Nanoscale Ferroelectrics and Multiferroics

Nanoscale Ferroelectrics and Multiferroics

Key Processing and Characterization Issues, and Nanoscale Effects

Edited by

MIGUEL ALGUERÓ
J. MARTY GREGG
LILIANA MITOSERIU

WILEY

This edition first published 2016
© 2016 John Wiley & Sons Ltd

Registered office
John Wiley & Sons Ltd, The Atrium, Southern Gate, Chichester, West Sussex, PO19 8SQ, United Kingdom

For details of our global editorial offices, for customer services and for information about how to apply for permission to reuse the copyright material in this book please see our website at www.wiley.com.

The right of the authors to be identified as the authors of this work has been asserted in accordance with the Copyright, Designs and Patents Act 1988.

All rights reserved. No part of this publication may be reproduced, stored in a retrieval system, or transmitted, in any form or by any means, electronic, mechanical, photocopying, recording or otherwise, except as permitted by the UK Copyright, Designs and Patents Act 1988, without the prior permission of the publisher.

Wiley also publishes its books in a variety of electronic formats. Some content that appears in print may not be available in electronic books.

Designations used by companies to distinguish their products are often claimed as trademarks. All brand names and product names used in this book are trade names, service marks, trademarks or registered trademarks of their respective owners. The publisher is not associated with any product or vendor mentioned in this book.

Limit of Liability/Disclaimer of Warranty: While the publisher and authors have used their best efforts in preparing this book, they make no representations or warranties with respect to the accuracy or completeness of the contents of this book and specifically disclaim any implied warranties of merchantability or fitness for a particular purpose. It is sold on the understanding that the publisher is not engaged in rendering professional services and neither the publisher nor the authors shall be liable for damages arising herefrom. If professional advice or other expert assistance is required, the services of a competent professional should be sought.

The advice and strategies contained herein may not be suitable for every situation. In view of ongoing research, equipment modifications, changes in governmental regulations, and the constant flow of information relating to the use of experimental reagents, equipment, and devices, the reader is urged to review and evaluate the information provided in the package insert or instructions for each chemical, piece of equipment, reagent, or device for, among other things, any changes in the instructions or indication of usage and for added warnings and precautions. The fact that an organization or Website is referred to in this work as a citation and/or a potential source of further information does not mean that the author or the publisher endorses the information the organization or Website may provide or recommendations it may make. Further, readers should be aware that Internet Websites listed in this work may have changed or disappeared between when this work was written and when it is read. No warranty may be created or extended by any promotional statements for this work. Neither the publisher nor the authors shall be liable for any damages arising herefrom.

Library of Congress Cataloging-in-Publication Data

Names: Algueró, Miguel, 1969- editor. | Gregg, J. Marty (John Marty), 1969- editor. | Mitoseriu, Liliana, editor.
Title: Nanoscale ferroelectrics and multiferroics : key processing and characterization issues, and nanoscale effects / [compiled by] Miguel Algueró, J. Marty Gregg, Liliana Mitoseriu.
Description: Hoboken : John Wiley & Sons, Inc., 2016. | Includes bibliographical references and index.
Identifiers: LCCN 2015042479 (print) | LCCN 2015046191 (ebook) | ISBN 9781118935750 (cloth) | ISBN 9781118935675 (ePub) | ISBN 9781118935705 (Adobe PDF)
Subjects: LCSH: Ferroelectric devices. | Nanoelectromechanical systems.
Classification: LCC TK7872.F44 N36 2016 (print) | LCC TK7872.F44 (ebook) | DDC 621.381–dc23
LC record available at http://lccn.loc.gov/2015042479

A catalogue record for this book is available from the British Library.

ISBN: 9781118935750

Set in 10/12pt Times by Aptara Inc., New Delhi, India.

1 2016

Contents

VOLUME I

List of Contributors xvii
Preface xxiii

Introduction: Why Nanoscale Ferroelectrics and Multiferroics? xxv
Miguel Algueró, J. Marty Gregg, and Liliana Mitoseriu

PART A 1

Nanostructuring: Bulk

1 Incorporation Mechanism and Functional Properties of Ce-Doped $BaTiO_3$ Ceramics Derived from Nanopowders Prepared by the Modified Pechini Method 13
Adelina-Carmen Ianculescu, Daniela C. Berger, Catalina A. Vasilescu, Marius Olariu, Bogdan S. Vasile, Lavinia P. Curecheriu, Andreja Gajović, and Roxana Truşcă

- 1.1 Why Cerium-Doped $BaTiO_3$? 13
- 1.2 Sample Preparation, Phase and Nano/Microstructural Characterization 18
  - 1.2.1 Powders 18
  - 1.2.2 Ceramics 22
- 1.3 Dielectric Properties 30
- 1.4 Raman Investigation 37
- 1.5 Conclusions 39
- Acknowledgments 40
- References 40

2 Synthesis and Ceramic Nanostructuring of Ferroic and Multiferroic Low-Tolerance-Factor Perovskite Oxides 44
Teresa Hungria, Covadonga Correas, and Alicia Castro

- 2.1 Introduction 44
- 2.2 Synthesis of Perovskites Oxides 47

2.2.1 General Information on the Preparation of Low-tolerance-Factor Perovskite Oxides 47
2.2.2 Mechanochemical Activation and Mechanosynthesis Applied to Low-Tolerance-Factor Perovskite Oxides 48
2.3 Processing of Ferroic and Multiferroic Materials: From the Ceramic Method to the Current Assisted Methods 54
2.3.1 SPS Applied to the Preparation of Ferroic Ceramic Materials 60
2.4 Combination of Mechanosynthesis and Spark Plasma Synthesis: The Right Track to the Nanoscale in Ferroic Materials 62
2.5 Conclusions 63
Acknowledgments 64
References 64

3 Core–Shell Heterostructures: From Particle Synthesis to Bulk Dielectric, Ferroelectric, and Multiferroic Composite Materials 72
Vincenzo Buscaglia and Maria Teresa Buscaglia

3.1 Introduction 72
3.2 Liquid-Phase Synthesis of Core–Shell Particles 74
3.2.1 Controlled Assembly of Preformed Nanoparticles 74
3.2.2 Precipitation 75
3.3 $BaTiO_3$@polymer Particles and Composites 77
3.4 Inorganic Core–Shell Particles with a Ferroelectric Core 78
3.5 Multiferroic Core–Shell Particles and Composites 83
3.6 Conclusions and Outlook 90
References 92

4 Modeling of Colloidal Suspensions for the Synthesis of the Ferroelectric Oxides with Complex Chemical Composition 100
Gregor Trefalt, Bosiljka Tadić, and Barbara Malič

4.1 Introduction 100
4.2 Solid-State Synthesis 102
4.3 Colloidal Interactions and Aggregation 103
4.3.1 DLVO Theory 103
4.3.2 Modeling of Aggregate Formation and Their Structure 105
4.4 Aggregation in the Three-Component System 106
4.5 Applying the Modeling Results to Enhance Properties of Ferroelectric Complex Oxides 109
4.5.1 PMN Synthesis by Controlled Aggregation of Reagent Particles 109
4.5.2 PMN–PT Synthesis by Controlled Aggregation of Reagent Particles 110
4.6 Conclusions and Outlook 112
Acknowledgments 114
References 114

Nanostructuring: Thin Films

5 Self-Assemblage and Patterning of Thin-Film Ferroic Nanostructures 118
Theodor Schneller

5.1 Introduction 118
5.2 Short Survey on Classical Top-Down Approaches 119
5.3 Non-invasive Procedures 121
5.3.1 Nanomask Techniques 124
5.3.2 Direct Self-Assembly of Ferroelectric Nanostructures 126
5.3.3 Nanoseeds Assisted Growth 131
5.4 Embedded Ferroelectric Nanograins 135
5.4.1 Embedded Lead Titanate-Based Nanograins 136
5.4.2 Further Embedding Concepts 137
5.5 Conclusions 139
References 140

6 Thin-Film Porous Ferroic Nanostructures: Strategies and Characterization 147
Alichandra Castro, Paula Ferreira, Stella Skiadopoulou, Liliana P. Ferreira, Margarida Godinho, Brian J. Rodriguez, and Paula M. Vilarinho

6.1 (Nano)Microelectronics Considerations 147
6.2 Ferroics and Nanoferroic Structures 148
6.3 Meso- and Nanoporosity in Advanced Functional Materials 151
6.4 Nanoporosity in Ferroelectric Thin Films 153
6.4.1 Lead Titanate ($PbTiO_3$) – Nanoporous and Nanopatterned Thin Films 153
6.4.2 Lead-Free Ferroelectric and Single-Phase Multiferroic – Bismuth Ferrite 156
6.5 Looking Ahead 158
Acknowledgments 160
References 160

7 Low-Temperature Photochemical Solution Deposition of Ferroelectric and Multiferroic Thin Films 163
Christopher De Dobbelaere, An Hardy, Marlies K. Van Bael, Iñigo Bretos, Ricardo Jiménez, and M. Lourdes Calzada

7.1 Introduction 163
7.2 Low-Temperature Processing of Ferroelectrics and Multiferroics 165
7.3 Low Environmental Impact Precursor Chemistry 165
7.4 Aquous Solution–Gel Precursors 166
7.4.1 Metal Ions in Water 166
7.4.2 Gel Formation and Decomposition 169
7.4.3 UV Activity 170

7.5 Photosensitive Sol–Gel Precursors 171
 7.5.1 Addition of UV-Absorbing Molecules to the Precursor Solution 172
 7.5.2 Synthesis of Highly Photosensitive Metal Complexes 175
7.6 Photochemical Solution Deposition (PCSD) 178
 7.6.1 Working Principle 178
 7.6.2 Low-Temperature Ferroelectric Oxide Films Prepared from Photosensitive Sol–Gel Precursors 182
 7.6.3 Low-Temperature Ferroelectric and Multiferroic Oxide Films Prepared from Aqueous Photochemical Solution Deposition (Aqueous PCSD) 185
7.7 Final Remarks 190
References 191

Nanostructuring: Fibers and Wires

8 Synthesis and Properties of Ferroelectric Nanotubes and Nanowires: A Review 200
Vincenzo Buscaglia and Maria Teresa Buscaglia

8.1 Introduction 200
8.2 Synthesis of Ferroelectric Nanowires and Nanotubes 202
 8.2.1 Direct Growth from the Liquid Phase 202
 8.2.2 Templated Growth 208
 8.2.3 Topochemical Solid-State Reactions 211
 8.2.4 Electrospinning 213
 8.2.5 Focused Ion Beam Lithography 213
8.3 Crystal Structure, Phase Transitions, and Ferroelectric Properties 213
8.4 Applications 219
 8.4.1 Nanogenerators for Energy Harvesting and Other Devices 219
 8.4.2 Dielectric Composites and Other Applications 221
8.5 Summary and Conclusions 222
References 223

9 Fabrication of One-Dimensional Ferroelectric Nano- and Microstructures by Different Spinning Techniques and Their Characterization 232
Tony Lusiola and Frank Clemens

9.1 Introduction 232
9.2 Fiber Synthesis 233
 9.2.1 One-Dimensional Nanostructures 233
 9.2.2 One-Dimensional Microstructures 236
9.3 Investigation of Nanostructure, Microstructure, and Phase Composition 240
 9.3.1 Microscopy 241
 9.3.2 Phase Composition 243
9.4 Investigation of Mechanical Properties 245
 9.4.1 Characterization of Nanowires/Fibers 246
 9.4.2 Characterization of Microfibers 248

9.5 Ferroelectric Characterization 249
  9.5.1 Characterization of Nanowires/fibers 250
  9.5.2 Characterization of Microfibers 252
9.6 Applications 255
  9.6.1 Potential Applications for Nanowires 255
  9.6.2 Applications for Microfibers 258
9.7 Summary and Outlook 259
References 260

PART B **269**

Characterization (of the Nanostructured Materials): Crystal Structure

10 Structural Characterization of Ferroelectric and Multiferroic Nanostructures by Advanced TEM Techniques **275**
Etienne Snoeck, Axel Lubk, and César Magén

10.1 Introduction: Advanced TEM Techniques for the Analysis of Ferroelectric and Multiferroic Materials 275
10.2 Transmission Electron Microscopy 276
  10.2.1 TEM and HRTEM Basics 276
  10.2.2 TEM and HRTEM Imaging of Ferroelectrics 280
10.3 HAADF–STEM Structure Determination 288
  10.3.1 Basics of HAADF–STEM Imaging 289
  10.3.2 Solid-State Properties 294
  10.3.3 Case Studies 297
10.4 Electron Energy Loss Spectroscopy 307
  10.4.1 EELS Basics 307
  10.4.2 EELS Applications in the Characterization of Multiferroics 310
10.5 Future and Challenges 317
References 319

11 Raman Spectroscopy of Nanostructured Ferroelectric Materials **325**
Marco Deluca and Andreja Gajovic

11.1 Introduction 325
11.2 Raman Spectroscopy Fundamentals 326
  11.2.1 The Raman Effect 326
  11.2.2 Selection Rules 328
  11.2.3 Phase Transitions 329
11.3 Raman Analysis of Relaxors 331
  11.3.1 Lead-Based Relaxors 333
  11.3.2 Lead-Free Relaxors 340
  11.3.3 Wrap-Up: Raman Analysis of Relaxors 351
11.4 Raman Analysis of Nanostructured Ferroelectrics 352
  11.4.1 Ferroelectric Nanostructured Ceramics 353

11.4.2 Ferroelectric 2D Nanostructures 357
11.4.3 Wrap-Up: Raman Analysis of Nanostructured Ferroelectrics 358
11.5 Tip-Enhanced Raman Spectroscopy (TERS) of Nanoscale Ferroelectrics 359
11.6 Summary 362
Acknowledgments 363
References 363

12 Neutron and Synchrotron X-Ray Scattering Studies of Bulk and Nanostructured Multiferroic and Ferroelectric Materials 375
Evagelia G. Moshopoulou, Pascale Foury-Leylekian, Katharine Page, Céline Doubrovsky, Martha Greenblatt, and Alan J. Hurd

12.1 Introduction 375
12.2 Synchrotron X-Ray and Neutron Facilities for Structural Characterization of Ferroelectrics and Multiferroics 378
12.3 Crystal Structure of $NdMn_2O_5$ in Powder and Single Crystalline Forms 381
12.3.1 Multiferroelectricity in RMn_2O_5 Compounds 381
12.3.2 Synthesis of $NdMn_2O_5$ 383
12.3.3 Synchrotron X-Ray Powder Diffraction Data Collection 384
12.3.4 Synchrotron X-Ray Powder Diffraction Data Analysis 384
12.3.5 Results 385
12.3.6 Discussion 385
12.4 Neutron Total Scattering Investigations of the $BaTiO_3$@SiO_2 Nanocomposites 390
12.4.1 Neutron and Synchrotron X-Ray Probes for Nanostructure Determination 390
12.4.2 Ferroelectricity in $BaTiO_3$ 392
12.4.3 Total Neutron Scattering Data Collection 393
12.4.4 Total Neutron Scattering Data Analysis 394
12.4.5 Results and Discussion 394
12.5 Concluding Comments 395
Acknowledgments 395
References 396

Characterization (of the Nanostructured Materials): Domains

13 Advanced Characterization of Multiferroic Materials by Scanning Probe Methods and Scanning Electron Microscopy 400
Michael R. Koblischka and Anjela Koblischka-Veneva

13.1 SPM-Related Methods in Advanced Materials Research 400
13.2 Magnetic Force Microscopy (MFM) and Related Methods 403
13.2.1 Magnetic Imaging 403
13.2.2 Magnetic Force Microscopy (MFM) 406
13.2.3 Further Developments (HF-MFM, MRFM) 406

13.3 Electrostatic Force Microscopy (EFM) and Piezo Force Microscopy (PFM) 408
  13.3.1 Electrostatic Force Microscopy (EFM) 408
  13.3.2 Piezo Force Microscopy (PFM) 408
13.4 Scanning Tunneling Microscopy (STM) and Related Methods 409
13.5 Imaging of Crystallographic Orientations (SEM/EBSD) 412
  13.5.1 EBSD Technique 412
  13.5.2 Examples of EBSD Measurements on Multiferroics 416
  13.5.3 EBSD Analysis of a Composite Multiferroic 418
  13.5.4 Future Directions 425
13.6 New Developments in the Field of EBSD 426
  13.6.1 3D EBSD 426
  13.6.2 Transmission EBSD (t-EBSD) 427
References 428

14 Electrostatic and Kelvin Probe Force Microscopy for Domain Imaging of Ferroic Systems 435
Brian J. Rodriguez

14.1 Introduction 435
14.2 Electrostatic Force Microscopy and Kelvin Probe Force Microscopy 438
  14.2.1 Electrostatic Force Microscopy 438
  14.2.2 Kelvin Probe Force Microscopy 438
14.3 EFM of Ferroelectric Materials 439
14.4 KPFM of Ferroelectric Materials 441
14.5 Recent Advances 445
  14.5.1 Open-Loop KPFM 445
  14.5.2 Time-Resolved KPFM 447
14.6 Summary and Outlook 447
Acknowledgments 448
References 448

VOLUME II

***List of Contributors* xvii**
***Preface* xxiii**

Introduction: Why Nanoscale Ferroelectrics and Multiferroics? xxv
Miguel Algueró, J. Marty Gregg, and Liliana Mitoseriu

PART C 461

Nanoscale Effects: Bulk Properties

15 Nanostructured Barium Titanate Ceramics: Intrinsic versus Extrinsic Size Effects 473
Liliana Mitoseriu and Lavinia P. Curecheriu

15.1 Introduction 473
15.2 Applications of $BaTiO_3$ Ceramics; Actual Demands for Passive Components 476
15.3 Size-Dependent Phenomena in Ferroelectrics 478
  15.3.1 General Properties 478
  15.3.2 Theoretical Description of Size-Dependent Phenomena in Ferroelectrics 479
15.4 Size-Dependent Properties in $BaTiO_3$ Ceramics: Intrinsic versus Extrinsic Size Effects 486
  15.4.1 Size-Dependent Properties of $BaTiO_3$ Ceramics with Grain Size in the Range of Micrometers 486
  15.4.2 Size-Dependent Properties of $BaTiO_3$ Nanoceramics 487
15.5 Conclusions 501
Acknowledgments 501
References 501

16 The Effects of Ceramic Nanostructuring in High-Sensitivity Piezoelectrics 512
Harvey Amorín, Ricardo Jiménez, Jesús Ricote, Alicia Castro, and Miguel Algueró

16.1 Technological Drive for Ceramic Nanostructuring of High-Sensitivity Piezoelectrics 512
16.2 State of the Art Ferroelectric Materials for Piezoelectric Technologies 514
  16.2.1 Commercial, PZT-Based Hard and Soft Piezoceramics 514
  16.2.2 Novel High-Sensitivity Piezoelectrics 516
16.3 Nanostructuring Effects in Perovskite Systems with PZT-like MPBs 519
  16.3.1 Basic Phenomenology 519
  16.3.2 Grain Size Dependence of Room Temperature Properties 525
  16.3.3 Grain Size Against Boundary Effects 533
16.4 Nanostructuring Effects in Perovskite Systems with Intrinsic Chemical Inhomogeneity 540
16.5 Summary and Future Perspectives 545
Acknowledgments 546
References 547

17 Correlation between Microstructure and Electrical Properties of Ferroelectric Relaxors 554
Jelena D. Bobic, Jan Macutkevic, Robertas Grigalaitis, Maksim Ivanov, Mirjana M. Vijatovic Petrovic, Juras Banys, and Biljana D. Stojanovic

17.1 Introduction 554
17.2 Perovskite Relaxors 558

17.2.1 Nanosized PMN Powders and Nanostructured Ceramics 558
17.2.2 Nanostructured $PbSc_{\frac{1}{2}}Nb_{\frac{1}{2}}O_3$ Ceramics 566
17.3 Aurivillius Lead-Free Ferroelectric Relaxors 570
17.3.1 Relaxor $BaBi_4Ti_4O_{15}$ Ceramic System 572
17.3.2 Grain Size-Dependent Electrical Properties of $BaBi_4Ti_4O_{15}$ Ceramics 574
17.3.3 $BaBi_4Ti_4O_{15}$ Doped Ceramics 577
17.4 Conclusions 580
References 581

18 Local Field Engineering Approach for Tuning Dielectric and Ferroelectric Properties in Nanostructured Ferroelectrics and Composites 588
Leontin Padurariu and Liliana Mitoseriu

18.1 Introduction 588
18.2 Finite Element Method 590
18.3 The Role of Local Electric Field Inhomogeneity on Tunability Properties 593
18.3.1 Nanostructured Ferroelectric Ceramics 596
18.3.2 Porous Ferroelectric Ceramics 599
18.3.3 Composites with Non-linear Matrix and Conductive Inclusions 600
18.4 Switching Properties in Inhomogeneous Ferroelectrics 603
18.4.1 Classical Preisach Model 603
18.4.2 Switching in Nanostructured Ferroelectric Ceramics 608
18.4.3 Switching in Porous Ferroelectrics 609
18.5 Conclusions 610
Acknowledgments 611
References 611

Nanoscale Effects: Thin-Film Properties

19 Ferroelectric Phase Transitions in Epitaxial Perovskite Films 617
Marina Tyunina

19.1 Introduction 617
19.2 Experimental Study of Phase Transition 618
19.2.1 Bulk Ferroelectrics and Relaxors 618
19.2.2 Epitaxial Thin Films 622
19.3 Dielectric Permittivity in Thin Films 623
19.3.1 Thin-Film Capacitor 623
19.3.2 Derivative of Inverse Permittivity 627
19.3.3 Thermo-optical Behaviour 634
19.4 Phase Transitions in Epitaxial Films 635
19.4.1 $Pb_{0.5}Sr_{0.5}TiO_3$ 635
19.4.2 $BaTiO_3$ 637

19.4.3 $KTaO_3$ 638
19.4.4 $PbSc_{0.5}Nb_{0.5}O_3$ 638
19.5 Concluding Remarks 639
Acknowledgments 640
References 640

20 Interfaces in Epitaxial Ferroelectric Layers/Multilayers and Their Effect on the Macroscopic Electrical Properties 645
Lucian Pintilie, Andra G. Boni, Cristina Chirila, Luminita M. Hrib, Alin Iuga, Lucian Trupina, Ioana Pintilie, Iuliana Pasuk, Raluca Negrea, Corneliu Ghica, Mihaela Botea, Nicoleta Apostol, and Cristian M. Teodorescu

20.1 Introduction 645
20.2 Electrode Interfaces in Ferroelectric Capacitors 647
20.2.1 Interface Effects on the Macroscopic Properties 647
20.2.2 Analysis of Free Surfaces and of Electrode Interfaces by AFM/PFM, XPS, and TEM 660
20.3 Interfaces in Complex Structures 667
20.3.1 PZT/ZnO 667
20.3.2 Ferroelectric/Multiferroic Multilayers 669
20.4 Conclusions 671
Acknowledgments 671
References 671

21 Electric Field Control of Magnetism Based on Elastically Coupled Ferromagnetic and Ferroelectric Domains 677
Kévin J.A. Franke, Tuomas H.E. Lahtinen, Arianna Casiraghi, Diego López González, Sampo J. Hämäläinen, and Sebastiaan van Dijken

21.1 Introduction 677
21.2 Domain Pattern Transfer 678
21.3 Elastic Coupling Between Magnetic and Ferroelectric Domain Walls 681
21.4 Domain Size Scaling of Pattern Transfer 686
21.5 Electric Field Control of Ferromagnetic Domains 688
21.6 Electric Field Driven Magnetic Domain Wall Motion 690
21.7 Summary and Outlook 693
Acknowledgments 695
References 695

Nanoscale Effects: Novel Phenomena and Applications

22 Ferroelectric Vortices and Related Configurations 700
Sergei Prosandeev, Ivan I. Naumov, Huaxiang Fu, Laurent Bellaiche, Michael P.D. Campbell, Raymond G.P. McQuaid, Li-Wu Chang, Alina Schilling, Leo J. McGilly, Amit Kumar, and J. Marty Gregg

22.1 Insights from Simulations and Theory 700
22.1.1 Introduction 700
22.1.2 Methods 701

22.1.3 Discovery of Unusual Patterns in Ferroelectric Nanostructures and Their Associated Order Parameters 704
22.1.4 Controlling and Switching of Single, Double, and Multiple Vortex States 708
22.1.5 Other Phenomena Related to Vortices and Complex Dipolar Patterns 712
22.1.6 Summary from the Simulations and Theory Perspective 714
22.2 Insights from Experiments 714
22.2.1 Introduction 714
22.2.2 Vortices and Topological Winding Numbers 715
22.2.3 Continuous versus Sudden Dipole rotation 718
22.2.4 Unique Core Singularity 719
22.2.5 Summary and Conclusions from an Experimental Perspective 723
Acknowledgments 723
References 723

23 Reentrant Phenomena in Relaxors 729
Alexei A. Bokov and Zuo-Guang Ye

23.1 Introduction 729
23.2 Reentrant Phases in Condensed Matter 730
23.3 Relaxor Ferroelectrics 736
23.4 Reentrant Relaxor Behavior in Ferroelectrics 741
23.4.1 Properties of Materials with Paraelectric–Ferroelectric–Relaxor Sequence of States 742
23.4.2 Models and Theories 752
23.5 Transverse Glassy Freezing and Canonical Relaxors 753
23.6 Reentrant Dipolar Glass State in Quantum Paraelectrics Doped with Dipolar Impurities 757
23.7 Summary and Concluding Remarks 758
Acknowledgments 759
References 759

24 Functional Twin Boundaries: Multiferroicity in Confined Spaces 765
Ekhard. K.H. Salje and Xiangdong Ding

24.1 Introduction 765
24.2 Ferroelectric Twin Boundaries 766
24.2.1 Polar Twin Walls in $CaTiO_3$ 768
24.2.2 Polar Twin Walls in $SrTiO_3$ 771
24.3 Conducting Twin Boundaries 773
24.4 Thermal Conductivity 775
24.5 Landau Theory of Coupled Order Parameters in Domain Walls 776
24.6 Chiral Twin Walls 778
24.7 High Wall Densities 780
24.8 Summary 783
Acknowledgment 784
References 784

25 Novel Approaches for Genuine Single-Phase Room Temperature Magnetoelectric Multiferroics 789
Lynette Keeney, Michael Schmidt, Andreas Amann, Tuhin Maity, Nitin Deepak, Ahmad Faraz, Nikolay Petkov, Saibal Roy, Martyn E. Pemble, and Roger W. Whatmore

25.1 Introduction to Single-Phase Multiferroic Materials 789
25.2 Aurivillius Phase Materials – Candidate Single-Phase Multiferroics? 796
25.3 Magnetoelectric Coupling in Multiferroic $Bi_6Ti_xFe_yMn_zO_{18}$ Systems at Room Temperature 801
25.3.1 Fabrication and Structural Analysis of $Bi_{m+1}Ti_3(Mn/Fe)_{m\text{-}3}O_{3m+1}$ Thin Films 801
25.3.2 Ferroelectric Investigations of $Bi_6Ti_xFe_yMn_zO_{18}$ thin films 804
25.3.3 Assessment of Ferromagnetism in $Bi_6Ti_xFe_yMn_zO_{18}$ Thin Films 804
25.3.4 Room Temperature Magnetoelectric Coupling in $Bi_6Ti_{2.8}Fe_{1.52}Mn_{0.68}O_{18}$ Thin Films 810
25.4 Confidence Level Assessment of Genuine Single-Phase Multiferroicity 810
25.4.1 Statistics of a Single Measurement 812
25.4.2 The Inclusion Size Distribution Function 813
25.4.3 Series of Measurements at Varying Resolutions 813
25.4.4 Upper Limit on the Contribution to Remanent Magnetization 814
25.5 Potential Devices/Applications Based on Single-Phase Magnetoelectric Multiferroics 816
25.6 Summary and Conclusions 820
References 821

26 Semiconducting and Photovoltaic Ferroelectrics 830
Andrew R. Akbashev, Vladimir M. Fridkin, and Jonathan E. Spanier

26.1 Introduction 830
26.2 Basic Principles of Photovoltaic Effect in Ferroelectrics 831
26.3 Experimental Evidence of the Bulk Photovoltaic Effect in Ferroelectrics 835
26.3.1 $BiFeO_3$ 835
26.3.2 Niobates 838
26.4 The Role of the Schottky Barrier and Depletion Layer 840
26.5 Photovoltaic Effect Mediated by Ferroelectric Domain Walls 840
26.6 Ferroelectric Solid Solutions: Chemical Tuning of Band-Gap 843
26.7 Conclusions 847
Acknowledgment 847
References 847

***Index* 851**

List of Contributors

Andrew R. Akbashev Drexel University, USA

Miguel Algueró Instituto de Ciencia de Materiales de Madrid (ICMM), Consejo Superior de Investigaciones Científicas (CSIC), Spain

Andreas Amann Tyndall National Institute, University College Cork, Ireland; and School of Mathematical Sciences, University College Cork, Ireland

Harvey Amorín Instituto de Ciencia de Materiales de Madrid (ICMM), Consejo Superior de Investigaciones Científicas (CSIC), Spain

Nicoleta Apostol National Institute of Materials Physics, Romania

Juras Banys Faculty of Physics, Vilnius University, Lithuania

Laurent Bellaiche Physics Department, University of Arkansas, USA

Daniela C. Berger Departement of Inorganic Chemistry, Physical-Chemistry and Electrochemistry, “Politehnica” University of Bucharest, Romania

J.D. Bobic Institute for Multidisciplinary Research, University of Belgrade, Serbia

Alexei A. Bokov Department of Chemistry and 4D LABS, Simon Fraser University, Canada

Andra G. Boni National Institute of Materials Physics, Romania

Mihaela Botea National Institute of Materials Physics, Romania

Iñigo Bretos Instituto de Ciencia de Materiales de Madrid (ICMM), Consejo Superior de Investigaciones Científicas (CSIC), Spain

Maria Teresa Buscaglia Institute of Energetics and Interphases, National Research Council, Italy

Vincenzo Buscaglia Institute of Energetics and Interphases, National Research Council, Italy

Michael P.D. Campbell School of Maths and Physics, Queen’s University Belfast, Northern Ireland, United Kingdom

Arianna Casiraghi NanoSpin, Department of Applied Physics, Aalto University School of Science, Finland

Alichandra Castro CICECO – Aveiro Institute of Materials, Department of Materials and Ceramic Engineering, University of Aveiro, Portugal

Alicia Castro Instituto de Ciencia de Materiales de Madrid (ICMM), Consejo Superior de Investigaciones Científicas (CSIC), Madrid, Spain

Li-Wu Chang School of Maths and Physics, Queen's University Belfast, Northern Ireland, United Kingdom

Cristina Chirila National Institute of Materials Physics, Romania

Frank Clemens Laboratory for High Performance Ceramics, Empa, Swiss Federal Laboratories for Materials Science and Technology, Switzerland

Covadonga Correas Instituto de Ciencia de Materiales de Madrid (ICMM), Consejo Superior de Investigaciones Científicas (CSIC), Spain; and College of Engineering, Swansea University, United Kingdom

Lavinia P. Curecheriu Department of Physics, "Alexandru Ioan Cuza" University, Romania

Nitin Deepak Tyndall National Institute, University College Cork, Ireland

Marco Deluca Materials Center Leoben Forschung GmbH, and Institut für Struktur- und Funktionskeramik, Montanuniversitaet Leoben, Austria

Xiangdong Ding State Key Laboratory for Mechanical Behavior of Materials, Xi'an Jiaotong University, China

Christopher De Dobbelaere Inorganic and Physical Chemistry Group, Institute for Materials Research, Universiteit Hasselt and imec vzw, Division imomec, Belgium

C. Doubrovsky Laboratoire de Physique des Solides, Université de Paris Sud, Campus d'Orsay, France

Ahmad Faraz Tyndall National Institute, University College Cork, Ireland

Liliana P. Ferreira Biosystems and Integrative Sciences Institute, Department of Physics, University of Coimbra, Portugal

Paula Ferreira CICECO – Aveiro Institute of Materials, Department of Materials and Ceramic Engineering, University of Aveiro, Portugal

Pascale Foury-Leylekian Laboratoire de Physique des Solides, Université de Paris Sud, Campus d'Orsay, France

Kévin J. A. Franke NanoSpin, Department of Applied Physics, Aalto University School of Science, Finland

Vladimir M. Fridkin Drexel University, USA; and Russian Academy of Sciences, Moscow, Russian Federation

Huaxiang Fu Physics Department, University of Arkansas, USA

Andreja Gajović Molecular Physics Laboratory, Institute Rudjer Boskovic, Croatia

Corneliu Ghica National Institute of Materials Physics, Romania

Margarida Godinho Biosystems and Integrative Sciences Institute, Department of Physics, Faculty of Sciences, University of Lisbon, Portugal

Martha Greenblatt Department of Chemistry and Chemical Biology, Rutgers, The State University of New Jersey, USA

J. Marty Gregg School of Maths and Physics, Queen's University Belfast, Northern Ireland, United Kingdom

R. Grigalaitis Faculty of Physics, Vilnius University, Lithuania

Sampo J. Hämäläinen NanoSpin, Department of Applied Physics, Aalto University School of Science, Finland

An Hardy Inorganic and Physical Chemistry Group, Institute for Materials Research, Universiteit Hasselt and imec vzw, Division imomec, Belgium

Luminita M. Hrib National Institute of Materials Physics, Romania

Teresa Hungria Instituto de Ciencia de Materiales de Madrid (ICMM), Consejo Superior de Investigaciones Científicas (CSIC), Spain; and Centre de Microcaractérisation Raimond Castaing, UMS 3623, France

Alan J. Hurd Los Alamos National Laboratory, USA

Adelina-Carmen Ianculescu Department of Oxide Materials Science and Engineering, "Politehnica" University of Bucharest, Romania

Alin Iuga National Institute of Materials Physics, Romania

Maksim Ivanov Faculty of Physics, Vilnius University, Lithuania

Ricardo Jiménez Instituto de Ciencia de Materiales de Madrid (ICMM), Consejo Superior de Investigaciones Científicas (CSIC), Spain

Lynette Keeney Tyndall National Institute, University College Cork, Ireland

Michael R. Koblischka Institute of Experimental Physics, Saarland University, Germany

Anjela Koblischka-Veneva Institute of Experimental Physics, Saarland University, Germany

Amit Kumar School of Maths and Physics, Queen's University Belfast, Northern Ireland, United Kingdom

Tuomas H.E. Lahtinen NanoSpin, Department of Applied Physics, Aalto University School of Science, Finland

Diego López González NanoSpin, Department of Applied Physics, Aalto University School of Science, Finland

M. Lourdes Calzada Instituto de Ciencia de Materiales de Madrid (ICMM), Consejo Superior de Investigaciones Científicas (CSIC), Spain

Axel Lubk Triebenberg Laboratory, Technische Universität Dresden, Germany

Tony Lusiola Laboratory for High Performance Ceramics, Empa, Swiss Federal Laboratories for Materials Science and Technology, Switzerland

Leo J. McGilly Ceramics Laboratory, École Polytechnique Fédérale de Lausanne (EPFL), Switzerland

Raymond G.P. McQuaid School of Maths and Physics, Queen's University Belfast, Northern Ireland, United Kingdom

J. Macutkevic Faculty of Physics, Vilnius University, Lithuania

César Magén Instituto de Nanociencia de Aragón-ARAID, Universidad de Zaragoza, Spain

Tuhin Maity Tyndall National Institute, University College Cork, Ireland

Barbara Malič Electronic Ceramics Department, Jožef Stefan Institute, Slovenia

Liliana Mitoseriu Faculty of Physics, University "Alexandru Ioan Cuza", Romania

Evagelia G. Moshopoulou Institute of Nanoscience and Nanotechnology, National Center for Scientific Research "Demokritos", Greece; and Laboratoire de Physique des Solides, Université de Paris Sud, Campus d'Orsay, France

Ivan I. Naumov Carnegie Institution of Washington, USA

Raluca Negrea National Institute of Materials Physics, Romania

Marius Olariu Department of Electrical Measurements & Materials, Technical University Gh. Asachi Iasi, Romania

Leontin Padurariu University "Alexandru Ioan Cuza", Romania

Katharine Page Spallation Neutron Source, Oak Ridge National Laboratory, USA

Iuliana Pasuk National Institute of Materials Physics, Romania

Martyn E. Pemble Tyndall National Institute, University College Cork, Ireland; and Department of Chemistry, University College Cork, Ireland

Nikolay Petkov Tyndall National Institute, University College Cork, Ireland

M.M. Vijatovic Petrovic Institute for Multidisciplinary Research, University of Belgrade, Serbia

Ioana Pintilie National Institute of Materials Physics, Romania

Lucian Pintilie National Institute of Materials Physics, Romania

Sergei Prosandeev Physics Department, University of Arkansas, USA and Physics Department and Research Institute of Physics, Southern Federal University, Russia

Jesús Ricote Instituto de Ciencia de Materiales de Madrid (ICMM), Consejo Superior de Investigaciones Científicas (CSIC), Spain

Brian J. Rodriguez Conway Institute of Biomolecular and Biomedical Research, University College Dublin, Ireland

Saibal Roy Tyndall National Institute, University College Cork, Ireland

Ekhard. K.H. Salje Department of Earth Sciences, University of Cambridge, United Kingdom

Alina Schilling School of Maths and Physics, Queen's University Belfast, Northern Ireland, United Kingdom

Michael Schmidt Tyndall National Institute, University College Cork, Ireland

Theodor Schneller Institut für Werkstoffe der Elektrotechnik II, RWTH Aachen University, Germany

Stella Skiadopoulou CICECO – Aveiro Institute of Materials, Department of Materials and Ceramic Engineering, University of Aveiro, Portugal

Etienne Snoeck Centre d'Elaboration de Matériaux et d'Etudes Structurales, CNRS, France

Jonathan E. Spanier Drexel University, USA

Biljana D. Stojanovic Institute for Multidisciplinary Research, University of Belgrade, Serbia

Bosiljka Tadić Department of Theoretical Physics, Jožef Stefan Institute, Slovenia

Cristian M. Teodorescu National Institute of Materials Physics, Romania

Gregor Trefalt Electronic Ceramics Department, Jožef Stefan Institute and Center of Excellence NAMASTE, Slovenia; and University of Geneva, Switzerland

Lucian Trupina National Institute of Materials Physics, Romania

Roxana Truşcă S.C. METAV – Research and Development, Romania

Marina Tyunina Microelectronics and Materials Physics Laboratories, University of Oulu, Finland

Marlies K. Van Bael Inorganic and Physical Chemistry Group, Institute for Materials Research, Universiteit Hasselt and imec vzw, Division imomec, Belgium

Sebastiaan van Dijken NanoSpin, Department of Applied Physics, Aalto University School of Science, Finland

Bogdan S. Vasile Department of Oxide Materials Science and Engineering, "Politehnica" University of Bucharest, Romania

Catalina A. Vasilescu Department of Oxide Materials Science and Engineering, "Politehnica" University of Bucharest, Romania

Paula M. Vilarinho CICECO – Aveiro Institute of Materials, Department of Materials and Ceramic Engineering, University of Aveiro, Portugal

Roger W. Whatmore Tyndall National Institute, University College Cork, Ireland; Department of Chemistry, University College Cork, Ireland and Department of Materials, Royal School of Mines, Imperial College London, United Kingdom

Zuo-Guang Ye Department of Chemistry and 4D LABS, Simon Fraser University, Canada

Preface

Multiferroics have been at the cutting edge of research and development in materials for ICTs for over a decade. During this period steady improvements in fundamental knowledge have been made. At the same time, nanoscale phenomena have assumed an increasing importance. Progress has benefited from the strong synergies with activities in nanoscale ferroelectrics, which are at a more mature stage. Multifunctionality and nanoscaling are widely acknowledged at present as the keys to the miniaturization of solid-state electronics, and specifically nanoferronics, which is emerging as a new area with large technological potential. The topic has now reached a maturity level that allows, and actually requires, books that provide a comprehensive revision of the topic, and an in-depth analysis of future trends. These are the objectives of *Nanoscale Ferroelectrics and Multiferroics: Key Processing and Characterization Issues, and Nanoscale Effects.*

It is intended to provide the increasing number of scientists and engineers, who are approaching the topic from a range of backgrounds, with a reference/guide text that should help them to roadmap their R&D activities. The volume reviews the key issues in processing and characterization of nanoscale ferroelectrics and multiferroics, and provides a comprehensive description of their properties. An emphasis is put on differentiating size effects of extrinsic ones like boundary or interface effects. Nanoscale novel, recently described, phenomena that are bound to be behind major advancement in the field during the coming years are also addressed.

The book is devised to stress, and take full advantage of, the synergies between nanoscale ferroelectrics and multiferroics. It covers materials nanostructured at all levels, from ceramic technologies like ferroelectric nanopowders, bulk nanostructured ceramics and thick films, and magnetoelectric nanocomposites, to thin films, either polycrystalline layer heterostructures or epitaxial systems, and to nanoscale free-standing objects with specific geometries, such as nanowires and tubes at different levels of development, but all technologically relevant. Nanostructuring is a requirement of the current tendency to miniaturization of ceramic technologies for microelectronics that imposes stringent conditions on processing, and has a deep impact on functional properties. Also, nanostructuring ultimately results in the ever-decreasing processing temperatures of thin films, a key issue to the integration of these multifunctional oxides with silicon devices and flexoelectronics. Last but not least, a range of novel physical phenomena has been described in nanoscale ferroelectrics and multiferroics that have the potential to enable a range of disruptive technologies, like magnetoelectric memory. Overall, the book reviews the current state of the art of these materials, stressing a range of specific topics at the cutting edge of research.

This project springs from the high-level European scientific knowledge platform built within the COST Action *Single and Multiphase Ferroics and Multiferroics with Restricted*

Geometries (SIMUFER, ref. MP0904), active between March 2010 and May 2014. COST (European Cooperation in Science and Technology) is a pan-European networking instrument that allows researchers from COST member countries and cooperating states to jointly develop their ideas and initiatives in a field or topic of common interest. SIMUFER established a multidisciplinary scientific network of groups from 24 European countries and 7 non-COST countries, experienced in synthesis, advanced characterization, and modeling of all nanoscale ferroics, single-phase multiferroics, and ferroic-based combinations of dissimilar materials. This book project arises primarily from their expertise, though it has been open to world renowned experts when necessary. Chapter contributors have been carefully selected and have all made major contributions to knowledge of the respective topics; overall, they are among the most respected scientists in the field.

Introduction

Why Nanoscale Ferroelectrics and Multiferroics?

Miguel Algueró[1], J. Marty Gregg[2], and Liliana Mitoseriu[3]

[1] *Instituto de Ciencia de Materiales de Madrid (ICMM), Consejo Superior de Investigaciones Científicas (CSIC), Spain*
[2] *School of Maths and Physics, Queen's University Belfast, Northern Ireland, United Kingdom*
[3] *Faculty of Physics, University "Alexandru Ioan Cuza", Romania*

I.1 Ferroics and Multiferroics

Single-phase ferroics are compounds that present one of the three (currently expanded to four) ferroic properties: ferroelectricity, ferromagnetism, or ferroelasticity, to which ferrotoroidicity has recently been added. The common feature of the four types of ferroics is the appearance of the ferroic order; either it is a spontaneous electrical polarization, magnetization, strain, or toroidal moment, in a phase transition from a high-temperature prototype phase to the low-temperature ferroic phase, related by a group/subgroup relationship. This transition is always accompanied by a decrease in symmetry and the splitting of the ferroic phase into domains (regions with a different orientation of the order parameter). A second feature, the direct consequence of the switchable nature of the order parameter and of the domain dynamics, is the characteristic ferroic hysteresis loop; that is, a distinctive hysteretic dependence of the order parameter on its conjugated field (electric or magnetic field, mechanical stress or toroidal source vector, respectively), with two remnant states of opposite sign [1]. The four phenomena are schematically shown in Figure I.1. Ferroics are highly topical, advanced functional materials that have not only enabled a range of mature and ubiquitous related technologies (like magnetic

Nanoscale Ferroelectrics and Multiferroics: Key Processing and Characterization Issues, and Nanoscale Effects, First Edition. Edited by Miguel Algueró, J. Marty Gregg, and Liliana Mitoseriu.

© 2016 John Wiley & Sons, Ltd. Published 2016 by John Wiley & Sons, Ltd.

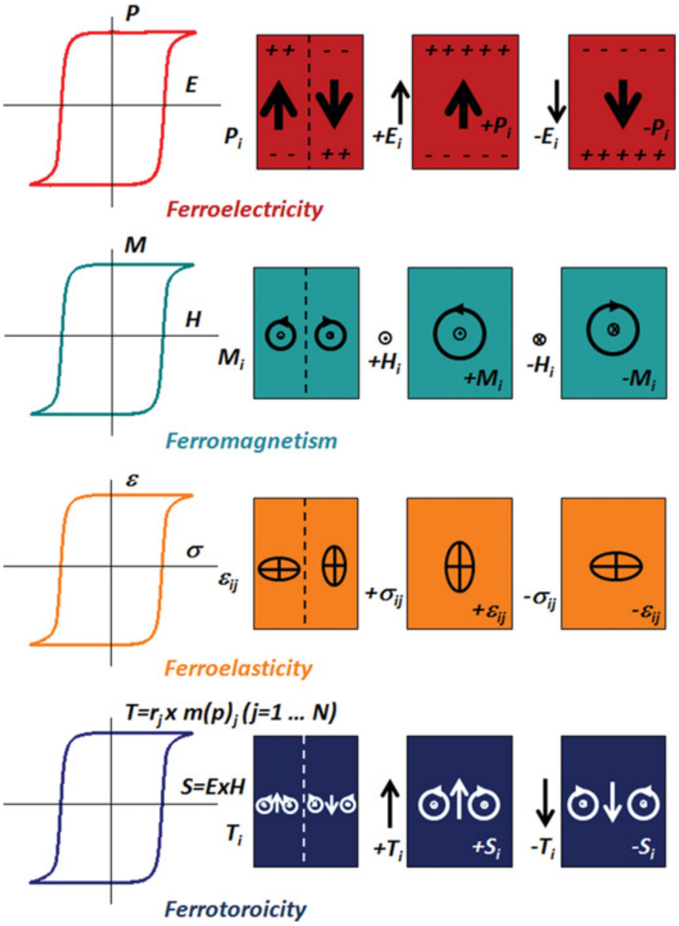
P
E
P_i
++ | - -
- - | ++
+E_i
+++++
+P_i
- - - - -
-E_i
- - - - -
-P_i
+++++
Ferroelectricity
M
H
M_i
+H_i
+M_i
-H_i
-M_i
Ferromagnetism
ε
σ
ε_ij
+σ_ij
+ε_ij
-σ_ij
-ε_ij
Ferroelasticity
T=r_j x m(p)_j (j=1 ... N)
S=ExH
T_i
+T_i
+S_i
-T_i
-S_i
Ferrotoroicity

Figure I.1 Schematics of domains and hysteretic switching for the four ferroic phenomena. Adapted by permission of IOP Publishing from [1]. © IOP Publishing. All rights reserved.

or ferroelectric information recording, ceramic ultrasound transducers, or shape memory alloys, to name only a few examples) but are also under extensive research for a number of novel, potentially disruptive, applications [2].

There are also compounds that simultaneously present two (or more) ferroic phenomena, known as multiferroics, among which those showing coexistence of ferroelectricity and ferromagnetism (initially termed ferroelectromagnets) are receiving increasing attention [3,4]. This is not only because of their inherent multifunctionality but also for the fact that they are liable to show magnetoelectric coupling, and have thus the potential to enable the electrical control of magnetism (and the magnetic control of polarization) [5].

This book specifically deals with ferroelectrics and ferroelectromagnets (either robust ferromagnetic materials or canted antiferromagnets showing weak ferromagnetism), though the general term multiferroics will be used following the current tendency to name ferroelectric–ferromagnetic materials, and in general any type of magnetic ordering compounds, in this way.

The choice of addressing them together only acknowledges the deep-rooted relationship between the two sets of materials; multiferroism requires ferroelectricity and thus multiferroics have to be electrically insulating to be functional (an issue not always acknowledged). This feature is not easily found in magnetic materials, most of them being metallic or narrow-band gap semiconductors. Indeed, chemical bonding requirements suggest the two ferroic phenomena to be incompatible [6]; transition metal or rare earth atomic species with partially filled outer *d* or *f* electronic shells (and unpaired electrons) are necessary for magnetism, while model ferroelectric perovskite oxides are characterized by covalently bonded transition metals (to oxygen) with empty *d* orbitals [7]. Nevertheless, an ever-increasing number of multiferroic single-phase materials have been reported over the last decade, exploring alternative mechanisms of ferroelectricity.

I.2 Ferroelectric Materials and Related Technologies

Ferroelectrics are thus materials that present a spontaneous electrical polarization, whose direction can be reversed with an electric field (by nucleation and growth of inversion domains, resulting in the distinctive ferroelectric hysteresis). The ferroic phase appears at a ferroelectric transition, driven by electrical polarization [8], which can be either of a displacive type, the most common one, associated with a crystal structure instability induced by condensation of a transverse optical phonon (the soft mode) [9], or of an order–disorder type. Its macroscopic phenomenological description according to Landau's theory of phase transitions can be found in Chapter 19.

All ferroelectrics are also pyroelectric and piezoelectric, as well as electrooptic, which turns them into a prototype of multifunctionality (even before magnetic order is added). Moreover, they are the only materials that can present these properties, intrinsically linked to the crystal structure, in polycrystalline form (thanks to the ability to reorient the polarization under an electric field).

Though ferroelectricity was first described for hydrogen-bonded compounds (Rochelle salt being the first one in 1921), and there are also examples among tellurides, fluorides, and iodides [10], a number of electroactive polymers like poly(vinylidene fluoride) [11], and recent reports of ferroelectric metal organic frameworks [12], clearly oxides stand out as the ones that have enabled a range of successful ferroelectric technologies.

I.2.1 Ferroelectric Bulk Technologies

Perhaps the best-known ferroelectric, and also the first oxide shown to be so in 1944, is $BaTiO_3$ with a perovskite structure. This model compound presents the ferroelectric transition at ~393 K and a succession of low-temperature polymorphic phase transitions between ferroelectric phases with decreasing symmetry, from tetragonal to orthorhombic and to rhombohedral, for which the polar axis (and thus the direction of the spontaneous polarization defined by the displacement of the Ti^{4+} cation from the centre of the oxygen octahedra) changes. Polymorphism is a quite common phenomenon in ferroelectric perovskite oxides and plays a very important role in their functionality. $BaTiO_3$ is also the base composition of multilayer ceramic capacitors (after the chemical tailoring of the ferroelectric transition down to room temperature), one of the two large-scale, mature bulk ceramic ferroelectric technologies. This material and its modifications are extensively addressed in this book (see Chapters 1, 11, 12, 15, and 18), for the miniaturization of these capacitors is a case study of the current trends in microelectronics that require the nanostructuring of the ceramic layers. In the last few years, nanostructured $BaTiO_3$ and its solid solutions have become the main candidates for active materials used in capacitive building blocks for energy storage applications.

The second successful technology is piezoelectric ceramics for electromechanical transduction. The state of the art material for these applications, which range from sensors and actuators (like accelerometers or positioning systems for scanning probe microscopy, respectively) and their combination in smart systems (to implement active vibration damping), to ultrasound generation and sensing (for medical imaging or non-destructive testing), and to submarine acoustics, is $Pb(Zr,Ti)O_3$, which also has a perovskite structure. This is an oxide solid solution, for which the best properties are found at a morphotropic phase boundary (MPB) between rhombohedral and tetragonal ferroelectric polymorphs, for which a monoclinic phase has been recently described [13]. This material can be regarded as a modification of $PbTiO_3$, a second model ferroelectric oxide that also shows a succession of polymorphic phase transitions, yet induced by hydrostatic pressure instead of temperature [14], which has been placed at one of these ferroelectric instabilities (the MPB) by building up chemical pressure (achieved by substitution of Zr^{4+} for Ti^{4+}). As a matter of fact, the very good electromechanical response of this material is a combination of two effects, a crystal contribution, associated with the existence of a transverse lattice instability at the monoclinic tetragonal boundary [15], and an extrinsic contribution, associated with the fact that ferroelectric perovskite oxides are also ferroelastic (and therefore multiferroic, but not ferroelectromagnets). The spontaneous strain develops at the ferroelectric transition along with the polarization (the two parameters are intrinsically coupled), and as a consequence ferrroelectric–ferroelastic domains appear (in addition to polarization inversion domains).The non-180° (90° in the tetragonal case) domain walls are mobile under stress and electric field (unlike 180° walls that only move under an electric field), giving way to a wall contribution to the piezoelectric effect [16]. Moreover, the domain dynamics is enhanced at the morphotropic phase boundary. In addition, chemical (or doping) engineering of $Pb(Zr,Ti)O_3$ has been developed that enables a range of soft and hard piezoelectric ceramics with tailored properties for specific applications. Piezoelectric ceramics are also being considered for novel applications, such as energy harvesting [17] and magnetoelectric composites (see later). Further explanations of the mechanisms, along with a review of alternative materials, can be found in Chapter 16. This technology is not oblivious to the general miniaturization trend and nanostructuring can also be anticipated.

Other examples of ferroelectric ceramic bulk technologies are infrared (IR) cameras for night vision (and, in general, IR detectors for a range of applications exploiting the pyroelectric effect) and electrooptic devices. Modifications of $PbTiO_3$ like $(Pb,La)TiO_3$ and transparent $(Pb,La)(Zr,Ti)O_3$ are usually the material choices, respectively. An excellent review of ferroelectric ceramics and related technologies can be found in [18].

Also successful ferroelectric single-crystal technologies are presently available. The best examples are surface acoustic wave (SAW) devices for radio frequency and microwave signal conditioning, based on ferroelectric $LiNbO_3$ substrates. At the very end of the last century, ultrahigh piezoelectricity and strain under an electric field was reported for single crystals of the relaxor–ferroelectric solid solutions $Pb(Zn_{1/3}Nb_{2/3})O_3$–$PbTiO_3$ and $Pb(Mg_{1/3}Nb_{2/3})O_3$–$PbTiO_3$ [19]. Their very large electromechanical response is obtained for plates cut along off-polar directions by a mechanism of polarization rotation that takes full advantage of the already mentioned lattice transverse instability [20, 21]. This crystal technology is now reaching reliability standards for commercialization and is especially suitable for ultrasonic and acoustic transducers [22].

I.2.2 Ferroelectric Thin-Film Technologies

Ferroelectric thin-film technologies can be seen as a first step in miniaturization, and comprise a range of microelectronic devices where the oxide layer is usually the integrated, active component with CMOS control electronics. They can also be reckoned as a first example of a nanostructured ferroelectric, for films on silicon-based substrates are usually polycrystalline or columnar with a grain size (or column diameter) below 100 nm, even though thickness is in the micrometer or submicrometer range.

Three main technologies have been proposed, although only one has succeeded in full commercialization: the ferroelectric random access memory (FeRAM) [23, 24]. This is a non-volatile memory, where the two binary states are defined as the two opposite directions of (reversible) spontaneous polarization. It is a low-power, fast-access device, whose capacity has steadily increased from 4 kbytes in 1992, when mass production started, to 64 Mbytes [25]. Commercial products are based on either columnar $Pb(Zr,Ti)O_3$ films with conducting oxide electrodes or $SrBi_2Ta_2O_7$ with Pt electrodes [26], and are used in applications such as IC cards and radio frequency tags [27]. $SrBi_2Ta_2O_7$ is an example of a wide family of oxides with a layered perovskite, Aurivillius-type crystal structure, which are also used as high-temperature piezoelectrics (see Chapter 17); multiferrroic examples have also been reported (see Chapter 25).

The second ferroelectric thin-film technology is the piezoelectric microelectromechanical system (pMEMS). These are bulk or surface micromachined structures, commonly in silicon, on to which a piezoelectric oxide layer has been integrated to implement sensing and/or actuation capabilities, along with the control electronics. Most commonly used microstructures are cantilevers and membranes. One device based on such a microcantilever is the piezoelectric force sensor for scanning probe microscopy, while cantilever arrays have been considered for applications like adaptative optics, micromirror image projectors, or radio frequency switches. Ultrasonic micromotors based on piezoelectrically actuated membranes have been fabricated, and micromembrane arrays are the basis of piezoelectric micromachined ultrasonic transducers (pMUTs) [25]. They are also being considered for ink-jet printing heads (an example out of a range of applications in microfluidics) [28].

Microwave microelectronics making use of the material high-dielectric permittivity and its tunability under the electric field can be considered the third ferroelectric thin-film technology. $(Ba,Sr)TiO_3$ films are being considered for varactors, even if non-negligible dielectric losses have hindered its development. A successful product, though based on non-ferroelectric piezoelectric AlN, is the bulk acoustic wave (BAW) thin-film resonator, which has been key to the miniaturization of mobile communication devices like cellular telephones [25, 28].

Integrated infrared sensors [29] and thin-film capacitors [30] are other examples of ferroelectric thin-film technologies. Electrothermal energy interconversion by means of the electrocaloric effect is also under extensive research [31]. A thorough description of applications and related material issues can be found in recent reviews [10, 25, 28].

I.3 Multiferroic Materials for Enabling Magnetoelectric Technologies

Multiferroics are liable to present different magnetoelectric coupling phenomena. They all show linear dependences of magnetic susceptibility and dielectric permittivity on the electric and magnetic fields (originating from linear–quadratic terms in the free energy: $\propto ExH^2$ and HxE^2, respectively), and can also show a large linear magnetoelectric effect as compared with non-multiferroic magnetoelectrics like Cr_2O_3 (this time from a bilinear $\propto HxE$ term). This latter effect is the development of an electrical polarization proportional to an applied magnetic field (direct effect) and of magnetization in response to an electric field (converse effect). Magnetoelectric materials are being investigated as an alternative to superconducting quantum interference devices (SQUIDs) for weak magnetic field detection and for electrically tunable microwave magnetic devices such as filters, resonators, and phase shifters [32, 33].

They are also liable to show magnetoelectric switching, which would be the reversal of the electric polarization with a magnetic field or of the magnetization with an electric field, phenomenon that could enable novel potentially disruptive information technologies like the magnetoelectric random access memory (MeRAM). This device would combine the best characteristics of ferroelectric memories (FeRAMs): an electrical low-power and ultrafast WRITE operation, with a magnetic non-destructive (no reset) READ operation [10, 34]. Destructive reading is a main shortcoming of FeRAMs, which determine architecture and ultimately limit downscaling and, thus, storage capacity.

Research and development are being intensified along two lines that progress in parallel: single-phase multiferroics and magnetoelectric composite materials.

I.3.1 Single-Phase Multiferroics

A lot of research has been, and still is, concentrated on magnetic or spin-induced ferroelectrics. These are improper ferroelectrics, in which a small spontaneous polarization ($\ll 1\ \mu C\ cm^{-2}$) develops as a byproduct of a magnetic transition, often involving complex incommensurate antiferromagnetic states like sinusoidal or spiral spin configurations. Such complex magnetic orders result from competing exchange interactions in systems with several different magnetic cations and from consequent magnetic frustration. First examples were orthorhombic Terbium manganites like $TbMnO_3$ and $TbMn_2O_5$ with ordering temperatures around 40 K. These oxides developed a ferroelectric state at low-temperature successive magnetic transitions involving spin reorientation (one system of this type is chosen in Chapter 12 to show the application of high-resolution synchrotron X-ray diffraction in the study of the crystal mechanisms underlying multiferroism). Large magnetoelectric effects, basically changes of permittivity and reorientation of polarization, even direction reversal, have been reported under high magnetic fields associated with phase-change responses at the instabilities of the antiferromagnetic state [35, 36]. Following works concentrated on finding systems that showed similar phenomenology but higher magnetic ordering temperatures, among which CuO at 230 K [37] and $Sr_3Co_4Fe_{24}O_{41}$ at 670 K stand out [38].

Similar effects have been described for different improper ferroelectrics like geometric or electronic ones, for which a comparatively large spontaneous polarization ($>1\ \mu C\ cm^{-2}$) develops independently of the magnetic order, usually at a high-temperature transition, either involving structural rearrangements or charge ordering. The best known examples are $YMnO_3$ and $LuFe_2O_4$, respectively [39, 40]. Nonetheless, magnetic ordering temperatures are also below room temperature and magnetoelectric effects again are phase-change responses associated with additional polarization components that appear at low-temperature magnetic transitions. Furthermore, the ferroelectricity of $LuFe_2O_4$ has been recently questioned [41]. Besides, reports on the electrical control of magnetization, let alone on its reversal (the key enabling property for the magnetoelectric memory), are scarce. An example is the development of a ferromagnetic Ho^{3+} state in $HoMnO_3$ under the electric field, switchable but not remnant below the ordering temperature of 80 K [42]. Therefore, and though research goes on covering an ever wider range of manganites, ferrites, chromites, and cobaltites [43], it is not clear that they can provide room temperature, electrically driven magnetization switching. Alternatives thus need to be (and are being) investigated.

An alternative approach to obtain oxides that do show independent ferroic orders is to chemically design ABO_3 perovskite systems where ferroelectricity and magnetism originate at different crystal lattice sites. $BiMnO_3$ stands out as an insulating ferromagnet, which has also been claimed to be ferroelectric, and is considered a model system of this strategy. Ferromagnetic order of the Mn^{3+} at the B-site develops at 100 K, while ferroelectric off-center distortion would be driven by the stereochemically active Bi^{+3} lone pair at the A-site [44]. However, later detailed structural characterizations, electrical measurements down to 77 K, and studies of the lattice dynamics have shown this oxide not to be ferroelectric [45–47]. This is consistent with studies of the $x\mathrm{BiMnO_3} - (1-x)\mathrm{PbTiO_3}$ solid solution that clearly indicated the disappearance of ferroelectricity for $x \geq 0.5$ [48].

$BiFeO_3$ is undoubtedly a multiferroic material, and perhaps the only compound that shows magnetic ordering and proper ferroelectricity at room temperature. This perovskite oxide has a ferroelectric transition temperature of 1100 K and G-type antiferromagnetism with an ordering temperature of 643 K. Crystal magnetoelectric coupling does exist and results in spin canting as well as a long-range incommensurate cycloid superstructure that cancels out the ferromagnetic component [49]. Weak ferromagnetism and a linear magnetoelectric effect are only obtained when the latter spin cycloid is destroyed by chemical modification [50], epitaxial strain [51], or due to a size effect [52]. These two latter phenomena are examples of multiferroism tailored by means of nanostructuring (see Figure I.2).

Recently, a strong phase-change magnetoelectric response has been anticipated by a first-principles investigation of phases in the $BiFeO_3$–$BiCoO_3$ perovskite binary system, associated with the existence of a morphotropic phase boundary (MPB) between multiferroic polymorphs of rhombohedral and tetragonal symmetries [53]. This might be a general property of multiferroic MPBs, like the enhancements of polarizability and of the electromechanical response are of analogous ferroelectric MPBs, and is a novel promising approach for room temperature magnetoelectricity. The mechanism would be the rotation of the magnetization easy axis following that of spontaneous polarization under the electric field, facilitated by the lattice transverse instability at the MPB, and the final electric field

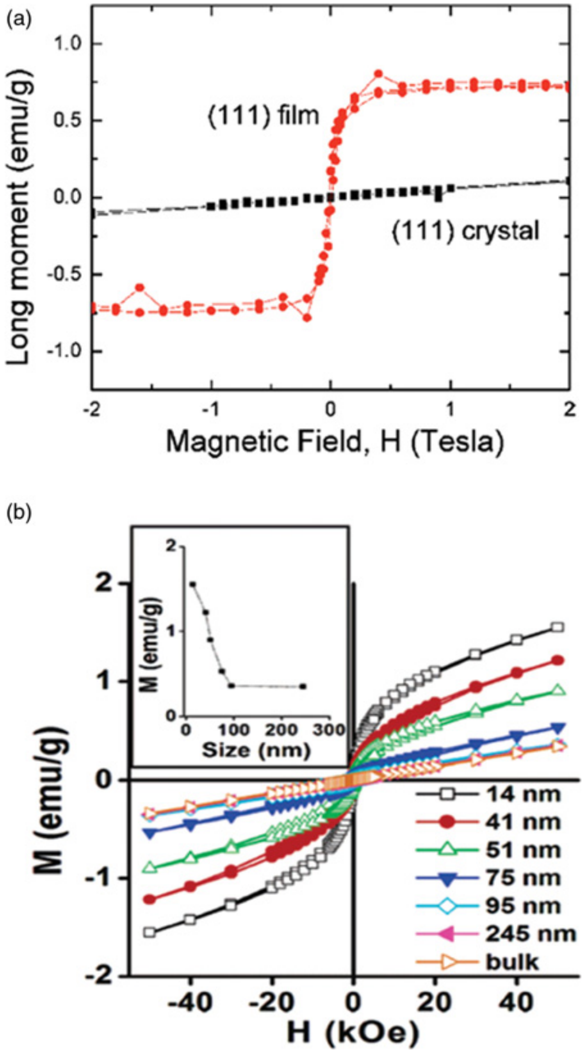

Figure I.2 *Uncovering the latent magnetization in $BiFeO_3$ (a) thin films (reprinted with permission from [51]. Copyright [2005], AIP Publishing LLC) and (b) nanoparticles (reprinted with permission from [52]. Copyright (2007) American Chemical Society).*

induced transformation from one ferroelectric (multiferroic) polymorphic phase to the other. This approach requires the identification and study of suitable material systems, like the $BiFeO_3$–$PbTiO_3$ solid solution, recently shown to present such a multiferroic MPB, for which the enhancement of properties was described [54, 55].

Nonetheless, the presence of coexisting, independently developed ferroic orders and of linear or/and phase-change magnetoelectric effects in a single-phase material does not guarantee the occurrence of magnetoelectric switching. This phenomenon requires direct coupling of the magnetic and ferroelectric domain configurations. This coupling has been demonstrated for antiferromagnetic multiferroics like $YMnO_3$ and $BiFeO_3$ and enables the reorientation of the antiferromagnetic domains following electrical switching of ferroelectric/ferroelastic ones [56–58]. However, an analogous phenomenon has not been found for ferromagnetic multiferroics.

A milestone in research of single-phase multiferroics, partially reversible ferroelectric domain reorientations under magnetic fields have been very recently described for $(1-x)\ Pb(Zr_{0.53}Ti_{0.47})O_3$–$x\ Pb(Fe_{1/2}Ta_{1/2})O_3$, with $x = 0.4$ at room temperature [59]. This is an example out of a number of perovskite solid solutions between ferroelectric phases and relaxor compounds (it is the second time that these polar materials are mentioned without being introduced; they are examples of intrinsically nanostructured compounds that will be addressed later on) containing magnetically active cations like $Pb(Fe_{1/2}Nb_{1/2})O_3$, $Pb(Fe_{2/3}W_{1/3})O_3$, and $Pb(Fe_{1/2}Ta_{1/2})O_3$ itself, which show weak ferromagnetism in coexistence with a range of polar states and different magnetoelectric coupling phenomena [60, 61]. Though the underlying mechanisms have not been elucidated, spin clustering is thought to be responsible for the ferromagnetic component in the otherwise expected paramagnetic state, while elastic interactions between the proposed magnetic nanoregions and the ferroelectric matrix would cause the magnetoelectric effects.

Ferroelectric domain reorientations under magnetic fields have also been recently reported for Aurivillius structure multiferroic single-phase materials [62]. These oxides are the topic of Chapter 25.

I.3.2 Magnetoelectric Composites

In spite of the extensive research briefly reviewed in the previous section, a single-phase material multiferroic at room temperature and with strong magnetoelectric response, either a linear response or fully controllable magnetoelectric switching, has not yet been reported.

An alternative to single-phase materials for room temperature magnetoelectricity are two-phase ferromagnetic–ferroelectric composites [63, 64]. In these materials, the magnetoelectric effect is obtained as a product property of the magnetostriction and piezoelectricity of the phases (it is thus strain mediated). Best results have been obtained with laminate composites of a high-permeability magnetostrictive FeBSiC alloy and ultra-high piezoelectricity $Pb(Mg_{1/3}Nb_{2/3})O_3$–$PbTiO_3$ fibers with a 2–1 connectivity, which showed a magnetoelectric coefficient $\alpha_E > 50\ V\ cm^{-1}\ Oe^{-1}$ (to be compared with $0.017\ V\ cm^{-1}\ Oe^{-1}$ for the $Sr_3Co_4Fe_{24}O_{41}$ hexaferrite). Magnetic field sensors with extremely low equivalent magnetic noise and sensitivity as high as 10 pT have been demonstrated with these laminates [65]. Ferromagnetic–ferroelectric composites are also promising bitunable materials (field-dependent permittivity and permeability) with a high potential for miniaturized low-weight wearable antennas (mostly in the radiofrequency range) with enhanced bandwidth, improved directivity, high efficiency, and tunable resonant frequency.

This is the last example of a technology that seems to be ready for commercialization: bulk magnetoelectric composites of ultrahigh magnetostriction alloys, such as terfenol or metglass, and high-sensitivity piezoelectrics. Research is also very active in all-oxide composites with 2–2 and 0–3 connectivities, for which spinel structure compounds based on $NiFe_2O_4$ are commonly selected as magnetostrictive components (Chapter 3 introduces one of the most topical nanotechnologies for the processing of these composites) and in polymeric-based ones.

The challenge is now to develop comparable materials in thin-film form for integrated technologies. It is clear that films on silicon-based substrates are required for the magnetoelectric memory, but integrated sensors and microwave components are also targeted. There is also a parallel activity on films of single phases, some of which have already been mentioned [60–62].

However, the current, most promising approaches for obtaining magnetoelectric switching are based on multiferroic epitaxial heterostructures. This is already within the realm of nanoscale ferroelectrics and multiferroics.

I.4 Nanoscale Ferroelectrics and Multiferroics

We have already presented several examples of how the miniaturization of bulk ferroelectric technologies requires the nanostructuring of the ceramic layers. We have also noted that thin films used for FeRAMs are nanostructured, and further miniaturization must lead to even smaller characteristic sizes. The successive FeRAM generations have complied with their own Moore law up to now and must continue doing it in the future for increasing capacity [25].

However, before introducing nanoscale ferroelectrics and multiferroics, we consider it necessary to make some remarks about the concept of critical size for ferroelectricity, highly topical at the turn of the last century. Ferroic phenomena, and thus ferroelectricity, are solid-state cooperative phenomena that result from the interaction of individual entities (electrical dipoles originating from the ion arrangement in the non-centrosymmetric crystal structure in this latter case). Therefore, one can anticipate a critical size below which the interacting units are not enough for the ferroic transition to take place. Even within these limits, ferroelectrics have been shown to withstand successive levels of nanostructuring down to very low sizes while preserving polar order. For instance, $PbTiO_3$ epitaxial films as thin as 3 monolayers (1D nanostructuring down to 1.2 nm) are ferroelectric and show inversion domains. These are formed to reduce the electrostatic energy associated with the increasing depolarization field. Ferroelectricity thus is only limited by an antiferrodistortive surface reconstruction [66]. Moreover, $BaTiO_3$ nanowires with 3 nm diameter (2D nanostructuring) are still ferroelectric, and extrapolation of the transition temperature trend allows their existence to be predicted down to 0.8 nm. In this case the depolarization field is thought to be screened by surface adsorbed chemical species [67]. Finally, linearly ordered and monodomain polarization states have been described in $BaTiO_3$ individual isolated cubic nanocrystals with characteristic dimensions below 10 nm (3D nanostructuring) [68]. This latter example is illustrated in Figure I.3.

Therefore, there remains plenty of room at the bottom for the nanostructuring of ferroelectrics before the ferroic order vanishes. This has shifted attention from determining the critical size to the description and the understanding of the effects of nanostructuring on the properties of ferroelectric materials. These do not only result from the size decrease, but also from the specific mechanical and electrical boundary conditions. The three levels of nanostructuring are being investigated extensively.

I.4.1 1D Nanostructured Ferroelectrics and Multiferroics

The ideal 1D nanostructured system would be a free-standing single-crystal plate. $BaTiO_3$ nanoscale thickness plates have been machined out of bulk single-crystal samples by

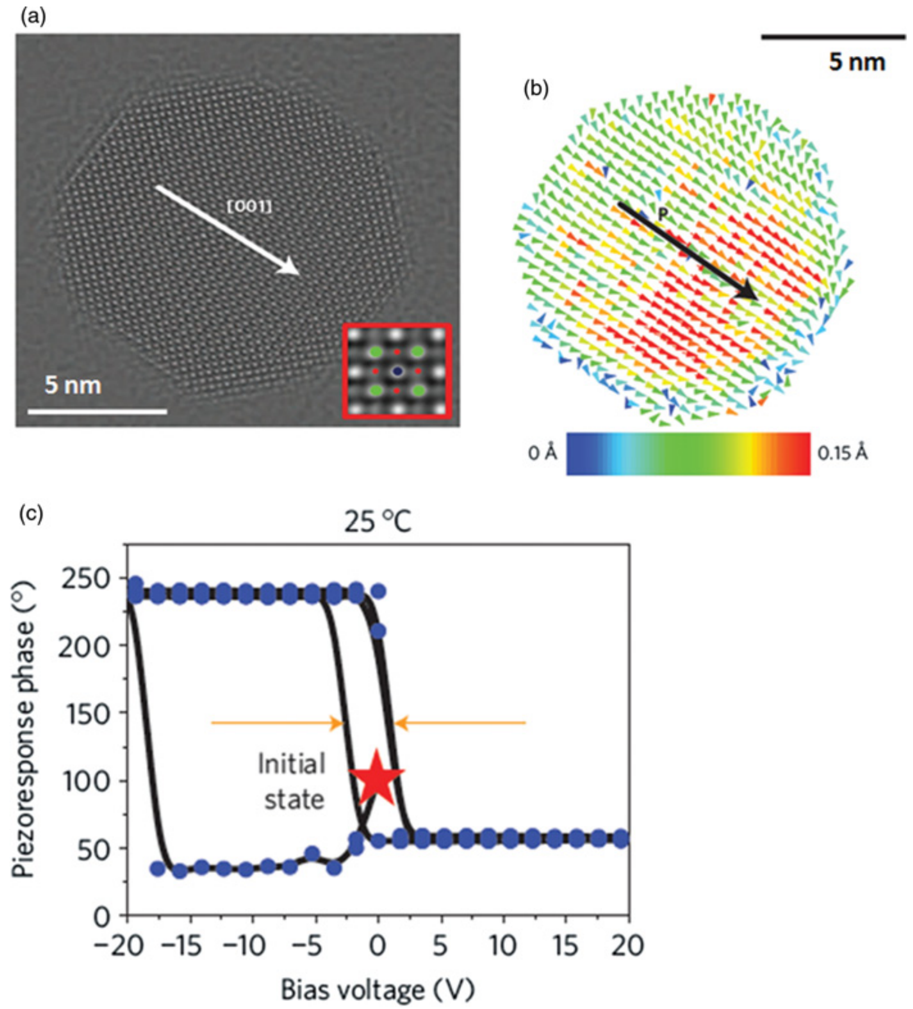

Figure I.3 *(a) Atomic resolution reconstructed phase image and (b) titanium displacement map of a single* $BaTiO_3$ *nanocrystal and (c) ferroelectric switching (followed with piezoresponse force microscopy) in a 10 nm crystal. Reprinted by permission from Macmillan Publishers Ltd (*Nature Materials*) [68], copyright (2012).*

focused ion beam milling and their domain configuration and dynamics, as well as electrical properties successfully characterized. This research has been the key to building up an understanding of the effect of the confined geometry in ferroelectrics [69]. However, the most topical and technologically relevant 1D nanostructured systems are epitaxial films (and specifically those very recently grown on buffered silicon; see Chapter 20).

I.4.1.1 Nanoscale Epitaxial Films for Novel Ferroelectric Memories

Ultra-thin epitaxial ferroelectric oxide films do not only maintain ferroelectricity but their properties can be tailored to the epitaxial strain, an approach referred to as strain engineering, which allows, for instance, enhanced spontaneous electrical polarization to be obtained [70]. In addition, these films are enabling materials for novel memory designs proposed to overcome current FeRAMs limitations, basically the capacitive and destructive reading, which hinders miniaturization. Three devices are under extensive investigation:

1. The first one to be raised was the ferroelectric field effect transistor (FeFET) memory. This is a one-transistor (1T) device as compared with one-transistor one-capacitor (1T–1C) current architectures. They are basically a metal oxide-semiconductor FET (MOSFET), for which the gate dielectric has been replaced by a ferroelectric layer. In MOSFETs, the charge carrier density within the channel and the current between the source and drain are controlled by polarization within the gate oxide. This layer being ferroelectric, a hysteretic resistance loop with two well-differentiated remnant states appears to be directly associated with the ferroelectric hysteresis and the two directions of the remnant polarization. The memory is a ferroelectric one, for information is still stored in the polarization state, but the reading is resistive and non-destructive, and the architecture is simplified. In spite of these advantages, reliability issues originating from the quality of the ferroelectric oxide–semiconductor interface have prevented full development (epitaxial growth is used, and still surface electronic states often compensate the electrical polarization and screen the electric field within the channel) [27]. This topic is addressed in Chapter 20.
2. A second promising, related, device is the ferroelectric tunnel junction (FeTJ) memory. It is based on the dependence of the tunnel electroresistance through an ultra-thin ferroelectric film capacitor structure on the polarization within the dielectric. This shows two well-differentiated resistance states, again directly associated with the two polarization directions. It is therefore also a ferroelectric memory with a resistive, non-destructive reading, but with a vertical instead of a planar configuration, and a 1C architecture that is also advantageous for miniaturization. All-oxide epitaxial capacitors are investigated, which provide very high quality interfaces. More information can be found in recent reviews [71, 72].
3. The last device is the ferroelectric scanning probe memory. This is an example of scanning probe technologies currently under extensive research, specifically based on the ability of writing arrays of very small ferroelectric domains in ultra-thin ferroelectric films with SPM electrically biased microcantilevers, and of probing their orientation with the piezoresponse force mode. Indeed, dense patterns up to 28 Gbit cm^{-2} have been written and imaged in epitaxial Pb(Zr,Ti)O_3 films with 37 nm thickness [73]. This technology requires parallel operation of large microcantilever arrays for fast access. SPM technologies for ferroelectrics are the topic of Chapters 13 and 14.

I.4.1.2 Nanoscale Film Epitaxial Heterostructures for Magnetoelectricity

Epitaxial multiferroic films are also under focus, and multiferroism has been described in films of $BiMnO_3$, not ferroelectric in bulk, and of (Bi,La)MnO_3, with which multiferroic tunnel junctions have been built and four-state memory effect demonstrated [74]. Multiferroism has also been strain engineered in $EuTiO_3$, taking advantage of spin-lattice coupling [75].

Moreover, magnetoelectricity has been shown to appear in a number of oxide epitaxial heterostructures consisting of ferroelectric and magnetic layers, and thus multiferroic by design. Different mechanisms of interaction between the ferroic layers, capable of generating the magnetoelectric response, have been described.

The first one to be reported was elastic interaction of the layers (or strain-mediated magnetoelectricity). This is the same mechanism responsible for the high magnetoelectric response of bulk composites. The simplest configuration is a magnetic layer deposited on to a ferroelectric single crystal, and indeed strong magnetoelectric effects can be obtained with such systems. An example is the electrical tuning of ferromagnetic resonance. This effect has been illustrated for a range of oxide heterostructures, like Fe_3O_4 films on $Pb(Zn_{1/3}Nb_{2/3})O_3$–$PbTiO_3$ single crystals, throughout the variation of magnetic susceptibility due to in-plane piezoelectric strains [76]. Direct electric field control of magnetism has been obtained on two-component systems with elastically coupled ferromagnetic and ferroelectric/ferroelastic domains (the topic of Chapter 21).

However, this approach is not directly transferable to epitaxial heterostructures on non-active substrates, such as $SrTiO_3$, or even better $SrTiO_3$/Si for their integration with electronics, for the piezoelectric or ferroelastic strains are strongly limited by the substrate in this configuration. This is why attention has mainly concentrated on epitaxial columnar nanostructures of magnetic spinel and ferroelectric perovskite structure oxides such as $CoFe_2O_4$ and $BaTiO_3$ or $BiFeO_3$ [77]. A 1–3 connectivity is engineered in these multiferroic epitaxial thin-film composites to avoid substrate clamping effects. Though magnetoelectric switching has been locally demonstrated and controlled [78], an analogous macroscopic effect has not been achieved, and only very recently an unambiguous magnetoelectric response was reported, though with low coefficients of 0.06 $V\ cm^{-1}\ Oe^{-1}$ [79]. The substrate clamping issue can also be minimized by selecting 0–3 connectivity, and the most promising results have been found for thin-film particulate nanocomposites of Co and $BaTiO_3$ with magnetoelectric coefficients of 0.16 $V\ cm^{-1}\ Oe^{-1}$ [80]. Chapter 6 presents a novel process for such thin-film composites.

Magnetoelectricity has also been obtained from magnetic interaction of the layers (exchange-mediated). This requires a heterostructure formed by an antiferromagnetic multiferroic with coupled domains, such as $YMnO_3$ or $BiFeO_3$, and a ferromagnet. Electrical control of the magnetism in the ferromagnetic component is obtained by means of exchange interaction with the multiferroic one, specifically by electrical modulation of the exchange bias [81,82].

Electrostatic interaction can also result in magnetoelectricity. This has been described for heterostructures of ferroelectrics and strongly correlated magnetic systems like $PbZr_{0.2}Ti_{0.8}O_3/La_{0.8}Sr_{0.2}MnO_3/SrTiO_3$ film epitaxial ones. The mechanism in this case is modification of the density of the charge carriers in the manganite compound and formation of depleted/accumulated layers, with the electrostatic field associated with the switchable electrical polarization in the ferroelectric oxide. This has a direct effect on magnetism (charge-mediated magnetoelectricity). Note the analogy with the ferroelectric field effect transistor [83].

Both effects can be operative and add up, such as in $BiFeO_3$/(La,Sr)MnO_3 heterostructures, for which reversible electric control of the exchange bias has been demonstrated using a field effect device [84]. Two examples of magnetoelectric response in epitaxial heterostructures are given in Figure I.4.

A phenomenon that is attracting increasing attention is interface room temperature multiferroism [85], such as that recently reported for $BaTiO_3$/Fe heterostructures [86]; see

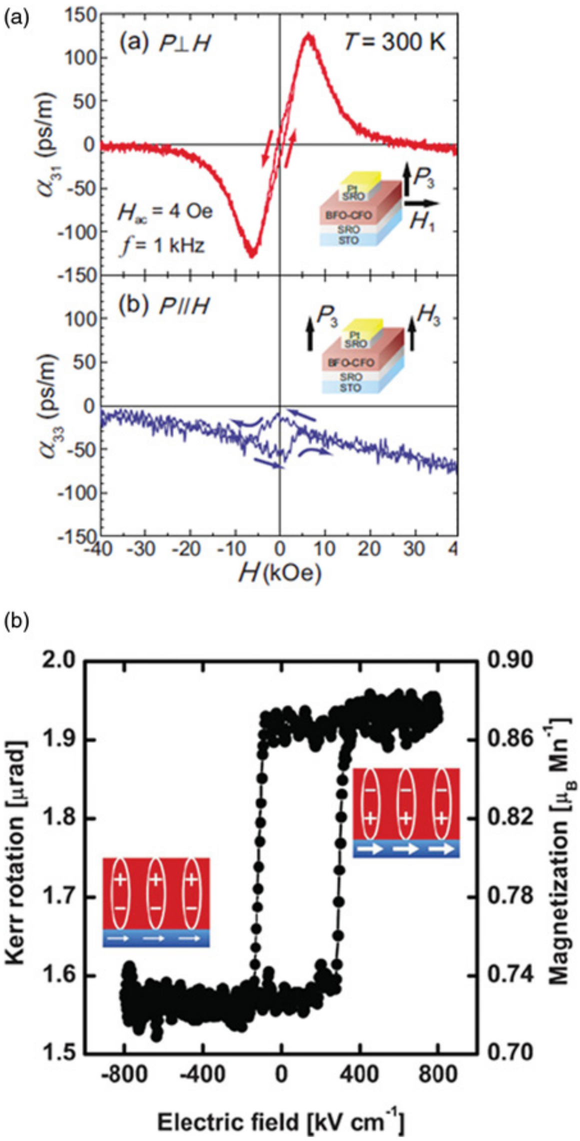

Figure I.4 *(a) Magnetoelectric response for a $BiFeO_3/CoFe_2O_4$ thin-film nanocomposite (reprinted with permission from [79]. Copyright [2010], AIP Publishing LLC) and (b) magnetoelectric hysteresis curve for a $Pb(Zr,Ti)O_3/(La,Sr)MnO_3$ heterostructure (reproduced with permission from [83]. Copyright © [2009] John Wiley & Sons).*

Chapter 10 for an atomic resolution analysis of the chemical nature of the interface. Ferroelectric control of the current spin polarization through magnetic tunnel junctions based on $BaTiO_3$/Fe has been demonstrated [87]. Multiferroic tunnel junctions consisting of a ferroelectric barrier between dissimilar ferromagnetic electrodes are an example out of a range of multiferroic devices under extensive investigation for spintronics [88].

Interface multiferroism has also been described for ferroelectric domain walls, the topic of Chapter 24.

A transversal issue for all type of memories, whether they are based on either ferroelectric or multiferroic film structures, is their patterning to obtain nanoscale cell arrays for very high densities. Different approaches used to prepare ordered arrays of 3D nanostructured ferroic elements on substrates are reviewed in Chapter 5.

I.4.2 2D Nanostructured Ferroelectrics and Multiferroics

Single-crystal nanowires do not only preserve ferroelectricity down to very small diameters but they can also show enhancement of axial polarization with the decrease in size [89] and a significant piezoelectric response [90]. They are being considered for a range of applications [91], among which energy harvesting stands out [92].

Single-crystal nanotubes have not been reported, though polycrystalline analogs are under extensive study. These are not actual 2D nanostructured systems, but ensembles of 3D nanostructured crystals under distinctive boundary conditions imposed by shape. Finite curvature effects leading to better downscaling behavior than films of a comparable thickness have been reported [93]. They are also under consideration for different applications [94], such as microfluidics, making use of piezoelectricity and random access memories. Coaxial capacitors can be formed with a large effective surface, providing increased specific charge.

These systems are extensively addressed in Chapters 8 and 9.

I.4.3 3D Nanostructured Ferroelectrics and Multiferroics

Though isolated ferroelectric and multiferroic single-crystal nanoparticles have been used for piezo- or photocatalysis [91], they are basically precursors, as ceramic nanopowders, for the processing of high-performance electroceramics and also an enabling technology for the nanostructuring of ceramic layers (see Chapters 1, 2, and 4).

In fact, most topical and technologically relevant 3D nanostructured systems are nanostructured ceramics, films, and nanotubes, which are actually ensembles of densely packed nanoparticles. Nanostructuring is a requirement of the current tendency to miniaturization of ceramic and film technologies. This has a deep impact on functional properties, not only as a consequence of actual size effects but also of the boundary conditions. This subject is dealt with in Chapters 15, 16, 17, and 18. Also, nanostructuring ultimately results from the ever-decreasing processing temperatures, a key issue to the integration of these multifunctional oxides into silicon devices and flexoelectronics (see Chapter 7).

I.4.4 Intrinsically Nanostructured Ferroelectrics and Multiferroics

There are single-crystal compounds that show nanoscale features, which highly determine their properties. This is the case of the hierarchical domain configuration characteristic of $Pb(Zr,Ti)O_3$ at the MPB, consisting of a first level of submicrometer size non-180° lamellar domains, within which a substructure, or second level, of nanoscale regular twinned domains exist. It is the dynamics of these nanotwins that is responsible for the high domain wall contribution to the piezoelectric coefficients [95].

However, the best known example is relaxor ferroelectrics like the model $Pb(Mg_{1/3}Nb_{2/3})O_3$, for which nanoscale chemical ordered regions (CORs) self-assemble within a disorder matrix, driven by electrostatic and elastic forces, and seed the nucleation of polar nanoregions (PNRs) [96]. The dynamics of these PNRs embedded within a paraelectric matrix is responsible for the distinctive electrical behavior of these short-range ordered polar and extensively studied materials [97]. Magnetoelectric relaxors, also named electric/magnetic birelaxors, have been described. Relaxors are extensively addressed in Chapters 11 and 17, and also in Chapter 23, where the intriguing reentrant phenomena are addressed.

I.5 Book Plan

Therefore, nanoscale ferroelectrics are a highly topical research field that is driven by technological interests. They are also being considered for novel applications like magnetoelectric and photovoltaic ones (here chosen as examples; see Chapters 25 and 26). Additionally, a range of novel physical phenomena have been described in nanoscale ferroelectrics and multiferroics, mainly relating to domain configurations in confined systems. The best known example is the finding of polarization closure domain configurations in nanoscale objects, within a general search of the predicted dipolar vortexes (electrical ferrotoroic order) [98].This is the topic of Chapter 22.

This book aims at reviewing the current state of the art of these materials, stressing a range of specific topics at the cutting edge of research. Key issues in processing (nanostructuring), characterization (of the nanostructured materials), and nanoscale effects are successively addressed in three specific sections.

References

(1) Schmid, H. (2008) Some symmetry aspects of ferroics and single phase multiferroics. *Journal of Physics: Condensed Matter*, **20**, art. no. 434201.

(2) Bibes, M. (2012) Nanoferronics is a winning combination. *Nature Materials*, **11**, 354–357.

(3) Spaldin, N.A. and Fiebig, M. (2005) The renaissance of magnetoelectric multiferroics. *Science*, **309**, 391–392.

(4) Eerenstein, W., Mathur, N.D., and Scott, J.F. (2006) Multiferroic and magnetoelectric materials. *Nature*, **442**, 759–765.

(5) Fiebig, M. (2005) Revival of the magnetoelectric effect. *Journal of Physics D: Applied Physics*, **38**, R123–R152.

(6) Hill, N.A. (2000) Why are there so few magnetic ferroelectrics? *Journal of Physical Chemistry B*, **104**, 6694–6709.

(7) Cohen, R.E. (1992) Origin of ferroelectricity in perovskite oxides. *Nature*, **358**, 136–138.

(8) Devonshire, A.F. (1954) Theory of ferroelectrics. *Advances in Physics*, **3**, 85–130.

(9) Cochran, W. (1960) Crystal stability and the theory of ferroelectricity. *Advances in Physics*, **9**, 387–423.

(10) Scott, J.F. (2007) Applications of modern ferroelectrics. *Science*, **315**, 954–959.

(11) Martins, P., Lopes, A.C., and Lanceros-Mendez, S. (2014) Electroactive phases of poly(vinylidene fluoride): determination, processing and applications. *Progress in Polymer Science*, **39**, 683–706.

(12) Guo, M., Cai, H.L., and Xiong, R.G. (2010) Ferroelectric metal organic framework (MOF). *Inorganic Chemistry Communications*, **13**, 1590–1598.

(13) Noheda, B., Gonzalo, J.A., Cross, L.E., et al. (2000) Tetragonal-to-monoclinic phase transition in a ferroelectric perovskite: the structure of $PbZr_{0.52}Ti_{0.48}O_3$. *Physical Review B*, **61**, 8687–8695.

(14) Ahart, M., Somayazulu, M., Cohen, R.E., et al. (2008) Origin of morphotropic phase boundaries in ferroelectrics. *Nature*, **451**, 545–549.

(15) Damjanovic, D. (2009) Comments on origins of enhanced piezoelectric properties in ferroelectrics. *IEEE Transactions on Ultrasonics, Ferroelectrics and Frequency Control*, **56**, 1574–1585.

(16) Damjanovic, D. (1998) Ferroelectric, dielectric and piezoelectric properties of ferroelectric thin films and ceramics. *Reports on Progress in Physics*, **61**, 1267–1324.

(17) Anton, S.R. and Sodano, H.A. (2007) A review of power harvesting using piezoelectric materials (2003–2006). *Smart Materials and Structuctures*, **16**, R1–R21.

(18) Haertling, G.H. (1999) Ferroelectric ceramics: history and technology. *Journal of the American Ceramic Society*, **82**, 797–818.

(19) Park, S.E. and Shrout, T.R. (1997) Ultrahigh strain and piezoelectric behavior in relaxor based ferroelectric single crystals. *Journal of Applied Physics*, **82**, 1804–1811.

(20) Fu, H. and Cohen, R.E. (2000) Polarization rotation mechanism for ultrahigh electromechanical response in single crystal piezoelectrics. *Nature*, **403**, 281–283.

(21) Kutnjak, Z., Petzelt, J., and Blinc, R. (2006) The giant electromechanical response in ferroelectric relaxors as a critical phenomenon. *Nature*, **441**, 956–959.

(22) Zhang, S., Li, F., Jiang, X., et al. (2015) Advantages and challenges of relaxor-$PbTiO_3$ ferroelectric crystals for electroacoustic transducers – a review. *Progress in Materials Science*, **68**, 1–66.

(23) Scott, J.F. and Paz de Araujo, C.A. (1989) Ferroelectric memories. *Science*, **246**, 1400–1405.

(24) Scott, J.F. (2000) *Ferroelectric Memories*, in Advanced Microelectronics Series, edited by K. Itoh and T. Sakurai, Springer-Verlag, Berlin, Heidelberg, Germany.

(25) Setter, N., Damjanovic, D., Eng, L., et al. (2006) Ferroelectric thin films: review of materials, properties and applications. *Journal of Applied Physics*, **100**, art. no. 051606.

(26) Paz de Araujo, C.A., Cuchiaro, J.D., McMillan, L.D., et al. (1995) Fatigue-free ferroelectric capacitors with platinum electodes. *Nature*, **374**, 627–629.

(27) Ishiwara, H. (2012) Ferroelectric random access memories. *Journal of Nanoscience and Nanotechnology*, **12**, 7619–7627.

(28) Eom, C.B. and Trolier-McKinstry, S. (2012) Thin-film piezoelectric MEMS. *MRS Bulletin*, **37**, 1007–1017.

(29) Whatmore, R.W., Zhang, Q., Shaw, C.P., et al. (2007) Pyroelectric ceramics and thin films for applications in uncooled infra-red sensor arrays. *Physica Scripta*, **T129**, 6–11.

(30) Brennecka, G.L., Ihlefeld, J.F., Maria, J.P., et al. (2010) Processing technologies for high permittivity thin films in capacitor applications. *Journal of the American Ceramic Society*, **93**, 3935–3954.

(31) Alpay, S.P., Mantese, J., Trolier-McKinstry, S., et al. (2014) Next-generation electrocaloric and pyroelectric materials for solid-state electrothermal energy interconversion. *MRS Bulletin*, **39**, 1099–1109.

(32) Sott, J.F. (2012) Applications of magnetoelectrics. *Journal of Materials Chemistry*, **22**, 4567–4574.

(33) Ma, J., Hu, J.M., Li, Z., and Nan, C.W. (2011) Recent progress in multiferroic magnetoelectric composites: from bulk to thin films. *Advanced Materials*, **23**, 1062–1087.

(34) Bibes, M. and Barthelémy, A. (2008) Towards a magnetoelectric memory. *Nature Materials*, **7**, 425–426.

(35) Kimura, T., Goto, T., Shintani, H., et al. (2003) Magnetic control of ferroelectric polarization. *Nature*, **426**, 55–58.

(36) Hur, N., Park, S., Sharma, P.A., et al. (2004) Electric polarization reversal and memory in a multiferroic material induced by magnetic fields. *Nature*, **429**, 392–395.

(37) Kimura, T., Sekio, Y., Nakamura, H., et al. (2008) Cupric oxide as an induced multiferroic with high T_C. *Nature Materials*, **7**, 291–294.

(38) Kitagawa, Y., Hiraoka, Y., Honda, T., et al. (2010) Low field magnetoelectric effect at room temperature. *Nature Materials*, **9**, 797–802.

(39) Van Aken, B.B., Palstra, T.T.M., Filippetti, A., and Spaldin, N.A. (2004) The origin of ferroelectricity in magnetoelectric $YMnO_3$. *Nature Materials*, **3**, 164–170.

(40) Ikeda, N., Ohsumi, H., Ohwada, K., et al. (2005) Ferroelectricity from iron valence ordering in the charge-frustrated system $LuFe_2O_4$. *Nature*, **436**, 1136–1138.

(41) Lafuerza, S., Garcia, J., Subias, G., et al. (2013) Intrinsic electrical properties of $LuFe_2O_4$. *Physical Review B*, **88**, art. no. 085130.

(42) Lottermoser, T., Lonkai, T., Amann, U., et al. (2004) Magnetic phase control by an electric field. *Nature*, **430**, 541–544.

(43) Preethi-Meher, K.R.S., Martin, C., Caignaert, V., et al. (2014) Multiferroics and magnetoelectrics: a comparison between some chromites and cobaltites. *Chemistry of Materials*, **26**, 830–836.

(44) Seshadri, R. and Hill, N.A. (2001) Visualizing the role of Bi 6s lone pairs in the off-center distortion in ferromagnetic $BiMnO_3$. *Chemistry of Materials*, **13**, 2892–2899.

(45) Belik, A.A., Kodama, K., Igaea, N., et al. (2010) Crystal and magnetic structures and properties of $BiMnO_{3+\delta}$. *Journal of the American Chemical Society*, **132**, 8137–8144.

(46) Castro, A., Correas, C., Peña, O., et al. (2012) Nanostructured $BiMnO_{3+\delta}$ obtained at ambient pressure: analysis of its multiferroicity. *Journal of Materials Chemistry*, **22**, 9928–9938.

(47) Golan, V., Kamba, S., Savinov, M., et al. (2012) Absence of ferroelectricity in $BiMnO_3$ ceramics. *Journal of Applied Physics*, **112**, art. no. 074112.

(48) Castro, A., Vila, E., Jiménez, R., et al. (2010) Synthesis, structural characterization, and properties of perovskites belonging to the x $BiMnO_3$–$(1 - x)$ $PbTiO_3$ system. *Chemistry of Materials*, **22**, 541–550.

(49) Catalan, G. and Scott, J.F. (2009) Physics and applications of bismuth ferrite. *Advanced Materials*, **21**, 2463–2485.

(50) Khomchenko, V.A., Kiselev, D.A., Vieira, J.M., et al. (2008) Effect of diamagnetic Ca, Sr, Pb, and Ba substitution on the crystal structure and multiferroic properties of the $BiFeO_3$ perovskite. *Journal of Applied Physics*, **103**, art. no. 024105.

(51) Bai, F.M., Wang, J.L., Wuttig, M., et al. (2005) Destruction of spin cycloid in $(111)_c$-oriented $BiFeO_3$ thin films by epitiaxial constraint: enhanced polarization and release of latent magnetization. *Applied Physics Letters*, **86**, art. no. 032511.

(52) Park, T.J., Papaefthymiou, G.C., Viescas A.J., et al. (2007) Size-dependent magnetic properties of single-crystalline multiferroic $BiFeO_3$ nanoparticles. *Nano Letters*, **7**, 766–772.

(53) Dieguez, O. and Iñiquez, J. (2011) First-principles investigation of morphotropic transitions and phase-change functional responses in $BiFeO_3$–$BiCoO_3$ multiferroic solid solutions. *Physical Review Letters*, **107**, art. no. 057601.

(54) Amorín, H., Correas, C., Ramos, P., et al. (2012) Very high remnant polarization and phase-change electromechanical response of $BiFeO_3$–$PbTiO_3$. *Applied Physics Letters*, **101**, art. no. 172908.

(55) Amorin, H., Correas, C., Fernandez-Posada, C.M., et al. (2014) Multiferroism and enhancement of material properties across the morphotropic phase boundary of $BiFeO_3$–$PbTiO_3$. *Journal of Applied Physics*, **115**, art. no. 104104.

(56) Fiebig, M., Lottermoser, Th., Fröhlich, D., et al. (2002) Observation of coupled magnetic and electric domains. *Nature*, **419**, 818–820.

(57) Zhao, T., Scholl, A., Zavaliche, F., et al. (2006) Electrical control of antiferromagnetic domains in multiferroic $BiFeO_3$ films at room temperature. *Nature Materials*, **5**, 823–829.

(58) Lebeugle, D., Colson, D., Forget, A., et al. (2008) Electric field induced spin flop in $BiFeO_3$ single crystals at room temperature. *Physical Review Letters*, **100**, art. no. 227602.

(59) Evans, D.M., Schilling, A., Kumar, A., et al. (2013) Magnetic switching of ferroelectric domains at room temperature in multiferroic PZTFT. *Nature Communications*, **4**, art. no. 1534.

(60) Sánchez, D.A., Ortega, N., Kumar, A., et al. (2011) Symmetries and multiferroic properties of novel room-temperature magnetoelectrics: lead ion tantalate–lead zirconate titanate (PFT/PZT). *AIP Advances*, **1**, art. no. 042169.

(61) Sánchez, D., Ortega, N., Kumar, A., et al. (2013) Room temperature single-phase multiferroic magnetoelectrics: $Pb(Fe,M)_x(Zr,Ti)_{1-x}O_3$ [M = Ta,Nb]. *Journal of Applied Physics*, **113**, art. no. 074105.

(62) Keeney, L., Maity, T., Scmidt, M., et al. (2013) Magnetic field induced ferroelectric switching in multiferroic Aurivillius phase thin films at room temperature. *Journal of the American Ceramic Society*, **96**, 2339–2357.

(63) Nan, C.W., Bichurin, M.I., Dong, S., et al. (2008) Multiferroic magnetoelectric composites: historical perspective, status, and future directions. *Journal of Applied Physics*, **103**, art. no. 031101.

(64) Vaz, C.A.F., Hoffman, J., Ahn, C.H., and Ramesh, R. (2010) Magnetoelectric coupling effects in multiferroic complex oxide composite structures. *Advanced Materials*, **22**, 2900–2818.

(65) Wang, Y.J., Gray, D., Berry, D., et al. (2011) An extremely low equivalent magnetic noise magnetoelectric sensor. *Advanced Materials*, **23**, 4111–4114.

(66) Fong, D.D., Stephenson, G.B., Streiffer, S.K., et al. (2004) Ferroelectricity in ultrathin perovskite films. *Science*, **304**, 1650–1653.

(67) Spanier, J.E., Kolpak, A.M., Urban, J.J., et al. (2006) Ferroelectric phase transition in individual single-crystalline $BaTiO_3$ nanowires. *Nano Letters*, **6**, 735–739.

(68) Polking, M.J., Han, M.G., Yourdkhani, A., et al. (2012) Ferroelectric order in individual nanometre scale crystals. *Nature Materials*, **11**, 700–709.

(69) Sharma, P., McQuaid, R.G.P., McGilly, L.J., et al. (2013) Nanoscale dynamics of superdomain boundaries in single crystal $BaTiO_3$ lamellae. *Advanced Materials*, **25**, 1323–1330.

(70) N. Schlom, D.G., Chen, L.Q., Eom, C.B., et al. (2007) Strain tuning of ferroelectric thin films. *Annual Review of Materials Research*, **37**, 589–626.

(71) Chanthbouala, A. Crassous, A., Garcia, V., et al. (2012) Solid-state memories based on ferroelectric tunnel junctions. *Nature Nanotechnology*, **7** (2), 101–104.

(72) Garcia, V. and Bibes, M. (2014) Ferroelectric tunnel junctions for information storage and processing. *Nature Communications*, **5**, art. no. 4289.

(73) Tybell, T., Paruch, P., Giamarchi, T., and Triscone, J.M. (2002) Domain wall creep in epitaxial ferroelectric $Pb(Zr_{0.2}Ti_{0.8})O_3$ thin films. *Physical Review Letters*, **89**, art. no. 097601.

(74) Gajek, M., Bibes, M., Fusil, S., et al. (2007) Tunnel junctions with multiferroic barriers. *Nature Materials*, **6**, 296–302.

(75) Lee, J.H., Fang, L., Vlahos, E., et al. (2010) A strong ferroelectric ferromagnet created by means of spin-lattice coupling. *Nature*, **466**, 954–959.

(76) Liu, M., Obi, O., Lou, J., et al. (2009) Giant electric field tuning of magnetic properties in multiferroic ferrite/ferroelectric heterostructures. *Advanced Functional Materials*, **19**, 1826–1831.

(77) Zheng, H., Wang, J., Lofland, S.E., et al. (2004) Multiferroic $BaTiO_3$–$CoFe_2O_4$ nanostructures. *Science*, **303**, 661–663.

(78) Zavaliche, F., Zheng, H., Mohaddes-Ardabili, L., et al. (2005) Electric field induced magnetization switching in epitaxial columnar nanostructures. *Nano Letters*, **5**, 1793–1796.

(79) Oh, Y.S., Crane, S., Zheng, H., et al. (2010) Quantitative determination of anistropic magnetoelectric coupling in $BiFeO_3$–$CoFe_2O_4$ nanostructures. *Applied Physics Letters*, **97**, art. no. 052902.

(80) Park, J.H., Jang, H.M., Kim, H.S., et al. (2008) Strain-mediated magnetoelectric coupling in $BaTiO_3$–Co nanocomposite thin films. *Applied Physics Letters*, **92**, art. no. 062908.

(81) Laukhin, V., Skumryev, V., Marti, X., et al. (2006) Electric-field control of exchange bias in multiferroic epitaxial heterostructures. *Physical Review Letters*, **97**, art. no. 227201.

(82) Chu, Y.H., Martin, L.W. Holcomb, M.B., et al. (2008) Electric field control of local ferromagnetism using a magnetoelectric multiferroic. *Nature Materials*, **7**, 476–482.

(83) Molegraaf, H.J.A., Hoffman, J., Vaz, C.A.F., et al. (2009) Magnetoelectric effects in complex oxides with competing ground states. *Advanced Materials*, **21**, 3470–3474.

(84) Wu, S.M., Cybart, S.A., Yu, P., et al. (2010) Reversible electric control of exchange bias in a multiferroic filed effect device. *Nature Materials*, **9**, 756–761.

(85) Rondinelli, J.M., Stengel, M., and Spaldin, N.A. (2008) Carrier-mediated mageto-electricity in complex oxide heterostructures. *Nature Nanotechnology*, **3**, 46–50.

(86) Valencia, S., Crassous, A., Bocher, L., et al. (2011) Interface-induced room temperature multiferroicity in $BaTiO_3$. *Nature Materials*, **10**, 753–758.

(87) García, V., Bibes, M., Bocher, L., et al. (2010) Ferroelectric control of spin polarization. *Science*, **327**, 1106–1110.

(88) Tsymbal, E.Y., Gruverman, A., García, V., et al. (2012) Ferroelectric and multiferroic tunnel junctions. *MRS Bulletin*, **37**, 138–143.

(89) Cai, M.Q., Zheng, Y., Wang, B., and Yang, G.W. (2009) Nanosize confinement induced enhancement of spontaneous polarization in a ferroelectric nanowire. *Applied Physics Letters*, **95**, art. no. 232901.

(90) Wang, Z., Hu, J., Suryavanshi, A.P., et al. (2007) Voltage generation from individual $BaTiO_3$ nanowires under periodic tensile mechanical load. *Nano Letters*, **7**, 2966–2969.

(91) Rørvik, P.M., Grande, T. and Einarsrud, M.A. (2011) One-dimensional nanostructures of ferroelectric perovskites. *Advanced Materials*, **23**, 4007–4034.

(92) Chen, X., Xu, S., Yao, N., and Shi, Y. (2010) 1.6 V nanogenerator for mechanical energy harvesting using PZT nanofibers. *Nano Letters*, **10**, 2133–2137.

(93) Nonnenmann, S.S., Leaffer, O.D., Gallo, E.M., et al. (2010) Finite curvature-mediated ferroelectricity. *Nano Letters*, **10**, 542–546.

(94) Zhu, X., Liu, Z., and Ming, N. (2010) Perovskite oxide nanotubes: synthesis, structural characterization, properties and applications. *Journal of Materials Chemistry*, **20**, 4015–4030.

(95) Theismann, R., Schmitt, L.A., Kling, J., et al. (2007) Nanodomains in morphotropic lead zirconate titanate ceramics: on the origin of the strong piezoelectric effect. *Journal of Applied Physics*, **102**, art. no. 024111.

(96) Burton, B.P., Cockayne, E., and Waghmare, U.W. (2005) Correlations between nanoscale chemical and polar order in relaxor ferroelectrics and the lengthscale for polar nanoregions. *Physical Review B*, **72**, art. no. 064113.

(97) Bokov, A.A. and Ye, Z.G. (2006) Recent progress in relaxor ferroelectrics with perovskite structure. *Journal of Materials Science*, **41**, 31–52.

(98) Naumov, I.I., Bellaiche, L., and Fu, H. (2004) Unusual phase transitions in ferroelectric nanodisks and nanorods. *Nature*, **432**, 737–740.

Part A

This first part of the book deals with the processing of the nanostructured ferroelectrics and multiferroics. It consist of nine chapters organized in three sections, which successively present the key issues in the processing of bulk nanostructured ceramics (and thus of the initial nanocrystalline ceramic powder), thin-film nanostructures, and nanoscale fibers and wires.

Nanostructuring: Bulk

The first section comprises four chapters that present selected case studies of the synthesis of nanopowders and the processing of ceramics structured at different scales from them, the emphasis put on the relationships among preparation, the nano- or microstructure, and the functionality for a number of perovskite systems with ferroelectric or multiferroic properties. $BaTiO_3$-based ferroelectrics, Bi-based multiferroics, complex core–shell structures with at least one perovskite component, and Pb-based relaxors are successively addressed. In the research of ferroelectric and multiferroic oxides, a key factor for producing dense nanostructured ceramics is the preparation of high-purity ultrafine powders, non-agglomerated and with the correct stoichiometry and controlled and reproducible nano/microstructures [1]. The usefulness of various non-conventional types of methods for the synthesis instead of the solid-state procedure is discussed by the authors by means of their original results put into the general context of a broad literature for each investigated system.

The section opens with Chapter 1, *Incorporation Mechanism and Functional Properties of Ce-Doped* $BaTiO_3$ *Ceramics Derived from Nanopowders Prepared by the Modified Pechini Method*. It presents the properties of $BaTiO_3$ ceramics with Ce substitutions on both the A or B sites of the ABO_3 perovskite unit cell, processed from the powders obtained by the wet chemistry route, and provides an exhaustive picture concerning the role of the incorporation mechanisms of the amphoteric Ce dopant into the perovskite structure on the functional properties of ceramics. Two compositions, one corresponding to the nominal formula $Ba_{0.95}Ce_{0.05}TiO_3$ and the second with built-in titanium vacancies

---

Nanoscale Ferroelectrics and Multiferroics: Key Processing and Characterization Issues, and Nanoscale Effects, First Edition. Edited by Miguel Algueró, J. Marty Gregg, and Liliana Mitoseriu.
© 2016 John Wiley & Sons, Ltd. Published 2016 by John Wiley & Sons, Ltd.

$Ba_{0.95}Ce_{0.05}Ti_{0.9875}(V_{Ti}'''')_{0.0125}O_3$, are analyzed. First of all, in the introductory part, the choice of Ce–$BaTiO_3$ as a case study for the large class of doped-$BaTiO_3$ systems, current state of the art materials for multilayer ceramic capacitors [2], is justified by the contradictory results reported in the literature as a step towards the understanding of the role of the incorporation mechanism on the functional properties. The authors present within the context of literature data of their own results concerning the two above-mentioned compositions obtained from nanopowders produced by the Pechini method.

The synthesis procedures and the morphology and crystalline structure of the resulting nanopowders are firstly described. The structural study carried out on ceramics sintered at different temperatures showed the formation of a major perovskite phase for all the compositions, with a significant decrease in the unit cell parameters and volume for the ceramics with built-in Ti vacancies, irrespective of the sintering temperature. The specimens sintered at higher temperatures show a mixture consisting of a cubic major phase and a minor tetragonal modification for the $Ba_{0.95}Ce_{0.05}Ti_{0.9875}(V_{Ti}'''')_{0.0125}O_3$ ceramic, whereas a pure tetragonal form was found for the $Ba_{0.95}Ce_{0.05}TiO_3$ sample. Only the specimen with built-in titanium vacancies sintered at 1300 °C showed a single-phase composition. Internal oxidation of Ce^{3+} to Ce^{4+} takes place in both samples sintered at a lower temperature (1200 °C), as well as in the specimen, without compensating defects sintered at 1300 °C. The Ce^{3+} oxidation is accompanied by segregation of Ti-rich secondary phases with various Ba/Ti ratios, as XRD and FE-SEM investigations revealed. All the ceramics show good dielectric properties, with permittivity values slightly below 1000.

The values of the phase transition temperatures indicated by dielectric data supported the assumption of an exclusive but incomplete incorporation (relative to the nominal formula) of the cerium as Ce^{3+} on the Ba site into the perovskite lattice for both ceramics sintered at a lower temperature and of a mixed incorporation of the cerium, mainly as Ce^{4+} on Ti sites, but in a less extent also as Ce^{3+} on Ba sites, in the case of the specimen without Ti vacancies and sintered at a higher temperature. Temperature-dependent Raman analyses also proved the mixed incorporation mechanism of cerium, with a predominant homovalent $Ce^{4+} \leftrightarrow Ti^{4+}$ substitution in the ceramic sample without built-in Ti vacancies sintered at higher temperature. Even related to a specific dopant on a $BaTiO_3$ perovskite structure, this study reveals the role of dopant incorporation mechanisms determined by the thermal treatment strategy and Ti vacancy level on the structural and macroscopic properties of $BaTiO_3$ solid solutions.

Magnetoelectric multiferroics, materials that simultaneously show some form of magnetic and ferroelectric order in the same structure, have excited condensed-matter researchers worldwide with the promise of coupling between electric and magnetic order parameters [3–5]. Among them, Bi-based multiferroics and, in particular, $BiFeO_3$ were mostly investigated for fundamental aspects and from the technological point of view, exploring the possibility of electrical control of magnetism and vice versa in innovative new devices for information storage and sensing and/or actuation. Regarding synthesis, only a few of the possible bismuth-containing perovskites can be prepared by conventional methods, while most of them require high pressures due to the small Bi^{3+} ionic radius and associated low tolerance factor [6]. Chapter 2, *Synthesis and Ceramic Nanostructuring of Ferroic and Multiferroic Low-Tolerance Factor Perovskite Oxides*, gives an overview of alternative non-conventional synthesis and processing methods suitable for these highly topical oxides, also aiming at their nanostructuring.

Focus is put on $BiMO_3$ systems (M = Fe, Mn) belonging to the class of multiferroics. $BiMnO_3$ is a case study of the well-known problems of lack of stability of low-tolerance perovskites due to its metastable character at ambient pressure [7, 8]. Until very recently, this perovskite oxide had only been obtained by using high-pressure methods, but these types of techniques are expensive and require a high energy cost. In this chapter, instead, the alternative use of mechanosynthesis as an optimal preparation route to obtain low-tolerance factor perovskite oxides and metastable phases in general is proposed. After an introductory part giving a general view about the properties of multiferroics and in particular on the low-tolerance factor systems, the synthesis methods of such peculiar systems are presented. Literature on the possible multiferroics with formula $BiMO_3$, for example $BiMnO_3$, $BiCrO_3$, $BiCoO_3$, and $BiFeO_3$, is reviewed, emphasizing how most of them need expensive high-pressure and high-temperature synthesis. High-pressure and high-temperature techniques are advantageous for the control of oxygen stoichiometry, but they do not allow the processing of ceramic materials with a controlled micro/nanostructure. As an alternative, the authors show that mechanochemical activation is a route with the advantage of easy operation and the ability to produce large amounts of nanocrystalline powders in a short time. This method was proposed in recent years as an effective, economical, and versatile method to stabilize materials that had previously only been obtained by high-pressure techniques. As a case study, the phase formation, microstructures, and some magnetic properties of nanosized $BiFeO_3$, $BiFeO_3$–$PbTiO_3$, and $BiMnO_3$–$PbTiO_3$ solid solutions by mechanochemical synthesis are presented.

Chapter 2 also reviews the methods of consolidation of nanopowders into dense nanostructured ceramics. The functional properties of ceramic materials strongly depend on their micro/nanostructures and, in particular, on the porosity and grain size. The conventional sintering method is not appropriate for nanostructuring dense ceramics, due to the inherent grain growth if a high temperature is used or low density if insufficiently sintered (lower temperature and time). Therefore, alternative sintering methods ensuring enhanced mass transport giving the possibility to reduce both the consolidation temperature and time in order to fully control grain growth have been developed (hot pressing, hot isostatic pressing, and field-assisted consolidation such as microwave sintering and spark plasma sintering) [9]. The last method started to be recently employed on a large scale for producing various types of dense ceramics up to full densification with nanosized grains. Its application to ferroelectrics and multiferroics is described here, underlying the role of the processing parameters on the densification process, for example DC current, heating rates, level of the applied pressure, along with a summary of the types of oxide ferroics and multiferroics consolidated by this method. It is further demonstrated that the combination of mechanosynthesis and spark plasma sintering is an optimum choice to achieve not only the stabilization of the low-tolerance perovskite phase in ceramics when sintering is carried out at low temperatures, but also to control grain growth, needed in order to produce dense nanostructured ceramics.

Obtaining multiple functionalities in the same material is nowadays a hot topic, and a lot of effort has been dedicated to combine dissimilar materials within a single structure [10, 11]. The coating of particles with shells of different compounds (“core–shell” structure) is an example of this approach for multifunctionality that also offers the possibility to tailor the surface properties and to produce valuable precursors for the fabrication of multifunctional composites with 0–3 connectivity. The synthesis of core–shell particles has rapidly developed in the last ten years and nowadays different types of materials, such as metals, oxides, polymers, etc., can be combined together in this unique geometry. Driven by the high interest in this field, Chapter 3, *Core–Shell Heterostructures: From Particle Synthesis to Bulk Dielectric, Ferroelectric and Multiferroic Composite Materials*, presents an overview of recent advances in the synthesis and characterization of core–shell particles and their corresponding composites, combining a ferroelectric phase with a different material.

After a general presentation of the core–shell concept and its usefulness in modifying the surface properties or surface functionalization, in providing 0–3 ferroelectric–magnetic composites with a low resistivity core fully covered by a high resistive material as shell, for which the percolation is prevented even for high-volume fractions of the core phase, or in improving the dielectric or tunability properties of dielectric–ferroelectric composites, the synthesis methods of core–shell structures are described. The three main approaches adopted for the realization of coatings on the surface of core particles suspended in a suitable liquid, and the role of control parameters during synthesis are reviewed: (i) the controlled assembly of one or more layers of preformed nanoparticles, (ii) the direct precipitation of the shell material from solution, and (iii) the reaction between functional groups at the core surface and shell precursor molecules introduced in solution. Furthermore, three classes of core–shell particles corresponding to the coupling of ferroelectrics with polymers, dielectrics, and magnetic oxides are separately addressed: (1) $BaTiO_3$@polymer particles and related composites, with a major advantage of avoiding percolation of the inorganic particles, even for high-volume fractions, and thus strongly reducing the breakdown field; (2) inorganic core–shell particles with a ferroelectric core, mainly $BaTiO_3$-based compounds coated with linear dielectrics (SiO_2, Al_2O_3, MgO) or with paraelectric compounds (TiO_2, $SrTiO_3$, $BaZrO_3$); and (3) multiferroic magnetoelectric core–shell particles, which are convenient precursors for the fabrication of 0–3 composites corresponding to non-percolative inclusions of the magnetic phase (usually with low resistivity) dispersed in a continuous high-resistivity matrix. The core–shell arrangement has the great advantage of maximizing the contact area between the two ferroic phases, improving the strain-mediated coupling between polarization and magnetization. Various types of core–shell geometries, such as spherical particles, coaxial fibers, and arrays of vertically aligned nanowires on a substrate produced by sonochemical synthesis, sol–gel, hydrothermal synthesis, by self-assembly of separately prepared and surface modified particles, and methods coupling colloid chemistry and solid-state reaction, are presented together with their related properties. In such core–shell composites mostly $BaTiO_3$ and $Pb(Zr,Ti)O_3$-based solid solutions were employed as the ferroelectric phase, while the magnetic counterparts were oxides with a kind of magnetic order, such as Fe_2O_3, Fe_3O_4, and different types of Co, Ni, and Zn ferrites.

The synthesis of pure ferroelectric or multiferroic oxides with a complex chemical composition like, for example, Pb-based relaxors is a challenging task, due to the fact that they are composed of several metallic cations and the precursors tend to form other stable compounds during the calcination step [12]. An example is the conventional solid-state synthesis of $PbMg_{1/3}Nb_{2/3}O_3$-based materials by mixing of constituent oxides, which yields, in addition to the desired perovskite, stable pyrochlore phases that are extremely detrimental for the electrical properties of the end product. This is the issue addressed in Chapter 4, *Modeling of Colloidal Suspensions for the Synthesis of the Ferroelectric Oxides with*

Complex Chemical Composition, which proposes a modeling-based approach to the solid-state synthesis of ferroelectric oxides with complex chemical compositions, based on designing particle contacts in the reagent particle mixture through control of particle–particle interactions in aqueous suspensions. The simulations enable a design to be produced during the experiment that will achieve the optimal configuration of reagent particles in the reaction mixture. Their success in improving and optimizing the solid-state synthesis strategy, and in providing the formation of a pure phase in complex perovskites is illustrated for $PbMg_{1/3}Nb_{2/3}$ (PMN) and its solid solution with $PbTiO_3$ (PMN-PT).

In this approach, the interaction forces between colloidal particles down to distances of a few nm are described by specific models based on the interaction potential governed by the competition between the double layer (repulsive) and van der Waals forces (attractive) between particles. The aggregation of the colloidal suspensions is then described by Monte Carlo simulations and applied to describe the formation of PMN starting from Pb, Mn, and Nb oxides. To avoid the formation of pyroclore phases, the desired arrangement of these components should avoid the $PbO–Nb_2O_5$ contacts in the reagent mixture.

The simulations enable the experiment to design in such a way that the optimal configuration of reagent particles in the reaction mixture can be obtained by adjusting the Z potential via modification of pH. The predictions were tested on two systems, PMN and its solid solution PMN-PT, which were prepared under the optimum designed conditions that resulted from the model ($pH = 12.5$). With this method, both materials were synthesized in a pure perovskite phase and exhibit excellent electrical properties.

Nanostructuring: Thin Films

The second section consists of three chapters. It is not intended to provide a detailed description of the different methods that have successfully been used to deposit ferroelectric and multiferroic thin films with a thickness below 100 nm, all nanostructured as either epitaxial, columnar, or polycrystalline. The growth of high-quality ultra-thin epitaxial films of general ferroic oxides has been achieved by a range of physical and chemical deposition methods like sputtering, pulsed laser deposition, and metal(lo) organic chemical vapor deposition (MOCVD) [13, 14]. Molecular beam epitaxy has gained importance during the last decade and has allowed, for instance, the deposition of fully strained $SrTiO_3$ (STO) epitaxial layers on single-crystal silicon wafers [15]. This development has been the key to the subsequent deposition of epitaxial films of a number of functional ferroelectrics, such as $Pb(Zr,Ti)O_3$ (PZT) and $Pb(Mg_{1/3},Nb_{2/3})O_3–PbTiO_3$ on STO/Si, doubtless a milestone in the field [16, 17]. Also, novel approaches like atomic layer deposition has very recently been demonstrated for the growth of a multiferroic oxide [18].

Nevertheless, epitaxial films on Si substrates have not yet been introduced into ferroelectric technologies. Devices like ferroelectric random access memories and piezoelectric microelectromechanical systems rely on columnar or polycrystalline films, usually deposited on platinized silicon. Sputtering or MOCVD techniques are used when conformal step coverage of surface micromachined patterns is required [19, 20], while chemical solution deposition (CSD) is selected when conformal deposition is not an issue. This encloses a wide range of highly versatile solution-based procedures, such as metallo-organic decomposition or sol–gel techniques that offer advantages like comparatively low cost, large homogeneity, and thickness uniformity over large areas, as well as enhanced compositional control [21, 22]. They have been demonstrated for the preparation of different thin-film nanostructures [23, 24] and will play a major role in the section.

The section on *nanostructuring: thin films* opens with Chapter 5, *Self-Assemblage and Patterning of Thin-Film Ferroic Nanostructures*, which provides a comprehensive overview of the different approaches that have been used to prepare 3D nanostructured ferroelectric elements on substrates (or nanoislands), the focus mainly put on how ordered arrays can be obtained and targeting high-density ferroelectric non-volatile random access memories (though the same approaches could be, and are being, applied to multiferroics for magnetoelectric memories).

The chapter starts by describing the application of standard top-down approaches to the nanopatterning of ferroelectric thin films. Roughly speaking, these techniques involve the deposition and patterning of a metal hard mask on to the ferroic film, which can be either epitaxial or polycrystalline, and can have been deposited by any physical or chemical means and the removal of the unmasked film material. Electron beam lithography, physical deposition of the metal, and a lift-off process are usually involved in mask patterning, while wet and mainly dry reactive ion etching (RIE) is used to remove the ferroic material. Maskless, focused ion beam (FIB) milling is also described, with which nanosislands as small as 70 nm have been machined out of a film.

After acknowledging material damage as a major issue in these top-down techniques, the rest of the chapter focuses on approaches for which the patterning is carried out in a precursor film before crystallization or which directly provide self-assembly and patterning, thus avoiding the mentioned damage. The term non-invasive techniques is used, while all are classified as bottom-up, even though not all are strictly bottom-up approaches in the common sense of the term [25, 26]. This is the case of electron beam direct writing, for which a precursor film (a dried as-deposited solution) is directly patterned with the electron beam that locally modifies its properties. This makes the exposed areas insoluble in an organic solvent and allows the pattern to be developed after soaking in the solvent. A crystallization step is necessary, after which arrays of nanostructures with lateral size down to 75 nm have been obtained.

Space is also devoted to procedures that combine scanning probe technologies and CSD, with which arrays of nanoislands with significantly smaller lateral sizes have been obtained. This is the case of dip-pen nanolithography, which is illustrated for the direct preparation of $PbTiO_3$ epitaxial features with 37 nm lateral dimension (arranged with a coverage density of 0.5×10^{12} in^{-2}), and also of thermochemical nanolithography, demonstrated for the local crystallization of spherical volumes with a diameter as small as 10 nm within a precursor film.

All these patterning procedures involving at some stage the scanning of electron or ion beams, or of cantilever probes, are serial (or sequential) writing techniques that require rather long processing times, which hinders mass production. Chapter 5 also addresses alternative non-sequential techniques, such as nanoimprint lithography. This is a CSD-based procedure that has allowed arrays of nanoislands with sizes down to 300 nm to be patterned by imprinting a precursor film with $Si–SiO_2$ molds. Other non-sequential techniques described are those that make use of nanopatterned masks, through which deposition is accomplished from a gas phase. Approach names usually refer to the type (or processing procedure) of the mask, such as gold nanotube membrane litography, ultra-thin ordered nanoporous anodic aluminum oxide (AOO) membrane lithography (these membranes have become a widely spread tool in nanotechnologies, also used for the preparation of nanotubes as presented in Chapter 8), and nanosphere lithography. Ordered arrays of ferroelectric nanostructures with typical sizes around 150 nm have been obtained by (usually) pulse laser deposition (PLD) though these masks.

A much lower feature size has been obtained by truly self-assemblage techniques. A straightfworward approach is the deposition of very diluted precursor solutions in CSD (making use of the microstructural instability) that is presented in detail, or by arresting a process of gas phase deposition (within the Volmer–Weber growth mode) in its first stages, though self-patterning does not occur in these cases. Nanoisland self-arrangement has been achieved with microemulsion (or micelle) mediated patterning or with block (or di-block) copolymer templates (with the oxide precursor molecule loaded in one specific block or subsequently incorporated on to specific sites of a self-assembled polymer thin-film template). Arrays of PZT grains of 20 nm lateral dimension have been obtained with a coverage density of $\sim 0.4 \times 10^{12}$ in^{-2} by one such copolymer micelle lithography, as illustrated.

Registration (the ability to place the nanostructures on specific places) is also discussed. Indeed, this is a main issue in truly self-assemblage approaches. Examples of the combination of different deposition techniques with the use of template substrates based on nanopatterned TiO_2 layers, which promote crystallization, are presented. All former patterning techniques can be (and many have been) used to prepare the seed layer. The smallest TiO_2 features reported were obtained with copolymer micelle lithography to prepare an Au hard mask, followed by reactive ion beam etching. This nicely illustrates how final successful approaches usually combine several of the techniques presented.

Chapter 5 finishes by introducing some approaches to the processing of nanostructures embedded in a low permittivity material. These procedures aim at enabling electrical characterization and also addressability in potential devices, both challenging issues. Though not acknowledged, these thin-film materials are examples of 0–3 (or 1–3) ferroelectric–dielectric nanocomposites that are under intensive investigation as moderate permittivity, low-loss materials for tunable microwave telecommunication devices [27].

Nanocomposites are explicitly targeted in the research reviewed in Chapter 6, *Thin-Film Porous Ferroic Nanostructures: Strategies and Characterization.* This second chapter describes an original CSD-based, bottom-up approach for the preparation of self-assembled and patterned nanoporous ferroic thin films.

A sol–gel method involving the use of inorganic precursors, an amphiphilic block copolymer as the patterning agent, and taking advantage of evaporation-induced self-assemblage phenomena is demonstrated for the preparation of self-patterned porous films of ferroelectric $BaTiO_3$ and $PbTiO_3$, and of multiferroic $BiFeO_3$ with hexagonal-type nanopore arrangements. Besides providing an in-depth discussion of the relationships among the preparation parameters and pore formation and organization, Chapter 6 also reviews the effects of the specific nanostructuring on the electrical and magnetic properties of the different oxides. Distinctive enhancements of ferroelectric switching and of magnetization are reported after nanopore introduction.

The approach presented for the preparation of thin-film porous nanostructures is an intermediate step within a general solution-based procedure for the processing of film nanoparticulate composites. This is proposed for the preparation of thin-film magnetoelectric composites by filling the nanopore array with a magnetic component. Indeed, film nanoparticulate magnetic metal–ferroelectric oxide composites are an alternative to multiferroic oxide epitaxial columnar nanostructures [28], also under extensive research [29], but whose magnetoelectric response is far from those reported for analogous bulk materials [30].

The thematics of the former two chapters are framed within current efforts to develop materials and processes for the miniaturization of film technologies for microelectronics, and review or present techniques for the processing of thin-film nanostructures. However, nanostructuring is often an untargeted result rather than an objective. Indeed, nanostructuring can ultimately result from the ever-decreasing processing temperatures, a key issue to the integration of these multifunctional oxides into silicon devices and flexoelectronics. Moreover, grain size effects have been shown to determine to a large extent the properties of the nanostructured films [31]. This is the topic of Chapter 7, *Low-Temperature Photochemical Solution Deposition of Ferroelectric and Multiferroic Thin Films*, which presents a comprehensive description of a successful family of solution-based procedures that have enabled the general preparation of oxide films below 450 °C.

Chapter 7 focuses on approaches that involve the use of ultraviolet (UV) radiation-sensitive solutions and thus of UV irradiation to aid the thermal decomposition of the gel films prior to crystallization, which can then be carried out at significantly lower temperatures than usual. The drive for lowering the processing temperature is not only enabling integration but also decreasing the environmental impact (not only by reducing the thermal budget but also the emission of toxic volatiles during the processing). Specifically, the chapter describes two photochemical solution deposition procedures respectively based on two environmentally benign solvents: water and a 1,3-propanodiol. In both cases, the devised precursor systems are intrinsically UV active in order to control the organic fraction that has to be eliminated during the pyrolysis step, which turned out to be a key aspect for success.

The aqueous solution–gel route is firstly presented, preceded by a description of the fundamentals of the stabilization of metal ions in water by introducing chelating agents – the basis of this first approach. Two diol-based sol–gel routes involving two different UV-active precursors, acetylacetone stabilized metal alkoxides and charge transfer complexes formed between a metal cation and *N*-metyldiethanolamine, are presented in this second section. Chapter 7 finishes by providing a number of examples of films processed below 450 °C that covers $PbTiO_3$, $(Pb,Ca)TiO_3$, $(Bi_{1/2}Na_{1/2})TiO_3$–$BaTiO_3$, and $BiFeO_3$.

Nanostructuring: Fibers and Wires

The final section of Part A comprises two chapters dedicated to the synthesis, processing, characterization, and properties of one-dimensional (1D) structures. Chapter 8, *Synthesis and Properties of Ferroelectric Nanotubes and Nanowires: A Review*, presents an overview concerning the fabrication, properties, and potential applications of ferroelectric nanowires and nanotubes over the last 15 years. The introduction paragraph presents the general properties of ferroelectrics and justifies the recent interest in producing and investigating 1D nanostructures (nanowires and nanotubes) [32]. Such nanostructures offer the opportunity to understand how ferroelectric properties and domain configuration and dynamics evolve with the morphology and aspect ratio in 1D systems, also providing useful information for the possibility of fabrication of next generation, fully three-dimensional FeRAM structures with high-bit density. Additionally, a new kind of ferroelectric order (circular or ferrotoroidal) should exist in nanorods and nanodisks of small diameter [33, 34], as predicted by ab initio calculations (see also Chapter 22). The need to obtain 1D nanostructures with controlled morphology has stimulated the development of a variety of synthesis techniques and fabrication strategies with a general validity that goes beyond the preparation of ferroelectric nanostructures.

The review focuses on three main aspects concerning 1D ferroelectric nanostructures: (i) synthesis methods developed for the preparation on nanowires and nanotubes, either free-standing or grown on a substrate; (ii) the crystal structure, the domain organization, and the ferroelectric properties of these nanostructures, including local scale properties by means of atomic force microscopy techniques; and (iii) potential applications. Regarding synthesis, the main synthesis strategies adopted to grow 1D ferroelectric nanostructures are presented. Direct growth from the liquid phase (hydrothermal synthesis), the use of reactive templates, both in wet methods and in solid-state reactions (topochemical hydrothermal reaction, topochemical solid state reactions), electrospinning, and focused ion beam lithography (top-down approach) are all reviewed.

The crystal structure, phase transitions, and ferroelectric properties of 1D structures are then presented. A reduction of tetragonal distortion when reducing the diameter of nanowires was observed and a corresponding reduction of Curie temperature as a size effect, similar to that predicted by ab initio calculations. Ferroelectric character and domain structures, even at very small sizes, was probed by scanning probe microscopy techniques. It was shown that remanent polarization perpendicular to the wire axis could be induced and switched, even in nanowires with diameters of 10–20 nm, although the stability of such perpendicular polarization is sensitive to the diameter of the nanowire and to the charge compensation conditions at the wire surface (boundary conditions). Modification of the domain patterns and of the orientation of the non-axial polarization component was found to be strongly dependent on the local morphology of the nanostructure. Manipulation of the domain pattern and polarization orientation can thus be realized by modifying the local aspect ratio of the column dimensions without the application of an electric field. This was demonstrated by the creation of bulges or notches along the $BaTiO_3$ nanocolumns directly patterned by FIB from single crystals (top-down approach).

Chapter 8 ends by presenting the possible applications of 1D ferroelectric structures, either as free-standing nanowires as well as on nanowire aligned arrays, for example nanogenerators for energy harvesting and other devices, dielectric composites with 1D ferrolectric fillers in polymer matrices and anisotropic dielectric characterization, microwave absorbers in the range of THz for electromagnetic shielding, applications of photocatalysis for degradation of organic pollutants in aqueous solution, and photosplitting of water or bimedical applications.

Chapter 9, *Fabrication of One-Dimensional Ferroelectric Nano- and Microstructures by Different Spinning Techniques and Their Characterization*, is devoted to the description of the fabrication methods used to produce one-dimensional ferroelectric micro- and nanostructures from different spinning techniques and the various methods of characterization. Their structural conformity, flexibility, and the tailoring of their acoustic impedance are still the main key issues for the research and development of such composites in view of their applications for structural health monitoring, energy harvesting, and transducers. The main methods for synthesis of micro- and nanoscale fibers on the industrial scale (e.g. viscous suspension spinning process, ALCERU-process, melt spinning process, sol–gel process, polysulfone process, etc.) with reproducible morphologies are described and compared, together with information concerning the effect of the synthesis parameters on the fiber diameter, surface morphology, and shape factors for different ferroelectric oxides. The role of the microstructural and phase characteristics on their macroscopical mechanical properties, such as Weibull strength, Young's modulus, and the proportional limit determined by means of tensile testing, as well as the local piezoelectric properties determined by piezoreponse force microscopy, are also comparatively analyzed for various types of fibers with different diameters, produced using different precursors and methods of preparation.

Chapter 9 also discusses the integration of 1D ferroelectric fillers into polymer-based composites and their electrical characteristics and potential applications. The electrical, piezoelectric, and mechanical properties of single fibers by comparison with ones of bulk corresponding material (PZT) are also shown. Finally, the standardization methods for characterization of micrometric sintered single fibers are presented.

Chapter 9 finishes by reviewing the potential applications of nano- and microwires as sensors and ultrasonic transducers, actuators, vibration-based harvesters based on the piezoelectric effect with the view of achieving self-powered electronic devices for remote/wireless sensing, charging batteries, and the powering of electronic devices.

References

(1) Garbovskiy, Y., Zribi, O., and Glushchenko, A. (2012) Emerging applications of ferroelectric nanoparticles in materials technologies, biology and medicine, in *Advances in Ferroelectrics*, edited by A. Peláiz-Barranco, InTech, ISBN: 978-953-51-0885-6.

(2) Kishi, H., Mizuno, Y., and Chazono, H. (2003) Base metal–electrode multilayer ceramic capacitors: past, present and future perspectives. *Japanese Journal of Applied Physics*, **42**, 1–15.

(3) Tokura, Y. (2007) Multiferroics – toward strong coupling between magnetization and polarization in a solid. *Journal of Magnetism and Magnetic Materials*, **310**, 1145–1150.

(4) Wang, K.F., Liu, J.M., and Ren, Z.F. (2009) Multiferroicity: the coupling between magnetic and polarization orders. *Advances in Physics*, **58**, 321–448.

(5) Vaz, C.A.F., Hoffman, J., Ahn, C.H., and Ramesh, R. (2010) Magnetoelectric coupling effects in multiferroic complex oxide composite structures. *Advanced Materials*, **22**, 2900–2918.

(6) Shannon, R.D. (1976) Revised effective ionic radii and systematic studies of interatomic distances in halides and chalcogenides. *Acta Crystallographica*, Section A, **32** (5), 751–767.

(7) Montanari, E., Righi, L., Calestani, G., et al. (2005) Room temperature polymorphism in metastable $BiMnO_3$ prepared by high-pressure synthesis. *Chemistry of Materials*, **17** (7), 1765–1773.

(8) Belik, A.A., Yusa, H., Hirao, N., et al. (2009) Peculiar high-pressure behavior of $BiMnO_3$. *Inorganic Chemistry*, **48** (3), 1000–1004.

(9) Maglia, F., Tredici, I.G., and Anselmi-Tamburini, U. (2013) Densification and properties of bulk nanocrystalline functional ceramics with grain size below 50 nm. *Journal of the European Ceramic Society*, **33**, 1045–1066.

(10) Caruso, R.A. and Antonietti, M. (2001) Sol–gel nanocoating: an approach to the preparation of structured materials. *Chemistry of Materials*, **13**, 3272–3282.

(11) Ramli, R.A., Laftah, W.A., and Hashim, S. (2013) Core–shell polymers: a review. *RSC Advances*, **3**, 15543–15565.

(12) Trefalt, G., Malic, B., Holc, J., and Kosec, M. (2012) Synthesis of $Pb(Mg_{1/3}Nb_{2/3})O_3$–$PbTiO_3$ by controlled agglomeration of precursor particles. *Journal of American Ceramic Society*, **95**, 1858–1865.

(13) Norton, D.P. (2004) Synthesis and properties of epitaxial electronic oxide thin-film materials. *Materials Science and Engineering R*, **43**,139–247.

(14) Martin, L.W., Chu, Y.H., and Ramesh, R. (2010) Advances in the growth and characterization of magnetic, ferroelectric, and multiferroic thin films. *Materials Science and Engineering R*, **68**, 89–133.

(15) Warusawithana, M.P., Cen, C., Sleasman, C.R., et al. (2009) A ferroelectric oxide made directly on silicon. *Science*, **324**, 367–370.

(16) Sambri, A., Gariglio, S., Torres-Pardo, A., et al. (2011) Enhanced critical temperature in epitaxial ferroelectric $Pb(Zr_{0.2}Ti_{0.8}O_3)$ thin films on silicon. *Applied Physics Letters*, **98**, art. no. 012903.

(17) Baek, S.H., Park, J., Kim, D.M., et al. (2011) Giant piezoelectricity on Si for hyperactive MEMS. *Science*, **334**, 958–961.

(18) Akbashev, A.R., Chen, G.N., and Spanier, J.E. (2014) A facile route for producing single-crystalline epitaxial perovskite oxide thin films. *Nano Letters*, **14**, 44–49.

(19) Auciello, O., Kingon, A.I., and Krupanidhi, S.B. (1996) Sputter synthesis of ferroelectric films and heterostructures. *MRS Bull.*, **21**, 25–30.

(20) Dey, S.K. and Alluri, P.V. (1996) PE-MOCVD of dielectric thin films: challenges and opportunities. *MRS Bull.*, **21**, 44–48.

(21) Tuttle, B.A. and Schwartz, R.W. (1996) Solution deposition of ferroelectric thin films. *MRS Bull.*, **21**, 49–54.

(22) Schwartz, R.W., Schneller, T., and Waser, R. (2004) Chemical solution deposition of electronic oxide films. *Comptes Rendus Chimie*, **7**, 433–461.

(23) Bassiri-Gharb, N., Bastani, Y., and Bernal, A. (2014) Chemical solution growth of ferroelectric oxide thin films and nanostructures. *Chemical Society Reviews*, **43**, 2125–2140.

(24) Obradors, X., Puig, T., Gibert, M., et al. (2014) Chemical solution route to self-assembled epitaxial oxide nanostructures. *Chemical Society Reviews*, **43**, 2200–2225.

(25) Yi, C.Q., Liu, D.D., and Yang, M.S. (2009) Building nanoscale architectures by directed synthesis and self-assembly. *Current Nanoscience*, **5**, 75–87.

(26) Einarsrud, M.A. and Grande, T. (2014) 1D oxide nanostructures from chemical solutions. *Chemical Society Reviews*, **43**, 2187–2199.

(27) Chung, U.C., Elissalde, C., Maglione, M., et al. (2008) Low-losses, highly tunable $Ba_{0.6}Sr_{0.4}TiO_3$ /MgO composite. *Applied Physics Letters*, **92**, art. no. 042902.

(28) Algueró, M., Ricote, J., Torres, M., et al. (2014) Thin film multiferroic nanocompoistes by ion implantation. *ACS Applied Materials and Interfaces*, **6**, 1909–1915.

(29) Zheng, H., Wang, J., Lofland, S.E., et al. (2004) Multiferroic $BaTiO_3$–$CoFe_2O_4$ nanostructures. *Science*, **303**, 661–663.

(30) Oh, Y.S., Crane, S., Zheng, H., et al. (2010) Quantitative determination of anisotropic magnetoelectric coupling in $BiFeO_3$–$CoFe_2O_4$ nanostructures. *Applied Physics Letters*, **97**, art. no. 052902.

(31) Algueró, M., Stewart, M., Cain, M.G., et al. (2010) Properties of morphotropic phase boundary $Pb(Mg_{1/3}Nb_{2/3})O_3$–$PbTiO_3$ films with submicrometre range thickness on Si-based substrates. *Journal of Physics D: Applied Physics*, **43**, art. no. 205401.

(32) Rørvik, P.M., Grande, T., and Einarsrud, M.A. (2011) One-dimensional nanostructures of ferroelectric perovskites. *Advanced Materials*, **23**, 4007–4034.

(33) Fu, H. and Bellaiche, L. (2003) Ferroelectricity in barium titanate quantum dots and wires. *Physical Review Letters*, **91**, art. no. 257601.

(34) Naumov, I.I., Bellaiche, L., and Fu, H. (2004) Unusual phase transitions in ferroelectric nanodisks and nanorods. *Nature*, **432**, 737–740.

1

Incorporation Mechanism and Functional Properties of Ce-Doped $BaTiO_3$ Ceramics Derived from Nanopowders Prepared by the Modified Pechini Method

Adelina-Carmen Ianculescu[1], Daniela C. Berger[2], Catalina A. Vasilescu[1,3], Marius Olariu[4], Bogdan S. Vasile[1], Lavinia P. Curecheriu[5], Andreja Gajović[6], and Roxana Truşcă[7]

[1]Department of Oxide Materials Science and Engineering, "Politehnica" University of Bucharest, Romania
[2]Department of Inorganic Chemistry, Physical-Chemistry and Electrochemistry, "Politehnica" University of Bucharest, Romania
[3]National Institute for Lasers, Plasma and Radiation Physics, Romania
[4]Department of Electrical Measurements and Materials, Technical University Gh. Asachi Iasi, Romania
[5]Department of Physics , "Alexandru Ioan Cuza" University, Romania
[6]Molecular Physics Laboratory, Institute Rudjer Boskovic, Croatia
[7]S.C. METAV – Research and Development Bucharest, Romania

1.1 Why Cerium-Doped $BaTiO_3$?

Donor-doped $BaTiO_3$ ceramics show very high endurance under DC field stress and a Curie temperature shift towards lower temperatures without flattening the permittivity

---

Nanoscale Ferroelectrics and Multiferroics: Key Processing and Characterization Issues, and Nanoscale Effects, First Edition. Edited by Miguel Algueró, J. Marty Gregg, and Liliana Mitoseriu.
© 2016 John Wiley & Sons, Ltd. Published 2016 by John Wiley & Sons, Ltd.

maximum, as the solute concentration increases within the solubility range [1,2]. Regarding the microstructure, above a critical donor dopant content of ~0.5 at% (also corresponding to an abrupt increase of the electrical resistivity), a strong grain growth inhibition known as a "grain growth anomaly" was observed [3–6]. For these reasons, donor-doped $BaTiO_3$ is suitable for the manufacture of multilayer capacitors with thin dielectric layers for applications as decoupling signals and high- and low-pass filters [1].

Due to its variable valence, cerium is a versatile solute for $BaTiO_3$. Therefore, the literature data regarding the oxidation state of cerium incorporated in a $BaTiO_3$ lattice seemed initially rather contradictory. Earlier, Kolar et al. reported a solubility of 18–20 mol% of CeO_2 incorporated as Ce^{4+} on Ti sites of $BaTiO_3$ [7]. Contrary to this result, Roth et al. [8] indicated the presence of Ce^{3+} in stable crystalline oxide phases (titanates, tantalates, and niobates), even if the cerium source was CeO_2 and sintering was carried out under an oxidizing atmosphere. Consistent with this view, Itakura et al. [9] found aliovalent substitution of Ba^{2+} by Ce^{3+} in $BaTiO_3$, induced by the close values of the ionic radii of these species in dodecahedral coordination ($r(Ba^{2+}) = 1.61$ Å, $r(Ce^{3+}) = 1.34$ Å). The incorporation of Ce^{3+} ions on Ti^{4+} sites as acceptors and the integration of Ce^{4+} on Ba^{2+} sites are very unlikely because of the high mismatch in ionic radius values of the substituting and substituted species ($r(Ti^{4+}) = 0.605$ Å and $r(Ce^{3+}) = 1.01$ Å for CN = 6; $r(Ba^{2+}) = 1.61$ Å and $r(Ce^{4+}) = 1.14$ Å for CN = 12). Later, some works of Hennings et al. [1], Makovec et al. [10], and Hwang and Han [11, 12] reconciled these apparent contradictory results. They showed that cerium may be incorporated either as Ce^{4+} on Ti^{4+} sites with the formation of homovalent $BaT_{1\text{-}y}Ce_yO_3$ solid solution or as Ce^{3+} on Ba^{2+} sites acting as donor dopant, or simultaneously as both Ce^{3+} on A sites and Ce^{4+} on B sites of the ABO_3 perovskite lattice, depending on the starting composition and oxygen partial pressure [1, 11, 13].

Based on the phase diagram of the $BaO–TiO_2–CeO_2$ system [14], the exhaustive study of Makovec et al. [10] showed that the starting Ba/Ti ratio plays a decisive role on the oxidation state of cerium, as well as on its solubility and lattice site occupancy into the host $BaTiO_3$ lattice. Thus, they concluded that: (i) for a Ba/Ti > 1 (CeO_2 is added to $BaTiO_3$ together with an excess amount of BaO), cerium is preferentially homovalently incorporated as Ce^{4+} on titanium sites and this solid solution extends along the $BaTiO_3–BaCeO_3$ tie line of the ternary $BaO–TiO_2–CeO_2$ system; (ii) for Ba/Ti < 1 (CeO_2 is added to $BaTiO_3$ with an excess amount of TiO_2), cerium is reduced and enters predominately as Ce^{3+} at barium sites acting as donor dopant; and (iii) for Ba/Ti = 1 (no excess of BaO or TiO_2), cerium is most likely incorporated both as Ce^{3+} at Ba sites and as Ce^{4+} at Ti sites in the ratio 3:4 and the solid solution extends on the tie-line $BaTiO_3–CeO_2$.

For Ba/Ti < 1, when cerium is entirely integrated as Ce^{3+} at Ba sites, several compensation mechanisms were proposed for the positive effective extracharge induced by the donor dopant. It is well known that the donor charge compensation mechanism is strongly dependent on several factors, such as partial pressure of oxygen in a firing atmosphere, sintering temperature, and donor concentration in the $BaTiO_3$ lattice [10, 15].

When sintering is carried out in air at high temperatures (above 1400 °C), the ceramics with a Ce^{3+} concentration below the critical value of 0.5 at% ($x < 0.005$) are described by the formula $Ba_{1-x}Ce^{\bullet}_{x}Ti_{1-x}Ti'_{x}O_3$ (or shortly $Ba_{1\text{-}x}Ce_xTiO_3$). These samples exhibit a dark gray colour and semiconducting behaviour, as the result of an electronic compensation of the donor extracharge. This kind of mechanism involves the formation of reduced titanium species, which act as acceptors and whose concentration is equal to the concentration of the donor dopant, that is $[\mathrm{Ce}^{\bullet}] = [\mathrm{Ti}']$. According to the Kröger–Vink notation [16] it can be described by:

$$2\mathrm{CeO}_2 + 2\mathrm{TiO}_2 \rightarrow 2\mathrm{Ce}^{\bullet}_{\mathrm{Ba}} + 2\mathrm{Ti}^{\times}_{\mathrm{Ti}} + 6\mathrm{O}^{\times}_{\mathrm{O}} + \mathrm{O}_2(g) + 2\mathrm{e}' \tag{1.1}$$

At a higher cerium content (>0.5 at%) ceramics sintered in air have reddish colour and are highly electrically insulating, which means that no electrons are available for conduction and, therefore, intrinsic effectively negatively charged defects as cation vacancies or interstitial anions are required for the compensation of the effective positive charge induced by the donor dopant.

Based on their calculations on defect energetics in barium titanate using computer simulation techniques, it was found [17] that interstitial incorporation of anions into the perovskite lattice, according to the theoretical formula $\mathrm{Ba}_{1\text{-}x}\mathrm{Ce}_x\mathrm{TiO}_{3+x/2}$, where $[\mathrm{Ce}^{\bullet}] = 2[\mathrm{O}_i'']$, as described by the following quation, is very unlikely to take place because of the high packing density of this structure:

$$2\mathrm{CeO}_2 + 2\mathrm{TiO}_2 \rightarrow 2\mathrm{Ce}^{\bullet}_{\mathrm{Ba}} + 2\mathrm{Ti}^{\times}_{\mathrm{Ti}} + 6\mathrm{O}^{\times}_{\mathrm{O}} + \mathrm{O}_i'' + \frac{1}{2}\mathrm{O}_2(\mathrm{g}) \tag{1.2}$$

In some perovskite systems, such as doped SrTiO$_3$ and doped PbTiO$_3$, the donor compensation involves the formation of vacancies on the *A* sites of the perovskite lattice [18, 19]. In the case of Ce-doped BaTiO$_3$, if $\mathrm{Ce}^{\bullet}$donors on Ba sites were to be entirely compensated by barium vacancies, then, according to the following equation, a ratio of co-additives $\mathrm{TiO}_2/\mathrm{CeO}_2 = 3{:}2$ relative to BaTiO$_3$ would be necessary to form a single-phase perovskite described by the formula $\mathrm{Ba}_{1\text{-}3x/2}\mathrm{Ce}_x\mathrm{TiO}_3$ (where $[\mathrm{Ce}^{\bullet}] = 2[\mathrm{V}''_{\mathrm{Ba}}]$):

$$2\mathrm{CeO}_2 + 3\mathrm{TiO}_2 \rightarrow 2\mathrm{Ce}^{\bullet} + \mathrm{V}''_{\mathrm{Ba}} + 3\mathrm{Ti}^{\times}_{\mathrm{Ti}} + 9\mathrm{O}^{\times}_{\mathrm{O}} + \frac{1}{2}\mathrm{O}_2(\mathrm{g}) \tag{1.3}$$

Another assumption considers the formation of an equal number of barium and titanium vacancies for the compensation of donor extracharge. If this mechanism involving the co-additives ratio $\mathrm{TiO}_2/\mathrm{CeO}_2 = 1{:}1$ is valid, then a single-phase perovskite with the nominal formula $\mathrm{Ba}_{1\text{-}7x/6}\mathrm{Ce}_x\mathrm{Ti}_{1\text{-}x/6}\mathrm{O}_3$ (where $[\mathrm{Ce}^{\bullet}] = 2[\mathrm{V}''_{\mathrm{Ba}}] + 4[\mathrm{V}''''_{\mathrm{Ti}}]$) would be formed, according to:

$$6\mathrm{CeO}_2 + 6\mathrm{TiO}_2 \rightarrow 6\mathrm{Ce}^{\bullet}_{\mathrm{Ba}} + 6\mathrm{Ti}^{\times}_{\mathrm{Ti}} + \mathrm{V}''_{\mathrm{Ba}} + \mathrm{V}''''_{\mathrm{Ti}} + 21\mathrm{O}^{\times}_{\mathrm{O}} + \frac{3}{2}\mathrm{O}_2(\mathrm{g}) \tag{1.4}$$

The experimental data of Hennings et al. [1], who reported the preparation and properties of Ce-doped BaTiO$_3$ ceramics with various Ti/Ce ratios ($0 \leq \mathrm{Ti/Ce} \leq 1.5$), showed that, actually, segregation of a Ti-rich second phase already occurred for the molar ratio $\mathrm{TiO}_2/\mathrm{CeO}_2 \cong 1$. Therefore, their results do not sustain the compensation mechanisms expressed by Equations (1.2) and (1.3). Consistent with this view, based on X-ray diffraction (XRD) and scanning electron microscopy (SEM), investigations corroborated with quantitative wavelength dispersive spectroscopy–electron probe microanalysis (WDS/EPMA), Makovec et al. [10] also showed that the compensation via double-ionized barium vacancy (Equation (1.3)) can be excluded. Similar to Hennings et al. [1], they found that when cerium is entirely incorporated as Ce^{3+} on Ba sites, the most likely compensation mechanism involves the generation of tetraionized titanium vacancies. This means that, for a monophasic composition described by the nominal formula $Ba_{1-x}Ce_xTi_{1-x/4}O_3$, a co-additives ratio $TiO_2/CeO_2 = 3{:}4$ is required, according to:

$$4CeO_2 + 3TiO_2 \rightarrow 4Ce^{\bullet}_{Ba} + 3Ti^{\times}_{Ti} + V''''_{Ti} + 12O^{\times}_{O} + O_2(g) \tag{1.5}$$

Even if earlier double-ionized barium vacancies were considered to be the most likely charge compensating defects [20], later experimental data and theoretical calculations [15, 17, 21] sustained the assertion of Jonker and Havinga [22] and converged to the conclusion that tetra-ionized titanium vacancies are the preferred defects for compensation of donors in $BaTiO_3$ systems.

However, some recent works concerning the characteristics of donor-doped $BaTiO_3$ and $(Ba,Sr)TiO_3$ ceramics [23, 24] do not exclude the conclusion that the compensation mechanism via mixed cation vacancies (equal amounts of barium double-ionized and titanium tetra-ionized vacancies) might take place in certain processing conditions. Even for Ce-doped $BaTiO_3$, the study of Hwang and Han [12], based on the equilibrium electrical conductivity of the ceramics corresponding to the nominal formula $Ba_{1-x}Ce_xTiO_3$, which involves equimolar amounts of TiO_2 and CeO_2 admixtures, proposed the defect model including both Ba and Ti vacancies as compensating defects for $Ce^{\bullet}_{Ba}$, according to Equation (1.4). It is worthy to mention that XRD and SEM analyses used in a previous study of the same authors [11], while investigating $Ba_{1-x}Ce_xTiO_3$ ceramics sintered in air, were not able to emphasize, in the solubility range, the presence of any secondary phases as CeO_2- or TiO_2-rich compounds, which normally should be identified if compensation mechanisms via exclusive formation of double-ionized barium vacancies or of tetra-ionized titanium vacancies would be valid. According to the following modified equations of (1.3) and (1.5), for $TiO_2/CeO_2 = 1{:}1$:

$$3CeO_2 + 3TiO_2 \rightarrow 2Ce^{\bullet} + V''_{Ba} + 3Ti^{\times}_{Ti} + 9O^{\times}_{O} + CeO_2 + \frac{1}{2}O_2(g) \tag{1.3$'$}$$

$$4CeO_2 + 4TiO_2 \rightarrow 4Ce^{\bullet}_{Ba} + 3Ti^{\times}_{Ti} + V''''_{Ti} + 12O^{\times}_{O} + TiO_2 + O_2(g) \tag{1.5$'$}$$

From this point of view, Makovec et al. [10] revealed aspects concerning the defect chemistry in Ce-doped $BaTiO_3$ solid solutions placed on a hypothetical tie-line between $BaTiO_3$ and the composition corresponding to the ratio $TiO_2/CeO_2 = 1$ only for ceramics sintered in a reducing atmosphere. Unfortunately, no data regarding the phase composition, microstructure, and defect chemistry of similar ceramics sintered in air were reported. Consequently, the compensation mechanism in some Ce-doped $BaTiO_3$ ceramics sintered in air when cerium is dissolved as Ce^{3+} at barium sites is still under debate.

Some authors showed that the type of compensating defects in donor-doped $BaTiO_3$ depends on several factors, such as the type of solute, its lattice site occupancy, stoichiometry (A/B ratio), and sintering temperature [22, 23].

Not only the compensation mechanism but also the solubility limit of cerium into the $BaTiO_3$ lattice is expected to be influenced by the incorporation mechanism and A/B ratio. For $BaTi_{1-x}Ce_xO_3$ ceramics prepared by solid state and sintered in air at 1350 °C for 5 days, the solubility extends up to a Ce^{4+} concentration of ~35 mol% [10], which is very close to the value of 33 mol% found by Ang et al. [25] for samples prepared by the same method and sintered at a higher temperature (1540 °C) for a much shorter time of 6 hours only. For

$Ba_{1-x}Ce_xTiO_3$ ceramics, a solubility limit for Ce^{3+} of 7 mol% for ceramics prepared by the Pechini method and sintered in air at 1350 °C for 5 hours was reported [11]. On the other hand, for the *A*-site cerium-doped $BaTiO_3$ with built-in titanium vacancies, described by the formula $Ba_{1-x}Ce_xTi_{1-x/4}V''''_{x/4}O_3$, Hennings et al. [1], Makovec et al. [10], and Jing et al. [26] found the same solubility limit of 8 mol%, for ceramics prepared by solid state and sintered in air, at temperatures above 1350 °C. The solubility of Ce^{3+} on Ba sites strongly decreases with sintering temperature, so that a solubility limit of only 4 mol% was found for ceramics prepared by the same route, but sintered at 1200 °C [10].

The *A*-site and *B*-site cerium-doped barium titanate ceramics also show different electrical behavior. Thus, according to the latest literature data for $BaTi_{1-y}Ce_yO_3$ solid solutions, the Curie temperature shifts slowly towards lower temperatures when increasing Ce^{4+} content, with a rate of about –7 °C/at% [27] or –3 °C/at% [28]. Besides, for a substitution degree $y > 0.1$, the increase of the solute content in $BaTi_{1-y}Ce_yO_3$ ceramics induces a gradual change in the electrical behavior, from a classic ferroelectric towards a relaxor [29,30]. Similarly, for the *A*-site cerium-doped solid solutions, a much faster linear decrease of the Curie temperature with the increase of Ce^{3+} content was found, with a rate of the Curie temperature decrease of –18 °C/at% [26] for $Ba_{1-x}Ce_xTi_{1-x/4}V''''_{x/4}O_3$, while values of –21 °C/at% [11, 31] and –22.5 °C/at% [32] were found for $Ba_{1-x}Ce_xTiO_3$ ceramics.

A specific feature of the ferroelectric–paraelectric phase transition in *A*-site cerium-doped $BaTiO_3$ ceramics sintered above 1350 °C is that the permittivity maxima remain very sharp, proving a typical ferroelectric behavior for all the compositions in the solubility limit [1, 11, 12, 26, 31]. Only Yasmin et al. [32] reported diffuse phase transitions and lower values of dielectric maxima ($\varepsilon_r < 3000$) for their fine-grained $Ba_{1-x}Ce_xTiO_3$ ($0 \leq x \leq 0.04$) ceramics sintered in air at 1200 °C/4 h.

Taking into account the fact that almost similar electrical behavior was reported for ceramics sintered in air, with identical Ce^{3+} content incorporated on Ba sites but with dissimilar (Ba+Ce)/Ti ratios and processed by different routes in different sintering conditions, we concluded that a systematic study concerning the influence of the cation stoichiometry (*A*/*B* ratio) on the dielectric characteristics of the Ce^{3+}-doped $BaTiO_3$ ceramics prepared by the same processing technique and sintered in air at different temperatures deserves more attention. For this purpose, we have chosen two compositions, with different *A*/*B* ratios, but both with the same cerium content, that is 5 at% Ce^{3+} incorporated on Ba sites into a $BaTiO_3$ lattice. Several works reported a shift of the Curie temperature value near to 25 °C [1, 11, 12, 31] for this Ce^{3+} concentration and, consequently, this kind of composition provides promising candidates for room temperature ceramic capacitor applications.

Various methods such as the solid-state reaction [1, 26, 32], sol–gel [33] and the Pechini method [11,12] have been utilized for preparing Ce^{3+}-doped $BaTiO_3$. The modified Pechini process is known as an excellent preparation technique for controlling stoichiometry and homogeneity of the oxide materials [34] and it was employed for the present study.

In the present work, 5% Ce-doped $BaTiO_3$ nanopowders were prepared by a modified Pechini method. Two types of solid solutions were comparatively investigated: (i) the first one is similar to the composition investigated by Hwang and Han [11, 12], which corresponds to the nominal formula $Ba_{0.95}Ce_{0.05}TiO_3$ (i.e. a cation ratio (Ba + Ce)/Ti = 1) and the lack of any compensating ionic defects, and (ii) one described by the nominal formula $Ba_{0.95}Ce_{0.05}Ti_{0.9875}(V''''_{Ti})_{0.0125}O_3$ ((Ba + Ce)/Ti ≅ 1.0127), which has the adjusted concentration of built-in titanium vacancies, as studied by Jing et al. [26]. Actually, for the first nominal composition $Ba_{0.95}Ce_{0.05}TiO_3$, taking into account the high cerium content (with an order of magnitude higher than the critical concentration), which excludes the charge compensation via the electronic mechanism, if a single-phase composition is assumed, the correct nominal formula would be $Ba_{0.95}Ce_{0.05}TiO_{3.025}$, which involves a charge compensation by oxygen ions on interstitial sites, according to Equation (1.2). Since this compensation mechanism is very unlikely, segregation of secondary phases should occur in this case. Therefore, we considered that we can refer to this composition as being described by the nominal formula $Ba_{0.95}Ce_{0.05}TiO_3$, as in other similar works concerning highly Ce^{3+}-doped $BaTiO_3$ [11, 12, 31, 32].

1.2 Sample Preparation, Phase and Nano/Microstructural Characterization

1.2.1 Powders

1.2.1.1 Powder Synthesis Procedure

Nanopowders with nominal compositions, $Ba_{0.95}Ce_{0.05}TiO_3$ and $Ba_{0.95}Ce_{0.05}Ti_{0.9875}(V_{Ti}^{''''})_{0.0125}O_3$, were prepared via a modified Pechini method [15] from titanium isopropoxide ($Ti(iOC_3H_7)_4$, Merck, Germany), cerium(III) carbonate ($Ce_2(CO_3)_3{\cdot}xH_2O$, Acros Organics, US), barium carbonate (Merck, Germany), citric acid (99.5% GR grade, Merck, Germany) as chelating agent and ethylene glycol (99.5% GR grade, Merck, Germany) as both solvent and polyesterification agent.

A solution of 5 mL of titanium isopropoxide was added to a solution previously obtained by dissolving under heating 5 g of citric acid in 20 mL of ethylene glycol. This reaction mixture was heated at 80 °C/2 h on a plate under magnetic stirring. Separately, for each nominal composition, two different solutions of barium citrate and cerium citrate were prepared. Barium citrate solutions were obtained by dissolving in 20 mL 4 *M* aqueous citric acid solution of 3.1864 g and 3.2267 g $BaCO_3$, for the preparation of the Ce–$BaTiO_3$ powders. Cerium citrate solutions were obtained by dissolving in 5 mL 4 *M* aqueous citric acid solution of 0.2415 g and 0.2445 g $Ce_2(CO_3)_3{\cdot}xH_2O$, respectively. In both cases barium citrate and cerium citrate solutions were added to the yellowish solution containing titanium ions. The resulting colourless solutions were kept under magnetic stirring at 80 °C/1 h. During this process, the solutions became increasingly viscous until yellow gels were produced. These gels were thermally treated on a sand bath at 135 °C/25 h (without stirring) for polyesterification reaction and water removal. The resulting orange-brown glassy resins were burnt out in air, at 400 °C/2 h in an electric furnace, to remove the organic matter. During the thermal treatment, the volume of resins has gradually increased, until foam-like, black residues or the so-called "precursors", were formed. After cooling, the residues were ground, so that fine powders, with a vitreous aspect, were obtained. The final thermal treatment at 900 °C/2 h was carried out to obtain yellowish Ce–$BaTiO_3$ oxide nanopowders.

1.2.1.2 Phase Composition and Structure

X-ray diffraction measurements at room temperature were performed with a Shimadzu XRD 6000 diffractometer (SHIMADZU, Kyoto, Japan) using Ni-filtered CuKα

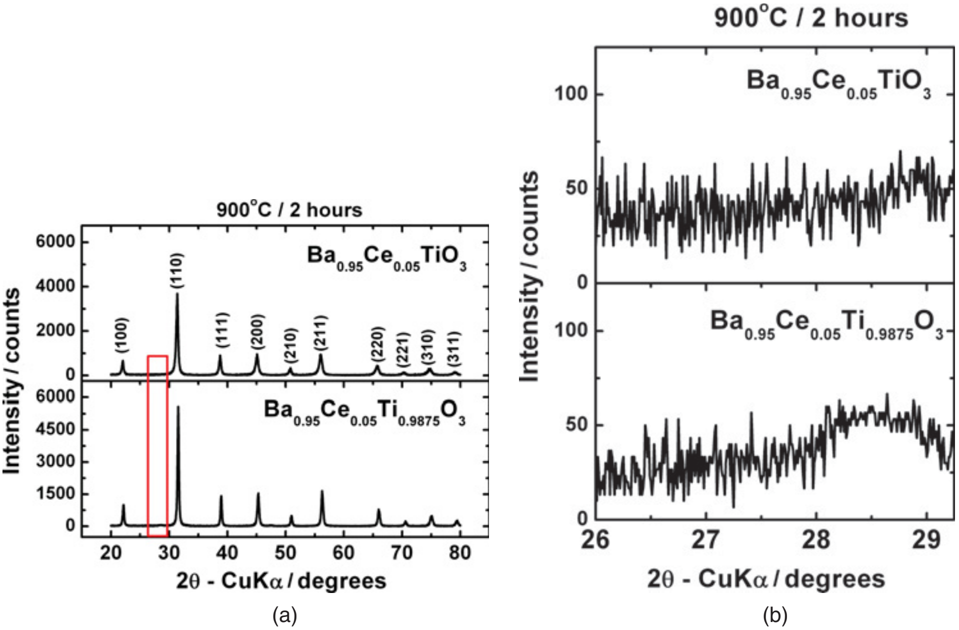

Figure 1.1 *(a) Room temperature XRD patterns of 5% Ce-doped $BaTiO_3$ powders thermally treated at 900 °C/2 h and (b) detail (rectangle in Figure 1.1(a)) of the region corresponding to diffraction angles 2θ =26–29.25°*

radiation ($\lambda = 1.5418$ Å), with a scan step of 0.02° and a counting time of 1 s/step, for $2\theta \in (20-80)°$.

The XRD patterns obtained for the powders thermally treated at 900 °C/2 h and slowly cooled at room temperature show the presence of a well-crystallized perovskite phase, identified by the main diffraction reflections specific to the $BaTiO_3$ structure, for both compositions (Figure 1.1(a)). The lack of visible, well-defined peaks corresponding to some secondary phases seems to indicate monophasic compositions. A careful examination of the region corresponding to diffraction angles of $2\theta = 26–29.25°$ in the XRD pattern of the $Ba_{0.95}Ce_{0.05}Ti_{0.9875}(V''''_{Ti})_{0.0125}O_3$ powder (Figure 1.1(b)) shows a very small, flattened feature centred around $2\theta = 28.5°$, which might correspond to small amounts of CeO_2 and polytitanates secondary phases, which proves that dopant was not yet entirely incorporated in the perovskite lattice. We cannot exclude the presence of these secondary phases also in the $Ba_{0.95}Ce_{0.05}TiO_3$ powders, but most likely they are below the detection limit.

Based on XRD data, structural characteristics as lattice constants and average crystallite size values were also calculated. Parameters to define the position, magnitude, shape, and integral breadth or full width at half maximum (FWHM) of the profile of the individual peaks are obtained using the pattern fitting and profile analysis of the original X-ray 5.0 program. The lattice constants calculation is based on the least squares procedure (LSP) using the linear multiple regressions for several XRD lines, depending on the unit cell symmetry. To deconvolute size-*D* and strain-*S* broadening from the XRD patterns of the powders, the multiple line analysis and integral breadth methods applied to the observed profiles

Table 1.1 *Structural parameters of 5% Ce–BaTiO$_3$ powders thermally treated at 900 °C/2 h*

	Composition		
Structural parameters	$Ba_{0.95}Ce_{0.05}TiO_3$		$Ba_{0.95}Ce_{0.05}Ti_{0.9875}O_3$
Symmetry	Cubic	Tetragonal	Cubic
a (Å)	4.0265(32)	4.0182(32)	4.0091(22)
c (Å)	4.0265(32)	4.0529(54)	4.0091(22)
c/a	1.000	1.0086(21)	1.000
V (Å3)	65.28(18)	65.44(19)	64.44(11)
<*D*> (Å)	741(39)	766(65)	792(78)
<*S*> $\times 10^{-3}$	0.26(3)	0.40(4)	0.10(2)

(properly approximated with Pearson's VII analytic functions) were used. Thus, analysis of the diffraction peak positions and profiles emphasizes a single cubic form in the sample with built-in compensating defects, whereas a mixture of cubic and tetragonal modifications was found in the $Ba_{0.95}Ce_{0.05}TiO_3$ powders. Calculation of structural parameters indicates that the presence of the titanium vacancies seems to favor the cubic modification, by inducing the shrinkage of the unit cell by decreasing the lattice constant (Table 1.1). Values corresponding to the average crystallite size, <*D*>, and internal microstrains, <*S*>, were also listed in Table 1.1. A slightly higher value of the crystallite size and lower internal microstrains were found for the powder with built-in Ti vacancies.

1.2.1.3 Powder Morphology

In order to analyze powder morphology and crystallinity degree, TEM (transmission electron microscopy) and HRTEM (high-resolution TEM) coupled with SAED (surface area electron diffraction) investigations were performed using a high-resolution transmission electron Tecnai G^2 F30 S-TWIN microscope (FEI Co., The Netherlands).

TEM investigations revealed uniform particles with an average size of 76 nm for the $Ba_{0.95}Ce_{0.05}TiO_3$ powder and 81 nm for the $Ba_{0.95}Ce_{0.05}Ti_{0.9875}(V_{Ti}^{''''})_{0.0125}O_3$ powder (Figure1.2(a) and 1.3(a)). This estimation is in good agreement with the average crystallite size calculated from XRD data and demonstrates the single-crystal nature of the particles of both compositions. The $Ba_{0.95}Ce_{0.05}TiO_3$ powder consists of isolated particles with polyhedral shape and well-defined edges, which are joined at sharp angles (Figure 1.2(a)), in comparison with the more rounded particles, exhibiting a higher agglomeration tendency, corresponding to the $Ba_{0.95}Ce_{0.05}Ti_{0.9875}(V_{Ti}^{''''})_{0.0125}O_3$ composition (Figure 1.3(a)). The high crystallinity degree of the particles of both powders was emphasized by the highly ordered fringes corresponding to the crystalline planes (111), (211), and (200) in the HRTEM images of Figure 1.2(b) and 1.3(b), respectively.

It is worthy of mention that no particles with dissimilar morphologies, which might indicate the presence of some secondary phases, were detected by TEM analyses. Indexing of HRTEM images taken on several particles at the maximum magnification of the microscope, as well as indexing of selected surface area electron diffraction (SAED) patterns

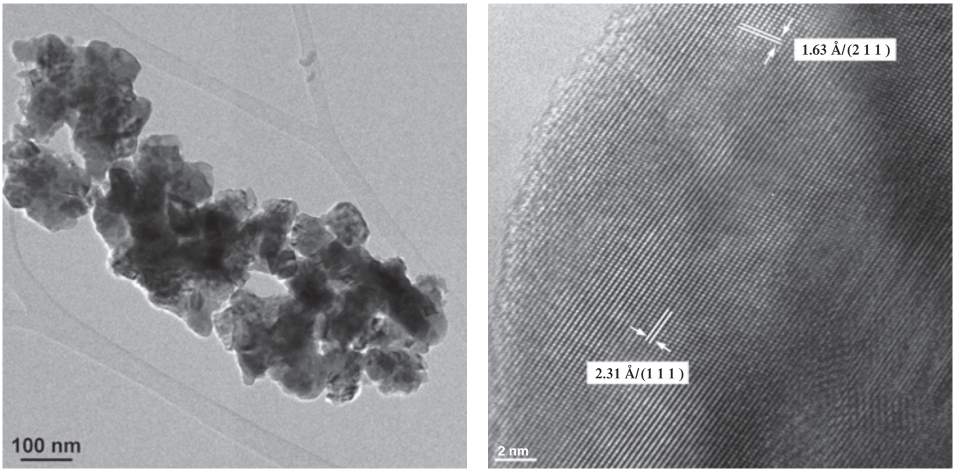

(a) (b)

Figure 1.2 *(a) TEM and (b) HRTEM images of $Ba_{0.95}Ce_{0.05}TiO_3$ powder thermally treated at 900 °C/2 h*

corresponding to several non-agglomerated areas and individual particles did not show the presence of CeO_2 or of any barium- or titanium-rich secondary phase. Moreover, EDX investigations carried out on several individual particles did not reveal any significant deviation of the Ba/Ti ratio (which should appear in Ba- or Ti-rich secondary phases) relative to $BaTiO_3$. However, this is not surprising, since the identification of small amounts of secondary phases in powdered samples is a harder task than detecting them by SEM in bulk ceramics.

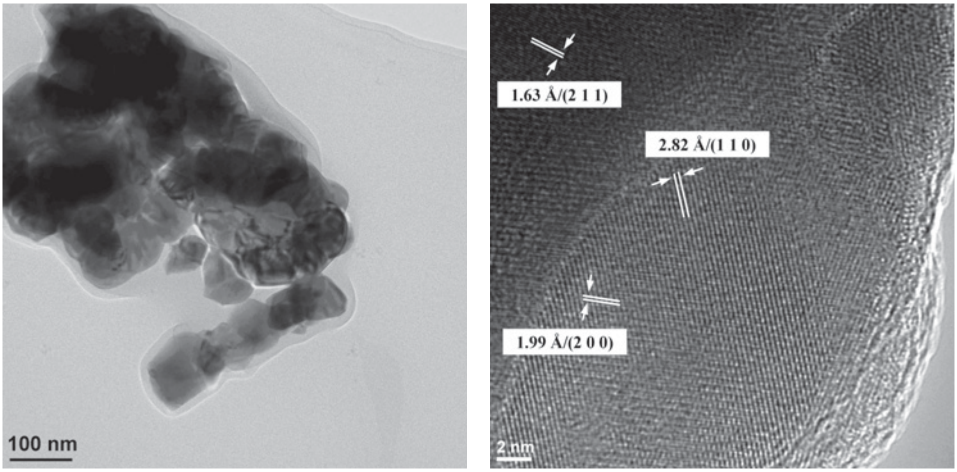

(a) (b)

Figure 1.3 *(a) TEM and (b) HRTEM images of $Ba_{0.95}Ce_{0.05}Ti_{0.9875}(V_{Ti}'''')_{0.0125}O_3$ powder thermally treated at 900 °C/2 h*

1.2.2 Ceramics

1.2.2.1 Ceramics Preparation

The powders were uniaxially pressed into pellets (of 13 mm diameter and ~2 mm thickness), using an organic binder (5% aqueous solution of polyvinyl alcohol). These pellets were sintered in air at temperatures of 1200 and 1300 °C, with a heating rate of 5 °C/min and a soaking time of 4 hours, and then they were slowly cooled down to room temperature at the normal cooling rate of the furnace.

Ceramic samples are denoted in the following as: A and B, representing specimens with the nominal composition $Ba_{0.95}Ce_{0.05}TiO_3$ sintered at 1200 and 1300 °C/4 h, respectively, while C and D refer to specimens with the nominal formula $Ba_{0.95}Ce_{0.05}Ti_{0.9875}(V_{Ti}^{''''})_{0.0125}O_3$ sintered in similar conditions. Ceramics A, B, and C exhibit a light-orange colour, while the ceramic D is intensely red.

1.2.2.2 Phase Composition and Structure

In order to check the phase purity in the ceramic samples, X-ray diffraction investigations were performed by means of an X'Pert Pro MPD diffractometer with a PIXcel detector (PANalytical, Almelo, The Netherlands), using the same radiation (Ni-filtered CuKα radiation), but with a scan step of 0.013° and a counting time of 150 s/step.

XRD patterns of both ceramics seem to indicate single-phase compositions, consisting of well-crystallized $BaTiO_3$ solid solutions, identified by the main reflections of the perovskite structure (Figure 1.4(a) and 1.5(a)). However, as in powders, the details (rectangles

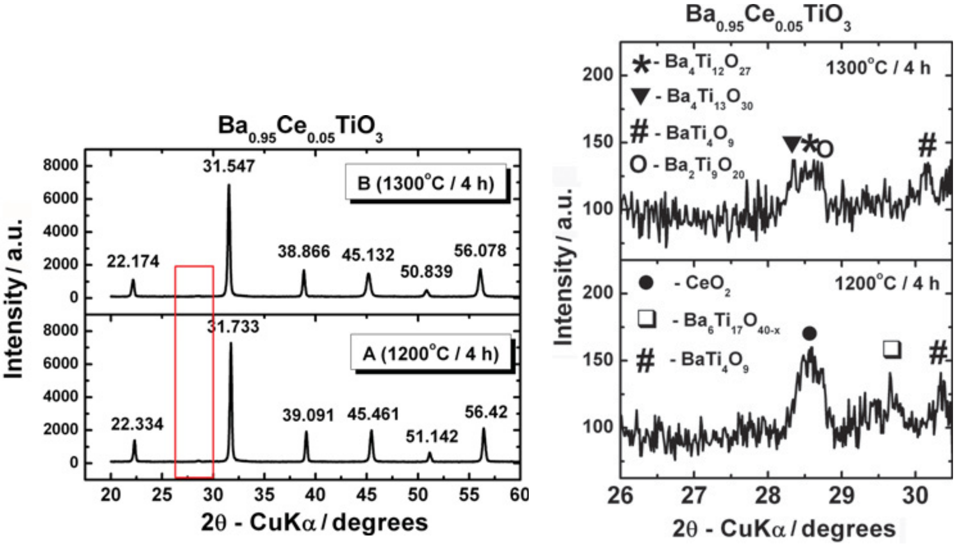

(a) (b)

Figure 1.4 *(a) Room temperature XRD patterns of ceramics corresponding to the nominal formula* $Ba_{0.95}Ce_{0.05}TiO_3$ *sintered in air at 1200 °C/4 h (sample A) and 1300 °C/4 h (sample B), respectively; (b) detail (rectangle in Figure 1.4(a)) of the region corresponding to diffraction angles* $2\theta = 26–30.5°$

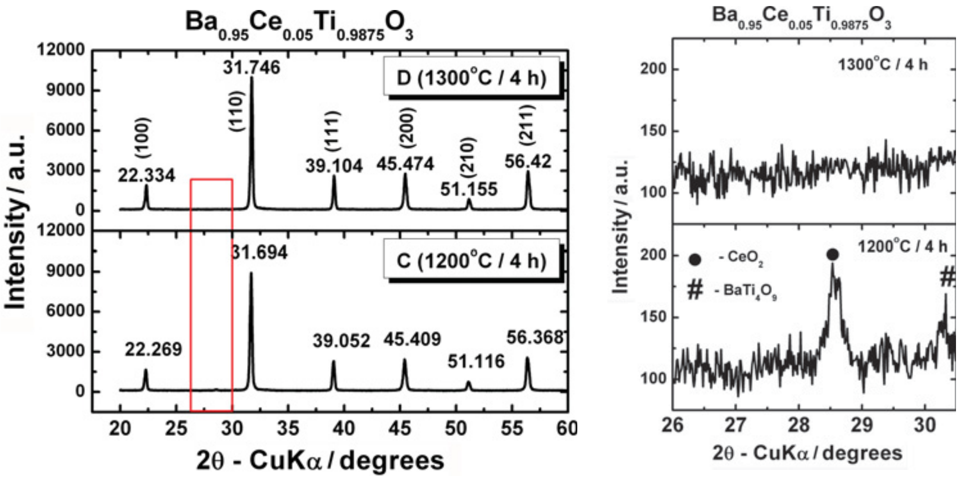

(a) (b)

Figure 1.5 *Room temperature XRD patterns of ceramics corresponding to the* $Ba_{0.95}Ce_{0.05}Ti_{0.9875}(V_{Ti}'''')_{0.0125}O_3$ *ceramic sintered in air at 1200 °C/4 h (sample A) and 1300 °C/4 h (sample B), respectively; (b) detail (rectangle in Figure 1.5(a)) of the region corresponding to diffraction angles* $2\theta = 26–30.5°$

in Figures 1.4(a) and 1.5(a)) of the region corresponding to diffraction angles $2\theta = 26–30.5°$ show the presence of small amounts of secondary phases (Figure 1.4(b) and 1.5(b)). Thus, for both ceramics sintered at 1200 °C, irrespective of the (Ba + Ce)/Ti ratio, CeO_2 (JCPDS file no. 43-1002) was identified by means of the main reflection (111) at $2\theta = 28.54°$. Typically, precipitation in solid solutions occurs at lower temperatures because of the reduced solid solubility of the dopant. As already mentioned, cerium, acting as a donor on Ba sites, exhibits a maximum solubility of only 4 at% Ce^{3+} on Ba sites at 1200 °C. Therefore, the Ce^{3+} concentration of 5 at% stipulated by the nominal compositions of our samples overpassed the solubility limit at 1200 °C, which might apparently explain the precipitation process. However, when the solubility limit is exceeded, Ce^{3+} should be precipitated and not Ce^{4+} [35]. Therefore, another explanation should be found for CeO_2 precipitation in the ceramic samples sintered at 1200 °C. According to the study of Makovec and Kolar [35], based on their HRTEM/SAED results on single phase Ce^{3+}-doped $BaTiO_3$ ceramics, internal partial oxidation of Ce^{3+} to Ce^{4+}, accompanied by heterogeneous precipitation of small amounts of fluorite CeO_2 and polytitanates in the perovskite matrix, takes place after annealing at higher temperatures of 1000–1100 °C. They demonstrated that this process is controlled by oxygen diffusion, which is strongly enhanced at the grain boundary regions and extended defects (subgrain boundaries and (111) twin boundaries) in comparison with oxygen diffusion in the perovskite lattice. The stoichiometry of the nominal compositions of Ce^{3+}–$BaTiO_3$ solid solutions demands that precipitation of CeO_2 be accompanied by precipitation of some TiO_2-rich secondary phases. Therefore, the partial reoxidation of Ce^{3+} induces the removal of Ce^{4+} ions together with Ti^{4+} ions in the atomic ratio Ce/Ti = 4/3, from the $Ba_{0.95}Ce_{0.05}Ti_{0.9875}(V_{Ti}'''')_{0.0125}O_3$ solid solution. For the $Ba_{0.95}Ce_{0.05}TiO_3$ solid solution, the amount of precipitated Ti-rich phases should be even larger (Ce/Ti = 1) by considering the lack of compensating defects.

Indeed, in Figure 1.4(b) one can observe that, beside CeO_2, small amounts of polytitanate phases consisting of a mixture of Ba_4TiO_9 (JCPDS file no. 77-1345) and $Ba_6Ti_{17}O_{40}$ (JCPDS file no. 43-0559) were identified for the $Ba_{0.95}Ce_{0.05}TiO_3$ ceramic sintered at 1200 °C/4 h. For the $Ba_{0.95}Ce_{0.05}Ti_{0.9875}(V_{\mathrm{Ti}}'''')_{0.0125}O_3$ specimen sintered in the same conditions only Ba_4TiO_9 was detected (Figure 1.5(b)).

The segregation of CeO_2 in the grain boundary regions induces the incorporation of a lower amount of cerium solute in the perovskite matrix than one corresponding to $x = 0.05$, stipulated by the nominal formulae. Consequently, for the ceramic specimens sintered at 1200 °C, the lowering of Ce^{3+} content incorporated on Ba sites into the perovskite lattice should be reflected in the Curie temperature, which should exhibit a higher value than one of ~25 °C, corresponding to the solid solution with 5 at% Ce^{3+} integrated on barium sites [1, 11, 12, 31]. Dielectric investigations shown later in Section 1.3 were aimed to clarify this aspect.

After sintering at 1300 °C, the ceramic corresponding to the nominal composition with built-in V_{Ti}'''' seems to be single phase, whereas for the ceramic without compensating defects, small amount of polytitanate phases with a variable Ba/Ti ratio (Ba/Ti = 3–4.5) are still identified. These polytitanates might be $Ba_4Ti_{12}O_{27}$ (JCPDS file no. 04-011-4266), $Ba_4Ti_{13}O_{30}$ (JCPDS file no. 73-1188), Ba_4TiO_9 (JCPDS file no. 77-1565), and $Ba_2Ti_9O_{20}$ (JCPDS file no. 40-0405) (Figures 1.4(b) and 1.5(b)). This indicates that, as was expected, in $Ba_{0.95}Ce_{0.05}TiO_3$ ceramic, the excess of titanium (relative to the nominal formula corresponding to the most likely charge compensation mechanism) could not be fully accommodated in the perovskite lattice and, consequently, it was expelled as Ti-rich secondary phases. CeO_2 precipitate was not identified in the ceramic with built-in compensating defects sintered at 1300 °C, which means that the increase of sintering temperature no longer favours the internal reoxidation process of Ce^{3+} ions, at least for the $Ba_{0.95}Ce_{0.05}Ti_{0.9875}(V_{\mathrm{Ti}}'''')_{0.0125}O_3$ composition. Therefore, in this case, the perovskite solid solution should present the same composition as one stipulated by the nominal formula. For the $Ba_{0.95}Ce_{0.05}TiO_3$ composition this assertion is difficult to sustain, since the main diffraction peak of the potential CeO_2 residual phase overlaps the main reflections of some polytitanate phases. Therefore, we concluded that an indubitable internal reoxidation process of Ce^{3+} involving CeO_2 precipitation takes place in the ceramics sintered at 1200 °C. Complementary investigations are required in order to establish what really happens with Ce^{3+} ions in the ceramics sintered at 1300 °C, especially in the one corresponding to the nominal formula $Ba_{0.95}Ce_{0.05}TiO_3$.

The structural parameter calculations based on the XRD data showed a significant decrease of the unit cell parameters and volume for the ceramic samples with built-in Ti vacancies, irrespective of the sintering temperature (Table 1.2).

For the ceramics sintered at 1200 °C, the evolution of the unit cell symmetry maintains the same tendency as in the precursor oxide powders, that is the composition with built-in compensating defects (C) favours the cubic modification, while the $Ba_{0.95}Ce_{0.005}TiO_3$ (A) sample consists of a mixture of tetragonal and cubic forms.

Concerning the specimens sintered at 1300 °C, a mixture consisting of a cubic major phase and a minor tetragonal modification was emphasized for the $Ba_{0.95}Ce_{0.05}Ti_{0.9875}$ $(V_{\mathrm{Ti}}'''')_{0.0125}O_3$ ceramic (D), whereas a pure tetragonal form was found for the

Table 1.2 *Structural parameters of 5% Ce–BaTiO$_3$ ceramics*

Structural parameters	Composition					
	$Ba_{0.95}Ce_{0.05}TiO_3$			$Ba_{0.95}Ce_{0.05}Ti_{0.9875}O_3$		
	A (1200 °C)		B (1300 °C)	C (1200 °C)	D (1300 °C)	
Symmetry	Cubic +	Tetragonal	Tetragonal	Cubic	Cubic +	Tetragonal
a (Å)	4.0155(13)	4.0067(19)	4.0239(11)	3.9974(4)	3.9721(24)	3.9878(7)
c (Å)	4.0155(13)	4.0173(44)	4.0465(26)	3.9974(4)	3.9721(24)	4.0006(9)
c/a	1.0000	1.0026(16)	1.0056(9)	1.0000	1.0000	1.0032(26)
V (Å^3)	64.74(6)	64.49(13)	65.52(8)	63.88(2)	62.67(11)	63.62(22)

$Ba_{0.95}Ce_{0.05}TiO_3$ sample (B). Fitting was carried out using JCPDS files no. 31-0174 for the cubic form and no. 05-0626 for the tetragonal form, respectively.

The presence of a mixture of two perovskite modifications (cubic and tetragonal) detected in some of the specimens might indicate the proximity of the ferroelectric–paraelectric phase transition close to room temperature, while the presence of a pure tetragonal form in the ceramic sample without built-in titanium vacancies and sintered at a higher temperature (B) seems to indicate a typical ferroelectric state.

In the case of $Ba_{0.95}Ce_{0.05}TiO_3$ specimens, higher values of lattice parameters were determined for the tetragonal form, when sintering was carried out at a higher temperature (1300 °C), while an opposite evolution against sintering temperature is indicated by the lattice parameter values corresponding to the major cubic phase of the $Ba_{0.95}Ce_{0.05}Ti_{0.9875}(V_{Ti}^{''''})_{0.0125}O_3$ sample. This latter evolution seems normal and is consistent with the slight shift of the main diffraction peaks of the perovskite phase towards higher values of the diffraction angle shown by the XRD pattern (Figure 1.5(a)). This shift, together with the lack of CeO_2 precipitate in the sample with built-in Ti vacancies sintered at 1300 °C seems to originate in an increasing amount of solute with a lower ionic radius incorporated on *A*-sites of the perovskite lattice, when the sintering temperature increased. Therefore, in the ceramic specimen sintered at 1300 °C, the whole cerium content stipulated by the nominal formula was incorporated as Ce^{3+} into the barium titanate lattice, in comparison with the sample with similar nominal composition sintered at 1200 °C. This latter sample should be in fact poorer in Ce^{3+}, taking into account the small amount of CeO_2 precipitate identified at the detection limit in its XRD pattern.

It remains to elucidate the unexpected shift of the diffraction peaks towards lower values of the diffraction angles (Figure 1.4(a)) and the significantly higher values of the lattice parameters for the sample described by the nominal formula $Ba_{0.95}Ce_{0.05}TiO_3$ sintered at 1300 °C, in comparison with those corresponding to the specimen with a similar nominal composition but sintered at 1200 °C (Table 1.2).

We also need to mention that in perovskite solid solutions sometimes the average cubic state can correspond at the local level to a non-centrosymmetric phase with a low distortion, close to the cubic one ("pseudocubic state") or to a mixture of such states. Therefore, dielectric investigations at different temperatures were performed to provide additional

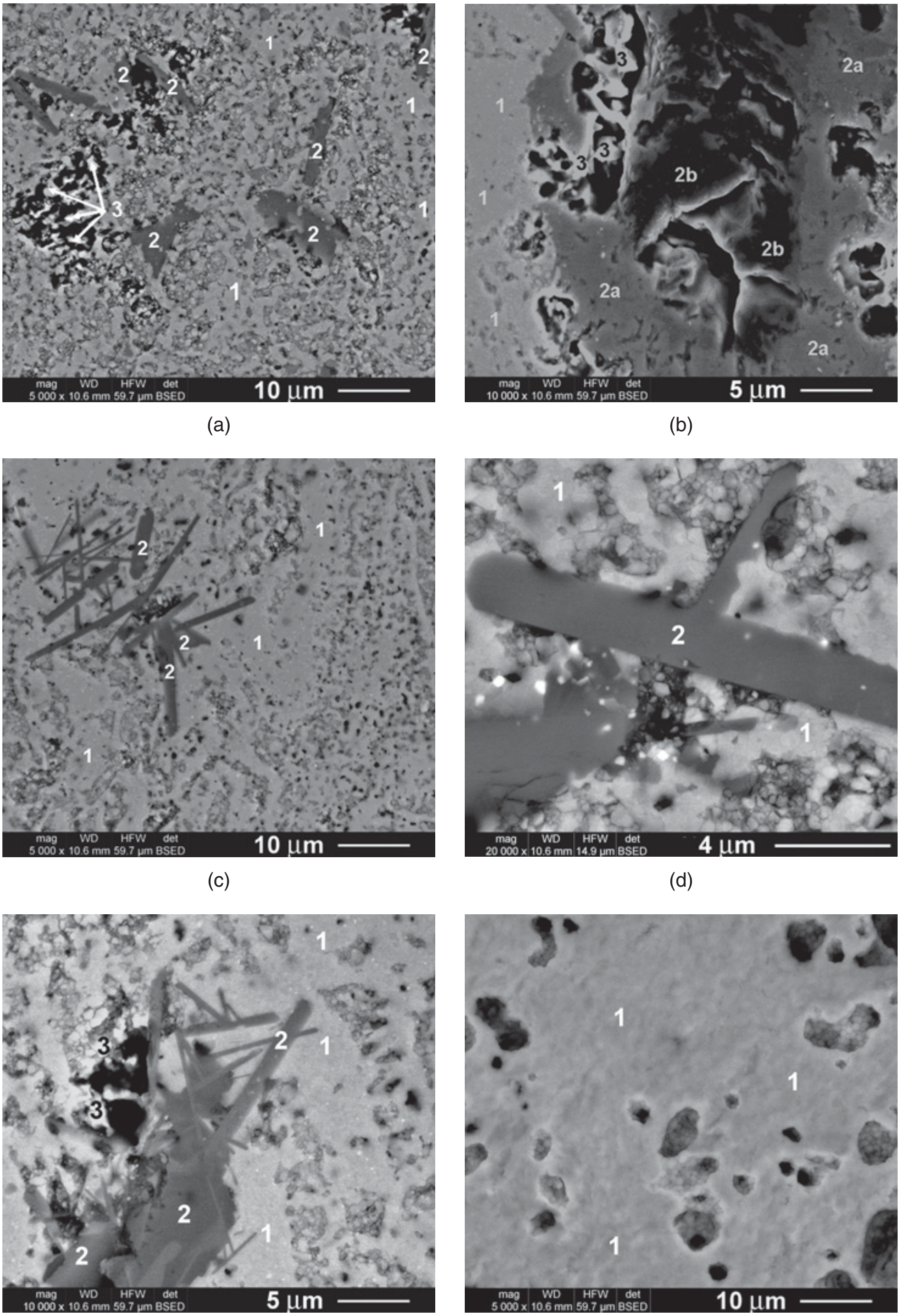
1
2
3
2a
2b
mag WD HFW det
5 000 x 10.6 mm 59.7 µm BSED
10 µm
10 000 x 10.6 mm 59.7 µm BSED
5 µm
20 000 x 10.6 mm 14.9 µm BSED
4 µm

(a) (b)

(c) (d)

(e) (f)

information and to explain the structural features determined by means of the XRD data at room temperature.

1.2.2.3 Ceramics Microstructure

A high-resolution scanning electron microscope Quanta Inspect F (FEI Co., The Netherlands) with a field emission (FE gun SEM coupled with energy-dispersive X-ray spectroscopy (EDX)) was used to analyze the microstructure and the chemical composition of the ceramics. To search for possible existing secondary phases, FE-SEM investigations were carried out first in BSE (back-scattered electron) mode on polished sections. After subsequent thermal etching, microstructural features were examined by performing analyses in SE (secondary electron) mode. The average grain size was calculated using the OriginPro 8.5 software (statistics on column) by taking into account equivalent size measurements on ~70 grains (from images of appropriate magnifications obtained from various microscopic fields) performed by means of the microscope software ImageJ. The relative density of the sintered ceramic pellets was calculated as the ratio between the apparent density measured by Archimedes' principle and the crystallographic (theoretical) density.

The FE-SEM image in BSE mode on a polished cross-section of the $Ba_{0.95}Ce_{0.05}TiO_3$ ceramic sintered at 1200 °C shows the presence of some dark-gray areas denoted 2, of various sizes and irregular shapes, but predominantly with an elongated aspect (i.e. fibrous, acicular and rod-like morphology), uniformly distributed in a light-gray matrix denoted 1 (Figure 1.6(a) and (b)). This indicates that titanium-rich secondary phases are formed in the whole matrix of perovskite grains. Such regions were observed in three of the four samples investigated here, that is both ceramics A and B corresponding to the nominal composition $Ba_{0.95}Ce_{0.05}TiO_3$, irrespective of sintering temperature, and the ceramic specimen C with built-in titanium vacancies sintered at 1200 °C. Small CeO_2 grains of bright-white color, denoted 3, were also identified in the ceramic samples A and C sintered at 1200 °C/4 h. Only ceramic D, with built-in Ti vacancies, sintered at 1300 °C, seems to be single phase. Figure 1.6(a) and (b) shows a general view indicating the distribution of phases and a detail of a region containing polytitanate phases with a variable Ba:Ti ratio (Ba:Ti ~ 1:3–1:4), corresponding mainly to $Ba_6Ti_{17}O_{40}$ (denoted 2a) and $BaTi_4O_9$ (denoted 2b), in a $Ba_{0.95}Ce_{0.05}TiO_3$ sample (A) sintered at 1200 °C, while Figure 1.6(c) and (d) reveals a general view and a detail showing the elongated shape of an area specific to the secondary polytitanate phase with a Ba:Ti ratio ~1:3 in ceramic sample B, with similar composition but sintered at 1300 °C. A distribution of phases similar to that indicated in Figure 1.6(a) was observed in ceramic sample C (Figure 1.6(e)), which corresponds to the

◀

Figure 1.6 FE-SEM images in the BSE mode on polished cross-sections of ceramics before thermal etching: (a) general view and (b) detail of sample A (without Ti vacancies and sintered at 1200 °C/4 hours), showing secondary phases denoted in accord with quantitative EDX analyses: (1) perovskite matrix; (2a) poly-titanate phase with a Ba:Ti ratio ~1:3; (2b) polytitanate phase with a Ba:Ti ratio ~1:4; (3) CeO_2; (c) general view and (d) detail of sample B (with similar composition, but sintered at 1300 °C/4 h), showing the predominantly elongated shape of poly-titanates areas; (e) detail of sample C (with built-in Ti vacancies sintered at 1200 °C/4 h) and (f) general view of the monophasic sample D (with built-in Ti vacancies sintered at 1300 °C/4 h)

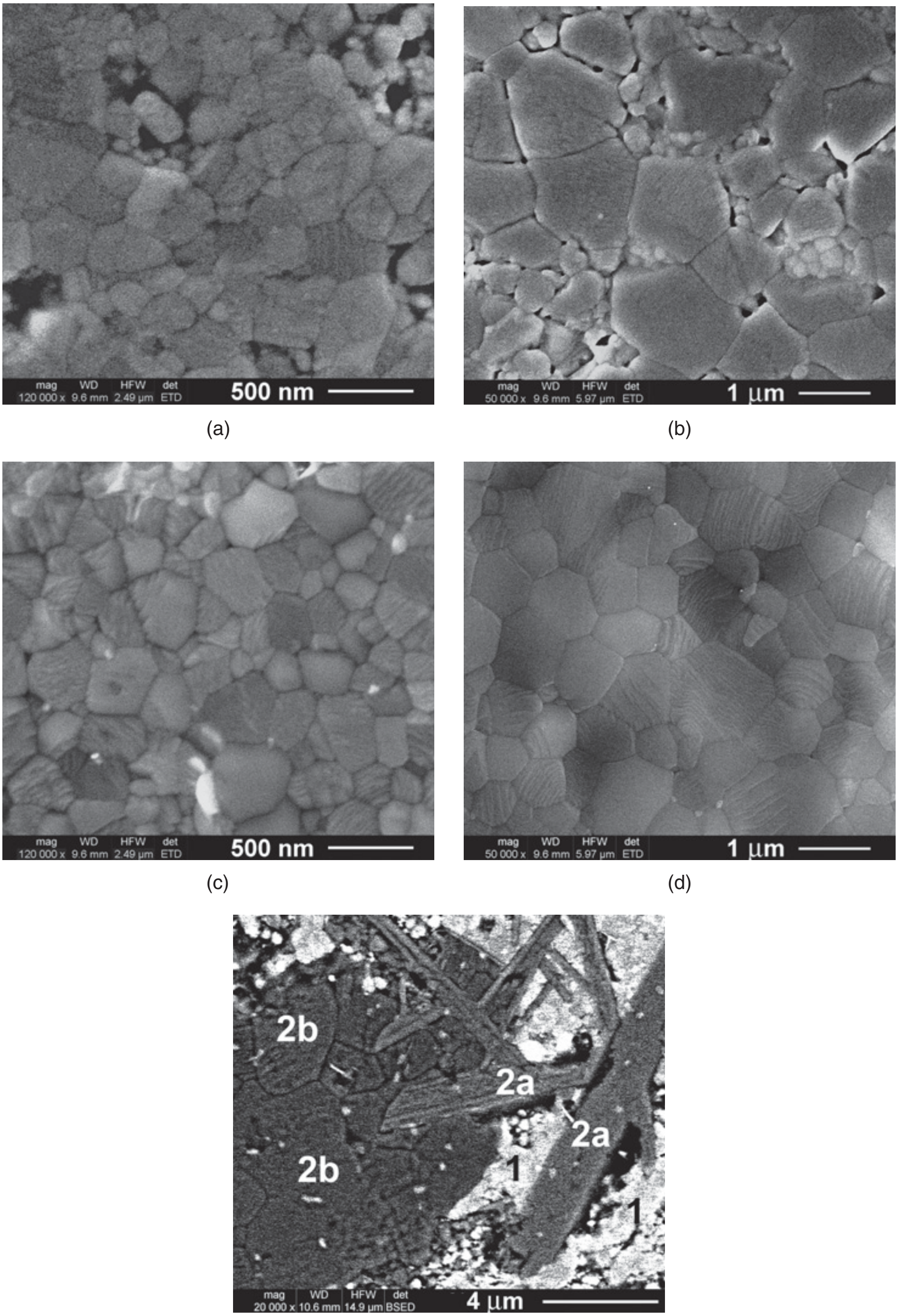
mag WD HFW det
120 000 x 9.6 mm 2.49 µm ETD
500 nm
mag WD HFW det
50 000 x 9.6 mm 5.97 µm ETD
1 µm
mag WD HFW det
120 000 x 9.6 mm 2.49 µm ETD
500 nm
mag WD HFW det
50 000 x 9.6 mm 5.97 µm ETD
1 µm
2b
2a
2a
2b
1
1
mag WD HFW det
20 000 x 10.6 mm 14.9 µm BSED
4 µm

(a) (b)

(c) (d)

(e)

specimen with built-in Ti vacancies, also sintered at 1200 °C. A general view of sample D sintered at 1300 °C and described by the same nominal formula indicates the single-phase composition of this ceramic (Figure 1.6(f)).

Values of the Ba:Ti ratio in several zones marked with numbers that correspond to each phase on FE-SEM images were determined by quantitative EDX analyses. Any possible difference in cerium amount in the samples sintered at 1200 °C in comparison with those sintered at 1300 °C is hard to determine in the regions corresponding to the perovskite phase. At this doping level, the results are not relevant since they are found in the margin of error of measurement. Moreover, because of overlapping of the strongest Ce line (Ce$L\alpha_{1,2}$) by the Ba$L\beta_{1,4}$ line, an accurate estimation of small cerium concentrations in barium titanate solid solutions becomes an even more difficult task. Given the high sensitivity of the Curie temperature value to very small amounts of Ce^{3+} incorporated on Ba sites, it is expected that dielectric measurements can provide a more realistic view in terms of dopant incorporation at different sintering temperatures in the investigated ceramic samples.

Regarding the charge compensation mechanism in perovskite phases, it is clear that exclusive compensation via a barium vacancy is very unlikely, since no barium-rich secondary phases were detected in any of our ceramics. Only in the single-phase ceramic sample D could one assume an exclusive compensation via Ti vacancies taking into account the starting formula and the lack of secondary phases. Based on the values of the Ba/Ti ratio estimated from quantitative EDX analyses, we were not able to find if the most likely compensating mechanism in the perovskite phase involves only Ti vacancies or an equal number of Ti and Ba vacancies in both ceramics sintered at 1200 °C (A and C), as well as in the ceramic sample without built-in compensating Ti vacancies (B) sintered at 1300 °C. This difficulty originates in the close values of the Ba/Ti ratio specific to the mentioned compensation mechanisms. Thus, if we assume an amount of 4 at% Ce^{3+} on Ba sites incorporated in the perovskite phase of both ceramics sintered at 1200 °C, compensation via exclusive Ti vacancies should involve a Ba/Ti ratio of ~0.97 in the perovskite solid solution, while the mechanism involving equal numbers of barium and titanium vacancies should lead to a Ba/Ti ratio of ~0.96. The capability of our equipment in providing very accurate quantitative results is not powerful enough to distinguish between them. We can only conclude that FE-SEM observations regarding the phase composition of the sintered specimens supported the XRD data.

FE-SEM investigations in the SE mode were carried out on polished cross-sections after thermal etching. The FE-SEM image of the ceramic sample A ($Ba_{0.95}Ce_{0.05}TiO_3$) sintered at 1200 °C/4 h shows a fine-grained, non-uniform, and porous microstructure, consisting of submicrometer grains (average grain size of 0.35 μm) with no well-marked grain boundaries and a significant amount of intergranular, interconnected porosity (Figure 1.7(a)). In some regions, these small grains exhibit an obvious aggregation tendency by neck formation, which indicates a rather incipient sintering stage. This explains the lower

Figure 1.7 *FE-SEM images in SE mode (a) to (d) and in BSE mode (e) on polished cross-sections after thermal etching of: (a), (b)* $Ba_{0.95}Ce_{0.05}TiO_3$ *and (c), (d)* $Ba_{0.95}Ce_{0.05}Ti_{0.9875}(V_{Ti}'''')_{0.0125}O_3$ *ceramics, obtained after sintering in air at: (a), (c) 1200 °C/4 h and (b), (d) 1300 °C/4 h, respectively; (e) detail showing the morphology of polytitanate phases in the* $Ba_{0.95}Ce_{0.05}TiO_3$ *ceramic sintered at 1300 °C/4 h*

value of the relative density of only 74% determined for this specimen. Ceramic sample C ($Ba_{0.95}Ce_{0.05}Ti_{0.9875}(V_{Ti}^{''''})_{0.0125}O_3$), sintered in similar conditions, also exhibits a fine-grained microstructure (Figure 1.7(c)), but the microstructure is more homogeneous, the grain's shape and size is uniform, grain boundaries are well defined, and the intergranular porosity is significantly lower, which suggests that the presence of built-in $V_{Ti}^{''''}$ as compensation defects exerts a favourable influence on the densification process. An almost similar average grain size of 0.33 μm and a relative density value of ~87 % were determined for this sample. The densification process is more effective in the temperature range of 1200–1300 °C. Thus, the fine-grained ceramics with compositions described by both nominal formulae, which resulted after sintering at 1300 °C/4 h (B and D), show denser microstructures (Figure 1.7(b) and (d)) and significantly higher relative density values, of 83 and 95%, respectively. The $Ba_{0.95}Ce_{0.05}TiO_3$ sample (B) sintered at 1300 °C/4 h exhibits a non-homogeneous microstructure with bimodal grain size distribution, consisting of a lower amount of smaller grains of ~0.29 μm randomly distributed into a matrix of polyhedral larger grains of ~1.14 μm (Figure 1.7(b)). A residual intergranular porosity was still detected. As for the specimens sintered at 1200 °C, the beneficial effect on the densification induced by the presence of the built-in Ti vacancies is clearly revealed by the microstructure of the $Ba_{0.95}Ce_{0.05}Ti_{0.9875}(V_{Ti}^{''''})_{0.0125}O_3$ ceramic sample (D) sintered at 1300 °C. In this case, uniform grain growth took place, so that a homogeneous, almost pore-free matrix-like microstructure with unimodal grain size distribution and consisting of polyhedral grains (average grain size of 0.87 μm) with well-defined grain boundaries and almost perfect triple junctions was observed (Figure 1.7(d)).

A careful investigation of the secondary polytitanate phases with different Ba/Ti ratios was performed in order to find if they are somewhat different from a morphological point of view. The FE-SEM image in the BSE mode on polished and thermally etched cross-section of sample B indicated that the polytitanate phases exhibit dissimilar grain morphology. Thus, the darker gray polytitanate area with a higher Ti content (denoted 2b), whose Ba:Ti ratio of ~1:4 seems to indicate the presence of $BaTi_4O_9$, represents an agglomerate of equiaxial grains, while the lighter shaded elongated areas (denoted 2a), with a lower Ba:Ti ratio (of ~1:3), which according to the XRD pattern of this sample should correspond to $Ba_4Ti_{12}O_{27}$ (Figure 1.4(b)), show no structuring. Therefore, these unidimensionally extended and randomly oriented areas are actually individual grains with fibrous or rod-like morphology (Figure 1.7(e)), which sometimes are welded into bundles.

1.3 Dielectric Properties

The electrical measurements were performed on a parallel-plate capacitor configuration, by applying Pd–Ag electrodes on the polished surfaces of the sintered ceramic disks. The complex impedance in the frequency range of 2–10^6 Hz and for temperatures of –150–160 °C was determined by using a dielectric spectrometer CONCEPT 40 Novocontrol Technologies.

Figure 1.8 (a) to (d) presents the temperature dependence of permittivity at a few selected frequencies, in the range of 1 Hz–1 MHz. All the samples show a well-defined frequency-independent maximum of permittivity assigned to the ferroelectric–paraelectric phase transition (Curie temperature T_C). A small frequency dispersion is observed only in the

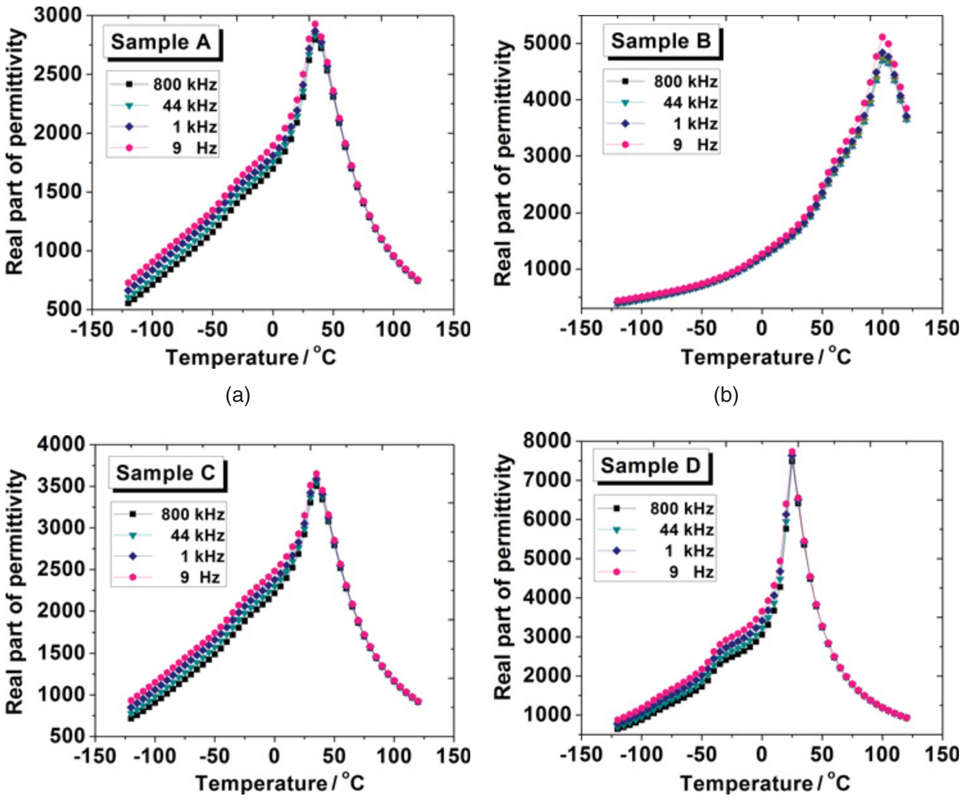

(a) (b)

(c) (d)

Figure 1.8 *Temperature dependence of the real part of the dielectric constant for: (a) sample A ($Ba_{0.95}Ce_{0.05}TiO_3$ sintered at 1200 °C/4 h); (b) sample B ($Ba_{0.95}Ce_{0.05}TiO_3$ sintered at 1300 °C/4 h); (c) sample C ($Ba_{0.95}Ce_{0.05}Ti_{0.9875}(V_{Ti}'''')_{0.0125}O_3$ sintered at 1200 °C/4 h); and (d) sample D ($Ba_{0.95}Ce_{0.05}Ti_{0.9875}(V_{Ti}'''')_{0.0125}O_3$ sintered at 1300 °C/4 h)*

ferroelectric phase for all the samples, with the exception of ceramic B (Figure 1.8(b)), while in the paraelectric state above T_C, the permittivity is almost frequency independent for all the ceramics.

For a better comparison of the dielectric data for all Ce-doped $BaTiO_3$ ceramics, the temperature dependence of the dielectric constant and tangent loss at a fixed frequency $f =$ 1 kHz are comparatively shown in Figure 1.9(a) and (b), respectively. The ceramics show good dielectric properties, with dielectric losses below 5% in the overall temperature range. In particular, the tangent loss values are significantly suppressed at temperatures above the Curie temperature T_C (Figure 1.9(b)). At the lowest temperature, the data revealed permittivity values slightly below 1000 for all of the ceramic samples. The ceramic with built-in titanium vacancies sintered at 1300 °C (sample D) presents the highest values of permittivity in the overall investigated temperature range, with a maximum at about ~7720, by comparison with values of about ~4910 (sample B), ~3620 (sample C), and ~2900 (sample A), at their corresponding ferroelectric–paraelectric transition temperatures (Figures 1.8

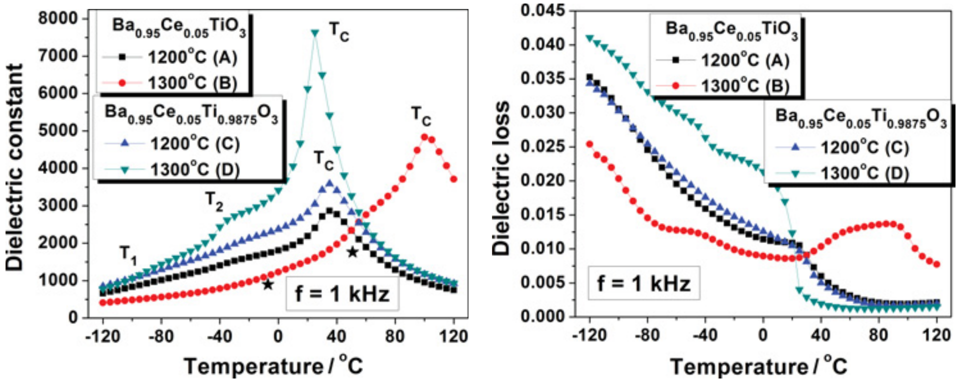

(a) (b)

Figure 1.9 *Comparative representation of the temperature dependence of the real part of the dielectric constant and (a) tangent loss, tan δ and (b) for 5% Ce–BaTiO$_3$ ceramics at frequency f = 1 kHz*

and 1.9(a)). The particular high permittivity determined for this sample is most likely due to its peculiar microstructure, showing almost full densification (Figure 1.7(d)), while the lowest permittivity of the A sample is mainly caused by its highest porosity (Figure 1.7(a)).

The ferroelectric–paraelectric phase transitions are clearly evidenced by the maximum permittivity, indicating a sharper ferroelectric–paraelectric phase transition for the ceramics sintered at a higher temperature (1300 °C) and a slightly more diffuse permittivity maxima for the samples sintered at a lower temperature (1200 °C). The phase transition diffuseness is most likely favoured by the lower densification and smaller grain size. The Curie temperature T_C is in the range of 25–35 °C, with the exception of the $Ba_{0.95}Ce_{0.05}TiO_3$ sample (B), for which T_C is much higher (around ~102 °C). This anomalous value is closer to the tetragonal–cubic phase transition temperature of undoped $BaTiO_3$ (110–120 °C) and confirms the pure tetragonal ferroelectric structure detected by XRD at room temperature, unlike the other sample (A) with a similar composition but sintered at a lower temperature, for which the mixture of cubic and tetragonal phases at room temperature is related to the proximity of the ferroelectric–paraelectric phase transition. However, one can observe that for both compositions sintered at a lower temperature (1200 °C), the Curie temperatures are slightly higher, of 36 and 35 °C for the ceramic samples A and C, respectively, by comparison with the value of 25 °C of specimen D, with built-in titanium vacancies, sintered at 1300 °C. According to Jing et al. [26], a T_C value of ~40 °C is obtained for the composition with 4 at% Ce^{3+} solubilized on Ba sites in $BaTiO_3$, so we can assume that an almost similar Ce^{3+} content must have been incorporated in the perovskite phase of our ceramics A and C sintered at 1200 °C. This value of Ce^{3+} concentration is similar to the solubility limit ($x = 0.04$) at 1200 °C found by Makovec et al. [10] for cerium incorporation as Ce^{3+} on Ba sites. These results support the conclusion emphasized by XRD data and FE-SEM observations that, at a lower sintering temperature, not the whole nominal cerium content was incorporated in the corresponding perovskite solid solutions because of the internal oxidation of Ce^{3+}, leading to precipitation of small amounts of CeO_2.

Only the single-phase ceramic sample D, with built-in compensating defects and sintered at 1300 °C, shows the normal Curie temperature value reported by the literature data for an incorporation of 5 at% Ce^{3+} on Ba sites into the $BaTiO_3$ lattice [1, 11, 12, 31]. Consequently, only in this specimen does the composition of the perovskite solid solution seem to coincide with the $Ba_{0.95}Ce_{0.05}Ti_{0.9875}(V_{Ti}'''')_{0.0125}O_3$nominal formula.

The features of the other structural phase transitions are not well defined in Figure 1.9(a). Values in the range of –25–40 °C were determined for the orthorhombic–tetragonal phase transition temperature T_1 for samples A, C, and D. Besides the significant decrease of the Curie temperature for Ce-doped compositions relative to undoped $BaTiO_3$, the additional shift of the orthorhombic–tetragonal phase transition temperature towards lower temperature values support the conclusions that for A, C, and D ceramics cerium was exclusively incorporated as Ce^{3+} on Ba sites into the perovskite lattice.

As in the case of the Curie temperature, one can observe that for both ceramics A and C sintered at a lower temperature (1200 °C), the values corresponding to the orthorhombic–tetragonal phase transition T_1 are slightly higher, of ∼ –25 °C, by comparison with the value of ∼ –39 °C determined for specimen D, proving once again that at 1200 °C not all the cerium content indicated by the nominal compositions was integrated in the perovskite lattice.

The rhombohedral–orthorhombic transition temperature T_2 was even more difficult to be observed. It was only detected from small anomalies of the derivative of permittivity versus temperature dependence. Values of about –93 and –91 °C for the A and D samples, respectively (similar to the ones of pure $BaTiO_3$), slightly higher for the C sample (–83 °C), and almost undetectable for the $Ba_{0.95}Ce_{0.05}TiO_3$ ceramic (B) sintered at a higher temperature were obtained for T_2. For the sample B, two anomalous features (indicated by star symbols in Figure 1.9(a)) at about –7 and 51 °C were observed besides the already mentioned Curie temperature $T_C = 102$ °C. They might be assigned to the rhombohedral–orthorhombic and orthorhombic–tetragonal transitions, respectively. However, if the anomaly at 51 °C is assigned to the orthorhombic–tetragonal phase transition, the room temperature symmetry should be predominantly orthorhombic and not tetragonal, as resulted from XRD analysis. However, for this composition, the XRD data were accurately fitted by using only the JCPDS file indexed for the tetragonal $BaTiO_3$ (i.e. JCPDS no. 05-0626), by comparison with any other JCPDS file corresponding to orthorhombic $BaTiO_3$. We concluded that the orthorhombic distortion in this Ce–$BaTiO_3$ specimen could be smaller or somewhat different from that of the pure $BaTiO_3$ orthorhombic state. Taking into account that the calculation of the structural parameters by XRD involves an averaging over about 10^4 unit cells, one can conclude that this investigation method is not sensitive enough to make a clear difference between the tetragonal and orthorhombic distortion in the case of such a solid solution and only the electrical measurements against the temperature are able to indicate the presence of the orthorhombic modification.

The anomalous behaviour of sample B relative to the Curie temperature value might be explained in terms of a significantly lower amount of Ce^{3+} ions replacing the host Ba^{2+} ions on their sites, rather than one corresponding to the nominal formula, in which a substitution degree of $x = 0.05$ (5 at%) on A sites of the ABO_3 perovskite lattice was considered. According to the dielectric data reported by Hwang and Han [11,12], a concentration of only ∼2 at% cerium incorporated as Ce^{3+} on Ba^{2+} sites can determine such a high value for T_C. This means that the rest of the cerium should be oxidized and precipitated as CeO_2.

This is not supported by XRD analyses or by SEM investigations. On the other hand, if we assume a lower Ce^{3+} amount exclusively incorporated on Ba sites, it should also contribute to the concurrent lowering of the orthorhombic–tetragonal phase transition temperature T_1, specific to the incorporation of donor dopants in $BaTiO_3$. As already mentioned, even if in A and C specimens sintered at lower temperature (1200 °C) Ce^{3+} was not entirely incorporated in the perovskite phase according to the nominal formula, the amount of Ce^{3+} integrated on Ba sites clearly contributed to the decrease of the orthorhombic–tetragonal phase transition temperature, relative to pure $BaTiO_3$. Unlike these specimens, ceramic B shows an opposite evolution consisting of a significant increase in T_1. Therefore, the lower amount of Ce^{3+} incorporated on Ba sites cannot explain the abnormal increase of T_1 in sample B. The only reasonable explanation for this strange behavior is homovalent incorporation of a certain amount of cerium as Ce^{4+} on Ti^{4+} sites.

It is well known that the homovalent incorporation of cerium as Ce^{4+} on Ti^{4+} sites induces a much less pronounced decrease of the Curie temperature and a concurrent strong increase of the rhombohedral – orthorhombic (T_2) and orthorhombic–tetragonal (T_1) phase transition temperatures compared with those of $\sim$–90 and $\sim$5 °C, respectively, specific to pure barium titanate [27].

If considering that the anomaly at $\sim$51 °C detected in the ceramic B can be attributed to the orthorhombic–tetragonal phase transition, which is shifted towards much higher temperatures than in the case of undoped $BaTiO_3$ and taking into account the high sensitivity of T_1 to the Ce^{4+} incorporation on the Ti-sites [27], one can conclude that, for this sample, it is most likely that a significant amount of cerium was incorporated as Ce^{4+} on Ti^{4+} sites. This suggests that in ceramic sample B, a higher sintering temperature induces a further internal oxidation of Ce^{3+} to Ce^{4+}. Unlike the samples sintered at lower temperatures, in this case Ce^{4+} is not expelled as CeO_2 precipitate, but instead replaces Ti^{4+} in the host lattice. This process is accompanied by exclusive segregation of Ti-rich precipitates with different Ba/Ti ratios, as XRD, FE-SEM, and EDX results indicated. Therefore, formation of polytitanate phases with various Ba/Ti ratios in the $Ba_{0.95}Ce_{0.05}TiO_3$ sample (B) sintered at 1300 °C might be determined by two concurrent phenomena: (i) predominant incorporation of cerium as Ce^{4+} on Ti^{4+} sites, which implies expelling from the perovskite lattice of a Ti^{4+} an amount equal to the amount of Ce^{4+} integrated on the Ti sites and the consequent enrichment in Ba of the perovskite phase and (ii) a charge compensation mechanism via Ti vacancies of the remaining Ce^{3+} incorporated on Ba sites, which should also lead to a supplementary segregation of Ti-rich secondary phases. It is hard to quantify the contribution of each of these phenomena to the appearance of the Ti-rich secondary phases, but it seems logical to assume that the segregation of polytitanates due to Ce^{4+} incorporation on Ti sites prevails over any charge compensation mechanism induced by a low content of Ce^{3+} (significantly lower than that stipulated by the nominal formula) incorporated on Ba sites, which might induce the same effect.

In contrast, sample D sintered in similar conditions but with built-in Ti vacancies is single phase, which means that no internal oxidation of Ce^{3+} occurred at 1300 °C. Moreover, it behaves normally from an electrical point of view, with a significant decrease of T_C and T_1 with the increase of Ce^{3+} content. Taking into account these aspects, one can conclude that the lack of compensating defects in sample B prevents the entire accommodation of Ce^{3+} on Ba sites, while the higher efficiency of *B*-site diffusion induced by the higher sintering temperature somehow facilitates a preferential incorporation of the solute as Ce^{4+} on Ti sites. The origin of this phenomenon is unclear and is still under investigation.

On the other hand, if we assume an exclusive incorporation of cerium as Ce^{4+} on Ti sites, then, according to data reported by Zhang et al. [28], the Curie temperature should be even higher, of ~120 °C. In fact, Zhang et al. [28] are the only ones to report the electrical behavior of $BaTi_{0.95}Ce_{0.05}O_3$ ceramic. A value T_1 of 77 °C for the orthorhombic–tetragonal phase transition temperature was also found [28]. Their results converge with those reported by Hwang and Han [11], where a T_C of 135 °C, practically composition-independent for Ce^{4+} amounts below 3 at% and a T_1 value of 70 °C for $BaTi_{0.97}Ce_{0.03}O_3$ ceramic, were found. A steeper decrease of T_C with the increase of Ce^{4+} amount integrated on Ti sites was reported by Jing et al. [27] and Ang et al. [30], who found for the $BaTi_{0.98}Ce_{0.02}TiO_3$ composition a T_C value of 118 °C and a T_1 value of 52 °C, while for the composition $BaTi_{0.94}Ce_{0.06}TiO_3$ a pinched phase transition at 108 °C was detected. Therefore, even if we refer to the results of Jing et al. [27], an entire Ce^{4+} homovalent incorporation of Ti^{4+} sites should involve a higher Curie temperature value than that (of 102 °C) already determined for sample B. Consequently, it was found that in ceramic specimen B a mixed incorporation involving both Ce^{3+} on Ba sites and of Ce^{4+} on Ti sites was most likely to take place. Comparing our results with the literature data regarding the values of the phase transition temperatures in Ce^{3+}- and Ce^{4+}-doped $BaTiO_3$, it seems that in our $Ba_{0.95}Ce_{0.05}TiO_3$ ceramic sintered at 1300 °C, a smaller amount of Ce^{3+} enters on Ba sites concurrently with a higher content of Ce^{4+}, which replaces Ti^{4+} in the host $BaTiO_3$ lattice. Thus, homovalent substitution of Ti^{4+} by Ce^{4+} is responsible for the shift of the rhombohedral–orthorhombic and orthorhombic–tetragonal phase transition temperatures towards higher temperature values, while the decrease of the Curie temperature is mainly induced by Ce^{3+} incorporated on Ba sites.

However, the orthorhombic–tetragonal phase transition temperature T_1 represents in this case the resultant between two opposite evolutions, that is a major increasing trend induced by Ce^{4+} incorporated on Ti sites, but also a certain contribution of Ce^{3+} incorporated on Ba sites to lowering this temperature. Based on the literature data [1, 11, 25–31], we approximated that a solid solution with 2 at% of Ce^{3+} on Ba sites and 3 at% Ce^{4+} on Ti sites might present T_C and T_1 values close to those found for this peculiar ceramic. As in the case of both ceramics A and C sintered at 1200 °C, we were not able to accurately estimate the composition corresponding to the perovskite phase in the sample B. Only for the $Ba_{0.95}Ce_{0.05}Ti_{0.9875}(V_{Ti}^{''''})_{0.0125}O_3$ single-phase ceramic sintered at a high temperature (1300 °C) does the experimental evidence allow a claim to be made without doubt of charge compensation via Ti vacancies. For other investigated samples, based on dielectric data versus temperature, we were only able to establish the site occupancy of the solute in the host perovsite lattice of $BaTiO_3$.

The mixed incorporation of both Ce^{3+} on Ba sites and Ce^{4+} on Ti sites seems to be in disagreement with the results of Hwang and Han [11], where no anomalous electrical behavior for the ceramics described by the $Ba_{1-x}Ce_xTiO_3$ formula was reported. Unlike our ceramic sample B, a T_C value of 26 °C and a T_1 value of –36 °C were found, which proves the exclusive incorporation of cerium as Ce^{3+} on Ba sites for the $Ba_{0.95}Ce_{0.05}TiO_3$ sample sintered in air at 1350 °C/5 h. No secondary phases were detected in the mentioned ceramic and, in a later work [12], they claimed the occurrence of a mixed compensation mechanism involving an equal number of V''_{Ba} and V''''_{Ti} for the effective positive extra charge induced by the donor dopant.

Therefore, further experiments aimed to reveal whether such abnormal behaviour might also occur for ceramics with similar $Ba_{0.95}Ce_{0.05}TiO_3$ nominal composition prepared by other wet-chemical methods and sintered in similar conditions.

The mixed incorporation of the cerium solute in the ceramic sample B is also supported by the values of the structural parameters calculated from the XRD data (Table 1.2). Thereby, the higher values of the lattice parameters for the specimen B sintered at 1300 °C compared to those specific to the sample A, with similar composition but sintered at a lower temperature (1200 °C), can be explained in terms of a predominant replacement of the smaller Ti^{4+} ions (ionic radius of 0.605Å [36]) with the slightly larger Ce^{4+} cations (ionic radius of 0.87Å [36]). The shift of the main diffraction peaks corresponding to the perovskite phase towards lower values of the diffraction angle, as indicated in Figure 1.4(a), also support the idea that the influence of homovalent incorporation of Ce^{4+} on Ti^{4+} sites prevails in ceramic B.

Empirical parameters are currently used to characterize the ferroelectric behavior. The dielectric constant versus temperature at the higher temperature above T_C follows the Curie–Weiss law:

$$\frac{1}{\varepsilon'} = \frac{T - T_0}{C}(T > T_C) \tag{1.6}$$

where T_0 is the Curie–Weiss temperature and C is the Curie constant. Figure 1.10 shows the reciprocal dielectric constant as a function of temperature at 1 kHz, which are well fitted by the Curie–Weiss law. The permittivity follows the Curie–Weiss law above T_C for all the samples with the parameters (T_0 and C) shown in Table 1.3.

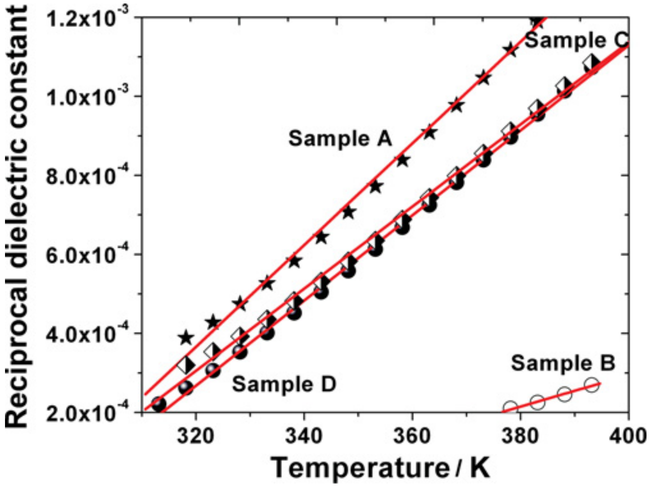

Figure 1.10 *Reciprocal permittivity as a function of temperature at 1 kHz for 5% Ce-doped* $BaTiO_3$ *and fits by the Curie–Weiss law*

Table 1.3 Fitting parameters (T_0 and C) of the Curie–Weiss law and ε_{max} and T_C determined at the frequency $f = 1$ kHz for the 5% Ce-doped BaTiO$_3$

Sample	$\varepsilon_{\mathrm{max}}$	T_{C} (°C)	T_0 (°C)	C (K)
A	2868	36	18	0.8×10^5
B	4838	102	53	2.5×10^5
C	3590	35	17	1.0×10^5
D	7640	25	22	0.9×10^5

The Curie–Weiss temperature increases by increasing the sintering temperature. The Curie constant is very similar (in the range of $(0.8–1.0) \times 10^5$ K), for the A, C, and D samples, while a 2.5 times larger value of $\sim 2.5 \times 10^5$ K is obtained for the B sample (Table 1.3). The higher Curie constant value is related to a stronger polar long-range order character (stronger ferroelectricity) of this ceramic, which correlates well with the high Curie temperature and with its higher structural polar distortion, which resulted from a lower level of Ce^{3+} incorporation on Ba sites and a predominant incorporation of Ce^{4+} on Ti sites. The dielectric data and the Curie–Weiss analysis sustain the results of the structural calculations, which indicated a high polar distortion at room temperature in this sample.

1.4 Raman Investigation

In order to emphasize the evolution of the phase transitions versus temperature and to explain the dissimilar Curie temperature values obtained for the ceramic samples sintered at 1300 °C/4 h but described by different nominal formula, temperature-dependent Raman spectroscopy was used as a complementary investigation method.

Raman spectra were obtained with a T64000 Raman system (Horiba/Jobin-Yvon, Villeneuve d'Ascq, France) working in micro-Raman mode and using a 514.5 nm Ar ion laser (Coherent Innova 400, Coherent, Santa Clara, CA, USA) as the excitation source. The laser light was focused on the sample surface by means of a long working distance ×50 objective lens with a numerical aperture NA = 0.5 (Olympus, Tokyo, Japan). The nominal power was set either to 20 mW or to 7 mW, depending of the temperature sensitivity of the sample. Spectra were collected in a true backscattering geometry with the aid of a liquid nitrogen-cooled charged coupled device (CCD) camera. Temperature-dependent (in situ) Raman experiments were performed by means of a Linkam THMS600 heating–cooling stage (Linkam, Tadworth, UK). Spectra were collected in the range of –190–110 °C in a triple subtractive configuration, in order to allow measurements in the low-wavenumber region (~50 cm^{-1}).

Figure 1.11 reports temperature-dependent Raman spectra of the previously mentioned B and D ceramic samples resulting after sintering at 1300 °C. For the ceramic sample B, without compensating defects, the Raman spectra clearly show a rhombohedral (R) modification at low temperatures (Figure 1.11(a)). This is indicated by the presence of the peaks at low wavenumbers (161 and 196 cm^{-1}) and especially by a distinct mode at ~490 cm^{-1}, which is only present in the R phase [39, 40]. These features seem to persist until –50 °C (Figure 1.11(a)). At higher temperatures, the damping of the mode at 490 cm^{-1} indicates the

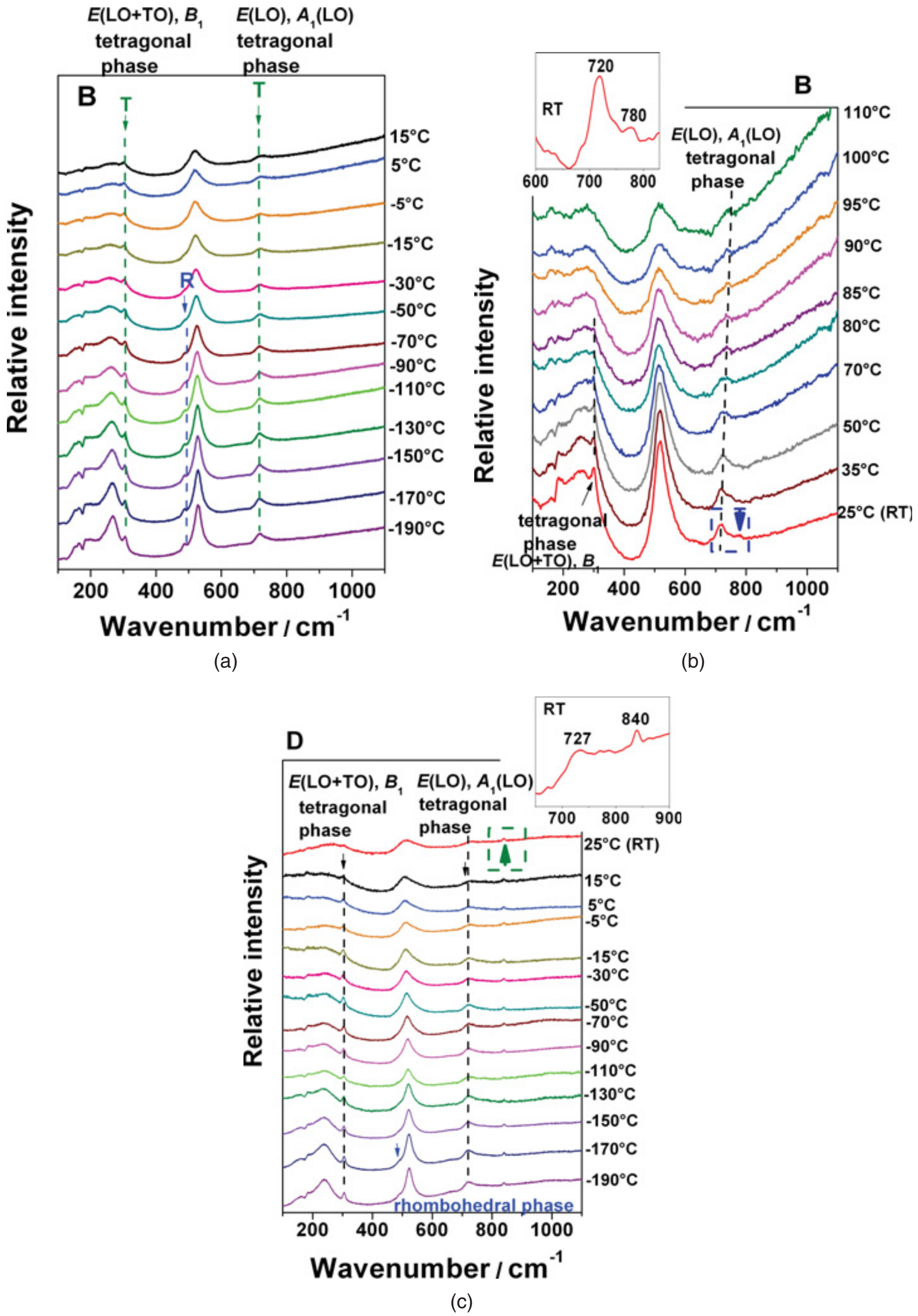

(a)

(b)

(c)

Figure 1.11 Evolution of Raman spectra versus temperature for the ceramic samples sintered at 1300 °C/4 h: (a) $Ba_{0.95}Ce_{0.05}TiO_3$ sample (B) in the temperature range of −190–15 °C; (b) sample B in the temperature range of 25–110 °C – inset: detail (dashed rectangle) of the wavenumber region 600–850 cm^{-1}; (c) $Ba_{0.95}Ce_{0.05}Ti_{0.9875}(V_{Ti}'''')_{0.0125}O_3$ sample (D) in the temperature range of −190–25 °C – inset: detail (dashed rectangle) of the wavenumber region 650–900 cm^{-1}.

transition from rhombohedral (R) to orthorhombic (O) symmetry. However, the persistence of the twin peaks at 160 and 183 cm^{-1} shows that a certain residual rhombohedral order still exists, so that in the temperature range of –50–50 °C a mixture of O and R modifications is more appropriate (Figure 1.11(a and (b)). This observation is in agreement with the results of the dielectric data (Figure 1.8), in which the room temperature state is located between the two anomalies at –7 and 51 °C, corresponding to the R–O and O–T phase transitions, respectively. The interference dip at 176 cm^{-1}, together with the "silent" mode at 302 cm^{-1} and the mode at 715 cm^{-1} represent clear indications that long-range ferroelectric order is present in the lattice [37, 38] at room temperature.

Transition to the cubic (C) paraelectric phase seems to occur above 100 °C, as indicated by the gradual disappearance of the "silent" mode at 302 cm^{-1} and the decrease in intensity of the mode at 715 cm^{-1}, both specific to the tetragonal phase. A Curie temperature of 102 °C was also detected by the permittivity versus temperature data. The evolution of the main features in the Raman spectra recorded at various temperatures suggests a diffuse character of the phase transition, as in relaxor ferroelectrics. The persistence of the Raman spectrum also in the C paraelectric phase above 100 °C is due to the presence of small distortions in the short-range polar nanoregions (PNRs), producing Raman activity even if it is forbidden by the long-range cubic crystalline structure [39]. Taking into account these observations, it is clear that the ceramic sample B sintered at 1300 °C/4 h is in its polar/ferroelectric state at room temperature. These results are in good agreement with both the structural parameters calculated from the XRD data and the Curie temperature estimated from the dielectric study. In the room temperature spectrum of this sample an additional small peak is noticed at 780 cm^{-1}, indicated by the arrow in Figure 1.11(b) and better pointed out by the inset placed in the top-left corner of the same figure. This small peak is generally related to a *B*-site substitution in BaTiO$_3$-based solid solutions [37, 40]. The presence of this peak supports our assumption regarding the predominant incorporation of cerium as Ce^{4+} on titanium sites in the perovskite lattice of the $Ba_{0.95}Ce_{0.05}TiO_3$ ceramic sintered at 1300 °C.

Unlike this case, in the $Ba_{0.95}Ce_{0.05}Ti_{0.9875}(V_{Ti}^{\prime\prime\prime\prime})_{0.0125}O_3$ specimen sintered in similar conditions, the rhombohedral distortion appears at much lower temperatures (< –150 °C) if only the presence of the mode located at 490 cm^{-1} is considered (Figure 1.11(c)).

Concerning the tetragonal modification, this is still identified at 15 °C by means of the "silent mode", but is missing at higher temperatures. This result is consistent with the dielectric properties, which revealed that for this composition the Curie temperature coincides with the room temperature. Another interesting feature in the Raman spectra of this ceramic is the presence of a small peak located at ~ 840 cm^{-1} (indicated by the arrow in Figure 1.11(c)), related to the substitution on the *A* sites of the perovskite lattice). This suggests that in this case the entire dopant amount is integrated as Ce^{3+} on Ba^{2+} sites. This mode is better visualized in the inset placed in the top-right corner of Figure 1.11(c). It is worth mentioning that this mode was not observed in the Raman spectra of the sample B described by the nominal formula $Ba_{0.95}Ce_{0.05}TiO_3$, most likely because of the significantly smaller amount of cerium incorporated on barium sites [41, 42].

1.5 Conclusions

Nanopowders of 5% Ce-doped BaTiO$_3$ with two nominal compositions involving the lack and the presence of Ti vacancies as charge compensating defects and described by the nominal formulae $Ba_{0.95}Ce_{0.05}TiO_3$ and $Ba_{0.95}Ce_{0.05}Ti_{0.9875}(V_{Ti}^{''''})_{0.0125}O_3$ were prepared by the modified Pechini method. From these powders ceramic samples were obtained after sintering in air at two temperatures, 1200 °C/4 h and 1300 °C/4 h, respectively. The phase purity, structural parameters, and microstructural characteristics were investigated.

Only the specimen with built-in titanium vacancies sintered at 1300 °C showed a single-phase composition. Internal oxidation of Ce^{3+} to Ce^{4+} takes place in both samples sintered at 1200 °C, as well as in the specimen without compensating defects sintered at 1300 °C. As a result, small amounts of CeO_2 precipitate were detected for the ceramics sintered at 1200 °C, while a predominant homovalent incorporation of cerium as Ce^{4+} on Ti sites was found in the specimen without Ti vacancies sintered at 1300 °C. The Ce^{3+} oxidation is accompanied by segregation of Ti-rich secondary phases with various Ba/Ti ratios, as revealed by XRD and FE-SEM investigations. The values of the structural parameters calculated from XRD data, as well as the values of the phase transition temperatures indicated by dielectric measurements versus temperature support the assumption of an exclusive but incomplete incorporation (relative to the nominal formula) of the cerium as Ce^{3+} on the Ba site into a perovskite lattice for both ceramics sintered at 1200 °C and of a mixed incorporation of the cerium, mainly as Ce^{4+} on Ti sites, but to a lesser extent also as Ce^{3+} on Ba sites, in the case of the specimen without Ti vacancies and sintered at 1300 °C.

All the ceramics investigated showed good dielectric properties characterized by low losses ($\tan \delta < 5\%$) and a high dielectric constant of 3000–8000 at their corresponding transition temperatures. Sharp ferroelectric–paraelectric phase transitions without a diffuse character and no apparent relaxor properties were determined.

Temperature-dependent Raman analyses sustain the XRD data and the results of the dielectric measurements, proving the mixed incorporation mechanism of cerium, with a predominant homovalent $Ce^{4+} \leftrightarrow Ti^{4+}$ substitution in the ceramic sample without built-in Ti vacancies, sintered at 1300 °C/4 h.

Acknowledgments

The financial support of the Romanian CNCS-UEFISCDI Projects No. PN-II-ID-PCE-2011-3-0668 and PN-II-PT-PCCA-2013-4-0470, as well as collaboration within COST MP0904 Action SIMUFER: “Single- and multiphase ferroics and multiferroics with restricted geometries”, are highly acknowledged. Raman measurements were performed in the frame of the Croatian Ministry of Science Education and Sport Project, “Physics and applications of nanostructures and bulk matter”, No. 098-0982904-2898.

References

(1) Hennings, D.F.K., Schreinemacher, B., and Schreinemacher, H. (1994) High-permittivity dielectric ceramics with high endurance. *Journal of the European Ceramic Society*, **13**, 81–88.

(2) Morrison, F.D., Sinclair, D.C., Skakle, J.M.S., and West, A.R. (1998) Novel doping mechanism for very-high-permittivity barium titanate ceramics. *Journal of the American Ceramic Society*, **81**, 1957–1960.

(3) Saburi, O. (1961) Semiconducting bodies in the family of barium titanates. *Journal of the American Ceramic Society*, **44**, 54–63.

(4) Jonker, G.H. (1964) Some aspects of semiconducting barium titanate. *Solid State Electronics*, **7**, 895–903.

(5) Drofenik, M., Popovic, A., and Kolar, D. (1984) Grain growth and related effects in doped $BaTiO_3$. *American Ceramic Society Bulletin*, **63**, 702–704.

(6) Desu, S.B., and Payne, D. (1990) Interfacial segregation in pervoskites: III, microstructure and electrical properties. *Journal of the American Ceramic Society*, **73**, 3407–3415.

(7) Kolar, D., Guha, J.P., and Buh, M. (1972) Ceramic and dielectric properties of selected compositions in the BaO-TiO_2-CeO_2 system. *Proceedings of the.British Ceramic Society*, **23**, 152–158.

(8) Roth, R.S., Negas, T., Parker, H.S., et al. (1977) Crystal chemistry of cerium titanates, tantalates and niobates. *Materials Research Bulletin*, **12**, 1173–1182.

(9) Itakura, G., Iguchi, T., and Kuroda, T. (1985) Ceramic dielectric materials with high dielectric constant for multilayer ceramic capacitors. *Natl Tech. Rep.* (Jpn), **31**, 145–156.

(10) Makovec, D., Samardžija, Z., and Kolar, D. (1996) Solid solubility of cerium in $BaTiO_3$. *Journal of Solid State Chemistry*, **123**, 30–38.

(11) Hwang, J.H. and Han, Y.H. (2000) Dielectric properties of $(Ba_{1-x}Ce_x)TiO_3$. *Japanese Journal of Applied Physics*, **39**, 2701–2704.

(12) Hwang, J.H. and Han, Y.H. (2001) Electrical properties of cerium-doped $BaTiO_3$. *Journal of the American Ceramic Society*, **84**, 1750–1754.

(13) Makovec, D., Samardžija, Z., and Kolar, D. (1993) Incorporation of cerium into the $BaTiO_3$ lattice, in *Proceedings of the Third European Ceramic Society Conference*, edited by P. Durán and J.P. Fernández, Faenza Editrice Ibérica S.L., Faenza, vol. 1, pp. 961–966.

(14) Guha, J.P. and Kolar, D. (1973) Subsolidus equilibria in the system BaO–CeO_2–TiO_2. *Journal of the American Ceramic Society*, **56**, 5–6.

(15) Chan, N.H. and Smyth, D.M. (1984) Defect chemistry of donor-doped $BaTiO_3$. *Journal of the American Ceramic Society*, **67**, 285–288.

(16) Kröger, F.A. and Vink, H.J. (1956) Relations between the concentrations of imperfections in crystalline solids, in *Solid State Physics*, edited by F. Seitz and D. Turnbull, Academic Press, New York, vol. 3, pp. 307–435.

(17) Lewis, C.V. and Catlow, C.R.A. (1986) Defect studies of doped and undoped barium titanate using computer simulation techniques. *Journal of Physics and Chemistry of Solids*, **47**, 89–97.

(18) Tien, T.Y. and Hummel, F.A. (1967) Solid solutions in the system.$SrTiO_3$–(La_2O_3:3TiO_2). *Transactions of the.British Ceramic Society*, **66**, 233–245.

(19) Hennings, D. (1971) The range of existence of perovskite phases in the system PbO–TiO_2–La_2O_3. *Materials Research Bulletin*, **6**, 329–339.

(20) Daniels, J., Härdtl, K.H., Hennings, D., and Wernicke, R. (1976) Defect chemistry and electrical conductivity of doped barium titanate ceramics. *Philips Research Reports*, **31**, 487–559.

(21) Chan, N.H., Harmer, M.P., and Smyth, D.M. (1986) Compensating defects in highly donor-doped $BaTiO_3$. *Journal of the American Ceramic Society*, **69**, 507–510.

(22) Jonker, G.H. and Havinga, E.E. (1982) The influence of foreign ions on the crystal lattice of $BaTiO_3$. *Materials Research Bulletin*, **17**, 345–350.

(23) Ianculescu, A., Mocanu, Z.V., Curecheriu, L.P., et al. (2011) Dielectric and tunability properties of La-doped $BaTiO_3$ ceramics. *Journal of Alloys and Compounds*, **509**, 10040–10049.

(24) Wang, L., Sakka, Y., and Shao, Y. (2010) Coexistence of A- and B-site vacancy compensation in La-doped $Sr_{1-x}Ba_xTiO_3$. *Journal of the American Ceramic Society*, **93**, 2903–2908.

(25) Ang, C., Yu, Z., Jing, Z., et al. (1997) Synthesis and characterization of $Ba(Ti_{1-x}Ce_x)O_3$ ceramics. *Journal of the European Ceramic Sociey*, **17**, 1217–1221.

(26) Jing, Z., Yu, Z., and Ang, C. (2002) Crystalline structure and dielectric behavior of $(Ce,Ba)TiO_3$ ceramics. *Journal of Materials Research*, **17**, 2787–2793.

(27) Jing, Z., Yu, Z., and Ang, C. (2003) Crystalline structure and dielectric properties of $Ba(Ti_{1-y}Ce_y)O_3$. *Journal of Materials Science*, **38**, 1057–1061.

(28) Zhang, Y., Sun, X., and Lu, D. (2006) Effects of cerium doping at Ti sites and europium doping at Ba sites on dielectric properties of $BaTiO_3$ ceramics. *Chem. Res. Chinese U.*, **22**, 515–519.

(29) Yu, Z., Ang, C., Jing, Z., et al. (1997) Dielectric properties of $Ba(Ti, Ce)O_3$ from 10^2 to 10^5 Hz in the temperature range 85–700 K. *Journal of Physics: Condensed Matter*, **9**, 3081–3088.

(30) Ang, C., Yu, Z., and Jing, Z. (2002) Ferroelectric relaxor $Ba(Ti,Ce)O_3$. *Journal of Physics: Condensed Matter*, **14**, 8901–8912.

(31) Klassens, H.A. and Philips, N.V. (1949) $BaTiO_3$–CeO_2 dielectric composition, German Patent No. 810 047.

(32) Yasmin, S., Choudhury, S., Hakim, M.A., et al. (2011) Effect of cerium doping on microstructure and dielectric properties of $BaTiO_3$ ceramics. *Journal of Materials Science and Technology*, **27**, 759–763.

(33) Cernea, M, Monereau, O., Llewellyn, P., et al. (2006) Sol–gel synthesis and characterization of Ce-doped- $BaTiO_3$. *Journal of the European Ceramic Society*, **26**, 3241–3246.

(34) Pechini, M.P. (1967) Method of preparing lead and alkaline earth titanates and niobates and coating method using the same for a capacitor, US Patent No. 3 330 697.

(35) Makovec, D. and Kolar, D. (1997) Internal oxidation of Ce^{3+}–$BaTiO_3$ solid solutions. *Journal of the American Ceramic Society*, **80**, 45–52.

(36) Shannon, R.D. (1976) Revised effective ionic radii and systematic studies of interatomic distances in halides and chalcogenides. *Acta Crystallographica A*, **32**, 751–767.

(37) Farhi, R., El Marssi, M., Simon, A., and Ravez, J. (1999) A Raman and dielectric study of ferroelectric $Ba(Ti_{1-x}Zr_x)O_3$ ceramics. *European Physical Journal B*, **9**, 599–604.

(38) Miao, S., Pokorny, J., Pasha, U.M., et al. (2009) Polar order and diffuse scatter in $Ba(Ti_{1-x}Zr_x)O_3$ ceramics. *Journal of Applied Physics*, **106**, art. no. 114111.

(39) Buscaglia, V., Buscaglia, M.T., Viviani, M., et al. (2005) Raman and AFM piezoresponse study of dense $BaTiO_3$ nanocrystalline ceramics. *Journal of the European Ceramic Society*, **25**, 3059–3062.

(40) Deluca, M., Vasilescu, C.A., Ianculescu, A.C., et al. (2012) Investigation of the composition-dependent properties of BaTi$_{1\text{-}x}$Zr$_x$O$_3$ ceramics prepared by the modified Pechini method. *Journal of the European Ceramic Society*, **32**, 3551–3566.

(41) Lu, D.Y., Sun, X.Y., and Toda, M. (2007) A novel high-*k* "Y5V" barium titanate ceramics co-doped with lanthanum and cerium. *Journal of Physics and Chemistry of Solids*, **68**, 650–664.

(42) Curecheriu, L.P., Deluca, M., Mocanu, Z.V., et al. (2013) Investigation of the ferroelectric–relaxor crossover in Ce-doped BaTiO$_3$ ceramics by impedance spectroscopy and Raman study. *Phase Transitions*, **86**, 703–714.

2

Synthesis and Ceramic Nanostructuring of Ferroic and Multiferroic Low-Tolerance-Factor Perovskite Oxides

Teresa Hungria[1,2], Covadonga Correas[1,3], and Alicia Castro[1]

[1] *Instituto de Ciencia de Materiales de Madrid (ICMM), Consejo Superior de Investigaciones Científicas (CSIC), Spain*
[2] *Centre de Microcaractérisation Raimond Castaing, UMS 3623, Toulouse, France*
[3] *College of Engineering, Swansea University, United Kingdom*

2.1 Introduction

The term multiferroism has been created to describe materials with at least two of the three primary orders (ferroelastic, ferro- or antiferromagnetic, and ferroelectric). Among them, those that are simultaneously ferroelectric and ferromagnetic are being extensively investigated due to their potential implementation in a range of applications [1]. Moreover, magnetoelectric coupling, that is the direct coupling between magnetization and polarization, may exist regardless of the nature of magnetic and electric orderings. Materials characterized by the simultaneous presence of both orderings, and a coupling between the order parameters, are called multiferroic magnetoelectrics [2,3] and a wide range of devices have been proposed that would take advantage of their distinctive properties [4].

Nanoscale Ferroelectrics and Multiferroics: Key Processing and Characterization Issues, and Nanoscale Effects, First Edition. Edited by Miguel Algueró, J. Marty Gregg, and Liliana Mitoseriu.
© 2016 John Wiley & Sons, Ltd. Published 2016 by John Wiley & Sons, Ltd.

Unfortunately, materials with simultaneous ferroelectric and magnetic orders are not very common, because the electronic structures needed for both orderings seem to be incompatible. On the one hand, ferromagnetism requires unpaired electrons and, on the other, typical ferroelectric materials (such as $BaTiO_3$ or $PbTiO_3$) require the transition-metal cation to have an empty outer shell of electrons [2, 5].

There are hundreds of different crystals with the ferroelectric transition temperature, T_c, above room temperature at atmospheric pressure, with approximately a lognormal distribution of transition temperatures [6]. Many of these materials are not oxides, yet almost all work on multiferroics has emphasized oxides. However, there is no a priori reason to expect that they will have the most interesting multiferroic physics or will make the best devices. Nevertheless, from a practical point of view, oxides are easy to prepare and relatively well known, and most of studies about high-T_C superconductors, colossal magnetoresistance manganites, and ceramics have been carried out on oxides [7].

Most approaches to make better multiferroic materials are based on the generation of ferroelectricity in magnetic materials, to sidestep the incompatibility described above.

Perhaps one of the most promising attempts so far is in the case of the perovskites of general formula ABO_3, to induce the distortion of the unit cell with the help of the lone pair of electrons belonging to the cation in the *A* position, resulting in the polarization, while the *B* position is occupied by a magnetically active cation. In this way, the polarization comes mostly from the cations located in the *A* position whereas the magnetization comes from the cations in the *B* sites. That is the case for the perovskites $BiMO_3$ with M = Fe, Mn, Co, and so forth. As a result of the potential multiferroic properties, this family has had an impact on the field of multiferroics that is comparable to that of yttrium barium copper oxide (YBCO) on superconductors, with hundreds of publications devoted to it in the past few years.

From the synthetic point of view, only some of these bismuth-containing perovskites can be prepared by conventional methods and usually high-pressure techniques are required. This fact can be attributed to the smaller Bi^{3+} ionic radius relative to that of the other *A* cations in typical ferroelectric perovskites (ionic radii in the cuboctahedral *A* position: $rBi^{3+} = 1.34$, $rPb^{2+} = 1.49$, and $rBa^{2+} = 1.61$ Å) [8], giving rise to very low tolerance factors and therefore, to low thermodynamic stability.

Among them, the most promising multiferroic material seems to be $BiFeO_3$. This oxide shows a rhombohedral structure (Space Group: R3c, No. 161), with lattice parameter $a = 3.965$ Å and angle $\alpha = 89.3°$, at room temperature. This material exhibits ferroelectric ($T_C = 825$ °C) and antiferromagnetic ($T_N = 370$ °C) behaviour. In the ABO_3 structure, as described above, the Bi^{3+} placed in the *A* position has a lone pair of electrons that makes the distortion of the perovskite possible, resulting in ferroelectricity, as shown in Figure 2.1, while the Fe^{3+} in the *B* site provides the antiferromagnetic order [7]. The main problems of this oxide from the point of view of its possible industrial application are due to its high conductivity, low thermal stability, and also its antiferromagnetic character, which does not allow a net magnetization.

Another highly topical material is $BiMnO_3$, the only oxide among $BiMO_3$ perovskites that has a true ferromagnetic state, although its ferroelectric character is under debate in the literature [9]. Despite the enormous number of papers about this compound that have appeared in the last five years, there is no consensus about the actual symmetry of the phase and its ferroelectric properties [9–13]. This fact suggests that the difficult synthesis and the

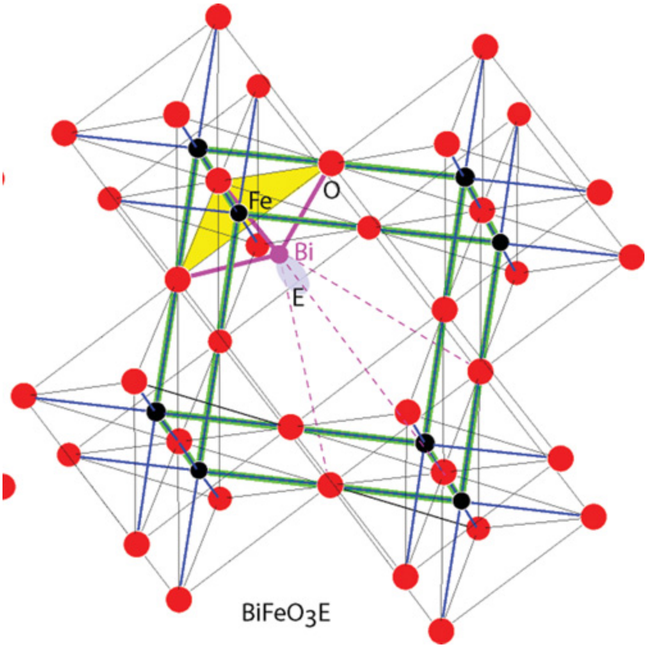

Figure 2.1 Structure of $BiFeO_3$ (E: lone pair of Bi). For a color version of this figure, see color plate section

lack of stability of the oxide make the reproducibility of the preparation and the control of the stoichiometry difficult. Moreover, it seems reasonable to think that the oxygen content plays a crucial role in the actual symmetry and the properties of the oxide.

In addition, a lot of work is being done to stabilize these low tolerance factor perovskites, through maintaining or even enhancing their properties, by the preparation of solid solutions based on $BiMO_3$. In this way, it is possible to find reports where the A position is occupied by La^{3+} or Ga^{3+}, while the B position can be doped with Sb^{5+} or Co^{3+} [14–17]. A good candidate for this purpose seems to be the $PbTiO_3$ ferroelectric perovskite. The $PbTiO_3$ is a tetragonal perovskite (S.G. P4 mm, No. 99) with a $T_C = 490$ °C and very good ferroelectric properties [18]. In the case of the binary system xBiMnO$_3$–$(1-x)$PbTiO$_3$, the substitution increases the stability of the perovskite structure [19, 20] and in the case of the xBiFeO$_3$–$(1-x)$PbTiO$_3$ system, the substitution of Ti^{4+} for Fe^{3+} also improves the magnetic properties [21–23], since the modulated antiferromagnetic spiral structure is destroyed and a weakly ferromagnetic state appears [24].

Moreover, some of the most studied examples among the ferroic solid solutions with a perovkite structure are the systems with morphotropic phase boundaries (MPB), due to their interesting properties. An MPB is defined as a compositional phase boundary at which the two adjacent phases in a phase diagram have equal Gibbs free energy, so usually it is defined as the steep near-vertical boundary where two neighboring phases are degenerate, and it is often observed in real systems as a narrow range of composition and temperature where different phases coexist [25]. Usually, it occurs because of the instability of one phase against another at a critical composition where the two phases are energetically very similar but structurally different and, thus, the mechanical strain to preserve one phase against the other is relaxed (or softened). Thus, in the case of solid solutions of ferroelectric compositions, many physical and electrical properties may change markedly at the MPB. This fact can be explained taking into account that elasticity constants are minimal for the MPB compositions, being easy to change. The decrease of the elasticity constants provides improved electrical properties, being possible maximum values of dielectric and piezoelectric parameters, electromechanical properties, spontaneous polarization, or pyroelectric coefficient [26]. For example, strong piezoelectricity in perovskite-type $PbZr_{1-x}Ti_xO_3$ (PZT) and $Pb(Zn_{1/3}Ti_{2/3})O_3$–$PbTiO_3$ (PZN–PT) systems is generally associated with the existence of separating regions with rhombohedral and tetragonal symmetry, together with a lower-symmetry phase in the vicinity of an MPB [27]. These very interesting results have stimulated further work to investigate systems with MPBs. That is the case for the solid solutions containing the $BiMO_3$ oxides: $x$$BiFeO_3$–(1− x)$PbTiO_3$ and $x$$BiMnO_3$–(1 − x)$PbTiO_3$.

The aim of the present chapter is therefore to provide a view that is as clear as possible of the pertinent works on the synthesis, stabilization, and ceramic processing of ferroic and multiferroic perovskite oxides.

2.2 Synthesis of Perovskites Oxides

2.2.1 General Information on the Preparation of Low-tolerance-Factor Perovskite Oxides

A main issue in the research on multiferroics is the preparation of high-quality ceramic materials, this is to say, with tailored stoichiometries and controlled microstructures. The potential multiferroic perovskites $BiMO_3$ are quite impossible to be obtained as single phases at low temperature and pressure, as described in the case of most of low-tolerance-factor perovskites. Indeed, only a few among possible $BiMO_3$ multiferroic oxides can be prepared by conventional synthesis methods, and high pressure (>5 GPa) and high temperatures are required, not only for $BiMnO_3$ but for most compounds, such as $BiCrO_3$, $BiCoO_3$, and even $BiFeO_3$ [28, 29]. Problems arise from the metastable character of the materials at ambient pressure. High-pressure and high-temperature techniques are advantageous for the control of oxygen stoichiometry, but they are expensive and do not allow the processing of ceramic materials with a controlled microstructure. The latter is a key issue, often not acknowledged, in the characterization of the electrical properties and, thus, in studying its ferroelectric nature.

In the case of $BiFeO_3$, the formation of impurities and oxygen vacancies is often observed during the synthesis step, especially when high-temperature methods are used. For this reason, various low-temperature chemical methods such as co-precipitation [30], hydrothermal [31, 32], combustion synthesis [33], sol–gel [34, 35], among others, have been developed and designed to prepare pure $BiFeO_3$.

On the other hand, $BiMnO_3$ needs to be synthesized at high pressure and high temperature in order to survive as a metastable phase at ambient conditions [11, 19, 36, 37].

In the case of the synthesis of the $x$$BiFeO_3$–(1 − x)$PbTiO_3$ system, the main problem is the appearance of secondary phases in the $BiFeO_3$-rich compositions, so most of the studies about this solid solution are focused on the research of low or moderated temperature methods [38–42]. As for the Bi and Mn oxide, the synthesis of the yBiMnO$_3$–(1 – y) PbTiO$_3$ system is also complicated, because BiMnO$_3$-rich compositions ($y > 0.8$) cannot be obtained as single phases without the use of high-pressure methods [20]. There is therefore a need for an efficient and reproducible synthesis method to obtain the whole system at ambient pressure.

Furthermore, it is possible to find studies of the zBiFeO$_3$–(1 – z)BiMnO$_3$ binary system, although in all of the cases the studied compositions have high z values because the BiMnO$_3$-rich compositions are difficult to obtain [43–45].

Therefore, it is still worth developing simple and low-cost procedures to obtain pure single-phase BiMO$_3$ (BiFeO$_3$ and in particular BiMnO$_3$) and their solid solutions with a homogeneous chemical composition and controlled particle size.

2.2.2 Mechanochemical Activation and Mechanosynthesis Applied to Low-Tolerance-Factor Perovskite Oxides

It is well known that mechanochemical activation is a route with many important advantages: it can be easily operated and produces large amounts of nanostructured powders in a short time. Although the first mechanochemical reactions were described at the end of the fourth century BC by Theophrastus of Erasus [46], mechanoactivation techniques were developed for the synthesis of intermetallics, alloys, and nanocrystalline materials during the twentieth century [47]. More recently, solid-state mechanochemistry has been employed to prepare new oxides or to improve the properties of known functional materials [48–50]. During the milling process, the homogeneity of the mixture is increased, the particle size decreased, and the contact area renewed. Localized heating and the combined action of pressure with shear at the points of impact may contribute to the activation of the milled sample [51]. Mechanochemical activation is usually a result of disordering of the crystal and generation of defects, or other metastable forms that cause higher reactivity, and even in some case the amorphization process is observed. Consequently, the necessary calcination step to form the designed phase is completed at a lower temperature and in a shorter time than in the traditional ceramic method. Moreover, in some cases, the formation of the desired phase is observed during the mechanical treatment; that is, it is mechanosynthesized and is usually constituted by nanosized particles [52, 53]. Figure 2.2 summarizes all the possible steps observed during the mechanochemical activation process. Furthermore, the high reactivity and low particle size obtained facilitate the sintering process, thus making it possible to obtain high-density ceramics at low temperatures [53, 54].

Recently, the mechanochemical method has been shown to be an effective, economical, and versatile means to successfully stabilize materials that had been obtained only by high-pressure techniques [55–57].

A first attempt to obtain BiMnO$_3$ by a mechanochemical route was carried out by Brankovic and coworkers and reported in two consecutive works [58, 59]. These authors announced the mechanosynthesis of BiMnO$_3$ at ambient pressure and room temperature. However, they admitted that the samples were contaminated by iron coming from the reaction media [58] and the existence of important amounts of unidentified amorphous phases, together with unreacted Mn$_2$O$_3$ [59]. Therefore, although these works summarize a very

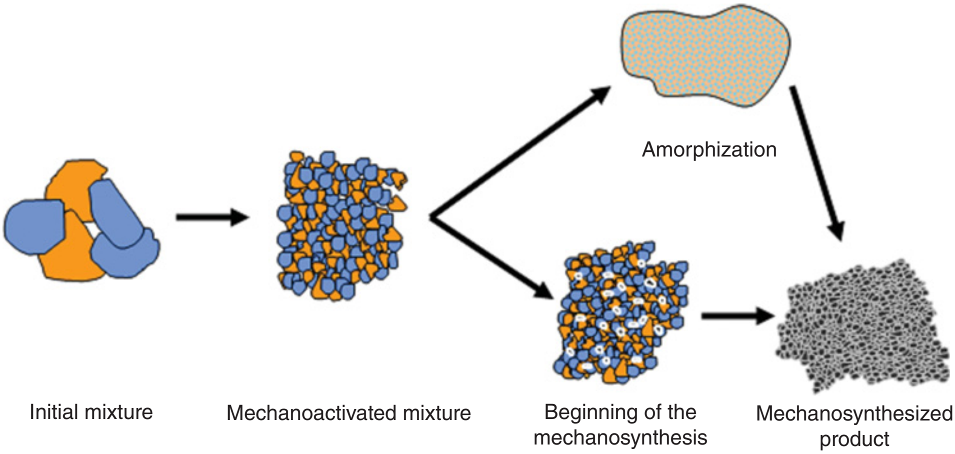
Amorphization
Initial mixture
Mechanoactivated mixture
Beginning of the mechanosynthesis
Mechanosynthesized product

Figure 2.2 *Different possible steps observed during a mechanochemical activation process. For a color version of this figure, see color plate section*

interesting approach, the synthesis of the perovskite as single phase seems to be incomplete and more work was necessary to succeed in this objective.

These preliminary results can be improved by using a tungsten carbide media [60]. The X-ray diffraction pattern of the final product, obtained after 18 h of mechanical treatment, of a mixture of Bi_2O_3 and Mn_2O_3 (1:1) oxides is shown in Figure 2.3(a). As can be observed, very broad diffraction lines, typical of nanocrystalline phases, are obtained and can be indexed as a pseudocubic symmetry. The nanometric crystal size of the mechanosynthesized powder was confirmed by transmission electron microscopy (Figure 2.3(b). This result is quite similar to those reported by Brankovic and coworkers [58, 59], although in

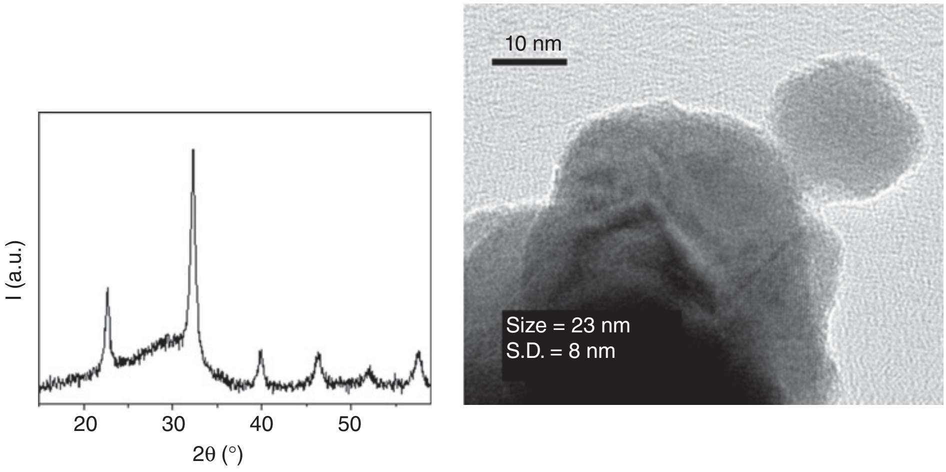

(a) (b)

Figure 2.3 *(a) XRD and (b) TEM image of the mechanosynthesized* $BiMnO_3$

the present case neither starting oxides nor secondary phases are detected by XRD in the final reaction product and the fraction of possible amorphous phases is very small. These facts can be explained as a consequence of the different reaction protocols employed. The use of an open reaction system favours the oxidation of Mn^{3+}, allowing $BiMnO_{3+\delta}$ or, more precisely, $Bi(Mn^{3+})_{1-4\omega}(Mn^{4+})_{3\omega}O_3$ phases to be obtained. Moreover, the nanocrystalline character of the obtained phases makes it difficult to ascertain the actual symmetry of the isolated phases, which is closely related to the δ value. It was necessary to combine the structural characterization carried out by SAED with the Mn/Bi and Mn^{4+}/Mn^{3+} ratios obtained by XPS and the magnetical characterization in order to conclude that the mechanosynthesized powder is ferromagnetic and most probably shows a δ value around 0.08 and a monoclinic P-type structure (S.G. $P2_1/c$, No. 14) [29].

In order to increase the crystallinity of the mechanosynthesized $BiMnO_{3+\delta}$ phase and to study its thermal behaviour, different annealings have been performed, also in open systems, which permit the metastable character of this phase to be established in perfect accordance with the already observed behaviour for the phases obtained by high-pressure and high-temperature treatments. The decomposition of the perovskite is observed at temperatures higher than 400 °C; a complete characterization of the phase annealed at 400 °C shows that an increase in the concentration of Mn^{4+} is obtained after a thermal treatment in air and spin glass behavior, previously described for an orthorhombic structure (S.G. Pnma, No. 62) with $\delta > 0.12$, is found [29].

Regarding $BiFeO_3$, the optimal conditions of mechanosynthesis for this oxide are the energetic milling during 18 h in a tungsten carbide medium of a stoichiometric mixture of Bi_2O_3 and Fe_2O_3 oxides. After milling, a nanocrystalline single-phase powder is obtained. Because of the nanometric crystal size, it is not possible to define from XRD data (Figure 2.4) the actual symmetry of these powdered phases. For this reason, different thermal treatments were carried out from the mechanosynthesized powder, in order to increase the crystal size and to allow the structural characterization to be carried out in more detail.

Figure 2.4 shows the X-ray diffraction patterns of the mechanosynthesized and subsequently thermally treated $BiFeO_3$ at different temperatures. During these thermal treatments, an abrupt change in the crystallinity of the $BiFeO_3$ phase is noted at 500 °C. Together with this crystallization, traces of the $Bi_{36}Fe_2O_{57}$ phase appear at 500 °C, the quantity of this compound decreasing with the temperature increase to finally disappear at the highest temperature (790 °C). Rhombohedral cell parameters corresponding to the sample mechanosynthesized material and subsequently thermally treated at 790 °C were calculated from XRD. Refinements were performed by using a least-squares refinement method (CELREF). The calculated lattice constants were $a_R = 3.972$ Å (±0.003) and $\alpha_R = 89.44°$ (±0.05), with a cell volume of 62.64 Å^3 (±0.05) [61], in good agreement with the data reported in the bibliography, considering the high variability of the α_R parameter [62].

Different magnetic experiments were carried out on samples mechanosynthesized and subsequently treated at 790 °C, as can be observed in Figure 2.5. The magnetic characterization reveals that the mechanosynthesized $BiFeO_3$ is temperature-independent paramagnetic, due to the size effect. Moreover, there is a spurious contribution due to the presence of secondary phases that disappears when the sample is thermally treated at 790 °C. In this case, the typical behavior of an antiferromagnetic character is observed.

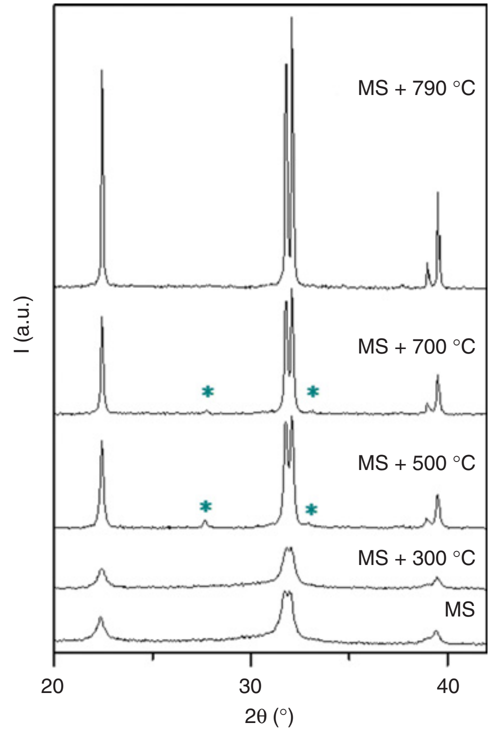

Figure 2.4 *XRD patterns of the mechanosynthesized (MS) and subsequently thermally treated* $BiFeO_3$ *at different temperatures (*: main peaks of the* $Bi_{36}Fe_2O_{57}$ *phase)*

$BiFeO_3$–$PbTiO_3$ and $BiMnO_3$–$PbTiO_3$ solid solutions were also prepared by mechanosynthesis in a WC media from the stoichiometric mixture of the binary oxides [61, 63], as can be observed in Figures 2.6(a) and 2.7(a), respectively. The mechanosynthesized powders were thermally treated at increasing temperatures, from 400 °C up to the melting point, so the final temperature of the synthesis depends on the composition. Tables 2.1 and 2.2 summarize the synthesis conditions for different members of the xBiFeO$_3$–(1 – x)PbTiO$_3$ and xBiMnO$_3$–(1 – x)PbTiO$_3$ systems, respectively.

The same synthesis approach was used in the case of the ternary system xBiFeO$_3$–yBiMnO$_3$–(1 – x – y)PbTiO$_3$, which has not been previously synthesized. Taking into account the interesting properties observed in the MPB regions, the chosen ternary compositions are in the region that connect the MPB regions of the xBiFeO$_3$–(1 – x)PbTiO$_3$ and yBiMnO$_3$–(1 – y)PbTiO$_3$ binary systems. The investigated compositions of the ternary solid solution are shown in Table 2.3 and Figure 2.8.

Once again, the use of the mechanochemical method in WC and air as the synthesis method has allowed different components of the solid solution to be obtained, regardless of the composition. Figure 2.9 shows the XRD patterns of different compositions obtained directly by mechanosynthesis. The synthesis was achieved after milling times depending on the composition, as can be observed in Table 2.4. It was possible to obtain the xBiFeO$_3$–(1 – x)PbTiO$_3$-rich compositions after 24 hour of milling (compositions 1 to 7), while the

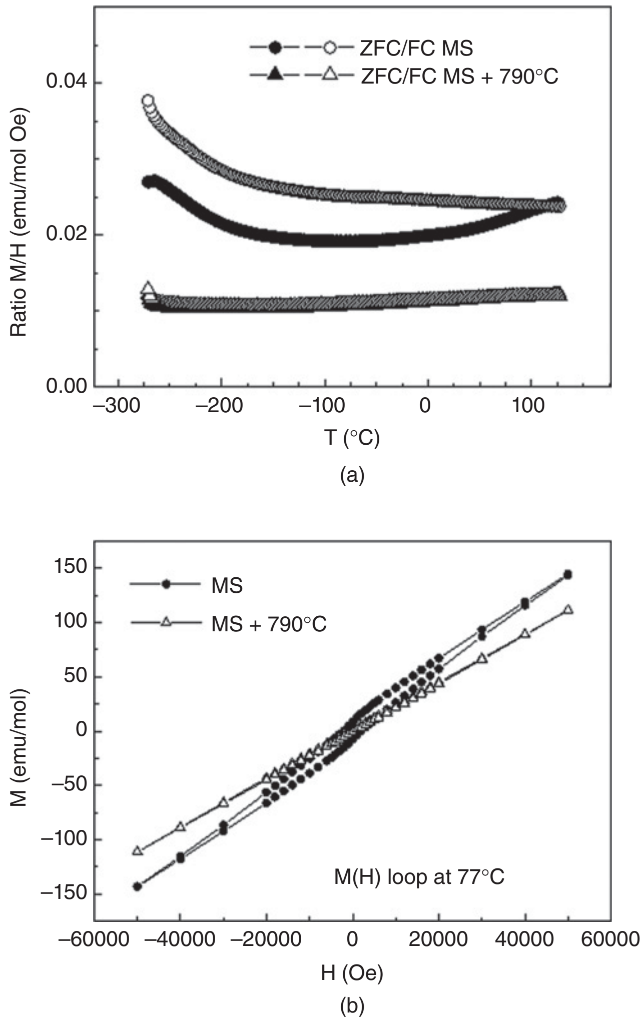

Figure 2.5 *(a) ZFC (closed symbols) and FC (open symbols) magnetization at 500 Oe for the two $BiFeO_3$ samples mechanosynthesized (MS) and thermally treated at 790 °C (MS + 790 °C); (b) isothermal magnetization curves measured at 77 °C for the same two $BiFeO_3$ samples*

yBiMnO$_3$–(1 − y)PbTiO$_3$-rich compositions were prepared in 18 hours (compositions 8 and 9).

The particle size of the samples obtained by mechanosynthesis is nanometric, so, as it has been done in the case of previous binary systems, different thermal treatments have been carried out, allowing an increase of particle size and revealing the crystalline symmetry of the phases. Figure 2.10 and Table 2.4 show the results and conditions employed for these treatments. These temperature values, named "crystallization temperatures", belong to the

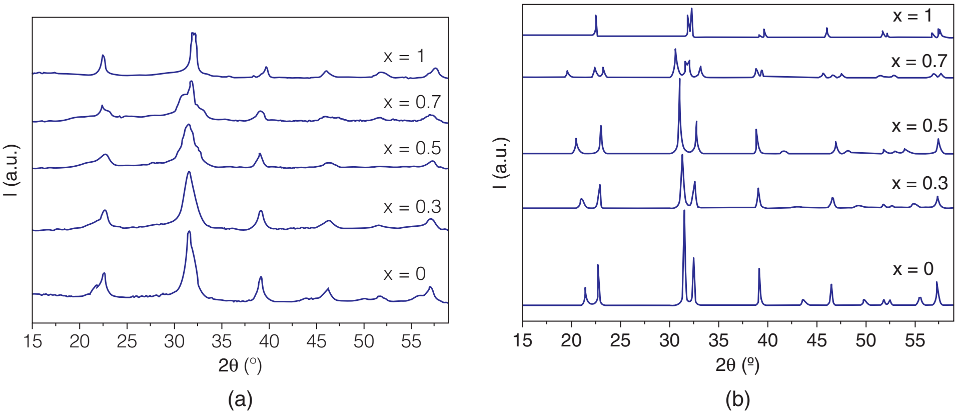

Figure 2.6 XRD patterns of the $xBiFeO_3$–$(1-x)PbTiO_3$ phases obtained by (a) mechanosynthesis in a WC medium during 24 h and (b) subsequently annealed at the final temperature. Reprinted from [61], Copyright (2011), with permission from Elsevier

highest temperatures before the decomposition, allowing isolated perovskite phases with high crystallinity to be obtained.

A zoom of the XRD patterns is depicted in Figure 2.11, showing a progressive evolution of the phases, from an MPB tetragonal/rhombohedral, typical of xBiFeO$_3$–(1 – x)PbTiO$_3$ MPB compositions, to an MPB tetragonal/orthorhombic, typical of yBiMnO$_3$–(1 – y)PbTiO$_3$ MPB compositions, being possible to group the compositions in three main regions: xBiFeO$_3$–(1 – x)PbTiO$_3$ rich compositions (composition 1), triphasic MPB compositions (compositions 2 to 7), and yBiMnO$_3$–(1 – y)PbTiO$_3$ rich compositions (compositions 8 and 9).

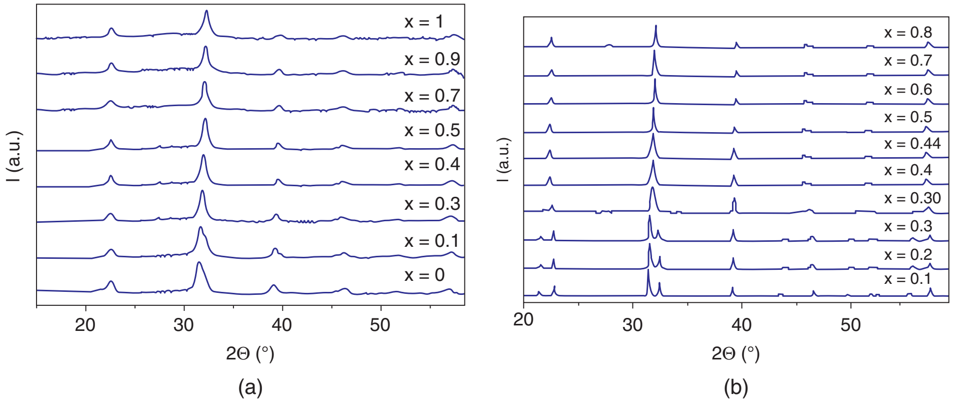

Figure 2.7 XRD patterns of the $xBiMnO_3$–$(1-x)PbTiO_3$ phases obtained by (a) mechanosynthesis in a WC medium and (b) subsequently annealed at the final temperature [63]. Reprinted from [63], Copyright © 2012 Wiley-VCH Verlag GmbH & Co. KGaA, Weinheim

Table 2.1 *Identified phases and experimental conditions of the mechanosynthesis of x$BiFeO_3$–(1 − x)$PbTiO_3$ system in WC and air conditions. Reprinted from [61], Copyright (2011), with permission from Elsevier*

Composition	Milling time (h)	Identified phases after milling process	Annealing temperature (°C) (annealing time (h))	Identified phases after thermal treatments
PT	24	PT (LC)	1050 (2)	$PbTiO_3$ (T)
0.1BF – 0.9PT	24	0.1BF – 0.9PT (LC)	1050 (2)	0.1BF – 0.9PT (T)
0.2BF – 0.8PT	24	0.2BF – 0.8PT (LC)	1050 (2)	0.2BF – 0.8PT (T)
0.3BF – 0.7PT	24	0.3BF – 0.7PT (LC)	1050 (2)	0.3BF – 0.7PT (T)
0.4BF – 0.6PT	24	0.4BF – 0.6PT (LC)	1050 (2)	0.4BF – 0.6PT (T)
0.5BF – 0.5PT	24	0.5BF – 0.5PT (LC)	1050 (2)	0.5BF – 0.5PT (T)
0.6BF – 0.4PT	24	0.6BF – 0.4PT (LC)	1050 (2)	0.6BF – 0.4PT (T)
0.625BF – 0.375PT	24	0.625BF – 0.375PT (LC)	1050 (2)	0.625BF – 0.375PT (R and T)
0.65BF – 0.35PT	24	0.65BF – 0.35PT (LC)	1050 (2)	0.65BF – 0.35PT (R and T)
0.675BF – 0.325PT	24	0.675BF – 0.325PT (LC)	1050 (2)	0.675BF – 0.325PT (R and T)
0.7BF – 0.3PT	24	0.7BF – 0.3PT (LC)	1050 (2)	0.7BF – 0.3PT (R and T)
0.75BF – 0.25PT	24	0.75BF – 0.25PT (LC)	1050 (2)	0.75BF – 0.25PT (R and T)
0.8BF – 0.2PT	24	0.8BF – 0.2PT (LC)	1000 (2)	0.8BF – 0.2PT (R)
0.9BF – 0.1PT	24	0.9BF – 0.1PT (LC)	850 (2)	0.9BF – 0.1PT (R)
BF	24	BF (LC)	790 (2)	$BiFeO_3$ (R)

LC = low crystalline perovskite, R = rhombohedral perovskite, T = tetragonal perovskite

2.3 Processing of Ferroic and Multiferroic Materials: From the Ceramic Method to the Current Assisted Methods

In many material applications there is a need for dense materials, often being very close to their theoretical density. Unfortunately, taking account of the fragility and refractory properties of ceramic materials and several difficulties inherent in the sintering process, the compaction without any additives becomes a real challenge from both practical and theoretical aspects.

The final properties of ferroic ceramic components greatly depend upon the history of the ceramic. Each step in the preparation of the material has to be carefully monitored and controlled to obtain the best product. The primary steps of the preparation of the ceramic material are synthesis of the precursor, fabrication of green bodies, and, last but not least, sintering of the pellet to achieve proper densification. This third step, which follows powder preparation, consists of thermal treatment with the aim of strengthening the desired piece. It occurs via bonding of the compact grains without melting. Such “welding” may be followed by a sintering – that is porosity reduction – depending on the application of the elaborated

Table 2.2 *Identified phases and experimental conditions of the mechanosynthesis of yBiMnO$_3$–(1 – y)PbTiO$_3$ system in WC and air conditions*

Composition	Milling time (h)	Identified phases after milling process	Annealing temperature (°C) (annealing time (h))	Identified phases after thermal treatments
PT	18	PT (LC)	1050 (2)	PbTiO$_3$ (T)
0.1BM – 0.9PT	18	0.1BM – 0.9PT (LC)	950 (2)	0.1BM – 0.9PT (T)
0.2BM – 0.8PT	18	0.2BM – 0.8PT (LC)	950 (2)	0.2BM – 0.8PT (T)
0.3BM – 0.7PT	18	0.3BM – 0.7PT (LC)	950 (2)	0.3BM – 0.7PT (T)
0.36BM – 0.64PT	18	0.36BM – 0.64PT (LC)	950 (2)	0.36BM – 0.64PT (T and O)
0.4BM – 0.6PT	18	0.4BM – 0.6PT (LC)	950 (2)	0.4BM – 0.6PT (T and O)
0.44BM – 0.56PT	18	0.44BM – 0.56PT (LC)	950 (2)	0.44BM – 0.56PT (T and O)
0.5BM – 0.5PT	18	0.5BM – 0.5PT (LC)	950 (2)	0.5BM – 0.5PT (O)
0.6BM – 0.4PT	18	0.6BM – 0.4PT (LC)	950 (2)	0.6BM – 0.4PT (O)
0.7BM – 0.3PT	18	0.7BM – 0.3PT (LC)	950 (2)	0.7BM – 0.3PT (O)
0.8BM – 0.2PT	18	0.8BM – 0.2PT (LC)	400 (1)	0.8BM – 0.2PT (*)
0.9BM – 0.1PT	18	0.9BM – 0.1PT (LC)	400 (1)	0.9BM – 0.1PT (*)
BM	18	BM (LC)	400 (1)	BiMnO$_3$ (M)

LC = low crystalline perovskite, T = tetragonal perovskite, O = orthorhombic perovskite, M = monoclinic perovskite, * = under study

product. However, even if a small-size powder is used, conventional sintering is often unable to provide dense, very fine-grained ceramics, due to the high temperatures still required for densification and the fact that the lowest grain size achievable by classical techniques remains about 0.5 μm or even higher, depending on the system. In addition, for ceramics containing volatile elements (for example Bi) or low-stability compounds (such as the low-tolerance-factor perovskites), exhaustive control of the processing is required in order to

Table 2.3 *xBiFeO$_3$–yBiMnO$_3$–(1 – x – y)PbTiO$_3$ ternary compositions*

Assigned number	xBiFeO$_3$–yBiMnO$_3$–(1 – x – y)PbTiO$_3$ composition
1	0.60BiFeO$_3$–0.06BiMnO$_3$–0.34PbTiO$_3$
2	0.52BiFeO$_3$–0.10BiMnO$_3$–0.38PbTiO$_3$
3	0.47BiFeO$_3$–0.13BiMnO$_3$–0.40PbTiO$_3$
4	0.40BiFeO$_3$–0.17BiMnO$_3$–0.43PbTiO$_3$
5	0.35BiFeO$_3$–0.20BiMnO$_3$–0.45PbTiO$_3$
6	0.30BiFeO$_3$–0.23BiMnO$_3$–0.47PbTiO$_3$
7	0.23BiFeO$_3$–0.27BiMnO$_3$–0.50PbTiO$_3$
8	0.17BiFeO$_3$–0.30BiMnO$_3$–0.53PbTiO$_3$
9	0.05BiFeO$_3$–0.37BiMnO$_3$–0.58PbTiO$_3$

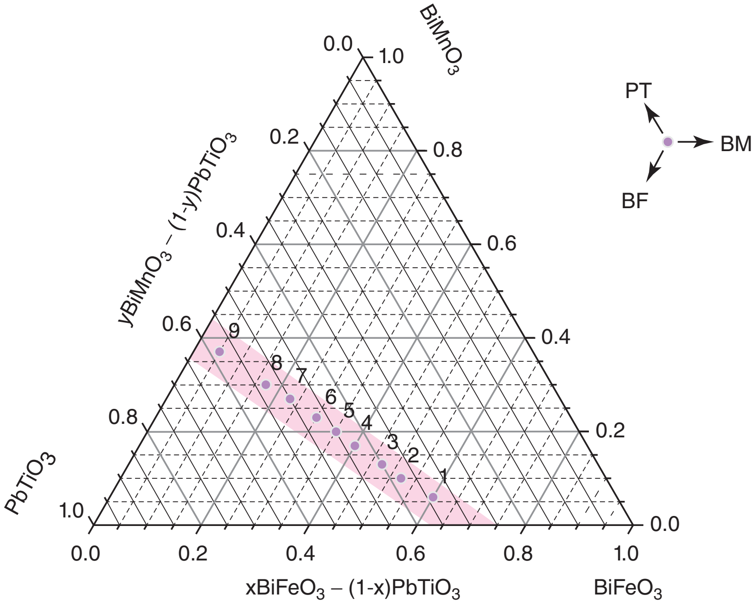
BiMnO$_3$
yBiMnO$_3$ – (1-y)PbTiO$_3$
PbTiO$_3$
xBiFeO$_3$ – (1-x)PbTiO$_3$
BiFeO$_3$
PT
BM
BF
0.0
0.2
0.4
0.6
0.8
1.0
1
2
3
4
5
6
7
8
9

Figure 2.8 *Compositional diagram of the* $xBiFeO_3$–$yBiMnO_3$–$(1-x-y)PbTiO_3$ *ternary system*

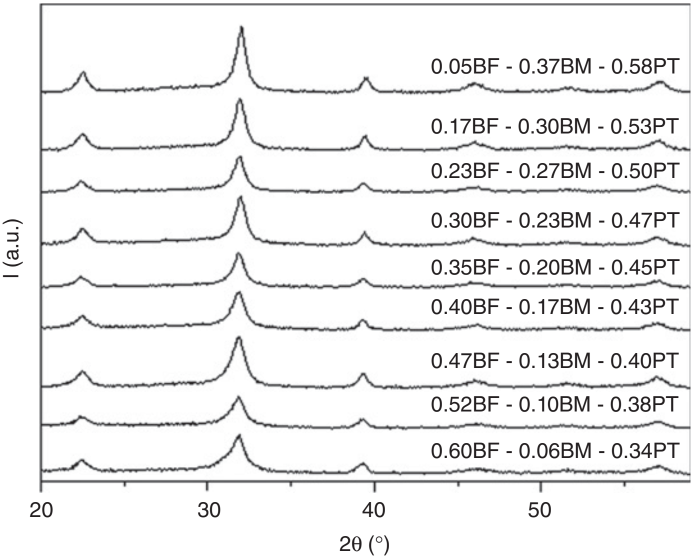

Figure 2.9 *XRD pattern of different compositions of the* $xBiFeO_3$–$yBiMnO_3$–$(1-x-y)PbTiO_3$ *solid solution obtained by mechanosynthesis*

Table 2.4 *Identified phases and experimental conditions of the mechanosynthesis of $xBiFeO_3$–$yBiMnO_3$–$(1 - x - y)PbTiO_3$ ternary system in WC and air conditions*

Composition	Milling time (h)	Identified phases after milling process	Annealing temperature (°C) (annealing time (h))	Identified phases after thermal treatments
0.7BF – 0.3PT	24	0.7BF – 0.3PT (LC)	1050 (2)	0.7BF – 0.3PT (T and R)
Composition 1	24	0.60BF – 0.06BM – 0.34PT (LC)	1000 (2)	0.60BF – 0.06BM – 0.34PT (T and R)
Composition 2	24	0.52BF – 0.10BM – 0.38PT (LC)	1000 (2)	0.52BF – 0.10BM – 0.38PT (Triphasic MPB)
Composition 3	24	0.47BF – 0.13BM – 0.40PT (LC)	1000 (2)	0.47BF – 0.13BM – 0.40PT (Triphasic MPB)
Composition 4	24	0.40BF – 0.17BM – 0.43PT (LC)	1000 (2)	0.40BF – 0.17BM – 0.43PT (Triphasic MPB)
Composition 5	24	0.35BF – 0.20BM – 0.45PT (LC)	950 (2)	0.35BF – 0.20BM – 0.45PT (Triphasic MPB)
Composition 6	24	0.30BF – 0.23BM – 0.47PT (LC)	950 (2)	0.30BF – 0.23BM – 0.47PT (Triphasic MPB)
Composition 7	24	0.23BF – 0.27BM – 0.50PT (LC)	950 (2)	0.23BF – 0.27BM – 0.50PT (Triphasic MPB)
Composition 8	18	0.17BF – 0.30BM – 0.53PT (LC)	950 (2)	0.17BF – 0.30BM – 0.53PT (T and O)
Composition 9	18	0.05BF – 0.37BM – 0.58PT (LC)	950 (2)	0.05BF – 0.37BM – 0.58PT (T and O)
0.4BM – 0.6PT	18	0.4BM – 0.6PT (LC)	950 (2)	0.4BM – 0.6PT (T and O)

LC = low crystalline perovskite, T = tetragonal perovskite, O = orthorhombic perovskite, R = rhombohedral perovskite

maintain compositional homogeneity and to avoid the decomposition of the phases. Hence, alternative sintering methods need to be investigated that enhance mass transport and make it possible to lower both the temperature and the time of consolidation, and, thus, to control grain growth.

Among the most used processing techniques, apart from natural sintering, those based on the application of pressure during the sintering process – for example hot pressing (HP) [64,65] and hot isostatic pressing (HIP) [66] – are the most commonly used, allowing dense ceramics to be obtained at lower temperatures whilst inhibiting grain growth. Interesting results have also been obtained by dual-stage sintering [67] and by the addition of sintering aids [68]. Other means of activating the sintering process involve the use of an electromagnetic field such as, for example, in microwave sintering and spark plasma sintering (SPS), in which pressure is applied simultaneously [69].

Although the widespread use of an electrical current to activate the sintering process is recent, generated by the availability of commercially built devices, its origin is much older [70]. Early patents describe methods in which an electric discharge is utilized to aid the sintering of powders [71, 72] and to obtain synthetic diamonds [73–75]. The use of a current to aid in the processing of different materials has been further developed over

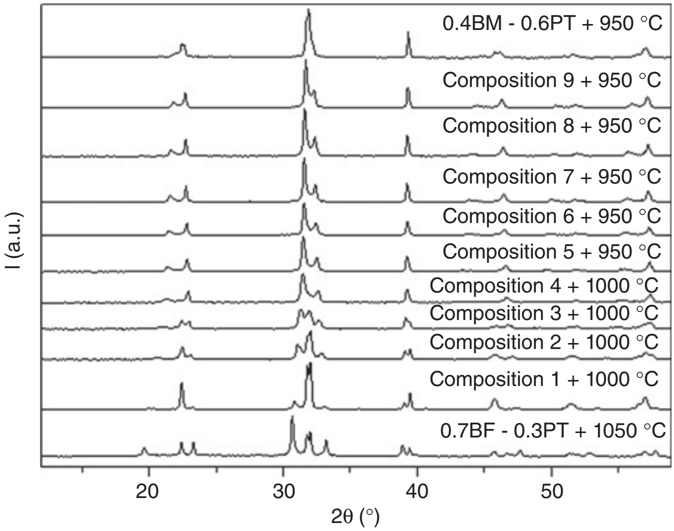

Figure 2.10 *XRD of different xBiFeO$_3$–yBiMnO$_3$–(1 − x − y)PbTiO$_3$ ternary compositions mechanosynthesized and subsequently thermally treated. The crystallization temperatures are shown. The binary compositions 0.7BF − 0.3PT and 0.4BM − 0.6PT are also shown, being the limits of the ternary compositions*

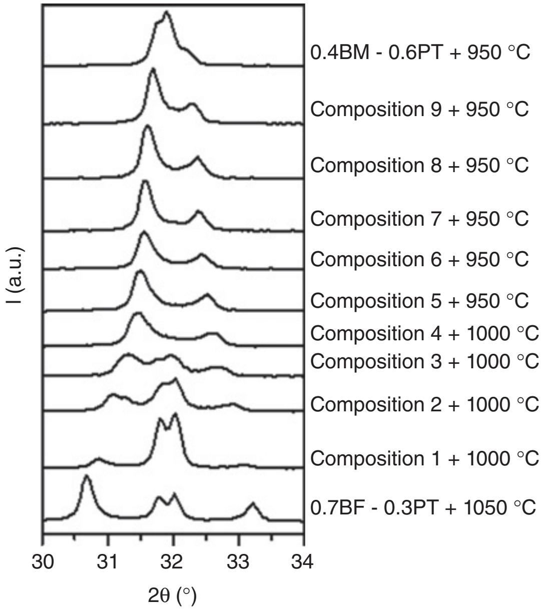

Figure 2.11 *Zoom of the XRD patterns between 30 and 34° (2θ) of the xBiFeO$_3$–yBiMnO$_3$–(1 − x − y)PbTiO$_3$ ternary compositions mechanosynthesized and subsequently thermally treated. The binary compositions 0.7BF − 0.3PT and 0.4BM − 0.6PT are also shown, being the limits of the ternary compositions*

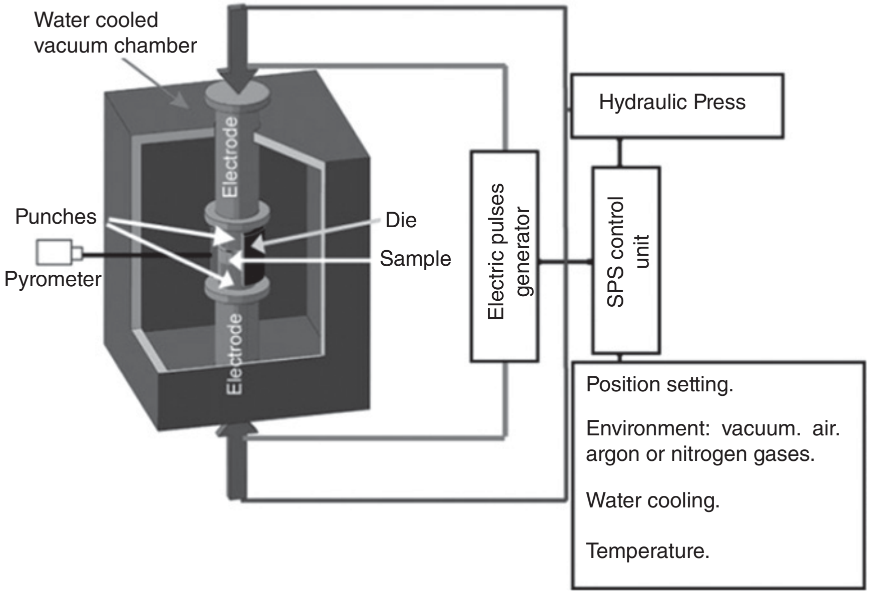
Water cooled vacuum chamber
Electrode
Punches
Pyrometer
Die
Sample
Electrode
Electric pulses generator
Hydraulic Press
SPS control unit
Position setting.
Environment: vacuum. air. argon or nitrogen gases.
Water cooling.
Temperature.

Figure 2.12 *Schematic drawing of an SPS machine. Reprinted from [69], Copyright © 2009 Wiley-VCH Verlag GmbH & Co. KGaA, Weinheim*

the past few decades. Examples of the new generation commercial units include: plasma assisted sintering (PAS); pulsed electric current sintering (PECS); electroconsolidation, also known as electric pulse assisted consolidation (EPAC); and, perhaps most commonly used, spark plasma sintering (SPS). SPS combines simultaneously the application of pressure and electric current directly on the sample. Joule heating provides high heating rates, allowing dense ceramics to be obtained under uniform heating at relatively low temperatures and in short processing times (typically a few minutes) [76]. The operation of an SPS unit is shown schematically in Figure 2.12. It consists of a uniaxial pressure device, in which the water-cooled punches also serve as electrodes, a reaction chamber that can be evacuated, a pulsed direct current (DC) generator, and pressure, position, and temperature regulating systems. In an SPS experiment, a weighed amount of powder is introduced in a die. The die may be built up with various materials, such as carbon, WC, refractory alloys, etc. The major interest in this process, when the sintering parameters have been mastered, is linked to the extreme rapidity of the thermal treatment. Thus, the consolidation time is greatly decreased from hours, in the case of conventional sintering, to a few minutes for the SPS process. Moreover, the sintering temperature can be diminished by a few hundred degrees compared to conventional sintering [53]. In short, SPS constitutes an innovative technique in the field of materials sintering. Three distinguishing factors contribute to its enhanced densification compared to conventional sintering processes: (i) DC current influence, (ii) high heating rates, and (iii) the simultaneous application of pressure [68].

(i) *The influence of DC current*. The main difference between SPS and other sintering methods is that both die and powder are directly heated by the Joule effect of the DC current. Such techniques make it possible to raise the temperature to 2000 °C at heating rates of up to 1000 °C min^{-1} or even higher. The roles of the current and the sintering mechanism are still subject of many debates between plasma formation [77–79] and electromigration supporters [80,81]; proof of either of these two phenomena is difficult to find. Compared to hot pressing, numerous studies have provided clear evidence that the densification of samples is greatly enhanced in the SPS process. Tokita has shown that, during sintering, matter necks appear between the grains, such a phenomenon being attributed to the presence of plasma between them [77]. Even if the presence of plasma can be debated, it is widely accepted that electric discharges occur at the microscopic level. Another important point has been settled: the influence of pulsing. It has been demonstrated that application of pulsed rather than constant DC current is directly related to the enhancement of the densification. The proposed hypothesis to account for this phenomenon is that the discharge of charges accumulated at the critical surface of the particle ionizes the corresponding volume by forming a plasma, which generates a drastic increase in the surface temperature of the particle.

(ii) *The effect of high heating rates*. The rapid sintering by SPS allows the low-temperature regime to be skipped, avoiding the non-densification mechanism (surface diffusion) and proceeding directly to the regime in which the densifying mechanisms (grain boundary and volume diffusion) are predominant [82]. Thus, the grain size decreases as the heating rate is increased [77]. Moreover, densification takes place in very short processing times, which further limits grain growth during the final sintering conditions; SPS provides a unique mechanism to separate grain growth from densification.

(iii) *Simultaneous application of pressure*. It is generally accepted that the application of mechanical pressure promotes the removal of pores and enhances diffusion. The use of mechanical pressure during the sintering step also increases the density of the green body and, thus, decreases the distance over which mass transfer must occur.

Moreover, the extent and rate of particle rearrangement are increased, while the agglomerates are destroyed. From studies carried out in different materials [77, 83], it is possible to conclude that the use of mechanical pressure involves a lowering of the sintering temperature and a limitation of the grain growth. Moreover, the possibility of separately programming the pressure and temperature during the SPS process allows both parameters to be combined in different ways [84].

2.3.1 SPS Applied to the Preparation of Ferroic Ceramic Materials

The SPS method has been used to obtain a large variety of piezoelectric ceramics, belonging to different structural types and with diverse chemical compositions. Here, the main results reported on 3-D perovskites are reviewed:

2.3.1.1 $BaTiO_3$-Based Lead-Free Materials

This system is one of the most studied using SPS, with the first work, reported in 1999 by Takeuchi et al. [85], showing the processing of dense $BaTiO_3$ ceramics (~95–97% densification). The starting powders were synthesized by different methods, either by hydrothermal, hydrolysis or, solid-state route (SSR), allowing submicrometer grain-sized materials (typically 0.1 to 0.6 μm) to be formed, with grain size similar to that of the starting powder. It has been demonstrated that the SPS process is effective for stabilizing the metastable cubic phase and also in reducing the influence of intergranular (grain boundary) effects on the permittivity and DC resistance, both characteristics of $BaTiO_3$ ceramics. Subsequent studies by the same research group [86] have also shown the influence of the synthesis method of perovskite powder on the properties of the final materials. For example, ceramics prepared from $BaTiO_3$ powder processed by a sol–gel method exhibit high room temperature permittivity values compared to conventional sintered ones. Several articles have been devoted to reporting the influence of the grain sizes of $BaTiO_3$ ceramics on their properties, down to the nanometer scale. SPS technology is particularly suitable for control of the grain size of the materials, of course depending on the average particle size of the precursor powders. The synthesis methods chosen to obtain nanosized powders are: sol–gel [87], coprecipitation [88–90], self-propagating high-temperature synthesis [91], and hydrothermal processing [92, 93].

SPS has also been applied to obtain dense ceramics belonging to different $BaTiO_3$-based solid solutions, such as $BaZr_{1-x}Ti_xO_3$ (BZT) [94] and $Ba_{1-x}Sr_xTiO_3$ [53, 95]. In the same way, other composite or nanocomposite materials, based on $BaTiO_3$, have been prepared by SPS, as, for example, densified multiwalled carbon nanotube (MWCNT)–$BaTiO_3$ [96], $BaTiO_3$/MgO/$BaTiO_3$ laminated composites [97], and $BaTiO_3$/Al_2O_3 nanocomposites [98].

2.3.1.2 Alkaline Niobate Lead-Free Materials

Although alkaline niobate-based piezoceramics exhibit an important combination of electrical and mechanical properties and an environmentally friendly character, the processing of high-quality ceramics remains a challenge. Moreover, for alkaline niobate ceramics, control of the processing is required in order to improve the compositional homogeneity, because high temperatures and long sintering times lead to volatilization of the alkaline metal [99].

The first attempts to apply the SPS method to obtain alkaline niobate-related ceramics were made by Wang et al. [100] and Wada et al. [101], who both succeeded in processing dense ceramics – $(1-y)(Na_{0.5}K_{0.5})NbO_3$–$yPbTiO_3$ ($y = 0.5$) and $NaNbO_3$, respectively – in order to study their electrical responses.

One of the more studied solid solutions of this system is $Na_xK_{1-x}NbO_3$, due to the good piezoelectric properties it is expected to have; however, because of its poor sinterability under ambient pressure, research has been devoted to new processing methods. The study by Wang et al. [102], using the SPS method, clearly showed that ceramics with ~98% densification can be obtained at temperatures of 1040–1100 °C.

2.3.1.3 High-Sensitivity Piezoelectrics Chemically Derived from $PbTiO_3$

The first works dealing with the application of SPS to $PbTiO_3$-related materials report results corresponding to the parent compound. It can, therefore, be deduced that the nature of the powdered precursors have a great influence on the results. Kakegawa et al. claim that lead titanate ($PbTiO_3$) is difficult to sinter without additives, even when an SPS technique is applied, if a simple mixture of PbO and TiO_2 is employed as the precursor [103]. This fact is attributed to the mechanical strain that resulted from the phase change from cubic – the stable polymorph at the sintering temperature – to the tetragonal stable phase at room temperature, after the sintering, which allows a decrease in the grain size rather than an increase of densification to be reached. In contrast, other authors have succeeded in obtaining dense

$PbTiO_3$ ceramics consisting of submicrometer-sized grains (0.1 μm) by using SPS [104]. This difference must be due to the precursor employed, in the latter case hydrothermally prepared $PbTiO_3$.

One of the PT-based systems to which the SPS technique has been widely applied in order to obtain ceramics with enhanced properties is the solid solution $Pb(Mg_{1/3}Nb_{2/3})O_3$–$PbTiO_3$ [105–108]. The SPS process has also been determined to be very effective for the densification of $0.65Pb(Mg_{1/3}$-$Nb_{2/3})O_3$–$0.35PbTiO_3$ ceramics. This fact is very important because, in this material as in the case of most of ceramic materials, the higher the density and the larger the average grain size, the better the dielectric and piezoelectric properties that are obtained. Moreover, the SPS process allows a capillary driven 0.65PMN – 0.35PT single crystal to be fabricated, with a high density, by increasing the density of the polycrystalline matrix precursor during heat treatment [105].

Similarly, the SPS method has been applied to obtaining dense ceramics belonging to the system $x Pb(Zn_{1/3}Nb_{2/3})O_3$–$y PbZrO_3$–$(1-x-y)PbTiO_3$. When a mixture of calcined materials having different compositions of this system was sintered by SPS, the compositional distribution in the starting mixture was almost maintained and such material exhibited a high pyroelectric coefficient, strongly related to the microstructure, over a wide temperature range [109, 110]. Moreover, SPS has also been used as a new method of preparing transparent $x Pb(Zn_{1/3}Nb_{2/3})O_3$–$y PbZrO_3$–$(1-x-y)PbTiO_3$ ceramics that could be promising candidates for applications in areas such as electrooptics and pyrooptics [111].

As a general conclusion, the SPS technique allows almost fully dense ceramics to be prepared with largely improved properties; this is mainly attributed to the control of their chemical compositions and microstructures. Obviously, the synthesis method for the powdered precursors and the resulting morphology of those powders also have a drastic effect on the characteristics of the final ceramic material.

2.4 Combination of Mechanosynthesis and Spark Plasma Synthesis: The Right Track to the Nanoscale in Ferroic Materials

Perhaps one of the most interesting applications of the SPS technique is the fabrication of nanostructured materials, when nanosized powdered precursors are used. This clear advantage over conventionally employed sintering methods can be attributed to the lower sintering temperature and shorter holding times needed, which allows nearly complete densification with little grain growth to be achieved. In this sense, the combination of mechanosynthesis and SPS makes it possible to control grain growth down to the nanometric scale, as well as to obtain homogeneous microstructures, demonstrating that synergy occurs by the joint utilization of these non-conventional methods. This approach had successfully been used to obtain high-density metallic materials [112], composites [113], and structural ceramics [114]. More recently, we have reported the first applications of this combination for the preparation of fully dense, fine-grained electroceramics of the $Ba_{1-x}Sr_xTiO_3$ [53], $(1-x)NaNbO_3$:$x SrTiO_3$ [99], and $BiScO_3$–$PbTiO_3$ systems [115]. The key to control grain growth in the nanoscale is to achieve a significant densification during initial stages of the SPS, mainly by particle rearrangement under pressure, before thermally activated processes are triggered. However, the advantages of this synergy can be used not only to control grain growth during the sintering process but also, and this is very important in the case of the low-tolerance factor perovskites, to stabilize some phases that could only be obtained by high-pressure methods. The first example is the PZN–PT, which presents ultra-high piezoelectric and electromechanical coefficients, which are significantly higher than those of the best lead zirconate titanate (PZT)-based piezoelectric ceramics typically used in applications [116]. The PZN–PT perovskite cannot be synthesized by the classical route due to phase instability issues that lead to the appearance of a paraelectric pyrochlore-type phase [117]. Moreover, even if the PZN–PT perovskite phase is obtained by high pressure or mechanochemical methods, as it is not stable under heating, the sintering process of the ceramic leads to its decomposition into pyrochlore, PbO and ZnO. The use of highly reactive nanocrystalline perovskite powder obtained by mechanosynthesis, together with spark plasma sintering, allows the stabilization of the 0.92PZN–0.08PT perovskite phase during the sintering and nanostructured ceramics with a grain size of 15–20 nm have been processed successfully [118]. Similar results were obtained in the case of the $Pb(Zn_{1/3}Nb_{2/3})O_3$–$Pb(Fe_{1/2}Nb_{1/2})O_3$–$PbTiO_3$ system [119].

The instability of the perovskite phase is also an issue in the case of the rare-earth manganites with orthorhombic perovskite structure $REMnO_3$ (RE: rare earth). These compounds have attracted much interest during the last few years due to their different and interesting properties, such as the colossal magnetoresistance observed in hole-doped $LaMnO_3$ [120] or the multiferroicity of many of their compositions [121]. The synthesis of such materials is not easy, as they belong to the group of rare-earth manganites with small ionic radii, for which the stable form is the hexagonal structure, with S.G. $P6_3cm$, instead of the orthorhombic perovskite one (OP), with S.G. Pbnm. As in the example of PZN–PT, the use of a combination of non-conventional methods prevent the decomposition of the perovskite, allowing dense ceramics to be obtained, keeping the OP structure at low temperatures, and maintaining the grain size at the nanoscale range [122].

As mentioned above, $BiMnO_{3+\delta}$ has been successfully obtained by mechanosynthesis, but when the oxide is annealed at temperatures higher than 400 °C, the decomposition of the perovskite is observed. This is the reason why, despite the numerous studies performed on this material and its foretold multiferroic properties, no processing studies have yet been conducted, which has limited its physical and mainly electrical characterization. Due to the metastable character of this material, very particular processing conditions are necessary to keep the structural characteristics of the final ceramic material. In this way, the optimum processing conditions have also been established in order to obtain high-quality ceramics of single-phase $BiMnO_{3+\delta}$ oxide. Soft thermal conditions (400 °C), medium pressures (1 GPa), and very short times (6 minutes) in a spark plasma sintering equipment are the unique conditions able to produce ceramics of good quality (relative density 92%). Different processing conditions, at a higher temperature and/or lower pressure and/or longer time, even by SPS, always result in decomposition of the compound. This processing route probably is adequate only for nanocrystalline precursors, like those obtained by mechanochemical routes [60].

2.5 Conclusions

It is difficult to summarize the research on a topic that is so popular and that is continuing to develop at such a rapid rate. Therefore, rather than just writing a summary about what is known so far about ferroic oxides, we have chosen to focus our attention on the problems observed during the synthesis of $BiMO_3$ (M = Fe and Mn) solid solutions. These problems are related to the lack of stability of the low-tolerance perovskites, especially in the case of $BiMnO_3$. Usually these problems are solved by the use of high-pressure methods, but these types of technique are expensive and require a high energy cost.

Instead of high-pressure methods, we propose the use of mechanosynthesis as an optimal preparation route to obtain low-tolerance-factor perovskite oxides and metastable phases in general. Remarkable results have been obtained in the case of PZN–PT, PZN–PFN–PT, $REMnO_3$, and $BiMO_3$ phases, among others.

However, even if the oxide is stabilized by mechanosynthesis, conventional sintering is often unable to provide dense ceramics of these low-stability phases, due to the high temperatures still required for densification. To solve this problem, we propose the use of spark plasma sintering, which has clear advantages over conventional sintering methods, making it possible to sinter mechanosynthesized powders to near full densification with no changes in the composition.

With this approach we achieved not only the stabilization of the low-tolerance perovskite phase in ceramics when sintering is carried out at low temperatures but also good control of the grain growth, necessary to produce nanostructured materials, while it has become increasingly important recently, with the miniaturization of electronic devices and the need to investigate size effects on the properties in the submicrometer range and approaching the nanometer scale ($\sim$100 nm).

Acknowledgments

This research has been funded by MINECO (Spain) through the MAT2014-58816-R Project. Technical support by Ms I. Martínez (ICMM) is acknowledged. The work has strongly benefited from synergies established within the ESF COST Action MP0904 SIMUFER.

References

(1) Schmid, H. (1994) Multi-ferroic magnetoelectrics. *Ferroelectrics*, **162** (1), 317–338.
(2) Hill, N.A. (2000) Why are there so few magnetic ferroelectrics? *Journal of Physical Chemistry B*, **104** (29), 6694–6709.
(3) Vaz, C.A.F., Hoffman, J., Ahn, C.H., and Ramesh, R. (2010) Magnetoelectric coupling effects in multiferroic complex oxide composite structures. *Advanced Materials*, **22** (26–27), 2900–2918.
(4) Wang, K.F., Liu, J.M., and Ren, Z.F. (2009) Multiferroicity: the coupling between magnetic and polarization orders. *Advances in Physics*, **58** (4), 321–448.
(5) Ramesh, R. (2009) Materials science: emerging routes to multiferroics. *Nature*, **461** (7268), 1218–1219.
(6) Scott, J.F. (1995) Transition temperatures in ferroelectrics. *Ferroelectrics*, **166** (1), 95–98.
(7) Catalan, G., and Scott, J.F. (2009) Physics and applications of bismuth ferrite. *Advanced Materials*, **21** (24), 2463–2485.

(8) Shannon, R.D. (1976) Revised effective ionic radii and systematic studies of interatomic distances in halides and chalcogenides. *Acta Crystallographica Section A*, **32** (5), 751–767.

(9) Belik, A., Kodama, K., Igawa, N., et al. (2010) Crystal and magnetic structures and properties of $BiMnO_{3+delta}$. *Journal of the American Chemical Society*, **132** (23), 8137–8144.

(10) Baettig, P., Seshadri, R., and Spaldin, N.A. (2007) Anti-polarity in ideal $BiMnO_3$. *Journal of the American Chemical Society*, **129** (32), 9854–9855.

(11) Belik, A.A., Iikubo, S., Yokosawa, T., et al. (2007) Origin of the monoclinic-to-monoclinic phase transition and evidence for the centrosymmetric crystal structure of $BiMnO_3$. *Journal of the American Chemical Society*, **129** (4), 971–977.

(12) Yokosawa, T., Belik, A.A., Asaka, T., et al. (2008) Crystal symmetry of $BiMnO_3$: Electron diffraction study. *Physical Review B*, **77** (2), art. no. 024111.

(13) Kodama, K., Iikubo, S., Shamoto, S.I., et al. (2007) Local crystal structure of multiferroic system $BiMnO_3$ by atomic pair distribution function analysis. *Journal of the Physical Society of Japan*, **76** (12), art. no. 124605.

(14) Comyn, T.P., Stevenson, T., and Bell, A.J. (2004) Piezoelectric properties of $BiFeO_3$–$PbTiO_3$ ceramics, in *Proceedings of the 14th IEEE International Symposium on Applications of Ferroelectrics*, IEEE, New York.

(15) Sakamoto, W., Yamazaki, H., Iwata, A., et al. (2006) Synthesis and characterization of $BiFeO_3$–$PbTiO_3$ thin films through metalorganic precursor solution. *Japanese Journal of Applied Physics*, **45** (9S), 7315–7320.

(16) Stevenson, T., Comyn, T.P., Daoud-Aladine, A., and Bell, A.J. (2006) Change in periodicity of the incommensurate magnetic order towards commensurate order in bismuth ferrite lead titanate. *Journal of Magnetism and Magnetic Materials*, **322** (22), L64–L66.

(17) Diéguez, O., and Íñiguez, J. (2011) First-principles investigation of morphotropic transitions and phase-change functional responses in $BiFeO_3$–$BiCoO_3$ multiferroic solid solutions. *Physical Review Letters*, **107** (5), art. no. 057601.

(18) Rabe, K.M., and Ghosez, P. (2007) First-principles studies of ferroelectric oxides, in *Physics of Ferroelectrics: A Modern Perspective*, 1st edition, edited by K. Rabe, Ch. H. Ahn, and J.M. Triscone, Springer-Verlag, Berlin, Heidelberg, pp. 117–174.

(19) Woodward, D.I., and Reaney, I.M. (2004) A structural study of ceramics in the $(BiMnO_3)(x)$–$(PbTiO_3)(1-x)$ solid solution series. *Journal of Physics: Condensed Matter*, **16** (49), 8823–8834.

(20) Castro, A., Vila, E., Jimenez, R., et al. (2010) Synthesis, structural characterization, and properties of perovskites belonging to the $xBiMnO_3$–$(1-x)$ $PbTiO_3$ system. *Chemistry of Materials*, **22** (2), 541–550.

(21) Zhang, X.Q., Sui, Y., Wang, X.J., et al. (2009) Influence of diamagnetic Pb doping on the crystal structure and multiferroic properties of the $BiFeO_3$ perovskite. *Journal of Applied Physics*, **105** (7), 07D918.

(22) Chaigneau, J., Haumont, R., and Kiat, J.M. (2009) Ferroelectric order stability in the $Bi_{1-x}Pb_xFeO_3$ solid solution. *Physical Review B*, **80** (18), art. no. 184107.

(23) Khomchenko, V.A., Kiselev, D.A., Kopcewicz, M., et al. (2009) Doping strategies for increased performance in $BiFeO_3$. *Journal of Magnetism and Magnetic Materials*, **321** (11), 1692–1698.

(24) Troyanchuk, O., Tereshko, N.V., Chobot, A.N., et al. (2009) Weak ferromagnetism in $BiFeO_3$ doped with titanium. *Physica B: Condensed Matter*, **404** (21), 4185–4189.

(25) Cao, W.W. and Cross, L.E. (1993) Theoretical-model for the morphotropic phase boundary in lead zirconate lead titanate solid-solution. *Physical Review B*, **47** (9), 4825–4830.

(26) Bhalla, A.S., Guo, R., and Alberta, E.F. (2002) Some comments on the morphotropic phase boundary and property diagrams in ferroelectric relaxor systems. *Materials Letters*, **54** (4), 264–268.

(27) Cox, D.E., Noheda, B., Shirane, G., et al. (2001) Universal phase diagram for high-piezoelectric perovskite systems. *Applied Physics Letters*, **79** (3), 400–402.

(28) McLeod, J.A., Pchelkina, Z.V., Finkelstein, L.D., et al. (2010) Electronic structure of $BiMO_3$ multiferroics and related oxides. *Physical Review B*, **81** (14), art. no. 144103.

(29) Belik, A.A. (2012) Polar and nonpolar phases of $BiMO_3$: a review. *Journal of Solid State Chemistry*, **195**, 32–40.

(30) Shetty, S., Palkar, V.R., and Pinto, R. (2002) Size effect study in magnetoelectric $BiFeO_3$ system. *Pramana – Journal of Physics*, **58** (5–6), 1027–1030.

(31) Wang, Y., Xu, G., Ren, Z., et al. (2007) Mineralizer-assisted hydrothermal synthesis and characterization of $BiFeO_3$ nanoparticles. *Journal of the American Ceramic Society*, **90** (8), 2615–2617.

(32) Basu, S., Pal, M., and Chakravorty, D. (2008) Magnetic properties of hydrothermally synthesized $BiFeO_3$ nanoparticles. *Journal of Magnetism and Magnetic Materials*, **320** (24), 3361–3365.

(33) Farhadi, S. and Zaidi, M. (2009) Bismuth ferrite ($BiFeO_3$) nanopowder prepared by sucrose-assisted combustion method: a novel and reusable heterogeneous catalyst for acetylation of amines, alcohols and phenols under solvent-free conditions. *Journal of Molecular Catalysis A: Chemical*, **299** (1), 18–25.

(34) Kim, J.K., Kim, S.S., and Kim, W.J. (2005) Sol–gel synthesis and properties of multiferroic $BiFeO_3$. *Materials Letters*, **59** (29), 4006–4009.

(35) Kumar, M., Yadav, K.I., and Varma, G.D. (2008) Large magnetization and weak polarization in sol–gel derived $BiFeO_3$ ceramics. *Materials Letters*, **62** (8), 1159–1161.

(36) Montanari, E., Righi, L., Calestani, G., et al. (2005) Room temperature polymorphism in metastable $BiMnO_3$ prepared by high-pressure synthesis. *Chemistry of Materials*, **17** (7), 1765–1773.

(37) Belik, A.A., Yusa, H., Hirao, N., et al. (2009) Peculiar high-pressure behavior of $BiMnO_3$. *Inorganic Chemistry*, **48** (3), 1000–1004.

(38) Bhattacharjee, S. and Pandey, D.J. (2010) Stability of the various crystallographic phases of the multiferroic $(1-x)BiFeO_3$–$xPbTiO_3$ system as a function of composition and temperature. *Journal of Applied Physics*, **107** (12), art. no. 124112.

(39) Comyn, T.P., McBride, S.P., and Bell, A.J. (2004) Processing and electrical properties of $BiFeO_3$–$PbTiO_3$ ceramics. *Materials Letters*, **58** (30), 3844–3846.

(40) Aguiar, E.C., Ramirez, M.A., Moura, F., et al. (2013) Low-temperature synthesis of nanosized bismuth ferrite by the soft chemical method. *Ceramic International*, **39** (1), 13–20.

(41) Bhattacharjee, S., Tripathi, S., and Pandey, D.J. (2007) Morphotropic phase boundary in $(1-x)BiFeO_3$–$xPbTiO_3$: phase coexistence region and unusually large tetragonality. *Applied Physics Letters*, **91** (4), art. no. 042903.

(42) Siddaramanna, A., Kothai, V., Srivastava, C., and Ranjan, R. (2014) Stabilization of metastable tetragonal phase in a rhombohedral magnetoelectric multiferroic $BiFeO_3$–$PbTiO_3$. *Journal of Physics D: Applied Physics*, **47** (4), art. no. 045004.

(43) Azuma, M., Kanda, H., Belik, A.A., et al. (2007) Magnetic and structural properties of $BiFe_{1-x}Mn_xO_3$. *Journal of Magnetism and Magnetic Materials*, **310** (2), 1177-1179.

(44) Selbach, S.M., Tybell, T., Einarsrud, M.A. and Grande, T. (2009) Structure and Properties of Multiferroic Oxygen Hyperstoichiometric $BiFe_{1-x}Mn_xO_{3+\delta}$. *Chemistry of Materials*, **21** (21), 5176–5186.

(45) Belik, A.A., Abakumov, A.M., Tsirlin, A.A., et al. (2011) Structure and magnetic properties of $BiFe_{0.75}Mn_{0.25}O_3$ perovskite prepared at ambient and high pressure. *Chemistry of Materials*, **23** (20), 4505–4514.

(46) Takacs, L. (2000) Quicksilver from Cinnabar: the first documented mechanochemical reaction? *JOM – Journal of the Minerals Metals and Materials Society*, **52** (1), 12–13.

(47) Benjamin, J.S. (1976) Mechanical alloying. *Scientific American*, **234** (5), 40–49.

(48) Giri, K. (1997) Nanocrystalline materials prepared through crystallization by ball milling. *Advanced Materials*, **9** (2), 163–166.

(49) Lacorre, P., and Retoux, R. (1997) First direct synthesis by high energy ball milling of a new lanthanum molybdate. *Journal of Solid State Chemistry*, **132** (2), 443–446.

(50) Castro, A., Millan, P., Pardo, L., and Jimenez, B. (1999) Synthesis and sintering improvement of Aurivillius type structure ferroelectric ceramics by mechanochemical activation. *Journal of Materials Chemistry*, **9** (6), 1313–1317.

(51) Boldyrev, V.V., and Tkacova, K. (2000) Mechanochemistry of solids: past, present, and prospects. *Journal of Materials Synthesis and Processing*, **8** (3–4), 121–132.

(52) Hungria, T., Hungria, A.B., and Castro, A. (2004) Mechanosynthesis and mechanical activation processes to the preparation of the $Sr_2[S_{n-1}Ti_nO_{3(n+1)}]$ Ruddlesden–Popper family. *Journal of Solid State Chemistry*, **177** (4–5), 1559–1566.

(53) Hungria, T., Hungria, A.B., Alguero, M., and Castro, A. (2005) Dense, fine-grained $Ba_{1-x}Sr_xTiO_3$ ceramics prepared by the combination of mechanosynthesized nanopowders and spark plasma sintering, *Chemistry of Materials*, **17** (24), 6205–6212.

(54) Lisoni, J.G., Millán, P., Vila, E., et al. (2001) Synthesis of ferroelectric $Bi_4Ti_3O_{12}$ by alternative routes: wet no-coprecipitation chemistry and mechanochemical activation. *Chemistry of Materials*, **13** (6), 2084–2091.

(55) Alguero, M., Ricote, J., and Castro, A. (2004) Mechanosynthesis and thermal stability of piezoelectric perovskite $0.92Pb(Zn_{1/3}Nb_{2/3})O_3$–$0.08PbTiO_3$ powders. *Journal of the American Ceramic Society*, **87** (5), 772–778.

(56) Alguero, M., Ricote, J., Hungria, T., and Castro, A. (2007) High-sensitivity piezoelectric, low-tolerance-factor perovskites by mechanosynthesis. *Chemistry of Materials*, **19** (20), 4982–4990.

(57) Moure, A., Hungria, T., Castro, A., et al. (2010) Mechanosynthesis of the orthorhombic perovskites $ErMn_{1-x}Ni_xO_3$ ($x = 0, 0.1$). Processing and characterization of nanostructured ceramics. *Chemistry of Materials*, **22** (9), 2908–2915.

(58) Brankovic, Z., Stanojevic, Z.M., Mancic, L., et al. (2010) Multiferroic bismuth manganite prepared by mechanochemical synthesis. *Journal of the European Ceramic Society*, **30** (2), 277–281.

(59) Stanojevic, Z.M., Brankovic, Z., Jaclicic, Z., et al. (2011) Structural and magnetic properties of nanocrystalline bismuth manganite obtained by mechanochemical synthesis. *Journal of Nanoparticle Research*, **13** (8), 3431–3439.

(60) Castro, A., Correas, C., Pena, O., et al. (2012) Nanostructured $BiMnO_{3+\delta}$ obtained at ambient pressure: analysis of its multiferroicity. *Journal of Materials Chemistry*, **22** (19), 9928–9938.

(61) Correas, C., Martínez, I., Castro, A. and Hungría, T. (2011) Optimization of the mechanochemical conditions for the synthesis of the xBiFeO$_3$–$(1-x)$PbTiO$_3$ multiferroic system. *Journal of Alloys and Compounds*, **509** (18), 5483–5487.

(62) Moreau, J.M., Michel, C., Gerson, R., and James, W.J. (1971) Ferroelectric $BiFeO_3$ X-ray and neutron diffraction study. *Journal of Physics and Chemistry Solids*, **32** (6), 1315–1320.

(63) Hungria, T., Correas, C., Houdellier, F., et al. (2012) Study of nanocrystalline $BiMnO_3$–$PbTiO_3$: synthesis, structural elucidation, and magnetic characterization of the whole solid solution. *Chemistry – A European Journal*, **18** (29), 9075–9082.

(64) Nagata, K., Kawatani, Y., and Okazaki, K. (1983) Anisotropies of hot-pressed transparent (Pb, Ba, La)Nb_2O_6 ceramics. *Japanese Journal of Applied Physics*, **22** (9R), 1353–1356.

(65) VanDamme, N.S., Sutherland, A.E., Jones, L., et al. (1991) Fabrication of optically transparent and electrooptic strontium barium niobate ceramics. *Journal of the American Ceramic Society*, **74** (8), 1785–1792.

(66) Kobune, M., Nishioka, Y., Inoue, T., and Yazawa, T. (2005) Growth and ferroelectric properties of $Pb(Zr_{0.52}Ti_{0.48})O_3$ thin films crystallized on MgO single-crystal substrates by hot isostatic pressing. *Journal of Crystal Growth*, **275** (1), E2421–E2425.

(67) Lee, H.Y., and Freer, R. (1997) The mechanism of abnormal grain growth in $Sr_{0.5}Ba_{0.4}Nb_2O_6$ ceramics. *Journal of Applied Physics*, **81** (1), 376–382.

(68) Nishiwaki, S., Takahashi, J., and Kodaira, K. (1994) Effect of additives on microstructure development and ferroelectric properties of $Sr_{0.3}Ba_{0.7}Nb_2O_6$ ceramics. *Japanese Journal of Applied Physics*, **33** (9S), 5477–5481.

(69) Hungria, T., Galy, J., and Castro, A. (2009) Spark plasma sintering as a useful technique to the nanostructuration of piezo-ferroelectric materials. *Advanced Engineering Materials*, **11** (8), 615–631.

(70) Munir, Z.A., Anselmi-Tamburini, U., and Ohyanagi, M. (2006) The effect of electric field and pressure on the synthesis and consolidation of materials: a review of the spark plasma sintering method. *Journal of Materials Science*, **41** (3), 763–777.

(71) Taylor, G.F. (1933) *Apparatus for Making Hard Metal Compositions*, US Patent, 1,896,854, filed July 7, 1931 and issued February 7, 1993.

(72) Cremer, G.D. (1944) *Powder Metallurgy*, US Patent, 2,355,954, filed March 4, 1942 and issued August 15, 1944.

(73) Inoue, K. (1960) *Electric Spark Machining Apparatus*, US Patent, 2,924,751, filed Jan. 31, 1958 and issued February 9, 1960.

(74) Honda, H., Sanada, Y., and Inoue, K. (1964) Diamond synthesis by electric discharge shock technique. *Carbon*, **1** (2), 127–128.

(75) Inoue, K. (1966) *Electric-Discharge Sintering*, US Patent, 3,241,956, filed October 29, 1963 and issued March 22, 1966.

(76) Wang, S.W., Chen, L.D., and Hirai, T. (2000) Densification of Al_2O_3 powder using spark plasma sintering. *Journal of Materials Research*, **15** (4), 982–987.

(77) Tokita, M. (1999) Development of large-size ceramic/metal bulk FGM fabricated by spark plasma sintering. *Materials Science Forum*, **308–311**, 83–88.

(78) Shen, Z.J., Johnsson, M., Zhao, Z., and Nygren, M. (2002) Spark plasma sintering of alumina. *Journal of the American Ceramic Society*, **85** (8), 1921–1927.

(79) Hulbert, D.M., Anders, A., Dudina, D.V., et al. (2008) The absence of plasma in "spark plasma sintering". *Journal of Applied Physics*, **104** (3), art. no. 033305.

(80) Wang, S.W., Chen, L.D., Hirai, T., and Kang, Y.S. (1999) Microstructure inhomogeneity in Al_2O_3 sintered bodies formed during the plasma-activated sintering process. *Journal of Materials Science Letters*, **18** (14), 1119–1121.

(81) Olevsky, E., and Froyen, L. (2006) Constitutive modeling of spark-plasma sintering of conductive materials. *Scripta Materialia*, **55** (12), 1175–1178.

(82) Wang, S.W., Chen, L.D., and Hirai, T. (2001) Formation of Al_2O_3 grains with different sizes and morphologies during the pulse electric current sintering process. *Jingkun Guo Journal: Journal of Materials Research*, **16** (12), 3514–3517.

(83) Anselmi-Tamburini, U., Garay, J.E., and Munir, Z.A. (2006) Fast low-temperature consolidation of bulk nanometric ceramic materials. *Scripta Materialia*, **54** (5), 823–828.

(84) Guillard, F., Allemand, A., Lulewicz, J.D., and Galy, J. (2007) Densification of SiC by SPS-effects of time, temperature and pressure. *Journal of the European Ceramic Society*, **27** (7), 2725–2728.

(85) Takeuchi, T., Betourne, E., Tabuchi, M., and Kageyama, H. (1999) Dielectric properties of spark-plasma-sintered $BaTiO_3$. *Journal of Materials Science*, **34** (5), 917–924.

(86) Takeuchi, T., Capiglia, C., Balakrishnan, N., et al. (2002) Preparation of fine-grained $BaTiO_3$ ceramics by spark plasma sintering. *Journal of Materials Research*, **17** (3), 575–581.

(87) Li, R., Wang, X.H., Cai, M.M., et al. (2003) Densification of uniformly small-grained $BaTiO_3$ using spark-plasma-sintering. *Materials Chemistry and Physics*, **82** (1), 173–180.

(88) Li, X., Wang, L., Li, H., et al. (2004) Dielectric properties of fine-grained $BaTiO_3$ prepared by spark-plasma-sintering. *Materials Chemistry and Physics*, **83** (1), 23–28.

(89) Buscaglia, M.T., Buscaglia, V., Viviani, M., et al. (2004) Ferroelectric properties of dense nanocrystalline $BaTiO_3$ ceramics. *Nanotechnology*, **15** (9), 1113–1117.

(90) Buscaglia, V., Buscaglia, M.T., Viviani, M., et al. (2005) Raman and AFM piezoresponse study of dense $BaTiO_3$ nanocrystalline ceramics. *Journal of the European Ceramic Society*, **25** (12), 3059–3062.

(91) Licheri, R., Fadda, S., Orru, R., et al. (2007) Self-propagating high-temperature synthesis of barium titanate and subsequent densification by spark plasma sintering (SPS). *Journal of the European Ceramic Society*, **27** (5), 2245–2253.

(92) Maiwa, H. (2008) Preparation and properties of $BaTiO_3$ ceramics by spark plasma sintering. *Japanese Journal of Applied Physics*, **47** (9S), 7646–7649.

(93) Deng, X.Y., Wang, X.H., Wen, H., et al. (2006) Ferroelectric properties of nanocrystalline barium titanate ceramics. *Applied Physics Letters*, **88** (25), 252905.

(94) Maiwa, H. (2008) Structure and properties of Ba($Zr_{0.2}Ti_{0.8}$)O_3 ceramics prepared by spark plasma sintering. *Journal of Materials Science*, **43** (19), 6385–6390.

(95) Liu, J., Shen, Z.J., Nygren, M., et al. (2006) Spark plasma sintering behavior of nanosized (Ba,Sr)TiO_3 powders: determination of sintering parameters yielding nanostructured ceramics. *Journal of the American Ceramic Society*, **89** (9), 2689–2694.

(96) Huang, Q., Gao, L., Liu, Y.Q., and Sun, J. (2005) Sintering and thermal properties of multiwalled carbon nanotube-$BaTiO_3$ composites. *Journal of Materials Chemistry*, **15** (20), 1995–2001.

(97) Rattanachan, S., Miyashita, Y., and Mutoh, Y. (2005) Fabrication of piezoelectric laminate for smart material and crack sensing capability. *Science and Technology of Advanced Materials*, **6** (6), 704–711.

(98) Zhan, G.D., Kuntz, J., Wan, J.L., et al. (2003) Spark-plasma-sintered $BaTiO_3/Al_2O_3$ nanocomposites. *Materials Science and Engineering A*, **356** (1), 443–446.

(99) Hungria, T., Alguero, M., and Castro, A. (2006) Synthesis of nanosized $(1 - x)$ $NaNbO_3$–$x$$SrTiO_3$ solid solution by mechanochemical activation, processing of ceramics, and phase transitions. *Chemistry of Materials*, **18** (22), 5370–5376.

(100) Wang, R.P., Xie, R.J., Sekiya, T., et al. (2002) Piezoelectric properties of spark-plasma-sintered ($Na_{0.5}K_{0.5}$)NbO_3–$PbTiO_3$ ceramics. *Japanese Journal of Applied Physics*, **41** (11S), 7119–7122.

(101) Wada, T., Tsuji, K., Saito, T., and Matsuo, Y. (2003) Ferroelectric $NaNbO_3$ ceramics fabricated by spark plasma sintering. *Japanese Journal of Applied Physics*, **42** (9S), 6110–6114.

(102) Wang, R.P., Xie, R.J., Sekiya, T., and Shimojo, Y. (2004) Fabrication and characterization of potassium–sodium niobate piezoelectric ceramics by spark-plasma-sintering method. *Materials Research Bulletin*, **39** (11), 1709–1715.

(103) Kakegawa, K., Kawai, Y., Wu, Y.J., et al. (2004) Sintering of lead titanate using a spark-plasma-sintering technique. *Journal of the American Ceramic Society*, **87** (4), 541–545.

(104) Takeuchi, T., Tabuchi, M., Kondoh, I., et al. (2000) Synthesis of dense lead titanate ceramics with submicrometer grains by spark plasma sintering. *Journal of the American Ceramic Society*, **83** (3), 541–544.

(105) Chen, K.P., Li, C.W., Zhang, X.W., and Huang, Y. (2002) Microstructure and electrical properties of $0.7Pb(Mg_{1/3}Nb_{2/3})O_3$–$0.3PbTiO_3$ ceramics by spark plasma sintering. *Materials Letters*, **57** (1), 20–23.

(106) Park, J.K., Chung, U.J., and Kim, D.Y. (2006) Application of spark plasma sintering for growing dense $Pb(Mg_{1/3}Nb_{2/3})O_3$–35 mol% $PbTiO_3$ single crystal by solid-state crystal growth. *Journal of Electroceramics*, **17** (2–4), 509–513.

(107) Zuo, R.Z., Granzow, T., Lupascu, D.C., and Rodel, J. (2007) PMN–PT ceramics prepared by spark plasma sintering. *Journal of the American Ceramic Society*, **90** (4), 1101–1106.

(108) Shimojo, Y., Wang, R., Shan, Y.J., et al. (2008) Dielectric characters of $0.7Pb(Mg_{1/3}Nb_{2/3})O_3$–$0.3PbTiO_3$ ceramics fabricated at ultra-low temperature by the spark-plasma-sintering method. *Ceramic International*, **34** (6), 1449–1452.

(109) Wu, Y.J., Uekawa, N., Sasaki, Y., et al. (2002) Microstructures and pyroelectric properties of multicomposition $0.9PbZrO_{3.}xPbTiO_{3.}(0.1 - x)Pb(Zn_{1/3}Nb_{2/3})O_3$ ceramics. *Journal of the American Ceramic Society*, **85** (8), 1988–1992.

(110) Kakegawa, K., Uekawa, N., Wu, Y.J., and Sasaki, Y. (2003) Change in the compositional distribution in perovskite solid solutions during the sintering by SPS. *Materials Science and Engineering B*, **99** (1), 11–14.

(111) Wu, Y.J., Kimura, R., Uekawa, N., et al. (2002) Spark plasma sintering of transparent $PbZrO_3$–$PbTiO_3$–$Pb(Zn_{1/3}Nb_{2/3})O_3$ ceramics. *Japanese Journal of Applied Physics*, **41** (2B), L219–L221.

(112) Paris, S., Gaffet, E., Bernard, F., and Munir, Z.A. (2004) Spark plasma synthesis from mechanically activated powders: a versatile route for producing dense nanostructured iron aluminides. *Scripta Materialia*, **50** (5), 691–696.

(113) Luo, Y.M., Li, S.Q., Chen, J., et al. (2002) Effect of composition on properties of alumina/titanium silicon carbide composites. *Journal of the American Ceramic Society*, **85** (12), 3099–3140.

(114) Won, J.H., Kim, K.H., Chae, J.H., and Shim, K.B. (2002) Sintering of attrition-milled TiN powders using a spark plasma sintering technique. *Journal of Ceramic Processing Research*, **3** (3), 166–170.

(115) Hungria, T., Amorin, H., Alguero, M., and Castro, A. (2011) Nanostructured ceramics of $BiScO_3$–$PbTiO_3$ with tailored grain size by spark plasma sintering. *Scripta Materialia*, **64** (1), 97–100.

(116) Park, S.E., and Shrout, T.R. (1997) Ultrahigh strain and piezoelectric behavior in relaxor based ferroelectric single crystals. *Journal of Applied Physics*, **82** (4), 1804–1811.

(117) Halliyal, A., Kumar, U., Newnham, R.E., and Cross, L.E. (1987) Stabilization of the perovskite phase and dielectric-properties of ceramic in the $Pb(Zn_{1/3}Nb_{2/3})O_3$-$BaTiO_3$ system. *American Ceramic Society Bulletin*, **66** (4), 671–676.

(118) Hungria, T., Amorin, H., Galy, J., et al. (2008) Nanostructured ceramics of $0.92PbZn_{1/3}Nb_{2/3}O_3$–$0.08PbTiO_3$ processed by SPS of nanocrystalline powders obtained by mechanosynthesis. *Nanotechnology*, **19** (15), 155609.

(119) Amorin, H., Jimenez, R. Hungria, T., et al. (2009) Relaxor behavior in nanostructured $Pb(Zn_{1/3}Nb_{2/3})O_3$–$Pb(Fe_{1/2}Nb_{1/2})O_3$–$PbTiO_3$ ceramics. *Applied Physics Letters*, **94** (15), art. no. 152902.

(120) Ramirez, P. (1997) Colossal magnetoresistance. *Journal of Physics: Condensed Matter*, **9** (39), 8171–8199.

(121) Cheong, S.W., and Mostovoy, M. (2007) Multiferroics: a magnetic twist for ferroelectricity. *Nature Materials*, **6** (1), 13–20.

(122) Moure, A., Hungria, T., Castro, A., et al. (2012) Influence of Ni and Co doping on the stability of the $ErMnO_3$ perovskites processed by mechanochemical synthesis. *Ceramic International*, **38** (2), 1507–1513.

3

Core–Shell Heterostructures: From Particle Synthesis to Bulk Dielectric, Ferroelectric, and Multiferroic Composite Materials

Vincenzo Buscaglia and Maria Teresa Buscaglia

Institute of Energetics and Interphases, National Research Council, Italy

3.1 Introduction

The nanoscale coating of small particles with materials of different composition, resulting in the formation of core–shell structures, is a relatively new and active area of research. The coating not only changes the interactions of the particles with the surrounding environment but also allows modification of the particle properties (optical, magnetic, catalytic, etc.). New functionalities can be imparted to the cores depending on the properties of the shell. Using a number of synthetic approaches, dissimilar materials (metals, semiconductors, ceramics, polymers, biomolecules, etc.) can be combined together for many different applications in the areas of coatings, electronics, catalysis, separations, diagnostics, and drug delivery [1–3].

Silica coatings have been used extensively in order to modify the surface properties of several types of colloidal particles (especially magnetic particles) and make them dispersible in a liquid or in a glass or glass–ceramic matrix. Silica-coated nanoparticles can be further modified by surface functionalization. Moreover, a silica coating can significantly

---

Nanoscale Ferroelectrics and Multiferroics: Key Processing and Characterization Issues, and Nanoscale Effects, First Edition. Edited by Miguel Algueró, J. Marty Gregg, and Liliana Mitoseriu.
© 2016 John Wiley & Sons, Ltd. Published 2016 by John Wiley & Sons, Ltd.

improve the properties of magnetic nanoparticles or modulate the optical properties. The optical resonances of SiO_2@Au particles (the A@B notation signifies A cores coated with B shell) could be varied over hundreds of nanometers in wavelenght by variation of the relative sizes of the core and shell [4]. Catalytic applications include Fe_3O_4@SiO_2 nanoparticles as support for biocatalyst for a more efficient separation and very thin anatase coating on gold nanoparticles [5,6]. Bimagnetic core–shell particles have also attracted interest due to the possibility to tailor the overall properties by the exchange interaction between the two constituents [7]. Hollow inorganic spheres can be obtained by coating polymer particles in suspension with a given material. Subsequent dissolution or oxidation of the organic core yields hollow ceramic or metal spheres. Hollow organic and hybrid nanostructured spheres are intensively studied as microcapsules for the encapsulation and controlled delivery of diverse substances (drugs, cosmetics, dyes, etc.) [1].

Core–shell particles can be used as building blocks for the fabrication of bulk composite multifunctional materials with 0–3 connectivity by means of appropriate densification techniques. The coating prevents percolation even for high-volume fractions of the core phase. Thanks to their high dielectric constant, ferroelectric oxide particles, either bare or coated with a polymeric shell, are used as fillers in dielectric polymeric materials to increase their effective permittivity. Capacitors fabricated from these composites are attractive owing to their ability to store energy with high density. The polymer shell improves the compatibility between the particles and the matrix resulting in homogeneous dispersion of the filler, avoiding agglomeration and segregation of the inorganic component. When the composite is fabricated by in situ polymerization, the polymer shell favors the anchoring of the monomer on the particle surface.

The dielectric properties of ferroelectric ceramics can be modified by coating the precursor particles with linear dielectric or paraelectric oxides, such as SiO_2, Al_2O_3, MgO, $SrTiO_3$, $BaZrO_3$, etc. The coating exerts a significant effect on temperature and frequency dependence of dielectric permittivity. An intriguing class of multifunctional composites that has attracted interest in recent years is the so-called magnetoelectric multiferroics. Multiferroic (MF) composites consist of a ferroelectric phase, in most cases $BaTiO_3$ or $Pb(Zr,Ti)O_3$, and a ferro- or ferrimagnetic compound, often a spinel ferrite [8]. In addition to the ferroic properties of the parent phases, MFs possess a complete new property, the magnetoelectric (ME) effect. In these materials the application of a magnetic field determines a variation of polarization whereas the application of an electric field results in a change of magnetization. Recent progress on the preparation of MF composites using core–shell particles was summarized by Schileo [9].

In the case of inorganic composites, the retention of the core–shell arrangement of the precursor particles along with high densification is not trivial. Inorganic composites are usually consolidated by sintering, a process that requires high temperatures. Consequently, the final microstructure and properties will be strongly conditioned by the amount of residual porosity, the occurrence of grain growth and coarsening, the extent of interdiffusion between the core and shell and the possible formation of intermediate phases by reaction at phase boundaries. These interface phenomena can be minimized by using rapid sintering methods, such as spark plasma sintering (SPS) and field-assisted sintering. With these methods a good densification is usually attained at a lower temperature (100–300 °C less) and in a shorter time (typically a few minutes) in comparison to conventional sintering and hot-pressing [10,11].

In this review paper, the synthesis and consolidation of ferroelectric and multiferroic core–shell particles and the properties of resulting composites will be addressed. A general overview on the liquid-phase synthesis of core–shell particles is given in Section 3.2. Section 3.3 reports a short survey on the synthesis of $BaTiO_3$@polymer particles and their use as fillers in polymer composites. The coating of ferroelectric cores with linear dielectric or paraelectric oxides and the fabrication of dielectric ceramics and composites are reviewed in Section 3.4. The topic of Section 3.5 is the preparation and consolidation of multiferroic core–shell particles.

3.2 Liquid-Phase Synthesis of Core–Shell Particles

Three main approaches are adopted for the realization of coatings on the surface of core particles suspended in a suitable liquid: (i) the controlled assembly of one or more layers of preformed nanoparticles; (ii) the direct precipitation of the shell material from solution; and (iii) the reaction between functional groups at the core surface and shell precursor molecules introduced in solution. The first two methods are mainly adopted for inorganic core–shell particles and the solvent is most often water. General principles and mechanisms are discussed in Subsections 3.2.1 and 3.2.2. The third approach is particularly useful for the growth of a polymeric coating on oxide particles. In this case, appropriate coupling molecules are first anchored on the core and then the monomer or polymer is grafted on the particle by formation of chemical bonds between the functional groups of the two molecules. The liquid media used in the different processing steps have to be good solvents of the organic species. A more detailed survey is given in Section 3.3.

3.2.1 Controlled Assembly of Preformed Nanoparticles

Useful guidelines for the coating of core particles by the ordered assembly of preformed nanoparticles are provided by the theory of colloids. When a solid is immersed in water or another polar solvent, it acquires a surface charge by adsorbing ions from the surrounding liquid. The control of the electrostatic interactions between particles in suspension is one of the most widely used methods to induce the ordered assembly of the shell nanoparticles at the surface of the cores. Near the isoelectric point, the attractive van der Waals forces predominate, thus causing the uncontrolled aggregation of the particles in suspension. However, by choosing appropriate experimental conditions (pH, temperature, ionic strength) at which two different types of particles have opposite charge, the self-assembly of the colloids in core–shell structures can be readily obtained by mixing two separate suspensions. The surface charge of one or both solids can be controlled by the adsorption of polymeric polyelectrolytes, such as polyacrilic acid (negative surface charge), polyethylenimine, and polydiallyldimethylammonium chloride (positive surface charge). Nanocomposite multilayers can be assembled on particle surfaces by using the layer-by-layer (LbL) method [1, 12], which consists of the multiple application of polyelectrolyte adsorption and nanoparticle assembly steps. The use of chemical assembly methods can lead to more robust particle aggregates. These methods rely on the formation of covalent bonds between functional groups anchored on the solid surfaces and reactive solute molecules. The Cu(I)-catalyzed azide-alkyne cycloaddition (CuAAC) reaction (often referred to as "click" chemistry) has recently emerged as a particularly versatile way to achieve chemical assembly [13, 14].

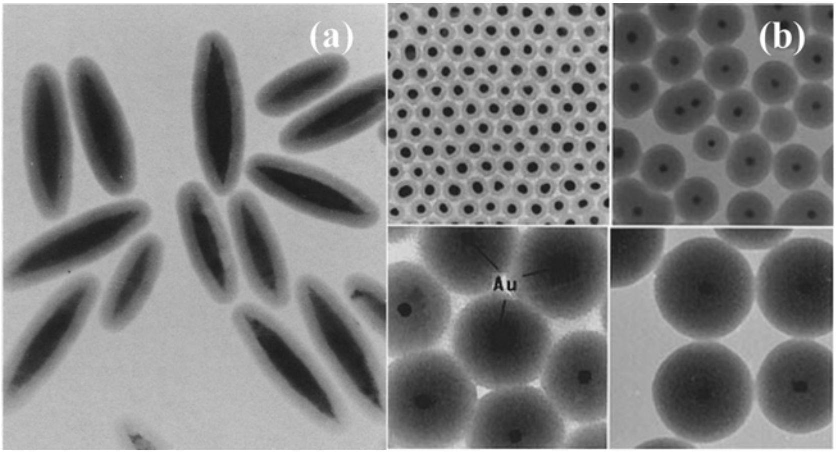

Figure 3.1 (a) Hematite (α-Fe_2O_3) particles coated with silica (reprinted from [16], Copyright (1992), with permission from Elsevier). (b) Gold nanoparticles coated with silica (reprinted with permission from [17]. Copyright (2005) American Chemical Society)

3.2.2 Precipitation

Inorganic core–shell particles considered in this review are mainly synthesized by this approach. The precipitation method has been widely employed to coat magnetic particles with silica using the Stöber process [15,16]. After coating, the surface properties are those of silica and the particles can be easily dispersed in different media. The method is not directly applicable to coating vitreophobic materials such as gold or silver nanoparticles. In this case, functionalization of the metal surface with aminosilane molecules is required to obtain thick and homogeneous coatings [17]. Similar approaches are often used to coat many types of inorganic colloids. Figure 3.1 shows the morphology of two core–shell model systems: $Fe_2O_3@SiO_2$ and $Au@SiO_2$.

In their pioneering work, Matijević and co-workers fabricated a variety of core–shell particles by combining inorganic compounds, mainly oxides, of zirconium, hafnium, titanium, iron, chromium, manganese, indium, and zinc [16, 18–25] as well as inorganic coatings on polystyrene (PS) spheres [26,27]. The availability of non-agglomerated core particles with controlled morphology and narrow size distribution is a fundamental prerequisite for the preparation of core–shell particles with controlled and reproducible properties [28,29]. Matijević and co-workers [26, 30] also investigated in some detail the shell formation mechanism. The surface coating may be formed either by surface nucleation and growth or heterocoagulation of preformed coating material with the core particle. The second process is mainly driven by interparticle electrostatic interactions. During the aging of a precursor solution of the shell material, hydrolysis occurs with formation of small clusters that can grow further with the formation of colloidal particles. When the cores and these colloidal moieties have opposite charge, the electrostatic attraction will spontaneously determine the formation of a coating by heterocoagulation. The coating formation is strongly dependent on temperature, pH, and concentration. At high concentration the nucleation rate is very high and a huge number of nanoparticles are generated in a very short time and

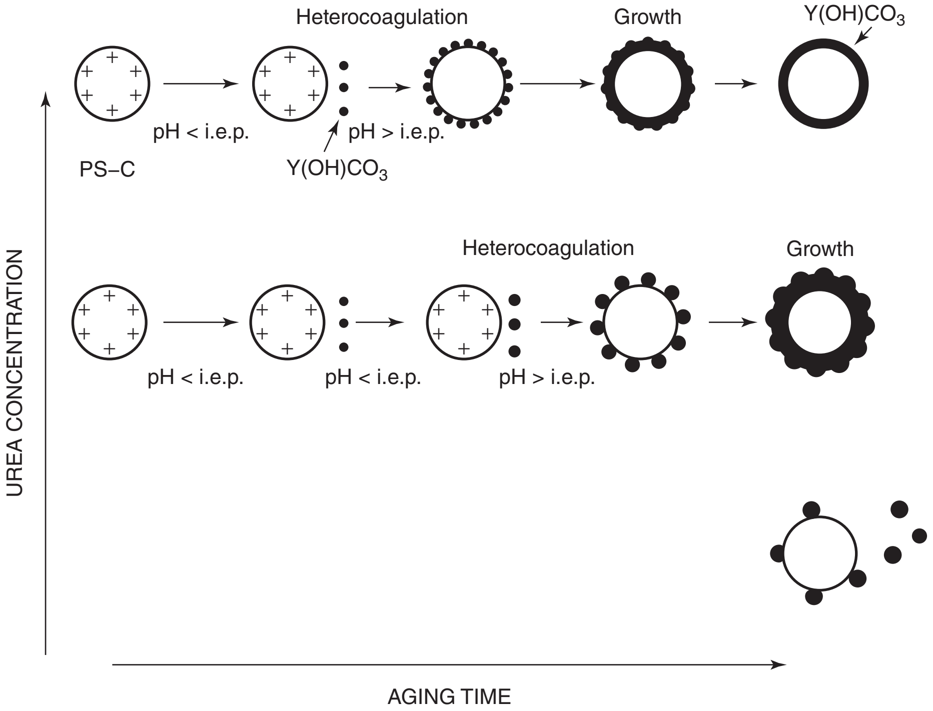

Figure 3.2 *Schematic presentation of the coating mechanisms of latex by yttrium basic carbonate at different urea concentrations as a function of the aging time. Reprinted from [26], Copyright (1990), with permission from Elsevier*

readily heterocoagulate with the cores, forming a smooth and uniform shell. In contrast, at low concentration, the number of nuclei is much smaller and growth becomes important, resulting in coatings with a rough surface or even the formation of a mixture of particles. Figure 3.2 illustrates the shell formation by heterocoagulation in the case of polystyrene microspheres suspended in a solution containing yttrium nitrate and urea.

The sequence of events include the decomposition of urea, which determines a rise of pH, the hydrolysis of the yttrium nitrate solution with subsequent formation of small yttrium basic carbonate particles, and finally the heterocoagulation of this colloid with the PS spheres. The PS cores are positively charged whereas the surface charge of the colloidal particles reverse from positive to negative with increasing pH determining their adhesion on the PS surface. With decreasing concentration (supersaturation) the growth of the yttrium compound particles become important and can result in the formation of a mixture of the two different colloids rather than core–shell particles.

Heterogeneous nucleation and growth of the shell compound on the core surface can be promoted when the concentration (supersaturation) is rather low. The most favorable circumstance corresponds to the heteroepitaxial growth of the shell compound. In this case the energy barrier for nucleation is strongly reduced, resulting in fast nucleation and only limited growth, with the formation of a homogeneous coating. Heteroepitaxial growth

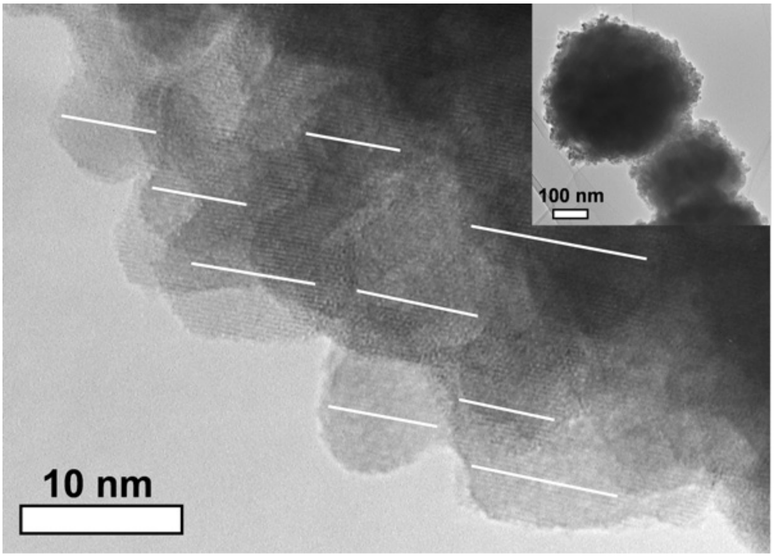

Figure 3.3 HR-TEM image of the shell morphology in a $BaTiO_3$@$BaZrO_3$ particle obtained by precipitation. The white lines show that the (100) lattice planes in different $BaZrO_3$ nanocrystals are oriented along the same crystallographic direction. Inset: particle morphology at low magnification

occurs when there is a high structural compatibility, at least along some crystallographic directions, between the two solids. A representative example of a heteroepitaxial arrangement has been observed in the case of $BaTiO_3$@$BaZrO_3$ particles [31]. As shown in Figure 3.3, the $BaZrO_3$ nanocrystals on the surface of $BaTiO_3$ are all aligned along the [100] crystallographic direction as well as along the [100] pseudocubic direction of the underlying $BaTiO_3$ lattice. However, there is not conclusive evidence that this situation originates from surface nucleation and growth rather than the ordered assembly of preformed nanoparticles.

3.3 $BaTiO_3$@polymer Particles and Composites

The coating of inorganic particles with polymers can be realized by in situ polymerization processes (*grafting from* methods) or by grafting preformed polymers on the particle surface (*grafting to* methods). First examples of core–shell particles obtained by in situ polymerization were reported about 20 years ago for different systems: poly(divinylbenzene) on silica and alumina [32], polyaniline on CuO [33], polypyrrole on different metal oxides [34], and polyacrylate [35] and polystyrene on silica [36, 37]. As a general approach, the shell can be produced by dispersing the inorganic particles in a suitable organic solvent in which the monomer is dissolved, adsorbing/anchoring the monomer on the particle surface, and then adding an initiator to induce the in situ polymerization of the monomer. Reducible metal oxides, such as CuO and CeO_2, can take part in the reaction by oxidizing the monomer and then facilitating the polymerization process, as happens in the case of aniline and pyrrole [33, 34]. In practice, the core surface has often to be modified to improve its compatibility with the monomer and the solvent, for example by binding a reactive coupling agent which matches the monomer/polymer or by precoating the cores with an inorganic layer that better matches the monomer or the coupling agent or the polymer. $BaTiO_3$ particles can be functionalized by different molecules, including different types of organosilanes [38], ethylenediamine [39], phosphonic acids [40–42], and oleic acid [43] to improve their dispersion in organic solvents and host polymers. The surface of $BaTiO_3$ can be hydroxilated by treatment with a hot solution of H_2O_2 to improve the compatibility with fluorinated polymers [44]. Moreover, the surface hydroxyl groups are very useful for anchoring molecules, such as oleic acid [43], methylaluminoxane (MAO) [45–47], and γ-aminopropyltriethoxysilane (γ-APS) [48–52]. The amine groups of γ-APS are then used to graft different monomers by chemical reaction. In order to avoid any possible adverse effect of the residual polymerization catalyst (CuCl, CuBr) on the dielectric properties of the composite, reversible addition–fragmentation chain transfer (RAFT) polymerization has been recently introduced for the in situ coating of $BaTiO_3$ [49, 52, 53]. RAFT polymerization is compatible with a wide range of functionalities in monomers and no metallic ion complexes are needed.

Recent results of the preparation of $BaTiO_3$@polymer particles and the dielectric properties of the corresponding 0-3 composites [48–56] are summarized in Table 3.1. The final materials typically contain 10–50 vol% of oxide particles with a typical diameter of the order of 100 nm. As a representative example, the morphology of PS@$BaTiO_3$ particles and the final composite containing 37 vol% $BaTiO_3$ are shown in Figure 3.4(a) and (b).

A simple method for the fabrication of the composites is by hot compression of the core–shell particles in a mould; the coalescence of the polymer shell determines the formation of a continuous matrix. When the polymer matrix has a composition different from that of the shell, the composite is often prepared by spin coating or casting of a dispersion of the coated $BaTiO_3$ particles in a solution of the polymer followed by solvent evaporation and a hot-compression stage. The addition of the filler results in a significant increase of the dielectric constant from a few units for the pure polymers to 15–30 for composites containing ≈30–40 vol% $BaTiO_3$ with an improvement of an order of magnitude (Table 3.1). Beside a high dielectric constant, application of the composite in capacitors requires a low loss tangent, of the order of 1% or less. Frequency dispersion should be absent or limited; a significant increase of ε_r at low frequency accompanied by a peak of $\tan\delta$ usually denotes dielectric relaxation or Maxwell–Wagner relaxation [50, 56]. The dielectric properties of composites prepared from PS@$BaTiO_3$ particles are shown in Figure 3.4(c) and (d). A major advantage of the use of BaTiO@polymer particles as fillers is that percolation of the inorganic particles is avoided even for volume fractions well above the percolation threshold of ≈16 vol% predicted for two-phase random composites. This results in a breakdown field much higher than that of the oxide, even for a filler loading of 50 vol% or larger.

3.4 Inorganic Core–Shell Particles with a Ferroelectric Core

The literature on this topic is mostly focused on the coating of ferroelectric particles, mainly $BaTiO_3$ and $(Ba,Sr)TiO_3$, with linear dielectrics (SiO_2, Al_2O_3, MgO) or paraelectric compounds (TiO_2, $SrTiO_3$, $BaZrO_3$). Appropriate densification of these particles produces microstructures characterized by a lower permittivity percolating grain boundary layer originated by the coalescence of the shells. The dielectric properties of these composites are

Table 3.1 *$BaTiO_3$@polymer particles and composites. Room temperature dielectric properties (ε_r: relative dielectric constant; tan δ: loss tangent) are reported at two different frequencies (10^3 and 10^6 Hz) and refer to the amount of filler indicated in the second-last column*

$BaTiO_3$ fraction (vol%)	Shell composition	Polymeric matrix	Composite fabrication method	ε_r		tan δ		$BaTiO_3$ fraction (vol%)	Ref.
				10^3 Hz	10^6 Hz	10^3 Hz	10^6 Hz		
10–33	Polystyrene-blockpoly(styrene-co-vinylbenzylchloride)	Polystyrene	Suspension spin coating	45	34	0.06	–	33	54
30 wt %	Hyperbranched copper phthalocyanine	Polyarylene ether nitrile	Suspension casting	5.9		0.028		30 wt%	55
15–32	Poly(methyl methacrylate)	–	Hot compression molding at 200 °C	14.5	13	0.038	0.022	32	48
7–41 wt%	Double shell: hyperbranched polyester + poly(methyl methacrylate)	–	Suspension spin coating and thermal treatment at 125 °C	86	14.5	5.8	0.21	41 wt%	56
37–48	Polystyrene (RAFT polymerization)	–	Hot compression molding at 200 °C	14.4	14.4	0.009	0.013	37	49
10–40	Hyperbranched aromatic polyamide	Poly(vinylidene fluoride-trifluoroethylene-chlorofluoroethylene)	Suspension casting	1470	90	3.5	0.66	40	50
25.5–56.7	Double shell: hyperbranched aromatic polyamide + poly(methyl methacrylate)	–	Suspension casting	15.3	13.8	0.042	0.02	41	51
10–50	Polyfluoroalkyl acrylate (RAFT polymerization)	Poly(vinylidene fluoride-co-hexafluoro propylene)	Hot compression molding	33–36	–	0.017–0.02	–	40	52
56–60	Polystyrene (RAFT polymerization)	–	Hot compression molding	29.5	28.5	0.0014	0.01	56	53
56–60	Poly(methyl methacrylate) (RAFT polymerization)	–	Hot compression molding	34	31.5	0.032	0.02	57	53

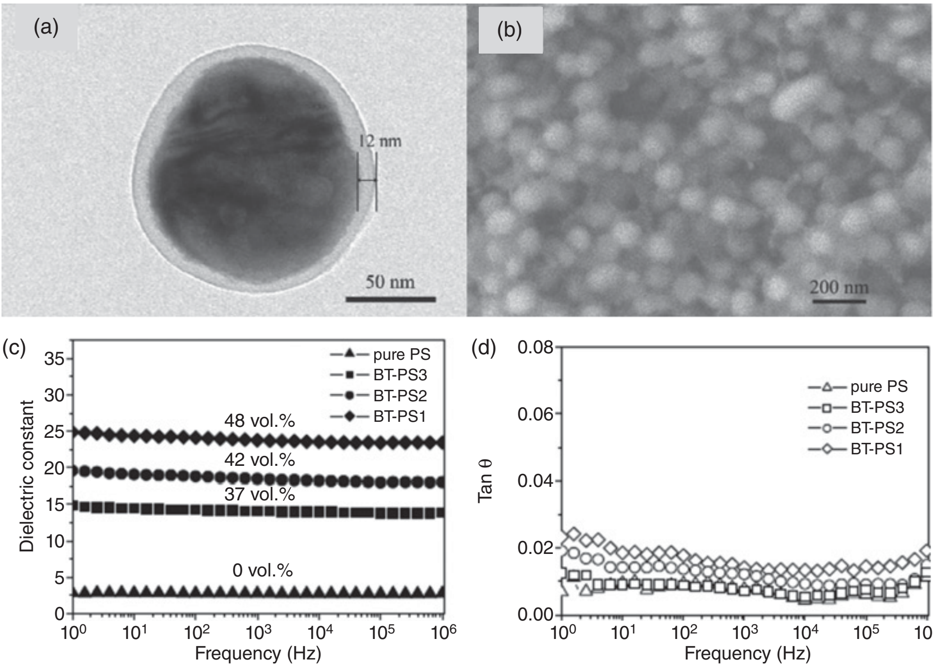

Figure 3.4 *(a) TEM image of a PS@BaTiO$_3$ particle and (b) SEM mage of the fracture surface of the composite with 37 vol% BaTiO$_3$. (c) Relative dielectric constant and (d) dielectric losses versus temperature of composites containing different amounts of BaTiO$_3$ particles. Reprinted with permission from [49]. Copyright (c) [2012] [Wiley-VCH Verlag GmbH & Co. KGaA, Weinheim].*

strongly modified in comparison to the corresponding pure ferroelectric ceramics because of the dilution effect exerted by this layer and the possible interdiffusion between core and shell materials.

In a series of papers [57–61], Elissalde and co-workers have investigated the encapsulation of $BaTiO_3$ and $Ba_{0.6}Sr_{0.4}TiO_3$ particles of different diameter with an amorphous silica shell by means of a modified Stöber process using tetraethoxysilane (TEOS) as precursor. In the case of $Ba_{0.6}Sr_{0.4}TiO_3$ particles, the thickness of the shell can be controlled between 2 and 80 nm with high accuracy [59]. The typical morphology of the particles is shown in Figure 3.5(a). Due to the silica shell, the sintering temperature can be decreased to 1000 °C in comparison to values of the order of 1400 °C required for the uncoated particles. Consequently, grain growth does not occur and this offers the possibility to investigate the dielectric and ferroelectric properties of the composite as a function of the core size. However, even using particles with an average size of ≈200 nm and narrow size distribution, good densification is not attained and a considerable level of porosity (20–30%) is retained. The Curie temperature of these composites is very close to that of the uncoated material, meaning that interdiffusion is limited at least when the silica shell is thin. The existence of a continuous silica network and the residual porosity are the main factors responsible for the low dielectric constant (usually <100) of the composites when compared to dense pure

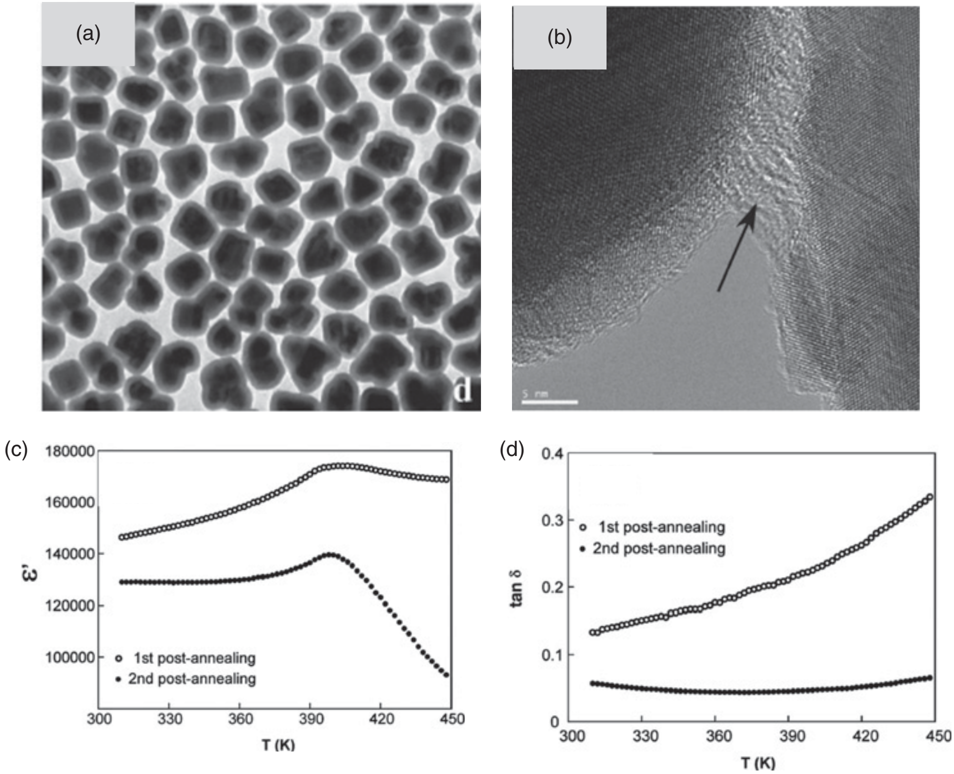

Figure 3.5 *(a) $Ba_{0.6}Sr_{0.4}TiO_3$@SiO_2 particles (reprinted with permission from [59]. Copyright (2005) American Chemical Society). (b) Grain boundary amorphous silica layer in $BaTiO_3$@SiO_2 ceramics densified by SPS at 1050 °C (reprinted with permission from [61]. Copyright (c) [2010] [The American Ceramic Society]). (c) Dielectric constant and (d) loss tangent of $BaTiO_3$@SiO_2 ceramics densified by SPS at 1100 °C and postannealed in air (reprinted with permission from [60]. Copyright [2009], AIP Publishing LLC)*

ceramics (a few thousands). Indeed, due to the low permittivity of silica (4) the electric field is mainly confined into the percolating linear dielectric and the high-permittivity ferroelectric cores give only a relatively small contribution to the effective dielectric constant. For the same reason, the loss tangent is lower ($1–5 \times 10^{-3}$ at 100–400 K) than in the corresponding pure ceramic. As expected, the dielectric constant decreases with increasing shell thickness, that is by increasing the volume fraction of silica. A good densification (97% relative density) of $BaTiO_3$@SiO_2 particles without significant grain growth can be achieved by spark plasma sintering at 1050–1100 °C for a few minutes [60, 61]. A detailed microstructural study [61] has shown a continuous amorphous silica layer at the grain boundaries with sporadic small fresnoite ($Ba_2TiSi_2O_8$) crystals (Figure 3.5(b)). Massive formation of fresnoite and diffusion of barium into the silica layer has been observed when the silica-coated particles are heated up to 1000 °C in the hot stage of a TEM. In this case heating is much slower and, consequently, there is enough time for the secondary phase formation. Despite fresnoite formation, T_C is not significantly affected, which can possibly be explained by the reduced thickness of the original silica layer (5–25 nm). However, the formation of fresnoite destroys the continuity of the grain boundary layer. Thus, in addition to a higher density, SPSed ceramics fully retain a continuous intergranular amorphous silica layer.

Good densification (92%) is also obtained by sintering in a microwave furnace. After postannealing at 800 °C in air, the SPSed ceramics exhibit (at 10 kHz) a giant dielectric constant ($>10^5$) and a relatively low loss tangent (≈ 0.05) in the range 300–450 K [60], as shown in Figure 3.5(c) and (d). This behavior can be explained by considering the heterogeneous electrical structure of the ceramics comprising an insulating grain-boundary layer and more conducting grain cores and modeled using two parallel RC circuits connected in series (internal barrier layer capacitor effect) [62]. The silica shell is a good dielectric and, moreover, slows down reoxidation of the inner region of the $BaTiO_3$ grains, which remain semiconducting after postannealing. At low frequency ($<10^5$ Hz) and above room temperature, the effective permittivity is controlled by the insulating grain boundary layer whereas at a higher frequency and lower temperature the contribution of grain cores predominates and the permittivity drops to values typical of $BaTiO_3$.

Significant modifications of the dielectric properties of barium titanate were observed after densification of $BaTiO_3$@$SrTiO_3$ and $BaTiO_3$@$BaZrO_3$ particles obtained by a precipitation method in aqueous solution [31]. Since the three compounds are isomorphous and display complete solid solubility without appearance of additional phases, partial interdiffusion between core and shell determines the formation of a composition gradient inside each grain responsible for the strong broadening and flattening of the permittivity peak. As a result, the temperature dependence of dielectric permittivity is strongly reduced over a wide temperature range. The observed enhanced dielectric losses in the THz range gives evidence of the core–shell interdiffusion [63].

$BaTiO_3$@MgO particles were synthesized by Berthelot et al. [64] by thermal decomposition of magnesium acetylacetonate at 120 °C inside a mixed organic solvent containing activated $BaTiO_3$ nanoparticles in suspension. The shell consists of a polycrystalline continuous layer comprising small MgO particles. Due to the poor adherence of the MgO nanoparticles to the underlying core and to their plastic flow, the core–shell arrangement is not preserved during the SPS densification and the final material consists of a dense mixture of MgO and $BaTiO_3$ grains of comparable size. Homogeneous and continuous layers of amorphous yttrium and dysprosium oxycarbonates can be deposited on $BaTiO_3$ submicrometer particles [65] by using the homogeneous precipitation process induced by urea decomposition as described by Kawahashi and Matijević [26]. Calcination at 700 °C transforms the amorphous shells in polycrystalline coatings consisting of Y_2O_3 and Dy_2O_3, respectively. $BaTiO_3$@ZrO_2 particles can be prepared by dispersing surface-modified $BaTiO_3$ submicrometer particles in a zirconyl nitrate solution and inducing precipitation and heterocoagulation of zirconia nanoparticles with $BaTiO_3$ by addition of aqueous ammonia [65]. The polyethyleneimine and polydiallyldimethylammonium chloride polyelectrolytes preventively adsorbed on the barium titanate surface carry a positive charge that promotes the adhesion of the negatively charged ZrO_2 nanoparticles.

The use of fillers obtained by encapsulation of high-permittivity ferroelectric nanoparticles with an oxide layer with intermediate dielectric permittivity between that of the core and the polymer is expected to result in polymer composites with higher dielectric strength and higher stored energy density because the intermediate layer reduces the inhomogeneous distribution of the electric field in the composite. Tanaka et al. [66] suggested and modeled a hypothetical multishell structure involving different layers to describe how the field interacts differently with the various components of a polymer nanocomposite dielectric.

$BaTiO_3$ particles coated with Al_2O_3 [45–47], SiO_2 [67], and TiO_2 [68] were investigated as improved fillers. Encapsulation of $BaTiO_3$, (Ba,Sr)TiO_3 and other oxides (TiO_2, ZrO_2, MgO), and nanoparticles with Al_2O_3 is realized by anchoring MAO molecules on to the nanoparticles via surface hydroxyl group reaction to form covalent Al–O bonds. Subsequent MAO decomposition by air exposure produces an alumina shell. The thickness of the shell can be controlled by the number of grafting and decomposition cycles [45–47]. Dense isotactic polyolefins containing a relatively small fraction (<10 vol%) of well-dispersed oxide@Al_2O_3 nanoparticles can be fabricated by in situ polymerization driven by metallocene olefin polymerization catalyst centers chemisorbed on the nanoparticle surface. These composites have a high breakdown field (up to 340 MV/m when the filler is $BaTiO_3$@Al_2O_3) and store energy with high efficiency. More than 80% recoverable energy can be retrieved from the charged capacitor at high field. The addition of $BaTiO_3$@TiO_2 particles to poly(vinylidene fluoride-hexafluoropropylene) determines a remarkable increase in the dielectric constant (70 for 40 vol% filler), breakdown field comparable or even higher than that of the pure polymer (up to 400 MV/m for 20% filler), and a doubling of the stored energy density, as shown in Figure 3.6. Successful encapsulation with a homogeneous amorphous silica shell is also reported for $BiFeO_3$ [69]. The silica coating modifies the magnetic properties of the ferrite, which exhibits weak ferromagnetism instead of the antiferromagnetic behavior of the uncoated particles.

3.5 Multiferroic Core–Shell Particles and Composites

A detailed introduction to composite multiferroic materials can be found in dedicated reviews [8, 70, 71] and only a few simple concepts are recalled here. Composite multiferroic materials combine constituents exhibiting two different ferroic order parameters. In the most common case that will be treated here, a ferro- or ferrimagnetic material is combined with a ferroelectric phase. The composite will manifest the ferroic properties of the parent phases and entirely new properties, such as the magnetoelectric (ME) effect, arising from the coupling of the two order parameters (i.e. polarization in ferroelectrics and magnetization in magnetics). The coupling of the two ferroic phases is mediated by strain and the ME effect results from the product of the magnetostrictive effect of the magnetic phase and the piezoelectric effect of the ferroelectric phase. Thus the application of a magnetic field determines a magnetostrictive deformation of the magnetic phase which, in turn, induces a variation of the polarization of the ferroelectric through the converse piezoelectric effect. The converse effect occurs by application of an electric field. A coupling much larger than in single-phase multiferroics can be obtained by choosing ferroelectrics with large piezoelectric coefficients and magnetic phases with high magnetostriction. Often the entity of coupling is quantified by measuring the voltage resulting by the application of an AC magnetic field and expressed by the ME voltage coefficient, α_E, with units of mV Oe^{-1} cm^{-1}. Considering the polycrystalline nature of composites, useful piezoelectric and magnetoelectric properties require the poling of the material using an external electric field. The poling process consists in the alignment of the orientation of the domains and associated polarization within the ferroelectric grains in the direction of the applied field. In sintered

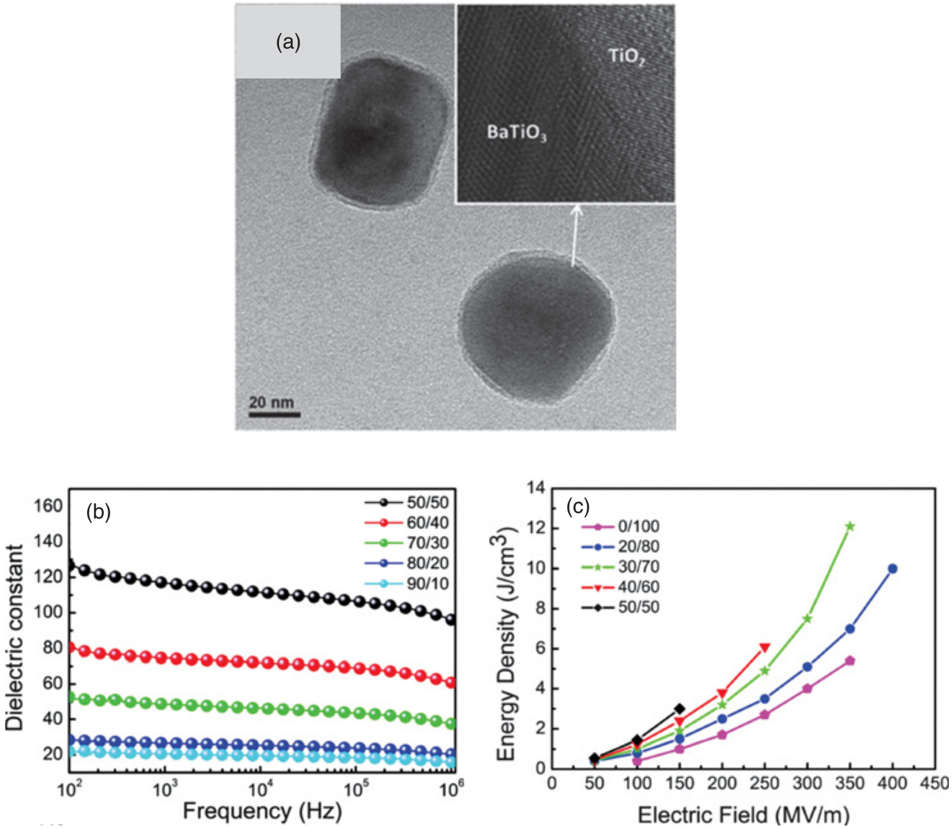

Figure 3.6 *(a) $BaTiO_3@TiO_2$ particles. (b) Dielectric constant versus frequency and (c) discharged energy density versus applied field for P(VDF-HFP)–$BaTiO_3@TiO_2$ nanocomposites. The legend in panels (b) and (c) reports the composite composition as polymer/filler and filler/polymer ratios, respectively. Reproduced from [68] with permission of the PCCP Owner Societies*

ceramics and composites, the polarization of the single ferroelectric domains is randomly oriented through the solid and the resulting piezoelectric effect is nil or very small.

Multiferroic core–shell particles are convenient precursors for the fabrication of 0–3 composites corresponding to non-percolative inclusions of phase 1 well dispersed in a continuous matrix of phase 2. The core–shell arrangement has a couple of potential advantages.

Firstly, the spherical geometry along with a well-adherent and dense shell maximizes the contact area between the two ferroic phases improving the strain-mediated coupling between polarization and magnetization. In particular, a good coupling can in principle be attained by heteroepitaxial growth of the shell on the core surface provided that the two crystal lattices are compatible, as happens with the spinel structure of ferrites and the perovskite structure of ferroelectric titanates. An example of excellent coupling is that observed in thin-film heteroepitaxial structures comprising $CoFe_2O_4$ pillars in a $BaTiO_3$ matrix [72]. Modeling of the ME coupling within the effective medium approximation has pointed out that a remarkable ME effect can be achieved in multiferroic composites with 0–3 connectivity [71] when the volume fraction of the magnetic phase (matrix) is in the range 0.6–0.8. Fabrication of composites with such a high concentration of non-percolating magnetic phase by random mixing of powders is rather difficult but becomes feasible using core–shell particles with magnetic cores. Magnetoelectric coupling in multiferroic coaxial nanofibers as well as in 1–3 composites has been predicted to be even higher than in 0–3 composites and bilayered film (2–2 connectivity) with the same composition [71, 73]. However, 1–3 composites are far much difficult to prepare than 0–3 composites.

Secondly, the dielectric losses can be lowered by coating the magnetic cores with the better insulating ferroelectric phase, thus avoiding the percolation of the usually more conductive magnetic phase in the final composite after densification. A high resistance is indeed required for the poling process, essential to obtain useful magnetoelectric properties and a high magnetoelectric coupling coefficient. However, even when the magnetic phase is not percolative, the insulating properties of the ferroelectric matrix can be degraded due to diffusion of transition metal elements such as Fe, Ni, and Co from the ferrite to the perovskite lattice.

Three kinds of multiferroic core–shell structures have been synthesized: (1) spherical particles, (2) coaxial fibers, and (3) arrays of vertically aligned nanowires on a substrate. In the case of spherical particles, both configurations, ferroelectric@magnetic and magnetic@ferroelectric, were often explored. $BaTiO_3$ (BT) and $Pb(Zr,Ti)O_3$ (PZT) are commonly used as ferroelectric phases. These compounds have a perovskite structure and possess high spontaneous polarization (25–50 $\mu C\ cm^{-2}$). Fe_2O_3, Fe_3O_4, $NiFe_2O_4$ (NFO), and $CoFe_2O_4$ (CFO) are usually adopted as magnetic phases. Fe_2O_3 has a hexagonal corundum structure and shows a weak ferromagnetic behavior. The other compounds have a cubic spinel structure with a soft ferrimagnetic behavior.

A survey of the most common preparation methods of multiferroic core–shell structures is reported in Table 3.2. The sonochemical synthesis is particularly useful for the coating of $BaTiO_3$ particles with a continuous nanocrystalline shell of iron oxides [74–77]. The $BaTiO_3$ particles are suspended in an $FeCl_2$ solution at a suitable pH. The application of ultrasounds at the suspension heated at 70 °C determines the nucleation and growth of a polycrystalline Fe_3O_4 shell on the perovskite surface (Figure 3.7(a)). The shell thickness can be controlled by varying the reaction time [76]. Oxidation at a moderate temperature (300 °C) determines the transformation of Fe_3O_4 in γ-Fe_2O_3.

Although the formation of core–shell particles at the synthesis stage is not clearly demonstrated, the sol–gel process is often used to obtain composites with 0–3 connectivity characterized by a good dispersion of the magnetic particles in a $BaTiO_3$ or PZT matrix up to a volume fraction of 50% and enhanced ME coefficient [78–88]. According to a common approach, the ferrite particles are suspended in a sol obtained by dissolving a Ba precursor (Ba acetate or $Ba(OH)_2$) and a Ti alkoxide (*n*-butoxide, isopropoxide) in an aqueous solution of acetic acid. Gelation is induced by heating and stirring. The resulting gel is then dried and calcined at 650–800 °C to transform the amorphous Ba–Ti precursor in crystalline $BaTiO_3$ [78–86]. A similar methodology is used when PZT is the ferroelectric phase [87, 88].

The main advantage of the hydrothermal synthesis is the possibility of growing homogeneous and continuous shells of a ferroelectric perovskite on magnetic particles [89, 90], as shown in Figure 3.7(b). Liu et al. [89] have proposed a general method for coating ferrites,

Table 3.2 *Synthesis methods of multiferroic core–shell particles and properties of corresponding composites. The values in parentheses (central column) denote the mol% of magnetic phase in the composite*

Synthesis method and investigated compositions	Magnetoelectric coefficient of composite (mV cm^{-1} Oe^{-1})	Piezoelectric coefficient d_{33}(pC N^{-1})
Sonochemical synthesis [74–77] $BaTiO_3$@γ-Fe_2O_3, $BaTiO_3$@Fe_3O_4	–	–
Sol–gel synthesis and calcination [78–88] $CoFe_2O_4$@$BaTiO_3$, $CoFe_2O_4$@PZT, $La_{0.7}Sr_{0.3}MnO_3$@$BaTiO_3$	$CoFe_2O_4$@$BaTiO_3$: 2540* (20) [78], 1.5 (50) [80], 6.7 (50) [82], 3.9 (50) [85] $La_{0.7}Sr_{0.3}MnO_3$@$BaTiO_3$: 54.4 (10) [83] $CoFe_2O_4$@PZT: 30 (25) [87]	24.1 [80]
Hydrothermal and solvothermal synthesis [89–91] $NiFe_2O_4$@$BaTiO_3$, Fe_3O_4@$PbTiO_3$, γ-Fe_2O_3@$PbTiO_3$,γ-Fe_2O_3@PZT, $CoFe_2O_4$@$BaTiO_3$, $CoFe_2O_4$@$PbTiO_3$, $CoFe_2O_4$@PZT, $NiFe_2O_4$@PZT	$NiFe_2O_4$@$BaTiO_3$: 12 (10) [90] PZT@$NiFe_2O_4$: 195 (26) [91]	60 [91]
Particle self-assembly [92–96] $BaTiO_3$@$NiFe_2O_4$, $NiFe_2O_4$@BaTiO3	$BaTiO_3$@$CoFe_2O_4$: 0.61 (27) [92] $NiFe_2O_4$@$BaTiO_3$: 0.5 (25) [93]	4.9 [92]
Combined methods [97–99] (Ni,Zn)Fe_2O_4@$BaTiO_3$, α-Fe_2O_3@$BaTiO_3$	–	–
Electrospinning [103–105] (coaxial fibers) CoFe2O4@PZT, PZT@ $NiFe_2O_4$, $NiFe_2O_4$@PZT	–	–
Templated growth [107–109] (nanowires and nanotubes) PZT@$NiFe_2O_4$, Fe@PZT, $CoFe_2O_4$@$BaTiO_3$	–	–

*Measured at resonant frequency

such as Fe_3O_4, Fe_2O_3, and CFO, with $BaTiO_3$, $PbTiO_3$, and PZT with a two-step process. An amorphous shell of Ti hydroxide is first deposited on the ferrite cores by hydrolysis of a $Ti(SO_4)_2$ solution. After coating, the resulting particles underwent a hydrothermal treatment at 120–180 °C in a $Ba(OH)_2$ solution ($BaTiO_3$ shell) or in a $Pb(NO_3)_2$/KOH solution ($PbTiO_3$ shell). The particles are finally annealed at 650–800 °C. NFO@$BaTiO_3$ particles were obtained by Zhou et al. [90] using a single-step hydrothermal treatment at 300 °C.

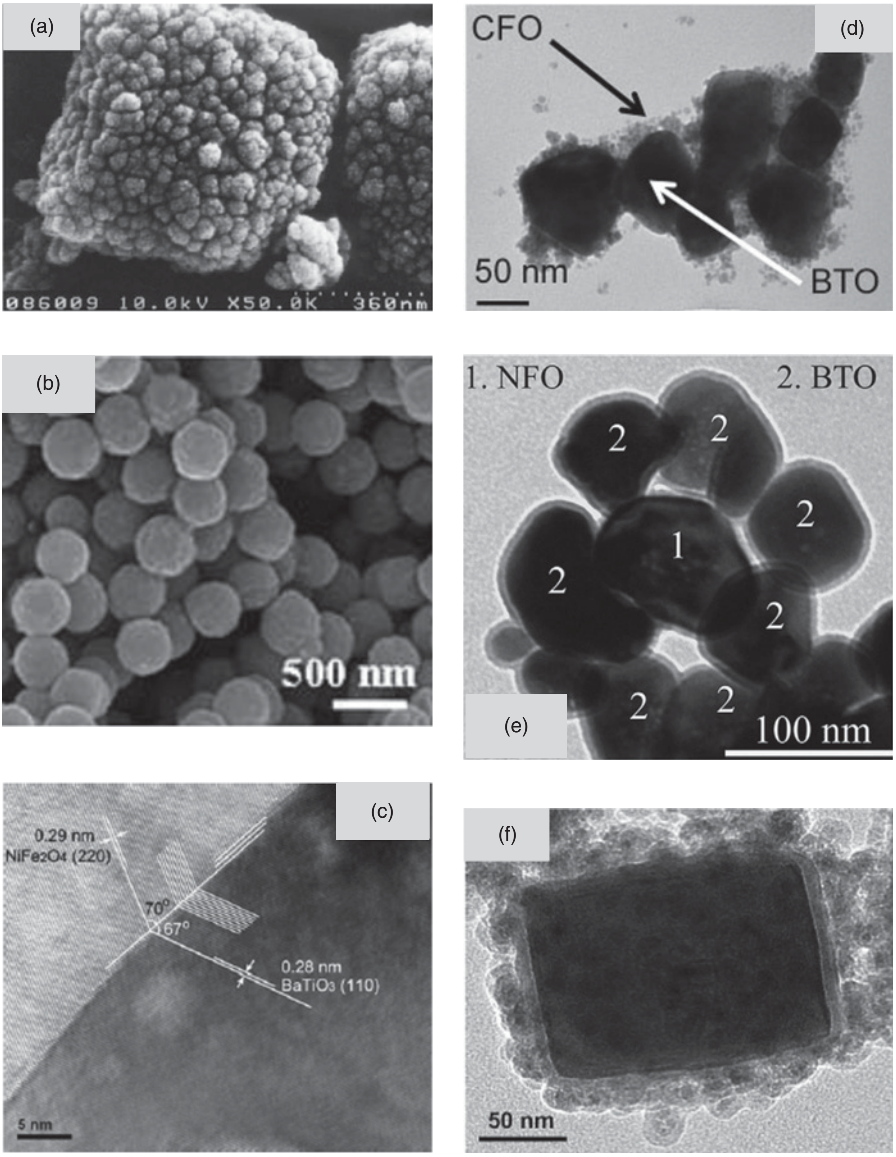
(a)
086009 10.0kV X50.0K 360nm
(d)
CFO
50 nm
BTO
(b)
500 nm
1. NFO
2. BTO
2
2
2
1
2
2
2
2
2
(e)
100 nm
(c)
0.29 nm
NiFe2O4 (220)
70°
67°
0.28 nm
BaTiO3 (110)
5 nm
(f)
50 nm

Figure 3.7 *Representative examples of multiferroic core–shell particles. (a) $BaTiO_3@Fe_3O_4$ (reprinted from [74], Copyright (2004), with permission from Elsevier). (b) $PZT@Fe_2O_3$ (reproduced from [89] with permission of The Royal Society of Chemistry). (c) $NFO@BaTiO_3$ (reproduced from [90] with permission. © National Institute for Materials Science (NIMS). CC BY-NC-SA). (d) $BaTiO_3@CoFe_2O_4$ (reprinted with permission from [92]. Copyright (c) [2010] [Wiley-VCH Verlag GmbH & Co. KGaA, Weinheim]). (e) $NFO@BaTiO_3$ (reprinted with permission from [93]. Copyright [2014], AIP Publishing LLC). (f) $(BST@SiO_2)@(\gamma\text{-}Fe_2O_3@SiO_2)$ (reprinted with permission from [96]. Copyright (2007) American Chemical Society). (g) $CoFe_2O_4@PZT$ (reproduced from [103] with permission of The Royal Society of Chemistry). (h) $PZT@NiFe_2O_4$ (reprinted with permission from [105]. Copyright [2014], AIP Publishing LLC). (i) Fe@PZT (reprinted with permission from [108]. Copyright (c) [2014] [Wiley-VCH Verlag GmbH & Co. KGaA, Weinheim])*

The NFO cores were suspended in a suspension of an amorphous precursor obtained by hydrolyzing a solution of $TiCl_4$ and $Ba(NO_3)_2$ with NaOH and adjusting the final pH to 13. The growth of the shell involves the formation of heteroepitaxial interfaces between $NiFe_2O_4$ and $BaTiO_3$ (Figure 3.7(c)) The thickness of the shell can be controlled, changing the amount of ferrite particles. Thus a wide range of composites characterized by different ferrite/perovskite molar ratios (0.1–0.5) can be prepared. A uniform coating of NFO on PZT particles can be obtained by a solvothermal method using a solvent with a high boiling point such as benzyl ether in which the PZT particles are suspended [91]. Nickel acetylacetonate and iron pentacarbonyl are used as precursors of NFO whereas oleic acid and oleylamine are added as growth controlling molecules. The growth of the shell is induced by heating the suspension at 295 °C.

A further classical approach to the preparation of multiferroic core–shell particles is by self-assembly of separately prepared and surface modified particles. Electrostatic self-assembly of $BaTiO_3$ and CFO particles in organic non-polar solvents is promoted by functionalizing the perovskite with phosphonic acid (negatively charged) and the ferrite with aminosilane molecules (positively charged) [92]. However, this interaction is relatively weak and the core–shell aggregates break down when they are transferred in water, a solvent with higher polarity. More robust assemblies (Figure 3.7(d)) can be obtained by promoting the formation of a covalent amide bond between the two surface functional groups by adding the chemical coupling agent *N*-*N*(-dicyclohexylcarbodiimide). In a series of more recent papers [93–95], self-assembly of nickel ferrite and barium titanate in $BaTiO_3$@NFO and NFO@$BaTiO_3$ (Figure 3.7(e)) particles was induced by a chemical reaction between complementary functional groups in the presence of a catalyst. The well-known Cu(I)-catalyzed azide–alkyne cycloaddition reaction was chosen for this purpose [13, 14].

Mornet et al. [96] have developed a different approach for self-assembling magnetic nanoparticles on ferroelectric cores by exploiting the possibility to switch the surface charge of silica from positive to negative by functionalization with aminosilane molecules. $BaTiO_3$ and γ-Fe_2O_3 particles were separately synthesized and coated with a thin silica film. After functionalization of the $BaTiO_3$@SiO_2 particles, spontaneous formation of ($BaTiO_3$@SiO_2)@(Fe_2O_3@SiO_2) assemblies occurs due to the interparticle electrostatic interaction when the two suspensions are mixed (Figure 3.7(f)).

Magnetic particles can be coated with $BaTiO_3$ combining different methods in a multistep process [97–99]. Firstly, an amorphous layer of titanium hydroxide is deposited on the magnetic particles by hydrolysis of a peroxotitanium solution at pH 10. Then a layer of $BaCO_3$ nanocrystals are self-assembled on the surface of the ferrite@TiO_2 particles exploiting the attractive electrostatic interactions between the two kind of particles at pH 8. Finally, a barium titanate shell is obtained by a solid-state reaction between TiO_2 and $BaCO_3$ at 700 °C. Due to the relatively low reaction temperature, the particle morphology is well preserved and parasitic boundary reactions are negligible.

Electrospinning is a simple and versatile method for generating ultra-thin fibers of a rich variety of ceramic materials including $BaTiO_3$ and PZT. This non-mechanical, electrostatic technique involves the use of a high-voltage electrostatic field to charge the surface of a precursor solution or suspension droplet and thus to induce the ejection of a liquid jet through a spinneret. The route of the charged jet is controlled by the electric field. The jet extends through spiraling loops; as the loops increase in diameter the jet grows longer and thinner until it solidifies or collects on the target [100]. $BaTiO_3$ fibers are typically produced from a sol obtained by dissolving a Ti alkoxide and Ba acetate in acetic acid and adding a poly(vinylpyrrolidone) (PVP) solution in ethanol. The polymer is required to maintain the necessary viscosity and surface tension needed for the spinning process and to bond together the inorganic particles in the dried green fibers. The dried fibers are amorphous; crystallization of the perovskite is determined by calcination at temperatures above 700 °C. Electrospinning can also be used for the fabrication of composite fibers including multiferroic fibers.

Different arrangements of the components in the fiber are possible: random [101], Janus-type (two joined cylindrical hemispheres) [102], and coaxial (core–shell) [103–105]. CFO@PZT, PZT@NFO, and NFO@PZT fibers are fabricated by coaxial electrospinning using PZT and ferrite precursor sols containing PVP or polymethylmethacrylate polymers. The two sols are separately injected in the inner (core) and outer (shell) parts of a coaxial spinneret assembled from two commercial blunt needles of different diameter, as illustrated in detail by Xie et al. [103]. The diameter of the coaxial fibers are in the range 100–500 nm for CFO@PZT fibers and 0.5–1 μm for NFO@PZT and PZT@NFO. The fibers have a well-defined core@shell geometry, as can be observed in Figure 3.7(g) and (h). The fibers can be aligned by means of a magnetic field and assembled in a thick film for property characterization [105]. Silicon nanowires with a PZT shell were investigated for application in electronic devices. The coaxial nanowire geometry facilitates large ferroelectric field-effect modulation ($> 10^4$) of nanowire conductivity [106].

Vertically aligned arrays of NFO@PZT and Fe@PZT nanowires are fabricated by templated growth using anodic aluminum oxide (AAO) and polycarbonate (PC) membranes with ordered cylindrical porosity [107, 108]. The fabrication process involves several steps. In the first case [107], a PZT precursor layer was coated on to the inner walls of the AAO template by infiltration with a sol and subsequent solvent evaporation. Annealing at 650 °C determines the formation of crystalline nanotubes. A copper layer was then sputtered on one side of the template containing the PZT nanotubes and used as a working electrode for the electrodeposition of $Ni_{33}Fe_{67}$ alloy inside the nanotubes. Oxidation at 800 °C determines the formation of coaxial NFO@PZT nanowires with a diameter of ≈200 nm. The alumina template is finally removed by etching with NaOH. In the second case [108], iron nanowires with a diameter of ≈800 nm are grown by electrodeposition in the pores of the PC template preventively coated on one side with a gold film and a copper layer. The polymer membrane was dissolved in dichloromethane and a film of PZT precursor was coated on the nanowires by spin coating. Crystallization of PZT at 700 °C results in well-aligned arrays of Fe@PZT nanowires, as shown in Figure 3.7(i). Raidongia et al. [109] fabricated CFO nanotubes with a diameter of ≈80 nm using PC templates. After template removal, an irregular coating of $BaTiO_3$ nanoparticles on the ferrite nanotubes was obtained by immersion in a $BaTiO_3$ precursor solution followed by drying and calcination at 780 °C.

Densification of multiferroic core–shell particles is commonly carried out by sintering. The fabrication of 0–3 composites is quite challenging because of the need to find a compromise between contrasting effects. For example, high sintering temperatures promote densification but can determine a microstructure modification and even the disappearance of the core–shell arrangement as a consequence of grain growth and coarsening processes. Moreover, high temperatures enhance phase boundary reactions and interdiffusion with deterioration of resistivity, piezoelelecric properties, and magnetoelectric coupling. Lower sintering temperatures must be adopted but this often results in the retention of a substantial amount (>10%) of residual porosity, which is again detrimental for properties. There are only a few systematic studies on the processing–microstructure–property relationships of multiferroic composites. Duong et al. [84–86] have investigated the effect of phase arrangement ($BaTiO_3$@CFO or CFO@$BaTiO_3$), compaction pressure (3–7.5 tons cm^{-2}), sintering temperature (1000–1250 °C), and time (1–20 h) on the ME coefficient and compared the results with those of composites obtained by random mixing of the two components and bilayered thick films. Depending on the experimental configuration, the ME coefficient can change by up to a factor of 20. Composites processed from core–shell particles exhibited a higher ME coefficient than random and bilayered composites. The highest ME coefficient (3.9 mV cm^{-1} Oe^{-1}) was obtained using CFO as the core, a sintering temperature of 1250 °C, and a sintering time of 4 h. In a detailed paper, Islam and Priya [110] investigated the effect of the grain size of the ferroelectric phase on the properties of PZT–NFO composites prepared from mechanically mixed powders. Resistivity, piezoelectric d_{33} coefficient and ME coefficient increase with PZT grain size and substantial property saturation above a grain size of 600 nm is observed. In particular, the ME coefficient improves from 54 to 158 mV Oe^{-1} cm^{-1} as the PZT grain size increased from 100 to 800 nm. However, the property improvement is in part determined by the parallel increase of the relative density from 93 to 98%. The strong impact of processing conditions and microstructure thus explains the broad dispersion of the ME coefficient observed in the literature (see Table 3.2). The remarkable coupling coefficient of 195 mV Oe^{-1} cm^{-1} reported for a PZT@NFO composite with 20 wt% NFO sintered at 950 °C [91] is the result of a careful optimization of both PZT grain size and NFO shell thickness. This value is significantly higher than that obtained by Ryu et al. (115 mV Oe^{-1} cm^{-1}) for optimized composites prepared by conventional powder mixing [111]. For the sake of comparison, α_E is 28 mV Oe $^{-1}$ cm $^{-1}$ in Cr_2O_3, one of the single-phase materials with highest ME coupling [8]. Good densification can be achieved at a lower temperature than those typically required by conventional sintering and in a shorter time using SPS [10, 11]. Mechanically mixed powders of PZT and NFO (30 vol%) could be sintered at 900–950 °C, obtaining a densification of 97–99% [112], d_{33} of 40 pC N^{-1} and α of 25 mV Oe^{-1} cm^{-1}. One of the main advantages offered by SPS is to minimize phase boundary reactions and interdiffusion during the consolidation process, making it possible to couple together phases that are thermodynamically incompatible. An example is represented by the densification of Fe_2O_3@$BaTiO_3$ particles [98]. Conventional sintering requires a temperature of 1050–1150 °C and results in the formation of the additional magnetic compounds $BaFe_{12}O_{19}$ and $Ba_{12}Fe_{28}Ti_{15}O_{84}$ by reaction between the two parent phases. Conversely, Fe_3O_4–$BaTiO_3$ and Fe_2O_3–$BaTiO_3$ composites with a high relative density (98–99%) are obtained by SPS at 1050–1100 °C for 3–4 min.

3.6 Conclusions and Outlook

As shown in this review, core–shell particles combining a ferroelectric compound with a different material have attracted considerable interest for potential application as fillers in dielectric polymer composites and as building blocks for the fabrication of dielectric ceramics and multiferroic composites.

The shell modifies the surface properties of the cores and, consequently, the particles can be dispersed more effectively in different matrices. Accordingly, a polymer coating can improve the compatibility between ferroelectric filler particles and a polymer matrix (or the monomer when polymerization is performed in situ), resulting in a good dispersion that enhances the dielectric permittivity and the breakdown field of the composite. The existence of a graded structure rather than a sharp interface is expected to further improve the dielectric properties and the stored energy density. In turn, this has fostered the development of more sophisticated filler particles comprising a ferroelectric core ($BaTiO_3$) and an oxide shell (Al_2O_3, SiO_2, TiO_2), with a dielectric constant intermediate between the polymer and the ferroelectric. The growth of uniform shells with controlled thickness in both aqueous and organic solvents has mainly relied on the use of colloid and precipitation chemistry. A further progress in the design and preparation of ferroelectric fillers with graded interfaces can be predicted.

Core–shell particles are convenient precursors for the fabrication of ceramic composites with 0–3 connectivity. The shell prevents percolation of the core phase, even for high-volume fractions (>50%), a result not attainable with the conventional preparation route based on the mechanical mixing of powders. Ceramics obtained by densification of $BaTiO_3$ particles coated with a linear dielectric or paraelectric phase exhibit a significant modification of the temperature and frequency dependence of dielectric permittivity due to the existence of a grain boundary layer originated by the coalescence of the shell regions. An interesting example is provided by the properties of dense $BaTiO_3@SiO_2$ ceramics obtained by SPS. Controlled reoxidation after sintering leads to the appearance of a giant dielectric constant ($>10^5$) and reasonable losses in a wide temperature range. The formation of a graded structure as observed after densification of $BaTiO_3@BaZrO_3$ and $BaTiO_3@SrTiO_3$ particles determines a significant broadening and flattening of the permittivity peak of barium titanate, which is shifted to lower temperatures.

A big effort has been devoted to the synthesis of multiferroic core–shell particles. Several synthesis approaches, including sonochemical synthesis, sol–gel methods, hydrothermal synthesis, self-assembly, and methods coupling colloid chemistry and solid-state reaction were successfully employed to combine ferrites such as Fe_2O_3, Fe_3O_4, $NiFe_2O_4$, and $CoFe_2O_4$ with the ferroelectric phases $BaTiO_3$ and PZT.

Modeling of multiferroic 0–3 composites within the effective medium approximation predicted remarkable values for the ME coefficient. However, properties comparable to bilayered laminated composites were obtained only in a very few cases. While notable progress has been made on synthesis methods, further processing of core–shell particles in composites has not received due attention. Densification and microstructure control of multiferroic composites are still challenging tasks. Even more difficult is the densification of multiferroic coaxial fibers in composites with 1–3 connectivity. Good properties require the removal of porosity, the formation of sharp interfaces between the two ferroic phases and optimal grain size of both compounds to maximize piezoelectric and magnetostrictive effects. Residual porosity, interdiffusion, and formation of parasitic phases determine a rapid degradation of the ME coupling. Moreover, useful ME properties can only be obtained if the ferroelectric component can be poled efficiently. Consequently, the formation of more conductive paths related to ferrite percolation or diffusion of transition metal ions in the perovskite lattice need to be avoided.

New rapid sintering methods such as spark plasma sintering and field-assisted sintering have a great potential for the fabrication of dense multiferroic composites with controlled microstructure and better properties, but systematic studies are missing. Since SPS is carried out in the locally reducing atmosphere dictated by the use of graphite dies, the final materials usually show higher electrical conductivity and dielectric losses than those conventionally sintered in air. Therefore a careful reoxidation annealing is required after densification.

References

(1) Caruso, F. (2001) Nanoengineering of particle surfaces. *Advanced Materials*, **13** (1), 11–22.

(2) Caruso, R.A. and Antonietti, M. (2001) Sol–gel nanocoating: an approach to the preparation of structured materials. *Chemistry of Materials*, **13** (10), 3272–3282.

(3) Ramli, R.A., Laftah, W.A., and Hashim, S. (2013) Core–shell polymers: a review. *RSC Advances*, **3** (36), 15543–15565.

(4) Oldenburg, S.J., Averitt, R.D., Westcott, S.L. and Halas, N.J. (1998) Nanoengineering of optical resonances. *Chemical Physics Letters*, **288**, 243–247.

(5) Lee, J., Lee, Y., Youn, J.K., et al. (2008) Simple synthesis of functionalized superparamagnetic magnetite/silica core/shell nanoparticles and their application as magnetically separable high-performance biocatalysts. *Small*, **4** (1), 143–152.

(6) Mayya, K.S., Gittins, D.I., and Caruso, F. (2001) Gold–titania core–shell nanoparticles by polyelectrolyte complexation with a titania precursor. *Chemistry of Materials*, **13** (11), 3833–3836.

(7) López-Ortega, A., Estrader, M., Salazar-Alvarez, G., et al. (2015) Applications of exchange coupled bi-magnetic hard/soft and soft/hard magnetic core/shell nanoparticles. *Physics Reports*, **553**, 1–32.

(8) Vaz, C.A.F., Hoffman, J., Ahn, C.H., and Ramesh, R. (2010) Magnetoelectric coupling effects in multiferroic complex oxide composite structures. *Advanced Materials*, **22** (26–27), 2900–2918.

(9) Schileo, G. (2013) Recent developments in ceramic multiferroic composites based on core/shell and other heterostructures obtained by sol–gel routes. *Progress in Solid State Chemistry*, **41** (4), 87–98.

(10) Munir, Z.A., Anselmi-Tamburini, U., and Ohyanagi, M. (2006) The effect of electric field and pressure on the synthesis and consolidation of materials: a review of the spark plasma sintering method. *Journal of Materials Science*, **41** (3), 763–777.

(11) Maglia, F., Tredici, I., and Anselmi-Tamburini, U. (2013) Densification and properties of bulk nanocrystalline functional ceramics with grain size below 50 nm. *Journal of the European Ceramic Society*, **33** (6), 1045–1066.

(12) Wang, Y., Angelatos, A.S., and Caruso, F. (2008) Template synthesis of nanostructured materials via layer-by-layer assembly. *Chemistry of Materials*, **20** (3), 848–858.

(13) Kolb, H.C., Finn, M.G., and Sharpless, K.B. (2001) Click chemistry: diverse chemical function from a few good reactions. *Angewandte Chemie International Edition*, **40** (11), 2004–2021.

(14) Cardiel, A.C., Benson, M.C., Bishop, L.M., et al. (2012) Chemically directed assembly of photoactive metal oxide nanoparticle heterojunctions via the copper-catalyzed azide–alkyne cycloaddition "click" reaction. *ACS Nano*, **6** (1), 310–318.

(15) Stöber, W., Fink, A., and Bohn, E. (1968) Controlled growth of monodisperse silica spheres in the micron size range. *Journal of Colloid and Interface Science*, **26** (1), 62–69.

(16) Ohmori, M. and Matijević, E. (1992) Preparation and properties of uniform coated colloidal particles. VII. Silica on hematite. *Journal of Colloid and Interface Science*, **150** (2), 594–598.

(17) Liz-Marzán, L.M., Giersig, M., and Mulvaney, P. (1996) Synthesis of nanosized gold−silica core−shell particles. *Langmuir*, **12** (18), 4329–4335.

(18) Garg, A. and Matijević, E. (1988) Preparation and properties of uniformly coated inorganic colloidal particles. 2. Chromium hydrous oxide on hematite. *Langmuir*, **4** (1), 38–44.

(19) Garg, A. and Matijević, E. (1988) Preparation and properties of uniform coated inorganic colloidal particles III. Zirconium hydrous oxide on hematite. *Journal of Colloid and Interface Science*, **126** (1), 243–250.

(20) Aiken, B. and Matijević, E. (1988) Preparation and properties of uniform coated inorganic colloidal particles. IV. Yttrium basic carbonate and yttrium oxide on hematite. *Journal of Colloid and Interface Science*, **126** (2), 645–649.

(21) Ocaña, M., Hsu, W.P., and Matijević, E. (1991) Preparation and properties of uniform-coated colloidal particles. 6. Titania on zinc oxide. *Langmuir*, **7** (12), 2911–2916.

(22) Yura, K. and Matijević, E. (1993) Preparation and properties of uniform-coated colloidal particles: VII. Hafnium oxide and indium oxide. *Journal of Colloid and Interface Science*, **155** (2), 328–333.

(23) Hsu, W.P., Yu, R., and Matijević, E. (1993) Paper whiteners: I. Titania coated silica. *Journal of Colloid and Interface Science*, **156** (1), 56–65.

(24) Ohmori, M. and Matijević, E. (1993) Preparation and properties of uniform-coated colloidal particles: 8. Silica on iron. *Journal of Colloid and Interface Science*, **160** (2), 288–292.

(25) ul Haq, I. and Matijević, E. (1997) Preparation and properties of uniform coated inorganic colloidal particles. 11. Nickel and its compounds on manganese compounds. *Chemistry of Materials*, **9** (12), 2659–2665.

(26) Kawahashi, N. and Matijević, E. (1990) Preparation and properties of uniform coated colloidal particles: V. Yttrium basic carbonate on polystyrene latex. *Journal of Colloid and Interface Science*, **138** (2), 534–542.

(27) Kawahashi, N., Persson, C., and Matijević, E. (1991) Zirconium compounds as coatings on polystyrene latex and as hollow spheres. *Journal of Materials Chemistry*, **1** (4), 577–582.

(28) Matijević, E. (1993) Preparation and properties of uniform size colloids. *Chemistry of Materials*, **5** (4), 412–426.

(29) Matijević, E. (1996) Controlled colloid formation. *Current Opinion in Colloid and Interface Science*, **1** (2), 176–183.

(30) Gherardi, P. and Matijević, E. (1986) Interactions of precipitated hematite with preformed colloidal titania dispersions. *Journal of Colloid and Interface Science*, **109** (1), 57–68.

(31) Buscaglia, M.T., Viviani, M., Zhao, Z., et al. (2006) Synthesis of $BaTiO_3$ core–shell particles and fabrication of dielectric ceramics with local graded structure. *Chemistry of Materials*, **18** (17), 4002–4010.

(32) Oyama, H.T., Sprycha, R., Xie, Y.M., et al. (1993) Coating of uniform inorganic particles with polymers, I. *Journal of Colloid and Interface Science*, **160** (2), 298–303.

(33) Huang, C.L., Partch, R.E., and Matijević, E. (1995) Coating of uniform inorganic particles with polymers: II. Polyaniline on copper-oxide. *Journal of Colloid and Interface Science*, **170** (1), 275–283.

(34) Huang, C.L. and Matijević, E. (1995) Coating of uniform inorganic particles with polymers: III. Polypyrrole on different metal-oxides. *Journal of Materials Research*, **10** (5), 1327–1336.

(35) Sondi, I., Fedynyshyn, T.H., Sinta, R., and Matijević, E. (2000) Encapsulation of nanosized silica by in situ polymerization of *tert*-butyl acrylate monomer. *Langmuir*, **16** (23), 9031–9034.

(36) Bourgeat-Lami, E. and Lang, J. (1998) Encapsulation of inorganic particles by dispersion polymerization in polar media. 1. Silica nanoparticles encapsulated by polystyrene. *Journal of Colloid and Interface Science*, **197** (2), 293–308.

(37) Bourgeat-Lami, E. and Lang, J. (1999) Encapsulation of inorganic particles by dispersion polymerization in polar media. 2. Effect of silica size and concentration on the morphology of silica–polystyrene composite particles. *Journal of Colloid and Interface Science*, **210** (2), 281–289.

(38) Ramesh, S., Shutzberg, B.A., Huang, C., et al. (2003) Dielectric nanocomposites for integral thin film capacitors: materials design, fabrication and integration issues. *IEEE Transactions on Advanced Packaging*, **26** (1), 17–24.

(39) Li, J., Claude, J., Norena-Franco, L.E., et al. (2008) Electrical energy storage in ferroelectric polymer nanocomposites containing surface-functionalized $BaTiO_3$ nanoparticles. *Chemistry of Materials*, **20** (20), 6304–6306.

(40) Kim, P., Jones, S.C., Hotchkiss, P.J., et al. (2007) Phosphonic acid-modified barium titanate polymer nanocomposites with high permittivity and dielectric strength. *Advanced Materials*, **19** (7), 1001–1005.

(41) Beier, C.W., Cuevas, M.A., and Brutchey, R.L. (2010) Effect of surface modification on the dielectric properties of $BaTiO_3$ nanocrystals. *Langmuir*, **26** (7), 5067–5071.

(42) Kim, P., Doss, N.M., Tillotson, J.P., et al. (2009) High energy density nanocomposites based on surface-modified $BaTiO_3$ and a ferroelectric polymer. *ACS Nano*, **3** (9), 2581–2592.

(43) Chang, S.J., Liao, W.S., Ciou, C.J., et al. (2009) An efficient approach to derive hydroxyl groups on the surface of barium titanate nanoparticles to improve its chemical modification ability. *Journal of Colloid and Interface Science*, **329** (2), 300–305.

(44) Zhou, T., Zha, J.W., Cui, R.Y., et al. (2011) Improving dielectric properties of $BaTiO_3$/ferroelectric polymer composites by employing surface hydroxylated $BaTiO_3$ nanoparticles. *ACS Applied Materials and Interfaces*, **3** (7), 2184–2188.

(45) Guo, N., DiBenedetto, S.A., Kwon, D.K., et al. (2007) Supported metallocene catalysis for in situ synthesis of high energy density metal oxide nanocomposites. *Journal of the American Chemical Society*, **129** (4), 766–767.

(46) Li, Z., Fredin, L.A., Tewari, P., et al. (2010) In situ catalytic encapsulation of core–shell nanoparticles having variable shell thickness: dielectric and energy storage properties of high-permittivity metal oxide nanocomposites. *Chemistry of Materials*, **22** (18), 5154–5164.

(47) Fredin, L.A., Li, Z., Ratner, M.A., et al. (2012) Enhanced energy storage and suppressed dielectric loss in oxide core–shell–polyolefin nanocomposites by moderating internal surface area and increasing shell thickness. *Advanced Materials*, **24** (44), 5946–5953.

(48) Xie, L., Huang, X., Wu, C., and Jiang, P. (2011) Core–shell structured poly(methyl methacrylate)/$BaTiO_3$ nanocomposites prepared by in situ atom transfer radical polymerization: a route to high dielectric constant materials with the inherent low loss of the base polymer. *Journal of Materials Chemistry*, **21** (16), 5897–5906.

(49) Yang, K., Huang, X.Y., Xie, L.Y., et al. (2012) Core–shell structured polystyrene/$BaTiO_3$ hybrid nanodielectrics prepared by in situ RAFT polymerization: A route to high dielectric constant and low loss materials with weak frequency dependence. *Macromolecular Rapid Communications*, **33** (22), 1921–1926.

(50) Xie, L.Y., Huang, X.Y., Huang, Y.H., et al. (2013) K core–shell structured hyperbranched aromatic polyamide/$BaTiO_3$ hybrid filler for poly(vinylidene fluoride-trifluoroethylenechlorofluoroethylene) nanocomposites with the dielectric constant comparable to that of percolative composites. *ACS Applied Materials and Interfaces*, **5** (5), 1747−1756.

(51) Xie, L.Y., Huang, X.Y., Huang, Y.H. et al. (2013) Core@double-shell structured $BaTiO_3$−polymer nanocomposites with high dielectric constant and low dielectric loss for energy storage application. *The Journal of Physical Chemistry A*, **117** (44), 22525−22537.

(52) Yang, K., Huang, X.Y., Huang, Y.H., et al. (2013) Fluoro-polymer@$BaTiO_3$ hybrid nanoparticles prepared via RAFT polymerization: toward ferroelectric polymer nanocomposites with high dielectric constant and low dielectric loss for energy storage application. *Chemistry of Materials*, **25** (11), 2327–2338.

(53) Yang, K., Huang, X.Y., Zhu, M., et al. (2014) Combining RAFT polymerization and thiol−ene click reaction for core−shell structured polymer@$BaTiO_3$ nanodielectrics with high dielectric constant, low dielectric loss, and high energy storage capability. *ACS Applied Materials and Interfaces*, **6** (3), 1812−1822.

(54) Jung, H.M., Kang, J.H., Yang, S.Y., et al. (2010) Barium titanate nanoparticles with diblock copolymer shielding layers for high-energy density nanocomposites. *Chemistry of Materials*, **22** (2), 450–456.

(55) Tang, H.L., Ma, Z., Zhong, J.C., et al. (2011) Effect of surface modification on the dielectric properties of PEN nanocomposites based on double-layer core/shell-structured $BaTiO_3$ nanoparticles. *Colloids and Surfaces A*, **384** (1–3), 311–317.

(56) Benhadjala, W., Bord-Majek, I., Béchou, L., et al. (2012) Improved performances of polymer-based dielectric by using inorganic/organic core-shell nanoparticles. *Applied Physics Letters*, **101** (14), art. no. 142901.

(57) Huber, C., Treguer-Delapierre, M., Elissalde, C., et al. (2003) New application of the core–shell concept to ferroelectric nanopowders. *Journal of Materials Chemistry*, **13** (4), 650–653.

(58) Hornebecq, V., Huber, C., Maglione, M., et al. (2004) Dielectric properties of pure (BaSr)TiO_3 and composites with different grain sizes ranging from the nanometer to the micrometer. *Advanced Functional Materials*, **14** (9), 899–904.

(59) Mornet, S., Elissalde, C., Hornebecq, V., et al. (2005) Controlled growth of silica shell on $Ba_{0.6}Sr_{0.4}TiO_3$ nanoparticles used as precursors of ferroelectric composites. *Chemistry of Materials*, **17** (17), 4530–4536.

(60) Chung, U.C., Elissalde, C., Mornet, S., et al. (2009) Controlling internal barrier in low loss $BaTiO_3$ supercapacitors. *Applied Physics Letters*, **94** (7), art. no. 72903.

(61) Chung, U.C., Elissalde, C, Mompiou, F., et al. (2010) Interface investigation in nanostructured $BaTiO_3$/silica composite ceramics. *Journal of the American Ceramic Society*, **93** (3), 865–874.

(62) Li, M., Feteira, A., and Sinclair, D.C. (2005) Origin of the high permittivity in $(La_{0.4}Ba_{0.4}Ca_{0.}2)(MnO_{.4}Ti_{0.6})O_3$ ceramics. *Journal of Applied Physics*, **98** (8), art. no. 084101.

(63) Nuzhnyy, D., Petzelt, J., Rychetsky, I., et al. (2009) THz and IR dielectric response of $BaTiO_3$ core–shell composites: evidence for interdiffusion. *Journal of Physics D: Applied Physics*, **42** (15), art. no. 155408.

(64) Berthelot, R., Basly, B., Buffière, S., et al. (2014) From core–shell $BaTiO_3$@MgO to nanostructured low dielectric loss ceramics by spark plasma sintering. *Journal of Materials Chemistry*, **2** (4), 683–690.

(65) Bassano, A., Buscaglia, V., Sennour, M., et al. (2010) Nanocrystalline oxide (Y_2O_3, Dy_2O_3, ZrO_2, NiO) coatings on $BaTiO_3$ submicron particles by precipitation. *Journal of Nanparticle Research*, **12** (2), 623–633.

(66) Tanaka, T., Kozako, M., Fuse, N., and Ohki, Y. (2005) Proposal of a multi-core model for polymer nanocomposite dielectrics. *IEEE Transactions on Dielectrics and Electrical Insulation*, **12** (4), 669–681.

(67) Yu, K., Niu, Y., Bai, Y., et al. (2013) Poly(vinylidene fluoride) polymer based nanocomposites with significantly reduced energy loss by filling with core–shell structured $BaTiO_3/SiO_2$ nanoparticles. *Applied Physics Letters*, **102** (10), art. no. 102903.

(68) Rahimabady, M., Sharifzadeh Mirshekarloo, M., Yao, K., and Lub, L. (2013) Dielectric behaviors and high energy storage density of nanocomposites with core–shell $BaTiO_3$@TiO_2 in poly(vinylidene fluoride-hexafluoropropylene). *Physical Chemistry Chemical Physics*, **15** (38), 16242–16248.

(69) Shirolkar, M.M., Das, R., Maity, T., et al. (2012) Observation of enhanced dielectric coupling and room-temperature ferromagnetism in chemically synthesized $BiFeO_3$@SiO_2 core−shell particles. *The Journal of Physical Chemistry C*, **116** (36), 19503−19511.

(70) Fiebig, M. (2005) Revival of the magnetoelectric effect. *Journal of Physics D: Applied Physics*, **38** (8), R123–R152.

(71) Nan, C.W., Bichurin, M.I., Dong, S.X., et al. (2008) Multiferroic magnetoelectric composites: historical perspective, status, and future directions. *Journal of Applied Physics*, **103** (3), art. no. 031101.

(72) Zheng, H., Wang, J., Lofland, S.E., et al. (2004) Multiferroic $BaTiO_3$–$CoFe_2O_4$ nanostructures. *Science*, **303** (5658), 661–663.

(73) Zhang, C.L., Chen, W.K., Xie, S.H., et al. (2009) The magnetoelectric effects in multiferroic composite nanofibers. *Applied Physics Letters*, **94** (10), art. no. 102907.

(74) Choi, S.H., Oh, J.H., and Ko, T. (2004) Preparation and characteristics of Fe_3O_4-encapsulated $BaTiO_3$ powder by ultrasound-enhanced ferrite plating. *Journal of Magnetism and Magnetic Materials*, **272–276**, Part 3, 2233–2235.

(75) Park, H.K., Choi, S.H., Oh, J.H., and Ko, T. (2004) Preparation and characteristics of a magnetic–dielectric ($Fe_3O_4/BaTiO_3$) composite by ferrite plating with ultrasound irradiation. *Physica Status Solidi B*, **241** (7), 1693–1696.

(76) Koo, Y.S., Bonaedy, T., Sung, K.D., et al. (2007) Magnetodielectric coupling in core/shell $BaTiO_3/\gamma$-Fe_2O_3 nanoparticles. *Applied Physics Letters*, **91** (21), art. no. 212903.

(77) Koo, Y.S., Song, K.M., Hur, N., et al. (2009) Strain-induced magnetoelectric coupling in $BaTiO_3/Fe_3O_4$ core/shell nanoparticles. *Applied Physics Letters*, **94** (3), art. no. 032903.

(78) Ren, S.Q., Weng, L.Q., and Song, S.H. (2005) $BaTiO_3/CoFe_2O_4$ particulate composites with large high frequency magnetoelectric response. *Journal of Materials Science*, **40** (16), 4375–4378.

(79) Duong, G.V., Groessinger, R., and Turtelli, R.S. (2006) Magnetoelectric properties of $CoFe_2O_4$–$BaTiO_3$ core–shell structure composite. *IEEE Transactions on Magnetics*, **42** (10), 3611–3613.

(80) Corral-Flores, V., Bueno-Baques, D., Carrillo-Flores, D., and Matutes-Aquino, J.A. (2006) Enhanced magnetoelectric effect in core–shell particulate composites. *Journal of Applied Physics*, **99** (8), art. no. 08J503.

(81) Corral-Flores, V., Bueno-Baques, D., and Ziolo, R.F. (2010) Synthesis and characterization of novel $CoFe_2O_4$–$BaTiO_3$ multiferroic core–shell-type nanostructures. *Acta Materialia*, **58** (3), 764–769.

(82) Shvartsman, V.V., Alawneh, F., Borisov, P., et al. (2011) Converse magnetoelectric effect in $CoFe_2O_4$–$BaTiO_3$ composites with a core–shell structure. *Smart Materials and Structures*, **20** (7), art. no. 075006.

(83) Nayek, C., Sahoo, K.K., and Murugavel, P. (2013) Magnetoelectric effect in $La_{0.7}Sr_{0.3}MnO_3$–$BaTiO_3$ core–shell nanocomposite. *Materials Research Bulletin*, **48** (3), 1308–1311.

(84) Duong, G.V. and Groessinger, R. (2007) Effect of preparation conditions on magnetoelectric properties of $CoFe_2O_4$–$BaTiO_3$ magnetoelectric composites. *Journal of Magnetism and Magnetic Materials*, **316** (2), e624–e627.

(85) Duong, G.V., Groessinger, R., and Turtelli, R.S. (2007) Effect of structure on magnetoelectric properties of $CoFe_2O_4$–$BaTiO_3$ multiferroic composites. *Journal of Magnetism and Magnetic Materials*, **310** (2), e361–e363.

(86) Duong, G.V., Groessinger, R., and Turtelli, R.S. (2007) Driving mechanism for magnetoelectric effect in $CoFe_2O_4$–$BaTiO_3$ multiferroic composite. *Journal of Magnetism and Magnetic Materials*, **310** (2), 1157–1159.

(87) Wan, J.G., Zhang, H., and Wang, X.W. (2006) Magnetoelectric $CoFe_2O_4$–lead zirconate titanate thick films prepared by a polyvinylpyrrolidone-assisted sol–gel method. *Applied Physics Letters*, **89** (12), art. no. 122914.

(88) Weng, L.Q., Fu, Y.D., and Song, S.H. (2007) Synthesis of lead zirconate titanate–cobalt ferrite magnetoelectric particulate composites via an ethylenediaminetetraacetic acid–citrate gel process. *Scripta Materialia*, **56** (6), 465–468.

(89) Liu, R., Zhao, Y., Huang, R., et al. (2010) Multiferroic ferrite/perovskite oxide core/shell nanostructures. *Journal of Materials Chemistry*, **20** (47), 10665–10670.

(90) Zhou, J.P., Lv, L., Liu, Q., et al. (2012) Hydrothermal synthesis and properties of $NiFe_2O_4$@$BaTiO_3$ composites with well-matched interface. *Science and Technology of Advanced Materials*, **13** (4), art. no. 045001.

(91) Islam, R.A., Bedekar, V., Poudyal, N., et al. (2008) Magnetoelectric properties of core–shell particulate nanocomposites. *Journal of Applied Physics*, **104** (10), art. no. 104111.

(92) Evans, G., Duong, G.V., Ingleson, M.J., et al. (2010) Chemical bonding assembly of multifunctional oxide nanocomposites. *Advanced Functional Materials*, **20** (2), 231–238.

(93) Sreenivasulu, G., Popov, M., Chavez, F.A., et al. (2014) Controlled self-assembly of multiferroic core–shell nanoparticles exhibiting strong magneto-electric effects. *Applied Physics Letters*, **104** (5), art. no. 052901.

(94) Popov, M., Sreenivasulu, G., Petrov, V.M., et al. (2014) High frequency magneto-dielectric effects in self-assembled ferrite-ferroelectric coreshell nanoparticles. *AIP Advances*, **4** (9), art. no. 097117.

(95) Sreenivasulu, G., Petrov, V.M., Chavez, F.A., and Srinivasan, G. (2014) Superstructures of self-assembled multiferroic core–shell nanoparticles and studies on magneto-electric interactions. *Applied Physics Letters*, **105** (7), art. no. 072905.

(96) Mornet, S., Elissalde, C., Bidault, O., et al. (2007) Ferroelectric-based nanocomposites: toward multifunctional materials. *Chemistry of Materials*, **19** (5), 987–992.

(97) Curecheriu, L.P., Buscaglia, M.T., Buscaglia, V., et al. (2010) Functional properties of $BaTiO_3$–$Ni_{0.5}Zn_{0.5}Fe_2O_4$ magnetoelectric ceramics prepared from powders with core–shell structure. *Journal of Applied Physics*, **107** (10), art. no. 104106.

(98) Buscaglia, M.T., Buscaglia, V., Curecheriu, L.P., et al. (2010) Fe_2O_3@$BaTiO_3$ core–shell particles as reactive precursors for the preparation of multifunctional composites containing different magnetic phases. *Chemistry of Materials*, **22** (16), 4740–4748.

(99) Curecheriu, L., Postolache, P., Buscaglia, M.T., et al. (2014) Novel magnetoelectric ceramic composites by control of the interface reactions in Fe_2O_3@$BaTiO_3$ core–shell structures. *Journal of Applied Physics*, **116** (8), art. no. 084102.

(100) Sigmund, W., Yuh, J., Park, H., et al. (2006) Processing and structure relationships in electrospinning of ceramic fiber systems. *Journal of the American Ceramic Society*, **89** (2), 395–407.

(101) Xie, S.H., Li, J.Y., Liu, Y.Y., et al. (2008) Electrospinning and multiferroic properties of $NiFe_2O_4$– $Pb(Zr_{0.52}Ti_{0.48})O_3$ composite nanofibers. *Journal of Applied Physics*, **104** (2), art. no. 024115.

(102) Starr, J.D. and Andrew, J.S. (2013) Janus-type bi-phasic functional nanofibers. *Chemical Communications*, **49** (39), 4151–4153.

(103) Xie, S.H., Ma, F.Y., Liu, Y.M., and Li, J.Y. (2011) Multiferroic $CoFe_2O_4$–$Pb(Zr_{0.52}Ti_{0.48})O_3$ core–shell nanofibers and their magnetoelectric coupling. *Nanoscale*, **3** (8), 3152–3158.

(104) Xie, S.H., Liu, Y.Y., and Li, J.Y. (2012) Synthesis, microstructures, and magnetoelectric couplings of electrospun multiferroic nanofibers. *Frontiers of Physics*, **7** (4), 399–407.

(105) Sreenivasulu, G., Popov, M., Zhang, R., et al. (2014) Magnetic field assisted self-assembly of ferrite–ferroelectric core–shell nanofibers and studies on magnetoelectric interactions. *Applied Physics Letters*, **104** (5), art. no. 052910.

(106) Nonnenmann, S.S., Islam, M.A., Beatty, B.R., et al. (2012) The ferroelectric field effect within an integrated core/shell nanowire. *Advanced Functional Materials*, **22** (23), 4957–4961.

(107) Liu, M., Li, X., Imrane, H., et al. (2007) Synthesis of ordered arrays of multiferroic $NiFe_2O_4$–$Pb(Zr_{0.52}Ti_{0.48})O_3$ core–shell nanowires. *Applied Physics Letters*, **90** (15), art. no. 152501.

(108) Baibarac, M., Sima, M., Matei, E., et al. (2014) Synthesis and Raman scattering of multiferroic Fe–$Pb(Zr_{0.2}Ti_{0.8})O_3$ core–shell wire arrays. *Phys. Status Solidi A*, **211** (1), 200–205.

(109) Raidongia, K., Nag, A., Sundaresan, A., and Rao, C.N.R. (2010) Multiferroic and magnetoelectric properties of core–shell $CoFe_2O_4$@$BaTiO_3$ nanocomposites *Applied Physics Letters*, **97** (6), art. no. 062904.

(110) Islam, R.A. and Priya, S. (2008) Effect of piezoelectric grain size on magnetoelectric coefficient of $Pb(Zr_{0.52}Ti_{0.48})O_3$–$Ni_{0.8}Zn_{0.2}Fe_2O_4$ particulate composites. *Journal of Materials Science*, **43**, 3560–3568.

(111) Ryu, J.H., Vazquez-Carazo, A., Uchino, K., and Kim, H.E. (2001) Piezoelectric and magnetoelectric properties of lead zirconate titanate/Ni-ferrite particulate composites. *Journal of Electroceramics*, **7** (1), 17–24.

(112) Jiang, Q.H., Shen, Z.J., Zhou, J.P., et al. (2007) Magnetoelectric composites of nickel ferrite and lead zirconate titanate prepared by spark plasma sintering. *Journal of the European Ceramic Society*, **27** (1), 279–284.

4

Modeling of Colloidal Suspensions for the Synthesis of the Ferroelectric Oxides with Complex Chemical Composition

Gregor Trefalt[1,2], Bosiljka Tadić[3], and Barbara Malič[4]

[1] *Electronic Ceramics Department, Jožef Stefan Institute and Center of Excellence NAMASTE, Slovenia*
[2] *Department of Inorganic and Analytical Chemistry, University of Geneva, Switzerland*
[3] *Department of Theoretical Physics, Jožef Stefan Institute, Slovenia*
[4] *Electronic Ceramics Department, Jožef Stefan Institute, Slovenia*

4.1 Introduction

Perovskite ferroelectric materials are known for their excellent dielectric, ferroelectric, piezoelectric, and electrostrictive responses. These properties enable their use in many practical applications, ranging from capacitors, transducers, memory elements, and precise positioning devices to microelectromechanical systems (MEMS) [1]. A subgroup of these materials are lead-based perovskites with the general chemical formula Pb(B1,B2)O_3, where B1 and B2 are low- and high-valence cations (e.g. Mg^{2+} or Zn^{2+} and Nb^{5+} or Ta^{5+}). These complex oxides are known for their large dielectric permittivity ($\varepsilon_r \sim 20\,000$) and electrostrictive (strain $\sim 0.1\%$) properties [1–3]. To further enhance or tune these properties synthesis of solid solutions is possible. One widely studied example of such a solid solution

---

Nanoscale Ferroelectrics and Multiferroics: Key Processing and Characterization Issues, and Nanoscale Effects, First Edition. Edited by Miguel Algueró, J. Marty Gregg, and Liliana Mitoseriu.
© 2016 John Wiley & Sons, Ltd. Published 2016 by John Wiley & Sons, Ltd.

is a relaxor–ferroelectric $(1-x)\mathrm{Pb}(\mathrm{Mg}_{1/3}\mathrm{Nb}_{2/3})\mathrm{O}_3$–$x\mathrm{PbTiO}_3$ (PMN–PT) with an extremely high dielectric and piezoelectric response [4, 5].

Due to their excellent properties, lead-based relaxor–ferroelectrics are good candidates for practical applications. However, one of the major drawbacks in these systems is their complex chemical composition. Since they are composed of several metallic cations, it is often challenging to prepare them in a homogeneous, phase-pure form. For example, conventional solid-state synthesis of PMN-based materials, which comprises simultaneous mixing of constituent oxides, yields in addition to desired perovskite also non-desired pyrochlore phases [2]. The latter can have an extremely detrimental effect on the properties of the end product.

The reaction sequence in a single-step synthesis of PMN from a mixture of constituent oxides was described by Inada [6]. In a homogeneous mixture of PbO, $\mathrm{Nb}_2\mathrm{O}_5$, and MgO, preferential reaction of lead and niobium oxide leads to a binary pyrochlore, $\mathrm{Pb}_x\mathrm{Nb}_y\mathrm{O}_z$, phases at relatively low temperatures. In further reactions at elevated temperatures, the pyrochlore phases subsequently react with magnesium oxide to form a perovskite PMN phase. However, due to high stability of the pyrochlores the reaction is not complete and the non-desirable pyrochlore phase may remain in the end product. To circumvent this problem, Swartz and Shrout proposed a two-step synthesis approach known as the columbite method [7]. In this procedure the columbite, $\mathrm{MgNb}_2\mathrm{O}_6$, is synthesized first:

$$\mathrm{MgO} + \mathrm{Nb}_2\mathrm{O}_5 \xrightarrow{1000\text{–}1200^\circ\mathrm{C}} \mathrm{MgNb}_2\mathrm{O}_6 \quad \text{(columbite precursor)} \tag{4.1}$$

and in the second step it is mixed with PbO to form a pure perovskite phase:

$$\mathrm{MgNb}_2\mathrm{O}_6 + 3\mathrm{PbO} \xrightarrow{900^\circ\mathrm{C}} 3\mathrm{Pb}(\mathrm{Mg}_{1/3}\mathrm{Nb}_{2/3})\mathrm{O}_3 \tag{4.2}$$

The first reaction to columbite is used to prevent the reaction between PbO and $\mathrm{Nb}_2\mathrm{O}_5$ and, consequently, the formation of the pyrochlores is limited/avoided. In this two-step method typically pure perovskite PMN phase is formed without secondary pyrochlore phases. However, in comparison to the traditional single-step synthesis method it requires at least two heating steps. The columbite method was also successfully extended to synthesize phase pure $(1-x)$PMN–xPT [8–10]. PMN-based materials were synthesized also by other methods including wet chemistry methods and mechanochemical synthesis; for details see Trefalt et al. [11, 12]. These methods are usually more complex and/or more expensive compared to the widely used solid-state synthesis methods.

In this chapter, we describe a new approach to the solid-state synthesis of ferroelectric oxides with complex chemical composition. We show how the design of particle contacts in the reagent particle mixture can lead to phase-pure products. The desired arrangements of the particles in the dried powders can be achieved through the control of particle–particle interactions in the aqueous suspensions. We explain how modeling of suspensions containing reagent particles can help us understand the process of aggregate formation. The simulations enable us to design the experiment is such way that we achieve the optimal configuration of reagent particles in the reaction mixture. The predictions were tested on two systems, PMN and its solid solution PMN–PT. With this method, both materials can be synthesized in a pure perovskite phase and they exhibit excellent electrical properties. In the end, we discuss the extension of the presented approach on other systems.

4.2 Solid-State Synthesis

Let us first outline some general concepts of solid-state synthesis. At elevated temperatures substances can react in the solid state to a solid product. These reactions are fundamentally different from reactions in liquids or gases. The diffusion in liquids and gases is extremely fast compared to the diffusion in solids. In the former cases, the rate-determining step is, therefore, chemical reactivity of reacting species. On the other hand, in the solid-state reactions the limiting factor is usually the diffusion rate. In this case, the crystal and/or defect structures are more important than the intrinsic chemical reactivities of the reacting species [13]. The typical mechanism of a binary solid-state reaction is shown in Figure 4.1(a).

The reaction starts at the interface between the two reacting phases. One or more solid products can be formed at the interface, which physically separates the two reacting components. Now the reactant atoms/ions have to diffuse through the layer of the intermediate product for the reaction to proceed. As mentioned above, the diffusion is slow and one way of enhancing it is to shorten the diffusion paths by creating more contacts between the reagent particles (see Figure 4.1(b)). The optimal situation for fast and effective reaction comprises small reagent particles, which are mixed homogeneously. In Figure 4.1(a),

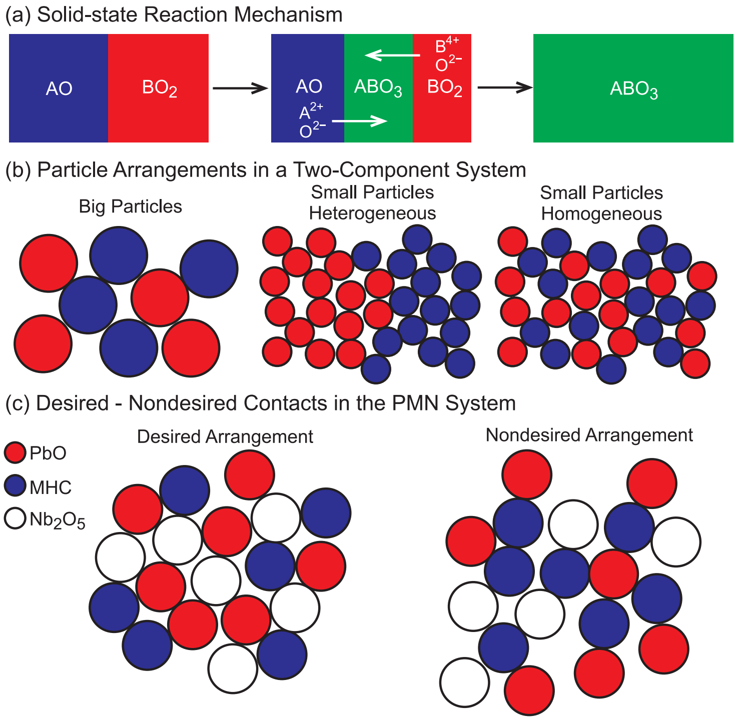
(a) Solid-state Reaction Mechanism
AO
BO_2
AO
A^{2+}
O^{2-}
ABO_3
B^{4+}
O^{2-}
BO_2
ABO_3
(b) Particle Arrangements in a Two-Component System
Big Particles
Small Particles Heterogeneous
Small Particles Homogeneous
(c) Desired - Nondesired Contacts in the PMN System
PbO
MHC
Nb_2O_5
Desired Arrangement
Nondesired Arrangement

Figure 4.1 *(a) Mechanism of a binary solid-state reaction assuming that the perovskite phase is the only reaction product. (b) Different reagent particle arrangements in the two-component system. (c) Desired and non-desired contacts in the mixture of reagent particles for the PMN synthesis. PbO: lead oxide, Nb_2O_5: niobium oxide, MHC: magnesium hydroxy carbonate. Adapted after [14]* a two-component system is presented. In this case, the only possible reaction is between two components AO and BO_2. The number of contacts between these two phases can be increased by decreasing the size of both AO and BO_2 particles and homogeneously mixing them. This conclusion leads to the accepted idea in solid-state synthesis, which states that, for fast reactions and phase pure products, homogeneous mixtures of small reagent particles are needed. However, this theory applies for two-component systems and cannot always be extended to multicomponent systems. In the case of three or more components, the homogenization is not always beneficial. In such systems multiple reactions can occur and not all of them may be desirable. Let us describe the problem on a three-component system containing particles A, B, and C. Here three different binary reactions are possible, namely reactions between A and B, A and C, and B and C. Let us presume that the reaction between A and B leads to the non-desired secondary phase, which prevents or slows down the reaction to the targeted product. Such a problem is encountered in the synthesis of PMN described above. In the mixture of PbO, Nb_2O_5, and MgO, the reaction between lead and niobium oxide leads to the non-desired pyrochlore phase. To circumvent this problem, one can design such an arrangement of the reagent particles, which would hinder the formation of pyrochlore phases and lead to the phase pure product (see Figure 4.1(c)). The homogeneous arrangement of reagent particles would lead to a lot of non-desired PbO–Nb_2O_5 contacts. On the other hand, arrangement where magnesium hydroxy carbonate (MHC) is separating PbO and Nb_2O_5 particles would be desired as it would hinder the reaction to pyrochlores. The question is how to achieve this confguration. A possible solution is to design the particle–particle interactions in aqueous suspension in such way that they would lead to the desired arrangement. We show in the next section how this aim can be achieved.

4.3 Colloidal Interactions and Aggregation

Interactions between surfaces in an aqueous media are of great importance in environmental science, biosciences, and material science. Some examples of their applications in material science include formation of ceramic green bodies [15], cement hardening [16], ink-jet printing [17], and material synthesis [11, 12, 18, 19]. In colloidal systems particle–particle interactions define their macroscopic properties, and therefore, it is crucial to understand and manipulate these forces.

4.3.1 DLVO Theory

When solid particles are immersed in water, they typically acquire charge on their surface. If the solution contains ions, a diffuse layer of these ions develops adjacently to the surface, resulting in an electrical double layer [20, 21]. When two particles approach each other their double layers overlap, resulting in an interaction force between them. Depending on the particle charge, these forces can be either attractive or repulsive. When the double-layer interactions are added to the omnipresent van der Waals interactions, one arrives at the classical DLVO theory, developed by Derjaguin and Landau [22] and Verwey and Overbeek [23]:

$$U^{\mathrm{DLVO}} = U^{\mathrm{DL}} + U^{\mathrm{vdW}} \tag{4.3}$$

where U^{DLVO} is the total interaction potential, U^{DL} is the double layer contribution, and U^{vdW} is the van der Waals interaction. The authors of the theory showed that it is able to predict the aggregation behavior of the colloidal suspensions [22, 23]. The forces between particles can be directly measured, for example, by the colloidal probe technique based on atomic force microscopy (AFM) [24, 25]. This enables the DLVO theory to be directly tested by confronting the calculated and measured force between charged colloidal particles in a solution. Numerous reports have shown that the DLVO theory is able to quantitatively describe the interaction forces between colloidal particles down to distances of a few nm [24–29]. Furthermore, it was shown that aggregation of the colloidal suspensions can also be quantitatively described by the DLVO theory [27, 28, 30–32].

Figure 4.2 shows the influence of the DLVO interaction potentials on the aggregation state of the suspension.

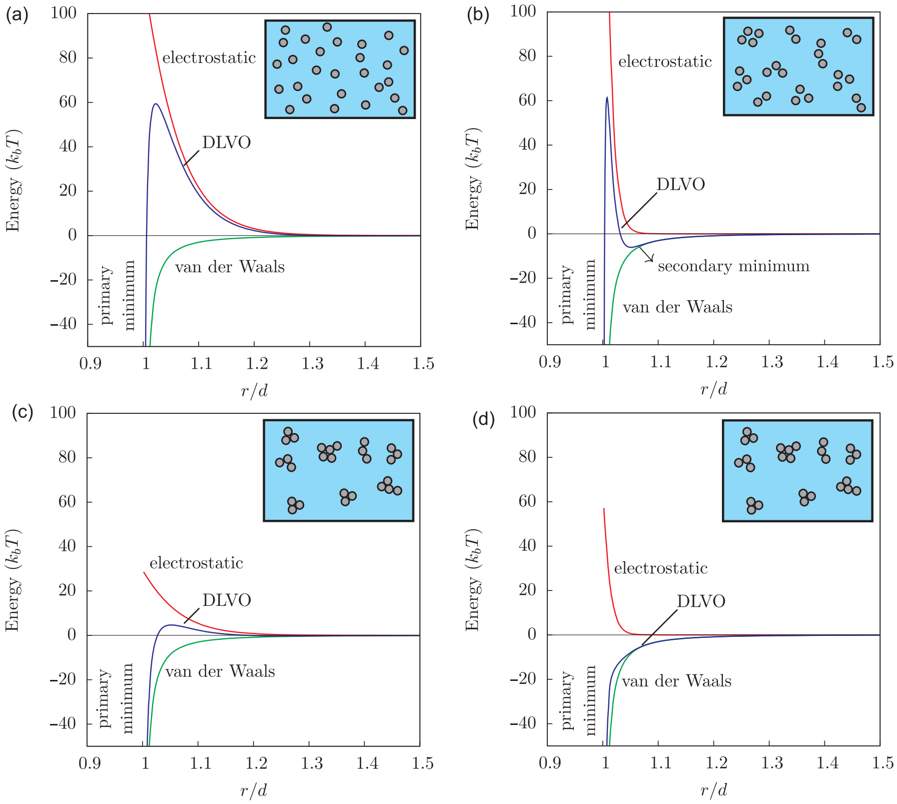

Figure 4.2 *Influence of the DLVO interaction potential on the colloidal stability. The DLVO potential with its van der Waals and double-layer (electrostatic) contributions is plotted for four different conditions with the scheme of the suspension state corresponding to the shown potential. (a) Repulsive forces are dominant – suspension is stable. (b) Repulsive forces with a shallow secondary minimum – weakly agglomerated system. (c) Low potential maximum, particles can overcome a potential barrier – aggregated suspension. (d) Attractive forces are dominant – aggregated suspension. Adapted after [14]*

According to the DLVO theory, the interaction potential is governed by the competition between the double-layer and van der Waals forces. The double layer between equally charged particles is repulsive, while the van der Waals forces are in most cases attractive. When the double-layer forces are dominant, the total interaction is repulsive, particles are not aggregating, and the suspension is stable (see Figure 4.2(a)). The strength of the repulsive double-layer forces can be reduced by reducing the surface charge of the particles or by screening the force with the addition of ions into the solution. In Figure 4.2(b) the strength of the double-layer force is reduced and the total interaction is still repulsive close to the surface. However, at larger distances the secondary minimum develops. The particles are trapped in this secondary minimum and the suspension is weakly aggregated. When the strength of the double-layer forces is further decreased, the repulsive energy barrier becomes small compared to the thermal energy (see Figure 4.2(c)). In this case, the particles overcome the barrier and strongly aggregate. In the last case, Figure 4.2(d), the van der Waals forces dominate and lead to attractive DLVO interaction, which also results in strong aggregation.

4.3.2 Modeling of Aggregate Formation and Their Structure

Colloidal suspension samples contain a big number of individual particles. The pair interactions between charged particles are governed by DLVO potential, as explained above. For the description of the whole system, all pairwise interactions have to be summed up. Typically, numerical simulations are used to model the particle ensembles. Monte Carlo (MC) or Brownian dynamics (BD) methods are most widely used to model aggregate formation in colloidal suspensions [33–42].

Next we shortly describe the basics of an MC simulation, since this method was used to predict the structure of the aggregates for PMN synthesis [40]. In the MC method different microscopic configurations of particle ensemble are sampled. For every microscopic state its energy is calculated by summing up the interaction potentials in the system. The properties of the states are then averaged and the average is weighted with the probability of finding the system in a certain state. In practice the Metropolis algorithm is usually used for sampling the configurational space (see Figure 4.3) [43].

In this approach, first a random arrangement of particles in the simulation box is created. Next, a particle is chosen and randomly moved to a new position. Then, the probability of transition from the initial to a new state is calculated. This probability is a function of the energy difference between the two states. If the transition probability is higher than randomly chosen number between 0 and 1, the new state is accepted; otherwise the new

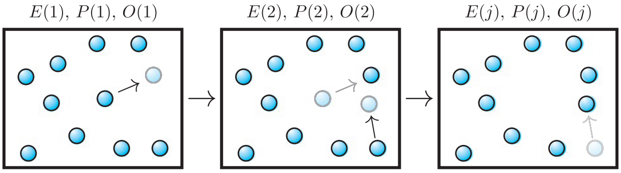

__Figure 4.3__ Metropolis sampling scheme. By moving one particle at the time, a Markov chain of states is formed. The properties are calculated as the average through these states. E: energy, P: transition probability, O: value of a certain property. Adapted after [14]

state is rejected and the system returns back to the old state. Now, a Markov chain of such states is formed and the properties are averaged through a large number of such states. A more detailed description of this method can be found in Allen and Tildesley [44] and Frenkel and Smit [45].

4.4 Aggregation in the Three-Component System

Synthesis of PMN requires three components, namely compounds containing lead, niobium, and magnesium. In Figure 4.1(c) the desired arrangement of these components is shown. As discussed, PbO–Nb_2O_5 contacts are not desired in the reagent mixture since they enhance the reaction to pyrochlores. In the presented method, instead of MgO, MHC was used as a source of magnesium for two reasons. Firstly, the carbonate compound is more reactive compared to the oxide compound and, secondly, the surface charge behavior of the MHC is beneficial to create the desired structure of aggregates [40]. One of the possibilities for creating a desired particle arrangement in the dried powders is by manipulating the particle–particle interactions in suspensions to invoke the formation of the desired structure of aggregates. The component of the DLVO forces that can be tuned is the double-layer force. One can change the interactions from repulsive to attractive and vice versa by changing the surface charge of the particles. The charge of the inorganic particles can often be adjusted by changing the pH. In Figure 4.4 zeta-potentials measurements of PbO, Nb_2O_5, and MHC particles in aqueous suspensions are presented as a function of the pH.

The zeta potential is closely related to surface charge of the particles [20,21]. The charge of PbO is positive at pH $\approx$ 9 and decreases with the increasing pH. At pH $\approx$ 12 the particles become neutral and further increase in pH leads to the negatively charged PbO. The charge of Nb_2O_5 particles also decreases with increasing pH, but it is always negative in the measured pH range. The MHC particles behave differently, their zeta potential increases with increasing pH, and the charge inversion is observed at pH $\approx$ 11. The two pH conditions, (i) pH = 11.4 and (ii) pH = 12.5, where markedly different structures of aggregates are

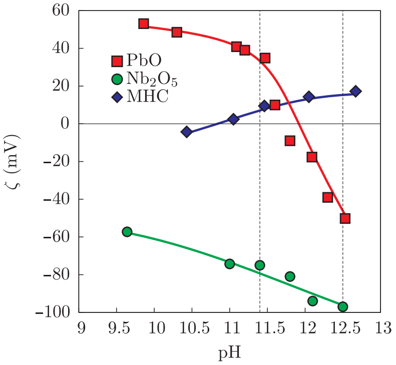

Figure 4.4 *Dependence of the zeta potential on the pH of the reagent particles, namely PbO, Nb_2O_5, and MHC. The two pH conditions considered in simulations are denoted by the dashed lines. Adapted from [40] with permission from The Royal Society of Chemistry*

expected, are denoted by the dashed lines. These two cases will be further abbreviated as pH11.4 and pH12.5. In the pH11.4 case, the PbO and MHC particles are positively charged, while Nb_2O_5 particles are negatively charged. At higher pH, PbO changes the charge from positive to negative, and in the pH12.5 case, both PbO and Nb_2O_5 are negatively charged, while MHC is positively charged. Therefore in the pH11.4 case the PbO–Nb_2O_5 interaction should be attractive and in the pH12.5 case the repulsive interaction is expected between the two.

The above-mentioned pH conditions were used in the MC simulations of aggregate formation in suspensions containing PbO, Nb_2O_5, and MHC particles. The parameters of the simulations were chosen in such a way to closely correspond to the aforementioned experimental conditions. Details of the simulation parameters and the used model are explained in Trefalt et al. [40]. The interactions between the particles were calculated with the DLVO theory and are presented in Figure 4.5(a) and (b) for the pH11.4 and pH12.5 cases, respectively.

In the three-component system there are six pairs of interactions. In the pH11.4 case, the PbO–PbO, Nb_2O_5–Nb_2O_5, and PbO–MHC interactions are repulsive, while PbO–Nb_2O_5, Nb_2O_5–MHC, and MHC–MHC interactions are attractive. In the pH12.5 case, the situation is different; here PbO–PbO, Nb_2O_5–Nb_2O_5, PbO–Nb_2O_5, and MHC–MHC interactions are repulsive, while PbO–MHC and Nb_2O_5–MHC are attractive. The most important difference between the two pH conditions is the difference in the PbO–Nb_2O_5 interactions, since the PbO–Nb_2O_5 contacts are important for the pure perovskite phase formation, as proposed in Figure 4.1.

The most instructive results from simulations regarding the aggregate structures are radial distribution functions (RDFs) and snapshots of spatial distribution of particles, presented in Figure 4.5(c) to (f). The RDFs show the average distribution of particles around the chosen particle. For clarity the RDF curves are systematically shifted upwards by 10 units.

In the pH11.4 sample, Figure 4.5(c), the RDFs can be divided into two groups: (i) functions with a large sharp peak at 400 nm, which is the distance of the closest approach between two particles, and (ii) the RDFs where the first peak is located at 450 nm. PbO–Nb_2O_5, PbO–MHC, Nb_2O_5–MHC, and MHC–MHC RDFs belong to group (i). In these cases, the large peak at 400 nm suggests that the respective pairs of particles are on average in close contact. The second group (ii) of RDFs contains PbO–PbO and Nb_2O_5–Nb_2O_5 pairs. Here the respective particles are not in contact. The results from the RDFs are in agreement with the snapshot shown in Figure 4.5(e), where a lot of PbO–Nb_2O_5 contacts are observed.

In the pH12.5 case large sharp peaks in the RDFs at 400 nm show that PbO–MHC and Nb_2O_5–MHC pairs are in contact, while other pairs are not directly connected. Detailed analysis of other RDFs reveals that PbO and Nb_2O_5 adsorb on MHC particles [40]. In this configuration the MHC particles separate the PbO and Nb_2O_5 particles, preventing them from coming into contact. The corresponding snapshot, Figure 4.5(f), shows exactly the situation predicted from the RDFs; there are no PbO–Nb_2O_5 contacts since MHC separates the two types of particles.

Comparison of the snapshots in Figure 4.5 with the schematic arrangements in Figure 4.1(c) reveals that the non-desired arrangement, with a lot of PbO–Nb_2O_5 contacts, corresponds to pH11.4 conditions, while the desired arrangement of reagent particles is obtained for the pH12.5 case.

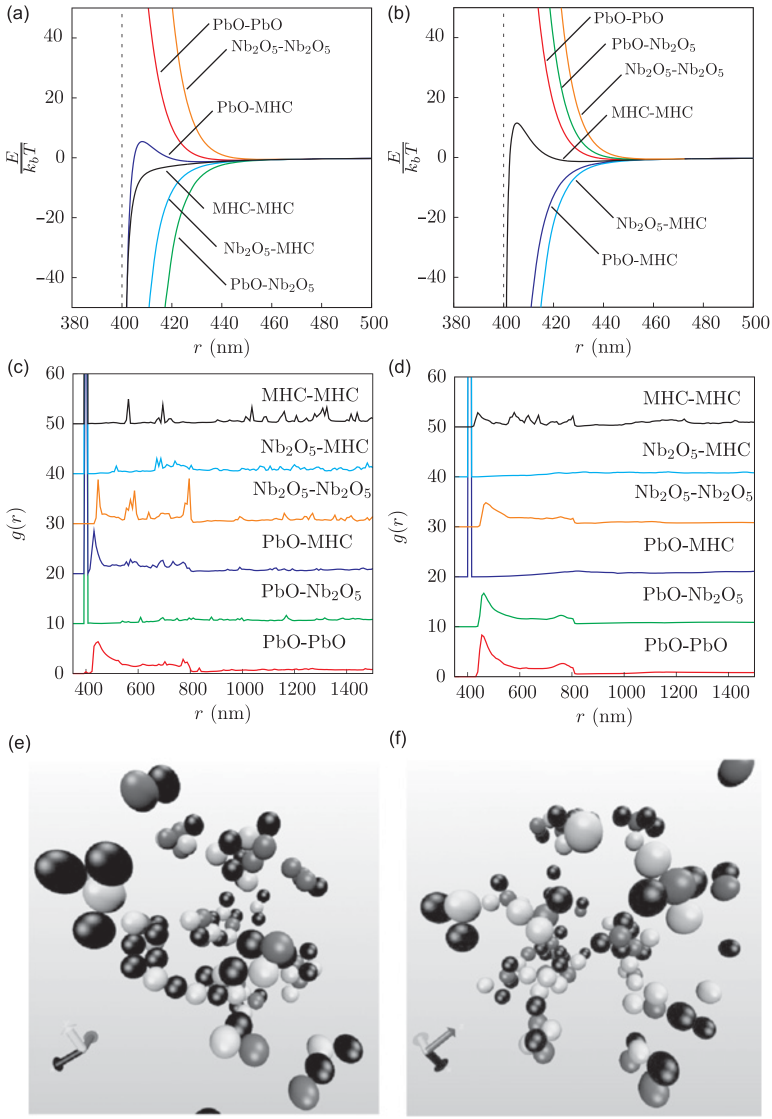

Figure 4.5 Interactions and simulation results. DLVO interaction potentials (a) and (b). Radial distribution functions (c) and (d). Snapshots of spatial distribution of particles (e) and (f). The pH11.4 case is shown on the left and the pH12.5 case on the right. PbO is colored black, Nb_2O_5 white, and MHC gray. All particles have a size of 400 nm. Adapted from [40] with permission from The Royal Society of Chemistry

The simulations give a detailed insight in the formation of aggregates at the conditions important for the PMN synthesis. The results imply that pH12.5 conditions should be superior for preparation of the phase pure perovskite PMN material as compared to the pH11.4 conditions.

4.5 Applying the Modeling Results to Enhance Properties of Ferroelectric Complex Oxides

The simulation results presented in the previous section can be used to optimize the synthesis of PMN-based materials. Here, two examples of synthesis by controlling the aggregation of reagent particles are presented. The first case presents the synthesis of PMN and in the second case PMN–PT synthesis is described.

4.5.1 PMN Synthesis by Controlled Aggregation of Reagent Particles

The simulation results were tested on the problem described in the introduction. In Figure 4.1(c) the optimal arrangement of the particles for the PMN synthesis was presented. This arrangement corresponds to the structure of the aggregates in the pH12.5 suspension as predicted by the simulations. Therefore, two sets of experiments were conducted to test the simulation results, namely pH11.4 and pH12.5 samples were prepared [11]. Suspensions were prepared by mixing constituent powders, namely PbO, Nb_2O_5, and MHC, in water. The lower pH case corresponds to the inherent pH of the suspension. For the pH12.5 sample, pH was adjusted by adding ammonia solution. The samples were attrition milled, dried, and then heated at elevated temperatures, where the solid-state reaction took place. The details about the experimental procedure can be found in [11].

In Figure 4.6 the X-ray diffraction (XRD) patterns of the pH11.4 and pH12.5 samples heated at 900 °C are presented.

Pure perovskite PMN powder is present only in the pH12.5 case, while the pH11.4 sample in addition to perovskite also contains the non-desired pyrochlore phase. As predicted by the simulations, the pure perovskite phase is only formed in the sample with higher pH. Analysis of the respective samples with a scanning electron microscope (SEM) is shown in Figure 4.7.

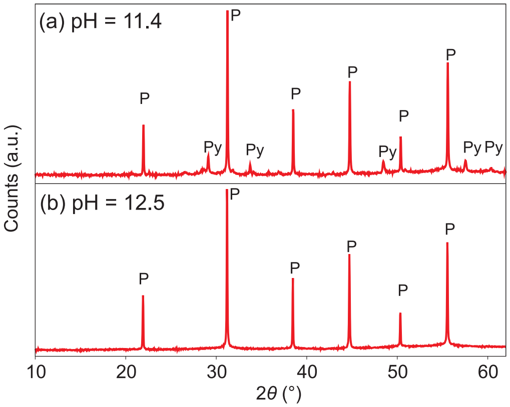

Figure 4.6 XRD patterns reagent powder mixtures for synthesis of PMN heated at 900 °C: (a) pH11.4 sample and (b) pH12.5 sample. P: perovskite $Pb(Mg_{1/3}Nb_{2/3})O_3$, Py: pyrochlore $Pb_{1.83}Nb_{1.71}Mg_{0.29}O_{6.39}$. Adapted with permission from [11]. Copyright © [2011] [The American Ceramic Society]

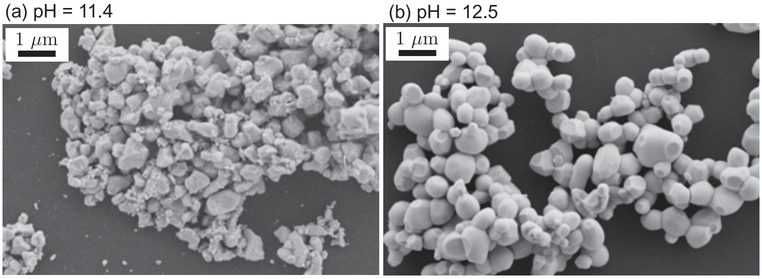

Figure 4.7 *Scanning electron micrographs of PMN powder mixtures heated at 900 °C for 5 h: (a) pH11.4 sample and (b) pH12.5 sample. Adapted with permission from [11]. Copyright © [2011] [The American Ceramic Society]*

The pH conditions strongly influence the morphology of the powders. In the pH12.5 case, the particles are uniform in size and shape, with sizes of roughly 1 μm. On the other hand, the powder from the pH11.4 sample, in addition to bigger micron-sized particles, contains also smaller particles of a few hundred nm. It was further shown with transmission electron microscopy (TEM) that the smaller particles contain both perovskite and pyrochlore phases [11].

The calcined powders were sintered to produce ceramics. The properties of the pH11.4 and the pH12.5 ceramic samples are presented in Figure 4.8.

Dielectric properties of the respective samples sintered at 1050 °C can be compared by observing Figure 4.8(a) and (b). The peak dielectric permittivity of the pH11.4 sample is about 50% lower as compared to the pH12.5 sample. Similarly, the electromechanical response of the pH11.4 sample is much lower than the response of the pH12.5 sample (see Figure 4.8(d)). The presence of the non-desired pyrochlore phase heavily deteriorates the properties of the ceramics. Furthermore, the phase pure pH12.5 sample can be sintered to high density at only 950 °C, which is about 200–300 K lower compared to the typically used sintering temperatures [7, 46, 47]. The dielectric properties of this sample are comparable to the pH12.5 sample sintered at a 200 K higher temperature (see Figure 4.8(c)).

4.5.2 PMN–PT Synthesis by Controlled Aggregation of Reagent Particles

The synthesis method described in the previous section was extended to the PMN–PT material [12]. Compared to the synthesis of PMN, one more component is added to the reaction mixture, namely TiO_2. The zeta potential of TiO_2 behaves similarly to Nb_2O_5. In the suspension containing reagent particles, PbO, Nb_2O_5, MHC, and TiO_2, similar structures of aggregates as in the PMN case are expected at pH11.4 and pH12.5 conditions. The pH11.4 sample should contain a lot of non-desired PbO–Nb_2O_5 contacts, whereas in the pH12.5 sample the PbO–Nb_2O_5 contacts should be prevented by MHC [12].

The pH11.4 and pH12.5 reagent powder mixtures were heated at 850 °C to synthesize the PMN–PT powder. The XRD patterns of the respective samples are shown in Figure 4.9.

Also in the case of PMN–PT synthesis only the pH12.5 sample contains the pure perovskite phase, while the pH11.4 sample contains both perovskite and detrimental pyrochlore phases. After sintering at 950 °C the pH11.4 and the pH12.5 samples reached

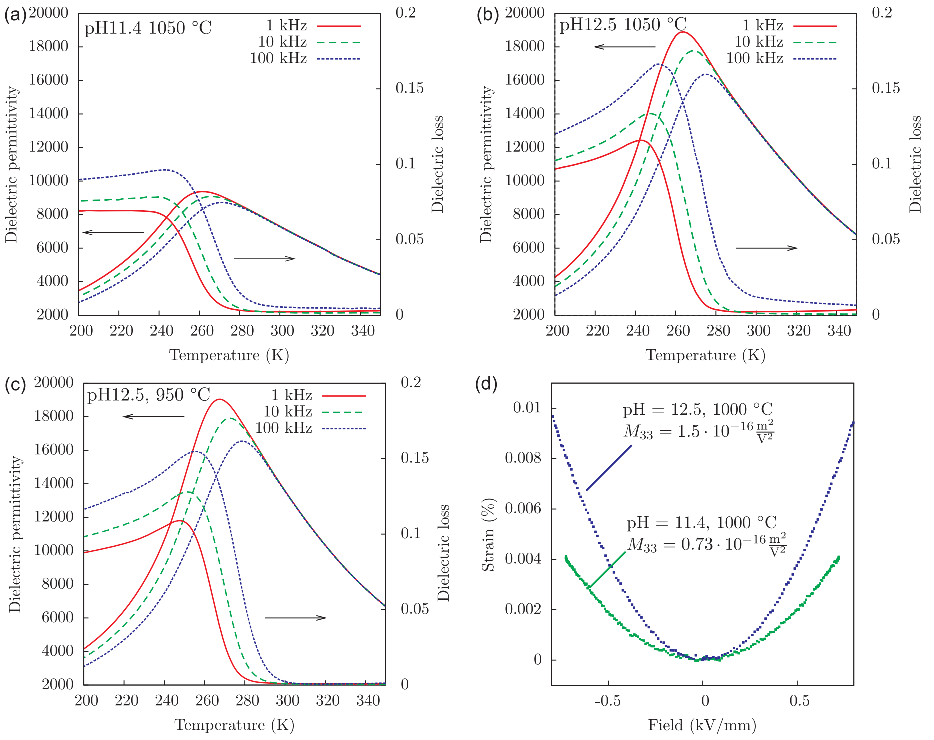

Figure 4.8 *Properties of the PMN ceramics. Dielectric permittivity as a function of temperature of the PMN ceramics sintered at 1050 °C for (a) pH11.4 and (b) pH12.5 samples. (c) Dielectric permittivity as a function of temperature of the pH12.5 sample sintered at 950 °C. (d) Strain as a function of the applied electric field for the pH11.4 and pH12.5 samples. Adapted with permission from [11]. Copyright © [2011] [The American Ceramic Society]*

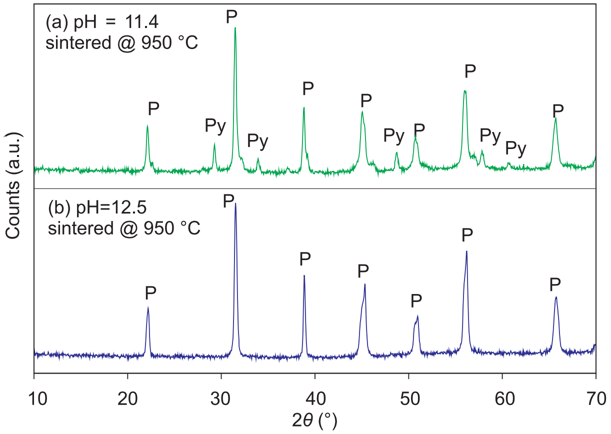

Figure 4.9 *XRD patterns of the PMN–PT ceramics: (a) pH11.4 and (b) pH12.5. Adapted with permission from [12]. Copyright © [2012] [The American Ceramic Society]*

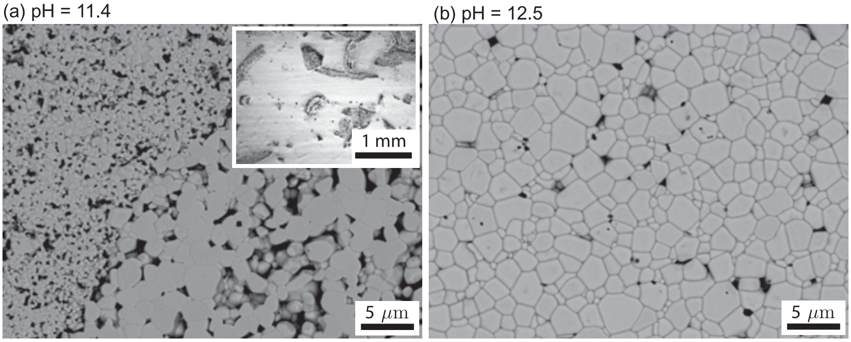

Figure 4.10 Microstructures of the polished PMN–PT ceramics: (a) pH11.4 sample and (b) pH12.5 sample. The inset in (a) is of a lower magnication image. Adapted with permission from [12]. Copyright © [2012] [The American Ceramic Society]

81 and 96% of theoretical density, respectively. The corresponding microstructures of the polished and thermally etched ceramics are presented in Figure 4.10.

The pH11.4 sample is non-homogeneous and consists of regions with smaller and larger grains. The two phases are also observed in a lower magnification image (see the inset in Figure 4.10(a)). On the other hand, the microstructure of the pH12.5 ceramics is highly homogeneous with a small amount of porosity and grains between 0.5 and 3 μm. Further differences between the pH11.4 and pH12.5 samples are evident when comparing dielectric, ferroelectric, and electrical properties of the two ceramic samples (see Figure 4.11).

The dielectric permittivity of the pH12.5 sample is considerably higher than the one measured for the pH11.4 sample. At the maximum the permittivity value of the pH12.5 sample is approximately five times higher compared to the value of the pH11.4 case. Ferroelectric hysteresis loops are observed in both pH11.4 and pH12.5 samples (see Figure 4.11(c) and (d)). However, the remnant polarization for the pH12.5 sample reaches a three times higher value as compared to the pH11.4 sample. Similarly, the peak-to-peak strain at 2 kV/mm is one order of magnitude higher in the case of the pH12.5 sample as compared to the pH11.4 case.

The functional properties of the pH11.4 ceramics are heavily deteriorated in comparison with those of the pH12.5 ceramics and this behavior was attributed to the presence of the pyrochlore and high porosity of the former samples [11].

4.6 Conclusions and Outlook

In this chapter, an approach to tailor the solid-state synthesis by designing the arrangements in the reactant powder mixtures was presented. The development of the synthesis method was supported by MC simulations, which were crucial for understanding the formation of aggregates and optimizing the experimental conditions. The predictions of the simulations were tested for two systems, namely PMN and PMN–PT. In both cases, the pure perovskite phase was formed only at pH = 12.5, which is consistent with simulation results. Furthermore, the ceramic samples obtained from the suspensions with pH = 12.5 had superior

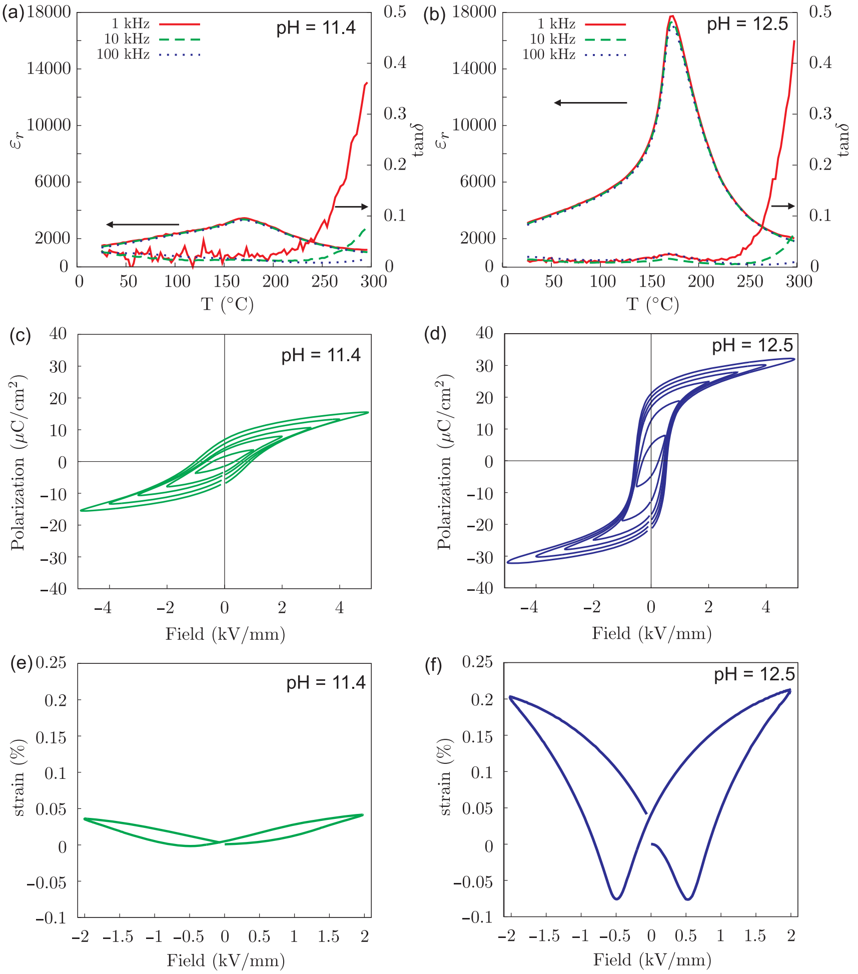

Figure 4.11 *Dielectric, ferroelectric, and electromechanical properties of PMN–PT ceramics. The pH11.4 sample is presented in the left panel and the pH12.5 sample in the right panel. Adapted with permission from [12]. Copyright © [2012] [The American Ceramic Society]*

properties as compared to the samples prepared at pH = 11.4. The difference between the properties was attributed to the presence of the non-desirable pyrochlore phase, which was present only in the pH11.4 samples.

The idea behind the presented synthesis method, where the contacts between the reagent particles are designed to control the solid-state reactions, is general. In the presented approach, the interactions between the particles were controlled by changing the zeta potential via the pH adjustment. In general, one can use other approaches to tune the interactions in the desired way. One of the possible ways to change the interactions is by adsorption of the charged molecules on the particle surfaces. The latter approach was used, for example, for the preparation of homogeneous Pb(Zr,Ti)O_3–ZrO_2 composites [19]. With such modifications, the presented method could be further extended to the synthesis of other ferroelectric materials with complex chemical compositions.

Acknowledgments

The authors gratefully acknowledge the contribution by Professor Dr Marija Kosec, who passed away in December 2012. They are grateful for the financial support from the Research Programs P2-0105 and P1-0044 funded by the Research Agency of the Republic of Slovenia.

References

(1) Setter, N. (2002) *Pezoelectric Materials in Devices*, Ceramics Laboratory, EPFL Swiss Federal Institute of Technology, Lausanne.

(2) Heartling, G.H. (1999) Feroelectric ceramics: "history and technology". *Journal of the American Ceramic Society*, **82**, 2341–2359.

(3) Swartz, S.L., Shrout, T.R., Schultze, W.A., and Cross, L.E. (1984) Dielectric properties of lead–magnesium niobate ceramics. *Journal of the American Ceramic Society*, **67**, 311–314.

(4) Park, S.E. and Shrout, T.R. (1997) Ultrahigh strain and piezoelectric behavior in relaxor based ferroelectric single crystals. *Journal of Applied Physics*, **82**, 1804–1811.

(5) Uršič, H., Hrovat, M., Holc, J., et al. (2008) A large-displacement 65Pb$(Mg_{1/3}Nb_{2/3})O_3$–35$PbTiO_3$/Pt bimorph actuator prepared by screen printing. *Sensors and Actuators B*, **133**, 699–704.

(6) Inada, M. (1977) Analysis of the formation process of the piezoelectric PCM ceramics. *Jpn. Natl. Tech. Rep.*, **27**, 95–102.

(7) Swartz, S.L. and Shrout, T.R. (1982) Fabrication of perovskite lead magnesium niobate. *Materials Research Bulletin*, **17**, 1245–1250.

(8) Kelly, J., Leonard, M., Tantigate, C., and Safari, A. (1997) Effects of composition on the electromechanical properties of $(1-x)Pb(Mg_{1/3}Nb_{2/3})O_3$–$xPbTiO_3$ Ceramics. *Journal of the American Ceramic Society*, **80**, 957–964.

(9) Kwon, S., Sabolsky, E., and Messing, G. (2001) Low-temperature reactive sintering of 0.65 PMN–0.35 PT. *Journal of the American Ceramic Society*, **84**, 648–650.

(10) Leite, E., Scotch, A., Khan, A., et al. (2002) Chemical heterogeneity in PMN–35PT ceramics and effects on dielectric and piezoelectric properties. *Journal of the American Ceramic Society*, **85**, 3018–3024.

(11) Trefalt, G., Malič, B., Kuščer, D., et al. (2011) Synthesis of $Pb(Mg_{1/3}Nb_{2/3})O_3$ by self-assembled colloidal aggregates. *Journal of the American Ceramic Society*, **94**, 2846–2856.

(12) Trefalt, G., Malič, B., Holc, J., and Kosec, M. (2012) Synthesis of $Pb(Mg_{1/3}Nb_{2/3})O_3$ – $PbTiO_3$ by controlled agglomeration of precursor particles. *Journal of the American Ceramic Society*, **95**, 1858–1865.

(13) Rao, C.N.R. and Gopalakrishnan, J. (1997) *New Directions in Solid State Chemistry*, Cambridge University Press, Cambridge.

(14) Trefalt, G. (2012) *New Synthesis Route to Pb(*$Mg_{1/3}Nb_{2/3}$*)*O_3 *Based Materials by Controlled Agglomeration of Reagent Particles*, PhD Thesis, Jozef Stefan Interantional Postgraduate School.

(15) Balzer, B., Hruschka, M.K.M., and Gauckler, L.J. (1999) Coagulation kinetics and mechanical behavior of wet alumina green bodies produced via DCC. *Journal of Colloid and Interface Science*, **216**, 379–386.

(16) Labbez, C., Jonsson, B., Pochard, I., et al. (2006) Surface charge density and electrokinetic potential of highly charged minerals: experiments and Monte Carlo simulations on calcium silicate hydrate. *Journal of Physical Chemistry B*, **110**, 9219–9230.

(17) Kuščer, D., Stavber, G., Trefalt, G., and Kosec, M. (2012) Formulation of an aqueous titania suspension and its patterning with ink-jet printing technology. *Journal of the American Ceramic Society*, **95**, 487–493.

(18) Aschauer, U., Burgos-Montes, O., Moreno, R., et al. (2011) A toolkit for the calculation of particle interactions and suspension stability and its application to mullite synthesis by colloidal methods. *Journal of Dispersion Science and Technology*, **32**, 470–479.

(19) Trefalt, G., Benčan, A., Kamplet, M., et al. (2014) Evaluation of the homogeneity in Pb(Zr,Ti)O_3–zirconia composites prepared by the heteroagglomeration of precursors using the Voronoi-diagram approach. *Journal of the European Ceramic Society*, **34**, 669–675.

(20) Russel, W.B., Saville, D.A., and Schowalter, W.R. (1991) *Colloidal Dispersions*, Cambridge University Press, Cambridge.

(21) Elimelech, M., Gregory, J., Jia, X., and Williams, R.A. (1998) *Particle Deposition and Aggregation*, Butterworth-Heinemann, Woburn.

(22) Derjaguin, B.V. and Landau, L.D. (1941) Theory of the stability of strongly charged lyophobic sols and the adhesion of strongly charged particles in solutions of electrolytes. *Acta Physicochimica USSR*, **14**, 633–662.

(23) Verwey, E.J.W. and Overbeek, J.T.G. (1948) *Theory of the Stability of Lyophobic Colloids: The Interaction of Sol Particles Having an Electric Double Layer*, Elsevier Publishing Company, Amsterdam.

(24) Ducker, W.A., Senden, T.J., and Pashley, R.M. (1991) Direct measurement of colloidal forces using an atomic force microscope. *Nature*, **353**, 239–241.

(25) Butt, H.J. (1991) Measuring electrostatic, van der Waals, and hydration forces in electrolyte solutions with an atomic force microscope. *Biophysical Jounal*, **60**, 1438–1444.

(26) Hartley, P.G., Larson, I., and Scales, P.J. (1997) Electrokinetic and direct force measurements between silica and mica surfaces in dilute electrolyte solutions. *Langmuir*, **13**, 2207–2214.

(27) Sinha, P., Szilagyi, I., Montes Ruiz-Cabello, F.J., et al. (2013) Attractive forces between charged colloidal particles induced by multivalent ions revealed by confronting aggregation and direct force measurements. *Journal of Physical Chemistry Letters*, **4**, 648–652.

(28) Ruiz-Cabello, F.J.M., Trefalt, G., Csendes, Z., et al. (2013) Predicting aggregation rates of colloidal particles from direct force measurements. *Journal of Physical Chemistry B*, **117**, 11853–11862.

(29) Ruiz-Cabello, F.J.M., Maroni, P., and Borkovec, M. (2013) Direct measurements of forces between different charged colloidal particles and their prediction by the theory of Derjaguin, Landau, Verwey, and Overbeek (DLVO). *Journal of Chemical Physics*, **138**, art. no. 234705.

(30) Behrens, S., Christl, D., Emmerzael, R., et al. (2000) Charging and aggregation properties of carboxyl latex particles: experiments versus DLVO theory. *Langmuir*, **16**, 2566–2575.

(31) Szilagyi, I., Sadeghpour, A., and Borkovec, M. (2012) Destabilization of colloidal suspensions by multivalent ions and polyelectrolytes: from screening to overcharging. *Langmuir*, **28**, 6211–6215.

(32) Szilagyi, I., Polomska, A., Citherlet, D., et al. (2013) Charging and aggregation of negatively charged colloidal latex particles in the presence of multivalent oligoamine cations. *Journal of Colloid and Interface Science*, **392**, 34–41.

(33) Cerbelaud, M., Videcoq, A., Abélard, P., et al. (2008) Heteroaggregation between Al_2O_3 submicrometer particles and SiO_2 nanoparticles: experiment and simulation. *Langmuir*, **24**, 3001–3008.

(34) Hütter, M. (1999) Coagulation rates in concentrated colloidal suspensions studied by Brownian dynamics simulation. *Physical Chemistry Chemical Physics*, **1**, 4429–4436.

(35) Blunt, M.O., Stannard, A., Pauliac-Vaujour, E., et al. (2010) Patterns and pathways in nanoparticle self- organization, in *The Oxford Handbook of Nanoscience and Technology*, edited by A.V. Narlikar and Y.Y. Fu, Oxford University Press, Oxford, pp. 214–249.

(36) Bianchi, E., Tartaglia, P., Zaccarelli, E., and Sciortino, F. (2008) Theoretical and numerical study of the phase diagram of patchy colloids: ordered and disordered patch arrangements. *Journal of Chemical Physics*, **128**, art. no. 144504.

(37) Hong, L., Cacciuto, A., Luijten, E., and Granick, S. (2008) Clusters of amphiphilic colloidal spheres. *Langmuir*, **24**, 621–625.

(38) Lopéz-Lopéz, J.M., Schmitt, A., Moncho-Jordá, A., and Hidalgo-Álvarez, R. (2006) Stability of binary colloids: kinetic and structutal aspects of heteroaggregation processes. *Soft Matter*, **2**, 1025–1042.

(39) Tadič, B., Šuvakov, M., and Trefalt, G. (2011) Modelling structure of collodal assemblies: methodology and examples, in *Proceedings of the 2011 International Conference on Computational and Mathematical Methods in Science and Engineering*, CMMSE, Benidorm, pp. 1097–1103.

(40) Trefalt, G., Tadič, B., and Kosec, M. (2011) Formation of colloidal assemblies in suspensions for $Pb(Mg_{1/3}Nb_{2/3})O_3$ synthesis: Monte Carlo simulation study. *Soft Matter*, **7**, 5566–5577.

(41) Dijkstra, M. (2001) Computer simulations of charge and steric stabilised colloidal suspensions. *Current Opinion in Colloid and Interface Science*, **6**, 372–382.

(42) Chen, J.C. and Kim, A.S. (2004) Brownian dynamics, molecular dynamics, and Monte Carlo modeling of colloidal systems. *Advances in Colloid and Interface Science*, **112**, 159–173.

(43) Metropolis, N., Rosenbluth, A.W., Rosenbluth, M.N., et al. (1953) Equation of state calculations by fast computing machines. *Journal of Chemical Physics*, **21**, 1087–1092.

(44) Allen, M.P. and Tildesley, D.J. (1987) *Computer Simulation of Liquids*, Clarendon Press, Oxford.
(45) Frenkel, D. and Smit, B. (2002) *Understanding Molecular Simulation: From Algorithms to Applications*, Academic Press, San Diego.
(46) Ravindranathan, P., Komarneni, S., Bhalla, A.S., and Roy, R. (1990) Dielectric properties of sol–gel derived lead magnesium niobate ceramics. *Ferroelectric Letters Section*, **11**, 137–144.
(47) Wang, C.H. and Schultze, W.A. (1990) The role of excess magnesium oxide or lead oxide in determining the microstructure and properties of lead magnesium niobate. *Journal of the American Ceramic Society*, **73**, 825–832.

5

Self-Assemblage and Patterning of Thin-Film Ferroic Nanostructures

Theodor Schneller

Institut für Werkstoffe der Elektrotechnik II, RWTH Aachen University, Germany

5.1 Introduction

The continuing trend of device miniaturization in the electronic industry, which is driven by the need to integrate more and more functionalities on the same area and by Moore's Law [1] requires an increasing technological and scientific effort. For memory devices such as non-volatile ferroelectric random accessible memory (FERAM) [2] increasing the memory density typically leads to a continuous reduction of the ferroelectric capacitor down to the 10 nm range and below. This means that ferroelectric nanograins in this dimension have to be integrated into a circuit, which raises technical questions of the manufacturability and physical questions concerning the limit of ferroelectricity, which is a cooperative phenomenon of interacting dipoles. Thus deviations from the bulk behavior are expected as the number of contributing unit cells decreases. The ultimate volume below which spontaneous polarization ceases is referred to as the "superparaelectric limit" [3], which marks the ultimate size limit of the device concept.

In order to study scaling effects in ferroelectrics, different approaches have been applied to fabricate three-, two-, and one-dimensional nanopatterned materials, either supported on substrates or unsupported. For general reviews on nanoscaled ferroelectric particles, rods, wires, and tubes the reader is referred to Chapters 1, 2, 8, and 9, and to the literature [4, 5]. In case of thin-film ferroic nanostructures the methods are often classified

Nanoscale Ferroelectrics and Multiferroics: Key Processing and Characterization Issues, and Nanoscale Effects, First Edition. Edited by Miguel Algueró, J. Marty Gregg, and Liliana Mitoseriu.
© 2016 John Wiley & Sons, Ltd. Published 2016 by John Wiley & Sons, Ltd.

into top-down and bottom-up methods and/or invasive and non-invasive methods. Standard top-down approaches, which are known from the semiconductor industry, start with the fabrication of suitable film stacks, e.g. (bottom)electrode–insulator–(top)electrode (e.g. metal–ferroelectric–metal (MFEM)[1]). Subsequently these multilayered films are patterned after crystallization by methods such as the focused ion beam (FIB) method [6, 7]. Ferroic nanostructures obtained by these rather classical top-down approaches usually suffer from damage by, for example, ion bombardment, which makes it difficult to decide between real size effects and those induced by the patterning method. Such methods may therefore also be defined as invasive methods. Hence numerous studies have been conducted to develop non-invasive techniques to avoid such damage, either by doing the patterning step prior to the final crystallization (e.g. e-beam direct writing [8] etc.) or by using other bottom-up approaches, where patterning is obtained by free and site-induced self-assembly (SA) methods. In principle the fabrication methods for ferroic thin films and nanostructures can be based on physical principles such as sputtering or evaporation or on chemistry either from the gas phase, for example (metal organic) chemical vapor deposition (MOCVD/CVD), or from the liquid phase (chemical solution deposition (CSD) [9]). Common to all these chemical methods is the use of metal(lo) organic compounds as precursors, which are typically decomposed by thermal treatment to form the corresponding amorphous complex metal oxides. A heat treatment at higher temperatures leads to the desired crystalline material by a nucleation and growth driven process. Among the chemical methods, CSD offers a number of advantages, such as high flexibility with regard to composition (stoichiometry and possible doping) and coating technique. Compared to gas-phase methods it is cheap regarding operation and technical equipment and therefore ideally suited for research and development as well as applications where no conformal step coverage of ultra-small trenched structures is required. Thus in this chapter predominantly wet chemical preparation methods with a focus on the various non-invasive procedures often combined with true bottom-up steps are discussed. The reported approaches will be limited to those that yield ferroic nanostructures on suitable substrates. Sometimes wet chemical techniques combined with vapor-based deposition techniques are the method of choice.

5.2 Short Survey on Classical Top-Down Approaches

It is self-evident that the first attempts to prepare sub-1 μm ferroelectric capacitors and in the further course of the research sub-100 nm lateral-sized capacitors relied on top-down approaches known from the semiconductor industry. Reactive ion etching (RIE) processes are largely used since they provide anisotropic etch profiles and relatively high etch selectivity as well [10]. Typically these processes involve both physical processes, such as ion bombardment for directional etching, and chemical processes through the use of highly reactive chemicals to form volatile etching byproducts. Based on (e-beam) lithography and dry etching or mask-free FIB milling, these techniques enabled lateral capacitor stack dimensions down to approximately 70 nm (Figure 5.1). In any case the high energy impact between the

---

[1] Typical capacitor structure used for ferroic capacitors with M = Pt. Often one or both metals forming the electrodes are replaced by an oxide conductor such as IrO_2, $SrRuO_3$, etc., to improve fatigue properties.

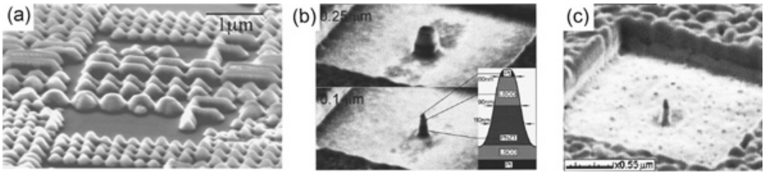

Figure 5.1 (a) Scanning electron and (b, c) scanning ion beam images of lead zirconate titanate (PZT) and niobium doped PZT (PNZT) nanostructures prepared by top-down approaches. (a) RIE-derived mesoscopic $Pb(Zr_{0.4}Ti_{0.6})O_3$ (PZT40/60) patterns in the range from 100 nm to 1 μm of lateral size. Reprinted with permission from [11]. Copyright [2002], AIP Publishing LLC. (b) Examples of FIB milled capacitor test structures of different sizes (0.25 μm × 0.25 μm and 0.1 μm × 0.1 μm). The inset shows the cross-section of the capacitor stack consisting of PNZT sandwiched between oxide LSCO/Pt electrodes. Reprinted with permission from [12]. Copyright [1999], AIP Publishing LLC. (c) Micrograph of the smallest capacitor structure prepared by FIB with dimension of 70 nm × 70 nm. Reprinted with permission from [13]. Copyright [1999], AIP Publishing LLC

Ga^+ beam and the milled specimen involved with FIB has to be taken into account. A lot of damage in the region that is directly milled can be produced, but also damaging of side walls can occur.

Bühlmann et al. used a combination of e-beam lithography and lift-off processing to deposit a patterned chromium layer as a hard mask on top of an epitaxial $Pb(Zr_{0.40}Ti_{0.60})O_3$/Nb-doped $SrTiO_3$ (100) (PZT40/60/STO:Nb) stack [11]. Reactive radio frequency magnetron sputtering has been used here to deposit the 200 nm thick epitaxial PZT film. The pattern was then transferred into mesoscopic PZT grains in the range of 1 μm down to 100 nm by RIE. Rounded PZT grains (Figure 5.1(a)) resulted from the dry etching process due to a continuous reduction of the thinner border of the Cr mask. However, it was impossible to prepare sub-100 nm grains. Damage caused by the dry etching step could be recovered by postannealing or wet cleaning [14, 15]. Nevertheless, the extent of recovery has not been quantified in any of these post-treatments. However, piezoelectric activity of the as-deposited and patterned films could be proven by means of piezoelectric sensitive atomic force microscopy (AFM) in the contact mode [16–19].

Ferroelectric nanocapacitors with lateral dimensions between 70 and 100 nm (Figure 5.1(b) and (c)) have been manufactured by FIB milling of heterostructures such as MFeM with M(BE)[2] = Pt, $(La,Sr)CoO_3$, FE = $Pb((Nb)Zr,Ti)O_3$ (P(N)ZT), $SrBi_2Ta_2O_9$ (SBT), and M(TE)[3] = $(La,Sr)CoO_3$, Pt [12, 13, 20], in which the polycrystalline PNZT thin films of the composition $Pb_{1.0}(Nb_{0.04}Zr_{0.28}Ti_{0.68})O_3$ and SBT were deposited by CSD processing onto the M(BE) stack. In this mask-less patterning technique a 10 nm Ga^+ ion spot is used to pattern the area by "cutting out" the structures. However, slow processing, restriction to small sample areas, and implantation of Ga^+ ions into the structures are the drawbacks of FIB. Removal of the latter effect is possible by an annealing step under oxygen. It should be noted that although it has been possible to fabricate 70 nm size capacitors, due to a problem of Pt lift-off during annealing none of them could be electrically measured [13].

---

[2] M(BE) = bottom electrode (typically on $TiO_x/SiO_2/Si$ wafers)

[3] M(TE) = top electrode

5.3 Non-invasive Procedures

In order to avoid damages of the fabricated nanostructures by the patterning technique great efforts have been undertaken to develop non-invasive methods, in which the crystalline nanoscopic ferroelectrics grow from the bottom up. It should be noted that, strictly speaking, the term "bottom-up approach" usually denotes techniques that rely on the physical–chemical principles of molecular/atomic self-assembly. In this section, however, all methods where the final functional nanoscopic ferroelectric material is crystallized unaffected from the applied patterning method are classified as the bottom-up approach. Hence the methods reviewed here include e-beam direct writing (EBDW), e-beam lithography mediated patterning, self-patterning, true self-assembly and SA-assisted approaches, template controlled growth, and dip-pen nanolithography (DPN).

EBDW, which was earlier used for the patterned deposition of metals such as gold [21] or palladium [22], was introduced to patterned metal oxide and ferroelectric oxide processing as one of the first non-destructive methods [23, 24]. It is based on the deposition of a suitable CSD precursor solution, which is often of metallo-organic decomposition (MOD)-type, onto a substrate by, for example, spin coating followed by a drying step at moderate temperatures (~40–100 °C). The thus-formed (physical[4]) gel is locally exposed to an electron beam of, for example 3 nm in diameter, rendering the exposed area insoluble in an organic solvent. Subsequently, the pattern is developed by removal of the unexposed areas with a proper solvent such as toluene or xylene. Finally, the patterned nanostructures are pyrolyzed and annealed to crystallize the metal oxide and ferroelectric oxide, respectively. By this technique Alexe et al. prepared arrays of typically polycrystalline SBT and PZT grains below 100 nm [8, 25, 26] (Figure 5.2). While in the case of binary oxides such as Al_2O_3 even lines down to 20 nm width have been prepared [23], the smallest lateral sizes of ferroelectric oxides fabricated by this method are approximately 75 nm [26].

Later the combination of an e-beam lithography (EBL) structured soft template and CSD processing has been used to prepare arbitrary arranged ferroelectric nanopillars [27] and nanotubes [28]. In this approach the e-beam was used to pattern a spin-coated polymeric e-beam resist which can be either directly used as the template [27] or after a subsequent atomic layer deposition of a sub-10 nm thin Al_2O_3 layer onto the resulting formed soft template [28]. The latter leads to mechanical consolidation and prevents chemical reactions between the polymeric template and the subsequently applied precursor solution of the functional material. A sol–gel type $PbZr_{0.52}Ti_{0.48}O_3$ (PZT52/48) precursor solution was infiltrated into this polymeric template under reduced pressure, yielding ferroelectric PZT nanotubes (Figure 5.3) after a two-step thermal processing (pyrolysis at 300 °C and

---

[4] Contrary to chemical gels, which are typically formed in true sol–gel processes by a chemical inorganic polymerization leading to three-dimensional metal–oxygen–metal networks, physical gels have no chemical bonds and can be redissolved in suitable solvents, such as toluene, xylene, etc.

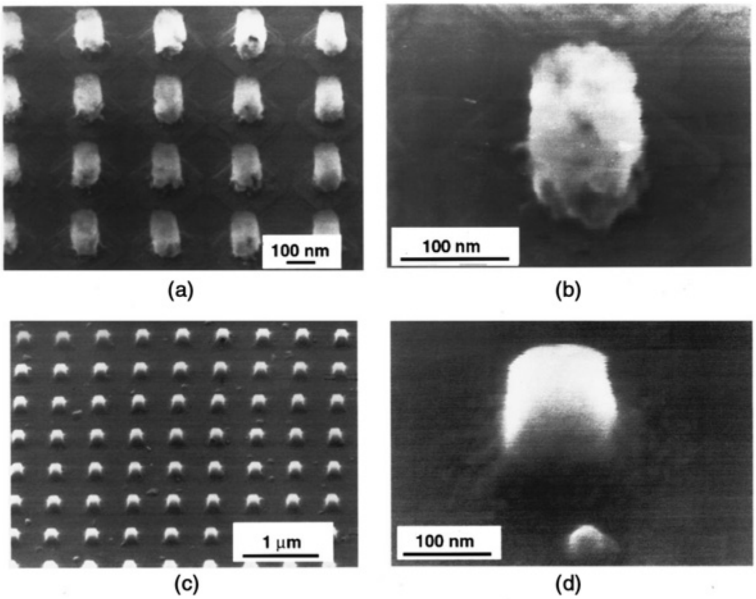

Figure 5.2 SEMs showing (a) an SBT cell array on an $SrTiO_3$:Nb substrate after crystallization annealing at 800 °C, (b) one 100 nm SBT cell, (c) a PZT cell array after crystallization annealing at 650 °C, and (d) a 100 nm PZT cell. Reprinted with permission from [8]. Copyright [1999], AIP Publishing LLC

crystallization in a ramp from 600 to 800 °C). During the high-temperature processing step PZT crystallization and decomposition of the organic soft template simultaneously took place. The remaining thin Al_2O_3 layer connects the build adjacent PZT nanotubes. Generally the height and width of the EBL structured resist determines the aspect ratio of the generated PZT nanostructures. Thus by varying the rotation speed during the spin-on process

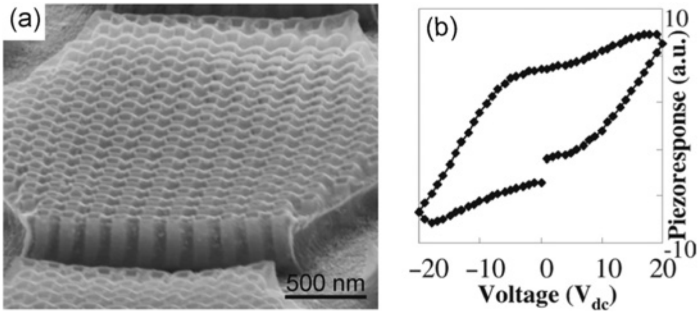

Figure 5.3 Ferroelectric nanostructures processed via soft-template infiltration. (a) Scanning electron microscopic (SEM) image showing 100 nm wide PZT nanotubes with an aspect ratio of 5:1; (b) piezoresponse measurement for a single PZT nanotube of this array (arbitrary units). Reprinted with kind permission from [28], Copyright © 2012 Wiley-VCH Verlag GmbH & Co. KGaA, Weinheim

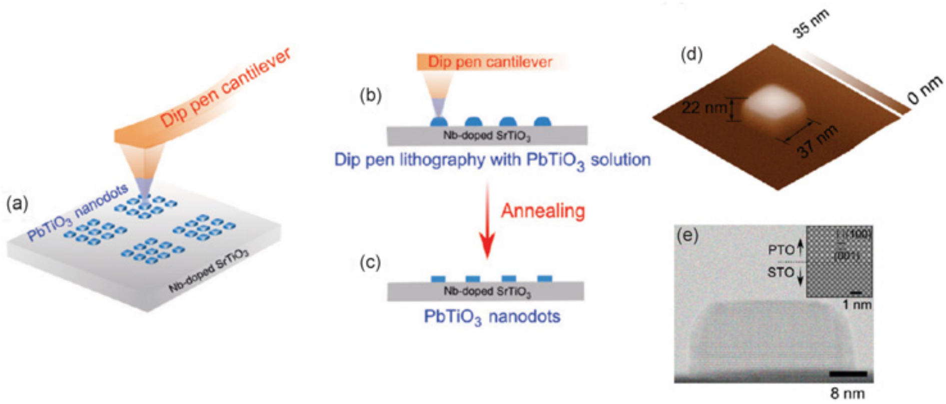

Figure 5.4 *Schematic illustrations of DPN of ferroelectric PTO nanodots and images of the smallest PTO dots produced by this method. (a) Patterns of PTO nanodots formed by DPN; (b) deposition of a nanopattern from a PTO precursor solution on the surface of STO:Nb by DPN; (c) transformation of the as-deposited PTO–sol nanodots to the well-crystallized PTO nanopattern by annealing; (d) three-dimensional AFM image of a minimum-sized PTO nanodot with a lateral dimension of 37 nm and a height of 22 nm; (e) high-resolution transmission electron microscopy (HRTEM) image of such a PTO nanograin. Reprinted with permission from [30], Copyright (2009) American Chemical Society*

of the e-beam resist the polymer template thickness and hence the height of the PZT nanotubes could be altered. Aspect ratios from 1.2:1 up to 5:1 have been demonstrated so far. In order to prove crystallinity and the ferroelectric nature of the fabricated nanostructures [28] micro-Raman spectroscopy and piezoresponse force microscopy (PFM) techniques were applied. It was concluded that this approach can be tailored for a variety of ceramic materials by appropriate choice of the CSD processing conditions (precursors and annealing temperatures) [28].

Dip-pen nanolithography (DPN) is another rather serial writing technique that may be one of the feasible solutions for the fabrication of position-controlled ferroelectric nanostructures. It has been originally developed by the group of Mirkin [29] for the patterning of 1-octadecanethiol polymers and later adapted to the requirements of $PbTiO_3$ (PTO) precursor solutions [30], which are typically used in CSD processing. In contrast to the routine originally developed for polymers, in this study a sequential drying and annealing process for the fabrication of ferroelectric PTO nanodots has been applied. The required PTO precursor solution was modified with a low-viscosity alcohol. At first PTO precursor sol nanodots were deposited with the AFM tip on a STO:Nb substrate (Figure 5.4(b)). The as-deposited PTO nanodot arrays (cf. Figure 5.4(a)) were slowly dried for a week at room temperature and finally rapid thermally annealed under an oxygen atmosphere at 650 °C to yield the corresponding array of crystalline perovskite PTO nanodots (Figure 5.4(c)). By a suitable adjustment of the dip-pen deposition time the size of the nanodots can be controlled. The smallest PTO nanodots were square shaped with a lateral dimension of 37 nm and a thickness of ~22 nm (Figure 5.4(d) and (e)) corresponding to a maximum storage density of ~0.5 Tbit in^{-2} for FeRAM applications. Electric force microscopy (EFM) and PFM were applied to prove the ferroelectric behavior of the PTO nanograins.

5.3.1 Nanomask Techniques

The major drawback of the sequential patterning techniques such as EBL and DPN is their slow processing speed, which makes them less suitable for potential mass production. A promising approach in this respect is *nanoimprint lithography* (NIL), which came up as a fast, low-cost technique for the fabrication of nanostructures in polymer films such as polymethylmethacrylate (PMMA) with structure sizes well below the limit of traditional lithography methods [31–33]. In this technique a suitable mold with the desired nanostructures on its surface is pressed into a thin polymer resist, which has been deposited before by, for example, spin coating. The removal of the mold yields the patterned resist in the form of a thickness contrast pattern. Anisotropic etching is typically used to remove residual resist in the compressed areas in order to transfer the pattern to the entire resist. Harnagea et al. have adapted NIL to CSD-derived PZT precursor gel films to generate ferroelectric PZT cells down to ~300 nm [34]. In this approach the deposited chemical or physical gel layer is patterned by imprinting a SiO_2–Si mold into the film at a typical pressure of 1 kbar. After this process the imprinted gel layers are pyrolized and subsequently crystallized at 650 °C in air. Finally, the ferroelectric nature of the fabricated PZT nanostructures was probed by PFM. Hitherto lateral ferroelectric nanostructures in the range of 20 nm, as demonstrated for polymers, have not been obtained in this way. However, as concluded by Bernal et al. [28], the creation and use of the soft templates mentioned above by NIL with the subsequent impregnation with a PZT precursor solution, etc., may enable larger patterned areas of ferroelectric nanostructures or more precisely nanotubes down to ~100 nm.

In addition, different types of "nano shadow mask" techniques have been proposed that have some specific advantages, such as fabrication of relatively large-area arrays of nanoscale structures. In this sense a technique called "gold nanotube-membrane lithography" [35, 36] was realized by at first covering a perfectly ordered nanoporous anodic aluminum oxide (AAO) [37] with a thin gold plating base by sputtering (Figure 5.5(a)). This thin gold layer on the top part of the inner nanochannel surface as well as on the top surface of the AAO template was subsequently thickened by electrochemical deposition of Au from an electrolyte. By wet-chemical etching with phosphoric acid the alumina was removed and the resulting gold nanotube membrane remained floating on the surface of the etching solution. After neutralization the membranes with sizes of 2×2 mm^2 to 10×10 mm^2 could easily be transferred to the desired substrate ($SrRuO_3/SrTiO_3$ or Nb-doped $SrTiO_3$). Large arrays of hexagonally ordered $Pb(Zr_{0.4},Ti_{0.6})O_3$ [35] or $(Bi,La)_4Ti_3O_{12}$ (BLT) [36] ferroelectric nanodots with lateral sizes of about 150 nm have been fabricated by PLD of these materials through this gold nanotube shadow mask (Figure 5.5(b)). In a subsequently developed optimized variant ultra-thin, self-ordered AAO membranes have been prepared and used as a high-temperature stable stencil for PLD prepared epitaxial PZT20/80 nanocapacitors on Pt(200)/MgO(200) substrates [38].

Furthermore, the so-called "natural lithography" [39] or "nanosphere lithography" [40] – a combination of self-assembly and vapor deposition of the ferroelectric material – was applied for the first time by Ma et al. to fabricate oxide ferroelectric nanostructures [41]. Here the triangular interstices of well-ordered hexagonally close-packed monolayers of monodisperse latex spheres (1 or 0.5 μm in size) serve as a deposition mask for pulsed laser deposition (PLD) of $BaTiO_3$ (BTO) or SBT [42] at room temperature. The required masks (Figure 5.6(a)) were created by spin-coating and self-assembly of commercial

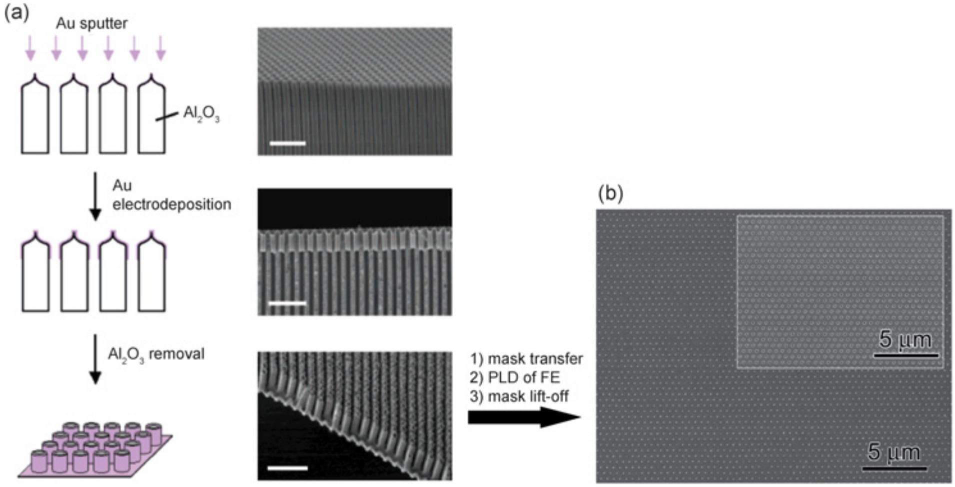

Figure 5.5 *(a) Process flow of the fabrication procedure of the free-standing gold nanotube membrane with corresponding SEM images at the right side showing the different intermediate states of the process (scale bar: 2 μm). The gold nanotube mask, obtained after detaching the membrane by wet chemical etching from the alumina pore structure, is subsequently transferred to the desired substrate. After PLD of the ferroelectric (FE) material followed by the mask lift-off, a high-temperature annealing step leads to crystalline ferroelectric nanostructures. Reprinted with permission from [35], Copyright (2005) American Chemical Society. (b) SEM plan-view image of an as-deposited BLT nanostructure array on an* $SrRuO_3$ *(SRO) electrode covered STO single-crystal substrate. The inset shows a top view SEM image of part of the gold nanotube mask used for patterning. Reprinted with permission from [36]. Copyright [2005], AIP Publishing LLC*

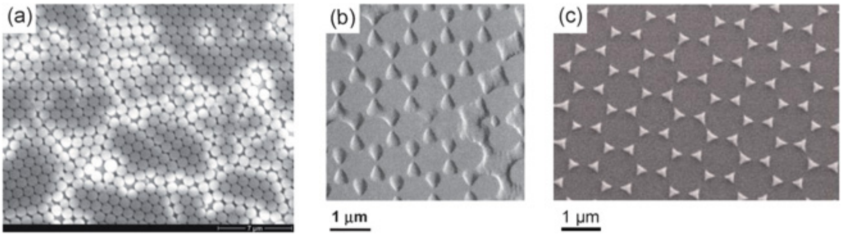

Figure 5.6 *(a) Top view of an SEM image of a self-assembled, hexagonally close-packed monolayer of polystyrene latex spheres of 1 μm diameter (scale bar: 7 μm). Reprinted from [44], Figure 10, © 2006 Springer Science + Business Media, Inc. with kind permission of Springer Science and Business Media. (b) Contact mode AFM image (deflection image) of the resulting well-ordered PLD-derived BTO nanostructures after annealing. Reprinted with permission from [41]. Copyright [2003], AIP Publishing LLC. (c) Top view of an SEM image of an SBT array fabricated from the self-assembled monolayer of latex spheres. Reprinted from [44], Figure 11a, © 2006 Springer Science + Business Media, Inc. with kind permission of Springer Science and Business Media*

dispersed polystyrene latex spheres. After the PLD process the polystyrene latex mask was lifted off in methylene chloride and the as-deposited nanostructures, for example BTO (Figure 5.6(b)), were finally crystallized at 650 or 950 °C (SBT, Figure 5.6(c)) in air. Although for metals lateral dimensions down to approximately 35 nm have been demonstrated, the smallest ferroelectric grain produced by this method had a diameter of 160 nm [43].

5.3.2 Direct Self-Assembly of Ferroelectric Nanostructures

Self-assembly principles can not only be used to enable nanolithographic steps, as shown above, but also to directly obtain a local self-patterning. Such self-assembly[5] approaches often use the microstructural instability observed by Seifert et al. for the epitaxial growth relationship between ultra-thin PTO films and $SrTiO_3$ (STO) single crystalline substrates. It leads to the formation of single-crystal islands instead of continuous films [45]. The usually undesirable process was adapted to semiconductor substrates with bottom electrodes in a tailored way to generate separated three-dimensional nanograins by Waser et al. [46] as one of the first methods to grow ferroelectric nanograins with sub-100 nm lateral dimensions without the destructive influence of the patterning method. Highly diluted PTO precursor solutions were deposited onto $Pt(111)/TiO_2/SiO_2/Si$ substrates, subsequently pyrolized, and finally crystallized. By control of the CSD conditions, that is the concentration of the initial PTO coating solution, different grain sizes and grain size distributions, ranging from 200 nm to about 10 nm, were obtained at typical crystallization temperatures of 700 °C (Figure 5.7).

A detailed AFM study on the grain height as a function of the grain diameter revealed that: (i) with increasing precursor dilution the maximum grain height decreases from 18 to 10 nm, (ii) for grains between a diameter of 10 to 30 nm this correlation is almost linear and independent of the dilution of the precursor solution, and (iii) an extrapolation of the size leads to a critical nucleus size of about 10 nm [47]. All nuclei formed during crystallization that are smaller than 10 nm are not stable and will coalesce with larger neighboring grains. This diameter apparently marks the lower limit for this CSD method.

Compared with the deposition on single crystalline STO substrates, the grain boundaries of the Pt layer reduce the nucleation energy and act as a preferential nucleation site for perovskite structures, thus lowering the necessary temperature. Consequently the temperatures for the formation of single-crystal PZT ferroelectric nanostructures with lateral sizes of 40–90 nm on conducting STO:Nb model substrates were significantly higher (800–1100 °C) [48]. Epitaxial growth of these ferroelectric nanostructures was proven by X-ray diffraction (XRD) and TEM investigations.

A similar approach involves using MOCVD and terminating the deposition before dense films are formed. Following this idea, Fujisawa and co-workers studied the nucleation and growth behavior of PZT grains on platinized (111) silicon substrates [49, 50]. They found triangular-shaped single crystalline PZT islands, which points to a (111) orientation. Their typical dimensions were between 80 and 100 nm width and 20 and 30 nm height. However, grains with 1.7 nm height and 38 nm width are also reported to have shown ferroelectricity [51].

---

[5] Terms like *self-assembly* or *self-patterning* are typically used to express local structural ordering (assembly) or long-range ordering (patterning). To express similar mechanisms with weaker coupling they are also used for ferroelectrics here.

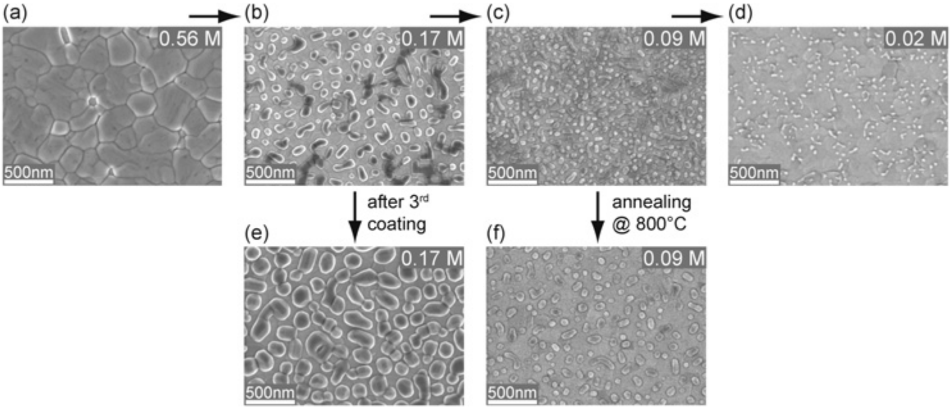

Figure 5.7 *Top view of SEM images of self-assembled PTO nanograins on Pt/*TiO_2*/*SiO_2*/Si substrates prepared by CSD with different processing conditions. (a) Almost dense PTO film after a single coating and annealing step of a PTO precursor solution with standard concentration. (b) to (d) Effect of lowering the coating solution concentrations (indicated in the figures) after a single coating and annealing step (700 °C). Greater dilution results in smaller and fewer grains. A closer look to the SEM image (d) reveals that the PTO islands preferentially nucleate at grain boundaries of the underlying platinum electrode. (e) Result of two additional coating and annealing steps on the already deposited and crystallized grains. (f) Effect of a higher annealing temperature (800 °C) step*

The mechanism of this kind of CSD-based PZT nanoisland formation on single crystalline substrates such as STO or STO:Nb was investigated and compared to the formation of Ge islands on Si by Dawber et al. [52]. The experimentally determined volume distributions of domes and superdomes could be fitted with the distribution function of Williams and co-workers [53, 54]:

$$\ln[\omega_X(V)] = -\left(B_X V^{2/3} + A_X V^{1/3} + \frac{B_X^2}{4A_X} V \right) \tag{5.1}$$

indicating that the mechanism of substrate-mediated strain is similar to analogous semiconductor systems. In Equation (5.1) ω_X is the frequency of a crystal of species X with a particular volume V, B_X is the facet energy, and A_X is the edge energy parameter. At a crystallization temperature of 800 °C a transition from superdomes to domes has been observed if the thickness of the initially deposited amorphous PZT layer decreased. In contrast to the expectations based on the Ge on Si systems at higher temperatures (1100 °C) the superdomes become dominant again in the case of the thinnest as-deposited PZT films. It is assumed that this is due to an easier generation of dislocations at these temperatures, which favours the formation of superdomes as they contain multiple dislocations.

Hydrothermal methods can also be used to prepare ferroelectric nanocrystals in a self-assembly way [55]. In this method strongly alkaline solutions of lead nitrate $Pb(NO_3)_2$ and anatase TiO_2 were reacted under moderate temperatures (130–180°C) in a teflon bomb in the presence of a single crystalline substrate (STO and $LaAlO_3$ (LAO)) to form separated PTO nanoislands on top of the substrate. However, it should be noted that the strong alkaline reaction environment is not suitable for the typically used silicon substrates and possibly remaining hydroxyl groups in the nanoscaled ferroelectric material may also cause problems.

CSD or, in some cases, more precisely spoken chemical solution based methods have also been used to generate one- and three-dimensional ferroelectric nanostructures, such as $BaTiO_3$ (BTO) nanorods [56,57], PZT, BTO, and SBT nanotubes [58], and BTO nanoparticles [59–62]. The synthesis of BTO and STO nanorods has been accomplished by solution-phase decomposition of bimetallic alkoxide precursors such as $BaTi[OCH(CH_3)_2]_6$ and $SrTi[OCH(CH_3)_2]_6$ in the presence of coordinating ligands [56, 57] at 280 °C. This reaction yields well-isolated nanowires with diameters ranging from 5 to 70 nm and lengths varying from a few hundred nanometers up to tens of micrometers. Ferroelectric nanotubes were obtained either by dip-coating of porous alumina [63] and silica matrices with suitable precursor solutions [64] or by liquid source misted chemical deposition into porous, photonic Si crystals [65].

Mixed barium/titanium alkoxides, for example $BaTi[OCH(CH_3)_2]_6$ mentioned above, can also be used to fabricate nanocrystalline ferroelectric particles [59–62] by microemulsion mediated syntheses. These microemulsions are based on water droplets of inverse micelles in oil, thus forming a “nanoreactor” for ideally stoichiometric sol–gel type hydrolysis and polycondensation reactions of the highly reactive bimetallic alkoxide precursors. Due to the confinement of the reaction space and if optimum reaction conditions are fulfilled, the final product consists of monodisperse nanosize particles. Consequently, the droplet size, which in turn can be tailored by the length of the hydrophilic part of the surfactant, determines the size of the resulting crystallites. This method was used to prepare BTO nanoparticles and to tune their crystallite size in the range of 6–17 nm by employing different microemulsions prepared with various surfactants [60].

By using a microemulsion route consisting of cyclohexane as the oil phase, Brij 30 (polyoxyethylene(4) lauryl ether) as the surfactant, and barium titanium ethylhexano-isopropoxide as the bimetallic precursor, BTO nanoparticles dispersed in a solvent have been prepared. The resulting dispersions have been deposited onto single crystalline STO:Nb substrates to form randomly distributed BTO grains of 50–60 nm in diameter [59]. However, no data of the ferroelectric properties of these self-assembled BTO nanograins (Figure 5.8(a)) were given.

By adding the same type of microemulsion (i.e. surfactant Brij 30, cyclohexane, and water) to a diol-based PTO precursor the corresponding PTO precursor dispersion has been prepared [66,67]. After homogenization in an ultra-sonicator the formed transparent sol has been deposited onto single crystalline STO substrates by spin-coating, dried at ~30 °C for 7 d and finally RTA crystallized at 650 °C. The analysis of the coated STO surface revealed that the particles have an average size of ~ 40 nm and have a periodical order in some regions (Figure 5.8(b)). Local piezoelectric activity could be demonstrated by a PFM analysis of the fabricated nanostructures. It is interesting to note that in both studies the particle size in the dispersion prior to the coating step has not been given and that the hexagonal pattern of the nanograins that could be expected from such a micelle-assisted approach [68] was not observed. The reason is not yet completely clear. While Bhattacharyya et al. [59] state that the size of the particles were still too big for self-assembly since the crystal field would need a size below 10 nm to lock the nanodots at some preferred sites, Torres

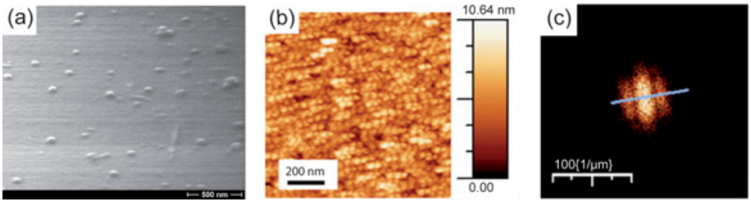

Figure 5.8 *(a) SEM image of STO:Nb substrate surface after coating with the ultra-sonicated microemulsion after coating and annealing. It was observed that there was a distribution in the size of these BTO particles with an average size in the range of 50–60 nm. From [59], with permission. © 2003 Materials Research Society. (b) Topography image obtained by scanning force microscopy (SFM), showing nanosized and uniform PTO particles with a periodic order. (c) Two-dimensional fast Fourier transform of the image (b) where a short range one-dimensional periodicity is detected. $PbTiO_3$ particles placed along parallel lines. From [66]. © IOP Publishing. Reproduced by permission of IOP Publishing. All rights reserved*

et al. [67] postulate that the rather short-range periodical arrangement may be related to the thickness of the coating layer and to wetting issues.

Block copolymers and di-block copolymers, respectively, can also form micelles and are thus basically suitable for self-assembly approaches [69]. The used copolymers consist of two chemically different macromolecular chain segments that do not mix, but form microdomains. The size and mesomorphic order of these so-called A–B diblock copolymers largely depend on the length of the blocks and their molecular weight distribution [70–72]. Typical periodicities are in the range of 10 ± 200 nm. In thin films, the domain structure is affected by the interfacial energies and the geometrical constraints introduced by the flat interfaces [73–76].

Kim et al. [77] incorporated PTO precursor molecules into polystyrene-block-poly(4-vinylpridine) (PS-b-P4VP) copolymer micelles and used them for the direct SA-modulated deposition of PTO nanograins. The stable incorporation of the PTO precursor is based on the selective coordination of the metal cations (Pb^{2+} and Ti^{4+}) at the polar pyridine moiety inside the core of the P4VP block. Chemically this incorporation has been accomplished by a solvent change-driven micelle inversion from the initially PS block core, which is formed inside the (polar) 2-methoxyethanol-based PTO precursor solution, to a P4VP core by careful addition of a toluene/tetrahydrofurane mixture [77]. By spin-coating of such PTO precursor-loaded PS-b-P4VP micelle solutions with suitable concentrations onto STO:Nb substrates, monolayers of laterally well-ordered epitaxial PTO nanograins have been obtained after thermal annealing (Figure 5.9). The nanoislands possess a lateral dimension of 22 nm and a height of 7 nm and exhibit a distinct piezoresponse, which confirms the existence of ferroelectricity at this size. It is expected that ferroelectric nanoislands with smaller volumes could also be prepared easily by tuning the molecular weight of the PS-b-P4VP macromolecules [77].

More recently another block copolymer approach takes advantage of the noticeable chemical difference between PS and PEO to allow selective metal ion inclusion by the coordinating properties of the polar block. It was originally developed for hexagonal superparamagnetic iron oxide (FeO_x) nanodots [78] and has been transferred to the fabrication of ferroelectric $PbZr_{0.30}Ti_{0.70}O_3$ (PZT30/70) nanograins [79]. Though in

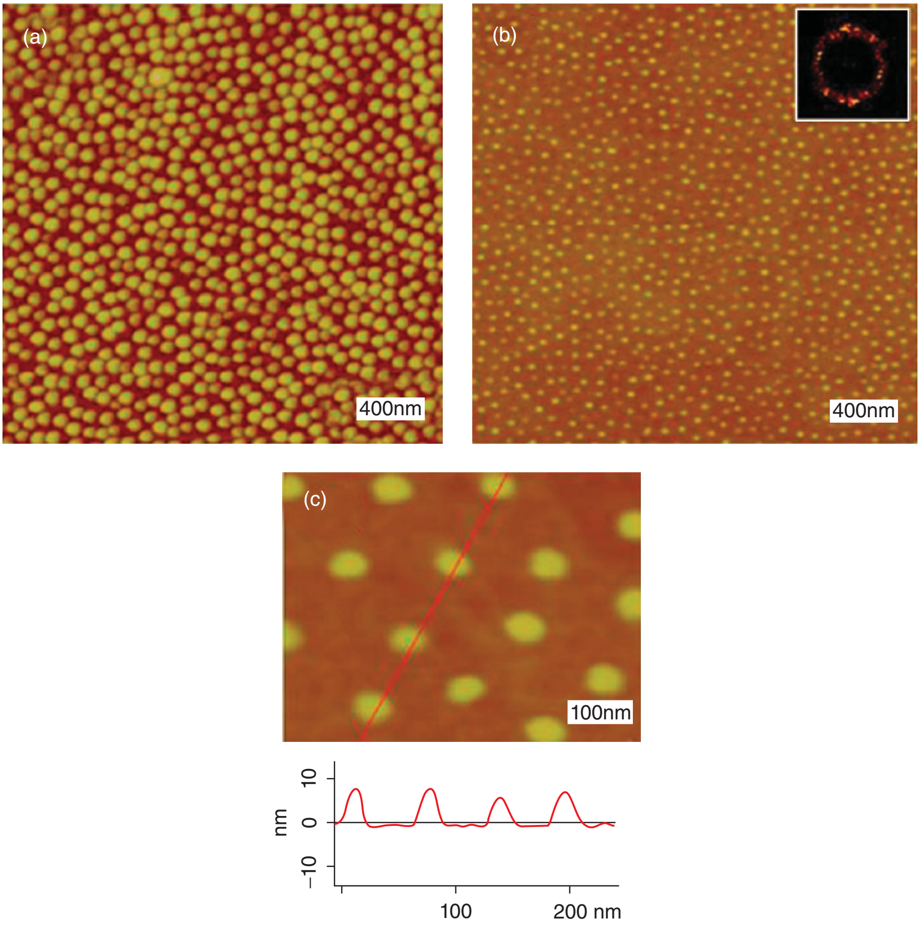

Figure 5.9 *AFM topography images of the array of (a) precursor-loaded micelles and (b) the PTO nanoislands after crystallization. Inset shows fast Fourier transform of the image. (c) Enlarged image of part of (b) and the AFM height profile along the red line. Reprinted with permission from [77], Copyright (2010) American Chemical Society*

contrast to the method mentioned above no preformed metal-loaded block copolymer micelles have been used here for the self-assembly process, using self-assembled thin-film templates of polystyrene-block-polyethylene oxide (PS-b-PEO) block copolymers instead (Figure 5.10(a)), which are subsequently loaded with metal cations such as Fe^{3+} (FeO_x) or Pb^{2+}, Zr^{4+}, Ti^{4+} (PZT). The required highly ordered SA template is generated by solvent annealing [80, 81] in a mixed toluene/water environment of the spin-coated as-deposited polymer film followed by ethanol treatment at 40 °C for 15 h. Based on the copolymer microphase separation, cylindrical microdomains result (one block hexagonally arranged in a matrix of the other block). After spin-coating of the low concentrated PZT precursor solution the lone pairs of the oxygen atoms in the polar PEO block cylinders selectively coordinate the metal cations. A subsequent UV/ozone treatment was used to oxidize the

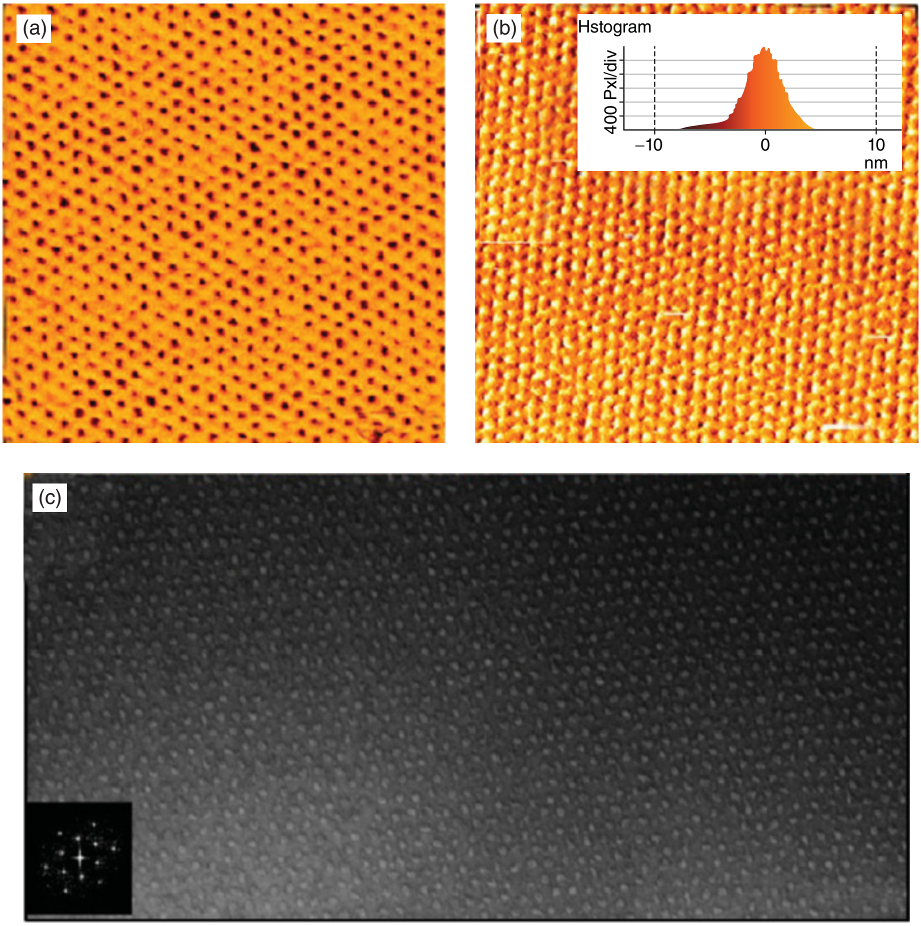

Figure 5.10 *AFM topography image of: (a) a PS-b-PEO (32-11) self-assembled thin film formed on an n-doped Si substrate and (b) arrays of PZT nanodots formed using a PS-b-PEO (32-11) thin film (inset shows the histogram of the nanodot size). (c) Plan-view SEM image of an array of PZT nanodots formed from a PS-b-PEO (32-11) template; the FFT pattern in the inset shows the hexagonal ordering of the nanodots. (Scale bars, 200 nm). Reprinted with permission from [79], Copyright (2013) American Chemical Society*

metallo-organic precursor and remove the polymer template. Crystalline PZT nanograins with a lateral width of 20 nm and a height of 10 nm, and a coverage density of $\sim 68 \times 10^9$ cm^{-2} were obtained by a final annealing step at 600 °C (Figure 5.10(b) and (c)). By XRD, X-ray photoelectron spectroscopy, and PFM, crystallinity and ferroelectricity in these PZT nanodot arrays were proven.

5.3.3 Nanoseeds Assisted Growth

Although these self-assembly and self-patterning methods have the advantage of being non-invasive, one major drawback remains as the position on the substrate, that is registration,

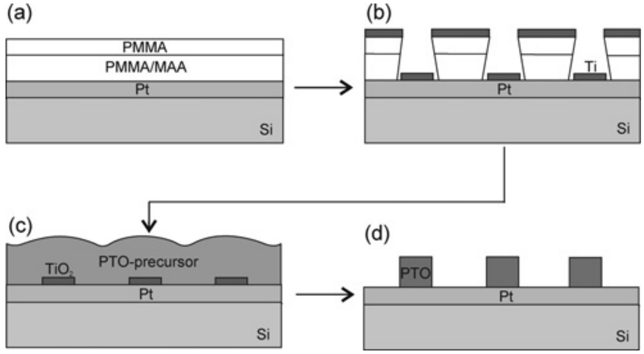

Figure 5.11 *Schematic process flow of PTO nanostructure fabrication by a TiO_2 nanoseed template pattern. (a) A two-layer resist system is spin-coated onto the platinized substrate; (b) the resist is exposed by e-beam, developed and covered by a thin Ti layer by evaporation; (c) lift-off in N-methyl pyrollidone, followed by an oxidation anneal to form the TiO_2 seeds and spin-coating of a PTO–precursor solution onto the preannealed TiO_2 structures; (d) the precursor film is pyrolized and crystallized. Reprinted from [3], Figure 4, © Springer-Verlag 2005. With kind permission of Springer Science and Business Media*

and size distribution of the deposited nanograins is governed by thermodynamics and therefore randomized. Based on the fact that ultra-thin TiO_2 seed layers promote the nucleation and growth of (111) textured PZT films on (111) oriented platinized substrates [82], a template technique to gain control on the arrangement of perovskite structures in the nanoscale regime has been proposed [83]. The concept consisted of the preparation of predefined nano-sized TiO_2 patterns on a suitable bottom electrode such as Pt to act as seeds for the subsequent deposition of ferroelectric PTO or PZT. The basic impact of this nanoseed approach was soon after confirmed by two groups [84, 85]. In the first attempt sputter-deposited PZT40/60 grains were grown onto 150 nm wide TiO_2 dot structures that were patterned by lift-off of a Cr hard mask followed by a reactive ion etching step [84].

Clemens et al. presented a different technique leading to even smaller templates of TiO_2 dots and lines (diameter 30–100 nm) based on electron beam lithography and lift-off processing, as illustrated in Figure 5.11 [85]. This specific lift-off relies on a two-layer e-beam resist system consisting of a polymethylmethacrylate (PMMA) top and a polymethylmethacrylate/methacrylic acid (PMMA/MAA) bottom layer. PMMA is used for nanostructure fabrication due to its very high resolution among conventional electron beam resists, while PMMA/MAA is higher in sensitivity. Consequently the combination of both in a two-layer resist system leads to undercut resist profiles after exposure and development.

A 2 nm thick titanium layer was evaporated on top of the structured resist employing an electron beam evaporation tool since sputtering the titanium layer provided a high step coverage of the resist structures and therefore was inapplicable for lift-off processing. Finally, lift-off was fulfilled in *N*-methyl-2-pyrollidone (NMP). Although it is obvious that the initially deposited titanium layer converts into titanium oxide (TiO_x) due to contact with oxygen from the environment, a subsequent oxygen annealing was performed to ensure the complete oxidation into TiO_2. The smallest TiO_2 lines had a line width and edge-to-edge

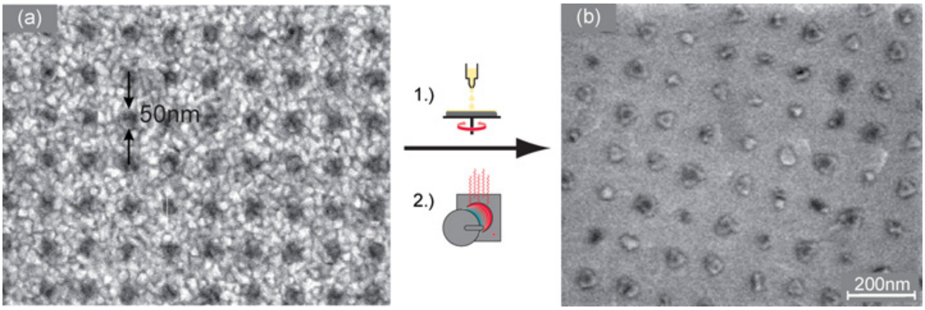

Figure 5.12 *(a) SEM images of the TiO_2 template and (b) the resulting ferroelectric PTO nanograins. The seed structures appear as round shadows on the bright platinum substrate. The dots are 50 nm in diameter and have a distance of 75 nm. After the CSD process of a 0.032 M PTO precursor solution mainly triangular-shaped PTO grains were formed. The separation distance is preserved. Reprinted from [3], Figure 5, © Springer-Verlag 2005. With kind permission of Springer Science and Business Media*

distance of 50 nm, respectively, and the smallest dots that were fabricated reproducibly were 30 nm in diameter and had a distance of 75 nm. By CSD processing of the PTO precursor solution PTO grains down to lateral dimensions of 50 nm and a separation distance of 75 nm were grown onto the 50 nm wide nucleation sites, where nucleation of the PTO grains almost exclusively took place on the TiO_2 nanoseed structures (Figure 5.12). Most of the nanograins were triangular shaped, which points to a (111) orientation in agreement with the literature.

Since it is known [86] that Pb cations can easily and fast diffuse under the given annealing conditions (700 °C under oxygen) it is apparent that these ultra-thin TiO_2 seeds are incorporated into the perovskite structures during the crystallization process. This is also reasonable since the precursor solution contains a lead excess of typically 15%, which helps to adjust the stoichiometry of the final $PbTiO_3$ nanograins. However, in this study only 80% of the nanograins exhibited a piezoresponse [85]. The origin is not yet fully clear. Probably not all the nanograins or not the complete nanograins, respectively, have a perfect perovskite structure. This can be due to PbO deficiency, which might be caused by a non-sufficient lead excess in the initial precursor solution or by segregation effects caused by the above-mentioned easy migration of lead ions leading to Pb-rich and Ti-rich regions [86].

Although the e-beam lithography mediated nucleation site concept described above yields excellent results there are still drawbacks such as the serial working principle, that is time consumption, relatively high cost, and the typical covering of only small surface areas. As shown in Section 5.3.2, self-assembly approaches, on the other hand, allow for an efficient parallel generation of nanopatterns. These methods can either lead to a direct SA deposition of the precursor with subsequent crystallization of nanoscopic ferroelectric grains, for example PTO and PZT, or can be used for the SA generation of lithographic nanomasks. The aim is here at first to implement a suitable process that allows a high degree of structural ordering, which is then transferred to suitable templates with dimensions of a few nanometers. Möller and others [87–89] made considerable progress in the fabrication of such highly ordered nanostructures by using "copolymer micelle lithography".

In order to explore the potential of this method for bottom-up fabrication of sub-100 nm structures and functional oxide particles, Kronholz et al. used gold-loaded diblock-copolymer micelles, which arrange in a hexagonal pattern according to the balance of different forces (e.g. capillary forces, long-range van der Waals interactions and adhesion forces), for the generation of such defined oxidic nanostructures [90]. The first steps of the preparation process involved the formation of micelles from poly(vinylpiridine)-b-poly(styrene) (PVP-b-PS) diblock copolymers and the loading of the micellar core with the gold salt. Dip coating of an ultra-thin titania layer coated platinized silicon substrate (TiO_2[2nm]/Pt/TiO_2/SiO_2/Si) into the solution of PVP-b-PS yielded a monolayer micellar film. In the subsequent process step the organic compounds are removed by reactive ion beam etching (RIBE) with an oxygen plasma. The plasma treatment leads to a reduction of the Au salt and finally to one Au nanocluster per micelle by thermal annealing. The resulting Au nanoparticles are suitable as hard mask for the patterning of the ultra-thin TiO_2 film on top of the Pt electrode with reactive ion etching (RIE) using a CF_4 plasma. Subsequently the residual Au nanoparticles are removed by an RIBE Ar plasma treatment step (Figure 5.13).

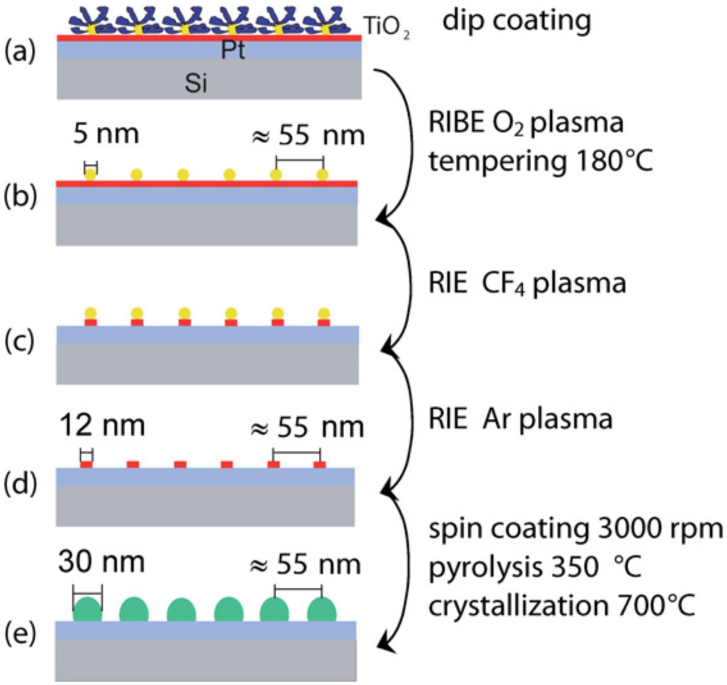

Figure 5.13 Process flow for the template-based preparation of $PbTiO_3$ nanograins: (a) self-assembled gold-loaded PVP-b-PS micelles; (b) gold nanoparticles after reduction and temperature treatment (RIBE: reactive ion beam etching); (c) gold-covered TiO_2 seeds after reactive ion etching (RIE); (d) elimination of the Au template by RIE; and (e) $PbTiO_3$ grains grown on TiO_2 seeds. Reprinted from [90], Copyright © 2006 Wiley-VCH Verlag GmbH & Co. KGaA, Weinheim

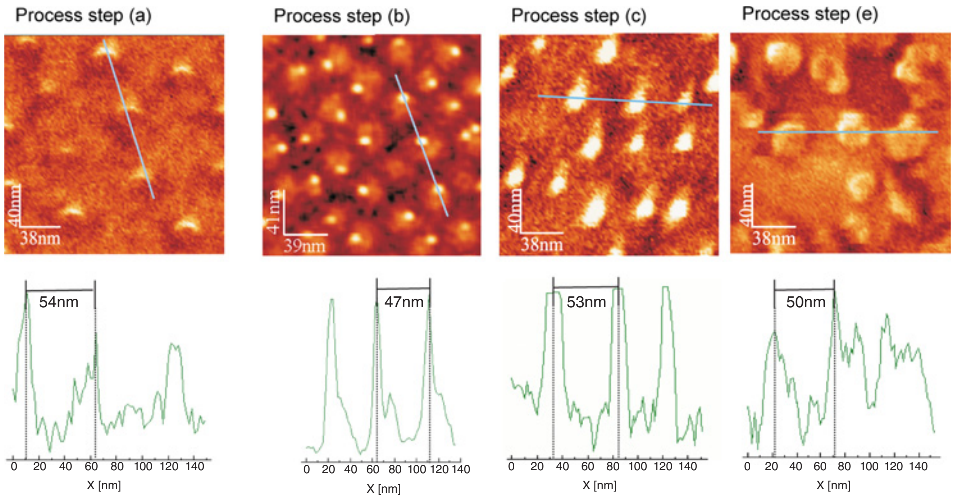

Figure 5.14 *AFM photographs and results of line scans yielding the interparticle distances taken at process steps (a), (b), (c), and (e) (see Figure 5.13) during the preparation of PTO nanograins on a* TiO_2 *surface. Reprinted from [90], Copyright © 2006 Wiley-VCH Verlag GmbH & Co. KGaA, Weinheim*

The resulting TiO_2 nanodots act again as nanoseeds for the controlled growth of PTO nanograins by the basically same chemical solution deposition technique that has already been applied for e-beam patterned TiO_2 described above. The results of an AFM study showed that the initial SA pattern of the Au loaded micelles could be transferred to the PTO nanograins including the interparticle distances (Figure 5.14).

5.4 Embedded Ferroelectric Nanograins

In order to enable direct electrical characterization of bottom-up grown ferroic nanograins either top electrodes have to be deposited directly or their integration has to be pushed to a level where the ferroelectric cells can be provided with top electrodes. In any case nanocapacitors have to be fabricated in order to characterize their ferroelectric response under "device-like" conditions. Single top electrode deposition on individual ferroelectric nanograins in the sub-100 nm range still imposes an obstacle to the integration of ferroelectric nanograins. One early approach used the segregation effect of bismuth at high temperatures. During the PLD deposition of epitaxial ferroelectric $Bi4Ti_3O_{12}$ thin films on single-crystal $SrTiO_3$ substrates at 825 ± 40 °C the excess Bi segregates and migrates to the surface, where it forms a self-organized planar array of rectangular epitaxial mesas showing metallic conductivity. Hence "nanoelectrodes" of about 200 nm in size have been formed and hence defined capacitors could be measured electrically [91].

A second, more universal, concept is to embed the ferroelectric nanoislands into an isolating matrix of a typically glassy or amorphous material. Referring to this in the following subsections, a number of examples will be presented.

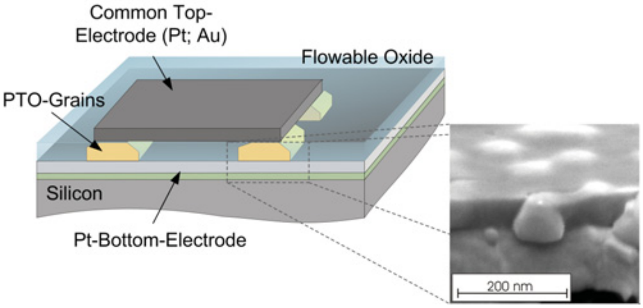

Figure 5.15 Schematic of the sample setup of fully embedded PTO nanograins provided with collective gold or platinum top electrodes. The inset on the right shows a cross-sectional scanning electron image of an embedded and polished PTO island of about 60 nm in height. The PTO islands were prepared according to the self-patterning method described above in Section 5.3.2. Reprinted with permission from [94]. Copyright [2008], AIP Publishing LLC

5.4.1 Embedded Lead Titanate-Based Nanograins

One of the first approaches relies on a flowable oxide layer in combination with chemical mechanical polishing (CMP) [92] and subsequent collective top electrode deposition [93] (Figure 5.15).

In the first step flowable spin-on glasses (SOG) were used as dielectric matrix layers for embedding the ferroelectric nanocells since they feature excellent gap-fill and planarization properties. Different low-*k* dielectric SOG materials like hydrogen silsesquioxane (HSQ) or methyl silsesquioxane (MSQ) were applied – polymers with the empirical formula $(\mathrm{R\text{-}SiO_{3/2}})_n$ [95,96]. The name silsesquioxane is derived from the one and a half (sesqui) stoichiometry of oxygen bound to silicon. HSQ is an inorganic polymer that contains hydrogen bonded to the silicon atoms in the Si–O backbone (R = H). MSQ includes an organic substitution of 10 wt% CH_3 groups to silicon ($R = CH_3$). The low dielectric constant of the materials is due to the low polarizability of the Si–R bond in comparison to the Si–O bond in SiO_2 [96]. Moreover, the presence of cage structures increases the larger free volume of the films compared to films of amorphous SiO_2 networks. In order to obtain mechanically stable films, cross-linking of the silsesquioxane polymer structures was achieved by thermal curing of the films after deposition at temperatures around 400 °C in inert (nitrogen) atmosphere in order to prevent oxidation of the films. The processing route itself is likewise a CSD route where the SOG materials are dispensed in a liquid state, that is they are spin-coated onto the substrate. After curing, a layer of low permittivity glass ($\varepsilon_r \approx 4$) with characteristics similar to those of SiO_2 is formed. These low-*k* SOG dielectrics are widely used as interlayer dielectric (ILD) or overcoat passivation in the manufacture of ICs in the standard semiconductor industry [97].

The dielectric layers were spin-coated to thicknesses that just covered the highest PTO grain tops. The excessive dielectric material on top of the grains was subsequently removed by CMP [93,94, 98]. Due to the planarizing properties of the matrix layers and the marginal surface corrugation after embedding (see Figure 5.16(b)), the polishing process could be carried out on a commercial tabletop polisher (which in contrast to a dedicated CMP tool

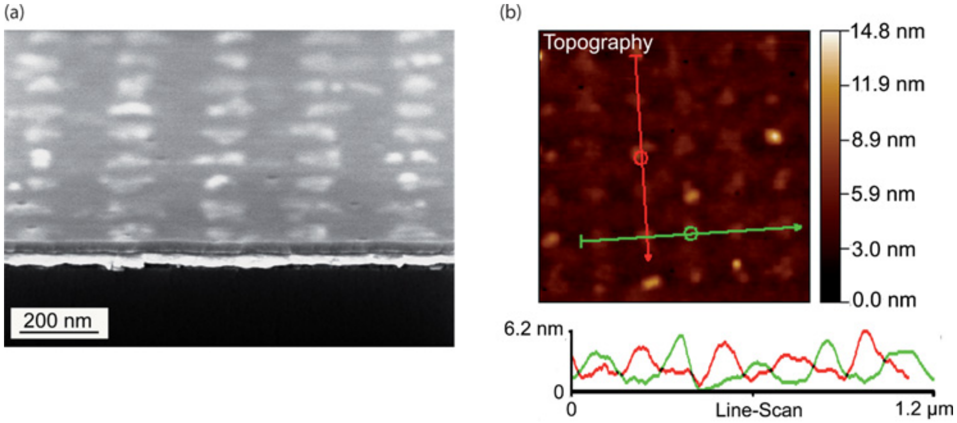

Figure 5.16 *(a) Cross-sectional SEM image of smoothly embedded 100 nm wide PTO grains. (b) Only a small surface corrugation is remaining, as shown in the AFM image on the right, where the PTO grains lift the dielectric layer to 5 nm high humps. The line scan also indicates the high degree of in-plane grain registration in this example. From [98]. © IOP Publishing. Reproduced by permission of IOP Publishing. All rights reserved*

barely features any global planarization impact). Figure 5.16 displays an exemple of such a ferroelectric nanostructure array of highly arranged PTO cells about 100 nm wide and 15 nm high on a 250 nm pitch that were embedded in MSQ and made electrically accessible by polishing [98]. The embedded PTO grains appear as bright shades within the dielectric layer, arranged in lines on top of the sample (Figure 5.16(a)).

Although the embedding process is obviously not restricted with regard to the smallest structural dimensions, direct electrical characterization of such structures is hampered as the electric charge to detect scales with lateral cell dimension. As this charge readily drops below any background noise, parasitic capacitances, and leakage during measurement, the method of choice for proving ferroelectricity on nanoscaled ferroelectrics is still piezoresponse force microscopy.

However, direct electrical characterization of sub-100 nm ferroelectric islands becomes feasible when measuring several structures in parallel. For this, collective Au and Pt top electrodes with diameters in the range of 100 μm (cf. the schematic in Figure 5.15) were deposited onto embedded and electrically accessible PTO nanoislands of typically below 100 nm in lateral dimensions that were grown, for example, by the microstructure instability-based self-assembly route discussed in Section 5.3.1 [94].

I–V plots as shown in Figure 5.17 were recorded that show displacement current peaks close to those measured on continuous PTO thin films with related characteristics regarding frequency and applied voltage, which gives a strong hint on the eligibility of the applied integration route.

5.4.2 Further Embedding Concepts

Ferroic nanostructures may also be embedded in other glassy or amorphous matrices. As such the surrounding amorphous precursor matrix of the ferroic material itself or binary

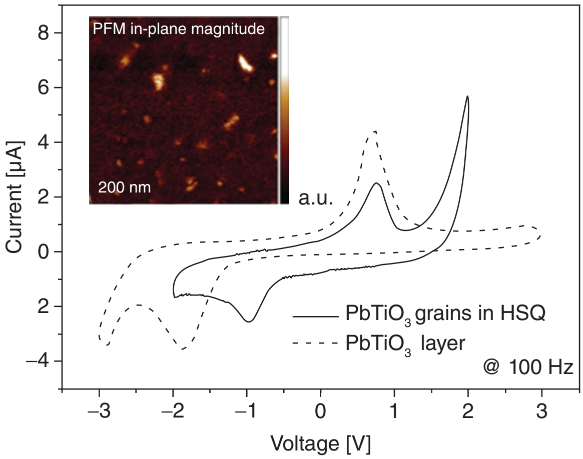

Figure 5.17 *I–V curves of HSQ embedded PTO grains (solid) of about 40 nm in height and of an approximately 80 nm thick continuous PTO thin film (dashed). Both curves were measured at 100 Hz using Pt top electrodes of 200 μm (grains) and 80 μm (layer) in diameter. The PFM inset on the top left displays the percentage of piezoelectric activity that could be recorded on the embedded PTO grain surface. Reprinted with permission from [94]. Copyright [2008], AIP Publishing LLC*

metal oxides such as TiO_2 may serve. The first example is based on the use of resistively heated AFM cantilever tips, which represents another way to use a technically adapted AFM setup not for analysis but for generation of nanostructures [99]. In general this technique allows controlled local deposition of materials, which are normally immobile at room temperature, and local chemical reactions such as conversion to other functional groups [100, 101] or local reduction of, for example, graphene oxide [102]. This so-called thermochemical nanolithography was recently also employed to locally crystallize a ferroelectric CSD-derived amorphous precursor film [103]. The amorphous PZT52/48 and PTO films have been prepared by spin-coating and a subsequent short drying/pyrolysis step at moderate temperatures of 250–300 °C. Thus, beyond the standard silicon-based substrates a large variety of typically too temperature-sensitive substrates such as plastics (e.g. Kapton) or soda-lime glass can be used as long as they withstand at least ~250 °C. In summary, this maskless method enabled the direct creation of ferroelectric lines with widths > 30 nm and spheres with a diameter >10 nm and densities up to ~33 Gbit cm^{-2} (~213 Gbit in^{-2}) [103] by local nanoscale crystallization. The authors conclude that the method can potentially be parallelized in order to have high registry and alignment quality for fabrication of real devices.

The application of a reversed nucleation site concept offers the second possibility of integrating ferroic PZT nanostructures into a glassy matrix consisting of TiO_2 in this case [104]. In order to explain the working principle it has to be mentioned that only adequately thin and (110) oriented rutile TiO_2 layers act as efficient seeding layers for the perovskite phase [82], while thicker amorphous TiO_2 layers on platinized silicon substrates do not show the seeding effect. Based on this fact, amorphous, 50 nm thick TiO_2 layers on platinized silicon substrates were provided with holes ranging from 100 to 500 nm using a focused ion beam

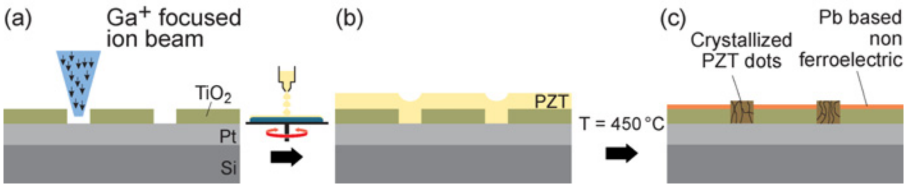

Figure 5.18 *Schematic diagram of the processing steps used in the fabrication of ferroelectric nanostructures. (a) FIB patterning of the spun-on TiO_2-coated platinized silicon wafer; (b) the structure after spin-coating of the PZT precursor solution; (c) actual structure after annealing at 450 °C. It has been shown that the PZT material inside the dot is raised above the surrounding matrix and that it has individual crystallites. The figure is according to [104]*

(FIB) technique. Subsequent crystallization of a low-temperature PZT40/60 precursor solution (400 °C) yielded a perovskite PZT phase that only emerged within the milled holes. This effect was explained by an amorphous TiO_2 layer that actively drives away the PZT nucleation to the FIB-generated holes where bare platinum is present, that is the reversal of the seeds compared to Section 5.3.3. Platinum of the bottom electrode reacts with metallic lead, which forms during the reducing conditions of pyrolysis an intermetallic $PbPt_x$ phase. The formation of such intermediate $PbPt_x$ alloys during PZT crystallization was at first discussed by Chen and Chen, who investigated this mechanism in order to explain the texture selection of their MOD-derived PZT films [105]. Later it was confirmed by a number of groups [106–109] and a summary of these findings may be found in Hoffmann-Eifert and Schneller [110]. Due to the good lattice match of the $PbPt_x$ phase it serves as an excellent nucleation seed for the ferroelectric PZT phase. Thus it is mandatory to keep the annealing temperature as low as possible in order to just enable crystallization of the PZT but inhibit crystallization of the glassy TiO_2. Figure 5.18 illustrates the important steps of this method.

Finally, embedded lead zirconate titanate (PZT) crystal dots down to 100 nm in the lateral dimension without the need for additional processing steps resulted. By means of PFM their ferroelectricity was proven.

5.5 Conclusions

The fabrication and characterization of nanoscale ferroic materials as (ultra-)thin layers and well-defined ferroelectric nanostructures for research as well as for larger-scale production represents a challenging task. With the advent of suitable characterization techniques beyond SEM and TEM, such as AFM and in particular its PFM variant in the late 1990s, a characterization of sub-100 nm ferroelectric structures was basically possible, but often lacking suitable samples, due to the difficulties with established top-down patterning techniques based on photolithography and etching steps. By using FIB techniques first ferroelectric capacitors well below 1 μm and down to ~100 nm were successfully prepared and characterized. Even $70 \times 70\ nm^2$ structures could be prepared but not electrically measured. Due to the patterning induced damages encountered with the typical top-down approaches other methods were sought in the past decade that enable an undisturbed grain growth from the bottom. These comprise true bottom-up methods that rely on self-assembly principles as well as the growth of individual ferroelectric nanoislands by crystallization of a prepatterned amorphous precursor film. Self-assembly and self-patterning methods, respectively, thereby enabled the preparation of ferroelectric nanostructures with lateral sizes down to ∼10 nm on different substrates, which is significantly below the dimensions accessible by any of the top-down techniques. Even high-quality epitaxial or single crystalline nanostructures could be processed that facilitated the study of fundamental physical issues such as general size effects, domain pinning at the nanoscale, or the determination of the superparaelectric limit. Nevertheless, the lack of registry of these self-assembled nanostructures represents a major obstacle for the processing of devices. Hence other fabrication routes using site-induced nucleation at predefined TiO_2 nanoseed pattern, the local arbitrary deposition by DPN followed by crystallization, or the local crystallization of a precursor film by resistively heated AFM cantilever tips have been developed. Furthermore, different nanomasks, which have also been prepared by self-assembly and self-ordering methods, or nanoimprint lithography may help to gain control over the registration, although the hitherto achieved minimum grain sizes do not yet reach the 10 nm range of the randomized self-assembly derived nanostructures.

In summary, a bunch of applicable preparation methods to obtain high-quality nanoscale ferroics are now available on a lab scale. Some of them, such as nanoimprint lithography and stencil masks, basically have the potential to be applied on larger areas and scales. SOG-embedded fully functional ferroelectric nanograins, for exemple, showed a possible approach for the integration into devices. In spite of this substantial progress the discussion and the study of the issues related to upscaling of the methods and solving the encountered challenges for the integration into real devices, such as the way of contacting these small capacitor structures electrically, the processing temperatures, etc., remain an ambitious task and have to be the subject of further work. In any case the developed preparation routes may also be of interest for other application areas, where the capability of generating nanostructured functional oxide patterns with predictable shapes, controlled sizes, and arbitrary positions on the substrate are required.

References

(1) Moore, G.E. (1965) Cramming more components onto integrated circuits. *Electronics*, **38**, 114–117.

(2) Scott, J.F. (2000) *Ferroelectric Memories*, Springer, Berlin.

(3) Rüdiger, A., Schneller, T., Roelofs, A., et al. (2005) Nanosize ferroelectric oxides: tracking down the superparaelectric limit. *Applied Physics A: Materials Science and Processing*, **80** (6), 1247–1255.

(4) Varghese, J., Whatmore, R.W., and Holmes, J.D. (2013) Ferroelectric nanoparticles, wires and tubes: synthesis, characterisation and applications. *Journal of Material Chemistry C*, **1**, 2618–2638.

(5) Rørvik, P.M., Grande, T., and Einarsrud, M.A. (2011) One-dimensional nanostructures of ferroelectric perovskites. *Advanced Materials*, **23**, 4007–4034.

(6) Utke, I., Hoffmann, P., and Melngailis, J. (2008) Gas-assisted focused electron beam and ion beam processing and fabrication. *Journal of Vacuum Science and Technology B*, **26**, 1197–1276.

(7) Melngailis, J. (1987) Focused ion beam technology and applications. *Journal of Vacuum Science and Technology B*, **5**, 469–495.

(8) Alexe, M., Harnagea, C., Hesse, D., and Gösele, U. (1999) Patterning and switching of nano-size ferroelectric memory cells. *Applied Physics Letters*, **75**, 1793–1795.

(9) Schneller, T., Waser, R., Kosec, M., and Payne, D. (eds) (2013) *Chemical Solution Deposition of Functional Oxide Thin Films*, Springer, Wien.

(10) Steinbrüchel, C. (1992) Ion–surface interactions: from sputtering to reactive ion etching. *Materials Science and Technology*, **8**, 565–573.

(11) Bühlmann, S., Dwir, B., Baborowski, J., and Muralt, P. (2002) Size effect in mesoscopic epitaxial ferroelectric structures: increase of piezoelectric response with decreasing feature size. *Applied Physics Letters*, **80**, 3195–3197.

(12) Ganpule, C.S., Stanishevsky, A., Su, Q., et al. (1999) Scaling of ferroelectric properties in thin films. *Applied Physics Letters*, **75**, 409–411.

(13) Ganpule, C.S., Stanishevsky, A., Aggarwal, S., et al. (1999) Scaling of ferroelectric and piezoelectric properties in Pt/$SrBi_2Ta_2O_9$/Pt thin films. *Applied Physics Letters*, **75**, 3874–3876.

(14) Lee, J.K., Kim, T.Y., Chung, I., and Desu, S.B. (1999) Characterization and elimination of dry etching damaged layer in Pt/$Pb(Zr_{0.53}Ti_{0.47})O_3$/Pt ferroelectric capacitor. *Applied Physics Letters*, **75**, 334–336.

(15) Saad, M.M., Bowman, R.M., and Gregg, J.M. (2004) Characteristics of single crystal "thin film" capacitor structures made using a focused ion beam microscope. *Applied Physics Letters*, **84**, 1159–1161.

(16) Alexe, M. and Gruverman, A. (eds) (2004) *Nanoscale Characterisation of Ferroelectric Materials*, Springer, Berlin.

(17) Gruverman, A., Tokumoto, H., Prakash, A.S., et al. (1997) Nanoscale imaging of domain dynamics and retention in ferroelectric thin films. *Applied Physics Letters*, **71**, 3492–3495.

(18) Colla, E.L., Hong, S., Taylor, D.V., et al. (1998) Direct observation of region by region suppression of the switchable polarization (fatigue) in $Pb(Zr,Ti)O_3$ thin film capacitors with Pt electrodes. *Applied Physics Letters*, **72**, 2763–2765.

(19) Abplanalp, M., Eng, L.M., and Günter, P. (1998) Mapping the domain distribution at ferroelectric surfaces by scanning force microscopy. *Applied Physics A: Materials Science and Processing*, **66**, S231–S234.

(20) Stanishevsky, A., Aggarwal, S., Prakash, A.S., et al. (1998) Focused ion-beam patterning of nanoscale ferroelectric capacitors. *Journal of Vacuum Science and Technology B*, **16**, 3899–3902.

(21) Craighead, H. and Schiavone, L. (1986) Metal deposition by electron beam exposure of an organometallic film. *Applied Physics Letters*, **48**, 1748–1750.

(22) Lohau, J., Friedrichowski, S., Dumpich, G., et al. (1998) Electron-beam lithography with metal colloids: direct writing of metallic nanostructures. *Journal of Vacuum Science and Technology B*, **16**, 77–79.

(23) Saifullah, M.S.M., Namatsu, H., Yamaguchi, T., et al. (1999) Effect of chelating agents on high resolution electron beam nanolithography of spin-coatable alumina gel films. *Japanese Journal of Applied Physics*, **38**, 7052–7058.

(24) Okamura, S., Mori, K., Tsukamoto, T., and Shiosaki, T. (1997) Fabrication of ferroelectric $Bi_4Ti_3O_{12}$ thin films and micropatterns by means of chemical solution

decomposition and electron beam irradiation. *Integrated Ferroelectrics*, **18**, 311–318.

(25) Alexe, M., Harnagea, C., Erfurth, W., et al. (2000) 100-nm lateral size ferroelectric memory cells fabricated by electron-beam direct writing. *Applied Physics A: Materials Science and Processing*, **70**, 247–251.

(26) Alexe, M., Harnagea, C., Hesse, D., and Gösele, U. (2001) Polarization imprint and size effects in mesoscopic ferroelectric structures. *Applied Physics Letters*, **79**, 242–244.

(27) Hirano, S., Shimada, S., and Kuwabara, M. (2005) Fabrication and optical reflection behavior of a two-dimensional barium titanate ceramic photonic crystal. *Applied Physics A: Materials Science and Processing*, **80**, 783–786.

(28) Bernal, A., Tselev, A., Kalinin, S., and Bassiri-Gharb, N. (2012) Free-standing ferroelectric nanotubes processed via soft-template infiltration. *Advanced Materials*, **24**, 1160–1165.

(29) Piner, R.D., Zhu, J., Xu, F., et al. (1999) "Dip-pen" nanolithography. *Science*, **283**, 661–663.

(30) Son, J.Y., Shin, Y.H., Ryu, S., et al. (2009) Dip-pen lithography of ferroelectric $PbTiO_3$ nanodots. *Journal of the American Chemical Society*, **131**, 14676–14678.

(31) Chou, S., Krauss, P., and Renstrom, P. (1995) Imprint of sub-25 nm vias and trenches in polymers. *Applied Physics Letters*, **67**, 3114–3117.

(32) Chou, S.Y., Krauss, P.R., and Renstrom, P.J. (1996) Nanoimprint lithography. *Journal of Vacuum Science and Technology B*, **14**, 4129–4133.

(33) Chou, S.Y., Krauss, P.R., Zhang, W., et al. (1997) Sub-10 nm imprint lithography and applications. *Journal of Vacuum Science and Technology B*, **15**, 2897–2904.

(34) Harnagea, C., Alexe, M., Schilling, J., et al. (2003) Mesoscopic ferroelectric cell arrays prepared by imprint lithography. *Applied Physics Letters*, **83**, 1827–1829.

(35) Lee, W., Alexe, M., Nielsch, K., and Gösele U. (2005) Metall membranes with hierarchically organized nanotubes arrays. *Chemistry of Materials*, **17**, 3325–3327.

(36) Lee, S.K., Lee, W., Alexe, M., et al. (2005) Well-ordered large-area arrays of epitaxial ferroelectric $(Bi,La)_4Ti_3O_{12}$ nanostructures fabricated by gold nanotube-membrane lithography. *Applied Physics Letters*, **86**, art. no. 152906.

(37) Choi, J., Nielsch, K., Reiche, M., et al. (2003) Fabrication of monodomain alumina pore arrays with an interpore distance smaller than the lattice constant of the imprint stamp. *Journal of Vacuum Science and Technology B*, **21**, 763–766.

(38) Lee, W., Han, H., Lotnyk, A., et al. (2008) Individually addressable epitaxial ferroelectric nanocapacitor arrays with near Tb inch^{-2} density. *Nature Nanotechnology*, **3**, 402–407.

(39) Deckmann, H.W. and Dunsmuir, J.H. (1982) Natural Lithography. *Applied Physics Letters*, **41**, 377–379.

(40) Hulteen, J.C. and Van Duyne, R.P. (1995) Nanosphere lithography: a materials general fabrication process for periodic particle array surfaces. *Journal of Vacuum Science and Technology A*, **13**, 1553–1558.

(41) Ma, W., Harnagea, C., Hesse, D., and Gösele, U. (2003) Well-ordered arrays of pyramid-shaped ferroelectric $BaTiO_3$ nanostructures. *Applied Physics Letters*, **83**, 3770–3772.

(42) Ma, W. and Hesse, D. (2004) Microstructure and piezoelectric properties of sub-80 nm high polycrystalline $SrBi_2Ta_2O_9$ nanostructures within well-ordered arrays. *Applied Physics Letters*, **85**, 3214–3216.

(43) Ma, W. and Hesse, D. (2004) Polarization imprint in ordered arrays of epitaxial ferroelectric nanostructures. *Applied Physics Letters*, **84**, 2871–2873.

(44) Alexe, M. and Hesse, D. (2006) Self-assembled nanoscale ferroelectrics. *Journal of Materials Science*, **41**, 1–11.

(45) Seifert, A., Vojta, A., Speck, J.S., and Lange, F.F. (1996) Microstructural instability in single-crystal thin films. *Journal of Materials Research*, **11**, 1470–1482.

(46) Waser, R., Schneller, T., Hoffmann-Eifert, S., and Ehrhart, P. (2001) Advanced chemical deposition techniques – from research to production. *Integrated Ferroelectrics*, **36**, 3–20.

(47) Roelofs, A. (2004) *Size Effects in Ferroelectric Thin Films*, PhD Thesis, Verlag für Wissenschaft und Forschung, Berlin.

(48) Szafraniak, I., Harnagea, C., Scholz, R., et al. (2003) Ferroelectric epitaxial nanocrystals obtained by a self-patterning method. *Applied Physics Letters*, **83**, 2211–2214.

(49) Fujisawa, H., Morimoto, K., Shimizu, M., et al. (2000) Observations of island structures at the initial growth stage of $PbZr_xTi_{1-x}O_3$ thin films prepared by metalorganic chemical vapor deposition. *Japanese Journal of Applied Physics*, **39**, 5446–5450.

(50) Nonomura, H., Fujisawa, H., Shimizu, M., et al. (2003) Self-assembled $PbTiO_3$ nano-islands prepared on $SrTiO_3$ by metalorganic chemical vapor deposition. *Japanese Journal of Applied Physics*, **42**, 5918–5921.

(51) Fujisawa, H., Okinawa, M., Nonomura, H., et al. (2004) Ferroelectricity of the 1.7 nm-high and 38 nm-wide self-assembled $PbTiO_3$ island. *Journal of the European Ceramic Society*, **24**, 1641–1645.

(52) Dawber, M., Szafraniak, I., Alexe, M., and Scott, J.F. (2003) Self-patterning of arrays of ferroelectric capacitors: description by theory of substrate mediated strain interactions. *Journal of Physics: Condensed Matter*, **15**, L667–L671.

(53) Williams, R.S., Medeiros-Ribeiro, G., Kamins, T.I., and Ohlberg, D.A.A. (2000) Thermodynamics of the size and shape of nanocrystals: epitaxial Ge on Si(001). *Annual Review of Physical Chemistry*, **51**, 527–551.

(54) Rudd, R.E., Briggs, G.A.D., Sutton, A.P., et al. (2003) Equilibrium model of bimodal distributions of epitaxial island growth. *Physical Review Letter*, **90**, art. no. 146101.

(55) Szafraniak, I. and Alexe, M. (2003) Hydrothermal growth of nanosize ferroelectrics, *Ferroelectrics*, **291**, 19–26.

(56) Urban, J.J., Spanier, J.E., Ouyang, L., et al. (2003) Single-crystalline barium titanate nanowires. *Advanced Materials*, **15**, 423–426.

(57) Urban, J.J., Yun, W.S., Gu, Q., and Park, H. (2002) Synthesis of single-crystalline perovskite nanorods composed of barium titanate and strontium titanate. *Journal of the American Chemical Society*, **124**, 1186–1187.

(58) Morrison, F.D., Luo, Y., Szafraniak, I., et al. (2003) Ferroelectric nanotubes. *Review of Advanced Materials Science*, **4**, 114–122.

(59) Bhattacharyya, S., Chattopadhyay, S., and Alexe, M. (2003) Fabrication of isolated ferroelectric nanostructures. *Materials Research Society Symposium Proceedings*, **740**, I10.3.1–I10.3.6.

(60) Beck, Ch., Härtl, W. and Hempelmann, R. (1998) Size-controlled synthesis of nanocrystalline $BaTiO_3$ by a sol–gel type hydrolysis in microemulsion-provided nanoreactors. *Journal of Materials Research*, **13**, 3174–3180.

(61) Herrig, H. and Hempelmann, R. (1996) A colloidal approach to nanometre-sized mixed oxide ceramic powders. *Materials Letters*, **27**, 287–292.

(62) Pithan, C., Shiratori, Y., Waser, R., et al. (2006) Preparation, processing, and characterization of nano-crystalline $BaTiO_3$ powders and ceramics derived from microemulsion-mediated synthesis. *Journal of the American Ceramic Society*, **89**, 2908–2916.

(63) Hernandez, B.A., Chang, K.S., Fisher, E.R., and Dorhout, P.K. (2002) Sol–gel template synthesis and characterization of $BaTiO_3$ and $PbTiO_3$ nanotubes. *Chemistry of Materials*, **14**, 480–482.

(64) Luo, Y., Szafraniak, I., Zakharov, N.D., et al. (2003) Nanoshell tubes of ferroelectric lead zirconate titanate and barium titanate. *Applied Physics Letters*, **83**, 440–442.

(65) Morrison, F.D., Ramsay, L., and Scott, J.F. (2003) High aspect ratio piezoelectric strontium–bismuth–tantalate nanotubes. *Journal of Physics: Condensed Matter*, **15**, L527–L532.

(66) Calzada, M.L., Torres, M., Fuentes-Cobas, L.E., et al. (2007) Ferroelectric self-assembled $PbTiO_3$ perovskite nanostructures onto (100) $SrTiO_3$ substrates from a novel microemulsion aided sol–gel preparation method. *Nanotechnology*, **18**, art. no. 375603.

(67) Torres, M., Ricote, J., Pardo, L., and Calzada, M.L. (2008) Nanosize ferroelectric $PbTiO_3$ structures onto substrates. Preparation by a novel bottom-up method and nanoscopic characterization. *Integrated Ferroelectrics*, **99**, 95–104.

(68) Grosso, D., Boissiere, C., Smarsly, B., et al. (2004) Periodically ordered nanoscale islands and mesoporous films composed of nanocrystalline multimetallic oxides. *Nature Materials*, **3**, 787–792.

(69) Lazzari, M. and López-Quintela, M.A. (2003) Block copolymers as a tool for nanomaterial fabrication. *Advanced Materials*, **15**, 1583–1594.

(70) Bates, F.S. and Frederickson, G.H. (1990) Block copolymer thermodynamics: theory and experiment. *Annual Review of Physical Chemistry*, **41**, 525–557.

(71) Milner, S.T. (1991) Polymer brushes. *Science*, **251**, 905–914.

(72) Leibler, L. (1980) Theory of microphase separation in block copolymers. *Macromolecules*, **13**, 1602–1617.

(73) Kellogg, G.J., Walton, D.G., Mayes, A.M., et al. (1996) Observed surface energy effects in confined diblock copolymers. *Physical Review Letters*, **76**, 2503–2506.

(74) Morkved, T.L., Lu, M., Urbas, A.M., et al. (1996) Local control of microdomain orientation in diblock copolymer thin films with electric fields. *Science*, **273**, 931–933.

(75) Mansky, P., Russell, T.P., Hawker, C.J., et al. (1997) Interfacial segregation in disordered block copolymers: effect of tunable surface potentials. *Physical Review Letters*, **79**, 237–240.

(76) Mansky, P., Liu, Y., Huang, E., et al. (1997) Controlling polymer–surface interactions with random copolymer brushes. *Science*, **275**, 1458–1460.

(77) Kim, Y., Han, H., Kim, Y., et al. (2010) Ultrahigh density array of epitaxial ferroelectric nanoislands on conducting substrates. *Nano Letters*, **10**, 2141–2146.

(78) Ghoshal, T., Maity, T., Godsell, J.F., et al. (2012) Large scale monodisperse hexagonal arrays of superparamagnetic iron oxides nanodots: a facile block copolymer inclusion method. *Advanced Materials*, **24**, 2390–2397.

(79) Varghese, J., Ghoshal, T., Deepak, N., et al. (2013) Fabrication of arrays of lead zirconate titanate (PZT) nanodots via block copolymer self-assembly. *Chemistry of Materials*, **25**, 1458–1463.

(80) Peng, J., Kim, D.H., Knoll, W., et al. (2006) Morphologies in solvent-annealed thin films of symmetric diblock copolymer. *Journal of Chemical Physics*, **125**, art. no. 064702.

(81) Peng, J., Han, Y.C., Knoll, W., and Kim, D.H. (2007) Development of nanodomain and fractal morphologies in solvent annealed block copolymer thin films. *Macromolecules Rapid Communications*, **28**, 1422–1428.

(82) Muralt, P., Maeder, T., Sagalowicz, L., et al. (1998) Texture control of $PbTiO_3$ and PZT thin films with TiO_2 seeding. *Journal of Applied Physics*, **83**, 3835–3841.

(83) Schneller, T. and Waser, R. (2002) Chemical solution deposition of ferroelectric thin films – state of the art and recent trends. *Ferroelectrics*, **267**, 293–301.

(84) Bühlmann, S., Muralt, P., and von Allmen, S. (2004) Lithography-modulated self-assembly of small ferroelectric $Pb(Zr,Ti)O_3$ single crystals. *Applied Physics Letters*, **84**, 2614–2616.

(85) Clemens, S., Schneller, T., van der Hart, A., et al. (2005) Registered deposition of nanoscale ferroelectric grains by template-controlled growth. *Advanced Materials*, **17**, 1357–1361.

(86) Roelofs, A., Szot, K., and Waser, R. (2004) Domain switching and self-polarization in perovskite thin films, in *Nanoscale Phenomena in Ferroelectric Thin Films*, edited by S. Hong, Kluwer Academic Publishers, Dordrecht, pp. 135–155.

(87) Spatz, J.P., Mossmer, S., Hartmann, C., et al. (2000) Ordered deposition of inorganic clusters from micellar block copolymer films. *Langmuir*, **16**, 407–415.

(88) Haupt, M., Miller, S., Ladenburger, A., et al. (2002) Semiconductor nanostructures defined with self-organizing polymers. *Journal of Applied Physics*, **91**, 6057–6059.

(89) Glass, R., Möller, M., and Spatz, J.P. (2003) Block copolymer micelle nanolithography. *Nanotechnology*, **14**, 1153–1160.

(90) Kronholz, S., Rathgeber, S., Karthäuser, S., et al. (2006) Self-assembly of diblock-copolymer micelles for template-based preparation of $PbTiO_3$ nanograins. *Advanced Functional Materials*, **16**, 2346–2354.

(91) Alexe, M., Scott, J.F., Curan, C., et al. (1998) Self-patterning nano-electrodes on ferroelectric thin films for gigabit memory applications. *Applied Physics Letters*, **73**, 1592–1594.

(92) Steigerwald, J.M., Murarka, S.P., and Gutmann, R.J. (1997) *Chemical Mechanical Planarization of Microelectronic Materials*, John Wiley & Sons, Inc., New York.

(93) Clemens, S., Schneller, T. Waser, R., et al. (2005) Integration of ferroelectric lead titanate nanoislands for direct hysteresis measurements. *Applied Physics Letters*, **87**, art. no. 142904.

(94) Clemens, S., Dippel, A.C., Schneller, T., et al. (2008) Direct electrical characterization of embedded ferroelectric lead titanate nanoislands. *Journal of Applied Physics*, **103**, art. no. 034113.

(95) Baney, R.H., Itoh, M., Sakakibara, A., and Suzuki, T. (1995) Silsesquioxanes. *Chemical Reviews*, **95**, 1409–1430.

(96) Maex, K., Baklanov, M.R., Shamiryan, D., et al. (2003) Low dielectric constant materials for microelectronics. *Journal of Applied Physics*, **93**, 8793–8841.

(97) ITRS (2011) *The International Roadmap for Semiconductors: Interconnect*, http://www.itrs.net/Links/2011ITRS/2011Chapters/2011Interconnect.pdf (accessed 18 February 2013).

(98) Clemens, S., Röhrig, S., Rüdiger, A., et al. (2009) Embedded ferroelectric nanostructure arrays. *Nanotechnology*, **20**, 075305–075310.

(99) Sheehan, P.E., Whitman, L.J. King, W.P., and Nelson, B.A. (2004) Nanoscale deposition of solid inks via thermal dip pen nanolithography. *Applied Physics Letters*, **85**, 1589–1591.

(100) Szoszkiewicz, R., Okada, T., Jones, S.C., et al. (2007) High-speed, sub-15 nm feature size thermochemical nanolithography. *Nano. Letters*, **7**, 1064–1069.

(101) Wang, D., Kodali, V.K., Underwood II, W.D., et al. (2009) Thermochemical nanolithography of multifunctional nanotemplates for assembling nano-objects. *Advanced Functional Materials*, **19**, 3696–3702.

(102) Wei, Z., Wang, D., Kim, S., et al. (2010) Nanoscale tunable reduction of graphene oxide for graphene electronics. *Science*, **328**, 1373–1376.

(103) Kim, S., Bastani, Y., Lu, H., et al. (2011) Direct fabrication of arbitrary-shaped ferroelectric nanostructures on plastic, glass, and silicon substrates. *Advanced Materials*, **23**, 3786–3790.

(104) Nagarajan, V., Stanishevsky, A., and Ramesh, R. (2006) Ferroelectric nanostructures via a modified focused ion beam technique. *Nanotechnology*, **17**, 338–343.

(105) Chen, S.Y. and Chen, I.W. (1994) Phase transformations of oriented $Pb(Zr_{1-x}Ti_x)O_3$ thin films from metallo-organic precursors. *Ferroelectrics*, **152**, 25–30.

(106) Dippel, A.C., Schneller, T., Waser, R., et al. (2010) Formation sequence of lead platinum interfacial phases in chemical solution deposition derived $Pb(Zr_{1-x}Ti_x)O_3$. *Chemistry of Materials*, **22**, 6209–6211.

(107) Kaewchinda, D., Chairaungsri, T., Naksata, M., et al. (2000) TEM characterisation of PZT films prepared by a diol route on platinised silicon substrates. *Journal of the European Ceramic Society*, **20**, 1277–1288.

(108) Huang, Z., Zhang, O., and Whatmore, R.W. (1998) The role of an intermetallic phase on the crystallization of lead zirconate titanate in sol–gel process. *Journal of Materials Science*, **17**, 1157–1159.

(109) Brooks, K.G., Reaney, I.M., Klissurska, R., et al. (1994) Orientation of rapid thermally annealed lead zirconate titanate thin films on (111) Pt substrates. *Journal of Materials Research*, **9**, 2540–2553.

(110) Hoffmann-Eifert, S. and Schneller, T. (2013) Orientation and microstructure design, in *Chemical Solution Deposition of Functional Oxide Thin Films*, Edited by T. Schneller, R. Waser, M. Kosec, and D. Payne, Springer, Wien, Chapter 17.

6

Thin-Film Porous Ferroic Nanostructures: Strategies and Characterization

Alichandra Castro[1], Paula Ferreira[1], Stella Skiadopoulou[1], Liliana P. Ferreira[2], Margarida Godinho[3], Brian J. Rodriguez[4], and Paula M. Vilarinho[1]

[1] *CICECO–Aveiro Institute of Materials, Department of Materials and Ceramic Engineering, University of Aveiro, Portugal*
[2] *Biosystems and Integrative Sciences Institute, Department of Physics, University of Coimbra, Portugal*
[3] *Biosystems and Integrative Sciences Institute, Department of Physics, Faculty of Sciences, University of Lisbon, Portugal*
[4] *Conway Institute of Biomolecular and Biomedical Research, University College Dublin, Ireland*

6.1 (Nano)Microelectronics Considerations

The world of digital content grows exponentially every day. The semiconductor industry has been characterized for more than five decades by a fast rate of development in its products. Improvement trends at the integration level, cost, speed, power, compactness, and functionality are on the basis of progresses such as increasing number of components/chip (Moore's law), low cost per function, high microprocessor throughput, long battery life, small and lightweight products, non-volatile memories (among others).

Nanoscale Ferroelectrics and Multiferroics: Key Processing and Characterization Issues, and Nanoscale Effects, First Edition. Edited by Miguel Algueró, J. Marty Gregg, and Liliana Mitoseriu.
© 2016 John Wiley & Sons, Ltd. Published 2016 by John Wiley & Sons, Ltd.

These trends have been generically called “scaling” the device size [1]. However, since 2007 a new concept, “More than Moore” (MtM) that addresses functional diversification, has emerged. Besides the small size, devices should incorporate functionalities that provide additional value to the end customer. The MtM approach typically allows for the non-digital functionalities (e.g. RF communication, power control, passive components, sensors, actuators) to migrate from the system board level into a particular package level (SiP) or chip level (SoC) system solution [1]. Heterogeneous integration of multiple technologies is a key aspect for the further generation of new semiconductor applications beyond the traditional semiconductor logic and memory products.

As many physical device dimensions are expected to cross the 10 nm threshold, it is becoming clear that fundamental geometrical limits will be reached and by fully utilizing the vertical dimension it will be possible to stack layers of devices on top of each other; this three-dimensional (3D) approach will continue to increase the number of components per area and moreover adding functionality [1]. This 3D integration technology enables system and sensor functions at a nanoscale via the implementation of a highly integrated nanosemiconductor as well as the fabrication of a single chip with multiple functions [2].

A paradigmatic example of the benefits of the 3D technology are memories. 3D memory devices by stacking memory arrays vertically results in higher archival device storage, smaller chips, and lower power and costs. Stacking memory elements vertically permits a smaller die area for a given density than traditional memories and by decreasing the chip size and increasing the yield, memories can be produced at considerable lower costs [3].

With 3D the opportunities go far beyond just connecting together the bond pads; increasing functionality to a chip is another main advantage. Adding components to the integrated circuit can be done without applying processes to it, and the cost burden may be considerably reduced. Although the exploitation of 3D semiconductor technology has just started and much research is still needed, it opens unprecedented opportunities, for example, for the integration of passive components (such as capacitors, among others) at the level of integrated circuitry and the exploitation of new materials that will permit new functionalities.

A greater degree of creativity at the level of materials and, as a consequence, of functions will be possible to be implemented. This is the case, for example, of multiferroic materials that with the coexistence of at least two ferroic orders, ferroelectric, ferromagnetic, or ferroelastic, may have great potential applications as multifunctional devices. Within this context ferroics will be briefly discussed in the next section.

6.2 Ferroics and Nanoferroic Structures

Ferroic is the general name given to a material exhibiting the property of ferroelasticity, ferromagnetism, and ferroelectricity. In common, ferroelastics, ferromagnets, and ferroelectrics exhibit a large variation in their physical properties when a phase transition takes place around a critical temperature value (commonly designated as T_c and within a quite narrow temperature interval). Above the critical temperature the material exhibits a non-ferroic state, generally with properties of low practical relevance. When cooling down below T_c the material undergoes a spontaneous phase transition accompanied by a crystal symmetry reduction. The breaking of the symmetry is associated with the ferroic behavior emergence and appearance of technological important physical properties. The largest response of such materials is usually obtained in the vicinity of the phase transitions, where the domain structure is destabilized due to the transformation of the lattice.

In ferroelastics, the transition from the non-ferroic (for example cubic structure) to the ferroic state (tetragonal one) is accompanied by the formation of spontaneous strains. In the case of ferromagnets upon the phase transition with symmetry breaking from a paramagnetic to a ferromagnetic phase a spontaneous magnetization is created. In this case T_c is known as the Curie temperature. Ferromagnetism is the physical phenomenon widely known in permanent magnets. Applications such as electromagnets and hard disk drives are based on this phenomenon. Similarly, for ferroelectrics below the transition temperature spontaneous dipole moments are created along one of the axis of the unit cell that as a whole may generate important polarization values without an applied field, justifying some of the most important electrical properties of ferroelectrics. Examples of applications are ferroelectric random access memories, actuators, sensors, and transducers.

The ferroics interact with the external electromagnetic, elastic, and temperature fields manifesting four important collective effects connected with the change of the free energy, namely: phase transition, followed by the change of the lattice symmetry; anomalous temperature behavior of the susceptibilities, elastic constants, heat capacitance, and thermal expansion coefficients; transformation of the domain structure; nonlinear hysteresis change of the parameters.

In recent years a new class of ferroics designated “multiferroics” has been raising interest due to the promising potential applications. Multiferroics, as the name indicates, exhibit simultaneously more than one ferroic property in a single material [4]. These properties exist in the presence of an electric polarization, magnetization, or elastic deformation and can be hysterically switched by the action of an electric field, a magnetic field, or a stress, respectively. Recently, the multiferroic term has been extended to materials with other magnetic orders, like ferrimagnetism or antiferromagnetism [5], and even to a ferrotoroid order (though controversial) [6, 7].

In the form of thin films, multiferroics can be used in devices based on magnetoelectric coupling, such as spintronic devices, tunnel magneto resistance sensors, and spin valves with electric field tunable functions [4]. Moreover, these materials offer the possibility of fabricating a new type of storage device combining the best qualities of ferroelectric random access memories (FeRAMs) and magnetic random access memories (MRAMs), like fast low-power electric write operation and non-destructive magnetic read operation [8, 9].

However, the development of multiferroic materials and devices is in part a consequence of the development of high-quality ferroelectric thin films and, depending on the application, the thickness of the ferroelectric films also plays an important role. For example, for tunnel junction devices the required thickness is <10 nm [10]. It is well known that upon reduction of the physical dimension of the ferroelectric thin films, the change in the physical properties associated with size reduction become extremely difficult to characterize and understand. This is due to a complicated interplay between structures, surfaces properties, strain effects from substrates, domain nucleation and configuration, wall motions, depolarization effects and absence of long-range cooperative interactions as well as elastic constraints [11]. Nevertheless, in the last decade, new ferroelectric properties have been discovered for many nanosized materials, proving that ferroelectricity can be present in ultra-low thin films, and the spontaneous polarization can be sustained in a material below a critical size of a few tens of nanometers [12, 13].

Generally, two types of multiferroics are considered: single-phase multiferroics and nanocomposite multiferroics [14, 15]. Single-component multiferroics, also called intrinsic multiferroics, are characterized by the coexistence of ferroelectricity and magnetism in a single crystallographic phase. Currently, bismuth ferrite, $BiFeO_3$, is the only material coupling magnetic and ferroelectric activity at room temperature [16], although it is yet to be applied by the industry as multiferroic.

At this time it is believed that in order to obtain an applicable multiferroic it is important to engineer multiphase composites with a sufficiently high magnetoelectric coupling [14, 15]. Mainly three architectures of nanocomposite multiferroics have been studied (Figure 6.1). The nanoparticulate multiferroics are formed by dispersion of ferromagnetic nanoparticles in a ferroelectric matrix (0–3 geometry). Horizontal multilayered thin-film composites consist of alternating layers of ferroelectric and magnetic phases and are named 2–2 type. Usually both 0–3 and 2–2 composites exhibit a weak magnetoelectric effect due to large *in-plane* constraints from the substrate. The vertical heterostructured (1–3 type)

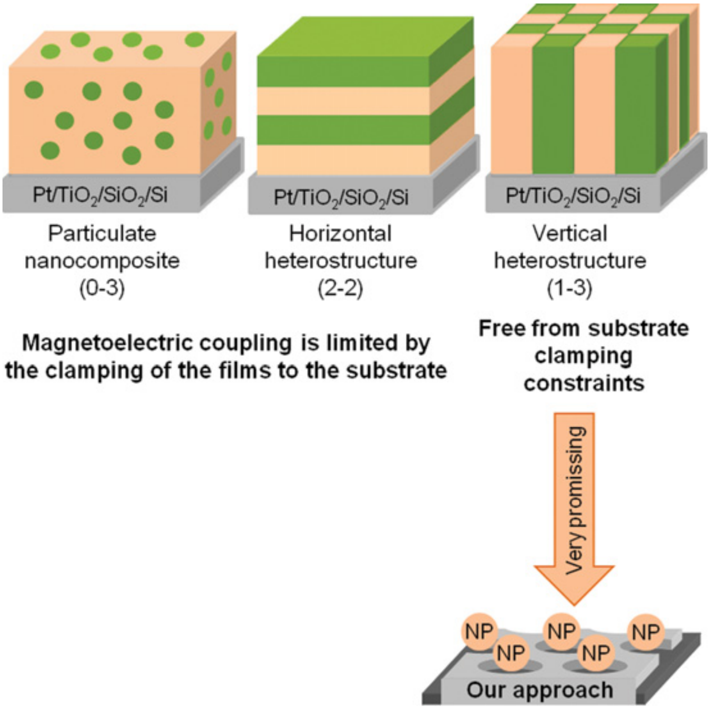
Pt/TiO2/SiO2/Si
Pt/TiO2/SiO2/Si
Pt/TiO2/SiO2/Si
Particulate nanocomposite (0-3)
Horizontal heterostructure (2-2)
Vertical heterostructure (1-3)
Magnetoelectric coupling is limited by the clamping of the films to the substrate
Free from substrate clamping constraints
Very promising
NP
NP
NP
NP
NP
Our approach

Figure 6.1 *Schematic illustration of three kinds of magnetoelectric composite nanostructures: particulate nanocomposite (0–3) films with magnetic particles (0) embedded in a ferroelectric film matrix (3); horizontal heterostructure (2–2) with alternating ferroelectric (2) and magnetic (2) layers; and vertical heterostructure (1–3) with one-phase nanopillars (1) embedded in a matrix of another phase (3). The* $Pt/TiO_2/SiO_2/Si$ *is the used substrate (Pt: platinum,* TiO_2*: titanium oxide,* SiO_2*: silica, and Si: silicon)*

composite consists of vertical structures of one of the ferroic phases embedded vertically within the other phase. These films are intrinsically heteroepitaxial in three dimensions, with low substrate-imposed mechanical clamping. This, together with a large interfacial surface area, allows achieving, theoretically, strong magnetoelectric coupling.

There are some examples of vertical epitaxially-embedded magnetic phases in ferroelectric matrices thin films prepared by physical methods [17–19]. Pillars of $CoFe_2O_4$ epitaxially embedded into $BaTiO_3$ films present a strong coupling manifested as a distinct drop in the magnetization of ca. 16 emu cm^{-3} (5% of magnetization at 100 Oe external field) around the ferroelectric Curie temperature. No temperature dependence of magnetization at 100 Oe was observed for a $CoFe_2O_4$–$BaTiO_3$ multilayer horizontal composite film with a layer thickness of 30 nm around the ferroelectric Curie temperature [17–19]. However, the magnetoelectric coupling values, limited by clamping of the films to the substrate, were much lower than required for applications. In the case of vertical heterostructured composites different types of strains should be taken into consideration. Typically, the substrate induces a tension (lateral strain), giving rise to out-of-plane compression. Additionally, the presence of two different crystallographic phases originates a vertical strain at the interface. In order to achieve a good magnetoelectric coupling, it is important that the vertical strain dominates. This happens when the vertical interface area exceeds the area of the film–substrate interface and the thickness of the films is kept relatively low [19, 20]. A careful control of the geometry of the film at the nanoscale allows a relatively simple strain field distribution to be achieved and to optimize and enhance the coupling. The physical methods generally applied for and in the preparation of vertical heterostructures, such as pulse laser deposition, usually provide a relatively low control of the nanostructure [17–19]. Reports are available on composite magnetoelectric thin films with magnetoelectric couplings comparable to those of bulk multiferroics but, because the magnetoelectric voltage output signal depends on the film's thickness, the values are far too low for application [6].

Recent review reports describe magnetoelectric thin films as being at an infant stage and emphasize the need to explore vertical nanostructures with long-range order and to ensure precise control of each ferroic phase composition, atomic arrangements, and interfaces [6, 10, 21–23]. Moreover, it is crucial to accomplish magnetoelectric films presenting room-temperature coupling at a cost allowing their mass production and application in a wide variety of applications.

6.3 Meso- and Nanoporosity in Advanced Functional Materials

Since 1992, when it was discovered that the micellar and lyotropic liquid-crystal phases could behave as templates for the formation of mesoporous materials [24, 25], an explosive growth of research in this field has occurred envisaging their application in catalysis, as sorbents, gas sensors, photonics, etc. Many reports described mesostructured and mesoporous materials with different chemical compositions, in diverse morphologies, using a variety of synthetic routes and template molecules [26]. Initially mainly silica and aluminosilicate mesoporous materials with amorphous structures were reported [27]. The great attraction of mesoporous non-silica oxides started in 1995 when a porous powder TiO_2 network was first organized [28]. Since then a large effort has been dedicated to the preparation of mesoporous non-silica oxide thin films. The coexistence of crystallinity and

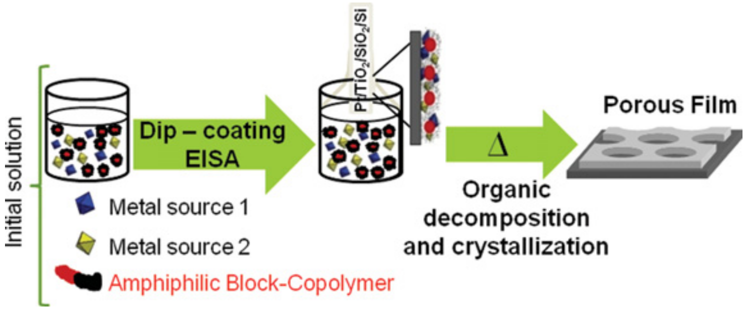

Figure 6.2 *Illustrative scheme describing the preparation method used to prepare porous thin films*

meso-ordering showed it to be notably difficult. A careful control of the chemical, processing, and treatment conditions on the synthesis are required to avoid the collapse of meso-ordering during the thermal crystallization. In 2004, a controlled process of preparation of ordered mesoporous crystalline networks and mesostructure nanoisland single layers, composed of multimetallic oxides having perovskite or ilmenite type structures was reported [29]. Nanocrystalline mesoporous films of $SrTiO_3$, $MgTa_2O_6$, and $Co_xTi_{(1\text{-}x)}O_{(2\text{-}x)}$ were then prepared, starting from metal chloride precursors and using a copolymer with higher chemical and thermal stability than the often used Pluronics. Careful control of the self-assembly (by in situ techniques) and of the kinetics allowed the preservation of meso-ordering and prevented cation separation during the crystallization.

Nanostructured multimetallic oxide porous thin films can be achieved by evaporation-induced self-assembly (EISA) [30]. In fact, this chemical-based methodology (Figure 6.2) offers excellent control of the physical and chemical properties of nanostructured materials such as stoichiometry, thickness, size, array, and porous distribution. Moreover, the self-assembly of block copolymers provides a versatile platform to prepare functional nanostructured materials, namely mesostructured oxide thin films, due to their capability to form large pores and thick walls, apart from being industrially available and hazard-free. The block copolymers are easy to remove from the mineral framework and have high thermal stability, avoiding the dehydration of the nanoporous network before organic decomposition.

The importance of this first work [29] lies in the fact that it opens the possibility of preparing a multitude of multimetallic oxide structures with ferroic properties as porous thin films. Evidence of the opportunity created by this fundamental work can be found in the literature, namely on studies reporting the synthesis of piezo and ferroelectric porous films of $BaTiO_3$ and $PbTiO_3$ [31, 32], PZT [33], and synthesis of magnetic mesoporous oxides such as $CoFe_2O_4$ [34, 35], $NiMo_2O_4$ [36], among others [37].

Besides the functional properties of these porous films by themselves, they are extremely promising to achieve multiferroic composites with applicable magnetoelectric coupling as typically porosity may be tuned to be vertically oriented, reducing the substrate clamping effect. Moreover, the high specific surface of this type of porous film may be very promising for composite formation. Additionally, this chemical-assembly method allows direct nanopatterning of large substrate areas with a functional oxide at a cost-effective price, in the absence of expensive equipment or etching processes (which typically affect negatively the ferroic properties).

In lieu of these opportunities we at CICECO of the University of Aveiro have been developing a pioneer work of preparing and characterizing ferroelectric porous thin-film matrices. The following subsection describes some of this work, in particular our observations in the systems of $PbTiO_3$ and $BiFeO_3$.

6.4 Nanoporosity in Ferroelectric Thin Films

6.4.1 Lead Titanate ($PbTiO_3$) – Nanoporous and Nanopatterned Thin Films

As mentioned before, due to their interesting properties, ferroelectric materials are widely used in the microelectronics industry as radio frequency (RF) devices, non-volatile memories, sensor and actuator applications, capacitors, and in tunable microwave circuits [11]. Nowadays, ferroelectric films are used in a number of commercial and widespread products including novel memories, microwave electronic components, and microdevices with pyroelectric and piezoelectric microsensors/actuators [11]. Up to now the most used inorganic ferroelectrics possess a perovskite-type structure, such as lead titanate ($PbTiO_3$), barium titanate ($BaTiO_3$), lead zirconium titanate ($Pb_xZr_{(1-x)}TiO_3$), and bismuth ferrite ($BiFeO_3$).

Among the most common preparation methods used to synthesize $PbTiO_3$ and $BiFeO_3$ are the sol–gel process, hydrothermal methods, organometallic chemical vapor deposition (MOCVD), or sputtering, being the most used nanolithographic techniques to prepare nanostructured thin films. Although these nanostructured thin films present well-defined structures, the application of such methods is limited by equipment high costs and difficulty to cover large surface areas. In addition, and importantly from the fabrication point of view, etching methods usually associated with lithographic techniques are typically harmful to the electric and magnetic properties of the ferroic materials.

Our work has been devoted to developing a strategy to prepare porous piezo- and ferroelectric thin films by dip-coating deposition of a sol–gel solution containing an amphiphilic block copolymer, followed by evaporation-induced self-assembly (EISA). Piezo- and ferroelectric thin films (about 100 nm thick) of barium titanate and lead titanate were prepared. Both film types presented functional properties at nanoscale. The drawback of this strategy was the partial loss of the organization of the porous structure during the thermal treatment required to achieve a tetragonal crystallographic structure for the ferroelectric phase [31]. This problem was more relevant for barium titanate films as the crystallization temperature to obtain the required tetragonality is significantly higher (700 °C) than the temperature of decomposition of the block copolymer (350 °C).

In order to understand the effect of porosity on the crystallization of tetragonal $PbTiO_3$, after the deposition of the sol–gel solution in silicon platinized substrates, we have followed the structural and morphological evolution of the films using different heat treatments. We have compared porous and dense counterparts with around 100 nm of thickness to investigate the differences between them. Figure 6.3 shows the scanning electron micrographs of the $PbTiO_3$ films upon treatment at 600 °C.

Extended bright areas are observed in the nanoporous films, which were associated with areas with a tetragonal structure as seen in the Raman spectrum (not shown). Moreover, these bright zones have a strong piezoelectric response. From these facts, we concluded

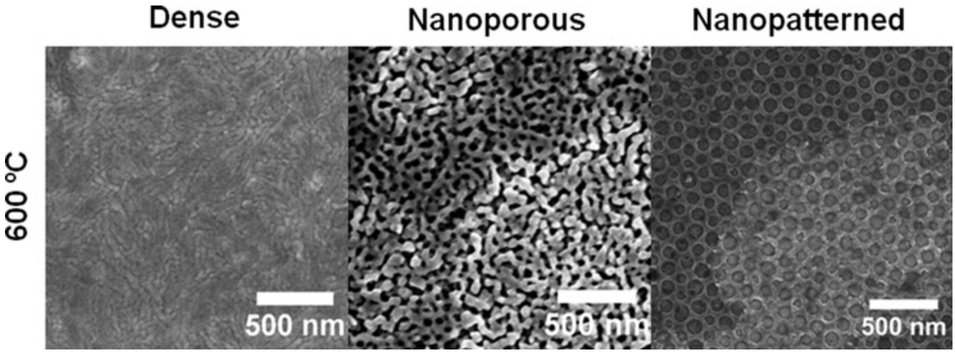

Figure 6.3 *SEM micrographs illustrating the typical morphology of dense, nanoporous, and nanopatterned* $PbTiO_3$ *thin films thermally treated at 600 °C. The dense thin film presents a crack-free surface with well-defined grains. The nanoporous thin film presents some interconnected pores, the porosity order is lost and bright areas appear. In the nanopatterned thin film the order and porosity over a large range remain, even in the bright areas, which correspond to the crystalline areas*

that nanoporosity acts as a facilitator of the crystallization of the tetragonal phase at lower temperatures when compared with the bulk dense counterparts [32]. We hypothesized that the presence of pores act as defect nucleation centers that trigger nucleation and crystallization, leading to the formation of the tetragonal phase in nanoporous films at lower temperatures than in dense ones. We also advocate that pores may facilitate the transport of oxygen to the nearby regions, promoting nucleation and crystallization. Hence under identical thermal conditions, porous films exhibit enhanced piezoelectric coefficients, switchable polarization, and low local coercivity (Table 6.1) [32]. Our observations in fact reveal an added value for the porous ferroelectric thin films not reported up to now.

Both nanoporous and dense $PbTiO_3$ thin films revealed well-defined hysteresis loops that clearly confirm the ferroelectric behavior at room temperature. Nevertheless, the hysteresis loops are not symmetric, since the positive and negative coercive fields and positive and negative remanent polarizations are not similar. This effect is known as imprint. The horizontal shift (coercive fields) provides a measure of the internal field, and the vertical shift (remanent polarizations) provides information on regions with frozen polarization, that can be associated with regions having a non-switching polarization and, therefore, a preferred polarization direction. Imprint behaviour can also be related to the self-polarization that depends, to a large extent, on the film deposition technology. In the case of sol–gel deposited films, it was reported that the self-polarization effect is thickness-dependent, suggesting that the alignment of domains occurs locally near the film–bottom electrode interface [38–40]. From our results the observed imprint can be associated with the incipient crystallization of the tetragonal phase. Thus, as the heat treatment temperature increases, the imprint effect slightly decreases for both thin films (nanoporous and dense). Imprint can also be related with the presence of defects in the films, including oxygen vacancies and surface/interface defects (e.g. lattice distortion due to the difference in the thermal expansion coefficient between the film and the substrate). From coercivity values of Table 6.1, it is observed that nanoporous films present values slightly lower when compared with the dense thin films,

Table 6.1 *Average values of coercivity, imprint, switchable polarization, and* $(d_{33})_{eff}$ *calculated from at least ten phases, amplitudes, and mixed hysteresis loops (Piezo Force Microscopy loops) for dense, nanoporous, and nanopatterned thin films. Switchable polarization corresponds to the difference between the positive saturated piezoresponse and negative ones* $(Rm = (RS)^{+} - (RS)^{-})$ *taken from the mixed hysteresis loops. The higher coercivity values present in nanopatterned thin films show how the ferroelectric behavior is affected by the low thickness of the nanopatterned thin films. However in terms of the vertical shift, nanopatterned thin films present a reduced imprint effect, probably due to the high-porosity area of this kind of structure. Consequently, the switchable polarization and* $(d_{33})_{eff}$ *coefficient are slightly higher than those obtained for dense ones, where the cross-talk effect provoked by the domain movement or thermal diffusion is not excluded*

	Thickness (nm)	Coercivity (V)	Imprint (V)	Imprint (pm V^{-1})	Switchable polarization (pm V^{-1})	$(d_{33})_{eff}$ (pm V^{-1})
Dense	100	2.5 ± 0.1	1.2 ± 0.1	31.8 ± 5.1	85.1 ± 2.0	35.7 ± 0.8
Nanoporous	100	2.4 ± 0.1	1.0 ± 0.1	16.7 ± 3.7	261.3 ± 6.6	148.8 ± 5.5
Nanopatterned	22	5.3 ± 0.5	1.3 ± 0.5	7.7 ± 2.1	137.6 ± 6.7	49.6 ± 0.7

suggesting that the crystallinity degree and porosity present in nanoporous films can affect the switching ability.

In terms of values of ferroelectric properties, nanoporous films exhibit enhanced piezoelectric coefficients and switchable polarization for the same thermal conditions. These observations suggest that the crystallinity degree and porosity present in nanoporous films affect the switching ability, leading to a reduction of the energy necessary to reorient the dipoles in the ferroelectric structures and, consequently, a reduction of coercivity when compared with dense films. On the other hand, as the porosity induces instability in the dipole–dipole interactions, the reverse polarization can be favored for low-bias values. This increase of the piezoelectric coefficient and decrease of the coercivity for nanoporous thin films is indeed a critically important result, since porosity can be used as a tool to tailor the coercive field of ferroelectric nanostructures.

By decreasing the thickness of the films from 100 to 20 nm, we were able to enhance the order of the nanostructured films, achieving highly ordered nanopatterned films with an hexagonal type arrangement of the pores [41]. Figure 6.3 presents an example of a top view scanning electron microscopy (SEM) micrograph of one of our nanopatterned 20 nm thick $PbTiO_3$ films. A long-range porous order over an extended coverage area was obtained. This film was crystallized at 600 °C, under carefully adjusted conditions to preserve the nanopatterning. Similar bright areas to the ones referred to above were present in these films. The nanoscale electric properties of the nanopatterned films are summarized in Table 6.1 and are compared to those of nanoporous films. The high coercivity value in the thinnest nanopatterned films clearly demonstrate how the ferroelectric behaviour is affected by the low thickness of the nanopatterned thin films. The reduced vertical shift (7.7 ± 2.1 pm V^{-1}) in the thinnest nanopatterned films is plainly visible. We hypothesized that this observation is related to the fact that the nanopatterned films have large pore diameters (ca. 82 nm), being the underneath platinum electrode almost 50% accessible. The piezoelectric coefficient and switchable polarization are lower than the ones of the 100 nm thick $PbTiO_3$ nanoporous films. The degradation of the electrical properties may result from the decrease of the film thickness with consequent reduction of the tetragonality. The decrease of the tetragonality leads to a drop on the spontaneous polarization of the films, due to a residual unscreened depolarization field. Comparing the values with the values reported for dense films it is possible to observe that the nanopatterned films present higher switchable polarization and $(d_{33})_{\text{eff}}$ piezoelectric coefficient than dense thin films. The strains of the substrate are probably of minor importance in nanopatterned compared to nanoporous and dense films.

6.4.2 Lead-Free Ferroelectric and Single-Phase Multiferroic – Bismuth Ferrite

Bismuth ferrite ($BiFeO_3$) is the only single-phase multiferroic presenting simultaneously magnetic and ferroelectric order at room temperature, thus considered as the multiferroic archetype and the most adequate recruit for the pursuit of solutions in multiferroic's perplexities. In addition it is lead free.

Its properties are a result of the two distorted perovskite blocks, connected along the pseudocubic [111], building a rombohedral unit cell. A clockwise and a counterclockwise rotation of the two oxygen octahedra connected along the [111], as well as a shift of the Fe ion also along the [111], are responsible for conferring spontaneous polarization [4, 16]. One of the most widely accepted theories accounting for the ferromagnetic ordering is the Dzyaloshinskii–Moriya interaction, which corresponds to spin-exchange in combination with the spin-orbit coupling, leading to canting of the magnetic sublattices [10, 42]. The $BiFeO_3$ ferroelectric Curie temperature is 1103 K and the antiferromagnetic Néel temperature is 643 K [43]. Concerning its chemical nature, $BiFeO_3$ is a metastable and off-stoichiometric compound, easily forming secondary phases, like Bi_2O_3, $Bi_2Fe_4O_9$, and sillenite $Bi_{25}FeO_{39}$ [44].

Considering the current environmental concerns and the rigid regulations towards the banishment of lead from most of the applications (European Directive 2002/95/EC and California Health and Safety Code 25214.9–25214.10.2), the use of more environment-friendly materials has been pursued. Within this context $BiFeO_3$ as well as some other niobate- and titante-based ferroelectrics are being considered promising as lead-free ferroelectrics. The large remnant polarization of $BiFeO_3$ (100 μC cm^{-2} along the polar [111] direction) is the biggest known switchable polarization in perovskites and is almost double the remanent polarization of PZT [16].

Within this context we have prepared by EISA, using nitrate metal salts and a commercial block copolymer as the structure-directing agent, nanopatterned thin films of $BiFeO_3$ with large vertical porosity [45]. Similarly to $PbTiO_3$, these observations provide evidence that the sol–gel based method can be successfully used to achieve crystalline and well-organized nanopatterned $BiFeO_3$ surfaces with an average pores size of ca. 100 nm and 65 nm of thickness at 600 °C (Figure 6.4). A dense film counterpart with similar thickness was prepared and treated in the same thermal conditions (Figure 6.4). A vertical porosity towards the substrate is observed in the nanopatterned films.

Comparing the hysteresis loops measured in a single grain of both nanopatterned and dense films (Figure 6.5(e)) significant differences can be identified. The coercivity and the effective piezoelectric coefficient $(d_{33})_{\text{eff}}$ are estimated to be respectively around 5.5 ± 0.4 V and 69.8 ± 2.5 pm V^{-1} (in nanopatterned thin film) and 6.3 ± 0.9 V and 28.9 ± 1.8 pm V^{-1} (in dense thin film). The lowest coercivity in nanopatterned thin films means an easier

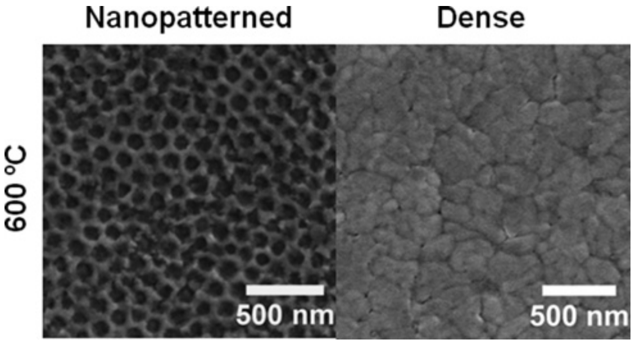

Figure 6.4 *SEM micrographs of nanopatterned and dense BiFeO$_3$ thin films thermally treated at 600 °C for 5 min. The nanopatterned thin film treated at 600 °C presents some interconnected pores, but the order and porosity over a large range remain. Dense thin films are crack-free with a bigger grain size than nanopatterned films*

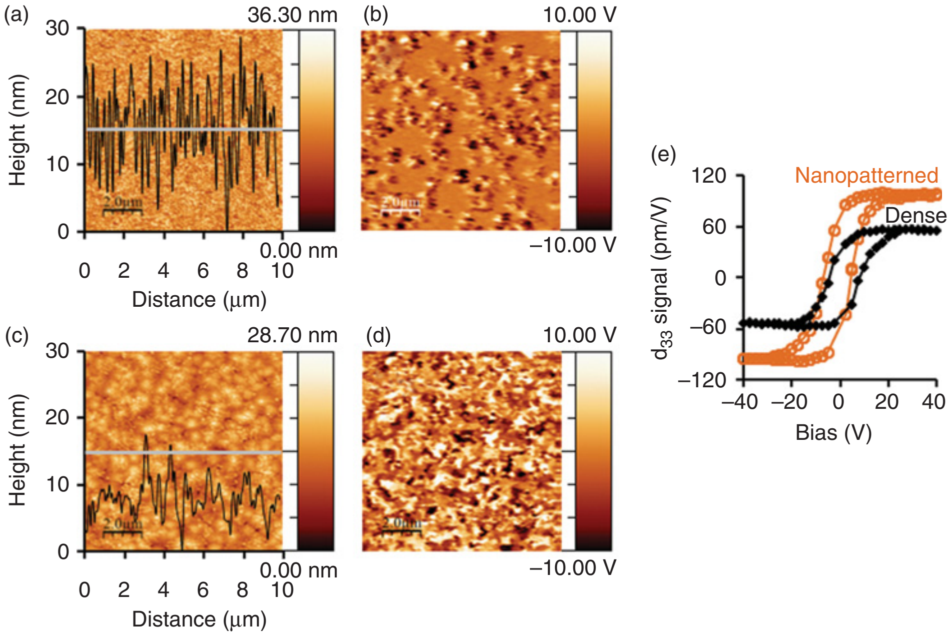

Figure 6.5 *Topography and VPFM mixed signal images for nanopatterned (a and b) and dense (c and d) thin films thermally treated at 600 °C, respectively. The data scale for VPFM mixed signal image ranges from −10 to 10 V. This 20 V scale corresponds to 360°, thus opposite domains oscillate 180° out of phase, as expected. The representative remanent local hysteresis loops obtained for both thin films are presented in (e). The circles correspond to the nanopatterned thin films and the lozenges to the dense ones. Nanopatterned thin films present enhanced ferroelectric properties as a consequence of its porous structure. The line profiles along the gray line present in the image (a) and (c) reveals the roughness difference between the well-defined porous order of the nanopatterned and the flat surface of the dense thin films*

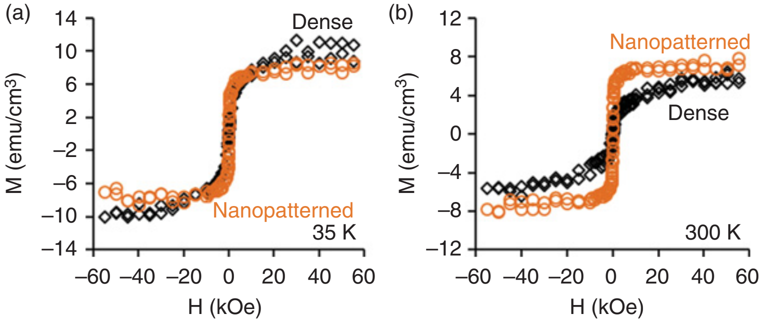

Figure 6.6 In-plane magnetic properties of the nanopatterned and dense thin films thermally treated at 600 °C, where (a) and (b) are the hysteresis loops at 35 and 300 K. The circles correspond to the nanopatterned thin films and the lozenges to the dense ones. At room temperature nanopatterned thin films present enhanced ferromagnetic properties. The nanoporosity inhibits the typical antiferromagnetic behavior of the nanopatterned $BiFeO_3$ thin films

polarization switch. On the other side the highest $(d_{33})_{\mathrm{eff}}$ value of nanopatterned thin film reveals the enhancement of the nanoscale electric properties in the presence of nanopatterned porosity. Comparing the obtained values with the literature, the $(d_{33})_{\mathrm{eff}}$ value for nanopatterned thin films is in good agreement with the $(d_{33})_{\mathrm{eff}}$ values reported for epitaxial $BiFeO_3$ thin films with a tetragonal phase [43] and for heteroepitaxially constrained $BiFeO_3$ thin films [46].

The vertical large porosity orients electrical domains and reduces the necessary energy to reorient the dipoles. The induced instability in the dipole–dipole interactions results in an increase of the effective piezoelectric coefficient, $(d_{33})_{\mathrm{eff}}$. On the other hand, the porous structure can accommodate more domains partly uncompensated, which may be situated at the edge of the pore, showing that magnetic anisotropy within the nanopatterned thin films can overcome the shape anisotropy to produce a higher remanent magnetization (Figure 6.6). The vertical porosity thus inhibits the typical antiferromagnetic behavior, leading to a ferromagnetic signal around 50% stronger than the ferromagnetic component obtained for the counterpart dense film.

6.5 Looking Ahead

In the last decade the functional oxides community has been concerned in developing new methods to afford efficient multiferroic oxide-based nanocomposites through direct chemical-based bottom-up nanopatterning of functional oxides over extensive substrate areas.

Our work proves that the deposition of a solution containing an amphiphilic block copolymer, inorganic precursors, and volatile solvents by EISA permits the formation of nanopatterned thin films with tunable thickness and ordered porosity. The deep understanding on the way porosity affects the ferroic properties is, however, needed, since it will allow the definition of optimized conditions aimed at enhanced performance.

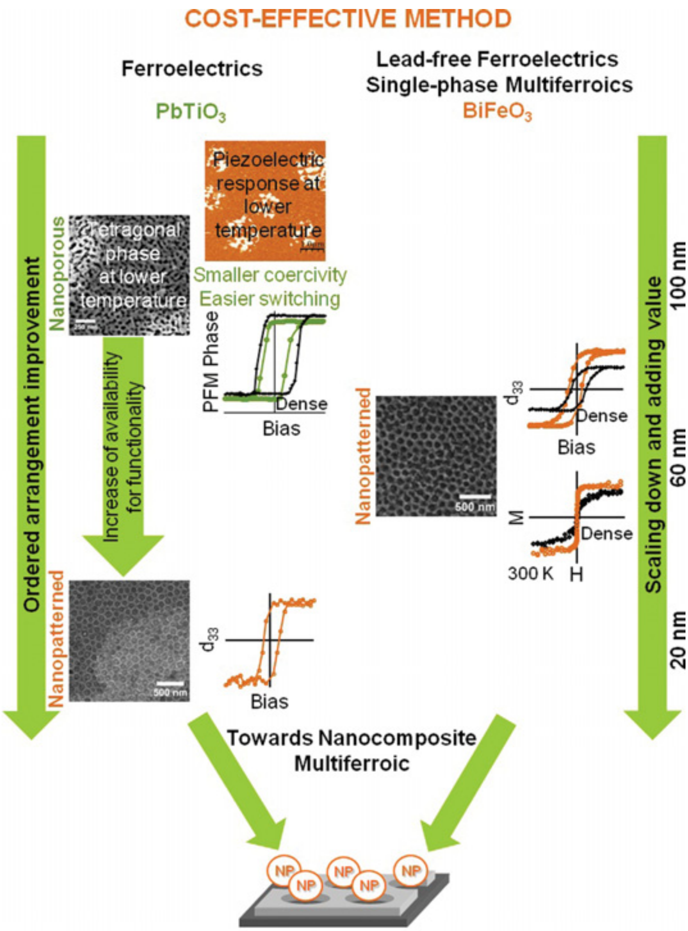
COST-EFFECTIVE METHOD
Ferroelectrics
PbTiO3
Lead-free Ferroelectrics
Single-phase Multiferroics
BiFeO3
Ordered arrangement improvement
Nanoporous
Tetragonal phase at lower temperature
Piezoelectric response at lower temperature
Smaller coercivity
Easier switching
PFM Phase
Dense
Bias
Increase of availability for functionality
Nanopatterned
500 nm
d33
Bias
Nanopatterned
500 nm
d33
Dense
Bias
M
Dense
300 K
H
Scaling down and adding value
100 nm
60 nm
20 nm
Towards Nanocomposite Multiferroic
NP

Figure 6.7 *Strategy to achieve functional nanocomposite multiferroics*

Our strategy can also be viewed as a new concept to prepare multiferroic nanocomposite thin films. Figure 6.7 is the illustration of the state-of-the-art research of our group and looks out over future nanocomposite multiferroic structures with enhanced cross-coupling properties, which need to be cost-effective.

Indeed, if the vertical ordered porosity of the ferroelectric/single-phase multiferroic matrix is filled with ferromagnetic nanoparticles and interfaces are improved, we should be able to enhance the magnetoelectric coupling of the composite. According to preview studies [19], the transition from substrate strain control to vertical strain control occurs when the vertical interface area within ferroic phases exceeds the one with the substrate. Extrapolating the latest study results to our nanopatterned thin films, we expected control of the vertical strains over the lateral ones in all of our films as their thickness is always lower than half of the diameter of the vertical pore.

Important features to be taken into account are the good crystallinity, especially of the ferroelectric phase, and the quality of the interfaces. It is important that the integrity of each ferroic phase is preserved. In this way, the ferroic phases must be carefully selected, including cations with ionic radium sufficiently different, in order to avoid the intermixing of the phases during full crystallization of ferroic crystallographic phases and/or interface improvement.

Acknowledgments

This work was developed within the scope of the Project CICECO–Aveiro Institute of Materials POCI-01-0145-FEDER-007679 (Ref. FCT UID/CTM/50011/2013), financed by Portuguese funds through the FCT/MEC and when applicable co-financed by FEDER under the PT2020 Partnership Agreement. The authors are grateful to FCT and POPH/FSE, for doctoral fellowship SFRH/BD/67121/2009 and investigator fellowship IF/00327/2013. Some of the measurements were performed on equipment funded by the Science Foundation Ireland (SFI07/IN1/B931). COST Action MP0904 SIMUFER is acknowledged for funding the Short Term Scientific Mission of A. Castro.

References

(1) *International Technology Roadmap for Semiconductors 2012* (ITRS 2012).
(2) Kim, A., Son Choi, E., Hyungbin, P., and Sung, G. (2014) Development and applications of 3-dimensional integration nanotechnologies. *Journal of Nanoscience and Nanotechnology*, **14**, 2001–2011.
(3) *Matrix® 3-D Memory (3DM)*, SanDisk. Accessed at: http://www.sandisk.com/.
(4) Martin, L.W., Crane, S.P., Chu, Y.H., et al. (2008) Multiferroics and magnetoelectrics: thin films and nanostructures. *Journal of Physics: Condensed Matter*, **20**, art. no. 434220.
(5) Eerenstein, W., Mathur, N.D., and Scott, J.F. (2006) Multiferroic and magnetoelectric materials. *Nature*, **442**, 759–765.
(6) Ma, J., Hu, J., Li, Z., and Nan, C.W. (2011) Recent progress in multiferroic magnetoelectric composites: from bulk to thin films. *Advanced Materials*, **23**, 1062–1087.
(7) Schmid, H. (2001) On ferrotoroidics and electrotoroidic, magnetotoroidic and piezotoroidic effects. *Ferroelectrics*, **252**, 41–50.
(8) Gajek, M., Bibes, M., Fusil, S., et al. (2007) Tunnel junctions with multiferroic barriers. *Nature Materials*, **6**, 296–302.
(9) Scott, J.F. (2007) Multiferroic memories. *Nature Materials*, **6**, 256–258.
(10) Scott, J.F. (2012) Applications of Magnetoelectrics. *Journal of Materials Chemistry*, **22**, 4567–4574.
(11) Setter, N., Damjanovic, D., Eng, L., et al. (2006) Ferroelectric thin films: review of materials, properties, and applications. *Journal of Applied Physics*, **100**, art. no. 051606.
(12) Lichtensteiger, C., Dawber, M., and Triscone, J.M. (2007) Ferroelectric size effects, in *Physics of Ferroelectrics: A Modern Perspective*, edited by K. Rabe, C.H. Ahn, and J.M. Triscone, Springer-Verlag, Berlin, Heidelberg, pp. 305–338.

(13) Rabe, K.M., Dawber, M.P., Lichtensteiger, C., et al. (2007) Modern physics of ferroelectrics: essential background, in *Physics of Ferroelectrics: A Modern Perspective*, edited by K. Rabe, C.H. Ahn and J.M. Triscone), Springer-Verlag Berlin Heidelberg, pp. 1–30.

(14) Ramesh, R. and Spaldin, N.A. (2007) Multiferroics: progress and prospects in thin films. *Nature Materials*, **6**, 21–29.

(15) Wang, Y., Hu, J., Lin, Y., and Nan, C.W. (2010) Multiferroic magnetoelectric composite nanostructures. *NPG Asia Materials*, **2**, 61–68.

(16) Catalan, G. and Scott, J.F. (2009) Physics and applications of bismuth ferrite. *Advanced Materials*, **21**, 2463–2485.

(17) Zheng, H., Wang, J., Lofland, S.E., et al. (2004) Multiferroic $BaTiO_3$–$CoFe_2O_4$ nanostructures. *Science*, **303**, 661–663.

(18) Vaz, C.A.F., Hoffman, J., Ahn, C.H., and Ramesh, R. (2010) Magnetoelectric coupling effects in multiferroic complex oxide composite structures. *Advanced Materials*, **22**, 2900–2918.

(19) MacManus-Driscoll, J.L., Zerrer, P., Wang, H., et al. (2008) Strain control and spontaneous phase ordering in vertical nanocomposite heteroepitaxial thin films. *Nature Materials*, **7**, 314–320.

(20) Levin, I., Li, J., Slutsker, J., and Roytburd, A.L. (2006) Design of self-assembled multiferroic nanostructures in epitaxial films. *Advanced Materials*, **18**, 2044–2047.

(21) Andrew, J.S., Starr, J.D., and Budi, M.A.K. (2014) Prospects for nanostructured multiferroic composite materials. *Scripta Materialia*, **74**, 38–43.

(22) Marchack, N. and Chang, J.P. (2012) Chemical processing of materials on silicon: more functionality, smaller features, and larger wafers. *Annual Review of Chemical and Biomolecular Engineering*, **3**, 235–262.

(23) Kim, Y., Pham, C., and Chang, J.P. (2015) Potentials and challenges of integration for complex metal oxides in CMOS devices and beyond. *Journal of Physics D: Applied Physics*, **48**, art. no. 063001.

(24) Kresge, C.T., Leonowicz, M.E., Roth, W.J., et al. (1992) Ordered mesoporous molecular sieves synthesized by a liquid–crystal template mechanism. *Nature*, **359**, 710–712.

(25) Beck, J.S., Vartuli, J.C., Roth, W.J., et al. (1992) A new family of mesoporous molecular sieves prepared with liquid crystal templates. *Journal of the American Chemical Society*, **114**, 10834–10843.

(26) Sanchez, C., Boissière, C., Grosso, D., et al. (2008) Design, synthesis, and properties of inorganic and hybrid thin films having periodically organized nanoporosity. *Chemistry of Materials*, **20**, 682–737.

(27) Soler-Illia, G.J.A.A., Sanchez, C., Lebeau, B., and Patarin, J. (2002) Chemical strategies to design textured materials: from microporous and mesoporous oxides to nanonetworks and hierarchical structures. *Chemical Reviews*, **102**, 4093–4138.

(28) Antonelli, D.M. and Ying, J.Y. (1995) Synthesis of hexagonally packed mesoporous TiO_2 by a modified sol–gel method. *Angewandte Chemie International Edition*, **34**, 2014–2017.

(29) Grosso, D., Boissière, C., Smarsly, B., et al. (2004) Periodically ordered nanoscale islands and mesoporous films composed of nanocrystalline multimetallic oxides. *Nature Materials*, **3**, 787–792.

(30) Grosso, D., Cagnol, F., Soler-Illia, G.J.A.A., et al. (2004) Fundamentals of mesostructuring through evaporation-induced self-assembly. *Advanced Functional Matererials*, **14**, 309–322.

(31) Ferreira, P., Hou, Z.R., Wu, A., et al. (2012) Nanoporous piezo- and ferroelectric thin films. *Langmuir*, **28**, 2944–2949.

(32) Castro, A., Ferreira, P., Rodriguez, B., and Vilarinho, P.M. (2015) The role of nanoporosity on local piezo and ferroelectric properties of lead titanate thin films. *Journal Material Chemistry C*, **3**, 1035–1043.

(33) Reitz, C., Leufke, P.M., Hahn, H., and Brezesinski, T. (2014) Ordered mesoporous thin film ferroelectrics of biaxially textured lead zirconate titanate (PZT) by chemical solution deposition. *Chemistry of Materials*, **26**, 2195–2202.

(34) Quickel, T.E., Le, V.H., Brezesinski, T., and Tolbert, S.H. (2010) On the correlation between nanoscale structure and magnetic properties in ordered mesoporous cobalt ferrite ($CoFe_2O_4$) thin films. *Nano Letters*, **10**, 2982–2988.

(35) Haetge, J., Suchomski, C., and Brezesinski, T. (2010) Ordered mesoporous MFe_2O_4 (M = Co, Cu, Mg, Ni, Zn) thin films with nanocrystalline walls, uniform 16 nm diameter pores and high thermal stability: template-directed synthesis and characterization of redox active trevorite. *Inorganic Chemistry*, **49**, 11619–11626.

(36) Haetge, J., Djerdj, I., and Brezesinski, T. (2012) Nanocrystalline $NiMoO_4$ with an ordered mesoporous morphology as potential material for rechargeable thin film lithium batteries. *Chemical Communications*, **48**, 6726–6728.

(37) Reitz, C., Suchomski, C., Haetge, J., et al. (2012) Soft-templating synthesis of mesoporous magnetic $CuFe_2O_4$ thin films with ordered 3D honeycomb structure and partially inverted nanocrystalline spinel domains. *Chemical Communications*, **48**, 4471–4473.

(38) Alexe, M., Harnagea, C., Hesse, D., and Gösele, U. (2001) Polarization imprint and size effects in mesoscopic ferroelectric structures. *Applied Physics Letters*, **79**, 242–244.

(39) Kholkin, A.L., Brooks, K.G., Taylor, D.V., et al. (1998) Self-polarization effect in $Pb(Zr,Ti)O_3$ thin films. *Integrated Ferroelectrics*, **22**, 525–533.

(40) Frey, J., Schlenkrich, F., and Schönecker, A. (2001) Self-polarization and texture of wet chemically derived lead zirconate titanate thin films. *Integrated Ferroelectrics*, **35**, 105–113.

(41) Castro, A., Ferreira, P. and Vilarinho, P.M. Sustainable bottom-up nanopatterning of lead titanate for advanced electronic, submitted.

(42) Ederer, C. and Spaldin, N.A. (2005) Weak ferromagnetism and magnetoelectric coupling in bismuth ferrite. *Physical Review B*, **71**, art. no. 060401.

(43) Wang, J., Neaton, J.B., Zheng, H., et al. (2003) Epitaxial $BiFeO_3$ multiferroic thin film heterostructures. *Science* **299**, 1719–1722.

(44) Lahmar, A., Zhao, K., Habouti, S., et al. (2011) Off-stoichiometry effects on $BiFeO_3$ thin films. *Solid State Ionics*, **202**, 1–5.

(45) Castro, A., Martins, M.A., Ferreira, L.P., et al. Scalable cost-effective nanopatterned multifunctional $BiFeO_3$ thin films, submitted.

(46) Chu, Y.H., Zhao, T., Cruz, M.P., et al. (2007) Ferroelectric size effects in multiferroic $BiFeO_3$ thin films. *Applied Physics Letters*, **90**, art. no. 252906.

7

Low-Temperature Photochemical Solution Deposition of Ferroelectric and Multiferroic Thin Films

Christopher De Dobbelaere[1], An Hardy[1], Marlies K. Van Bael[1], Iñigo Bretos[2], Ricardo Jiménez[2], and M. Lourdes Calzada[2]

[1] *Inorganic and Physical Chemistry Group, Institute for Materials Research, Universiteit Hasselt and imec vzw, Division imomec, Belgium*
[2] *Instituto de Ciencia de Materiales de Madrid (ICMM), Consejo Superior de Investigaciones Científicas (CSIC), Spain*

7.1 Introduction

The synthesis of functional materials is currently moving towards low-temperature routes due to environmental and economic reasons. Specifically, the growing number of applications for oxide layers on semiconductor and flexible substrates and for organic–inorganic composites or hybrid materials has largely fueled the current efforts devoted to the low-temperature fabrication of these materials [1].

For solution-based precursor systems, chemical solution deposition (CSD) routes are the most common ones for the deposition of electronic oxide thin films [2]. Moreover, low-temperature solution processed metal oxides have turned out to be an enabling technology for the cost-effective integration of high-performance functional layers into devices. To date, major efforts are focused on oxide semiconductors, where advanced solution methods are being investigated to reduce the formation temperature of the crystalline semiconductor phase, making the preparation of these oxides compatible with low melting point substrates

---

Nanoscale Ferroelectrics and Multiferroics: Key Processing and Characterization Issues, and Nanoscale Effects, First Edition. Edited by Miguel Algueró, J. Marty Gregg, and Liliana Mitoseriu.
© 2016 John Wiley & Sons, Ltd. Published 2016 by John Wiley & Sons, Ltd.

[3]. The crystalline state strongly improves the characteristics of semiconductor oxides, and it is also a requisite for most physical properties of many other oxides. This is the case of inorganic ferroelectric and multiferroic compounds, for which the functional response is intrinsically linked to their non-centrosymetric crystal structure. In this case, the limitation for their integration with semiconductors is the high crystallization temperature necessary to obtain the desired crystal phase, typically over 600 °C [4,5]. Nevertheless, the perspective of the integration of active, non-semiconductor layers into Si-technology or flexible electronics to increase the device functionality offers a major opportunity for these oxide thin films. Their intrinsic multifunctionality (ferro-, pyro-, and piezoelectricity, and even ferromagnetism in the case of multiferroics) enables diverse operations in electronic devices such as memories, sensors, actuators, transducers, or detectors, realizing new applications which were not possible before (e.g. smart skin, flexible sensitive displays, photovoltaic cells, or eye-type imagers) [6–11].

In this scenario, solution deposition techniques provide the unique advantage of tailoring the solution chemistry to decrease the Gibbs free energy barrier for the formation of the crystalline oxide layer and, therefore, its integration with the substrate [2]. Among the different low-temperature deposition methods for ferroelectric and multiferroic oxide thin films reported in the literature, special attention has been paid to those based on chemical solution deposition [12–26], among which seeded solutions [16, 27, 28], crystal growth under high (oxygen) pressure [29, 30], microwave annealing [24, 31], or solution combustion synthesis [10] are being actively explored.

A low-temperature processing method for inorganic ferroelectric thin oxide films is considered successful if the applied temperature is below the requirement for its integration into CMOS (complementary metal–oxide–semiconductor) technology [32]. In this case, the resulting films should ideally display values of the switching charge density close to those demanded for practical applications such as non-volatile ferroelectric random access memories (NVFeRAMs; 12 μC cm^{-2} by 2020, according to the International Technology Roadmap for Semiconductors (ITRS)) [32]. A further step towards the universal applicability of the low-temperature process would involve annealing temperatures close to those applied for oxide semiconductors [33–35] or organic ferroelectrics [36–38] (below 300 °C). Because these temperatures are still a long way off for inorganic ferroelectrics, the challenge at this point is the use of annealing temperatures within the thermal stability of semiconductors and flexible polymer substrates, of 450 and 400 °C, respectively [32–34].

Specifically, photochemical solution deposition (PCSD) is a successful low-temperature solution-based deposition method for complex oxide thin films [15, 17, 22, 23, 26]. This route combines the use of a light-sensitive sol(ution) with UV irradiation. UV light susceptible precursors contain UV-absorber molecules or fragments that are at least present in the as-deposited layer. The typical penetration depth of UV photons is limited to the surface region of condensed matter [15, 17]; thus the effectiveness of UV irradiation would be optimum in deposited thin gel layers. Energetic photons coming from the UV source electronically excite the chemical bonds of these photosensitive compounds, which enhances their decomposition and promotes the formation of the crystalline oxide at a reduced temperature [15, 17, 23, 26].

This chapter reviews our activity on the development of different solution-based methods to attain photosensitive precursors for complex oxide material synthesis (ferroelectric and multiferroic compounds in particular). We take advantage of the photoreactivity of the layers deposited from these solutions to prepare functional crystalline oxide thin films at the low temperatures currently demanded for their integration with Si technologies and flexible electronics.

7.2 Low-Temperature Processing of Ferroelectrics and Multiferroics

For the preparation of functional oxide films by means of CSD, a thermal treatment is necessary to convert the as-deposited amorphous layer into a crystalline film. The crystallization of ferroelectric or multiferroic oxides typically requires temperatures above 600 °C [4, 5]. Two important undesirable phenomena occur at these high temperatures: (i) the interdiffusion between film and substrate, which could result in the formation of secondary phases at the substrate–film interface and (ii) the volatilization of high vapor pressure elements, resulting in non-stoichiometric surface compositions [39]. Both the substrate–film interface layer and surface non-stoichiometry are detrimental for the properties of the ferroic thin film. These problems should be added to those derived from the use of high thermal budgets in the current semiconductor technology, which mainly are cross-contamination and circuitry degradation in the device [32]. Moreover, problems will exacerbate if flexible substrates are being used, for example plastics, textiles, or paper. Also, these challenges are difficult to tackle for films of most important ferroelectric compositions, which contain diffusible and high vapor pressure elements such as lead or bismuth and additionally require high crystallization temperatures to form the desired crystal phase [39–41].

Related to the technological interest of preparing ferroelectric thin oxide films at low temperature, the environmental and economic impact of the fabrication process should be considered. High annealing temperatures might result in the emission of toxic volatiles and elevated energy costs. Therefore, these considerations are pushing the low-temperature processing of ferroic thin films forward, while performance demands for current microelectronic devices are maintained.

7.3 Low Environmental Impact Precursor Chemistry

Environmental awareness pushes research towards more thoughtful processing. This results in an increasing interest for life cycle assessments (LCAs) [42, 43], environmental, health and safety (EHS) [44] properties, and cost–benefit analyses. Nevertheless, not only the hazards (e.g. toxicity and flammability) [44] but also the physicochemical properties of solvents have to be taken into account when adapting a chemical process, in addition to economic aspects such as recovery characteristics and possible reuse. Generally, technical advantages should be balanced with any environmental danger, financial cost, or other disadvantage [45].

Although a solvent-free environment is envisaged, functional oxide materials syntheses still benefit from "wet chemistry" for the preparation of their precursors. For ferroelectric and multiferroic oxide materials, 2-methoxyethanol [46, 47], 1,3-propanediol [48, 49], and water [50–53] are often the solvents of choice because of favorable quantitative properties such as the dielectric constant, dipole moment, and solvatochromic parameters, such as the Kamlet–Taft [54] and the ET(30) parameters [55]. Nevertheless, 2-methoxyethanol is a possible teratogen [56, 57], it contributes to photochemical smog formation, and is indicated by the *United States' Clear Air Act* as to be avoided. Diol-based routes use non-toxic dihydroxy alcohols as their solvent and have a very low environmental impact [58]. However, water is probably the greenest, most benign solvent available. Due to its high polarity, dielectric constant, and extensive hydrogen bonding, it is a popular medium for water-based precursor systems in which ionic compounds are initially dissolved. Nevertheless, water has a high heat capacity that causes heating or cooling of aqueous phases to be energy demanding. Also, its purification is difficult, as organic compounds have a very low degree of solubility in water.

In addition to the solvent, the toxicity of the metal reagents is also taken into consideration. Nowadays, the development of less hazardous compounds is considered a crucial challenge in the electronic industry, where legislations enforce the use of alternative non-hazardous materials [59]. In the particular case of ferroelectrics, strong efforts are underway in the direction of finding lead-free alternatives to the commercially applied lead zirconate titanate, $Pb(Zr_x,Ti_{1-x})O_3$ (PZT) [60, 61]. Limitations for these compounds are often related to the high annealing temperatures necessary to crystallize the perovskite phase in the desired crystal structure.

Here we will introduce and discuss the application of two environmental benign solvents, that is water and 1,3-propanediol, within the PCSD route. These solution-based routes have been applied mainly to the preparation of lead-based and bismuth-based perovskite thin films (e.g. $PbTiO_3$ and $BiFeO_3$), but the general concept is transferrable to the preparation of other oxides as well.

7.4 Aquous Solution–Gel Precursors

Water is probably the most benign solvent available. Nevertheless, dissolving metal ions in aqueous media is challenging. In this paragraph, the approach to stabilize metal ions by the introduction of chelating agents in water will be presented. This is the foundation of the aqueous solution–gel route.

7.4.1 Metal Ions in Water

Once brought into water, metal ions will be subjected to solvation, hydrolysis and condensation reactions. The extent will depend on the kind of metal ion and will determine if the ion can stay freely in solution or will polymerize and/or eventually precipitate [62–64].

7.4.1.1 Solvation and Hydrolysis

Cations of a metal, M, will be solvated by surrounding water molecules, forming aqua complexes:

$$M^{z+} + N\mathrm{H_2O} \rightarrow \left[M(\mathrm{OH_2})_N\right]^{z+} \tag{7.1}$$

The charge or the oxidation state of the cation and the coordination number are respectively indicated as $z+$ and N. The amount of water molecules involved is related to the size and charge of the cation, z/r^2, where r is the radius of M^{z+} [65, 66]. The water molecules in the first solvation shell are in direct contact with the metal ion and are involved in possible hydrolysis and condensation reactions. Molecules in the second or higher solvation shells are constantly being interchanged with the solvent and thus do not participate in further reactions.

The formed aqua complexes can release a proton depending on the size and the charge of the cation and the acidity of the medium. Thus, the cation is involved in an equilibrium in which aqua (H_2O), hydroxo (HO^-) or oxo ligands (O^{2-}) can be formed in the coordination shell [63]:

$$\left[M-\mathrm{OH_2}\right]^{z+}\overset{\mathrm{H_2O}}{\longleftrightarrow}[M-\mathrm{OH}]^{(z-1)+}+\mathrm{H_3O^+}\overset{\mathrm{H_2O}}{\longleftrightarrow}[M-\mathrm{O}]^{(z-2)+}+2\mathrm{H_3O^+} \tag{7.2}$$

Or, more generally:

$$\left[M\left(\mathrm{OH_2}\right)_N\right]^{z+}+h\mathrm{H_2O}\leftrightarrow\left[M(\mathrm{OH})_h\left(\mathrm{OH_2}\right)_{N-h}\right]^{(z-h)+}+h\mathrm{H_3O^+} \tag{7.3}$$

If h, the hydrolysis, equals 0, no hydrolysis occurs, no protons are released, and the cation is a pure aqua complex. As h equals $2N$, all protons are released, forming a pure oxo complex: $[MO_N]^{(z-2N)+}$. In between those extrema, aqua–hydroxo complexes $[M(OH)_h(OH_2)_{N-h}]^{(z-h)+}$ ($0 < h < N$), hydroxo complexes $[M(OH)_N]^{(z-N)+}$ ($h = N$), or oxo–hydroxo complexes $[MO_{h-N}(OH)_{2N-h}]^{(z-h)+}$ ($N < h < 2N$) are formed. The hydrolysis state of the cation can be derived from the pH of the medium [64]:

$$h=\left(\frac{1}{1+0.0138\cdot\mathrm{pH}}\right)\left[(1.36z)+N(0.038\cdot\mathrm{pH}-0.25)-\frac{2.62-0.02\cdot\mathrm{pH}-\chi_M^*}{\sqrt{\chi_M^*}}\right] \tag{7.4}$$

where χ_M^* is the Allred–Rochow electronegativity of the cation. Equation (7.4) allows the amount of H^+ ions to be theoretically determined when M^{z+} is brought into solution and to evaluate the base–acid behavior of the cation in an aqueous medium [62]. This model agrees well with empirical results [63].

For any metal cation, the species present in an aqueous medium in a function of the pH value can differ. This is presented in a so-called charge–pH diagram (Figure 7.1), making the assumption that only aqua ligands are present [63, 67]. The z-pH domain with H_2O, OH^- or O^{2-} ligands are respectively called the aqua, the hydroxo, or the oxo domain.

The decisive factor for the level of hydrolysis and coordination of metal M is the charge of the cation, z. Note that, for example, tetravalent cations ($z = 4$) lie in a boundary region and thus can adopt various hydrolysis products. The boundary of the aqua–hydroxo formation $[M(OH_2)_{(N-1)}(OH)_1]^{(z-1)+}$ and oxo–hydroxo formation $[M(O)_{N-1}(OH)_1]^{(z-2N+1)+}$ in a function of pH and charge can be obtained using Equation (7.4), assuming $h = 1$ and $h = 2N - 1$, respectively.

7.4.1.2 Condensation

Condensation reactions convert monomeric hydrolysis units into more complex structures by inorganic polymerization reactions. These reactions occur in three steps: initiation, propagation, and termination [62].

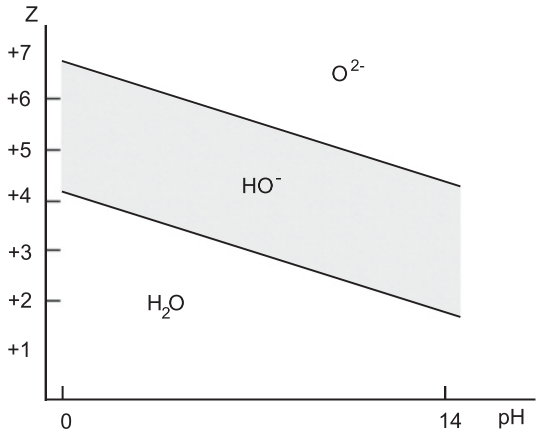

Figure 7.1 *Ligands in the coordination shell of the cation as a function of the charge z and the pH*

Initiation. Only complexes in the hydroxo domain of Figure 7.1 are eligible for condensation as nucleophilic hydroxo ligands (OH^-) are necessary to initiate polymerization. The electrophilic character of the metal cation has to be high and positive in order to participate in the condensation reaction. Empirical work has demonstrated that the following requirements have to be met (δ is the partial charge) [64]:

$$\delta(\mathrm{OH}) < 0 \text{ and } \delta(M) > 0.3 \tag{7.5}$$

Propagation. Olation and oxolation are respectively responsible for the introduction of a hydroxo, *M*–OH–*M*, or oxo bridge, *M*–O–*M*, between hydrolyzed metal cations. Which reaction occurs is determined by the type of hydrolysis complex in solution.

Olation occurs according to a two-step dissociative nucleophile substitution reaction (S_N1):

$$M-\mathrm{OH}+M-\mathrm{OH_2} \rightarrow M-\mathrm{OH}\cdots M+\mathrm{H_2O} \rightarrow M-\mathrm{OH}-M+\mathrm{H_2O} \tag{7.6}$$

The aqua ligand leaves the coordination shell, leaving an unsaturated coordination behind. This intermediate reacts with the negatively charged hydroxo group of the incoming nucleophile, forming an *–OH–* bridge between two metal cations. This reaction typically occurs for aqua-hydroxo complexes $[M(OH)_h(OH_2)_{N-h}]^{(z-h)+}$ ($0<h<N$) if $\delta(H_2O) < 0$. The reaction rate increases with decreasing charge *z* and increasing radius *r*, thus for a lower polarizing character of the cation.

Oxolation occurs according to an associative nucleophilic substitution reaction (S_N2):

$$M-\mathrm{OH}+M-\mathrm{OH} \rightarrow M-\mathrm{OH}-M-\mathrm{OH} \rightarrow M-\mathrm{O}-M-\mathrm{OH_2} \rightarrow M-\mathrm{O}-M+\mathrm{H_2O} \tag{7.7}$$

Nucleophilic addition of the hydroxo ligand on the electrophile metal initiates the reaction. The hydrogen atom on the temporary “ol” bridge is more acid than the hydrogen atom on the terminal hydroxo group of the attacked metal ion. Proton transfer to the terminal hydroxo group creates an aqua ligand, which will act as a leaving group if

$\delta(H_2O) > 0$, forming an –O– bridge between two metal cations. Oxolation reactions usually occur if no aqua ligands are present in the coordination shell, that is for oxo, hydroxo, and oxo–hydroxo complexes: $MO_{h-N}\,(OH)_{2N-h}^{(z-h)+}$ $(N \leq h \leq 2N)$ with a high oxidation state.

Termination. Termination depends on the degree of hydrolysis of the metal cations as this determines the species present in solution. The condensation of charged, hydroxo-containing monomers results in a network of charged polycations. These polymers stay in solution unless the hydroxo ligands lose their nucleophilic properties ($\delta(OH) > 0$) or the cations are less electrophilic ($\delta(M) < 0.3$). Charged hydrolysis products do not form a solid phase as the network keeps its positive charge during polymerization. However, electrically neutral hydrolysis clusters can lead to the formation of a solid hydroxide, oxyhydroxide, or a (hydrated) oxide. Hydroxides $M(OH)_z$ are theoretically formed via the endless olation of non-charged aqua–hydroxo complexes and can be transformed into oxyhydroxides $MO_x(OH)_{z\text{-}2x}$ or hydrated oxides $MO_{z/2}.xH_2O$ via dehydration.

7.4.1.3 Complexation

In order to prepare aqueous precursor solutions for multi-metal oxide syntheses, hydrolysis and condensation reactions of the cation have to be controlled. By suppressing hydrolysis of the cation, further condensation reactions, and thus possible precipitation, can be avoided. Hydrolysis is influenced by the presence of chelating agents in the solution, as these electron-donating ligands compete for complexation. Polydentate compounds such as tartrates [68], lactates [69], citrates [53, 70], malonates [71], ethylenediaminetetraacetates [72], or oxalates [73] are often used. These chelants are able to form stable, water-soluble complexes with the cation, shielding it from other reagents and protecting it from further reactions. The substitution of coordinated water molecules by a ligand X^{n-} can be presented as follows:

$$\left[M(OH_2)_N\right]^{z+} + aX^{n-} \rightarrow \left[MX_a\left(OH_2\right)_{N-\alpha a}\right]^{(z-\alpha a)+} + \alpha a H_2O \tag{7.8}$$

N being the amount of initially bonded aqua ligands, n the charge of the coordinating ligand, and α the amount of coordinating bonds between the ligand X^{n-} and the metal ion M^{z+}; $\alpha = 1$, 2, or 3 are respectively called monodentate, bidentate, or tridentate ligands. As aqua ligands in the coordination shell of the metal ion are replaced by more bulky ligands, the hydrolysis rate of the ion is decreased and steric hindrance towards the central ion is increased. Due to the electron-donating character of the ligand, the charge on the metal cation is decreased, which lowers the probability of hydrolysis even further. For a more elaborated study on how chelation inhibits precipitation, the reader is referred to Kakihana [74].

The principle of suppressing further condensation by the addition of electron-donating ligands is the core of the aqueous solution–gel route. By formation of water-soluble metal ion complexes, the reactivity of the cations is suppressed and more stable entities are formed.

7.4.2 Gel Formation and Decomposition

The water-based precursor solution is converted into a glassy, amorphous gel by solvent evaporation. Metal ion complexes are immobilized as stable entities in a gel matrix obtained from the complexing agents, and hence the name “aqueous solution–gel route”. The core of this route is the interaction between the metal ion and the chelating α-hydroxy-carboxylates, forming water-soluble α-hydroxy-carboxylate metal ion complexes. Citric acid is shown to be a potent complexing agent regarding precursor stability [50–53,75–77]. Citric acid (H_3Cit) is a polyprotic acid. Depending on the pH of the solution, it takes different forms in water: H_2Cit^- ($pK_{a1} = 3.13$), $HCit^{2-}$ ($pK_{a2} = 4.76$), and Cit^{3-} ($pK_{a3} = 6.40$) [78]. Free groups can thus be involved in the crosslinking reactions between the different metal ion complexes, allowing the formation of the gel matrix. As ammonia (NH_3) is usually used to regulate the pH of the solution, ammonium ions (NH_4^+) are also involved in this crosslinking process. Precipitate formation during the evaporation of water is thus inhibited by crosslinking of the metal ion complexes. Thereby, a rigid, viscous structure is formed in which diffusion is delayed and phase segregation prevented [79].

To finally form the desired oxide, the amorphous gel has to be treated at high temperatures.

7.4.3 UV Activity

An important parameter for the PCSD route being successful is the (remaining) UV activity of the precursor film during its thermal decomposition. To obtain UV activity, additional photoactive organic compounds are frequently added to a precursor system [49, 80, 81]. This methodology increases the amount of organics in the precursor, which can be detrimental for decreasing the crystallization temperature. However, the water-based precursor system is intrinsically UV active, as shown in Figure 7.2. The intense absorption at high energy (<200 nm) is attributed to $\pi \rightarrow \pi^*$ transitions of free carboxylate groups or intra

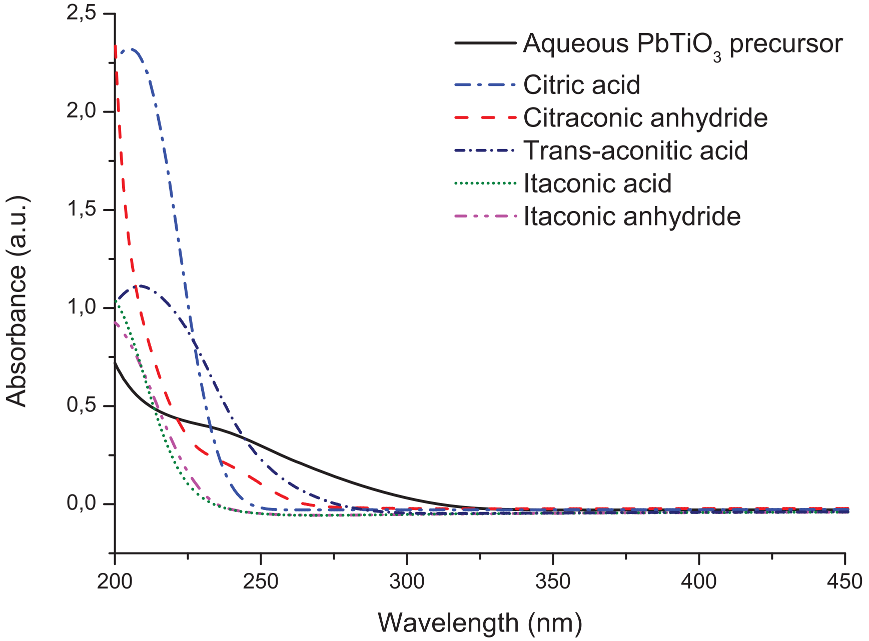

Figure 7.2 *UV-Vis spectra of the aqueous solution–gel $PbTiO_3$ precursor and of the typical decomposition products for a citric acid-based aqueous precursor system*

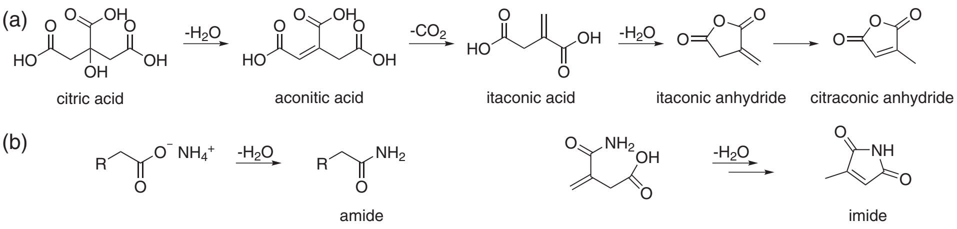

Figure 7.3 *(a) Schematic thermal decomposition of citric acid. (b) Schematic formation of amides or imides*

ligand transitions [82]. As the aqueous solution–gel route is based on soluble α-hydroxy-carboxylate complexes with the cation, this precursor concept is generally applicable within the PCSD route (*vide infra*).

The thermal decomposition pathway of aqueous solution–gel precursors based on citric acid containing metal ion complexes has been intensively studied [52, 83, 84]. Built on this knowledge, the broad UV susceptibility of the precursor throughout a wide temperature window can be rationalized. The precursor gel generally decomposes in three arbitrary temperature domains. The first temperature domain (<270 °C) comprises the decomposition of the uncoordinated ammonium citrate gel matrix surrounding the metal ion complexes. Non-coordinated ammonium carboxylate groups decompose into carboxylic acids and NH_3, amides are formed, α-hydroxy-carboxylates dehydroxylate and transform into anhydrides, and unsaturated carboxylic acids decarboxylate and evaporate (see Figure 7.3) [52]. These transformations result in UV-absorbing carboxylate derivates, (cyclic) anhydrides, amides, and imides. The UV activity of these decomposition products is shown in Figure 7.2.

In the second temperature domain from 270 to 420 °C, the direct coordination of the metal ion is decomposed, resulting in the formation and release of UV-active carboxylate derivatives comparable to those formed during decomposition of pure citric acid [52, 83, 84]. Additionally, UV absorption spectra of deposited precursor films show that the remaining precursor films also retain their activity during thermal treatment (Figure 7.4), ensuring the UV sensitivity of the system.

Around 420 °C, metal carboxylates and residual organics further decompose and the oxide is formed.

The aqueous solution–gel precursor film as well as its decomposition products are intrinsically UV active throughout the different stadia of the thermal decomposition process. This allows advantage to be taken of the PCSD route even at elevated temperatures of the thermal profile.

7.5 Photosensitive Sol–Gel Precursors

The preparation of metal oxide ferroelectric thin films by sol–gel processing dates from the middle 1970s. Advantages such as compositional control, film homogeneity and relatively low cost have certainly made this technique a main tool for the scientific understanding

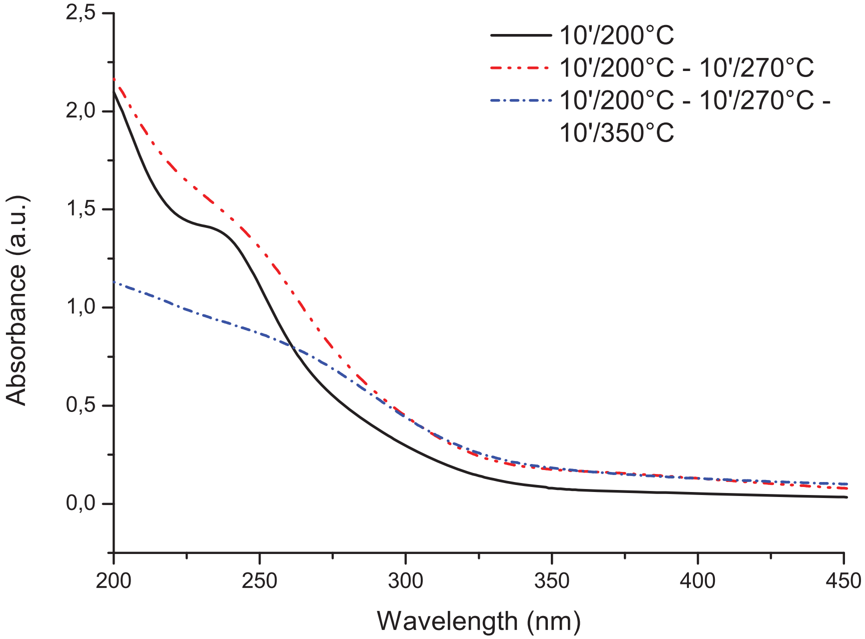

Figure 7.4 UV-Vis spectra of thermally treated aqueous solution–gel $PbTiO_3$ precursor films. Reprinted (adapted) with permission from [23]. Copyright (2011) American Chemical Society

of these materials today. The fundamentals of sol–gel processing can be found in many textbooks and reviews [85–88]. A key point that determines the physicochemical properties of both the solution and the film derived from it is the nature of the selected metal precursor. Metallo-organic compounds are widely used as precursors for the preparation of metal oxide films by wet chemistry-based routes. These compounds include species such as carboxylates, alkoxides, and β–diketonates, and their choice can depend on many factors such as toxicity, price, and solubility or volatility in case of deposition from liquid or gas media, respectively. During the last decade, the effects of UV light on sol–gel materials have enabled the development of new processing technologies for the fabrication of ferroelectric and multiferroic thin films [89]. In this section, two types of photosensitive sol–gel systems will be shown on the basis of the potential interaction that the different UV-absorbing molecules may have with the rest of the chemical compounds present in the solution.

7.5.1 Addition of UV-Absorbing Molecules to the Precursor Solution

For a precursor solution to be photosensitive, it must contain molecules with electronic transitions accompanying light absorption. In the ultraviolet region of the electromagnetic spectrum (between 100 and 400 nm), these absorptions correspond to the low-energy transitions $n \rightarrow \pi^*$ and $\pi \rightarrow \pi^*$. Therefore, the direct addition of compounds displaying such absorptions was initially investigated to obtain sol–gel precursors sensitive to UV light [80, 90]. Figure 7.5 shows the molecular structure of such UV-absorbing compounds that can be

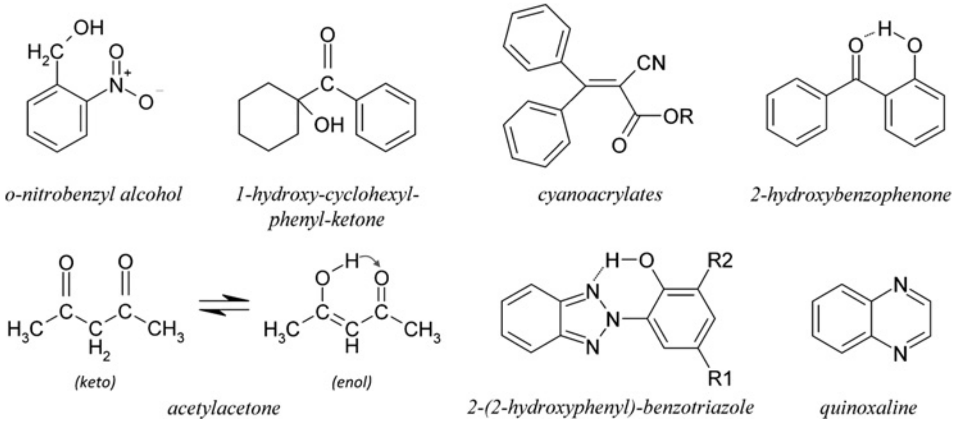

Figure 7.5 *Molecular structure of some UV-absorbing compounds*

added to sol–gel precursors, such as *o*-nitrobenzyl alcohol (NBA), 1-hydroxy-cyclohexyl-phenyl-ketone (HPK) or acetylacetone (acac). Cyanoacrylates are also compounds with a high absorption in the UV range due to the conjugated system formed by a large number of unsaturated chemical bonds. Another important family of UV-absorbing molecules are those containing phenolic groups in their structure [91]. Among them, compounds with either O−H…:O (salicylates, 2-hydroxybenzophenone, or xanthone) or O−H…:N (2-(2-hydroxyphenyl)-benzotriazole) bonds stand out.

Considering a thin-film fabrication process starting from a precursor solution, the formation of the crystalline oxide phase is assumed not to proceed until the precursor material is completely decomposed [2]. The addition of the aforementioned UV-absorbing compounds to a precursor can alter the decomposition pathway of the resulting film. This could happen either by an increase of the organic fraction that must be eliminated during pyrolysis or by the formation of undesired inter- or intramolecular interactions with the rest of the reagents present in the system (metal precursor reagents, solvents). In addition, most of these UV absorbers are aromatic compounds with a high associated toxic load. Table 7.1 gives an overview of some alternative UV-absorbing species [92]. Acrylates contain vinyl groups directly attached to a carbonyl carbon and their properties significantly vary depending on the type of organic fraction attached to this fragment. Their derivatives are implemented in solar filters and acrylic paints, but mainly serve as photoactivators for polymer plastics due to the high reactivity of the double bond. Azo compounds represent the functional group R−N=N−R’, which accounts for their UV absorption. Stable derivatives with aryl groups absorb in the visible light wavelengths, showing applications as a dye or as pigments for acid–base indicators. Alkyl azo compounds result in the formation of free radicals after rupture of the C−N bond by UV irradiation, which forms the basis of the photoinitiation step in the polymerization process. Derivatives with conjugated alkyl groups show molar extinction coefficients of 15 600 M^{-1} cm^{-1} at wavelengths near 250 nm. This value increases up to 30 000 M^{-1} cm^{-1} for conjugated polyene systems involving $\pi \rightarrow \pi^*$electronic transitions [93]. Isoprene is an example with a strong absorption in the ultraviolet–visible region of the electromagnetic spectrum (222 nm), although it is highly volatile and may be toxic

Table 7.1 *Potential UV-absorbing compounds to be introduced in sol–gel precursor solutions*

Group	Compound	Formula	λ(nm)/ε ($M^{-1}cm^{-1}$)
Acrylates	Poly(methyl methacrylate)	$[CH_2{=}C(CH_3)COOCH_3]n$	
	Acrylamide	$CH_2{=}CHCONH_2$	214
Azo compounds	Azo-*tert*-butane	$(CH_3)_3CN{=}NC(CH_3)_3$	
	Azoisobutyronitrile	$(CH_3)_2C(CN)N{=}NC(CH_3)_2CN$	345
	Azodicarboxamide	$H_2NCON{=}NCONH_2$	
	Ethyl diazoacetoacetate	$CH_3COC(N_2)CO_2C_2H_5$	
	Ethyl diazoacetate	$N{=}N{=}CHCOOC_2H_5$	250/15600
	tert-Butyl diazoacetate	$N_2CHCO_2C(CH_3)_3$	
	Diazodimedone	$C_8H_{10}N_2O_2$	
	Diazolidinyl urea	$C_8H_{14}N_4O_7$	
Conjugated polyenes	Isoprene	$CH_2{=}CHC(CH_3){=}CH_2$	222/20000
Alkynes	2,4,6,8-Decatetraene-1,10-diol	$HO{-}CH_2\text{-}C{=}C\text{-}C{=}C\text{-}C{=}C\text{-}C{=}C\text{-}CH_2\text{-}OH$	240/>10^5
Nitriles	Acetonitrile	CH_3CN	<190
Nitro compounds	*o*-Nitrobenzyl alcohol	$O_2NC_6H_4CH_2OH$	260/5000
	Nitromethane	CH_3NO_2	203/4400
	2-Methyl-2-nitropropane	$(CH_3)_3\text{-}C\text{-}O\text{-}N{=}O$	220/1000
O=C–C=C–	Methyl vinyl ketone	$CH_2{=}CHCOCH_3$	219
	3-Penten-2-one	$CH_3CH{=}CHCOCH_3$	220/15850
	Propylene aldehyde	$CH_3\text{-}CH{=}CH\text{-}C{=}OH$	218/19953
	Crotonic acid	$CH_3\text{-}CH{=}CH\text{-}COOH$	220/12590
Amines	*N*-methyldiethanolamine	$CH_3N(CH_2CH_2OH)_2$	
	N-methylethanolamine	$CH_3NHCH_2CH_2OH$	
	Triethylamine	$(C_2H_5)_3N$	200/3163
	Diethanolamine	$HN(CH_2CH_2OH)_2$	
β-Diketones	Acetylacetone	$CH_3COCH_2COCH_3$	275
	Camphorquinone	$C_{10}H_{14}O_2$	400–500

following repeated exposure. Similar to these compounds, conjugated acetylenes (alkynes) feature a high electronic density along π bonds responsible for UV absorption. However, they can display a rather long catenation of carbon atoms (see the example in Table 7.1) that increases the organic fraction of the precursor to get decomposed. Nitriles are UV-absorbing compounds comprising $n \rightarrow \pi^*$ electronic transitions with low molar extinction coefficients (<10 M^{-1} cm^{-1}). The high stability of the $-C{\equiv}N$ functional group makes these species not very reactive. Nitro compounds, on the other hand, display a large molar absorption ($\sim$103 M^{-1} cm^{-1}) at wavelengths around 200–260 nm. They have two absorption maxima associated with electronic $n \rightarrow \pi^*$ and $\pi \rightarrow \pi^*$ transitions (e.g. nitromethane), for which the intensity of the last one significantly increases for conjugated systems. The O=C–C=C– functional group (e.g. propylene aldehyde) is among the most active chromophores [93]. Conjugation with its carbonyl group results in a displacement of the $\pi \rightarrow \pi^*$ electronic transition to the 200–250 nm range with molar extinction coefficients close to 20 000 M^{-1} cm^{-1}, with the $n \rightarrow \pi^*$ electronic transition to 310–330 nm displaying a much lower intensity. This band displays a certain charge-transfer character, since the charge density in the excited electronic state is more focused on the carbonyl group rather than on the vinyl group. Despite amines being widely used to promote polymerization reactions as photoinitiators, their photosensitivity in the UV region is rather low. However, compounds with terminal hydroxyl groups display a more intense absorption in the UV-Vis range owing to $n \rightarrow \pi^*$ electronic transitions [94]. Finally, acetylacetone (acac) and related β-diketonates have traditionally been employed to stabilize metal alkoxides against hydrolysis [95]. These molecules show additional $\pi \rightarrow \pi^*$transitions at 275 nm [96] based on the conjugated system induced by keto-enol tautomerism (Figure 7.5), which makes them perfect candidates to provide photosensitivity compatible with the sol–gel processing of ferroelectric and multiferroic materials.

7.5.2 Synthesis of Highly Photosensitive Metal Complexes

The addition of UV-absorbing molecules to metal oxide precursor solutions provides a system that bestows light sensitivity to the corresponding as-deposited thin film. This photosensitivity depends exclusively on the molecular structure of the active species, capable of undergoing electronic transitions upon light absorption. As previously mentioned, the addition of these external compounds certainly increases the organic weight fraction that has to be eliminated during the thermal decomposition of the precursor. An alternative strategy for the addition of UV absorbers is the synthesis of metal complexes with an intrinsic high photosensitivity, which can be directly used as a metal precursor for the envisaged oxide layer [15, 49, 97]. A clear example is the stabilization of transition metal alkoxides by acetylacetone (acac).

Pure metal alkoxides have historically been employed in the sol–gel processing of oxide materials [85]. However, their high reactivity towards hydrolysis and their possible uncontrolled precipitation made the stabilization by the formation of glycolated compounds with acetylacetone ligands necessary [95]. These resulting β–diketonate complexes are more stable against hydrolysis than the initial pure alkoxides and display characteristic absorption bands in the near-ultraviolet region due to $\pi \rightarrow \pi^*$electronic transitions [98]. Figure 7.6(a) depicts the molecular structure of a modified titanium alkoxide [titanium di-isopropoxide bis(acetylacetonate), $[Ti(OC_3H_7)_2(CH_3COCHCOCH_3)_2]$, where the

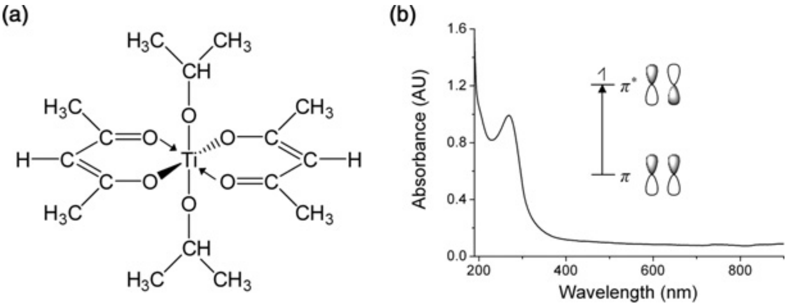

Figure 7.6 *(a) Molecular structure of titanium di-isopropoxide bis(acetylacetonate) and (b) the corresponding UV-Vis spectrum in solution*

presence of two acetylacetonate groups provides the inherent photosensitivity. This precursor has been widely used for the synthesis of complex oxide materials based on perovskite titanates such as $PbTiO_3$ or $Pb(Zr,Ti)O_3$. A maximum at ~275 nm is observed in the UV-Vis spectrum of Figure 7.6(b), corresponding to the electronic transitions within this complex.

Recently, another family of metal complexes has demonstrated its effectiveness as a new precursor with enhanced photosensitivity for the preparation of ferroelectric and multiferroic thin films. Those complexes consist of charge-transfer complexes formed between a metal cation and *N*-methyldiethanolamine (mdea) [22, 99, 100]. Coordination of the ion occurs via the hydroxy (–OH) and/or amino ($-NH_2$, –NHR, $-NR_2$) groups of this alkanolamine, which gives rise to either simple or cyclic complexes. The bond between nitrogen and the metal cation may incorporate new functionalities to the resulting compound, such as photosensitivity [101,102]. Absorption bands in charge-transfer complexes arise from electronic transfers between molecular orbitals predominantly with a metal-like and ligand-like character, usually induced by ultraviolet or visible light. The presence of charge-transfer bands can increase the molar absorptivity of these metal complexes up to 50 000 M^{-1} cm^{-1}, several orders of magnitude higher with respect to other UV-absorbing molecules. Metal cations comprising the perovskite ABO_3 structure are in principle optimal candidates to generate these bands since their electronic configuration involves either fully occupied (d^{10} elements, A-site cations) or empty (d^0 elements, B-site) molecular orbitals, enabling their respective metal-to-ligand (MLCT) and ligand-to-metal (LMCT) charge transfer.

Figure 7.7 shows the molecular structure of the charge-transfer complex resulting from the reaction between bismuth(III) nitrate and *N*-methyldiethanolamine. This approach has been succesfully used to prepare different thin films of bismuth-based functional oxides [Bi_2O_3, $BiFeO_3$, $(Bi_{0.5}Na_{0.5})_{0.945}Ba_{0.055}TiO_3$] using processing temperatures between 350 and 400 °C [100]. The ^1H-NMR spectra were first obtained in a bismuth nitrate solution (Figure 7.7(a)), which then was refluxed with the *N*-methyldiethanolamine compound (Figure 7.7(b)). Only chemical shifts associated with the protons of acetic acid (δHa ~1.87 ppm and δHb ~8.58 ppm) and 1,3-propanediol (δHe ~1.78 ppm, δHc ~1.85 ppm, and δHd ~3.54/3.96 ppm) solvents are recorded in the spectrum of this Bi(III) solution. Multiplets appear in the spectrum of the Bi(III)-mdea solution, which account for the presence of sterically non-equivalent mdea groups resulting from the coordination of this ligand to bismuth and the formation of a dimeric metal complex [103].

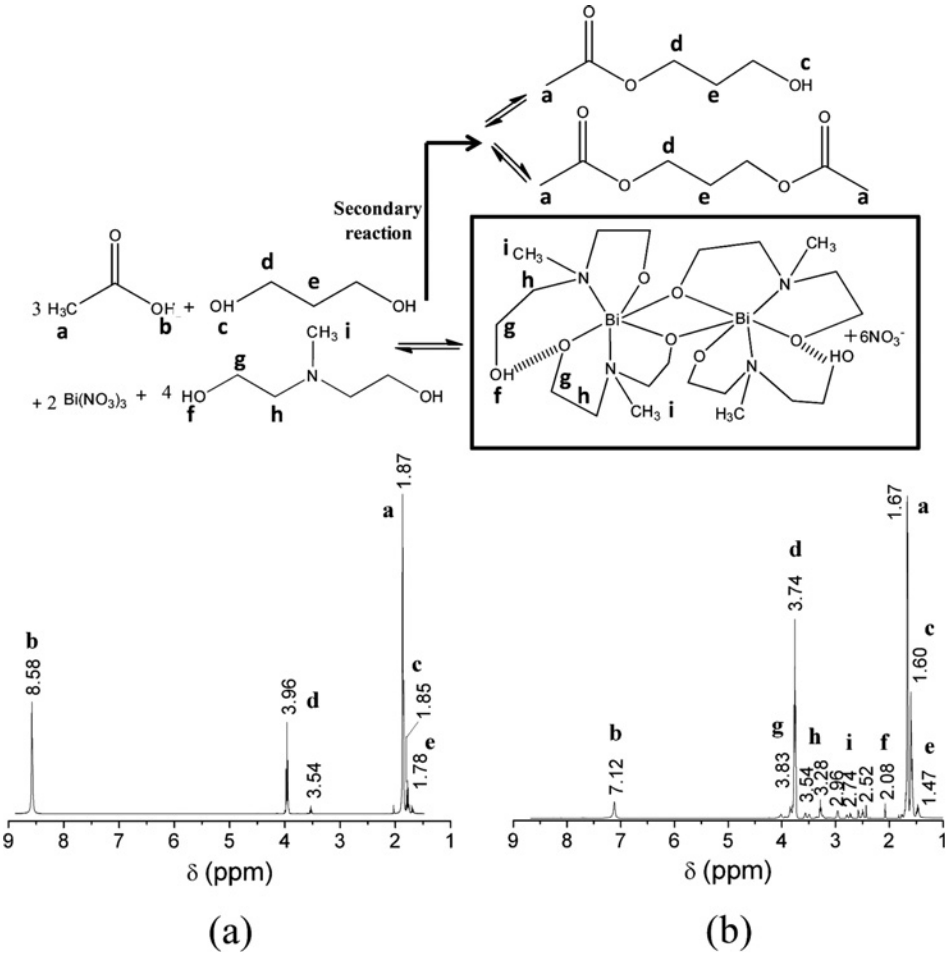

Figure 7.7 Reaction and ^{1}H-NMR spectra of (a) a bismuth nitrate solution (with acetic acid and 1,3-propendiol as solvents) and (b) the same solution after reflux with the N-methyldiethanolamine (mdea) compound, where the molecular structure of the resulting charge-transfer complex is depicted. Reproduced from [100] by permission of The Royal Society of Chemistry

The UV-Vis spectra of both Bi(III) and Bi(III)-mdea precursor solutions and their macroscopic appearances are compared in Figure 7.8. The color of the mixture changes from pale yellowish to dark brownish, which is caused by the occurrence of electronic transitions induced by the absorption of visible light. The maximum at ~250 nm in the Bi(III)-mdea solution is not observed for the pure Bi(III) solution, and neither for pure *N*-methyldiethanolamine (not shown), which confirms the photosensitive nature of the synthesized charge-transfer complex.

In the case of a reaction between a titanium(IV) alkoxide and *N*-methyldiethanolamine, the ligands of the metal ion are replaced by the mdea molecules, leading to the formation of

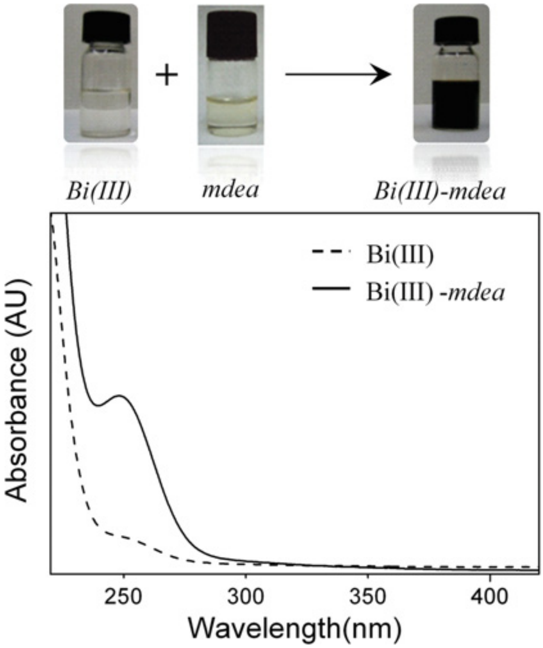

Figure 7.8 Macroscopic appearance and UV-Vis spectra of Bi(III) and Bi(III)-mdea precursor solutions. Reproduced from [100] by permission of The Royal Society of Chemistry

a new corresponding charge-transfer complex with improved photosensitivity. Figure 7.9(a) shows the IR spectrum of a titanium di-isopropoxide bis(acetylacetonate) solution, which was refluxed with *N*-methyldiethanolamine (Figure 7.9(b)). Note how the spectrum of the former displays the ν(C=O) and ν (C=C) bands characteristic of acetylacetonate groups (1583 and 1525 cm^{-1}) and how they disappear in the titanium precursor modified with mdea. The inset shows the molecular structure of the formed charge-transfer complex of titanium, as inferred from NMR studies [99].

7.6 Photochemical Solution Deposition (PCSD)

7.6.1 Working Principle

The study on the effects of UV irradiation on sol–gel materials started in the early 1990s in Japan [104]. Thin films were considered as ideal candidates for these studies, since the penetration depth of the photons is limited to the surface region of matter. In contrast to the thermal excitation produced by other illumination sources (visible, infrared), energetic photons of UV light additionally and predominately induce the electronic excitation of both inorganic and organic compounds present in the gel film [89]. The first phenomena investigated were the photoinduced densifications of single oxide films such as Ta_2O_5, SiO_2, and TiO_2 [90, 104, 105]. Crystallization and reduction were other physicochemical changes achieved by the direct activation of the inorganic gel network upon UV irradiation

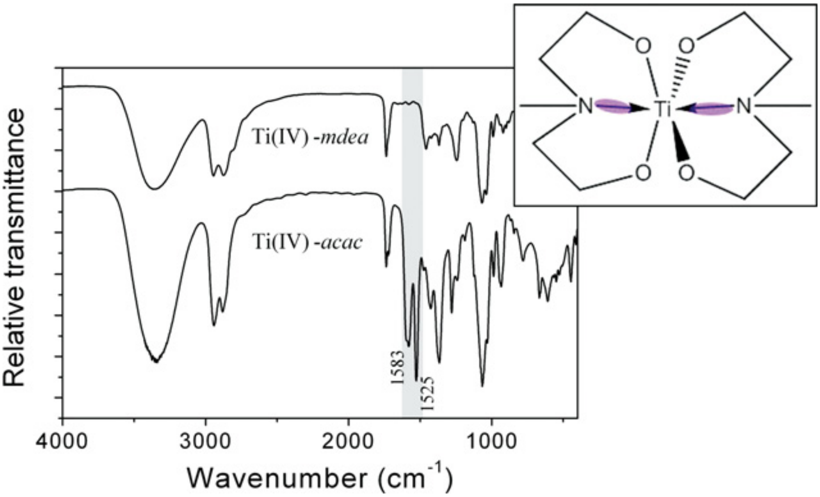

Figure 7.9 *FTIR spectrum of (a) an acac-modified titanium alkoxide solution (with 1,3-propendiol as the solvent) and (b) after reflux with N-methyldiethanolamine (mdea). The molecular structure of the resulting charge-transfer complex is depicted*

[106,107]. Additionally, the activation of organic compounds was used for the patterning of gel films [108] and as a pretreatment towards the annealing of functional oxide films, that is to lower the temperature of the subsequent heating process for film crystallization [98, 109, 110]. It is this last phenomenon, together with the development of new narrow-banded excimer UV lamps (108–354 nm) and high-density radiation, which forms the basis of the advanced technique termed photochemical solution deposition (PCSD). As a variant of the general method known as chemical solution deposition (CSD) [2], PCSD includes the conventional steps of solution deposition: removal of organic fragments and film crystallization. However, the decomposition of the metal precursors in the film is in this case assisted by irradiation with UV light. The aim of this UV irradiation is to induce electronic excitations within the UV-absorbing species present in the gel film, thereby promoting precursor decomposition prior to the crystallization of the oxide phase and thus resulting in a lower annealing temperature for the final heating step. By photon absorption, UV-active compounds are excited into an unstable and thus reactive state. This excitation induces the dissociation of chemical bonds and the formation of a metal-O-metal network, enabling film crystallization at a reduced temperature. This approach was initially employed for the low-temperature processing of ZrO_2 and Ta_2O_5 thin films [98, 110], where a reduction on the leakage current density of the capacitor after UV treatment was observed due to a decreased concentration of oxygen vacancies. Nevertheless, the challenge of crystallizing complex oxide systems at reduced temperatures by means of PCSD was not addressed until the past decade. Indeed, the effective integration of functional oxide films, which must be crystalline to reach the full potential of their physical properties, into microelectronics required radically new developments, as their crystallization temperatures are rather high (>600 °C). Nowdays, PCSD has demonstrated to be a facile and highly versatile solution-based method that enables the preparation of metal oxide layers with complex

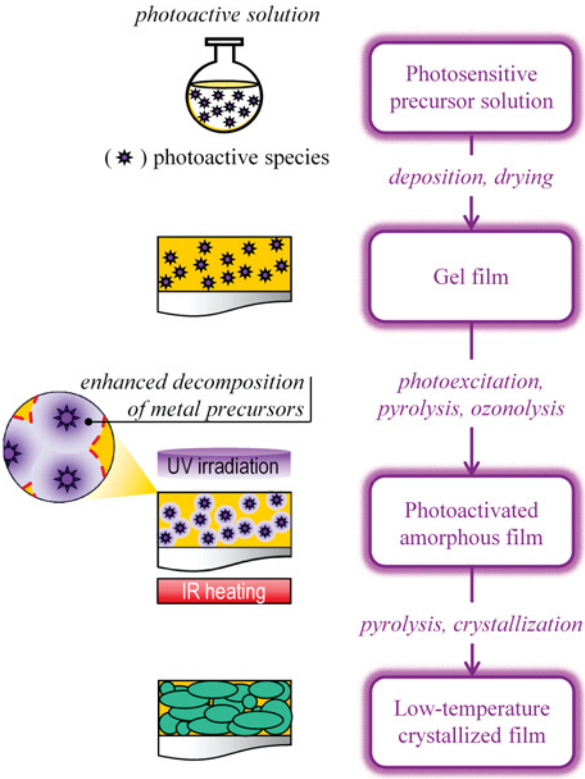
photoactive solution
(✸) photoactive species
Photosensitive precursor solution
deposition, drying
Gel film
enhanced decomposition of metal precursors
UV irradiation
IR heating
photoexcitation, pyrolysis, ozonolysis
Photoactivated amorphous film
pyrolysis, crystallization
Low-temperature crystallized film

Figure 7.10 *Generalized flowchart of the photochemical solution deposition (PCSD) method. Reprinted from [26], Copyright © 2014 Wiley-VCH Verlag GmbH & Co. KGaA, Weinheim*

perovskite structures at temperatures below 450 °C [15, 17, 22, 23, 26, 39, 99, 100, 111, 112]. This was the last hurdle to overcome before their successful integration into the current standard CMOS (complementary metal oxide semiconductor) processes for semiconductors [32].

Figure 7.10 depicts a flowchart for the photochemical solution deposition process. The presence of photosensitive compounds in the precursor solution is certainly responsible for the light absorption. However, for a multimetal precursor system to take full advantage of the effects induced by UV irradiation (in this case, as a pretreatment prior to film annealing), electronic excitations must stem from the metal precursor constituent of the envisioned material composition. The activation of organic components non-inherent to the precursor solution (additionally added UV-absorbing compounds) may lead to unappreciated changes in the metal oxide network of the system. Therefore, the use of highly photosensitive metal ion complexes as metal precursors is regarded as an asset within the low-temperature processing of functional oxide films by PCSD. Once deposited from the solution, these species remain in the gel layer, resulting in a thin UV-susceptible film. Obviously, thermal treatment of this film has to be carried out below the decomposition temperature of the photosensitive compounds.

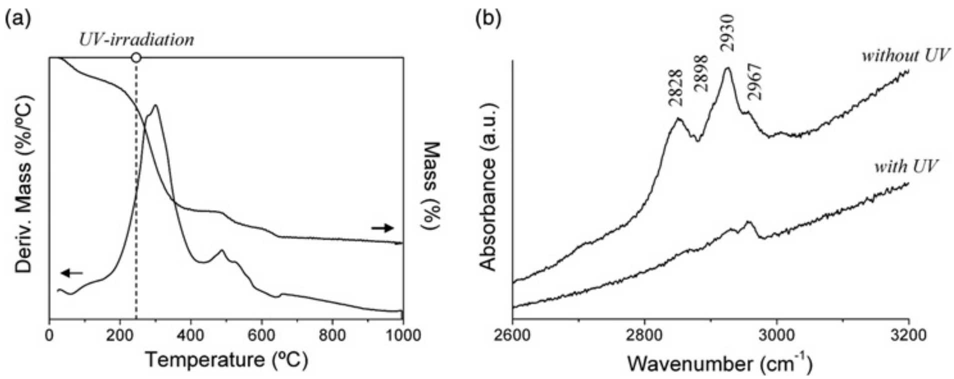

Figure 7.11 *(a) DTA/TGA profile of a gel powder derived from a precursor solution for* $(Pb_{1-x}Ca_x)TiO_3$ *and (b) FTIR spectra of deposited layers annealed at 250 °C with and without UV irradiation during thermal treatment*

Figure 7.11(a) shows the typical thermal decomposition profile of a gel powder for a complex oxide, derived from a precursor solution containing β–diketonate complexes of titanium di-isopropoxide bis(acetylacetonate) [15]. Most of the organic compounds are eliminated from this system in the temperature range between 200 and 500 °C. Therefore, in this particular case, 250 °C was selected as the temperature at which the corresponding thin films are irradiated. Only this value guarantees the presence of photosensitive acetylacetonate groups in the gel film, which is necessary to guarantee the occurrence of electronic excitations during UV irradiation.

Electronic excitations induced in the conjugated system promote the decomposition of the metal precursor and the formation of the amorphous oxide phase. The removal of organic species in the system promoted by this process can be inferred by infrared analysis, as shown in Figure 7.11(b) [15]. The data are obtained for thin films from a complex oxide system annealed at 250 °C with and without UV irradiation. The Fourier transform infrared (FTIR) spectrum of the non-irradiated film shows vibrational modes ascribed to groups typically involved in most organic compounds, such as CH_2 groups (ν_{asym} ~2930 cm^{-1} and ν_{sym} ~ ~2828 cm^{-1}) and CH_3 groups (ν_{asym} ~ ~2967 cm^{-1} and ν_{sym} ~2898 cm^{-1}). These bands almost disappear for the irradiated film. UV irradiation results in the cleavage of C–H bonds, enhancing the elimination of organics from the film by radical formation. Finally, the resulting photoactivated film requires a lower energy (via thermal heating) to crystallize into the desired oxide phase by further annealing at a comparatively lower temperature. Additionally, if the samples are irradiated in an oxygen atmosphere, active oxygen species $O(^1D)$ are formed in the process chamber [113] and ozone (O_3) is simultaneous formed:

$$O_2 + h\nu \rightarrow O + O\left(^1D\right) \tag{7.9}$$

$$O + O_2 \rightarrow O_3 \tag{7.10}$$

Ozone is a strong oxidizer which further assists the decomposition of precursors by an ozonolysis process in which active oxygen species further react with suboxides present in the film, thus improving the stoichiometry and decreasing the amount of defects and oxygen vacancies in the film [114, 115].

7.6.2 Low-Temperature Ferroelectric Oxide Films Prepared from Photosensitive Sol–Gel Precursors

Low-temperature processing of ferroelectric oxide films involves a series of chemical and physical features in the resulting material that makes them substantially differ from those films obtained by conventional annealing at higher temperatures. Processing effects derived from the use of a low crystallization temperature affect the (micro)structure of the film, which ultimately determines the functionality of the material. One of the main consequences may even go back to the solution chemistry. Low-temperature crystallization of PCSD processed films has shown to effectively avoid the volatilization of lead from the film [17], making the fabrication of these lead-based perovskite compositions possible without the widely used, apparently unavoidable lead excess in the system [39]. Figure 7.12 depicts a schematic cross-sectional representation deduced from Rutherford backscattering spectroscopy (RBS) measurements of three $(Pb_{0.76}Ca_{0.24})TiO_3$ thin films deposited on $Pt/TiO_2/SiO_2/(100)Si$ substrates processed by (a) conventional CSD at 650 °C with lead excess and by PCSD at (b) 450 °C with and (c) without the addition of lead excess to the precursor solution. These films were prepared from a photosensitive sol–gel precursor involving β–diketonate complexes of titanium (the respective alkoxide compound modified with acetylacetonate groups).

The presence of an inhomogeneous interfacial layer between the film and the substrate was identified and their characteristics analysed in all these samples. In the high-temperature processed film, this interface accounts for 13% of the total film thickness and its composition results basically from the diffusion of metallic elements from the film into the platinum bottom electrode of the substrate [116]. The formation of this interface is

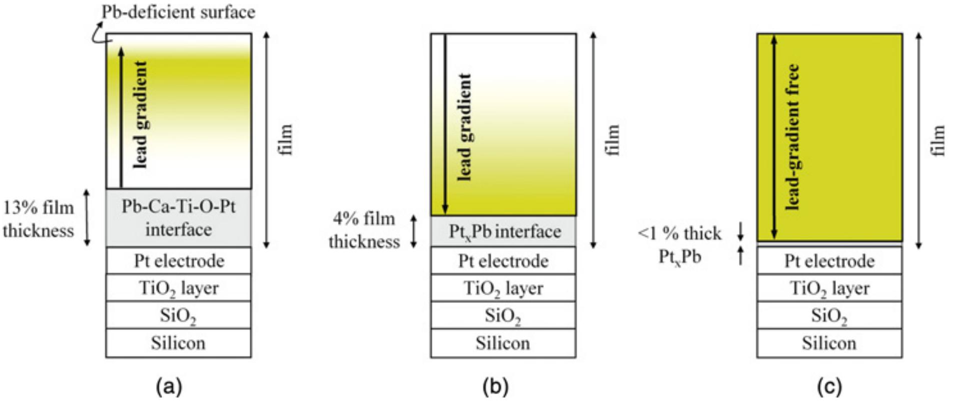
Pb-deficient surface
lead gradient
film
13% film thickness
Pb-Ca-Ti-O-Pt interface
Pt electrode
TiO₂ layer
SiO₂
Silicon
(a)
lead gradient
film
4% film thickness
PtₓPb interface
Pt electrode
TiO₂ layer
SiO₂
Silicon
(b)
lead-gradient free
film
<1 % thick PtₓPb
Pt electrode
TiO₂ layer
SiO₂
Silicon
(c)

Figure 7.12 *Schematic cross-sectional representations deduced from RBS analyses of* $(Pb_{0.76}Ca_{0.24})TiO_3$ *thin films prepared with a lead excess at (a) high (650 °C) and (b) low (450 °C) temperature and (c) without any lead excess at low temperature. Arrows indicate an increasing concentration of lead. Adapted from [17] and [19]*

strongly reduced for the films prepared at low temperature, where the presence of a fine interlayer with a composition generally assumed to be Pt_xPb is detected. This intermetallic compound is usually formed in the early stages of crystallization of the film, in which a reductive local atmosphere, present due to oxygen depletion during combustion of organic fragments, promotes the reduction of Pb^{2+} to Pb^0 and its subsequent reaction with Pt to form the aforementioned alloy [16, 117]. At higher temperatures, metallic lead is reoxidized and the intermetallic phase disappears. This is not the case for the low-temperature processed film, in which this transient compound remains in the heterostructure, as confirmed by RBS. Note that the formation of this interlayer is significantly minimized for the stoichiometric film prepared without any lead excess (<1% of the total film thickness) at low temperature, suggesting that the excess amount acts as a preferential source for lead reduction in the film. The reduction of detrimental interfaces in ferroelectric oxide films is expected to improve their electrical properties based on the approximation of an in-series capacitor with a ferroelectric bulk film and a non-ferroelectric interface [118]. Overall, the distribution of lead is not uniform in the films prepared with a lead excess. Surface volatilization of this element or Pt_xPb interlayer formation account for the lead gradients detected by RBS in the respectively high-temperature (up-graded increasing concentration) and low-temperature (down-graded increasing concentration) processed films. Both effects generate fluctuations for the chemical potential of this element that is responsible for its migration throughout the bulk film. The tendency of lead to diffuse is usually responsible for the compositional gradients observed in lead-based perovskite films prepared by a multiple coating procedure. This phenomenon induces variations on the physical properties of the material through the film thickness that can deteriorate the functionality of the device [119]. In contrast, the film prepared at a low temperature without lead excess has a homogeneous compositional film profile. The diminished lead volatilization from this film, together with the virtual suppression of Pt_xPb formation at the interface, results in the absence of compositional variations in the sample. Figure 7.13 shows the ferroelectric hysteresis loops of the low-temperature (450 °C) processed films prepared with and without a lead excess [17].

The compositional gradient obtained in the excess containing film may be responsible for the internal bias field generated, as inferred from different positive and negative coercive field values (–86 versus 148 kV cm^{-1}) for the corresponding loop. The presence of such internal fields in ferroelectric oxide films is known to be a source for imprint of the ferroelectric polarization [118]. For the film without lead excess, on the other hand, a symmetric ferroelectric loop with no bias field is measured. The remanent polarization of this film (14 μC cm^{-2}) is moderately high considering the low annealing temperature applied (450 °C). The higher value obtained for the film prepared with lead excess can likely be explained on the basis of an improved crystal quality resulting from this addition. Thus, the lead excess present in the film may act as a flux for crystal growth or as a network modifier, improving the mobility of the system and enhancing crystallization kinetics, as a sintering aid [17]. For conventional films annealed at higher temperatures (650 °C), even larger ferroelectric polarization values are obtained. Obviously, one of the main reasons is the enhanced crystallinity and microstructure obtained with higher thermal budgets, which results in improved dielectric and ferroelectric properties for the film. As an example, Figure 7.14 shows the microstructure of two thin films annealed at different temperatures. Crystallization at a high temperature leads to the nucleation of a relatively low number of crystal nuclei, promoting grain growth phenomena and the formation of large

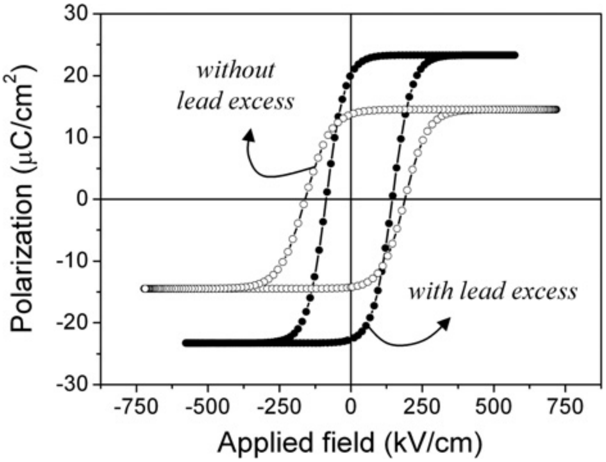

Figure 7.13 *Ferroelectric hysteresis loops of* $(Pb_{0.76}Ca_{0.24})TiO_3$ *thin films prepared by PCSD at 450 °C with and without a lead excess. Reprinted (adapted) with permission from [17]. Copyright (2008) American Chemical Society*

polycrystalline grains (Figure 7.14(a)). Low-temperature processed films, on the other hand, are nanostructured (Figure 7.14(b)), having an average grain size of ~30 nm owing to the higher number of crystal nuclei developed at such a low crystallization temperature. Nanostructuring can result in a variety of different characteristics for the material properties, such as the reduction of the remanent polarization, increasing coercive field, decrease of the dielectric constant, change in the domain structure, etc. Thus, the crystal quality and microstructure of the low-temperature processed films are obviously compromised by the

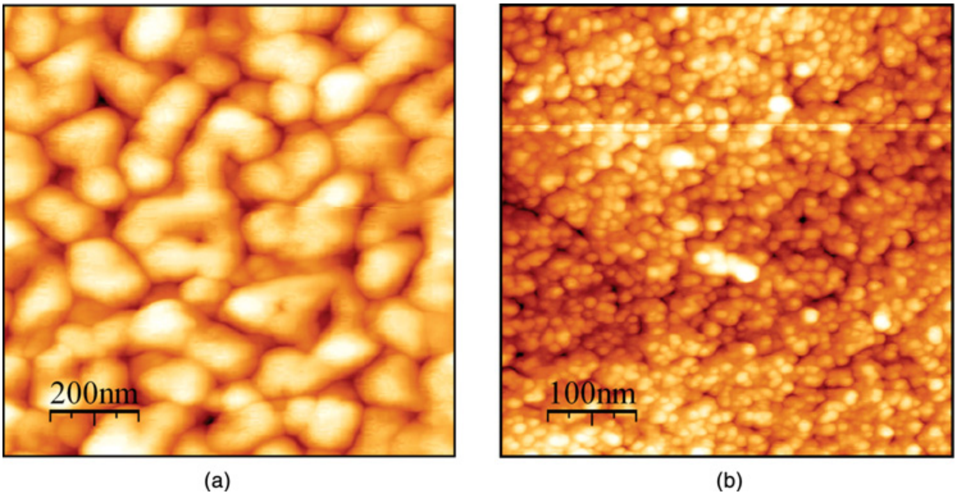

(a) (b)

Figure 7.14 *Surface microstructure obtained by AFM of* $(Pb_{0.76}Ca_{0.24})TiO_3$ *thin films prepared at (a) 650 °C or (b) 450 °C*

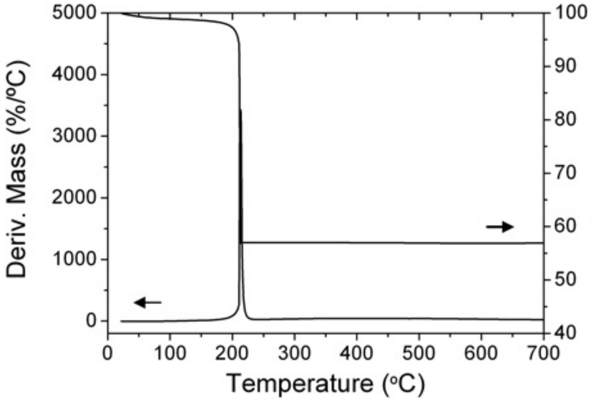

Figure 7.15 DTA/TGA profiles of a gel powder derived from a precursor solution for $PbTiO_3$ containing charge-transfer metal complexes of mdea

reduced thermal budget employed. However, as stated in the introduction to this chapter, high-temperature treatments involve technological drawbacks for a reliable integration with CMOS microelectronics and future flexible electronics.

Charge-transfer complexes with *N*-methyldiethanolamine (mdea) have also demonstrated their effectiveness for the low-temperature PCSD processing of ferroelectric thin films with adequate functionality. In this case, the thermal decomposition process of the precursor presents a highly exothermic anomaly (probably related to the presence of nitrogen-based compounds) that additionally contributes to the low-temperature formation of the oxide phase. Figure 7.15 shows the DTA/TGA profiles of a gel powder derived from an mdea–$PbTiO_3$ precursor solution. The exothermic energy released at ~215 °C further increases the internal temperature of the system during decomposition.

Perovskite thin films of $PbTiO_3$ on $Pt/TiO_2/SiO_2/(100)Si$ can both be obtained at 400 °C either with or without the UV-assisted annealing step (Figure 7.16(a)). However, the effect of UV irradiation is crucial with regard to the crystal quality and hence ferroelectric response measured for these films (Figure 7.16(b)). A remanent polarization value of 12 $\mu C\ cm^{-2}$ is obtained for the photoactivated film, whereas this value is approximately three times smaller for the non-irradiated film. These results confirm the critical role of the PCSD method on low-temperature processing of ferroelectric oxide films.

7.6.3 Low-Temperature Ferroelectric and Multiferroic Oxide Films Prepared from Aqueous Photochemical Solution Deposition (Aqueous PCSD)

The PCSD method has also been demonstrated for the low-temperature deposition of ferroelectric $PbTiO_3$ and multiferroic $BiFeO_3$ films obtained from aqueous systems [23].

7.6.3.1 $PbTiO_3$ Films

Figure 7.17 shows SEM images of single-layered $PbTiO_3$ films obtained from an aqueous $PbTiO_3$ precursor solution [53] deposited on $Pt/IrO_2/Ir/SiO_2/Si$ substrates. The following thermal treatment is applied: 10′/100 °C + 10′/200 °C + 10′/270 °C + 10′/350 °C +

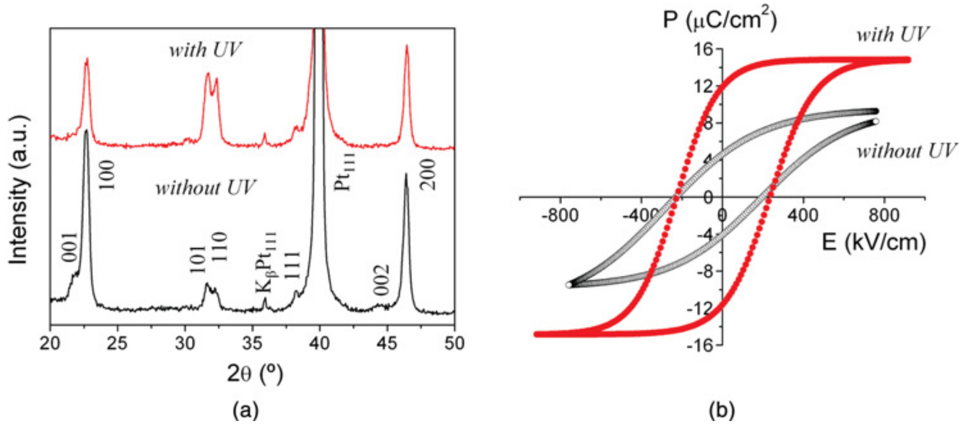

Figure 7.16 (a) XRD patterns and (b) ferroelectric hysteresis loops of $PbTiO_3$ thin films obtained from mdea-based precursors prepared at 400 °C by means of PCSD with or without UV irradiation during thermal decomposition of the precursor gel

60′/450 °C, with or without UV treatment at 270 and 350 °C [UV treatment is later indicated with square brackets]. Until 200 °C, the treatment is carried out on a hot plate in ambient air. The treatment at 270 and 350 °C is carried out in a UV-assisted thermal processor chamber with or without UV in dry air, and the final anneal step is performed in a rapid thermal processor (RTP) in dry air. If the film is not UV irradiated, a uniform but porous film is obtained (Figure 7.17(a)). Setting the UV treatment at 270 and 350 °C results in a significantly reduced film porosity (Figure 7.17(b)). This pretreatment with UV light before crystallization is a known procedure to reduce the roughness of the final oxide layer [109, 120].

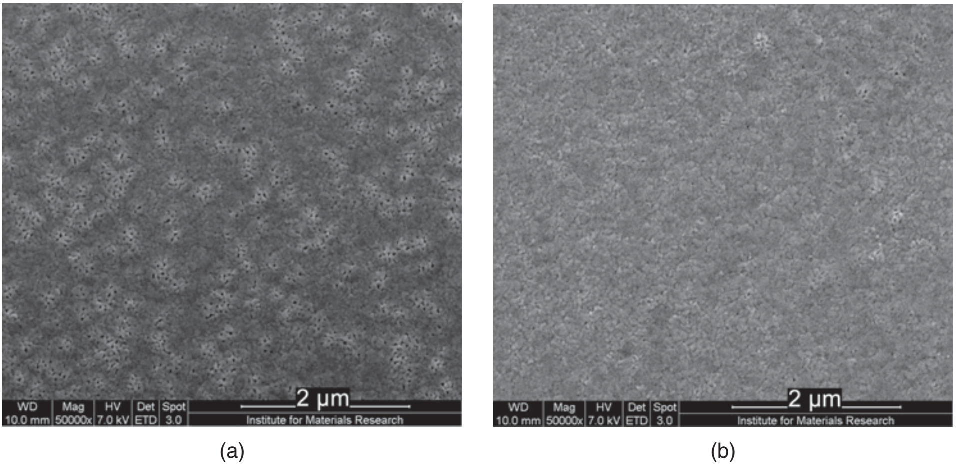
WD 10.0 mm
Mag 50000x
HV 7.0 kV
Det ETD
Spot 3.0
2 μm
Institute for Materials Research
WD 10.0 mm
Mag 50000x
HV 7.0 kV
Det ETD
Spot 3.0
2 μm
Institute for Materials Research

(a) (b)

Figure 7.17 SEM images of single-layered $PbTiO_3$ films obtained from an aqueous precursor system. Left, thermal treatment at: 10′/200 °C + 10′/270 °C + 10′/350 °C + 60′/450 °C; right: 10′/200 °C + [10′/270 °C] + [10′/350 °C] + 60′/450 °C (all in dry air)

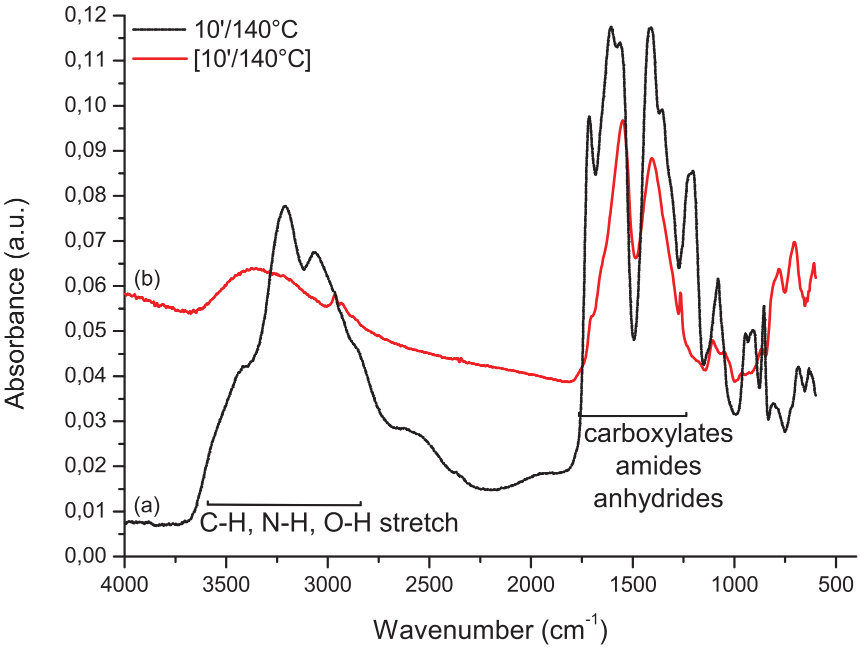

Figure 7.18 *GATR–FTIR spectra of aqueous $PbTiO_3$ precursor films treated at 140 °C: (a) without UV treatment and (b) with UV treatment during thermal treatment*

Irradiation with energetic UV photons during thermal decomposition of a precursor film accelerates the decomposition of organics inside the film [80, 89]. Grazing angle attenuated total reflection (GATR)–FTIR spectroscopy is applied to confirm the decomposition of organics inside the aqueous solution–gel $PbTiO_3$ precursor films (Figure 7.18). Metal citrate complexes are characterized by the following vibrations: C–O of the α-hydroxy group $\nu(C–O)_{COH}$ (1080 cm^{-1}), $\nu_{as}(COO^-)$ and $\nu_{sym}(COO^-)$ (respectively 1600 and 1400 cm^{-1}). By UV irradiation at 140 °C, the citrate ligand loses its α-hydroxy in a typical decarboxylation reaction (Figure 7.3). This is inferred from a diminishing $\nu(C–O)_{COH}$ absorption, indicating the formation of ammonium aconitate or aconitate metal complexes [83]. Moreover, the infrared absorbance is decreased in general, confirming the enhanced decomposition of organic fragments.

UV-assisted thermal treatment at 200 °C results in the complete disappearance of this characteristic $\nu(C–O)_{COH}$ vibration. The intense peak around 1710 cm^{-1} ($\nu(C{=}O)_{COOH}$) indicates that ammonium citrate and ammonium aconitate decompose into NH_3 and citric acid/aconitic acid according to:

$$R - COO^- \cdots H - {}^{+}NH_3 \rightarrow R - COOH + NH_3 \uparrow \qquad (7.11)$$

Various derivatives of citric acid are present below 270 °C, but due to peak shifts and peak overlap, their precise assignment is difficult.

UV irradiation at 270 and 350 °C enhances the decomposition of organics in the film, as inferred from the decreased IR absorption in the spectrum in Figure 7.19 for the UV

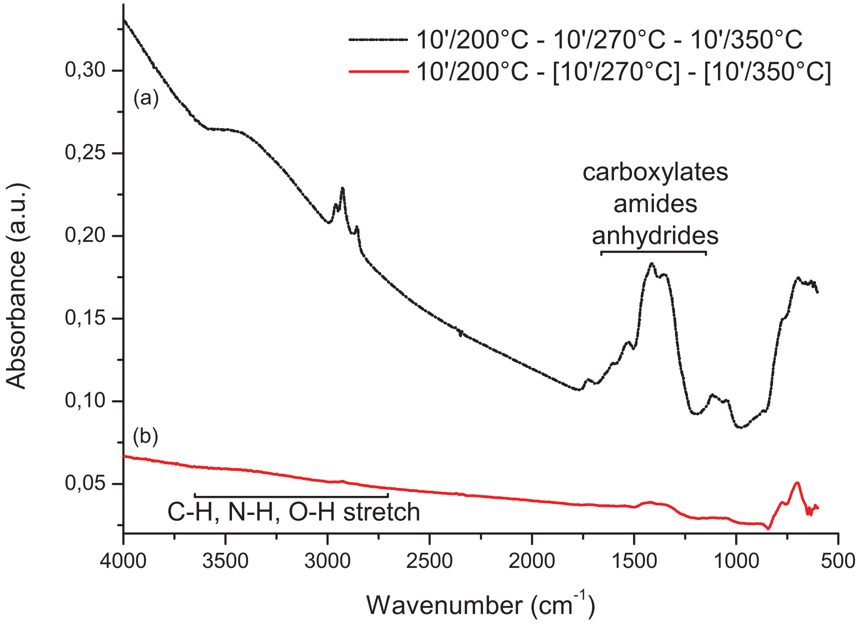

Figure 7.19 *GATR–FTIR spectra of treated PbTiO$_3$ precursor films. (a) No UV treatment and (b) UV treated at 270 and 350 °C. Reprinted (adapted) with permission from [23]. Copyright (2011) American Chemical Society*

treated sample. Decomposition is mainly driven by decarboxylation and dehydroxylation reactions of remaining carboxylic acids, as evidenced from the decreasing absorption in the characteristic area of the carboxylate groups. Nevertheless, UV-Vis spectroscopy proves the UV activity of the precursor film even at these high irradiation temperatures (Figure 7.4). The initial UV activity of the aqueous precursor is retained throughout the whole process due to the formation of UV active metal carboxylates, anhydrides, amides, and imides. The UV activity of these formed and released fragments is shown by the UV-Vis spectra in Figure 7.2.

The right SEM image in Figure 7.17 shows the obtained morphology for a single-layered PbTiO$_3$ film after UV–temperature treatment at [270°C] and [350°C]. However, in order to measure macroscopic electrical properties, four layered films are deposited. As UV penetration for sol–gel layers is limited to ~100 nm, UV treatment is carried out on each individual layer [17]. Films treated in an oxygen atmosphere with or without UV treatment contain phase pure PbTiO$_3$, as shown by the (GI)XRD patterns in Figure 7.20. No secondary phases are detected within the detection limit of the device. Diffraction at 2θ 38.3° is attributed to the (111) reflection of an fcc Pt$_x$Pb intermetallic phase at the interface with the PbTiO$_3$ layer, as was indicated in a previous section [17].

Phase purity is no guarantee for ferroelectricity. Therefore, macroscopic ferroelectric loops are measured to confirm ferroelectric behavior [121]. The compensated hysteresis loops for the obtained films are shown in Figure 7.21. The film UV-treated in oxygen has the largest remanent polarization (P_r = 8.8 μC cm^{-2}) and saturation polarization

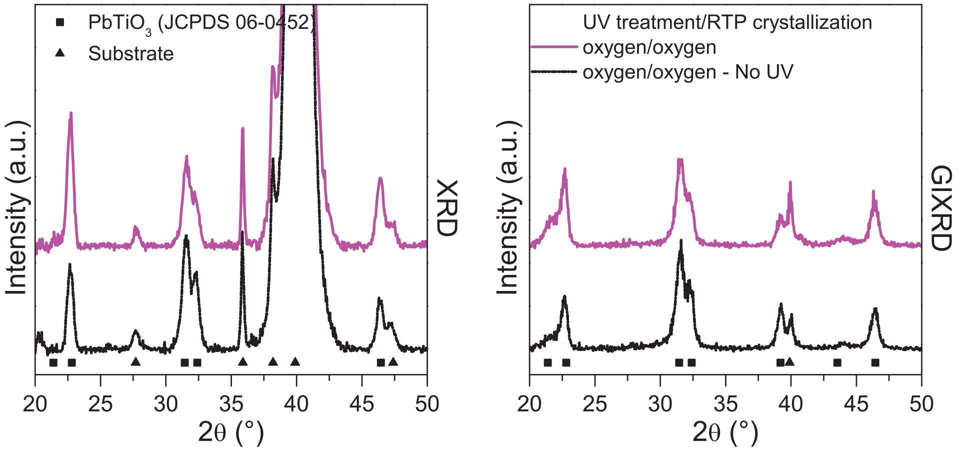

Figure 7.20 (Grazing incidence) XRD patterns of $PbTiO_3$ films obtained by PCSD processing and crystallized at 400 °C. UV treatment and the annealing step are carried out in an oxygen atmosphere

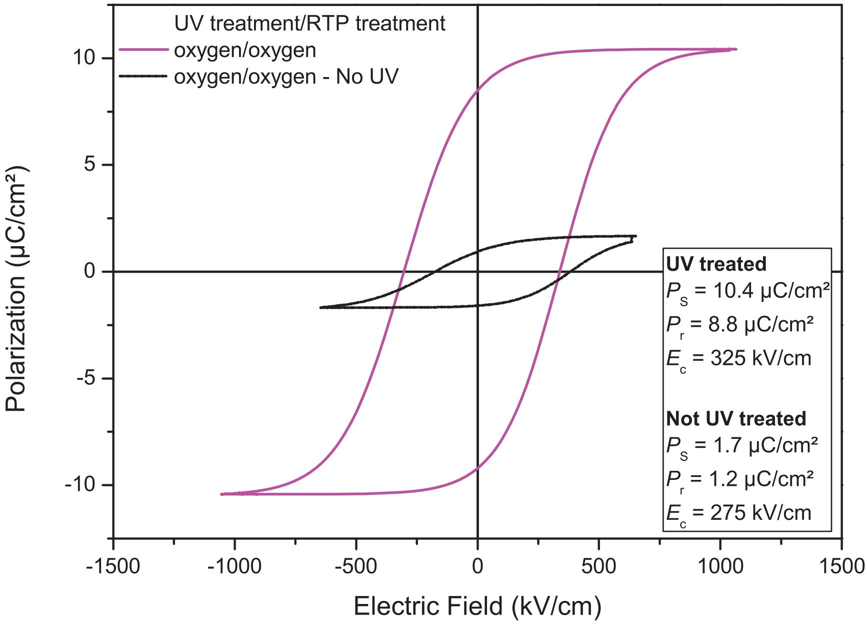

Figure 7.21 Polarization hysteresis loops (compensated) for $PbTiO_3$ films. Thermal treatment: 10′/200 °C + 10′/270 °C + 10′/350 °C + 60′/400 °C. UV treatment and crystallization in an oxygen atmosphere. UV irradiation is carried out at 270 and 350 °C. Reprinted (adapted) with permission from [23]. Copyright (2011) American Chemical Society

($P_S = 10.4$ μC cm^{-2}) and is more square than the non-UV-treated film (P_r and P_S are respectively 1.2 and 1.7 μC cm^{-2}).

UV treatment in an oxygen-rich atmosphere results in the dissociation of O_2, forming oxidizing species such as active oxygen (O^1D) and ozone (O_3) (Equations (7.9) and (7.10)). Ozone enhances the decomposition of organic compounds in a so-called ozone-oxidation process [115] and active oxygen reacts with suboxides to improve the stoichiometry and reduce the amount of oxygen vacancies and defects in the film [114, 115]. Specifically for the aqueous precursor [52, 84], the release of water leads to the formation of reactive atomic hydrogen and hydroxyl radicals [90,122]. Photolysis of released ammonia, formed during the decomposition of ammonium carboxylates or amides [52], results in the formation of reactive H, NH, and NH_2 radicals [122, 123]. Due to the UV activity of (partially) decomposed citrate complexes and the released decomposition products, the addition of photoactive compounds becomes superfluous for the aqueous PCSD method.

7.6.3.2 BiFeO$_3$ Films

Low-temperature deposition is challenging for all ferroic materials.[124, 125]. To illustrate the general applicability of the aqueous PCSD route, an aqueous citric acid-based precursor for multiferroic $BiFeO_3$ has also been demonstrated within the PCSD method [23, 75].

UV-Vis absorption spectra show that the deposited films are UV absorbing during all stages of the applied thermal profile (not shown, similar to Figure 7.4). UV absorption is assigned to $\pi \rightarrow \pi^*$ transitions in (partially decomposed) ammonium and metal citrate complexes [82] and is therefore intrinsically connected to the chemistry of the precursor system. GATR–FTIR spectroscopy indicates that the organic content in the film is subjected to an enhanced decomposition (not shown, similar to Figure 7.19). After the UV-enhanced thermal decomposition step, a crystalline $BiFeO_3$ film is obtained at only 400 °C, as inferred from the XRD pattern in Figure 7.22.

7.7 Final Remarks

The growing potential of chemical solution deposition methods oriented towards the low-temperature fabrication of ferroelectric and multiferroic thin films is illustrated by the photochemical solution deposition process (PCSD). Water- and diol solution-based chemical precursors with a low environmental impact are used for the preparation of multifunctional oxide films. The efficiency of different strategies for film deposition towards their application as a photosensitive precursor within the PCSD process is demonstrated in this chapter. Metal reagents with UV-absorber ligands, soluble UV-absorber charge-transfer metal complexes, or UV-absorbing molecules formed during the thermal decomposition of the deposited gel layers are evaluated for this purpose. Taking advantage of the photoreactivity of these precursors, lead titanate and bismuth ferrite perovskite thin films are being prepared at temperatures below 450 °C. Nanostructured thin films with an average grain size below 50 nm diameter are obtained as a result of the low-temperature thermal treatment for crystallization. In spite of the size effects on the functional properties, the small interactions between substrate and film, and the balance of the film composition by avoiding lead or bismuth losses by volatilization, contribute to obtain films with a homogeneous

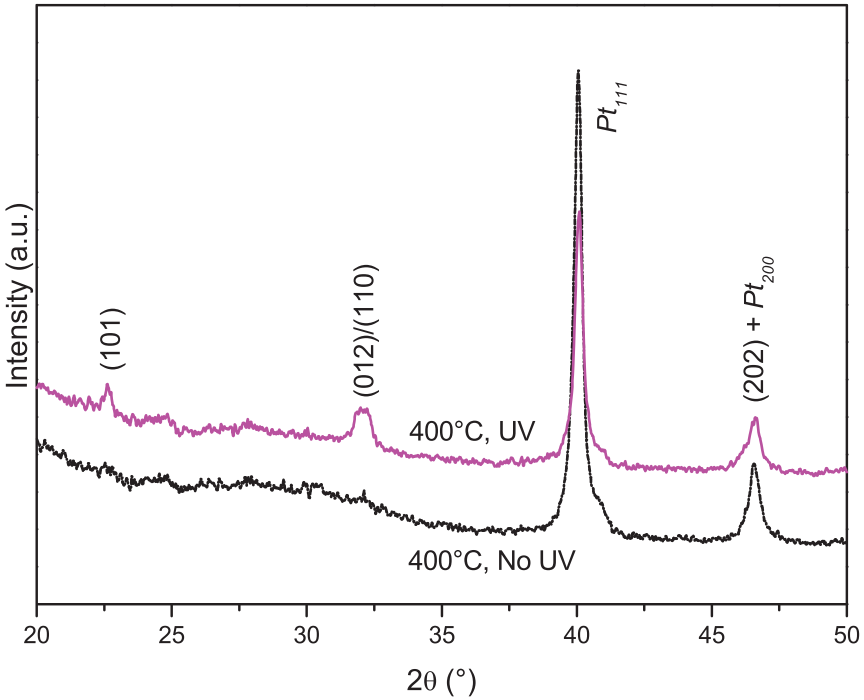

Figure 7.22 XRD patterns of PCSD deposited films obtained from an aqueous $BiFeO_3$ *precursor. Thermal treatment: 10′/200 °C + 120′/270 °C + 120′/350 °C, with or without UV irradiation at 270 and 350 °C. The crystallization is carried out at 400 °C in an oxygen atmosphere (JCPDS 86-1518). Reprinted with permission from [23]. Copyright (2011) American Chemical Society*

composition profile. As a result, these films present functional properties that fulfill the current demands necessary for their realistic integration in current Si technology and future flexible electronics.

References

(1) Wang, L., Yoon, M.H., Lu, G., et al. (2006) High-performance transparent inorganic–organic hybrid thin-film n-type transistors. *Nature Materials*, **5** (11), 893–900.

(2) Schwartz, R.W., Schneller, T., and Waser, R. (2004) Chemical solution deposition of electronic oxide films. *Comptes Rendus Chimie*, **7** (5), 433–461.

(3) Jeong, S. and Moon, J. (2012) Low-temperature, solution-processed metal oxide thin film transistors. *Journal of Materials Chemistry*, **22** (4), 1243–1250.

(4) Lefevre, M.J., Speck, J.S., Schwartz, R.W., et al. (1996) Microstructural development in sol–gel derived lead zirconate titanate thin films: the role of precursor stoichiometry and processing environment. *Journal of Materials Research*, **11** (8), 2076–2084.

(5) Kwok, C.K. and Desu, S.B. (1992) Pyrochlore to perovskite phase-transformation in sol–gel derived lead–zirconate–titanate thin-films. *Applied Physics Letters*, **60** (12), 1430–1432.

(6) Kim, D.H., Ahn, J.H., Choi, W.M., et al. (2008) Stretchable and foldable silicon integrated circuits. *Science*, **320** (5875), 507–511.

(7) Mitzi, D.B., Kosbar, L.L., Murray, C.E., et al. (2004) High-mobility ultrathin semiconducting films prepared by spin coating. *Nature*, **428** (6980), 299–303.

(8) Talapin, D.V. and Murray, C.B. (2005) PbSe nanocrystal solids for n- and p-channel thin film field-effect transistors. *Science*, **310** (5745), 86–89.

(9) Ahn, J.H., Kim, H.S., Lee, K.J., et al. (2006) Heterogeneous three-dimensional electronics by use of printed semiconductor nanomaterials. *Science*, **314** (5806), 1754–1757.

(10) Kim, M.G., Kanatzidis, M.G., Facchetti, A., et al. (2011) Low-temperature fabrication of high-performance metal oxide thin-film electronics via combustion processing. *Nature Materials*, **10** (5), 382–388.

(11) van der Wilt, P., Kane, M.G., Limanov, A.B., et al. (2006) Low-temperature polycrystalline silicon thin-film transistors and circuits on flexible substrates. *Mrs Bulletin*, **31** (6), 461–465.

(12) Bharadwaja, S.S.N., Dechakupt, T., Trolier-McKinstry, S., et al. (2008) Excimer laser crystallized (Pb,La)(Zr,Ti)O_3 thin films. *Journal of the American Ceramic Society*, **91** (5), 1580–1585.

(13) Mandeljc, M., Malic, B., and Kosec, M. (2003) PZT thin films with decreasing thickness crystallized at 400 degrees C. *Integrated Ferroelectrics*, **52**, 205–213.

(14) Xue, K.H., Celinska, J., and de Araujo, C.A.P. (2009) Low temperature preparation of ferroelectric bismuth titanate thin films. *Applied Physics Letters*, **95** (5), 052908.

(15) Calzada, M.L., Bretos, I., Jimenez, R., et al. (2004) Low-temperature processing of ferroelectric thin films compatible with silicon integrated circuit technology. *Advanced Materials*, **16** (18), 1620–1624.

(16) Wu, A., Vilarinho, P.M., Reaney, I., et al. (2003) Early stages of crystallization of sol–gel-derived lead zirconate titanate thin films. *Chemistry of Materials*, **15** (5), 1147–1155.

(17) Bretos, I., Jimenez, R., Garcia-Lopez, J., et al. (2008) Photochemical solution deposition of lead-based ferroelectric films: avoiding the PbO-excess addition at last. *Chemistry of Materials*, **20** (18), 5731–5733.

(18) Moon, J.W., Tazawa, S., Shinozaki, K., et al. (2006) Impact of thin $SrTiO_3$ seed layer to achieve low-temperature crystallization below 300 degrees C and ferroelectricity of lead zirconate titanate thin film. *Applied Physics Letters*, **89** (20), 202907.

(19) Hayashi, T., Iizawa, N., Togawa, D., et al. (2003) Excimer UV processing of $(Bi,Nd)_4Ti_3O_{12}$ ferroelectric thin films by chemical solution deposition method. *Japanese Journal of Applied Physics Part 1: Regular Papers Brief Communications and Review Papers*, **42** (9B), 5981–5985.

(20) Shannigrahi, S.R., Lim, X., and Tay, F.E.H. (2007) Excimer UV-assisted rapid thermal annealing of PbLa(Zr,Ti)O_3 thin films by a sol–gel deposition method. *Journal of Applied Physics*, **101** (2), 024107.

(21) Li, J.W., Kameda, H., Trinh, B.N.Q., et al. (2010) A low-temperature crystallization path for device-quality ferroelectric films. *Applied Physics Letters*, **97** (10), 102905.

(22) Martin-Arbella, N., Bretos, I., Jimenez, R., et al. (2011) Photoactivation of sol–gel precursors for the low-temperature preparation of $PbTiO_3$ ferroelectric thin films. *Journal of the American Ceramic Society*, **94** (2), 396–403.

(23) De Dobbelaere, C., Calzada, M.L., Jiménez, R., et al. (2011) Aqueous solutions for low-temperature photoannealing of functional oxide films: reaching the 400 °C Si-technology integration barrier. *Journal of the American Chemical Society*, **133** (33), 12922–12925.

(24) Wang, Z.J., Cao, Z.P., Otsuka, Y., et al. (2008) Low-temperature growth of ferroelectric lead zirconate titanate thin films using the magnetic field of low power 2.45 GHz microwave irradiation. *Applied Physics Letters*, **92** (22), 222905.

(25) Song, Y.J., Zhu, Y.F., and Desu, S.B. (1998) Low temperature fabrication and properties of sol–gel derived (111) oriented $Pb(Zr_{1-x}Ti_x)O_3$ thin films. *Applied Physics Letters*, **72** (21), 2686–2688.

(26) Bretos, I., Jimenez, R., Wu, A.Y., et al. (2014) Activated solutions enabling low-temperature processing of functional ferroelectric oxides for flexible electronics. *Advanced Materials*, **26** (9), 1405–1409.

(27) Moon, J., Kerchner, J.A., LeBleu, J., et al. (1997) Oriented lead titanate film growth at lower temperatures by the sol–gel method on particle-seeded substrates. *Journal of the American Ceramic Society*, **80** (10), 2613–2623.

(28) Kwok, C.K. and Desu, S.B. (1993) Low-temperature perovskite formation of lead zirconate titanate thin-films by a seeding process. *Journal of Materials Research*, **8** (2), 339–344.

(29) Zhang, X.D., Meng, X.J., Sun, J.L., et al. (2005) Low-temperature preparation of highly (100)-oriented $Pb(Zr_xTi_{1-x})O_3$ thin film by high oxygen-pressure processing. *Applied Physics Letters*, **86** (25), 252902.

(30) Naoyama, T., Noda, M., Okuyama, M., et al. (2006) Low temperature crystallization of $Pb(Zr,Ti)O_3$ and $PbTiO_3$ MOCVD thin film by hydrothermal treatment at 240 degrees C. *Integrated Ferroelectrics*, **84**, 137–146.

(31) Wang, Z.J., Chen, Y.N., Otsuka, Y., et al. (2011) Crystallization of ferroelectric lead zirconate titanate thin films by microwave annealing at low temperatures. *Journal of the American Ceramic Society*, **94** (2), 404–409.

(32) Semiconductor Industry Association (2009) International roadmap for semiconductors (ITRS). http://www.itrs.net/links/2009ITRS/Home2009.htm.

(33) Sun, Y.G. and Rogers, J.A. (2007) Inorganic semiconductors for flexible electronics. *Advanced Materials*, **19** (15), 1897–1916.

(34) Nathan, A., Ahnood, A., Cole, M.T., et al. (2012) Flexible electronics: the next ubiquitous platform. *Proceedings of the IEEE*, **100**, 1486–1517.

(35) Kim, Y.H., Heo, J.S., Kim, T.H., et al. (2012) Flexible metal-oxide devices made by room-temperature photochemical activation of sol–gel films. *Nature*, **489** (7414), 128–132.

(36) Chen, S.T., Yao, K., Tay, F.E.H., et al. (2010) Comparative investigation of the structure and properties of ferroelectric poly(vinylidene fluoride) and poly(vinylidene fluoride-trifluoroethylene) thin films crystallized on substrates. *Journal of Applied Polymer Science*, **116** (6), 3331–3337.

(37) Guan, F.X., Pan, J.L., Wang, J., et al. (2010) Crystal orientation effect on electric energy storage in poly(vinylidene fluoride-co-hexafluoropropylen) copolymers. *Macromolecules*, **43** (1), 384–392.

(38) Xu, H.S., Fang, X.R., Liu, X.B., et al. (2011) Fabrication and properties of solution processed all polymer thin-film ferroelectric device. *Journal of Applied Polymer Science*, **120** (3), 1510–1513.

(39) Bretos, I., Jimenez, R., Rodriguez-Castellon, E., et al. (2008) Heterostructure and compositional depth profile of low-temperature processed lead titanate-based ferroelectric thin films prepared by photochemical solution deposition. *Chemistry of Materials*, **20** (4), 1443–1450.

(40) Ramesh, R., Aggarwal, S., and Auciello, O. (2001) Science and technology of ferroelectric films and heterostructures for non-volatile ferroelectric memories. *Materials Science and Engineering R: Reports*, **32** (6), 191–236.

(41) Calzada, M.L., Gonzalez, A., Garcia-Lopez, J., et al. (2003) Crystallization, heterostructure, microstructure, and properties of ferroelectric strontium bismuth tantalate films derived from tantalum glycolate solutions. *Chemistry of Materials*, **15** (25), 4775–4783.

(42) Lankey, R.L. and Anastas, P.T. (2002) Life-cycle approaches for assessing green chemistry technologies. *Industrial and Engineering Chemistry Research*, **41** (18), 4498–4502.

(43) Clark, J.H. and Tavener, S.J. (2007) Alternative solvents: shades of green. *Organic Process Research and Development*, **11** (1), 149–155.

(44) Capello, C., Fischer, U., and Hungerbuhler, K. (2007) What is a green solvent? A comprehensive framework for the environmental assessment of solvents. *Green Chemistry*, **9** (9), 927–934.

(45) Lancaster, M. (2002) *Green Chemistry: An Introductory Text*, Royal Society of Chemistry, Cambridge,UK.

(46) Malic, B., Kosec, M., Smolej, K., et al. (1999) Effect of precursor type on the microstructure of $PbTiO_3$ thin films. *Journal of the European Ceramic Society*, **19** (6–7), 1345–1348.

(47) Wang, D.G., Chen, C.Z., Ma, J., et al. (2008) Lead-based titanate ferroelectric thin films fabricated by a sol–gel technique. *Applied Surface Science*, **255** (5), 1637–1645.

(48) Pardo, L., Poyato, R., Gonzalez, A., et al. (2002) Ca and La-modified lead titanate sol–gel thin films by UV-assisted processing for piezoelectric sensors. *Ferroelectrics*, **267**, 335–340.

(49) Pardo, L., Poyato, R., Gonzalez, A., et al. (2002) Low temperature preparation of piezoelectric thin films by ultraviolet-assisted rapid thermal processing. *Materials Science in Semiconductor Processing*, **5** (2–3), 77–83.

(50) Hardy, A., D'Haen, J., Goux, L., et al. (2007) Aqueous chemical solution deposition of ferroelectric Ti^{4+} cosubstituted $(Bi,La)_4Ti_3O_{12}$ thin films. *Chemistry of Materials*, **19** (12), 2994–3001.

(51) Van Bael, M.K., Nelis, D., Hardy, A., et al. (2002) Aqueous chemical solution deposition of ferroelectric thin films. *Integrated Ferroelectrics*, **45**, 113–122.

(52) Van Werde, K., Vanhoyland, G., Mondelaers, D., et al. (2007) The aqueous solution–gel synthesis of perovskite $Pb(Zr_{1-x},Ti_x)O_3$ (PZT). *Journal of Materials Science*, **42** (2), 624–632.

(53) De Dobbelaere, C., Hardy, A., D'Haen, J., et al. (2009) Morphology of water-based chemical solution deposition (CSD) lead titanate films on different substrates: towards island formation. *Journal of the European Ceramic Society*, **29** (9), 1703–1711.

(54) Kamlet, M.J., Abboud, J.L., and Taft, R.W. (1977) Solvatochromic comparison method. 6. Pi-star scale of solvent polarities. *Journal of the American Chemical Society*, **99** (18) 6027–6038.

(55) Taft, R.W. and Kamlet, M.J. (1976) Solvatochromic comparison method. 2. Alpha-scale of solvent hydrogen-bond donor (Hbd) acidities. *Journal of the American Chemical Society*, **98** (10), 2886–2894.

(56) Cheever, K.L., Swearengin, T.F., Edwards, R.M., et al. (2001) 2-Methoxyethanol metabolism, embryonic distribution, and macromolecular adduct formation in the rat: the effect of radiofrequency radiation-induced hyperthermia. *Toxicology Letters*, **122** (1), 53–67.

(57) Eisses, K.T. (1999) Concurrent teratogenic and mutagenic action of 2-methoxyethanol in *Drosophila melanogaster* larvae resulted in similar phenotypes: close resemblance to directed mutations. *Teratogenesis Carcinogenesis and Mutagenesis*, **19** (3), 183–204.

(58) Phillips, N.J., Calzada, M.L., and Milne, S.J. (1992) Sol gel-derived lead titanate films. *Journal of Non-crystalline Solids*, **147**, 285–290.

(59) EU-Directive 2011/65/EU (2011) Restrictions of the use of certain substances in electrical and electronic equipments (RoHS).

(60) Saito, Y., Takao, H., Tani, T., et al. (2004) Lead-free piezoceramics. *Nature*, **432** (7013), 84–87.

(61) Rödel, J., Jo, W., Seifert, K.T.P., et al. (2009) Perspective on the development of lead-free piezoceramics. *Journal of the American Ceramic Society*, **92** (6), 1153–1177.

(62) Livage, J., Henry, M., and Sanchez, C. (1988) Sol–gel chemistry of transition-metal oxides. *Progress in Solid State Chemistry*, **18** (4), 259–341.

(63) Baes, C.F. and Mesmer, R.E. (1976) *The Hydrolysis of Cations*, John Wiley & Sons, Inc., New York.

(64) Jolivet, J.-P. (2000) *Metal Oxide Chemistry and Synthesis: From Solution to Solid State*, John Wiley & Sons, Inc., New York.

(65) Magini, M., Licheri, G., Paschina, G., et al. (1988) *X-ray Diffraction of Ions in Aqueous Solutions: Hydration and Complex Formation*, University of Michigan, CRC Press.

(66) Ohtaki, H. and Radnai, T. (1993) Structure and dynamics of hydrated ions. *Chemical Reviews*, **93** (3), 1157–1204.

(67) Kepert, D.L. (1972) *The Early Transition Metals*, Academic Press, New York.

(68) Van Bael, M.K., Kareiva, A., Nouwen, R., et al. (1999) Sol–gel synthesis and properties of $YBa_2(Cu_{1-x}M_x)_4O_y$ (M = Co, Ni) and effects of additional replacement of yttrium by calcium. *International Journal of Inorganic Materials*, **1** (3–4), 259–268.

(69) Schieber, M., Tsach, T., Maharizi, M., et al. (1990) Films of Bscco superconductors prepared by spray pyrolysis of carboxylates. *Cryogenics*, **30** (5), 451–454.

(70) Ma, K.S. and Pierre, A.C. (1992) Sol–gel processing of high-T(C) superconductors in the Bi–(Pb)–Sr–Ca–Cu–O system. *Journal of Materials Research*, **7** (6), 1328–1335.

(71) Camargo, E.R. and Kakihana, M. (2002) Low temperature synthesis of lithium niobate powders based on water-soluble niobium malato complexes. *Solid State Ionics*, **151** (1–4), 413–418.

(72) Vanderbiest, O., Kwarciak, J., Dierickx, D., et al. (1991) Ceramic superconductors synthesized by sol–gel methods. *Physica C*, **190** (1–2), 119–121.

(73) Chiang, C., Shei, C.Y., Huang, Y.T., et al. (1990) Preparation of high-purity 110-K phase in the (Bi, Pb)–Sr–Ca–Cu–O superconductor system ssing a solution method. *Physica C*, **170** (5–6), 383–387.

(74) Kakihana, M. (1996) "Sol–gel" preparation of high temperature superconducting oxides. *Journal of Sol–Gel Science and Technology*, **6** (1), 7–55.

(75) Hardy, A., Gielis, S., Van den Rul, H., et al. (2009) Effects of precursor chemistry and thermal treatment conditions on obtaining phase pure bismuth ferrite from aqueous gel precursors. *Journal of the European Ceramic Society*, **29** (14), 3007–3013.

(76) Nelis, D., Mondelaers, D., Vanhoyland, G., et al. (2005) Synthesis of strontium bismuth niobate ($SrBi_2Nb_2O_9$) using an aqueous acetate–citrate precursor gel: thermal decomposition and phase formation. *Thermochimica Acta*, **426** (1–2), 39–48.

(77) Peys, N., Adriaensens, P., Van Doorslaer, S., et al. (2014) Aqueous citrato-oxovanadate(IV) precursor solutions for VO_2: synthesis, spectroscopic investigation and thermal analysis. *Dalton Transactions*, **43** (33), 12614–12623.

(78) Martell, A.E., and Smith, R.M. (1977) *Critical Stability Constants*, 3rd edition, Plenum Press.

(79) Narendar, Y. and Messing, G.L. (1997) Mechanisms of phase separation in gel-based synthesis of multicomponent metal oxides. *Catalysis Today*, **35** (3), 247–268.

(80) Calzada, M.L., Gonzalez, A., Poyato, R., et al. (2003) Photo-sensitive sol–gel solutions for the low-temperature UV-assisted processing of $PbTiO_3$ based ferroelectric thin films. *Journal of Materials Chemistry*, **13** (6), 1451–1457.

(81) Uozumi, G., Kageyama, K., Atsuki, T., et al. (1999) Evaluation of self-patterned $PbZr_xTi_{1-x}O_3$ thin film from photosensitive solution. *Japanese Journal of Applied Physics, Part 1: Regular Papers, Short Notes and Review Papers*, **38** (9B), 5350–5353.

(82) Szyper, M. and Zuman, P. (1976) Electronic absorption of carboxylic-acids and their anions. *Analytica Chimica Acta*, **85** (2), 357–373.

(83) Van Werde, K., Mondelaers, D., Vanhoyland, G., et al. (2002) Thermal decomposition of the ammonium zinc acetate citrate precursor for aqueous chemical solution deposition of ZnO. *Journal of Materials Science*, **37** (1), 81–88.

(84) Hardy, A., Van Werde, K., Vanhoyland, G., et al. (2003) Study of the decomposition of an aqueous metal-chelate gel precursor for $(Bi,La)_4Ti_3O_{12}$ by means of TGA–FTIR, TGA–MS and HT–DRIFT. *Thermochimica Acta*, **397** (1–2), 143–153.

(85) Brinker, C.J. and Sherer, G.W. (1990) *Sol–Gel Science: The Physics and Chemistry of Sol–Gel Processing*, Academic Press, Boston.

(86) Sakka, S. (2005) *Handbook of Sol–Gel Science and Technology. Processing Characterization and Applications*, edited by S. Sakka, Vol. **1**, Kluwer Academic Publishers, Dordrecht, The Netherlands.

(87) Klein, L.C. (1988) *Sol–Gel Technology for Thin Films, Fibers, Preforms, Electronics and Specialty Shapes*, Noyes Publishers, New Jersey.

(88) Livage, J. and Sanchez, C. (1992) Sol–gel chemistry. *Journal of Non-Crystalline Solids*, **145** (1–3), 11–19.

(89) Imai, H. (2005) Ultraviolet (UV) irradiation, in *Handbook of Sol–Gel Science and Technology*, edited by S. Sakka, Kluwer Academic Publishers, Boston, pp. 639–650.

(90) Van de Leest, R.E. (1995) UV photo-annealing of thin sol-gel films. *Applied Surface Science*, **86** (1-4), 278–285.

(91) Zayat, M., Parejo, P.G., and Levy, D. (2007) Preventing UV-light damage of light sensitive materials using a highly protective UV-absorbing coating. *Chemical Society Reviews*, **36** (8), 1270–1281.

(92) Martin-Arbella, N. (2012) *Fotoactivación de Precursores Sol–Gel para la Preparación de Láminas Delgadas Ferroeléctricas de $PbTiO_3$ a Baja Temperatura*, PhD Thesis, Universidad de Navarra.

(93) Hirayama, K. (1967) *Handbook of Ultraviolet and Visible Absorption Spectra of Organic Compounds*, Plenum Press, New York.

(94) Kikuta, K., Suzumori, K., Takagi, K., et al. (1999) Patterning of tin oxide film from photoreactive precursor solutions prepared via the addition of *N*-phenyldiethanolamine. *Journal of the American Ceramic Society*, **82** (8), 2263–2265.

(95) Mehrotra, R.C., Bohra, R., and Gaur, D.P. (1978) *Metal β-Diketonates and Allied Derivatives*, Academic Press, London.

(96) Barnum, D.W. (1961) Electronic absorption spectra of acetyl–acetonato complexes. 1. Complexes with trivalent transition metal ions. *Journal of Inorganic and Nuclear Chemistry*, **21** (3-4), 221–237.

(97) Gonzalez, A., Poyato, R., Pardo, L., et al. (2002) Photo-activated Ca–$PbTiO_3$ solutions for the preparation of films at low temperatures. *Ferroelectrics*, **271**, 1635–1640.

(98) Yu, J.J. and Boyd, I.W. (2002) Structural and electrical characteristics of zirconium oxide layers derived by photo-assisted sol–gel processing. *Applied Physics A: Materials Science and Processing*, **74** (2), 143–146.

(99) Martin-Arbella, N., Bretos, I., Jimenez, R., et al. (2011) Metal complexes with *N*-methyldiethanolamine as new photosensitive precursors for the low-temperature preparation of ferroelectric thin films. *Journal of Materials Chemistry*, **21** (25), 9051–9059.

(100) Pérez-Mezcua, D., Sirera, R., Jimenez, R., et al. (2014) UV-absorber bismuth(III)-*N*-methyldiethanolamine complex as low temperature precursor for bismuth-based oxide thin films. *Journal of Materials Chemistry C*, **2**, 8750–8760.

(101) Vogler, A. and Kunkely, H. (1998) Photoreactivity of metal-to-ligand charge transfer excited states. *Coordination Chemistry Reviews*, **177**, 81–96.

(102) Sharples, J.W. and Collison, D. (2014) The coordination chemistry and magnetism of some 3d–4f and 4f amino–polyalcohol compounds. *Coordination Chemistry Reviews*, **260**, 1–20.

(103) Le Bris, J., Hubert-Pfalzgraf, L.G., Daniele, S., et al. (2007) Cost efficient synthesis of bismuth aminoalkoxides from bismuth oxide: molecular structure of [Bi-2(mdea)(2)(mdeaH)(2)](mdeaH(2))(2). *Inorganic Chemistry Communications*, **10** (1), 80–83.

(104) Ohishi, T., Maekawa, S., and Katoh, A. (1992) Synthesis and properties of tantalum oxide-films prepared by the sol–gel method using photoirradiation. *Journal of Non-crystalline Solids*, **147**, 493–498.

(105) Imai, H., Hirashima, H., Awazu, K., et al. (1994) Novel modification method of sol–gel thin-films – densification of silica–gel films with electronic excitation. *Nippon Seramikkusu Kyokai Gakujutsu Ronbunshi – Journal of the Ceramic Society of Japan*, **102** (11), 1094–1096.

(106) Asakuma, N., Hirashima, H., Fukui, T., et al. (2002) Photoreduction of amorphous and crystalline ZnO films. *Japanese Journal of Applied Physics Part 1: Regular Papers Short Notes and Review Papers*, **41** (6A), 3909–3915.

(107) Imai, H., Tominaga, A., Hirashima, H., et al. (1999) Ultraviolet-reduced reduction and crystallization of indium oxide films. *Journal of Applied Physics*, **85** (1), 203–207.

(108) Ohishi, T. and Katoh, A. (1993) Photopatterning of tantalum oxide-films by a sol–gel method using a Krf excimer-laser. *British Ceramic Transactions*, **92** (2), 79–80.

(109) Nishizawa, K., Miki, T., Suzuki, K., et al. (2002) Photo-assisted control of surface morphology of alkoxy-derived ZrO_2 thin films. *Asian Ceramic Science for Electronics II and Electroceramics in Japan V, Proceedings*, **228–229**, 147–152.

(110) Boyd, I.W. and Zhang, J.Y. (2000) Low temperature photoformation of tantalum oxide. *Microelectronics Reliability*, **40** (4–5), 649–655.

(111) Calzada, M.L., Bretos, I., Jimenez, R., et al. (2007) Low-temperature ultraviolet sol–gel photoannealing processing of multifunctional lead-titanate-based thin films. *Journal of Materials Research*, **22** (7), 1824–1833.

(112) Vilarinho, P.M., Wu, A., Calzada, M.L., et al. (2009) PCT/IB2009/055699. *Universidade de Aveiro, CSIC.*

(113) JIPELEC, a division of Qualiflow Therm. http://www.jipelec.com/.

(114) Boyd, I.W. and Zhang, J.Y. (2001) Photo-induced growth of dielectrics with excimer lamps. *Solid-State Electronics*, **45** (8), 1413–1431.

(115) Zhang, Y., Terrill, R.H., and Bohn, P.W. (1999) Ultraviolet photochemistry and ex situ ozonolysis of alkanethiol self-assembled monolayers on gold. *Chemistry of Materials*, **11** (8), 2191–2198.

(116) Sirera, R., Leinen, D., Rodriguez-Castellon, E., et al. (1999) Processing effects on the compositional depth profile of ferroelectric sol–gel Ca–$PbTiO_3$ thin films. *Chemistry of Materials*, **11** (12), 3437–3444.

(117) Chen, S.Y. and Chen, I.W. (1994) Temperature–time texture transition of $Pb(Zr_{1-x}Ti_x)O_3$ thin-films.1. Role of Pb-rich intermediate phases. *Journal of the American Ceramic Society*, **77** (9), 2332–2336.

(118) Dawber, M., Rabe, K.M., and Scott, J.F. (2005) Physics of thin-film ferroelectric oxides. *Reviews of Modern Physics*, **77** (4), 1083–1130.

(119) Calame, F. and Muralt, P. (2007) Growth and properties of gradient free sol–gel lead zirconate titanate thin films. *Applied Physics Letters*, **90** (6), 062907.

(120) Habouti, S., Solterbeck, C.H., and Es-Souni, M. (2007) UV assisted pyrolysis of solution deposited $BiFeO_3$ multiferroic thin films. Effects on microstructure and functional properties. *Journal of Sol–Gel Science and Technology*, **42** (3), 257–263.

(121) Jimenez, R., Alemany, C., Calzada, M.L., et al. (2002) Processing effects on the microstructure and ferroelectric properties of strontium bismuth tantalate thin films. *Applied Physics A: Materials Science and Processing*, **75** (5), 607–615.

(122) McNesby, J.R., Okabe, H., and Tanaka, I. (1962) Vacuum ultraviolet photochemistry.3. Primary processes in vacuum ultraviolet photolysis of water and ammonia. *Journal of Chemical Physics*, **36** (3), 605–607.

(123) Kenner, R.D., Rohrer, F., and Stuhl, F. (1987) Generation of NH($^{a1\delta}$) in the 193 nm photolysis of Ammonia. *Journal of Chemical Physics*, **86** (4), 2036–2043.

(124) Xue, K.-H., Celinska, J., and Paz de Araujo, C.A. (2009) Low temperature preparation of ferroelectric bismuth titanate thin films. *Applied Physics Letters*, **95** (5), 052908.

(125) Malic, B., Mandeljc, M., Drazic, G., et al. (2008) Strategy for low-temperature crystallization of titanium-rich PZT thin films by chemical solution deposition. *Integrated Ferroelectrics*, **100**, 285–296.

8

Synthesis and Properties of Ferroelectric Nanotubes and Nanowires: A Review

Vincenzo Buscaglia and Maria Teresa Buscaglia

Institute of Energetics and Interphases, National Research Council, Italy

8.1 Introduction

Polar or pyroelectric materials have a non-centrosymmetric structure and possess an electrical dipole moment even in the absence of an external electric field. The macroscopic polarization resulting from these elementary dipole moments is called spontaneous polarization, P_S. Ferroelectric materials are a subset of polar crystals in which the polarization vector can be switched between two different equilibrium orientations by an external electric field. Because of their polar axis all ferroelectric crystals are also pyroelectric and piezoelectric. A piezoelectric crystal can be polarized, in addition to the electric field, by the application of a stress. Moreover, application of an electric field to a piezoelectric crystal determines a change of its dimensions. The related strain (contraction or expansion) depends on the sign of the electric field. Piezoelectric and, consequently, ferroelectrics also show the second harmonic generation or frequency doubling effect. In the following paragraphs a short and qualitative description of the properties of ferroelectric materials more closely related to the specific topic of this review is given. Readers interested in a more detailed introduction to ferroelectricity and related subjects can refer to classical textbooks and review articles [1–4].

Nanoscale Ferroelectrics and Multiferroics: Key Processing and Characterization Issues, and Nanoscale Effects, First Edition. Edited by Miguel Algueró, J. Marty Gregg, and Liliana Mitoseriu.
© 2016 John Wiley & Sons, Ltd. Published 2016 by John Wiley & Sons, Ltd.

Since the discovery of ferroelectricity in Rochelle salt (sodium potassium tartrate tetrahydrate) and potassium dihydrogen phosphate, many ferroelectric compounds have been reported [2]. Most are oxides and in particular oxides with perovskite or a perovskite-like structure, but ferroelectricity has also been described in halides [5], organic crystals [6], and polymers [7]. The interest in ferroelectricity started to rise in 1944 after the discovery of ferroelectricity in barium titanate, $BaTiO_3$. Ferroelectricity in this compound, as well as in many other ferroelectric oxides, is associated with other useful properties that made barium titanate, even in the form of a polycrystalline ceramic, very attractive for different applications. Due the complex elastic and electric boundary conditions, the grains spontaneously split in domains and, consequently, in as-sintered ceramics the polarization through the solid is randomly oriented and the material has not useful pyroelectric and piezoelectric properties. The domains and the associated polarization within the ceramic grains can be oriented in the direction of the applied field by the poling process, resulting in piezoelectric and pyroelectric properties comparable to those of the much more expensive single crystals. The poling process has made possible the large-scale industrial production of piezoelectric transducers and actuators. The reference ferroelectric ceramic material for piezoelectric applications is lead zirconate titanate $Pb(Zr,Ti)O_3$ (PZT). The very high relative dielectric constant (1500–5000 depending on grain size) and relatively low losses have made polycrystalline barium titanate the ceramic material most widely used in the electronic industry, mainly as a dielectric in multilayer ceramic capacitors. Other important applications of ferroelectric materials are non-volatile memories, IR radiation detectors, and thermistors with a positive temperature coefficient of resistivity.

Most ferroelectrics undergo a phase transition from a high-temperature paraelectric phase to a low-temperature ferroelectric modification. The transition occurs at the Curie temperature, T_C. Since most of the investigated 1D ferroelectric materials have a perovskite structure, we will take $BaTiO_3$ as a representative example. In barium titanate the transition from the parent paraelectric cubic phase to the ferroelectric tetragonal phase occurs at about 125 °C. The appearance of the spontaneous polarization is accompanied by a spontaneous strain of the cubic structure, which elongates along one of the crystallographic axes, lowering the symmetry. Both the spontaneous strain and polarization are determined by the off-centre displacement of the Ti ions along the direction of the tetragonal axis. As a result of this displacement, the centers of gravity of negative and positive charges are no longer coincident and the unit cell acquires a spontaneous electrical dipole. Thus ferroelectricity can be considered as a cooperative phenomenon that involves the long-range ordering of ions inside the crystal lattice and alignment of the associated spontaneous dipoles. Owing to the long-range nature of ferroelectric order, the properties of ferroelectric materials are not only determined by the composition and external field but also by the geometry and the size of the system, as well as by the specific boundary conditions. An example is provided by epitaxial ferroelectric thin films in which the magnitude and orientation of spontaneous polarization as well as the Curie temperature can be greatly modified by the bidimensional strain exerted by the substrate on the lattice [8, 9]. Moreover, the variation of thin-film properties with thickness is markedly different from the evolution observed in ceramics with decreasing grain size [10].

Monodimensional ferroelectric nanostructures such as nanowires (NWs) and nanotubes (NTs) have attracted much attention in recent years for two main reasons. Firstly, these nanostructures offer the opportunity to understand how ferroelectric properties and domain configuration and dynamics evolve with morphology and aspect ratio in 1D systems. Many NWs have a non-circular cross-section and this introduces an additional degree of freedom. The study of these systems was expected also to provide useful information for the fabrication of next-generation, fully three-dimensional FeRAM structures with the required bit density [11]. Secondly, it was theoretically predicted that a new kind of ferroelectric order (circular or toroidal ordering of dipoles) should appear in nanorods and nanodisks of small diameter [12, 13]. This arrangement is characterized by the absence of a depolarizing field and could open a new avenue for the use of ferroelectric nanostructures in data storage. Moreover, the need to obtain 1D nanostructures with controlled morphology has stimulated the development of a variety of synthesis techniques and fabrication strategies with a general validity that goes beyond the preparation of ferroelectric nanostructures.

This review focuses on three main aspects concerning monodimensional ferroelectric nanostructures: (i) the synthesis methods developed for the preparation on NWs and NTs either free-standing or grown on a substrate, (ii) the crystal structure, the domain organization, and the ferroelectric properties of these nanostructures, including local scale measurement by means of atomic force microscopy techniques, and (iii) the potential applications.

8.2 Synthesis of Ferroelectric Nanowires and Nanotubes

The most widely investigated 1D nanoferroelectrics are perovskites of general formula ABO_3 where A = Sr, Ba, Pb and B = Ti, Zr or A = Na, K, and B = Nb, Ta. Although $SrTiO_3$ is not ferroelectric, it is very close to the ferroelectric instability (incipient ferroelectric). Ferroelectric bismuth compounds such as $BiFeO_3$ and $Na_{0.5}Bi_{0.5}TiO_3$ have also attracted a large interest. The compound $Bi_4Ti_3O_{12}$ has a layered perovskite structure composed of alternating $(Bi_2Ti_3O_{10})^{2-}$ perovskite blocks and $(Bi_2O_2)^{2+}$ layers. Most of the preparation methods are "bottom-up" strategies corresponding to the synthesis of these nanoobjects starting at the atomic or molecular level. Common "bottom-up" approaches involve the direct growth from a liquid phase in which suitable precursors are dissolved or suspended and include hydrothermal, solvothermal, and molten salt synthesis [14–43]. A high level of morphological control can be attained using appropriate templates [44–76]. There are two kinds of templates: reactive precursor templates and porous membranes (silicon, polycarbonate, anodic alumina) with ordered cylindrical pores. In the latter case the pores of the membrane are impregnated by a solution or sol–gel precursor. After drying, calcination and removal of the membrane by chemical etching, free-standing or supported nanowires and nanotubes can be produced. Reactive templates usually consisting of nanowires or nanotubes of suitable oxides (TiO_2, alkali titanates, etc.) are converted into ferroelectric materials by means of hydrothermal, molten salt, or solid-state topochemical reactions. Long, polycrystalline ferroelectric nanofibers can be produced from suitable sol–gel precursors by electrospinning and subsequent calcination [77–90]. Most common "top-down" approaches consist in directly cutting nanocolumns from a ferroelectric single crystal using a focused ion beam (FIB) milling inside an electron microscope [91, 92].

8.2.1 Direct Growth from the Liquid Phase

The term "hydrothermal synthesis" usually refers to the crystallization of substances by means of heterogeneous reactions in aqueous media above 100 °C and 1 bar. The method exploits the strong acceleration of heterogenous reactions and the increased solubility of most inorganic compounds in hot water. The pressure inside the autoclave is essentially determined by the vapour pressure of water at the given temperature (autogenous pressure), which increases from 1 bar at 100 °C to 221 bar at 374 °C, the critical point of water. In most cases, pressure has a minor effect in comparison to temperature and pH. Nowadays heterogeneous reactions that occur in aqueous solution, even at temperatures lower than 100 °C, are sometimes indicated with the term "hydrothermal", because the same chemical processes often occur over a broad temperature range. Solvothermal synthesis can be considered as a generalization of the hydrothermal method when water is replaced by organic solvents (ethanol, ethylene glycol, heptadecane) or water—organic solvent mixtures. The same techniques can be applied for growing vertical arrays of nanorods on the surface of suitable substrates. Molten salt synthesis exploits the relatively low melting point of NaCl or the eutectic NaCl–KCl and the high solubility of appropriate oxide and carbonate precursors in the resulting liquid to induce the crystallization of a new compound.

Hydrothermal synthesis of ferroelectric perovskites can be carried out by using a broad variety of precursors, including soluble inorganic salts of alkaline and alkaline-earth elements (nitrates, chlorides, and acetates) and binary transition metal oxides (TiO_2, ZrO_2, Nb_2O_5, Ta_2O_5). The reaction is usually performed at very high pH (>11) and in the temperature range 100–250 °C. The highly alkaline conditions are usually provided by the addition of a strong base, such as NaOH, KOH, and tetraalkylammonium hydroxide, denoted as mineralizer. A high pH is required for two main reasons. Firstly, many ferroelectric perovskites of interest are thermodynamically unstable at acidic or even neutral pH. The thermodynamic modeling of the hydrothermal synthesis of ferroelectric perovskites and comparison with experimental results has been reported in detail by Riman and co-workers [14–17]. The predominant aqueous and solid species, the yield of reaction, and the influence of chelating species have been investigated as a function of pH, concentration, and temperature for several compounds. Two examples of predominance and yield diagrams are shown in Figure 8.1. The calculations reveal, for instance, that quantitative formation of $BaTiO_3$ occurs at pH ≥ 10, whereas phase pure $PbTiO_3$ is only obtained in a relatively narrow window of pH and lead concentration [15]. Secondly, the increase of pH has a strong kinetic effect. For the above-cited binary oxides a significant solubility is only attained when the hydroxide ion concentration is high enough, of the order of 0.1 mol L^{-1} or more. The increase in solubility determines an acceleration of the hydrothermal reaction. For this reason hydrous amorphous titania suspensions obtained by rapid hydrolisys of a Ti alkoxide (butoxide, isopropoxide) or a $TiOCl_2$ solution with ammonia or other strong bases are often used as titanium precursors as they show higher solubility and higher reactivity in comparison to the crystalline polymorphs anatase and rutile.

The cation of the mineralizer does not usually take part in the reaction, unless the desired product is a sodium or potassium compound, such as $KTaO_3$ or $Na_{0.5}Bi_{0.5}TiO_3$ [16]. The hydroxides $Ba(OH)_2$ and $Sr(OH)_2$ can be used for the synthesis of $BaTiO_3$ and $SrTiO_3$ without the addition of a mineralizer, owing to their high solubility and basicity. The thermodynamic calculations also indicate that the synthesis should be carried out in a CO_2-free environment as alkaline-earth carbonates are very stable and tend to precipitate determination of contamination of the hydrothermal reaction product [14].

Some selected examples of the nanowire morphologies obtained by liquid-phase synthesis are reported in Figure 8.2. The morphology and sometimes the crystallographic structure

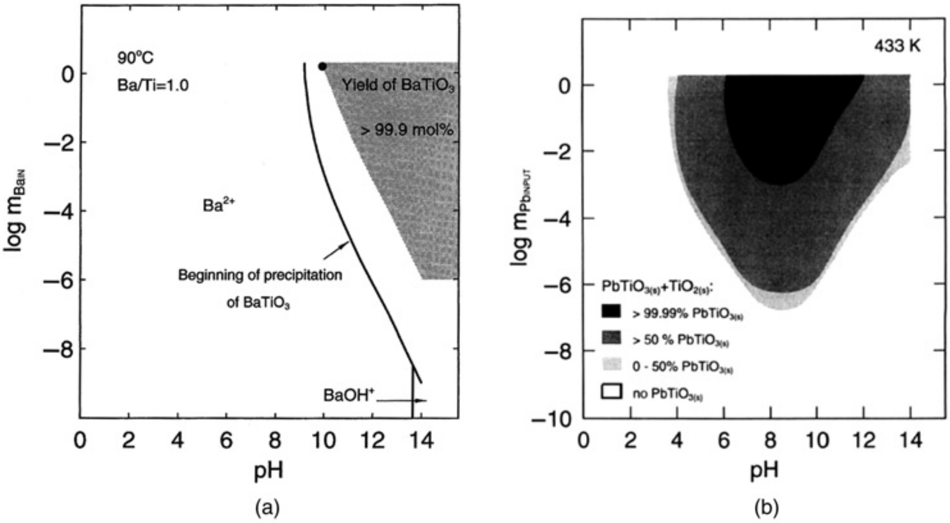

(a) (b)

Figure 8.1 Yield and stability diagrams for the hydrothermal synthesis of ferroelectric perovskites: (a) $BaTiO_3$ at 90 °C (reprinted with permission from [17]. Copyright © 2005, John Wiley & Sons) and (b) $PbTiO_3$ at 160 °C (reprinted with permission from [15]. Copyright © 2005, John Wiley & Sons)

of the particles can be modified by changing the chemical and physicochemical parameters, such as the solvent composition, type of precursor, temperature, and concentration, as well as by adding specific growth modifiers, usually organic molecules and hydrophilic polymers. The hydrothermal synthesis of $PbTiO_3$ and Pb(Zr,Ti)O_3 represents an interesting example. When the reaction is carried out at a moderate mineralizer concentration or, most often, when polyacrylic acid (PAA) or polyvynilic alcohol (PVA) are used as additives, formation of long single-crystalline nanowires with homogeneous morphology of the metastable PX phase (nonferroelectric tetragonal structure with I4/m space group) rather than the perovskite modification is observed [18–22] (Figure 8.2(a)). The PX structure is characterized by an open channel with diameter of 5 Å oriented along the *c* axis [22]. Transformation into the stable perovskite phase with a tetragonal structure occurs via a topochemical reaction induced by prolonged hydrothermal treatment (Figure 8.2(b) and (c)) or high-temperature (600 °C) calcination. However, because of the competition between the morphology-preserving topochemical transformation and dissolution-reprecipitation processes, like Ostwald ripening determining the formation of cubic crystals, the final morphology is strongly dependent on temperature, Pb/Ti ratio, mineralizer concentration, and soaking time [19, 20]. Often a mixture of NWs and cubic particles is obtained (Figure 8.2(c)).

Hydrothermal synthesis of $BaTiO_3$ and $SrTiO_3$ usually results in the formation of cubic or spherical particles. Single-crystal NWs with diameter of 50–100 nm and length up to a few micrometers were obtained by Joshi and co-workers [23, 24] (Figure 8.2(d)) using alkaline earth hydroxide and titania particles as precursors and adding ammonia as a mineralizer. Similarly, randomly oriented single-crystal NWs on a conductive glass were obtained using a TiO_2 nanoparticle seed layer deposited on the substrate by hydrothermal treatment in a

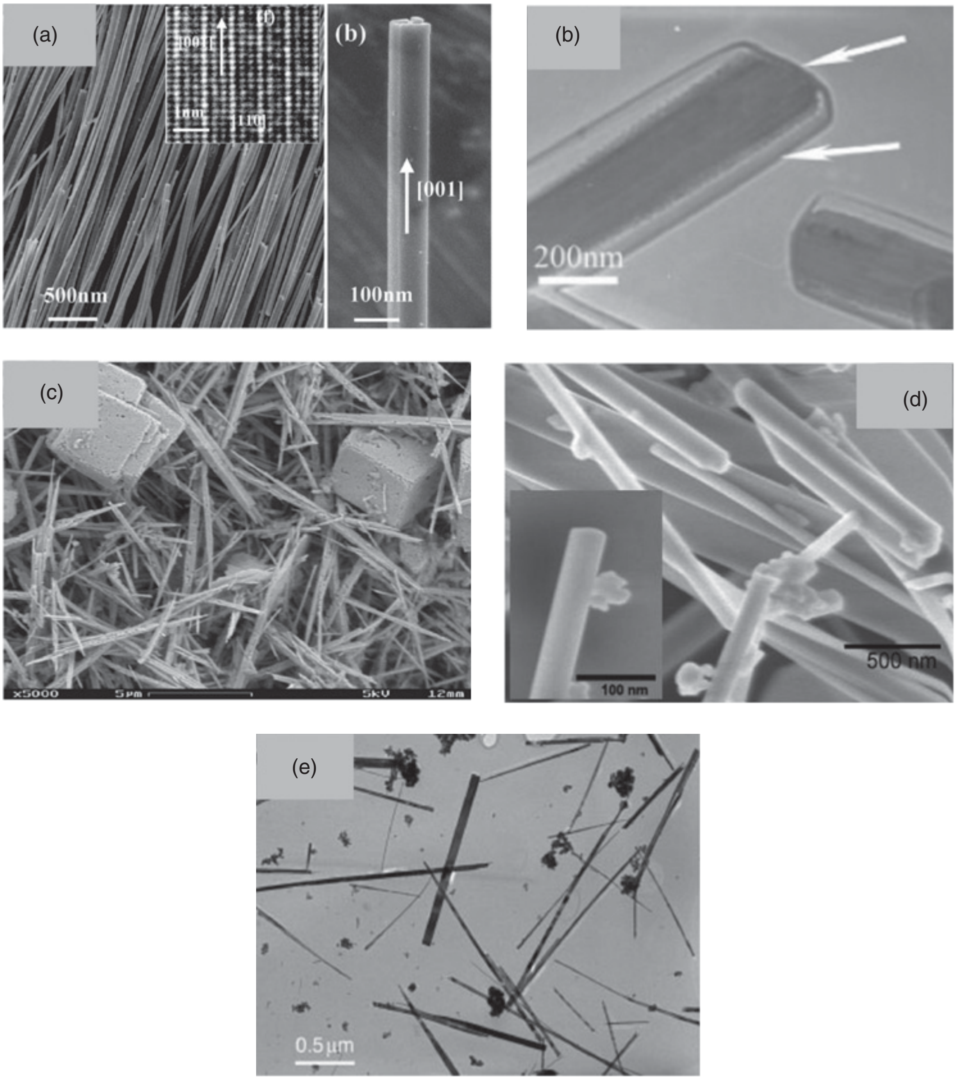

Figure 8.2 *Free-standing nanowires: (a) PbTiO$_3$, PX phase (reprinted with permission from [22]. Copyright (2010) American Chemical Society); (b) PZT. The arrows indicate a polymeric PVA coating (reprinted with permission from [21]. Copyright © 2005 Wiley-VCH Verlag GmbH & Co. KGaA, Weinheim). (c) PZT (reprinted from [19], Copyright (2001), with permission from Elsevier); (d) BaTiO$_3$ (reprinted with permission from [24]. Copyright (2006) American Chemical Society); (e) BaTiO$_3$ (reprinted with permission from [26]. Copyright © 2003 Wiley-VCH Verlag GmbH & Co. KGaA, Weinheim); (f) BaTiO$_3$ (reprinted with permission from [28]. Copyright (2003) American Chemical Society); (g) KNbO$_3$ (reprinted with permission from [33]. Copyright (2006) American Chemical Society); (h) KNbO$_3$ (reprinted with permission from [34]. Copyright (2005) American Chemical Society); and (i) SrTiO$_3$ mesocrystals (reprinted with permission from [52]. Copyright (2011) American Chemical Society)*

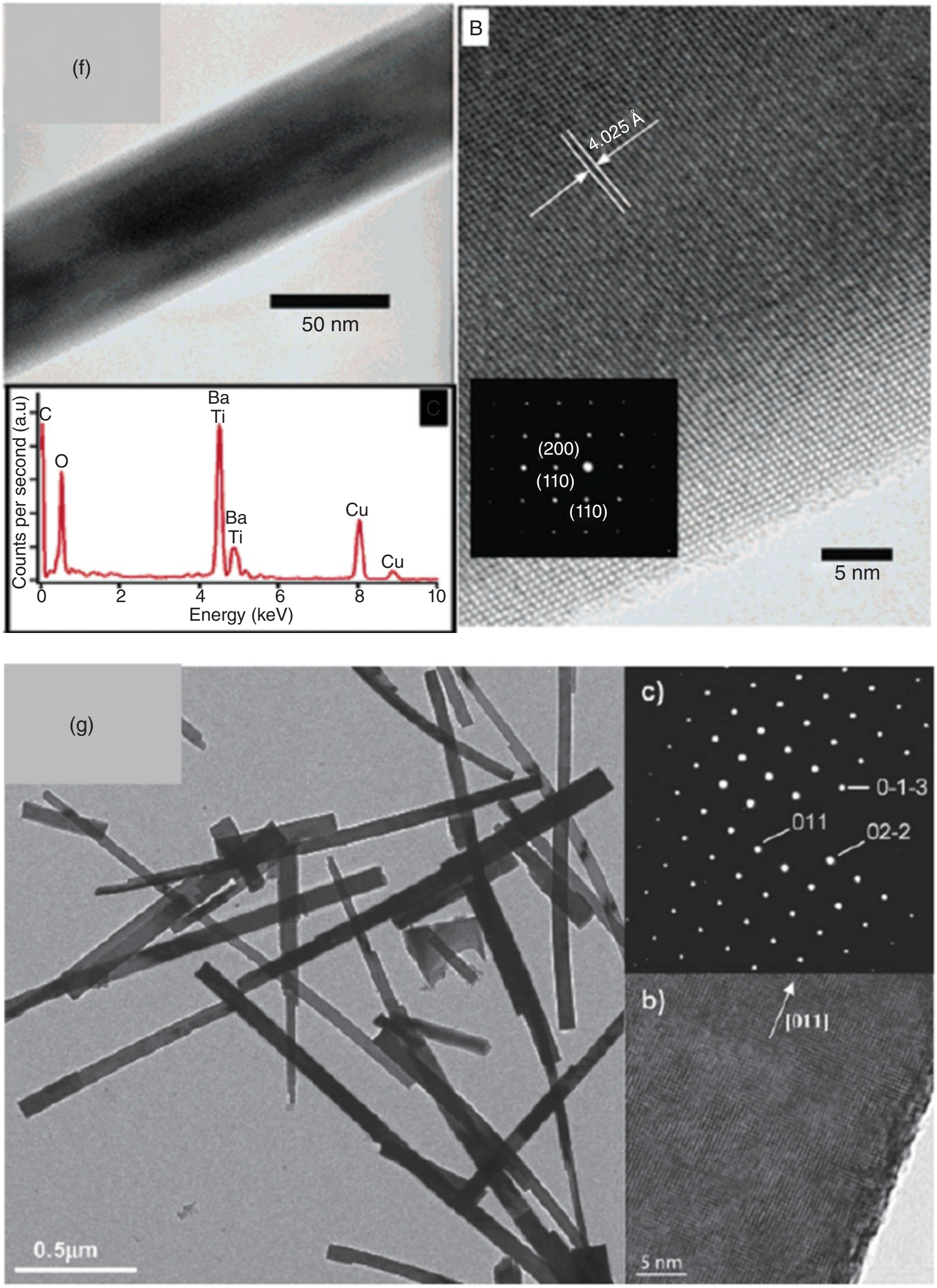
(f)
50 nm
B
4.025 Å
(200)
(110)
(110)
5 nm
C
Ba
Ti
C
O
Ba
Ti
Cu
Cu
Counts per second (a.u)
0
2
4
6
8
10
Energy (keV)
(g)
0.5μm
c)
0-1-3
011
02-2
b)
[011]
5 nm

Figure 8.2 (Continued)

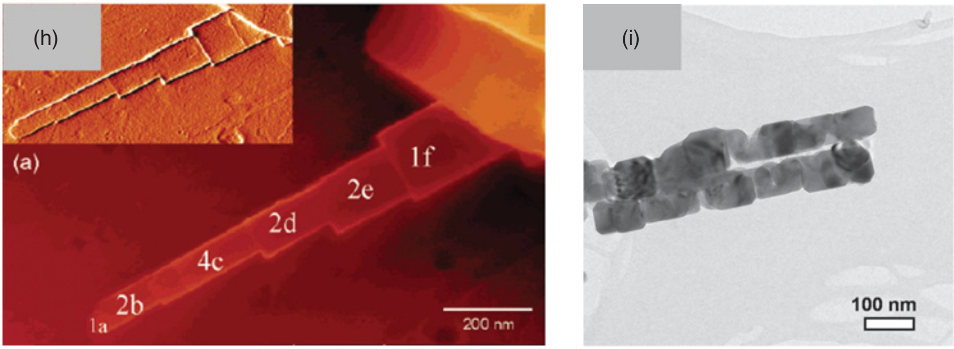

Figure 8.2 *(Continued)*

mixed $Ba(OH)_2$–ammonia solution at 170 °C [25]. Thus, ammonia is likely to play a fundamental role in morphology evolution. Solvothermal reaction at 280 °C for 6 h of bimetallic alkoxides, such as barium titanium isopropoxide and strontium titanium isopropoxide, dissolved in heptadecane with the addition of oleic acid resulted in thin single-crystal NWs (5–60 nm in diameter) [26] (Figure 8.2(e)). Very thin (6 nm in diameter) $BaTiO_3$ NWs with aspect ratio >1000 were obtained by reaction of $Ba(OH)_2$ and Ti tetrabutoxide at 200 °C in a mixed ethanol–water solvent using PEG as additive and KOH as mineralizer. A two-step process involving the initial formation of potassium titanate nanowires followed by the topochemical conversion to $BaTiO_3$ was proposed [27].

Single-crystal $BaTiO_3$ NWs can also be obtained by molten salt synthesis. BT nanorods grown along the [100] direction were synthesized at 820 °C in molten NaCl starting from a mixture of Ba oxalate and TiO_2 prepared in the presence of a non-ionic surfactant [28] (Figure 8.2(f)). When Ba is replaced by Sr, the reaction gives ST nanocubes. $PbTiO_3$ NWs were obtained in molten NaCl at 700 °C using a similar approach [29]. In a more recent reinvestigation, Rørvik et al. [30] pointed out that the molten salt synthesis at 760–820 °C not always yields NWs of the target perovskites $BaTiO_3$ and $PbTiO_3$. Although NWs were detected, electron diffraction revealed that the crystal structure corresponded to $BaTi_2O_5/BaTi_5O_{11}$ and $Na_2Ti_6O_{13}$ for the two different systems. It was shown that NaCl reacted with BaO (PbO), resulting in loss of volatile $BaCl_2$ ($PbCl_2$) with formation and preferential growth of titanium oxide-rich nanorods instead of the target phase $BaTiO_3$ ($PbTiO_3$). Indeed, alkali titanate NWs are easily obtained when TiO_2 particles are reacted in molten sodium or potassium chloride [31]. Likewise the simpler perovskites, pure and rare-earth doped bismuth titanate NWs can also be prepared by hydrothermal synthesis [32].

A rather rich literature also exists on the hydrothermal growth of $KNbO_3$ and $NaNbO_3$ NWs. The most common approach corresponds to the reaction of Nb_2O_5 powder at 150–200 °C in a highly concentrated NaOH or KOH solution for several days. A systematic study on the composition and morphology has shown that phase-pure $KNbO_3$ NWs with uniform morphology can only be obtained in a narrow window of experimental conditions (Figure 8.2(g)) [33]. Outside this narrow window, different morphologies or different phases are observed [33–36]. A peculiar "nanofinger" morphology corresponding to stacked nanocubes of decreasing size was observed after hydrothermal treatment at 200 °C [34] (Figure 8.2(h)). The growth kinetics of these "nanofingers" has been investigated and modeled in detail. The anisotropic growth is the result of a depletion phenomenon of the solution concentration at the nanostructure lateral faces and accumulation of defects blocking the coarsening of the successive cubes. The formation of $KNbO_3$ NWs can be promoted by the addition of a surfactant such as sodium dodecyl sulfate (SDS) [35, 36]. A detailed TEM investigation provided some support to an oriented attachment mechanism for the growth of these 1D structures. The concentration of SDS is crucial for the growth of the NWs. A similar mechanism was also suggested for the growth of $KTa_{1-x}Nb_xO_3$ NWs in the presence of PEG [37]. In that system a continuous evolution passing through different morphologies (octahedra, cubes, square prisms, "nanofingers", and truncated octahedra) is reported as the Nb/Ta ratio increases. Hydrothermal potassium niobate NWs usually possess an orthorhombic structure, which is the stable modification observed at RT in bulk crystals. However, $KNbO_3$ NWs with monoclinic structure and uniform morphology can be prepared by hydrothermal treatment of metallic Nb powder in 15 *M* KOH [38]. The synthesis of antiferroelectric $NaNbO_3$ was much less investigated. The hydrothermal reaction of Nb_2O_5 in 10 *M* NaOH at 180 °C evolves through the successive formation of three different phases with dissimilar morphology: $Na_{8-x}(H_3O)_xNb_6O_{19}\cdot 14H_2O$ nanorods, thin $Na_2Nb_2O_6\cdot 2/3H_2O$ NWs, and, finally, $NaNbO_3$ nanocubes [39].

Arrays of crystallographically oriented NWs can be grown on appropriate substrates by using hydrothermal reactions similar to those described above. As an example, $PbTiO_3$ aligned nanorods were obtained on polycrystalline $PbTiO_3$ and single-crystal $SrTiO_3$ substrates in the presence of sodium dodecylbenzenesulfonate (Figure 8.3(a)). The orientation of the NWs can be controlled by changing the crystallographic orientation of the substrate [40, 41]. A two-step growth mechanism was demonstrated: first an epitaxial layer was formed on the substrate; followed by self-assembly of nanocrystals forming a mesocrystal layer which matured into arrays of $PbTiO_3$ nanorods. The surfactant plays an essential role in the growth of the nanorods by oriented attachment of small primary nanocrystals [40–42]. Similarly, single-crystal, vertically aligned PZT NWs were grown at 175 °C on an oxidized Ti foil in the presence of PAA and PVA [43] (Figure 8.3(b)). The growth of vertically aligned $KNbO_3$ NWs on $SrTiO_3$ substrates was also described [38].

8.2.2 Templated Growth

The particle morphology resulting from hydrothermal/solvothermal synthesis can also be controlled by using reactive templates. If the transformation of the template occurs by means of a topochemical reaction or by heteroepitaxial growth, both the shape and the crystallographic order of the template are preserved in the final product. A typical example is the synthesis of 1D $BaTiO_3$ ($SrTiO_3$) structures by hydrothermal reaction of sodium titanate, potassium titanate, and hydrogen titanate NWs or NTs in an aqueous solution of $Ba(OH)_2$ ($Sr(OH)_2$). Alkaline titanates NWs and NTs can be easily grown by hydrothermal treatment of TiO_2 particles in concentrated NaOH or KOH solutions [44]. The crystallographic structure of these compounds corresponds to anatase-like layers consisting of corner-shared TiO_6 octahedra separated by interlayers containing alkaline ions and variable quantities of water. Owing to the layered structure and the weaker interactions along the stacking direction, the alkaline ions can be easily exchanged with ions of similar or smaller size, such as H_3O^+ and alkaline-earth cations [45]. The transformation occurs by a topochemical reaction that preserves the crystallographic order of the parent compound. This approach has

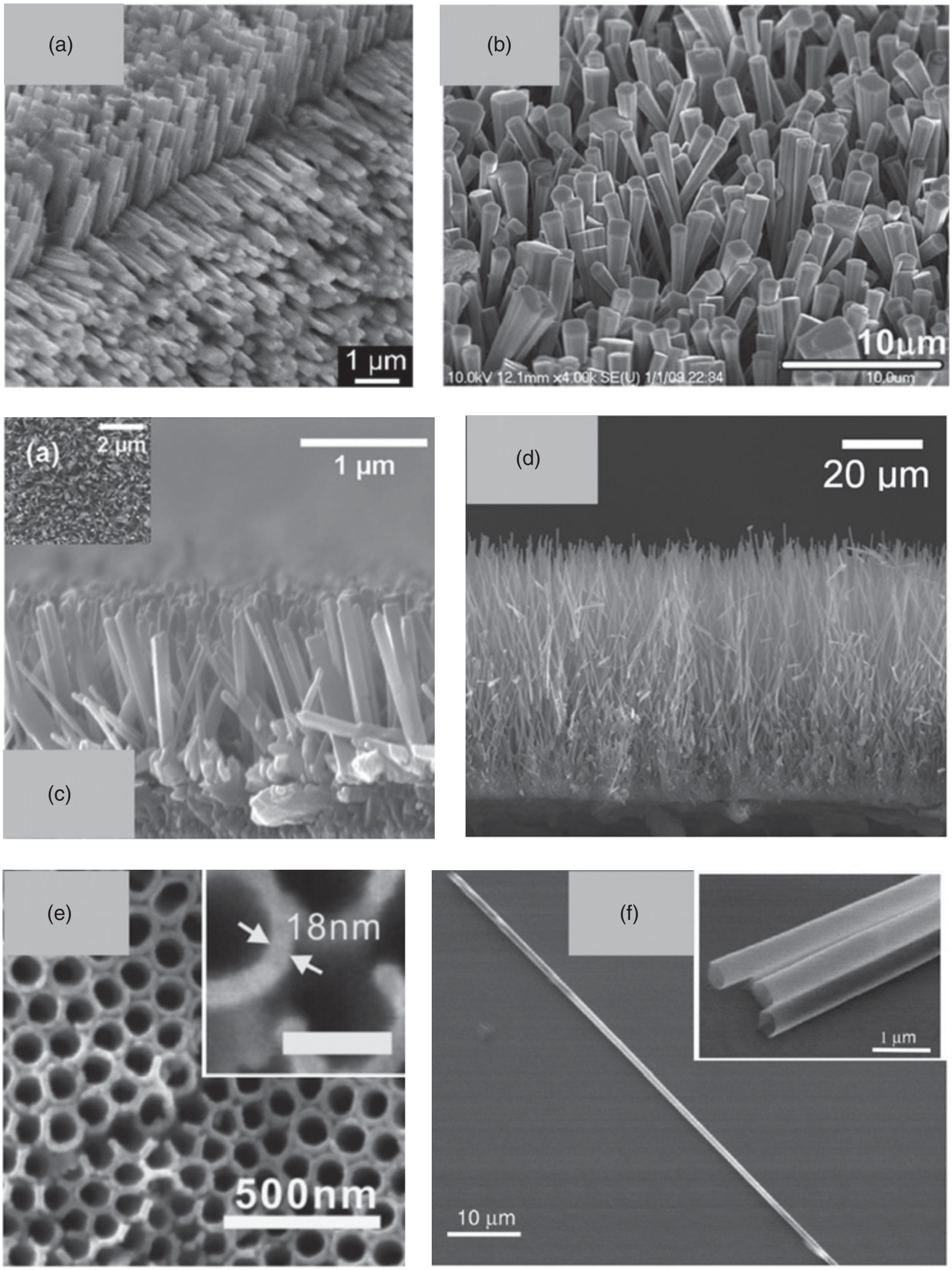
(a)
1 μm
(b)
10μm
10.0kV 12.1mm x4.00k SE(U) 1/1/09 22:34
10.0um
(a)
2 μm
1 μm
(c)
(d)
20 μm
(e)
18nm
500nm
(f)
1 μm
10 μm

Figure 8.3 *Vertical arrays of ferroelectric nanowires and nanotubes: (a)* $PbTiO_3$ *(from [40]. © IOP Publishing. Reproduced by permission of IOP Publishing. All rights reserved); (b) PZT (reprinted with permission from [43]. Copyright [2009], AIP Publishing LLC); (c)* $BaTiO_3$ *(reproduced from Ref. 54 with permission of The Royal Society of Chemistry); (d)* $BaTiO_3$ *(reprinted by permission from Macmillan Publishers Ltd [Nature Communications] [55], copyright (2013)); (e)* $SrTiO_3$ *(reprinted with permission from [62]. Copyright © 2010 The American Ceramic Society); (f and g) PZT (reprinted with permission from [67]. Copyright [2003], AIP Publishing LLC); and (h) PZT (reproduced from [69] by permission. Copyright (2008) American Chemical Society)*

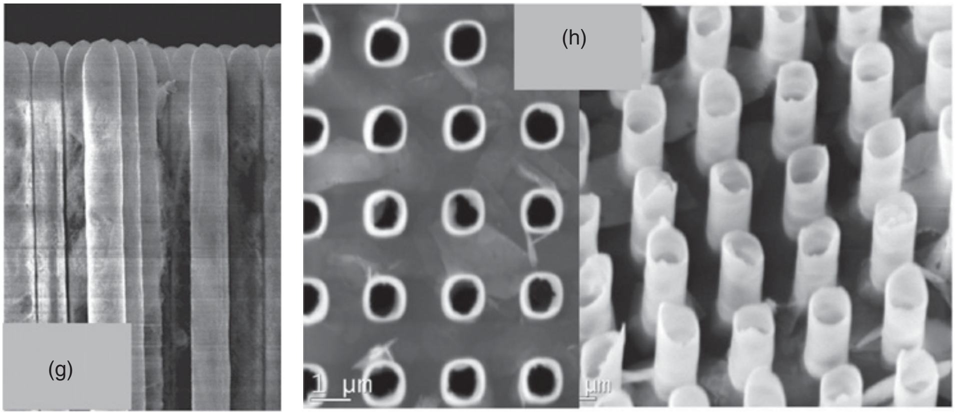

Figure 8.3 *(Continued)*

been investigated in some detail for the synthesis of $CaTiO_3$, $SrTiO_3$, and $BaTiO_3$ and is particularly suitable for the fabrication of $BaTiO_3$ nanowire arrays. The aspect ratio of the NWs can be controlled by changing the morphology and the composition of the template. Longer and thicker NWs can be obtained using $K_2Ti_4O_9$ in comparison to $Na_2Ti_3O_7$ [46]. The aspect ratio of the NWs can be increased to values >30 by optimizing the synthesis conditions [47]. Owing to the competition between topochemical reaction and dissolution–precipitation processes, the templated growth usually takes place in a narrow window of experimental conditions. Depending on barium hydroxide concentration, temperature, and reaction time, for a given precursor the product morphology can change from nanowire to different types of dendritic crystals and to cubic nanocrystals [48, 49]. Formation of the perovskite sometimes occurs by heterogeneous nucleation and growth on the surface of the alkali titanate template rather than a topochemical transformation.

Consequently the hydrothermal reaction results in polycrystalline NWs or NTs with rough surfaces [50,51]. Formation of $SrTiO_3$ mesocrystals retaining the wire-like morphology of the precursor has been observed after the hydrothermal treatment of anatase NWs [52] (Figure 8.2(i)). The mesocrystals result from heteroepitaxial nucleation and growth of perovskite nanocubes on opposite surfaces of anatase NWs. This transformation mechanism is intermediate between topochemical transformation and random heterogeneous and growth of the product on the template surface.

When the templated growth approach is applied to $CaTiO_3$, the reaction first produced bundles of NWs that later recrystallize with formation of hollow prismatic crystals with square section [50]. Topochemical transformation of anatase NWs in $BaTiO_3$ was also obtained by reaction with $BaCO_3$ in molten KCl–NaCl mixture at 700 °C [53]. Topochemical hydrothermal reactions of appropriate templates are of crucial importance for the fabrication of aligned arrays of NWs. Vertically aligned $BaTiO_3$ NWs on fluorine-doped tin oxide (FTO) glass substrates can be obtained by a two-step hydrothermal process [54] (Figure 8.3(c)). The first step corresponds to the growth of rutile NWs on the FTO substrate in acidic solution using Ti isopropoxide as precursor. Transformation of the TiO_2 NWs in $BaTiO_3$ was then carried out by the conventional treatment in a $Ba(OH)_2$ solution. A two-step hydrothermal process was also described for growing long (45 μm) NWs with a high aspect ratio (75) on a Ti foil preoxidized at high temperature [55] (Figure 8.3(d)).

Fabrication of single-crystal perovskite NTs by topochemical conversion of NT precursors seems to be more difficult owing to the lower stability of the templates. The synthesis of $BaTiO_3$ and $SrTiO_3$ NTs from hydrogen titanate NTs was initially described by Mao et al. [56]. However, the experimental conditions were not reported in detail. Later investigations [48, 57, 58] have shown that the nanotube geometry is hardly preserved during hydrothermal treatment at 110–200 °C; formation of dendritic structures and/or spherical/rounded particles is generally observed. The morphology evolution and the reaction kinetics were investigated in detail by Maxim et al. [58]. Formation of dendritic crystals occurs by heterogeneous nucleation on the NT surface and further growth proceeds by dissolution–precipitation controlled by a phase-boundary reaction. Synthesis of $BaTiO_3$ NTs by reaction of thin (20 nm) hydrogen titanate NTs with a $Ba(OH)_2$ solution in an ethanol/water mixture at mild temperature (50 °C) has been recently reported [59].

Vertically aligned arrays of $BaTiO_3$ and $SrTiO_3$ NTs can be obtained by hydrothermal treatment in $Ba(OH)_2$ and $Sr(OH)_2$ solution of highly ordered titania NT arrays fabricated by the well-known anodization process of titanium plates [60–65] (Figure 8.3(e)). The morphology of the titania NTs can be controlled by changing the composition of the electrolyte [63]. The as-prepared titania NTs are amorphous but can be transformed in anatase by thermal treatment at moderate temperature, fully retaining the ordered structure. Often the hydrothermal conversion is incomplete, with formation of $TiO_2/SrTiO_3$ heterostructures.

The most common types of physical templates for the fabrication of NTs and NWs are anodic aluminum oxide, silicon, and polycarbonate (PC) in the form of membranes with ordered cylindrical porosity [66–71]. A solution containing the appropriate metal ions or a convenient sol–gel precursor is then infiltrated into the membrane pores and dried. The thickness of the nanotubes can be controlled by the number of infiltration/drying cycles. Examples of PZT NTs grown using porous inorganic membranes are shown in Figure 8.3(f) to (h). Nanorods can be obtained by filling the pores of the membrane by electrophoretic deposition using a sol suspension [71]. The membrane can be removed by chemical etching (Al_2O_3, Si) as reported in Figure 8.3(f) and (g) or by thermal treatment in air (PC). A thermal treatment is also necessary to convert the precursor in the corresponding polycrystalline perovskite. Arrays of PZT nanotubes can also be obtained by deposition of the perovskite by magnetron sputtering or pulsed laser deposition on a positive template represented by vertically aligned ZnO nanorods on a silicon substrate [72]. Zinc oxide template and silicon substrate were removed by chemical etching.

8.2.3 Topochemical Solid-State Reactions

Solid-state topochemical transformations can be exploited for the fabrication of nanowires and nanotubes by thermal treatment of reactive templates at moderate temperature (500–800 °C). In a seminal paper, Fan et al. [73] reported the fabrication of long monocrystalline $ZnAl_2O_4$ nanotubes by reactive diffusion of core–shell $ZnO@Al_2O_3$ templates. The growth of the ternary compound at the interface occurs by a topochemical transformation and, consequently, the single-crystal nature of the ZnO core is preserved in the spinel nanotube. Formation of the central cavity involves the Kirkendall effect. The Kirkendall effect is a consequence of the different diffusivities of atoms in a diffusion couple causing a movement of the initial interface and a supersaturation of lattice vacancies. This supersaturation may lead to a condensation of extra vacancies in the form of so-called "Kirkendall voids" close to the interface on the side of the fastest moving component. Owing to the constrained core–shell geometry used in the experiment, the porosity coagulates at the centre of the ZnO core, resulting in a single cylindrical cavity when the reaction is completed. Opposite, when the component with higher mobility is located in the shell region, the reaction will result in a dense NW as the Kirkendall porosity will be eliminated as the shell is progressively consumed during the reaction. Diffusion-controlled topochemical solid-state reactions coupled with the Kirkendall effect can be considered as generic fabrication routes to a range of hollow nanostructures [74]. These strategies were applied to the solid-state synthesis of $BaTiO_3$ NWs and of $Bi_4Ti_3O_{12}$ NWs and NTs. Single-crystal barium titanate NWs were obtained by reaction at 700 °C of $TiO_2@BaCO_3$ templates prepared by coating hydrogen titanate NWs with nanocrystalline carbonate [75] (Figure 8.4(a)). The morphology of

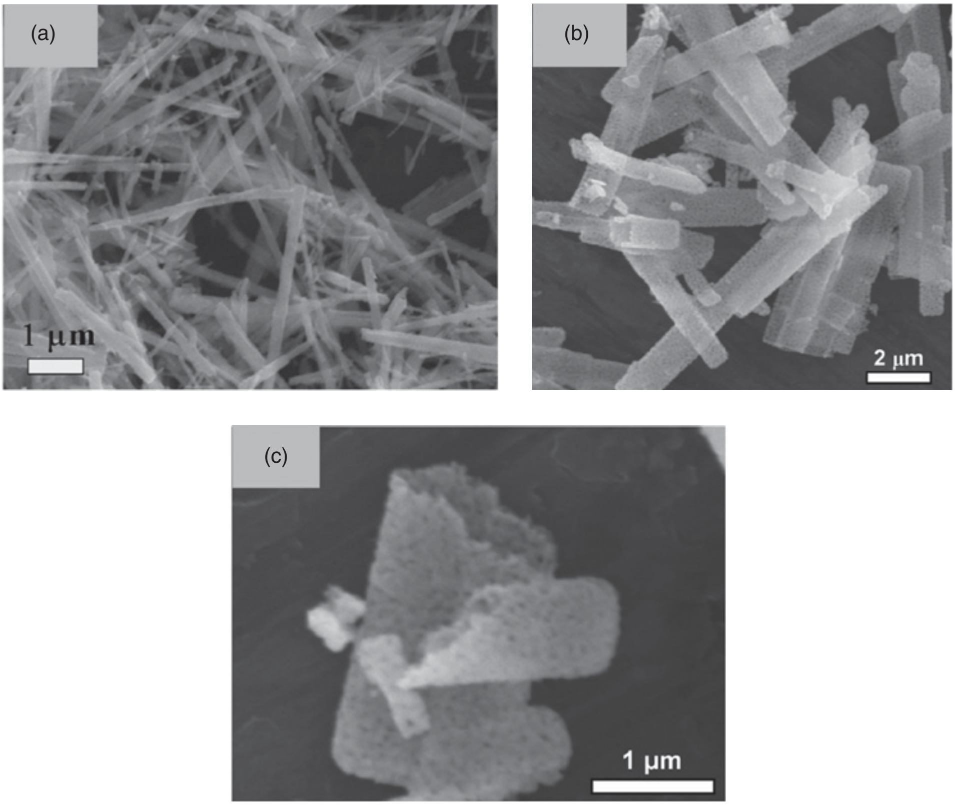

Figure 8.4 *Nanowires and nanotubes obtained by solid-state reaction of reactive templates: (a) $BaTiO_3$ nanowires (reprinted with permission from [75]. Copyright (2009) American Chemical Society); (b) porous $Bi_4Ti_3O_{12}$ nanowires; and (c) porous $Bi_4Ti_3O_{12}$ nanotubes (reprinted with permission from [76]. Copyright (2011) American Chemical Society)*

bismuth titanate was determined by the different assembly of the reactive templates [76]. $Bi_2O_3@TiO_2$ templates produced porous NWs or porous NTs depending on the thickness of the starting Bi_2O_3 rods (Figure 8.4(b) and (c)). In contrast, $TiO_2@Bi_2O_3$ templates led to single crystals of $Bi_4Ti_3O_{12}$ NWs.

8.2.4 Electrospinning

Electrospinning is a simple and versatile method for generating ultra-thin fibers of a rich variety of materials that include polymers, composites, and ceramics. This non-mechanical, electrostatic technique involves the use of a high-voltage electrostatic field to charge the surface of a polymer solution droplet and thus to induce the ejection of a liquid jet through a spinneret. The route of the charged jet is controlled by the electric field. The jet extends through spiraling loops; as the loops increase in diameter the jet grows longer and thinner until it solidifies or collects on the target [77]. Ceramic fibers are fabricated starting from a sol–gel precursor suspension. A spinnable sol commonly used in the preparation of $BaTiO_3$ fibers is obtained by (i) dissolution of Ba acetate and Ti isoproxide in acetic acid and (ii) addition of a solution of PVP in ethanol to the Ba–Ti precursor solution [78–82]. The spinnability depends on the relative amounts of acetic acid, ethanol, and metal precursors [78]. The dried electrospun fibers are amorphous; crystallization of the perovskite is induced by calcination at temperatures above 700 °C. The final inorganic fibers have a length up to several cm, a diameter in the range 100–500 nm depending on the specific experimental conditions, and consist of connected nanoparticles with a size from a few tenths to about 100 nm. If the calcination temperature is exceedingly high, the fibers develop a necklace morphology or even collapse. Beside barium titanate, electrospun fibers were also reported for $PbTiO_3$, PZT, $Bi_4Ti_3O_{12}$, $BiFeO_3$, and $NaTaO_3$ [83–90]. The main advantages of the electrospinning process are the low cost, the uniform diameter, and the considerable length of the fibers, as well as the possibility to produce large amounts of material. The polycrystalline structure makes the fibers less attractive for piezoelectric and ferroelectric applications since they do not have a net macroscopic polarization and poling is required to develop suitable properties. In contrast, electrospun fibers have a potential as fillers in polymer–ceramic composites to increase the dielectric constant.

8.2.5 Focused Ion Beam Lithography

Nanocolumns with a square or rectangular base and lateral size of 100–500 nm were directly patterned from $BaTiO_3$ single crystals using a focused ion beam microscope (FIB). The lateral edges of the columns were oriented along the three ⟨100⟩ pseodocubic directions. The columns remain attached to the parent crystals by their extremities. More complex morphologies corresponding to creation of bumps and notches on individual nanocolumns can be fabricated for studying the influence of size and aspect ratio on domain configuration and domain dynamics [91, 92].

8.3 Crystal Structure, Phase Transitions, and Ferroelectric Properties

Considering the very small size of NWs and NTs, the crystal structure is commonly investigated by powder X-ray diffraction methods, which provide the average structure of a large number of nanoobjects with a more or less wide size and aspect ratio distributions. Rich information on crystal structure, lattice arrangement, growth direction, domain patterns, and the existence of defects in individual NWs can be obtained by means of high-resolution transmission electron microscopy (HRTEM) and scanning transmission electron microscopy (STEM).

Ferroelectric properties and domain configuration in 1D nanostructures can be investigated using scanning force microscopy techniques such as piezoresponse force microscopy (PFM) and electrostatic force microscopy (EFM). PFM is a modification of the contact atomic force microscopy (AFM) that was initially introduced to investigate the properties of ferroelectric thin films and later extended to ceramics and different kinds of nanostructures [93, 94]. The technique is based on the detection of local electromechanical vibrations of a ferroelectric/piezoelectric sample caused by an external AC electric field applied between a conducting AFM tip and a counterelectrode. The deflection of a cantilever that oscillates together with the surface of the sample is detected by using a lock-in amplifier. Ferroelectric domains are visualized by monitoring the first harmonic of the deflection signal. Its amplitude is proportional to the local longitudinal piezoelectric coefficient, and the phase reflects the polarization direction (phase = 0° if the probing electric field is parallel to the local polarization and phase = 180° if the electric field is antiparallel). By measuring the signal corresponding to a torsional deformation of the cantilever, one can obtain information about the distribution of in-plane components of the polarization. Considering that the piezoelectric coefficient is proportional to the polarization through the dielectric constant and the electrostrictive coefficient, PFM allows for full imaging of the local polarization distribution with a high spatial resolution, which can be even of the order of 10 nm.

In EFM, the surface potential and the surface charge density can be obtained by measuring the electrostatic force acting on the AFM tip. This technique is particularly useful for imaging the domain structure and its evolution as determined by a temperature variation or application of a DC voltage between the tip and the sample [95].

For perovskites with a tetragonal structure at room temperature, XRD measurements usually indicate that the polar structure is preserved in the NWs although the spontaneous strain and tetragonality of the structure (defined as $c/a - 1$, where c and a are the lattice parameters of the unit cell where the electric dipole is oriented along the c direction) are reduced in comparison to the single-crystal value. Nevertheless, a polar structure is observed down to diameters of less than 10 nm. $BaTiO_3$, $PbTiO_3$, and PZT free-standing NWs obtained by hydrothermal or solvothermal synthesis usually grow along a pseudocubic [100] direction. During cooling through the Curie temperature a spontaneous polarization develops parallel to the elongation direction, which becomes the tetragonal [001] direction [21, 26–28, 40, 55, 96–98]. Accordingly, the existence of single-domain NWs with polarization aligned along the major axis has been documented by PFM investigations [99, 100]. Growth along one of the [100] pseudocubic directions is also reported for orthorhombic $KNbO_3$ and $KTa_{1\text{-}x}Nb_xO_3$ NWs [33, 36, 37, 101].

A decrease in tetragonality implies a diminution of spontaneous polarization and Curie temperature as these quantities are directly related in tetragonal ferroelectric perovskites. The T_C of $BaTiO_3$ NWs of different diameters prepared by solvothermal synthesis [26] and capped with oleic acid was determined by EFM [102]. T_C decreases linearly with the reciprocal of the NW diameter (d_{nw}) and drops to room temperature when d_{nw} = 3 nm (Figure 8.5(a)).

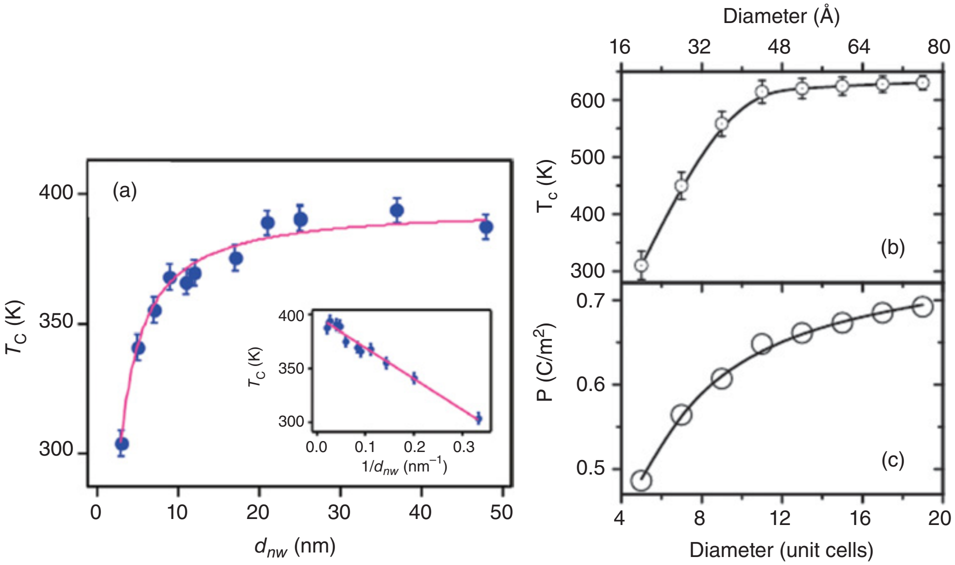

Figure 8.5 *(a) Ferroelectric phase transition temperature (T_C) in $BaTiO_3$ as a function of nanowire diameter. The solid circles are the experimentally determined data and the error bars are uncertainties. The solid line is the result of the fit to the data using the $1/d_{nw}$ scaling relation (reprinted with permission from [102]. Copyright (2006) American Chemical Society). (b) T_C and (c) magnitude of polarization at 64 K of PZT nws as a function of d_{nw} from an ab initio study. The diameter is in units of Å (bulk lattice constant) for the upper (lower) horizontal axis. The fitted result using the $1/d_{nw}$ scaling law is shown as a solid line in (c) (reprinted (Figure 3) with permission from [103]. Copyright (2005) by the American Physical Society)*

These results are in line with the temperature-dependent atomistic simulations of PZT NWs based on the use of first-principle derived effective Hamiltonians [103]. A sharp para/ferro transition corresponding to the appearance of polarization along the major axis of the NW was predicted. The Curie temperature slightly decreases below the bulk value down to a diameter of 4.4 nm and then rapidly drops and attains room temperature when $d_{nw} = 2$ nm (Figure 8.5(b)). The polarization follows a $1/d_{nw}$ scaling law (Figure 8.5(c)). First-principle calculations on $BaTiO_3$ NWs resulted in a critical diameter of 1.2 nm for ferroelectric instability [104].

One of the key factors for the stability of nanoscale ferroelectricity is an efficient screening of the surface charges associated with polarization. In bulk samples and ferroelectric devices the surface charges can be screened by the deposition of suitable electrodes in a planar capacitor configuration. If the surface charges are not efficiently screened, the resulting depolarization field, which opposes spontaneous polarization, will reduce or even suppress ferroelectricity. Thus the polarization perpendicular to the major axis in thin NWs is destroyed by the depolarization field whereas the dipoles are allowed to be parallel to the elongation direction. According to the DFT calculations of Spanier et al. [102], retention of ferroelectricity in thin NWs is also determined by the effective screening operated by chemiadsorbed hydroxyl groups (always present when the NWs are grown from

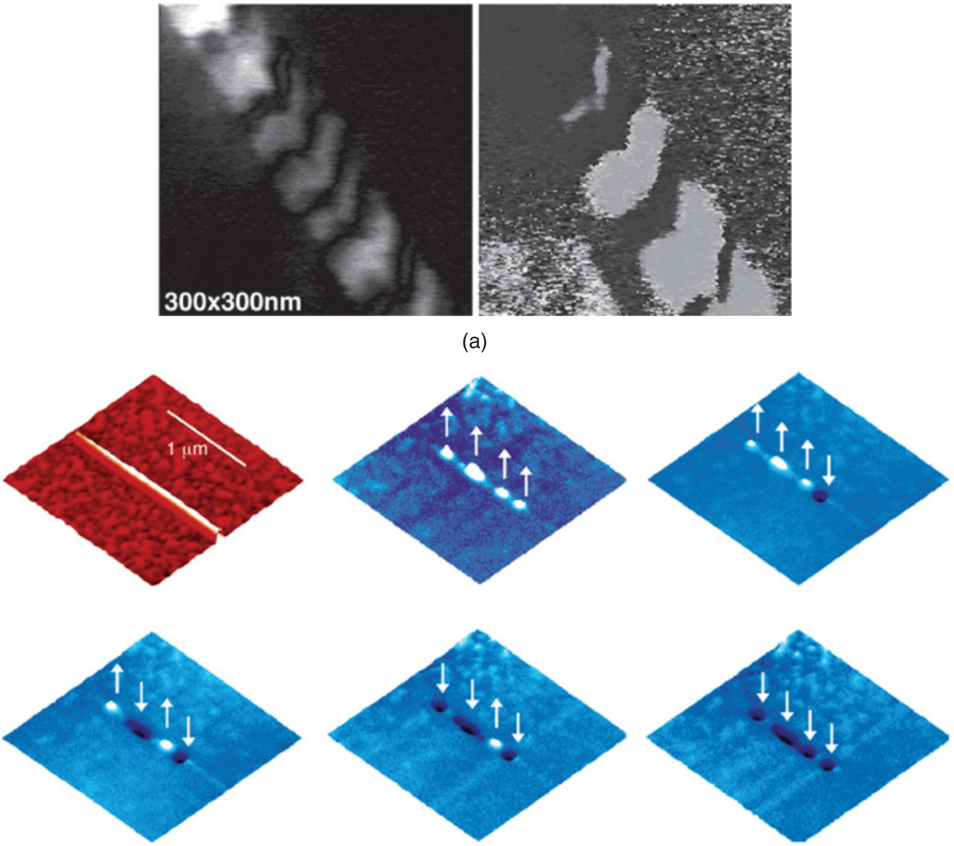

(a)

(b)

Figure 8.6 *(a) Piezoforce response images of K($Nb_{0.8}Ta_{0.2}$)O_3. Left: phase; right: amplitude (reprinted with permission from [101]. Copyright (2004) American Chemical Society). (b) EFM images of a $BaTiO_3$ nanowire showing that four distinct polarization domains can be independently manipulated by an external electric field (reprinted with permission from [96]. Copyright (2002) American Chemical Society). (c and d) Examples of piezoresponse hysteresis loops. (c) PZT nanotube (see Figure 8.3(g)) (reprinted with permission from [67]. Copyright [2003], AIP Publishing LLC). (d) $Bi_4Ti_3O_{12}$ nanowire (see Figure 8.4(b)) (reproduced with permission from [108]. Copyright (2012) IEEE)*

aqueous solutions or exposed to ambient air) and polar organic molecules such as carboxylic acids. The direction of spontaneous polarization can also change depending on the screening efficiency [105] and can deviate from the elongation direction of the NW, in particular when the crystal symmetry is lower than tetragonal [98,101,106], as indicated by the stripe domain pattern in the PFM images of Figure 8.6(a). Evident stripe domain patterns with domain walls perpendicular to the elongation direction were also observed in $BaTiO_3$ NWs obtained by a solid-state topochemical reaction [75]. The low dimensionality and the depolarizing field can also alter the phase transitions. The phase sequence characteristic of bulk $BaTiO_3$ and $KNbO_3$ is, moving from high to low temperature, cubic, tetragonal,

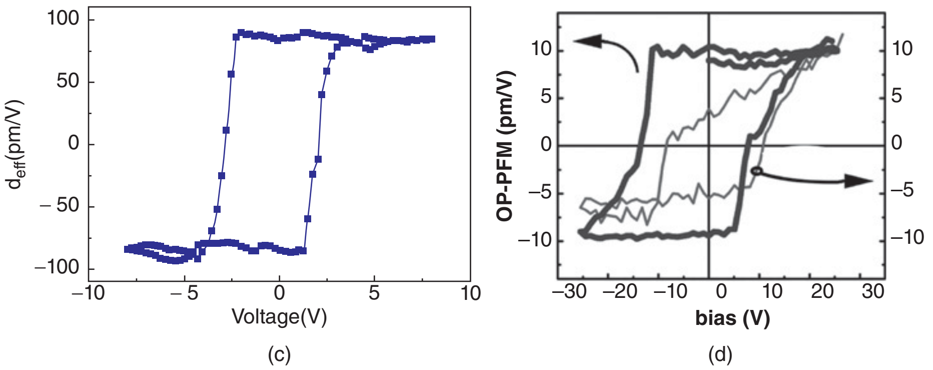

Figure 8.6 *(Continued)*

orthorhombic, and rhombohedral. However, it has been observed in $KNbO_3$ and predicted for $BaTiO_3$ [106] that the orthorhombic/rhombohedral transition is suppressed and the low-temperature phase is monoclinic. The monoclinic modification of potassium niobate NWs can also be stabilized at room temperature using metallic niobium as the precursor for the hydrothermal synthesis [38]. The orthorhombic phase is restored after thermal treatment at 450 °C.

The domain configuration and polarization can be imaged and manipulated with both PFM and EFM (Figure 8.6(b)) by applying a DC bias between the tip and the sample [96, 100, 107]. Polarization switching as well as measurement of piezoresponse hysteresis loops represent the ultimate tests to prove that the investigated nanostructure is ferroelectric. Examples of PFM loops [67, 108] are shown in Figure 8.6(c) and (d). Local electrical poling, using scanning probe microscopy techniques, has shown that remanent polarization perpendicular to the wire axis can be induced and switched even in nanowires with diameters of 10–20 nm, although the stability of such perpendicular polarization is sensitive to the diameter of the nanowire and to the charge compensation conditions at the wire surface (Figure 8.6(b)) [96].

The $BaTiO_3$ nanocolumns directly patterned by FIB [91] from single crystals cannot freely deform to accommodate the spontaneous strain associated with the cubic/tetragonal transition when they are cooled through T_C, as happens for free-standing NWs. The need to release the elastic energy leads to the formation of domain patterns with 90° domain walls (Figure 8.7(a)). There is a balance to be found between the decrease of energy related to domain formation and the increase of energy determined by the creation of domain walls. This leads to the well-known relationship between the domain width and square root of thickness of lamellae or width of column (Figure 8.7(b)), which is observed for a wide size range. Reduction of the column width at constant thickness results in a modification of the domain pattern corresponding to the reorientation of the non-axial component of polarization. More generally, the orientation of the non-axial polarization component is strongly dependent on the local morphology of the nanostructure. Manipulation of the domain pattern and polarization orientation can thus be realized by modifying the local aspect ratio of the column dimensions without the application of an electric field (Figure 8.7(c)). This was demonstrated by the creation of bulges or notches along the nanocolumns [91, 109].

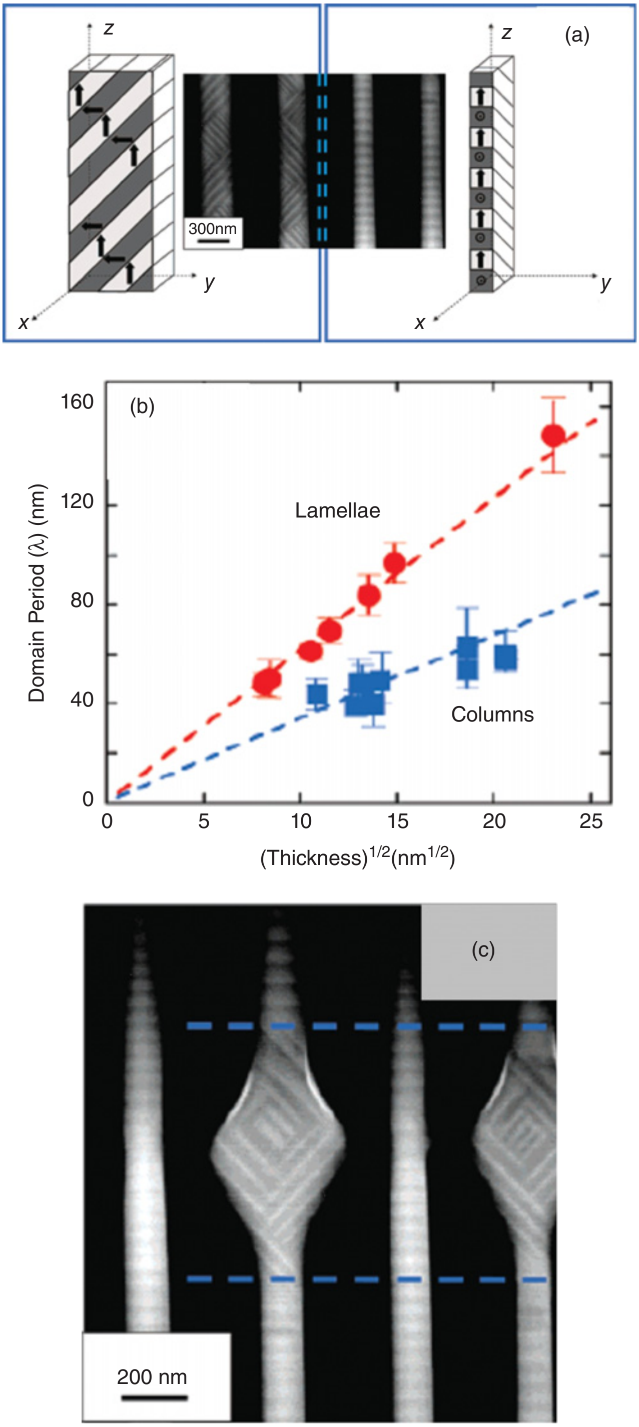
(a)
z
y
x
300nm
z
y
x
(b)
Domain Period (λ) (nm)
0
40
80
120
160
0
5
10
15
20
25
(Thickness)^1/2(nm^1/2)
Lamellae
Columns
(c)
200 nm

The domain wall mobility and switching characteristics are also strongly affected by the morphology of the specific nanostructure. This appears to be related to the local electric field distribution and to a faster nucleation of the reverse domains in nanowires [92].

8.4 Applications

8.4.1 Nanogenerators for Energy Harvesting and Other Devices

Applications of ferroelectric NWs are directly related to some properties, such as piezoelectric activity and high dielectric constant, which are a direct consequence of ferroelectricity. The ability of ferroelectric NWs and fibers to convert mechanical/vibrational energy into electrical energy by means of the piezoelectric effect has been recently demonstrated [110, 111]. This capability remains intact even at a reduced scale and nanogenerators (NGs) and nanoelectromechanical systems developed on the laboratory scale using ferroelectric nanowires have gained interest due to their ability to generate electrical power by harnessing several different sources of mechanical energy such as vibrations and sound waves. An advantage of the NW geometry is its responsiveness to small mechanical stimuli. Owing to the higher electromechanical coefficients, ferroelectric NWs exhibit a higher energy conversion efficiency in comparison to energy harvesting devices based on aligned ZnO NWs [112, 113]. There are two main fabrication strategies for NW-based NGs. A first type of device is fabricated starting from vertical arrays of NWs grown on a conductive substrate and putting an electrode to make contact with the top side of the vertical NWs (Figure 8.8(a)). The substrate acts as the bottom electrode. The output current is collected by an external circuit connected to the electrodes. Energy harvesting was demonstrated using vertical arrays of $BaTiO_3$, $KNbO_3$, and PZT NWs, even in devices with a multilayer design [38, 97, 113].

A similar approach has also been adopted for the realization of a highly accurate accelerometer using vertically aligned $BaTiO_3$ NWs [55]. A second type of energy harvesting device consists of a flexible composite layer obtained by dispersing ferroelectric NWs or NTs in polydimethylsiloxane (PDMS) with metal electrodes deposited on the opposite major surfaces (Figure 8.8(b)). Other polymeric layers are added to provide protection and mechanical strength to the NG [114, 115]. In a different design, PZT fibers obtained by electrospinning were deposited on fine interdigited electrodes fabricated on

◄

Figure 8.7 Configuration and properties of domains in $BaTiO_3$ nanocolumns. (a) Schematic illustration of the domain patterns typically observed in the $BaTiO_3$ nanocolumns under STEM with the electron beam parallel to the x axis (left). Decreasing the column dimension along the y axis while keeping x constant (right) results in a reorientation of the non-axial polarization and an associated change in the domain contrast. (b) Domain period as a function of the square root of either the thickness of a $BaTiO_3$ single-crystal slab/lamella or the width of a $BaTiO_3$ single-crystal column. (c) When the width of the wire is locally increased the non-axial component of polarization reorients to be in the plane of the micrograph, giving stripe domain contrast at 45° to the wire axis. Reprinted with permission from [91]. Copyright (2007) American Chemical Society

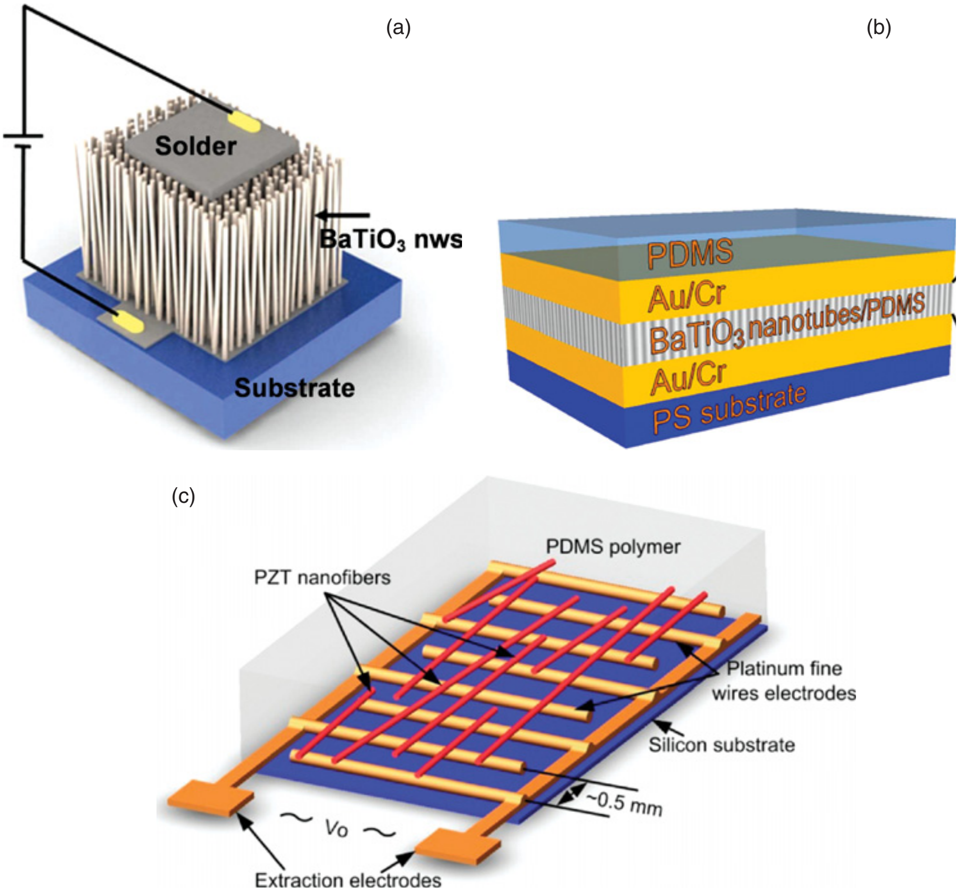
(a)
Solder
$BaTiO_3$ nws
Substrate
(b)
PDMS
Au/Cr
$BaTiO_3$ nanotubes/PDMS
Au/Cr
PS substrate
(c)
PDMS polymer
PZT nanofibers
Platinum fine wires electrodes
Silicon substrate
~0.5 mm
Vo
Extraction electrodes

Figure 8.8 *Schematic diagrams of piezoelectric nanogenerators for energy harvesting and sensor applications based on ferroelectric nanowires. (a) Vertically aligned NWs grown on a substrate (reprinted by permission from Macmillan Publishers Ltd [Nature Communications] [55], copyright (2013)). (b) Dispersion of ferroelectric NWs in the PDMS matrix (reprinted with permission from [114]. Copyright (2012) American Chemical Society). (c) Nanofibers deposited on interdigited electrodes and embedded in a PDMS flexible matrix (reprinted with permission from [116]. Copyright (2010) American Chemical Society)*

an Si substrate and then coated with a PDMS layer [116] (Figure 8.8(c)). Overall, the above results have shown the feasibility of using piezoelectric nanogenerators based on ferroelectric NWs for powering mobile and even personal microelectronics as well as to build nanoelectromechanical systems for sensors and other devices. One of the most innovative potential applications of multiferroic compounds is the realization of four-state memories corresponding to two orientation states for polarization and two orientations for magnetization [117]. High-density four-state memories have been realized using vertically aligned Mn-doped $BaTiO_3$ nanowires fabricated by filling the pores of an anodic alumina template with a sol precursor followed by thermal treatment [118]. The polarization switching by an external electric field does not influence the magnetization of the nanowires owing to a negligible degree of cross-coupling. Similarly, the magnetic-field-induced magnetization switching is unaffected by the ferroelectric polarization.

8.4.2 Dielectric Composites and Other Applications

Owing to the high dielectric constant and the relatively low losses of $BaTiO_3$ and PZT, ferroelectric particles can be used as fillers in polymeric composites for the fabrication of flexible dielectric layers with improved permittivity while preserving the high dielectric strength of the polymer. Capacitors fabricated from these composites are attractive owing to their ability to store energy with high density. The most used matrix is polyvinylidene fluoride (PVDF), a ferroelectric polymer with a dielectric constant of the order of 10. For a given volume fraction, the wire geometry of the inclusions determines a substantial enhancement of the effective permittivity of the composite (ε_{eff}) in comparison to spherical and equiaxed particles [47, 119]; ε_{eff} is maximized when the NWs are aligned along the direction of the applied field whereas the breakdown field is rather insensitive to the orientation of the filler as in the case of PVDF/PZT composites [120]. Although the breakdown field decreases with increasing filler amount, the maximum energy density of PVDF–PZT composites can be enhanced above that of pure polymer owing to strong improvement of ε_{eff} when the amount of filler is higher than 30 wt% [120, 121]. A strong dependence of ε_{eff} on the fiber orientation was also reported in the case of epoxy resin/$BaTiO_3$ composites [82]. The effective permittivity and the energy density can be also controlled by varying the aspect ratio (length/diameter) of the NWs: both quantities improve with increasing the aspect ratio. [122]. The aspect ratio has also a strong impact on the electromechanical properties of the composites [123, 124]. A progressive increase of ε_{eff} and energy density with filler amount is reported for composites containing paraelectric $Ba_{0.2}Sr_{0.8}TiO_3$ NWs [125]. In this case the compatibility between the filler and the polymer was increased by functionalization of the perovskite surface with amine groups, resulting in better dispersion and a stronger bond at the interface. The use of a paraelectric composition reduces the dissipated energy related to ferroelectric hysteresis.

Ferroelectric NWs have also promising properties in the field of microwave radiation. Barium titanate NWs and NTs show excellent microwave absorption properties in the range 5–12 THz and can be used for the preparation of polymer composites for shielding electromagnetic waves [27, 59]. The strong 2–8 THz emission obtained from vertically aligned PZT NTs in a silicon template shows the potential for filling the spectral gap generally not satisfied by conventional semiconductor devices [69]. The emission was attributed to the nanoscale geometry of the tubes as it was absent in bulk material and thin film.

$SrTiO_3$, $TiO_2/SrTiO_3$ heterostructures, $KNbO_3$, and $Bi_4Ti_3O_{12}$ with NT and NW morphology were proposed for several applications in the field of photocatalysis, including degradation of organic pollutants in aqueous solution and photosplitting of water [32, 61–63, 126–132]. Arrays of $SrTiO_3$ NWs have shown good biocompatibility and slow release of strontium in *in vitro* experiments. The NTs are capable of stimulating precipitation of hydroxyapatite from simulated body fluids and enhance osseointegration of bone implants [60]. Strong superhydrophilicity (contact angle with water: 3°) has been reported [133]. However, the surface becomes strongly hydrophobic (contact angle: 140°)

when oleic acid is added during synthesis. Exposure to UV light determines a progressive decrease of the contact angle due to the photocatalytic oxidation of the organic molecules.

8.5 Summary and Conclusions

From the overview presented in this paper, it is clear that our knowledge on 1D ferroelectric nanostructures has significantly advanced in the last 15 years. Many efforts have been devoted to develop new and improved synthesis methods for producing NWs and NTs with controlled size and morphology. Most investigated materials are ternary oxides with a perovskite structure such as $BaTiO_3$, $PbTiO_3$, $Pb(Zr,Ti)O_3$, and $KNbO_3$. Reproducibility of results is still an important issue, as small uncontrolled variations in the synthetic procedures can determine a major deviation from the expected composition and morphology. Liquid-phase preparation methods such as hydrothermal, solvothermal, and molten salt synthesis, with or without the use of reactive templates, are relatively simple and often produce single-crystal NWs of high quality. Topochemical conversion of reactive templates is particularly useful for controlling the final morphology and crystallographic orientation. A recent and important achievement is the extension of the hydrothermal methods to the growth of vertically aligned arrays of nanorods and NWs on suitable substrates. This has paved the way for the realization of miniaturized devices for mechanical/vibrational energy harvesting and sensors. Nanotubes and aligned arrays of NTs are mainly fabricated using physical templates such as alumina, silicon, and polycarbonate membranes with ordered cylindrical porosity. The membrane channels are typically impregnated by a sol–gel precursor and the final NTs are obtained by crystallization of the precursor at high temperatures and template removal. Some membranes are commercially available and then offer better opportunities in terms of availability and reproducibility of the final product.

In more recent years the focus of research on 1D nanostructures is gradually moving towards a better understanding of their ferroelectric and piezoelectric properties as well as the development of applications. Scanning force microscopy techniques are powerful tools for investigating the existence of ferroelectricity, the domain arrangement, and the domain switching in 1D nanostructures. Domains and polarization can be manipulated at the nanoscale by application of an electric field. Thus the existence of ferroelectricity in NWs with a diameter down to a few nm, as predicted by first-principle calculations, has been demonstrated. The Curie temperature and the spontaneous strain of the perovskite lattice are strongly affected by size effects and both decrease with decreasing NW diameter. The 1D morphology can lead to the stabilization of ferroelectric phases that are not observed in bulk single crystals and ceramics, such as the monoclinic modification of $KNbO_3$. Of fundamental importance for the retention of ferroelectricity in NWs is an efficient screening of the surface charges related to polarization in order to avoid the deleterious effect of the depolarizing field. Domain arrangement in 1D ferroelectric structures is strongly dependent on the specific morphology and the alteration of local geometry offers the possibility to manipulate the domain patterns and polarization as well as the domain wall mobility without the application of an electric field.

Among the applications already developed at the laboratory scale, nanogenerators and sensors based on free-standing NWs as well as on aligned arrays of NWs are of remarkable interest. Flexible miniaturized devices can be obtained by dispersing the NWs in a polymeric matrix. One of the main obstacles to the use of ferroelectric NWs and NTs, even in niche applications, is the scale-up of production from laboratory level to amounts of industrial interest. Scale-up of hydrothermal and solvothermal methods is challenging because of their extreme sensitivity to small and often uncontrolled variations in the synthesis conditions. However, large-scale hydrothermal synthesis of very fine powders for electronic applications was successfully implemented at the end of the 1990s after many years of intensive laboratory research and the same will hopefully happen even with NWs and NTs. For large-scale and cost-effective production of ferroelectric fibers, electrospinning is probably the most versatile and cost-effective method. However, these fibers have a polycrystalline structure and their main potential application is as fillers in polymer–ceramic composites with a high dielectric constant. Capacitors fabricated from these composites are attractive owing to their ability to store energy with high density.

References

(1) Fatuzzo, E. and Merz, W.J. (1967) *Ferroelectricity*, North-Holland Publishing Co., Amsterdam.

(2) Jaffe, B., Cook Jr, W.R., and Jaffe, H. (1971) *Piezoelectric Ceramics*, Academic Press, London and New York.

(3) Lines, M.E. and Glass, A.M. (1979) *Principles and Applications of Ferroelectrics and Related Materials*, Clarendon, Oxford.

(4) Damjanovic, D. (1998) Ferroelectric, dielectric and piezoelectric properties of ferroelectric thin films and ceramics. *Reports on Progress in Physics*, **61** (9), 1267–1324.

(5) Ederer, C. and Spaldin, N.A. (2006) Origin of ferroelectricity in the multiferroic barium fluorides $BaMF_4$: a first principles study. *Physical Review B*, **74**, art. no. 024102.

(6) Horiuchi, S. and Tokura, Y. (2008) Organic ferroelectrics. *Nature Materials*, **7**, 357–366.

(7) Lovinger, A.J. (1983) Ferroelectric polymers. *Science* **220** (4602), 1115–1121.

(8) Haeni, J.H., Irvin, P., Chang, W., et al. (2004) Room-temperature ferroelectricity in strained $SrTiO_3$. *Nature* **430** (7001), 758–761.

(9) Choi, K.J., Biegalski, M., Li, Y.L., et al. (2004) Enhancement of ferroelectricity in strained $BaTiO_3$ thin films. *Science*, **306**, 1005–1009.

(10) Shaw, T.M., Trolier-McKinstry, S., and McIntyre, P.C. (2000) The properties of ferroelectric films at small dimensions. *Annual Review of Materials Science*, **30**, 263–298.

(11) Scott, J.F., Morrison, F.D., Miyake, M., et al. (2005) Recent materials characterizations of [2D] and [3D] thin film ferroelectric structures. *Journal of the American Ceramic Society*, **88**, 1691–1701.

(12) Fu, H. and Bellaiche, L. (2003) Ferroelectricity in barium titanate quantum dots and wires. *Physical Review Letters*, **91**, art. no. 257601.

(13) Naumov, I.I., Bellaiche, L., and Fu, H. (2004) Unusual phase transitions in ferroelectric nanodisks and nanorods. *Nature* **432**, 737–740.

(14) Lencka, M.M. and Riman, R.E. (1993) Thermodynamic modeling of hydrothermal synthesis of ceramic powders. *Chemistry of Materials*, **5**, 61–70.

(15) Lencka, M.M. and Riman, R.E. (1993) Synthesis of lead titanate: thermodynamic modelling and experimental verification. *Journal of the American Ceramic Society*, **76**, 2649–2659.

(16) Lencka, M.M., Oledzka, M., and Riman, R.E. (2000) Hydrothermal synthesis of sodium and potassium bismuth titanates. *Chemistry of Materials*, **12**, 1323–1330.

(17) Eckert Jr, J.O., Hung-Houston, C.C., Gersten, B.L., et al. (1996) Kinetics and mechanisms of hydrothermal synthesis of barium titanate. *Journal of the American Ceramic Society*, **79**, 2929–2939.

(18) Cheng, H.M., Ma, J.M., Zhao, Z.G., et al. (1992) Synthesis of acicular lead titanate fine powders. *Journal of the American Ceramic Society*, **75** (5), 1123–1128.

(19) Cho, S.B., Oledzka, M., and Riman, R.E. (2001) Hydrothermal synthesis of acicular lead zirconate titanate (PZT). *Journal of Crystal Growth*, **226** (2–3), 313–326.

(20) Wang, J., Durussel, A., Sandu, C.S., et al. (2012) Mechanism of hydrothermal growth of ferroelectric PZT nanowires. *Journal of Crystal Growth*, **347**, 1–6.

(21) Xu, G., Ren, Z.H., Du, P.Y., et al. (2005) Polymer-assisted hydrothermal synthesis of single-crystalline tetragonal perovskite $PbZr_{0.52}Ti_{0.48}O_3$ nanowires. *Advanced Materials*, **17**, 907–910.

(22) Ren, Z.H., Xu, G., Liu, Y., et al. (2010) $PbTiO_3$ nanofibers with edge-shared TiO_6 octahedra. *Journal of the American Chemical Society*, **132**, 5572–5573.

(23) Joshi, U.A. and Lee, J.S. (2005) Template-free hydrothermal synthesis of single-crystalline barium titanate and strontium titanate nanowires. *Small*, **1**, 1172–1176.

(24) Joshi, U.A., Yoon, S., Baik, S., and Lee, J.S. (2006) Surfactant-free hydrothermal synthesis of highly tetragonal barium titanate nanowires: a structural investigation. *Journal of Physical Chemistry B*, **110**, 12249–12256.

(25) Im, B., Joshi, U.A., Lee, K.H., and Lee, J.S. (2010) Growth of single crystalline barium titanate nanowires from TiO_2 seeds deposited on conducting glass. *Nanotechnology* **21**, art. no. 425601.

(26) Urban, J.J., Spanier, J.E., Lian, O.Y., et al. (2003) Single-crystalline barium titanate nanowires. *Advanced Materials*, **15**, 423–426.

(27) Yang, J., Zhang, J., Liang, C.Y., et al. (2013) Ultrathin $BaTiO_3$ nanowires with high aspect ratio: a simple one-step hydrothermal synthesis and their strong microwave absorption. *ACS Applied Materials and Interfaces*, **5**, 7146–7151.

(28) Mao, Y.B., Banerjee, S., and Wong, S.S. (2003) Large-scale synthesis of single-crystalline perovskite nanostructures. *Journal of the American Chemical Society*, **125** (51), 15718–15719.

(29) Deng, Y., Wang, J.L., Zhu, K.R., et al. (2005) Synthesis and characterization of single-crystal $PbTiO_3$ nanorods. *Materials Letters*, **59** (26), 3272–3275.

(30) Rørvik, P.M., Lyngdal, T. Sæterli, R., et al. (2008) Influence of volatile chlorides on the molten salt synthesis of ternary oxide nanorods and nanoparticles. *Inorganic Chemistry*, **47** (8), 3173–3181.

(31) Xu, C.Y., Zhang, Q., Zhang, H., et al. (2005) Synthesis and characterization of single-crystalline alkali titanate nanowires. *Journal of the American Chemical Society*, **127** (33), 11584–11585.

(32) Lin, X., Guan, Q.F., and Zou, C. (2013) Photocatalytic degradation of an azo dye using $Bi_{3.25}M_{0.75}Ti_3O_{12}$ nanowires (M = La, Sm, Nd, and Eu). *Materials Science and Engineering B*, **178**, 520–526.

(33) Magrez, A., Vasco, E., Seo, J.W., et al. (2006) Growth of single-crystalline $KNbO_3$ nanostructures. *Journal of Physical Chemistry B*, **110** (1), 58–61.

(34) Vasco, E., Magrez, A., Forró, L., and Setter, N. (2005) Growth kinetics of one-dimensional $KNbO_3$ nanostructures by hydrothermal processing routes. *Journal of Physical Chemistry B*, **109** (30), 14331–14334.

(35) Wang, G.Z., Yu, Y.D., Grande, T., and Einarsrud, M.A. (2009) Synthesis of $KNbO_3$ nanorods by hydrothermal method. *Journal for Nanoscience and Nanotechnology*, **9** (2), 1465–1469.

(36) Wang, G.Z., Selbach, S.M., Yu, Y.D., et al. (2009) Hydrothermal synthesis and characterization of $KNbO_3$ nanorods. *CrystEngComm*, **11** (9), 1958–1963.

(37) Hu, Y.M., Gu, H.S., Hu, Z.L., et al. (2008) Controllable hydrothermal synthesis of $KTa_{1\text{-}x}Nb_xO_3$ nanostructures with various morphologies and their growth mechanisms. *Crystal Growth and Design*, **8** (3), 832–837.

(38) Kim, S., Lee, J.H., Lee, J., et al. (2013) Synthesis of monoclinic potassium niobate nanowires that are stable at room temperature. *Journal of the American Chemical Society*, **135** (1), 6–9.

(39) Zhu, H., Zheng, Z., Gao, X., et al. (2006) Structural evolution in a hydrothermal reaction between Nb_2O_5 and NaOH solution: from Nb_2O_5 grains to microporous $Na_2Nb_2O_6{\cdot}2/3H_2O$ fibers and $NaNbO_3$ cubes. *Journal of the American Chemical Society*, **128**, 2373–2384.

(40) Rørvik, P.M., Almli, Å., van Helvoort, A.T.J., et al. (2008) $PbTiO_3$ nanorod arrays grown by self-assembly of nanocrystals. *Nanotechnology*, **19**, art. no. 225605.

(41) Rørvik, P.M., Grande, T., and Einarsrud, M.A. (2009) Hierarchical $PbTiO_3$ nanostructures grown on $SrTiO_3$ substrates. *Crystal Growth and Design*, **9** (4), 1979–1984.

(42) Wang, G.Z., Sæterli, R., Rørvik, P.M., et al. (2007) Self-assembled growth of $PbTiO_3$ nanoparticles into microspheres and bur-like structures. *Chemistry of Materials*, **19** (9), 2213–2221.

(43) Lin, Y., Liu, Y., and Sodano, H.A. (2009) Hydrothermal synthesis of vertically aligned lead zirconate titanate nanowire arrays. *Applied Physics Letters*, **95**, art. no. 122901.

(44) Pradhan, S.K., Mao, Y., Wong, S.S., et al. (2007) Atomic-scale structure of nanosized titania and titanate: particles, wires, and tubes. *Chemistry of Materials*, **19**, 6180–6186.

(45) Feng, Q., Hirasawa, M., and Yanagisawa, K. (2001) Synthesis of crystal-axis-oriented $BaTiO_3$ and anatase platelike particles by a hydrothermal soft chemical process. *Chemistry of Materials*, **13** (2), 290–296.

(46) Bao, N.Z., Shen, L.M., Gupta, A., et al. (2009) Size-controlled one-dimensional monocrystalline $BaTiO_3$ nanostructures. *Applied Physics Letters*, **94**, art. no. 253109.

(47) Tang, H.X., Lin, Y.R., and Sodano, H.A. (2013) Synthesis of high aspect ratio $BaTiO_3$ nanowires for high energy density nanocomposite capacitors. *Advanced Energy Materials*, **3** (4), 451–456.

(48) Bao, N.Z., Shen, L.M., Srinivasan, G., et al. (2008) A shape-controlled monocrystalline ferroelectric barium titanate nanostructures: from nanotubes and nanowires to ordered nanostructures. *Journal of Physical Chemistry C*, **112** (23), 8634–8642.

(49) Kang, S.O., Park, B.H., and Kim, Y.I. (2008) Growth mechanism of shape-controlled barium titanate nanostructures through soft chemical reaction. *Crystal Growth and Design*, **8** (9), 3180–3186.

(50) Li, Y., Gao, X.P., Li, G.R., et al. (2009) Titanate nanofiber reactivity: fabrication of $MTiO_3$ (M = Ca, Sr, and Ba) perovskite oxides. *Journal of Physical Chemistry C*, **113** (11), 4386–4394.

(51) Dong, W.J., Li, B.J., Li, Y., et al. (2011) General approach to well-defined perovskite $MTiO_3$ (M = Ba, Sr, Ca, and Mg) nanostructures. *Journal of Physical Chemistry C*, **115** (10), 3918–3925.

(52) Kalyani, V., Vasile, B.S., Ianculescu, A., et al. (2012) Hydrothermal synthesis of $SrTiO_3$ mesocrystals: single crystal to mesocrystal transformation induced by topochemical reactions. *Crystal Growth and Design*, **12**, 4450–4456.

(53) Huang, K.C., Huang, T.C., and Hsieh, W.F. (2009) Morphology-controlled synthesis of barium titanate nanostructures. *Inorganic Chemistry*, **48** (19), 9180–9184.

(54) Koka, A., Zhou, Z. and Sodano, H.A. (2014) Vertically aligned $BaTiO_3$ nanowire arrays for energy harvesting. *Energy and Environmental Science*, **7**, 288–296.

(55) Koka, A. and Sodano, H.A. (2013) High-sensitivity accelerometer composed of ultra-long vertically aligned barium titanate nanowire arrays. *Nature Communications* **4**, art. no. 2682.

(56) Mao, Y.B., Banerjee, S., and Wong, S.S. (2003) Hydrothermal synthesis of perovskite nanotubes. *Chemical Communications*, 408–409.

(57) Maxim, F., Ferreira, P., Vilarinho, P.M., and Reaney, I. (2008) Hydrothermal synthesis and crystal growth studies of $BaTiO_3$ using Ti nanotube precursors. *Crystal Growth and Design*, **8**, 3309–3315.

(58) Maxim, F., Vilarinho, P.M., Ferreira, P., et al. (2011) Kinetic study of the static hydrothermal synthesis of $BaTiO_3$ using titanate nanotubes precursors. *Crystal Growth and Design*, **11**, 3358–3365.

(59) Zhu, Y.F., Zhang, L., Natsuki, T., et al. (2012) Facile synthesis of $BaTiO_3$ nanotubes and their microwave absorption properties. *ACS Applied Materials and Interfaces*, **4**, 2101–2106.

(60) Xin, Y.C., Jiang, J., Huo, K., et al. (2009) Bioactive $SrTiO_3$ nanotube arrays: strontium delivery platform on Ti-based osteoporotic bone implants. *ACS Nano*, **3** (10), 3228–3234.

(61) Zhang, J., Bang, J.H., Tang, C.C., and Kamat, P.V. (2010) Tailored TiO_2–$SrTiO_3$ heterostructure nanotube arrays for improved photoelectrochemical performance. *ACS Nano*, **4** (1), 387–395.

(62) Zhang, X.M., Huo, K.F., Hu, L.S., et al. (2010) Synthesis and photocatalytic activity of highly ordered TiO_2 and $SrTiO_3/TiO_2$ nanotube arrays on Ti substrates. *Journal of the American Ceramic Society*, **93**, 2771–2778.

(63) Sun, Y., Liu, J.W., and Li, Z.H. (2011) Design of highly ordered Ag–$SrTiO_3$ nanotube arrays for photocatalytic degradation of methyl orange. *Journal of Solid State Chemistry*, **184**, 1924–1930.

(64) Zhao, J.L., Wang, X.H., Chen, R.Z., and Li, L.T. (2005) Synthesis of thin films of barium titanate and barium strontium titanate nanotubes on titanium substrates. *Materials Letters*, **59**, 2329–2332.

(65) Yang, Y., Wang, X.H., Sun, C.K., and Li, L.T. (2009) Structure study of single crystal $BaTiO_3$ nanotube arrays produced by the hydrothermal method. *Nanotechnology* **20**, art. no. 055709.

(66) Hernandez, B.A., Chang, K.S., Fisher, E.R., and Dorhout, P.K. (2002) Sol–gel template synthesis and characterization of $BaTiO_3$ and $PbTiO_3$ nanotubes. *Chemistry of Materials*, **14**, 480–482.

(67) Luo, Y., Szafraniak, I., Zakharov, N.D., et al. (2003) Nanoshell tubes of ferroelectric lead zirconate titanate and barium titanate. *Applied Physics Letters*, **83**, 440–442.

(68) Hernandez-Sanchez, B.A., Chang, K.S., Scancella, M.T., et al. (2005) Examination of size-induced ferroelectric phase transitions in template synthesized $PbTiO_3$ nanotubes and nanofibers. *Chemistry of Materials*, **17**, 5909–5919.

(69) Scott, J.F., Fan, H.J., Kawasaki, S., et al. (2008) Terahertz emission from tubular $Pb(Zr,Ti)O_3$ nanostructures. *Nano Letters*, **8** (12), 4404–4409.

(70) Kim, J., Yang, S.A., Choi, Y.C., et al. (2008) Ferroelectricity in highly ordered arrays of ultra-thin-walled $Pb(Zr,Ti)O_3$ nanotubes composed of nanometer-sized perovskite crystallites. *Nano Letters*, **8**, 1813–1818.

(71) Limmer, S.J., Seraji, S., Wu, Y., et al. (2002) Template-based growth of various oxide nanorods by sol–gel electrophoresis. *Advanced Functional Materials*, **12**, 59–64.

(72) Alexe, M., Hesse, D., Schmidt, V., et al. (2006) Ferroelectric nanotubes fabricated using nanowires as positive templates. *Applied Physics Letters*, **89** (17), art. no. 172907.

(73) Fan, H.J., Knez, M., Scholz, R., et al. (2006) Monocrystalline spinel nanotube fabrication based on the Kirkendall effect. *Nature Materials*, **5**, 627–631.

(74) Fan, H.J., Gösele, U., and Zacharias, M. (2007) Formation of nanotubes and hollow nanoparticles based on Kirkendall and diffusion processes: a review. *Small*, **3** (10), 1660–1671.

(75) Buscaglia, M.T., Harnagea, C., Dapiaggi, M., et al. (2009) Ferroelectric $BaTiO_3$ nanowires by a topochemical solid-state reaction. *Chemistry of Materials*, **21**, 5058–5065.

(76) Buscaglia, M.T., Sennour, M., Buscaglia, V., et al. (2011) Formation of $Bi_4Ti_3O_{12}$ one-dimensional structures by solid-state reactive diffusion. From core-shell templates to nanorods and nanotubes. *Crystal Growth and Design*, **11**, 1394–1401.

(77) Chronakis, I.S. (2005) Novel nanocomposites and nanoceramics based on polymer nanofibers using electrospinning process – a review. *Journal of Materials Processing Technology*, **167**, 283–293.

(78) Yoko, T., Kamiya, K., and Tanaka, K. (1990) Preparation of multiple oxide barium titanate ($BaTiO_3$) fibers by the sol–gel method. *Journal of Materials Science*, **25**, 3922–3929.

(79) Yuh, J., Nino, J.C., and Sigmund, W.A. (2005) Synthesis of barium titanate ($BaTiO_3$) nanofibers via electrospinning. *Materials Letters*, **59**, 3645–3647.

(80) Maensiri, S., Nuansing, W., Klinkaewnarong, J., et al. (2006) Nanofibers of barium strontium titanate (BST) by sol–gel processing and electrospinning. *Journal of Colloid and Interface Science*, **297** (2), 578–583.

(81) Sà, P., Barbosa, J., Bdikin, I., et al. (2013) Ferroelectric characterization of aligned barium titanate nanofibres. *Journal of Physics D: Applied Physics*, **46**, art. no. 105304.

(82) Avila, H.A., Ramajo, L.A., Góes, M.S., et al. (2013) Dielectric behavior of epoxy/$BaTiO_3$ composites using nanostructured ceramic fibers obtained by electrospinning. *ACS Applied Materials and Interfaces*, **5** (3), 505–510.

(83) Selvaraj, U., Prasadarao, A.V., Komarneni, S., et al. (1992) Sol–gel processing of $PbTiO_3$ and $Pb(Zr_{0.52}Ti_{0.48})O_3$ fibers. *Journal of Materials Research*, **7** (4), 992–996.

(84) Toyoda, M., Hamaji, Y., and Tomono, K. (1997) Fabrication of $PbTiO_3$ ceramic fibers by sol–gel processing. *Journal of Sol–Gel Science and Technology*, **9** (1), 71–84.

(85) Park, Y.I., Kim, C.E., and Lee, H.W. (1999) Effects of catalyst and solvent on $PbTiO_3$ fibers prepared from triethanolamine complexed titanium isopropoxide. *Journal of Sol–Gel Science and Technology*, **14** (2), 149–162.

(86) Liao, M., Zhong, X.L., Wang, J.B., et al. (2007) Nd-substituted bismuth titanate ferroelectric nanofibers by electrospinning. *Journal of Crystal Growth*, **304**, 69–72.

(87) Tang, M.H., Shu, W., Yang, F., et al. (2009) The fabrication of La-substituted bismuth titanate nanofibers by electrospinning. *Nanotechnology*, **20**, art. no. 385602.

(88) Hou, D., Luo, W., Huang, Y., et al. (2013) Synthesis of porous $Bi_4Ti_3O_{12}$ nanofibers by electrospinning and their enhanced visible-light-driven photocatalytic properties. *Nanoscale*, **5**, 2028–2035.

(89) Xie, S.H., Li, J.Y., Proksch, R., et al. (2008) Nanocrystalline multiferroic $BiFeO_3$ ultrafine fibers by sol–gel based electrospinning. *Applied Physics Letters*, **93**, art. no. 222904.

(90) Yi, X. and Li, J.L. (2010) Synthesis and optical property of $NaTaO_3$ nanofibers prepared by electrospinning. *Journal of Sol–Gel Science and Technology*, **53**, 480–484.

(91) Schilling, A., Bowman, R.M., Catalan, G., et al. (2007) Morphological control of polar orientation in single-crystal ferroelectric nanowires. *Nano Letters*, **7** (12), 3787–3791.

(92) McQuaid, R.G.P., McMillen, M., Chang, L.W., et al. (2012) Domain wall propagation in meso- and nanoscale ferroelectrics. *Journal of Physics: Condensed Matter*, **24**, art. no. 024204.

(93) Shvartsman, V.V., Dkhil, B., and Kholkin, A.L. (2013) Mesoscale domains and nature of the relaxor state by piezoresponse force microscopy. *Annual Review of Materials Research*, **43**, 423–449.

(94) Harnagea, C., Pignolet, A., Alexe, M., and Hesse, D. (2002) Piezoresponse scanning force microscopy: What quantitative information can we really get out of piezoresponse measurements on ferroelectric thin films? *Integrated Ferroelectrics*, **44**, 113–124.

(95) Hong, J.W., Noh, K.H., Park, S., et al. (1998) Surface charge density and evolution of domain structure in triglycine sulfate determined by electrostatic-force microscopy. *Physical Review B*, **58**, 5078–5084.

(96) Yun, W.S., Urban, J.J., Gu, Q., and Park, H.K. (2002) Ferroelectric properties of individual barium titanate nanowires investigated by scanned probe microscopy. *Nano Letters*, **2**, 447–450.

(97) Zhou, Z., Tang, H.X., and Sodano, H.A. (2013) Vertically aligned arrays of $BaTiO_3$ nanowires. *ACS Applied Materials and Interfaces*, **5** (22), 11894–11899.

(98) Wang, J., Sandu, C.S., Colla, E. et al. (2007) Ferroelectric domains and piezoelectricity in monocrystalline Pb(Zr,Ti)O_3 Nanowires. *Applied Physics Letters*, **90**, art. n° 133107.

(99) Wang, Z.Y., Hu, J., and Yua, M.F. (2006) One-dimensional ferroelectric monodomain formation in single crystalline $BaTiO_3$ nanowire. *Applied Physics Letters*, **89**, art. no. 263119.

(100) Wang, Z.Y., Suryavanshi, A.P., and Yu, M.F. (2006) Ferroelectric and piezoelectric behaviors of individual single crystalline $BaTiO_3$ nanowire under direct axial electric biasing. *Applied Physics Letters*, **89**, art. no. 082903.

(101) Suyal, G., Colla, E., Gysel, R., et al. (2004) Piezoelectric response and polarization switching in small anisotropic perovskite particles. *Nano Letters*, **4** (7), 1339–1342.

(102) Spanier, J.E., Kolpak, A.M., Urban, J.J., et al. (2006) Ferroelectric phase transition in individual single-crystalline $BaTiO_3$ nanowires. *Nano Letters*, **6** (4), 735–739.

(103) Naumov, I.I. and Fu, H.X. (2005) Spontaneous polarization in one-dimensional Pb(ZrTi)O_3 nanowires. *Physical Review Letters*, **95**, art. no. 247602.

(104) Geneste, G., Bousquet, E., Junquera, J., and Ghosez, P. (2006) Finite-size effects in $BaTiO_3$ nanowires. *Applied Physics Letters*, **88** (11), art. no. 112906.

(105) Ponomareva, I.I., Naumov, I.I., Kornev, I., et al. (2005) Atomistic treatment of depolarizing energy and field in ferroelectric nanostructures. *Physical Review B*, **72**, art. no. 140102(R).

(106) Louis, L., Gemeiner, P., Ponomareva, I., et al. (2010) Low-symmetry phases in ferroelectric nanowires. *Nano Letters*, **10** (4), 1177–1183.

(107) Zhou, Z.H., Gao, X.S., Wang, J., et al. (2007) Giant strain in $PbZr_{0.2}Ti_{0.8}O_3$ nanofibers. *Applied Physics Letters*, **90**, art. no. 052902.

(108) Azodi, M., Harnagea, C., Buscaglia, V., et al. (2012) Ferroelectric switching in $Bi_4Ti_3O_{12}$ nanorods. *IEEE Transactions on Ultrasonics, Ferroelectrics and Frequency Control*, **59**, 1903–1911.

(109) McMillen, M., McQuaid, R.G.P., Haire, S.C., et al. (2010) The influence of notches on domain dynamics in ferroelectric nanowires. *Applied Physics Letters*, **96**, art. no. 042904.

(110) Chang, J.Y., Dommer, M., Chang, C., and Lin, L.W. (2012) Piezoelectric nanofibers for energy scavenging applications. *Nano Energy*, **1**, 356–371.

(111) Wang, Z.Y., Hu, J., Suryavanshi, A.P., et al. (2007) Voltage generation from individual $BaTiO_3$ nanowires under periodic tensile mechanical load. *Nano Letters*, **7** (10), 2966–2969.

(112) Sun, C., Shi, J., and Wang, X. (2010) Fundamental study of mechanical energy harvesting using piezoelectric nanostructures. *Journal of Applied Physics*, **108**, art. no. 034309.

(113) Xu, S., Hansen, B.J., and Wang, Z.L. (2010) Piezoelectric-nanowire-enabled power source for driving wireless microelectronics. *Nature Communications*, **1**, art. no. 93.

(114) Lin, Z.H., Yang, Y., Wu, J.M., et al. (2012) $BaTiO_3$ nanotubes-based flexible and transparent nanogenerators. *Journal of Physical Chemistry Letters*, **3**, 3599–3604.

(115) Jung, J.H., Lee, M., Hong, J.I., et al. (2011) Lead-free $NaNbO_3$ nanowires for a high output piezoelectric nanogenerator. *ACS Nano*, **5** (12), 10041–10046.

(116) Chen, X., Xu, S., Yao, N., and Shi, Y. (2010) 1.6 V nanogenerator for mechanical energy harvesting using PZT nanofibers. *Nano Letters*, **10**, 2133–2137.

(117) Scott, J.F. (2007) Data storage: multiferroic memories. *Nature Materials*, **6**, 256–257.

(118) Son, J.Y., Lee, J.H., Song, S.W., et al. (2013) Four-states multiferroic memories embodied using Mn-doped $BaTiO_3$ nanorods. *ACS Nano*, **7**, 5522–5529.

(119) Guo, N., DiBenedetto, S.A., Tewari, P., et al. (2010) Nanoparticle, size, shape, and interfacial effects on leakage current density, permittivity, and breakdown strength of metal oxide-polyolefin nanocomposites: experiment and theory. *Chemistry of Materials*, **22**, 1567–1578.

(120) Tang, H.X., Lin, Y.R., and Sodano, H.A. (2012) Enhanced energy storage in nanocomposite capacitors through aligned PZT nanowires by uniaxial strain assembly. *Advanced Energy Materials*, **2** (4), 469–476.

(121) Tang, H.X., Malakooti, M.H., and Sodano, H.A. (2013) Relationship between orientation factor of lead zirconate titanate nanowires and dielectric permittivity of nanocomposites. *Applied Physics Letters*, **103** (22), art. no. 222901.

(122) Tang, H.X., Lin, Y.R., Andrews, C., and Sodano, H.A. (2011) Nanocomposites with increased energy density through high aspect ratio PZT nanowires. *Nanotechnology*, **22** (1), art. no. 015702.

(123) Feenstra, J. and Sodano, H.A. (2008) Enhanced active piezoelectric 0–3 nanocomposites fabricated through electrospun nanowires. *Journal of Applied Physics*, **103**, art. no. 124108.

(124) Andrews, C., Lin, Y., and Sodano, H.A. (2010) The effect of particle aspect ratio on the electroelastic properties of piezoelectric nanocomposites. *Smart Materials and Structures*, **19**, art. no. 025018.

(125) Tang, H.X. and Sodano, H.A. (2013) Ultra high energy density nanocomposite capacitors with fast discharge using $Ba_{0.2}Sr_{0.8}TiO_3$ nanowires. *Nano Letters*, **13** (4), 1373–1379.

(126) Zhang, X.M., Huo, K., Hu, L., et al. (2010) Synthesis and photocatalytic activity of highly ordered TiO_2 and $SrTiO_3/TiO_2$ nanotube arrays on Ti substrates. *Journal of the American Ceramic Society*, **93**, 2771–2778.

(127) Sun, Y., Liu, J., and Li, Z. (2011) Design of highly ordered Ag–$SrTiO_3$ nanotube arrays for photocatalytic degradation of methyl orange. *Journal of Solid State Chemistry*, **184** (8), 1924–1930.

(128) Cao, T.P., Li, Y.J., Wang, C.H., et al. (2011) A facile in situ hydrothermal method to $SrTiO_3/TiO_2$ nanofiber heterostructures with high photocatalytic activity. *Langmuir*, **27** (6), 2946–2952.

(129) Ng, J.W., Xu, S.P., Zhang, X.W., et al. (2010) Hybridized nanowires and cubes: a novel architecture of a heterojunctioned $TiO_2/SrTiO_3$ thin film for efficient water splitting. *Advanced Functional Materials*, **20** (24), 4287–4294.

(130) Ding, Q.P., Yuan, Y.P., Xiong, X., et al. (2008) Enhanced photocatalytic water splitting properties of $KNbO_3$ nanowires synthesized through hydrothermal method. *Journal of Physical Chemistry C*, **112** (48), 18846–18848.

(131) Hou, D.F., Luo, W., Huang, Y.H., et al. (2013) Synthesis of porous $Bi_4Ti_3O_{12}$ nanofibers by electrospinning and their enhanced visible-light-driven photocatalytic properties. *Nanoscale*, **5**, 2028–2035.

(132) Lin, X., Guan, Q.F., Zhang, Y., et al. (2013) Visible light photocatalytic properties of $Bi_{3.25}Eu_{0.75}Ti_3O_{12}$ nanowires. *Journal of Physics and Chemistry of Solids*, **74** (9), 1254–1262.

(133) Miyauchi, M. (2007) Thin films of single-crystalline $SrTiO_3$ nanorod arrays and their surface wettability conversion. *Journal of Physical Chemistry C*, **111** (33), 12440–12445.

9

Fabrication of One-Dimensional Ferroelectric Nano- and Microstructures by Different Spinning Techniques and Their Characterization

Tony Lusiola and Frank Clemens

Laboratory for High Performance Ceramics, Empa, Swiss Federal Laboratories for Materials Science and Technology, Switzerland

9.1 Introduction

Ferroelectric materials display an extensive range of functional properties, for example piezoelectricity, pyroelectricity, high non-linear optical activity, switchable polarization, and non-linear dielectric behavior [1]. Ferroelectric materials in fiber form are suitable for incorporation into smart ceramic–polymer composites. The main advantage to the use of fibers instead of monolithic ferroelectric ceramics is the attained improvement in the design flexibility of the composites. Such composites are also called smart, intelligent, or adaptive composites. The concept of adaptive composite materials with integrated fibers for sensing and actuation is still an essential spur that drives the development of piezoelectric ceramic fibers. Nowadays a wide range of smart composites like piezoelectric, magnetostrictive, electrostrictive, magnetorheological, electrorheological, shape-memory, and thermoelectric materials [2] are under investigation for a number of applications. Piezoelectric fiber

---

Nanoscale Ferroelectrics and Multiferroics: Key Processing and Characterization Issues, and Nanoscale Effects, First Edition. Edited by Miguel Algueró, J. Marty Gregg, and Liliana Mitoseriu.
© 2016 John Wiley & Sons, Ltd. Published 2016 by John Wiley & Sons, Ltd.

composites [3] (i.e. 1–3 composites) and active fiber composites (AFCs) [4] are attractive for transducers, structural health sensors, and mechanical energy harvesters [5]. A very good overview about the theoretical organization of smart composites is given by Newnham et al. [6]. Nowadays such composites are also published as smart hybrid materials. In these hybrid materials the active fibrous inorganic material is embedded in a passive polymeric matrix.

As already mentioned, microfiber and hollow fiber hybrids have been of interest for structural health monitoring, energy harvesting, and transducers. Structure conformity, flexibility, and the tailoring of acoustic impedance are still the main key issues for the research and development of such composites. Nanorods, nanowires, and nanotubes have also become popular due to their potential use in non-volatile ferroelectric random access memory, nanoelectromechanical systems, energy-harvesting devices, advanced sensors, and in photocatalysis [7]. The fabrication of the nanostructures with well-aligned morphology and strong ferroelectric responses is technologically challenging [8]. Techniques used to create nano- and microstructures include molecular self-assembly [9], nanocasting [10], extrusion [11], spinning [12,13], etc. Ferroelectric and ferromagnetic materials have been synthesized to perform as functional compositions and have been employed to invent or improve nanoelectronic, nanophotonic, and nanogenerator devices [14].

This chapter will give an overview of the different processing methods, for example fiber-spinning techniques and the special techniques used to characterize their properties. Finally, different applications for fiber composites will be discussed.

9.2 Fiber Synthesis

9.2.1 One-Dimensional Nanostructures

One-dimensional (1D) nanostructures, such as nanorods, nanowires, nanofibers, etc., represent materials with at least one dimension spanning 1 to 100 nm. The difference between rods, wires, and fibers according to the Oxford English Dictionary are that rods are cylinders, wires are metals drawn into thin flexible threads, while fibers are threads or filaments formed from various materials including composites [15], though these definitions are not strictly adhered to by researchers. In order to increase the performance of the active nanoelements, a higher aspect ratio is desirable, as 1D nanofiber structures with high surface–volume ratios can increase the electromechanical coupling in nanocomposites and enable adsorption of molecules on the surface of sensors [8]. These materials have become the focus of intensive research, owing to their unique and superior application in the fabrication of electronic, optoelectronic, and sensor devices when compared to bulk structures.

1D ferroelectric materials have potential applications in high-density ferroelectric random access memory (FeRAM) and high-performance nanogenerators, thus generating worldwide interest in this field [16]. They possess novel properties intrinsically associated with low dimensionality and size confinement, making "bottom-up" construction of nanodevices possible, whereby smaller components are arranged into more complex assemblies. According to Xia et al. [17], it is generally accepted that quantum confinement of electrons by the potential wells of nanometer-sized structures may provide one of the most powerful (and yet versatile) means to control the electrical, optical, magnetic, and thermoelectric properties of solid-state functional materials. Research into 1D nanostructures was previously hindered by difficulties encountered in exercising control of the dimensions, morphology, phase purity, and chemical composition [18]. The development of new techniques at fabricating 1D structures with more control throughout the process has resulted in much interest from many materials and device research groups.

The use of piezoelectric nanofibers as the building blocks in nanogenerators and nanosensors makes them promising candidates for energy harvesting [14]. In the past decade, different methods have been employed to synthesize 1D $Pb(Zr,Ti)O_3$ nanostructures, such as hydrothermal synthesis [19], electrospinning [20], near migration and restricted growth technology [16], etc. Chen et al. designed and fabricated a high-efficiency nanogenerator based on PZT nanofibers, which produced 1.6 V output [21].

9.2.1.1 Hydrothermal Synthesis

Numerous natural occurring minerals have formed under hydrothermal conditions, that is in aqueous medium over 100 °C and 1 bar [22]. Hydrothermal synthesis involves various techniques that all include the crystallization of substances from high-temperature aqueous solutions at high vapour pressures and depends on the solubility of minerals in the aqueous media under high pressure. The hydrothermal method has been used extensively to produce low-dimensional nanostructures. The advantage of producing nanomaterials by the hydrothermal synthesis method includes lower energy requirements using simple equipment with a single step within the process and the process has a fast reaction time and is environmentally friendly [23].

Hydrothermal synthesis is performed in a steel pressure vessel called an autoclave, where the crystal growth occurs and a nutrient is supplied along with water. In the standard hydrothermal method a temperature gradient is maintained between the opposite ends of the growth chamber as it has been observed that certain metastable phases are only formed under these conditions. At the hotter end the nutrient solute dissolves, while at the cooler end it is deposited on a seed crystal, growing the desired crystal [22]. In Table 9.1 there are

Table 9.1 *An overview of hydrothermal synthesis produced 1D nanostructures by different researchers*

Raw material	Solvent	Composition	Diameter (nm)	References
Tetrabutyl titanate and lead nitrate	KOH (aq)	$PbTiO_3$	100–400	[16]
Ilmenite	NaOH (aq)	TiO_2	20–90	[23]
Anatase	NaOH (aq)	TiO_2	~20	[24]
Bismuth nitrate pentahydrate and titanium oxide	NaOH (aq)	$Bi_{0.5}Na_{0.5}TiO_3$	~200	[25]
Zirconium propoxide, titanium isopropoxide, and lead nitrate	KOH (aq)	PZT	50–200	[26]

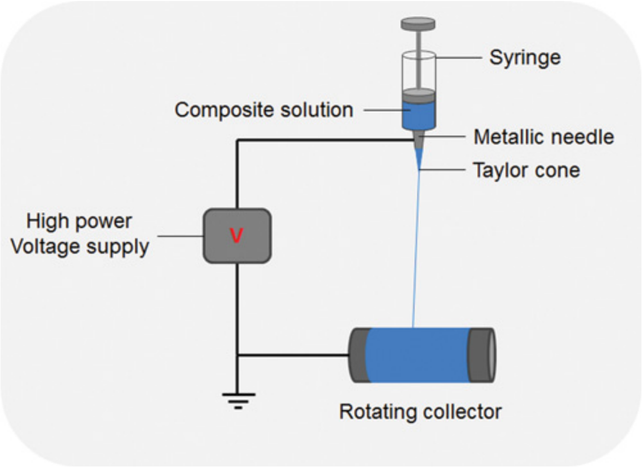

Figure 9.1 *An illustration of the electrospinning setup which involves the use of a high voltage applied between the needle attached to a syringe (filled with a ceramic–polymer solution) and a collector*

some summarized examples of ferroelectric and oxygen semiconductor fibrous materials produced by hydrothermal synthesis.

9.2.1.2 Electrospinning

Electrospinning involves the drawing of very fine fibers through a metallic needle under electric potential, from a precursor solution or liquid. Electrospinning is one of the most simple, versatile, low-cost, and effective ways to produce 1D nanostructures. Through electrospinning it is possible to produce ferroelectric nanofibers with diameters ranging from tens of nanometers to micrometers using a mixture of polymers, inorganic salts, and/or metal alkoxides [20]. Electrospun fibers have a very high surface-to-volume ratio and a relatively defect-free structure at the molecular level, which may open up the possibility of making high-mechanical-performance composite materials. Disadvantages related to electrospinning include the difficulty in controlling the shapes of the fibers and low yields [27]. In general a non-woven tissue gathers on the collector and therefore it is difficult to separate single fibers and disperse them homogeneously in a polymeric matrix. Figure 9.1 shows a schematic diagram of the electrospinning process.

The applied high voltage plays an important role during the electrospinning process [28], making the understanding of the polarity between metallic needle and collector very important. Depending on the type of power supply and electrode connection, electrospinning leads to different fiber diameters and deposition areas.

It has been reported by Chen et al. that nanofibers prepared by the electrospinning process should exhibit an extremely high piezoelectric voltage constant, high bending flexibility, and high mechanical strength. Therefore utilizing nanofibers in the assembly of 1D nanostructures provides a way to make portable, flexible, highly efficient devices with a low-frequency vibrational nature, since the nanofibers could be woven into fabrics and

Table 9.2 *An overview of electrospun fibers by different researchers*

Raw material	Polymer	Composition	Diameter (nm)	References
Barium acetate, calcium acetate, titanium isopropoxide, and zirconium propoxide	Polyvinylpyrrolidone	$(Ba_{0.85}Ca_{0.15})$–$(Ti_{0.9}Zr_{0.1})O_3$	~200	[14]
Zinc acetate dihydrate	Polyvinyl alcohol	ZnO_2	~250	[20]
Lead zirconate titanate sol–gel	Polyvinylpyrrolidone	$PbZr_{0.52}T_{0.48}O_3$	52–150	[21]
Titanium isopropoxide and barium acetate	Polyvinylpyrrolidone	$BaTiO_3$	100–300	[29]
Bismuth nitrate, potassium nitrate, sodium acetate, and titanium butoxide	Polyvinylpyrrolidone	$(Na_{0.82}K_{0.18})_{0.5}Bi_{0.5}TiO_3$	300–900	[30]
Potassium sodium niobate	Polyvinylpyrrolidone	$K_{0.5}Na_{0.5}NbO_3$	~500	Empa

integrated into composite materials [21]. Table 9.2 shows an overview of electrospun fibers by different research groups.

9.2.2 One-Dimensional Microstructures

One-dimensional (1D) microstructures, such as filaments, microrods, microwires, microfibers, and hollow fibers are desirable due to the fact that they can be operated with increased magnification and actuation with lower electrical power [31]. Such fibrous structures are often used for 0–3, 1–3, or 3–3 smart hybrid materials. The first number of the notation specifies the connectivity pattern (percolation direction) for a particular arrangement of ferroelectric particles, fibers, or rods in a surrounding matrix material [6].

Shaping of macrofibrous structures include the viscous suspension spinning process (VSSP), the ALCERU process, the melt-spinning process, the sol–gel process, etc. These production processes differ principally in the precursor materials, whether a mixed oxide powder (suspension spinning) or wet chemical (sol–gel) routes are selected [32]. The control of several processing parameters within these processing methods determines other fiber characteristics, for example surface morphology, shape, length, diameter, etc. Many of the methods used to produce 1D microstructures allow the use of nearly any material capable of formation into fine, stable fibers. Table 9.3 shows a summary of the different processes discussed that are used to produce fibers, indicating relative fiber diameters that may be achieved by each process.

Table 9.3 *Summary of the different processes and general fiber diameters achieved*

Process	Company/ institute	Material	Fiber thickness and remarks	References
VSSP	Advanced Cerametrics Inc. (ACI)	Cellulose in an alkaline medium (production of viscose)	15–400 μm, high environmental pollution, naturally fluctuating	[33], [34]
ALCERU process	Thuringian Institute of Textile and Plastics Research (TITK)	Cellulose in NMMNO–MH (further development of the Lyocell process)	20–1000 μm, high costs caused by necessary tempering, naturally fluctuating	[35], [36], [37]
Melt spinning (extrusion)	CeraNova Corp. Empa	Plastic alloy out of PZT–powder and binder	80–600 μm	[31], [38], [39], [40], [41]
Sol–gel process	Fraunhofer ISC	Fusable PZT–sols	10–50 μm, preferentially for sensory use	[12], [39], [42], [43]
Polysulfonic process	Fraunhofer IGB, Fa. Mann and Hummel	Polymer in NMP	Mostly hollow fibers for filtration processes	[44], [45], [46], [47], [48]

9.2.2.1 Viscous Suspension Spinning Process (VSSP)

Using a common textile technique, that is rayon fiber technology, the VSSP is used to produce high-purity ceramic fibers. Utilizing fibrous cellulose's past history as a natural material, its strengths as a material used in the textile industry, as well as applications as an energy source, building materials, etc., have been harnessed and used to aid production of ferroelectric fibers. Trace amounts of ceramic powders were used as additives to the rayon precursor to modify the properties of rayon yarns and the VSSP is an extension of this practice.

Submicrometer ceramic powders are mixed with viscose (cellulose dissolved in caustic soda) and extruded through a multihole spinneret into a solidifying bath of acid, creating a fibrous coagulate. Due to the fact that a multihole spinneret is inside the coagulation bath, this fabrication method belongs to the wet spinning technology. The fibers are drawn down to smaller diameters either in the solidifying bath or out in various regeneration and washing steps, attaining superfine fiber diameters (10–20 μm per filament). Prior to debinding and sintering, fibers can be formed into 2D and 3D shapes using conventional textile and composite forming processes [49]. The process is inexpensive and allows ceramic powder weight loadings in the 85% range, which may enable sufficient fiber green strength for efficient in-plant handling.

Control of several process parameters determines other fiber characteristics, for example fiber shape, diameter, surface morphology, length, etc. The VSSP method, patented by Janas and TenHuisen [33] has been used to produce ferroelectric fibers, bioresorbable ceramic fibers used as bone grafts, fuel cell filler material, highly conductive ceramic fibers for secondary battery system electrodes, etc. [34]. VSSP is a robust technology for the manufacture of green ceramic fibers.

9.2.2.2 ALCERU Process

The Thüringisches Institut für Textil- und Kunststoff-Forschung (TITK) developed a processing variant to produce their products, a process they named ALternative CEllulose from RUdolstadt (ALCERU), which is trademarked. The dissolution of cellulose in *N*-methylmorpholine oxide (NMMO), on which the ALCERU process is based, was developed as a reaction to the production of cellulose fibers through an environmentally unfriendly method that utilized viscose, which was found to cause significant air and water pollution. This led to increased research activity to find alternative processing routes with a lower environmental impact [35], resulting in the implementation of the continuous dissolution process of cellulose in NMMO, which is carried out in two ways, by mixing/kneading and thin-film technological paths, with the main differences being the instrumentation used for cellulose dissolution.

The ALCERU process utilizes LIST AG's mixing/kneading technology and by the addition of several functional additives to cellulose dissolution, innovative functional cellulose materials may be produced including 1D ferroelectric fibers, cushion bristles for automobile seats, fibers and filaments for use in filtration equipment, etc. Fibers from the ALCERU process can be produced from a minimum diameter of 20 μm up to 1000 μm. This spinning process is nowadays commercially used to produce PZT fibers [36,37]. Similar to the VSSP method the fibers are solidified using a coagulation bath and the method is considered as a wet spinning technology.

9.2.2.3 Melt Spinning

Melt spinning was developed for rapid cooling of liquids like metal or polymer melts and is used to develop materials that require extremely high cooling rates in order to form, such as metallic glasses, thermoplastics, or nanocomposites. The cooling rates achievable by melt spinning are on the order of 101–107° C/s [38]. For polymer fiber processing this method is frequently used. Typically thermoplastic materials are used and solidification occurs due to cooling below the melting point of the polymer. The melt-spinning process developed to produce ferroelectric fibers is considered to be simple and economical with low variation in fiber diameter and can be performed without the use of auxiliary spinning devices, and additionally the spinning mass has a long shelf-life [11,39].

The process chain of the thermoplastic-ceramic shaping technique as an example (Figure 9.2) includes the following steps: (a) feedstocks compounding, which involves the mixing of a ceramic powder with an organic vehicle (which may be done by the high or low

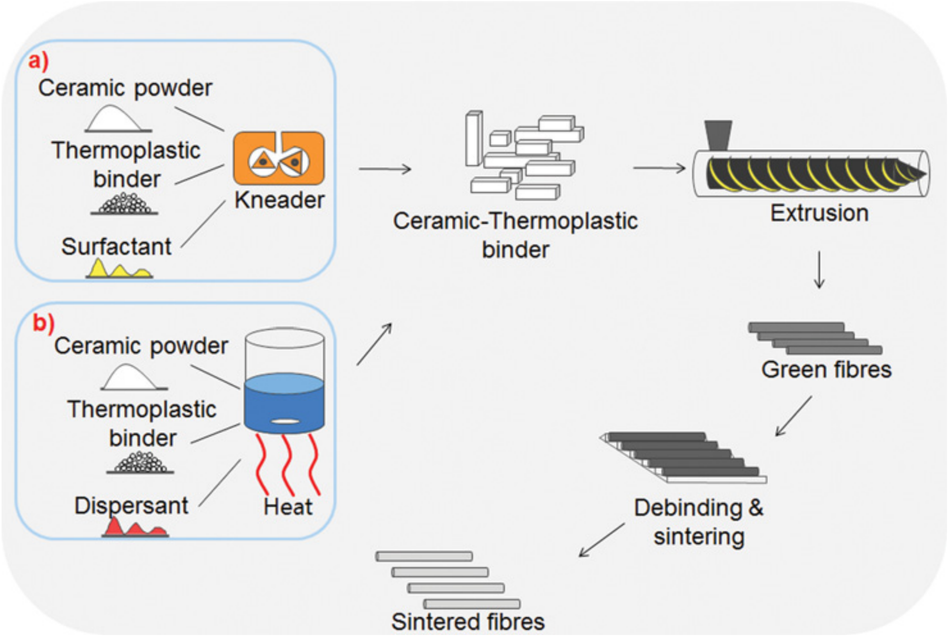
a)
Ceramic powder
Thermoplastic binder
Surfactant
Kneader
Ceramic-Thermoplastic binder
Extrusion
b)
Ceramic powder
Thermoplastic binder
Dispersant
Heat
Green fibres
Debinding & sintering
Sintered fibres

Figure 9.2 *A process schematic for thermoplastic extrusion of ceramic bodies. The ceramic-thermoplastic feed stock may be prepared by (a) a high-shear mixing method or (b) a low-shear mixing method*

shear mixing methods), (b) extrusion, which shapes the material into the final geometry, (c) debinding, which is the removal of the organic vehicle, and, finally, (d) sintering of the body to achieve sufficient density and grain size [11,40]. An advantage of the extrusion process is that it is easily adapted for mass production, allowing numerous fibers to be made simultaneously [31].

9.2.2.4 Sol–Gel

Sol–gel-derived PZT microfibers were developed in the mid-1990s by different groups aimed at active fiber materials for ultrasound transducers and smart structures [42]. The sol–gel process allows for the preparation of ceramics that are difficult to make through conventional methods, allowing the control of geometry and microstructure [12]. This dry spinning technique allows the continuous production of single-filament gel fibers that can be drawn up to several kilometers in length and offers the advantages of chemical homogeneity in multicomponent systems [43]. The metal–organic precursors are mixed in the desired stoichiometry. The sol–gel technique relies on hydrolization and polycondensation of a metal alkoxide or a metal salt precursor solution. These reactions are initiated by the addition of water, acid, and alcohol. The solution's viscosity rises as the reaction proceeds, resulting in a gel-like material. Fibers are formed by extruding the gel through a spinneret or drawing with a glass rod, etc., drying and sintering at between 700 and 1250°C.

Glass-rod-drawn fibers tend to vary in diameter, in the range of 10–200 μm. The obtained diameters of sol–gel-derived extruded PZT fibers range between 10 and 80 μm [12, 42, 43].

Glaubitt, Jahn, and Merklein developed a process that involves the mixing of organometallic (consisting of straight, branched, and cyclic alkyl groups having 1 to 10 carbon atoms) raw materials in an alcohol and reacting the mixture in an organic acid. Volatile components are removed from the combined mixture by hydrolytic condensation and a solid mass is formed at ambient temperatures. After removal of the volatile components under a vacuum, fibers of about 1 m in length can be drawn with a glass rod from the resultant heated viscous liquid. The 1997 patent by Glaubitt, Jahn, and Merklein spun PZT fibers for use as sensors and actuator applications [39].

9.2.2.5 Polysulfone Process

Polysulfone is a thermoplastic with good thermal and chemical stability, high mechanical strength, good solubility, and relative hydrophobicity, making it a suitable candidate for spinning hollow fiber membranes [44, 45]. The process involves the preparation of slurry containing ceramic, polysulfone, and a solvent suitable for polysulfone, which is degassed under stirring in vacuum and filled into cartridges. Fiber spinning may be carried out either (a) directly spun into a coagulation bath with summary controlled deposition or (b) spun on a rotating conveyor disk before entering the coagulation bath. The wet spinning process is carried out by extruding the slurry through a needle with a constant pressure into a non-solvent coagulation bath. Straight fibers may be produced by deposition into grooved spinning supports placed in the coagulation bath (either H_2O or isopropanol alcohol). The fibers are dried and the resulting green fibers heat-treated to remove organic binder, followed by sintering at the suited temperature of the selected ceramic [46–48].

Sintered PZT fibers cut to a length of 160 mm with diameters ranging from 100 to 800 μm could be prepared by the polysulfone process [49]. Dittmer et al. investigated the properties of fibers produced by the ALCERU, extrusion, and polysulfone methods. It could be assumed that mainly microstructural defects influenced the properties of the fibers and not the processing method [50].

9.3 Investigation of Nanostructure, Microstructure, and Phase Composition

Scientific progress in the field of ferroelectric materials would be impossible without reliable tools for the characterization of structural, physical, and chemical properties of materials and devices at a micro-, nano-, and atomic level [51]. The investigation of nanostructure and microstructure of nano- and microfibers may be carried out using scanning electron microscopy (SEM) or transmission electron microscopy (TEM) amongst several other techniques. These investigations normally involve precise preparation of samples in order to properly study the internal structure of the materials in question. Phase composition is investigated by X-ray iffraction (XRD), Raman spectroscopy, and element mapping, which are carried out in order to carry out material identification, analysis, and elemental makeup investigations.

9.3.1 Microscopy

9.3.1.1 SEM Investigations

SEM is an excellent tool to investigate the microstructure (grain size and porosity) of fibrous samples. The SEM creates magnified images by using electrons instead of light waves, allowing higher magnification. SEM investigations are carried out to observe and analyze surface topography and material composition. It involves scanning a sample with a focused beam of electrons and producing an image. The emitted electrons are scanned in a rectangular raster format and interaction with the sample results in different types of signals produced, such as secondary electrons (SE), back-scattered electrons (BSE), characteristic X-rays, cathodoluminescence (CL), auger, specimen current, and transmitted electrons, with SE being a standard attachment to most SEM machines [52]. SEM can produce very high resolution images of a sample surface, revealing details in the area of nanometers. Sintered samples may be characterized for density, grain size, and diameter measurements using SEM [43].

The main parts of an SEM machine include the electron column, scanning system, detector(s), display, vacuum system, and electronics controls. The electron gun contained within the electron column emits an electron beam, focused into a fine spot as small as 1 nm in diameter on to the sample surface. The electron beam is scanned over the specimen and the intensities of the signals created are collected by a detector and the resulting signal is amplified and displayed on a TV screen or computer monitor [52]. The sample holder in the top left corner of Figure 9.3(a) is an example of a special fibre sample holder that enables the examination of micrometer-sized fibres, as seen in Figure 9.3(b).

To determine the porosity and the grain size Heiber et al. embedded lead zirconate titanate (PZT) fibers in a three-component epoxy resin (Technovit 4000, Heraeus Kulzer GmbH & Co. KG) and polished it (a detailed description of the polishing procedure is in [53]). An example of a polished epoxy resin-based sample can be seen in the top-middle of Figure 9.3(a).

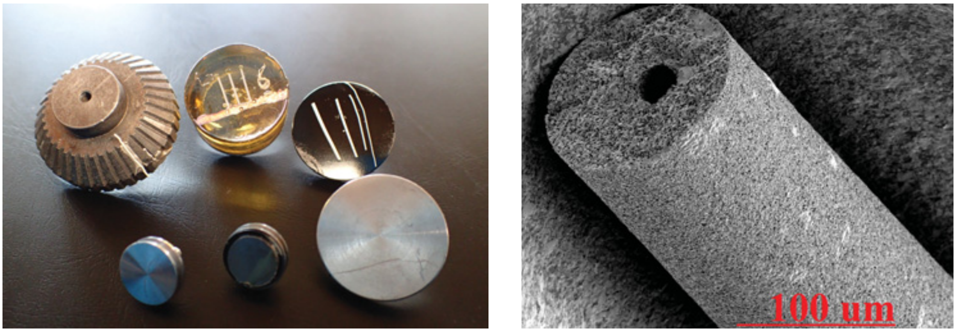

(a) (b)

Figure 9.3 Diagram showing (a) various sample holders with an assortment of samples attached on some and (b) an SEM trace of a KNN sintered fiber with a large void attached to a novel fiber sample holder

An image analysis involves the extraction of meaningful information from images, mainly from digital images by means of digital image processing techniques. The use of digital imaging software that can be run as online applets or downloadable applications is used to process, analyse, and present images obtained from a SEM. Some of the software packages used includes Image J (NIH) [54], Digital Micrograph (Gatan Inc.) [55], Lince (2.3.2 beta) [56], etc. The software may be used to determine porosity, grain size, fibre diameters, etc.

A new technique has enabled spatial resolutions better than 10 nm to be carried out and is suited for routine electron backscatter diffraction (EBSD) characterization of both nanostructured and highly deformed samples. In EBSD a stationary electron beam strikes a tilted crystalline sample and the diffracted electrons form a pattern on a fluorescent screen [57]. The new technique allows a spatial resolution improvement of up to one order of magnitude for EBSD and results can be achieved with the transmission Kikuchi diffraction (TKD) technique. SEM–TKD uses existing EBSD hardware but requires software adaptations and electron transparent samples [58]. Despite the burden of preparing thin, electron-transparent samples, orientation mapping using SEM–TKD is likely to become invaluable for routine characterization of nanocrystalline and, potentially, highly deformed microstructures [59].

An investigation at Empa to determine whether the high shear stress during the melt-spinning process resulted in grain-oriented fibres by using templated grain growth textured KNN powders was attempted (Figure 9.4).

The results of the analysis indicated (Figure 9.4) that no grain orientation occurred in the fibres due to the high shear stress during the melt-spinning process.

9.3.1.2 TEM Investigations

TEM is a technique where a beam of electrons are transmitted through an ultra-thin specimen (without adversely affecting the sample) and the transmitted electrons interact with

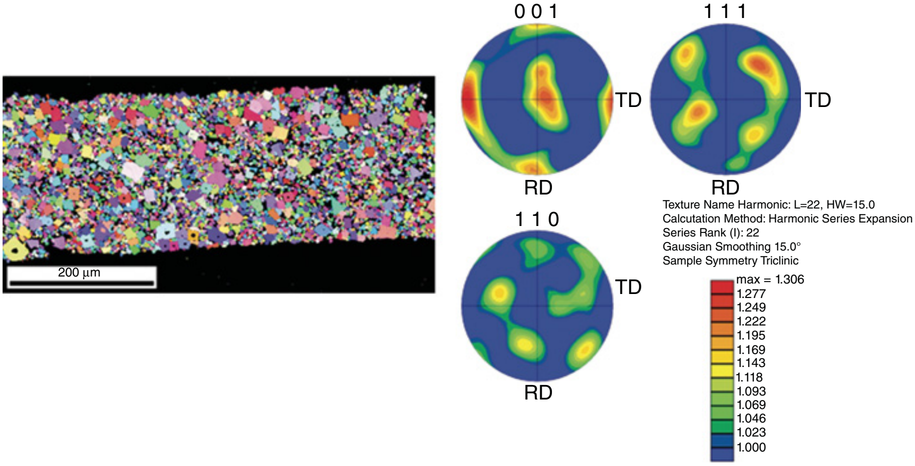

(a) (b)

Figure 9.4 *(a) The crystal orientation of a KNN fibre and (b) the same data plotted as (001), (111), and (110) texture plots of KNN fibre showing limited texturing inside the fibres. For a color version of this figure, see color plate section* the specimen as they pass through it. TEM is used to investigate the crystalline structure of ferroelectric nano- and microstructures with high-resolution TEM (HRTEM) used to investigate the crystal phase [60]. Normally a TEM sample must be no thicker than a few hundred nanometers. Electrons are easily immobilized or deflected by matter (an electron is nearly 2000× smaller and lighter than the smallest atom) so the microscope has to be evacuated and samples under investigation made very thin. TEM exploits the very small wavelengths of high-energy electrons to probe solids at the atomic scale and, in addition, information about local structure (by imaging of defects such as dislocations), average structure (using diffraction to identify the crystal class and lattice parameter), and chemical composition may be collected almost simultaneously. However, use of the TEM is highly skilled and along with the interpretation of the information gained requires a good understanding of the processes occurring in the microscope and the structure of materials under investigation [52, 61].

9.3.2 Phase Composition

9.3.2.1 Phase Compositions by XRD Across the Fiber Diameter

X-ray diffraction (XRD) is an analytical technique used to quickly identify the crystalline phase and may also provide information about unit cell dimensions of novel or unknown crystalline materials. XRD patterns may be experimentally determined or computed based on the crystal structure and Bragg's law. It is normally used to identify phases by comparison with data from known structures, quantify changes in the cell parameters, orientation, crystallite size, and other structural parameters, and is designed for use with a diffractometer (measuring instrument for analyzing the structure of materials from the scattering pattern produced when a beam of radiation interacts with the materials) [61].

One difficulty during the fabrication of (PZT) materials is the high partial pressure and the accompanying evaporation of PbO during sintering, which is extremely critical, especially when fibers with a high ratio of surface area to volume are concerned. To overcome this issue powder atmospheres are used during sintering and as a result a composition and microstructure gradient across the fiber radius is expected. In comparison with ferroelectric bulk materials, it is not possible to remove this gradient by mechanical grinding and therefore it will influence the performance of the fibers depending on their size (a larger influence as the diameter decreases) [53, 62]. The effect of the atmospheric powder on the microstructure as well as on the chemical and phase composition was investigated and their influence on the ferroelectric properties analyzed, as shown in Figure 9.5, in a Heiber et al. study [53].

9.3.2.2 Element Mapping

Elemental mapping of microstructures by electron-excited X-ray spectrometry has a history of more than 60 years. An element map is an image showing the spatial distribution of elements in a sample under investigation. Samples normally need to be polished and thus the map is a 2D section through the sample. It is one of many investigative and analytical techniques that can be used to investigate ferroelectric nano- and microstructures. Element maps are extremely useful as an additional material examination technique as they help to display element distributions in a textural context, particularly for showing compositional zonation. The physical principle of the technique is the generation of characteristic

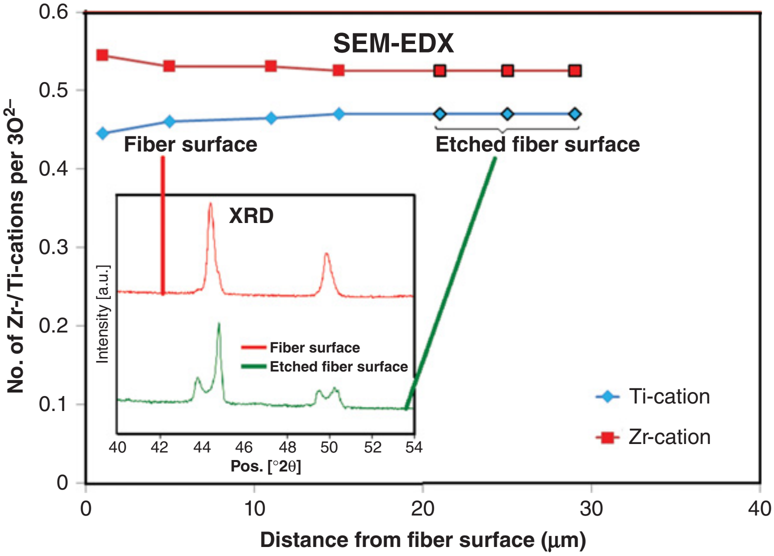

Figure 9.5 *SEM–EDX of a PZT fiber as sintered and after chemical etching (removal of a 20 micrometer layer from the fiber surface). Inset: X-ray diffraction (Debye-Scherrer Method) of the fiber*

X-rays by inelastic scattering of energetic electrons from an incident beam that is focused to a diameter from nm to μm, with the beam energy typically selected in the range 5 to 30 keV [63].

Specific X-ray wavelengths or energies are selected and counted, either by energy-dispersive X-ray spectroscopy (EDX, EDAX, EDS, or XEDS) or wavelength-dispersive X-ray spectroscopy (WDS or WDXRF), producing element maps, and these analysis methods may be incorporated into SEM hardware and are the main analysis tool of electronic microprobes (EMP). With EDX and WDS the image is produced by progressively rastering the electron beam in three different ways, that is spot, line, or rectangular area, point by point over the area of interest on the sample under investigation. The spot and line modes produce quantifiable elemental concentrations but analysis techniques usually limit the presentation of the elemental distribution to dots on a micrograph [64]. The resolution is determined by the beam size and the relative response of each element is determined by the beam dwell time at each point as well as the actual elemental concentration. Longer analysis leads to greater elemental distinction [65].

EDX is typically a faster technique when compared to WDS, but sacrifices resolution and detection limits. The best element maps are acquired using a WDS system on an electron microprobe as it has a much finer spectral resolution, but the trade-off in using the spectrometers is a longer acquisition time [63, 65]. Sometimes element maps have the different elements displayed in a color image and by doing so increase the possibility of distinguishing the different elements. The black and white micrographs of the single-element mappings are imported to a graphics editing program, where each element is given a unique color. Finally, this combined color image is pasted over the original black and white micrograph of the element mapping. Using a combination of element mapping (EDX) and XRD, Heiber et al. were able to discover the presence of a radial gradient structure within a PZT fiber [53].

The investigations showed that significant differences were found in terms of the chemical composition and hence the phase composition across the radial gradient of the fiber [53].

9.3.2.3 Phase Compositions by Raman Scattering Across the Fiber Diameter

Raman spectroscopy is a non-destructive spectroscopic technique used to observe vibrational, rotational, and various low-frequency modes in a system and provides information on the phase composition and the crystalline state (structure and texture) of materials and can be used to identify substances from their characteristic spectral patterns (fingerprinting). In Raman scattering, light interacts with a molecule and distorts (polarizes) the cloud of electrons round the nuclei to form a short-lived state called a "virtual state", which is not stable and the photon is quickly re-radiated. Infrared spectroscopy and Raman scattering are often complementary and may be used together, to give a better view of the vibrational structure of a molecule as they give quite different intensity patterns [66]. Raman scattering measures the difference in energy between the vibrational energy states by subtracting the energy of the scattered photon from that of the incident beam [67].

9.4 Investigation of Mechanical Properties

While structural information about a sample can be obtained using SEM, TEM, etc., high-resolution examination of local electronic structure, electric potential, and chemical functionality requires a different technology [68]. Imaging and manipulation tools have been extremely important for nanotechnological research without which nanoscience would be impossible [69]. The development of ferroelectric-based technology has necessitated imaging ferroelectric materials and local electromechanical measurements on the nanometer scale [68]. The arrangement of domain structures within ferroelectric materials has a direct effect on the macroscopic properties of the samples; thus it is important to be able to examine the ferroelectric domain structure at the smallest possible scale [70]. Scanning probe microscopy (SPM) is a branch of microscopy that forms images of surfaces using a physical probe that scans the sample. SPM was founded with the invention of the scanning tunneling microscope (STM) in 1981 at IBM-Zurich by G. Binnig and H. Rohrer, for which they were awarded the Nobel Prize in 1986. STM is based on quantum mechanical tunneling between an atomically sharp metallic tip and a conductive surface, generating real-space images of surfaces with atomic resolution, and is limited to the imaging of very clean (or chemically very well-defined) conducting surfaces [51, 69]. The development of this technique led to the development of atomic force microscopy (AFM), piezo-response force microscopy (PFM), and others such as magnetic force microscopy (MFM), electrostatic force microscopy (EFM), scanning capacitance microscopy (SCM), near-field scanning optical microscopy (NSOM), lateral (friction) force microscopy (LFM), etc., for the first time providing an opportunity for non-destructive visualization of ferroelectric domain structures at the nanoscale [1, 51].

The SPM techniques have demonstrated that besides imaging these methods allow the control and modification of the local structure and material functionality at the nano- and atomic scale [51]. Another physical property that may be investigated is the viscoelasticity of samples, which may be investigated by nanoindentation hardware [71]. Depending on the type of interaction force between the probing tip and the sample, that is attraction or repulsion, the SPM has two different modes of operation, namely non-contact or contact. In the non-contact mode, the tip is scanned over the surface at a distance of 10–100 nm, which may be controlled by monitoring the resonant frequency of the cantilever. Non-contact SPM can be used for ferroelectric domain imaging by sensing the electrostatic field of the surface polarization charges and is known as EFM [1]. Contact domain imaging methods can be divided into static and dynamic methods. Static imaging methods, for example AFM and LFM, use the surface domain-dependent properties of ferroelectrics, enabling a simple and non-destructive method for studying domain patterns in epitaxial ferroelectric films by topographic imaging of their surfaces. Dynamic methods, which include scanning nonlinear dielectric microscopy (SNDM) and PFM are based on the detection of electrical and mechanical responses, respectively, of the sample to an AC voltage applied via a conductive probing tip [1].

9.4.1 Characterization of Nanowires/Fibers

9.4.1.1 AFM

In 1986 Binnig *et al.* developed the atomic force microscope based on the mechanical detection of the van der Waals forces between a tip and a surface using a pliable cantilever [51]. Due to AFM's ability to image samples on an atomic scale, it has been vital to the advance of nanotechnology [61]. Almost immediately after its inception AFM was shown to be able to map forces of various types, for example magnetic and electrostatic forces, as well as an ability to probe chemical interactions [51]. The AFM differed in many ways from current instruments as it relied on an integrated STM tip. An advantage of AFM over STM is that besides conducting surfaces, insulating surfaces can also be measured. An AFM works by scanning a sharp probe over the surface of a sample in a raster pattern, applying a low AC voltage across the AFM tip–sample system. By monitoring the movement of the probe mounted on a cantilever spring using a laser and detector, a 3D image of the surface can be constructed, as the measurement is made in three dimensions [61, 72]. AFM has three differing modes of operation. These are:

- Contact (static) mode
- Intermittent, semi or tapping contact mode
- Non-contact mode.

9.4.1.2 LFM

LFM, also known as friction force microscopy (FFM), is a technique that detects lateral force variations on an atomic scale by sliding a microfabricated cantilever with a sharp tip over a flat surface. The sliding often takes the form of a stick-slip movement, with the same periodicity as the atomic lattice. LFM, a variation of the contact mode AFM, measures friction in the smallest sliding contacts, providing extremely high sensitivity, and thus atomic forces that act in the sliding of few-atom contacts may then provide a very direct insight into the microscopic origins of the friction. When the sample starts sliding with respect to the tip, the lateral force acting on the tip can be recorded as a twisting of the cantilever measured by means of the deflection of a reflected light beam [73]. The lateral deflection of the cantilever results from the force applied to the cantilever when it moves horizontally across the sample surface. The magnitude of the deflection is determined by the frictional coefficient, the topography of the sample surface, the direction of movement of the cantilever, and the cantilever's lateral spring constant [74].

LFM is a simple and quick technique that can map the orientation of a sample nondestructively, reproducibly, and at high resolution. The technique is standard on conventional commercial AFMs, is simple to apply, requires no sample preparation, and offers complementary information to electron microscopy and Raman spectroscopy [75].

The distributed friction force was determined by Dorogin et al. investigating the friction forces of a ZnO nanowire elastically bent on a flat substrate by LFM. The nanowire rested on a silicon wafer substrate and was pushed near its centre, perpendicular to its axis, by an AFM tip inside an SEM. Over several micrometers of travel, the initially straight profile of the nanowire transformed into the characteristic arc shape. With knowledge of the ZnO nanowire Young's modulus, the distributed kinetic friction was calculated and a distributed kinetic friction of q_{kin} – 1.8 nN nm^{-1} was found [76].

9.4.1.3 SEM/TEM (Nanoindenter)

Nanoindentation has become a popular technique for the measurement of mechanical properties at small scales, but may have even greater importance as a technique for experimental studies of fundamental materials physics. For more than a century, it has been known that surface contacts between materials are highly dependent on their mechanical properties. In the past few decades, due to the development of new sensors and actuators that allow indentations to be consistently performed at submicrometer scales, a revolution has occurred in indentation testing [77].

Indentation techniques may be used to measure hardness, elastic modulus, strain-hardening exponent, fracture toughness, viscoelastic properties of samples, scratch resistance, properties at high temperatures, film adhesion, residual stresses, and in some cases van der Waals type surface forces. New capabilities in ex situ and in situ imaging, acoustic emission detection, and high-temperature testing are being used to probe nm-scale phenomena such as mechanical instabilities or strain localization, defect nucleation, and dynamics, as well as phase transformations [71, 77].

Generally indentation involves making contact with a sample with unknown properties, such as the elastic modulus or hardness with a material whose properties are known. The principal components in a nanoindentation experiment are the sample, the sensors, and actuators used to measure the applied mechanical load and indenter displacement, with the indenter tip typically made from diamond. Nanoindentation measurements are normally indirect measurements of the contact area, whereby the area of contact is determined by measuring the depth of penetration of the indenter into the sample surface, which is then combined with the known geometry of the indenter to provide a measurement in the nm scale [71, 77].

In a nanoindentation test, the size of the residual impression is often only a few micrometers, making it very difficult to obtain direct measurements using optical techniques. The depth of penetration beneath the specimen surface during nanoindentation testing is measured as the load is applied to the indenter, whereby the known geometry of the indenter enables the determination of the size of the area of contact. This response may be plotted as the load–displacement curve (i.e. the *P–H* curve), which differs between different materials and usually reflects different mechanical properties. The nanoindentation procedure also facilitates determination of the modulus of the specimen material from a measurement of the "stiffness" of the contact, that is the rate of change of load and depth [71, 77]. The shape of the load–displacement curve is often found to be a rich source of information, not only for providing a means to calculate the modulus and hardness of the specimen material but also for identification of non-linear events such as phase transformations, cracking, and delamination of films [71].

9.4.2 Characterization of Microfibers

9.4.2.1 Tensile Test Method

Mechanical testing for material behavior characterization has brought much understanding into the mechanics of materials at the macroscale, but as micro/nanofibers are processed routinely, unexpected new mechanical micromechanisms have been revealed [78]. Fibers for advanced applications require a good combination of strength, stiffness, and toughness, but characterizing these properties for micro/nanofibers is challenging because of their low stiffness. With respect to the fiber processing and the low-dimensional structure, most chemical bonds in a fiber are oriented along the fiber axis, leading to large differences in mechanical properties along the fiber axis compared to the perpendicular direction. It is thus not accurate to interpret fiber properties from bulk properties [79].

The most common testing machines are universal testers, which test materials in tension, compression, or bending and their primary function is to create the stress–strain curve. Testing machines are either electromechanical or hydraulic, with the principal difference being the method by which the load is applied [80].

The most effective method for mechanical characterization of fibers is the uniaxial tensile test. During a tensile test, a fiber specimen mounted in a machine is pulled at a specified rate and the resulting reaction force is measured. With the knowledge of the initial fiber dimensions using the measured force and displacement, some of the parameters that can be calculated include ultimate tensile strength, Young's modulus, yield stress, yield strain, and failure strain; the force-elongation data collected can be converted to engineering stress and strain, resulting in a stress–strain curve that is virtually independent of sample dimensions. As the fiber diameter decreases, the crystallinity and arrangement of the molecules within a spun fiber usually results in the enhancement of the Young's modulus and tensile strength [79, 80].

The microstructure and mechanical properties of sintered PZT fibers fabricated from the three different routes (i.e. ALCERU, extrusion, and polysulfone processes) were investigated by Dittmer et al. [50] and Kornmann and Huber [81] (Table 9.4). In both studies, fibers were glued on to frames and the frames were mounted in the tensile testing machine. In the Dittmer et al. study the tensile test was carried out using a preload of 0.05 N at a test speed of 0.3 mm min^{-1} while a preload force of 0.2 N at a testing speed of 0.3 mm min^{-1} was used in the Kornmann and Huber study. In addition to the Weibull strength, Young's

Table 9.4 *The mechanical properties for the PZT fiber batches investigated by a tensile testing technique*

Process – powder	Fiber ø (μm)	Young's modulus (GPA)	Weibull strength (MPa)	Weibull modulus (MPa)	References
ALCERU – PZT	250	43.3	72	21.5 ± 2.4	[50]
Extrusion – PZT	250	34.4	40	22.4 ± 2.0	
Polysulfone – PZT	500	45.2	40	12.1 ± 1.3	
ALCERU – PZT	800	50.9	64	13.7 ± 1.5	
Extrusion – PZT	800	n/a	9	n/a	
Polysulfone – PZT	800	39.2	33	14.7 ± 1.1	
ALCERU – PZT–PMN	250	30.9	46	19.0 ± 4.0	
Extrusion – PZT-PMN	250	35.2	57	23.7 ± 4.1	
ALCERU – PZT–PMN	800	46.6	26	14.1 ± 1.3	
Extrusion – PZT–PMN	800	59.9	22	13.6 ± 3.0	
Extrusion – PZT	268	38.5	64	11.7	[81]
VSSP – PZT	266	40.0	50	3.9	
Sol–gel – PZT	264	37.7	68	9.6	

modulus and the proportional limit were determined by means of tensile testing and Young's modulus was calculated from the linear beginning of the stress–strain curves [50, 81].

The conclusion drawn from the study was that an overview on mechanical properties of selected PZT fibers investigated, where comparison of the mechanical properties was presented. The data were considered to be essential information for the engineering of the adaptive mechanical structures [50].

9.4.2.2 SEM/TEM (Nanoindenter)

In a study by Kozielski et al. nanoindentation was used to determine the hardness, Young's modulus, and defect structure of 140 μm radius PZT fibers, obtained by the extrusion method. A decrease in the measured values as the edge was approached was observed. The hardness values decreased from 8.4 GPa in the middle to 6.7 GPa at the edge of the fiber with reduced modulus values, decreasing from 120 to 108 GPa, respectively. The decreasing values of these parameters were associated with the surface defect structure resulting from an increasing number of Pb^+ vacancies. The outer surface is directly exposed to the lead evaporation, while the center has a larger Pb^+ diffusion distance, resulting in fewer structural defects. The increasing number of point defects affects the hardness value due to a higher degree of empty spaces (Pb vacancies) in unit cells. Thus the nanoindentation measurement revealed that both the hardness and Young's modulus exhibited the tendency to decrease along the radius of the fiber [82].

9.5 Ferroelectric Characterization

It has become increasingly important to characterize the performance of piezoelectric materials under conditions relevant to their eventual application. Piezoelectric materials are being operated at, for example, ever increasing stresses, either for high-power acoustic generation or high-load/stress actuation, etc. As a consequence, measurements of properties such as permittivity (capacitance), dielectric loss, and piezoelectric displacement at high driving voltages are required, which can be used either in device design or materials processing to enable the production of enhanced products [83]. Ferroelectric characterization comprises ferroelectric polarization measurements like P-E hysteresis loops, S-E butterfly curves, and low-voltage signal characterization as a function of frequency, temperature, and thermostimulated current measurements using dynamic and static methods to obtain the pyroelectric coefficient, etc. [84].

9.5.1 Characterization of Nanowires/fibers

9.5.1.1 AFM

AFM has been used for the direct measurements of the piezoelectric coefficient [72]. Due to the very small curvature of the AFM probe tip, a very high electric field can be generated by application of a relatively low potential, making AFM a very promising technique for the alteration of domain structure by local polarization reversal and for the creation of a highly ordered domain structure [61]. Using a conductive cantilever under a variable electric potential, a controlled local switching of polarization in the ferroelectric crystal may be achieved and the dynamics of domain nucleation, growth, and interaction may be investigated at a nanoscale resolution. AFM promises to be a powerful tool for the study of ferroelectric domains providing the nanoscale resolution of domain structure [70].

In a Sá et al. study they reported the synthesis, structural, and ferroelectric characterization of continuous well-aligned nanofibers of $BaTiO_3$ produced by the electrospinning technique, where the ferroelectric properties and domain structure were reported. The piezoelectric response was implemented by AFM to examine the ferroelectric properties; PFM allows local polarization imaging and characterization by means of local piezoresponse analysis. The PFM image revealed a pronounced electromechanical response sensed by the AFM tip on the $BaTiO_3$ nanofiber. In the study, the tetragonal phase present in the fibers was revealed by X-ray diffraction and Raman spectroscopy, the second harmonic generation (SHG) and also confirmed by piezoresponse force microscopy (PFM) using an AFM instrument. The PFM revealed a pronounced electromechanical response sensed by the AFM tip on the calcined $BaTiO_3$ nanofiber. The magnitude of the effective piezoelectric coefficient was evaluated by comparison with the PFM signal calibrated using a PZT thin film, where Sa et al. observed a value of 20 pmV^{-1} [29].

9.5.1.2 PFM

Initially developed to qualitatively investigate domain structures in ferroelectric materials where morphological information was sufficient for material characterization, the PFM technique has been used to study local hysteresis loop spectroscopy and ferroelectric domain patterning for applications such as high-density data storage and ferroelectric lithography [68].

PFM was established as a powerful tool for nanoscale imaging, spectroscopy, and manipulation of ferroelectric and piezoelectric materials (see Table 9.5). In PFM, a local oscillatory electric field is generated by applying an AC voltage to a conducting tip in contact with

Table 9.5 *Electromechanical properties of selected piezoelectric nanowires measured by PFM*

Material	Piezoelectric properties (pm/V)	Size (nm)	Characterization method	References
$BaTiO_3$ nanowire	16.5	ø = 120	PFM	[85]
GaN nanowires	$d_{15} \sim 10$	ø = 64	PFM	[86]
$KNbO_3$ nanowire	7.9	ø = 100	PFM	[87]
$NaNbO_3$ nanowire	~2.02 (ave.)	ø = 100	PFM	[88]
PZT nanowires	145	ø = 75	PFM	[89]

a sample and the deformation due to the piezoelectric effect is detected. PFM is based on the strong coupling between polarization and mechanical displacement whereby coupling can be measured by applying a highly localized electric field to the material and probing the resultant minute surface displacements within picometer precision. In addition to the vertical displacement of the cantilever, torsion of the cantilever can also be measured allowing measurement of both vertical and lateral PFM signals though the magnitude of these signals cannot be compared directly [68].

9.5.1.3 Composites

There are several methods available to characterize nanowires/fibers that have been mixed into a composite matrix solution. A method for measuring the conductivity of ceramic powders has been developed using effective medium theory (analytical/theoretical modeling describing macroscopic properties of composites) and impedance spectroscopy. The powder solution composite (PSC) method can be used to obtain the conductivity of nanowires from impedance spectroscopy measurements of nanowires dispersed in solution. The PSC method may be calibrated by comparing impedance spectroscopy measurements of ceramic powder/nanowires under study dispersed in solution with four-point probe measurements on the ceramic's bulk pellets. The PSC method utilizing nanowire solutions avoids the difficult process of forming electrical contacts to nanowires, enabling the non-destructive in situ measurement of the average electrical properties of large quantities of nanowires [90,91].

In an internal study at Empa, electrospun $K_{0.5}Na_{0.5}NbO_3$ nanofibers were integrated into a nylon 1,1 solid solution to produce a 0–3 ceramic–thermoplastic polymer composite disk, with the intended use for different sensor and actuator applications [92]. With an Ag electrode on either side of the sample impedance spectroscopy measurements could be carried out on this sample revealing the dielectric properties of the sample, as shown in Table 9.6.

The results indicated that the electrospun fiber KNN–nylon composite disk had less than optimal dielectric properties when compared to the nylon disk or the KNN–nylon composite disk, suggesting that the sample would not be best suited to it desired use, due to the lower quality factor and dielectric loss when compared to the PZT–nylon composite disk. The result suggested that further investigation of the microstructure was required.

Table 9.6 Dielectric properties of an electrospun fiber (ESF) KNN–nylon composite, KNN powder–nylon, and PZT–nylon composite disks as well as a nylon disk measured at 1 kHz

1 kHz	Nylon 1,1	KNN powder: nylon	PZT powder: nylon	ESF KNN: nylon
Q-factor	64	11	52	2
$\|Z\|$ (ohms)	34 114 000	41 614 900	13 754 500	332 070
$\angle\theta$ (°)	–89	–85	–89	–60
C (pF)	0.3	0.6	0.8	26
ε_r	4	5	12	333
tan δ (%)	–2	–9	2	–57

9.5.2 Characterization of Microfibers

A variety of piezoelectric composite materials can be made by combining piezoceramic elements with a passive polymer such as epoxy or active polymers. Piezocomposites are classified according to their connectivity (e.g. 2–2, 1–3, 0–3, etc.). Connectivity is defined as the number of dimensions through which the material is continuous. It is conventional for the first digit to refer to the active phase, that is the piezoelectric, while the second one refers to the matrix [6]. Small fiber diameters make common characterization techniques difficult or impossible to use. Normally fiber properties are determined by measuring the properties of 1–3 composites, which are then compared with analytical equations [93]. The piezoelectric, ferroelectric, dielectric, and elastic properties are determined by conventional or quasi-static methods, but the properties of the polymeric matrix have to be known in order to extrapolate the fiber ones. Additionally, the fabrication of composites with a high filling level is a time-consuming process [62].

9.5.2.1 Composite Characterization and Calculation of Single-Fiber Properties

Knowledge of the overall coupled electromechanical behavior in the constituent phases of composites is quite important. Different techniques utilizing algorithms have been used for the evaluation of piezoelectric, elastic, and dielectric constants for the prediction of piezoelectric sensitivity and optimization of properties of piezoelectric composites allowing for theoretical predictions. Nevertheless, the range between the calculated limits can be very wide for certain overall (i.e. bulk) moduli [94, 95].

The micromechanical method provides the overall behavior of the piezoelectric fiber composites from known properties of their constituents (fiber and matrix) through an analysis of a periodic representative volume element (RVE) or a unit cell model. This method evaluates a globally homogeneous medium equivalent to the original composite, using a representative volume element (RVE). It may also be utilized to predict the effective coefficients of 1–3 periodic composites made of piezoelectric unidirectional cylindrical fibers embedded in a soft non-piezoelectric matrix. The properties of composites do not depend solely on the type and portion of volume of the individual phases but also on their interconnection, which brings about a new dimension for optimizing material [95–97].

In a Bowen et al. study of viscous plastic processed PZT microfibers were arranged in a low-viscosity epoxy resin matrix in a 1–3 composite formation, where a systematic characterization of the macrostructure, microstructure, phase composition, and low- and high-field piezoelectric properties occurred. Fiber properties were extracted after poling from composite properties using an isostrain model (displacement continuity across all layers) and the relationships between composite and fiber d_{33} and $s^E{}_{33}$ (constant field elastic compliance for the fibers in the poling direction) were calculated. This was done by using knowledge of the fiber volume fraction and the elastic compliance of the polymer. The fiber results were compared to those of a bulk sintered PZT sample and were found to be very similar to those of the bulk material with no significant degradation of properties in forming and sintering the fine-scale fibers [98].

9.5.2.2 Single-Fiber Measurements

The capacity to investigate single fibers is required in order to optimize their manufacturing processes, for quality control purposes and for modeling the response of components and structures. Porosity, grain size, and phase composition are normally investigated to correlate the microstructure to the ferroelectric properties. Fibers with the best ferroelectric performance, in particular the piezoelectric coefficient, highest saturation, and remnant polarization, the lowest coercive field, and the highest polarization evolution (PE) loop squareness, tend to be fibers with low porosity, sufficiently large grain size, and a phase composition near the morphotropic phase boundary [99]. Table 9.7 shows the ease of measurement of single-fiber properties using instruments at different institutions.

In a study to validate a new composite feedstock processing method that utilized a polyethylene oxide binder system as opposed to the low-density polyethylene binder system, single-fiber measurements were employed to investigate the feasibility of the new low-shear processing method. Ferroelectric behavior of single fibers was measured with a novel piece of equipment (FerroFib) developed from a collaboration between Empa and aixACCT System GmbH (Figure 9.6).

The sintered fibers were cut to a length of ~2.5 mm and glued vertically on to a PMMA disk with Ag epoxy paste (Electrodag 5915, Acheson Colloids Co.), with Ag epoxy paste used for the top electrode on the free end of the fiber. The bottom part of the disk was connected with a metallic electrode, which was used as the contact between the fiber and the

Table 9.7 *The ease of measurement of single-fiber properties using instruments at different institutions*

	MIT, USA	Penn State, USA	Martin-Luther-Uni. Halle-Wittenberg, DE	ETHZ and Empa, CH
Characterization	Single fiber	Single fiber	Single fiber	Single fiber
Characteristics	S(E) and E_c	P(E) and ε_r	S(E) and d_{33}	S(E), P(E), d_{33} blocking force
Deviation	- - -	?	+ + -	+ + +
Handling	+ - -	- - -	+ + -	+ + +
Preparation	+ + +	+ - -	+ + -	+ + -
Temperature	RT	RT	RT	RT
Frequency	1 Hz	10 Hz	Variable	Variable

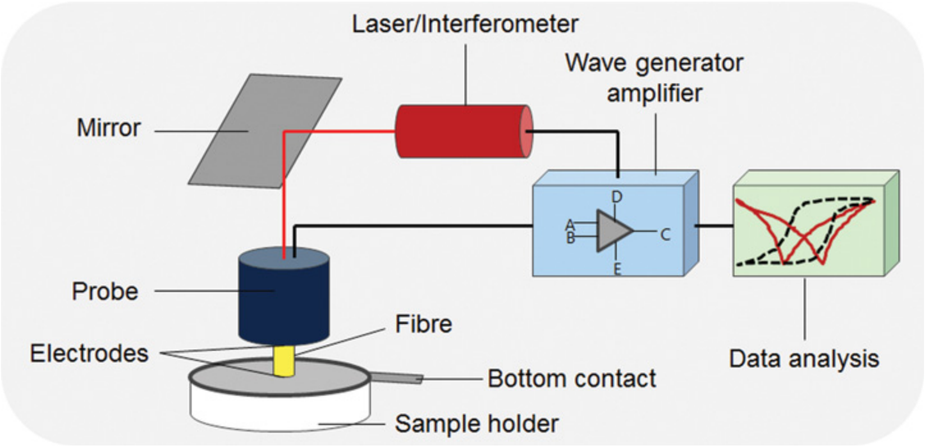

Figure 9.6 *A sketch of the FerroFib equipment.*

FerroFib, as shown in Figure 9.6. A full description of sample fabrication is also described in detail by Heiber et al. [53, 99].

In a Lusiola et al. study the validation of a novel low-shear feedstock preparation method against a standard high-shear mixing method was investigated [41]. A commercial lead zirconate titanate (PZT) powder was used to prepare a feedstock with both techniques for the first evaluation of useful thermoplastic binder systems and extruded to produce sintered ceramic fibers. Table 9.8 shows the electromechanical properties of PZT sintered fibers.

The validation of the low-shear feedstock preparation method against the standard high-shear mixing method proved successful where single electromechanical fiber characterization of low shear produced PZT fibers, in terms of PE, SE loops, and d_{33} measurements, demonstrated the reproducibility of the results when compared to a standard ceramic–thermoplastic high-shear mixing process. The repeatability of the measurements showed the proposed procedure to be robust, validating the new compounding method for wide-scale use [41].

Table 9.8 *Electromechanical properties of PZT sintered fibers measured at 10 Hz*

$PbZr_{0.52}Ti_{0.48}O_3$ (SP505)		Poled @ 3.5 kV mm^{-1} [41]	Manufacturer Spec. PZT SP505 [100]
Piezoelectric coefficient	Binder system	d_{33} (pC N^{-1})	
Low shear	PEO	392 ± 20	440
High shear	LDPE	388 ± 46	
Dielectric loss		tan δ (%)	
Low shear	PEO	6.7 ± 1.9	1.2 (1 kHz)
High shear	LDPE	7.3 ± 1.2	
Relative permittivity		ε^{t}_{33}	
Low shear	PEO	2372 ± 132	1850 (1 kHz)
High shear	LDPE	2458 ± 321	

9.5.2.3 *AFM/PFM*

PFM was used to investigate the ferroelectric domain switching of a PZT microfiber in a Kozielski et al. study [82]. The polarization line histograms provided details on piezoresponse amplitudes inside the examined areas. The polarization condition applied to the center of the fiber revealed a 20% higher change in switched volume of reversed domains in comparison to the edge of the fiber, which was statistically indicated on line histograms. The different pattern of the polarization contrast observed particularly for the central area of the fibers appeared to be caused by higher domain mobility in the part of the structure without defects [82].

9.6 Applications

Ferroelectric ceramics are used in multilayer capacitors, PTC thermistors, piezoelectric transducers, electro-optic devices, etc. The number of applications expanded steadily during the next three decades and is now entering an age of integration and miniaturization in which three-dimensional ceramic circuitry is being developed. Multilayer structures on a low-dimensional scale incorporate resistors, capacitors, dielectrics, metal interconnects, and piezoelectric transducers. Further advances will undoubtedly occur in the years ahead as the field of electroceramics follows in the footsteps of the semiconductor industry [101].

9.6.1 Potential Applications for Nanowires

Piezoelectric nanowires have attracted tremendous interest in nanotechnology energy applications as they possess an excellent electromechanical energy conversion capability that remains intact even with their reduced scale [102].

9.6.1.1 *Sensor*

Nanowire sensors have attracted much attention due to their high surface-to-volume ratios allowing ultra-sensitivity. The size of the nanostructures is similar to the size of species being sensed; consequently the nanostructures make good candidate transducers for producing the signals that are then detected and recorded by conventional instruments, all combining to enable higher selectivity, low power consumption, and a fast response [103, 104]. The underlying phenomenon exploited in using nanowires is the field effect on which field effect transistors (FETs) are based. The wire acts as the channel from the source to drain for the FET. If functional groups attached to the nanowire can act as a receptor to bind with a target species (particularly a biological entity that possesses a charge), then the charge on the surface of the nanowire changes. Since this can influence electronic behavior into the depth of the nanowire, a gating effect occurs that can be used for sensing [103].

9.6.1.2 *Nanogenerators*

Vibration-based mechanical energy is an abundant and accessible energy source that can be harvested with the use of piezoelectric materials. The harvesting of ambient mechanical energy at the nm scale holds great promise towards the goal of achieving self-powered electronic devices. The self-powering capability allows electronic device packages to exclude bulky battery components. The piezoelectric nanogenerator is a nanoscale power generator that transforms ambient mechanical energy into a useful form of electrical energy and the design of nanogenerators is mostly based on the cantilever-beam configuration [105, 106]. Many piezoelectric materials, for example ZnO, InN, ZnS, $BaTiO_3$, PZT, $NaNbO_3$, PVDF, etc., shaped into nanowires have been used for fabricating nanogenerators. While low piezoelectric coefficient and electromechanical conversion efficiency hinders ZnO-based nanogenerators, PZT and $BaTiO_3$, which have high piezoelectric coefficients, are brittle and difficult to manipulate for the fabrication of nanogenerators. Portable, personal, and wearable self-powered nano/microsystems require the piezoelectric materials to be flexible and lightweight [107]. Nanogenerators offer great potential for remote/wireless sensing, charging batteries, and the powering of electronic devices [105].

9.6.1.3 Energy Harvesting

Nanoelectromechanical systems (NEMSs) have been developed using piezoelectric nanowires and have gained a lot of attention for use in energy harvesting applications as they are able to convert several different forms of mechanical energy (e.g. sound waves [108], ultrasonic waves [109], vibrational energy [110], biomechanical energy [111], etc.) into electric power and thereby function as reliable power sources for ultra-low power wireless electronics. Many nanowire-based energy harvesting devices use ZnO [112–114], but among NEMS, those made of ferroelectric perovskite nanostructures and thin films such as PZT and $BaTiO_3$ can produce greater energy transfer due to their higher electromechanical coupling coefficients, thus providing an efficient means to harvest mechanical energy. Koka et al. poled ferroelectric nanowire arrays that were characterized through direct vibration excitation and demonstrated to provide efficient harvesting of mechanical vibrational energy, producing an average power density of $\sim$6.27 mW cm^{-3} from 1*g* acceleration [102].

9.6.1.4 Nanoelectromechanical systems

Nanoelectromechanical systems (NEMSs) are an important new type of device with a growing range of applications, such as nanoscale measurements, through many possible sensors to tests of basic quantum mechanics [115]. There is an increasing interest to form ferroelectric thin films into three-dimensional structures for microelectromechanical system (MEMS) applications. Additionally, piezoelectric materials are tailor-made for MEMSs, as the energy density does not decrease with the dimensions, as happens with electromechanical or magnetomechanical systems. However, piezoelectric ceramics constrained to a thin film within an MEMS results in limits on the design of the device and typically requires the use of the lower piezoelectric coefficient (k_{31}) [116]. By exploring nanoscale effects, NEMSs present interesting and unique characteristics, which deviate greatly from their MEMS predecessor [117]. Vertically aligned nanowires show promise due to the higher aspect ratio, which leads to highly deformable structures and size effects that act to enhance the piezoelectricity of the ceramic. As a result, nanowires have tremendous potential to be applied in the emerging field of nanoelectromechanical systems (NEMSs) [116]. The special characteristics of NEMS devices enable their use in applications such as force sensors, chemical sensors, biological sensors, and ultra-high frequency resonators [117]. Table 9.9 is a list of selected nanowire/fiber material devices with properties.

Table 9.9 *Some of the nanowire/fiber ferroelectric materials investigated for use in various devices*

Material	Synthesis	Diameter (nm)	Use	Input	Output	References
PZT	Electrospinning	52–150	Energy harvester	Stress	1.63 V 0.03 μW	[21]
$BaTiO_3$	Hydrothermal	90	Energy harvester	1*g* acceleration	~6.27 μW cm^{-3}	[102]
ZnO	Hydrothermal	~100	Energy harvester	1*g* acceleration	~0.4 μW cm^{-3}	[102]
ZnO	Vapor–liquid–solid process	60–100	Nanogenerator	–	8 mV ~0.05 fJ ~0.10 pW μm^{-2}	[105]
PZT	Electrospinning	200–400	Nanogenerator	Stress	6 V 45 nA	[107]
ZnO	Chemical vapour deposition	~150	Nanogenerator	~100 decibel	~50 mV	[108]
$NaNbO_3$	Hydrothermal	~200	Nanogenerator	Strain 0.23%	3.2 V 72 nA	[118]
$BaTiO_3$	Molten salt synthesis	~280	Energy harvester	Stress	~0.3 aJ	[119]
PZT	Hydrothermal	500	Nanogenerator	–	~0.7 V 4 μA/cm^2 2.8 mW/cm^3	[120]

9.6.2 Applications for Microfibers

9.6.2.1 Ultrasonic Transducers

With a short wavelength ultrasound waves can be reflected off very small surfaces, for example internal material defects, enabling its use for non-destructive testing of materials. The most common technique used to generate and receive ultrasound signals is through the use of piezoelectric materials. Piezoelectric ultrasonic transducers convert mechanical energy to electrical energy and vice versa, with the application of pressure (sound) or an electrical field, respectively, which saves on cost and design complexity [121]. Combining a piezoelectric ceramic and a passive polymer to form a piezoelectric composite allows the design of new piezoelectric devices that offers substantial advantages over the conventional piezoelectric ceramics and polymers [122].

Fibers containing piezoelectric stacks are developed to allow an increased signal-to-noise ratio for both acoustic emission and acoustic reception. Electrical impedance measurements are normally used to characterize and understand the electromechanical properties of both the fiber transducer and its active component materials. These long and flexible fibers can easily be assembled into large-scale conformal constructs, such as fabrics and sparse meshes. Furthermore, monolithic integration of electrodes into the fiber enables straightforward electrical connection of the device to an external electrical circuit. An issue faced with piezoelectric composite devices is the trade-off made between the requirement of maximizing the surface area of the acoustic device and the inherent energy penalty associated with generating large area interfaces [123].

9.6.2.2 Structural Health Monitoring

Structural reliability is a major concern for all existing structures that are in use and the monitoring of the condition of complex engineering structures is an important aspect of modern engineering, eliminating unnecessary work and enabling planned maintenance, preventing structural failure. The use of continuous non-destructive structural health monitoring enables focused investigation, optimizing the timing of structural repairs or replacements and thus reducing costs [124,125]. Composites of piezoelectric ceramics and polymers have been produced, combining the dielectric constant and the piezoelectricity of the ceramics with the low density and flexibility of polymers. Applications of these smart ceramic–polymer composites include rod composites (1–3 composites) and active fiber composites (AFCs). In these systems ceramic fibers are embedded in a polymeric matrix and their electromechanical properties depend on fiber content, distribution, diameter, and material composition [126]. The 1–3 composites are typically used for transducer applications like sonar, hydrophones, energy harvesting systems, or medical diagnostic applications, while AFC structures are used for sensor and actuator applications such as structural health monitoring, structural actuation and energy harvesting systems [41].

9.6.2.3 Structure Actuation

Piezoelectric actuators have been used in structure control due to their high energy density, wide range of response frequencies, good linear features, flexible location, and direct loading [127]. Traditional piezoelectric actuators are typically capable of exerting high pressures, but with small strains that have limited their applicability. These limitations have

Table 9.10 Some of the ferroelectric materials investigated for use in various devices

Material	Synthesis	Diameter (μm)	Use	Form	Output	References
Pb-based	Alceru	n/a	Actuator	Macrofiber composite	Displacement 63 μm	[128]
PLZT	Sol/gel	25	Transducer	1–3 composite	Bandwidth 170%	[132]
PSMT	Sol/gel	40	Transducer	1–3 composite	Bandwidth 150%	[132]
PZT	Pressing	2	Sensor	1–3 composite	–60 mV 0.6 nA	[133]
PZT	Alceru	300	Energy harvester	1–3 composite	0.33 mJ	[130], [131]
PZT	Extrusion	250	Actuator	1–3 composite	Voltage	[134]
PZT	Dicing	178	Sensor and actuator	1–3 composite	80% vibration suppression	[135], [136]

been overcome with the use of lower-dimensional structures such as microfibers. The control of surfaces that keep the benefits of morphing wings (geometrical changes to aeroplane wings) presents a challenge that can be addressed with the use of microfiber composite (MFC) actuators [128].

The use of the non-linear ferroelectric response, which involves large remnant strains, has also been used to overcome the limitations faced with the use of traditional piezoelectric actuators. Since the domain-switching phenomenon gives rise to strains that are considerably larger than the strains observed under the linear piezoelectric effect, Kushnir and Rabinovitch suggest that this effect can be used in order to overcome the strain actuation limits and to enhance the capabilities of the actuator. The proposed technique may be applied to rod actuators, to an active layer in a stack actuator, or to an active fiber in an MFC actuator [129].

9.6.2.4 Energy Harvesting

Piezoelectric materials have a superior performance when compared to other materials that can be used for energy harvesting from ambient vibrations because of their highly efficient method used to convert mechanical strain to an electric charge [130]. Harvesting energy from ambient vibrations has seen an increasing interest over the past few years due to the urge to find alternative energy sources. Ferroelectric devices have proven to be extremely effective energy harvesters for low-power devices, as often found in portable electronics, sensor controlled systems, and condition monitoring systems due to the wide usable frequency range and adaptability [131]. Table 9.10 is a list of selected microfiber material devices with properties.

9.7 Summary and Outlook

This chapter has been devoted to the description of the fabrication methods used to produce one-dimensional ferroelectric nano- and microstructures from different spinning techniques and the various methods of characterization. Material characterization results in an increase in the stock of knowledge and the use of this stock of knowledge to devise new applications [137]. Normally researchers apply a number of approaches to obtain reliable material characteristics and electromechanical behavior evaluations, making the characterization of elastic, dielectric, and electromechanical properties extremely important.

Knowledge of material characteristics enables the application of specific materials to specific needs, reducing research timelines, costs, etc., thus allowing faster production of novel devices for new and old applications. An example is the ferroelectric ceramic–polymer hybrid composites, which display higher flexibility in comparison to ferroelectric ceramics and higher piezoelectric charge and dielectric constant when compared to pure piezoelectric polymer materials that are used for transducer applications like sonar, hydrophones, energy harvesting systems, structural health applications, as well as large area actuators, etc. Parameters obtained through material characterization may be utilized to develop and validate the numerous analytical models developed to describe ferroelectric materials. Characterization of one-dimensional ferroelectric nano- and microstructures enables researchers to understand how the process of production affects eventual material properties, facilitating tailoring of processing methods to produce desired electromechanical properties suited to particular applications.

Over the years researchers continue to discover novel ways to characterize the complex electromechanical properties and as this occurs new processing methods and applications are revealed. The number of articles on composite processing, characterization, and application has continued to grow and thus ferroelectric materials have continued to be an important component in the field of materials science [2].

References

(1) Gruverman, A. and Kholkin, A. (2006) Nanoscale ferroelectrics: processing, characterization and future trends. *Reports on Progress in Physics*, **69** (8), 2443–2474.

(2) Jordan, T.L. and Ounaies, Z. (2001) *Piezoelectric Ceramics Characterization*, NASA, Langley Research Center, Hampton.

(3) Janas, V.F. and Safari, A. (1995) Overview of fine-scale piezoelectric ceramic/polymer composite processing. *Journal of the American Ceramic Society*, **78** (11), 2945–2955.

(4) Hagood, N. and Bent A. (1993) Development of piezoelectric fiber composites for structural actuation, in *AIAA/ASME/ASCE/AHS/ASC Structures, Structural Dynamics, and Materials Conference*, pp. 3625–3638.

(5) Persano, L., Dagdeviren, C., Su, Y., et al. (2013) High performance piezoelectric devices based on aligned arrays of nanofibers of poly(vinylidenefluoride-co-trifluoroethylene). *Nature Communications*, **4**, art. no. 1633.

(6) Newnhan, R.E., Skinner, D.P., and Cross, L.E. (1978) Connectivity and piezoelectric–pyroelectric composites. *Materials Research Bulletin*, **13** (5), 525–536.

(7) Rørvik, P.M., Grande, T., and Einarsrud, M.A. (2011) One-dimensional nanostructures of ferroelectric perovskites. *Advanced Materials*, **23** (35), 4007–4034.

(8) Sá, P., Barbosa, J., Bdikin, I., et al. (2013) Ferroelectric characterization of aligned barium titanate nanofibres. *Journal of Physics D: Applied Physics*, **46** (10), art. no. 105304.

(9) Boden, N. (2003) Molecular self-assembly: the future, in *Self-Assembly*, edited by B.H. Robinson, IOS, Amsterdam, p. 42.

(10) Polarz, S. and Antonietti, M. (2002) Porous materials via nanocasting procedures: innovative materials and learning about soft-matter organization. *Chemical Communications*, **22**, 2593–2604.

(11) Heiber, J., Clemens, F., Graule, T., and Hülsenberg, D. (2005) Thermoplastic extrusion to highly-loaded thin green fibres containing $Pb(Zr,Ti)O_3$. *Advanced Engineering Materials*, **7** (5), 404–408.

(12) Zhang, M., Wang, X.D., Wang, F.M., et al. (2005) Preparation and ferroelectric behaviour of PZT-fibres. *Ceramics International*, **31**, 281–286.

(13) Glauß, B., Steinmann, W., Walter, S., et al. (2013) Spinnability and characteristics of polyvinylidene fluoride (PVDF)-based bicomponent fibers with a carbon nanotube (CNT) modified polypropylene core for piezoelectric applications. *Materials*, **6**, 2642–2661.

(14) Jalalian, A., Grishin, A.M., and Dou S.X. (2011) Ferroelectric and ferromagnetic nanofibers: synthesis, properties and applications, in *Journal of Physics: Conference Series*, IOP Publishing, p. 012006.

(15) Oxford Dictionaries, Oxford University Press, Oxford 2014 [cited 2014 November 04]. Available from: http://www.oxforddictionaries.com/.

(16) Xiao, Z., Ren, Z., Liu, Z., et al. (2011) Single-crystal nanofibers of Zr-doped new structured $PbTiO_3$: hydrothermal synthesis, characterization and phase transformation. *Journal of Materials Chemistry*, **21**, 3562–3564.

(17) Xia, Y., Wang, P., Sun, Y., et al. (2003) One-dimensional nanostructures: synthesis, characterization, and applications. *Advanced Materials*, **15** (4), 353–389.

(18) Zhou, W., Zhang, Y., Niu, X., and Min, G. (2008) One-dimensional SiC nanostructures: synthesis and properties, in *One-Dimensional Nanostructures*, edited by Z.M. Wang, Springer, pp. 17–59.

(19) Zhu, M.W., Huang, N., Gong, J., et al. (2011) Growth of ZnO nanorod arrays by sol–gel method: transition from two-dimensional film to one-dimensional nanostructure. *Applied Physics A – Materials Science and Processing*, **103**, 159–166.

(20) Baranowska-Korczyc, A., Reszka, A., Sobczak, K., et al. (2012) Magnetic Fe doped ZnO nanofibers obtained by electrospinning. *Journal Sol–Gel Science Technology*, **61**, 494–500.

(21) Chen, X., Yao, N., and Shi, Y. (2011) Energy harvesting based on PZT nanofibers, in *Energy Efficiency and Renewable Energy Through Nanotechnology*, edited by L. Zang, Springer, London, pp. 425–438.

(22) Rabenau, A. (1985) The role of hydrothermal synthesis in preparative chemistry. *Angewandte Chemie International Edition*, **24** (12), 1026–1040.

(23) Simpraditpan, A., Wirunmongkol, T., Pavasupree, S., and Pecharapa, W. (2013) Hydrothermal synthesis of nanofibers from natural ilmenite mineral and their utilization for dye-sensitized solar cell. *Integrated Ferroelectrics*, **149**, 135–142.

(24) Tacchini, I., Ansón-Casaos, A., Yu, Y., et al. (2012) Hydrothermal synthesis of 1D TiO_2 nanostructures for dye sensitized solar cells. *Materials Science and Engineering B*, **177** (1), 19–26.

(25) Lu, R., Yuan, J., Shi, H., et al. (2013) Morphology-controlled synthesis and growth mechanism of lead-free bismuth sodium titanate nanostructures via the hydrothermal route, *CrystEngComm*, **15** (19), 3984–3991.

(26) Wang, J., Durussel, A., Sandu, C.S., et al. (2012) Mechanism of hydrothermal growth of ferroelectric PZT nanowires. *Journal of Crystal Growth*, **347** (1), 1–6.

(27) Song, J.H., Nam, J.H., Cho, J.H., et al. (2011) Microstructures and multiferroic properties of electrospun $BiFeO_3$ nanofibers. *Journal of the Korean Physical Society*, **59** (3), 2308–2312.

(28) Ali, U., Wang, X., and Lin, T. (2012) Effect of nozzle polarity and connection on electrospinning of polyacrylonitrile nanofibers. *The Journal of the Textile Institute*, **103** (11), 1160–1168.

(29) Sá, P., Bdikin, I., Almeida, B., et al. (2012) Production and PFM characterization of barium titanate nanofibers. *Ferroelectrics*, **429** (1), 48–55.

(30) Chen, Y.Q., Zheng, X.J., Feng, X., et al. (2010) Fabrication of lead-free $(Na_{0.82}K_{0.18})_{0.5}Bi_{0.5}TiO_3$ piezoelectric nanofiber by electrospinning. *Materials Research Bulletin*, **45** (6), 717–720.

(31) Ismael, M.R., Clemens, F., Bohac, W.M. et al. (2009) Effects of rheology on the interface of $Pb(Zr, Ti)O_3$ monofilament composites obtained by co-extrusion. *Journal of the European Ceramic Society*, **29** (14), 3015–3021.

(32) Dent, A.C., Nelson, L.J., Bowen, C.R. et al. (2005) Characterisation and properties of fine scale PZT fibres. *Journal of the European Ceramic Society*, **25**, 2387–2391.

(33) Janas, V.F. and TenHuisen, K.S. (inventors) (2002) *Viscous Suspension Spinning Process for Producing Resorbable Ceramic Fibers and Scaffolds*, US Patent US6451059 B1.

(34) Cass, R.B., Loh, R., and Luke, J. (2008) Recent developments, performance improvements, and new ceramic fibers produced by the viscous suspension spinning process, in *Proceedings of the 18th Annual Conference on Composites and Advanced Ceramic Materials – A: Ceramic Engineering and Science Proceedings*, edited by J.B. Watchman, The American Ceramic Society, Westerville, pp. 131–132.

(35) Diener, A. and Raouzeos, G. (1999) Continuous dissolution process of cellulose in NMMO [cited 2014 March 11]. Available from: http://www.listdryprocessing.com/fileadmin/user_upload/download/publications/continuous-dissolution-process-of-cellulose-in-nmmo.pdf.

(36) Meister, F., Vorbach, D., Niemz, F., et al. (2003) Functional high-tech-cellulose materials by the ALCERU-process. *Materialwissenschaft und Werkstofftechnik*, **34** (3), 262–266.

(37) Büttner, R., Markwitz, H., and Knobelsdorf, C. (2006) ALCERU® silver – A new ALCERU® Fibre with versatile application potential. *Lenzinger Berichte*, **85**, 131–136.

(38) Böttner, H., Ebling, D.G., Jacquot, A., et al. (2007) Melt spinning preparation of bismuth telluride and partially alloying with IV–VI compounds for thermoelectric applications. *Materials Research Society Proceedings*, **1044**, 1044-U04-01.

(39) Glaubitt, W., Jahn, R., and Merklein, S. (inventors) (1997) *Molded Article Based on PZT (Pb(Zr,Ti)O_3, Lead Zirconate–Lead Titanate), Method and Intermediate Product for its Manufacture*, US Patent US5656073.

(40) Ismael, M.R., Clemens, F., Graule, T., and Hoffmann, M.J. (2011) Effects of different thermoplastic binders on the processability of feedstocks for ceramic co-extrusion process. *Ceramics International*, **37** (8), 3173–3182.

(41) Lusiola, T., Scharf, D., Graule, T. and Clemens, F. (2014) Low shear compounding process for thermoplastic fabrication of ferroelectric lead-free fibres. *Journal of the European Ceramic Society*, **34** (10), 2265–2274.

(42) Schönecker, A. (2008) Piezoelectric fiber composite fabrication, in *Piezoelectric and Acoustic Materials for Transducer Applications*, edited by A. Safari and E.K. Akdogan, Springer, pp. 261–287.

(43) Meyer, R., Shrout, T., and Yoshikawa, S. (1998) Lead zirconate titanate fine fibers derived from alkoxide-based sol–gel technology. *Journal of the American Ceramic Society*, **81** (4), 861–868.

(44) Bai, Y., Liu, Z., and Sun, D. (2014) Preparation and performance of polysulfone hollow fiber ultrafiltration membranes. *Applied Mechanics and Materials*, **457–458**, 309–312.

(45) Park, S.J. and Kim, H.C. (2001) Thermal stability and toughening of epoxy resin with polysulfone resin. *Journal of Polymer Science Part B: Polymer Physics*, **39** (1), 121–128.

(46) Kaiser, S., Reichelt, E., Gebhardt, S.E., et al. (2014) Porous perovskite fibers – preparation by wet phase inversion spinning and catalytic activity. *Chemical Engineering and Technology*, **37** (7), 1146–1154.

(47) Hohlfeld, K., Gebhardt, S., Schönecker, A., and Michaelis, A. (2013) Piezoceramic fibers and pearls derived by the polysulfone spinning process, in *Electroceramics for End-Users Conference*, Les Arcs, France, pp. 9–12.

(48) Gebhardt, S., Michaelis, A., Scheithauer, U., et al. (inventors) (2010) *Producing Ceramic Molded Body Comprises Producing a Dispersion of Ceramic Powder and Solvent for Polysulfone, Adding a Mixture of Solvent and Polysulfone, Subjecting the Dispersion to Molding, and Sintering the Molded Body*, Patent DE 102008056721 A1.

(49) French, J.D., Weitz, G.E., Luke, J.E., et al. (1997) Production of continuous piezoelectric ceramic fibers for smart materials and active control devices, in *Smart Structures and Materials 1997: Industrial and Commercial Applications of Smart Structures Technologies*, pp. 406–412.

(50) Dittmer, R., Clemens, F., Schoenecker, A., et al. (2010) Microstructural analysis and mechanical properties of Pb(Zr,Ti)O_3 fibers derived by different processing routes. *Journal of the American Ceramic Society*, **93** (8), 2403–2410.

(51) Kalinin, S.V. and Gruverman, A. (2007) *Scanning Probe Microscopy*, Springer Science+Business Media, Berlin.

(52) Field Emission Inc. (2010) *An Introduction to Electron Microscopy*. Hillsboro [cited 2014 March 20]. Available from: www.fei.com/documents/introduction-to-microscopy-document/.

(53) Heiber, J., Clemens, F., Helbig, U., et al. (2007) Properties of Pb(Zr,Ti)O_3 fibres with a radial gradient structure. *Acta Materialia*, **55** (19), 6499–6506.

(54) National Institutes of Health (online) *Image Processing and Analysis in Java* [cited 2014 March 20]. Available from: http://imagej.nih.gov/ij/.

(55) Gatan, Inc. Software Products (online, 2007) [cited 2014 March 20]. Available from: http://www.gatan.com/software/.

(56) Technical University of Darmstadt. Software (online) [cited 2014 March 20]. Available from: http://www.mawi.tu-darmstadt.de/naw/nawstartseite/service/software/sv_software.de.jsp.

(57) Oxford Instruments. Introduction to EBSD (online, 2013) [cited 2014 March 20]. Available from: http://www.ebsd.com/index.php/ebsd-explained/introduction-to-ebsd.

(58) Bruker Corporation (online, 2014) [cited 2014 March 20]. Available from: http://www.bruker.com/service/education-training/webinars/eds-ebsd-and-micro-ct-for-sem/transmission-kikuchi-diffraction-in-the-sem.html.

(59) Trimby, P.W. (2015) Orientation mapping of nanostructured materials using transmission Kikuchi diffraction in the scanning electron microscope. *Ultramicroscopy*, **120**, 16–24.

(60) Tang, M., Shu, W., Yang, F., et al. (2009) The fabrication of La-substituted bismuth titanate nanofibers by electrospinning. *Nanotechnology*, **20**, art. no. 385602.

(61) University of Cambridge (online, 2004-3013) *Dissemination of IT for the Promotion of Materials Science (DoITPoMS)* [cited 2012 November 30]. Available from: http://www.doitpoms.ac.uk/tlplib/piezoelectrics/pzt.php.

(62) Bortolani, F., Michen, M.I., Graule, T., and Clemens, F. (online, 2014) Small and large signal ferroelectric properties of single PZT fibers. *Journal of Intelligent Material Systems and Structures*, DOI: 10.1177/1045389X14533434.

(63) Newbury, D.E. and Ritchie, N.W.M. (2013) Elemental mapping of microstructures by scanning electron microscopy-energy dispersive X-ray spectrometry (SEM-EDS): extraordinary advances with the silicon drift detector (SDD). *Journal of Analytical Atomic Spectrometry*, **28** (7), 973–988.

(64) Jansen, W. and Slaughter M. (1982) Elemental mapping of minerals by electron microprobe. *American Minerologist*, **67**, 521–553.

(65) Goodge J. (online, 2012) *Integrating Research and Education* [cited 2014 March 19]. Available from: http://serc.carleton.edu/research_education/geochemsheets/elementmapping.html.

(66) Swain, D., Bhadram, V.S., Chowdhury, P., and Narayana, C. (2012) Raman and X-ray Investigations of ferroelectric phase transition. *The Journal of Physical Chemistry A*, **16** (1), 223–230.

(67) Smith, E. and Dent, G. (2004) *Modern Raman Spectroscopy: A Practical Approach*, John Wiley & Sons, Ltd, Chichester.

(68) Kalinin, S.V., Rar, A., and Jesse, S. (2006) A decade of piezoresponse force microscopy: progress, challenges and opportunities. *IEEE Transactions on Ultrasonics, Ferroelectrics and Frequency Control*, **53** (12), 2226–2252.

(69) Lindsey, S.M. (2010) *Introduction to Nanoscience*, Oxford University Press, Oxford.

(70) Gruverman, A., Kolosov, O., Hatano, J., et al. (1995) Domain structure and polarization reversal in ferroelectrics studied by atomic force microscopy. *The Journal of Vacuum Science and Technology B: Microelectronics and Nanometer Structures*, **13** (3), 1095–1099.

(71) Fischer-Cripps, A.C. (2011) *Nanoindentation*, SpringerScience+Busines Media, New York.

(72) Agronin, A.G., Rosenwaks, Y., and Rosenman, G.I. (2003) Piezoelectric coefficient measurements. *Nano Letters*, **3** (2), 169–171.

(73) Bennewitz, R. (2005) Friction force microscopy. *Materials Today*, **8** (5), 42–48.

(74) Nanowerk. http://www.nanowerk.com/ (online). [cited 2014 April 11]. Available from: http://www.nanowerk.com/nanobusiness/showroom/Park_Systems/downloads/Lateral_Force_Microscopy.pdf

(75) Marsden, A.J., Phillips, M., and Wilson, N.R. (2013) Friction force microscopy: a simple technique for identifying graphene on rough substrates and mapping the orientation of graphene grains on copper. *Nanotechnology*, **24** (25), art. no. 255704.

(76) Dorogin, L.M., Polyakov, B., Petruhins, A., et al. (2014) Modeling of kinetic and static friction between an elastically bent nanowire and a flat surface. *Journal of Materials Research*, **27**, 580–585.

(77) Schuh, C.A. (2006) Nanoindentation studies of materials. *Materials Today*, **9** (5), 32–40.

(78) Bergers, L.I.J.C., Hoefnagels, J.P.M., Dekkers, E.C.A., and Geers, M.G.D. (2011) A nano-tensile tester for creep studies, *in Conference Proceedings of the Society for Experimental Mechanics Series*, pp. 25–29.

(79) Agilent Technologies Inc. (online, 2013) [cited 2014 April 10]. Available from: http://cp.literature.agilent.com/litweb/pdf/5991-2269EN.pdf.

(80) ASM International (2004) Introduction to tensile testing, in *Tensile Testing*, edited by J.R. Davis, 2nd edition, ASM International, Materials Park, p. 283.

(81) Kornmann, X. and Huber, C. (2004) Microstructure and mechanical properties of PZT fibres. *Journal of the European Ceramic Society*, **24** (7),1987–1991.

(82) Kozielski, L., Piechowiak, M., Czekaj, D., et al. (2008) Mechanical examination of PZT microfibre defects structure. *Phase Transitions: A Multinational Journal*, **81** (11–12), 1081–1088.

(83) Stewart, M., Cain, M.G., and Hall, D.A. (online at www.npl.co.uk); 1999 [cited 2012 May 28]. Available from: http://interactive.npl.co.uk/multiferroics/images/7/7a/CMMT_A(152).pdf.

(84) Jiménez, R. (online at www.icmm.csic.es) [cited 2014 April 15]. Available from: http://www.icmm.csic.es/gf2/tecnicas/ferroelectric.pdf.

(85) Wang, Z., Suryavanshi, A.P., and Yu, M.F. (2006) Ferroelectric and piezoelectric behaviors of individual single crystalline $BaTiO_3$ nanowire under direct axial electric biasing. *Applied Physics Letters*, **89**, art. no. 082903.

(86) Minary-Jolandan, M., Bernal, R.A., and Espinosa, H.D. (2011) Strong piezoelectricity in individual GaN nanowires. *MRS Communications*, **1** (1), 45–48.

(87) Wang, J., Stampfer, C., Roman, C., et al. (2008) Piezoresponse force microscopy on doubly clamped $KNbO_3$ nanowires. *Applied Physics Letters*, **93** (22), art. no. 223101.

(88) Ke, T.Y., Chen, H.A., Sheu, H.S., et al. (2008) Sodium niobate nanowire and its piezoelectricity. *Journal of Physical Chemistry C*, **112** (24), 8827–8831.

(89) Nguyen, T.D., Nagarah, J.M., Qi, Y., et al. (2010) Wafer-scale nanopatterning and translation into high-performance piezoelectric nanowires. *Nano Letters*, **10** (11), 4595–4599.

(90) Ingram, B.J. and Mason, T.O. (2003) Powder–solution-composite technique for measuring electrical conductivity of ceramic powders. *Journal of the Electrochemical Society*, **150** (8), E396–E402.

(91) Murali, S., Prasertpalichat, S., Huang, C.C., et al. (2011) Conductivity measurement of ZnO nanowires using the powder–solution-composite technique. *Journal of the Electrochemical Society*, **158** (10), G211–G216.

(92) Arlt, K. and Wegener, M. (2010) Piezoelectric PZT/PVDF-copolymer 0–3 composites: aspects on film preparation and electrical poling. *IEEE Transactions on Dielectrics and Electrical Insulation*, **17** (4), 1178–1184.

(93) Nelson, L.J., Bowen, C.R., Stevens, R. et al. (2003) Modelling and measurement of piezoelectric fibres and interdigitated electrodes for the optimisation of piezofibre composites, in *Proceedings of the Society of Photo-Optical Instrumentation Engineers (SPIE)*, **5053**, pp. 556-567.

(94) Bowen, C.R. and Topolov, V.Y. (2003) Piezoelectric sensitivity of $PbTiO_3$-based ceramic/polymer composites with 0–3 and 3–3 connectivity. *Acta Materialia*, **51**, 4965–4976.

(95) Berger, H., Kari, S., Gabbert, U., et al. (2006) Unit cell models of piezoelectric fiber composites for numerical and analytical calculation of effective properties. *Smart Materials and Structures*, **15**, 451–458.

(96) Medeiros, Rd., Moreno, M.E., Marques, F.D., and Tita, V. (2012) Effective properties evaluation for smart composite materials. *Journal of the Brazilian Society of Mechanical Sciences and Engineering*, **34**, 362–370.

(97) Berger, H., Kari, S., Gabbert, U., et al. (2005) Calculation of effective coefficients for piezoelectric fiber composites based on a general numerical homogenization technique. *Composite Structures*, **71** (3–4), 397–400.

(98) Bowen, C.R., Stevens, R., Nelson, L.J., et al. (2006) Manufacture and characterization of high activity piezoelectric fibres. *Smart Materials and Structures*, **15**, 295–301.

(99) Heiber, J., Belloli, A., Ermanni, P., and Clemens, F. (2009) Ferroelectric Characterization of Single PZT Fibers. *Journal of Intelligent Material Systems and Structures*, **20**, 379–385.

(100) Smart Material Corporation [online] (2003–2015) [cited 2014 July 26]. Available from: http://www.smart-material.com/media/Datasheet/fibers-Version-2011.pdf.

(101) Cross, L.E. and Newnham, R.E. (1987) History of ferroelectrics, in *Ceramics and Civilization*, edited by R.W. Chan, vol, 111, High-Technology Ceramics – Past, Present and Future, USA, pp. 289–291.

(102) Koka, A., Zhou, Z., and Sodano, H.A. (2014) Vertically aligned $BaTiO_3$ nanowire arrays for energy harvesting. *Energy and Environmental Science*, **7**, 288–296.

(103) US Environmental Protection Agency [online]; 2012 [cited 2014 April 15]. Available from: http://www.epa.gov/rpdweb00/docs/cleanup/nanotechnology/chapter-3-nanowire.pdf.

(104) Chen, X., Wong, C.K.Y., Yuan, C.A., and Zhang G. (2013) Nanowire-based gas sensors. *Sensors and Actuators B: Chemical*, **177**, 178–195.

(105) Wang, X. (2012) Piezoelectricnanogenerators – harvesting ambient mechanical energy at the nanometer scale. *Nano Energy*, **1** (1), 13–24.

(106) Lee, T.I., Lee, S., Lee, E., et al. (2013) High-power density piezoelectric energy harvesting using radially strained ultrathin trigonal tellurium nanowire assembly. *Advanced Materials*, **25** (21), 2920–2925.

(107) Wu, W., Bai, S., Yuan, M., et al. (2012) Lead zirconate titanate nanowire textile nanogenerator for wearable energy-harvesting and self-powered devices. *ACS Nano*, **6** (7), 6231–6235.

(108) Cha, S.N., Seo, J.S., Kim, S.M., et al. (2010) Sound-driven piezoelectric nanowire-based nanogenerators. *Advanced Materials*, **22** (42), 4726–4730.

(109) Wang, X., Song, J., Liu, J., and Wang, Z.L. (2007) Direct-current nanogenerator driven by ultrasonic waves. *Science*, **316**, 102–105.

(110) Chen, X., Xu, S., Yao, N., and Shi, Y. (2010) 1.6 V nanogenerator for mechanical energy harvesting using PZT nanofibers. *Nano Letters*, **10** (6), 2133–2137.

(111) Hansen, B.J., Liu, Y., Yang, R., and Wang, Z.L. (2010) Hybrid nanogenerator for concurrently harvesting biomechanical and biochemical energy. *ACS Nano*, **4** (7), 3647–3652.

(112) Wang, Z.L. and Song, J. (2006) Piezoelectric nanogenerators based on zinc oxide nanowire arrays. *Science*, **312** (5771), 242–246.

(113) Soomro, M.Y., Hussain, I., Bano, N., et al. (2012) Piezoelectric power generation from zinc oxide nanowires grown on paper substrate. *Physica Status Solidi – Rapid Research Letters*, **6** (2), 80–82.

(114) Riaz, M., Song, J., Nur, O., et al. (2011) Study of the piezoelectric power generation of ZnO nanowire arrays grown by different methods. *Advanced Functional Materials*, **21** (4), 628–633.

(115) Hao, L., Gallop, J., and Cox, D. (National Physical Laboratory, online) [cited 2014 April 16]. Available from: http://www.npl.co.uk/science-technology/quantum-detection/research/nems/.

(116) Koka, A. and Sodano, H.A. (2013) High-sensitivity accelerometer composed of ultra-long vertically aligned barium titanate nanowire arrays. *Nature Communications*, **4**, art. no. 2682.

(117) Ke, C. and Espinosa, H.D. (2006) Nanoelectromechanical systems and modeling, in *Handbook of Theoretical and Computational Nanotechnology*, edited by M.R.W. Schommers, American Scientific Publishers, Karlsruhe, p. 8000.

(118) Jung, J.H., Lee, M., Hong, J.I., et al. (2011) Lead-free $NaNbO_3$ nanowires for a high output piezoelectric nanogenerator. *ACS Nano*, **5** (12), 10041–10046.

(119) Wang, Z., Hu, J., Suryavanshi, A.P., et al. (2007) Voltage generation from individual $BaTiO_3$ nanowires under periodic tensile mechanical load. *Nano Letters*, **7** (10), 2966–2969.

(120) Xu, S., Hansen, B.J., and Wang, Z.L. (2010) Piezoelectric-nanowire-enabled power source for driving wireless microelectronics. *Nature Communications*, **1**, art. no. 93.

(121) Cochran, S. (2012) Piezoelectricity and basic configurations for piezoelectric ultrasonic transducers, in *Ultrasonic Transducers: Materials and Design for Sensors, Actuators and Medical Applications*, edited by K. Nakamura, Elsevier, pp. 3–35.

(122) Smith, W.A. (1989) The role of piezocomposites in ultrasonic transducers, in *IEEE – Ultrasonics Symposium*, Institute of Electrical and Electronics Engineers, Montreal, pp. 755–766.

(123) Chocat, N., Lestoquoy, G., Wang, Z., et al. (2012) Piezoelectric fibers for conformal acoustics. *Advanced Materials*, **24** (39), pp 5327–5332.

(124) Pickwell, A.J., Dorey, R.A., and Mba, D. (2011) Thick-film acoustic emission sensors for use in structurally integrated condition-monitoring applications. *IEEE Transactions on Ultrasonics, Ferroelectrics, and Frequency Control*, **58** (9), 1994–2000.

(125) Wang, C.S., Wu, F., and Chang, F.K. (2001) Structural health monitoring from fiber-reinforced composites to steel-reinforced concrete. *Smart Materials and Structures*, **10** (3), 548–552.

(126) Bowen, C.R., Dent, A.C., Nelson, L.J., et al. (2006) Failure and volume fraction dependent mechanical properties of composite sensors and actuators. *Proceedings of the Institution of Mechanical Engineers, Part C: Journal of Mechanical Engineering Science*, **220** (11), 1655–1663.

(127) Li, M., Yuan, J.X., Guan, D., and Chen, W.M. (2011) Application of piezoelectric fiber composite actuator to aircraft wing for aerodynamic performance improvement. *Science China Technological Sciences*, **54** (2), 395–402.

(128) Usher, T.D., Ulibarri Jr, K.R.U., and Camargo, G.S. (2013) Piezoelectric microfiber composite actuators for morphing wings. *ISRN Materials Science*, art. ID 189659.

(129) Kushnir, U. and Rabinovitch, O. (2008) Non-linear piezoelectric and ferroelectric actuators – analysis and potential advantages. *Journal of Intelligent Material Systems and Structures*, **19**, 1077–1088.

(130) Ali, W.G. and Ibrahim, S.W. (2012) Power analysis for piezoelectric energy harvester. *Energy and Power Engineering*, **4**, 496–505.

(131) Smart Material Corp. (Online), 2014 [cited 2014 April 16]. Available from: http://www.smart-material.com/EH-product-main.html.

(132) Chan, H.L.W., Li, K., and Choy, C.l. (2003) Piezoelectric ceramic fibre/epoxy 1–3 composites for high-frequency ultrasonic transducer applications. *Materials Science and Engineering B*, **99** (1-3), 29–35.

(133) Yang, Y., Zhou, Y., Wu, J.M., and Wang, Z.L. (2012) Single micro/nanowire pyroelectric nanogenerators as self-powered temperature sensors. *ACS Nano*, **6** (9), 8456–8461.

(134) Brunner, A.J., Barbezat, M., Huber, C., and Flüeler, P.H. (2005) The potential of active fiber composites made from piezoelectric fibers for actuating and sensing applications in structural health monitoring. *Materials and Structures*, **38** (5), 561–567.

(135) Sodano, H.A. (2003) *Macro-Fiber Composites for Sensing, Actuation and Power Generation*, MSc Thesis, Faculty of the Virginia Polytechnic Institute and State University.

(136) Wilkie, W., High, J., and Bockman, J. (ntrs.nasa.gov.) (online). Available from: http://ntrs.nasa.gov/archive/nasa/casi.ntrs.nasa.gov/20030014135.pdf.

(137) Organisation for Economic Co-operation and Development (2002) *The Measurement of Scientific and Technological Activities*, Paris.

Part B

The second part of the book deals with the characterization of the nanostructured ferroelectrics and multiferroics. It consists of five chapters organized in two sections, which successively present the key techniques for the characterization of the crystal structure and domain configuration of nanoscale ferroics and multiferroics, both critical to the determination of their actual ferroic nature.

Ferroelectricity is a solid-state property intrinsically linked to crystalline order. Indeed, the presence of a spontaneous polarization requires crystal structure to belong to one of the 10 polar (or pyroelectric) point groups [1]. Therefore, symmetry and group determinations have always played a main role when the potential ferroelectricity of new compounds was investigated, even though this is a necessary but not sufficient condition (polarization must also be reversible under an electric field). This is often the approach taken in the recent, fast-growing literature on novel single-phase multiferroics, for many of them show significant electrical conduction that hinders a sound ferroelectric characterization (see Chapter 25 and references therein).

Structural characterizations play an even more relevant role when nanostructured materials, and the persistence of ferroelectricity at the reduced dimensions, are studied. Macroscopic electrical measurements for the characterization of the pyroelectric and ferroelectric responses of nanoscale systems, such as ultrathin epitaxial films, single-crystal nanowires, and ultra-fine particles are very challenging, if not unfeasible. Therefore, the determination of the crystal symmetry and point group has very often been the only means of establishing ferroelectricity (yet, strictly speaking, of the possibility of having it). Good examples are the number of X-ray and electron diffraction studies on nanoparticles of tetragonal perovskites like $PbTiO_3$ or $BaTiO_3$ that proposed a critical size for ferroelectricity from the disappearance of the tetragonal distortion with the decrease in size [2–5].

However, later reports showed that average crystal structures obtained by conventional diffraction techniques provide an incomplete picture of the actual crystal structure of the nanoparticles [6, 7] and that ferroelectric crystal distortions can persist below the apparent critical sizes, though with correlation lengths below those required by the diffraction techniques to uncover them (and below the system size, because of the presence of intrinsic structural disorder). Neither are these techniques capable of characterizing key

Nanoscale Ferroelectrics and Multiferroics: Key Processing and Characterization Issues, and Nanoscale Effects,
First Edition. Edited by Miguel Algueró, J. Marty Gregg, and Liliana Mitoseriu.
© 2016 John Wiley & Sons, Ltd. Published 2016 by John Wiley & Sons, Ltd.

nanoscale structural features of bulk ferroelectrics like short-ranged chemical order in relaxors (thought to be the seed of polar nanoregions, whose dynamics largely determine the material properties; see Chapters 17 and 23 for an in-depth description) or nanotwin arrays in high-sensitivity piezoelectrics (whose dynamics is known to make a large contribution to the very high piezoelectric response; see Chapter 16 for this topic).

Characterization (of the Nanostructured Materials): Crystal Structure

The first section consists of three chapters that describe the same number of techniques, or families of techniques, that are among the most widely applied ones to the structural characterization of nanostructured ferroelectrics and multiferroics nowadays: advanced transmission electron microcopies, Raman spectroscopy, and neutron or synchrotron X-ray scattering techniques, with decreasing spatial resolution but all capable of analyzing crystal order extended over very small lengths.

Advanced transmission electron microscopy techniques are addressed in Chapter 10. This term encloses a wide family of developments in transmission electron microscopy (TEM) beyond conventional imaging and diffraction modes, whose application to ferroelectrics and multiferroics has contributed on a large scale to the build-up of our current understanding of the materials. Highly controversial issues like the actual nature of the nanoscale chemical ordered regions in relaxors [8–10], the symmetry of nanotwins in high-sensitivity piezoelectrics [11,12], which is directly related to the disputed existence of monoclinic phases in the morphotropic phase boundary region of the perovskite solid solutions [13], or the actual presence of ferroelectricity in hastily claimed multiferroics like $BiMnO_3$ [14] could not have been settled without the help of these techniques.

Specifically, the chapter concentrates on three advanced transmission electron microscopy techniques: high-resolution transmission electron microscopy (HRTEM), scanning transmission electron microscopy (STEM), and electron energy loss spectroscopy (EELS). Emphasis is put on capabilities enabled by state of the art spherical aberration corrected microscopes, which allow subangstrom spatial resolutions of about 40 to 80 pm. This is a quite recent development (the first microscopes were installed in the mid-2000s) that has already made a large impact in the field. Indeed, atomic resolution aberration corrected either by HRTEM or high-angle annular dark field (HAADF) STEM have enabled the determination of the relative ions displacements (from the quantitatively resolved atomic column positions) and thus of the actual electric dipoles and strain fields at the unit cell level.

This has allowed, for instance, the identification of a nanoscale region in a $PbZr_{0.2}Ti_{0.8}O_3$ epitaxial film, next to the $SrTiO_3$ substrate, where the local dipoles rotate continuously, forming a flux closure structure connecting two inversion domains [15]. This was the first direct experimental proof of continuous polarization rotation on the atomic scale (see Chapter 22 for implications).

It has also been applied to study the polarization structure and scaling limit of ferroelectric order in nanoscale systems. A recent study reported the persistence of a linearly ordered and monodomain polarization state in $BaTiO_3$ individual isolated cubic nanocrystals with characteristic dimensions below 10 nm [16].

HRTEM and HAADF-STEM sections both start with a comprehensive description of the fundamentals and specificities of the techniques, which is followed by selected case studies of their application to the characterization of nanoscale features of ferroelectrics and multiferroics, chosen out of the recent literature on epitaxial films. Specifically, it is illustrated how these techniques have allowed determination of the atomic level structure of domain walls (that is of how the unit cell level lattice distortions and dipole moments change through the walls), both for inversion (or 180°) walls in tetragonal $Pb(Zr,Ti)O_3$ and ferroelectric/ferroelastic 109° domain walls in rhombohedral $BiFeO_3$. Domain walls are currently the center of a strong activity after the finding that they can have differentiated properties from the bulk and progresses in the ability to tailor domain configurations in epitaxial films (see Chapter 24).

Significant space is also given to the procedures for determining strain fields, which involves the comparison of the actual atomic column positions with those of a reference lattice (usually the substrate in the case of epitaxial films). This is illustrated with authors' own work, where out-of plane and in-plane strain gradients are obtained for regularly twinned $PbTiO_3$ epitaxial films on $DyScO_3$ substrates. The study demonstrated the existence and relevance of flexoelectric components in the polarization.

Atomic resolution aberration-corrected transmission electron microscopy, in this case EELS, has also enabled chemical (and chemical bonding) analysis at the unit cell level. This tool is widely being applied to the study of interfaces in oxide epitaxial heterostructures. The EELS section also consists of a comprehensive description of fundamentals and a number of case studies. $LuFe_2O_4$, one of the hastily claimed multiferroics [17], is chosen to illustrate the ability of the technique to resolve oxygen bonding at the atomic scale, while the $La_{0.7}Sr_{0.3}MnO_3/BiFeO_3$ and $BiFeO_3/Fe$ systems are selected to demonstrate how the interface chemistry can be analyzed with atomic resolution. EELS analysis in these cases has been key to shed light into distinctive interface phenomena. The section finishes with a very recent first example of the application of EELS to the chemical analysis of domain walls, specifically in (this time doubtless) multiferroic$TbMnO_3$ that has allowed relating the ferromagnetism of epitaxial films to the characteristic chemistry of the walls.

Raman spectroscopy is addressed in Chapter 11. This optical spectroscopy is specially suited to probing crystal lattice dynamics, namely optical phonon branches, and thus is sensitive to crystal structure. It has been widely applied to the study of ferroelectrics and ferroelectric displacive phase transitions [18, 19], for it readily allows identifying and following the ferroelectric soft mode [20].

Once again, the chapter starts with a brief description of fundamentals, to subsequently provide an exhaustive review of the recent Raman work carried out on nanostructured ferroelectrics. The technique reflects crystal order extended over very small lengths, and is thus capable of uncovering nanoscale structural features that are not revealed by conventional diffraction techniques.

This is the case for short-ranged chemical or polar orders in bulk ferroelectric relaxors, the topic of the first and largest section that reviews Raman studies of main perovskite relaxor systems. All lead-based and lead-free relaxors, caused by either heterovalent or homovalent substitutions, are dealt with. $(Pb,La)(Zr,Ti)O_3$, $Pb(Mg_{1/3}Nb_{2/3})O_3$ and $Pb(Mg_{1/3}Nb_{2/3})O_3$-$PbTiO_3$, $BaTiO_3$-based solid solutions, and $(Bi_{1/2}Na_{1/2})TiO_3$-based ones are successively addressed in detail. Emphasis is put on how Raman spectroscopy has contributed to build up our understanding of the respective crystal structures, their evolution with temperature and the origin of the relaxor behavior, on how the Raman features associated with cationic disorder, short-ranged chemical order, and polar nanoregions can be differentiated, and on the use of the technique to identify relaxor states in new systems. This might be very useful, for instance, in the search for novel perovskite solid solutions that show nanoscale, self-assembled chemical magnetic order within ferroelectric matrices, one of the most promising single-phase approaches for multiferroism and magnetoelectricity [21]. Raman is a lab-scale technique that requires little sample preparation, ideally suited to readily detect these nanoscale features within a material under investigation.

Raman is also shown capable of identifying and characterizing ferroelectric order in nanoscale systems beyond apparent critical sizes. This is illustrated in a second section for nanostructured ceramics of two functional materials: $BaTiO_3$ and high-sensitivity piezoelectric $BiScO_3$–$PbTiO_3$. Research on nanowires is also reviewed.

Raman spectroscopy is not only sensitive to crystal structure but also to crystal orientation when polarized light is used. Along with the ability to reach a spatial resolution of about 1 μm this makes the technique, namely polarized micro-Raman spectroscopy, capable of imaging ferroelectric domains (and phase coexistence) in bulk systems [22,23]. The last section describes one of the latest developments, tip-enhanced Raman spectroscopy (TERS), which increases resolution up to a few tens of nanometers, and is thus capable of imaging domains of nanoscale objects. This is illustratred for $BaTiO_3$ nanorods.

Advanced neutron and synchrotron X-ray scattering techniques are addressed in Chapter 12. High-resolution diffraction studies carried out at synchrotron radiation or neutron large facilities have played (and will play) a main role in determining the crystal and magnetic orders associated with the ferroic phenomena and specific crystal characteristics key to functionality. The description of a monoclinic phase at the morphotropic phase boundary of the $Pb(Zr,Ti)O_3$ perovskite solid solution, which provides a structural bridge between the ferroelectric rhombohedral and tetragonal polymorphs (along with a mechanism for its high piezoelectric response), might be a good example [24]. This capability is illustrated in the chapter with a synchrotron X-ray diffraction study of the orthorhombic rare-earth manganite, $NdMn_2O_5$, and a discussion of the crystal mechanisms underlying multiferroism for this family of magnetic ferroelectrics.

As already anticipated, the previous diffraction techniques require structural correlation lengths over macroscopic scales, and they are not thus suitable to determine the crystal structure of nanostructured material systems. However, this can be done with methods enabled by the new generation of synchrotron X-ray and neutron sources, such as pair distribution function (PDF) analysis of the total scattering intensity (consisting of both the Bragg and diffuse components). The application of the neutron total scattering method to the characterization of $BaTiO_3$ nanoparticles and $BaTiO_3/SiO_2$ core–shell nanostructures is presented in the chapter as an example.

Characterization (of the Nanostructured Materials): Domains

The second section consists of two chapters, which discuss some of the characterization techniques that are employed to map ferroelectric and multiferroic structure at the nanoscale. Chapter 13 highlights the relative merits of different magnetic mapping tools ranging from Lorentz microscopy to scanning SQUID microscopy. Spatial resolution is considered alongside flux density sensitivity and scanning or image capture speed. Destructive methods, where specialized sample preparation is needed, are contrasted with non-destructive ones. Methods for imaging ferroelectric systems, or at least electrostatic fields are outlined, as are some aspects of scanning tunneling microscopy. The chapter finishes with a detailed discussion of electron backscattered diffraction (EBSD) and its usefulness in mapping and understanding multiferroic composites. The key characteristics of EBSD are in rapid phase imaging (identifying different regions in the composite with different crystallographies that can be attributed to different phases) and in local orientation mapping (and hence identification of grain structure). These capabilities are particularly important in multiferroic composites where ferroelectric and ferromagnetic phase distribution and interface characteristics are vital in determining magnetoelectric coupling performance.

Chapter 14 focuses particularly on scanning probe methodologies for imaging ferroelectric domains. The chronological development of various atomic force microscopy (AFM)-based techniques are presented and the exact way in which they allow imaging of either surface electrostatic potential (electric force microscopy (EFM) and Kelvin probe force microscopy (KPFM)) or local piezoelectric variations (through piezoelectric force microscopy (PFM)) is presented in detail. Views of the history of scanning probe microscopy (SPM) in ferroelectric research is given alongside a view on the latest techniques still under development and the likely future areas in which SPM should be critical.

References

(1) Damjanovic, D. (1998) Ferroelectric, dielectric and piezoelectric properties of ferroelectric thin films and ceramics. *Reports on Progress in Physics*, **61**, 1267–1324.
(2) Chattopadhyay, S., Ayyub, P., Palkar, V.R., and Multani, M. (1995) Size-induced diffuse phase transition in the nanocrystalline ferroelectric $PbTiO_3$. *Physical Review B*, **52**, 177–183.
(3) Frey, M.H. and Payne, D.A. (1996) Grain-size effect on structure and phase transformations for barium titanate. *Physical Review B*, **54** (5), 3158–3168.
(4) Tsunekawa, S., Ito, S. Mori, T., et al (2000) Critical size and anomalous lattice expansion in nanocrystalline $BaTiO_3$ particles. *Physical Review B*, **62**, 3065–3070.
(5) Akdogan, E.K., Rawn, C.J., Porter, W.D., et al. (2005) Size effects in $PbTiO_3$ nanocrystals: effect of particle size on spontaneous polarization and strain. *Journal of Applied Physics*, **97**, art. no. 084305.
(6) Petkov, V., Gateshki, M., Niederberger, M., and Ren, Y. (2006) Atomic scale structure of nanocrystallone $Ba_xSr_{1-x}TiO_3$ (x)1, 0.5, 0) by X-ray diffraction and the atomic pair distribution function technique. *Chemistry of Materials*, **18**, 814–821.
(7) Smith, M.B., Page, K., Siegrist, T., et al. (2008) Crystal structure and the paraelectric to ferroelectric phase transition on nanoscale $BaTiO_3$. *Journal of the American Chemical Society*, **130**, 6955–6963.
(8) Husson, E., Chubb, M., and Morell, A. (1988) Superstructure in $PbMg_{1/3}Nb_{2/3}O_3$ ceramics revealed by high resolution electron microscopy. *Materials Research Bulletin*, **23**, 357–361.

(9) Boulesteix, C., Varnier, F., Llevaria, A., and Husson, E. (1994) Numerical determination of the local ordering of $PbMg_{1/3}Nb_{2/3}O_3$ (PMN) from high resolution electron microscopy images. *Journal of Solid State Chemistry*, **108**, 141–147.

(10) Xu, Z., Gupta, S.M., Viehland, D., et al. (2000) Direct imaging of atomic ordering in undoped and La doped $Pb(Mg_{1/3}Nb_{2/3})O_3$. *Journal of the American Ceramic Society*, **83**, 181–188.

(11) Schierholz, R., Fuess, H., Tsuda, K., et al. (2008) Crystal symmetry in single domains of $PbZr_{0.54}Ti_{0.46}O_3$. *Physical Review B*, **78**, art. no. 024118.

(12) Hungría, T., Houdellier, F., Algueró, M., and Castro, A. (2010) Monoclinic symmetry of twin-free nanocrystals in the $BiScO_3$–$PbTiO_3$ solid solution as revealed by aberration-corrected TEM. *Physical Review B*, **81**, art. no. 100102.

(13) Wang, Y.U. (2007) Diffraction theory of nanotwin superlattices with low symmetry phase: application to rhombohedral nanotwins and monoclinic M_A and M_B phases. *Physical Review B*, **76**, art. no. 024108.

(14) Yokosawa, T., Belik, A.A., and Asaka, T. (2008) Crystal symmetry of $BiMnO_3$: electron diffraction study. *Physical Review B*, **81**, art. no. 100102.

(15) Jia, C.L., Urban, K.W., Alexe, M., et al. (2011) Direct observation of continuous electric dipole rotation in flux-closure domains in ferroelectric $Pb(Zr,Ti)O_3$. *Science*, **331**, 1420–1423.

(16) Polking, M.J., Han, M.G., Yourdkhani, A., et al. (2012) Ferroelectric order in individual nanometre scale crystals. *Nature Materials*, **11**, 700–709.

(17) Lafuerza, S., García, J., Subias, G. (2013) Intrinsic electrical properties of $LuFe_2O_4$. *Physical Review B*, **88**, art. no. 085130.

(18) Burns, G. and Scott, B.A. (1970) Raman studies of underdampled soft modes in $PbTiO_3$. *Physical Review Letters*, **25**, 167–170.

(19) Husson, E. (1998) Raman spectroscopy applied to the study of phase transitions. *Key Engineering Materials*, **155**, 1–40.

(20) Cochran, W. (1960) Crystal stability and the theory of ferroelectricity. *Advances in Physics*, **9**, 387–423.

(21) Evans, D.M., Schilling, A., Kumar, A., et al (2013) Magnetic switching of ferroelectric domains at room temperature in multiferroic PZTFT. *Nature Communications*, **4**, art. no. 1534.

(22) Deluca, M., Sakashita, T., and Pezzotti, G. (2007) Polarized Raman scattering of domain structures in polycrystalline lead zirconate titanate. *Applied Physics Letters*, **90**, art. no. 051919.

(23) Deluca, M., Bermejo, R., Grünbichler, H., et al. (2010) Raman spectroscopy for the investigation of indentation-induced domain texturing in lead zirconate titanate piezoceramics. *Scripta Materialia*, **63**, 343–346.

(24) Noheda, B, Gonzalo, J.A., Cross, L.E., et al. (2000) Tetragonal-to-monoclinic phase transition in a ferroelectric perovskite: the structure of $PbZr_{0.52}Ti_{0.48}O_3$. *Physical Review B*, **61**, 8687–8695.

10

Structural Characterization of Ferroelectric and Multiferroic Nanostructures by Advanced TEM Techniques

Etienne Snoeck[1], Axel Lubk[2], and César Magén[3]

[1] *Centre d'Elaboration de Matériaux et d'Etudes Structurales, CNRS, France*
[2] *Triebenberg Laboratory, Technische Universität Dresden, Germany*
[3] *Instituto de Nanociencia de Aragón-ARAID, Universidad de Zaragoza, Spain*

10.1 Introduction: Advanced TEM Techniques for the Analysis of Ferroelectric and Multiferroic Materials

Transmission electron microscopy (TEM) techniques play an increasingly prominent role in illuminating ferroelectric and multiferroic solid-state properties on the atomic scale. In particular, the development of high-resolution transmission electron microscopy (HRTEM), scanning transmission electron microscopy (STEM), and electron energy loss spectroscopy (EELS) have been fueled by the relative ease with which atomic resolution images are obtained by state of the art aberration-corrected instruments, leading many research groups to conduct atomic resolution (S)TEM and spectroscopic investigations of the local crystal structure and chemical properties of ferroelectrics. From that, solid-state properties like lattice constants, crystal symmetries, lattice strains, defect structures, as well as stoichiometry,

---

Nanoscale Ferroelectrics and Multiferroics: Key Processing and Characterization Issues, and Nanoscale Effects, First Edition. Edited by Miguel Algueró, J. Marty Gregg, and Liliana Mitoseriu.
© 2016 John Wiley & Sons, Ltd. Published 2016 by John Wiley & Sons, Ltd.

bonding types, and atomic valences could be extracted, often by combining the TEM data with other experimental data and theoretic models.

Important breakthroughs[1] were, for instance, the observation of the atomic-scale structure of inversion domain walls [1], of electric dipole rotations in flux closure domain structures [2], of diffuse ferroelectric domain wall steps in $BiFeO_3$ [3], of a strain-driven morphotropic phase boundary in $BiFeO_3$ [4], of electromechanical coupling between edge dislocations and domain walls in $BiFeO_3$ [5], and of flexoelectric rotation of polarization in $PbTiO_3$ [6].

The results of these investigations often reflect the peculiarities of the TEM technique applied. Two main branches can be distinguished: (a) HRTEM yielding an atomic resolution image by greatly magnifying the homogeneously illuminated specimen area and (b) high-resolution STEM providing atomic resolution information by scanning a highly focused atomic size electron probe over the sample and collecting the scattered electrons in a certain angular range. One can furthermore gain valuable information from intermediate modi. For instance, convergent beam electron diffraction (CBED) is highly useful to determine local symmetries and unit cell parameters [7, 8].

10.2 Transmission Electron Microscopy

This section is devoted to the introduction to the image formation process in TEM and HRTEM, focusing on the influence of aberrations on the image formation in HRTEM. This is illustrated with HRTEM studies on ferroelectrics. Subsequently, the benefits of aberration correctors to provide higher resolution and enhanced contrast images is discussed, and several examples of the potential of aberration corrected TEM imaging for probing nanoscaled ferroelectrics are presented. Special attention is given to the method of geometrical phase analysis for the measurement of local strain fields in ferroelectric and piezoelectric nanostructures.

10.2.1 TEM and HRTEM Basics

10.2.1.1 Transmission Electron Microscopy is Electron Diffraction

In a TEM, electrons of high energy (between 60 and 300 kV in modern TEMs) can be approximated as plane waves, when impinging on the object in the bright field mode. When propagating through a crystalline material, this plane wave is diffracted and, as a result of the interaction, the electron wave at the exit surface of the sample is a superposition of several diffracted beams associated with different spatial frequencies $\boldsymbol{g}$. This exit wave can then be expressed as:

$$\Psi_{\text{obj}}(\boldsymbol{r}) = \sum_{g} \tilde{\Psi}(\boldsymbol{g}) \exp(2\pi i \boldsymbol{g r}) \tag{10.1}$$

where $\tilde{\Psi}(\boldsymbol{g})$ are the diffracted beams in the $\boldsymbol{g}$ direction.

---

[1] The following compilation is very incomplete and not intended to give an overview of all important works in the field.

The phase and amplitude of these diffracted beams contain information on the local atomic structure of the periodic crystal. These diffracted beams are recombined by the objective lens of the TEM to an interference pattern in the image plane, the so-called HRTEM image. In the back focal plane of the objective lens, the electron beams converge to form a Fraunhofer diffraction pattern, which corresponds to the Fourier transform (FT) $\tilde{\Psi}(\boldsymbol{u})$ of the exit wave $\Psi_{obj}(\boldsymbol{r})$. Its systematic Bragg reflections located at $\boldsymbol{g}$ can be used to determine the lattice parameters of the crystal and to get information about its symmetry.

The final image recorded on the TEM detector is formed by modulated exit waves, which have passed through the imaging system of the microscope. During this imaging process, the exit wave is modified by the microscope optics and undergoes phase changes, which are not related to the object. Therefore, it is important to understand that the recorded image is not a direct representation of the projected crystallographic structure. The lattice periodicities are conserved thanks to the fact that the diffracted beams follow the Bragg relation and their scattering angle is related to the lattice periodicities. However, the relationship between the exit wave and the contrast of the final image is highly non-linear and is a function of the aberrations of the microscope.

A scheme of the electron wave transfer in the microscope can be drawn as follows (Figure 10.1). In general, the HRTEM image formation results from the combination of diffracted beams, which have been scattered within the crystal of given thickness and orientation and whose amplitude and phase have been differently modified due to dynamical interactions (multiple scattering). The diffracted beams are additionally phase shifted as a

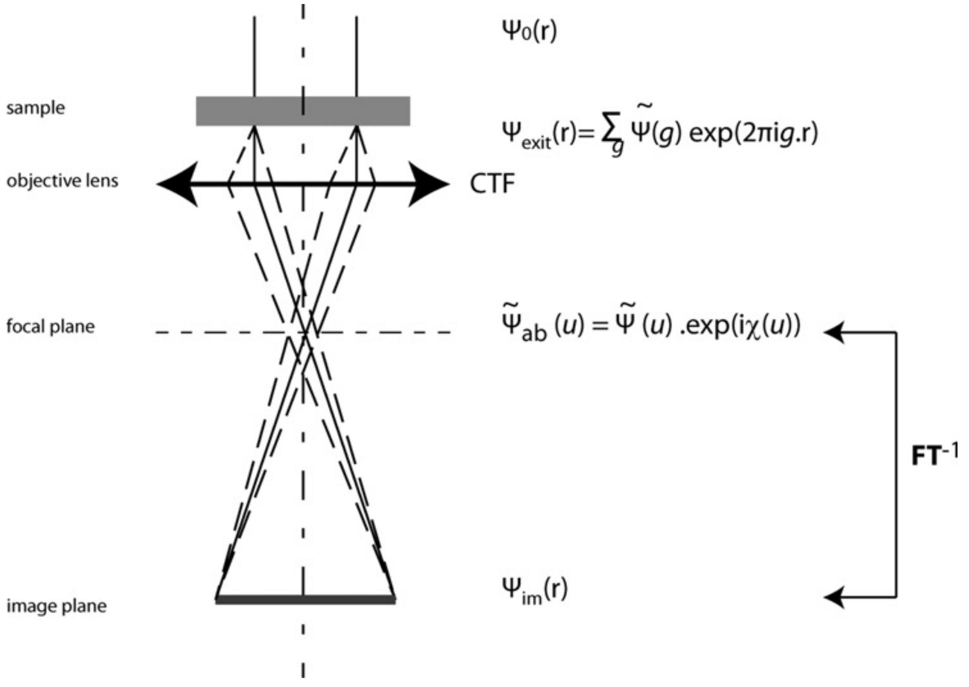

Figure 10.1 *Scheme of the electron wave transfer in a TEM*

function of their scattering angles due to the optical system. A detailed analysis of HRTEM image formation can be found in Spence [9].

The effect of the optical system on the exit wave is generally described by the *wave transfer function* (WTF), which produces a damping and a modulation of the diffracted beams $\tilde{\Psi}(\boldsymbol{g})$ due to the non-perfect optical system, as a function of the scattering angle (i.e. spatial frequency).

10.2.1.2 The Phase Contrast Transfer Function

In the case of very thin TEM samples modifying only the phase of the electron beams, the image formation can, however, be simplified in the so-called "weak phase object" approximation. In this particular case the phase transfer function (PCTF) comprehensively describes the optical transfer. The PCTF describes mainly the effect of objective lens aberrations, incoherency of the incident beam, and instabilities that affect the electron wave passing through the microscope. It depends on:

- The aperture limiting the maximum scattering angle $\boldsymbol{u}$ of the diffracted beams selected to create the HRTEM image.
- The electrical, mechanical, and thermal instabilities, beam incoherence, and detector modulation transfer.
- The different aberrations of the imaging lenses of the TEM (mainly the objective lens aberrations).

In such a case the PCTF can be expressed in the Fourier space as:

$$\mathrm{PCTF}(\boldsymbol{u}) = A(\boldsymbol{u})E(\boldsymbol{u})\sin\chi(\boldsymbol{u}) \tag{10.2}$$

where:

$A(\boldsymbol{u})$ = the *aperture function*, that is a top-hat function
$E(\boldsymbol{u})$ = an *envelope function* describing the attenuation of the wave towards high-spatial frequencies due to the instabilities, beam incoherence, and non-ideal detectors and
$\chi(\boldsymbol{u})$ = introduces the effect of the coherent isoplanatic aberrations of the electron optical system

The *aperture function* cuts off beams scattered above a certain critical angle limiting the resolution.The *envelope function* $E(u)$ has a similar effect, as it dampens the beams scattered at high angles and imposes a maximum to the transmitted spatial frequency. The latter depends on the spatial and temporal coherence of the electron source, the chromatic aberration, instrumental instabilities (specimen drift, vibrations, electronic noise, etc.) as well as the detector response.

10.2.1.3 The Spherical Aberration and the Defocus

The last sinusoidal term in Equation (10.2) of the PCTF, $\sin\chi(\boldsymbol{u})$, determines the sign with which a diffracted beam of frequency u contributes to the contrast in the final image.

If we consider only the leading orders of optical aberrations, which have a rotational symmetry about the optical axis, $\chi(\boldsymbol{u})$ can be expressed as:

$$\chi(\boldsymbol{u}) = \frac{\pi}{2} C_s \lambda^3 \boldsymbol{u}^4 - \pi \Delta f \lambda \boldsymbol{u}^2 \tag{10.3}$$

where:

C_s = the spherical aberration coefficient
λ = the electron wavelength
Δf = the defocus

The defocus Δf can easily be controlled and measured precisely as it only depends on the electric current flowing through the objective coils, while C_s is constant and only depends on the geometry and quality of the objective lens. Due to the $\sin\chi(\boldsymbol{u})$ term, the PCTF oscillates with $\boldsymbol{u}$ and depends on the defocus Δf. The first zero of the PCTF oscillations determines the *point resolution* of the microscope: diffracted beams whose frequencies are larger than this value are transferred with a sign-changing phase-shift, making the HRTEM contrast much less straightforward to analyze. Scherzer [10] showed that there is a particular defocus (*Scherzer defocus*) for which the microscope transfers the widest band of the spatial frequencies without contrast reversal:

$$\Delta f_{Scherzer} = -1.2\sqrt{C_s \lambda} \tag{10.4}$$

Figure 10.2 shows a typical PCTF of a 200 kV microscope with C_s = 1.2 mm at an optimal Scherzer focus of Δf = 66 nm.

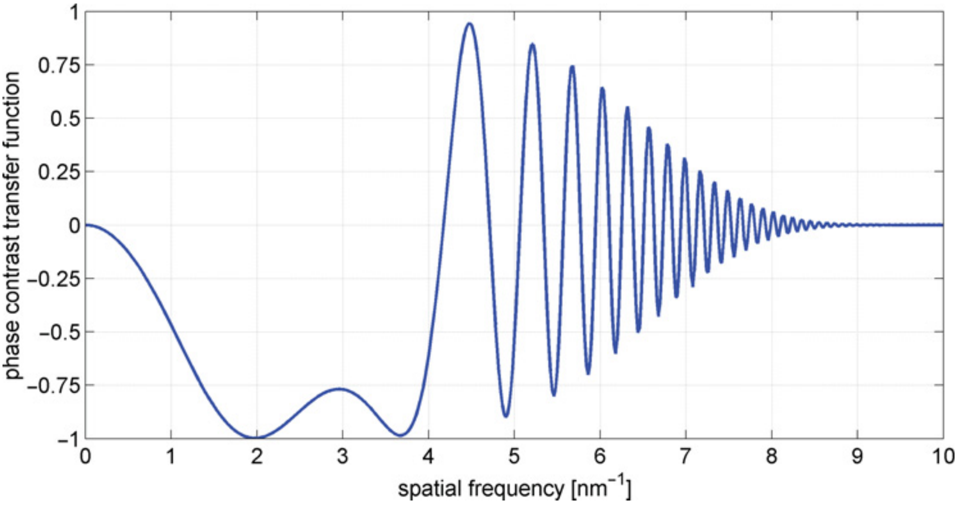

Figure 10.2 *PCTF function for a 200 kV microscope with C_s = 1.2 mm at Scherzer defocus (−66 nm)*

The electron wave in the image plane modulated by the objective lens is given by the PCTF acting on the diffracted beams in reciprocal space:

$$\tilde{\Psi}_{\mathrm{obj}}(\boldsymbol{u})\mathrm{PCTF}\,(\boldsymbol{u},\,\Delta f) \tag{10.5}$$

and a subsequent inverse FT:

$$\Psi_{\mathrm{img}}(\boldsymbol{r}) = \mathbf{FT}^{-1}\left\{\tilde{\Psi}_{\mathrm{obj}}\mathrm{PCTF}\,(\boldsymbol{u},\,\Delta f)\right\} \tag{10.6}$$

It is therefore mainly the *spherical aberration* C_s (and the *chromatic aberration* C_c not described here) together with current and voltage instabilities. Those factors limit the spatial resolution achievable in TEM. Before the development of spherical aberration correctors for TEM in the mid-1990s [11], the optimal spatial resolution of a 200 kV microscope was around 2.1 Å (1.4 Å for 400 kV TEM) while the information limit was close to 1 Å. The latter can be improved using extremely stable, noise-free environments, improving the stability of the electric power supplies and using highly coherent electron sources, namely cold-field emission guns (C-FEGs) or Schottky-field emission guns (S-FEG). The increase in the point resolution necessitates the correction of the spherical aberration coefficient of the objective lens and, to get an even better spatial resolution, to correct for higher-order aberration coefficients, that is axial coma, three-fold astigmatism, etc. (these higher-order aberrations have not been detailed here).

In the mid-2000s, the first spherical aberration correctors developed by CEOS were installed in commercial microscopes, representing a huge step forward for TEM [11]. These highly innovative multipolar optical systems facilitated the correction of the first three orders (nowadays five orders) of aberration coefficients, leading to an almost flat but also very small PCTF up to the information limit of the microscope. In order to increase the weak phase contrast again, a small negative Cs is typically adjusted with the help of the hardware corrector [12].

Spherical aberration-corrected microscopes nowadays allow spatial resolutions of about 40 to 80 pm depending on the microscope and accelerating voltage. Due to the flatness of the PCTF for $C_s \cong 0$, the optimal resolution is obtained for a defocus value close to 0 (i.e., Gaussian focus), facilitating a more straightforward interpretation of Cs-corrected images. The capabilities of Cs-corrected microscopes for the analysis of ferroelectric properties from HRTEM images are illustrated in the following section.

10.2.2 TEM and HRTEM Imaging of Ferroelectrics

10.2.2.1 Conventional Transmission Electron Microscopy

TEM is very efficient to image ferroelectric domains at the nanometer scale as contrast can be generated by the domains themselves and/or by the domain walls. The different diffraction contrasts arising in conventional TEM that can be used are summarized below.

Structure Factor Difference. Domain contrast can be observed by selecting only one diffracted beam coming from a single type of domain. For instance, in a tetragonal non-centrosymmetric ferroelectric structure (space group *P*4*mm*) whose polarization is pointing along the *c* axis, three ferroelastic twin domain types having their *c* axis oriented at approximately 90° with respect to each other occur. Additionally, for each ferroelastic domain two

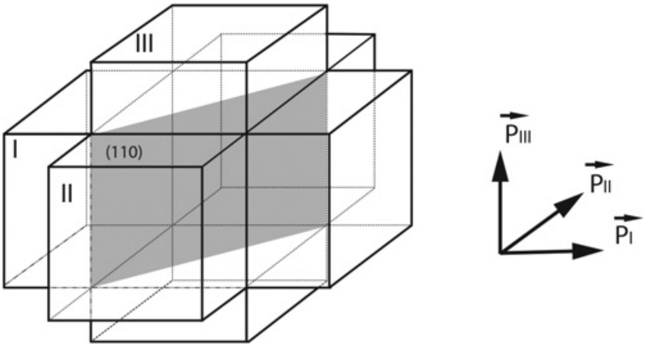

Figure 10.3 *Scheme of the three 90° ferroelectric/ferroelastic domains appearing in a tetragonal non-centrosymmetric ferroelectric structure*

ferroelectric variants exist corresponding to the two possible polarization directions parallel to *c*. The total number of six ferroelectric domains may be separated by 90° or 180° domain walls (DWs). The former are parallel to the (110), (101), or (011) planes [13, 14], (Figure 10.3) and the latter to (010), (100), or (001). When recording the diffraction pattern of such a multiple domain structure one observes the superimposition of the diffraction patterns of the different domains. For instance, if we consider 90° domains I and II with a (110) symmetry plane between them $(hkl)^{I}$ type reflections of one domain (I) would correspond to $(k-hl)^{II}$ reflections of the other domain (II).

As an example we analyze the diffraction pattern of the archetype $BaTiO_3$ ferroelectric compound observed along the [001] zone axis in Figure 10.4(a). Here, one clearly observes the superposition of the two diffraction patterns of domains I and II connected by symmetry leading to split reflections. The latter may have different structure factors and therefore, when selecting in the diffraction plane the nearby $(hkl)^{I}$ and $(k-hl)^{II}$ reflections to create a so-called "dark-field" image, one observes domain contrasts as shown in Figure 10.4(b) (domains I and II).

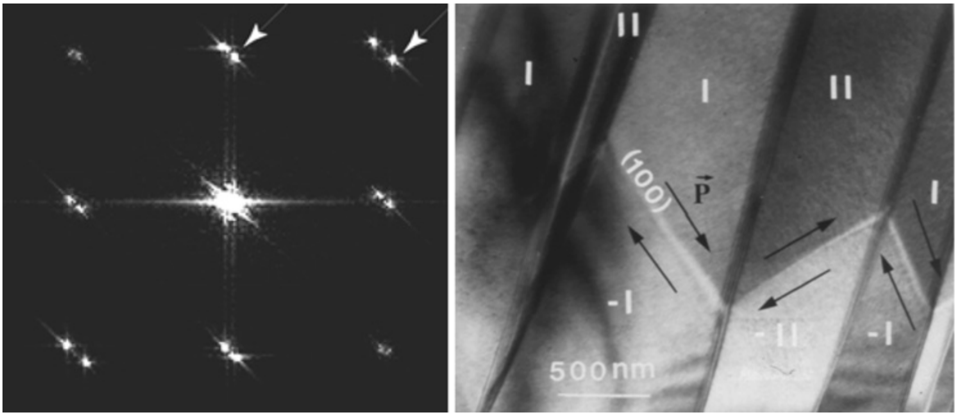

Figure 10.4 *$BaTiO_3$ crystal studied in TEM along its [001] zone axis. (a) Electron diffraction pattern and (b) (110) dark-field image*

Strain Contrast Associated to Domain Walls. Ferroelectric/ferroelastic DWs have a finite thickness in which atoms are locally displaced from their crystallographic positions they have far from the DW. These shifts induce a local strain field (which can be measured by HRTEM and STEM; see later) [15,16], which gives rise to a variation of diffraction contrast localized along the DW and then allows imaging of the boundary.

Fresnel Fringes. When the electron beam is propagating along a DW, the boundary induces a phase shift of the electron wave, resulting in the appearance of alternate dark and bright fringes running parallel to the intersection of the DW and the foil surface. Such Fresnel fringes can barely be observed on the TEM image in Figure 10.4(b). In addition to the localization of the DWs, the analysis of these fringes allows possible lattice defects associated to the boundary to be determined.

Dynamical Contrast in 180° DW. When domains are related to one another by an inversion symmetry (as 180° purely ferroelectric domains) because of Friedel's law, $F(hkl) = F(-\mathrm{h}-\mathrm{k}-\mathrm{l})$, no diffraction contrast is expected. Such 180° DW contrasts are, however, observed [17, 18], as can be clearly seen in Figure 10.4(b) (DWs between domains *I* and –*I* and between domains II and –II). The appearance of these contrasts can be explained by dynamical scattering theory and arise from differences of the dynamical interactions of the electron beam for the two orientations $[hkl]$ and $[-h-k-l]$ in a non-centrosymmetric crystal. These contrasts have been discussed in detail by Gevers et al. [19] and Portier [20]. Such a dynamical contrast drastically depends on the thickness of the foil.

10.2.2.2 High-Resolution Transmission Electron Microscopy

Local Polarization Determination from HRTEM Images. HRTEM is a powerful technique for imaging periodical crystal structures and visualizing atomic column projected potentials with a spatial resolution of a few tens of picometers. That is because the Cs correctors enable HRTEM images to be obtained with much better resolution (up to 50 pm), but also with a much better contrast and a higher signal-to-noise ratio compared to uncorrected ones. This is due to the fact that in non-corrected images, electrons scattered into high angles above the limited spatial resolution contribute to the blurring background while in Cs-corrected HRTEM they contribute to the signal. Cs-corrected HRTEM contains much more information than non-corrected HRTEM, which implies that subtle structural features can be accurately extracted.

For example, Cs-corrected HRTEM experiments have been carried out to study the fine structure of DWs in ferroelectric $PbZr_{0.2}Ti_{0.8}O_3$ (PZT) thin films [1]. Thanks to the flatness of the PCTF for spatial frequencies up to 1/80 pm^{-1}, the oxygen columns could be eventually distinguished from the cationic ones under dedicated imaging conditions. That includes the use of very thin specimens of about 10 nm thick in order to reduce the dynamical scattering effects. Figure 10.5 shows an HRTEM recorded along the [1–10] direction, which allowed Jia et al. [1] to resolve the oxygen octahedron and the Ti/Zr columns position within each PZT unit cell and therefore to study the local polarization changes associated with the distortion of the oxygen–cation dipoles across 180° DWs.

Local Strain Measurements from HRTEM: The GPA Method. HRTEM images can also be used to measure strain fields with a precision a few picometers using advanced microscopes.

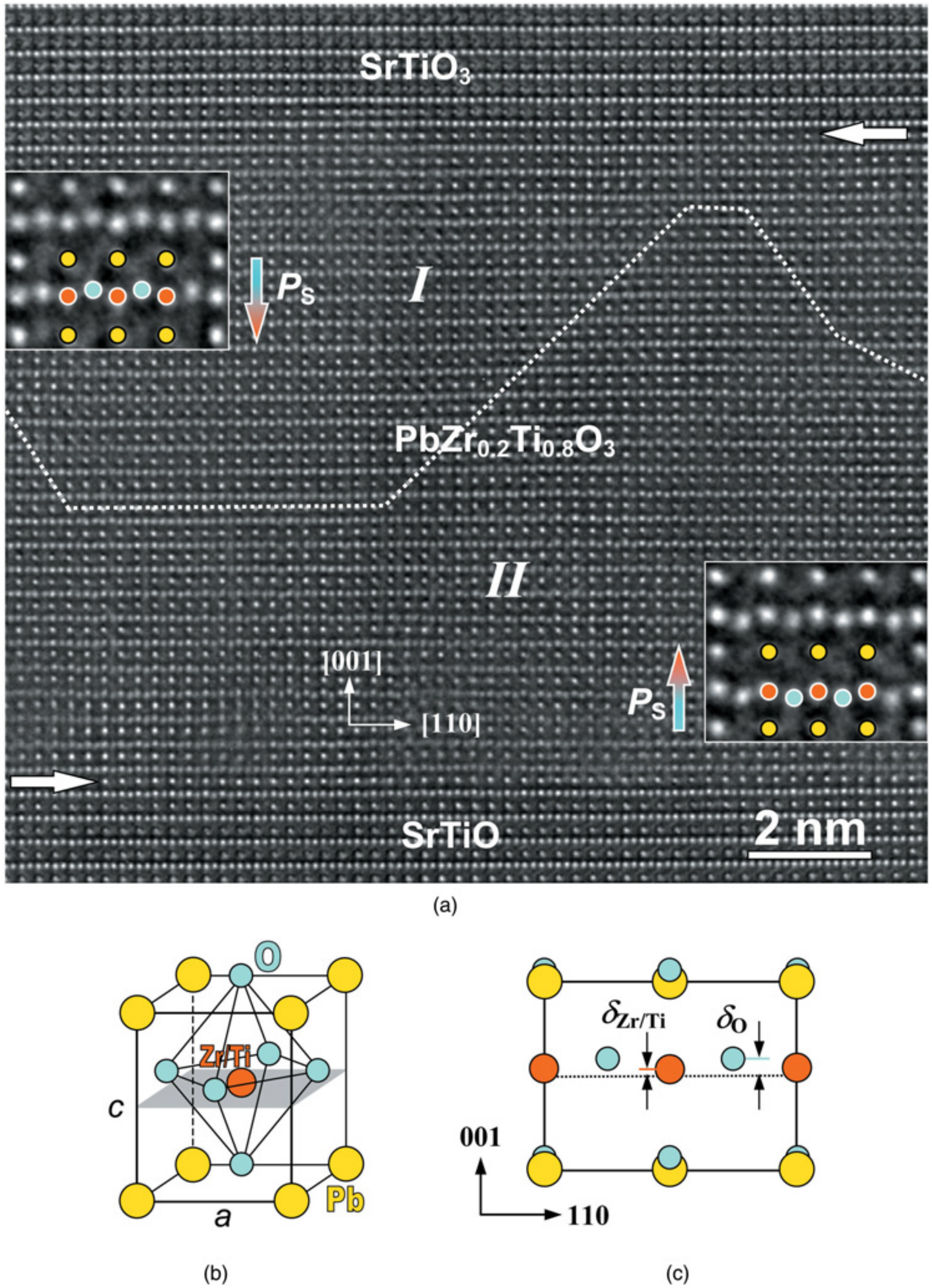
SrTiO$_3$
P_S
I
PbZr$_{0.2}$Ti$_{0.8}$O$_3$
II
[001]
[110]
P_S
SrTiO
2 nm
O
Zr/Ti
c
a
Pb
$\delta_{Zr/Ti}$
δ_O
001
110

(a)

(b)

(c)

Figure 10.5 *Cs-corrected HRTEM image of PZT (a) together with the schematic drawing of the PZT structure (b) projected along [1–10], (c) allowing the polarization change to be studied across a 180° domain wall. Reprinted by permission from Macmillan Publishers Ltd: [Nature Materials] [1]. Copyright © 2008. For a color version of this figure, see color plate section.*

That is because the periodicity of the lattice and small deviations from it are preserved in the HRTEM image even if the contrast modulation is too complicated to distinguish single atomic column positions. Strain can therefore be determined directly by comparing the HRTEM image of a deformed crystalline lattice with respect to a reference region of unstrained material. This can be carried out using image-processing techniques such as peak-finding [21] or geometric phase analysis (GPA)[2]. The latter was initially developed by M.J. Hÿtch et al. to study strain across a DW in PZT [16], and has been applied later to a number of systems, from strained multilayers to quantum dots and semiconductors. With such quantitative HRTEM methods, strain can be measured with remarkable precision using conventional microscopes.

An HRTEM micrograph of a strained crystalline sample reveals a 2D periodical contrast associated to the set of lattice fringes parallel to the electron beam. The intensity of such distorted periodic images can be decomposed in Fourier space:

$$I(\boldsymbol{r}) = \sum_{g} H_g(\mathbf{r}) \exp\{2\pi i \boldsymbol{g}\boldsymbol{r}\} \tag{10.7}$$

where:

$\boldsymbol{g}$ = the reciprocal lattice vector within the image which correspond to each Bragg reflection;

$H_{\boldsymbol{g}}(\boldsymbol{r})$ = the complex Fourier coefficient of each set of fringes of periodicity $\boldsymbol{g}$ which, however, must vary very slowly over the length scale $\boldsymbol{g}^{-1}$. This may be re-written as:

$$H_g(\boldsymbol{r}) = A_g(\boldsymbol{r}) \exp\left\{iP_g(\boldsymbol{r})\right\} \tag{10.8}$$

where:

$A_{\boldsymbol{g}}(\boldsymbol{r})$ = the average amplitude of the set of sinusoidal lattice fringes of frequency $\boldsymbol{g}$ around the position $\boldsymbol{r}$

$P_{\boldsymbol{g}}(\boldsymbol{r})$ gives the average position of the fringes in the image around the position $\boldsymbol{r}$

In the case of a perfect crystal free of deformation, the Fourier coefficients are constant (A_g and P_g do not depend on $\boldsymbol{r}$) and each set of lattice fringes can be written:

$$I_g(\boldsymbol{r}) = 2A_g \cos(2\pi \boldsymbol{g}\boldsymbol{r} + P_g) \tag{10.9}$$

which corresponds to the image that could be obtained by performing a Bragg filtering of the original HRTEM image selecting the $\pm\boldsymbol{g}$ reflections in the FT.

A deformation field in the crystal leads to a displacement of the set of fringes and the Fourier coefficients $H_{\boldsymbol{g}}$ become space dependent, that is ($A_g(\boldsymbol{r})$ and $P_g(\boldsymbol{r})$) will depend weakly on $\boldsymbol{r}$:

$$I_g(\boldsymbol{r}) = 2A_g(\boldsymbol{r}) \cos(2\pi \boldsymbol{g}\boldsymbol{r} + P_g(\boldsymbol{r})) \tag{10.10}$$

Considering a displacement field $\boldsymbol{u}(\boldsymbol{r})$ which translates $\boldsymbol{r} \to \boldsymbol{r} + \boldsymbol{u}(\boldsymbol{r})$, the set of fringes can be then rewritten:

$$I_g(\boldsymbol{r}) \approx 2A_g(\boldsymbol{r}) \cos(2\pi \boldsymbol{g}\boldsymbol{r} + 2\pi \boldsymbol{g}\boldsymbol{u}(\boldsymbol{r}) + P_g) \tag{10.11}$$

---

[2] The GPA method for measuring local strain from an HRTEM image has been fully described by Hytch et al. [16] and a software commercialized by HREM Research Inc. (http://www.hremresearch.com/) is available for Digital Micrograph platform (Gatan©).

Ignoring the constant phase term, this leads to:

$$P_g(r) = 2\pi \boldsymbol{g}u(\boldsymbol{r}) \tag{10.12}$$

Thus, the phase image $P_g(\boldsymbol{r})$ yields the displacement field $\boldsymbol{u}(\boldsymbol{r})$ in the direction of the reciprocal lattice vector $\boldsymbol{g}$. By combining two sets of lattice fringes in two non-collinear directions $\boldsymbol{g}_1$ and $\boldsymbol{g}_2$, the in-plane x and y components $(u_x(\boldsymbol{r}), u_y(\boldsymbol{r}))^{\mathrm{T}}$of the displacement field $\boldsymbol{u}(\boldsymbol{r})$ can be recovered, solving the equations:

$$P_{g1}(\boldsymbol{r}) = -2\pi \left[g_{1x}u_x(\boldsymbol{r}) + g_{1y}u_y(\boldsymbol{r})\right]$$

$$P_{g2}(\boldsymbol{r}) = -2\pi \left[g_{2x}u_x(\boldsymbol{r}) + g_{2y}u_y(\boldsymbol{r})\right] \tag{10.13}$$

The local strain $\varepsilon_{xx}(\boldsymbol{r})$ and $\varepsilon_{yy}(\boldsymbol{r})$, the local shear $\varepsilon_{xy}(\boldsymbol{r})$, as well as the local rotation $\omega_{xy}(\boldsymbol{r})$ of the 2D projected lattice can then be deduced from the spatial derivative of local displacement components $u_x(\boldsymbol{r})$, $u_y(\boldsymbol{r})$ by:

$$\varepsilon_{xx} = \frac{\partial u_x}{\partial x}, \varepsilon_{yy} = \frac{\partial u_y}{\partial y}, \varepsilon_{xy} = \frac{1}{2}\left(\frac{\partial u_x}{\partial y} + \frac{\partial u_y}{\partial x}\right), \omega_{xy} = \frac{1}{2}\left(\frac{\partial u_x}{\partial y} - \frac{\partial u_y}{\partial x}\right) \tag{10.14}$$

In practice the GPA method consists of: (1) calculating the FT of either an HRTEM or an High Resolution HAADF-STEM images of a strained crystal; (2) selecting two non-collinear $\boldsymbol{g}$ vectors in that pattern; and (3) centering a mask on each of them before performing two inverse FT. This leads to two complex images ($I_{g1}(\boldsymbol{r})$ and $I_{g2}(\boldsymbol{r})$) from which the amplitude images $A_{g1}(\boldsymbol{r})$ and $A_{g2}(\boldsymbol{r})$ and the phase images $P_{g1}(\boldsymbol{r})$ and $P_{g2}(\boldsymbol{r})$ can be calculated separately. The phase variations from a reference region expected to be strain-free allow the $u_x(\boldsymbol{r})$, and $u_y(\boldsymbol{r})$ components of the displacement field $\boldsymbol{u}(\boldsymbol{r})$ to be calculated. Strain, shear, and rotation can then be easily deduced following Equations (10.14).

The GPA method is very efficient to analyze the strain associated to DWs in ferroelectric materials. The GPA procedure is illustrated below, where the strain and rotation associated to 90° ferroelectric domains in an epitaxial $PbTiO_3$ thin film is studied from an high-angle annular dark field (HAADF)–STEM image. Figure 10.6 displays a low-magnification HAADF–STEM image of a $PbTiO_3$/$SrRuO_3$/$DyScO_3$ stacking grown by pulsed laser deposition [22] with its corresponding FT.

The $\boldsymbol{g}_1$and$\boldsymbol{g}_2$ reflections can be successively selected in the FT (Figure 10.6) and the corresponding complex images (I_{g1}andI_{g2}) can be calculated by inverse FT. The amplitude images $A_{g1}(\boldsymbol{r})$ and $A_{g2}(\boldsymbol{r})$ and the phase images $P_{g1}(\boldsymbol{r})$ and $P_{g2}(\boldsymbol{r})$ can then be extracted from these complex images (Equation 10.10). The two phase images are shown in Figure 10.7 using the spatial periodicity of $DyScO_3$ as reference.

Following Equation (10.13), the in-plane components $(u_x(\boldsymbol{r}), u_y(\boldsymbol{r}))$ of the displacement field $\boldsymbol{u}(r)$ can be measured giving access to the local strain, shear, and rotation of the 2D projected lattice following Equations (10.14).

Figure 10.8(a) and (b) show the measured in-plane strain $\varepsilon_{xx}(\boldsymbol{r})$ and rotation $\omega_{xy}(\boldsymbol{r})$ of the $PbTiO_3$ layer relative to the $DyScO_3$ substrate chosen as reference, respectively (note that in case of a fully relaxed epitaxial layer, the $\varepsilon_{\mathrm{xx}}$ relative strain corresponds to the layer/substrate misfit).

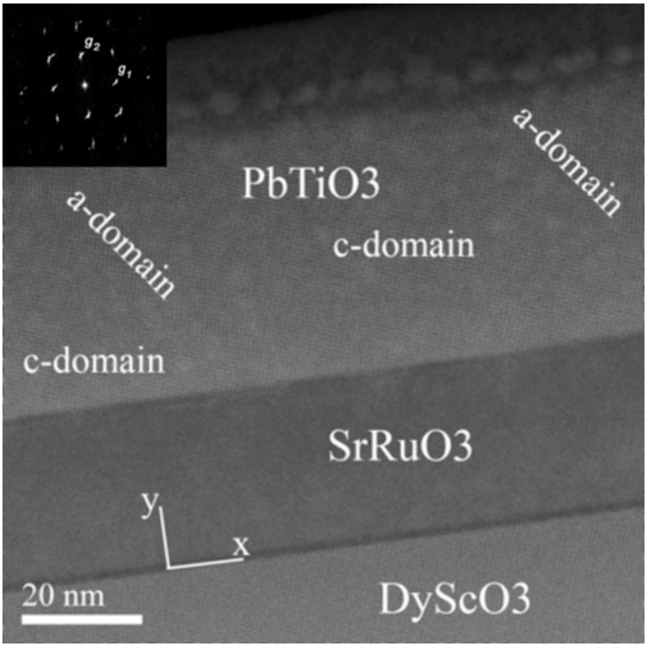

Figure 10.6 *HAADF–STEM image of a ferroelectric $PbTiO_3$ layer grown on $SrRuO_3$/$DyScO_3$(001). Inset shows the FT of the image evidencing all spatial periodicities appearing in the image. Adapted from Catalan et al. [6].*

In the $PbTiO_3$/$SrRuO_3$/$DyScO_3$ stacking studied here, the GPA analysis clearly reveals the rotation associated to the *a–c* domain configuration and also evidences a gradient of the out-of-plane strain and a rotation in a direction parallel to the interface as well as in the growth direction. This strain gradient has been shown to stimulate a flexoelectric modulation of the electric polarization [6], which will be detailed in Section 10.3.3.1.

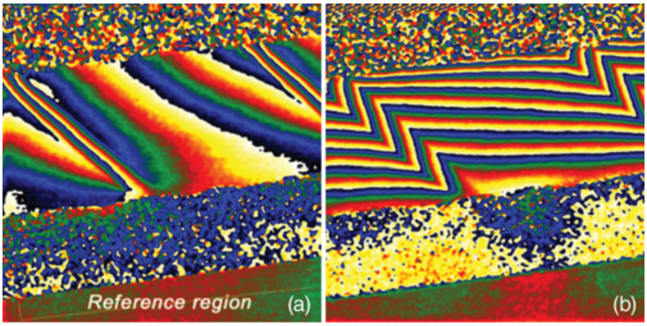

Figure 10.7 $P_{g1}(\boldsymbol{r})$ *and* $P_{g2}(\boldsymbol{r})$ *phase images calculated from the* $\boldsymbol{g}_1$ *(a) and* $\boldsymbol{g}_2$*(b) reflections indicated in the FT of (b). The $DyScO_3$ substrate is chosen as the reference area for the phase shift calculation.*

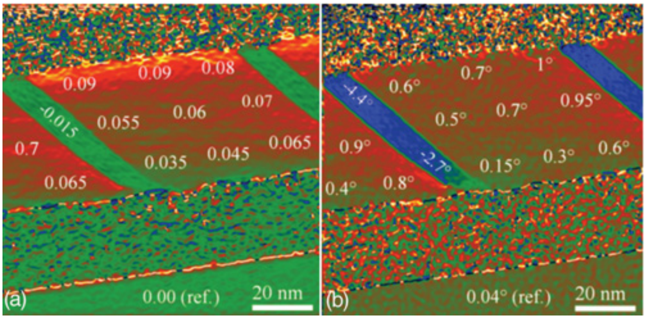

Figure 10.8 *The ε_{YY} strain and ω_{xy} rotation images calculated from the phase images in Figure 10.7. Adapted from Catalan et al. [6].*

Limitations and Accuracy of the GPA Method for Measuring Strain. For effective strain mapping, the contrast of the image needs to be uniform across the field of view. Although the GPA method was first developed to measure strain from HRTEM images, GPA is even more efficient studying high resolution STEM images as they generally exhibit a homogeneous contrast, mainly depending on the atomic number Z, and not so much on sample thickness. In addition, for sample thickness variations close to the extinction distance contrast inversion arises in HRTEM [23], complicating the application of the GPA method in samples of such thicknesses. Strain mapping from HRTEM images therefore requires the preparation of specimens with uniform thickness. This becomes even more crucial for non-centrosymmetric ferroelectric crystals or for imaging away from a zone axis. Specimens should therefore have a relatively flat exit surface and, provided that significant tilting was not used to align the crystal, the effective defocus should be constant. The drawback in using GPA on HAADF–STEM images is that the scanning of the probe in STEM may induce artifacts in the direction perpendicular to the scanning direction, resulting in a "diffuse line" in the Fourier transform of the STEM–HAADF images corresponding to an additional phase shift in the phase image. These additional phase shifts can, however, be corrected to some extend a-posteriori by image processing or by acquiring a second HAADF image rotated by 90°, which may be combined with the first one.

Precision. GPA strain mapping determines displacements from the local positions of lattice fringes. The accuracy with which this can be carried out depends on the signal-to-noise ratio of the HRTEM image. Apart from the noise inherent in counting statistics and detector characteristics, a substantial part of the noise in experimental HRTEM images comes from the amorphous layers covering the specimen surfaces. These can be native oxides or layers damaged by the thinning processes. In either case, the contrast from amorphous or badly crystallized material will perturb the contrast from the underlying crystal. These layers are in general thin and act like weak phase objects. Here again HAADF–STEM images are less sensitive to these amorphous layers, resulting in images of much flatter and more homogeneous contrast.

Contrast. Let us first consider the contrast of an individual set of lattice fringes observed in HRTEM. Theoretically, the contrast of lattice fringes depends on the PCTF of the objective lens, both for linear and non-linear interference. The maximum contrast obtainable for each of these terms individually depends ultimately on the envelope function and is independent of whether the specimen is thick or thin. For example, if we consider only linear interference, the defocus that will maximize the contrast will depend on the phase difference between the diffracted and transmitted beams. However, the maximum value will only depend on the linear transfer envelope function for the particular frequency of the lattice fringes.

It is interesting to note that aberration correction provides considerable advantages here as it addresses the main limitations in HRTEM strain mapping, namely precision, spatial resolution, and thin-film relaxation. Aberration correction improves the envelope function by effectively eliminating the damping function due to spatial incoherence. Non-linear interference terms also contribute to the contrast of a particular set of lattice fringes. The contrast of each non-linear interference term will be maximized for different values of defocus. Aberration correction provides a smoothly varying transfer function, which will optimize the non-linear contrast for a wider range of defocus values compared a conventional microscope. An additional and maybe more important feature is that the non-linear contrast will most likely by positive. Symmetric beams will have no phase difference and hence be imaged in positive contrast. This effect is independent of defocus. By choosing conditions for positive linear contrast, the linear and non-linear terms will add constructively. Aberration correction uniquely allows the choice of the sign of the spherical aberration coefficient, thus allowing positive contrast for under-focus images of weak phase objects.

For the overall image contrast, which is a sum of the contrast of the individual lattice fringes, only general arguments can be used. Aberration correction, by virtue of the smoother PCTF, will allow a large band of spatial frequencies to have near-optimum contrast for the same defocus setting. If contrast is of the same sign, all interference will be constructive. Aberration correction also allows creating the final HRTEM image with additional diffracted beams of higher spatial frequencies, exploiting the improved envelope function. The overall contrast will therefore, in general, be higher.

10.3 HAADF–STEM Structure Determination

This section is dedicated to the role of (quasi-)elastic high-resolution HAADF–STEM imaging in investigating ferroelectric solids. To that end we continue along the following red ribbon. First, the HAADF–STEM imaging process is discussed including both the scattering of the electron probe in the sample and the optical transfer by the elements of the microscope. That allows us to understand the similarities and differences to HRTEM. Second, we introduce the solid-state properties accessible by HAADF–STEM. Similar to HRTEM, these are mainly atomic column positions and their weight – hence the lattice structure. In a third step, we combine the imaging properties and parameter estimation theory to extract the relevant ferroelectric solid-state properties. The modus operandi will be illustrated in detail with the help of two case studies in the final section. Throughout the chapter we will focus more on general concepts than on technological details as the latter can expire quickly with the arrival of new generations of microscopes. We will furthermore concentrate on how to use STEM to obtain the desired information rather than on the interpretation of the obtained results itself. The latter is by and large discussed in the other chapters of this book.

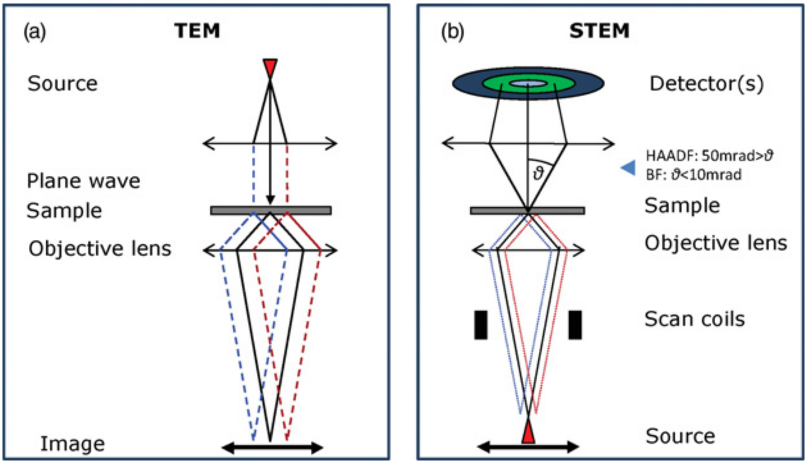

Figure 10.9 *Optical setup of (a) broad-beam TEM and (b) STEM imaging (reversed). Source, sample, and detector plane are indicated. The annular detectors employed in STEM can be distinguished according to their collection angle interval. Bright-field (BF) STEM records very small scattering angles, annular dark field covers the intermediate range, and high-angle annular dark-field (HAADF)–STEM collects electrons scattered into very large angles only*

10.3.1 Basics of HAADF–STEM Imaging

Modern TEMs facilitate the use of several imaging modes mainly differing in the beam formed in the specimen plane and the plane chosen for detecting the scattered electrons. Even though the nature of electron scattering within the sample does not depend on these modes, we will see in the following that they are highly useful to analyze particular aspects of the scattering. We will mainly concentrate on HAADF–STEM and refer to the literature for a thorough treatment of STEM imaging in general (e.g. [24–26]).

One main classification of the imaging modes is based on the relation between the source, object, and detector plane. Following E. Abbe, the wave optical action of a lens can be described by Fourier transforms connecting the object with the back focal plane and the back focal plane with the image plane, respectively. Accordingly, in classical broad-beam TEM, the object plane is conjugated to the Fourier plane of the source and the detector is placed conjugated to the object plane, see Figure 10.9(a). STEM utilizes a (demagnified) source in the object plane, which, after scattering, is recorded in the Fourier plane of the sample, as shown in Figure 10.9(b). The STEM image is obtained by scanning the probe over the sample and collecting the intensity on a detector. It is interesting to note that broad-beam TEM and bright-field STEM are equivalent upon reversing the beam direction (compare Figure 10.9(a) and (b)), which is referred to as the reciprocity principle [27].

The optical elements between the particular conjugated planes would ideally only (de)magnify the various conjugated planes. In STEM a system of condenser lenses demagnifies the electron source into the object plane. Unfortunately, lens aberrations are unavoidable in this process. In a systematic classification two types of geometric aberrations are distinguished, one depending on real space (image) and the other on Fourier space (back focal plane) coordinates. The latter typically leads to a blurring of the image in real space while the former distorts the image without decreasing resolution. Furthermore, mixed aberrations may also occur. After sustained research and efforts in instrumental developments of aberration correctors, which drastically decrease the Fourier space aberrations and thereby increase resolution, they finally became available around the beginning of this millennium [28,29]. What followed was a small revolution in (S)TEM, for instance leading to the abovementioned number of breakthroughs in the field of ferroelectric material characterization.

In the case of STEM, the geometric size of the demagnified probe in the object plane is increased by the aberrations of the condenser lens. To mitigate this effect one can introduce an aperture to limit the convergence angle by cutting off aberrated electrons. Such an aperture, however, also decreases resolution and the current in the probe, and one chooses an aperture size providing some compromise between cut-off and resolution decrease. State of the art aberration-corrected STEM instruments permit very large convergence angles in the range of several tens of mrad, yielding probe sizes down to 50 pm. However, such small probes also lead to a small depth of focus in the order of some nanometers, and it was noted that the size of the convergence angle might be chosen to prolongate the depth of focus instead of minimizing the probe size only [30]. A typical STEM beam formed under a convergence angle of 19 mrad at an acceleration voltage of 300 kV is depicted in Figure 10.10. One clearly observes the rapid delocalization over a propagation range of several nanometers. This reduces the specimen thickness that can be investigated at similar illumination conditions, that is resolution. We emphasize, however, that the shape of the electron beam can significantly change upon scattering (on strong scatterers such as heavy atoms), rendering the depth of focus an inappropriate measure for describing the beam shape (see below).

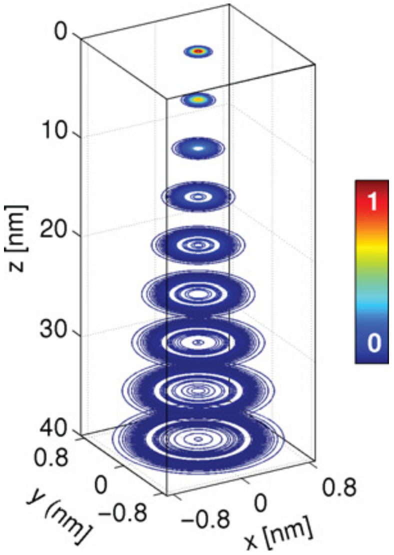

Figure 10.10 Three-dimensional STEM electron beam shape focused at the specimen plane (z = 0 nm). The beam parameters are 300 kV acceleration voltage and 19 mrad convergence angle

Inspite of the reciprocity principle, substantial differences make HRTEM and STEM rather complementary techniques. While HRTEM records images in one shot, typically within some seconds of exposure time, STEM image acquisition may take tens of seconds, depending on the resolution and scanning area. Therefore specimen drift as well as the scanning unit can lead to severe image artifacts, obscuring the original geometry. The scanning error occurs when the scanning probe jumps from one line to the next, thereby producing artificial shifts in the probe position. STEM techniques, on the other hand, allow the angular distribution of the scattered electrons to be resolved (see Figure 10.9(b)). For example, one typically distinguishes between forward scattered electrons, which can be collected on a bright field detector or exploited for EELS spectroscopy (see Section 10.4 of this chapter) and high-angle scattered electrons recorded on an annular detector. This degree of freedom is not readily available in bright-field TEM. For instance, the reciprocal TEM technique to annular dark-field STEM would require particular hollow cone beam shapes, which are technically demanding to be realized. An important difference between STEM and TEM is furthermore given by the electron dose impinging the sample. That can be an important selection criterion, especially if samples are very sensitive to beam damage.

In order to understand why it is so useful to use a HAADF detector, we have to understand what type of information is recorded on such a detector. To that end we shortly sketch the electron scattering process in the sample. On a very general basis we could imagine the scattering process to be the sum of single scattering processes taking place at the atoms making up the solid. For instance, within the first-order Born approximation, referred to as kinematical scattering, the scattering matrix is given by the Fourier transform of the total potential, that is the sum of Fourier transforms of atomic potentials. Such a sum depends strongly on the spatial arrangement of the atoms as the positional phase factors can sum up constructively or destructively. The latter leads to reflections characteristic for certain crystal symmetries [31]. One furthermore has to consider perturbations to such a scheme imposed by the thermal motion of the atoms. This influence can be described analytically within the first-order Born approximation, leading to a Debye–Waller damping of the systematic reflections and incoherent superposition of atomic scattering into the large angles [32].

This behavior is to a certain extend preserved at scattering formalisms going beyond the first-order Born approximation, referred to as dynamical scattering, which are generally required to describe electron scattering in the TEM. Accordingly, the following picture can be established. The electron wave undergoes a transformation when traversing the crystal lattice, resulting from a complex sum of partial waves scattered by the individual atoms. However, the small fraction of electrons scattered at each atom into large angles sum up incoherently as any phase relation was destroyed by the thermal motion [33]. Thus, an annular detector, integrating over large scattering angles only, intercepts an electron flux given by the product of an incoming flux, the atomic density, and the atomic large-angle scattering cross-section. The latter is to a good approximation proportional to Z^2 (Rutherford scattering), conferring the atomic resolution HAADF–STEM signal its characteristic peaked contrast at atomic column positions proportional to the atomic number ("Z-contrast" [26]). For our purposes, however, we also have to consider the influence of the incoming flux, that is the dynamical scattering of the electron wave, mainly because it determines the depth dependence as well as the spatial localization of the recorded signal. An explicit example will be given in Section 10.3.3.2.

We conclude that, in a first approximation the atomic-resolution HAADF contrast can be considered to emerge locally from the atomic column under the focused electron probe. However, due to dynamical scattering of electrons in the material in combination with the contrast mechanism of HAADF–STEM imaging, a direct quantitative interpretation of the observed image contrast in terms of material properties (e.g., column positions) has to be supported by dynamic scattering simulations (see below). In particular, the growing diffusion of the electron probe within the sample must not be neglected. If the probe smears out, both the HAADF signal stemming from the central atomic column under the focused beam will be attenuated and the relative signal from neighboring columns will increase at the same time. Thus, depending on the sample and imaging conditions, the column contrast is usually dominated by the crystal structure in the upper part of the sample traversed by the beam and the concept of uncorrelated HAADF column contrasts will be obscured at a certain thickness.

10.3.1.1 Model-Based Image Analysis

In this section we lay out the principal steps to extract atomic column parameters (mainly positions) from high-resolution HAADF–STEM micrographs. Our vehicle towards this goal will be the repeated refinement of a model for the local contrast in an HAADF–STEM image. The most accurate model would be a full-scale dynamic scattering simulation of HAADF–STEM contrast with all atomic positions and weights as free parameters. Such an approach is currently beyond reach for several reasons. Most notably, the objective function to be minimized in the refinement procedure (e.g., the Euclidean distance between the model and experimental contrast) has a complicated shape with multiple local minima. That leads to a very complicated and time-consuming, if not unfeasible, search for the global minimum with respect to a large set of parameters (the number of atoms within typical fields of view easily exceeds 1000). Thus, the main problem consists of how to decrease the number of refined parameters in approximate models without introducing too many systematic errors in describing the image contrast. In the previous section it was argued that a single atomic column contrast model could provide a suitable model provided that specimen thickness and probe convergence angle stay within certain limits. This approach does not require an evaluation of the scattering equations, thereby drastically reducing computing time. The feasibility of this type of position measurements was demonstrated by several authors (e.g., [34, 35]).

The refinement of the contrast model is performed within the framework given by parameter estimation theory, a subdiscipline of probability theory and statistics. Accordingly, we proceed by: (a) deriving a likelihood function $f\,[I;p]$ for the fluctuations of the experimentally observed image intensity around the mean intensity $I(\mathbf{R})$ and (b) relate the latter to a contrast model. This contrast model $I_{\mathrm{M}}\,(\mathbf{R};p)$ depends on a set of free parameters p, which is obtained by maximizing the likelihood of the observed intensity, that is $\max\limits_{p} f\,[I;p] \rightarrow p$.

(a) Generally, HAADF image acquisition can be regarded as a scanning-stepwise uncorrelated electron counting experiment following a Poisson statistic modified by the detector, i.e., $\mathrm{Cov}(I_n, I_{n'}) = \sigma_n^2 \delta_{n,n'}$ and $\sigma_n^2 = \rho_n(\sigma_d^2 + g^2)$ [36]. Here, n counts the pixels, g is the detector conversion rate, σ_d the detector noise, that is the standard deviation of the HAADF output when recording one primary electron, and ρ_n the input shot noise variance, that is the average electron density. In order to considerably simplify the maximum likelihood estimation we approximate the input shot noise by the recorded gain-corrected intensity $\rho_n \approx I_n/g$, that is we assume the covariance is known and must not be estimated. The covariance matrix of this likelihood then reads:

$$\begin{aligned}\mathrm{Cov}\left(I_n, I_{n'}\right) &\approx I_n\left(\frac{\sigma_d^2}{g} + g\right)\delta_{n,n'} \\ &\equiv \mathrm{C}I_n\delta_{n,n'}\end{aligned} \tag{10.15}$$

Considering that the Poisson statistic is well approximated by a Gaussian for the amount of electrons typically recorded, the experimental fluctuations around the mean intensity $\bar{\mathbf{I}} = \bar{I}(R_n)$ at scanning positions $\mathbf{R}_n$ then follow a joint Gaussian probability distribution ($\cong$ the likelihood function):

$$f\,[\mathbf{I};p] = \exp\left(-\frac{1}{2}(\mathbf{I}-\bar{\mathbf{I}})\mathbf{Cov}^{-1}(\mathbf{I}-\bar{\mathbf{I}})^{\mathrm{T}}\right) \tag{10.16}$$

incorporating the covariance matrix **Cov**. Here and henceforth, the collection of pixel-wise intensities (i.e., the image) is denoted by the intensity vector **I**.

(b) In the above formulation maximizing the likelihood would yield $I = \bar{\mathbf{I}}$, as the average image intensities $\bar{\mathbf{I}}$ are the free parameters of the likelihood function, which implies that no column positions are estimated. Based on physical reasoning and the evaluation of a large number of atomic resolution HAADF–STEM micrographs, we now postulate that a bivariate Gaussian plus background is a suitable contrast model for the column intensity, that is:

$$\bar{\mathbf{I}} = \mathbf{I}_{\mathrm{M}} = B + A\ \exp\left(-\frac{1}{2}(\mathbf{R}_n - \mathbf{R}_0)\mathbf{M}(\mathbf{R}_n - \mathbf{R}_0)\right) \tag{10.17}$$

where the component matrix:

$$\mathbf{M} = \mathbf{O}(\phi)^T\begin{pmatrix} a^{-2} & 0 \\ 0 & b^{-2}\end{pmatrix}\mathbf{O}(\varphi) \tag{10.18}$$

of the symmetric bilinear form in the exponent is a function of three different parameters, the extensions of two principal axes a and b and the rotation angle φ of the corresponding ellipse determining the orthogonal rotation matrix **O** (see Figure 10.11). Under certain conditions, namely small intercolumn scattering and a well-aligned zone axis, the following relationships to properties of the atomic columns can be established. $\mathbf{R}_0$ corresponds to the atomic column position, the integrated intensity of the Gaussian ~Aab is (nonlinearly) proportional to the atomic weight of the column [37], and the eccentricity $\sqrt{a^2 - b^2}/a$ as well as the angle φ can be related to a possible tilt or rotation of the sample with respect to the electron beam or a residual coma. The background B is a measure of scattering from neighboring columns, since it is a direct consequence of those parts of the probe diffusing from the original spot position. Within the above noted approximations maximizing the likelihood:

$$f\,[\mathbf{I};p] = \exp\left(-\frac{1}{2}(\mathbf{I}-\mathbf{I}_{\mathrm{M}}(p))\mathbf{Cov}^{-1}(\mathbf{I}-\mathbf{I}_{\mathrm{M}}(p))^{\mathrm{T}}\right) \tag{10.19}$$

corresponds to a weighted least-square fit with weight I_{n} [38].

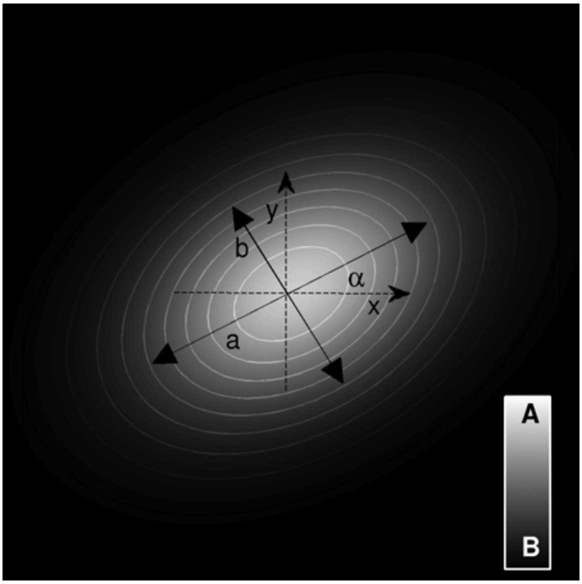

Figure 10.11 Two-dimensional Gaussian as an atomic column contrast model. The set of free parameters (background, peak height, large and small principle axis, rotation angle) is indicated

This model-based analysis of local column contrast has to be performed for each atomic column. We will show below that choosing a certain fitting order and taking fitting results from previous atomic columns into account for the next fitting step can approximately take into account column correlations. If that is not sufficient the local contrast model can be enhanced to a sum of bivariate Gaussians, each for a different atomic column. The parameter fit is then performed for all parameters in parallel. Keeping the number of Gaussians as small as possible has the advantage of yielding a high precision and small computing time of the fit. The main drawback of the method is its susceptibility to failures in the contrast model, which therefore has to be verified against the experimental images.

10.3.2 Solid-State Properties

Ferroelectric materials can be characterized by an order parameter, the spontaneous electric polarization $\mathbf{P}_s$ vector whose direction may be reversibly inverted. Frequently, the ferroelectric phase is stable only within a certain range of thermodynamic variables (e.g., temperature, pressure) and the susceptibility obeys a Curie–Weiss law when approaching the phase transition from the paraelectric phase. The spontaneous polarization is intimately related to the atomic structure of the material. According to the conventional theory, the distance between the positive (ionic) and negative (electronic) charge center of mass of the so-called natural unit cell determines the spontaneous polarization (e.g., [31]). This concept, however, lacked a clear definition of the natural unit cell, which was remedied by R.D. King-Smith and D. Vanderbilt in their seminal paper [39]. They expressed the polarization by integrating a current flowing when polarizing the material.[3] The modern theory allows more accurate computations of polarizations and related quantities, if nothing else, because the integrated current is the charge accumulated on the capacitor plates of the typical Sawyer–Tower setup employed to measure the $\mathbf{E}(\mathbf{P})$ hysteresis [40]. The latter equivalence can be explained by separating the total electric field $\mathbf{E}$ into the displacement field $\mathbf{D}$ due to free charge carriers and the polarization $\mathbf{P}$ due to bound charges:

$$\epsilon_0 \mathbf{E} = \mathbf{D} - \mathbf{P} \tag{10.20}$$

and noting that the bulk ground state of a ferroelectric material is characterized by a zero electric field. It follows that the spontaneous polarization of the bulk is completely screened by the electric displacement generated by surface charges located at the boundary of the bulk material (i.e., the capacitor plates in the Sawyer–Tower setup). Non-ground state configurations such as domain boundaries or externally distorted lattices (piezoelectric effect) are characterized by a non-zero electric field. These non-zero electric fields are referred to as depolarization fields due to the resulting force $\mathbf{F} = q\mathbf{E}$ acting on the ions and electrons with charge q in the material in the opposite direction of the polarization.

Within the linear response approach (e.g., [41]) the following relationship between the depolarization field $\mathbf{E}$ and the *induced* polarization $\mathbf{P}_\mathrm{i}$:

$$\mathbf{P}_\mathrm{i} = \epsilon_0 \chi \mathbf{E} \tag{10.21}$$

can be established with the help of the linear susceptibility χ. Note that changes in the polarization with respect to the ground state, rather than the total polarization itself, occur on the left-hand side. Otherwise the spontaneous polarization itself would imply unrealistically large electric fields, which is a frequently encountered misinterpretation in electron holography measurements of spontaneous polarizations [42–46] (see Section 10.5 for more details on this point).

Linear response theory can also be applied to derive a direct relationship between the ion positions and the electric polarization according to:

$$\mathrm{d}\mathbf{P} = \frac{1}{\Omega} \sum_n \mathbf{Z}_n^* \mathrm{d}\mathbf{r}_n \tag{10.22}$$

where $\mathbf{Z}^*$ are the so-called Born effective charge (BEC) tensors defined as the change of polarization $Z_{ijn}^* = \Omega \partial P_i / \partial x_{jn}$ upon a displacement $\mathrm{d}\mathbf{r}_n$ of the nth atom in the unit cell with a volume Ω (see Figure 10.12). The total spontaneous polarization is obtained by integrating the change in polarization according to Equation (10.22) along a path connecting a nonpolar (i.e., paraelectric) configuration with the polar one:

$$\mathbf{P}_s = \sum_n \int_{\mathrm{para}}^{\mathrm{ferro}} \mathbf{Z}_n^*(l) \frac{\partial \mathbf{r}_n}{\partial l} \mathrm{d}l \tag{10.23}$$

---

[3] This current can be related to a particular Berry or geometric phase, which is why the modern polarization theory is also referred to as the Berry phase approach.

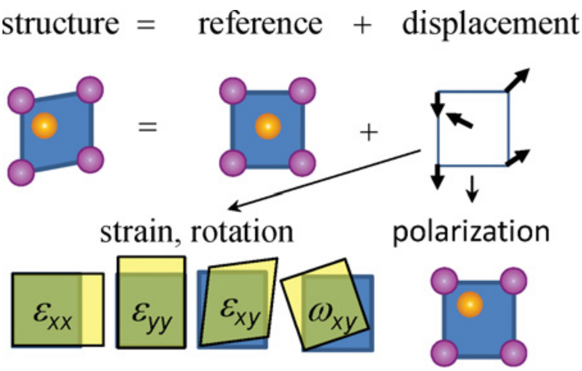

Figure 10.12 *Schematics of lattice structure modifications by strain, lattice rotation, and polarization. Upper row: lattice structure as the sum of reference lattice and atomic displacements. Lower row: strain and rigid lattice rotation derived from displacement of the unit cell and polarization resulting from relative displacement of all atoms in the unit cell*

The Born effective charge tensors used in the following are calculated with the help of the above-mentioned modern theory of polarization. In practice, one usually computes Born effective charges for some discrete states and approximates the spontaneous polarization by:

$$\mathbf{P}_s \approx \sum_n \mathbf{Z}_n^* \int_{\text{para}}^{\text{ferro}} \mathrm{d}\mathbf{r}_n \approx \sum_n \mathbf{Z}_n^* \delta\mathbf{r}_n \tag{10.24}$$

The BEC tensor contains both ionic and electronic contributions to polarization, the combination of which is responsible for the particularly large magnitudes observed in typical ferroelectrics (e.g., [47]).

One can furthermore extend the concept of BECs to the collective motion of groups of atoms, which is useful when not all atomic positions are known. In STEM investigations this is often the case, either due to projection effects along one column (different atomic species occupy one atomic column) or due to the generally weak contrast of light elements such as oxygen (see Section 10.3.3. for examples). Thus, one has to establish an additional relationship between the missing atom displacements and the known column displacements, either by ab initio calculations or other measurements. In a similar spirit one can derive unknown vectorial components of the polarization from the known ones. That is useful because the polarization component along the electron beam direction is usually not observable. An example will be given in Section 10.3.3.2.

Equation (10.24) provides probably the most important link between structural data resolved in TEM and properties of ferroelectrics. It facilitates the unit-cell-wise computation of the ferroelectric ordering parameter, that is the $\mathbf{P}_s$ field, from high-resolution micrographs, provided that atomic positions could be accurately determined in three dimensions. To the date of this book, this goal has not yet been achieved because several limitations are present and have to be considered when mapping electric polarization. For instance, although reconstruction of three-dimensional atomic lattices of metallic nanoparticles by means of HAADF–STEM tomography have been recently reported [48, 49], it remains highly questionable whether these data contain atomic position information with an accuracy of the order of several pm required for measuring polarizations. The difficulties arise not only from the limited number of projections decreasing resolution but also from dynamic scattering obscuring standard linear tomographic approaches. Furthermore, an HAADF–STEM signal diminishes with decreasing atomic weight, rendering the detection of light atomic species, let alone their position, very challenging [50]. We will come back to these points when discussing the prospects of (S)TEM for investigating ferroelectrics in Section 10.5. In the following we either use approximations, for instance facilitating a computation of the polarization from a restricted number of positions (see above), or we will focus on aspects not requiring fully quantitative polarization values.

Apart from electric polarization, the geometry of the unit cell plays an important role for ferroelectrics because unit cell distortions and polarization are usually coupled. For instance, ferroelectrics are typically ferroelastic as well, meaning that different distortions of the unit cell can be reversibly switched. Consequently, a domain wall can separate not only two regions with different polarizations but also distortion directions (see Section 10.3.3). Additionally, a change in distortion (i.e., strain) can lead to a change in polarization and vice versa. In the lowest (linear) order of the coupling this phenomenon is referred to as piezoelectric coupling. Higher orders involve electrostrictive or flexoelectric couplings.

In order to determine a displacement field **u** in HAADF–STEM images, the actual column positions are compared to a deliberately chosen reference lattice (see Figure 10.12). Note that similar to the polarization only components perpendicular to the beam direction are accessible. We furthermore point out that instead of directly measuring the column positions, analyzing changes in the scattering angle of systematic reflections is frequently used in TEM investigations for measuring the displacement (see Section 10.2). The engineering strain tensor ε as well as the lattice rotation ω are readily calculated from the displacement field according to (see also Section 10.2):

$$\varepsilon_{ij} = \frac{1}{2}\left(\frac{\partial u_i}{\partial r_j} + \frac{\partial u_j}{\partial r_i}\right), \omega_{ij} = \frac{1}{2}\left(\frac{\partial u_i}{\partial r_j} - \frac{\partial u_j}{\partial r_i}\right) \qquad (10.25)$$

In order to obtain the physically significant strain values, such as occurring within piezoelectric or purely elastic coupling terms, one should use an induced-polarization-free or strain-free lattice as reference.

Consequently, an atomic-resolution HAADF–STEM image can be analyzed in terms of atomic column types and positions in order to provide unit-cell-wise maps of strain and polarization. This high-resolution capability is unique among other characterization methods and highly useful for investigating heterogeneous structures, such as domain walls, dislocations, and interfaces, very important for the properties of ferroelectrics. The next section is concerned with case studies elucidating the above-noted principles.

10.3.3 Case Studies

We will focus on two ferroelectric materials with a particularly large spontaneous polarization, namely $PbTiO_3$ and $BiFeO_3$. This choice is motivated by the following reasons.

Firstly, they both belong to the perovskite family, whose members show a remarkable diversity in physical properties realized on a simple lattice structure. Perovskites have therefore been extensively investigated in the past, leading to important breakthroughs in the understanding of ferroelectricity and a large number of technologically important applications [51] such as ferroelectric non-volatile memories, which require large spontaneous polarizations and stable ferroelectric distortion [52]. $PbTiO_3$ [53] and $BiFeO_3$ as lead-free alternative are therefore used in ferroelectric random access memories [54] and other devices. $PbTiO_3$ is furthermore the aristotype of $Pb(Zr,Ti)O_3$ (PZT), most frequently used in piezoelectric transducers. $BiFeO_3$ is intensely investigated because of its large room temperature ferroelectric polarization and simultaneous (antiferro-)magnetic ordering. Such multiferroic materials show a wealth of complex physical properties caused by their coexisting electrical and magnetic order parameters, which in turn suggest potential applications in novel magnetoelectronic devices [55, 56].

Secondly, both materials consist of heavy and light atomic species covering a wide range of scattering powers. Thus, they adequately elucidate the limits of HAADF–STEM imaging posed by dynamic scattering and small scattering cross-sections.

Thirdly, the investigation of both materials, in particular focusing on various types of characteristic defects occurring in them, is part of our extensive studies on ferroelectric materials. The results on flexoelectric coupling in $PbTiO_3$ thin films have been published by Catalan et al. [6] whereas various defect studies in $BiFeO_3$ have been reported in Refs. [3–5]. The interest in defect structures arises amongst others from the fact that the suitability of ferroelectric materials for various applications is determined not only by the magnitude of their ferroelectric polarization but also by factors such as switchability, fatigue, and loss. These are in turn influenced by the structure of the domains and particularly by the boundaries between them. The detailed structure and formation energies of domain walls in some conventional ferroelectrics are now well established (see, for example, [57, 58] for experimental studies and [59, 60] for calculations). Here we will focus on domain walls in $PbTiO_3$ and $BiFeO_3$. The material presented in this chapter contains various new aspects not presented in the above-noted publications.

We begin with the investigations on $PbTiO_3$ since it is more apt to illustrate the basic aspects of HAADF–STEM characterization of ferroelectrics. More subtle details like light atom detection, cross-column talk, and polarization evaluation will be discussed with the help of the subsequent $BiFeO_3$ studies.

10.3.3.1 $PbTiO_3$ Domain Walls

Besides the Ti–O hybridization, the so-called stereochemically inactive $6s^2$ electron lone pair is the driving force behind the large polarization in $PbTiO_3$ (tetragonal space group $P4mm$). The c/a distortion of the tetragonal unit cell as well as the displacement of the Ti atom with respect to the center of the unit cell gives rise to a very large ferroelectric polarization of $\sim 88\ \mu C\ cm^{-2}$ [61], which makes the material attractive for various applications. In Figure 10.13(a) and (b) the unit cell, structure parameters, and domain wall configurations of $PbTiO_3$ allowed by symmetry are summarized.

In the following, we investigate the same system studied in Section 10.2.2.2. It is an epitaxial $PbTiO_3$ layer grown on $DyScO_3$ with a $SrRuO_3$ buffer layer (Figure 10.6). We aim to gain insight into the interplay between domain structure, polarization, and strain. The

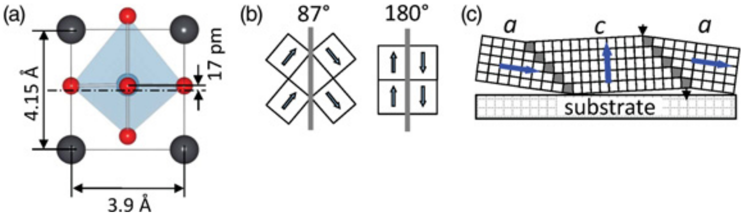

Figure 10.13 *(a) Unit cell of tetragonal $PbTiO_3$ (space group P4mm) with lattice parameters (a = 3.908 Å, c = 4.188 Å) obtained from XRD measurements [62], (b) possible domain wall configurations, and (c) a–c twinning incorporating ≈ 90° domain walls. The clamping to the substrate is indicated by a black arrow*

thin films have been grown by pulsed laser deposition under growth conditions detailed in Catalan et al. [6]. Such films exhibit different domain structures, such as periodic ferroelectric, non-ferroelastic, domains in ultra-thin films (5 nm, [63]), or alternating 90° domains at larger thickness (>10 nm, [22]), such as the *a–c* twins seen in Figure 10.13(c). These different twinning structures are imprinted on the tetragonal film upon minimizing the misfit strain when relaxing on the (pseudo)cubic lattice and depend on various growth parameters [64].

Figure 10.14 shows an atomic resolution HAADF–STEM image. It contains *a–c* twins, which will become clear after the subsequent analysis. However, we first take a closer look at the atomic HAADF contrast, revealing several characteristics discussed in Section 10.3.2. The strongly scattering Pb column (large high-angle cross-section) can be easily

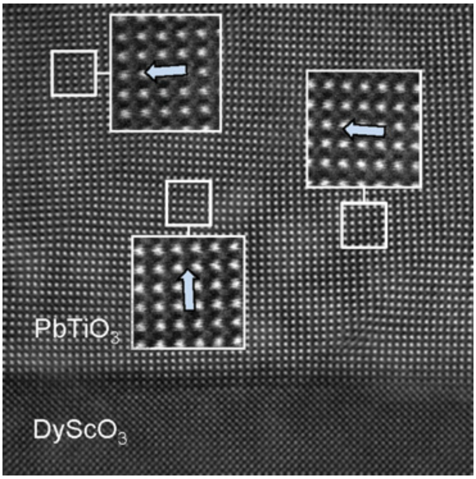

Figure 10.14 *Atomic resolution HAADF–STEM analysis of the epitaxial $PbTiO_3$ layer (the lower magnification image of the stacking is shown in Figure 10.6). The zoom-ins reveal bright Pb and weak TiO column contrasts. Both tetragonal distortion as well as off-center displacement of the TiO column allow a visual determination of the polarization direction, indicated by arrows*

distinguished from the TiO column, whereas the weakly scattering O column (small high-angle cross-section) cannot be observed at all. We show in Section 10.3.3.2 how a change in the electron probe convergence angle may result in a better visibility of the O column, however at the price of a more complicated interpretation. The unit cell spanned by four adjacent Pb columns displays a visible tetragonal distortion, which changes over the field of view (see zoom-ins in Figure 10.14). Furthermore, when comparing the position of the TiO column with the Pb column one observes a small displacement from the center of the tetragonal unit cell, indicating the presence of an electric polarization.

We will now apply the above-described model-based analysis to obtain unit-cell-wise strain, lattice rotation, and polarization maps. In principle two different reference lattices based on the Pb or Ti sublattice could be chosen for computing the strain, however, because of the larger precision of the fit at the heavier Pb column, the Pb sublattice was used for determining the displacement field **u**(**r**). Figure 10.15 shows the x and y strains obtained from Figure 10.14. The alternating *a*–*c* domains separated by sharp (width ≃1 unit cell) domain walls are readily observed. The change in lattice orientation (visible in the rigid

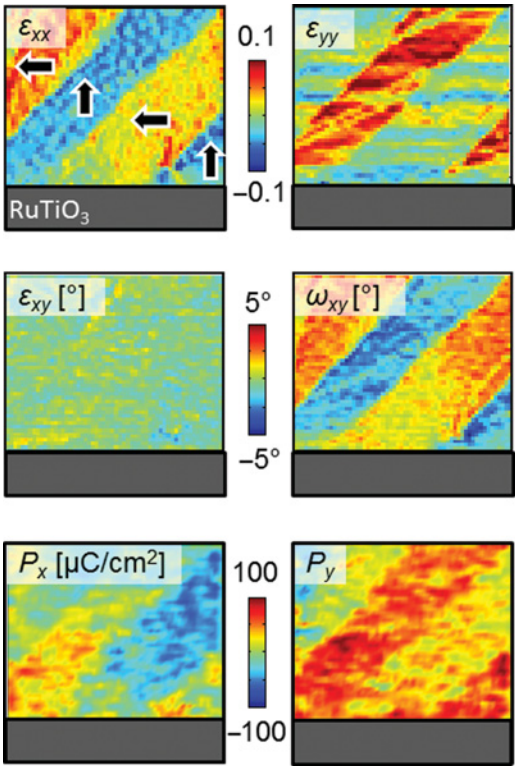

Figure 10.15 *Strain and polarization in a–c domain configuration in PbTiO$_3$ thin film. Top row: axial strain components. Second row: shear and rigid lattice rotation. Bottom row: polarization components. Large polarization and lattice rotation changes superimpose in the vicinity of the interface with the substrate. The characteristic horizontal lines in ε_{yy} are scanning error artifacts*

lattice rotation ω_{xy}) across the domain wall corresponds to the 87° domain wall angle due to the tetragonal unit cell. Furthermore, a strong change in lattice rotation is visible close to the $RuTiO_3$ buffer (indicated in Figure 10.15), which originates from the clamping of the zig-zag strain-free *a–c* domain pattern (see Figure 10.13(c) and [6] for more details). The clamping in combination with the biaxial lattice misfits additionally introduces a gradient in the axial strain components (visible in the ε_{xx} component).

The inhomogeneous strain and lattice rotation within the domains influence the electric polarization via various coupling paths. In the leading order, piezoelectric coupling leads mainly to a change in the polarization component in the direction of the corresponding axial strain component. That could explain the attenuation of P_x in the acute corner of the *a* domain. Flexoelectric coupling, on the other hand, introduces a coupling between strain gradients of an axial strain component and the corresponding perpendicular polarization component. Indeed, the large change in P_x visible in the *c* domain has been argued to originate from the corresponding ε_{yy} gradient via flexoelectric coupling [6].

We can conclude that the model-based atomic position parameter estimation from atomic resolution HAADF images reveals valuable information about the *a–c* twinning in the $PbTiO_3$ thin films. Both strain and polarization maps show the domain structure, sharp domain walls, and long-range strain and polarization gradients within the domains. However, we also observe artifacts such as the scanning error, which will be addressed in more detail in the following paragraph about $BiFeO_3$ domain walls.

10.3.3.2 $BiFO_3$ Domain Walls

At ambient conditions $BiFeO_3$ has the rhombohedral space group *R*3*c* with a very small rhombohedral distortion (rhombohedral angle = 59.35° ≈ 60°, $a = 5.63$ Å [65]). The rhombohedral symmetry can be derived from the cubic perovskite space group *Pm3m* by imposing two distinct distortions: (i) a polar Γ_4^- distortion, consisting of polar displacements along the pseudocubic $(111)_{pc}$ direction and a symmetric breathing of adjacent oxygen triangles [66], yielding a very large ferroelectric polarization of ~90 μC cm^{-2} [67] into the $\langle 111\rangle_\mathrm{pc}$ direction (driven by the stereochemically active Bi^{3+} lone pair [68]); (ii) an alternating rotation of adjacent oxygen octahedron. In the ideal rhombohedral system ($\alpha = 60°$) only angles of ±71°, ±109°, or 180° between different polarization orientations at a domain wall are allowed by symmetry [69]; the different variants are denoted by that ideal domain boundary angle in the following. Such relative domain orientations and reorientation angles have been confirmed experimentally [70]. In Figure 10.16 the unit cell and possible domain wall configurations of $BiFeO_3$ are summarized.

Domain walls in $BiFeO_3$ have attracted considerable interest after discovering strongly increased conductivity along the domain walls [70]. Furthermore, novel routes towards domain wall engineering have been analyzed in $BiFeO_3$ [71]. The structural and electronic properties of $BiFeO_3$ domain walls as predicted by DFT calculations exhibit two fingerprint quantities: the structural distortions of atomic columns at the wall and the electrostatic potential jump due to the polarization fluctuations [72]. It has been argued that the latter is the origin for charge-carrier accumulation and thus enhanced conductivity. The possibilities of measuring electrostatic potentials in ferroelectrics such as occurring at domain walls by means of electron holography will be discussed separately in Section 10.5.

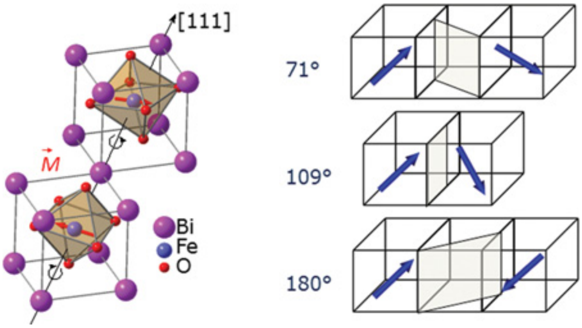

Figure 10.16 *Unit cell of bulk BiFeO$_3$. Electric polarization is indicated by arrows in the [111] direction. The antiparallel Fe-magnetic moments (arrows centered on Fe atoms) are perpendicular to the electric polarization. The right column shows the three types of domain wall geometries allowed by symmetry*

In the following, we show 109° domain walls observed in an approximately 140 nm thick layer of pure BiFeO$_3$, which was epitaxially grown in a $(001)_{pc}$ orientation on low miscut DyScO$_3$(110) single-crystal substrate ($a_{pc} = 0.3945$ nm) by pulsed laser deposition. Figure 10.17 shows an overview image and an atomic resolution HAADF image of the thin-film layers. HAADF–STEM was carried out using the aberration-corrected TEAM 0.5 microscope [73] operated at 300 kV with a collection angle interval of 45–290 mrad in order to increase the signal from the light FeO atomic column. The probe convergence angle was adjusted to ~ 19 mrad in order to provide a sufficiently small probe size (60 pm) minimizing cross-talk between the atomic columns. The 109° domain walls are visible as contrast changes along the $[010]_{pc}$ direction (see Figure 10.17(a)).

The HAADF contrast (see zoom-in) has a similar appearance to that of PbTiO$_3$. However, beside the strongly scattering Bi columns (large Z) and the medium scattering FeO also the weakly scattering O column displays a barely discernible contrast [74]. The oxygen contrast was obtained by decreasing the lower collection angle of the HAADF detector to 45 mrad facilitating the detection of the oxygen octahedron rotation in BiFeO$_3$ [74]. By closely inspecting the atomic column contrasts one can also distinguish the individual scanning lines from the STEM instrument, which are slightly shifted with respect to each other due to the imperfect, scanning coils.

Before discussing the strain and position maps, we will now focus on some important details, which have been omitted in the former example of PbTiO$_3$ for instructive reasons. We will particularly discuss the delocalization and corruption of the position information due to (a) the probe diffusion and (b) the scanning error, which typically represent the two most important error sources.

(a) As explained in Section 10.3.2, the diffusion of the probe eventually increases its size to cover several atomic columns. As a consequence high-angle scattering is produced from all the covered atomic columns and the position information is delocalized. In order to quantify this effect it is indispensable to simulate the scattering process of the electron probe at the crystal. We used the (S)TEM simulation software SEMI, implementing a numerical integration of the paraxial approximation of the Klein–Gordon

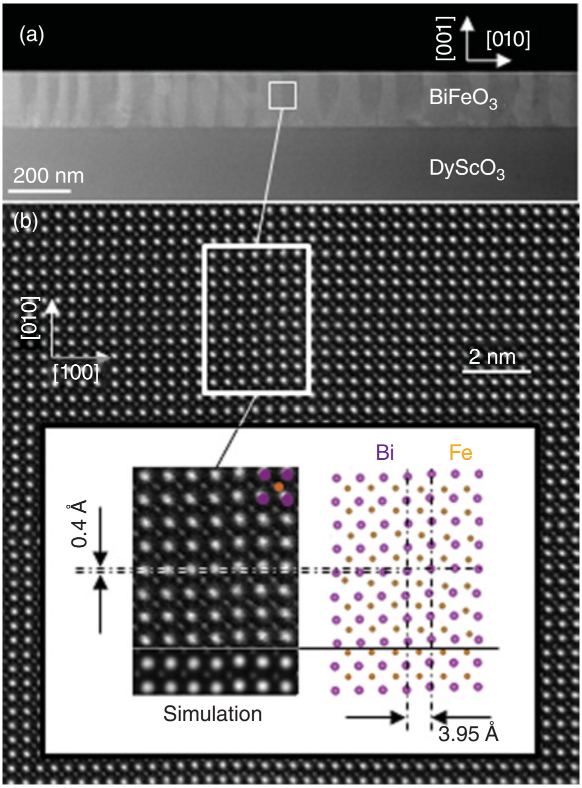

Figure 10.17 (a) Overview of BiFeO$_3$ layer grown on DyScO$_3$. (b) Atomic resolution HAADF image containing a vertical domain wall. The inset contains a zoom-in as well as the corresponding fitted lattice with the domain wall width indicated. The domain wall is readily discerned by inspecting the displacement of the Fe column with respect to the Bi column. The bottom of the line contains a simulation and a corresponding fit of the HAADF contrast in order to validate the accuracy of the fitting procedure and thus the fitting results

wave equation with predefined step size, referred to as multislice in the literature [75] to accurately propagate the electron probe through [001]-oriented BiFeO$_3$. Figure 10.18 shows the shape of the probe when propagating along the FeO column.

The growing delocalization of the wave function is clearly visible as a reduction of intensity within the central part. However, the delocalization is significantly reduced compared to the freely propagating STEM probe (Figure 10.10) due to the attracting force exerted by the atomic potentials on the electron wave. This phenomenon is referred to as channeling in the context of dynamic electron scattering and helps to increase the electron flux and hence the HAADF signal produced by the atomic columns. Besides, one can observe an oscillation of intensity characteristic for dynamic scattering (see, for example, local maximum at a depth of 5 nm), which renders the depth dependency of the HAADF signal non-linear. One consequence of that scattering behavior is that the signal is typically produced by the upper part of the specimen since the probe is focused at the top face of the specimen. This is the reason why atomic

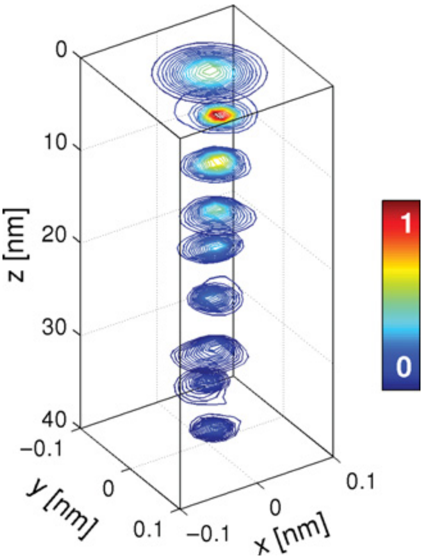

Figure 10.18 *Intensity of the FeO-column-centered STEM probe during propagation. The oscillation of the spot position results from not-aligned Fe and O positions in the* $BiFeO_3$ *structure. Simulation parameters separated into TEM (A), crystallographic (B), and numerical (C) parameters are summarized in the following: (A)* $U_a = 300$ kV, $\theta_{conv} = 19$ mrad, $\theta_{\mathrm{HAADF}} = [45,290]$ *mrad;* $t = 40$ *nm*

resolution HAADF–STEM images may be obtained from a comparatively thick specimen compared to HRTEM investigations, where small specimen thicknesses around 10 nm are typically employed. Another ramification is the relative insensitivity of the HAADF–STEM contrast to zone-axis misalignment or defects; for example the latter produce a significant effect only if they are in a depth where the electron probe is still sufficiently focused.

In order to quantify the correlation between neighboring atomic column contrasts, we centered the probe (probe size approximately 60 pm) on the Bi and FeO column, respectively, and calculated the relative weight w of the respective neighboring columns in the final HAADF signal. Those weights are determined by integrating the intensity of the probe within the Voronoi cell of the respective neighboring column along z, multiplying the result by the Rutherford-like cross-section proportional to Z^2 [76], and normalizing with the respective value from the central column, that is $w = Z_n^2 \int_0^t I_n(z)dz / Z_p^2 \int_0^t I_p(z)\mathrm{d}z$. If the beam is centered on the Bi (or FeO) column we obtain $\mathrm{w}_{\mathrm{FeO|Bi}} \approx 0.002$ ($\mathrm{w}_{\mathrm{Bi|FeO}} \approx 0.621$, $\mathrm{w}_{\mathrm{FeO|FeO}} \approx 0.02$).

From the obtained values of w, we can infer that the Bi column contrast is uncorrelated to the next neighbors, whereas the FeO column contrasts experience a certain influence from next neighbor Bi column scattering. Consequently, in order to account for the influence of tails of the probe in combination with scattering from neighboring columns, it is sufficient to first determine the Bi sublattice and then fit the weak FeO column contrast, taking into account the previously determined Bi column contrasts. This result can be generalized to other materials insofar as the local atomic contrast fits

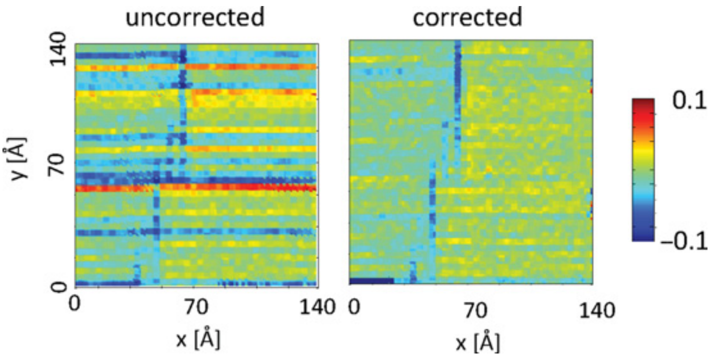

Figure 10.19 Influence of the scanning error on the strain analysis. The shear is depicted before (a) and after (b) removing the scanning error. The scanning error is visible as characteristic streaks stemming from a large $\partial u_x/\partial y$ term

should be ordered according to their contrast, beginning with the strongest one. This order was used for the $PbTiO_3$ as well as the $BiFeO_3$ investigations.

(b) The scanning error as noted in the high-resolution image can have a large impact on the position analysis. As an example we show a typical result of a shear field ε_{xy} around a 109° domain wall in Figure 10.19(a). Similar to Figure 10.15, one observes characteristic lines in $\partial u_i/\partial y$ introduced by the abrupt jumps of the probe into the y direction introduced by the scanning unit. Here we applied the following procedure to remove them. (i) Firstly, they are identified by applying a threshold. (ii) The erroneous part of the displacement field $\mathbf{u}_{\mathrm{err}}$ is obtained by integrating these derivatives in $\partial u_i/\partial y$. (iii) Subsequently, $\mathbf{u}_{\mathrm{err}}$ is subtracted from the column positions and the displacement field is determined again (see Figure 10.19(b)).

Additionally, the domain wall was aligned perpendicular to the scanning direction. Since the scanning error within one line scan is rather small, changes at the domain wall can be ascribed to the domain wall and not the scanning error within that orientation.

Having discussed the two most important error sources we continue with the quantitative evaluation of strain and polarization similar to the $PbTiO_3$ example. In order to obtain a polarization value we now have to deal with the problem of missing oxygen position information. We will infer the missing oxygen positions by choosing one (detectable) reference atom and extending the linear response model to the displacements of the other (unknown) atoms with suitable proportionality constants. For the particular case of $BiFeO_3$, $\mathbf{P}$ within this linear response model is given by the Fe displacement $\delta\mathbf{R}_{\mathrm{Fe}}$ only ($\delta\mathbf{R}_{\mathrm{Bi}}$ is set to zero by choosing Bi as reference) if assuming that the shift $\delta\mathbf{R}_{\mathrm{O}}$ of O depends linearly (with some factor c) on that of Fe, that is:

$$\begin{aligned}\mathbf{P} &\approx \frac{1}{\Omega}\left(\mathbf{Z}^*_{\mathrm{Fe}}\delta\mathbf{R}_{\mathrm{Fe}} + \mathbf{Z}^*_{\mathrm{O}}\delta\mathbf{R}_{\mathrm{O}}\right)\\ &= \frac{1}{\Omega}\left(\mathbf{Z}^*_{\mathrm{Fe}} + \mathbf{Z}^*_{\mathrm{O}}c\right)\delta\mathbf{R}_{\mathrm{Fe}} \qquad (10.26)\\ &= \frac{\mathbf{Z}^*}{\Omega}\delta\mathbf{R}_{\mathrm{Fe}}\end{aligned}$$

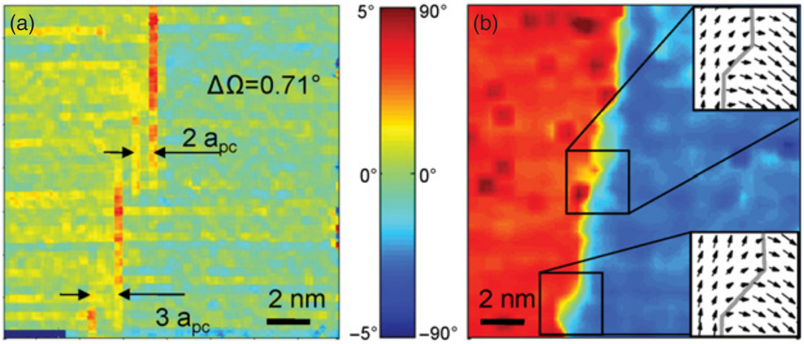

Figure 10.20 *(a) Lattice and (b) polarization rotation field at the* $BiFeO_3$ *109° domain wall containing steps. The polarization vector field at the steps (enlarged squares) shows a rotation across a diagonal boundary. For a color version of this figure, see color plate section.*

In the following we use this approximation and refer to the relative displacement of Fe with respect to the center of the current unit cell as the polarization equivalent or short polarization.

Strain and polarization maps of several domain wall regions (for an example see Figure 10.20) now reveal several interesting characteristic features. The general shape of the domain walls consists of long straight faces interrupted by short steps comprising 2–4 pseudocubic unit cells. The steps always occur in one direction and could therefore be related to a frozen-in motion of the domain wall (see further below). The straight unperturbed parts of the domain wall have a width of 1–2 pseudocubic unit cells, which together with the determined atomic positions agrees very well with *ab initio* predictions obtained from LDA+U DFT [72]. The staircase shape could be related to a frozen-in domain wall motion by considering the details of the motion process. Miller and Weinreich [77] noted that for energetic reasons a domain wall is not shifting as a whole when moving to the left or right. According to their model it rather develops sharp 90° steps, which are shifted vertically along the whole domain wall eventually increasing the size of one domain at the cost of the other. That resembles the working principle of a loom, where the wefts shooting in from the sides play the role of the steps. Based on theoretic considerations, Shin et al. [78] noted that the polarization in the vicinity of these steps should be attenuated over a certain region ("diffuse domain walls") in order to facilitate experimentally observed domain wall motions. The polarization values estimated from atomic resolution HAADF images are now suited to support these findings in the case of $BiFeO_3$. An inspection of the unit-cell-wise polarization in Figure 10.20(b) at the steps reveals a gradual rotation and small attenuation smeared out over several unit cells. For more details we refer to Lubk et al. [3].

Similar to the previous $PbTiO_3$ thin-film investigations we can conclude that both strain and polarization obtained by means of HAADF–STEM and model-based parameter estimation theory are suited for quantitative characterization. In comparison to HRTEM (Section 10.2), the HAADF–STEM contrast is less susceptible to specimen bending, with adsorbents at the specimen surface and dynamic scattering effects yielding atomic contrast images under relaxed experimental conditions (e.g., several tens of nanometers thick specimen). However, these advantages can be delusive and compensated by disadvantages when extracting quantitative specimen properties such as atomic positions from the STEM micrographs. For instance, we have seen that the STEM scanning error can shift the determined atomic positions, light elements are difficult to see with HAADF–STEM, and the atomic HAADF contrast stems from a thin layer of the specimen only because of the small depth of focus of the STEM probe. We therefore conclude that HRTEM is better suited for high-precision extraction of strain and polarization on the level of unit cells if specimen preparation, alignment, and aberration correction are under perfect control. HAADF–STEM is experimentally less demanding while offering a similar spatial resolution like HRTEM and might therefore be readily applied to a larger class of problems. However, certain aspects of HAADF–STEM require further improvement in order to attain the precision of state of the art HRTEM investigations.

10.4 Electron Energy Loss Spectroscopy

This section focuses on the use of EELS techniques to investigate the chemical composition and electronic properties of ferroelectric and multiferroic materials. A particular insight will be provided on the importance of the interfaces of nanoscaled multiferroics with other materials, specially ferromagnets. The chemical and electronic states of the interfaces, which can be mapped and spectroscopically analyzed by STEM–EELS techniques, will determine their macroscopic properties and eventually their functionality.

10.4.1 EELS Basics

Electrons are highly energetic charged particles that interact strongly with matter. In a TEM, in addition the elastic scattering, there is a significant probability of inelastic interaction in which the electrons transfer some energy to the sample. This occur, depending on the amount of energy transferred (from low to high), in the form of heat (excitation of phonons), collective excitation of conduction electrons (plasmons), interband transitions from weakly bonded electron bands, and electron excitations from core levels to unoccupied states above the Fermi level. Thus, the spectroscopic analysis of the energy lost by the transmitted electrons, the electron energy loss spectroscopy (EELS), provides invaluable information on the physical properties of the material. Firstly, these excitations are associated to transitions between specific energy levels that are characteristic for the chemical elements present in the material. As the intensity of the transitions is proportional to the concentration of that element, EELS is extremely valuable to quantify the composition of the specimen. Furthermore, as inelastic interactions can only induce transitions to unoccupied electron levels, EELS probes the local density of states (LDOS) above the Fermi level. The latter is dramatically affected by the local environment of the atom in its specific position on the crystal structure. Consequently, the fine structure of the EELS edges reflects the influence of coordination, bonding, and electronic state of the atom, which can be analyzed qualitatively (fingerprinting) or quantitatively by complementary theoretical simulations [79].

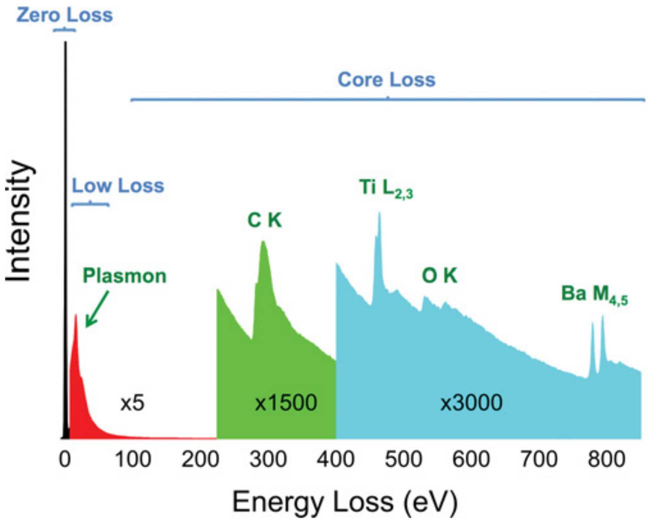

Figure 10.21 *The EEL spectrum*

10.4.1.1 The EEL Spectrum

The amount of energy lost determines the type of electron transition induced and, as a consequence, the type of physical property or phenomena that can be probed. Following this criterion, three main energy ranges can be distinguished in a typical EEL spectrum, which are illustrated in Figure 10.21:

(a) The quasi-elastic region or *zero-loss peak* (ZLP) is usually below 1 eV. Its width is the result of the convolution between the energy resolution of the spectrometer (including the point-spread function of the detector) and the temporal coherence (or energy spread) of the electron source. It is an important component of the spectrum. From the practical point of view, the ZLP is the reference to define the quality of the spectra and tune the spectrometer. Furthermore, its relative intensity with respect to the rest of the EELS spectrum determines the number of inelastic interactions occurring with respect to the elastic ones. As this ratio is related to the specimen thickness, the ZLP may be used to determine or at least estimate the thickness of the sample.

(b) The *low-loss* region contains the electrons generating low-energy excitations revealing fine details of the electronic structure close to the Fermi level, such as band gap transitions, collective electronic excitations (volume and surface plasmons), or interband transitions, up to 20–30 eV of energy loss. This regime hosts low-energy and low-lifetime excitations characterized by wide peaks with no fine structure, but is frequently dependent on composition (band gaps or plasmons) or geometry (plasmons).

(c) The *core-loss* region is beyond the low-loss regime, where edges associated to transitions from the core atomic-like levels appear. Core-loss edges usually show a fine structure related to the specific electronic structure of the chemical species and the chemical environment of the atom, as it is associated mostly to dipolar transitions from core states to the unoccupied atomic levels. As these transitions originate from inner shell electron levels, core-loss excitations are very localized near the atomic positions. Thus, they are both used for chemical quantification and electronic structure determination with high spatial resolution down to the atomic level. They are identified with the standard spectroscopic nomenclature for ionization edges in X-rays (e.g. in Figure 10.21, K for transitions from the 1s level, $L_{2,3}$ for 2p levels, $M_{4,5}$ for 3d, etc.).

Two regimes are considered when analyzing core loss edges: *electron loss near edge spectroscopy* (ELNES) refers to the energy loss region tens of eVs above the ionization energy, where the excited electron has little excess energy and undergoes multiple scattering with the surrounding atoms, and *extended energy loss fine structure* (EXELFS), in which the excess energy is hundreds of eVs above the ionization energy, so the multiple scattering is rare and the expelled electron behaves as a single scattering electron wave diffracted by the surrounding lattice. As we will see later, ELNES provides valuable information about the coordination and bonding with the nearest neighbors and it is more widely used because, in spite of the complexity of the interactions, its intensity is remarkably higher and overlaps with other edges less likely than the EXELFS region.

Due to the influence of subtle changes in the local chemical composition, electronic state, and crystal structure in their physical properties, the core-loss EELS, with particular attention to the ELNES fine structure, is mostly exploited in the study of nanoscale multiferroics, and hereafter we will focus on it.

10.4.1.2 Instrumentation

Modern spectrometers employ magnetic prisms that, producing a magnetic field perpendicular to the electron trajectory, bend the electron path with a radius depending on the energy of the electrons. The overall effect is an energy dispersion of the electrons combined with a focusing action for electrons of a given energy. Two configurations are currently available: in-column omega filters (more suitable for energy filtered imaging) and post-column spectrometers/image filters, which consist of magnetic prisms and additional optical elements to facilitate both spectroscopy and image filtering [79].

10.4.1.3 Experimental Consideration

Most of the inelastic electrons are dispersed within a few mrad around the transmitted beam, close to the optical axis, so EELS certainly approaches 100% collection efficiency, contrary to other TEM-based spectroscopies employing X-rays or cathodolumininescence, where the emission is nearly isotropic and therefore a significant amount of the signal is wasted. This implies that EELS easily produces high-intensity spectra with decent statistics in short acquisition times (from seconds to milliseconds). Furthermore, electron optics in modern spectrometers is so advanced that the energy resolution is only limited by the temporal coherence of the electron source. To improve the energy resolution beyond the intrinsic energy spread of electron sources, *electron monochromators* have been developed to reach energy resolution well below 100 meV, competing with synchrotron radiation albeit with much higher spatial resolution. In addition to extremely fine detail in the core-loss edges, monochromated electron beams enable the study of very small energy (< 1 eV) low-loss interactions such as surface plasmons, band gaps, excitons and even vibrational modes [80].

One of the main drawbacks of EEL spectroscopy is the fact that the inelastic scattering cross-section decreases quickly as a function of the energy lost by the electrons. Therefore, EELS intensity diminishes so quickly that it is impractical to probe energy losses beyond 2–3 keV. Therefore, EELS is not as convenient for heavy atoms as X-ray spectroscopy. Furthermore, complex inelastic interactions and multiple scattering can only obtain reliable quantitative information in very thin specimens, and band structure calculations to model the EEL spectrum as a function of the electronic state of the atoms and their chemical environment are required to interpret the fine structure provided by high-energy resolution EELS.

10.4.1.4 STEM–EELS Spectrum Imaging

Most of the EELS experiments performed nowadays rely on the possibility of collecting spectra in selected positions of a sample by controlling the position of the incident beam with the scan coils of the microscope in STEM mode. Consequently, the incident beam can be scanned along the sample with a certain dwell time and EEL spectra collected at each point enabling the *spectrum imaging* (SI), that is 1D or 2D arrays of EEL spectra, to be collected pixel by pixel in a region of the sample as depicted in Figure 10.22 [76]. The advent of aberration correctors for STEM, permitting subangstrom probes, has opened the door for atomic resolution SI, which, considering the weak delocalization of inelastic scattering of core loss edges (in many cases smaller than the atomic distances), provides atomically resolved information (maps) of the chemical composition and the electronic state of the chemical elements in the compound.

10.4.2 EELS Applications in the Characterization of Multiferroics

A good example of the potential of EELS in the study of multiferroics is the case of $LuFe_2O_4$. Although the real nature of ferroelectricity in this material is still under debate, it is traditionally considered as one of the systems presenting multiferroicity at the highest temperature. Whereas a charge ordering transition in the Fe position causes ferroelectricity at $T_{CO} = 320$ K, the system orders ferrimagnetically at $T_N = 240$ K [26].

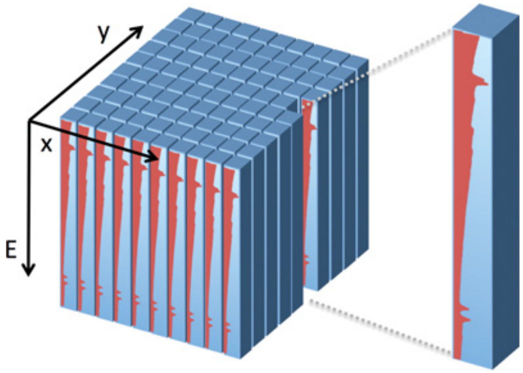

Figure 10.22 *Scheme of the spectrum imaging 3D cube*

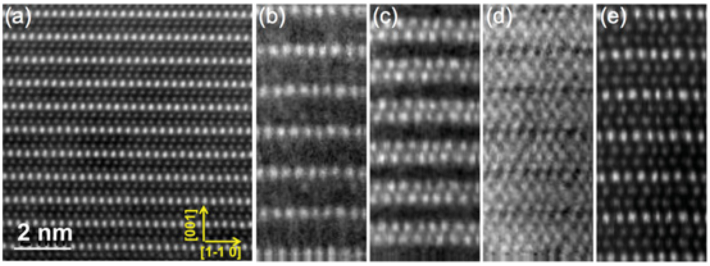

Figure 10.23 *(a) HAADF–STEM image of a* $LuFe_2O_4$ *thin film observed along the [110] orientation, showing the alternation of Lu and double Fe layers. Integrated intensities of (b) Lu* $M_{4,5}$*, (c) Fe* $L_{2,3}$*, and (d) O K edges of a STEM–EELS spectrum image. (e) Annular dark-field signal collected simultaneously. Reprinted with permission from [82]. Copyright [2012], AIP Publishing LLC*

Thin films of $LuFe_2O_4$ have been recently studied in order to probe the distribution of chemical elements in the structure and the type of bonds the oxygen forms with neighboring atoms depending on the two distinct environments in which it is placed [81, 82].

The atomic resolution mapping demonstrates the nearly perfect alternation of Fe and Lu planes, and how the oxygen lattice is nicely resolved, their atomic positions differentiated from the metal ions. In addition to the confirmation of the expected chemical structure, it also evidences the presence of Fe/Lu chemical intermixing, in this particular case clearly observable in the Lu map, which presents atomic contrast in the Fe layers (see Figure 10.23).

The layered hexagonal structure of this material can be pictured as the alternation of two atomic planes of Fe, each enclosed by an oxygen trigonal bipyramid, and one plane of Lu along the [110] direction. Depending on the layer, oxygen is then surrounded by a trigonal bipyramid of four Fe atoms with one Lu atom in one of the apexes in the Fe layers, whereas the oxygen next to the Lu planes presents a tetrahedral environment with three Lu ions and one Fe ion in the apex. High-energy resolution SI can also provide information on the chemical bonds sustaining the crystal structure of $LuFe_2O_4$, down to atomic resolution. In particular, in the dipolar approximation the O K edge is sensitive to the LDOS of the unoccupied O 2p levels, which are hybridized with the d orbitals of the adjacent metal ions, Fe 3d and Lu 5d. Thus, the changing features of the ELNES fine structure of the O K edge of oxygen are related to the coordination of oxygen in the Fe and Lu layers, and thus to the electron population of these levels in the metal sites.

As illustrated in Figure 10.24, three main peaks at 530, 535, and 540 eV characterize the O K edge of $LuFe_2O_4$. In the case of the Fe-bonded oxygen, the first peak is remarkably more intense due to the contribution to the LDOS of the hybridization of O p and Fe d orbitals. On the other hand, the oxygen in the Lu layers shows a first peak diminished in intensity, with an increase of the second one at 535 eV. *Ab initio* LDOS calculations demonstrate that the first peak is related to the hybridization of O p with Lu d orbitals. These two different oxygen fine structures, integrated from their respective areas in the sample, can be incorporated to a non-linear least square fit to determine their spatial distribution along the SI. The result is a chemical bonding map where the spatial distribution of the two different environments of the oxygen atoms is displayed, exhibiting a complete correspondence

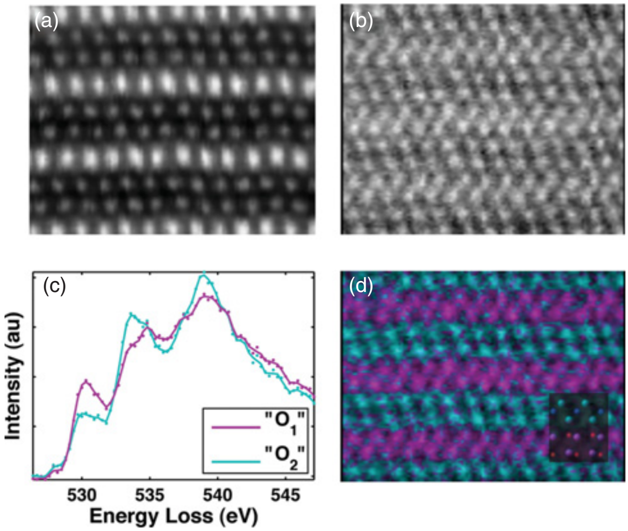

Figure 10.24 *Spectrum imaging of the local oxygen bonding in* $LuFe_2O_4$ *(110). (a) HAADF–STEM collected simultaneously to the EELS spectra. (b) Integrated intensity of the O K edge. (c) EELS fine structure of the two distinct O K edges found in the spectrum imaging, labeled* O_1 *and* O_2*. (d) Spatial distribution of the* O_1 *and* O_2 *chemical environment of oxygen atoms in the structure. Reprinted with permission from [82]. Copyright [2012], AIP Publishing LLC. For a color version of this figure, see color plate section.*

between this fine structure, the dominant atomic bonding, and its spatial location in the Fe and Lu layers.

Even though EELS spectrum imaging is valuable for the study of bulk or nanoscaled multiferroics, the most interesting applications in which this technique shows up all its potential is the analysis of interfaces. There is a growing interest in the design of heterostructures, usually thin multilayers composed of multiple materials with different properties, in order to confer to the integrated system new functionalities, either derived from the coexistence of both materials or new ones emerging from the integration itself through interface phenomena. Charge redistribution, chemical diffusion, or structural modifications due to strain give rise to new interface properties different from those of the bulk or isolated materials. A paradigmatic example is the appearance of a 2D electron gas at the interfaces of $LaAlO_3$–$SrTiO_3$ multilayers, both of them being model insulators separately. In the case of ferroelectrics there are two situations that are worth studying: (a) the influence of the substrate/vicinal layers on the ferroic properties of the original material and (b) the effect of the interface on the functionality of integrated heterostructures.

$SrTiO_3$ is one of the basic substrates for the growth of oxide heterostructures, particularly of perovskites. As many ferroelectric or multiferroics are perovskite-based oxides, the consequences of integrating these thin films on $SrTiO_3$ substrates is of great importance. An example of this is the $PbTiO_3$–$SrTiO_3$ system. Ferroelectricity of $PbTiO_3$ thin films is directly related to the tetragonality of the lattice, and both are influenced by the hybridization of Pb 6sp and Ti 3d orbitals with the O 2p orbital [83]. Thus, substrate-induced strain

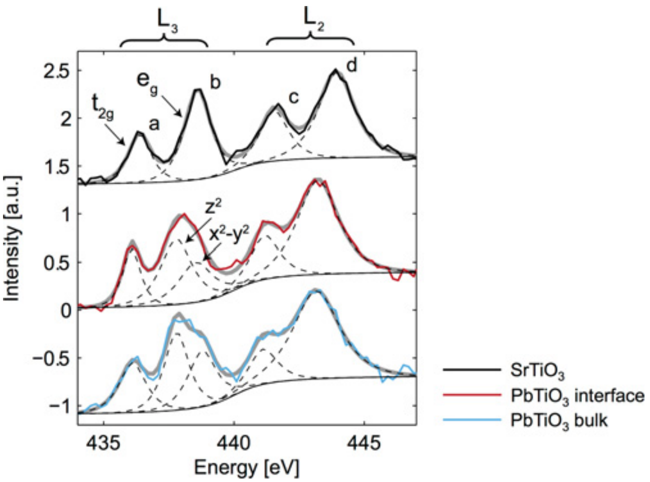

Figure 10.25 *Normalized Ti $L_{2,3}$ edge of $PbTiO_3$ far from the interface (bottom curve), $PbTiO_3$ near the interface (mid-level curve), and the $SrTiO_3$ substrate (top curve) in a $PbTiO_3$ epitaxial thin film grown on $SrTiO_3$ (100). Dashed lines represent the fitted models for the contributions of the different 3d orbitals. Reprinted with permission from Ref. [85]. Copyright [2011], AIP Publishing LLC*

in an epitaxially grown system can modify the *c*/*a* ratio and affect significantly the electric polarization. Indeed, tetragonality decreases in the case of very thin (< 20 nm) PTO films grown on $SrTiO_3$ [84]. High spatial resolution EELS is able to probe the Ti $L_{2,3}$ fine structure in the "bulk" film and at the interface (3 nm next to the substrate), and we can observe how the typical features of Ti in $PbTiO_3$ are modified. L_2 and L_3 peaks of Ti correspond to transitions from the $2p_{1/2}$ and $2p_{3/2}$ atomic levels to unoccupied 3d levels, which are split into t_{2g} and e_g levels due to the crystal field of the octahedral site symmetry at Ti in $SrTiO_3$. The presence of tetragonal distortion in $PbTiO_3$ produces several effects with respect to cubic $SrTiO_3$. In particularly the e_g degeneracy is broken (z^2 and x^2–y^2 orbitals are split). Figure 10.25 shows how this effect is present in the Ti at the interface and, to a lesser extend, in the first 2–3 nm of the $PbTiO_3$ layer with respect to bulk, which reflects a smaller tetragonality of the lattice, and, thus, weaker electric polarization [85].

Integration with other functional materials such as ferromagnets is another context where EELS provide useful information on the interface properties. A representative case is the control of the ferroelectric polarization in a thin film by tuning the interface properties, particularly the atomic termination in contact with another material, which was experimentally demonstrated by Yu et al. [86]. This work investigates the correlation between the ferroelectric properties and the structure of the interface $La_{0.7}Sr_{0.3}MnO_3$–$BiFeO_3$. This interface can be atomically engineered to present two different terminations: $La_{0.7}Sr_{0.3}O$–MnO_2–BiO–FeO_2 and MnO_2–$La_{0.7}Sr_{0.3}O$–FeO_2–BiO. Atomic resolution STEM–EELS gives the experimental evidence of the presence of these terminations, which cannot be identified by any other imaging technique. Figure 10.26 evidences how the chemical termination can be accurately determined by STEM–EELS line profiles. The valence mismatch at the interface builds up an electrostatic potential step that

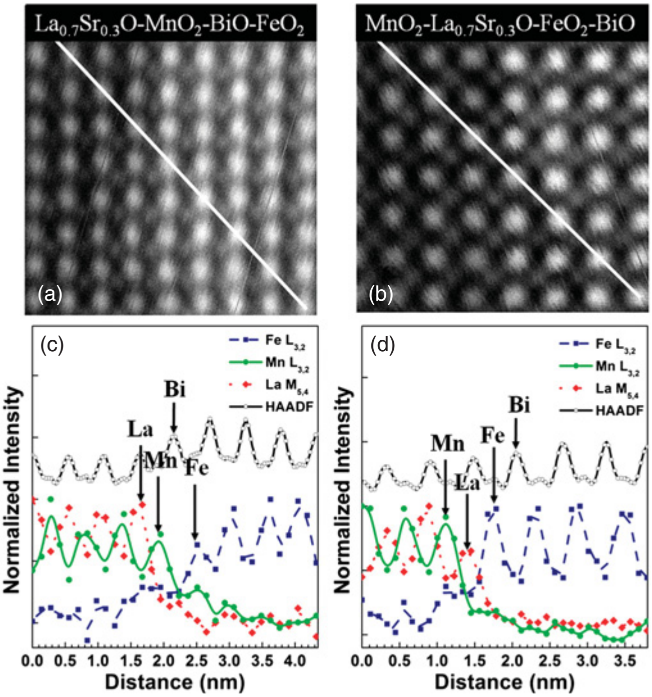

Figure 10.26 *HAADF–STEM images of* $La_{0.7}Sr_{0.3}MnO_3$*/* $BiFeO_3$ *interfaces with terminations (a)* MnO_2*–BiO and (b)* $La_{0.7}Sr_{0.3}O$*–*FeO_2*; (c) and (d) correspond to the chemical profiles obtained from spectrum lines across interfaces of both types, respectively, acquired diagonally from top left to bottom right along the white lines. Adapted with permission from [86], courtesy of Yu et al. Copyright © 2012, National Academy of Sciences*

causes a bias voltage and modifies the depolarization fields, and thus the spontaneous polarization. Then each one of these atomic terminations gives rise to different orientations of the as-grown ferroelectric polarization and ferroelectric hysteresis.

Another example of atomic-scale characterization of multiferroicity at interfaces is the investigation of the $BaTiO_3$–Fe interface. This interface has been theoretically predicted to support interface multiferroicity due to charge redistribution inducing magnetoelectric coupling and the existence of net magnetic moment in the interfacial $BaTiO_3$ [87–89]. This has been experimentally demonstrated in $La_{0.7}Sr_{0.3}MnO_3$–$BaTiO_3$–Fe ferroelectric tunnel junctions showing strong tunnel electroresistance (variation of the electric resistivity with the polarization orientation of the ferroelectric barrier) and tunnel electromagnetoresistance (variation of the magnetoresistance as a function of the electric polarization) [90]. An atomic resolution STEM–EELS analysis of the $BaTiO_3$–Fe interface was carried out by Bocher et al. [91]. This study shows that at the interface the decay of the oxygen signal is delayed with respect to that of Ba and Ti across the interface, coinciding with the increase of the Fe signal of the top electrode. This indicates the presence of a very thin iron oxide layer at the interface. As shown in Figure 10.27, the ELNES spectrum at the interface also presents features that do not match the fine structure of metallic iron. Analysis of the ELNES

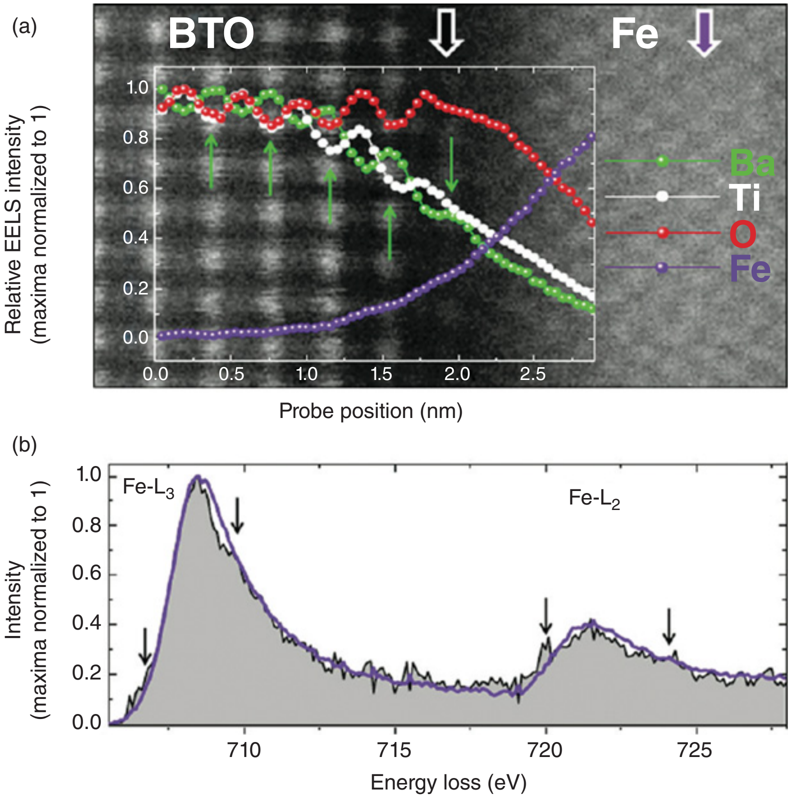

Figure 10.27 *(a) Normalized intensity profiles of Ba, Ti, O, and Fe obtained from STEM–EELS spectrum lines across the* $BaTiO_3$*—Fe interface superimposed over a HAADF–STEM image of the interface used as a reference. (b) ELNES of the Fe* $L_{2,3}$ *edge at the interface (line) and the Fe layer (shadowed line), where arrows indicate the specific features of* Fe^{2+} *and* Fe^{3+}*. Adapted with permission from [91]. Copyright (2012), American Chemical Society*

fine structure at the interface by fitting the interfacial Fe fine structure to a linear combination of reference spectra for metallic Fe, Fe^{2+}, and Fe^{3+} demonstrate that the main ionic contribution is Fe^{2+}, together with metallic Fe coming from the neighboring Fe layer due to delocalization and beam broadening. Finally, multiple atomic models have been proposed to calculate the resulting HAADF images in order to compare them with the experimental one, demonstrating that an interface structure is Fe–FeO–TiO_2–$BaTiO_3$. Further analysis by X-ray resonant magnetic scattering and DFT calculations has demonstrated the presence of magnetic moments in Ti atoms of the interface caused by the enhanced ferromagnetism of the FeO layer and the hybridization of spin-polarized Fe and O with Ti orbitals [91].

We have already discussed in this chapter the importance of ferroelectric DWs to understand the physical properties of nanoscale ferroelectrics. Ferroelastic walls are particularly interesting because they are accompanied by strong elastic deformations that can drastically affect the local physical properties, for instance the electric polarization orientation (see Section 10.3.3.1). Furthermore, DWs can give rise to the formation of new structural and chemical phases different from "bulk" domain structures and with radically new physical properties that can even be observed macroscopically. An example is the emergence of ferromagnetism in the epitaxially strained multiferroic $TbMnO_3$. This manganite is an orthorhombically distorted perovskite that is an incommensurate antiferromagnet (T_N = 42 K) at low temperatures, and becomes a commensurate spin spiral antiferromagnet at T_{N2} = 28 K in bulk. This new ordering breaks inversion symmetry and induces ferroelectricity with a strong magnetoelectric coupling [92]. Highly strained $TbMnO_3$ thin films present the unexpected peculiarity of becoming weakly ferromagnetic below 40 K and, interestingly, the magnetization scales with the density of DWs formed to accommodate epitaxial strain. The thinner the film, the higher is the number of DWs nucleated and thus the higher the ferromagnetic signal [93].

We finish this section illustrating how aberration-corrected STEM–EELS has been used to explore the local properties of these domain walls. Surprisingly, these domain walls are not only accompanied by a remarkable structural relaxation (-3% in-plane strain release with respect to the domains) but they also show an unprecedented chemical ordering driving this strain relaxation [93]. As shown in Figure 10.28, the atomic resolution spectrum image evidences that the DWs are characterized by the alternating substitution of Tb along the growth direction by Mn, a smaller ion. This particular arrangement is atomically flat and thin, perpendicular to the substrate plane and confined in the DWs. In addition to a strain relaxation, this chemical ordering also triggers the onset of local ferromagnetism at the domain walls. DFT calculations have demonstrated that these Mn ions occupying Tb sites are located in chemical environments different from those of the "bulk" domains and exhibit different magnetic moments and exchange interactions. Even though antiferromagnetic interactions are predominant in the DW environment, they collectively give rise to an overall ferromagnetic coupling at remanence around the defect, whereas deep into the domain the spins are fully compensated as in bulk antiferromagnetic $TbMnO_3$. Indeed, the effect of the replacement of Tb by Mn at the DW exceeds the defect itself around two Mn planes beyond the DW, and a net magnetic moment of ~10 μ_B is induced by each Mn atom

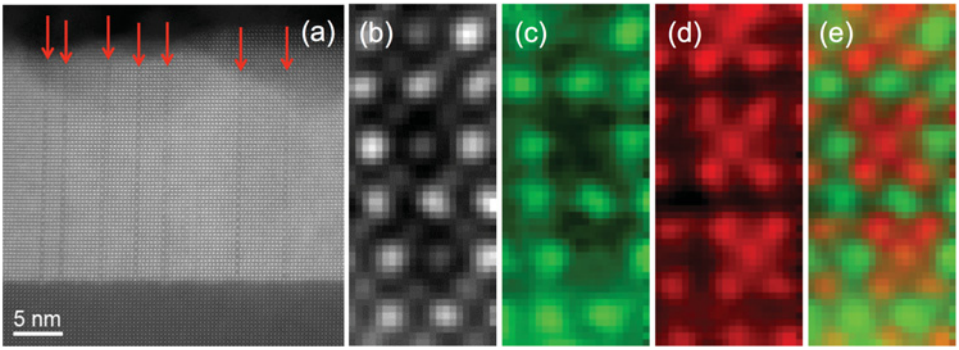

Figure 10.28 Strained $TbMnO_3$ film grown on $SrTiO_3$ (100). (a) HAADF image of the film, where the domain walls are marked with arrows. (b) to (e) Spectrum image of one of the domain walls: simultaneously acquired HAADF signal (b), EELS integrated intensities of the Tb $M_{4,5}$ (c), and Mn $L_{2,3}$ (d) edges, and a color map composed with the later EELS maps (e). Adapted from [93].

in a Tb site. Once the experimental domain wall density is taken into account, the average net magnetic moment calculated theoretically is 0.15 μ_B/*f.u*, which matches nicely with the macroscopic remanent magnetization, about 0.10 μ_B/*f.u*. Fine structure analysis of the O K edge also reveals a significant decrease in the nominal oxidation state of Mn in the DW, which reflects that the different chemical environment of Mn atoms replacing Tb positions causes a different electronic state for these ions, yet to be explored in depth.

10.5 Future and Challenges

The previous chapters demonstrated the state of the art capabilities of TEM techniques for investigating ferroelectrics. On several occasions we referred to the large progress in the field mainly fueled by instrumental developments such as hardware aberration correction. Since further advances are on their way, similar progress is expected in the future and we will expound in the following its probable direction and character.

Advanced equipment for better resolution. Classical HR(S)TEM focusing on atomic column positions and unit cell dimensions will continue to provide valuable insight into ferroelectric properties. We will see an expansion of the investigations towards a larger class of ferroelectrics and a larger focus on defect structures, such as domain walls and interfaces. Here, the additional resolving power and beam intensity provided by using next-generation hardware correction [94] and gun technology will enable a higher precision in the measured atomic column positions and a better detection of light atoms. A non-conventional technique such as annular bright field (ABF) has been recently revisited in the framework of aberration corrected technologies for its potential for the simultaneous observation of heavy and light atoms in STEM, and the next years are bound to witness its exploitation in the field of multiferroics for the analysis of the oxygen lattice. That will, for instance, facilitate a better characterization of oxygen vacancies, local modulations of the polarization around defects, and the polarization variations in complicated domain structures such as flux closure domains. Better quality of the obtained structure data will also open pathways towards the direct analysis of coupling phenomena, most notably between strain and polarization (e.g., piezoelectricity, electrostriction, flexoelectricity). Unit-cell-wise strain and polarization maps from inhomogeneous strain states (see also in situ TEM below) could be quantitatively analyzed with respect to correlations between strain and polarization, for instance yielding certain components of the piezoelectric tensor. Due to the smaller amount of artifacts, HRTEM will be the favorable choice for high-precision work and problems where light atoms have to be detected. HRSTEM, on the other hand, is experimentally less demanding when it comes to specimen preparation and aberration correction, and will therefore be most frequently applied, exploiting the potential of ABF to obtain a complete picture of the atomic structure at the atomic level. Analytical techniques will also benefit from technical advances, pushing the limits of sensitivity, resolution, and accuracy in EELS fine structure determination. Together with the relentless improvement of spectrometer performance, a new generation of gun monochromators combined in highly stable environments will push the energy resolution down to the meV regime to provide, in combination with the new possibilities for deconvolution of plural scattering, an unprecedented detail in the fine structure of the LDOS that might boost our capacity to explore the local electronic structure and its correlation to the ferroic properties.

Electron tomography. Eventually, three-dimensional structure determination based on high-resolution tomographic techniques like HAADF–STEM tomography could also become a valuable tool in the field. We envisage a high potential of these techniques for resolving local lattice defects like vacancies. It should be noted, however, that several obstacles have to be resolved for determining atomic positions in 3D with pm accuracy. For instance, the above-noted dynamic scattering of the electron probe varying for different angles during the tilt series must be properly taken into account.

Electron holography. Another line of development deals with the application of electron holographic techniques to measure electric fields related to ferroelectric properties [42–46]. Here, one intends to exploit the fact that, under certain conditions, the phase φ of an electron wave reconstructed by electron holography is directly proportional to the electrostatic potential projected along the beam direction z: $\varphi(x, y) = C_E \int V(x, y, z)\,\mathrm{d}z$ (proportionality constant C_E). Thus, holography can be used to measure the total projected electric field $\mathbf{E} = (\mathbf{D} - \mathbf{P})/\varepsilon_0$, which is referred to as the depolarizing field within the nomenclature of ferroelectrics (because it forces the ions in the crystal lattice to reduce polarization; see Section 10.3.2). In the ground state bulk ferroelectric, those depolarizing fields are zero because the spontaneous polarization $\mathbf{P}_\mathrm{s}$ is perfectly screened by surface charges generating $\mathbf{D}$. However, a still growing number of publications claims spontaneous polarization measurements based on the expression $\mathbf{P} = \varepsilon_0 \chi \mathbf{E}$, which does hold in the linear response regime (i.e., the superimposed or induced polarization on top of the ground state) but not for the spontaneous polarization itself (see Section 10.3.2). Indeed, the published findings, in particular the change of reconstructed phases upon paraelectric–ferroelectric phase transition [45, 46] are rather due to dynamical scattering effects and beam-induced charging [95, 96]. Those two effects change upon phase transition and can therefore be easily misinterpreted in terms of a change in spontaneous polarization. A conclusive holographic evidence of depolarizing fields such as occuring at domain walls remains a future goal.

In situ electron microscopy. A whole new level of insight into ferroelectric properties is expected to come from the growing capabilities of in situ TEM. Here, a large variety of dedicated TEM specimen holders facilitate heating and cooling or the application of stress, traction, and electric fields. The simplest in situ TEM experiments, either in imaging or diffraction mode, aim at investigating the phase diagram and analyze locally the paraelectric to ferroelectric phase transition, particularly studying the domain formation when passing the Curie temperature [86, 97]. Other in situ TEM investigations were carried out to study the domain wall motion under an applied field [18] and some results obtained at large bias show highly complicated domain patterns. More recent in situ experiments have even been performed at atomic resolution: Gao et al. [98] showed time-resolved domain wall dynamics in $PbTiO_3$ *a–c* thin films by applying electric fields through connected top and bottom electrodes, studying in situ the polarization reversal and domain wall propagation at the nanometer scale. Future experiments probably have to combine in situ TEM techniques and quantitative (S)TEM imaging methods to investigate, for instance, the “electric field–temperature” or “strain field–temperature” phase diagrams measuring locally the strain fields together with polarization rotations as a function of electrical biasing or external stress at various temperatures. In situ electron holography may also reveal valuable information studying charge displacement during polarization reversal. Eventually such nanometer-scale TEM experiments might give direct insight into the emergence of ferroelectric ordering and domain formation, eventually also elucidating the displacement and order–disorder polarization mechanisms that have been debated for a long time.

References

(1) Jia, C.L., Mi, S.B., Urban, K., et al. (2008) Atomic-scale study of electric dipoles near charged and uncharged domain walls in ferroelectric films. *Nature Materials*, **7** (1), 57–61.

(2) Jia, C.L., Urban, K.W., Alexe, M., et al. (2011) Direct observation of continuous electric dipole rotation in flux-closure domains in ferroelectric $Pb(Zr,Ti)O_3$. *Science*, **331** (6023), 1420–1423.

(3) Lubk, A., Rossell, M.D., Seidel, J., et al. (2012) Evidence of sharp and diffuse domain walls in $BiFeO_3$ by means of unit-cell-wise strain and polarization maps obtained with high resolution scanning transmission electron microscopy. *Physical Review Letters*, **109**, art. no. 047601.

(4) Zeches, R.J., Rossell, M.D., Zhang, J.X., et al. (2009) A strain-driven morphotropic phase boundary in $BiFeO_3$. *Science*, **326** (5955), 977–980.

(5) Lubk, A., Rossell, M.D., Seidel, J., et al. (2013) Electromechanical coupling among edge dislocations, domain walls, and nanodomains in $BiFeO_3$ revealed by unit-cell-wise strain and polarization maps. *Nano Letters*, **13**, 1410–1415.

(6) Catalan, G., Lubk, A., Vlooswijk, A.H.G., et al. (2011) Flexoelectric rotation of polarization in ferroelectric thin films. *Nature Materials*, **10** (12), 963–967.

(7) Tsuda, K., Sano, R., and Tanaka, M. (2012) Nanoscale local structures of rhombohedral symmetry in the orthorhombic and tetragonal phases of $BaTiO_3$ studied by convergent-beam electron diffraction. *Physical Review B*, **86**, art. no. 214106.

(8) Tsuda, K., Sano, R., and Tanaka, M. (2013) Observation of rhombohedral nanostructures in the orthorhombic phase of $KNbO_3$ using convergent-beam electron diffraction. *Applied Physics Letters*, **102** (5), art. no. 051913.

(9) Spence, J.C.H. (2003) *High-Resolution Transmission Electron Microscopy*, Oxford University Press, Oxford.

(10) Scherzer, O. (1949) The theoretical resolution limit of the electron microscope. *Journal of Applied Physics*, **20**, 20–29.

(11) Haider, M., Braunshausen, G., and Schwan, E. (1995) Correction of the spherical-aberration of a 200-kV TEM by means of a hexapole-corrector. *Optik*, **99** (4), 167–179.

(12) Jia, C.L., Houben, L., Thust, A., et al. (2010) On the benefit of the negative-spherical-aberration imaging technique for quantitative HRTEM, Ultramicroscopy.

(13) Sapriel, J. (1975) Domain-wall orientations in ferroelastics. *Physical Review B*, **12**, 5128–5140.

(14) Aizu, K. (1970) Possible species of ferromagnetic, ferroelectric, and ferroelastic crystals. *Physical Review B*, **2**, 754–772.

(15) Tsai, F., Khiznichenko, V., and Cowley, J.M. (1992) High-resolution electron microscopy of 90° ferroelectric domain boundaries in $BaTiO_3$ and $Pb(Zr_{0.52}Ti_{0.48})O_3$. *Ultramicroscopy*, **45**, 55–63.

(16) Hÿtch, M.J., Snoeck, E., and Kilaas, R. (1998) Quantitative measurement of displacement and strain fields from HREM micrographs. *Ultramicroscopy*, **74** (3), 131–146.

(17) Tanaka, M. and Honjo, G. (1964) Electron optical studies of barium titanate single crystal films. *Journal of the Physical Society of Japan*, **9**, 954.

(18) Snoeck, E., Normand, L., Thorel, A., and Roucau, C. (1994) Electron microscopy study of ferroelastic and ferroelectric domain wall motions induced by the in-situ application of an electric field in $BaTiO_3$. *Phase Transition*, **46**, 77–88.

(19) Gevers, R., Blank, H., and Amelinckx, S. (1966) Extension of the Howie–Whelan equations for electron diffraction to non-centro symmetrical crystals. *Physica Status Solidi*, **13**, 449.

(20) Portier, R. (1997) *Etudes Microstructurales d'Oxydes Mixtes Ordonnés Dérivant de Structure Spinelle ou Perovskite*, PhD Thesis, University Pierre et Marie Curie (Paris VI).

(21) Bierwolf, R., Hohenstein, M., Philipp, F., et al. (1993) Direct measurement of local lattice distortions in strained layer structures by HREM. *Ultramicroscopy*, **49**, 273–285.

(22) Vlooswijk, A.H.G., Noheda, B., Catalan, G., et al. (2007) Smallest 90° domains in epitaxial ferroelectric films. *Applied Physics Letters*, **91**, art. no. 112901.

(23) Hÿtch, M.J. and Plamann, T. (2001) Imaging conditions for reliable measurement of displacement and strain in high-resolution electron microscopy. *Ultramicroscopy*, **87**, 199–212.

(24) Reimer, L. and Kohl, H. (2008) *Transmission Electron Microscopy: Physics of Image Formation*, Springer, New York.

(25) Erni, R. (2010) *Aberration-Corrected Imaging in Transmission Electron Microscopy*, Imperial College Press, London.

(26) Pennycook, S.J. and Nellist, P.D. (eds) (2011) *Scanning Transmission Electron Microscopy*, Springer, New York.

(27) Cowley, J.M. (1969) Image contrast in a transmission scanning electron microscope. *Applied Physics Letters*, **15**, 58–59.

(28) Haider, M., Uhlemann, S., Schwan, E., et al. (1998) Electron microscopy image enhanced. *Nature*, **392**, 768–769.

(29) Batson, P.E., Dellby, N. and Krivanek, O.L. (2002) Sub-angstrom resolution using aberration corrected electron optics. *Nature*, **418** (6898), 617–620.

(30) Erni, R., Rossell, M.D., Kisielowski, C., and Dahmen, U. (2009) Atomic-resolution imaging with a sub-50-pm electron probe. *Physical Review Letters*, **102**, art. no. 096101.

(31) Ashcroft, N.W. and Mermin, N.D. (1996) *Solid State Physics*, Saunders College Publishing, New York.

(32) Lubk, A. (2010) *Quantitative Off-Axis Electron Holography and (Multi-)ferroic Interfaces*, PhD Thesis, TU Dresden.

(33) Howie, A. (1979) Image contrast and localized signal selection techniques. *Journal of Microscopy*, **117** (1), 11–23.

(34) Ernst, F. and Rühle, M. (eds) (2003) *High-Resolution Imaging and Spectrometry of Materials*, Springer, Berlin.

(35) Aert, S.V., den Dekker, A.J., den Bos, A., et al. (2005) Maximum likelihood estimation of structure parameters from high resolution electron microscopy images. Part II: A practical example. *Ultramicroscopy*, **104**, 107–125.

(36) Niermann, T., Lubk, A., and Röder, F. (2012) A new linear transfer theory and characterization method for image detectors. Part I: Theory. *Ultramicroscopy*, **115**, 68–77.

(37) Van Aert, S., Verbeeck, J., Erni, R., et al. (2009) Quantitative atomic resolution mapping using high-angle annular dark field scanning transmission electron microscopy. *Ultramicroscopy*, **109** (10), 1236–1244.

(38) den Dekker, A.J., Aert, S.V., van den Bos, A., and Dyck, D.V. (2005) Maximum likelihood estimation of structure parameters from high resolution electron microscopy images. Part I: A theoretical framework. *Ultramicroscopy*, **104**, 83–106.

(39) King-Smith, R.D. and Vanderbilt, D. (1993) Theory of polarization of crystalline solids. *Physical Review B*, **47**, R1651–R1654.

(40) Gonzalo, J.A. and Jiménez, B. (eds) (2005) *Ferroelectricity*, John Wiley & Sons, Weinheim.

(41) Jackson, J.D. (2006) *Classical Electrodynamics*, de Gruyter, New York.

(42) Lichte, H., Reibold, M., Brand, K., and Lehmann, M. (2002) Ferroelectric electron holography. *Ultramicroscopy*, **93**, 199–212.

(43) Rother, A., Reibold, M., Lichte, H., et al. (2006) X-ray investigation, high-resolution electron holography, and density functional calculations of single-crystalline $BaTiO_3$. *Physical Review B*, **74** (13), art. no. 134116.

(44) Lichte, H., Formanek, P., Lenk, A., et al. (2007) Electron holography: applications to materials questions. *Annual Review of Materials Research*, **37**, 539–588.

(45) Matsumoto, T., Koguchi, M., Suzuki, K., et al. (2008) Ferroelectric 90° domain structure in a thin film of $BaTiO_3$ fine ceramics observed by 300 kV electron holography. *Applied Physics Letters*, **92** (7), 072902.

(46) Polking, M. J., Han, M.G., Yourdkhani, A., et al. (2012) Ferroelectric order in individual nanometre-scale crystals. *Nature Materials*, **11** (8), 700–709.

(47) Rabe, K., Ahn, C., and Triscone, J. (eds) (2007) *Physics of Ferroelectrics: A Modern Perspective*, Springer, New York.

(48) Goris, B., Bals, S., Van den Broek, W., et al. (2012) Atomic-scale determination of surface facets in gold nanorods. *Nature Materials*, **11** (11), 930–935.

(49) Scott, M.C., Chen, C.C., Mecklenburg, M., et al. (2012) Electron tomography at 2.4-angstrom resolution. *Nature*, **483** (7390), 444–447.

(50) Ishikawa, R., Okunishi, E., Sawada, H., et al. (2011) Direct imaging of hydrogen-atom columns in a crystal by annular bright-field electron microscopy. *Nature Materials*, **10** (4), 278–281.

(51) Lines, M.E. and Glass, A.M. (1977) *Principles and Applications of Ferroelectrics and Related Materials*, Oxford University Press, Oxford.

(52) Okuyama, M. and Ishibashi, Y. (2005) *Ferroelectric Thin Films: Basic Properties and Device Physics for Memory Applications*, Springer, New York.

(53) Ishiwara, H., Okuyama, M., and Arimoto, Y. (2004) *Ferroelectric Random Access Memories: Fundamentals and Applications*, Springer, Berlin.

(54) Scott, J.F. and Paz de Araujo, C.A. (1989) Ferroelectric memories. *Science*, **246** (4936), 1400–1405.

(55) Zhao, T., Scholl, A., Zavaliche, F., et al. (2006) Electrical control of antiferromagnetic domains in multiferroic $BiFeO_3$ films at room temperature. *Nature Materials*, **5**, 823–829.

(56) Chu, Y.H., Martin, L.W., Holcomb, M.B., et al. (2008) Electric-field control of local ferromagnetism using a magnetoelectric multiferroic. *Nature Materials*, **7**, 478–482.

(57) Stemmer, S., Streiffer, S., Ernst, F., et al. (1995) Domain configurations in ferroelectric $PbTiO_3$ thin films: the influence of substrate and film thickness. *Solid State Ionics*, **75**, 43–48.

(58) Floquet, N. and Valot, C. (1999) Ferroelectric domain walls in $BaTiO_3$: structural wall model interpreting fingerprints in XRPD diagrams. *Ferroelectrics*, **234** (1–4), 107–122.

(59) Padilla, J., Zhong, W., and Vanderbilt, D. (1996) First-principles investigation of 180° domain walls in $BaTiO_3$. *Physical Review B*, **53**, R5969–5973.

(60) Meyer, B. and D. Vanderbilt, D. (2002) *Ab initio* study of ferroelectric domain walls in $PbTiO_3$. *Physical Review B*, **65**, art. no. 104111.

(61) Sághi-Szabó, G., Cohen, R.E., and Krakauer, H. (1998) First-principles study of piezoelectricity in $PbTiO_3$. *Physical Review Letters*, **80** (19), 4321–4324.

(62) Mabud, S.A. and Glazer, A.M. (1979) Lattice parameters and birefringence in $PbTiO_3$ single crystals. *Journal of Applied Crystallography*, **12** (1), 49–53.

(63) Catalan, G., Janssens, A., Rispens, G., et al. (2006) Polar domains in lead titanate films under tensile strain. *Physical Review Letters*, **96**, art. no. 127602.

(64) Pompe, W., Gong, X., Suo, Z., and Speck, J.S. (1993) Elastic energy release due to domain formation in the strained epitaxy of ferroelectric and ferroelastic films. *Journal of Applied Physics*, **74**, 6012–6019.

(65) Kubel, F. and Schmid, H. (1990) Structure of a ferroelectric and ferroelastic monodomain crystal of the perovskite $BiFeO_3$. *Acta Crystallographica B*, 1990, **46**, 698–702.

(66) Fennie, C.J. (2008) Ferroelectrically induced weak ferromagnetism by design. *Physical Review Letters*, **100**, 167203.

(67) Lebeugle, D., Colson, D., Forget, A., and Viret, M. (2007) Very large spontaneous electric polarization in $BiFeO_3$ single crystals at room temperature and its evolution under cycling fields. *Applied Physics Letters*, **91**, art. no. 022907.

(68) Neaton, J.B., Ederer, C., Waghmare, U.V., et al. (2005) First-principles study of spontaneous polarization in multiferroic $BiFeO_3$. *Physical Review B*, **71**, art. no. 014113.

(69) Streiffer, S.K., Parker, C.B., Romanov, A.E., et al. (1998) Domain patterns in epitaxial rhombohedral ferroelectric films. I. Geometry and experiments. *Journal of Applied Physics*, **83** (5), 2742–2753.

(70) Seidel, J., Martin, L.W., He, Q., et al. (2009) Conduction at domain walls in oxide multiferroics. *Nature Materials*, **8** (3), 229–234.

(71) Jang, H.W., Ortiz, D., Baek, S.H., et al. (2009) Domain engineering for enhanced ferroelectric properties of epitaxial (001) $BiFeO_3$ thin films. *Advanced Materials*, **21** (7), 817–823.

(72) Lubk, A., Gemming, S., and Spaldin, N.A. (2009) First-principles study of ferroelectric domain walls in multiferroic bismuth ferrite. *Physical Review B*, **80** (10), art. no. 104110.

(73) Kisielowski, C., Freitag, C., Bischoff, B.M., et al. (2008) Detection of single atoms and buried defects in three dimensions by aberration-corrected electron microscope with 0.5 A information limit. *Microscopy and Microanalysis*, **14**, 469–477.

(74) Borisevich, A., Ovchinnikov, O.S., Chang, H.J., et al. (2010) Mapping octahedral tilts and polarization across a domain wall in $BiFeO_3$ from Z-contrast scanning transmission electron microscopy image atomic column shape analysis. *ACS Nano*, **4** (10), 6071–6079.

(75) Cowley, J.M. and Moodie, A.F. (1957) The scattering of electrons by atoms and crystals. I. A new theoretical approach. *Acta Crystallographica*, **10**, 609–619.

(76) Williams, D.B. and Carter, C.B. (1996) *Transmission Electron Microscopy*, Plenum Press, New York.

(77) Miller, R.C. and Weinreich, G. (1960) Mechanism for the sidewise motion of 180° domain walls in barium titanate. *Physical Review B*, **117** (6), 1460–1466.

(78) Shin, Y.H., Grinberg, I., Chen, I.W., and Rappe, A.M. (2007) Nucleation and growth mechanism of ferroelectric domain-wall motion. *Nature*, **449** (7164), 881–884.

(79) Egerton, R. (1996) *Electron Energy-Loss Spectroscopy in the Electron Microscope*, Plenum Press, New York.

(80) Krivanek, O.L., Lovejoy, T.C., Dellby, N., et al. (2014) Vibrational spectroscopy in the electron microscope. *Nature*, **514** (7521), 209–212.

(81) Lee, J., Trugman, S.A., Batista, C.D., et al. (2013) Probing the interplay between quantum charge fluctuations and magnetic ordering in $LuFe_2O_4$. *Scientific Reports*, **3**, art. no. 2654.

(82) Mundy, J.A., Mao, Q., Brooks, C.M., et al. (2012) Atomic-resolution chemical imaging of oxygen local bonding environments by electron energy loss spectroscopy. *Applied Physics Letters*, **101** (4), art. no. 042907.

(83) Cohen, R.E. (1992) Origin of ferroelectricity in perovskite oxides. *Nature*, **358**, 136–138.

(84) Lichtensteiger, C., Triscone, J.M., Junquera, J., and Ghosez, P. (2005) Ferroelectricity and tetragonality in ultrathin $PbTiO_3$ films. *Physical Review Letters*, **94**, art. no. 047603.

(85) Eberg, E., van Helvoort, A.T.J., Takahashi, R., et al. (2011) Electron energy loss spectroscopy investigation of Pb and Ti hybridization with O at the $PbTiO_3$/$SrTiO_3$ interface. *Journal of Applied Physics*, **109** (3), art. no. 034104.

(86) Yu, P., Luo, W., Yi, D., et al. (2012) Interface control of bulk ferroelectric polarization. *Proceedings of the National Academy of Sciences*, **109** (25), 9710–9715.

(87) Duan, C.G., Jaswal, S.S., and Tsymbal, E.Y. (2006) Predicted magnetoelectric effect in Fe/$BaTiO_3$ multilayers: ferroelectric control of magnetism. *Physical Review Letters*, **97**, art. no. 047201.

(88) Fechner, M., Maznichenko, I.V., Ostanin, S., et al. (2008) Magnetic phase transition in two-phase multiferroics predicted from first principles. *Physical Review B*, **78**, art. no. 212406.

(89) Lee, J., Sai, N., Cai, T., Niu, Q., and Demkov, A.A. (2010) Interfacial magnetoelectric coupling in tricomponent superlattices. *Physical Review B*, **81**, art. no. 144425.

(90) Valencia, S., Crassous, A., Bocher, L., et al. (2011) Interface-induced room-temperature multiferroicity in $BaTiO_3$. *Nature Materials*, **10** (10), 753–758.

(91) Bocher, L., Gloter, A., Crassous, A., et al. (2012) Atomic and electronic structure of the $BaTiO_3$/Fe interface in multiferroic tunnel junctions. *Nano Letters*, **12** (1), 376–382.

(92) Kimura, T., Goto T., Shintani, H., et al. (2003) Magnetic control of ferroelectric polarization. *Nature*, **426**, 55–58.

(93) Farokhipoor, S., Magén, C., Venkatesan, S., et al. (2014) Artificial chemical and magnetic structure at the domain walls of an epitaxial oxide. *Nature*, **515**, 379–383.

(94) Kabius, B., Hartel, P., Haider, M., et al. (2009) First application of Cc-corrected imaging for high-resolution and energy-filtered TEM. *Journal of Electron Microscopy*, **58** (3), 147–155.

(95) Szwarcman, D., Lubk, A., Linck, M., et al. (2012) Ferroelectric effects in individual $BaTiO_3$ nanocrystals investigated by electron holography. *Physical Review B*, **85**, art. no. 134112.

(96) Gatel, C., Lubk, A., Pozzi, et al. (2013) Counting elementary charges on nanoparticles by electron holography. *Physical Review Letters*, **111**, art. no. 025501.

(97) Tan, X., Ma, C., Frederick, J., et al. (2011) The antiferroelectric–ferroelectric phase transition in lead-containing and lead-free perovskite ceramics. *Journal of the American Ceramic Society*, **94** (12), 4091–4107.

(98) Gao, P., Britson, J., Jokisaari, J.R., et al. (2013) Atomic-scale mechanisms of ferroelastic domain-wall-mediated ferroelectric switching. *Nature Communications*, **4**, art. no. 2791.

11

Raman Spectroscopy of Nanostructured Ferroelectric Materials

Marco Deluca[1] **and Andreja Gajovic**[2]

[1]*Materials Center Leoben Forschung GmbH and Institut für Struktur- und Funktionskeramik, Montanuniversitaet Leoben, Austria*
[2]*Molecular Physics Laboratory, Institute Rudjer Boskovic, Croatia*

11.1 Introduction

Nanostructured ferroelectrics are nowadays increasing their importance, since coexistence of phases on the nanoscale or disordered/glassy behavior leads to enhanced electromechanical and dielectric properties. Relaxors, for instance, are being studied for actuator applications and also as thermally stable dielectrics [1].

Fine structural tuning of these materials offers further possibilities to enhance their properties. In order to improve both performance and lifetime, well-defined compositions and suitable processing routes must be identified. To ease this task, high spatial resolution characterization methods are needed to study phases and structures on the nanoscale and relate them to the temperature and pressure dependence of macroscopic electromechanical and dielectric properties.

Among the available techniques, Raman spectroscopy (RS) offers unique advantages. It is a non-destructive laboratory-scale method with almost no need for sample preparation. RS can readily convey information about phases, crystal orientation, and strain in the

---

Nanoscale Ferroelectrics and Multiferroics: Key Processing and Characterization Issues, and Nanoscale Effects, First Edition. Edited by Miguel Algueró, J. Marty Gregg, and Liliana Mitoseriu.
© 2016 John Wiley & Sons, Ltd. Published 2016 by John Wiley & Sons, Ltd.

investigated material [2]. It is a vibrational spectroscopy method, and as such it is sensitive to small differences in phases that influence ferroic behavior (e.g. ferroelectric (FE) and paraelectric (PE) phases). RS is useful in detecting phase transitions as functions of temperature, pressure, and composition [3–6]. Despite being an optical method making use of monochromatic radiation in the visible range, the information the Raman spectrometer accesses originates from the unit cell scale [7]. The spatial resolution of typical Raman instruments is of the order of micrometers [8], and hence RS results can be compared (and are complementary) to synchrotron X-ray diffraction (XRD) and neutron diffraction analyses.

In this chapter an overview of the application of RS to nanoscale ferroelectrics will be presented. We will first explain the basics of RS in solid-state materials. Then we will describe (i) how RS can be applied to lead-based and lead-free relaxors and (ii) the application of RS in nanosize-grained ceramics and 2D nanostructures (nanotubes, nanowires). The presented Raman results will be compared with results from other micro- and macroscale techniques, to highlight the benefits and the complementary nature of RS.

11.2 Raman Spectroscopy Fundamentals

11.2.1 The Raman Effect

RS is a type of molecular spectroscopy in which the spectral lines occur due to the inelastic scattering of light by molecules or their complexes (crystals). Energy changes involve vibrational and rotational (for gas molecules) states of the system or electronic transitions [9]. Being related to the energy landscape of the system, inelastic scattering spectra give information on the structure, bond strength, defects, etc., of the investigated material.

During scattering, incident photons interact with the electric dipole of a molecule. Most incident photons are elastically scattered without energy exchange (elastic “Rayleigh” scattering). A small fraction of light is scattered at different energies. Raman scattering is the inelastic scattering of light by optical phonons [10] and is much weaker (between 10^{-5} and 10^{-8}) than elastic Rayleigh scattering.

The classical and quantum theories of Raman scattering are very well described by Long [11], so we will briefly overview here only the latter. Scattering can be explained by transitions from vibrational states by absorption of an incident photon of energy $\hbar\omega_i$ to virtual states that are energetically lower than real electronic transitions. The radiation is absorbed or emitted during the transition to and from the virtual state (Figure 11.1(a)), and depending on the energy transfer process (being it either an energy-loss or energy-gain mechanism), Stokes or anti-Stokes bands can be observed in the spectrum, respectively (Figure 11.1(b)).

In the case of Rayleigh scattering, there is no change in the energy of the photon. In the case of Stokes scattering the energy of the emitted photon is smaller than that of the incident photon, while in the case of anti-Stokes scattering the energy of the emitted photon is larger than the incident photon energy. At room temperature, the Stokes process is more probable due to the larger population of ground vibrational states with respect to higher vibrational states. Since the energy of the transition depends on the energy of vibrational states in the molecule/crystal, the Raman spectrum is a fingerprint of the investigated substance.

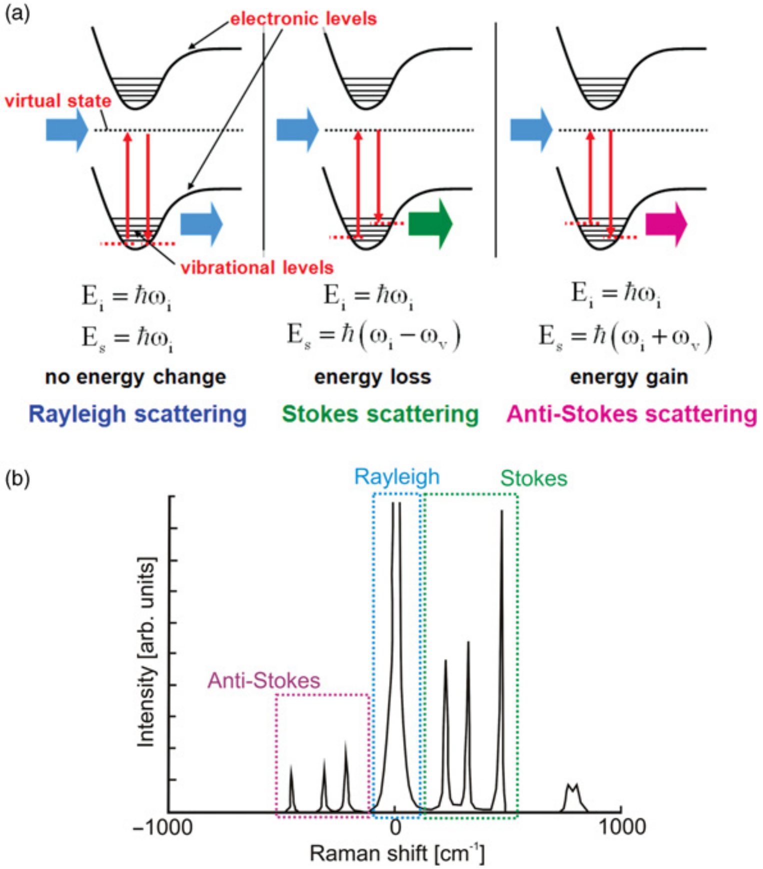
(a)
electronic levels
virtual state
vibrational levels
$E_i = \hbar\omega_i$
$E_s = \hbar\omega_i$
no energy change
Rayleigh scattering
$E_i = \hbar\omega_i$
$E_s = \hbar(\omega_i - \omega_v)$
energy loss
Stokes scattering
$E_i = \hbar\omega_i$
$E_s = \hbar(\omega_i + \omega_v)$
energy gain
Anti-Stokes scattering
(b)
Rayleigh
Stokes
Anti-Stokes
Intensity [arb. units]
−1000
0
1000
Raman shift [cm^{-1}]

Figure 11.1 *(a) Schematic showing the Raman effect from a quantum mechanical viewpoint. Inelastic scattering is related to an energy loss or energy gain mechanism between the incident radiation energy and the vibrational energy of the crystal. (b) The room-temperature Raman spectrum of* CCl_4

Vibrations in crystals can be represented as quantized group motions with a quasi-particle character (phonons). Figure 11.2(a) shows the dispersion curve for optical phonons (OPs) and acoustic phonons (APs) in the case of a one-dimensional diatomic lattice. In a three-dimensional lattice there are 3n phonon branches, from which 3 branches represent acoustic phonons and 3n – 3 the optical phonons. During the interaction of the electromagnetic (EM) radiation with the crystal, if the phonon has frequency ω_q and the excitation field has frequency ω_0, then frequency of the induced dipole moment and scattered radiation is:

$$\omega_k = \omega_0 \pm \omega_q \tag{11.1}$$

This is the condition for constructive interference of the scattered radiation. A second condition is the momentum conservation:

$$\mathbf{k_r} = \mathbf{k_0} - \mathbf{q} \tag{11.2}$$

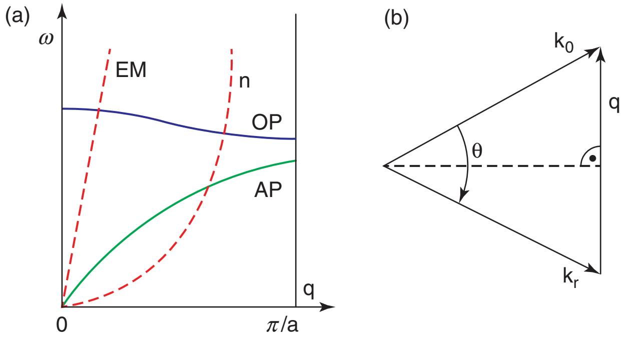

Figure 11.2 *(a) Example of a phonon dispersion curve within the first Brillouin zone for a 1D, two-atomic crystal (lattice dimension a). EM is the electromagnetic radiation and OP and AP are the optical and acoustic phonon branches, respectively. (b) Schematic of the scattering geometry*

where:

$\mathbf{k_0}$ = wave vector of incident excitation radiation
$\mathbf{k_r}$ = wave vector of scattered radiation
$\mathbf{q}$ = wave vector of phonon (cf. Figure 11.2(b)).

since $\omega_q \ll \omega_0$, $\mathbf{k_r} \approx \mathbf{k_0}$ and the magnitude of the wave vector of the phonon is:

$$q = 2k_0 \sin(\theta/2) \tag{11.3}$$

In the most-used backscattering configuration, $\theta = 180°$, and thus $q = 2k_0$. An important consequence of Equations (11.2) and (11.3) is that the visible EM radiation can be scattered only by phonons with $q \approx 0$ (center of the Brillouin zone) and thus the change in frequency is practically independent of the scattering angle since the optical phonon frequency does not change for small q. This argument is valid for first-order Raman scattering.

Common Raman spectrometers make use of monochromatic laser radiation, an optical microscope for focusing and collecting scattered radiation (in backscattering) and high-end single spectrographs or double and triple monochromators. Modern detectors are always multichannel ones, such as CCDs. A very good treatise on Raman equipment and the influence of instrumental parameters on spectral resolution and spectral coverage can be found in McCreery's book [12].

11.2.2 Selection Rules

Due to its intrinsic structure, every solid has a different number of normal modes of vibration (phonons). Their number, type, and symmetry depend on the number of atoms (N) in the primitive unit cell of the crystal, and on the symmetry of the lattice.

Selection rules for Raman scattering require that components of the polarizability tensor transform by the same symmetry operations as normal modes. The number of Raman active modes determines the number of the bands that can be observed in the spectrum of a specific material. The limitation to the $q \approx 0$ phonons means that the wavelength of the excited phonons is of the order of magnitude of the crystal size (many unit cells); in other words, neighboring unit cells oscillate in phase and the determination of the normal mode (phonon) symmetry for a crystal is the same as treating the unit cell as a molecule. Therefore, in the group theoretical treatment, the point group of the unit cell is considered as isomorph to the space group of the crystal.

Normal mode determination by group theory is very well detailed in many treatises [9, 13] and thus will be only briefly mentioned.

To determine the symmetry of the molecular motions, first the symmetry group should be determined and then the characters of the symmetry operation have to be found. This is called the reducible representation of the symmetry group of molecules. Normal modes of vibration can be calculated by decomposing a reducible representation into an irreducible one that represents normal modes. From the symmetry of the specific mode (which can also be found in the character tables), the activity of the mode can be determined. Modes with x, y, z components produce changes in the dipole moment of the lattice and are infrared (IR) active. Modes with higher-order components (x^2, y^2, z^2, xy, xz, yz, etc.) produce changes in the polarizability of the lattice, and are thus Raman active. The symmetry of the modes can be determined by polarized Raman measurements by changing sample orientation or scattering geometry, as reported by Loudon [14].

In the case of disordered crystals, activation of phonons is possible within π/d of the center of the Brillouin zone, where d is the spatial length of the extended disorder (smaller than the lattice parameter) [15]. Thus, scattering can occur also by phonons with $q \neq 0$. This is referred to as selection rule breaking; namely a different number of modes is observed than that predicted by group theory. Disorder can be extended, such as uncorrelated ion displacements or local phases (amorphous or due to chemical segregation), or local: point defects that vibrate with their own frequency and cause either extra-bands or coupling to the Brillouin zone boundary (which excites the whole phonon density of states) [15]. Disorder can also be dynamic; cations can dynamically spring (hop) from one potential well to the other when the kinetic energy of the vibrating atoms in the crystal is increased. This leads to the appearance of a central mode at low frequencies. This phenomenon should not be confused with the Bose–Einstein population [16], and therefore can be recognized with confidence only after Bose–Einstein correction of the spectrum.

11.2.3 Phase Transitions

The application of Raman spectroscopy to the characterization of phase transitions in perovskite materials is excellently reviewed by Husson [17]. Structural phase transitions alter the crystal vibrational behavior. Specifically, in a displacive phase transition, the number of Raman modes is greater in the structural phase with lower symmetry than in the phase with higher symmetry. Moreover, an unstable "soft" optical phonon should always be present. This mode "softening" is the decrease of mode frequency with the change of temperature and a soft mode is directly involved in the FE–PE transition, since FE originates from the cooperative displacement of cations inducing spontaneous polarization (Figure 11.3(a)). The fundamental mechanism that drives those transitions is the weakening of the restoring force on ions as a displacement transition is approached, leading to a decrease of mode frequency ("softening") (Figure 11.3(b)). At the transition point, the frequency of soft phonon modes tends to zero [18]. In the neighborhood of the phase transition (Curie point, T_C) the observation of the soft mode is hampered by three aspects: (1) the anharmonic terms

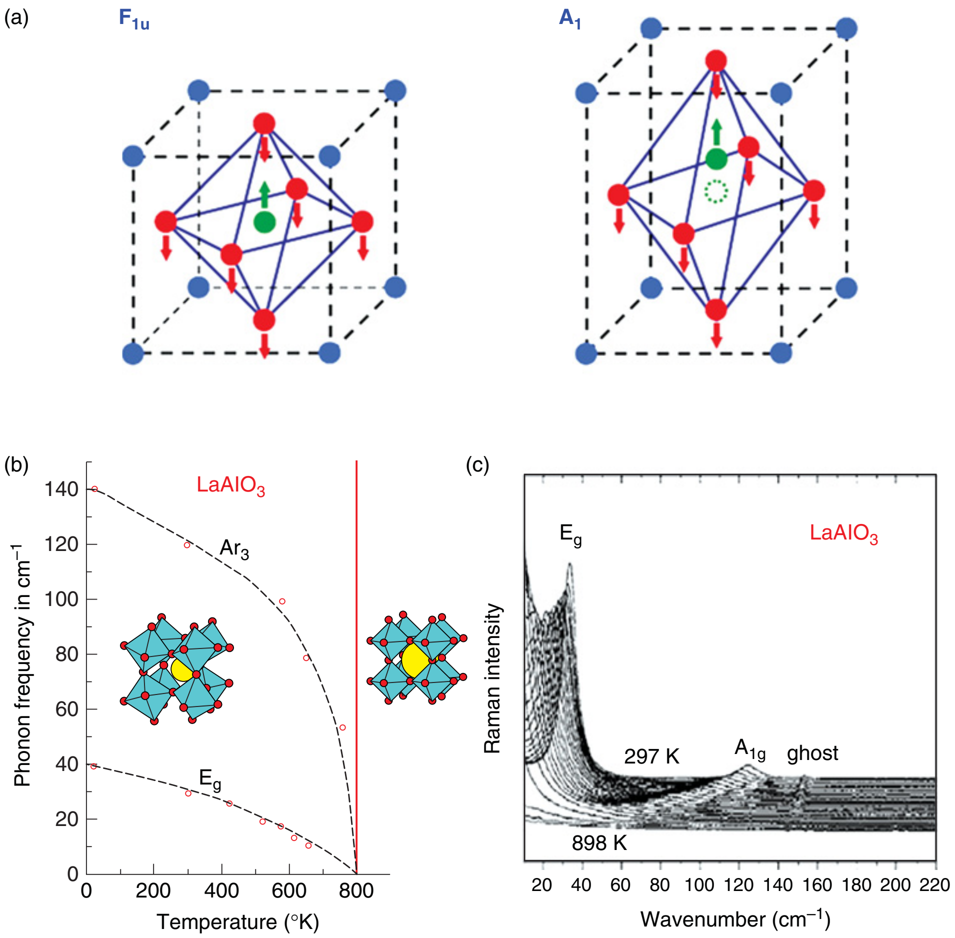

Figure 11.3 *(a) Formation of the soft mode. (b) Soft mode behavior in* $LaAlO_3$ *near the phase transition (octahedral rotation) driven by temperature (reprinted with permission from [20]. Copyright (1969) by the American Physical Society). (c) Shape of the Raman spectra during mode softening (reprinted with permission from [21]. Copyright (2005) by the American Physical Society)*

contribute to the damping of the soft mode; (2) a diffusion peak centered at $\omega = 0$ (central peak) always appears due to the partially order–disorder behavior near T and lattice imperfections (vacancies, defects etc.), and (iii) Rayleigh scattering. Soft modes occur typically well below 100 cm^{-1} (Figure 11.3(c)), therefore special care is needed to filter out Rayleigh radiation (with notch or edge filters on the scattered light path, or the use of a triple monochromator [12]). Modelling of anharmonic and dielectric relaxation effects is also necessary [19].

In order–disorder phase transitions, symmetry lowering and/or crystal twinning can take place, but the soft mode does not appear. Instead, atomic fluctuation becomes important near T_C. Ordering and dynamic fluctuations can be detected by Raman spectroscopy. The former induces a lack of periodicity of the crystal network and thus the detection of non-zone-center phonons, while the latter leads to the existence of the central peak.

If a soft mode is not present or is difficult to detect, phase transitions can be studied by monitoring the hard-mode phonons [22]. The idea is to treat the high-frequency phonons as Einstein oscillators so their frequencies and optical cross-sections depend on the local bond properties. If the bonds change during the phase transition, changes are produced in the Raman spectrum. This method is applicable in both displacive or order–disorder transitions. Since the changes in phonon frequencies are usually very small, the order parameter dependence of frequencies is usually treated using perturbation theory.

11.3 Raman Analysis of Relaxors

Relaxors are perovskite compounds characterized by nanoscale disorder that gives them peculiar dielectric and electromechanical properties [23,24]. The distinctive trait of relaxors is the existence of a broad, frequency-dependent maximum of the dielectric permittivity versus temperature (cf. Figure 11.4(a)), peaking at T_m [23]. All ferroelectrics in the PE phase above the Curie temperature (T_C) are subject to random (uncorrelated) short-range displacements of ions among near-site potential wells (cf. Figure 11.4(b)) [23]. In relaxors these displacements can become correlated due to the presence of random electric fields (RF) generated by local (nanoscale) phenomena (polar nanoregions (PNRs)) originating from compositional inhomogeneities (chemically ordered and disordered regions, COR and CDR, respectively) [25].

Relaxors are characterized by a disordered distribution of different ions on the equivalent lattice sites. Typical relaxors belong to complex perovskite compounds. For $A(B'_{1/2}B''_{1/2})O_3$, ordering in this chemical scheme implies site diffusion between B′ and B″ cations, which has an infinite characteristic time at low temperatures, but occurs with different finite times (depending on the chemical species) at the sintering temperature. Fast cooling can lead to quenched order and thus, generally, these compounds possess a mixture of COR and CDR, which can be distributed with matrix-dispersant or core–shell schemes (cf. Figure 11.4(c)) [23]. The mixture between COR and CDR occurs on the nanoscale, with the COR regions constituted by few unit cells (cf. Figure 11.4(c)). For this reason the overall structure appears always as cubic on average (i.e. by XRD). The presence of this local disorder can be confirmed by the observation of weak superlattice reflections (F-spots) [23] or by Raman spectroscopy [3, 26, 27]. Both COR and CDR are responsible for the formation of electric RFs and consequently of PNRs, but the mechanism by which this occurs is different depending on the character of the substitution [25, 26].

In *heterovalent-substituted complex perovskites*, a cation with a different charge is substituted either on the A-site or on the B-site of the perovskite. This is the case, for instance, of $Pb_{1-x}La_x(Zr_{1-y}Ti_y)_{1-x/4}O_3$ (PLZT), where La^{3+} substitutes on the A-site, of $Pb(Sc_{1/2}Ta_{1/2})O_3$, where Sc^{3+} and Ta^{5+} substitute on the B-site, and of $Pb(Mg_{1/3}Nb_{2/3})O_3$, where Mg^{2+} and Nb^{5+} substitute on the B-site. The arrangement of these substituents with different charges in nanoscale COR produces local charge decompensations and the formation of space charges, which eventually lead to local depolarization fields, thus giving rise to RFs [25].

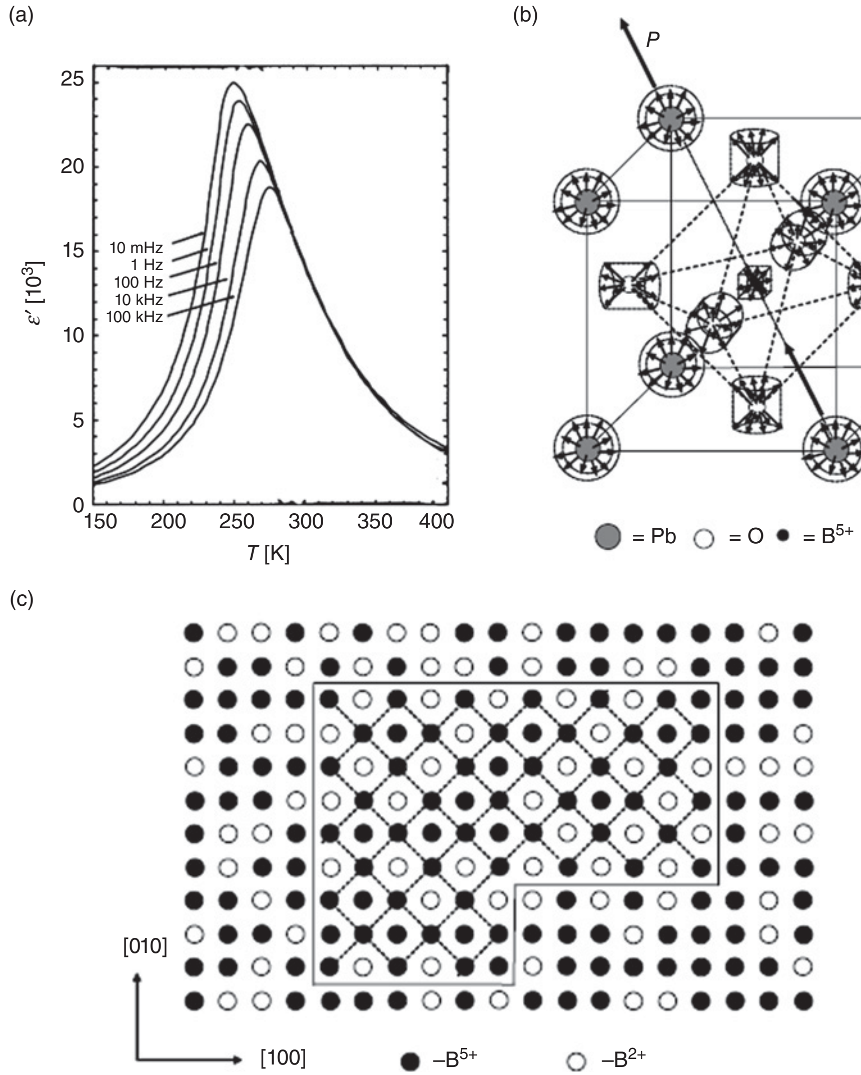

Figure 11.4 *(a) Temperature dependence of the real part of the dielectric permittivity measured at different frequencies for a* $Pb(Mg_{1/3}Nb_{2/3})O_3$ *single crystal. (b) Typical uncorrelated ion displacements (small arrows) in the unit cell of a lead-containing perovskite relaxor. Thick arrows show the direction of the local spontaneous polarization (in the PNR) caused by correlated ion displacements with neighboring cells. (c) Schematic of a COR – the area delimited by the solid line – within the disordered matrix of a Pb-containing complex perovskite. One of the two sublattices inside the COR (highlighted by dashed lines) is formed by the* B^{5+} *ions only (referring to the perovskite* ABO_3 *structure [28]). Pb and O ions are not shown. Reproduced from [23] with kind permission from Springer Science and Business Media*

In *homovalent-substituted complex perovskites*, the substituted cation has the same valence as the substituent. In this condition, no space charge should appear if the ions have the same size. This is, of course, never the case. Ferroelectricity is due generally to a cooperative shift of B-site cations with respect to the surrounding lattice. Larger B-site substituent cations distort the lattice locally and cannot go off-center, which causes the random breaking of the correlated displacement along B–O bond chains [29–31]. As the amount of substituent increases, regions with an accumulated concentration of broken spatial correlation increase in size. Consequently, FE domains are less likely to nucleate, but due to the local distortions caused by cation substitutions, a redistribution of the charges and the formation of local charged centers results. These are sources of local RFs. This kind of RF is assumed to be much weaker than those stemming from heterovalent cation substitution, and in fact the crossover to relaxor behavior occurs only at relatively high doping levels for homovalent substituents [25,26]. Typical examples of this case are $Ba(Sn_xTi_{1-x})O_3$ (substitution by Sn^{4+}) and $Ba(Zr_xTi_{1-x})O_3$ (substitution by Zr^{4+}).

PNRs are a direct consequence of the existence of these random fields. Since correlation between neighboring COR/CDR is dependent on temperature [32,33], PNRs also evolve and increase their mutual interaction with decreasing temperature. At high temperatures, relaxors possess a non-polar PE phase similar to that of normal ferroelectrics – the overall structure is cubic. Upon cooling they transform into an ergodic relaxor state in which PNRs with randomly distributed and non-interacting dipole moments appear. The temperature at which the PNRs start to form is called the Burns temperature (T_B), and is not associated with a definite structural rearrangement of the crystal structure. PNRs at temperatures close to T_B are very dynamic, but their behavior soon starts to slow down as PNRs grow and increasingly interact while the temperature is decreased, until a freezing temperature T_F is reached (normally below room temperature). Below T_F the state is non-ergodic and an FE state can be generally induced (irreversibly) by applying a sufficiently high electric field [23]. Neither T_F nor T_m (the position of the broad and dispersive permittivity maxima) are related to a structural phase transition, even if T_m is of the same order of magnitude as the peaks at the Curie point in traditional FE perovskites. Maxima at T_m are a consequence of the randomness in size distribution and mutual interaction of the PNRs. PNRs can be evidenced experimentally by the deviation of temperature dependences of the refractive index [34,35] or of the thermal expansion coefficient [36] from the behavior predicted for the PE state.

11.3.1 Lead-Based Relaxors

11.3.1.1 $Pb_{1-x}La_x(Zr_{1-y}Ti_y)_{1-x/4}O_3$ (PLZT)

Lead zirconate titanate (PZT) is the most well-known ferroelectric ceramic. It is used in piezoelectric sensor and actuator applications owing to its excellent electromechanical coupling, with d_{33} values peaking (depending on composition) above 600 pC N^{-1} [37]. The properties of PZT are based on a very complicated crystal structure, and depend largely on doping content, ionic size, and bonding character. The maximum response is obtained in the neighborhood of the morphotropic phase boundary (MPB), which occurs for a definite Ti/Zr ratio [37]. In the compositional range around the MPB, the crystal structure of PZT is unclear. The most widely accepted view is that of a finely twinned nanodomain structure, in which rhombohedral, tetragonal, and monoclinic symmetries coexist [38–41]. RS has also been used, confirming that a coexistence of phases is the most probable picture at the MPB [42]. The presence of this structure flattens the free energy surface in the neighborhood of the B-site, thus producing a very high polarizability of the unit cell [43].

Phases in undoped PZT are predominantly FE or PE, and may possess or not an antiferrodistortive (AFD) rotation of oxygen octahedra, which (at low temperatures) doubles the unit cell. This phenomenon can be detected by Raman mode splitting [44, 45]. For Zr contents higher than 90% the antiferroelectric (AFE) structure of $PbZrO_3$ is obtained. Lanthanum (La) doping introduces relaxor behavior. This is due to the La-driven A-site disorder: La^{3+} replaces Pb^{2+} and the charge difference is compensated by $1/2V'_{Pb}$ vacancies. Another mechanism leads to the formation of Ti^{4+} vacancies upon La addition [46]. The presence of these defects disrupts the long-range FE order and ultimately induces a relaxor state as the concentration of La increases [47]. Other effects produced by La addition are the lowering of T_C [48], the decrease of the permittivity maximum, and the induction of transparency (by lowering the optical anisotropy). Therefore, La-doped PZT (PLZT) is used, with varying compositions, in capacitors, transducers, and electrooptic devices [28, 49–51]. PLZT is generally mentioned as PLZT $100x/100y/100(1-y)$, where x and y are the respective atomic fractions of La and Zr. In this section, we shall restrict ourselves to two different Zr contents, one on the Ti-rich side of the phase diagram (PLZT x/40/60) and one on the Zr-rich side (PLZT x/90/10) [47,48].

PLZT x/40/60, for $x = 0$, possesses a tetragonal structure at room temperature and undergoes a first-order transition to the cubic PE state at ~330 °C. La addition causes T_C to decrease down to ~80 °C for $x > 12\%$. Concurrently, the phase transition becomes diffuse, leading to relaxor behavior with PNR size increasing with the amount of La [48, 52]. Buixaderas et al. [48] have examined the Raman spectra as a function of temperature for both FE and relaxor PLZT x/40/60 compositions: 5/40/60 and 15/40/60, respectively (Figure 11.5). The displayed spectra appear consistent with a tetragonal undoped PZT structure at temperatures below RT, but two important differences occur: (i) in 15/40/60, modes much broader than normal are observed. This is due to increased anharmonicity by La addition, while the 15/40/60 sample is closer to the cubic phase at lower temperatures than undoped PZT or PLZT 5/40/60. (ii) The number of modes is higher than predicted by group theory. This aspect pairs with the appearance of a Raman spectrum in both compositions above the Curie point, where the presence of a cubic centrosymmetric structure should forbid Raman activity. Buixaderas et al. [48] were able to explain this phenomenon by combining Raman and IR analyses and performing factor-group analyses for both cubic and tetragonal phases taking into account different cation arrangements, thus highlighting disorder effects. The presence of a Raman signal in the cubic phase is due to symmetry breakdown at the nanoscale. Taking into account short-range off-site displacements of Zr and Ti atoms, the number of IR and Raman active modes calculated by factor-group analysis is close to the number of the observed modes. Concerning spectra below the Burns temperature, the signal is not related to polarization fluctuations [53], since a very similar spectrum can also be obtained above T_B. Therefore, symmetry breakdown due to short-range displacements of cations (promoted by chemical substitution) is the most probable mechanism in these compositions. The number of observed Raman modes never matches perfectly the number of modes predicted by the *modified* factor-group analysis. The reason for this is that some modes can be too weak to be detected or could be hidden in the spectra due to high damping of the vibrations. Unit cell doubling could occur (even on a local scale), with a consequent

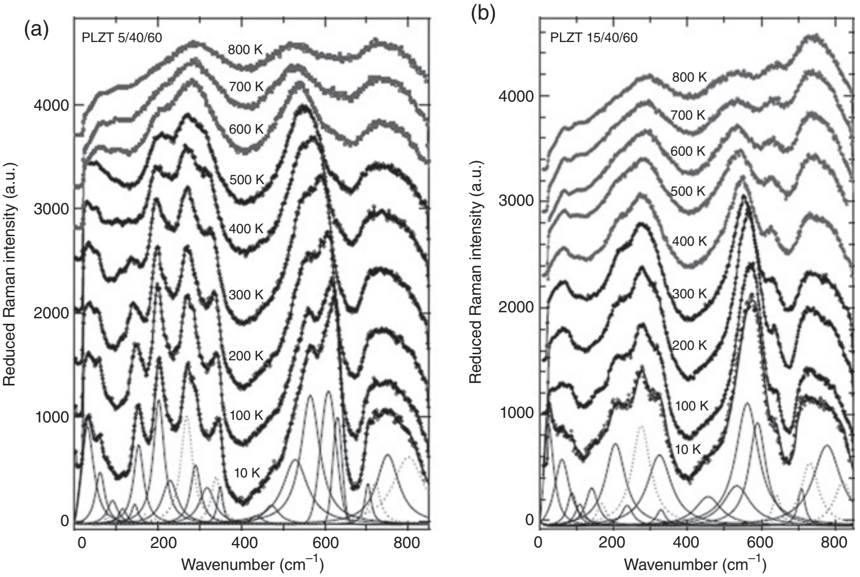

Figure 11.5 *Bose–Einstein corrected Raman spectra of (a) PLZT 5/40/60 and (b) PLZT 15/40/60 as functions of temperature. The fit at 10 K and the oscillators used in the fit are also shown. The dotted peaks refer to modes that are only Raman-active [48]. © IOP Publishing. Reproduced by permission of IOP Publishing. All rights reserved*

increase of the observable Raman modes. Moreover, dynamic disorder in the B-site leads to the appearance of a central mode in the neighborhood of the FE–PE phase transition [48].

The influence of La addition on the Raman spectra of PLZT is generally indirect, related to the induced symmetry changes. However, there is one direct effect, namely the appearance of an extra mode at ~640 cm^{-1}. This mode is not an La-driven A-site vibration as its frequency is too high, but it is due to the presence of Ti and Zr vacancies promoted by La addition. These vacancies affect locally the vibrations of the surrounding oxygen octahedra at high frequencies. Oxygen atoms without one positive charge inside the octahedral are subject to higher repulsion forces because of charge compensation, with consequent weakening of the bonding and decrease of Raman frequency [48]. In other words, this extra mode is due to a sort of two-mode behavior [54] of the oxygen octahedra in the presence or absence of vacancies. Its intensity is directly proportional to La (and thus vacancy) content. At higher La contents (>15%) Mesquita et al. [55] found a direct correlation between the intensity of the E(TO$_3$) mode at ~500 cm^{-1} and the size of La-induced disordered regions, showing this intensity to saturate below T_m in a way similar to the freezing of PNRs. This result may suggest that highly doped PLZT *x*/40/60 may display irreversible field-induced transitions to the FE state below room temperature ($T_m < 0$ °C for $x = 0.21$).

For *PLZT x/90/10*, although the $x = 0$ composition was widely believed to possess FE rhombohedral *R*3*c* structure (double-unit cell) [56], neutron and electron diffraction data [57] suggested that on the Zr-rich side the symmetry is lower than rhombohedral, and pointed out either a monoclinic *Pc* structure or a multiphase system. The latter is indeed the

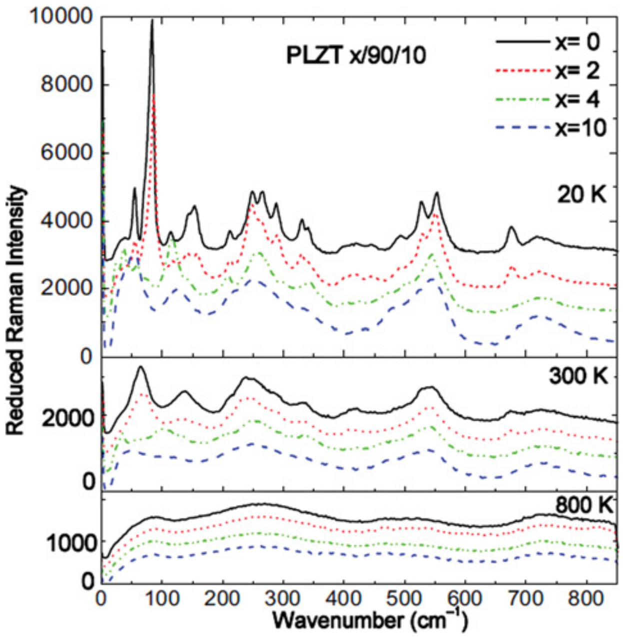

Figure 11.6 *Raman spectra of PLZT x/90/10 at different temperatures. Reprinted with permission from [58]. Copyright [2009], AIP Publishing LLC*

most probable mechanism if La substitution is taken into account; this conclusion has been drawn by dielectric and IR spectroscopy measurements supported by RS [47, 58]. With La addition, the system experiences a crossover from FE to AFE behavior between 2 and 4% of La; above 4% the material is AFE and shows relaxor characteristics. The structure responsible for this behavior is not yet fully clarified, and many researchers invoked a mixture of rhombohedral and orthorhombic phases [59], or an incommensurate modulation along the [110] direction [57, 60]. Buixaderas et al. [47, 58] attempted to clarify this with combined dielectric, IR, and Raman studies. We shall report here on the latter.

The Raman spectrum of PLZT x/90/10 with $x = 0$, 2%, 4%, and 10% is shown in Figure 11.6 at three different temperatures (20 K, 300 K, and 800 K). At 20 K, for low La contents a much higher number of modes is detected, which is compatible with the double-unit cell associated with the rhombohedral $R3c$ symmetry. Above 4% La the number of modes decreases drastically, which confirms that transition to a higher-symmetry tetragonal (AFE) phase occurs. At 300 K the spectra appear damped due to increased anharmonic interactions and the proximity to the cubic phase, whereas above T_C a Raman spectrum can still be measured, which is ascribed to short-range displacements of Ti^{4+} and Zr^{4+} cations.

Temperature-dependent Raman spectra of both PLZT 2/90/10 and 4/90/10 compositions are shown in Figure 11.7(a), whereas in Figure 11.7(b) the phonon modes observed in both Raman and IR measurements are plotted versus T. Transition to the PE phase occurs for both compositions almost at the same temperature, but for 2/90/10 a second transition related to the AFD rotation of oxygen octahedra is also present. The transition was detected by a

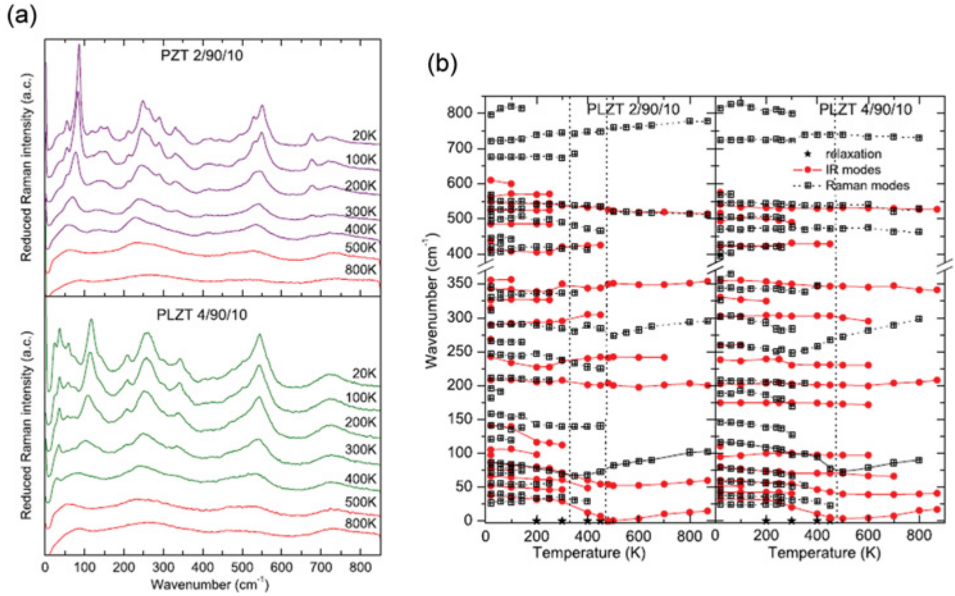

Figure 11.7 (a) Raman spectra of PLZT 2/90/10 and 4/90/10 dependent on temperature. (b) Temperature dependence of the Raman and IR transverse frequencies for PLZT 2/90/10 and 4/90/10. Vertical lines correspond to the phase transition temperatures. Reprinted with permission from [47]. Copyright [2010], AIP Publishing LLC

(~80 cm^{-1}) soft mode anomaly and was confirmed by dielectric measurements. In other words, an intermediate phase with rotated octahedra is present for low La contents, and the transition points tend to merge for higher La contents. A similar effect was pointed out in pure Zr-rich PZT by Cordero et al. [38] using anelastic and dielectric spectroscopy. This suggests that a multiphase system (AFE and FE) is present in PLZT. Soft-mode splitting was detected in PLZT *x*/90/10 [47] and was explained as a two-mode behavior due to the two-cation occupancy of the perovskite B-site. The effect of further La addition on PLZT *x*/90/10 is to reduce the total volume of FE polar regions, causing a modulated AFE phase to extend within the material at the expense of the FE phase. The signature of this in the Raman spectra (cf. Figure 11.7(a)) is the appearance of an intense AFE mode at 100 cm^{-1} in PLZT 4/90/10, which is related to the loss of the strength of the soft mode at 80 cm^{-1} as the FE regions reduce their size. The mode at ~640 cm^{-1} that was detected with La addition in PLZT 40/60 is not so evident here, which is probably related to its shifting with La content [47].

11.3.1.2 $Pb(Mg_{1/3}Nb_{2/3})O_3$ (PMN) and $Pb(Mg_{1/3}Nb_{2/3})O_3$–$PbTiO_3$ (PMN–PT)

Relaxor $(PbMg_{1/3}Nb_{2/3}O_3)_{1-x}(PbTiO_3)_x$ (PMN–PT) materials present a very high dielectric constant with good voltage stability and excellent electrostrictive and piezoelectric properties, and thus often replace PZT and PLZT in multilayer capacitors, actuators, and electrooptic devices, especially in virtue of their low sintering temperature [50]. The parent compound, PMN, possesses the same properties but is less optimized for piezoelectric applications. Structural differences between PMN and PMN–PT are consistent. PMN presents an average cubic $Pm\bar{3}m$ symmetry over the whole temperature range, with a frequency-dispersed permittivity maximum at T_m = 270 K and a field-induced phase transition at ~210 K. This relaxor behavior arises from elliptically shaped PNRs 15 to 25 nm in size superposed on spherically shaped CORs less than 5 nm in size, as determined by TEM analyses [61]. In addition, a phase transition below 225 K was detected by angular dependent Raman measurements isolating a soft mode (at ~26 cm^{-1}) from the dominating Pb^{2+} lattice mode (at ~45 cm^{-1}) [19]. Needless to say, the Raman spectrum in PMN is a consequence of the disordered structure, since in a cubic centrosymmetric crystal no Raman activity should be allowed. PNRs persist in PMN up to above 600 K (T_B = ~615 K at 1 kHz), and this has been confirmed also by hyper-Raman measurements applying Cochran law to a split low-frequency soft mode [62].

$PbTiO_3$ addition lowers the average symmetry of PMN, stabilizing rhombohedral, monoclinic, orthorhombic, and tetragonal phases, depending on temperature and composition. At high temperatures the PMN–PT system possesses a PE cubic phase [64–66]. The Raman spectrum of PMN–PT consists of a series of broad bands (cf. Figure 11.8(a)), which do not change much with temperature variation, similar to other relaxor systems. Specifically, the PMN–PT solid solution is also characterized by the presence of CORs and PNRs, which are sources of short- to long-range intrinsic disorder [2, 67]. CORs in PMN–PT are very complicated due to the high number of different substituent species. There are three different ions at the B site: Nb, Mg, and Ti (cf. Figure 11.8(b)), which constitute sub-μm sized domains rich in one chemical species or the other. RS can detect signals from all these regions, provided that they are of sufficient size (a few nanometers [54]), but the finite size of the

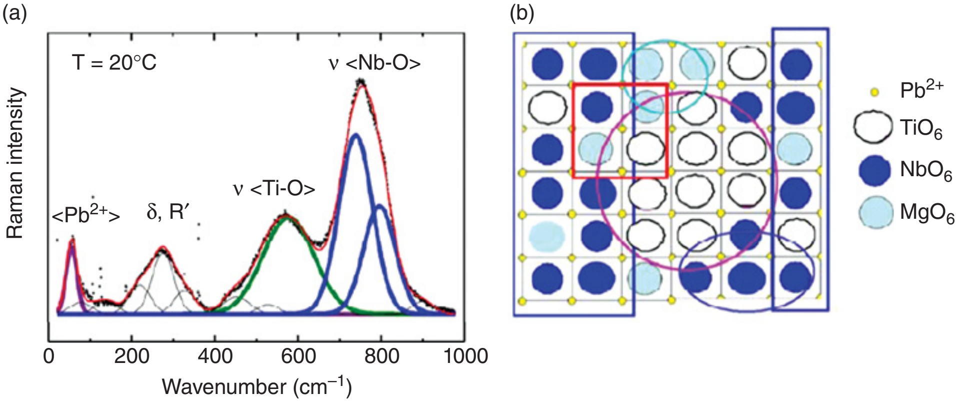

Figure 11.8 *(a) Raman spectrum and spectral decomposition of PMN–PT. Mode assignment is performed according to the sublattice model: ν are BO_6 stretching modes, δ are bending modes, R′ were interpreted as librations and <Pb^{2+}> translations of the lead cation. (b) Schematic of the local distribution of different BO_6 octahedra depending on the different chemical species in PMN–PT: Ti-based, Nb-based, Mg-based and the regions between the "pure" ones [63]*

laser probe (lateral resolution ~0.5 μm) makes it impossible to distinguish between them if their dimensions are smaller than the probe diameter [63]. As shown in Figure 11.8(b), in the case of the investigated PMN–PT, at least four domain types are present: Ti-based, Mg-based, Nb-based, and boundary regions; each can give a Raman spectrum: The higher the distortion from cubic symmetry, the higher the Raman intensity. Moreover, since the Raman cross-section depends mainly on bond polarizability, that is the number of electrons involved in the bond, Raman spectra will not reflect the signature of all regions but only of the ones that possess stronger polarizability [2, 68]. In the case of PMN–PT, chemical bond considerations lead to the following ranking of the expected Raman mode intensities: Nb–O $>$ Ti–O $\gg$ Mg–O. As a consequence, the contribution of Mg-rich regions is too weak to be observed. By comparison with Raman mode assignment in other perovskite compounds, the broad bands of PMN–PT can be roughly divided as follows: the low-frequency region can be attributed to the vibrations of the Pb^{2+} sublattice, the modes from the intermediate-frequency region can be classified as mixed B–O–B bending modes, while those from the high-frequency region as BO_6 stretching vibrations [63].

A more complete assignment has been attempted by Lima and co-workers [69] using lattice dynamical calculations. Their results are displayed in Table 11.1. They also performed a temperature-dependent Raman study in morphotropic PMN–PT and were able to detect a new transition point at ~170 K by studying the anomalous behavior of the 90 cm^{-1} phonon (cf. Figure 11.9). They pointed out that this phonon is twofold degenerate in the tetragonal

Table 11.1 *Experimental and calculated phonon wavenumber, their respective irreducible representations, and tentative assignment of normal modes for tetragonal PMN–PT. Reproduced with permission from [69]. Copyright © [2009] [John Wiley & Sons]*

$PbTiO_3$ [73]	PMN–PT (exp)	PMN–PT (calc)	Irreducible representations	Assignment
	43		?	Lattice
	57		?	Lattice
88 [E(TO$_1$)]	91		E(TO$_1$)?	Lattice
128 [E(LO$_1$)]	137	146	E(LO$_1$)	(Lattice)$^{x+y}$
147 [A$_1$(TO$_1$)]				
189 [A$_1$(LO$_1$)]	208	187	A$_1$(LO$_1$)	(Lattice)^{z}
220 [E(TO$_2$)]				
289 [B$_1$]	265	260	E(LO$_2$)	Oxygen
289 [E(LO$_2$)]	286	260	B$_1$	Oxygen
289 [E(TO$_3$)]				
359 [A$_1$(TO$_2$)]	317		A$_1$(TO$_2$)?	
439 [E(LO$_3$)]	434	425	E(LO$_3$)	B-O
	514		E(TO$_4$)?	
465 [A$_1$(LO$_2$)]	580	589	A$_1$(LO$_2$)	B-O
505 [E(TO$_4$)]				
646 [A$_1$(TO$_3$)]				
723 [E(LO$_4$)]	751	714	E(LO$_4$)	B-O
796 [A$_1$(LO$_3$)]	797	853	A$_1$(LO$_3$)	B-O

? stands for a non-definite assignment

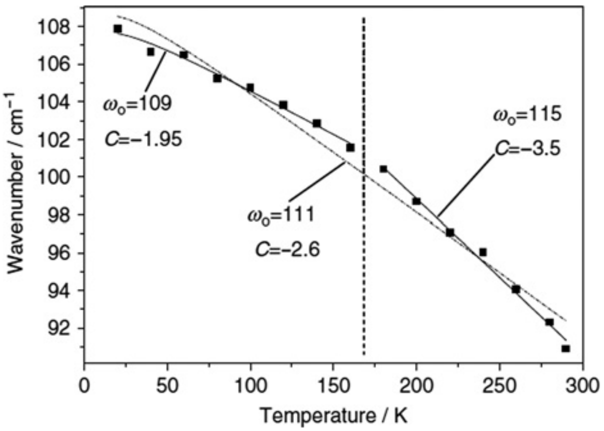

Figure 11.9 *Temperature dependence of the 90 cm^{-1} Raman mode of PMN–PT. The slope change at 170 K underlines a possible structural phase transition. Reproduced with permission from [69]. Copyright © [2009] [John Wiley& Sons]*

phase, whereas it splits into A′+A″ modes in the monoclinic phase. Since the temperature dependence of the center of mass of the band would change sensibly in the presence of a phase transition, they took this anomaly as a signature of the tetragonal–monoclinic transition. This is indeed a practice that recently has become common in the detection of phase transitions in the absence of soft-mode behavior [70–72], and confirms the great role of RS in detecting subtle changes in crystal structure. Concerning PMN and PMN–PT, Raman studies picture a solid with multiscale inhomogeneities, composed of two sublattices with a different degree of order: a Pb sublattice governed by ionic interactions, whose role is mainly in the formation of PNRs, and a BO_6 covalent-bonded sublattice, which determines the short-range structure upon chemical substitution (CORs) [63]. Soft-mode behavior is mainly related to the former structure [61], whereas the CORs are responsible for the disordered signature and the other phonon anomalies. Both mechanisms are at the basis of its peculiar dielectric and electromechanical behavior.

11.3.2 Lead-Free Relaxors

11.3.2.1 $BaTiO_3$ (BT)-Based Solid Solutions

In this section, we focus on A- or B-site substituted barium titanate (BT) and examine how the changes in the Raman spectrum reveal the signature of phase transitions and even subtle structural changes in function of both composition and temperature. Hence, the Raman spectrum of BT is the starting point of our consideration. Cubic phase $BaTiO_3$ has five atoms in the primitive unit cell; the expected phonon modes are three triply-degenerate F_{1u} modes and one triply-degenerate F_{2u} optical mode: $\Gamma_{OPcub} = 3F_{1u} + F_{2u}$. The modes with F_{1u} and F_{2u} symmetry are not Raman active, so first-order vibrational bands in Raman spectra are not expected for cubic $BaTiO_3$ [74]. In the tetragonal phase, because of the shift of the titanium ion with respect to the oxygens, the F_{1u} modes split into three A_1 modes and

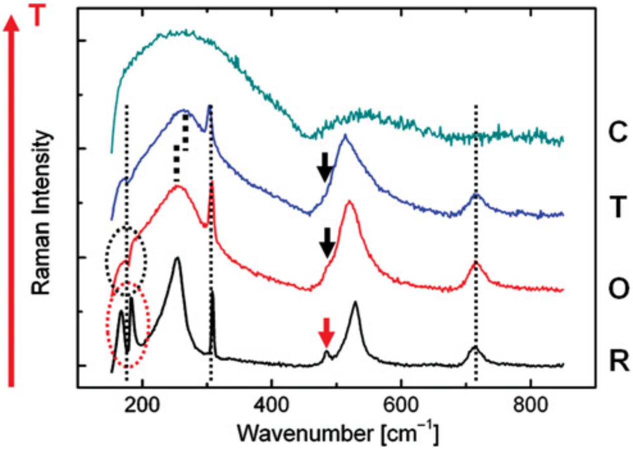

Figure 11.10 Raman spectra of pure, polycrystalline BT ceramics in the rhombohedral (R), orthorhombic (O), tetragonal (T), and cubic (C) phases. Thin, dashed vertical lines indicate modes present in FE phases. Circles indicate low-frequency modes that become damped in the O phase; arrows indicate the mode at 490 cm^{-1} that disappears in the tetragonal phase. The appearance of a spectrum in the C phase is a result of local spatial disorder. Temperature increases from the bottom to the top of the diagram

three (doubly-degenerate) E modes, while the F_{2u} mode splits into one B_1 and one (doubly-degenerate) E mode [75]: $\Gamma_{OPtet} = 3A_1 + B_1 + 4E$. Due to long-range electrostatic forces, the A_1 and E optical modes are further split into transversal (TO) and longitudinal (LO) components. All Raman active modes in the tetragonal phase can be represented as follows: $\Gamma_{OPtet} = 3[A_1(TO) + A_1(LO)] + B_1 + 4[E(TO) + E(LO)]$. In practice, the measured Raman spectra of the BT tetragonal phase in ceramics present four dominant bands at 250 (A_1 (TO)), 307 (B_1, E (TO + LO)), 515 (A_1(TO), E (TO)) and 715 cm^{-1} (A_1(LO), E(LO)) [75–77]. In randomly oriented polycrystalline ceramics the directions of phonon wave vectors are randomly distributed with respect to the crystallographic axes and thus quasi-modes rather than polar phonons are observed. For this reason, Raman lines appear broader than in single crystals and none of them possesses true A_1, E, or B_1 symmetry [78, 79].

At the liquid N_2 temperature (~80 K), BT is in a long-range rhombohedral FE structure and the Raman spectrum (cf. Figure 11.10) presents sharp modes due to the reduction of anharmonic interactions and the slowing down of dynamic disorder. Sharp peaks appear below 200 cm^{-1} and at ~490 cm^{-1}, and are regarded as signatures of the rhombohedral phase [5, 80]. Peaks at ~305 cm^{-1} and ~715 cm^{-1} originate from the correlated displacement of the Ti cation with respect to the oxygens; they are present in all FE phases of BT and are thus considered an indication of the FE state of the material [26, 80]. The dip at 180 cm^{-1} was reported as being caused by antiresonance between the narrow $A_1(TO_1)$ and broad $A_1(TO_2)$ modes [81]. An alternative explanation invokes an anharmonic coupling of three A_1 phonons [77, 82]. This feature also appears only in FE phases. The very sharp mode at ~305 cm^{-1} is the B_1 "silent" mode [83]. With increasing temperature, the sharp modes below 200 cm^{-1} become damped; the same happens to the mode at 490 cm^{-1}, which also shifts to higher wavenumbers. The spectrum is broader; this is the signature of the orthorhombic phase. Further increasing T above 0 °C, the modes below 200 cm^{-1} become indistinguishable (except from the dip at 180 cm^{-1}), there is a shift of the main feature at 250 cm^{-1} to 270 cm^{-1}, and the mode at 490 cm^{-1} becomes undetectable. This is the spectrum of tetragonal BT. Increasing T above the Curie point, a spectrum composed by two broad bands is observed, although due to the cubic centrosymmetric structure Raman activity should be forbidden. This spectrum is due to the presence of short-range disorder in the cubic phase. Activation of phonons is possible in this case within π/d of the center of the Brillouin zone, where d is the length scale of the disorder [15]. Since d is smaller than the lattice parameter, these modes are not properly first-order (they do not originate from the Γ-point of the Brillouin zone), but neither are they second-order modes, since their activation does not strictly require a two-phonon process. Similar disorder-related effects appear in all perovskites and could be due either to cation displacements (CDs) in pure compounds, such as the case of BT, or to chemically ordered or disordered regions (CORs, CDRs) when cations of different charge or ionic size are substituted in the crystal. Only the latter could give rise to PNRs as found in relaxors. Although in these systems the average crystal structure is cubic, the detection of a Raman spectrum is the proof that local spatial disorder is present in the material. There is no easy way to distinguish between CDs, CORs, and CDRs with RS, but one can use the rule-of-thumb that CORs and CDRs will generally produce more lattice distortion than CDs or would be present on a larger spatial scale, thus producing higher coherency of vibration. Consequently, Raman spectra from CORs and CDRs should appear sharper and more intense than those from CDs. Additionally, in some cases formation of chemical clusters like CORs or CDRs produces extra modes in the Raman spectrum. This does not happen for CDs.

In the following, we shall concentrate only on a few systems to give an example of how the Raman spectrum changes with substitution-induced structural rearrangements. We chose the following systems (cf. Figure 11.11):

$BaSn_xTi_{1-x}O_3$ (BST) – homovalent substituted at the B-site (Sn^{4+})
$BaZr_xTi_{1-x}O_3$ (BZT) – homovalent substituted at the B-site (Zr^{4+})
$(Bi_{1/2}Na_{1/2})_xBa_{1-x}TiO_3$ (BBNT) – twofold heterovalent (Na^+ and Bi^{3+}) substituted at the A-site
$Ba_{1-x}Bi_xTi_{1-x}Yb_{x/2}Fe_{x/2}O_3$ (BBTYF) – simultaneous heterovalent substituted at the B-site (Yb^{3+}, Fe^{3+}) and at the A-site (Bi^{3+})

Depending on composition (x), some common traits can be found in the development of Raman spectra for all these systems, which reflect the structural changes taking place upon chemical substitution (cf. Figure 11.11):

Loss of ferroelectricity. By increasing x above a certain amount, A- or B-site substitution disrupts the long-range cooperative displacement of Ti atoms and suppresses FE order. This produces at room temperature disappearance of all peaks belonging to the FE phases, which are related with Ti long-range order. These are the interference dip at 180 cm^{-1}, the "silent" mode at 305 cm^{-1}, and the mode at 715 cm^{-1}. This behavior can be seen, for instance, in BST at $x = 0.15$, in BBNT at $x = 0.15$, and in BBTYF at $x = 0.06$.

Increased disorder. Substitution promotes the formation of CORs and CDRs, which can be randomly and evenly distributed in the lattice or segregated. In both cases, lattice disorder increases with x, which is a direct consequence of the introduction of ions with different

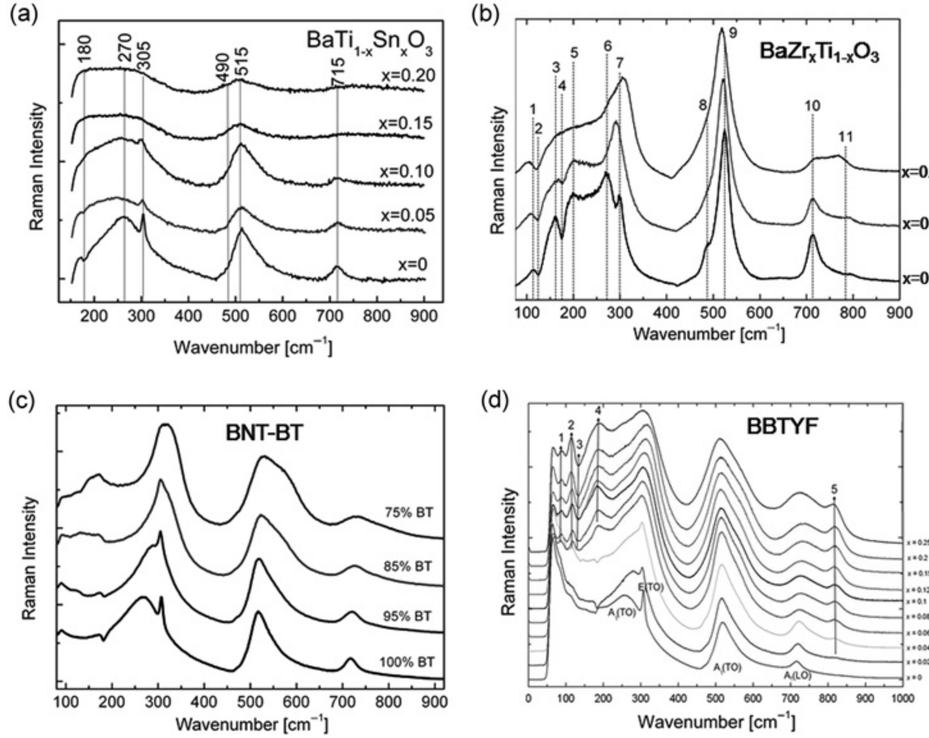

Figure 11.11 *Composition dependence of the Raman spectrum of several BT modifications. (a) BST (reprinted with permission from [3]. Copyright [2012], AIP Publishing LLC); (b) BZT [26] (© IOP Publishing. Reproduced by permission of IOP Publishing. All rights reserved); (c) BBNT (reprinted with permission from [84]. Copyright [2015], AIP Publishing LLC); (d) BBTYF (reprinted from [85], Copyright (2013), with permission from Elsevier)*

charge or ionic size, producing local lattice distortion by electrical or steric effects. The trace of this is seen in the Raman spectra: with increasing x, much broader modes are observed over the whole spectral range.

Shift of the BO$_6$ polar phonons. The introduction of an ion of different size at the A- or B-site changes the local crystal environment and influences the strength of the bonds. This produces a shift in the phonon modes because of changes in the interatomic spring constant [86]. This is particularly true if Bi^{3+} is the substituent atom because of the lone-pair effect. Hybridization with neighboring oxygen atoms in fact produces a considerable off-centering of the Bi cation [87], which impacts also on B-site vibrations, namely on the polar Ti–O vibration (the mode at 270 cm^{-1}) and on BO$_6$ vibrations (at 515 and 715 cm^{-1}) [70, 84, 88, 89]. These changes are evident in both BBNT and BBTYF. It should be noted that also in BZT the Ti–O phonon at 270 cm^{-1} shifts with increasing x. This is obviously not related to a lone-pair effect, but is rather due to the ionic size difference between Zr^{4+} and Ti^{4+} (0.72 and 0.605 Å, respectively [26]). This produces a much smaller change in the Raman spectrum: the shift of the Ti–O phonon is ~20 cm^{-1} per

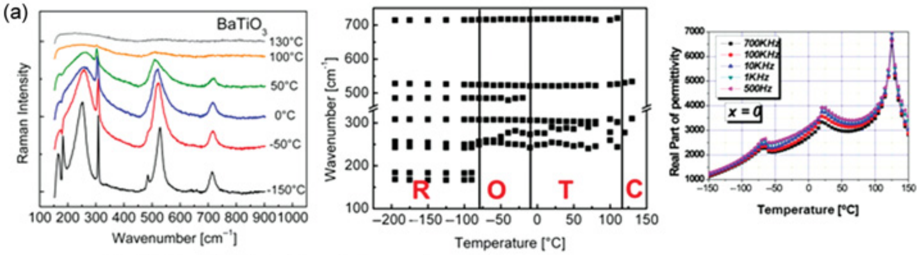

$BaTiO_3$: Well-defined phase transitions

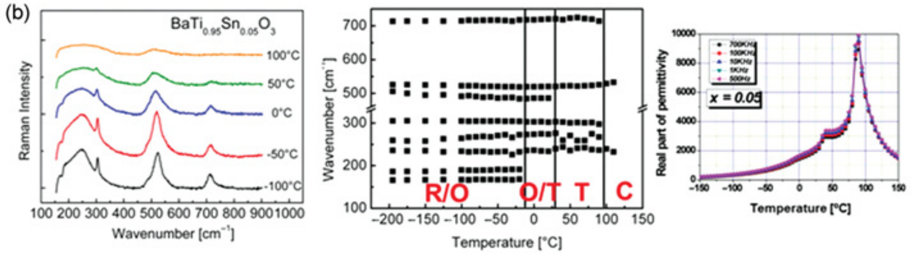

$BaSn_{0.05}Ti_{0.95}O_3$: R-O-T transitions are diffuse (phase coexistence)

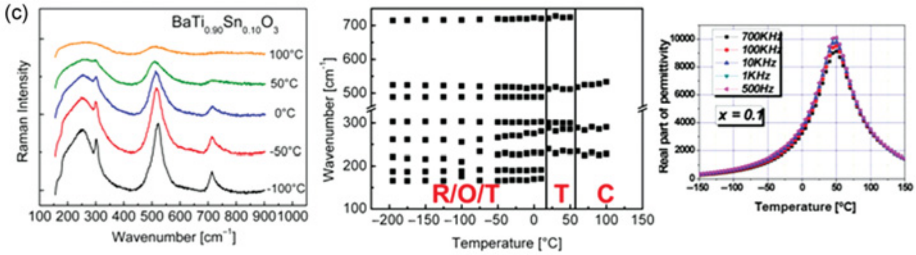

$BaSn_{0.10}Ti_{0.90}O_3$: R-O-T transitions are diffuse (phase coexistence)

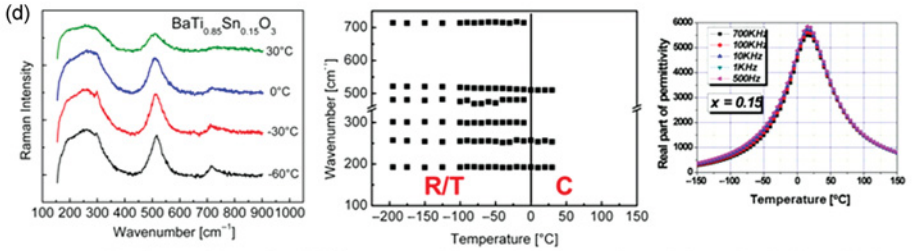

$BaSn_{0.15}Ti_{0.85}O_3$: Diffuse transition at T_c, ferroelectricity only below RT

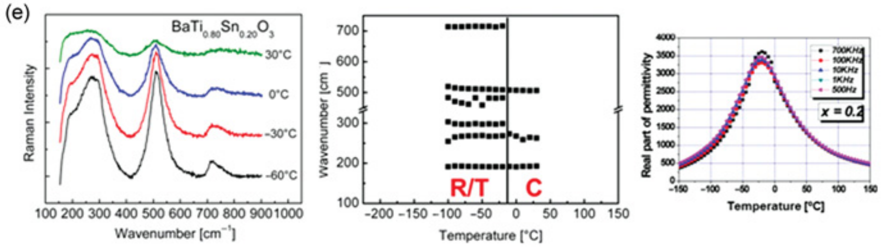

$BaSn_{0.20}Ti_{0.80}O_3$: Diffuse transition but no ferroelectricity (relaxor)

20% substituent content (it is ~40 cm^{-1} for the same amount of substituted Bi) and the BO_6 modes are unaffected.

Formation of chemical clusters. Increased substitution leads to the formation of CORs or CDRs. If these regions are of sufficient size (above 1 nm), their coherent scattering at frequencies different from those of the pure compound produces extra modes (a process similar to the defect-induced local modes). This is especially evident for materials substituted on the A-site like BBNT or BBTYF, for which extra peaks appear in the region of A-site vibrations (below 150 cm^{-1}). The presence of several peaks in materials with multiple substitutions like BBNT and BBTYF proves segregation of these constituents into chemical clusters rich in Bi, Ba, or Na. In fact, due to the different ionic size and mass, these constituents vibrate at different frequencies (the strength of the bond is different), which produces a definite peak (two-mode behavior [54]). In BZT, no additional peak can be observed, but a prominent dip appears at 125 cm^{-1}. This feature is an interference effect between two B–O polar phonons produced by octahedral environments that have at the B-site cations of different size [90]. Thus, this confirms that in BZT Zr-based and Ti-based octahedra retain their individuality and can cluster together, forming, respectively, non-polar and polar CORs [26]. This result in BZT has been also confirmed by EXAFS and neutron diffraction analyses [91,92].

It is clear that Raman spectra, if correctly interpreted, have a tremendous potential to elucidate compositional-driven changes in substituted BT systems. In particular, they give information on the FE character of the material. The crossover to relaxor behavior and the arrangement of phases as a function of composition can be investigated with temperature-dependent measurements, and we shall explain this by comparing results on two similar systems: BST and BZT.

$BaSn_xTi_{1-x}O_3$ (BST). In pure BT, by increasing T, as expected, a sharp border between the rhombohedral (R), orthorhombic (O), tetragonal (T), and cubic (C) phases can be observed (cf. Figure 11.12). The Raman spectrum in the cubic phase comes from CD. Increasing the substituent content, the border between long-range phases smears out, and only diffuse phase transitions are measured even with the smallest amount of Sn. Diffuseness increases with x and mirrors the dielectric behavior reported on the third column of Figure 11.12 for all compositions. The diagrams in the middle report the Gaussian–Lorentzian fit of the main phonon modes. It is clear that with higher x it becomes increasingly difficult to distinguish between R, O, and T phases, so it is supposed that a mixture of phases is present. In addition, the boundary to the C phase (the PE phase) shifts to lower temperatures, mirrored by the shift of the permittivity maximum, T_m. Consequently, the FE–PE crossover temperature

◄

Figure 11.12 *Temperature- and composition-dependent Raman and dielectric study in BST. (a) Pure BT; (b) BST with 5% Sn; (c) BST with 10% Sn; (d) BST with 15 % Sn; (e) BST with 20% Sn. (First column) Raman spectra of BST as a function of temperature. (Second column) Peak positions versus temperature for all observed modes; vertical lines indicate phase transitions, whereas phases are indicated with bold letters (R = rhombohedral, O = orthorhombic, T = tetragonal, C = cubic). (Third column) Temperature and frequency dependence of the real part of the dielectric permittivity in the investigated compositions. Reprinted with permission from [3]. Copyright [2012], AIP Publishing LLC*

decreases with x. It has to be mentioned that for the $x = 0.20$ composition the FE modes at 180 and 305 cm^{-1} were not detected. However, the mode at 715 cm^{-1} was still prominent at low temperatures, while an overall suppression of the Raman signature across T_{m}, albeit diffuse, can be noticed. This can be interpreted as a diffuse transition from a mixed non-FE R/T structure to a cubic structure, whereby XRD indicated an average cubic structure (*Pm*–3*m*) for all temperatures. In the cubic phase, for all compositions, a Raman spectrum can still be measured (also from CORs or PNRs, since it is more intense than in pure BT), but its intensity is considerably lower than below T_{m}. Hence, in BST T_{m} seems to be related to a phase transition involving the creation of a low-symmetry mixed structure that probably originates from the chemical arrangement. This has also been suggested in BST by dielectric spectroscopy and first-order reversal curves (FORC) measurements [3] and is similar to the view of Fu et al. for PMN [61]. The $x = 0.20$ composition presents incipient relaxor behavior, and this is also reflected in the Raman modes, since the overall spectral signature within the mixed R/T phase is the same and changes only by (diffuse) transition to the C phase.

$BaZr_xTi_{1-x}O_3$ (BZT). Temperature-dependent Raman spectra of BZT ceramics with $x = 0.10$, 0.20, and 0.40 are presented in Figure 11.13. All compositions show an intense Raman spectrum well above T_C, that is in the cubic PE phase, confirming the presence of

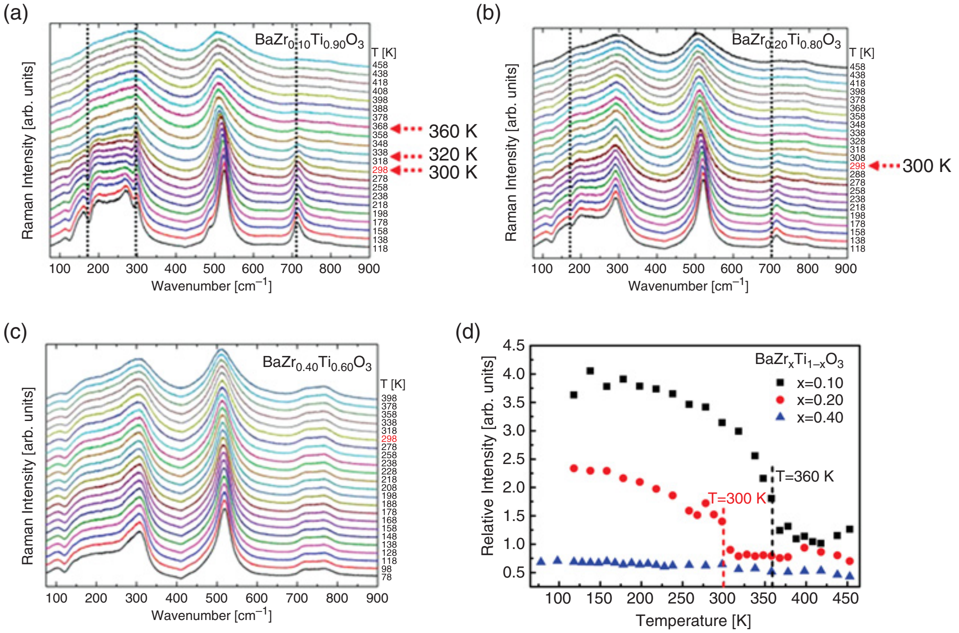

Figure 11.13 *(a), (b), and (c) Temperature dependence of Raman spectra in BZT with 10, 20, and 40% Zr content, respectively. Arrows indicate the observed phase transitions. (d) Relative intensity of the two modes at 715 and 780 cm^{-1} versus temperature. Vertical dashed lines indicate the temperature of the FE–PE phase transition. The composition with 40% Zr is in the relaxor state, as no transition is detected [26]. © IOP Publishing. Reproduced by permission of IOP Publishing. All rights reserved*

CORs. The Raman spectra of BZT with $x = 0.10$ shows R symmetry up to room temperature. Above this temperature the Raman spectrum resembles that of the O phase of BT (absence of the "triple mode" below 200 cm^{-1}, shift of the peak at ~490 cm^{-1}). Increasing T above 318 K the spectrum matches that of the T phase of BT (shift of the mode at 270 cm^{-1} to higher wavenumbers). Coexistence of O and T phases cannot be excluded in this temperature range. The transition to the C phase is diffuse, which is expected for a solid solution (cf. BST) and is completed by 358 K, as signaled by the simultaneous disappearance of the interference dip at 180 cm^{-1}, the "silent" mode at 305 cm^{-1} and the mode at 715 cm^{-1}. This phase sequence is typical for BZT [4, 93, 94] and matches the results of Rietveld refinements on the same compositions [26].

Upon increasing Zr content ($x = 0.20$), Raman data suggest a coexistence of R and C phases at room temperature. Here the transition to the PE phase is diffuse. The absence of the 'silent' mode complicates the observation of the transition to PE, although the presence of both the dip at 180 cm^{-1} and the mode at 715 cm^{-1} suggests that FE order is present. These two features disappear above 300 K, which is then taken as FE–PE transition temperature. A very different picture is offered by the Raman spectrum of BZT with $x = 0.40$ in dependence of T. Raman peaks belonging to the R symmetry are not seen for the whole temperature range. In addition, the Raman spectra look alike at all temperatures; that is no FE–PE transition is detected by RS. This, together with the prominent dip at 125 cm^{-1} that indicates B-site cation ordering, hints at a possible relaxor state. Note that cation ordering and the absence of a clear structural phase transition are characteristics of relaxor systems [23, 27]. Rietveld refinements on the same composition also suggest a relaxor state [26]. The precise FE–PE transition point and the crossover to relaxor behavior can be detected by monitoring the relative intensity of the Raman features above 700 cm^{-1}. The mode at 715 cm^{-1} is in fact a mixed A_1 and E mode associated with the breathing of BO_6 octahedra in the FE phase [5, 95], whereas the mode at 780 cm^{-1} is a stretching mode of BO_6 octahedra related to A- or B-site substitution of BT. The latter may appear regardless of the presence or absence of an FE phase [26, 95]. The relative intensity of these two modes (I_{715}/I_{780}) can thus be used as an indicator of the FE state of the material. Values of (I_{715}/I_{780}) much higher than unity indicate a highly coherent long-range FE phase. Values closer to unity indicate a system with only short-range correlation of dipoles. Values of one or lower are indicative of a PE system. Figure 11.13(d) shows a plot of (I_{715}/I_{780}) versus temperature for the present BZT compositions. In BZT with $x = 0.10$ and $x = 0.20$ the (I_{715}/I_{780}) intensity ratio initially decreases smoothly with temperature, then takes an abrupt drop at 358 K and 298 K for $x = 0.10$ and $x = 0.20$, respectively, remaining constant with a value close to unity at higher temperatures. These temperatures correspond to the FE–PE transitions for these compositions. The overall (I_{715}/I_{780}) intensity ratio observed for BZT with $x = 0.20$ is lower than for BZT with $x = 0.10$, suggesting a lower FE degree in the former. When $x = 0.40$, the (I_{715}/I_{780}) intensity ratio stays constant and below one across the whole temperature range. This suggests that this composition is PE and also does not exhibit a structural phase transition with changing temperature, in line with the findings of the Rietveld refinements [26]. This is indeed a feature of relaxor systems and explains the dielectric properties of Zr-rich BZT compositions [27, 96]. By monitoring the integrated intensity of BO_6 phonons it is possible to determine the size evolution of local order in relaxor systems, including BZT [27, 93]. An intensity plateau is generally reached for low temperatures, indicating the temperature at which local order freezes. In BZT this happens at around 150 K [26] and the overall size evolution (and symmetry) was confirmed by *ab initio* calculations [97, 98] and synchrotron XRD results [26].

The detected transition temperatures correspond to the maximum of the dielectric permittivity of the respective BZT ceramics, and are close to the values reported in previous dielectric and Raman studies [4, 93, 94]. Also in the case of BZT, RS highlights that a combination of local polar and chemical order is at the basis of the observed dielectric behavior.

These considerations about BST and BZT are generally valid for all A-site and B-site substituted BT. In summary, substitution produces (i) a shift of the FE–PE transition temperature to lower values; (ii) increased disorder and diffuseness of phase transitions, which is related to phase coexistence or the formation of CORs and CDRs, and (iii) as a consequence, relaxor behavior is induced.

The compositional threshold at which relaxor behavior appears depends on whether the substitution is homo- or heterovalent. In heterovalent substitution, it is the difference in charge that produces polar regions; in homovalent substitution, this is due to the difference in ionic size. The former effect (charge-driven) is much stronger, as pointed out by Kleemann [25] and Buscaglia et al. [26], and thus induces relaxor behavior for lower substituent contents.

Table 11.2 reports the transition temperatures and the character of the transition for many differently substituted BT solid solutions. Its scope is to provide a comprehensive picture of these systems at one sight. The included results were obtained by different authors and different groups, also on the same systems.

11.3.2.2 $(Bi_{1/2}Na_{1/2})TiO_3$ (BNT) and Solid Solutions

Bismuth sodium titanate, $Bi_{1/2}Na_{1/2}TiO_3$ (BNT), is a complex perovskite that recently attracted much attention after the report of very high field-induced electromechanical strain for some of its solid solutions [100, 101]. The material is thus very promising for lead-free actuator applications. The crystal structure of BNT and its solid solutions is quite complex. At room temperature, pure BNT possesses an FE rhombohedral phase ($R3c$). Upon A-site substitution, this phase evolves into a tetragonal ($P4bm$) one [102], forming a morphotropic phase boundary (MPB) in between [103]. It was demonstrated that this MPB is different from that of PZT and can be understood as a high-temperature polymorphic phase transition that is driven down to RT by doping [104]. Consequently, this MPB is not temperature invariant but occurs over a wide temperature range, leading to strong temperature dependences of the dielectric and electromechanical properties. Phase evolution has been confirmed by high-resolution XRD and neutron scattering techniques [54,105–107]. Transmission electron microscopy (TEM) measurements indicated a stronger unstable nature of BNT: different researchers have found different symmetries for the same nominal compositions, both within the same sample [107, 108], and even within the same grain [109, 110], forming in some cases a core–shell structure [111]. In other words, there is evidence that the room-temperature phase is composed of three different symmetries ($Pm\bar{3}m$, $P4bm$, and $R3c$) [110, 112] that coexist without macroscopic separation, which are very difficult to detect with traditional diffraction methods. RS can be used to detect structural changes in BNT, and in fact Raman studies have confirmed the above-mentioned results in function of composition in BNT-based solid solutions [54,103,113], also allowing the MPB (for BNT–BT) to be located [103, 114].

Table 11.2 *Summary of phase transition temperatures and of the character of the phase transition for various A-site and B-site substituted BT compositions. "n.d." stands for "non-detected"*

System	Substituents	Composition (x)	Transition points (notes)
$BaSn_xTi_{1-x}O_3$ (BST) [3]	Sn^{4+} (B-site homovalent)	$x = 0.05$	R–O (diffuse) O–T, 15–30 °C T–C, 95 °C
		$x = 0.10$	R–O (diffuse) O–T, 10 °C T–C, 50 °C
		$x = 0.15$	R–O n.d. O–T (diffuse) T–C, –5 °C
		$x = 0.20$	R–O n.d. O–T (diffuse) T–C (diffuse)
$BaZr_xTi_{1-x}O_3$ (BZT)	Zr^{4+} (B-site homovalent)	$x = 0.05$	O–T, 28 °C [80]
		$x = 0.10$	T–C, 81.5 °C (Pechini method) [4] 85 °C (solid-state) [26]
		$x = 0.15$	R–O/T, –193 °C [80] T–C, 47 °C [80], 50 °C (Pechini method) [4]
		$x = 0.20$	T–C 25 °C (Pechini method) [4] 25 °C (solid-state) [26]
		$x = 0.25$	T–C, 7 °C [80]
		$x = 0.35$	T–C n.d. [80]
		$x = 0.40$	T–C n.d. [26, 96]
		$0.5 < x < 1$	T–C n.d. [26, 96]
$BaCe_xTi_{1-x}O_3$ (BCT) [99]	Ce^{4+} (B-site homovalent)	$x = 0.06$	O–T, 0 °C T–C, 120 °C
		$x = 0.10$	n.d.
		$x = 0.20$	n.d.
$(Bi_{1/2}Na_{1/2})_xBa_{1-x}TiO_3$ (BBNT) [84]	Bi^{3+} (A-site heterovalent) Na^{+} (A-site heterovalent)	$x = 0.05$	T–C, 150 °C
		$x = 0.15$	T–C, 180 °C (diffuse)
		$x = 0.25$	T–C, 205 °C (diffuse)
$Ba_{1-x}Bi_xTi_{1-x}Yb_{x/2}Fe_{x/2}O_3$ (BBTYF) [85]	Bi^{3+} (A-site heterovalent) Yb^{3+} and Fe^{3+} (B-site heterovalent)	$x = 0.02$	T–C, 117 °C
		$x = 0.04$	T–C, 90 °C
		$x = 0.06$	Diffuse
		$x > 0.08$	n.d.

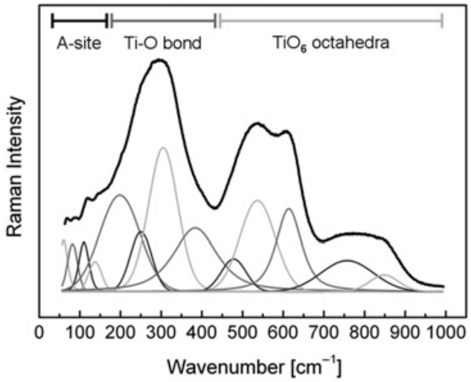

- < 150 cm^{-1}: **A-O bonds (Na-O, Bi-O)**
- 200 - 400 cm^{-1}: **Ti-O bond**
- High-frequency bands: TiO$_6$ **polyhedral vibrations** (oxygen atoms)

Figure 11.14 *Raman spectrum of BNT (doped with K and Li) and mode assignment. Adapted with permission from [89]. Copyright © [2012] [WILEY-VCH Verlag GmbH & Co. KGaA, Weinheim]*

More difficulties have been encountered by researchers in studying the temperature dependence of BNT and its solid solutions. The material loses its ferroelectric character well below the Curie point, at a temperature that is universally known as the "depolarization temperature", T_d. This loss in long-range ferroelectricity is not related to a macroscopic first-order phase but rather to an increase in short-range disorder leading to depolarization [70, 89, 107, 115]. Temperature-dependent Raman analyses based merely on the observation of the spectral signature were not able to detect such subtle structural changes [103]. The Raman spectrum of pure BNT is in fact dominated by broad bands originating from the intrinsic spatial disorder (cf. Figure 11.14, reporting also mode assignment [89]). Raman signals from second phases of nanometer scale but with the same correlation length are superimposed on this overall broad signal [44, 63, 95, 116] and are difficult to distinguish, unless a more detailed analysis on specific phonon modes is carried out [6, 54, 117–119].

An example of this kind of analysis is the study Aksel et al. [70] carried out on undoped BNT. By modeling the temperature dependence of the Ti–O (A_1-type) phonon at ~270 cm^{-1} taking into account anharmonic phonon behavior [120] (cf. section 11.4.1.2.), they were able to show that the depolarization temperature corresponds to an anomaly of this phonon mode (cf. Figure 11.15). This anomaly can be related to changes in the Ti–O bond upon nucleation of a different phase. The presence in the lattice of short-range domains with (non-polar *P4bm*) tetragonal phase produces the local reorientation of A site cations along the [001] pseudocubic direction. This is expected to influence the strength of the Ti–O bond, thus causing the observed phonon anomaly at T_d. Domain nucleation is at the basis of depolarization. This conclusion is supported by synchrotron XRD studies [70] and TEM analyses [107].

A possible explanation for the nucleation of this phase as a function of temperature and also for the high field-induced strain has been suggested by Schütz et al. in a K-doped BNT composition, also by RS [89]. By monitoring the peak position of the A-site mode

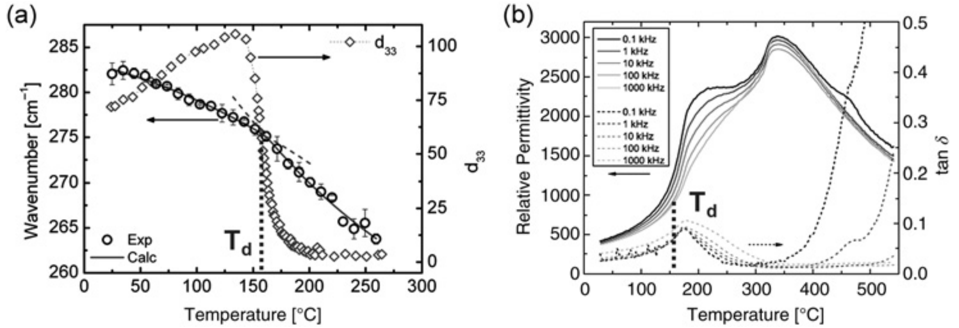

Figure 11.15 *(a) Phonon wavenumber versus temperature of the Ti–O phonon at ~270 cm^{-1}, plotted together with the macroscopic depolarization (d_{33} versus T). The depolarization temperature, T_d, corresponds to an anomaly in the phonon behavior. Solid lines show fitting by the Balkanski formula (cf. [70] and Equation (11.5)). (b) Temperature and frequency dependence of the real part of the dielectric permittivity and loss tangent for the same composition. T_d is indicated by an anomalous peak in the loss tangent and consequent frequency dispersion of the permittivity. Reprinted with permission from [70]. Copyright (2012) by the American Physical Society*

related to Bi–O vibrations (at ~65 cm^{-1}) as a function of temperature and applied field, they were able to observe phonon anomalies in correspondence of T_d and of changes in the electromechanical regime. This suggests an involvement of the Bi–O bond in the short-range phase rearrangements, possibly through a weakening of the Bi–O hybridization.

In BNT-based materials, RS has to be taken as a complementary method. The Raman spectrum of the pure compound, in fact, is already affected by disorder effects. With respect to pure BT, for which the spectral signature greatly changes with phase transitions, a mere visual comparison is not sufficient for BNT. Therefore, a more detailed analysis employing the principles of hard-mode spectroscopy (i.e. study of phonon position, intensity, and width in dependence of the relevant physical quantity) [22] is necessary.

11.3.3 Wrap-Up: Raman Analysis of Relaxors

RS is very powerful for the study of relaxor systems. As can be deduced from the above sections, its short-range sensitivity allows the detection of structural features complementary to other techniques like XRD. The most important result of RS is the detection of transition points between structural phases and the crossover to PE phases. Raman can also give information on the order and disorder on the short range and on phase coexistence. All these aspects contribute to the electromechanical and dielectric responses of the materials. The following considerations can be drawn in relaxors:

- Temperature-dependent RS can discern between FE and relaxor states. FE systems generally have first-order phase transitions that can be detected as the sudden appearance/disappearance/shift of phonon modes by increasing/decreasing temperature. They also display soft-mode behavior. Incipient relaxor systems, on the other hand, have only diffuse phase transitions and full relaxors display the same spectrum from low to very high temperatures [3, 26, 27, 80].

- The presence of cation disorder (CD) and CORs/CDRs can be detected by Raman experiments. Despite the overall cubic structure of relaxors, CD and CORs/CDRs break the local symmetry and activate order- or disorder-related Raman modes that should normally be forbidden in a cubic centrosymmetric structure. Chemical clusters can be detected if their size exceeds 1 nm. The measurable spectrum in relaxors is much more intense than the one appearing, for instance, in PZT and BT above the Curie temperature, which is due to CD only. This means that Raman is capable of distinguishing CD and chemical clusters, given the bigger size and higher coherency of scattering of the latter.
- The growth and the freezing temperature of local order can be determined by RS. Since the intensity of Raman modes is dependent on the size of coherently scattering regions through the fluctuation–dissipation theorem [93, 121], increasing intensity with decreasing T indicates local order growth. Below T_F the intensity saturates and reaches a plateau.

11.4 Raman Analysis of Nanostructured Ferroelectrics

FE materials are very sensitive to electromechanical boundary conditions because of long-range electrostatic interactions and the high correlation between polarization and strain [122]; consequently, ferroelectricity is influenced by grain size due to the constraint posed by grain boundaries on strain, polarization, and electrostatic forces. In general, there is a critical grain size below which the FE phase becomes unstable, and transition to the PE phase occurs at room temperature [18, 123–125]. In grains larger than the critical size, in the FE phase the typical polydomain structure is obtained to minimize electrostatic and elastic energies [123]. On the other hand, in grains smaller than the critical size, the polydomain structure cannot fully compensate for stresses that are present near the edges, and it becomes energetically unfavorable [126]. This can induce a macroscopic PE state even if local FE distortions may be present. Many authors tried to define a limiting grain size for the disappearance of ferroelectricity. A few tens of nanometers was proposed as the critical crystallite size in the case of BT [122,123, 127–130], whereas some authors suggested that there is no particular size at which long-range polar order vanishes, but instead a gradual loss of coherency of the structural distortion, which leads to an average cubic phase as the crystal dimension decreases [131–133]. Since RS is sensitive to short-range order, observing a Raman spectrum in grains with a certain size would raise expectation of finding macroscopic FE behavior. However, this is not always backed up by electrical measurements, especially in the case of nanopowders [127]. This is because a distortion on the short range is not always related to macroscopically measurable ferroelectricity, similar to the scenario previously described for the PE phase in BT above the Curie point. Raman measurements represent the structure of the nanocrystal on the scale of unit cells, whereas electrical measurements represent macroscopic effects most often measured on pellets, which could also be affected by ceramic–electrode interfaces and are averaged over a larger volume [134]. Grain size also influences the temperature of the FE phase transition and its character. Concerning the rate of the phase transition with respect to temperature, some authors showed that the phase transition in nanograined ceramics is diffuse [128, 132, 133], whereas other authors showed a sharp phase transition in the case of nanosized BT powder [131].

11.4.1 Ferroelectric Nanostructured Ceramics

11.4.1.1 $BaTiO_3$ Nanostructured Ceramics

The grain-size effect on the structure and phase transitions of BT was discussed in 1996 by Frey and Payne [123]. The aim of their investigation was to clarify the loss of driving force for the FE transformation for very small grain sizes. They investigated the grain-size dependence of the lattice structure of BT ceramics prepared by a sol–gel method. They showed that nanocrystalline $BaTiO_3$ (grain size <0.1 μm), which was free of hydroxyl defects and displayed cubic structure according to XRD, showed Raman spectra belonging to the orthorhombic phase, and supported these data with thermal analysis. These authors stated that due to acentric distortions in ultra-fine $BaTiO_3$ the driving force for the FE transformation is present even for very small grain sizes. Successively, Buscaglia et al. [135] compared RS results with piezoresponse force microscopy (PFM) in order to study local polar character, phase transitions, and switching properties of dense nanocrystalline ceramics with the aim of obtaining information about local order changes induced by size effects. Dense nanocrystalline BT ceramics with a grain size (GS) of around 50 nm obtained by spark plasma sintering (SPS) were macroscopically weakly tetragonal at 300 K. Raman spectra measured in a temperature range from 80 to 770 K showed all the typical crystalline phases of BT with some differences in the temperature range of stability of each phase. Few Raman modes persisted at temperatures a few hundred degrees above the T–C phase transition, mainly due to the broken translational symmetry (supposedly by the high density of grain boundaries, rather than by CD), and a clear reduction of the T_c to around 368 K was indicated by the strong decrease of the $A_1(TO_1)$ mode. The PFM study showed a much weaker piezoelectric response signal than in the bulk BT as a consequence of the reduced FE polarization related to the lower average tetragonality. These results indicate that the critical GS for FE behavior in dense BT nanocrystalline ceramics was below 50 nm.

In a later work, Buscaglia et al. [134] prepared dense nanocrystalline BT ceramics with a GS of ~50, ~100, and ~300 nm using SPS and a GS of ~500 and ~1200 nm using conventional sintering. BT ceramics were studied by XRD, differential scanning calorimetry (DSC), impedance spectroscopy, and Raman spectroscopy. XRD results indicated a gradual reduction of the spontaneous tetragonal distortion (directly related to the spontaneous polarization) and of the non-centrosymmetric character of the BT lattice with decreasing GS, and supported the existence of an intrinsic size effect in BT ceramics. However, a dielectric anomaly was clearly observable for all samples, indicating FE behavior although the permittivity was strongly depressed for fine-grained samples. Raman spectra collected in the range 80–800 K provided evidence of all crystalline phases of BT. However, decreasing GS all structural phase transitions assumed a diffuse character. The persistence of Raman activity at temperatures higher than T_c in nanocrystalline ceramics was interpreted in terms of broken translational symmetry due to the high density of grain boundaries carrying out frozen (non-switchable) polar states. The overall properties of nanocrystalline BT could be explained with a combination of intrinsic effects due to the decrease of tetragonality with reducing GS and extrinsic contributions due to the higher density of non-FE grain boundaries influencing the FE properties compared to bulk BT.

Shiratori et al. [130] used RS to study dense $BaTiO_3$ ceramics with different GS from 5.6 μm down to 35 nm. Their results reveal tetragonal symmetry for the nanograined ceramics with an average GS of 35 nm at room temperature, thus experimentally demonstrating that the tetragonal phase is much more stabilized in the nanograined ceramic than in powders with comparable crystallite sizes, for which tetragonal symmetry is lost. This can be explained by the formation of local dipoles at the grain edges that can stabilize the tetragonal phase through intergranular electrostatic interaction with surrounding dipoles from neighboring grains. The micrograined ceramic showed the well-known spectra and phase transition behavior expected for bulk BT, whereas the nanograined ceramic with an average GS of 35 nm showed diffuse phase transitions, which can be explained by internal stress variation. The T_c of the nanograined ceramic is 20 degrees lower than that observed for coarse-grained ceramics as well as for nanoparticles of different sizes. They compared the phase transition behavior (by RS) of the ceramics with that obtained on small-grained powders. They showed that rather long phonon mean free paths can exist even in such ultrafine grains, but the phonon characteristics originating from various grains are diffuse due to the effect of internal stress. As a general conclusion from the study by RS, these authors stated that the behavior of nano-FE BT (particles, aggregates, and ceramics) is dominated by both intrinsic and extrinsic effects. In other words, the tetragonal character of nanocrystalline BT is retained on a molecular level within a mainly pseudocubic matrix, and the presence of a highly distorted pseudocubic layer on the grain boundaries leads to a depression of the dielectric constant in such fine-grained materials. The authors also gave the alternative explanation that local tetragonal clusters or inclusions may be embedded in the interior of mainly pseudocubic grains.

The phase stability of BT nanopowders is a crucial point for the production of ceramics with desired properties and minimized defect density, especially if different production methods are used. Therefore, numerous authors also systematically studied the size effect on the phase stability of $BaTiO_3$ powders by Raman spectroscopy [124, 128, 129, 132, 136, 137].

11.4.1.2 $BiScO_3$–$PbTiO_3$ (BS–PT) Nanostructured Ceramics

$BiScO_3$–$PbTiO_3$ (BS–PT) is considered an alternative to PZT for high-temperature applications, since it exhibits higher T_C and comparable piezoelectric coefficients [138, 139]. The best properties are found around an MPB analogous in phases to that of PZT [140, 141]. It has been shown that BS–PT ceramics can maintain significant piezoelectric activity even if nanostructured down to a grain size of ~80 nm, and thus possess promising down-scaling properties [142]. It is thus very important to understand the phenomena governing FE phase formation when further reducing grain size in this material. RS can help in this task: We report below a study on both coarse-grained (GS = 1.6 μm) and nanostructured (GS = 24 nm) BS–PT ceramics [143].

Figure 11.16 shows the deconvoluted room-temperature Raman spectrum of the coarse-grained BS–PT ceramic. The spectrum presents up to 11 modes in the frequency range 100–1000 cm^{-1}, which have been preliminarily assigned according to the classification for tetragonal $PbTiO_3$ [45, 73]. In the case of the present material, however, A-site (Bi) and B-site (Sc) substitution are likely to produce site disorder, lattice distortion, and CDRs, leading to a relaxation of the selection rules [144, 145]. Hence, the spectrum appears much broader than that of pure $PbTiO_3$ and Raman mode assignment only according to group theory is challenging [145, 146]. This might be the reason why some of the predicted modes

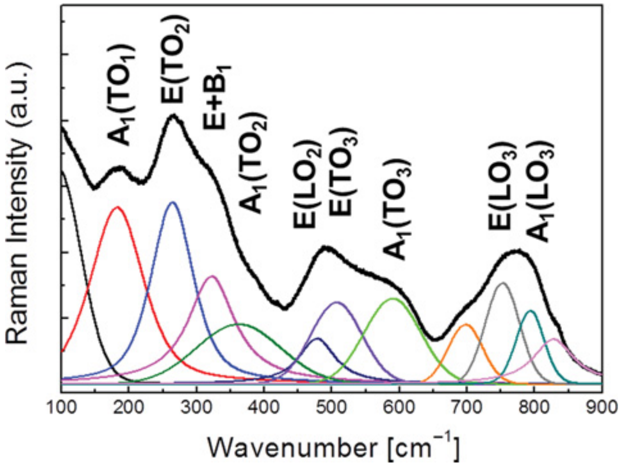

Figure 11.16 *Room-temperature Raman spectrum of the coarse-grained ceramic. Modes were assigned according to the classification for tetragonal PbTiO$_3$ [45, 73]. Extra modes at 700 and 825 cm^{-1} could be related to a monoclinic symmetry at MPB. Reprinted with permission from [143]. Copyright © [2014] [The American Ceramic Society]*

of lead titanate are not visible, whereas the presence of some extra modes (at 700 cm^{-1} and 825 cm^{-1}) is probably linked to the monoclinic symmetry of the MPB region. The number of modes is consistent to *P*4*mm* and *Cm* symmetries, or a mixture of both. TO–LO splitting [14] occurs also in this material.

The mode at 189 cm^{-1} (henceforth referred to as mode *A*) is likely a combination of the A$_1$(TO$_1$) soft phonon mode described for PbTiO$_3$ (located at ~150 cm^{-1}) and of the A$_1$(LO$_1$) + E(LO$_1$) mode [45, 73], shifted and convoluted into a single mode due to the straining of chemical bonds upon A- and B-site substitution. Mode *A* thus presents two different softening contributions upon increasing temperature. One is the soft-mode contribution from the A$_1$(TO$_1$) phonon and one the anharmonic softening due to A$_1$(LO$_1$) + E(LO$_1$) phonons. The former contribution is present only when the material has ferroelectric character and the latter is present for all PE materials.

Bose–Einstein-corrected Raman spectra of the coarse-grained and nanostructured ceramics are shown in Figure 11.17(a) and (b), respectively, as a function of temperature. The evolution of mode *A* is indicated with the dashed arrow. Spectra are similar, in particular at low temperature, which indicates that the polar structures present in the coarse-grained material persist with decreasing GS down to 24 nm. In both cases, Raman spectra were obtained in the cubic *Pm*$\bar{3}$*m* phase (i.e. above 480 °C), although Raman activity is forbidden for this structure. This is probably due to the local polar order, but not to CORs, since the overall spectral intensity is low. Upon increasing temperature, the mode *A* shifts to lower wavenumbers and its intensity decreases, until a temperature above which the mode becomes indistinguishable from the rest of the spectrum. This temperature is 465 °C for the coarse-grained ceramic and 405 °C for the nanostructured material.

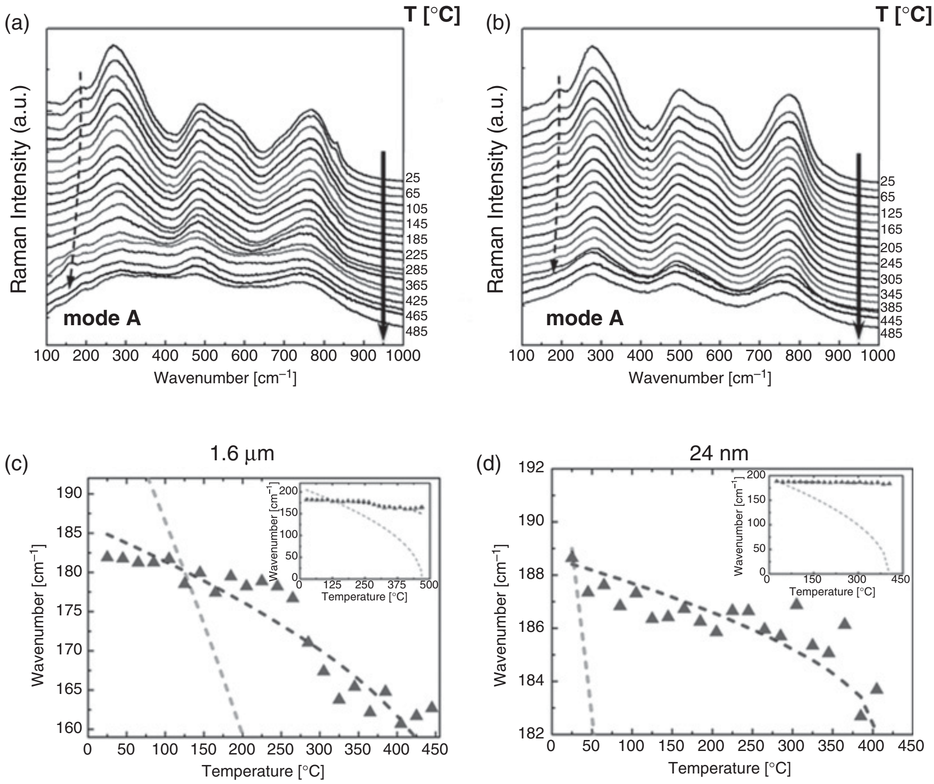

Figure 11.17 (a) and (b) Temperature-dependent Raman spectra for the coarse-grained and nanostructured BS–PT ceramics, respectively. The dashed arrows indicate the evolution of the mode A. (c) and (d) Softening behavior of mode A for both the coarse-grained and nanostructured samples [(c) and (d), respectively]. The symbols represent the observed mode A wavenumber and the dark dashed line is the best fit of Equation (11.6) to the experimental data. The fully Cochran-like soft mode contribution (dashed light line) is also represented. In the inset the observed wavenumber, the fit according to Equation (11.6) and the soft mode contribution is shown in the wavenumber range down to 0. Reprinted with permission from [143]. Copyright © [2014] [The American Ceramic Society]

In FE materials, the frequency of the soft mode tends to zero upon approaching a structural (displacive) phase transition, and the softening behavior should obey, in first approximation, the Cochran law [147]:

$$\omega_{\mathrm{SM}}^{2}(T) = A(T - T_{\mathrm{C}}) \tag{11.4}$$

where ω_{SM} is the soft mode frequency, T_{C} is the Curie temperature, and A is a constant. Recently it has been demonstrated [148] that this description is not complete and the frequency of the soft mode never reaches zero; Equation (11.4) will, however, be used here since mode A has only a partially soft mode character.

Raman mode softening with temperature is due to anharmonic terms in the vibrational potential energy and has been observed also in ferroelectrics and multiferroics for modes not displaying typical soft mode behavior, as previously stated [70–72]. Considering terms up to four phonons, the anharmonic behavior can be modeled according to the following equation [120]:

$$\omega_{\mathrm{Anh}}(T) = \omega_0 + B\left[1 + \frac{2}{e^x - 1}\right] + C\left[1 + \frac{3}{e^y - 1} + \frac{3}{(e^y - 1)^2}\right] \tag{11.5}$$

where $x = \hbar\omega_0/2kT$, $y = \hbar\omega_0/3kT$, $\hbar$ is the reduced Planck's constant, k the Boltzmann's constant; ω_0 is the wavenumber at $T = 0$ K (taken as the fitting parameter), and B and C are constants (also taken as fitting parameters). Considering that mode A has soft-mode and anharmonic components, its behavior can be represented by combining Equations (11.4) and (11.5):

$$\omega_{\mathrm{obs}}(T) = \delta\omega_{\mathrm{Anh}}(T) + (1 - \delta)\omega_{\mathrm{SM}}(T) \tag{11.6}$$

where $\delta(0 < \delta < 1)$ is the weight. Figure 11.17 shows the softening behavior of mode A for both the coarse-grained and nanostructured samples ((c) and (d), respectively). The symbols represent the observed mode A wavenumber, the dashed dark line is the best fit of Equation (11.6) to the experimental data. The fully Cochran-like soft-mode contributions are represented as dashed light lines. Values of T_C corresponding to the apparent disappearance of mode A (cf. Figure 11.17(a) and (b)) were taken for the fit (405 °C for the nanostructured material and 465 °C for the coarse-grained material). In the inset the observed wavenumber, the fit according to Equation (11.6), and the soft-mode contribution are shown in the wavenumber range down to 0 cm^{-1}, highlighting the fact that by taking a full Cochran behavior the soft mode wavenumber tends to zero towards T_C.

It has to be mentioned that, in both materials, fitting of the observed wavenumber only by considering anharmonic components did not give consistent results, that is, a ferroelectric soft mode contribution is always present. Less softening observed for the nanostructured ceramic can be explained with a high contribution of the $\mathrm{A_1(LO_1) + E(LO_1)}$ modes to mode A (the value of δ resulting from the fit is 0.97 for the nanostructured material and 0.82 for the coarse-grained material). In other words, the FE component is reduced with respect to the PE one for the nanostructured material. Nevertheless, Raman data clearly demonstrate that ferroelectricity is still present in nanostructured BS–PT, in accord with previous studies [142].

11.4.2 Ferroelectric 2D Nanostructures

2D nanostructures are increasingly gaining importance in miniaturized devices for energy applications, and in this sense FE materials play a decisive role. BT nanorods were recently synthesized by a template-assisted sol–gel procedure [5]. These materials were studied at different temperatures by RS, evidencing a multiphase composition of the nanorods. These were largely tetragonal, but showed an intrinsic phase transition towards the cubic phase and, depending on the synthesis routes, contained some orthorhombic and/or hexagonal phases. The existence of a high-temperature hexagonal phase at room temperature is characterized by a band at ~640 cm^{-1}, where bands of other BT phases are not expected. During the in situ heating process, it was shown that the phase transition was diffuse with respect to temperature, which is explained by the morphology of the nanorods consisting of nanocrystallites. It was also revealed that the phase transition to the cubic structure was completed at higher temperatures than would be expected for nanocrystalline or even bulk samples. This was explained with strain in the investigated nanorods induced by the presence of the hexagonal nanolamellae.

Fully crystallized $BaTiO_3$ nanofibers were synthesized by Yuh et al. [149] via electrospinning and subsequent annealing. To prove the tetragonality of the fibers prepared using different heat treatment conditions, room temperature RS was applied. The authors discussed intermediate phases and phase formations in the view of Raman results. It was observed that nanofibers obtained from heat treatments at or above 600 °C for 16 h showed the bands of tetragonal BT, but in nanofibers annealed at 750 °C for 16 h these bands became better defined and of higher intensity, indicating that those fibers were completely crystalline. They also observed an additional band at around 640 cm^{-1}, but they assigned it to extended (111) planar defects, rather than to a hexagonal phase.

Hernandez et al. [127] prepared $BaTiO_3$ and $PbTiO_3$ nanotubes by sol–gel template synthesis. XRD identified the long-range crystal structure of $PbTiO_3$ as tetragonal and that of BT nanotubes as cubic. RS, however, also revealed a tetragonal component in BT. Dielectric analysis showed that this tetragonal phase did not contribute to the FE behavior in the nanotubes.

Louis et al. investigated the phase transition sequence of $KNbO_3$ (KNO) and BT FE bulk materials and nanowires (mean diameter of about 50 nm and mean length of about 5 μm along the [001]-pseudocubic direction) as a function of temperature by using XRD, RS, and first principles [150]. The low-temperature (80 K) rhombohedral phase of the bulk KNO had a clear Raman spectrum with characteristic vibrational modes, but such a feature was not found in the nanowires. The Raman spectrum at 80 K was rather close to an orthorhombic one. In order to describe this structure better, the authors performed a Rietveld refinement on a full XRD pattern recorded at 8 K and demonstrated that the low-temperature ground state is monoclinic, which is of great interest due to the high achievable piezoelectric responses.

11.4.3 Wrap-Up: Raman Analysis of Nanostructured Ferroelectrics

Nanostructured FE ceramics generally maintain local structural distortions, albeit the macroscopic FE response is weakened or suppressed. In ceramic systems, the higher density of grain boundaries increases the disorder of the lattice and puts a constraint to domain movement, inhibiting domain formation below a certain grain size. RS can contribute investigating nanostructured FE ceramics in a twofold manner: It can reveal the increased disorder due to grain boundary contributions and it can detect phases, transition points, and their diffuseness. Even if a macroscopic FE response cannot be measured, a Raman spectrum can help clarifying whether FE order is retained at least locally. Raman is especially powerful if used during changing temperatures and an applied electric field, or by comparing different chemical compositions and production methods.

Due to space restrictions, this overview of results is obviously not complete. Nevertheless, it again shows that RS is complementary to laboratory XRD and works on the same scale as synchrotron XRD, though with laboratory-size equipment. Combining Raman and XRD with dielectric measurements, ferroelectric loops, and PFM allows short- and long-range structures to be linked with macro- and microscopic dielectric and FE properties. RS is essential to study the intrinsic properties of nanoscale FE ceramics and in combination with the aforementioned techniques is the ideal tool to finely tune processing methods and compositions to obtain desired properties.

11.5 Tip-Enhanced Raman Spectroscopy (TERS) of Nanoscale Ferroelectrics

The spatial resolution of RS is limited by optical diffraction, and thus the investigation volume is of the order of μm^3 [151]. In some cases, such as the study of ferroelectric domain orientation, this may not be enough.

Tip-enhanced Raman spectroscopy (TERS) appeared in the last 15 years as an evolution of surface-enhanced Raman spectroscopy (SERS), to which it adds the capability of performing scanning-resolved measurements [152, 153]. SERS, in fact, relies on a random (or hardly controllable) distribution of field enhancement centers [154]. The local field enhancement that is realized in TERS produces a twofold advantage compared with traditional RS: (i) Raman selection rules can be relaxed, which allows detection of additional features from the material [155], and (ii) since the enhanced field is confined to a very small volume near the tip, TERS can probe nanoscale variations in the material by scanning the tip across the material surface. The spatial resolution is limited by the nanometer-scale sharpness of the tip [156–160]. Thus, much higher resolution than in traditional micro-RS can in principle be achieved.

In TERS, the laser is focused off-axis on the tip of a metallic (or metal-coated) cantilever (cf. Figure 11.18(a)), similar to the ones used in AFM microscopy. The electric field from the laser is concentrated at the bottom of the tip and field enhancement processes allow a near-field signal to be generated. The same focusing objective generally collects the scattered signal, which is a combination of near-field and far-field (from conventional micro-RS) signals. The field enhancement results from a combination of two factors [161]:

1. *Lightning rod effect*. The electric field of incident light is amplified in regions of high curvature, such as an AFM tip. Field enhancement increases with the aspect ratio of the tip until saturation for aspect ratio $> \sim 40$ is reached. Since the incident field must have a strong component along the long axis of the tip, illumination is realized off-axis at shallow angles with linearly polarized light.
2. *Localised surface plasmon (LSP) resonance*. LSPs are collective excitations at the surface of metallic materials, which have typical resonance frequencies corresponding to plasma frequencies of the metal. If the tip is illuminated with an excitation source with a frequency close to the plasmon resonance, the near-field Raman enhancement factor M can be increased.

M is determined from the measured near- and far-field optical intensities I_{NF} and I_{FF}, respectively, the size of the far-field focus A_{FF}, and the spatial extent of the tip-enhanced region, A_{NF} [152]:

$$M = \frac{I_{\mathrm{NF}} A_{\mathrm{FF}}}{I_{\mathrm{FF}} A_{\mathrm{NF}}} \tag{11.7}$$

A_{FF} can be calculated considering the size of the probed volume for the illuminating wavelength [12, 151], whereas A_{NF} is determined by the tip apex size, which is generally of the order of ~10 nm. In TERS, enhancement factors of $M = \sim 10^4 – 10^5$ have been measured in crystalline samples [162]. A possible issue affecting field enhancement is the metal tip degradation due to oxidation. A numerical study has shown that a thin protective layer made of SiO_2 can improve the enhancement factor [163].

Two setups are possible for TERS measurements: the *transmission mode* and the *reflection mode*. In the former, an inverted microscope is used to deliver the laser light and to collect the Raman signal. The metallic tip is mounted above the scanning microscope table. Transmission-mode TERS is especially useful for thin or transparent samples, but it cannot be used for opaque samples [153]. In the reflection mode, the optical system is placed above the sample surface at some angle with respect to it (cf. Figure 11.18a) [164–167]);

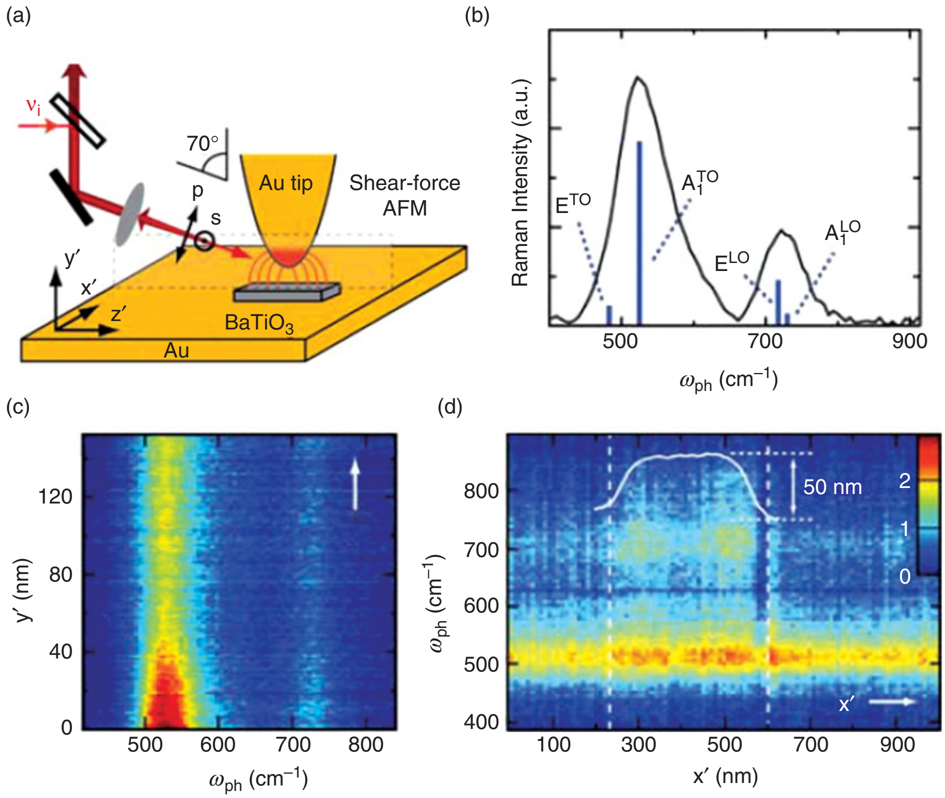

Figure 11.18 *(a) Schematic of the experimental reflection TERS setup for the measurement of BT nanocrystals. (b) TERS spectrum of BT acquired on a nanorod. The fluorescent background has been subtracted and phonon mode assignment is reported on the spectrum. (c) Tip-sample distance dependence and (d) spectrally resolved linescan across a BT nanorod. The abrupt signal change at 580 cm^{-1} is due to an acquisition artifact. Reprinted by permission from Macmillan Publishers Ltd: [175], copyright (2009). For a color version of this figure, see color plate section*

this mode, however, has the drawback that a huge far-field background results from the larger focused spot of the low numerical aperture (NA) objective lens used for illumination. This strong background needs to be minimized in order to extract useful near-field information. Berweger and Raschke [168] estimated in Si (considering a near-field probe volume of 10^3 nm^3 and a realistic TERS enhancement factor $M = 10^4$) a near- to far-field contrast $I_{NF}/I_{FF} = 2.6 \times 10^{-4}$. While this provides a lower estimate and experimentally measured values are generally larger, this poor contrast presents a significant concern for TERS studies of bulk crystalline materials in general [152]. Consequently, TERS has not been so popular for ferroelectric materials, which notoriously have much lower (and broader) scattering cross-sections compared to Si. In addition, in crystalline systems field enhancement cannot be improved by using metallic substrates. The depolarization of light scattered by the tip provides a means to overcome this limitation. The tip, considered as a nanoscopic scatterer, modifies the polarization state of ~10% of the tip-scattered TERS signal [169]. For conditions where the TERS selection rules predict the detection of p-polarized light only, a small portion of near-field signal will then be detected in the s-polarized configuration as well. By orienting the crystallographic directions of the sample and incident and detected polarization such that far-field Raman scattering is forbidden, the observation of near-field modes with enhanced contrast, at the expense of an overall reduced signal level, is enabled [170–174].

The most notable example of TERS applied to ferroelectric materials is the study by Berweger et al. on domains in $BaTiO_3$ (BT) nanorods [175]. Figure 11.18(b) shows an unpolarized TERS spectrum acquired on a BT nanorod. The two main peaks are the $A_1(TO_1)$ mode at 515 cm^{-1} and the E(LO) mode at 715 cm^{-1}. Also contributing to the signal are the weaker $A_1(LO_1)$ mode at 727 cm^{-1} and the E(TO) mode at 487 cm^{-1} [78]. The authors linked the observation of the Raman-active LO modes to the presence of the FE state but did not show the low-wavenumber spectrum, so it is not clear if the "silent" mode at 305 cm^{-1} can be measured for this material. Although this would unambiguously prove FE order, the argument concerning LO phonons supporting an FE phase is correct. An approach curve, shown in Figure 11.18(c), verifies the tip-enhanced near-field localization of the signal. A linescan across the rod (Figure 11.18(d), where topography is displayed as a white line) shows a Raman enhancement of 10^4–10^5, which is consistent with the typical field enhancement of the tips of order ~ 10–20.

Imaging of FE domains in BT is shown in Figure 11.19. Panel (a) shows the AFM topography of the BT crystal with the corresponding spectrally integrated optical Raman signal (b). In addition to the overall reduced signal observed with the tip positioned above the rod, a region ~ 60 nm × 200 nm of a significantly stronger near-field signal is seen. By symmetry and polarization considerations, the authors proved that most of the crystal has c-domain orientation, whereas the stronger signal is contributed by a-domains. Furthermore, by using domain shape considerations, they were able to distinguish between parallel and perpendicular a-domains, which judging from the intensity of E-modes alone is not possible. The spatial resolution of the TERS measurements was in this case better than 30 nm. Direct conclusions from their results are that while the rods are smaller than typical FE domains, they are not necessarily single domain. Thus, an increase in surface-to-volume ratios and the associated increasing importance of the surface free energy, including adsorbates and surface defects, may induce finite size effects on FE ordering. This supports the findings on nanosize-grained ceramics we reviewed above.

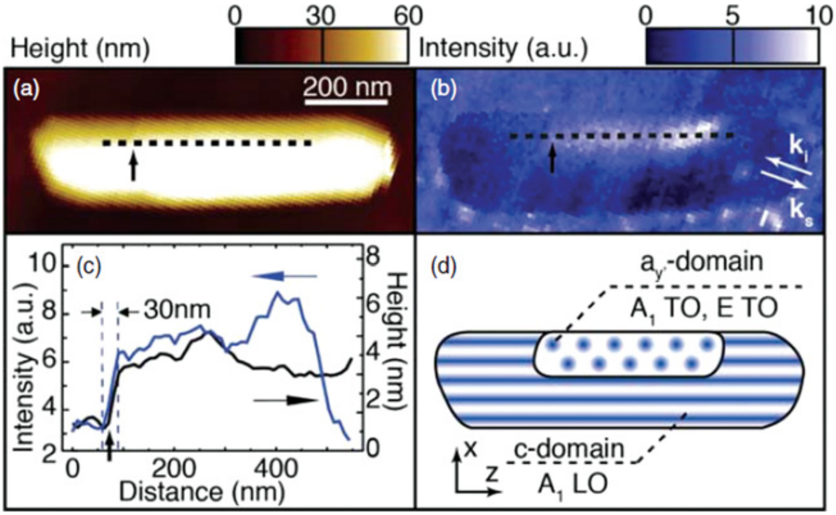

Figure 11.19 *(a) AFM topography (shear force) of a BT microcrystal. (b) Spectrally integrated TERS image on the same area, showing FE domain contrast. (c) Topography and TERS signals in cross-section along the dashed lines in (a) and (b). (d) Domain assignment based on the Raman selection rules. Reprinted by permission from Macmillan Publishers Ltd: [175], copyright (2009)*

In the next years, it is expected that TERS will grow in importance, especially by technical improvements that should allow better tip positioning, laser alignment, and data interpretation. This technique will surely find a place in the characterization of FE nanostructures, as it has the potential to surpass conventional micro-Raman or confocal Raman, not only for the analysis of FE domain nanostructures but also to sample phase mixtures in nanosized ferroelectric bulks and relaxors, such as PNRs (by combining TERS and PFM) and CORs/CDRs.

11.6 Summary

In this contribution, we presented a review of Raman studies conducted on nanostructured ferroelectric materials. We focused mainly on: (i) bulk materials owing their excellent electromechanical and dielectric properties to nanoscale phase, charge, or compositional variations (relaxors) and (ii) materials that have been nanostructured on purpose (such as nanorods and nanocrystalline ceramics). In both cases, RS has established itself as a technique capable of detecting fine structural variations originating on the short range, often outperforming laboratory XRD. RS, in fact, owing to a smaller coherence length, delivers information that can be compared to synchrotron XRD, but with much smaller and easy-to-use equipment. RS conveys information on short-range phases and phase transitions, charge and bonding anomalies, strain, and domain orientation (but not polarization – for which it is complementary to PFM). The interpretation of Raman results is not straightforward. In the case of ferroelectrics, group theory alone is not sufficient to explain the observed spectral signature and first-principles calculations are needed (but are often not available, due to high computational requirements). All in all, RS is very advantageous if used together with other methods (XRD, permittivity, and piezoelectric loops measurements (PFMs)), in order to explain the link between short- and long-range structures and the micro- and macroscopic dielectric and piezoelectric properties, also in dependence of temperature and pressure. In this sense, RS is truly complementary to other most-used techniques for the characterization of nanostructured FE ceramics. The spatial resolution of common micro-Raman spectrometers is of the order of micrometers; this limit is expected to improve with the further development of TERS, whose spatial sensitivity reaches the nanometer scale.

Acknowledgments

Marco Deluca gratefully acknowledges financial support by the Austrian Federal Government (in particular from the Bundesministerium für Verkehr, Innovation und Technologie and the Bundesministerium für Wirtschaft Famile und Jugend) represented by Österreichische Forschungsförderungsgesellschaft mbH and the Styrian and the Tyrolean Provincial Government, represented by Steirische Wirtschaftsförderungsgesellschaft mbH and Standortagentur Tirol, within the framework of the COMET Funding Programme. Dr Elena Buixaderas (Institute of Physics, Prague, Czech Republic), Dr Roger Morrell (National Physical Laboratory, Teddington, UK), and Professor Robert Danzer (Institut für Struktur- und Funktionskeramik, Montanuniversitaet Leoben, Leoben, Austria) are gratefully acknowledged for critical reading of the manuscript.

References

(1) Acosta, M., Zang, J., Jo, W., and Rödel, J. (2012) High-temperature dielectrics in $CaZrO_3$-modified $Bi_{1/2}Na_{1/2}TiO_3$-based lead-free ceramics. *Journal of the European Ceramic Society*, **32** (16), 4327–4334.

(2) Gouadec, G. and Colomban, P. (2007) Raman spectroscopy of nanomaterials: how spectra relate to disorder, particle size and mechanical properties. *Progress in Crystal Growth and Characterization of Materials*, **53** (1), 1–56.

(3) Deluca, M., Stoleriu, L., Curecheriu, L.P. et al. (2012) High-field dielectric properties and Raman spectroscopic investigation of the ferroelectric-to-relaxor crossover in $BaSn_xTi_{1-x}O_3$ ceramics. *Journal of Applied Physics*, **111** (8), art. no. 084102.

(4) Deluca, M., Vasilescu, C.A., Ianculescu, A.C. et al. (2012) Investigation of the composition-dependent properties of $BaTi_{1-x}Zr_xO_3$ ceramics prepared by the modified Pechini method. *Journal of the European Ceramic Society*, **32** (13), 3551–3566.

(5) Gajovic, A., Plestina, J.V., Zagar, K., et al. (2013) Temperature-dependent Raman spectroscopy of $BaTiO_3$ nanorods synthesized by using a template-assisted sol–gel procedure. *Journal of Raman Spectroscopy*, **44** (3), 412–420.

(6) Kreisel, J., Glazer, A.M., Bouvier, P., and Lucazeau, G. (2001) High-pressure Raman study of a relaxor ferroelectric: the $Na_{0.5}Bi_{0.5}TiO_3$ perovskite. *Physical Review B*, **63** (17), art. no. 174106.

(7) Jorio, A., Dresselhaus, M.S., Saito, R., and Dresselhaus, G. (2010) *Raman Spectroscopy in Graphene Related Systems*, John Wiley & Sons, Weinheim.

(8) Colombi Ciacchi, L., Gregori, G., Lughi, V., et al. (1999) Piezo-spectroscopy: a materials science perspective. *Recent Research Developments in Applied Spectroscopy*, **2**, 243–272.

(9) Harris, D.C. and Bertolucci, M.D. (1978) *Symmetry and Spectroscopy: An Introduction to Vibrational and Electronic Spectroscopy*, Courier Dover Publications, New York.

(10) Raman, C.V. and Krishnan, K.S. (1928) A new type of secondary radiation. *Nature*, **121** (3048), 501–502.

(11) Long, D.A. (1977) *Raman Spectroscopy*, McGraw-Hill, New York.

(12) McCreery, R.L. (2005) *Raman Spectroscopy for Chemical Analysis*, John Wiley & Sons, Inc., New York.

(13) Nakamoto, K. (1978) *Infrared and Raman Spectra of Inorganic and Coordination Compounds*, John Wiley & Sons, Inc., Hoboken.

(14) Loudon, R. (1964) The Raman effect in crystals. *Advances in Physics*, **13** (52), 423–482.

(15) Trodahl, H.J., Budde, F., Ruck, B.J., et al. (2005) Raman spectroscopy of nanocrystalline and amorphous GaN. *Journal of Applied Physics*, **97** (8), art. no. 084309.

(16) Ashcroft, N.W. and Mermin, D. (1976) *Introduction to Solid State Physics*, Saunders, Philadelphia.

(17) Husson, E. (1998) Raman spectroscopy applied to the study of phase transitions. *Key Engineering Materials*, **155**, 1–40.

(18) Lines, M.E. and Glass, A.M. (1977) *Principles and Applications of Ferroelectrics and Related Materials*, Oxford University Press, Oxford.

(19) Taniguchi, H., Itoh, M., and Fu, D. (2011) Raman scattering study of the soft mode in $Pb(Mg_{1/3}Nb_{2/3})O_3$. *Journal of Raman Spectroscopy*, **42** (4), 706–714.

(20) Scott, J.F. (1969) Raman study of trigonal-cubic phase transitions in rare-earth aluminates, *Physical Review*, **183** (3), 823.

(21) Hayward, S.A., Morrison, F.D., Redfern, S.A.T., et al. (2005) Transformation processes in $LaAlO_3$: neutron diffraction, dielectric, thermal, optical, and Raman studies. *Physical Review B*, **72** (5), art. no. 054110.

(22) Salje, E.K.H. and Bismayer, U. (1997) Hard mode spectroscopy: the concept and applications. *Phase Transitions: A Multinational Journal*, **63** (1–4), 1–75.

(23) Bokov, A.A. and Ye, Z.G. (2006) Recent progress in relaxor ferroelectrics with perovskite structure. *Journal of Materials Science*, **41** (1), 31–52.

(24) Shvartsman, V.V. and Lupascu, D.C. (2012) Lead-free relaxor ferroelectrics. *Journal of the American Ceramic Society*, **95** (1), 1–26.

(25) Kleemann, W. (2012) Random fields in relaxor ferroelectrics – a jubilee review. *Journal of Advanced Dielectrics*, **2**, art. no. 1241001.

(26) Buscaglia, V., Tripathi, S., Petkov, V., et al. (2014) Average and local atomic-scale structure in $BaZr_xTi_{1-x}O_3$ ($x = 0.10, 0.20, 0.40$) ceramics by high-energy X-ray

diffraction and Raman spectroscopy. *Journal of Physics: Condensed Matter*, **26** (6), art. no. 065901.

(27) Karan, N.K., Katiyar, R.S., Maiti, T., et al. (2009) Raman spectral studies of Zr^{4+}-rich $BaZr_xTi_{1-x}O_3$ ($0.5 < x < 1.00$) phase diagram. *Journal of Raman Spectroscopy*, **40** (4), 370–375.

(28) Moulson, A.J. and Herbert, J.M. (2003) *Electroceramics: Materials, Properties, Applications*, John Wiley & Sons, Ltd, Southern Gate.

(29) Shvartsman, V.V., Dec, J., Xu, Z.K., et al. (2008) Crossover from ferroelectric to relaxor behavior in $BaTi_{1-x}Sn_xO_3$ solid solutions. *Phase Transitions*, **81** (11–12), 1013–1021.

(30) Shvartsman, V.V., Kleemann, W., Dec, J., et al. (2006) Diffuse phase transition in $BaTi_{1-x}Sn_xO_3$ ceramics: an intermediate state between ferroelectric and relaxor behavior. *Journal of Applied Physics*, **99** (12), 124111.

(31) Simon, A., Ravez, J., and Maglione, M. (2004) The crossover from a ferroelectric to a relaxor state in lead-free solid solutions. *Journal of Physics: Condensed Matter*, **16** (6), 963–970.

(32) Qian, H. and Bursill, L.A. (1996) Random-field Potts model for the polar domains of lead magnesium niobate and lead scandium tantalate. *International Journal of Modern Physics B*, **10** (16), 2027–2047.

(33) Semenovskaya, S. and Khachaturyan, A.G. (1998) Ferroelectric transition in a random field: possible relation to relaxor ferroelectrics. *Ferroelectrics*, **206** (1),157–180.

(34) Burns, G. and Dacol, F.H. (1983) Glassy polarization behavior in ferroelectric compounds $Pb(Mg_{1/3}Nb_{2/3})O_3$ and $Pb(Zn_{1/3}Nb_{2/3})O_3$. *Solid State Communications*, **48** (10), 853–856.

(35) Westphal, V., Kleemann, W., Glinchuk, M.D. (1992) Diffuse phase transitions and random-field-induced domain states of the "relaxor" ferroelectric $PbMg_{1/3}Nb_{2/3}O_3$, *Physical Review Letters*, **68** (6), 847–850.

(36) Samara, G.A. (2003) The relaxational properties of compositionally disordered ABO_3 perovskites. *Journal of Physics: Condensed Matter*, **15** (9), R367–R411.

(37) Jaffe, B., Cook Jr, W.R., and Jaffe, H. (1971) *Piezoelectric Ceramics*, Academic Press, London.

(38) Cordero, F., Trequattrini, F., Craciun, F., and Galassi, C. (2013) Merging of the polar and tilt instability lines near the respective morphotropic phase boundaries of $PbZr_{1-x}Ti_xO_3$. *Physical Review B*, **87** (9), art. no. 094108.

(39) Gorfman, S., Keeble, D.S., Glazer, A.M., et al. (2011) High-resolution X-ray diffraction study of single crystals of lead zirconate titanate. *Physical Review B*, **84** (2), art. no. 020102.

(40) Schönau, K.A., Schmitt, L.A., Knapp, M., et al. (2007) Nanodomain structure of $Pb[Zr_{1-x}Ti_x]O_3$ at its morphotropic phase boundary: investigations from local to average structure. *Physical Review B*, **75** (18), art. no. 184117.

(41) Zhang, N., Yokota, H., Glazer, A.M., and Thomas, P.A. (2011) Neutron powder diffraction refinement of $PbZr_{1-x}Ti_xO_3$. *Acta Crystallographica Section B: Structural Science*, **67** (5), 386–398.

(42) Buixaderas, E., Berta, M., Kozielski, L., Gregora, I. (2011) Raman spectroscopy of $Pb(Zr_{1-x}Ti_x)O_3$ graded ceramics around the morphotropic phase boundary. *Phase Transitions*, **84** (5–6), 528–541.

(43) Damjanovic, D. (2005) Contributions to the piezoelectric effect in ferroelectric single crystals and ceramics. *Journal of the American Ceramic Society*, **88** (10), 2663–2676.

(44) Deluca, M., Fukumura, H., Tonari, N., et al. (2011) Raman spectroscopic study of phase transitions in undoped morphotropic $PbZr_{1\text{-}x}Ti_xO_3$. *Journal of Raman Spectroscopy*, **42** (3), 488–495.

(45) Frantti, J., Lantto, V., Nishio, S., and Kakihana, M. (1999) Effect of A-and B-cation substitutions on the phase stability of $PbTiO_3$ ceramics. *Physical Review B*, **59** (1), 12–15.

(46) Härdtl, K.H. and Hennings, D. (1972) Distribution of A-site and B-site vacancies in (Pb, La)(Ti, Zr)O_3 ceramics. *Journal of the American Ceramic Society*, **55** (5), 230–231.

(47) Buixaderas, E., Bovtun, V., Veljko, S., et al. (2010) Ultrabroadband dielectric spectroscopy and phonons in $(Pb_{1\text{-}x/2}La_x)(Zr_{0.9}Ti_{0.1})O_3$. *Journal of Applied Physics*, **108** (10), art. no. 104101.

(48) Buixaderas, E., Gregora, I., Kamba, S., et al. (2008) Raman spectroscopy and effective dielectric function in PLZT *x*/40/60. *Journal of Physics: Condensed Matter*, **20** (34), art. no. 345229.

(49) Buixaderas, E., Nuzhnyy, D., Veljko, S., et al. (2007) Far-infrared and dielectric spectroscopy of relaxor ferroelectric $(Pb_{1\text{-}x}La_x)(Zr_{0.4}Ti_{0.6})O_3$. *Journal of Applied Physics*, **101** (7), art. no. 074106.

(50) Haertling, G.H. (1999) Ferroelectric ceramics: history and technology. *Journal of the American Ceramic Society*, **82** (4), 797–818.

(51) Robinson, M.C., Morris, D.J., Hayenga, P.D., et al. (2006) Structural and electrical characterization of PZT on gold for micromachined piezoelectric membranes. *Applied Physics A*, **85** (2), 135–140.

(52) Kamba, S., Bovtun, V., Petzelt, J., et al. (2000) Dielectric dispersion of the relaxor PLZT ceramics in the frequency range 20 Hz–100 THz. *Journal of Physics: Condensed Matter*, **12** (4), 497–519.

(53) El Marssi, M., Farhi, R., Dai, X., et al. (1996) A Raman scattering study of the ferroelectric ordering in rhombohedral and tetragonal La-modified lead zirconate titanate ceramics. *Journal of Applied Physics*, **80** (2), 1079–1084.

(54) Kreisel, J., Glazer, A.M., Jones, G., et al. (2000) An X-ray diffraction and Raman spectroscopy investigation of A-site substituted perovskite compounds: the $(Na_{1\text{-}x}K_x)_{0.5}Bi_{0.5}TiO_3$ $(0 < x < 1)$ solid solution. *Journal of Physics: Condensed Matter*, **12** (14), 3267–3280.

(55) Mesquita, A., Michalowicz, A., Pizani, P.S., et al. (2014) Local order of $Pb_{1\text{-}x}La_xZr_{0.40}Ti_{0.60}O_3$ ferroelectric ceramic materials probed by X-ray absorption and Raman spectroscopies. *Journal of Alloys and Compounds*, **582**, 680–687.

(56) Glazer, A.M. and Mabud, S.A. (1978) Powder profile refinement of lead zirconate titanate at several temperatures. II. Pure $PbTiO_{3.}$ *Acta Crystallographica Section B: Structural Crystallography and Crystal Chemistry*, **34** (4), 1065–1070.

(57) Knudsen, J., Woodward, D.I., and Reaney, I.M. (2003) Domain variance and superstructure across the antiferroelectric/ferroelectric phase boundary in $Pb_{1\text{-}1.5\,x}La_x(Zr_{0.\,9}TiM_{0.1})O_3$. *Journal of Materials Research*, **18** (2), 262–271.

(58) Buixaderas, E., Gregora, I., Kamba, S., et al. (2009) Phonon anomalies in $Pb_{1-x}La_x(Zr_{0.9}Ti_{0.1})O_3$ ceramics. *Applied Physics Letters*, **94** (5), art. no. 052903.

(59) Pelaiz-Barranco, A., Guerra, J.D.S., Garcia-Zaldivar, O., et al. (2008) Effects of lanthanum modification on dielectric properties of $Pb(Zr_{0.90}Ti_{0.10})O_3$ ceramics: enhanced antiferroelectric stability. *Journal of Materials Science*, **43** (18), 6087–6093.

(60) Dai, X., Xu, Z., Li, J.F., and Viehland, D. (1996) Effects of lanthanum modification on rhombohedral Pb $(Zr_{1-x}Ti_x)O_3$ ceramics: Part I. Transformation from normal to relaxor ferroelectric behaviors. *Journal of Materials Research*, **11** (3), 618–625.

(61) Fu, D., Taniguchi, H., Itoh, M., et al. (2009) Relaxor $Pb(Mg_{1/3}Nb_{2/3})O_3$: a ferroelectric with multiple inhomogeneities. *Physical Review Letters*, **103** (20), art. no. 207601.

(62) Al-Zein, A., Hlinka, J., Rouquette, J., and Hehlen, B. (2010) Soft mode doublet in $PbMg_{1/3}Nb_{2/3}O_3$ relaxor investigated with hyper-Raman scattering. *Physical Review Letters*, **105** (1), art. no. 017601.

(63) Slodczyk, A. and Colomban, P. (2010) Probing the nanodomain origin and phase transition mechanisms in (un)poled PMN–PT single crystals and textured ceramics. *Materials*, **3** (12), 5007–5028.

(64) Noheda, B., Cox, D.E., Shirane, G., et al. (2002) Phase diagram of the ferroelectric relaxor $(1-x)PbMg_{1/3}Nb_{2/3}O_3$–$xPbTiO_3$. *Physical Review B*, **66** (5), art. no. 054104.

(65) Stock, C., Ellis, D., Swainson, I.P., et al. (2006) Damped soft phonons and diffuse scattering in 40% $Pb(Mg_{1/3}Nb_{2/3})O_3$–60% $PbTiO_3$. *Physical Review B*, **73** (6), art. no. 064107.

(66) Ye, Z.G., Bing, Y., Gao, J., et al. (2003) Development of ferroelectric order in relaxor $(1-x)Pb(Mg_{1/3}Nb_{2/3})O_3$–$xPbTiO_3$ $(0 < x < 0.\,1\,5)$. *Physical Review B*, **67** (10), art. no. 104104.

(67) Chemarin, C., Rosman, N., Pagnier, T., and Lucazeau, G. (2000) A high-pressure Raman study of mixed perovskites $BaCe_xZr_{1-x}O_3$ $(0 < x < 1)$. *Journal of Solid State Chemistry*, **149** (2), 298–307.

(68) Colomban, P. (2003) Raman analyses and "smart" imaging of nanophases and nanosized materials. *Spectroscopy Europe*, **15** (6), 8–16.

(69) Lima, J.A., Paraguassu, W., Freire, P.T.C., et al. (2009) Lattice dynamics and low-temperature Raman spectroscopy studies of PMN–PT relaxors. *Journal of Raman Spectroscopy*, **40** (9), 1144–1149.

(70) Aksel, E., Forrester, J.S., Kowalski, B., et al. (2012) Structure and properties of Fe-modified $Na_{0.5}Bi_{0.5}TiO_3$ at ambient and elevated temperature. *Physical Review B*, **85** (2), art. no. 024121.

(71) Fukumura, H., Hasuike, N., Harima, H., et al. (2007) Spin-coupled phonons in multiferroic $YbMnO_3$ epitaxial films by Raman scattering. *Journal of Physics: Conference Series*, **92**, art. no. 012126.

(72) Fukumura, H., Matsui, S., Harima, H., et al. (2007) Raman scattering studies on multiferroic $YMnO_3$. *Journal of Physics: Condensed Matter*, **19** (36), art. no. 365239.

(73) Freire, J.D. and Katiyar, R.S. (1988) Lattice dynamics of crystals with tetragonal $BaTiO_3$ structure. *Physical Review B*, **37** (4), 2074–2085.

(74) DiDomenico Jr, M., Wemple, S.H., Porto, S.P.S., and Bauman, R.P. (1968) Raman spectrum of single-domain $BaTiO_3$. *Physical Review*, **174** (2), 522.

(75) Joshi, U.A., Yoon, S., Baik, S., and Lee, J.S. (2006) Surfactant-free hydrothermal synthesis of highly tetragonal barium titanate nanowires: a structural investigation. *The Journal of Physical Chemistry B*, **110** (25), 12249–12256.

(76) Perry, C.H. and Hall, D.B. (1965) Temperature dependence of the Raman spectrum of $BaTiO_3$. *Physical Review Letters*, **15** (17), 700–702.

(77) Venkateswaran, U.D., Naik, V.M., and Naik, R. (1998) High-pressure Raman studies of polycrystalline $BaTiO_3$. *Physical Review B*, **58** (21), art. no. 14256.

(78) Jang, M.S., Takashige, M., Kojima, S., and Nakamura, T. (1983) Oblique phonons with special concern to the soft phonon in tetragonal $BaTiO_3$. *Journal of the Physical Society of Japan*, **52** (3), 1025–1033.

(79) Merten, L. (1968) Zur Richtungsdispersion der optischen Gitterschwingungen des tetragonalen $BaTiO_3$ bei Zimmertemperatur. *Physica Status Solidi (b)*, **25** (1), 125–130.

(80) Miao, S., Pokorny, J., Pasha, U.M., et al. (2009) Polar order and diffuse scatter in $Ba(Ti_{1\text{-}x}Zr_x)O_3$ ceramics. *Journal of Applied Physics*, **106** (11), art. no. 114111.

(81) Scalabrin, A., Chaves, A.S., Shim, D.S., and Porto, S.P.S. (1977) Temperature dependence of the A_1 and E optical phonons in $BaTiO_3$. *Physica Status Solidi (b)*, **79** (2), 731–742.

(82) Fleury, P.A. and Lazay, P.D. (1971) Acoustic-soft-optic mode interactions in ferroelectric $BaTiO_3$. *Physical Review Letters*, **26**, 1331–1334.

(83) Burns, G. (1974) Lattice modes in ferroelectric perovskites. II. $Pb_{1\text{-}x}Ba_xTiO_3$ including $BaTiO_3$. *Physical Review B*, **10** (5), 1951–1959.

(84) Deluca, M., Picht, G., Hoffmann, M.J., et al. (2014) Chemical and structural effects on the high-temperature mechanical behavior of $(1-x)(Bi_{1/2}Na_{1/2})TiO_3$–$x$$BaTiO_3$. *Journal of Applied Physics*, **117**, art. no. 134110.

(85) Schileo, G., Luisman, L., Feteira, A., et al. (2013) Structure–property relationships in $BaTiO_3$–$BiFeO_3$–$BiYbO_3$ ceramics. *Journal of the European Ceramic Society*, **33** (8), 1457–1468.

(86) Maradudin, A.A., Ganesan, S., and Burstein, E. (1967) Use of morphic effects for the study of vibrational and optical properties of impurity atoms in crystals. *Physical Review*, **163** (3), 882–895.

(87) Halasyamani, P.S. (2004) Asymmetric cation coordination in oxide materials: influence of lone-pair cations on the intra-octahedral distortion in d_0 transition metals. *Chemistry of Materials*, **16** (19), 3586–3592.

(88) Feteira, A. and Sinclair, D.C. (2009) The influence of nanometric phase separation on the dielectric and magnetic properties of $(1-x)BaTiO_3$–$x$$LaYbO_3$ $(0 < x < 0.60)$ ceramics. *Journal of Materials Chemistry*, **19** (3), 356–359.

(89) Schütz, D., Deluca, M., Krauss, W., et al. (2012) Lone-pair-induced covalency as the cause of temperature- and field-induced instabilities in bismuth sodium titanate. *Advanced Functional Materials*, **22** (11), 2285–2294.

(90) Lu, D.Y., Sun, X.Y., and Toda, M. (2007) A novel high-k “Y5V” barium titanate ceramics co-doped with lanthanum and cerium. *Journal of Physics and Chemistry of Solids*, **68** (4), 650–664.

(91) Laulhé, C., Hippert, F., Bellissent, R., et al. (2009) Local structure in $BaTi_{1\text{-}x}Zr_xO_3$ relaxors from neutron pair distribution function analysis. *Physical Review B*, **79** (6), art. no. 064104.

(92) Levin, I., Cockayne, E., Krayzman, V., et al. (2011) Local structure of Ba(Ti,Zr)O_3 perovskite-like solid solutions and its relation to the band-gap behavior. *Physical Review B*, **83** (9), art. no. 094122.

(93) Farhi, R., El Marssi, M., Simon, A., and Ravez, J. (1999) A Raman and dielectric study of ferroelectric ceramics. *The European Physical Journal B – Condensed Matter and Complex Systems*, **9** (4), 599–604.

(94) Maiti, T., Guo, R., and Bhalla, A.S. (2008) Structure-property phase diagram of $BaZr_xTi_{1-x}O_3$ system. *Journal of the American Ceramic Society*, **91** (6), 1769–1780.

(95) Feteira, A., Sinclair, D.C., and Kreisel, J. (2010) Average and local structure of $(1-x)BaTiO_3$–$xLaYO_3$ ($0 < x < 0.50$) ceramics. *Journal of the American Ceramic Society*, **93** (12), 4174–4181.

(96) Dixit, A., Majumder, S.B., Dobal, P.S., et al. (2004) Phase transition studies of sol–gel deposited barium zirconate titanate thin films. *Thin Solid Films*, **447**, 284–288.

(97) Akbarzadeh, A.R., Prosandeev, S., Walter, E.J., et al. (2012) Finite-temperature properties of Ba(Zr,Ti)O_3 relaxors from first principles. *Physical Review Letters*, **108** (25), art. no. 257601.

(98) Prosandeev, S., Wang, D., Akbarzadeh, A.R., et al. (2013) Field-induced percolation of polar nanoregions in relaxor ferroelectrics. *Physical Review Letters*, **110** (20), art. no. 207601.

(99) Curecheriu, L.P., Deluca, M., Mocanu, Z.V., et al. (2013) Investigation of the ferroelectric-relaxor crossover in Ce-doped $BaTiO_3$ ceramics by impedance spectroscopy and Raman study. *Phase Transitions*, **86** (7), 703–714.

(100) Zhang, S.T., Kounga, A.B., Aulbach, E., et al. (2007) Giant strain in lead-free piezoceramics $Bi_{0.5}Na_{0.5}TiO_3$–$BaTiO_3$–$K_{0.5}Na_{0.5}NbO_3$ system. *Applied Physics Letters*, **91** (11), art. no. 112906.

(101) Zhang, S.T., Kounga, A.B., Jo, W., et al. (2009) High-strain lead-free antiferroelectric electrostrictors. *Advanced Materials*, **21** (46), 4716–4720.

(102) Rödel, J., Jo, W., Seifert, K.T.P., et al. (2009) Perspective on the development of lead-free piezoceramics. *Journal of the American Ceramic Society*, **92** (6), 1153–1177.

(103) Wylie-van Eerd, B., Damjanovic, D., Klein, N., et al. (2010) Structural complexity of $(Na_{0.5}Bi_{0.5})TiO_3$–$BaTiO_3$ as revealed by Raman spectroscopy. *Physical Review B*, **82** (10), art. no. 104112.

(104) Hiruma, Y., Nagata, H., and Takenaka, T. (2009) Formation of morphotropic phase boundary and electrical properties of $(Bi_{1/2}Na_{1/2})TiO_3$-$Ba(Al_{1/2}Nb_{1/2})O_3$ solid solution ceramics. *Japanese Journal of Applied Physics*, **48** (9), art. no. 09KC08.

(105) Aksel, E., Forrester, J., Jones, J.L., et al. (2011) Monoclinic crystal structure of polycrystalline $Na_{0.5}Bi_{0.5}TiO_3$. *Applied Physics Letters*, **98** (15), art. no. 152901.

(106) Gorfman, S. and Thomas, P.A. (2010) Evidence for a non-rhombohedral average structure in the lead-free piezoelectric material $Na_{0.5}Bi_{0.5}TiO_3$. *Journal of Applied Crystallography*, **43** (6), 1409–1414.

(107) Ma, C., Tan, X., Dul'Kin, E., and Roth, M. (2010) Domain structure-dielectric property relationship in lead-free $(1-x)(Bi_{1/2}Na_{1/2})TiO_3$–$xBaTiO_3$ ceramics. *Journal of Applied Physics*, **108** (10), art. no. 104105.

(108) Tan, X., Aulbach, E., Jo, W., et al. (2009) Effect of uniaxial stress on ferroelectric behavior of $(Bi_{1/2}Na_{1/2})TiO_3$-based lead-free piezoelectric ceramics. *Journal of Applied Physics*, **106** (4), art. no. 044107.

(109) Schmitt, L.A. and Kleebe, H.J. (2010) Single grains hosting two space groups: a transmission electron microscopy study of a lead-free ferroelectric. *Functional Materials Letters*, **3** (1), 55–58.

(110) Schmitt, L.A., Kling, J., Hinterstein, M., et al. (2011) Structural investigations on lead-free $Bi_{1/2}Na_{1/2}TiO_3$-based piezoceramics. *Journal of Materials Science*, **46** (12), 4368–4376.

(111) Acosta, M., Scherrer, M.C., Brilz, M., et al. (2014) Designing lead-free piezoceramics: core–shell approach. *Journal of the American Ceramic Society*, submitted for publication.

(112) Simons, H., Daniels, J., Jo, W., et al. (2011) Electric-field-induced strain mechanisms in lead-free 94% $(Bi_{1/2}Na_{1/2})TiO_3$–6% $BaTiO_3$. *Applied Physics Letters*, **98** (8), art. no. 082901.

(113) Rout, D., Moon, K.S., Rao, V.S., and Kang, S.J.L. (2009) Study of the morphotropic phase boundary in the lead-free $Na_{1/2}Bi_{1/2}TiO_3$–$BaTiO_3$ system by Raman spectroscopy. *Journal of the Ceramic Society of Japan*, **117** (7), 797–800.

(114) Foronda, H., Deluca, M., Aksel, E., et al. (2014) Thermally-induced loss of piezoelectricity in ferroelectric $Na_{0.5}Bi_{0.5}TiO_3$–$BaTiO_3$. *Materials Letters*, **115**, 132–135.

(115) Matsuura, M., Iida, H., Hirota, K., et al. (2013) Damped soft phonons and diffuse scattering in $(Bi_{1/2}Na_{1/2})TiO_3$. *Physical Review B*, **87** (6), art. no. 064109.

(116) Slodczyk, A., Daniel, P., and Kania, A. (2008) Local phenomena of $(1 - x)PbMg_{1/3}Nb_{2/3}O_3$–$xPbTiO_3$ single crystals ($0 < x < 0.38$) studied by Raman scattering. *Physical Review B*, **77** (18), art. no. 184114.

(117) Luo, L., Ge, W., Li, J., et al. (2011) Raman spectroscopic study of $Na_{1/2}Bi_{1/2}TiO_3$–x% $BaTiO_3$ single crystals as a function of temperature and composition. *Journal of Applied Physics*, **109** (11), art. no. 113507.

(118) Petzelt, J., Kamba, S., Fabry, J., et al. (2004) Infrared, Raman and high-frequency dielectric spectroscopy and the phase transitions in $Na_{1/2}Bi_{1/2}TiO_3$. *Journal of Physics: Condensed Matter*, **16** (15), 2719–2731.

(119) Rout, D., Moon, K.S., Kang, S.J.L., and Kim, I.W. (2010) Dielectric and Raman scattering studies of phase transitions in the $(100 - x)Na_{0.5}Bi_{0.5}TiO_3 - xSrTiO_3$ system. *Journal of Applied Physics*, **108** (8), art. no. 084102.

(120) Balkanski, M., Wallis, R.F., and Haro, E. (1983) Anharmonic effects in light scattering due to optical phonons in silicon. *Physical Review B*, **28** (4), 1928–1934.

(121) Kumar, A., Rivera, I., and Katiyar, R.S. (2009) Investigation of local structure of lead-free relaxor $Ba(Ti_{0.70}Sn_{0.30})O_3$ by Raman spectroscopy. *Journal of Raman Spectroscopy*, **40** (4), 459–462.

(122) Yashima, M., Hoshina, T., Ishimura, D., et al. (2005) Size effect on the crystal structure of barium titanate nanoparticles. *Journal of Applied Physics*, **98**(1), art. no. 014313.

(123) Frey, M.H. and Payne, D.A. (1996) Grain-size effect on structure and phase transformations for barium titanate. *Physical Review B*, **54** (5), 3158–3168.

(124) Nakamura, T. (1988) Ferroelectricity involved in structural phase transitions (in Japanese). *Shoukabou*, **169**, 103.

(125) Rabe, K.M., Ahn, C.H., and Triscone, J.M. (eds) (2007) *Physics of Ferroelectrics: A Modern Perspective*, Springer, Berlin.

(126) Arlt, G. (1990) The influence of microstructure on the properties of ferroelectric ceramics. *Ferroelectrics*, **104** (1), 217–227.

(127) Hernandez, B.A., Chang, K.S., Fisher, E.R., and Dorhout, P.K. (2002) Sol–gel template synthesis and characterization of $BaTiO_3$ and $PbTiO_3$ nanotubes. *Chemistry of Materials*, **14** (2), 480–482.

(128) Hou, R.Z., Ferreira, P., and Vilarinho, P.M. (2009) Nanoporous $BaTiO_3$ crystallites. *Chemistry of Materials*, **21** (15), 3536–3541.

(129) Shiratori, Y., Pithan, C., Dornseiffer, J., and Waser, R. (2007) Raman scattering studies on nanocrystalline $BaTiO_{3.}$ Part I: Isolated particles and aggregates. *Journal of Raman Spectroscopy*, **38** (10), 1288–1299.

(130) Shiratori, Y., Pithan, C., Dornseiffer, J., and Waser, R. (2007) Raman scattering studies on nanocrystalline $BaTiO_{3+.}$ Part II: Consolidated polycrystalline ceramics. *Journal of Raman Spectroscopy*, **38** (10), 1300–1306.

(131) Dobal, P.S. and Katiyar, R.S. (2002) Studies on ferroelectric perovskites and Bi-layered compounds using micro-Raman spectroscopy. *Journal of Raman Spectroscopy*, **33** (6), 405–423.

(132) Smith, M.B., Page, K., Siegrist, T., et al. (2008) Crystal structure and the paraelectric-to-ferroelectric phase transition of nanoscale $BaTiO_{3.}$ *Journal of the American Chemical Society*, **130** (22), 6955–6963.

(133) Szwarcman, D., Vestler, D., and Markovich, G. (2010) The size-dependent ferroelectric phase transition in $BaTiO_3$ nanocrystals probed by surface plasmons. *ACS Nano*, **5** (1), 507–515.

(134) Buscaglia, V., Buscaglia, M.T., Viviani, M., et al. (2006) Grain size and grain boundary-related effects on the properties of nanocrystalline barium titanate ceramics. *Journal of the European Ceramic Society*, **26** (14), 2889–2898.

(135) Buscaglia, V., Buscaglia, M.T., Viviani, M., et al. (2005) Raman and AFM piezoresponse study of dense $BaTiO_3$ nanocrystalline ceramics. *Journal of the European Ceramic Society*, **25** (12), 3059–3062.

(136) Hwang, U.Y., Park, H.S., and Koo, K.K. (2004) Low-temperature synthesis of fully crystallized spherical $BaTiO_3$ particles by the gel–sol method. *Journal of the American Ceramic Society*, **87** (12), 2168–2174.

(137) Wada, S., Yasuno, H., Hoshina, T., et al. (2003) Preparation of nm-sized barium titanate fine particles and their powder dielectric properties. *Japanese Journal of Applied Physics*, **42**, 6188–6195.

(138) Eitel, R.E., Shrout, T.R., and Randall, C.A. (2006) Nonlinear contributions to the dielectric permittivity and converse piezoelectric coefficient in piezoelectric ceramics. *Journal of Applied Physics*, **99** (12), art. no. 124110.

(139) Zhang, S., Randall, C.A., and Shrout, T.R. (2005) Recent developments in high Curie temperature perovskite single crystals. *IEEE Transactions on Ultrasonics Ferroelectrics and Frequency Control*, **52** (4), 564–569.

(140) Chaigneau, J., Kiat, J.M., Malibert, C., and Bogicevic, C. (2007) Morphotropic phase boundaries in $(BiScO_3)_{1-x}(PbTiO_3)_x$ ($0.60 < x < 0.75$) and their relation

to chemical composition and polar order. *Physical Review B*, **76** (9), art. no. 094111.

(141) Datta, K., Walker, D., and Thomas, P.A. (2010) Structural investigations of the bismuth scandate-lead titanate $x\mathrm{BiScO_3}$–$(1 - x)\mathrm{PbTiO_3}$ solid solution for $0.10 < x < 0.40$. *Physical Review B*, **82** (14), art. no. 144108.

(142) Algueró, M., Amorin, H., Hungria, T., et al. (2009) Macroscopic ferroelectricity and piezoelectricity in nanostructured $BiScO_3$–$PbTiO_3$ ceramics. *Applied Physics Letters*, **94** (1), art. no. 012902.

(143) Amorín, H., Jiménez, R., Deluca, M., et al. (2014) Grain size versus boundary effects on the macroscopic properties of $BiScO_3$–$PbTiO_3$ nanostructured ceramics. *Journal of the American Ceramic Society*, **97** (9), 2802–2809.

(144) Carreaud, J., Gemeiner, P., Kiat, J.M., et al. (2005) Size-driven relaxation and polar states in $PbMg_{1/3}Nb_{2/3}O_3$-based system. *Physical Review B*, **72** (17), art. no. 174115.

(145) Haumont, R., Gemeiner, P., Dkhil, B., et al. (2006) Polar and chemical states at a nanometer scale in a $PbSc_{1/2}Nb_{1/2}O_3$–$PbTiO_3$ system investigated by Raman spectroscopy. *Physical Review B*, **73** (10), art. no. 104106.

(146) Zhu, M.K., Lu, P.X., Hou, Y.D., et al. (2006) Analysis of phase coexistence in Fe_2O_3-doped 0.2 PZN–0.8 PZT ferroelectric ceramics by Raman scattering spectra. *Journal of the American Ceramic Society*, **89** (12), 3739–3744.

(147) Cochran, W. (1959) Crystal stability and the theory of ferroelectricity. *Physical Review Letters*, **3** (9), 412–414.

(148) Jang, H.M., Oak, M.A., Lee, J.H., et al. (2009) Softening behavior of the ferroelectric A 1 (TO) phonon near the Curie temperature. *Physical Review B*, **80** (13), art. no. 132105.

(149) Yuh, J., Perez, L., Sigmund, W.M., and Nino, J.C. (2007) Electrospinning of complex oxide nanofibers. *Physica E: Low-dimensional Systems and Nanostructures*, **37** (1), 254–259.

(150) Louis, L., Gemeiner, P., Ponomareva, I., et al. (2010) Low-symmetry phases in ferroelectric nanowires. *Nano Letters*, **10** (4), 1177-1183.

(151) Everall, N.J. (2010) Confocal Raman microscopy: common errors and artefacts. *Analyst*, **135** (10), 2512–2522.

(152) Atkin, J.M., Berweger, S., Jones, A.C., and Raschke, M.B. (2012) Nano-optical imaging and spectroscopy of order, phases, and domains in complex solids. *Advances in Physics*, **61** (6), 745–842.

(153) Tarun, A., Hayazawa, N., and Kawata, S. (2009) Tip-enhanced Raman spectroscopy for nanoscale strain characterization. *Analytical and Bioanalytical Chemistry*, **394** (7), 1775–1785.

(154) Fang, Y., Seong, N.H., and Dlott, D.D. (2008) Measurement of the distribution of site enhancements in surface-enhanced Raman scattering. *Science*, **321** (5887), 388–392.

(155) Hayazawa, N., Yano, T., Watanabe, H., et al. (2003) Detection of an individual single-wall carbon nanotube by tip-enhanced near-field Raman spectroscopy. *Chemical Physics Letters*, **376** (1), 174–180.

(156) Anderson, N., Hartschuh, A., and Novotny, L. (2007) Chirality changes in carbon nanotubes studied with near-field Raman spectroscopy. *Nano Letters*, **7** (3), 577–582.

(157) Demming, A.L., Festy, F., and Richards, D. (2005) Plasmon resonances on metal tips: understanding tip-enhanced Raman scattering. *The Journal of Chemical Physics*, **122** (18), art. no. 184716.

(158) Hayazawa, N., Inouye, Y., Sekkat, Z., and Kawata, S. (2001) Near-field Raman scattering enhanced by a metallized tip. *Chemical Physics Letters*, **335** (5), 369–374.

(159) Hayazawa, N., Inouye, Y., Sekkat, Z., and Kawata, S. (2002) Near-field Raman imaging of organic molecules by an apertureless metallic probe scanning optical microscope. *The Journal of Chemical Physics*, **117** (3), 1296–1301.

(160) Stöckle, R.M., Suh, Y.D., Deckert, V., and Zenobi, R. (2000) Nanoscale chemical analysis by tip-enhanced Raman spectroscopy. *Chemical Physics Letters*, **318** (1), 131–136.

(161) Mangum, B., Shafran, E., Johnston, J., and Gerton, J. (2012) Near-field scanning optical microscopy, in *Optical Techniques for Solid-State Materials Characterization*, edited by R.P. Prasankumar and A.J. Taylor, CRC Press, Boca Raton, pp. 619–660.

(162) Roy, D., Wang, J., and Williams, C. (2009) Novel methodology for estimating the enhancement factor for tip-enhanced Raman spectroscopy. *Journal of Applied Physics*, **105** (1), art. no. 013530.

(163) Cui, X., Erni, D., Zhang, W., and Zenobi, R. (2008) Highly efficient nano-tips with metal-dielectric coatings for tip-enhanced spectroscopy applications. *Chemical Physics Letters*, **453** (4), 262–265.

(164) Anderson, M.S. and Pike, W.T. (2002) A Raman-atomic force microscope for apertureless-near-field spectroscopy and optical trapping. *Review of Scientific Instruments*, **73** (3), 1198–1203.

(165) Hayazawa, N., Tarun, A., Inouye, Y., and Kawata, S. (2002) Near-field enhanced Raman spectroscopy using side illumination optics. *Journal of Applied Physics*, **92** (12), 6983–6986.

(166) Pettinger, B., Ren, B., Picardi, G., et al. (2004) Nanoscale probing of adsorbed species by tip-enhanced Raman spectroscopy. *Physical Review Letters*, **92** (9), art. no. 096101.

(167) Sun, W.X. and Shen, Z.X. (2001) A practical nanoscopic Raman imaging technique realized by near-field enhancement. *Materials Physics and Mechanics*, **4**, 17–21.

(168) Berweger, S. and Raschke, M.B. (2010) Signal limitations in tip-enhanced Raman scattering: the challenge to become a routine analytical technique. *Analytical and Bioanalytical Chemistry*, **396** (1), 115–123.

(169) Poborchii, V., Tada, T., and Kanayama, T. (2005) Subwavelength-resolution Raman microscopy of Si structures using metal-particle-topped AFM probe. *Japanese Journal of Applied Physics*, **44** (6), L202–L204.

(170) Gucciardi, P.G., Lopes, M., Déturche, R., et al. (2008) Light depolarization induced by metallic tips in apertureless near-field optical microscopy and tip-enhanced Raman spectroscopy. *Nanotechnology*, **19** (21), art. no. 215702.

(171) Lee, K.G., Kihm, H.W., Kihm, J.E., et al. (2007) Vector field microscopic imaging of light. *Nature Photonics*, **1** (1), 53–56.

(172) Merlen, A., Valmalette, J.C., Gucciardi, P.G., et al. (2009) Depolarization effects in tip-enhanced Raman spectroscopy. *Journal of Raman Spectroscopy*, **40** (10), 1361–1370.

(173) Motohashi, M., Hayazawa, N., Tarun, A., and Kawata, S. (2008) Depolarization effect in reflection-mode tip-enhanced Raman scattering for Raman active crystals. *Journal of Applied Physics*, **103** (3), art. no. 034309.

(174) Ossikovski, R., Nguyen, Q., and Picardi, G. (2007) Simple model for the polarization effects in tip-enhanced Raman spectroscopy. *Physical Review B*, **75** (4), art. no. 045412.

(175) Berweger, S., Neacsu, C.C., Mao, Y., et al. (2009) Optical nanocrystallography with tip-enhanced phonon Raman spectroscopy. *Nature Nanotechnology*, **4** (8), 496–499.

12

Neutron and Synchrotron X-Ray Scattering Studies of Bulk and Nanostructured Multiferroic and Ferroelectric Materials

Evagelia G. Moshopoulou[1,2], Pascale Foury-Leylekian[2], Katharine Page[3], Céline Doubrovsky[2], Martha Greenblatt[4], and Alan J. Hurd[5]

[1]*Institute of Nanoscience and Nanotechnology, National Center for Scientific Research "Demokritos", Greece*
[2]*Laboratoire de Physique des Solides, Université de Paris Sud, Campus d'Orsay, France*
[3]*Spallation Neutron Source, Oak Ridge National Laboratory, USA*
[4]*Department of Chemistry and Chemical Biology, Rutgers, The State University of New Jersey, USA*
[5]*Los Alamos National Laboratory, USA*

12.1 Introduction

Since its discovery [1] about a century ago, the phenomenon of ferroelectricity has been investigated in relation to the host material's crystal lattice. A ferroelectric crystal is defined as a material that possesses a spontaneous electrical polarization that is stable, can be switched hysteretically by an applied electric field, and is manifested in the form of cooperative structural displacements. As a consequence, whereas knowledge of the crystal structure is the *sine qua non* of understanding the properties of any material, ferroelectrics exemplify clearly and beautifully the inseparability between crystal structure and physical properties.

Nanoscale Ferroelectrics and Multiferroics: Key Processing and Characterization Issues, and Nanoscale Effects, First Edition. Edited by Miguel Algueró, J. Marty Gregg, and Liliana Mitoseriu.
© 2016 John Wiley & Sons, Ltd. Published 2016 by John Wiley & Sons, Ltd.

The first material, where ferroelectricity was observed was Rochelle salt [1] (potassium sodium tartrate, $KNaC_4H_4O_6.4H_2O$). This salt was initially synthesized at the French city La Rochelle in 1665 and was called "sel polychreste" [2], which means a salt (sel) of many and various uses (polychreste is a word derived from the Greek word "$\pi o\lambda \upsilon\chi\rho\eta\sigma\tau o\varsigma$"). Interestingly, for over two centuries, this salt was widely used "only" as a mild drug. Its physical properties were first approached [3] in 1824, nearly two centuries after its discovery, and it was investigated in more detail later by Pierre and Paul-Jacques Curie [4] in 1880. The term ferroelectricity was coined, however, even later, in 1912, by Schrodinger [5], following earlier theoretical work by Debye [6], which suggested that permanent dielectric polarization can exist even in the absence of an external electric field. The seminal work of Joseph Valasek [1, 7], however, on the properties of Rochelle salt at the University of Minnesota, actually opened the field of ferroelectricity. Valasek stated that "permanent polarization is the natural state" for Rochelle salt and published the first hysteresis curve for a ferroelectric material. Since then the academic interest of understanding the phenomenon of ferroelectricity and the role of the underlying crystal structure was exploded and it was almost always intertwined with the potential applications of ferroelectrics. Several other ferroelectric materials were discovered during the last century, among the most known being $BaTiO_3$, KH_2PO_4, etc. Some of them form the basic components of various electronic devices today; for example they can be commonly found in ferroelectric random access devices. From the numerous investigations of the structure–property relationship in ferroelectrics, it is now well-established that the crystal symmetry of a ferroelectric material (including inversion symmetry) is broken from a nonpolar state at high temperature to a polar state at low temperature, having the symmetry of one of the ten pyroelectric polar groups.

In addition to the discovery of the ferroelectricity, Valasek also pointed out for first time the "magnetic analogy" [7], that is the parallelism between the ferroelectric behavior of Rochelle salt and the phenomenon of ferromagnetism as described by the Weiss theory of magnetism. He noticed that "some of the features of Weiss's theory of magnetism may find their counterpart in the phenomena in Rochelle salt". Valasek based this on the analogy between the (E, P) hysteresis curves of ferroelectrics and the (H, M) ones of ferromagnets, where E is the applied external electric field, P is the induced polarization, H is the applied external magnetic field, and M is the induced magnetization. The striking similarities between ferroelectric and ferromagnetic materials, pointed out since these early days of ferroelectricity and ferromagnetism, were: (i) their response to external electric and magnetic fields, respectively, (ii) the anomalies at a critical temperature (Curie point) of the electric polarization and magnetization correspondingly, and (iii) the presence of domain structures.

Since this first study, ferroelectricity and ferromagnetism were investigated as distinct classes of materials, mostly in parallel. However, the effect that bridges these two classes of materials, namely the magnetoelectric effect, had already been discovered [8] in 1888 by Röntgen. The magnetoelectric effect describes the influence of a magnetic (electric) field on the electric polarization (magnetization) of a material. In addition to the discovery of the magnetoelectric effect, the crystallographic symmetry requirements for a crystal to exhibit intrinsic magnetoelectric behavior were pointed out [9] for first time by Pierre Curie in 1894. Since these first studies, the magnetoelectric effect and the mechanism behind this effect, the magnetoelectric coupling, were extensively investigated and till a few years ago they appeared to form a rather mature area of science. However, in the last decade,

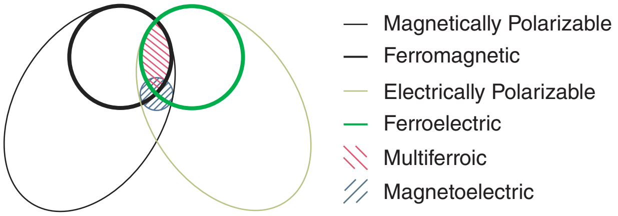

Figure 12.1 *Relationship between ferroelectric, ferromagnetic, multiferroic, and magnetoelectric materials. Reprinted by permission from Macmillan Publishers Ltd: [Nature] [11], copyright (2005)*

this area has undergone a surprising and impressive renaissance [10] thanks to: (i) the discovery and the strong significance (fundamental and applied) of materials exhibiting magnetoelectric coupling and (ii) the advanced synchrotron X-rays and neutron facilities that allow, through scattering, spectroscopy and imaging, to investigate the microscopic coupling mechanism(s) behind the magnetoelectric effect.

This coupling between electric and magnetic order parameters can take place whatever the nature of the electric or magnetic order parameters (antiferro-, ferro-, ferri-) and can be direct or indirect. Direct magnetoelectric coupling (proper or inproper) occurs, through various mechanisms [10–13], in single-phase multiferroics – materials that possess two of the so-called "ferroic" properties of ferroelectricity, ferromagnetism, and ferroelasticity, even if the current trend is to exclude the requirement for ferroelasticity but to include antiferroic order. Indirect magnetoelectric coupling occurs when the magnetic and electric order parameters arise in separate but intimately connected compounds, i.e. in (nano)composite materials (layered heterostructures, core–shell nanoparticles, etc). This indirect coupling is either strain-mediated and/or due to interfacial effects [10–12].

It is important to emphasize that the presence of electric and magnetic order in single-phase or composite materials does not guarantee the strong coupling among them. Therefore, given the various "sources" of magnetoelectric coupling just mentioned in the previous paragraph, the overlap of the terms "multiferroic" and "magnetoelectric" is incomplete, as shown in Figure 12.1, which also presents schematically the taxonomy of the materials involving ferroic properties.

Understanding the microscopic origin of ferroelectricity and multiferroelectricity requires understanding of the role of the lattice on the electric order in the case of ferroelectrics and on the electric and magnetic orders (and their magnetoelectric coupling) in the case of multiferroics. This challenging problem requires key information on: (i) the detailed crystal structure (including disorder and defects) of the material; (ii) the atomic displacements and the structural phase transitions that are cooperative to the magnetoelectric coupling; (iii) the detailed magnetic and/or charge order that favors such coupling; and (iv) the dynamics (spin waves, phonons, electromagnons) related to the magnetoelectric coupling. All these issues fall in the realm of science taking place at neutron and synchrotron X-ray facilities worldwide: scattering, spectroscopy, imaging.

The scope of this chapter is not to review the plethora of structural results reported in the literature on ferroelectric, multiferroic, and magnetoelectric materials obtained at neutron and synchrotron X-ray facilities. Our aim is rather to highlight neutron and synchrotron

X-ray elastic scattering as unique probes to provide detailed quantitative information on the structural parameters at various length scales, which is critical for establishing the microscopic mechanism behind ferroelectricity and multiferroelectricity for any material bulk or nanostructure. We begin by discussing briefly the use of neutron and synchrotron X-ray facilities for the scattering studies of materials in general, and ferroelectrics or multiferroics in particular. We then turn to our synchrotron X-ray scattering results on the single-phase multiferroic $NdMn_2O_5$. The structural differences between the various forms of this material will be presented and the structure–property relationship will be discussed. Finally, we discuss the neutron total scattering method (and the associated pair distribution function analysis) for nanostructure determination, and present the room temperature structure of the core/shell $BaTiO_3/SiO_2$ nanocomposite deduced by this method.

12.2 Synchrotron X-Ray and Neutron Facilities for Structural Characterization of Ferroelectrics and Multiferroics

Today's materials researcher has a wide variety of synchrotron X-ray and neutron scattering techniques at his/her disposal to probe the structure and dynamics of multiferroics and ferroelectric materials (bulk and nanostructured). Rarely used alone, scattering complements microscopy and measurements of behavior such as transport, electrical, magnetic, mechanical, acoustic, and thermodynamic response functions. Structural insights from scattering are often a good first experiment to formulate hypotheses about a material's physics and functionality.

This chapter concentrates on neutron and X-ray scattering, themselves mutually complementary, though light scattering, electron scattering, and muon spectroscopy are commonly used as well in multiferroic and ferroelectric materials. In addition to diffraction, spectroscopy and imaging are also widely used at synchrotron X-ray and neutron facilities to provide the complete, precise, and accurate structure at local, nano-, meso-, and average length scales of the material. The powerful instruments at leading synchrotron and neutron user facilities offer world-class capability and world-class expertise at very low cost to the user, and when used together neutrons and X-rays offer great acuity on the behavior of complex materials.

Neutron–synchrotron X-ray complementarity occurs at several levels of technical detail. Synchrotron X-rays excel in flux and high throughput, strong scattering at high atomic numbers, fluorescence, high temporal and lateral resolution, and zero sample activation. Coherent X-ray sources based on free-electron lasers now deliver an outstanding new capability including polarization, which will greatly enhance experiments on ferroelectrics and multiferroics. Neutrons offer deep penetration depth, sensitivity to low atomic numbers and certain isotopes, superior magnetic sensitivity, and a flat form factor extending to high scattering angles for pair distribution correlation functions. In addition, synchrotron X-rays can explore routinely even tiny samples, in contrast to neutrons, which often impose lower limits on the size of the samples, especially for inelastic scattering experiments.

Tables 12.1 and 12.2 provide a comprehensive list of synchrotron and neutron facilities across the world including regional and university facilities. Most of the facilities sponsor a general access user program through which anyone may apply. Outside of general access, additional beam time may be available to certain communities or member states.

Table 12.1 *List of synchrotron facilities across the world including regional and university facilities*

Continent	Country	Synchrotron
Americas	USA	ALS – Advanced Light Source
Americas	USA	APS – Advanced Photon Source
Americas	USA	CAMD – Center for Advanced Microstructures and Devices
Americas	USA	CHESS – Cornell High Energy Synchrotron Source
Americas	Canada	CLS – Canadian Light Source
Americas	USA	CTST – UCSB Center for Terahertz Science and Technology
Americas	USA	DFELL – Duke Free Electron Laser Laboratory
Americas	USA	Jlab – Jefferson Lab
Americas	USA	LCLS – Linac Coherent Light Source
Americas	Brazil	LNLS – Laboratorio Nacional de Luz Sincrotron
Americas	USA	NSLS and NSLSII – National Synchrotron Light Source
Americas	USA	SRC – Synchrotron Radiation Center
Americas	USA	SSRL – Stanford Synchrotron Radiation Lightsource
Americas	USA	SURF – Synchrotron Ultraviolet Radiation Facility
Americas	USA	VU FEL – W.M. Keck Vanderbilt Free-Electron Laser Center
Asia	PR China	BSRF – Beijing Synchrotron Radiation Facility
Asia	Armenia	CANDLE
Asia	Japan	HSRC – Hiroshima Synchrotron Radiation Center
Asia	Japan	iFEL – Institute of Free Electron Laser
Asia	India	INDUS 1/INDUS 2
Asia	Japan	IR FEL Research Center – FEL–SUT
Asia	Japan	Medical Synchrotron Radiation Facility
Asia	Japan	Nano-Hana
Asia	PR China	NSRL – National Synchrotron Radiation Laboratory
Asia	Taiwan	NSRRC – National Synchrotron Radiation Research Center
Asia	Japan	NUSRC – Nagoya University Synchrotron Radiation Research Center
Asia	Japan	KSR – Nuclear Science Research Facility
Asia	Korea	PAL – Pohang Accelerator Laboratory
Asia	Japan	PF – Photon Factory KEK
Asia	Japan	Ritsumeikan University (Rits) Synchrotron Radiation Center
Asia	Japan	SACLA – SPring-8 Angstrom Compact Free Electron Laser
Asia	Japan	SAGA-LS – Saga Light Source
Asia	Thailand	SLRI – Synchrotron Light Research Institute
Asia	Japan	SPring-8
Asia	Singapore	SSLS – Singapore Synchrotron Light Source
Asia	Russian Federation	SSRC – Siberian Synchrotron Research Center
Asia	PR China	SSRF – Shanghai Synchrotron Radiation Facility

(continued)

Table 12.1 *(Continued)*

Continent	Country	Synchrotron
Asia	Japan	SuperSOR – SuperSOR Synchrotron Radiation Facility
Asia	Japan	TSRF – Tohoku Synchrotron Radiation Facility
Asia	Japan	UVSOR – Ultraviolet Synchrotron Orbital Radiation Facility
Europe	Spain	ALBA – Synchrotron Light Facility
Europe	Germany	ANKA – Angstromquelle Karlsruhe
Europe	Germany	BESSY II – Helmholtz–Zentrum Berlin (HZB)
Europe	Czech Republic	CESLAB – Central European Synchrotron Laboratory
Europe	France	CLIO – Centre Laser Infrarouge d′Orsay
Europe	Italy	DAFNE Light
Europe	Russian Federation	DELSY – Dubna ELectron SYnchrotron
Europe	Germany	DELTA – Dortmund Electron Test Accelerator
Europe	UK	Diamond Light Source
Europe	Germany	European XFEL - European X-ray Free Electron Laser
Europe	Italy	ELETTRA – Synchrotron Light Laboratory
Europe	Germany	ELSA – Electron Stretcher Accelerator
Europe	France	ESRF – European Synchrotron Radiation Facility
Europe	Germany	FELBE – Free-Electron Lasers at the ELBE radiation source at the FZD
Europe	The Netherlands	FELIX – Free Electron Laser for Infrared eXperiments
Europe	Germany	HASYLAB – Hamburger Synchrotronstrahlungslabor at DESY
Europe	Denmark	ISA – Institute for Storage Ring Facilities
Europe	Ukraine	ISI-800 – Institute of Metal Physics
Europe	Ukraine	Kharkov Institute of Physics and Technology
Europe	Russian Federation	KSRS – Kurchatov Synchrotron Radiation Source
Europe	Sweden	MAX IV Laboratory
Europe	Germany	MLS – Metrology Light Source
Europe	Poland	PSLS – Polish Synchrotron Light Source
Europe	Switzerland	SLS – Swiss Light Source
Europe	France	SOLEIL
Europe	Italy	SuperB FEL
Europe	Russian Federation	TNK – F.V. Lukin Institute
Middle East	Iran	ILSF – Iranian Light Source Facility
Middle East	Jordan	SESAME
Oceania	Australia	AS – Australian Synchrotron

A growing number of scattering experiments taking place at synchrotron X-ray and neutron facilities probes the structure of nanostructured materials. Quantitative determination of the nanostructure [14] is far from trivial and it lies beyond traditional crystallographic methods, which break down at the nanoscale. It is known, however, that the nanostructure is as essential [15] for understanding the nanomaterial's physics, properties, and functionalities as the knowledge that the crystal structure of bulk compounds (inorganic, organic, biological) has been fundamental for the spectacular advances in almost all physical sciences in the last nearly hundred years. For this reason, experimental, non-destructive

Table 12.2 *List of neutron facilities across the world including regional and university facilities*

Continent	Country	Neutron facility
Asia	Japan	ISSP Neutron Scattering Laboratory
Asia	Japan	JAEA Research Reactors
Asia	Japan	KENS Neutron Scattering Facility
Asia	Korea	Hi-Flux Advanced Neutron Application Reactor
Asia	India	Bhabha Atomic Research Centre
Asia	China	China Spallation Neutron Source (CSNS)
Europe	Austria	Austron Spallation Neutron Source
Europe	Sweden	European Spallation Source (ESS)
Europe	United Kingdom	ISIS-Rutherford-Appleton Laboratories
Europe	France	Institut Laue-Langevin
Europe	France	Leon Brillouin Laboratory
Europe	Germany	Berlin Neutron Scattering Center
Europe	Germany	GEMS at Helmholtz-Zentrum Geesthacht
Europe	Germany	Juelich Center for Neutron Science
Europe	Germany	FRM-II
Europe	Hungary	Budapest Neutron Centre
Europe	Netherlands	RID
Europe	Switzerland	SINQ
Europe	Russia	Frank Laboratory of Neutron Physics
Europe	Russia	St. Petersburg Neutron Physics Institute
North America	USA	Oak Ridge Neutron Facilities (SNS/HFIR)
North America	USA	Los Alamos Neutron Science Center (LANSCE)
North America	USA	University of Missouri Research Reactor Center
North America	Canada	Canadian Neutron Beam Centre
North America	USA	Indiana University Cyclotron Facility
Oceania	Australia	Bragg Institute

tools, based at neutron and synchrotron X-ray facilities, have been proposed [15], conceived, and developed in recent years. Experiments at such beamlines, in conjunction with advanced data analysis and complex modeling, extend quantitatively, rather than reiterate qualitatively, the structural studies carried out at laboratories using transmission electron microscopes (TEMs). Moreover, the high complexity of advanced materials, as is the case of ferroelectrics and multiferroics, bulk or nanostructured (single- or multi-component), and the need to find unique, quantitative, comprehensive, and robust nanostructure solutions [14] impose the combined use of different beamlines providing highly complementary information.

12.3 Crystal Structure of $NdMn_2O_5$ in Powder and Single Crystalline Forms

12.3.1 Multiferroelectricity in RMn_2O_5 Compounds

Ferroelectricity and magnetism in solids have, in general, different origins and they do not interfere with each other: whereas magnetism results from the ordering of the spins of electrons in incomplete *d* or *f* ionic shells, ferroelectricity is induced by relative shifts of cations and anions so that they share electron pairs between them and thus attain complete shells, that is stable electronic configurations through covalent bonding. Not only are these two ordered states seemingly mutually exclusive [16, 17] but also, if they are present in the same material, they are not [18, 19] necessarily coupled. However, work for bringing ferroelectricity and magnetism together in the same material started about six decades ago, leading to interesting and promising results [20–23]. These studies were mainly driven by the prospect of controlling charges (electric properties) by an externally applied magnetic field and spins (magnetic properties) by applied voltages, with the ultimate aim to obtain multifunctional materials. However, the magnetoelectric effects were too small to be useful for applications. The challenging and long-sought search for "strong magnetoelectric coupling" was achieved about a decade ago by Kimura et al. [24] who "found gigantic magnetoelectric and magnetocapacitance effects in $TbMnO_3$, which can be attributed to switching of the electric polarization induced by magnetic fields". Such observation of magnetically induced ferroelectricity is reminiscent (but based on completely different mechanisms) of the magnetically mediated superconductivity [25] in heavy-fermion systems. Kimura discovered strong magnetoelectric coupling in a rather unexpected class of materials known as "frustrated magnets".

In frustrated magnets, localized magnetic moments interact through competing exchange interactions that cannot be simultaneously satisfied (because of the geometric arrangement of the moments), giving rise to a large degeneracy of the material's ground state and precluding simple magnetic orders. The resulting low-temperature complex magnetic structures often lack the inversion symmetry of the higher-temperature underlying crystal structure. In such magnetic states, two main microscopic mechanisms are usually proposed to account for the emergence of a spin-induced ferroelectricity, depending on the collinearity or not of the magnetic structure. (a) In the case of a magnetic order of collinear spins, an exchange-striction mechanism can explain the shift of the ions in such a way that the spin-exchange energy is minimized, leading to lattice distortions, which may be polar and thus induce electric polarization, that is ferroelectricity. (b) When the ground state is a non-collinear magnetic structure, then the antisymmetric Dzyaloshinskii–Moriya interaction between the non-collinear ordered spins favors the displacement of the negatively charged ligands, breaks the inversion symmetry, and thus induces electric polarization in the system.

A key step leading to the rational design and discovery of new multiferroics or to the optimization of the properties of the known ones is to understand the underpinning principle(s) of the presence, absence, and scaling of multiferroic behavior among the members of a class of compounds. The orthorhombic rare-earth manganites RMn_2O_5 (R: rare earth elements, Y or Bi) are particularly suited to this aim. All the members of the class RMn_2O_5 adopt [26] the centrosymmetric orthorhombic space group P*bam* at RT with Mn^{3+} ions in oxygen pyramids, Mn^{4+} ions in oxygen octahedra and R atoms in oxygen bicapped trigonal prisms (i.e. eightfold coordinated to oxygen atoms). However, recent high-resolution synchrotron X-ray experiments on single crystal [27] suggested interesting slight deviations from this average structure for all members of the series. The $[Mn^{4+}O_6]$ octahedra share edges between them and form infinite chains parallel to the *c* axis. These chains are linked, through corner sharing, with the $Mn^{4+}O_5$ pyramids that form edge-sharing dimmers (Figure 12.2) [28]. All RMn_2O_5 compounds are isostructural, at least at RT, and they all exhibit rich magnetic phase diagrams at low temperatures (due to complex patterns of

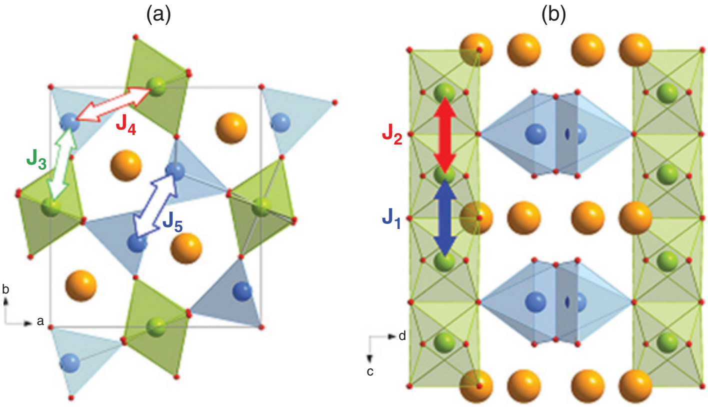

Figure 12.2 *Projections of the crystal structure of RMn$_2$O$_5$ (a) along the c axis and (b) along the b axis. The superexchange interactions J_i ($i = 1, 2, 3, 4, 5$) are indicated. Reprinted (Figure 1) with permission from [28]. Copyright (2012) by the American Physical Society*

magnetic interactions). However, the role that the nature (i.e. size, number of *f* electrons) of the R^{3+} ion plays on whether ferroelectricity emerges or not at an RMn$_2$O$_5$ compound and on the strength of the concomitant magnetoelectric coupling is at present an active area of research. In the members with smaller R^{3+} sizes (i.e. from Tb to Yb) magnetism and ferroelectricity coexist and couple; in contrast, the member with intermediate R^{3+} size (i.e. Pr) is not ferroelectric and does not undergo a transition to an incommensurate magnetic state. In order to uncover the underlying reasons of such contrasting behavior among the members of the same family of isostructural compounds, and thus of the intrinsic causes of the magnetically induced ferroelectricity in RMn$_2$O$_5$ materials, it is significant to study, in addition to PrMn$_2$O$_5$, the other member with rather large R^{3+} sizes (i.e. Nd) and compare it with their ferroelectric counterparts with smaller R^{3+} sizes. Such studies, while appealing, have been delayed for several years mainly because of the difficulty to synthesize high-quality (i.e. clean) polycrystalline samples and especially to grow high-quality single crystals of NdMn$_2$O$_5$ and PrMn$_2$O$_5$. This difficulty was overcome recently, opening to us the possibility to investigate these compounds.

The present study was undertaken against the above background. It is focused on NdMn$_2$O$_5$ in both powder and single-crystal forms and explores the subtle differences of their crystal structures determined by high-resolution synchrotron X-ray diffraction. Our aim was to establish the basis for further structural investigations [29] at low temperatures and/or under a magnetic field, which address the reasons (structural and/or magnetic) that allow small polar displacements and thus induce weak ferroelectricity in this material.

12.3.2 Synthesis of NdMn$_2$O$_5$

High-purity polycrystalline NdMn$_2$O$_5$ was synthesized following the method described by previous work [30]. Initially, highly pure Nd$_2$O$_3$ was dried for 24 h at 650 °C, and metallic Mn was washed with dilute HCl. Stoichiometric amounts of both these ingredients were dissolved in HNO$_3$ solution and dried overnight at 250 °C. The obtained precursor was heated again at 600 °C for 12 h in an alumina crucible. The obtained powder was thoroughly ground and pressed into pellets, which were sintered at 1100 °C for 48 h under oxygen flow.

Single crystals of $NdMn_2O_5$ were grown [31] by electrolysis of a mixture of molten salts Na_2MoO_4, MoO_3, $MnCO_3$, and Nd_2O_3 in high density alumina crucibles using Pt electrodes. The obtained crystals are black and have two habit types: plates and needles.

12.3.3 Synchrotron X-Ray Powder Diffraction Data Collection

High-resolution synchrotron X-ray powder diffraction experiments were carried out at RT on two powder samples: (a) the as-prepared powder of $NdMn_2O_5$ and (b) powder resulting from hand-ground and shifted $NdMn_2O_5$ single crystals with a plate-type habit. The synchrotron X-ray diffraction experiments were performed on the CRISTAL beamline [32], a high-resolution undulator-based beamline, at the Synchrotron Light Source SOLEIL (France) using a two-circle diffractometer. The accuracy of the diffractometer and its instrumental resolution were determined at the beginning of the experiments by collecting the diffraction data of the standard material LaB_6. This reference data collection is of critical importance for both high accuracy (i.e. agreement with the physically correct values as established by independent measurements) and precision (i.e. small standard deviations) of the resulting structural parameters since accurate determination of the instrumental resolution is the key prerequisite for determination of peak profile parameters, which are intrinsic to the samples. The data were collected in the 2θ range 4°–25° with a step of 0.002° for all three samples. A wavelength of 0.5773 Å was selected for the powder sample resulting from the hand-ground and shifted $NdMn_2O_5$ single crystals and a wavelength 0.6207 Å was chosen for the as-prepared powder $NdMn_2O_5$ sample; these wavelengths were optimal in order to minimize absorption effects.

12.3.4 Synchrotron X-Ray Powder Diffraction Data Analysis

The synchrotron X-ray diffraction data were analyzed by the Rietveld method using the general structure analysis system (GSAS) [33]. The initial structural model, introduced in GSAS, was the crystal structure of $NdMn_2O_5$ obtained by Euzen et al. [34]. The instrumental background was fitted by a Chebyshev polynomial with six coefficients to be refined. The high-resolution powder diffractometer at the CRISTAL beamline has a well-defined instrumental line-shape, which is described by the profile function 2 of GSAS. This function integrates pseudo Voigt functions characterized by the mixing coefficient between the Lorentzian and Gaussian functions. The coefficients of the function can be interpreted in order to provide both strain and particle size information. The initial values of all profile coefficients for each sample were the values deduced from the refinement of the standard LaB_6 using profile function 2 as well.

The same refinement procedure was followed for the two samples. At the first steps of the refinement only the scale factor and the background coefficients were refined. In the next few cycles, the cell constants of $NdMn_2O_5$ were refined as well. No impurities were present in any of our samples. The profile coefficients LX and LY, which describe particle size and peak broadening, respectively [33], were then refined, improving the fit considerably. A few exploratory refinements were next carried out where other profile coefficients were varied, but these refinements either result in meaningless values or they even diverge.

Among the positional parameters of $NdMn_2O_5$, the x and y parameters of Nd, the z parameter of Mn1, the x and y parameters of Mn2, the z parameter of O1, the x and y parameters of O2 and O3, and the x, y, and z parameters of O4 are not fixed by symmetry and thus these parameters were also varied successively for Nd, Mn1 and Mn2, and O1, O2, O3, and O4. Corrections for absorption and zero-point shifts were applied next. Subsequently, isotropic atomic displacement parameters were also allowed to vary successively for Nd, Mn1 and Mn2, and O1, O2, O3, and O4. In the next few cycles the occupancies of the Nd, Mn's, and O's where allowed to vary successively. Because of the fact that atomic displacement parameters and site occupancies have too much correlation for independent refinement, at the next cycles the atomic displacements were fixed and the site occupancies were allowed to vary together with all previously refined parameters. Convergence was achieved, and at the final cycles the atomic displacements were allowed to vary as well, together with the site occupancies and all previous parameters. It is worth noting that, despite the great care taken at every step of data collection, data reduction, and structure refinement, a small negative value for the isotropic atomic displacement parameter Mn1 resulted, which obviously does not have any physical meaning. It may have been due to thermal diffuse scattering, which can seriously affect the thermal parameters. Thermal diffuse scattering corrections could not be applied to our data because not only the experimental conditions but also the elastic constants of the materials have to be known. Also, anharmonic atomic motions can affect the thermal parameters. In addition, refinements were carried out after fixing the occupancies of the O sites to 1, taking into consideration the fact that occupancies of light atoms cannot be accurately determined by X-rays. The obtained values of the lattice constants, atomic coordinates, and atomic displacements (including the small negative value of Uiso of Mn1) remained the same (within the estimated standard deviation) as the values listed in Table 12.3.

12.3.5 Results

Table 12.3 lists the structural parameters, the profile coefficients, as well as the numerical criteria of the fit (R_p, and χ^2) of $NdMn_2O_5$. Nd and O2 ions are at 4g (x, y, 0) positions; Mn1 (Mn^{4+}) at 4f (0, 1/2, z); Mn2 (Mn^{3+}) and O3 at 4h (x, y, 1/2); O1 at 4e (0, 0, z); and O4 at 8i (x, y, z) positions. The diffraction profiles for the powder and crashed single-crystal samples are shown in Figures 12.3 and 12.4, respectively.

Selected interatomic distances and angles calculated from the refined cell constants and atomic coordinates are listed in Table 12.4.

12.3.6 Discussion

A number of important conclusions can be drawn from Tables 12.3 and 12.4. Both single crystalline and powder samples exhibit deviations from the stoichiometric composition $NdMn_2O_5$, these deviations being more severe for the single crystalline sample. As a result, the lattice constants and the cell volume of the single crystalline sample are significantly smaller than the corresponding ones of the powder sample. The positional parameters x, y, and z of all atoms differ slightly among the single crystalline and powder samples.

The above differences between the two samples affect the basic polyhedra (octahedra, rectangular pyramids, and bicapped prisms) of the structure, which present different distortions and thus different metal–metal distances. The most significant (for the physics of the

Table 12.3 *Refined structural parameters of $NdMn_2O_5$ powder and single crystals at room temperature*

Parameters	Powders	Single crystals (plates)
a (Å)	7.512329(20)	7.469203(31)
b (Å)	8.623612(22)	8.583076(33)
c (Å)	5.704554(15)	5.678176(24)
V (Å^3)	369.560(1)	364.020(3)
x_Nd	0.142936(43)	0.142459(79)
y_Nd	0.173043(51)	0.172476(94)
z_Nd	0	0
x_Mn1	0	0
y_Mn1	0.5	0.5
z_Mn1	0.25925(16)	0.26008(29)
x_Mn2	0.41006(10)	0.41027(20)
y_Mn2	0.35149(10)	0.35271(20)
z_Mn2	0.5	0.5
x_O1	0	0
y_O1	0	0
z_O1	0.277388(63)	0.28104 (93)
x_O2	0.16022(51)	0.15062(92)0
y_O2	0.45307(44)	0.44540(75)
y_O2	0	0
x_O3	0.15186(49)	0.14911(91)
y_O3	0.435979(370)	0.43999(69)
z_O3	0.5	0.5
x_O4	0.40011(29)	0.40284 (54)
y_O4	0.20477(30)	0.20568(54)
z_O4	0.24886(38)	0.25381(69)
U_{iso}_Nd	0.214(6)	0.366(15)
U_{iso}_Mn1	−0.004(20)	−0.251(47)
U_{iso}_Mn2	0.115(22)	0.336(57)
U_{iso}_O1	0.603(114)	2.184(255)
U_{iso}_O2	0.918(121)	0.952(249)
U_{iso}_O3	0.760(96)	0.610(205)
U_{iso}_O4	0.681 (76)	2.171(204)
Occupancy coefficient_Nd	0.952(1)	0.885(1))
Occupancy coefficient_Mn1	0.964(2)	0.876(3)
Occupancy coefficient_Mn2	0.956(2)	0.858(3)
Occupancy coefficient_O1	0.979(8)	1.067(14)
Occupancy coefficient _O2	1.005(8)	0.924(13)
Occupancy coefficient _O3	1.055 (8)	0.924 (12)
Occupancy coefficient _O4	1.006(6)	1.005(11)
LX	0.3564(117)	0.1765(111)
LY	15.68(9)	12.90(9)
R_p	10.62%	10.20%
χ^2	2.656	1.555

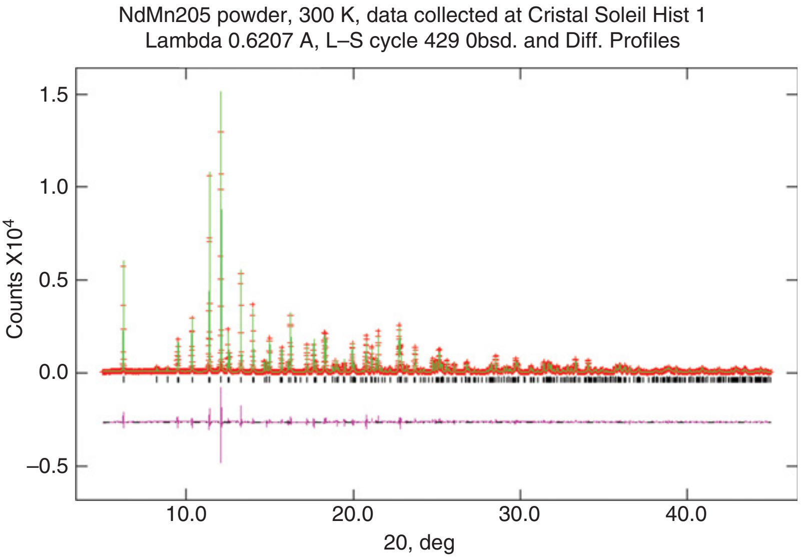

Figure 12.3 Observed (crosses), calculated, and difference synchrotron X-ray powder diffraction profiles of NdMn$_2$O$_5$ powder

materials) differences between the interatomic distances are the ones among the Mn magnetic cations, since Mn–Mn distances affect directly the superexchange interactions and thus the physical properties of these materials. There are totally five non-equivalent, nearest-neighbor superexchange interactions between the Mn^{3+} and Mn^{4+} magnetic cations. J_1

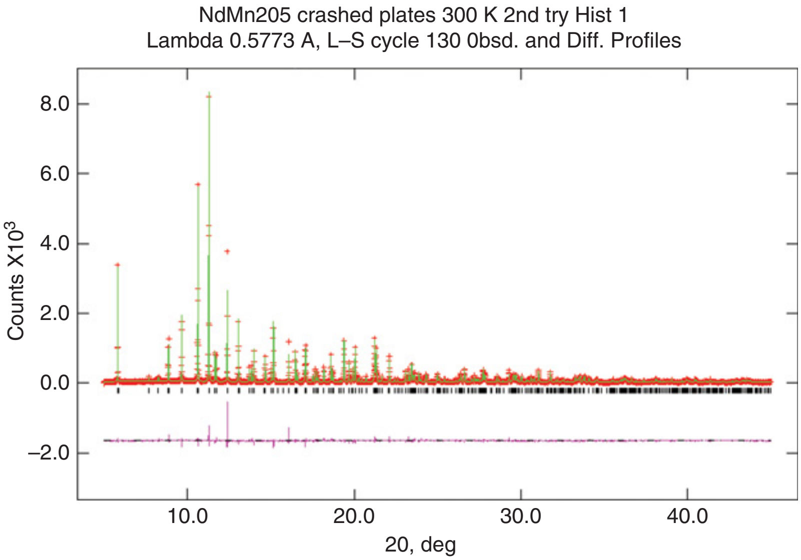

Figure 12.4 Observed (crosses), calculated, and difference synchrotron X-ray powder diffraction profiles of NdMn$_2$O$_5$ crushed single crystals

Table 12.4 *Select interatomic distances and angles of NdMn$_2$O$_5$ powder and single crystals at room temperature deduced from the refined atomic positions and cell constants*

[Mn1O$_6$] octahedra		
Interatomic distances (Å)	Powder	Single crystals (plates)
Mn1 - O2 × 2	1.9493(25)	1.915(4)
Mn1 - O3 × 2	1.8688(24)	1.833(4)
Mn1 - O4 × 2	1.9196(25)	1.909(5)
Angles (°)	Powder	Single crystals (plates)
O2 - Mn1 - O2	81.30(17)	79.06(32)
O2 - Mn1 - O3	96.85(12)	98.48(21)
O2 - Mn1 - O4	85.76(13)	89.35(23)
O3 - Mn1 - O3	85.41(17)	84.02(33)
O3 - Mn1 - O4	89.40(13)	89.14(24)
[Mn2O$_5$] tetragonal pyramid		
Interatomic distances (Å)	Powder	Single crystals (plates)
Mn2 - O1 × 2	1.9259(25)	1.899(4)
Mn2 - O4 × 2	1.9129(25)	1.884(4)
Mn2 - O3	2.072(4)	2.090(7)
Angles (°)	Powder	Single crystals (plates)
O1 - Mn2 - O1	82.50(17)	82.24(29)
O1 - Mn2 - O3	95.43(7)	95.21(15)
O1 _ Mn2 _ O4	87.69(10)	88.18(17)
O3 _ Mn2 _ O4	101.30(9)	102.28(17)
O4 _ Mn2 _ O4	97.00(15)	95.80(27)
[NdO$_7$] bicapped prism		
Interatomic distances (Å)	Powder	Single crystals (plates)
Nd - O1 × 2	2.4256(23)	2.419(4)
Nd - O2	2.418(4)	2.343(6)
Nd - O2	2.405(4)	2.487(7)
Nd - O4 × 2	2.4130(22)	2.437 (4)
Nd - O4 × 2	2.5403(22)	2.525(4)
Angles (°)	Powder	Single crystals (plates)
O1 _ Nd _ O1	81.44(13)	82.18(22)
O1 _ Nd _ O2	77.70(6)	78.10(11)
O1 _ Nd _ O4	92.32(7)	91.95(12)
O2 _ Nd _ O2	138.98(6)	140.12(10)
O2 _ Nd _ O4	66.25(9)	66.69(17)
O4 _ Nd _ O4	67.95(10)	69.61 (16)

(continued)

Table 12.4 *(Continued)*

Metal–metal distances		
Interatomic distances (Å)	Powder	Single crystals (plates)
Mn1 _ Mn1 (J1)	2.9579(18)	2.9436(33)
Mn1 _ Mn1 (J2)	2.7467(18)	2.7246(33)
Mn1 _ Mn2 (J3)	3.3957(9)	3.3867(17)
Mn1 - Mn2 (J4)	3.6077(8)	3.5839(16)
Mn2 - Mn2 (J5)	2.8959(17)	2.8617(33)
Mn2 - Mn2	4.1440(8)	4.1299(15)
Nd - Nd	3.98378(29)	3.9646(5)
Nd - Nd	3.6769(8)	3.6468(15)
Nd - Mn1	3.3601(6)	3.3492(10)
Nd - Mn1	3.4072(5)	3.3914(9)
Nd - Mn2	3.3527(5)	3.3342(9)
Nd - Mn2	3.8119(6)	3.8017(12)
Nd - Mn2	3.9979(7)	3.9684(13)

couples Mn^{4+}–Mn^{4+} along the c axis through the Nd^{3+} layers. The corresponding interatomic distance Mn1–Mn1 is 2.7467(18) Å and 2.7246(33) Å for the powder and single crystalline sample, respectively. J_2 couples Mn^{4+}–Mn^{4+} also along the c axis but through the Mn^{3+} layers and it is ferromagnetic. The corresponding interatomic distance Mn1–Mn1 is 2.9579(18) Å and 2.9436(33) Å for the powder and the single crystalline sample, respectively. J_3 is the Mn^{4+}–Mn^{3+} superexchange interaction through the pyramidal base corners (i.e. through a shared O) in the (a, b) plane and its main contribution is antiferromagnetic. The corresponding interatomic distance Mn1–Mn2 is 3.3957(9) Å and 3.3867(17) Å for the powder and single crystalline sample, respectively, i.e. almost the same. J_4 couples antiferromagnetically Mn^{4+}–Mn^{3+} through the pyramidal apex (i.e. through a shared O) in the (a, b) plane. The corresponding interatomic distance Mn1–Mn2 is 3.6077(8) Å and 3.5839(16) Å for the powder and single crystalline sample, respectively. Finally, J_5 couples Mn^{3+}–Mn^{3+} antiferromagnetically in connected pyramids in the (a, b) plane. The corresponding interatomic distance Mn2–Mn2 is 2.8959(17) Å and 2.8617(33) Å for the powder and single crystalline sample, respectively.

The last three superexchange interactions result in magnetic frustration since five nearest-neighbor, antiferromagnetically coupled Mn1 (Mn^{4+}) and Mn2 (Mn^{3+}) cations form closed loops in the (a, b) plane. Therefore small displacements of the Mn ions can release frustration, resulting in differences in the physical properties of the two samples.

Indeed, detailed investigations [30] of the temperature dependence of the specific heat, the magnetization, the real part of the dielectric permittivity, and the electric polarization have revealed that the behavior of the two samples is not identical. Interestingly, however, both samples exhibit ferroelectricity, albeit weaker than that of $TbMn_2O_5$, the prototypical compound of the series. This observation establishes unambiguously that weak ferroelectricity, induced by an incommensurate magnetic structure, is an intrinsic property of $NdMn_2O_5$. Furthermore, such multiferroic behavior implies that $NdMn_2O_5$ actually bridges its close neighboring RMn_2O_5 compounds, that is the paraelectric $PrMn_2O_5$ and ferroelectric $SmMn_2O_5$. Thus the study of $NdMn_2O_5$ contributes decisively in understanding the role of the size of the R cations in the presence or not of ferroelectricity in RMn_2O_5 compounds.

Finally, comparison of the cell constants and the positional parameters resulting from the Rietveld refinements of the synchrotron X-ray powder diffraction data of the crushed plate-like crystals and those deduced [27] from the least-squares refinements of conventional X-ray single crystal diffraction data reveals interesting differences. The cell constants of the former are considerably smaller than the corresponding ones of the latter. Some positional parameters also differ slightly between these two sets of results. Given that the powder diffraction data were obtained from several crashed crystals, whereas single-crystal data were obtained on one crystal, it is possible that there is sample dependence (i.e. slight deviations from the composition) among the plate-like crystals of nominal $NdMn_2O_5$. The issue of deviations of the crystallographic parameters and thus of the bond lengths in nominal $NdMn_2O_5$ was also pointed out by Volkova and Marinin [35], which was attributed to possible off-stoichiometries and/or to structural instability (non-rigidity) of the structure.

12.4 Neutron Total Scattering Investigations of the $BaTiO_3@SiO_2$ Nanocomposites

12.4.1 Neutron and Synchrotron X-Ray Probes for Nanostructure Determination

As mentioned in the introduction, the electrical polarization of ferroelectrics is manifested in the form of cooperative structural displacements; thus ferroelectrics exemplify clearly and beautifully the inseparability between crystal structure and physical properties. For bulk ferroelectrics (powder and single crystals with no disorder), what reflects such inseparability are the changes of the crystal structure at average, meso-, nano-, and local length scales when the transition from the paraelectric to the ferroelectric state takes place. For nanostructured ferroelectrics (in which, by definition, the atomic order is limited at nanoscale), the structure–property inseparability is reflected in the fact that the very details of the nanostructure are the key prerequisites to understanding emergent, cooperative phenomena at nanoscale, especially the scaling of ferroelectricity and the polar discontinuities at the surfaces and interfaces. The nanostructure is defined as the atomic arrangement (atomic structure), including disorder and defects, at length scales ranging from tenths of nanometer (nm) up to the order of ten nm.

Experimental structural methods that can yield *direct* information on the atomic arrangement at nanoscale belong to two categories:

(i) Local probes of the nanoscale structure can probe tiny, nm- to μm-sized regions of the sample. The most widely used technique of this category is transmission electron microscopy (TEM). Modern TEMs combine diffraction, imaging, and spectroscopy and enable atomically resolved structural and chemical information.
(ii) Average bulk probes of the nanoscale structure can probe the entire sample. The bulk average structural probes of this category are total neutron or synchrotron X-ray scattering and X-ray absorption fine structure spectroscopy. They are the only direct

techniques that determine quantitatively the nanostructure (i.e. the atomic arrangements, including disorder and defects) as a function of length from tenths of nm to the order of 10 nm for the entire sample. Such quantitative and detailed nanostructure determination cannot be done by any other technique. These two methods are discussed briefly in the following paragraphs.

Conventional, well-established diffraction methods using neutrons or X-rays (both conventional and synchrotron) comprise the key pillars of structure determination of bulk materials (single crystals and powders) of any type (organic, inorganic, biological). However, these methods give only poor-quality information when used for nanostructured materials. The reason is that these techniques are based on the assumption that the scatterer (i.e. the material) is infinitely periodic, and thus it has *structural coherence* at the macroscopic length-scale. By their very nature, nanostructured materials have structural coherence at the nm length-scale and thus the conventional diffraction techniques are inapplicable.

Neutron or synchrotron X-ray total scattering (along with pair distribution function analysis) at spallation sources and third-generation synchrotron sources, respectively, is a very powerful method for addressing this so-called "nanostructure problem" [14], that is the need to determine atomic arrangements in nanostructured materials quantitatively and with high precision. "Total scattering" means that the total scattered intensity (i.e. both the Bragg and diffuse parts) from a sample is collected over a wide range of the reciprocal space where coherent scattering exists. The total scattering data are processed to provide the real space atomic pair distribution function (PDF). The PDF yields the probability of finding pairs of atoms separated by a distance r; therefore the PDF does not presume periodicity and thus no limitation of the particle size. PDF is obtained by a sine Fourier transformation of the reciprocal space total scattering structure function $S(Q)$, where Q is the magnitude of the scattering vector, $Q = 4\pi \sin \theta/\lambda$, where θ is the Bragg angle and λ the wavelength of neutrons or X-rays. For nanostructured materials, in order to obtain the best possible real-space resolution, Q ranges up to about $Q_{\max} \approx 50$ Å are necessary. This requires short wavelength X-rays or neutrons. For this reason, reliable total scattering experiments became possible only with the advent of spallation neutron sources (reactor neutron energies are too low) and third synchrotron sources, where dedicated total scattering instruments were built. As an exception, reactor-based neutron diffraction instruments (like the D4 diffractometer at the Institut Laue-Langevin) are preferable for samples containing isotopes with strong λ-dependent neutron absorption (e.g. Eu, Ag, Gd, Sm, etc.). Also, the choice between a neutron or synchrotron X-ray experiment depends on the nature of the sample (type of elements that it contains, i.e. light, heavy, close neighbors in the periodic table) and on what information is sought (which usually requires special sample environments). It is also possible to obtain chemically resolved PDFs (differential PDFs*)* making use of the different scattering strengths of isotopes (neutrons) or resonantly scattering elements (synchrotron X-rays). Also, in situ total scattering experiments, that is time-resolved PDFs, are possible.

The raw total scattering data are processed to obtain the PDF using freely available software: PDFgetN or GUDRUN and PDFgetX2 or PDFgetX3 for neutron and synchrotron X-ray total scattering data, respectively. Once a PDF is obtained, it can be analyzed directly by fitting models to the data. The software commonly used is PDFgui. This quantitative modeling is the real-space analog of Rietveld refinement. Because PDFgui applies a spherical envelope function to account for the finite size of the nanoparticle, it excludes non-spherical nanoparticles, core–shell structures, surface relaxation, surface defects, etc. This limitation was recently overcome by more versatile tools for complex nanoparticles. The implementation of whole-particle refinement [36] within two programs, DISCUS and DIFFEV, enables one to build up and refine the atomic structure (including defects, strain, and various types of disorder), the nanoparticle size, shape, and the architecture (including core–shell structures, surface relaxation, and ligand capping) of complex multicomponent nanoparticles.

Complementary to the total scattering method is the widely applied spectroscopic technique of X-ray absorption fine structure (XAFS), comprising extended X-ray absorption fine structure (EXAFS) and X-ray absorption near-edge structure (XANES). The complementarity emerges at several key issues. (i) EXAFS probes only the first few coordination shells of an ion and thus reveals the local (up to about 1 nm) structure, complementing the nm-scale structure deduced from total scattering; thus EXAFS provides information on the near-neighbor distance distributions, coordination numbers, and bond angles. (ii) EXAFS data contain crucial, chemical-specific, local, structural information; thus they complement nicely total scattering data when chemically resolved PDFs are not possible. (iii) Related to the EXAFS technique, XANES is mainly used to determine the coordination type and oxidation state of selected chemical species and thus it also complements chemically unresolved PDFs. The EXAFS spectra are initially subjected to background subtraction using the ATHENA software and then they are fitted by FEFFIT using photoelectron scattering paths that are constructed with the FEFF8 program.

12.4.2 Ferroelectricity in $BaTiO_3$

Barium titanate, $BaTiO_3$, is the archetypical ferroelectric material. It is also one of the most extensively investigated functional materials because of its RT ferroelectricity, its high dielectric constant, its versatile crystal chemistry, and its wide range of applications. For nearly seventy years efforts to determine the very details of the structure–property relationship in $BaTiO_3$ were mostly focused on ceramics, single crystals, thin films, and multilayers. In the past decade, the race to understand this material has been extended to $BaTiO_3$ nanoparticles and $BaTiO_3$-based nanocomposites. These studies were enabled by the tremendous advances made in nanomaterials synthesis, which led to the synthesis of $BaTiO_3$ nanoparticles and $BaTiO_3$-based nanocomposites with unprecedented control over their size, shape, composition, strain, dispersity, self-assembly, interface, and surface states. The main focus of these investigations was/is to understand: (i) the correlation of the ferroelectricity with size, (ii) the scaling of the ferroelectricity at the surface/interface(s), and (iii) the concomitant structure (crystal and electronic) response to such scaling of ferroelectricity at local and nanometer length scales. These issues are not only academically exciting but also important from an applied perspective, given the current technological trend towards nanoscale.

Bulk $BaTiO_3$ adopts a cubic crystal structure and is paraelectric above 393 K (at ambient pressure). Below this critical temperature (Curie temperature), upon cooling it undergoes a series of structural phase transitions as a function of temperature [37, 38, 39]. Thus, the material is tetragonal between 393 K and 278 K, orthorhombic between 278 K and 183 K, and rhombohedral below 183 K. Each of these structures is a distortion of the initial cubic structure: the tetragonal cell comes from elongation along the edge [001] of the cubic cell, the orthorhombic cell results from elongation along the face diagonal [011] of the cubic cell, and finally the rhombohedral cell coming from elongation along the body diagonal [111] of the cubic cell. All these distortions result in a net displacement of the Ti cation from its cubic centrosymmetric position and thus in the creation of permanent electric dipoles, that is ferroelectricity.

We now turn to nanocrystalline $BaTiO_3$. At ambient pressure, the above phase transitions are influenced by the particle size. Although reviewing the studies on the size dependence of ferroelectricity in nanostructured $BaTiO_3$ is beyond of the scope of this chapter (the reader can find such revision in Chapter 15), it is worth pointing out here that the phase transition from the paraelectric to ferroelectric transition becomes increasingly broadened with decreasing particle size [40, 41] and disappears at a critical size of about 26 nm, even if there are reports [42, 43] of ferroelectric $BaTiO_3$ nanoparticles as small as 6 nm. Behind this behavior, there is a counterexpectation of structural evolution [41]: the distortions (Ba–Ti distances and Ti off-centering) actually increase with the decrease of the particle size and the tetragonal metric (c/a) decreases (because of a loss of coherence relative to the bulk material).

$BaTiO_3$-based nanocomposites are relatively less investigated, especially regarding the structural aspects associated with the evolution of ferroelectricity with size and/or temperature, mainly because of difficulties in the synthesis of such systems and the complexity of the associated structural characterization. For nanocomposites of the same $BaTiO_3$ core size, what is especially fascinating is to understand the structural signatures at: (i) the transition from a ferroelectric to a paraelectric state upon heating and (ii) the subsequent transition to a new ferroelectric state, due to the formation of a new ferroelectric material produced by a solid-state reaction between the core and shell at nanoscale. A recent advance [44] in this area was the synthesis of $BaTiO_3/SiO_2$ core/shell particles and the controlled transformation of the amorphous SiO_2 shell into crystalline $Ba_2TiSi_2O_8$ (fresnoite), which is itself ferroelectric. In order to understand the structural aspects associated with this transformation, and given the importance of local distortions for the presence of ferroelectricity at $BaTiO_3$ nanoparticles outlined above, it is necessary to initially determine the local structure of the $BaTiO_3$ cores at RT. We investigated the $BaTiO_3/SiO_2$ core/shell particles by total neutron scattering. We focus here only on the comparison of the RT local structure of the 300 nm $BaTiO_3$ cores with the corresponding ones of bulk $BaTiO_3$ and nanoparticles of $BaTiO_3$ with a diameter of 5 nm studied recently [44]. Our goal here is to provide the basis for further structural investigations aiming to determine the structure response of the nanocomposite to the evolution of its ferroelectricity as a function of temperature.

12.4.3 Total Neutron Scattering Data Collection

The $BaTiO_3/SiO_2$ sample consisted of $BaTiO_3$ nanoparticles of diameter 300 nm individually coated with homogeneous silica shell with thickness of 10 nm [44]. Details on the synthesis are given by Chung et al. [44]. Neutron total scattering data were collected on the NPDF diffractometer [45] at the Lujan Center at Los Alamos National Laboratory. The diffractometer's large Q maximum enables one to detect local structural distortions of ~0.01 nanometer, and its high Q resolution provides usable PDF data for atom–atom distances of more than 20 nanometers.

Table 12.5 *Results of real space PDF refinements (R_w = 10.55%) of time-of-flight total neutron scattering data for 300 nm $BaTiO_3$ nanoparticles at RT. The refined cell constants are: a = b = 3.9987(15) Å and c = 4.06369(32) Å*

Atom	*x*	*y*	*z*	U_{iso}
Ba	0	0	0	0.151807(1)
Ti	0.5	0.5	0.48539(2)	0.009835(9)
O	0.5	0.5	0.00268(8)	0.011374(4)
O	0.5	0	0.533153(1)	0.011374(4)

12.4.4 Total Neutron Scattering Data Analysis

Initially the data were corrected for instrument background, incident neutron spectrum, absorption, and multiple scattering, and finally normalized using the program PDFgetN [46]. Full profile PDF structure refinements were next carried out using the program PDFgui [47]. The $BaTiO_3$ cores were modeled with a tetragonal cell and space group P4*mm*. Lattice parameters, isotropic atomic displacement parameters, and atom positions were refined successively.

12.4.5 Results and Discussion

Table 12.5 summarizes the results of the real space PDF analysis of the spherical $BaTiO_3$ cores of the $BaTiO_3/SiO_2$ core/shell nanoparticles. The spherical $BaTiO_3$ cores have a diameter of 300 nm. The corresponding fit is shown in Figure 12.5. No unfitted peaks were observed; therefore its local structure is well described by the average tetragonal structure. Our results are in excellent agreement with those obtained [48] by Rietveld refinements

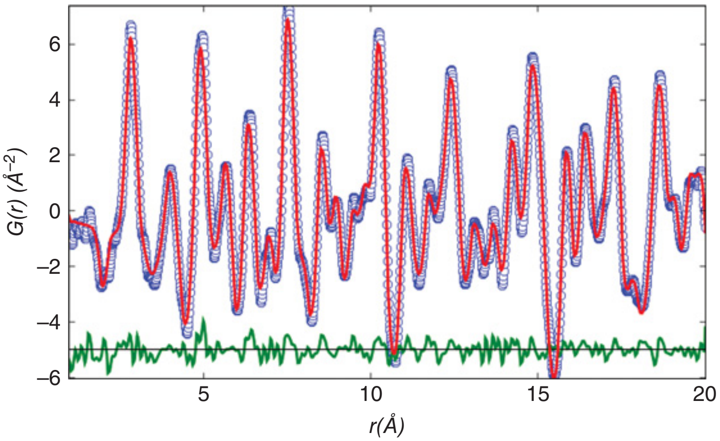

Figure 12.5 *Neutron pair distribution function G(r) analysis of $BaTiO_3/SiO_2$ core/shell nanoparticles. The size of the spherical $BaTiO_3$ cores is 300 nm (diameter). Experimental data are displayed as points; the fit and difference are also shown*

of neutron diffraction data for uncoated $BaTiO_3$ nanoparticles of similar size but synthesized by a modified two-step thermal decomposition method from barium titanyl oxalate. Recent high-resolution synchrotron X-ray studies revealed [49], through Rietveld analysis of the powder diffraction data, that uncoated $BaTiO_3$ nanoparticles have a composite average crystal structure. However, given the resolution of NPDF [50], our data on SiO_2-coated $BaTiO_3$ particles could not be fitted, through Rietveld analysis, by such an average composite structure. It is also interesting to compare the average and local structure of the 300 nm $BaTiO_3$ cores obtained here with the corresponding ones of free-standing, capped $BaTiO_3$ nanoparticles, with sizes near 5 nm [50]. While the former maintain their tetragonal symmetry in both their average and local structures, the latter present an average structure that is metrically more cubic but retain the tetragonal distortion locally [50]. Ongoing studies aim to clarify whether this structural distinction among the SiO_2-coated $BaTiO_3$ cores of 300 nm and the free-standing capped $BaTiO_3$ nanoparticles of 5 nm is due only to their size difference or to the SiO_2 coating of the former.

12.5 Concluding Comments

The synthesis, structure, and properties of ferroelectrics and multiferroics are all intimately connected. Therefore, the use of synchrotron X-ray and neutron facilities to obtain information on their structure and dynamics at length scales ultimately responsible for their macroscopic properties is essential. Furthermore, this information underpins the functionality of these materials and thus is critical for their applications. The two examples discussed in this chapter give only a flavor of the importance of synchrotron X-ray and neutron scattering for the structure determination of ferroelectrics and multiferroics. The breadth, power, and versatility of neutron and synchrotron X-ray facilities extend far beyond these two examples and cover a vast array of samples coming from almost every branch of natural sciences, life sciences, and even cultural heritage.

The complete characterization of ferroelectrics and multiferroics is a multiscale, multidimensional problem often requiring the combination of data from multiple beamlines based on different neutron and synchrotron X-ray facilities and the use of sophisticated data analysis software. Furthermore, experiments under complex sample environments are essential to probe the structure and dynamics response of these materials to an external control parameter, like temperature, pressure, magnetic, electric field, and combinations thereof. Such advanced structural characterization of ferroelectrics and multiferroics at neutrons and synchrotrons is a ripe and yet rapidly evolving area of science, and we hope that this contribution will stimulate further progress in this area.

Acknowledgments

E.G. Moshopoulou acknowledges support from CNRS for her work at the Laboratoire de Physique du Solide (UMR 8502 Université Paris-Sud 11 and Centre National de la Recherche Scientifique). She thanks Dr. Erik Elkaim and Dr. Pierre Fertey for assistance during the data collection at the French National Synchrotron Facility Soleil and for useful discussions. She is grateful to Dr. Jean-Paul Pouget, Dr. Victor Balédent, and Dr. Luc Ortega for fruitful discussions. She also thanks Joan Siewenie for her assistance during the total neutron scattering experiment at NPDF (Lujan Center at LANSCE).

The authors would like to acknowledge networking support by the European Science Foundation-Cooperation in Science and Technology Framework, Action MP0904 "Single and Multiphase Ferroics and Multiferroics with Restricted Geometries". E.G. Moshopoulou has also been supported by this Action, through a Short Term Scientific Mission grant, for her work at the Institut de Chimie de la Matière Condensée de Bordeaux, CNRS, Université Bordeaux. She is also grateful to Dr. Catherine Elissalde, Dr. U-Chan Chung, and Dr. Mario Maglione for providing her the $BaTiO_3@SiO_2$ sample for the total scattering experiment.

This work has benefited from the use of NPDF at the Lujan Center at Los Alamos Neutron Science Center, funded by the US DOE Office of Basic Energy Sciences. Los Alamos National Laboratory is operated by Los Alamos National Security LLC under US DOE contract DE-AC52-06NA25396. The National Science Foundation is acknowledged as an upgrade of the NPDF instrument at Los Alamos (Grant No. DMR00-76488).

Work at Los Alamos National Laboratory was performed under the auspices of the US Department of Energy.

References

(1) Valasek, J. (1920) Piezoelectric and allied phenomena in Rochelle salt. *Physical Review*, **17**, 475–481.

(2) Soenen, M. (1910) *La Pharmacie à La Rochelle. Les Seignettes et le Sel Polychreste* (English translation: *The Pharmacy at La Rochelle. The Seignettes and the Salt of Many Uses*), Thèse de Doctorat, University of Bordeaux.

(3) Brewster, D. (1824) Observation on the pyro-electricity in minerals. *Edinburgh Journal of Science,* **1** (II), 208–218.

(4) Curie, J. and Curie, P. (1880) Développement par pression de l'électricité polaire dans des crystaux hémiédriques à faces inclinées (English translation: Development of polarized electricity induced by pressure in hemiedric crystals of tilted faces). *Comptes Rendus*, **91**, 294–295 and 383–387.

(5) Schrödinger, E. (1912). Studien üder kinetik der dielektrika, dam schmelzpunkt, pyro- und piezoelekrizität (English translation: Study of the kinetics of a dielectric, its melting point and its pyro- and piezoelectricity). *Colloquium Academy of Sciences in Vienne*, November 1912.

(6) Debye, P. (1912) Results of kinetic theory of insulators. *Physikalische Zeitschrift*, **13**, 97–100.

(7) Valasek, J. (1922) Piezo-electric activity of Rochelle salt under various conditions. *Physical Review*, **19**, 478–491 (Reprinted: PhD Thesis, University of Minnesota).

(8) Rontgen, W.C. (1888) Ueber die durch bewegung eines im homogenen electrischen felde befindlichen dielectricums hervorgerufene electrodynamische (English translation: On the motion of a dielectric in a homogeneous electric field and about the induced electrodynamic force). *Annalen der Physik (Leipzig)*, **35**, 264–270.

(9) Curie, P. (1894) Sur la symétrie dans les phénomènes physiques, symétrie d'un champ électrique et d'un champ magnétique (English translation: On the symmetry of the

physical phenomena, and the symmetry of an electric and magnetic field). *Journal de Physique Theorique et Appliqué*, **3** (1), 393–415.

(10) Fiebig, M. (2005) Revival of the magnetoelectric effect. *Journal of Physics D: Applied Physics*, **38**, R123–R152.

(11) Eerenstein, W., Mathur, N.D. and Scott, J.F. (2005) Multiferroic and magnetoelectric materials. *Nature*, **442**, 759–765.

(12) Birol, T., Benedek, N.A., Das, H., et al. (2012) The magnetoelectric effect in transition metal oxides: insights and the rational design of new materials from first principles. *Current Opinion in Solid State and Materials Science*, **16**, 227–242.

(13) Tokura, Y., Seki, S., and Nagaosa, N. (2014) Multiferroics of spin origin. *Reports on Progress in Physics*, **77**, 076501–076546.

(14) Billinge, S.J.L. and Levin, I. (2007) The problem with determining atomic structure at the nanoscale. *Science*, **316**, 561–565.

(15) National Nanotechnology Initiative, DOE-NIST-NSF (2005) Anderson, I.S., Horton, L., Isaacs, E., and Ratner M.A. X-rays and Neutrons: Essential Tools for Nanoscience Research. National Nanotechnology Initiative Report.

(16) Hill, N.A. (2000) Why are there so few magnetic ferroelectrics? *Journal of Physical Chemistry B*, **104**, 6694–6709.

(17) Khomskii, D.I. (2001) Magnetism and ferroelectricity: why do they so seldom coexist? *Bulletin American Physical Society*, abstract no. C21.002, in Proceedings of the American Physical Society, Annual March Meeting, March 12–16, 2001, Washington State Convention Center Seattle, Washington Meeting.

(18) Katsufuji, T., Mori, S., Masaki M., et al. (2001) Dielectric and magnetic anomalies and spin frustration in hexagonal $RMnO_3$ (R = Y, Yb, and Lu). *Physical Review B*, **64**, art. no. 104419.

(19) Kimura, T., Kawamoto, S., Yamada I., et al. (2003) Magnetocapacitance effect in multiferroic $BiMnO_3$. *Physical Review B*, **67**, art. no. 180401.

(20) Smolenskii, G.A. and Chupis, I.E. (1982) Ferroelectromagnets. *Uspekhi Fizicheskikh Nauk*, **137**, 415–448.

(21) Smolenskii, G.A. and Chupis, I.E. (1982) Ferroelectromagnets. *Soviet Physics Uspekhi,* **25**, 475–493.

(22) Scott, J.F. (1979) Phase transitions in $BaMnF_4$. *Reports on Progress in Physics,* **42**, 1055–1084.

(23) Fox, D.L. and Scott, J.F. (1977) Ferroelectrically induced ferromagnetism. *Journal of Physics C*, **10**, L329–L331.

(24) Kimura, T., Goto, T., Shintani, H., et al. (2003) Magnetic control of ferroelectric polarization. *Nature*, **426**, 55–58.

(25) Mathur, N.D., Grosche F.M., Julian S.R., et al. (1998) Magnetically mediated superconductivity in heavy fermion compounds. *Nature*, **394**, 39–43.

(26) Quezel-Ambrunaz, S., Bertaut, F., and Buisson G. (1964) Structure des composés des terres rares et de manganese de formule TMn_2O_5. *Comptes Rendus de l'Académie des Sciences Paris*, **258**, 3025–3027.

(27) Balédent, V., Chattopadhyay, S., Fertey, P., et al. (2015) Evidence for room-temperature electric polarization in RMn_2O_5 multiferroics. *Physical Review Letters*, **114**, 117601–117604.

(28) Doubrovsky, C., André, G., Gukasov, A., et al. (2012) Magnetic phase transitions in $PrMn_2O_5$: importance of ion-size threshold size effects in RMn_2O_5 compounds (R = rare earth). *Physical Review B*, **86**, art. no. 174417.

(29) Chattopadhyay, S., Balédent, V., Damay, F., et al. First evidence of the multiferroicity in $NdMn_2O_5$. *Physical Review B, submitted.*

(30) Chattopadhyay, S., Balédent, V., Auban-Senzier, P., et al. (2015) Thermodynamic and neutron diffraction studies on multiferroic $NdMn_2O_5$. *Physica B: Condensed Matter*, **460**, 214–217.

(31) Popov, G., Greenblatt, M., and McCarroll, W.H. (2000) Synthesis of RMn_2O_5 (R = Nd, Pr) crystals using fused salt electrolysis. *Materials Research Bulletin*, **35**, 1661–1667.

(32) http://www.synchrotron-soleil.fr/Recherche/LignesLumiere/CRISTAL.

(33) Larson, A.C. and Von Dreele, R.B. (2001). General Structure Analysis System, LAUR 86–748, Los Alamos National Laboratory, New Mexico, USA.

(34) Euzen, P., Leone, P., Gueho, C., et al. (1993) Structure of $NdMn_2O_5$. *Acta Crystallographica*, **C49**, 1875–1877.

(35) Volkova, L.M. and Marinin, D.V. (2009) Crystal chemistry aspects of the magnetically induced ferroelectricity in $TbMn_2O_5$ and $BiMn_2O_5$. *Journal of Physics: Condensed Matter*, **21**, 015903–015916.

(36) Page, K., Hood, T.C., Proffen, T., et al. (2011) Building and refining complete nanoparticle structures with total scattering data. *Journal of Applied Crystallography*, **44**, 327–336.

(37) Jona, F. and Shirane, G. (1993) *Ferroelectric Crystals*, Dover Publications, Inc., New York.

(38) Strukov, B.A. and Levanyuk, A.P. (1998) *Ferroelectric Phenomena in Crystals*, Springer-Verlag, Berlin.

(39) Keeble D.S. and Thomas, P.A. (2009) On the tetragonality of the room-temperature ferroelectric phase of barium titanate $BaTiO_3$. *Journal of Applied Crystallography*, **42**, 480–484, and references therein.

(40) Nuraje, N. and Su, K. (2013) Perovskite ferroelectric nanomaterials. *Nanoscale*, **5**, 8752–8780, and references therein.

(41) Smith, M.B., Page, K., Siegrist, T., et al. (2008) Crystal structure and the paraelectric-to-ferroelectric phase transition of nanoscale $BaTiO_3$. *Journal of the American Chemical Society*, **130**, 6955–6963.

(42) Nuraje, N., Su, K., Haboosheh, A., et al. (2006) Room temperature synthesis of ferroelectric barium titanate nanoparticles using peptide nanorings as templates. *Advanced Materials*, **18**, 807–811

(43) Polking, M.J., Han, M.-G., Yourdkhani, A., et al. (2012) Ferroelectric order in individual nanometre-scale crystals. *Nature Materials*, **11**, 700–709.

(44) Chung, U.C., Elissalde, C., Mompiou, F., et al. (2010) Interface investigation in nanostructured $BaTiO_3$/silica composite ceramics. *Journal of the American Ceramic Society*, **93** (3), 865–874.

(45) Proffen, T., Egami, T., Billinge, S.J.L., et al. (2002) Building a high-resolution total scattering powder diffractometer – upgrade of NPD at MLNSC. *Applied Physics A – Materials Science and Processing,* **74** (1), S163–S165.

(46) Peterson, P.F., Gutmann, M., Proffen, T., et al. (2000) PDFgetN: a user-friendly program to extract the total scattering structure factor and the pair distribution function from neutron powder diffraction data. *Journal of Applied Crystallography*, **33**, 1192–1192.

(47) Farrow, C.L., Juhas, P., Liu, J.W., et al. (2007) PDFfit2 and PDFgui: computer programs for studying nanostructure in crystals. *Journal of Physics: Condensed Matter,* **19**, art. no. 335219.

(48) Yashima, M., Hoshina, T., Ishimura, D., et al. (2005) Size effect on the crystal structure of barium titanate nanoparticles. *Journal of Applied Physics*, **98**, art. no. 014313.

(49) Hoshina, T., Wada, S., Kuroiwa, Y., et al. (2008) Composite structure and size effect of barium titanate nanoparticles. *Applied Physics Letters*, **93**, art. no. 192914.

(50) Page, K., Proffen, T., Niederberger, M., et al. (2010) Probing local dipoles and ligand structure in $BaTiO_3$ nanoparticles. *Chemistry of Materials*, **22**, 4386–4391.

13

Advanced Characterization of Multiferroic Materials by Scanning Probe Methods and Scanning Electron Microscopy

Michael R. Koblischka and Anjela Koblischka-Veneva

Institute of Experimental Physics, Saarland University, Germany

13.1 SPM-Related Methods in Advanced Materials Research

The scanning probe methods (SPM) are the most important research tool for nanoscience and nanostructured materials. However, all these techniques are limited to an investigation of the surfaces of the materials. These developments towards the nanoscale are only possible if the resulting physical properties of the materials can effectively be controlled on the same length scale. For this purpose, the commonly applied measurement techniques like electron microscopy have to be enhanced by the possibility of measuring the physical properties on the nanoscale, and not only in an integral way like, for example, in magnetometry, transport or AC susceptibility measurements.

Firstly, we have to make a distinction between purely topographic analysis and an analysis of physical properties. To the topographic methods belong techniques like light microscopy, scanning electron microscopy (SEM), transmission electron microscopy (TEM), and interferometry for thickness determination. Furthermore, the various X-ray techniques providing chemical information and measurements of mechanical properties

Nanoscale Ferroelectrics and Multiferroics: Key Processing and Characterization Issues, and Nanoscale Effects, First Edition. Edited by Miguel Algueró, J. Marty Gregg, and Liliana Mitoseriu.
© 2016 John Wiley & Sons, Ltd. Published 2016 by John Wiley & Sons, Ltd.

belong to this class. Special modes of the techniques just mentioned may enable the spatial-resolved analysis of crystallographic data (for example electron backscatter diffraction (EBSD)), which is found to be very fruitful for a detailed understanding of a given sample [1–4]. The scanning probe techniques (SPM) are universal tools in the field of nanotechnology and have undergone vast development in a variety of directions [5].

All these methods share a raster operation in the (x, y) direction, a piezomotor for the z approach, and an electronic feedback element responsible for keeping the proper distance between the scanning element and the sample surface. Among the various methods developed in the literature, scanning force microscopy (AFM) and scanning tunneling microscopy (STM) are the most representative. Of course, both AFM and STM can provide topographic information as well, but both techniques enable further measurements to be made of physical quantities as their main application.

Techniques providing physical information are mainly based on scanning probe techniques (SPM) in general, with the exception of some developments of electron microscopy, including Lorentz microscopy [6] and low-temperature (LT)-SEM [7]. The SPM techniques measure in parallel the topography and the physical quantity, as the topography may interact with the desired information. An example of such a technique is magnetic force microscopy (MFM), where in two subsequent scans a topographic signal (close to the sample surface) and a magnetic signal (in a selected distance from the sample surface) are detected. This principle is employed also in similar techniques like electric field microscopy (EFM) or piezoforce microscopy (PFM). The use of the various SPM techniques with respect to questions of materials science were reviewed by Bonnell [8].

Figure 13.1 gives a schematic drawing of all SPM methods in general. The probe, together with the piezoactuators, the sensor, the feedback loop, and the scan electronics are shared between all SPM methods [9]. In general, there is an interaction between the tip (probe) and the sample, which can be measured by a respective sensor. There are two fundamentally different approaches of SPM techniques, namely STM and AFM. In the case of STM, there is a current flow between the tip and the sample and, in this way, the local density of states (LDOS) can be measured. This is indicated by a dashed line in Figure 13.1. In contrast, the AFM-related methods measure a force between the probe and the sample. The "pure" AFM detects van der Waals forces (hence, also, the name atomic force microscopy), whereas long-ranged forces like magnetic and electric ones can be measured as well by EFM, MFM, and PFM techniques.

In order to achieve a complete picture and a better understanding of the images obtained on samples of technological interest, a combination of a method of type (i) providing details of the topography with a method of type (ii) providing information on physical properties may be very useful. One has to note that MFM or EFM provide such combined information, but both measurements are done with a coated tip so that the topography images are not completely free of additional effects caused by the interaction of this coating with the sample. Furthermore, there is no crystallographic or chemical information available.

Figure 13.2 gives a schematic sketch concerning the appropriate length scales and the appropriate measurement techniques. Here, superconducting high-T_C oxides serve as an example. The "industrial" length scale above a 1 m sample length is out of the scope of this chapter, but it is important for technical production of samples to control the sample properties. This is done with measurement systems like the so-called tape recorder based on AC susceptibility and a continuously moving sample [10]. To develop such industrial fabrication of superconducting tapes, the main obstacles like secondary phases, cracks, and

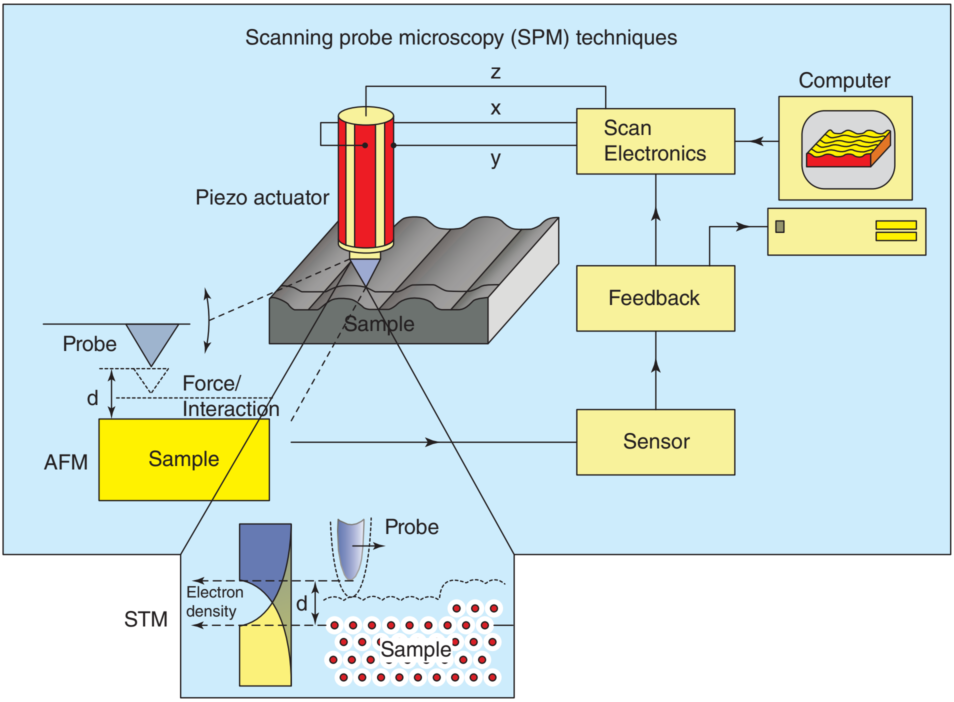
Scanning probe microscopy (SPM) techniques
z
x
y
Computer
Scan Electronics
Piezo actuator
Sample
Feedback
Probe
Force/ Interaction
d
AFM
Sample
Sensor
Probe
Electron density
d
STM
Sample

Figure 13.1 Schematic drawing of the arrangement for scanning probe microscopy (SPM). The type of interaction between the probe and the sample defines the two basic methods, scanning tunneling microscopy (STM) and atomic force microscopy (AFM)

sausaging had to be overcome by achieving a good texture of the material itself. In this way, the length scale down to about 1 µm was mastered [11]. However, from this point on, it is essential to tackle the problems occurring on the nanoscale, which have a direct influence on the intrinsic properties of the superconducting material and hence to flux

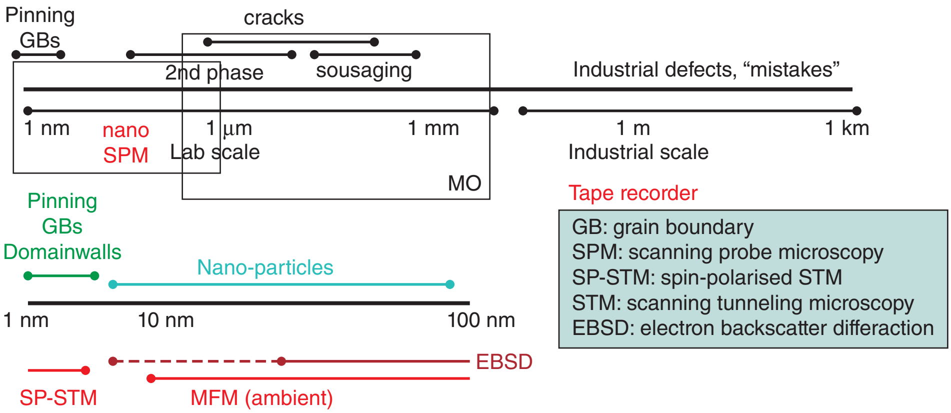
Pinning GBs
cracks
2nd phase
sousaging
Industrial defects, “mistakes”
1 nm
nano SPM
1 µm
Lab scale
1 mm
1 m
Industrial scale
1 km
MO
Tape recorder
Pinning GBs
Domainwalls
Nano-particles
1 nm
10 nm
100 nm
EBSD
SP-STM
MFM (ambient)
GB: grain boundary
SPM: scanning probe microscopy
SP-STM: spin-polarised STM
STM: scanning tunneling microscopy
EBSD: electron backscatter differaction

Figure 13.2 Illustration of the appropriate length scales in superconductors and the corresponding analysis methods

pinning and the resulting maximum critical current densities, which should reach, in the ideal case, the thermodynamic depairing limit. This now includes the study of natural sample inhomogeneities – both structurally and electronically – on the nanoscale, the addition of nanoparticles to improve the flux pinning and their effect on the superconducting matrix, the electronic character of the grain boundaries, and the study of flux pinning properties on the respective length scale.

This goal can only be reached if the sample characterization, which is commonly carried using magnetometry and transport measurements, is accompanied by a thorough investigation using methods of nanotechnology, which includes electron microscopy and the scanning probe techniques working in various environments. The EBSD technique is just reaching the interesting area for superconductors; a highest spatial resolution of about 20 nm on ceramic samples is already enabling the orientation analysis of nanoparticles embedded within the superconducting matrix [12] or of details of the twin structure [13]. AFM/MFM techniques offer a resolution in the range 1–40 nm, which is therefore an ideal combination with the EBSD technique described in Section 13.5.

This type of combined measurement can even be further enhanced by a detailed knowledge about the sample properties like crystallographic orientation, texture, grain boundaries, misorientation angles, etc. If, for example, AFM or MFM is combined together with the EBSD technique operating within the SEM environment [14], such a combination may provide very important details on crystallography or mechanical properties, which further contributes to an improved understanding of the physical quantities measured by the SPM technique. The EBSD and MFM share a similar spatial resolution, so a combined measurement is very effective [15]. The main problem encountered here is that there is a need to find back the same sample section in a completely different experimental environment. This problem can be largely facilitated by means of FIB milling, where markers can be milled into the sample, which allow an unambiguous relocation of the section of interest.

Another interesting approach for the research on multiferroic materials could be the use of a magnetic tip in STM or MFM to induce a strong magnetic field very near to the sample surface, which can be employed for a magnetically induced switching. In a similar way, a high voltage applied on an STM tip (or on a C-AFM) creates a strong electrical field, which could serve the same purpose. In this way, a very localized electric or magnetic switching becomes possible on the nanoscale.

13.2 Magnetic Force Microscopy (MFM) and Related Methods

13.2.1 Magnetic Imaging

As magnetic force imaging (MFI) and its further developments are playing an important role in the current research, we will focus on this technique and present a comparison of MFM to other techniques existing in the literature for magnetic imaging. Among these other techniques is magneto-optic imaging (MOI) based on the interaction of polarized light with a magnetic material. There are two main versions to be considered: (i) the Kerr effect for measurements of domain structures of magnetic materials and (ii) the Faraday effect taking place within a magneto-optical active layer for superconducting materials and magnetic materials with weak signals. The difference between the two methods is the type of interaction of the polarized light with the sample. In the Kerr technique, the polarized light is reflected directly at the sample surface and therefore interacts directly with the magnetic structure of the sample, while the Faraday effect works in transmission through the magneto-optical active layer. This layer can be either a thin film of a Eu-chalcogenide [16, 17] or a yttrium-iron garnet (YIG) material [18]. As the light is also reflected at the sample surface in this case, the MO layer is passed twice by the polarized light. In both techniques, several additional "tricks" can be applied to further enhance the imaging quality. This is done by an additional ZnS layer for the Kerr effect and a thickness criterion for the MO layer in the Faraday effect, which may act as antireflective coating providing a destructive interference of light with and without magnetic information. The application of the Kerr effect on magnetic materials is discussed in detail in the book by Hubert and Schäfer [19]; the use of the Faraday technique was reviewed by Koblischka and Wijngaarden [20], Jooss et al. [21], and Koblischka [22, 23].

The two other SPM techniques measuring local magnetic fields, the scanning Hall probe microscopy (SHPM), which has developed into a strong rival to the MFM technique, was reviewed by Bending [24] and the scanning superconducting quantum interference device (SQUID) microscopy technique and its application on superconducting materials was reviewed by Kirtley [25]. The SHPM is a niche technique operating with a miniaturized Hall probe element as the magnetic field sensor, which provides a unique compromise between spatial resolution (about 200 nm) and sensitivity (about 100 nT $\mathrm{Hz}^{-1/2}$), making it particularly well adapted for investigating vortices in superconductors. Video rate imaging is likely to become possible in the near future. Furthermore, the technique is non-invasive and measures the local magnetic field, B_{i}, directly. The scanning SQUID technique operates with a SQUID circuit as the sensing element and therefore exhibits an unprecedented field sensitivity [26]. The problems of this technique are the miniaturization of the SQUID element, where recently progress has been made, and the problem of a separate cooling of the SQUID element and of the sample to be investigated. For comparison, data of electron microscopy techniques like Lorentz microscopy [6] and of the classical Bitter decoration technique [27–29] are also included in this discussion.

Figure 13.3(a) shows a diagrammatic plan of the current state of the art in magnetic field sensitivity and spatial resolution for the six magnetic imaging techniques considered here, namely Lorentz microscopy, magnetic force microscopy (MFM), Bitter decoration, scanning Hall probe microscopy (SHPM), magneto-optical (MO) imaging with the two indicator materials, EuS/EuSe and YIG, and scanning SQUID microscopy. A measurement bandwidth of 1 Hz has been assumed (except for the "static" case of Bitter decoration). What is immediately evident from a plot of this type is the trade-off between field sensitivity and spatial resolution. This is well illustrated by the limiting cases of Lorentz microscopy (high spatial resolution) and scanning SQUID microscopy (high field resolution), while SHPM and MO provide a compromise between these two. The diagonal lines running across the figure represent the equivalent flux sensitivity $B_{\mathrm{min}} \times l2_{\mathrm{min}}$ expressed in fractions of a superconducting flux quantum $\Phi_0 = h/2e$ and it is interesting that many of the techniques lie in the range $(10^{-4}–10^{-6})\Phi_0$, although for a variety of different reasons. The notable exception to this rule is MO imaging, which has significantly worse flux resolution – depending on the MO indicator employed – but is nevertheless an important technique owing to its very high intrinsic temporal resolution and the possibility to perform observations in magnetic fields, which can either be static or pulsed [20].

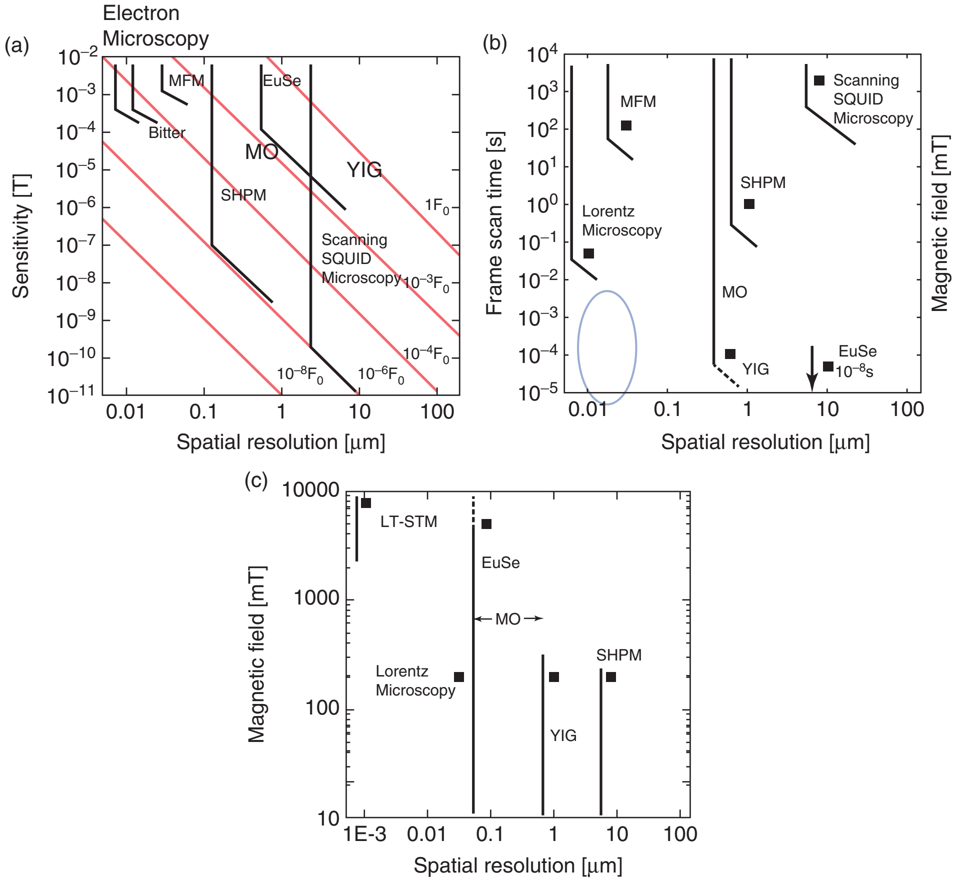

Figure 13.3 *(a) Diagram comparing the magnetic field sensitivity and spatial resolution of electron microscopy, MFM, Bitter decoration, SHPM, MO imaging, and scanning SQUID microscopy. (b) Diagram comparing the image acquisition time and spatial resolution. The circle in (b) marks an area of interest for many magnetic applications (after [24]). (c) Diagram plotting the spatial resolutions versus the applied magnetic fields for the same techniques presented in (a) and (b), plus low-temperature STM. For all techniques, the imaging is done in remnant fields; only the MO technique works in applied magnetic fields up to 5 T (experimentally proven), but higher fields are possible using Eu-chalcogenide indicators. LT-STM measures the vortex cores only, so high fields are required in order to get several vortex cores into the experimental window. Compiled using data of [24]*

Figure 13.3(b) shows a similar diagram where the time to capture one image frame is plotted against spatial resolution. Since in many cases the limit on scanning speed is set by signal-to-noise ratios, the optimized data points in this figure generally do not correspond to those of Figure 13.3(a). It is evident from this plot that the temporal resolution of MO imaging far exceeds all the other techniques although Lorentz microscopy can be performed at video rates with much higher spatial resolution. High scanning rates have, however, not been a priority in the development of many of these techniques and there is considerable scope for improvements in this area [24]. Figure 13.3(c) plots the spatial resolution versus the applied field where measurements can be taken.

13.2.2 Magnetic Force Microscopy (MFM)

In Figures 13.4(a) to (c), a series of MFM images is presented obtained on a polycrystalline ferrite film prepared by DC sputtering on a (111) Si substrate, showing the remnant state after saturation. The edge length of the images is (a) 20 µm, (b) 8 µm, and (c) 1 µm. Another example of an MFM measurement on ferrite grains within a sintered, artificial multiferroic sample is presented in Figure 13.4(d) to (f), together with the topography information. Together with an EBSD analysis of the grain orientations, it becomes possible to interpret the obtained magnetic information in detail.

In this way, MFM has proven to be a very versatile analysis method of magnetic domain information at a high spatial resolution of up to 10 nm [30, 31]. A minimum of sample preparation is required on thin-film samples, whereas for bulk magnetic samples polishing to a roughness below the optical wavelength is required when MFM should be performed. Such a surface quality of the sample surfaces can be achieved by mechanical polishing similar to the preparation of EBSD-suited samples, as discussed below.

13.2.3 Further Developments (HF-MFM, MRFM)

Due to the demands of the development of the magnetic recording industry, the MFM technique was further developed into high-frequency magnetic force microscopy (HF-MFM), where it became possible to record magnetic stray fields from hard disk writer poles that operate at frequencies above 1 GHz [32–36]. In this way, the study of the switching behavior of magnetic domains in this frequency regime became possible [37]. This might be an interesting development also for the analysis of the performance of multiferroic devices in the future. Another long-standing topic is the improvement of the spatial resolution of the MFM technique beyond the current limit of about 10 nm. An interesting approach is the near-field magnetic force microscopy (NF-MFM), which shares principle ideas with the HF-MFM technique [38,39].

Finally, the true three-dimensional magnetic imaging is achieved using the so-called magnetic resonance force microscopy (MRFM), which shares the basic principle with magnetic resonance imaging (MRI) [40–43]. The MRFM concept combines the ideas of MRI and atomic force microscopy (AFM). Conventional MRI employs an inductive coil as an antenna to sense resonant nuclear or electronic spins in a magnetic field gradient. MRFM uses a cantilever equipped with a ferromagnetic (iron cobalt) particle on top to directly detect a modulated spin gradient force between sample spins and the tip. The magnetic particle is characterized using the technique of cantilever magnetometry [44]. As the ferromagnetic tip moves close to the sample, the atoms' nuclear spins become attracted to it and generate a small force on the cantilever. The spins are then repeatedly flipped, causing the cantilever to gently sway back and forth in a synchronous motion. That displacement is measured with a laser beam to create a series of 2D images of the sample, which are combined to generate a 3D image. The interferometer measures resonant frequency of the cantilever. Smaller ferromagnetic particles and softer cantilevers increase the signal-to-noise ratio.

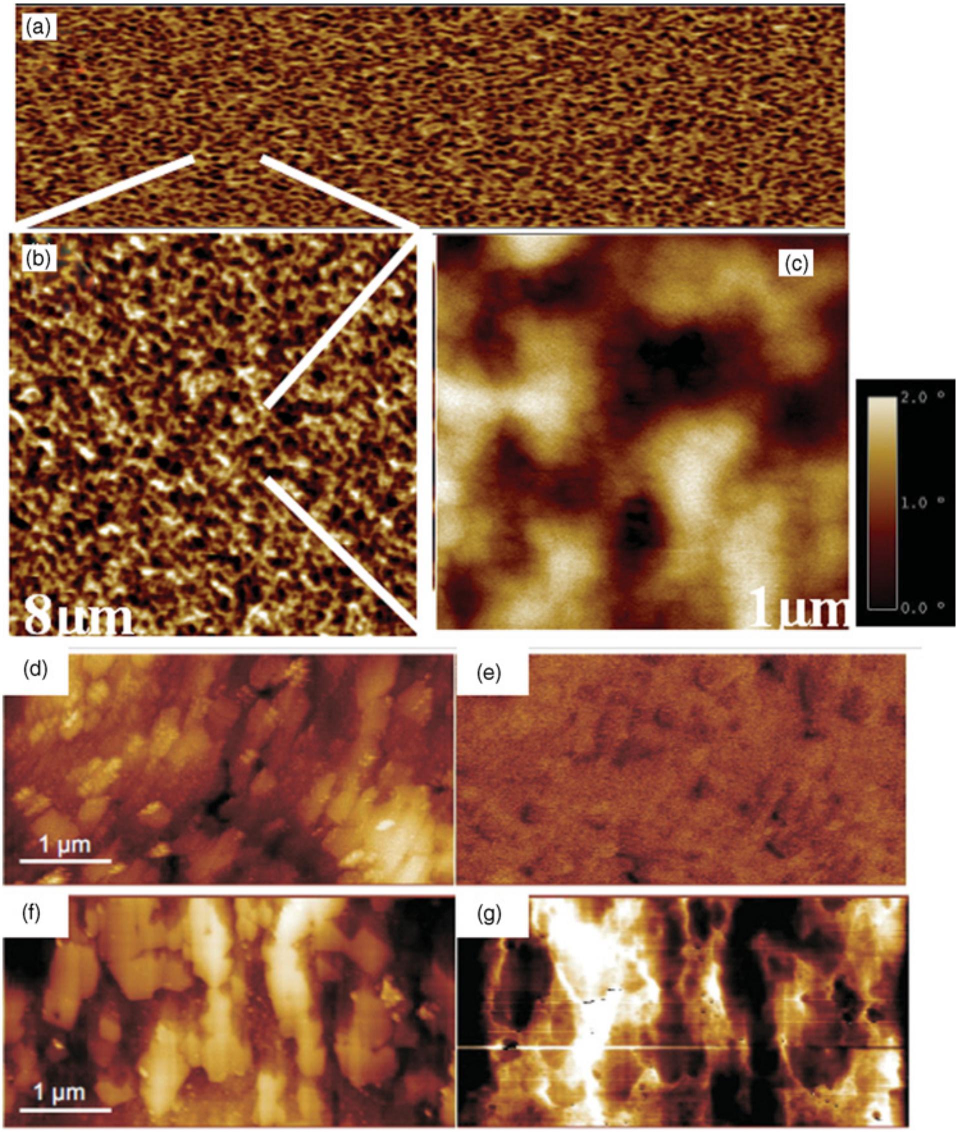

Figure 13.4 *MFM images are presented obtained on a pure, polycrystalline (Ni,Zn)*Fe_2O_4 *ferrite film prepared by DC sputtering on a (111) Si substrate, showing the remanent state after saturation. The edge length of the images is (a) 20 μm, (b) 8 μm, and (c)1 μm. Images (d) to (f) present topography images and MFM images of sintered, artificial multiferroic samples* $BaTiO_3$ *(BT) + (Ni,Zn)*Fe_2O_4 *(NZF) (see also the EBSD analysis shown later in Figures 13.17 and 13.18). Images (d) and (e) are from a sample with a mixture of (BT:NZF) = 60:40 and (f) and (g) of a sample (BT:NZF) = 70:30. The MFM images represent the remnant state after saturation. The MFM signal from the ferrite grains is much stronger in (g) and several grains are coupled together, while in (e) only some individual grains are observed. This corresponds to the result of the EBSD measurements on the same samples, indicating larger and well-developed ferrite grains in the sample (BT:NZF) = 70:30*

Unlike the inductive coil approach, MRFM sensitivity scales favorably as a device and sample dimensions are reduced. The setup using microwave fields stemming from a waveguide is also similar to the HF-MFM technique mentioned above. Using the MRFM technique, the detection of the magnetic spin of a single electron was achieved [45, 46]. Due to the capability of the 3D magnetic imaging, the MRFM technique plays an important role for the future development of 3D magnetic structures, including 3D magnetic recording [47–49].

13.3 Electrostatic Force Microscopy (EFM) and Piezo Force Microscopy (PFM)

13.3.1 Electrostatic Force Microscopy (EFM)

Electrostatic SPM techniques are based on the dynamic response of the probe to a mechanical or voltage modulation. These techniques are usually implemented in the lift mode, similar to the MFM technique. The tip first acquires the surface topography using standard intermittent contact AFM. Electrostatic data are collected in the second scan, during which the tip retraces the topographic profile with constant tip–sample separation. In the mechanically driven mode, an actuator induces cantilever oscillations. The force gradient acting on the cantilever is detected through the resonant frequency shift (frequency detection) using external phase-locked loop electronics or directly by amplitude or phase shifts. In the case of electrostatic force microscopy (EFM), sensitivity to the electrostatic field is enabled by using a biased tip. Measuring an electrostatic force gradient signal allows mapping of local surface potentials. However, the interpretation of EFM data is complicated by the fact that the imaging is non-linear and strongly dependent on surface topography. An alternative approach involves voltage modulation. Here, the tip is not mechanically driven; rather, a conductive tip is biased by an AC voltage. In this regime, the piezoactuator is disengaged and an oscillating bias is applied to the tip during the lift mode scan. The surface potential is directly measured by adjusting the potential offset on the tip and keeping the first harmonic response at zero. It is noteworthy that the signal is independent of the geometric properties of the tip–surface system and the modulation voltage. This technique allows very high potential resolution [8].

13.3.2 Piezo Force Microscopy (PFM)

Piezoresponse force microscopy (PFM) is based on the mechanical deformation of a sample due to the converse piezoelectric effect. The application of an electric field causes a change of thickness and/or a shearing of the material, depending on the direction of the electric field with respect to the piezoelectric tensor elements. For PFM measurements, a scanning force microscope is operated in the contact mode with a voltage (typically $\sim$ 10 V) applied to the tip. A schematic drawing of the necessary arrangement is shown in Figure 13.5. The electric field causing the piezoelectric deformations is thus applied only locally between the sharp tip and a back-electrode underneath the sample, resulting in a local deformation of the sample in a restricted volume of a few cubic μm at its very surface. As the amplitude of the resulting deformations is extremely small (that is of the order of a few pm only), the voltage applied to the tip is frequency modulated (typically using a modulation frequency of some 10 kHz) and the readout is performed with a lock-in amplifier. The PFM technique

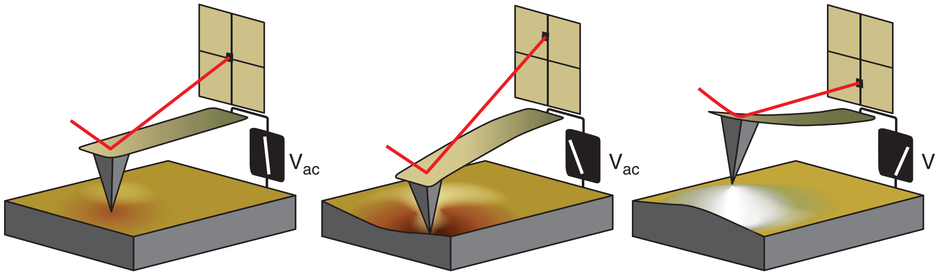

Figure 13.5 *Schematic sketches of PFM operation. The sample deforms in response to the applied voltage. This causes the cantilever to be deflected as well, which can be measured and interpreted in terms of the piezoelectric properties of the sample. A topographic image (V = 0 V) can be recorded together with the vertical and lateral PFM phase. Image by S. Jesse, ORNL (reproduced with permission)*

has thus become a very versatile tool for the investigation of ferroelectric domain patterns [50–55]. This is due to the fact that ferroelectricity entails piezoelectricity, and consequently a ferroelectric domain pattern can be recorded by PFM. An important advantage of PFM concerning multiferroic materials is given by the fact that PFM can be carried out using the same setup as for MFM, which enables parallel measurements of both physical properties. Similar to every other scanning probe technique, the lateral resolution of the measurements is of major interest. In the case of PFM, the width of a (atomically sharp) domain wall reflects the lateral resolution. The contrast in PFM is due to the local mechanical deformation of the sample surface. Therefore, this limits by nature the possible lateral resolution due to clamping effects. When scanning across a domain boundary, one side expands whereas the other side contracts [56].

In analogy to MFM, a topographic image can be obtained when the voltage is switched off and two images result for the vertical and the lateral PFM phase recorded by the lock-in amplifier. In this form, many analyses of ferroelectric domain patterns are performed in the literature, and naturally also on multiferroic samples [57, 58]. The PFM technique can be combined with MFM in order to measure both the ferromagnetic and ferroelectric response on one sample, but only in the sense that the same basic setup is employed. The different characteristics of the required tips (electrically conducting in the contact mode and magnetically covered for non-contact MFM) do not allow such combined information to be recorded simultaneously. This could be easier to achieve when combining the PFM technique with SHPM or in an all-optical method to record the domain information. Another important combination is PFM with EBSD, which yields information on the grain orientation together with the ferroelectric response. An example of this is presented in Figure 13.6. Here, the so-called SSPM technique is applied, which is a variant of PFM, measuring the grain potential via a shift of the contact potential difference.

13.4 Scanning Tunneling Microscopy (STM) and Related Methods

The STM technique requires a conducting sample in order to perform the measurements. This fact is naturally limiting the use of STM on multiferroic materials, which are often

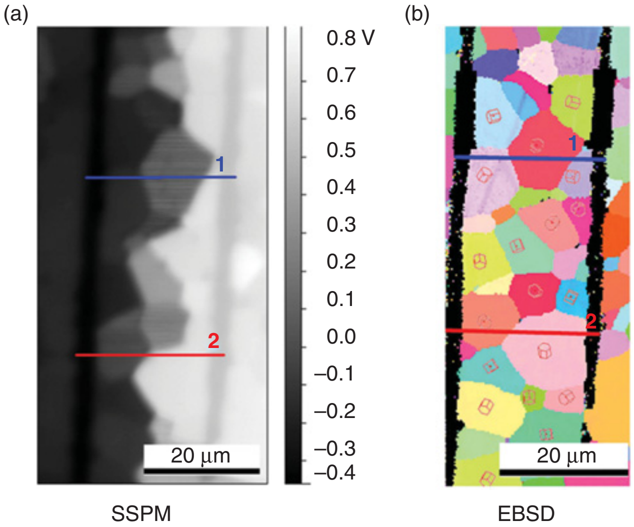

Figure 13.6 *SPM investigation on a Pr-doped polycrystalline ZnO ceramic material. (a) SSPM image at +1 V applied to the right electrode and (b) EBSD map of the area marked by the rectangle in (a). The lines in (a) and (b) represent the location of selected profiles (not shown here). The grain orientations in (b) are indicated by unit cell/crystal symbols included at each grain. This double measurement enables an improved understanding of the SSPM information. Reprinted from [59], Copyright (2013), with permission from Elsevier*

insulators. However, the STM technique is useful for topographical investigations on thin-film materials, which do not require a surface preparation, that is on thin-film materials. High-resolution topographical imaging was performed in the literature on various multiferroic samples using variable temperature STM under UHV conditions (see, for example, [60–62]). The spectroscopic data measured by STM (often abbreviated as STS) provide a direct insight to the electronic properties of a given sample, and valuable results can be obtained on existing growth defects, which may have a direct influence on the performance of such a sample. Figure 13.7 presents such a measurement on a twin boundary of a superconducting sample.

An interesting development took place in the field of high-T_C superconductors, which are also of a ceramic nature. STS data obtained were evaluated showing the superconducting gap, and this gap was plotted as a function of position. While doing this, a so-called gap map results, which can provide important information on the spatial distribution of the selected property [63–66]. This is shown in Figure 13.8 for different materials. Figure 13.8(a) and (b) present such gap maps for a $Bi_2Sr_2CaCu_2O_8$ (Bi-2212) single crystal, where the crystal in (a) is underdoped (i.e. of reduced oxygen content) and (b) gives the situation of an as-grown crystal [63]. Figure 13.8(c) finally presents data obtained on a melt-textured (Nd, Eu, Gd)$Ba_2Cu_3O_x$ sample, which is a material of application interest. These data were taken at 77 K on a 25 × 25 nm^2 area [67]. These data demonstrate clearly that it is important to control the growth of such materials on the nanometer scale. Furthermore, such a type of analysis may also play an important role on multiferroic materials to understand the resulting electric/magnetic behavior.

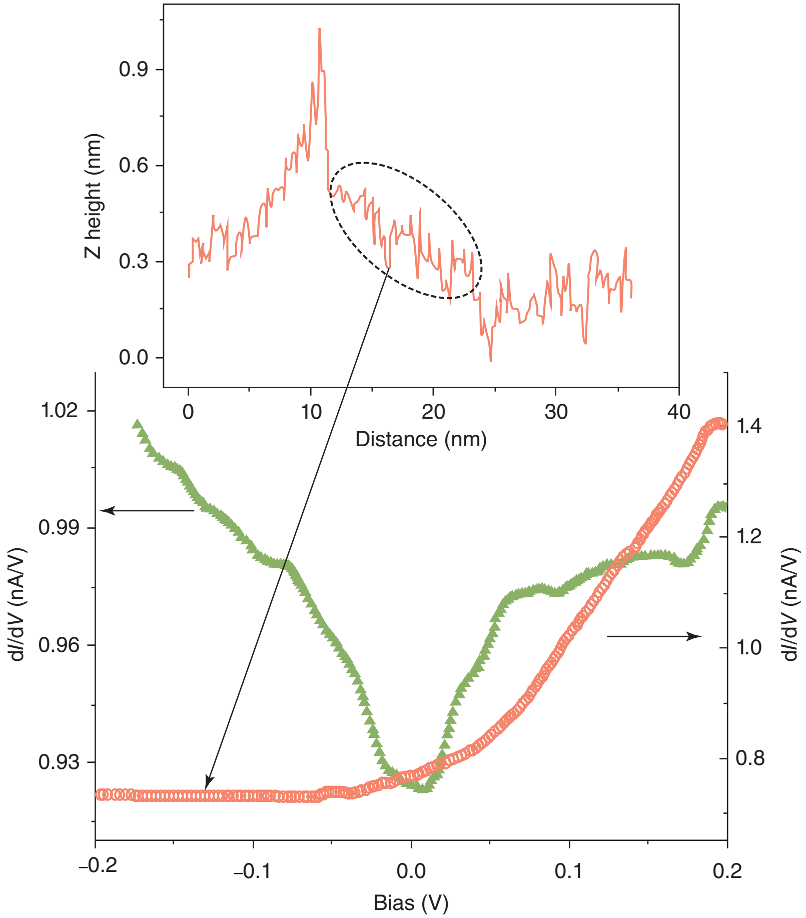

Figure 13.7 *Spectra across a twin boundary. The inset (top) shows a cross-section of the boundary. Unfilled circles mark a typical curve observed on the shoulder (indicated by an arrow). The curve shown by filled triangles is representative for the entire superconducting matrix*

A derivate of the STM technique is the spin-polarized scanning tunneling microscopy (SP-STM, which requires a ferromagnetic (or antiferromagnetic) tip for imaging. In an STM experiment this combines ultimate spatial resolution with spin-sensitivity, which enables the investigation of magnetic phenomena of conducting samples down to the atomic length scale. Details of the SP-STM technique were reviewed by Bode [68]. Magnetic tips for SP-STM can be prepared starting from bulk material (e.g. wires of Fe, Ni, Cr, or Co) or prepared by coating non-magnetic tips with a thin film of magnetic material using sputtering or electron-beam evaporation. Ferromagnetic materials like Fe as well as antiferromagnets such as Cr are used for tips. Spin-polarized tips can also be obtained by picking up magnetic material from the sample surface, which enables interesting experiments.

Spin-polarized tunneling was demonstrated on $La_{0.7}Sr_{0.3}MnO_3$ epitaxial thin film with an $La_{0.7}Sr_{0.3}MnO_3$-coated PtIr tip at room temperature. A magnetic-field-dependent gap

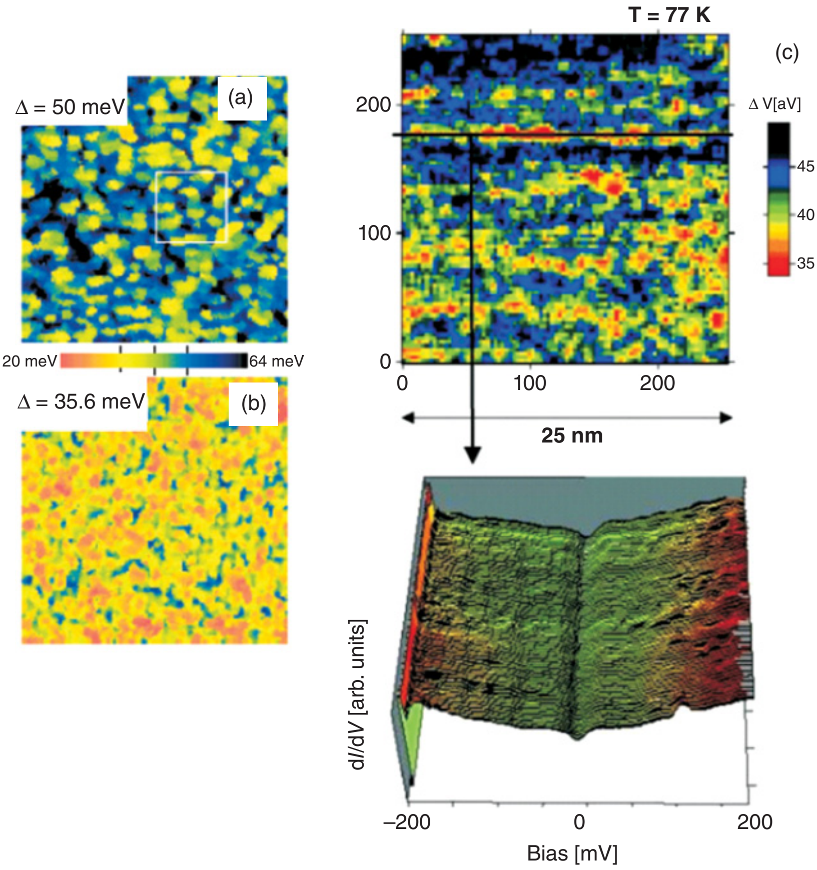

Figure 13.8 *Spatially resolved electronic inhomogeneities detected by low-temperature STM in high-T_C superconductors. (a) An experimental gap-map determined on an underdoped and (b) on an as-grown Bi-2212 single crystal. (c) Gap-map (peak voltage difference) of a 25 × 25 nm^2 area of the melt-textured NEG sample, measured at 77 K. The measured dI/dV curves taken along the black line are given in detail in the lower graph. Adapted from [37]*

structure was found in the differential tunneling spectra due to the spin-valve effect. The spatial mapping of the differential tunneling conductance shows strongly contrasting variations, which demonstrates the presence of magnetic domains with different spin alignments [69].

13.5 Imaging of Crystallographic Orientations (SEM/EBSD)

13.5.1 EBSD Technique

In the field of multiferroics, one encounters a large variety of materials, which are often of a ceramic nature. Even more challenging, artificially engineered multiferroics have been successfully prepared and reported in the literature by using thin-film technology [70–74] or, for example, by sintering a ferromagnetic component together with a ferroelectric one [75–77]. The resulting microstructure and texture of such multiferroic compounds may exhibit a complicated pattern, where grains of one phase can be embedded within the other. Therefore, it is an interesting question as to how the grains of the two constituents interact with each other during the fabrication or sintering process. Such an investigation requires a high spatial resolution entering the nanometer dimensions. A possible tool for such an analysis is given by the electron backscatter diffraction (EBSD) technique working within an SEM system that enables multiphase crystallographic orientation scans to be performed with a relatively high spatial resolution (∼20 nm) [78–80] and thus can provide detailed information on each individual component, as not only the phase distribution or grain size is measured but also the individual misorientations of grains and boundaries for each phase separately. However, a good surface polishing/cleaning procedure is essential for the EBSD analysis to be carried out, as the EBSD method requires a perfect, undisturbed sample surface with a depth of about 50 nm in order to obtain a high image quality (IQ) of the recorded Kikuchi patterns. Together with the recent developments concerning the image recording system, a spatial resolution of about 20 nm can be achieved even on oxidic samples. In this contribution, we present experimental details of the EBSD technique and discuss the properties of the measured Kikuchi patterns of several multiferroic samples. Furthermore, we show some possibilities to obtain high-quality Kikuchi patterns and give some examples of EBSD mappings on multiferroic materials.

The Kikuchi patterns are generated in the scanning electron microscope (SEM) at an acceleration voltage of 20 kV. The electron beam is hitting the sample surface, which is inclined by an angle of 70° in order to increase the strength of the resulting signal. This is illustrated schematically in Figure 13.9. Next, the electrons enter the sample surface to a depth of 20 to 100 nm, depending on the acceleration voltage and the material itself, before the electrons are scattered. The scattered electrons will travel in directions such that they impinge on crystal planes at the Bragg angle and so satisfy the equation:

$$\lambda = 2d \sin\theta \tag{13.1}$$

Here, λ is the effective wavelength of the electrons, d is the spacing of the crystal planes, and θ is the glancing angle of incidence [81].

The electrons escape the sample again in the form of a cone with an opening of 2θ. Finally, this electron cone is interacting with a phosphor screen, where the Kikuchi patterns are imaged. These Kikuchi diffraction patterns are recorded by means of a DigiView$^{\text{TM}}$ camera system, allowing a maximum recording speed of the order of 0.05 s/pattern. The time employed in the case of a multiphase scan is much longer, of the order of 0.4 s/pattern, as a higher image quality/confidence index is required. The resulting diffraction pattern is superimposed on background noise caused by all the backscattered electrons that escape the surface without being diffracted or are inelastically scattered after the diffraction. Therefore, the signal-to-noise ratio is typically less than 0.1, and an image processing step (background subtraction) is required for proper imaging of the Kikuchi patterns. To produce a crystallographic orientation map, the electron beam is scanned over a selected surface area and the resulting Kikuchi patterns are indexed and analyzed automatically (i.e. the Kikuchi bands are detected by means of the software [82]) by the controlling computer. This process is depicted schematically in Figure 13.10. The figure also illustrates how the 70° angle

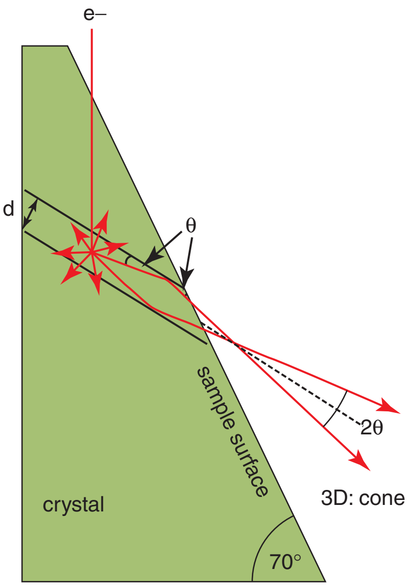
e–
d
θ
2θ
3D: cone
sample surface
crystal
70°

Figure 13.9 Scheme illustrating the electron scattering at the sample surface during an EBSD experiment. In order to increase the number of backscattered electrons, the sample is inclined by an angle of 70°

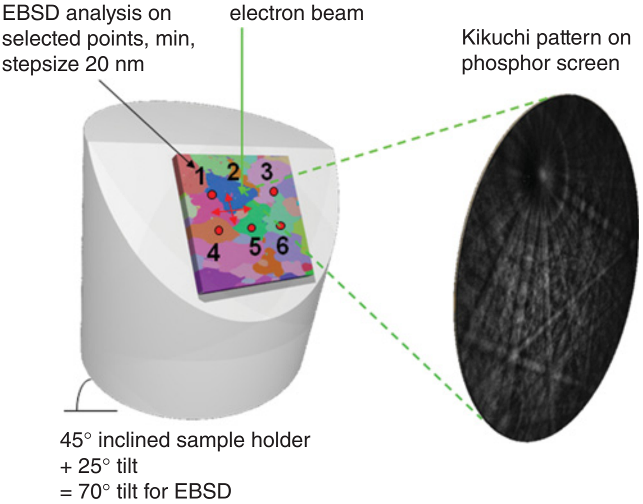
EBSD analysis on selected points, min, stepsize 20 nm
electron beam
Kikuchi pattern on phosphor screen
1
2
3
4
5
6
45° inclined sample holder
+ 25° tilt
= 70° tilt for EBSD

Figure 13.10 Scheme illustrating the EBSD mapping process. At each selected point on the sample surface, a Kikuchi pattern is recorded and indexed. It is also shown how the 70° angle is realized in a practical EBSD setup

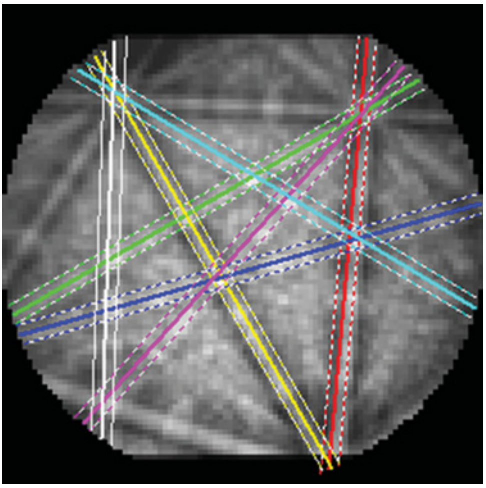

Figure 13.11 *Schematic illustration of the band indexing in a Kikuchi pattern. The bands can be approached by a simple line or by the full band with its specific width*

is experimentally realized using a special SEM sample holder, providing the larger part of the required angle (45°); the rest is done by inclining the entire sample holder by 25°. Of course, not the entire Kikuchi pattern is treated and stored by the controlling computer for each point measured, but a so-called Hough transform of the detected bands is used in order to save computing time. In the Hough transform, the bands are represented by peaks [82], which can be analyzed in a much simpler and, hence, faster way.

Furthermore, the user can influence the pattern recognition process by selecting, for example, the number of bands, and if only a line or an entire band width is to be fitted. This enables the user to adapt the process to the specific needs of a given sample. This indexing method is presented in Figure 13.11. Here, only six lines are chosen for the indexation, with the respective band width marked in the image. An image quality (IQ) parameter and a confidence index (CI) is recorded for each Kikuchi pattern [82]. The dimensionless IQ parameter is the sum of the detected peaks in the Hough transform employed in the image recording; the CI value yields information about how exact the indexation was carried out. The CI value ranges between 0 and 1. Based on the analysis of the recorded CI value, a mult-phase analysis is realized. As mentioned before, the sample surface preparation method is essential to achieve a high image quality of the Kikuchi patterns. After grinding the sample surface with polishing paper, several steps using diamond paste down to 1/4 μm particle size were employed. A final polishing step using colloidal silica solution (Struers OP-S) with a grain size of 25 nm was carried out. This polishing procedure ensures a high-quality polished surface for most types of samples [83], which is also useful for other experiments like magneto-optic imaging or even force microscopy (AFM/MFM). In several cases, we obtained nevertheless only weak Kikuchi patterns, which indicates that the area below the sample surface is not as homogeneous as required for EBSD. In order to solve this problem, we remove the surface layer using Ar ion polishing with Ar ions (5 keV, 5 min) on a low incident angle [84].

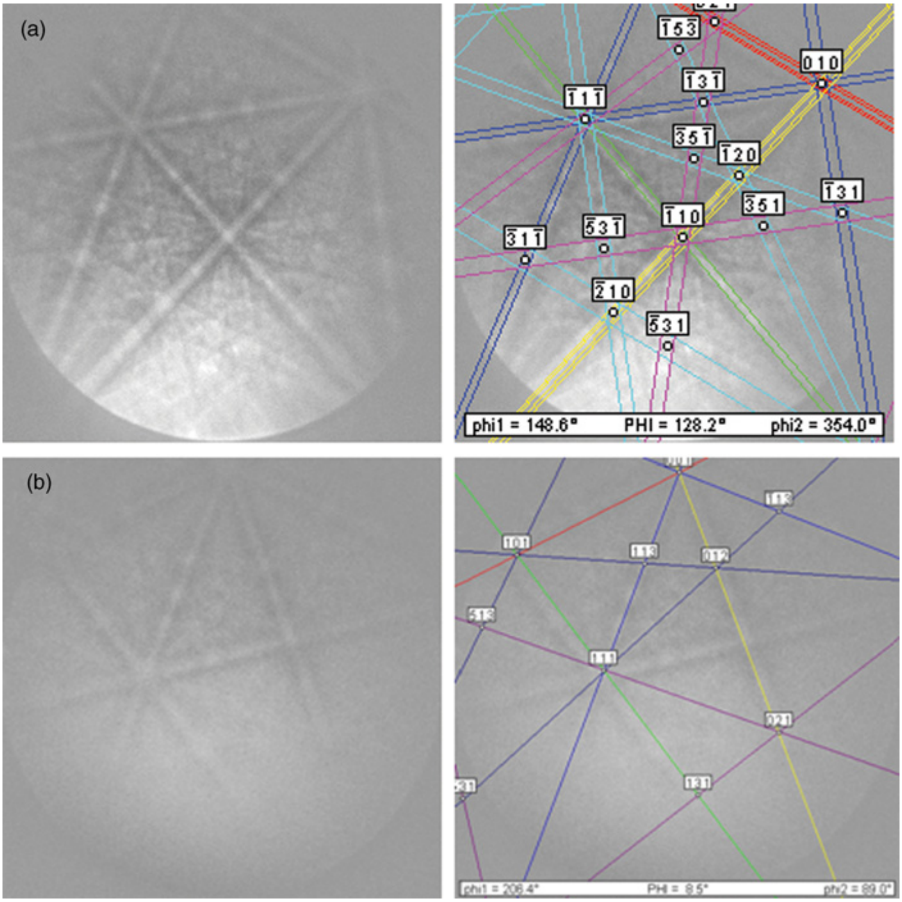

Figure 13.12 *(a) and (b) Kikuchi pattern and the respective indexation of a KNL–NTS sample. The determined Eulerian angles are (a)* $\varphi_1 = 148.6°$, $\Phi = 128.2°$, $\varphi_2 = 354.0°$ *and (b)* $\varphi_1 = 206.4°$, $\Phi = 8.5°$, $\varphi_2 = 89.0°$. *In (a) six bands with their respective width are selected for indexation, in (b) only five bands are represented as simple lines*

13.5.2 Examples of EBSD Measurements on Multiferroics

This procedure was found to work well on several metallic samples as well as on ferrites and multiferroic samples. Now we will discuss the properties of Kikuchi patterns and their indexation obtained on multiferroic samples and show the outcome of EBSD mappings.

In Figure 13.12, we present two Kikuchi patterns of KNL–NTS, fabricated according to earlier work [85]. In (a), a high image quality of the Kikuchi pattern is achieved and so it is possible to index the pattern using six bands, together with their respective bandwidths. The orientation represented by the Kikuchi pattern is summarized using the three Eulerian angles $\varphi_1 = 148.6°$, $\Phi = 128.2°$, and $\varphi_2 = 354.0°$. In (b), a similar indexation is performed, but only using lines to fit the five bands selected. The resulting Eulerian angles are $\varphi_1 = 206.4°$, $\Phi = 8.5°$, and $\varphi_2 = 89.0°$.

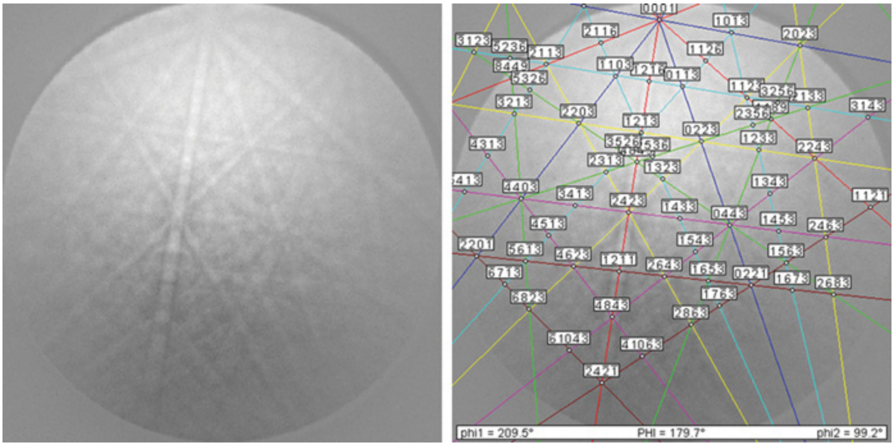

Figure 13.13 *Kikuchi pattern and the respective indexation of an $LuMnO_3$ sample. The determined Eulerian angles are $\varphi_1 = 209.5°$, $\Phi = 179.7°$, and $\varphi_2 = 99.2°$*

Another example is the $LuMnO_3$ compound, here in the form of a single crystal [86]. Here we can obtain excellent Kikuchi patterns, as illustrated in Figure 3.13, allowing an analysis to be performed with even eight bands at once. The determined Eulerian angles for this pattern are $\varphi_1 = 209.5°$, $\Phi = 179.7°$, and $\varphi_2 = 99.2°$. In Figure 3.14, we present an EBSD mapping on the sample surface in the (001) direction, that is normal to the surface. This mapping is called an inverse pole figure map, giving the crystallographic orientation at the sample surface. The color code for this map is given in the stereographic triangle. Even though the sample is a single crystal, we detect here several characteristic misorientations on the sample surface. These misoriented islands are, however, very tiny and have dimensions in the nanometer range, typically between 20 and 50 nm.

Figure 3.15 shows the Kikuchi patterns and their respective indexing of a polycrystalline $BaTiO_3$ sample. A new version of the EBSD software also includes the image parameters. The Eulerian angles and the image parameters are (a) IQ = 150.62, CI = 0.429, $\varphi_1 = 93.9°$, $\Phi = 52.3°$, $\varphi_2 = 320.1°$, (b) IQ = 123.71, CI = 0.714, $\varphi_1 = 80.5°$, $\Phi = 20.0°$, $\varphi_2 = 51.9°$, and (c) IQ = 79.8, CI = 0.8, $\varphi_1 = 123.7°$, $\Phi = 37.2°$, $\varphi_2 = 326.0°$. The problems that can arise when analyzing $BaTiO_3$ samples were discussed in detail by Skumryev et al. [87]. As $BaTiO_3$ has only a low electrical conductivity, problems of charging due to the incident electron beam may occur, especially when performing an EBSD mapping, but can be solved by applying a thin carbon layer on the top of the sample surface. The determination of the exact thickness of such a carbon layer is quite delicate, as presented by Muralidhar [67]; a thickness of 15 Å was found to work well, whereas a 20 Å-thick carbon layer obscures the Kikuchi pattern completely.

Figure 3.16 presents the Kikuchi patterns and their indexation of a polycrystalline nickel–zinc ferrite [$(Ni, Zn)Fe_2O_4$] sample, indexed with four bands only. The resulting Eulerian angles are (a) $\varphi_1 = 176.9°$, $\Phi = 89.2°$, $\varphi_2 = 270.1°$ and (b) $\varphi_1 = 89.0°$, $\Phi = 56.0°$, $\varphi_2 = 4.6°$. Details of the sample surface preparation of such ferrite samples have been presented [84, 88].

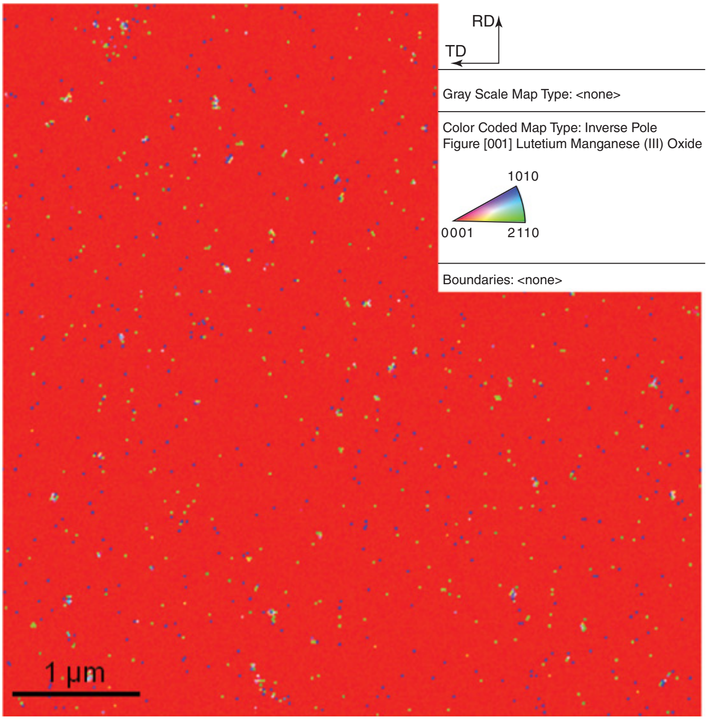
RD
TD
Gray Scale Map Type: <none>
Color Coded Map Type: Inverse Pole Figure [001] Lutetium Manganese (III) Oxide
1010
0001
2110
Boundaries: <none>
1 µm

Figure 13.14 *EBSD mapping of the crystal orientation, a so-called inverse pole figure (IPF) map in the (001) direction (i.e. normal to the sample surface). The color code is given in the stereographic triangle on top of the map. The sample is oriented in the (001) direction, but shows some characteristic misorientations of islands in the nanometer range*

Multiferroic materials can either be systems showing, for example, ferroelectric and ferromagnetic effects in a single compound or they can be formed artificially by a material mixture of a ferroelectric (here $BaTiO_3$, abbreviated BT) and a ferromagnetic ceramic (here $(Ni,Zn)Fe_2O_4$, abbreviated NZF). Such a mixtured multiferroic material can be sintered together in order to form ceramic composites [89–91]. The resulting microstructure and texture of such a compound may exhibit a complicated pattern, where grains of one phase can be embedded within the other. Therefore, it is an interesting question as to how the grains of the two materials interact with each other during the sintering process. A possible tool for such an analysis is given by the electron backscatter diffraction (EBSD) technique, which enables multiphase crystallographic orientation scans to be performed with a relatively high spatial resolution (~10 nm) and thus can provide detailed information on each individual component as not only the phase distribution or grain size is measured but also the individual misorientations, etc., for each phase.

13.5.3 EBSD Analysis of a Composite Multiferroic

Here we provide a detailed EBSD analysis of such composite multiferroic samples with three different compositions: $xBaTiO_3 - (1-x)(Ni_{0.5}Zn_{0.5})Fe_2O_4$ with $x = 0.50$, 0.60,

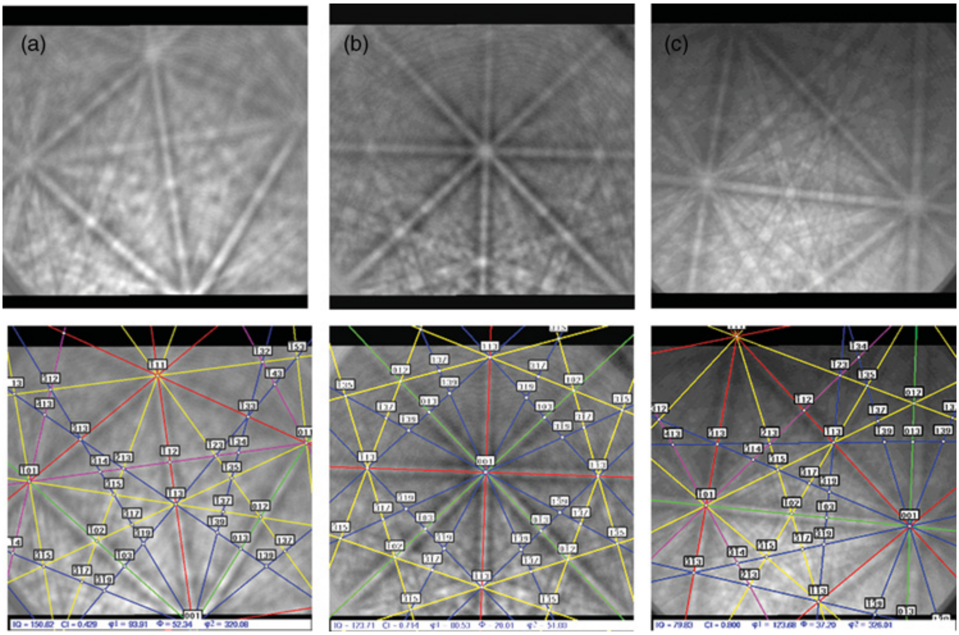
(a)
(b)
(c)
IQ = 150.82 CI = 0.429 φ1 = 93.91 Φ = 52.34 φ2 = 320.08
IQ = 79.83 CI = 0.800 φ1 = 123.68 Φ = 37.20 φ2 = 326.01

Figure 13.15 *(a), (b), and (c) Kikuchi patterns and their indexation of BaTiO$_3$. For the Eulerian angles and the image information see text*

and 0.70 (BT-NZF). These different mixing ratios were chosen in order to investigate the behavior of the ferrite grains in the BaTiO$_3$ matrix. The obtained EBSD data are presented as phase maps, orientation (IPF) maps, pole figures, grin size histograms, misorientation angle histograms, and orientation distribution functions (ODFs).

The EBSD measurement area is selected so as to cover a maximum region in order to be sure that the results obtained represent the entire sample under study. Further, several mappings with different step sizes are run for the same purpose. Firstly, we will take a closer look at the microstructure of sample C. Figure 13.17(a) presents an EBSD-determined phase map of sample C ($x = 0.70$). In this map, all detected grain boundaries are marked using thin black lines. The NZF is indicated in red, while the BT is given in green. It is clearly visible here that the ferrite grains are much larger than the BT grains, even though some small ferrite grains also exist. Together with the map, there is also an analysis of the total fraction of the two phases, 25.2% NZF and 74.8% BT (fraction of surface) as determined for the selected area. These values are close to the starting mixture, but these data tend always to be smaller as we only analyze the surface fractions. This was already observed in previous EBSD measurements on ferrites and superconductors [92, 93].

Knowing the phase distribution, it is now of great interest to obtain information about the distribution of crystallographic orientations of the two phases. Figure 13.17(b) presents an inverse pole figure (IPF) map in the (0 0 1) direction (that is perpendicular to the surface) for NZF only, with all other phases plotted in gray. The color code for the crystallographic orientation is given in the corresponding stereographic triangle. From this map, we learn

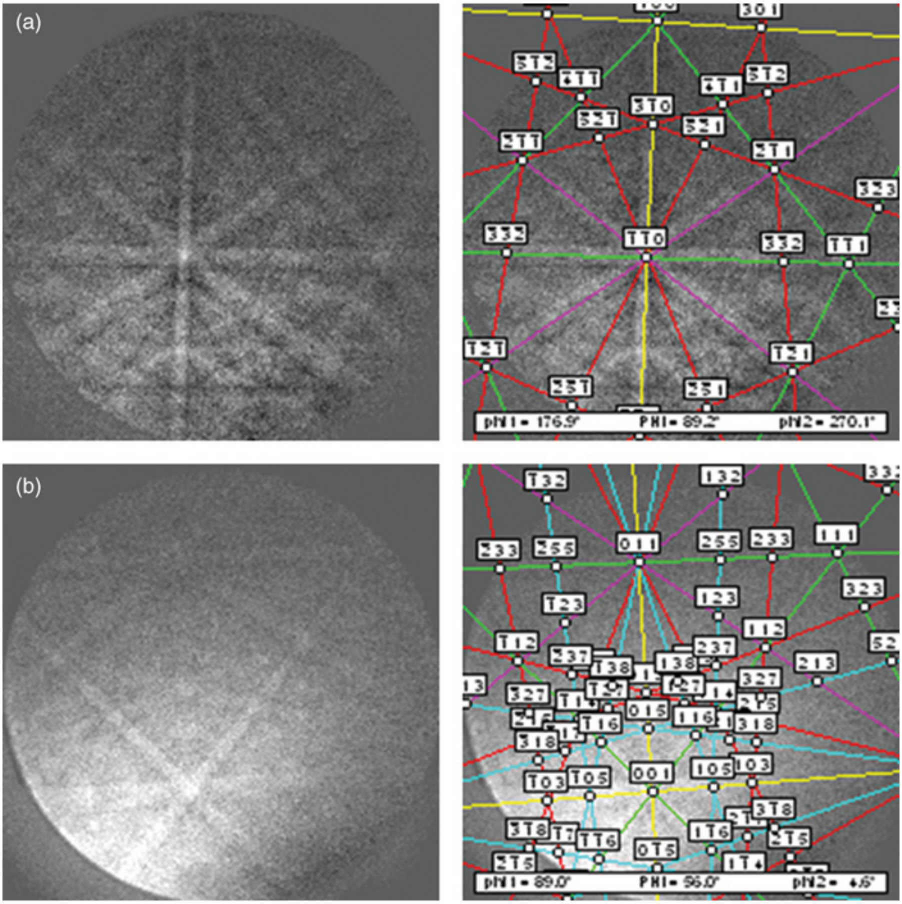

Figure 13.16 *(a) and (b) Kikuchi patterns and their indexation of nickel–zinc ferrite (Ni, Zn)*Fe_2O_4*. The determined Eulerian angles are (a)* $\varphi_1 = 176.9°$, $\Phi = 89.2°$, $\varphi_2 = 270.1°$ *and (b)* $\varphi_1 = 89.0°$, $\Phi = 56.0°$, $\varphi_2 = 4.6°$*. The indexation was performed using four bands only*

that the big NZF grains only exhibit some specific orientations, while the small NZF grains also show other orientations. Furthermore, one can see that the large NZF grains consist of subgrains (adjacent grains with slightly different orientations), or even have BT grains embedded in them.

From the data of these mappings, we can plot and calculate a pole figure for NZF and BT separately, given on the right side of the map (d). The data for the pole figures are normalized with respect to the NZF data. In the pole figure four intense maxima are clearly visible, together with four smaller ones, which indicate that the large ferrite grains only have four preferred orientations while being embedded in a BT matrix. In contrast to this behavior, the small BT grains within the selected area (Figure 13.17(c)) show random orientation. The orientation of the BT grains is more or less random. Furthermore, a direct comparison of Figure 13.17(b) and (c) reveals that the orientation of the small NZF grains is often induced by the orientation of the BT neighborhood.

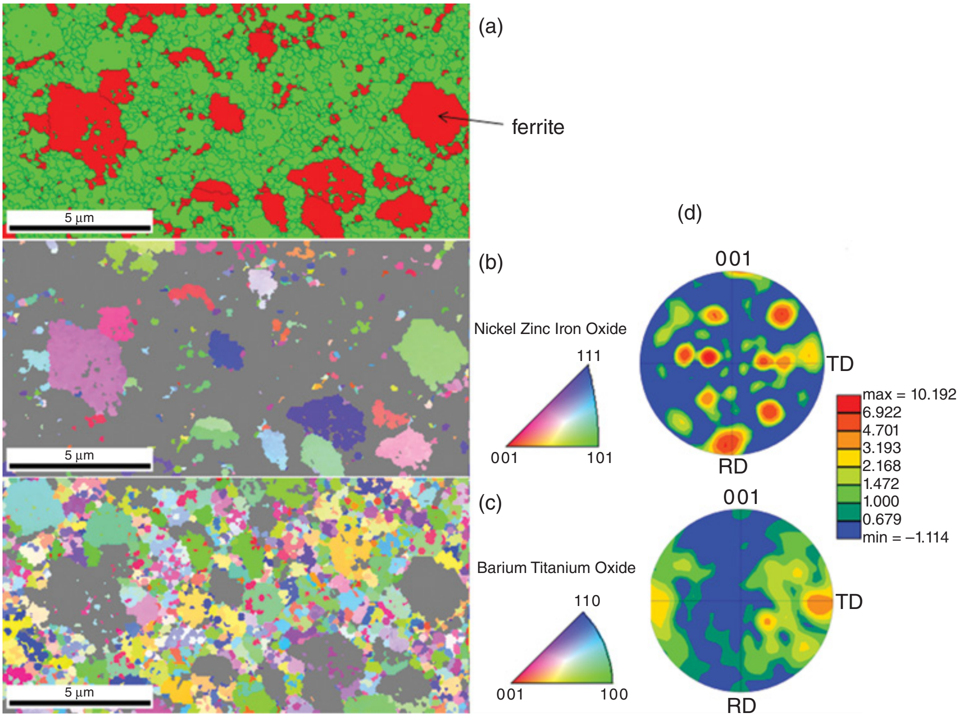

Figure 13.17 *EBSD analysis for sample C, where (a) gives the phase map and (b) gives the inverse pole figure (IPF) map in the (0 0 1) direction for the ferrite only, all other information being plotted in gray. The color code for the orientation is given in the stereographic triangle. (c) The same analysis as for* $BaTiO_3$. *(d) The corresponding pole figures in the (001) direction for the ferrite (left) and* $BaTiO_3$ *(right). Here the intensities are normalized with respect to the NZF data. For a color version of this figure, see color plate section*

On the other hand, the BT grains embedded within large NZF grains show only two specific orientations. Also here, the corresponding pole figure shows that the obtained crystallographic distribution is quite random with only two small maxima being present. This provides important information concerning the crystal growth in such a composite sample, showing the usefulness of detailed EBSD investigations on ceramic multiphase samples.

In Figure 13.18, an analogous analysis is presented for the sample A ($x = 0.50$). Figure 13.18(a) gives the phase map; furthermore, the EBSD-detected grain boundaries are marked in black. The analysis yields here 42.2% NZF and 57.8% BT (fraction of surface). The reduction of the grain size of the NZF grains is remarkable in comparison to sample C, whereas the BT grains still remain much smaller. Figure 13.18(b) presents the IPF map in the (0 0 1) direction for NZF. Now the NZF grains exhibit a nearly random orientation distribution. Some of the NZF grains also exhibit subgrains, as seen before, and some of the larger NZF grains have embedded BT grains in them. The number of subgrains is much larger in this sample and therefore the amount of high-angle misorientations detected in this sample is much larger (as we will see in Figure 13.19 below). The corresponding pole figure

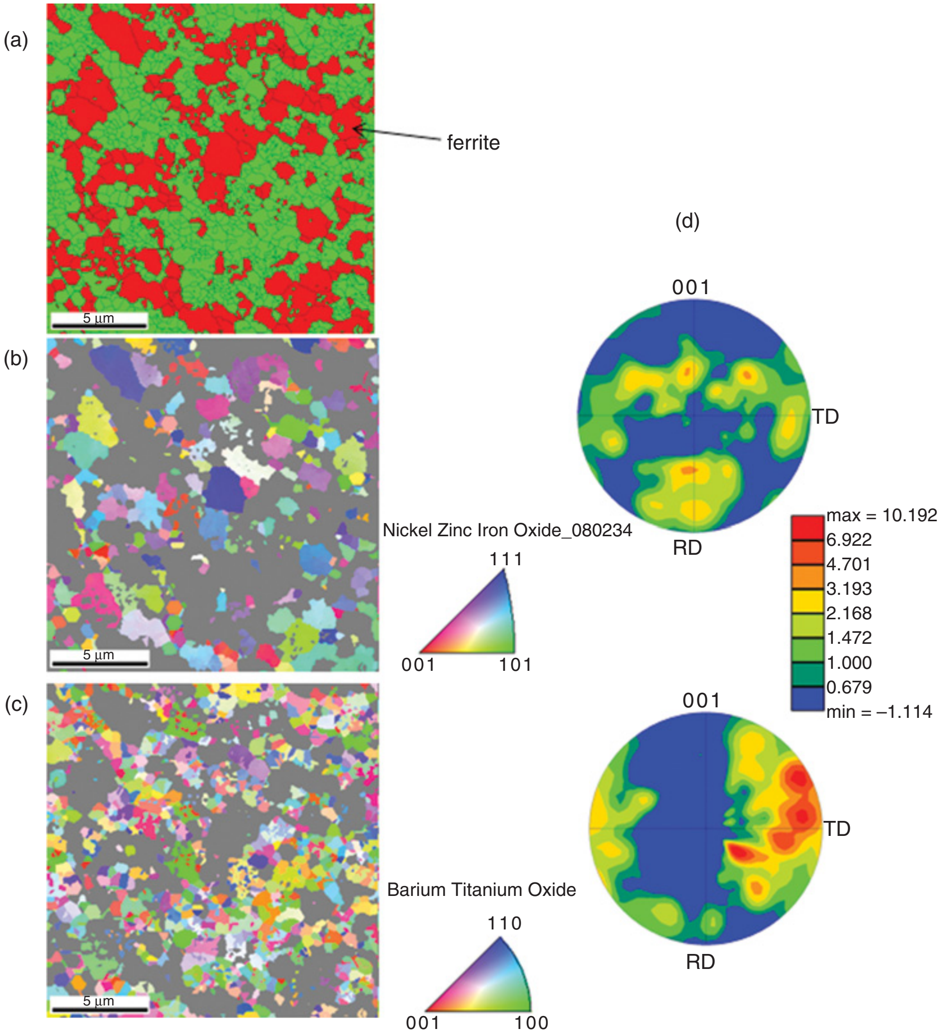

Figure 13.18 *EBSD analysis for sample A: (a) gives the phase map and (b) gives the inverse pole figure (IPF) map in the (0 0 1) direction for the ferrite only; all other information is plotted in gray. The color code for the orientation is given in the stereographic triangle. (c) The same analysis as for* $BaTiO_3$*. (d) The corresponding pole figures for NZF (left) and* $BaTiO_3$ *(right). Here, the recorded intensities are normalized with respect to the NZF data. For a color version of this figure, see color plate section*

in the (0 0 1) direction (normalized as before) manifests these observations. There are only three tiny intensity maxima for the ferrite, the majority of the grains being randomly oriented. Regarding the behavior of the BT phase of sample A as presented in Figure 13.18(c), the situation is clearly different from that of Figure 13.17(c). The IPF map in the (0 0 1) direction for the BT phase of sample A shows only small BT grains; large ones as in sample C are no longer present here. The corresponding pole figure (d) reveals some large maxima,

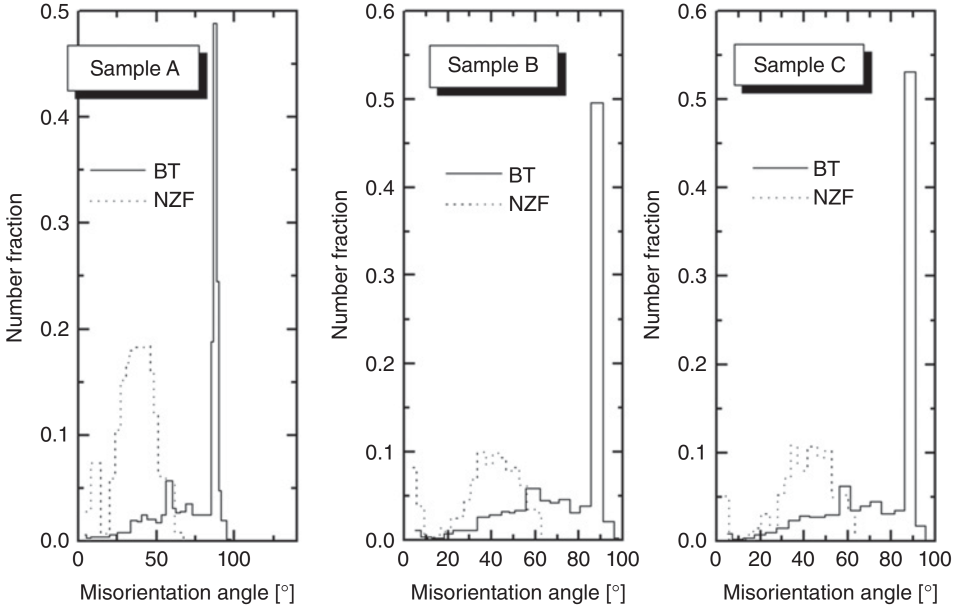

Figure 13.19 Misorientation angle histogram for all three samples under study. The ferrite data are given using dotted lines, the $BaTiO_3$ data using solid lines

which indicates that the BT grains are much more oriented as compared to sample C, even though this is not so clearly visible from the IPF map.

In Figure 13.19, we present an analysis of the EBSD-detected misorientation angles, which are obtained separately for each phase. All samples A to C are represented in these graphs. The plots give the number fraction as a function of the misorientation angle. Sample C shows a large number of misorientations for NZF in the range 30–50°; this ratio is reduced to about half in samples A and B. In contrast, the amount of small-angle misorientations is much larger in sample A. The behavior of BT is similar in all three samples.

Figure 13.20 gives the EBSD grain size analysis for all samples investigated. The NZF grain sizes range between 0.1 and 2 μm. The curves clearly show that sample C has the largest amount of big NZF grains of all samples, whereas the number of small grains in this sample is very small. The BT grains show a large maximum for a grain size of 0.1 μm in all samples investigated here; this indicates that the vast majority of the grains has a size of 0.1–0.2 μm. Grains larger than 1 μm do not exist in sample 50:50, whereas the other two samples show grains up to 2 μm being present.

The present EBSD analysis of composite multiferroic BT–NZF samples demonstrates the advantages of a spatially highly resolved analysis technique for microstructure characterization, which is also capable of performing a phase detection. In this way, it is possible to obtain information about the grain misorientations within each phase separately, and important conclusions concerning the behavior of NZF grains within a BT matrix (and vice versa) can be obtained. This information may contribute to the further design of such composite multiferroics. The EBSD technique provides a spatially highly resolved phase and

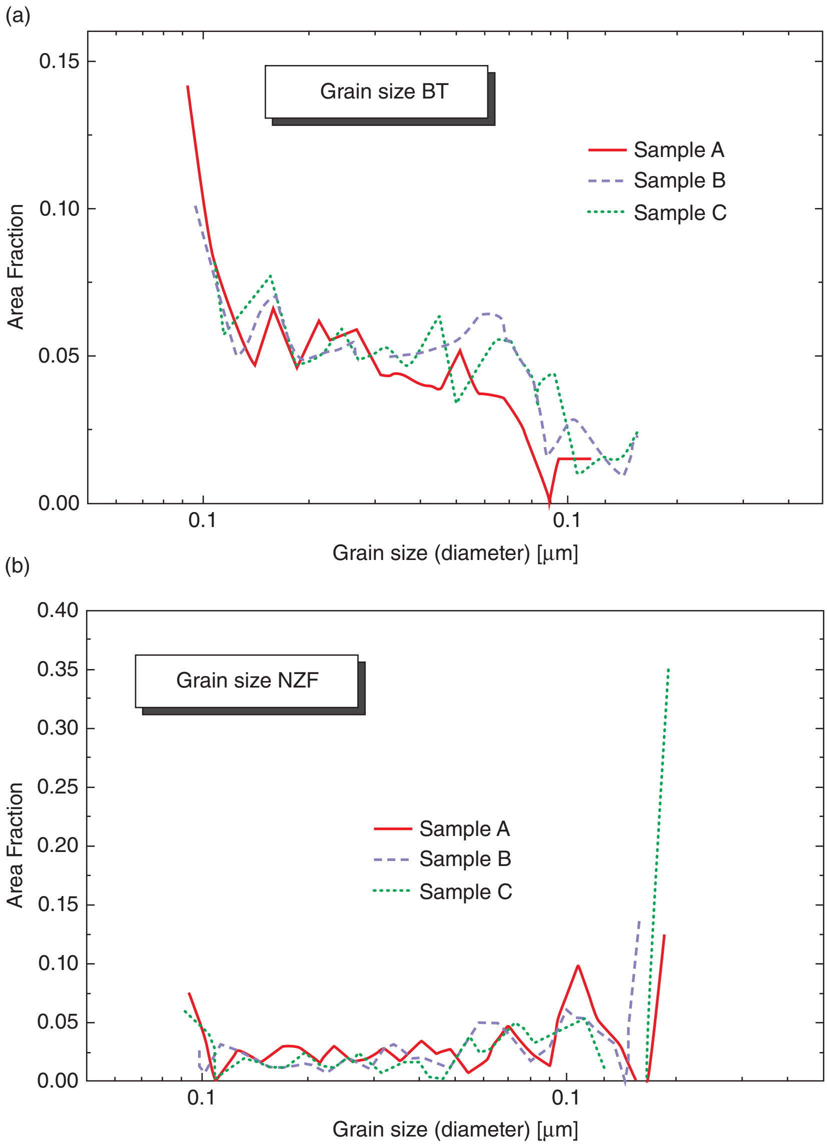

Figure 13.20 *Graphs of the EBSD-determined grain sizes for both phases for all three samples under study: (a) BT and (b) NZF. Sample A is represented by solid lines, sample B dotted lines, and sample C dashed lines*

orientation analysis, which is ideally suited for the investigation of such composite multiferroic samples, where information about the grain arrangement due to the interaction during the grain growth can be obtained.

From the above, we can draw the following conclusions. A high-resolution EBSD analysis can be performed with high accuracy on a multiferroic composite sample with two different phases, ferrite and $BaTiO_3$. The crystallographic orientations can be determined for both phases, ferrite and $BaTiO_3$, separately. The analysis clearly reveals that the grain size of ferrite and $BaTiO_3$ change upon changes in the starting composition ($x = 0.50$, 0.60, and 0.70).

The ferrite grains within a $BaTiO_3$ matrix show only four preferred orientations (sample C), whereas the $BaTiO_3$ remains randomly oriented. In sample A ($x = 0.50$), the situation is found to be the opposite. Only small ferrite grains with nearly random orientation prevail, while the $BaTiO_3$ phase shows an increased orientation. The measurements clearly demonstrate the advantages of the use of the EBSD technique to investigate such a two-phase composite multiferroic sample.

13.5.4 Future Directions

To conclude, the EBSD technique is now already a mature technique that can be employed to study multiferroic samples. The achievable high spatial resolution, which compares to that of force microscopy, enables valuable crystallographic information to be obtained. The possibility to analyze the properties of several phases simultaneously and independently from each other is very useful, especially for multiferroic composite samples. The key to achieve a high image quality of the Kikuchi patterns is the sample surface preparation step, which has been considerably developed further in the last few years. Besides the already mentioned magnetic force microscopy (MFM) and EBSD analysis, more detailed investigations on the nanometer scale need to be performed. A detailed review about scanning probe analysis of oxidic materials is given by Bonnell [94]. In order to investigate the ferroelectric behavior of multiferroic oxidic samples, the electric force microscopy (EFM) and the piezoresponse force microscopy (PFM) are essential tools [95]; the magnetic properties and effects of switching of magnetic objects can be analyzed by means of MFM. Noteworthy here is the fact that the spatial resolution of all methods mentioned above currently reach about 10 nm, which enables a variety of different analyses. Recently, the observation of room-temperature electronic conductivity at ferroelectric domain walls in the insulating multiferroic $BiFeO_3$ was a step forward. The origin and nature of the observed conductivity are probed using a combination of conductive atomic force microscopy (c-AFM), high-resolution transmission electron microscopy, and first-principles density functional computations [96].

Further, we may state that big advances in the field of multiferroics have been made, mainly within the last decade, but also further developments will be seen in the near future. We have reviewed recent progress in the study of multiferroic heterostructures, including those of epitaxial thin-film and bonded laminate heterostructure designs. There is continuous increasing interest in this topic in applied physics, materials science, and engineering communities. New materials used in multiferroic heterostructures remain relatively limited, but fabrication of the heterostructures and demonstration of related MF-based devices continue to receive great attention. Additionally, the integration of MF heterostructures with semiconductor platforms are likely to receive increased focus and attention, which may result in the development of novel tunable semiconductor microwave integrated devices based on the ME effect. Naturally, fabrication of epitaxial heterostructures is crucial to realizing all-thin-film MF devices, for which further refinement of epitaxial film processing of MF heterostructures is necessary. The heterostructures reported here are mostly constructed using ferromagnetic and ferroelectric oxides, especially for those of an epitaxial design. However, metal oxide heterostructures may have greater potential due to the strong intrinsic ME coupling and the greater selection of magnetic alloys and other compounds. Bonded laminate heterostructures provide a simple path to achieving larger devices (such as field generators), but improvement of the bonding quality is a key to realizing reliability and reproducibility in the operation and in the time-domain response of devices based upon multiferroic heterostructures.

13.6 New Developments in the Field of EBSD

13.6.1 3D EBSD

Any kind of nanostructured multiferroic material, for example a thin film of barium titanate with embedded nanorods of a ferrite, demands to be analyzed in three dimensions, and not only in two as usual. Furthermore, the arrangement of pores and defects in such a sample will give interesting additional information. Therefore, there is a large demand to carry out EBSD measurements, which is a typical two-dimensional method, also for true three-dimensional objects. A route towards this goal is given by the combination of scanning electron microscopy/EBSD together with the FIB technique. This approach, however, is a destructive one as several FIB slices have to be prepared and analyzed. Figure 13.21(a) illustrates this standard sample geometry relative to the electron and ion beams for an FIB–SEM. Cross-section milling is almost always used because this beam-to-sample geometry produces nominally flat surfaces, even when the milling rates of various microconstituents are vastly different. Differential milling is usually observed in polyphase and polycrystalline materials, because milling rates are dependent on a number of factors that include chemistry, crystallographic orientation, and surface topology. This technique has already been reviewed [97–99].

Each slice has to be ion-beam polished prior to the EBSD analysis. The demands and problems of this ion-polishing step have already been discussed in several papers in

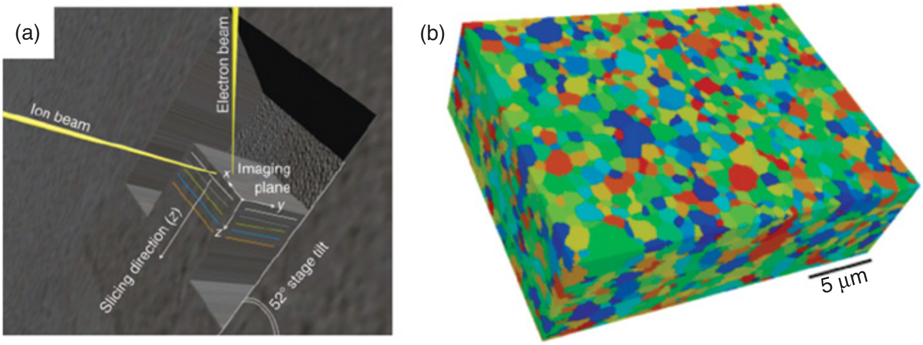

Figure 13.21 *(a) Typical sample geometry and beam orientation for an FIB–SEM tomography experiment using cross-section milling (from [97], reproduced with permission). (b) The results of the reconstruction of serial sections of EBSD data from undoped yttria. This dataset contains 43 individual slices (reprinted with permission from [99]. Copyright © [2009] [The American Ceramic Society])*

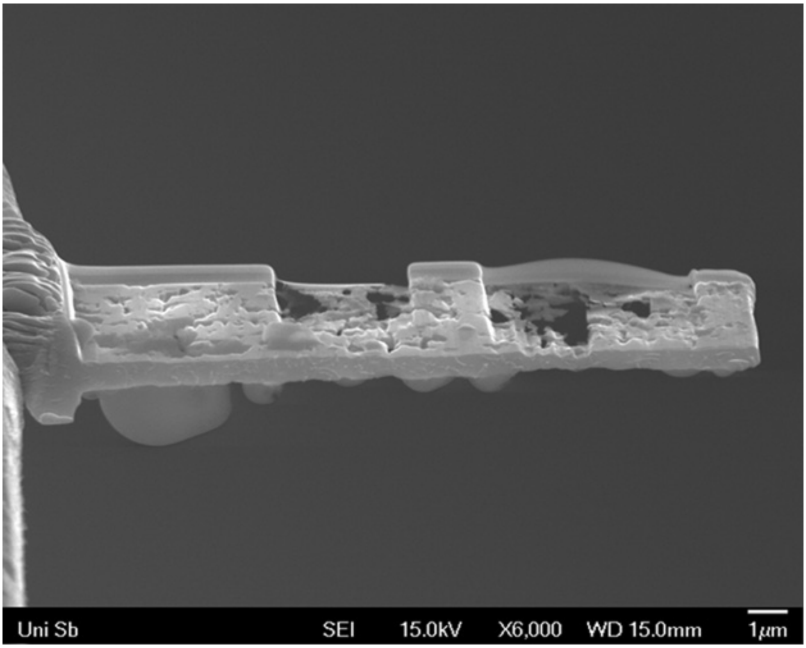

Figure 13.22 *SEM image of a prepared TEM-slice sample for transmission EBSD. The sample is a nanocrystalline* MgB_2 *superconductor with a mean grain size of ~200 nm*

the literature [100, 101]. The results obtained from each slice have then to be combined together using a computer. In the last few years, software modules have been developed. An example of such an analysis on a yttria sample is presented in Figure 13.21(b). Here only the primary alignment procedure provided by the commercial software was applied. This provides a resonable reconstruction and is an acceptable starting point for the reconstruction of the grain boundary planes [99]. Most of the current results of 3D EBSD published in the literature were obtained on metallic samples like steel or electroplated materials [102–104] with only a small amount carried out on ceramic samples, even though these materials offer the most interesting microstructures for such an analysis. Some of these materials, however, are extremely difficult to ion-polish. An example of this is magnetite (Fe_3O_4), where the so-called antiphase boundaries would be a very interesting subject for analysis, but experiments using FIB structuring have revealed an extreme sensitivity of magnetite to the ion bombardment, so the attempts to ion-polish the sample surfaces for EBSD analysis have failed. On the other hand, it is possible to use this again to structure magnetite samples [105]. Therefore, such 3D EBSD experiments have not yet been carried out on multiferroic samples.

13.6.2 Transmission EBSD (t-EBSD)

Another important new approach is the introduction of the so-called transmission EBSD (abbreviated t-EBSD) in some recent work [106–108]. In this case, a TEM slice is prepared form the sample via FIB milling. This slice is mounted on a copper grid, which can be applied on a specific sample holder also in the SEM environment. In this way, it becomes possible to operate the EBSD detector on a tiny sample in transmission, which in turn results in a much better spatial resolution, especially on samples with nanometer-sized grains. To operate the t-EBSD, a specific sample holder to enable the 70° inclination to the electron beam is required without changing the position of the phosphor detector screen.

An SEM image of a prepared TEM-slice sample for transmission EBSD is presented in Figure 13.22. The sample surface can be polished directly within the FIB environment (using the Ga^+ ions) or in an additional step using low-incident Ar^+ ions, which is a more gentle approach. A big advantage of the t-EBSD method is the fact that charging effects do not play a detrimental role, thus benefiting the high-resolution imaging. This method is currently applied to metals like Cu, Ti [106], Ni [109], Al [108], steels [106, 108], and also some ceramics like $LiFePO_4$ [110], but not yet on multiferroic samples. Here one may expect in the future some spectacular results, especially on nanometer-sized, multiphase multiferroics, where it should be possible to solve problems that arise during sample preparation.

References

(1) Dingley, D.J. and Randle, V. (1992) Microtexture determination by electron backscatter diffraction. *Journal of Materials Science*, **27**, 4545–4566.

(2) Baba-Kishi, K.Z. (2002) Electron backscatter Kikuchi diffraction in the scanning electron microscope for crystallographic analysis. *Journal of Materials Science*, **37**, 1715–1746.

(3) Randle, V. (1993) *The Measurement of Grain Boundary Geometry*, IOP Publishing, Bristol.

(4) Schwarzer, R.A. (2000) In *Electron Backscatter Diffraction in Materials Science*, edited by A.J. Schwartz, M. Kumar, and B.L. Adams, Kluwer Academic/Plenum Publishers, New York, p. 105.

(5) Ashby, M.F., Ferreira, P.J., and Shodek, D. (2009) *Nanomaterials, Nanotechnologies and Design*, Butterworth-Heinemann, Oxford.

(6) Tonomura, A., Kasai, H. Kamimura, O., et al. (2001) Observation of individual vortices trapped along columnar defects in high-temperature superconductors. *Nature*, **412**, 620–622.

(7) Koelle, D. and Gross, R. (1994) Low-temperature scanning electron microscopy of superconducting thin-films and Josephson junctions. *Reports on Progress in Physics*, **57**, 651–741.

(8) Bonnell, D.A. (1998) Local structure and properties of oxide surfaces: scanning probe analyses of ceramics. *Journal of the American Ceramic Society*, **81**, 3049–3070.

(9) Kalinin, S.V. and Gruverman, A. (2007) *Scanning Probe Microscopy*, vols 1 and 2, Springer, Berlin.

(10) Bentzon, M.D. and Vase P. (1999) Critical current measurements on long BSCCO tapes using a contact-free method. *IEEE Transactions on Applied Superconductivity*, **9**, 1594–1597.

(11) Larbalestier, D.C. (2001) Critical currents: Just how critical are they? *IEEE Transactions on Applied Superconductivity*, **11**, 2685–2685.

(12) Koblischka-Veneva, A., Mücklich, F., Koblischka, M.R., et al. (2007) Crystallographic orientation of $Y_2Ba_4CuMO_x$ (M = Nb, Zr, Ag) nanoparticles embedded in bulk, melt-textured YBCO studied by EBSD. *Journal of the American Ceramic Society*, **90**, 2582–2588.

(13) Koblischka-Veneva, A. and Koblischka, M.R. (2008) Analysis of twin boundaries using the electron backscatter diffraction (EBSD) technique. *Materials Science and Engineering B*, **151**, 60–64.

(14) Krieger Lassen, N.C., Juul Jensen, D., and Condradsen, C. (1994) Automatic recognition of deformed and recrystallized regions in partly recrystallized samples using electron back scattering patterns. *Materials Science Forum*, **157–162**, 149–158.

(15) Koblischka-Veneva, A., Koblischka, M.R., Wei, J., et al. (2007) Misorientations in [001] magnetite thin films studied by electron backscatter diffraction and magnetic force microscopy. *Journal of Applied Physics*, **101**, art. no. 09M507.

(16) Laeng, P. and Rinderer, L. (1972) Preparation of EuS/EuF_2 films for magneto-optical studies at low temperatures. *Cryogenics*, **12**, 315–318.

(17) Schuster, T., Koblischka, M.R., Ludescher, B., et al. (1991) EuSe as magneto-optical active coating for use with the high-resolution Faraday effect. *Cryogenics*, **31**, 811–816.

(18) Indenbom, M., Polyanskii, A., Vlasko-Vlasov, V.K., et al. (1990) In *Physics and Materials Science of High Temperature Superconductors*, Proceedings of the NATO Advanced Study Institute, edited by R. Kossowky, S. Methfessel, and D. Wohlleben, Kluwer, Dordrecht, p. 131.

(19) Hubert, A. and Schäfer, R. (2009) *Magnetic Domains*, 3rd edition, Springer, Berlin.

(20) Koblischka, M.R. and Wijngaarden, R.J. (1995) Magneto-optical investigations of superconductors. *Superconductor Science and Technology*, **8**, 199–213.

(21) Jooss, Ch., Albrecht, J., Kuhn, H., et al. (2002) Magneto-optical studies of current distributions in high-T_c superconductors. *Reports on Progress in Physics*, **65**, 651–788.

(22) Koblischka, M.R. (2002) In *Handbook of Thin Film Materials,* vol. **5***: Nanomaterials and Magnetic Thin Films*, edited by H.S. Nalwa, Academic Press, San Diego.

(23) Koblischka, M.R. (2009) *Magnetic Properties of High-T_c Superconductors*, Alpha Science, Oxford.

(24) Bending, S.J. (1999) Local magnetic probes of superconductors. *Advances in Physics*, **48**, 449–535.

(25) Kirtley, J.R. (2010) Fundamental studies of superconductors using scanning magnetic imaging. *Reports on Progress in Physics*, **73**, art. no. 126501.

(26) Kirtley, J.R., Tsuei, C.C., Rupp, M., et al. (1995) Direct imaging of integer and half-integer Josephson vortices in high-T_c grain boundaries. *Physical Review Letters*, **76**, 1336–1339.

(27) Sarma, N.V. and Moon, J.R. (1967) High resolution Bitter patterns on superconductors. *Philosophical Magazine*, **16**, 433–445.

(28) Träuble, H. and Eßmann, U. (1968) Ein hochauflösendes Verfahren zur Untersuchung magnetischer Strukturen von Supraleitern. *Physica Status Solidi* **18**, 813–828.

(29) Grigorieva, I.V. (1994) Magnetic flux decoration of type-II superconductors. *Superconductor Science and Technology*, **7**, 161–176.

(30) Koblischka, M.R. and Hartmann, U. (2003) Recent advances in magnetic force microscopy. *Ultramicroscopy*, **97**, 103–112.

(31) Koblischka, M.R., Hartmann, U., and Sulzbach, T. (2004) Improving the spatial resolution of the MFM technique to the 10 nm range. *Journal of Magnetism and Magnetic Materials*, **272–276**, 2138–2140.

(32) Li, S., Stokes, S., Liu, Y., Foss-Schrader, S., et al. (2002) Dual vibrational high-frequency magnetic force microscopy. *Journal of Applied Physics*, **91**, 7346–7348.

(33) Proksch, R., Neilson, P., Austvold, S., and Schmidt, J.J. (1999) Measuring the gigahertz response of recording heads with the magnetic force microscope. *Applied Physics Letters*, **74**, 1308–1310.

(34) Abe, M. and Tanaka, Y. (2001) High-frequency write head with the phase detection magnetic force microscope. *Journal of Applied Physics*, **89**, 6766–6768.

(35) Koblischka, M.R., Kirsch, M., Wei, J.D., and Hartmann, U. (2006) High-frequency magnetic force microscopy imaging of hard-disk write heads. *Japanese Journal of Applied Physics*, **45**, 2238–2241.

(36) Koblischka, M.R. and Hartmann, U. (2009) Theoretical description of the high-frequency magnetic force microscopy technique. *IEEE Transactions on Magnetics*, **45**, 3228–3232.

(37) Koblischka, M.R. (2013) *Nanoscale Investigations on Magnetic and Superconducting Materials*, Habilitation Thesis, Saarland University, Saarbrücken.

(38) Li, Z.H., Hatekayama, K., Egawa, G., et al. (2012) Stroboscopic imaging of an alternating magnetic field from a perpendicular magnetic recording head by frequency-modulated magnetic force microscopy. *Applied Physics Letters*, **100**, art. no. 222405.

(39) Li, Z., Liu, D., Li, X., and Ishio, S. (2014) Near surface magnetic domain observation with ultra-high resolution. *Nanoscale*, **6**, 11163–11168.

(40) Zuger, O. and Rugar, D. (1993) First images from a magnetic resonance force microscope. *Applied Physics Letters*, **63**, 2496–2498.

(41) Chao, S., Dougherty, W., Garbini, J., and Sidles, J. (2003) Nanometer-scale magnetic resonance imaging. *Review of Scientific Instruments*, **75**, 1175–1181.

(42) Zhang, Z., Hammel, P.C., and Midzor, M. (1998) Ferromagnetic resonance force microscopy on microscopic cobalt layer films. *Applied Physics Letters*, **73**, 2036–2038.

(43) Poggio, M. and Degen, C.L. (2010) Force-detected nuclear magnetic resonance: recent advances and future challenges. *Nanotechnology*, **21**, art. no. 342001.

(44) Stipe, B.C., Mamin, H.J., and Stowe, T.D. (2001) Magnetic dissipation and fluctuations in individual nanomagnets measured by ultrasensitive cantilever magnetometry. *Physical Review Letters*, **86**, 2874–2877.

(45) Rugar, D., Budakian, R., Mamin, H., and Chui, B. (2004) Single spin detection by magnetic resonance force microscopy. *Nature*, **430**, 329–332.

(46) Degen, C.L., Poggio, M., Mamin, H., et al. (2004) Nanoscale magnetic resonance imaging. *Proceedings of the National Academy of Sciences*, **106**, 1313–1317.

(47) Midzor, M.M., Wigen, P.E., Pelekhov, D., et al. (2000) Imaging mechanisms of force detected FMR microscopy. *Journal of Applied Physics*, **87**, 6493–6495.

(48) Vinante, A., Wijts, G., Usenko, O., et al. (2012) Magnetic resonance force microscopy of paramagnetic electron spins at millikelvin temperatures. *Nature Communications*, **2**, art. no. 572.

(49) Verbiest, G.J., Oosterkamp, T.H., and Rost, M.J. (2013) Cantilever dynamics in heterodyne force microscopy. *Ultramicroscopy*, **135**, 113–120.

(50) Jungk, T., Hoffmann, A., Fiebig, M., and Soergel, E. (2010) Electrostatic topology of ferroelectric domains in $YMnO_3$. *Applied Physics Letters*, **97**, art. no. 012904.

(51) Jungk, T., Hoffmann, A., and Soergel, E. (2009) New insights into ferroelectric domain imaging with piezoresponse force microscopy, in *Ferroelectric Crystals for Photonic Applications*, edited by P. Ferraro, S. Grilli, and P. de Natale, Springer Series in Materials Science, Chapter 8, pp. 209–228.

(52) Johann, F., Hoffmann, A., and Soergel, E. (2010). Impact of electrostatic forces in contact-mode scanning force microscopy. *Physical Review B*, **81**, art. no. 094109.

(53) Soergel, E. (2011) Piezoresponse force microscopy (PFM). *Journal of Physics D: Applied Physics*, **44**, art. no. 464003.

(54) Chu, Y.H., Zhan, Q., Martin, L.W., et al. (2006) Nanoscale domain control in multiferroic $BaFeO_3$ thin films. *Advanced Materials*, **18**, 2307–2311.

(55) Yang, C.H., Zavaliche, F., Zheng, H. and Ramesh, R. (2007) Ferroelectric size effects in multiferroic $BiFeO_3$ thin films. *Applied Physics Letters*, **90**, art. no. 252906.

(56) Vrejoiu, I., Le Rhun, G., Pintilie, L., et al. (2006) Intrinsic ferroelectric properties of strained tetragonal $PbZr_{0.2}Ti_{0.8}O_3$ obtained on layer-by-layer grown, defect-free single-crystalline films. *Advanced Materials*, **18**, 1657–1661.

(57) Chen, X., Yang, S., Kim, J.H., et al. (2011) Ultrathin $BaTiO_3$ templates for multiferroic nanostructures. *New Journal of Physics*, **13**, art. no. 083037.

(58) Gao, X.S., Bao, D.H., Birajdar, B., et al. (2009) Switching magnetic anisotropy in epitaxial $CoFe_2O_4$ thin films induced by $SrRuO_3$ buffer layer. *Journal of Physics D: Applied Physics*, **42**, art. no. 175006.

(59) Hofstätter, M., Nevosad, A., Teichert, C., et al. (2013) Voltage polarity dependent current paths through polycrystalline ZnO varistors. *Journal of the European Ceramic Society*, **33**, 3473–3476.

(60) Wiesendanger, R. (1994) *Scanning Pobe Microscopy and Spectroscopy: Methods and Applications*, Cambridge University Press, Cambridge.

(61) Martinez, J.M.P., Morales, E. H., Saidi, W.A., et al. (2012) Atomic and electronic structure of the $BaTiO_3$(001) (root 5 x root 5)R26.6 degrees surface reconstruction. *Physical Review Letters*, **109**, 256802.

(62) Forster, S. and Widdra, W. (2010) Growth, structure, and thermal stability of epitaxial $BaTiO_3$ films on Pt(111). *Surface Science*, **604**, 2163–2169.

(63) Lang, K.M., Madhavan, V., Hoffman, J.E., et al. (2002) Imaging the granular structure of high-T_c superconductivity in underdoped $Bi_2Sr_2CaCu_2O_{8+\delta}$. *Nature* **415**, 412-416.

(64) Lee, J., Slezak, J.A., and Davis, J.C. (2005) Spectroscopic imaging STM studies of high-Tc superconductivity. *Journal of Physics and Chemistry of Solids*, **66**, 1370–1375.

(65) Madhavan, V., Lang, K.M., Hudson, E.W., et al. (2000) Spatial variations in the superconducting order parameter of $Bi_2Sr_2CaCu_2O_{8+\delta}$ as revealed by low

temperature scanning tunneling spectroscopy. *Bulletin of the American Physical Society*, **45**, 416–418.

(66) Kinoda, G., Hasegawa, T., Nakao, S., et al. (2003) Observations of electronic inhomogeneity in heavily Pb-doped $Bi_2Sr_2CaCu_2O_y$ single crystals by scanning tunneling microscopy. *Physical Review B*, **67**, art. no. 224509.

(67) Muralidhar, M. (2012) Private communication.

(68) Bode, M. (2003) Spin-polarized scanning tunnelling microscopy. *Reports on Progress in Physics*, **66**, 523–582.

(69) Akiyama, R., Tanaka, H., Matsumoto, T., and Kawai, T. (2001) Spin-polarized scanning tunneling microscopy on half-metallic manganite thin film with half-metallic manganite tip. *Applied Physics Letters*, **79**, 4378–4380.

(70) Kimura, T., Goto, T., Shintani, H., et al. (2003) Magnetic control of ferroelectric polarization. *Nature*, **426**, 55–58.

(71) Zheng, H., Wang, J., Lofland, S.E., et al. (2004) Multiferroic $BaTiO_3$–$CoFe_2O_4$ nanostructures. *Science*, **303**, 661–663.

(72) Prellier, W., Singh, M.P., and Murugavel, P. (2005) The single-phase multiferroic oxides: from bulk to thin film. *Journal of Physics: Condensed Matter*,**17**, R803–R832.

(73) Cheong, S.W. and Mostovoy, M. (2007) Multiferroics: a magnetic twist for ferroelectricity. *Nature Materials*, **6**, 13–20.

(74) Ramesh, R. and Spaldin, N.A. (2007) Multiferroics: progress and prospects in thin films. *Nature Materials*, **6**, 21–29.

(75) Nan, C.W., Bichurin, M.I., Dong, Sh., et al. (2008) Multiferroic magnetoelectric composites: historical perspective, status and future directions. *Journal of Applied Physics*, **103**, art. no. 031101.

(76) Yang, Y., Priya, S., Li, J.F., and Viehland, D. (2009) Two-phase coexistence in single grain $BaTiO_3$–$(Mn_{0.5}Zn_{0.5})Fe_2O_4$ composites via solid state reaction. *Journal of the American Ceramic Society*, **92**, 1552–1555.

(77) Mitoseriu, L., Pallecchi, I., Buscaglia, V., et al. (2007) Magnetic properties of the $BaTiO_3$–$(Ni,Zn)Fe_2O_4$ multiferroic composites. *Journal of Magnetism and Magnetic Materials*, **316**, e603–e606.

(78) Humphreys, F.J. (2001) Grain and subgrain characterization by electron backscatter diffraction. *Journal of Materials Science*, **36**, 3833–3854.

(79) Humphreys, F.J. (2004) Characterisation of fine-scale microstructures by electron backscatter diffraction (EBSD). *Scripta Materialia*, **51**, 771–776.

(80) Koblischka-Veneva, A., Koblischka, M.R., Mücklich, F., et al. (2007) Comparative study of grain orientation in melt-textured HTSC with different additions. *Physica* C, **426–431**, 618–624.

(81) Dingley, D.J., Baba-Kishi, K.Z., and Randle, V. (1995) Atlas of backscattering Kikuchi diffraction patterns, in *Microscopy in Materials Science Series*, edited by B. Cantor and M. Goringe, IOP Publishing, Bristol.

(82) Software Version V4.0 (2004) *User Manual*, TexSEM Laboratories (TSL), Draper, UT.

(83) Koblischka-Veneva, A. and Koblischka, M.R. (2004) Surface preparation of high-T_c superconductors for MO-imaging, in *Magneto-Optical Imaging*, eedited by T.H. Johansen and D.V. Shantsev, Kluwer Academic Press, Dordrecht, pp. 242—246.

(84) Koblischka-Veneva, A., Schmauch, J., Koblischka, M.R., et al. (2009) Microstructural investigation of M-type $BaFe_{12}O_{19}$ hexaferrites using electron backscatter diffraction (EBSD), in *MC2009*, edited by W. Grogger, F. Hofer, and P. Pölt, vol. 3: *Materials Science*, Verlag TU Graz, Graz, pp. 525–526.

(85) Koblischka-Veneva, A. and Mücklich, F. (2002) Orientation imaging microscopy applied to $BaTiO_3$ ceramics. *Crystal Engineering*, **5**, 235–242.

(86) Ochoa, D.A., García, J.E., Pérez, R., et al. (2009) Extrinsic contribution and nonlinear response in lead-free KNN-modified piezoceramics. *Journal of Physics D: Applied Physics*, **42**, art. no. 025402.

(87) Skumryev, V., Laukhin, V., Fina, I., et al. (2011) Magnetization reversal by electric-field decoupling of magnetic and ferroelectric domain walls in multiferroic-based heterostructures. *Physical Review Letters*, **106**, art. no. 057206.

(88) Koblischka-Veneva, A., Koblischka, M.R., and Mücklich, F. (2010) Advanced microstructural analysis of ferrite materials by means of electron backscatter diffraction (EBSD). *Journal of Magnetism and Magnetic Materials*, **322**, 1178–1181.

(89) Mitoseriu, L. and Buscaglia, V. (2006) Intrinsic/extrinsic interplay contributions to the functional properties of ferroelectric-magnetic composites. *Phase Transitions*. **79**, 1095–1121.

(90) Mitoseriu, L., Buscaglia, V., Viviani, M., et al. (2007) $BaTiO_3$–$(Ni_{0.5}Zn_{0.5})Fe_2O_4$ ceramic composites with ferroelectric and magnetic properties. *Journal of the European Ceramic Society*, **27**, 4379–4382.

(91) Testino, A., Mitoseriu, L., Buscaglia, V., et al. (2006) Preparation of multiferroic composites of $BaTiO_3$–$Ni_{0.5}Zn_{0.5}Fe_2O_4$ ceramics. *Journal of the European Ceramic Society*, **26**, 3031–3036.

(92) Koblischka-Veneva, A., Koblischka, M.R., Teng, C.L., et al. (2010) EBSD analysis of electroplated magnetite thin films. *Journal of Magnetism and Magnetic Materials*, **322**, 1235–1238.

(93) Koblischka-Veneva, A. and Koblischka, M.R. (2003) Texture analysis of melt-textured and polycrystalline $YBa_2Cu_3O_y$ using EBSD. *Journal of Low Temperature Physics*, **131**, 653–657.

(94) Bonnell, D.A. (1998) Scanning tunneling microscopy and spectroscopy of oxide surfaces. *Progress in Surface Science*, **57**, 187–252.

(95) Seidel, J., Martin, L.W., He, Q., et al. (2009) Conduction at domain walls in oxide multiferroics. *Nature Materials*, **8**, 229–234.

(96) Chu, Y.H., Martin, L.W., Holcomb, M.B., et al. (2008) Electric-field control of local ferromagnetism using a magnetoelectric multiferroic. *Nature Materials*, **7**, 478–482.

(97) Uchic, M.D., Holzer, L., Inkson, B.J., et al. (2007) Three-dimensional microstructural characterization using focused ion beam tomography. *MRS Bulletin*, **32**, 408–416.

(98) Zaefferer, S., Wright, S.I., and Raabe, D. (2008) Three-dimensional orientation microscopy in a focused ion beam-scanning electron microscope: a new dimension of microstructure characterization. *Metallurgical and Materials Transactions A*, **39**, 374–389.

(99) Dillon, S.J. and Rohrer, G.S. (2009) Characterization of the grain boundary character and energy distribution of yttria using automated serial sectioning and EBSD in the FIB. *Journal of the American Ceramic Society*, **92**, 1580–1585.

(100) Snowadee, N., Aegersted, K., Ubhi, H.S. and Bowen, J.R. (2013) Ion beam polishing for three-dimensional electron backscatter diffraction. *Jounal of Miscroscopy*. **249**, 36-40.

(101) Xu, W., Ferry, M., Mateescu, N., et al. (2007) Techniques for generating 3-D EBSD microstructures by FIB tomography. *Materials Characterization*, **58**, 961–967.

(102) Calcagnotto, M., Ponge, D., Demir, E., and Raabe, D. (2010) Orientation gradients and geometrically necessary dislocations in ultrafine grained dual-phase steels studied by 2D and 3D EBSD. *Materials Science and Engineering A*, **527**, 2738–2746.

(103) Petrov, R., Garcia, O.L., Mourino, N.S., et al. (2007) Microstructure: texture related toughness anisotropy of API-X80 pipeline steel characterized by means of 3D-EBSD technique. *Materials Science Forum*, **558–559**, 1429–1434.

(104) Velichko, A. and Mücklich, F. (2009) Quantitative 3D characterization of graphite morphology in cast iron – correlation between microstructure, processing and properties. *International Journal of Materials Research*, **8**, 1031–1037.

(105) Koblischka-Veneva, A. and Koblischka, M.R. (2008) Ion damage during preparation of nanostructures in magnetite by means of focused ion-beam (FIB) milling. *Superlattices and Microstructures*, **44**, 468–475.

(106) Trimby, P.W. (2012) Orientation mapping of nanostructured materials using transmission Kikuchi diffraction in the scanning electron microscope. *Ultramicroscopy*, **120**, 16–24.

(107) Keller, R.R. and Geiss, R.H. (2012) Transmission EBSD from 10 nm domains in a scanning electron microscope. *Journal of Microscopy*, **245**, 245–251.

(108) Suzuki, S. (2013) Features of transmission EBSD and its applications. *JOM*, **65**, 1254–1263.

(109) Lohmiller, J., Grewer, M., Braun, C., et al. (2014) Untangling dislocation and grain boundary mediated plasticity in nanocrystalline nickel. *Acta Materialia*, **65**, 295–307.

(110) Robert, D., Douillard, T., Boulineau, A., et al. (2013) Multiscale phase mapping of $LiFePO_4$-based electrodes by transmission electron microscopy and electron forward scatter diffraction. *ACS Nano*, **7**, 10887–10894.

14

Electrostatic and Kelvin Probe Force Microscopy for Domain Imaging of Ferroic Systems

Brian J. Rodriguez

School of Physics and Conway Institute of Biomolecular and Biomedical Research,
University College Dublin, Ireland

14.1 Introduction

The advent of scanning probe microscopy has ushered in the age of nanotechnology, driven by the motivation to see, manipulate, and measure materials properties at the nanoscale [1]. This is particularly true for ferroelectric materials, where the macroscale properties of the ferroelectric are defined largely by the microscale and nanoscale behavior of the ferroelectric domains [2]. Thus, the drive to visualize ferroelectric domains has been an impetus for the development of techniques capable of domain imaging.

The first approaches for domain imaging relied on polarized light [3–7], etching [8–10], and transmission electron microscopy (TEM) [11, 12]. Initially, these approaches were predominantly used to investigate $BaTiO_3$. Etching and TEM are inherently destructive, and so other approaches emerged to image ferroelectric polarization. Domains have been decorated and observed optically using charged powders [13], solvent droplets [14], metallic particles [15], and aligned nematic liquid crystals [16]. More recently, domain decoration has been extended to tobacco mosaic virus particles [17], polystyrene spheres [18], and droplet arrays [19, 20], and polarization-dependent molecular adsorption [21, 22] and ice nucleation [23] have been demonstrated. These approaches, however, require specialized

---

Nanoscale Ferroelectrics and Multiferroics: Key Processing and Characterization Issues, and Nanoscale Effects,
First Edition. Edited by Miguel Algueró, J. Marty Gregg, and Liliana Mitoseriu.
© 2016 John Wiley & Sons, Ltd. Published 2016 by John Wiley & Sons, Ltd.

tools, such as scanning probe microscopy and photoemission spectroscopy. Similarly, to directly visualize nanoscale-sized domains, beyond the diffraction limit of optical microscopes, new techniques were required, based primarily on voltage-modulated atomic force microscopy (AFM) approaches. For an outstanding and detailed review of various techniques used to visualize ferroic domains, consult the book by Tagantsev et al. [2], and for an article tailored specifically for triglycine sulfate (TGS), consult Nakatani [24].

The use of AFM for domain imaging of ferroelectric materials was made possible by the invention of the scanning tunneling microscope (STM) by Binnig and Rohrer [25] and the AFM by Binnig et al. [26]. The development of the profilometer actually predates AFM [27]. Profilometers make use of a feedback loop to maintain constant probe–sample interactions [28] and, in some cases, employed an optical lever [29], as is widely used in AFM [30, 31], and piezoelectric activation to minimize lateral forces and unstable probe motion [32,33]. The Topographiner [34,35], based on sensing electron field emission current above the surface of conducting samples, also predated STM and used both feedback and piezoelectric activation. Another early scanning probe microscope was developed by Kaczér [36, 37], which was used to image ferromagnetic domains – a precursor to the AFM-based magnetic force microscopy (MFM) [38, 39], which is used widely to investigate magnetoelectric coupling in multiferroics [40].

Electrostatic force microscopy (EFM) was first reported in the late 1980s [41–43] and by 1990 had been applied to a ferroelectric material [44]. Subsequently, EFM was used to investigate domain writing in $Pb(Zr,Ti)O_3$ (PZT) [45] and the stability/screening of switched domains [46]. By 1991, STM and scanning near-field acoustic microscopy had been used to visualize domains in ferroelectric materials [47, 48], and in 1992, what we know today as piezoresponse force microscopy (PFM) had already been demonstrated on a ferroelectric polymer [49]. Contact and non-contact AFM modes were subsequently used to visualize domains and domain walls, respectively, of GASH crystals [50]. Time-dependent surface topography changes after cleaving were observed on TGS via contact mode AFM and attributed to the domain structure [51, 52]. Changes in topography were observed following the application of bias to the surface of GASH crystals and attributed to piezoelectric deformations resulting from domain switching [53,54]. Tunneling acoustic microscopy was used to image and switch domains in PZT [55] and friction force imaging of domains was performed on GASH [54] and TGS [56] as a function temperature [57] and time after cleaving (Figure 14.1) [58]. Two years after the first PFM paper, a second publication appeared [59], and shortly thereafter many followed [60–68].

Around this time, another technique emerged for imaging ferroelectric domains, the so-called dynamic contact mode EFM (DC-EFM) – not to be confused with an implementation of EFM [69–71], where the DC deflection of the lever in lift mode is recorded while the topography is retraced at a constant height above a surface. DC-EFM is basically an implementation of PFM whereby an AC excitation is applied via the conducting cantilever to the sample surface and the vibration of the lever is recorded. DC-EFM has been used to image domains in TGS [72, 73] and their evolution in an AC field [74] and under thermal cycling [75–79] to determine domain wall thickness, surface charge density, and the role of defects on domain pinning in TGS [80, 81], and also to switch [82–85] domains and study domain relaxation in PZT [86] and $Bi_{3.25}La_{0.75}Ti_3O_{12}$ [87]. In general, the proponents of DC-EFM claimed that the signal stemmed from the electrostatic force of the ferroelectric domains resulting from the polarization charge, and not from the piezoelectric deformation. Still

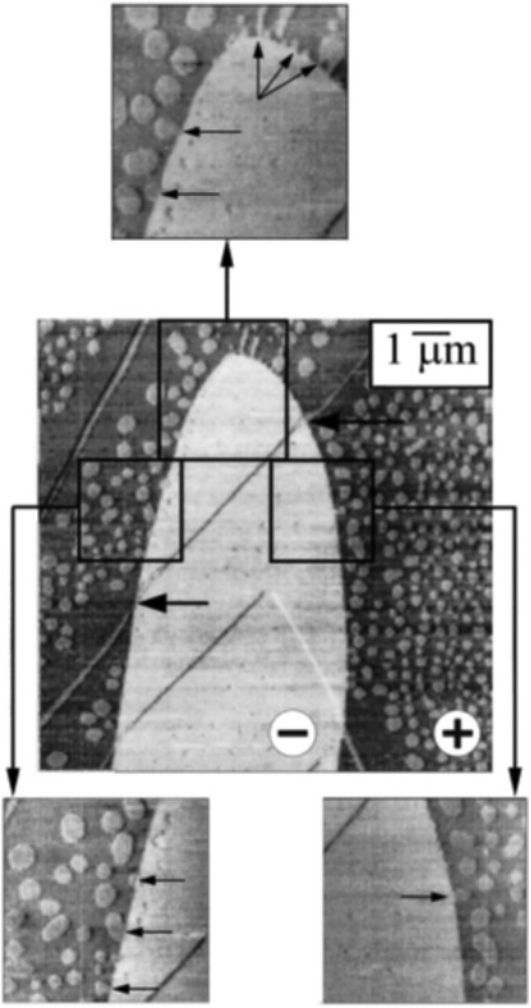

Figure 14.1 Friction images recorded several hours after cleaving a TGS crystal, showing positive and negative domains (dark and bright, respectively). The black arrows indicate certain interactions between domains. Reprinted with permission from [58]. Copyright [1996], AIP Publishing LLC

others claimed the signal may be related to electrochemical activity [82, 88], which brings the argument full circle now that PFM is being applied for electrochemical strain detection via electrochemical strain microscopy [89–92].

Despite being first reported in 1991 [93], Kelvin probe force microscopy (KPFM) was applied to measure surface potentials at the surface of ferroelectric materials only in 1999 [94,95]. Shortly thereafter, a series of papers by Kalinin and Bonnell set the standard for the use of KPFM to investigate surface potentials, phase transitions, and polarization screening of ferroelectric materials [96–98].

In the sections that follow, the operating principles of EFM and various KPFM modes are discussed, and specific examples of the use of EFM and KPFM to image domains and understand polarization screening are provided. In addition, the benefits of combined PFM and EFM and KPFM measurements are outlined, and some emerging modes for exploring, e.g., time-resolved behavior are discussed. While care was taken to reference as many unique examples of the use of EFM and KPFM to study ferroic materials, there are likely to be accidental omissions.

14.2 Electrostatic Force Microscopy and Kelvin Probe Force Microscopy

As described above, EFM appeared just two years after the first implementation of the AFM [26, 41]. Thus, the measurement of long-range electrostatic forces using dynamic AFM modes has long been of interest to the scanning probe community.

14.2.1 Electrostatic Force Microscopy

In EFM, the electric potential of a conductive AFM probe is modulated by applying a voltage to the tip, $V_{tip} = V_{dc} + V_{ac}\sin(\omega t)$, where V_{dc} is a DC potential (often $V_{dc} = 0$ during an EFM experiment), V_{ac} is the AC voltage, and ω, the modulation frequency, is typically selected to be close to the free cantilever resonance. Depending on the experimental configuration, V_{tip} can be applied either during the lift scan (i.e., the tip retraces the surface topography a certain distance from the surface) or simultaneously during the acquisition of topography, although at a different frequency than the free cantilever resonance. The application of V_{tip} results in a capacitive probe–surface electrical force, $F_{el} = -1/2C'_z(V_{tip} - V_{cpd})^2$, where C'_z is the tip-surface capacitance gradient and V_{cpd} is the contact potential difference between the tip and the surface [93]. In EFM, the first harmonic electrostatic force response of the cantilever, $F_{\omega} = -C'_z(V_{dc} - V_{cpd})V_{ac}\sin(\omega t)$, is monitored using a lock-in amplifier. While also present, the second harmonic component of the electrostatic force, $F_{2\omega} = 1/4C'_zV_{ac}^2\cos(2\omega t)$, which is independent of V_{cpd} and V_{dc}, is typically not recorded, although it has proven useful in mapping dielectric properties of samples [64, 99]. The implementation of EFM described above is referred to as the amplitude modulation (constant frequency) mode. EFM can also be implemented in the frequency modulation mode, whereby the electrostatic force gradient acting on the probe is determined from the frequency shift of the resonance of the voltage-modulated cantilever. Multifrequency implementations are also possible [100–103].

14.2.2 Kelvin Probe Force Microscopy

It is considered difficult to quantify EFM as the signal is sensitive to surface topography by way of the tip–surface capacitance gradient. Thus, in order to quantify the electrostatic properties of surfaces, KPFM was developed to be able to determine V_{cpd} and by extension the surface potential of the sample being studied [93]. In KPFM, a feedback loop acts to minimize the first harmonic response, or frequency shift in the case of frequency modulation KPFM [105–107], through the application of V_{dc} proportional to V_{cpd}. The key distinguishing features between EFM and KPFM operation are outlined schematically in Figure 14.2.

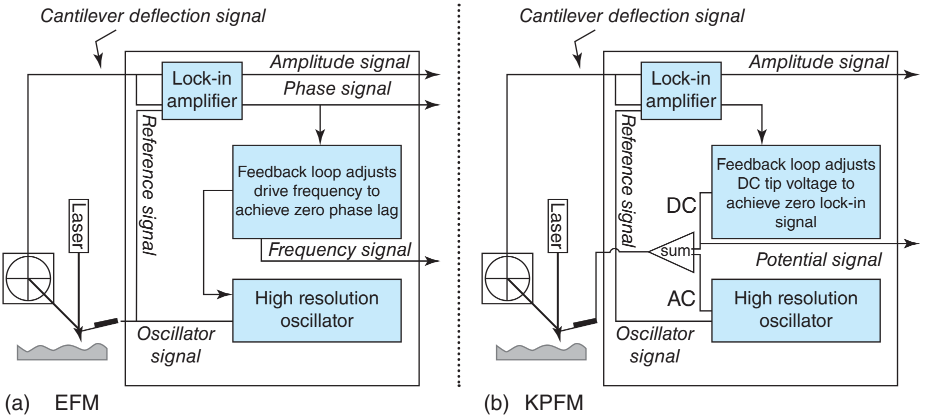
Cantilever deflection signal
Lock-in amplifier
Amplitude signal
Phase signal
Reference signal
Feedback loop adjusts drive frequency to achieve zero phase lag
Frequency signal
Laser
High resolution oscillator
Oscillator signal
(a) EFM
Cantilever deflection signal
Lock-in amplifier
Amplitude signal
Reference signal
Feedback loop adjusts DC tip voltage to achieve zero lock-in signal
DC
sum
Potential signal
AC
High resolution oscillator
Laser
Oscillator signal
(b) KPFM

Figure 14.2 *Schematics of EFM and KPFM operation. The electrostatic force measured in (a) EFM is simultaneously minimized in (b) KPFM using a feedback loop, which applies the required DC voltage. Adapted from [104]. © IOP Publishing. Reproduced by permission of IOP Publishing. All rights reserved*

EFM and KPFM have been widely used [108, 109] to study semiconductors and devices [110–115], dielectrics [116], solar materials [117], organic molecules [118–123], biomolecular systems [124, 125], and photo-induced phenomena [126–133]. Frequency-modulated KPFM can achieve atomic [134–137] and molecular [138] resolution, suggesting tremendous potential for this technique. In the following sections, the use of EFM and KPFM to study ferroelectric materials is discussed.

14.3 EFM of Ferroelectric Materials

As described above, Saurenbach and Terris were the first to use EFM to image ferroelectric domains (down to 10 μm in width) and domain walls by detecting the force gradient due to polarization charge in the ferroelectric–ferroelastic material $Gd_2(MoO_4)_3$ [44]. They reported that the signal changed sign at the domain wall, which appeared larger (several micrometers in width) than the expected width due to convolution with the tip shape and the long-range nature of the interactions, and noted that further improvements could be made by operating in vacuum [44].

Even at this early stage, the motivation for applying EFM to study ferroelectric materials centered on domain imaging, manipulation, and stability, with an eye towards the potential use of these materials in non-volatile memory applications. Ahn et al. [45] and Tybell et al. [46, 65] subsequently investigated domain writing and stability in PZT thin films using EFM (and PFM). In 1997, Ahn et al. reported electronic writing of domains in PZT with an electronic readout by EFM, noting also a tunable sheet resistance change in the $SrRuO_3$ bottom electrode [45]. Shortly thereafter, using PFM, Tybell et al. showed that domains smaller than 100 nm – approaching the size of the AFM tip – could be written in PZT [65]. In 1999, Tybell et al. went on to investigate the time dependence of the PFM and

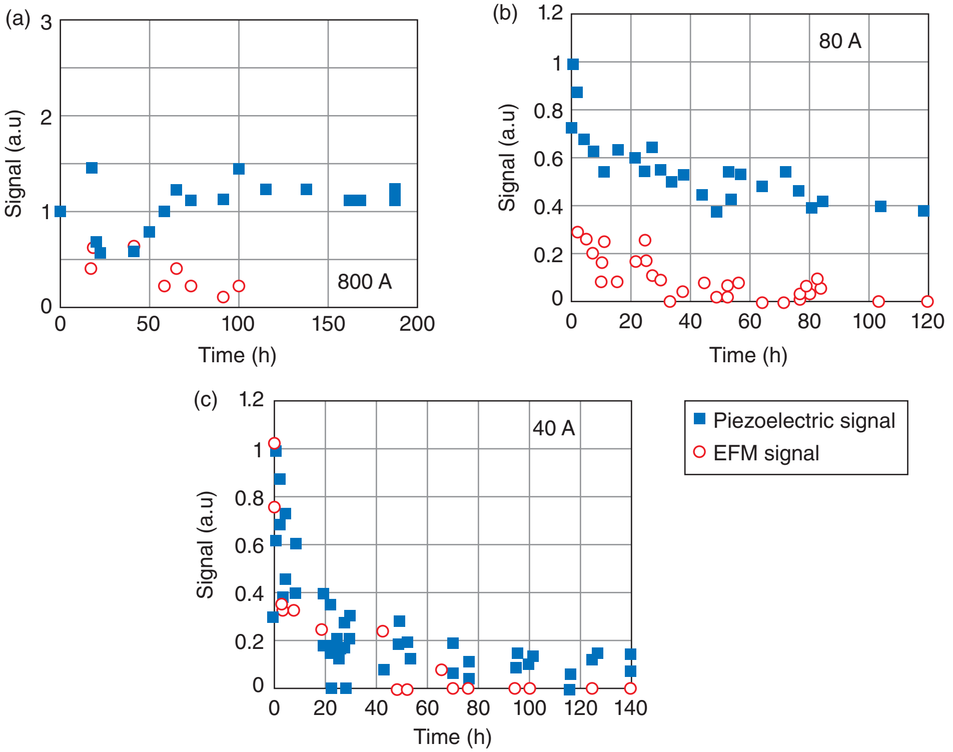

Figure 14.3 *The observed time-dependence of the EFM and PFM signals following polarization reversal in PZT thin films with thicknesses of (a) 800 Å, (b) 80 Å, and (c) 40 Å. Reprinted with permission from [46]. Copyright [1999], AIP Publishing LLC*

EFM signals following local polarization reversal in 800 Å, 80 Å, and 40 Å thick PZT thin films, reporting that the EFM signal goes to zero whereas the PFM signal remains nonzero (Figure 14.3) [46]. In the immediate years that followed, the EFM signal was also investigated as a function of distance from a PZT surface [139], and implemented using a tuning fork on domain-patterned PZT films [140].

As mentioned in Section 14.1, EFM is considered a dynamic AFM mode, typically operated in intermittent, non-contact, or lift modes, but the late 1990s and early 2000s saw the development of so-called dynamic contact EFM or DC-EFM, which was widely used to image domains, often as a function of temperature through a phase transition (Figure 14.4). In DC-EFM, the AFM is operated in contact mode and dynamic contact is assumed as a result of the modulation voltage applied to the tip. Thus, the images resemble those obtained by PFM [141]. Similarities between DC-EFM and contact resonance PFM are readily apparent in the work of Labardi et al. [73] and the cases for and against electrostatic versus electromechanical imaging mechanisms are laid out by Hong et al. [82, 142].

Generally, the EFM signal measured above a ferroelectric surface will result from a superposition of the polarization and screening charges. This explains why Tybell et al.

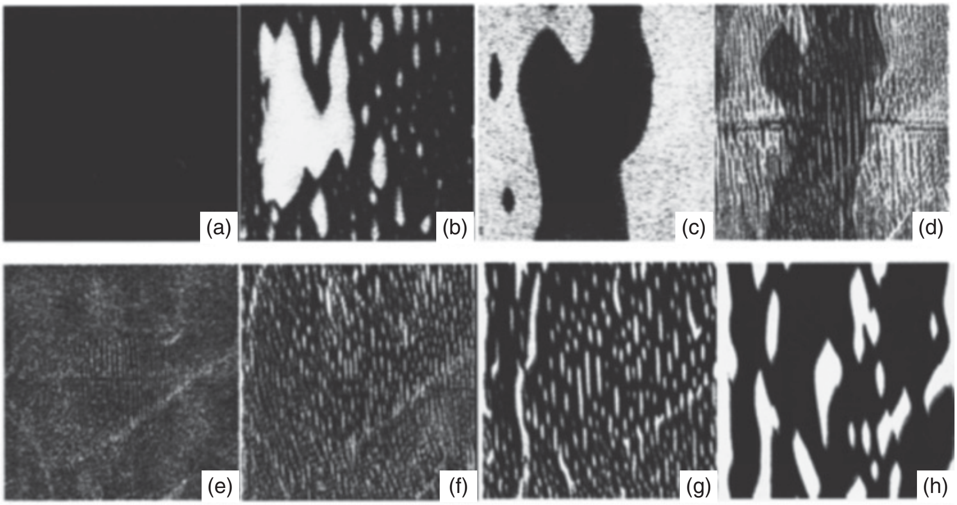

Figure 14.4 *DC-EFM images (40 μm × 40 μm) of a TGS surface on heating: (a) 35 °C, (b) 44.4 °C, (c) 46.5 °C, and (d) 48.2 °C; and cooling: (e) 49 °C, (f) 48.1 °C, (g) 47.7 °C, and (h) 46.7 °C. Reprinted with permission from [76]. Copyright (2000) by the American Physical Society*

[46] observed that the EFM signal decayed to zero following polarization reversal, why Lehnen et al. reported that unlike EFM, PFM reveals domains regardless of surface charge compensation [143], and also why it is possible for opposite domains to lack contrast in EFM (Figure 14.5).

More recently, EFM has been used to image domains written into $BaTiO_3$ nanowires (Figure 14.6) [146, 147], to detect domain walls in periodically poled $LiNbO_3$ and potassium titanyl phosphate via in-plane EFM [148], to quantify surface charge density of the z-cut [149], to compare the decay of PFM and EFM signals as a function of time after poling [150], to visualize mechanically-induced charging in ultrathin $BaTiO_3$ [151], and to observe variations in electrostatic force on periodically proton exchanged $LiNbO_3$ [152]. Despite advances in quantifying EFM signals to measure surface charge and dielectric constants [64, 99], KPFM allows quantification without taking into account, e.g., tip shape and changes in capacitance, and has therefore been more widely applied to study the quantitative electrostatic properties of ferroelectric materials, still with a view to understand domain-switching stability and screening mechanisms of ferroelectric surfaces.

14.4 KPFM of Ferroelectric Materials

KPFM was first applied to study the switching and time evolution of domains in ferroelectric films of PZT and polyvinylidene difluoride in 1999 by Chen et al. [94, 95]. Around the same time, Durkan et al. also reported using KPFM to measure the surface potential of

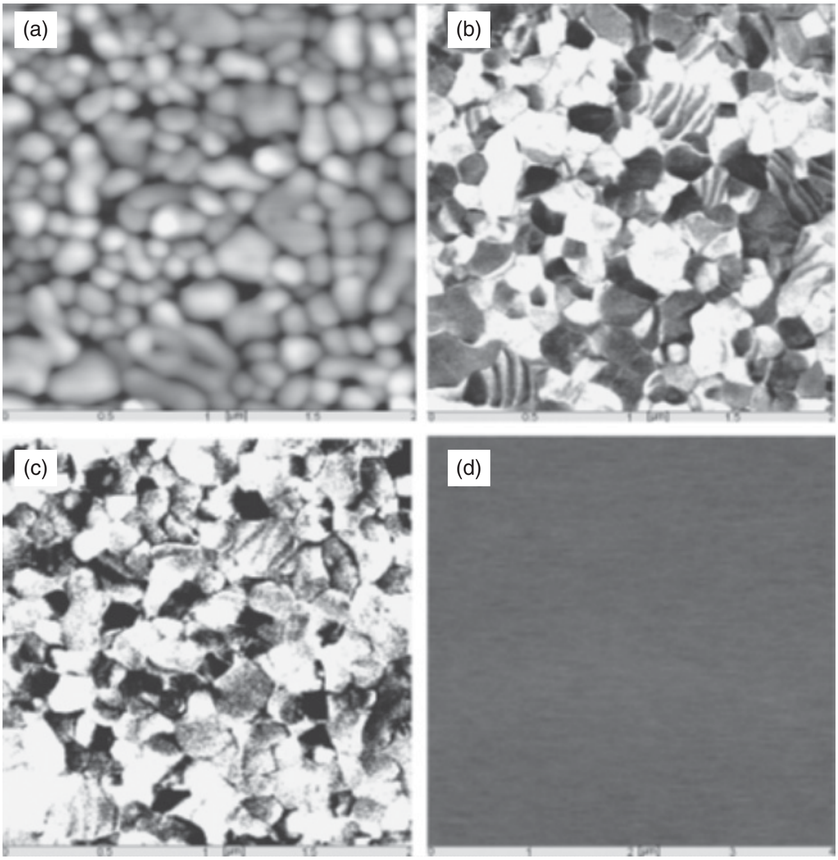

Figure 14.5 *(a) Topography, (b) in-plane PFM, (c) out-of-plane PFM, and (d) EFM image [144] recorded on a* $PbTiO_3$*(PT)/PZT/PT multilayer film showing that while the presence of domains are clearly evident from the PFM images, they are indistinguishable in the EFM image, presumably due to screening. Reprinted from [145] by permission of the publisher (Taylor & Francis Ltd, http://www.tandf.co.uk/journals)*

PZT films following localized switching by the AFM tip [153, 154]. In modeling the tip–sample system using a sphere-plane model, the calculated surface charge densities showed good agreement with experiment, and the influence of surface contaminants on domains formed and imaged with KPFM and PFM was described [153, 154].

In a series of papers by Kalinin et al., the potential of KPFM to study phase transitions and elucidate screening mechanisms at the surface of ferroelectric crystals was realized [96–98, 155, 156]. In 2000, Kalinin and Bonnell reported that the surface corrugations due to 90° domain boundaries disappeared above the Curie temperature and were able to monitor the surface potential during the ferroelectric–paraelectric transition and also to identify 90° and 180° domain walls, thereby reconstructing the domain structure on $BaTiO_3$ (100) surfaces [96]. They further noted that the time scales of the surface potential variations observed allowed different screening mechanisms to be identified; large surface potentials

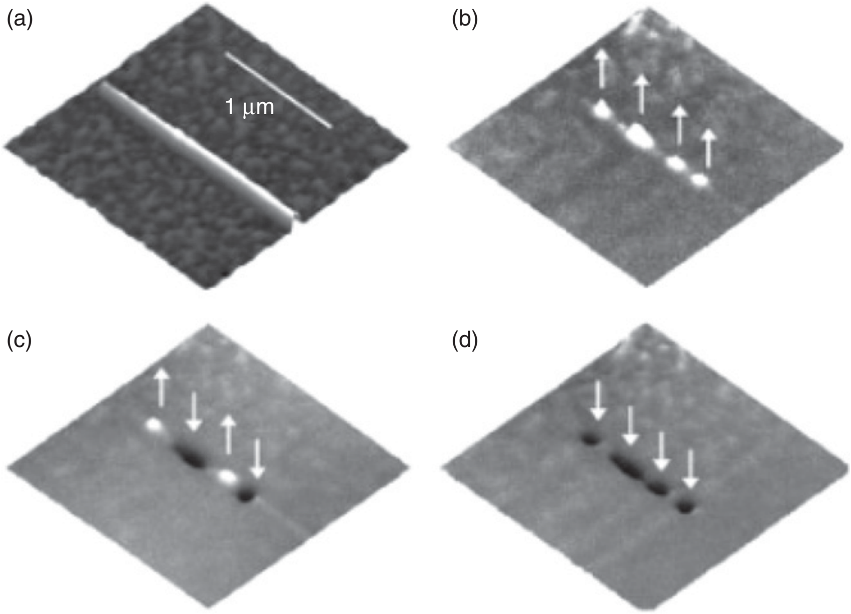

Figure 14.6 *(a) Topography and (b) to (d) EFM images recorded on a BaTiO$_3$ nanowire showing the manipulation of domain polarization through the application of ±10 V to the conducting tip. The arrows in (b) to (d) indicate the polarization direction. © 2003 WILEY-VCH Verlag GmbH & Co. KGaA, Weinheim*

were observed immediately after the ferroelectric phase transition and slowly decayed over tens of minutes [96]. In a subsequent study, they expanded upon this last point, using EFM and KPFM to study the evolution of the electrostatic force gradient and surface potential during the ferroelectric–paralectric transition in BaTiO$_3$, reporting that the surface potential measured reflects the complete screening of the polarization charge and that this is largely achieved by surface adsorbates [97]. In 2001, Kalinin and Bonnell used a combination of variable temperature KPFM and PFM to show that the sign of the surface potential is opposite to that expected from the polarization orientation determined by PFM [98]. Furthermore, upon heating the BaTiO$_3$ surface, the bound polarization charge was found to be reduced, leaving an uncompensated screening charge and an increase in surface potential [98]. The kinetics and dynamics of the screening process were studied in detail by Kalinin et al. [155]. The influence of the adsorbed charge on surface potential measurements and subsequent implications of screening for a wide range of materials and scanning probe microscopy techniques were outlined by Kalinin and Bonnell [156–158]. An example of the variable temperature KPFM measurements are shown in Figure 14.7 and a schematic illustrating the resulting charge dynamics is shown in Figure 14.8.

Later, the Bonnell group reported that UV illumination decreased the surface potential contrast between BaTiO$_3$ domains by introducing photogenerated charge [159]. Other groups have also studied BaTiO$_3$ using KPFM. For example, in 2011 He et al. investigated the evolution of the surface potential of a BaTiO$_3$ (100) with an electric field applied

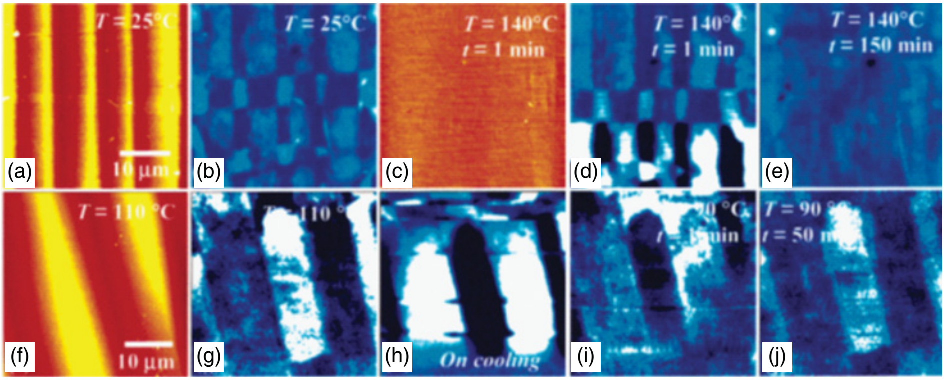
(a)
T = 25°C
10 µm
(b)
T = 25°C
(c)
T = 140°C
t = 1 min
(d)
T = 140°C
t = 1 min
(e)
T = 140°C
t = 150 min
(f)
T = 110 °C
10 µm
(g)
T = 110 °
(h)
On cooling
(i)
90 °C
t = 1 min
(j)
T = 90 °
t = 50 m

Figure 14.7 *(a), (c), and (f) Topography and (b), (d), (e), and (g) to (j) KPFM images of a* $BaTiO_3$ *surface. Topography and surface potential (a) and (b) before and (c) and (d) 1 minute after going through the phase transition (data scales are 0.1 V for (b) and 0.5 V for (d)). (e) Surface potential after 150 minutes of annealing at 140 °C (0.1 V data scale). (g) Topography and (f) surface potential at 110 °C, and (i) surface potential upon cooling to 90 °C and (j) after 50 minutes at 90 °C. Reprinted with permission from [156], Copyright (2004) American Chemical Society*

parallel to the (100) surface [160] and also as a function of relative humidity [161]. The influence of humidity on the surface potentials measured on PZT has also been investigated [162].

In addition to PZT [94, 153, 163–166] and $BaTiO_3$ [96–98, 155, 159–161], other ferroelectric materials have been studied by KPFM. For instance, Shvebelman et al. employed

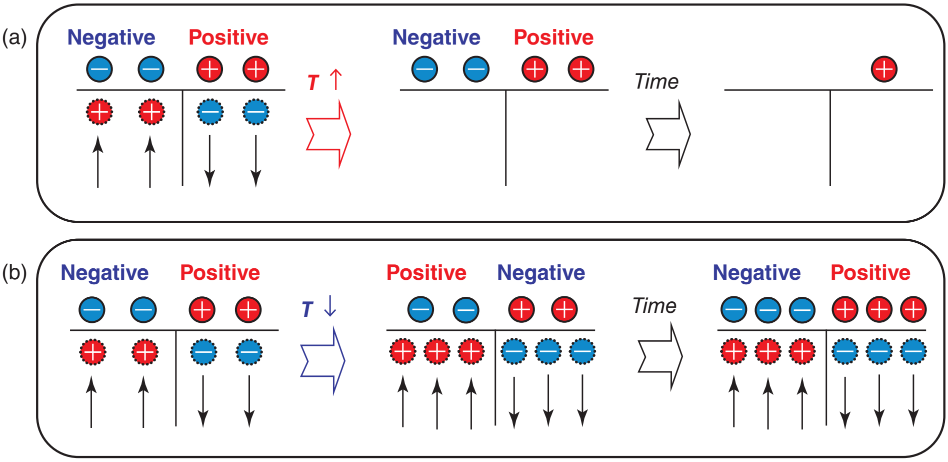
(a)
Negative
Positive
T ↑
Negative
Positive
Time
(b)
Negative
Positive
T ↓
Positive
Negative
Time
Negative
Positive

Figure 14.8 *Schematic of the charge dynamics observed experimentally in Figure 14.7 on (a) heating and (b) cooling the* $BaTiO_3$ *surface. Reprinted with permission from [156], Copyright (2004) American Chemical Society*

KPFM to visualize domains and measure surface potentials of uniform and periodically poled $KTiOPO_4$ crystals [167], Liu et al. reported on the relative surface potential differences between oppositely polarized $LiNbO_3$ domains [168], Zhukov et al. studied surface charge retention on $LiNbO_3$ [169], Lau et al. characterized $Pb(In_{1/2}Nb_{1/2})O_3$–$Pb(Mg_{1/3}Nb_{2/3})O_3$–$PbTiO_3$ by KPFM [170], Choi et al. studied the relaxation behavior of potential at poly(vinylidenefluoride-co-trifluoroethylene) thin-film surfaces [171], and Son et al. compared the suitability of PZT and $SrBi_2Ta_2O_9$ (SBT) films for non-volatile storage applications using KPFM [172]. Son et al. revealed that data storage is easier in PZT compared to SBT, which is more susceptible to charge injection during poling [172,173]. In 2004, Son et al. applied KPFM to study a multiferroic, apparently for the first time [174]. Orientation-dependent surface potentials have subsequently been measured in doped [175,176] and undoped $BiFeO_3$ [177]. In 2009, Son et al. went on to study surface charge dynamics following biased-tip-induced switching in PZT [178] and switching in lead titanate nanodots formed by dip pen lithography [179].

In a series of papers by Kim et al., KPFM was used to investigate the role of imprint on asymmetric switching in PZT [180] and in combination with conducting AFM (c-AFM) and PFM demonstrated that grain boundaries of a PZT film were at a lower potential than the grains themselves, probably as a result of leakage paths [181]. In polycrystalline films, the relaxation behavior of the surface potential was subsequently studied in the vicinity of grain boundaries [182]. Kim et al. also showed that charge transfer and polarization reversal occurs for a grounded tip and that the charge transfer can be negated by applying an offset bias [183], as previously reported by the same group [184]. In 2009, Kim et al. investigated the surface potential of switched domains in PT, correlating the KPFM with PFM measurements in order to elucidate the interplay of polarization, screening, and injected charge on the measured surface potentials (Figure 14.9) [185]. In terms of providing insight into the properties of ferroelectric materials, KPFM is most useful when it is used in combination with complementary techniques, including tip-bias-induced switching, PFM, and c-AFM studies.

14.5 Recent Advances

14.5.1 Open-Loop KPFM

In general, despite the quantitative nature of KPFM, it still has limitations as a technique, stemming from electronic offsets of the instrumentation used, thermomechanical and electrical noise, etc., and, in particular, the closed-loop bias feedback used in KPFM is susceptible to imaging and feedback artifacts [186–190]. These factors (and other reasons described below) have led to the development of open-loop KPFM approaches to determine the surface potential without the use of a feedback loop. In one implementation, this entails measuring the signal as a function of V_{dc} and then identifying the V_{cpd} from the signal minimum [102, 189, 191]. In a second bias- and feedback-free approach, V_{cpd} is determined by considering both the first and second (or half) harmonic response using dual harmonic (DH)-KPFM [103, 189, 192–196]. In DH-KPFM, V_{cpd} is determined as $V_{cpd} = \mathrm{sgn}(\cos\theta_\omega)(A_\omega/A_{2\omega})(V_{ac}/4X_{gain})$, where A_ω and $A_{2\omega}$ are the amplitude response of the first (F_ω) and second ($F_{2\omega}$) harmonic electrostatic force, respectively, $X_{gain} = G_\omega/G_{2\omega}$, where

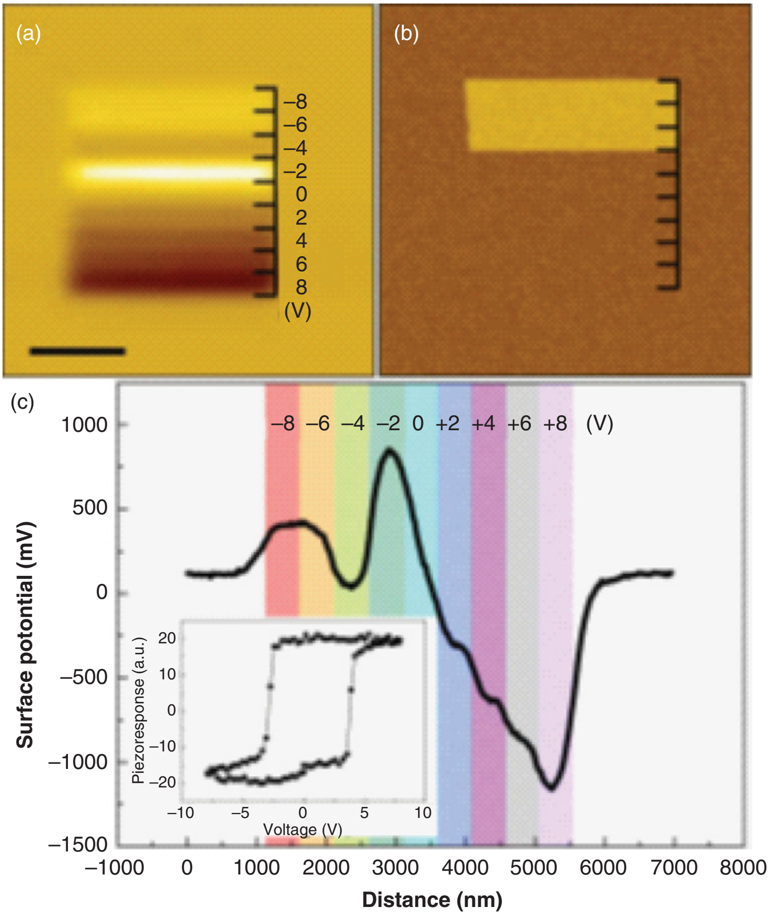

Figure 14.9 (a) KPFM and (b) PFM images recorded after scanning the central region from the top down with biases of −8 V to 8 V applied to the bottom electrode in 2 V increments. The scale bar in (a) is 2 μm. (c) Line profile of the surface potential image showing a maximum at −2 V as a result of positive screening charge. At −4 V, the negative polarization charge is almost completely screened by the positive screening charge, leading to a surface potential close to zero. The inset in (c) shows a piezoelectric hysteresis loop recorded from the sample. Reprinted with permission from [185]. Copyright [2009], AIP Publishing LLC

G_ω and $G_{2\omega}$ are the gains due to the cantilever transfer function at ω and 2ω, respectively, and θ_ω is the phase of the first harmonic response.

Given the previous examples of how the application [178] or absence [183] of bias has been shown to influence charge injection and the measurement of surface potentials in ferroelectrics, and the possibility that charge transfer occurs even during intermittent contact mode when the tip touches the surface, there is a possibility that the act of measuring KPFM on ferroelectric surfaces can influence what is being measured. In this regard, a feedback-free approach such as DH-KPFM may be suitable for determining surface potentials of ferroelectrics. DH-KPFM of several ferroelectric surfaces was first reported by Collins et al. [195]. As a precursor to DH-KPFM of ferroelectrics, Zavala et al. recorded the second harmonic signal of PZT films in order to determine the dielectric constant [64]. Subsequently, Li et al. demonstrated that open-loop KPFM could be used in conjunction with switching spectroscopy PFM [191]. In switching spectroscopy PFM (SS-PFM), local piezoelectric hysteresis loops are acquired in force volume mode (i.e., at every user-specified pixel in an image) and analyzed to yield two-dimensional maps of relevant switching parameters, which can be correlated with surface topography [197–199]. The implementation of switching spectroscopy KPFM by Li et al. may prove to be a useful technique for elucidating the roles of surface potential, polarization charge, and screening charge on the charge transport properties of ferroelectric surfaces, and could easily be extended to also map time-dependent processes, as shown by Rodriguez et al. [200] and Kalinin et al. [201].

Given the potential use of ferroelectrics in microfluidic applications [202], which exploit the presence of polarization charge and screening mechanisms, and that ferroelectric surfaces are used for the aqueous-based fabrication of metallic nanoarrays for possible biosensing applications [152], it would be useful to be able to locally probe electrostatics and surface potentials at the ferroelectric–liquid interface [203]. While KPFM has been shown to be feasible in non-polar solutions [204], the implementation of conventional KPFM is not suitable to probe surface potentials at the solid–liquid interface in solutions containing mobile ions [205], and even the bias-free DH-KPFM approach has limitations [196]. A recently developed open-loop approach called electrochemical force microscopy allows surface potentials to be extracted from surfaces under certain conditions and furthermore can be used to probe electrochemical reactions at the solid–liquid interface [205]. Such an approach may be useful for studying the local domain-dependent electrostatic and electrochemical properties of ferroelectric surfaces.

14.5.2 Time-Resolved KPFM

Recently Strelcov et al. developed a technique called time-resolved (tr)-KPFM to probe ion dynamics on dielectric surfaces [206, 207]. The tr-KPFM approach utilizes biased surface-deposited electrodes in bias on and bias off-states to map surface potential as a function of space and time, thus gaining insight into the transport properties, screening, and electrochemical phenomena on Ca-substituted $BiFeO_3$ [206] and $LiNbO_3$ [207] surfaces. Further improvements in the time resolution may allow more insight to be gained on the role of adsorbed charge and injected charge on polarization switching and screening.

14.6 Summary and Outlook

The drive to image ferroelectric domains, given their suitability for data storage applications, has been instrumental in the development of voltage-modulated AFM approaches. Thus, EFM and KPFM approaches have been widely used to visualize ferroelectric domains and to elucidate screening mechanisms at ferroelectric surfaces and have been particularly informative when implemented after local bias-induced polarization reversal and during temperature-induced phase transitions. In addition, EFM and KPFM have been shown to be powerful tools when used together with other complementary AFM techniques. EFM and KPFM approaches for investigating ferroelectric surfaces and properties are expected to continue to be relevant. Going forward, they are likely to be implemented to better understand and exploit domain wall functionality in potential nanoelectronics applications [208, 209]. In addition, they can further our understanding of resistive and mechanical switching [151] and can be used in tandem with the recently established charge gradient microscopy technique [210].

Acknowledgments

This work was supported by Cost Action MP0904, Single- and multiphase ferroics and multiferroics with restricted geometries (SIMUFER), UCD Research, Science Foundation Ireland (Grant no. 10/RFP/MTR2855), European Commission within FP7, Marie Curie Initial Training Network "Nanomotion" (Grant agreement no. 290158), and NANOREMEDIES, which is funded under the Programme for Research in Third Level Institutions Cycle 5 and co-funded by the European Regional Development Fund.

References

(1) Mody, C.C.M. (2011) *Instrumental Community: Probe Microscopy and the Path to Nanotechnology*, The MIT Press, Cambridge.
(2) Tagantsev, A., Cross, L.E., and Fousek, J. (2010) *Domains in Ferroic Crystals and Thin Films*, Springer Science+Business Media LLC, New York.
(3) Matthias, B. and von Hippel, A. (1948) Domain structure and dielectric response of barium titanate single crystals. *Physical Review*, **73**, 1378–1384.
(4) Forsbergh, P.W. (1949) Domain structures and phase transitions in barium titanate. *Physical Review*, **76**, 1187–1201.
(5) von Hippel, A. (1950) Ferroelectricity, domain structure, and phase transitions of barium titanate. *Review of Modern Physics*, **22**, 221–237.
(6) Mitsui, T. and Furuichi, J. (1953) Domain structure of rochelle salt and KH_2PO_4. *Physical Review*, **90**, 193–202.
(7) Kanzig, W. (1957) Ferroelectrics and antiferroelectrics, *in Solid State Physics*, edited by F. Seitz and D. Turnbull, Academic Press, New York.
(8) Hooton, J.A. and Merz, W.J. (1955) Etch patterns and ferroelectric domains in $BaTiO_3$ single crystals. *Physical Review*, **98**, 409–413.
(9) Nassau, K., Levinstein, H.J., and Loiacono, G.M. (1965) The domain structure and etching of ferroelectric lithium niobate. *Applied Physics Letters*, **6**, 228–229.
(10) Nassau, K., Levinstein, H.J., and Loiacono, G.M. (1966) Ferroelectric lithium niobate. 1. Growth, domain structure, dislocations and etching. *Journal of Physics and Chemistry of Solids*, **27**, 983–988.
(11) Pfisterer, H., Fuchs, E., and Liesk, W. (1962) Elektronenmikroskopische Abbildung Ferroelektrischer Domänen in Dünnen $BaTiO_3$–Einkristallschichten. *Naturwiss*, **49**, 178–179.
(12) Blank, H. and Amelinckx, S. (1963) Direct observation of ferroelectric domains in barium titanate by means of the electron microscope. *Applied Physics Letters*, **2**, 140–142.

(13) Person, G.L. and Feldmann, W.L. (1959) Powder-pattern techniques for delineating ferroelectric domain structures. *Journal of Physics and Chemistry of Solids*, **9**, 28–30.

(14) Fousek, J., Safránková, M., and Kaczér, J. (1966) A new dew method for revealing ferroelectric domains. *Applied Physics Letters*, **8**, 192–194.

(15) Distler, G.I., Konstantinova, V.P., Gerasimov, Y.M., and Tolmacheva, G.A. (1968) Interaction of defect and domain structures of triglycine sulphate crystals in ferroelectric and paraelectric states. *Nature*, **218**, 762–765.

(16) Furuhata, Y. and Toriyama, K. (1973) New liquid–crystal method for revealing ferroelectric domains. *Applied Physics Letters*, **23**, 361–362.

(17) Dunn, S., Cullen, D., Abad-Garcia, E., et al. (2004), Using the surface spontaneous depolarization field of ferroelectrics to direct the assembly of virus particles. *Applied Physics Letters*, **85**, 3537–3539.

(18) Habicht, S., Nemanich, R.J., and Gruverman, A. (2008) Physical adsorption on ferroelectric surfaces: photoinduced and thermal effects. *Nanotechnology*, **19**, art. no. 495303.

(19) Grilli, S., Miccio, L., Vespini, V., et al. (2008) Liquid micro-lens array activated by selective electrowetting on lithium niobate substrates. *Optics Express*, **16**, 8084–8093.

(20) Ferraro, P., Grilli, S., Micco, L., and Vespini, V. (2008) Wettability patterning of lithium niobate substrate by modulating pyroelectric effect to form microarray of sessile droplets. *Applied Physics Letters*, **92**, art. no. 213107.

(21) Zhang, Z., Sharma, P., Borca, C.N., et al. (2010) Polarization-specific adsorption of organic molecules on ferroelectric $LiNbO_3$ surfaces. *Applied Physics Letters*, **97**, art. no. 243702.

(22) Zhang, Z., González, R., Díaz, G., et al. (2011) Polarization mediated chemistry on ferroelectric polymer surfaces. *Journal of Physical Chemistry C*, **115**, 13041–13046.

(23) Ehre, D., Lavert, E., Lahav, M., and Lubomirshy, I. (2010) Water freezes differently on positively and negatively charged surfaces of pyroelectric materials. *Science*, **327**, 672–675.

(24) Nakatani, N. (2011) Observation of ferroelectric domain structure in TGS. *Ferroelectrics*, **413**, 238–265.

(25) Binnig, G. and Rohrer, H. (1982) Scanning tunneling microscopy. *Helvetica Physica Acta*, **55**, 726–735.

(26) Binnig, G., Quate, C.F., and Gerber, Ch. (1986) Atomic force microscope. *Physical Review Letter*, **56**, 930–933.

(27) Thomas, T.R. (1999) *Rough Surfaces*, Imperial College Press, 2nd edition, London.

(28) Schnell, A. and Oepen, H. (1982) *Arrangement for Measuring Surface Profiles*, US Patent **4**,359,892.

(29) Schmaltz, G. (1929) Über Glätte und Ebenheit als Physikalisches und Physiologisches problem. *Zeitschrift des Vereins Deutscher Ingenieure*, **73**, 144–161.

(30) Meyer, G. and Amer, N.M. (1988) Novel optical approach to atomic force microscopy. *Applied Physics Letters*, **53**, 1045–1047.

(31) Amer, N.M. and Meyer, G. (1988) A simple optical method for the remote sensing of stylus deflection in atomic force microscopy. *Bulletin of the American Physical Society*. **33**, 319–323.

(32) Becker, H., Bender, O., Bergmann, L., et al. (1955) *Apparatus for Measuring Surface Irregularities*, US Patent **2**, 728, 222.

(33) Lee, D. and Harrison, R.G. (1979) *Measuring and Recording Surface Profile*, UK Patent 2009409-A.

(34) Young, R.D. (1966) Field emission ultramicrometer. *Review of Scientific Instruments*, **37**, 275–278.

(35) Young, R., Ward, J., and Scire, F. (1972) The Topografiner: an instrument for measuring surface microtopography. *Review of Scientific Instruments*, **43**, 999–1011.

(36) Kaczér, J. (1955) A new method for investigating the domain structure of ferromagnetics. *Czechoslovak Journal of Physics*, **5**, 239–244.

(37) Kaczér, J. and Gemperle, R. (1956) Vibrating permalloy probe for mapping magnetic fields. *Czechoslovak Journal of Physics*, **6**, 173–184.

(38) Martin, Y. and Wickramasinghe, H.K. (1987) Magnetic imaging by "force microscopy" with 1000 Å resolution. *Applied Physics Letters*, **50**, 1455–1457.

(39) Hartmann, U., Göddenhenrich, T., and Heiden, C. (1991) Magnetic force microscopy – current status and future-trends. *Journal of Magnetism and Magnetic Materials*, **101**, 263–270.

(40) Zavaliche, F., Zhao, T., Zheng, H., et al. (2007) Electrically assisted magnetic recording in multiferroic nanostructures. *Nano Letters*, **7**, 1586–1590.

(41) Martin, Y., Abraham, D.W., and Wickramasinghe, H.K. (1988) High-resolution capacitance measurement and potentiometry by force microscopy. *Applied Physics Letters*, **52**, 1103–1105.

(42) Stern, J.E., Terris, B.D., Mamin, H.J., and Rugar, D. (1988) Deposition and imaging of localized charge on insulator surfaces using a force microscope. *Applied Physics Letters*, **53**, 2717–1719.

(43) Terris, B.D., Stern, J.E., Rugar, D., and Mamin, H.J. (1989) Contact electrification using force microscopy. *Physical Review Letters*, **63**, 2669–2672.

(44) Saurenbach, F. and Terris, B.D. (1990) Imaging of ferroelectric domain walls by force microscopy. *Applied Physics Letters*, **56**, 1703–1705.

(45) Ahn, C.H., Tybell, T., Antognazza, L., et al. (1997) Nonvolatile electronic writing of epitaxial $Pb(Zr_{0.52}Ti_{0.48})O_3/SrRuO_3$ heterostructures. *Science*, **276**, 1100–1103.

(46) Tybell, T., Ahn, C.H., and Triscone, J.M. (1999) Ferroelectricity in thin perovskite films. *Applied Physics Letters*, **75**, 856–858.

(47) Birk, H., Glatz-Reichenbach, J., Jie, L., et al. (1991) The local piezoelectric activity of thin polymer films observed by scanning tunneling microscopy. *Journal of Vacuum Science and Technology B*, **9**, 1162–1165.

(48) Günther, P., Glatz-Reichenbach, J., and Dransfeld, K. (1991) Investigation of local piezoelectric properties of thin copolymer films. *Journal of Applied Physics*, **69**, 7895–7897.

(49) Güthner P. and Dransfeld, K. (1992) Local poling of ferroelectric polymers by scanning force microscopy. *Applied Physics Letters*, **61**, 1137–1139.

(50) Lüthi, R., Haefke, H., Meyer, K.P., et al. (1993) Surface and domain structures of ferroelectric crystals studied with scanning force microscopy. *Journal of Applied Physics*, **74**, 7461–7471.

(51) Bae, M.K., Horiuchi, T., Hara, K. et al. (1994) Direct observation of domain structures in triglycine sulfate by atomic force microscope. *Japanese Journal of Applied Physics*, **33**, 1390–1393.

(52) Hara, K., Bae, M.K., Okada, H., et al. (1995) AFM observations of TGS crystal surface in microscopic levels. *Ferroelectrics*, **170**, 101–109.

(53) Kolosov, O., Gruverman, A., Hatano, J., et al. (1995) Nanoscale visualization and control of ferroelectric domains by atomic force microscopy. *Physical Review Letters*, **74**, 4309–4312.

(54) Gruverman, A., Kolosov, O., Hatano, J., et al. (1995) Domain structure and polarization reversal in ferroelectrics studied by atomic force microscopy. *Journal of Vacuum Science and Technology B*, **13**, 1095–1099.

(55) Takata, K. (1996) Strain imaging of a Pb(Zr,Ti)O_3 thin film. *Journal of Applied Physics*, **79**, 134–142.

(56) Bluhm, H., Schwarz, U.D., Meyer, K.P., and Wiesendanger, R. (1995) Anisotropy of sliding friction on the triglycine sulfate (010) surface. *Applied Physics A – Materials Science and Processing*, **61**, 525–533.

(57) Eng, L.M., Friedrich, M., Fousek, J., and Günter, P. (1996) Scanning force microscopy of ferroelectric crystals. *Ferroelectrics*, **186**, 49–52.

(58) Correia, A., Massanell, J., García, N., et al. (1996) Friction force microscopy study of a cleaved ferroelectric surface: time and temperature dependence of the contrast, evidence of domain structure branching. *Applied Physics Letters*, **68**, 2796–2798.

(59) Franke, K., Besold, J., Haessler, W., and Seegebarth, C. (1994) Modification and detection of domains on ferroelectric PZT films by scanning force microscopy. *Surface Science Letters*, **302**, L283–L288.

(60) Hidaka, T., Maruyama, T., Saitoh, M., et al. (1996) Formation and observation of 50 nm polarized domains in $PbZr_{1-x}Ti_xO_3$ thin film using scanning probe microscope. *Applied Physics Letters*, **68**, 2358–2359.

(61) Gruverman, A., Auciello, O., and Tokumoto, H. (1996) Scanning force microscopy for the study of domain structure in ferroelectric thin films. *Journal of Vacuum Science and Technology B*, **14**, 602–605.

(62) Gruverman, A., Auciello, O., and Tokumoto, H. (1996) Nanoscale investigation of fatigue effects in Pb(Zr,Ti)O_3 films. *Applied Physics Letters*, **69**, 3191–3193.

(63) Hidaka, T., Maruyama, T., Sakai, I., et al. (1997) Characteristics of PZT thin films as ultra-high density recording media. *Integrated Ferroelectrics*, **17**, 319–327.

(64) Zavala, G., Fendler, J.H., and Trolier-McKinstry, S. (1997) Characterization of ferroelectric lead zirconate titanate films by scanning force microscopy. *Journal of Applied Physics*, **81**, 7480–7491.

(65) Tybell, T., Ahn, C.H., and Triscone, J.M. (1998) Control and imaging of ferroelectric domains over large areas with nanometer resolution in atomically smooth epitaxial $Pb(Zr_{0.2}Ti_{0.8})O_3$ thin films. *Applied Physics Letters*, **72**, 1454–1456.

(66) Auciello, O., Gruverman, A., Tokumoto, H., et al. (1998) Nanoscale scanning force imaging of polarization phenomena in ferroelectric thin films. *MRS Bulletin*, **23**, 33–42.

(67) Abplanalp, M., Eng, L.M., and Günter, P. (1998) Mapping the domain distribution at ferroelectric surfaces by scanning force microscopy. *Applied Physics A – Materials Science and Processing*, **66**, S231–S234.

(68) Eng, L.M., Abplanalp, M., and Günter, P. (1998) Ferroelectric domain switching in tri-glycine sulphate and barium titanate bulk single crystals by scanning force microscopy. *Applied Physics A – Materials Science and Processing*, **66**, S679–S683.

(69) Johnson, A.S., Nehl, C.L., Mason, M.G., and Hafner, J.H. (2003) Fluid electric force microscopy for charge density mapping in biological systems. *Langmuir*, **19**, 10007–10010.

(70) Yang, Y., Mayer, K.M., and Hafner, J.H. (2007) Quantitative membrane electrostatics with the atomic force microscope. *Biophysical Journal*, **92**, 1966–1974.

(71) Yang, Y., Mayer, K.M., Wickremasinghe, N.S., and Hafner, J.H. (2008) Probing the lipid membrane dipole potential by atomic force microscopy. *Biophysical Journal*, **95**, 5193–5199.

(72) Hong, J.W., Park, S.I., and Khim, Z.G. (1999) Measurement of hardness, surface potential, and charge distribution with dynamic contact mode electrostatic force microscope. *Review of Scientific Instruments*, **70**, 1735–1739.

(73) Labardi, M., Likodimos, V., and Allegrini, M. (2000) Force-microscopy contrast mechanism in ferroelectric domain imaging. *Physical Review B*, **61**, 14390–14398.

(74) Hong, J.W., Koh, K.H., Park, S.I., et al. (1998) Surface charge density and evolution of domain structure in triglycine sulfate determined by electrostatic-force microscopy. *Physical Review B*, **58**, 5078–5084.

(75) Likodimos, V., Labardi, M., and Allegrini, M. (2002) Domain pattern formation and kinetics on ferroelectric surfaces under thermal cycling using scanning force microscopy. *Physical Review B*, **66**, art. no. 024104.

(76) Luo, E.Z., Xie, Z., Xu, J.B., et al. (2000) In situ observation of the ferroelectric–paraelectric phase transition in a triglycine sulfate single crystal by variable-temperature electrostatic force microscopy. *Physical Review B*, **61**, 203–206.

(77) Likodimos, V., Orlik, X.K., Pardi, L., et al. (2000) Dynamical studies of the ferroelectric domain structure in triglycine sulfate by voltage-modulated scanning force microscopy. *Journal of Applied Physics*, **87**, 443–451.

(78) Likodimos, V., Labardi, M., and Allegrini, M. (2000) Kinetics of ferroelectric domains investigated by scanning force microscopy. *Physical Review B*, **61**, 14440–14447.

(79) Orlik, X.K., Likodimos, V., Pardi, L., et al. (2000) Scanning force microscopy study of the ferroelectric phase transition in triglycine sulfate. *Applied Physics Letters*, **76**, 1321–1323.

(80) Shin, S., Baek, J., Hong, J.W., and Khim, Z.G. (2004) Deterministic domain formation observed in ferroelectrics by electrostatic force microscopy. *Journal of Applied Physics*, **96**, 4372–4377.

(81) Likodimos, V., Labardi, M., Orlik, X.K., et al. (2001) Thermally activated ferroelectric domain growth due to random defects. *Physical Review B*, **63**, art. no. 064104.

(82) Hong, J.W., Kahng, D.S., Shin, J.C., et al. (1998) Detection and control of ferroelectric domains by an electrostatic force microscope. *Journal of Vacuum Science and Technology B*, **16**, 2942–2946.

(83) Jo, W., Kim, D.C., and Hong, J.W. (2000) Reverse-poling effects on charge retention in Pb(Zr, Ti)O_3(001)/LaNiO_3(001) heterostructures. *Applied Physics Letters*, **76**, 390–392.

(84) Desfeux, R., Da Costa, A., Flambard, A., et al. (2004) Effect of crystallographic orientation upon switching properties of PZT films measured by electrostatic force microscopy. *Applied Surface Science*, **228**, 34–39.

(85) Jo, W. (2005) Electrostatic force microscopy of as-grown (001)-oriented Pb(Zr, Ti)O_3 nanolayers. *Ultramicroscopy*, **105**, 299–304.

(86) Oh, Y.J., Lee, J.H., and Jo, W. (2005) Dynamics of space and polarization charges of ferroelectric thin films measured by atomic force microscopy. *Ultramicroscopy*, **106**, 779–784.

(87) Kim, T.Y., Lee, J.H., Oh, Y.J., et al. (2007) Charge retention behavior of preferentially oriented and textured $Bi_{3.25}La_{0.75}Ti_3O_{12}$ thin films by electrostatic force microscopy. *Applied Physics Letters*, **90**, art. no. 082901.

(88) Takata, K. (1996) Comment on "Domain structure and polarization reversal in ferroelectrics studied by atomic force microscopy". *Journal of Vacuum Science and Technology B*, **14**, 3393–3394.

(89) Morozovska, A., Eliseev, E., and Kalinin, S.V. (2010) Electromechanical probing of ionic currents in energy storage materials. *Applied Physics Letters*, **96**, art. no. 222906.

(90) Morozovska, A., Eliseev, E., Balke, N., and Kalinin, S.V. (2010) Local probing of ionic diffusion by electrochemical strain microscopy: spatial resolution and signal formation mechanisms. *Journal of Applied Physics*, **108**, art. no. 053712.

(91) Balke, N., Jesse, S., Morozovska, A.N., et al. (2010) Nanoscale mapping of ion diffusion in a lithium-ion battery cathode. *Nature Nanotechnology*, **5**, 749–754.

(92) Balke, N., Jesse, S., Kim, Y. et al. (2010) Real space mapping of Li-ion transport in amorphous Si anodes with nanometer resolution. *Nano Letters*, **10**, 3420–3425.

(93) Nonnenmacher, N., O'Boyle, M.P., and Wickramasinghe, H.K. (1991) Kelvin probe force microscopy. *Applied Physics Letters*, **58**, 2921–2923.

(94) Chen, X.Q., Yamada, H., Horiuchi, T., et al. (1999) Surface potential of ferroelectric thin films investigated by scanning probe microscopy. *Journal of Vacuum Science and Technology B*, **17**, 1930–1934.

(95) Chen, X.Q., Yamada, H., Horiuchi, T., and Matsushige, K. (1999) Investigation of surface potential of ferroelectric organic molecules by scanning probe microscopy. *Japanese Journal of Applied Physics*, **38**, 3932–3935.

(96) Kalinin, S.V. and Bonnell, D.A. (2000) Effect of phase transition on the surface potential of the $BaTiO_3$ (100) surface by variable temperature scanning surface potential microscopy. *Journal of Applied Physics*, **87**, 3950–3957.

(97) Kalinin, S.V. and Bonnell, D.A. (2001) Local potential and polarization screening on ferroelectric surfaces. *Physical Review B*, **63**, art. no. 125411.

(98) Kalinin, S.V. and Bonnell, D.A. (2001) Temperature dependence of polarization and charge dynamics on the $BaTiO_3$ (100) surface by scanning probe microscopy, *Applied Physics Letters*, **78**, 1116–1118.

(99) Fumagalli, L., Ferrer, D.E., Cuervo, A., et al. (2012) Label-free identification of single dielectric nanoparticles and viruses with ultraweak polarization forces. *Nature Materials*, **11**, 808–816.

(100) Rodriguez, B.J., Callahan, C., Kalinin, S.V., and Proksch, R. (2007) Dual-frequency resonance-tracking atomic force microscopy. *Nanotechnology*, **18**, art. no. 475504.

(101) Jesse, S., Kalinin, S.V., Proksch, R., et al. (2007) The band excitation method in scanning probe microscopy for rapid mapping of energy dissipation on the nanoscale. *Nanotechnology*, **18**, art. no. 435503.

(102) Guo, S., Kalinin, S.V., and Jesse, S. (2012) Open-loop band excitation Kelvin probe force microscopy. *Nanotechnology*, **23**, art. no. 125704.

(103) Guo, S., Kalinin, S.V., and Jesse, S. (2012) Half-harmonic Kelvin probe force microscopy with transfer function correction. *Applied Physics Letters*, **100**, art. no. 063118.

(104) Oliver, R.A. (2008) Advances in AFM for the electrical characterization of semiconductors. *Reports on Progress in Physics*, **71**, art. no. 076501.

(105) Kitamura, S. and Iwatsuki, M. (1998) High-resolution imaging of contact potential difference with ultrahigh vacuum noncontact atomic force microscope. *Applied Physics Letters*, **72**, 3154–3156.

(106) Loppacher, C., Zerweck, U., and Eng, L.M. (2004) Kelvin probe force microscopy of alkali chloride thin films on Au (111). *Nanotechnology*, **15**, S9–S13.

(107) Loppacher, C., Zerweck, U., Teich, S., et al. (2005) FM demodulated Kelvin probe force microscopy for surface photovoltage tracking. *Nanotechnology*, **16**, S1–S6.

(108) Glatzel, T., Lux-Steiner, M.Ch., Strassburg, E., et al. (2007) Principles of Kelvin probe force microscopy, in *Scanning Probe Microscopy: Electrical and Electromechanical Phenomena on the Nanoscale*, edited by S.V. Kalinin and A. Gruverman, vol. **1**, Springer Science and Business Media, New York.

(109) Sadewasser, S. and Glatzel, T. (eds) (2012) *Kelvin Probe Force Microscopy*, Springer Series in Surface Sciences vol. **48**, Springer Science + Business Media, New York.

(110) Baumgart, C., Helm, M., and Schmidt, H. (2009) Quantitative dopant profiling in semiconductors: a Kelvin probe force microscopy model. *Physical Review B*, **80**, art. no. 085305.

(111) Henning, A.K., Hochwitz, T., Slinkman, J., et al. (1995) Two-dimensional surface dopant profiling in silicon using scanning Kelvin probe microscopy. *Journal of Applied Physics*, **77**, 1888–1896.

(112) Xu, Q. and Hsu, J.W.P. (1999) Electrostatic force microscopy studies of surface defects on GaAs/Ge films. *Journal of Applied Physics*, **85**, 2465–2472.

(113) Shikler, R., Meoded, T., Fried, N., and Rosenwaks, Y. (1999) Potential imaging of operating light-emitting devices using Kelvin force microscopy. *Applied Physics Letters*, **74**, 2972–2974.

(114) Rodriguez, B.J., Yang, W.C., Nemanich, R.J., and Gruverman, A. (2005) Scanning probe investigation of surface charge and surface potential of GaN-based heterostructures. *Applied Physics Letters*, **86**, art. no. 112115.

(115) Vatel, O. and Tanimoto, M. (1995) Kelvin probe force microscopy for potential distribution measurement of semiconductor devices. *Journal of Applied Physics*, **77**, 2358–2362.

(116) Cunningham, S., Larkin, I.A., and Davis, J.H. (1998) Noncontact scanning probe microscope potentiometry of surface charge patches: origin and interpretation of time-dependent signals. *Applied Physics Letters*, **73**, 123–125.

(117) Glatzel, T., Fuertes Marron, D., Schedel-Niedrig, T., et al. (2002) $CuGaSe_2$ solar cell cross section studied by Kelvin probe force microscopy in ultrahigh vacuum. *Applied Physics Letters*, **81**, 2017–2019.

(118) Palermo, V., Palma, M., and Samorì, P. (2006) Electronic characterization of organic thin films by Kelvin probe force microscopy. *Advanced Materials*, **18**, 145–164.

(119) Sugimura, H., Hayashi, K., Saito, N., et al. (2002), Surface potential microscopy for organized molecular systems. *Applied Surface Science*, **188**, 403–410.

(120) Lü, J., Delamarche, E., Eng, L., et al. (1999) Kelvin probe force microscopy on surfaces: investigation of the surface potential of self-assembled monolayers on gold. *Langmuir*, **15**, 8184–8188.

(121) Fujihira, M. and Kawate, H. (1994) Structural study of Langmuir–Blodgett films by scanning surface potential microscopy. *Journal of Vacuum Science and Technology B*, **12**, 1604–1608.

(122) Chi, L.F., Jacobi, S., and Fuchs, H. (1996) Chemical identification of differing amphiphiles in mixed Langmuir–Blodgett films by scanning surface potential microscopy. *Thin Solid Films*, **284**, 403–407.

(123) Fujihira, M. (1999) Kelvin probe force microscopy of molecular surfaces. *Annual Review of Materials Science*, **29**, 353–380.

(124) Sinensky, A.K. and Belcher, A.M. (2007) Label-free and high-resolution protein/DNA nanoarray analysis using Kelvin probe force microscopy. *Nature Nanotechnology*, **2**, 653–659.

(125) Rodriguez, B.J. and Kalinin, S.V. (2012) KPFM and PFM of biological systems, in *Kelvin Probe Force Microscopy*, Springer Series in Surface Sciences vol. **48**, edited by S. Sadewasser and T. Glatzel, Springer Science + Business Media, New York.

(126) Coffey, D.C. and Ginger, D.S. (2006) Time-resolved electrostatic force microscopy of polymer solar cells. *Nature Materials*, **5**, 735–740.

(127) Kronik, L. and Shapira, Y. (2001) Surface photovoltage spectroscopy of semiconductor structures: at the crossroads of physics, chemistry and electrical engineering. *Surface and Interface Analysis*, **31**, 954–965.

(128) Chavez-Pirson, A., Vatel, O., Tanimoto, M., et al. (1995) Nanometer-scale imaging of potential profiles in optically excited n-i-p-i heterostructure using Kelvin probe force microscopy. *Applied Physics Letters*, **67**, 3069–3071.

(129) Lee, I., Lee, J.W., Stubna, A., and Greenbaum, E. (2000) Measurement of electrostatic potentials above oriented single photosynthetic reaction centers. *Journal of Physical Chemistry B*, **104**, 2439–2443.

(130) Frolov, L., Rosenwaks, Y., Carmeli, C., and Carmeli, I. (2005) Fabrication of a photoelectronic device by direct chemical binding of the photosynthetic reaction center protein to metal surfaces. *Advanced Materials*, **17**, 2434–2437.

(131) Kuritz, T., Lee, I., Owens, E.T., et al. (2005) Molecular photovoltaics and the photoactivation of mammalian cells. *IEEE Transactions on NanoBioscience*, **4**, 196–200.

(132) Knapp, H.F., Mesquida, P., and Stemmer, A. (2002) Imaging the surface potential of active purple membrane. *Surface and Interface Analysis*, **33**, 108–112.

(133) Lee, I., Greenbaum, E., Budy, S., et al. (2006) Photoinduced surface potential change of bacteriorhodopsin mutant D96N measured by scanning surface potential microscopy. *Journal of Physical Chemistry B*, **110**, 10982–10990.

(134) Kitamura, S., Suzuki, K., Iwatsuki, M., and Mooney, C.B. (2000) Atomic-scale variations in contact potential difference on Au/Si(111) 7×7 surface in ultrahigh vacuum. *Applied Surface Science*, **157**, 222–227.

(135) Okamoto, K., Yoshimoto, K., Sugawara, Y., and Morita, S. (2003) KPFM imaging of Si[(111)]_$(5\sqrt{3} \times 5\sqrt{3})$-Sb surface for atom distinction using NC-AFM. *Applied Surface Science*, **210**, 128–133.

(136) Enevoldsen, G.H., Glatzel, T., Christensen, M.C., et al. (2008) Atomic scale Kelvin probe force microscopy studies of the surface potential variations on the $TiO_2(110)$ surface. *Physical Review Letters*, **100**, art. no. 236104.

(137) Sadewasser, S., Jelinek, P., Fang, C.K., et al. (2009) New insights on atomic-resolution frequency-modulation Kelvin-probe force-microscopy imaging of semiconductors. *Physical Review Letters*, **103**, art. no. 266103.

(138) Mohn, F., Gross, L., and Meyer, G. (2012) Imaging the charge distribution within a single molecule. *Nature Nanotechnolog*y, **7**, 227–231.

(139) Li, X., Mamchik, A., and Chen, I.W. (2001) Stability of electrodeless ferroelectric domains near a ferroelectric/dielectric interface. *Applied Physics Letters*, **69**, 809–811.

(140) Seo, Y., Jhe, W., and Hwang, C.S. (2002) Electrostatic force microscopy using a quartz tuning fork. *Applied Physics Letters*, **80**, 4324–4326.

(141) Bdikin, I., Wojtaś, M., Kiselev, D., et al. (2012) Ferroelectric–paraelectric phase transition in triglycine sulphate via piezoresponse force microscopy. *Ferroelectrics*, **426**, 215–222.

(142) Hong, S., Woo, J., Shin, H., et al. (2001) Principle of ferroelectric domain imaging using atomic force microscope. *Journal of Applied Physics*, **89**, 1377–1386.

(143) Lehnen, P., Dec, J., and Kleemann, W. (2000) Ferroelectric domain structures of $PbTiO_3$ studied by scanning force microscopy. *Journal of Physics D: Applied Physics*, **33**, 1932–1936.

(144) Note that the image may in fact be a KPFM surface potential image, however, the domains that are visible in PFM are not visible in this image.

(145) Wang, L., Yu, J., Wang, Z., et al. (2008) In situ investigation of retention properties of polydomain ferroelectric thin films by multimode scanning force microscopy. *Integrated Ferroelectrics*, **98**, 26–34.

(146) Urban, J.J., Spanier, J.E., Ouyang, L., et al. (2003) Single-crystalline barium titanate nanowires. *Advanced Materials*, **15**, 423–426.

(147) Spanier, J.E., Kolpak, A.M., Urban, J.J., et al. (2006) Ferroelectric phase transitions in individual single-crystalline $BaTiO_3$ nanowires. *Nano Letters*, **6**, 735–739.

(148) Jungk, T., Hoffman, Á., and Soergel, E. (2006) Detection mechanism for ferroelectric domain boundaries with lateral force microscopy. *Applied Physics Letters*, **89**, art. no. 042901.

(149) Johann, F. and Soergel, E. (2009) Quantitative measurement of the surface charge density. *Applied Physics Letters*, **95**, art. no. 232906.

(150) Guyonnet, J., Béa, H., Guy, F., et al. (2009) Shear effects in lateral piezoresponse force microscopy at 180° ferroelectric domain walls. *Applied Physics Letters*, **95**, art. no. 132902.

(151) Lu, H., Kim, D.J., Bark, C.W., et al. (2012) Mechanically-induced resistive switching in ferroelectric tunnel junctions. *Nano Letters*, **12**, 6289–6292.

(152) Carville, N.C., Manzo, M., Damm, S., et al. (2012) Photoreduction of SERS-active metallic nanostructures on chemically-patterned ferroelectric crystals. *ACS Nano*, **6**, 7373–7380.

(153) Durkan, C., Welland, M.E., Chu, D.P., and Migliorato, P. (1999) Probing domains at the nanometer scale in piezoelectric thin films. *Physical Review B*, **60**, 16198–16204.

(154) Durkan, C., Chu, D.P., Migliorato, P., and Welland, M.E. (2000) Investigations into local piezoelectric properties by atomic force microscopy, *Applied Physics Letters*, **76**, 366–368.

(155) Kalinin, S.V., Johnson, C.Y., and Bonnell, D.A. (2002) Domain polarity and temperature induced potential inversion on the $BaTiO_3$ (100) surface. *Journal of Applied Physics*, **91**, 3816–3823.

(156) Kalinin, S.V. and Bonnell, D.A. (2004) Screening phenomena on oxide surfaces and its implications for local electrostatic and transport measurements. *Nano Letters*, **4**, 555–560.

(157) Kalinin, S.V. and Bonnell, D.A. (2004) Local electronic transport at grain boundaries in Nb-doped $SrTiO_3$. *Physical Review B*, **70**, art. no. 235304.

(158) Kalinin, S.V. and Bonnell, D.A. (2000) Surface potential at surface–interface junctions in $SrTiO_3$ bicrystals. *Physical Review B*, **62**, art. no. 10419.

(159) Shao, R., Nikiforov, M.P., and Bonnell, D.A. (2006) Photoinduced charge dynamics on $BaTiO_3$ (001) surface characterized by scanning probe microscopy. *Applied Physics Letters*, **89**, art. no. 112904.

(160) He, D.Y., Qiao, L.J., and Volinsky, A.A. (2011) Humidity effect on $BaTiO_3$ c-domain surface potential inversion induced by electric field. *Journal of Applied Physics*, **110**, art. no. 074104.

(161) He, D.Y., Qiao, L.J., Volinsky, A.A., et al. (2011) Electric field and surface charge effects on ferroelectric domain dynamics in $BaTiO_3$ single crystal. *Physical Review B*, **84**, art. no. 024101.

(162) Segura, J.J., Domingo, N., Fraxedas, J., and Verdaguer, A. (2013) Surface screening of written ferroelectric domains in ambient conditions. *Journal of Applied Physics*, **113**, art. no. 187213.

(163) Shen, J., Zeng, H., Wang, Z., et al. (2006) Study of asymmetric charge writing on $Pb(Zr,Ti)O_3$ thin films by Kelvin probe force microscopy. *Applied Surface Science*, **252**, 8018–8021.

(164) Heo, J. (2010) A study of the ferroelectric properties of $PbZr_{0.4}Ti_{0.6}O_3$ (PZT) grains using Kelvin force microscopy analysis. *Transactions on Electrical and Electronic Materials*, **11**, 275–278.

(165) Jang, D., Heo, J., Yi, I., and Chung, I. (2002) Ferroelectric properties of very thin $Pb(Zr_{0.4}Ti_{0.6})O_3$ film determined by Kelvin force microscope. *Japanese Journal of Applied Physics*, **41**, 6739–6742.

(166) Lee, K., Ham, H., Yi, I., and Chung, I. (2003) Study on the surface potential behavior of ultra thin PZT utilizing SPM (scanning probe microscope). *Integrated Ferroelectrics*, **53**, 431–441.

(167) Shvebelman, M.M., Agronin, A.G., Urenski, R.P., et al. (2002) Kelvin probe force microscopy of periodic ferroelectric domain structure in $KTiOPO_4$ crystals. *Nano Letters*, **2**, 455–458.

(168) Liu, X., Kitamura, K., and Terabe, K. (2006) Surface potential imaging of nanoscale $LiNbO_3$ domains investigated by electrostatic force microscopy. *Applied Physics Letters*, **89**, art. no. 132905.

(169) Zhukov, R.N., Bykov, A.S., Kiselev, S.A., et al. (2014) Piezoelectric properties and surface potential behavior in $LiNbO_3$ thin films grown by the radio frequency magnetron sputtering. *Journal of Alloys and Compounds*, **586**, S3336–S3338.

(170) Lau, K., Liu, Y., Li, Q., et al. (2013) Surface characterization of a ferroelectric single crystal by Kelvin probe force microscopy. *Journal of Surface Engineered Materials and Advanced Technology*, **3**, 190–194.

(171) Choi, H., Hong, J., and No, K. (2012) Local surface potential distribution and its relaxation in ferroelectric poly(vinylidenefluoride-co-trifluoroethylene) thin films. *Applied Physics Letters*, **101**, art. no. 042904.

(172) Son, J.Y., Bang, S.H., and Cho, J.H. (2003) Kelvin probe force microscopy study of $SrBi_2Ta_2O_9$ and $PbZr_{0.53}Ti_{0.47}O_3$ thin films for high-density nonvolatile storage devices. *Applied Physics Letters*, **82**, 3505–3507.

(173) Son, J.Y., Kyhm, K., and Cho, J.H. (2006) Surface charge retention and enhanced polarization effect on ferroelectric thin films. *Applied Physics Letters*, **89**, art. no. 092907.

(174) Son, J.Y., Kim, B.G., Kim, C.H., and Cho, J.H. (2004) Writing polarization bits on the multiferroic $BiMnO_3$ thin film using Kelvin probe force microscopy. *Applied Physics Letters*, **84**, 4971–4973.

(175) Zhang, Q., Kim, C.H., Jang, Y.H., et al. (2010) Multiferroic properties and surface potential behaviors in cobalt-doped $BiFeO_3$ film. *Applied Physics Letters*, **96**, art. no. 152901.

(176) Yan, F., Xing, G.Z., Islam, M., et al. (2012) Orientation-dependent surface potential behavior in Nb-doped $BiFeO_3$. *Applied Physics Letters*, **100**, art. no. 172901.

(177) Jang, Y.H., Kim, C.H., Seo, S.J., and Cho, J.H. (2013) Relaxation of ferroelectric domains in epitaxial $BiFeO_3$ thin films on vicinal $SrTiO_3$ substrate. *Thin Solid Films*, **548**, 52–57.

(178) Son, J.Y., Lee, G., and Shin, Y.H. (2009) Surface charge dynamics on ferroelectric $PbZr_{0.48}Ti_{0.52}O_3$ films responding to the switching bias of electric force microscope. *Applied Physics Letters*, **94**, art. no. 162902.

(179) Son, J.Y., Shin, Y.H., Ryu, S., et al. (2009) Dip-pen lithography of ferroelectric $PbTiO_3$ nanodots. *Journal of the American Chemical Society*, **131**, 14676–14678.

(180) Kim, Y., Hong, S., Kim, S.H., and No, K. (2006) Surface potential of ferroelectric domain investigated by Kelvin force microscopy. *Journal of Electroceramics*, **17**, 185–188.

(181) Kim, Y., Bühlmann, S., Kim, J., et al. (2007) Local surface potential distribution in oriented ferroelectric thin films. *Applied Physics Letters*, **91**, art. no. 052906.

(182) Kim, Y., Park, M., Bühlmann, S., et al. (2010) Effect of local surface potential distribution on its relaxation in polycrystalline ferroelectric films. *Journal of Applied Physics*, **107**, art. no. 054103.

(183) Kim, Y., Kim, J., Bühlmann, S., et al. (2008) Screen charge transfer by grounded tip on ferroelectric surfaces. *Physica Status Solidi*, **(RRL) 2**, 74–76.

(184) Kim, J., Kim, Y., No, K., et al. (2006) Surface potential relaxation of ferroelectric domain investigated by Kelvin probe force microscopy. *Integrated Ferroelectrics*, **85**, 25–30.

(185) Kim, Y., Bae, C., Ryu, K., et al. (2009) Origin of surface potential change during ferroelectric switching in epitaxial $PbTiO_3$ thin films studied by scanning force microscopy. *Applied Physics Letters*, **94**, art. no. 032907.

(186) Jacobs, H.O., Knapp, H.F., and Stemmer, A. (1998) Resolution and contrast in Kelvin probe force microscopy. *Review of Scientific Instruments*, **84**, 1168–1174.

(187) Mélin, T., Barbet, S., Diesinger, H., et al. (2011) Note: Quantitative (artefact-free) surface potential measurements using Kelvin force microscopy. *Review of Scientific Instruments*, **82**, art. no. 036101.

(188) Diesinger, H., Deresmes, D., and Mélin, T. (2012) Capacitive crosstalk in AM-mode KPFM, in *Kelvin Probe Force Microscopy*, Springer Series in Surface Sciences vol. **48**, edited by S. Sadewasser and T. Glatzel, Springer Science + Business Media, New York.

(189) Collins, L., Kilpatrick, J.I., Weber, S.A.L., et al. (2013) Open loop Kelvin probe force microscopy with single and multi-frequency excitation. *Nanotechnology*, **24**, art. no. 475702.

(190) Polak, L., de Man, S., and Wijngaarden, R.J. (2014) Note: Switching crosstalk on and off in Kelvin probe force microscopy. *Review of Scientific Instruments*, **85**, art. no. 046111.

(191) Li, Q., Liu, Y., Wang, D., et al. (2012) Switching spectroscopic measurement of surface potentials on ferroelectric surfaces via an open-loop Kelvin probe force microscopy method. *Applied Physics Letters*, **101**, art. no. 242906.

(192) Takeuchi, O., Ohrai, Y., Yoshida, S., and Shigekawa, H. (2007) Kelvin probe force microscopy without bias-voltage feedback. *Japanese Journal of Applied Physics*, **46**, 5626–5630.

(193) Kobayashi, N., Asakawa, H., and Fukuma, T. (2010) Nanoscale potential measurements in liquid by frequency modulation atomic force microscopy. *Review of Scientific Instruments*, **81**, art. no. 123705.

(194) Kobayashi, N., Asakawa, H., and Fukuma, T. (2011) Quantitative potential measurements of nanoparticles with different surface charges in liquid by open loop electric potential microscopy. *Journal of Applied Physics*, **110**, art. no. 044315.

(195) Collins, L., Kilpatrick, J.I., Bhaskaran, M., et al. (2012) Dual harmonic Kelvin probe force microscopy for surface potential measurements of ferroelectrics, in *2012 International Symposium on Applications of Ferroelectrics*, held jointly with *2012 European Conference on the Applications of Polar Dielectrics and 2012 International Symposium on Piezoresponse Force Microscopy and Nanoscale Phenomena in Polar Materials (ISAF/ECAPD/PFM)*, pp. 1–4.

(196) Collins, L., Kilpatrick, J.I., Vlassiouk, I.V., et al. (2014) Dual harmonic Kelvin probe force microscopy at the graphene–liquid interface. *Applied Physics Letters*, **104**, art. no. 133103.

(197) Jesse, S., Lee, H.N., and Kalinin, S.V. (2006) Quantitative mapping of switching behavior in piezoresponse force microscopy. *Review of Scientific Instruments*, **77**, art. no. 073702.

(198) Jesse, S., Baddorf, A.P., and Kalinin, S.V. (2006) Switching spectroscopy piezoresponse force microscopy of ferroelectric materials. *Applied Physics Letters*, **88**, art. no. 062908.

(199) Rodriguez, B.J., Jesse, S., Baddorf, A.P., et al. (2007) Spatially resolved mapping of ferroelectric switching behavior in self-assembled multiferroic nanostructures: strain, size, and interface effects. *Nanotechnology*, **18**, art. no. 405701.

(200) Rodriguez, B.J., Jesse, S., Kim, J., et al. (2008) Local probing of relaxation time distributions in ferroelectric polymer nanomesas: time-resolved piezoresponse force spectroscopy and spectroscopic imaging. *Applied Physics Letters*, **92**, art. no. 232903.

(201) Kalinin, S.V., Rodriguez, B.J., Jesse, S., et al. (2009) Spatial distribution of relaxation behavior on the surface of a ferroelectric relaxor in the ergodic phase. *Applied Physics Letters*, **95**, art. no. 142902.

(202) Ferris, R., Yellen, B., and Zauscher, S. (2012) Ferroelectric thin films in fluidic environments: a new interface for sensing and manipulation of matter. *Small*, **8**, 28–35.

(203) Ferris, R.J., Lin, S., Therezien, M., et al. (2013) Electric double layer formed by polarized ferroelectric thin films. *ACS Applied Materials and Interfaces*, **5**, 2610–2617.

(204) Domanski, A.L., Sengputa, E., Bley, K., et al. (2012) Kelvin probe force microscopy in nonpolar liquids. *Langmuir*, **28**, 13892–13899.

(205) Collins, L., Jesse, S., Kilpatrick, J.I., et al. (2014) Probing charge screening dynamics and electrochemical processes at the solid–liquid interface with electrochemical force microscopy. *Nature Communications*, **5**, art. no. 3871.

(206) Strelcov, E., Jesse, S., Huang, Y.L., et al. (2013) Space- and time-resolved mapping of ionic dynamic and electroresistive phenomena in lateral devices. *ACS Nano*, **7**, 6806–6815.

(207) Strelcov, E., Ievlev, A.V., Jesse, S., et al. (2014) Direct probing of charge injection and polarization-controlled ionic mobility on ferroelectric $LiNbO_3$ surfaces. *Advanced Materials*, **26**, 958–963.

(208) Catalan, G., Seidel, J., Ramesh, R., and Scott, J.F. (2012) Domain wall nanoelectronics. *Review of Modern Physics*, **84**, 119–156.

(209) Whyte, J.R., Scott, J.F., McQuaid, R.G.P., et al. (2014) Ferroelectric domain wall injection. *Advanced Materials*, **26**, 293–298.

(210) Hong, S., Tong, S., Park, W.I., et al. (2014) Charge gradient microscopy. *Proceedings of the National Academy of Sciences of the United States of America*, **111**, 6566–6569.

Part C

The third and last part of the book deals with nanoscale effects in ferroelectrics and multiferroics. It consist of twelve chapters organized in three sections, which successively address the effects of nanostructuring on the properties of bulk and thin-film materials, the emphasis put on differentiating size and extrinsic effects, and a number of novel nanoscale phenomena among the current hottest topics in research.

Nanoscale Effects: Bulk Properties

Effects of nanostructuring on the properties of bulk materials are reviewed in the first section. It consists of four chapters aimed at describing the grain size downscaling characteristics for selected ceramic ferroelectrics down to the nanoscale. Size-dependent phenomena are among the most topical properties in ferroelectrics from a fundamental point of view, which also limit their scalability in applications. Ferroelectric ceramics are basic materials in passive components as multilayer ceramic capacitors and piezoelectric devices like actuators or ultrasounds transducers, whose current trend of miniaturization imposes a continuous search for downscaling [1–3]. Therefore, finding how the functional properties are changing when reducing grain size down to a few tens of nanometers has become highly important. New methods of ceramic consolidation, like, for example, spark plasma sintering or combined sintering methods, in the last few years have allowed the production of ceramics with almost full density, while preserving the grain size to ultra-small values (below 10 nm in the case of $BaTiO_3$) [4]. This offered the possibility of investigating scale-dependent phenomena in pore-free ferro/piezoelectric nanoceramics. For such fine ceramics, the functional properties (dielectric, ferroelectric, piezoelectric, tunability, etc.) are strongly influenced by the large number of grain boundaries. Grain boundaries with differentiated properties have been shown to play a major role and mostly determine the functionality of the nanostructured materials, even though ferroelectric phases persist at sizes as small as ten nanometers. They can be theoretically described as low-permittivity non-ferroelectric components and their role introduces a high level of local field

---

Nanoscale Ferroelectrics and Multiferroics: Key Processing and Characterization Issues, and Nanoscale Effects, First Edition. Edited by Miguel Algueró, J. Marty Gregg, and Liliana Mitoseriu.
© 2016 John Wiley & Sons, Ltd. Published 2016 by John Wiley & Sons, Ltd.

inhomogenization, as it will be shown in Chapter 18. Overall, this section shows that ceramic nanostructuring of ferroelectrics and high-sensitivity piezoelectrics is feasible while maintaining functionality. Additionally, the nanostructuring can be used in some cases as an additional tool for tailoring low- and high-field electrical properties towards desired values by local field engineering.

Chapter 15, *Nanostructured Barium Titanate Ceramics: Intrinsic versus Extrinsic Size Effects*, presents an overview of the role of grain size and grain boundaries on the functional properties of barium titanate when reducing the ceramic grain size below 1 μm. The need for a higher volume capacitance in multilayer ceramic capacitor structures and tunable components imposes the investigation of properties in dense $BaTiO_3$ ceramic single layers with thickness below 1 μm (i.e. grain sizes below 100 nm) [5]. In the introduction, the general properties of $BaTiO_3$ are described, followed by a review of the main applications of $BaTiO_3$ ceramics, underlying the actual demands for passive components and the need to produce and investigate dense nanostructured ceramics with a grain size below 100 nm, as small as possible. Next, the general size-dependent properties observed in ferroelectrics are presented. All the reduction of crystallographic distortion towards the cubic state and of the spontaneous polarization, that of the Curie and Curie–Weiss temperatures, the depletion of the values of the physical constants, and broadening of the ferroelectric-to-paraelectric phase transitions, changes of the domain wall structure and domain walls dynamics, when reducing grain size are discussed. Besides, the theoretical approaches developed for describing size effects in ferroelectric structures at various length scales, as *ab initio*, mesoscale, and macroscale models, are reviewed.

The chapter also describes experimental observations from the literature concerning the size-dependent properties of $BaTiO_3$ with grain sizes firstly in the range of micrometers and then for nanostructured ceramics. Dense $BaTiO_3$ ceramics with grains below 100 nm and high density have been produced from ultra-fine powders in the last few years, using special densification methods down to 8 nm, which represents to date the finest $BaTiO_3$ ceramic almost fully densified (99.6% relative density) [6, 7]. The main scale-dependent properties as structural modifications, permittivity, and critical temperatures as well as high-field ferroelectric and tunability properties are shown for a broad range of nanostructured ceramics produced by various groups by using different sintering methods. In particular, the influence of the structure and properties of grain boundaries on the dielectric properties as an extrinsic effect is discussed.

Chapter 16, *The Effects of Ceramic Nanostructuring in High-Sensitivity Piezoelectrics*, provides a comprehensive description of the effects of ceramic nanostructuring in high-sensitivity piezoelectrics, namely ferroelectric perovskite oxide solid solutions at morphotropic phase boundaries like $Pb(Zr,Ti)O_3$, $BiScO_3$–$PbTiO_3$, $Pb(Zn_{1/3}Nb_{2/3})O_3$–$PbTiO_3$, $Pb(Mg_{1/3}Nb_{2/3})O_3$–$PbTiO_3$, $(Bi_{1/2}Na_{1/2})TiO_3$–$BaTiO_3$, $(Bi_{1/2}Na_{1/2})TiO_3$–$(Bi_{1/2}K_{1/2})TiO_3$, and $(K,Na)NbO_3$, which all show an enhanced piezoelectric response at their ferroelectric instability [8, 9]. The actual technological drive for ceramic nanostructuring in such high-sensitivity piezoelectrics is firstly presented. Applications such as multilayer ceramic actuators or piezoelectrics for novel applications like energy harvesters and magnetoelectric transduction, along with the integration of mechanical elements into microelectromechanical systems for miniaturized sensors and actuators, demand specific functional properties, which scale with the size decrease down to nanoscale [10, 11].

A current state of the art in the field of ferroelectrics for piezoelectric technologies, starting with the classical PZT solid solutions is presented. Furthermore, the general properties of other selected novel high-sensitivity piezoelectrics are shown, including: (i) the $BiScO_3$–$PbTiO_3$ system as a case study of high-temperature, high-sensitivity materials, (ii) $Pb(Zn_{1/3}Nb_{2/3})O_3$–$PbTiO_3$ and $Pb(Mg_{1/3}Nb_{2/3})O_3$–$PbTiO_3$ relaxor–ferroelectric solid solutions for high sensitivity and power, and (iii) lead-free solid solutions from the family $(Bi_{1/2}Na_{1/2})TiO_3$–$BaTiO_3$.

The nanostructuring effects on the properties of the mentioned piezoelectric systems are next described. The most noticeable effect of decreasing the grain size of a high-sensitivity piezoelectric ceramic down to nanoscale on its dielectric properties is a progressive broadening and depletion of the maximum in permittivity at the temperature of the ferroelectric transition, until its disappearance below a threshold size. For high-sensitivity piezoelectrics like $BiScO_3$–$PbTiO_3$ or $Pb(Zr,Ti)O_3$, no maximum in permittivity or in another property at a given grain size (as happens for $BaTiO_3$ around 1 μm) was reported, due to the different domain configurations formed in these systems. However, and similarly to $BaTiO_3$ this time, a gradual disappearance of ferroelectric switching and a reduction of ferroelectric loops is shown for $(1-x)$ $BiScO_3$–$xPbTiO_3$ ceramics with $x = 0.64$ when decreasing grain size down to 25 nm, at which ferroelectricity apparently vanishes. Ferroelectric switching is present in nanostructured materials with an average grain size of 80 and 60 nm that present single-domain grains and this behavior is explained as being related to the presence of the inversion superdomains. The piezoelectric coefficients slowly decrease in the submicrometer range and drop dramatically for grain sizes below 150 nm. The observed size effects are compared with ones reported in PZT materials with composition at the morphotropic phase boundary.

Further aspects related to the grain size against grain boundary interplay effects on the functional properties of such materials are discussed. The impedance spectroscopy technique allowed the impedance response of grain cores and boundaries to be discriminated in ceramics with various grain sizes. The results clearly have shown that the electrical response of the nanostructured materials is fully dominated by grain boundaries, as in the case of nanostructured $BaTiO_3$. Using values for the permittivity and conductivity of the grain bulk and boundary, a simulation of the electrical response of ceramic nanomaterials with an increasing fraction of grain boundaries was performed. As in experiments, a strong broadening and depletion of the dielectric anomaly, down to its disappearance, resulted from simulations as a grain boundary effect, while the temperature corresponding to the permittivity maximum does not change with the increase in volumetric fraction of boundaries, showing that the experimental shift observed in $BiScO_3$–$PbTiO_3$ ceramic materials is an intrinsic size effect.

Nanostructuring effects in perovskite systems with intrinsic chemical inhomogeneity such as relaxor–ferroelectric $Pb(Mg_{1/3}Nb_{2/3})O_3$–$xPbTiO_3$ materials with composition in the morphotropic phase boundary are separately described in the chapter. Phase coexistence is influenced by grain size and an evolution from micrometer-sized lamellar domains towards submicrometer/nanometer-sized crosshatched domains (considered to be intermediate states between the relaxor and ferroelectric ones) was found. This was interpreted in the literature as due to the fact that size effects were the consequence of the slowing down of the relaxor to ferroelectric transition up to the final stabilization of the relaxor state at room temperature, when size decreases down to the submicrometer range, unlike in materials with conventional ferroelectric transitions like $Pb(Zr, Ti)O_3$ and $BiScO_3–PbTiO_3$. Summary and future perspectives are presented at the end of the chapter.

Chapter 17, *Correlation between Microstructure and Electrical Properties of Ferroelectric Relaxors*, starts with an introductory part in which the general properties of relaxors, together with the main theoretical approaches, the microscopic origin of polar nanoregions, and the empirical behavior of relaxors compared with classical ferroelectrics and spin glasses, are presented. Also, grain size-dependent phenomena of a few types of relaxors are reviewed as case studies.

First of all, the broadband dielectric properties of nanosized $Pb(Mg_{1/3}Nb_{2/3})O_3$ powders (particle size in the range from 15 nm to 1 μm) and nanostructured ceramics (50–115 nm) are discussed. To find out the influence of the mean grain size on the properties of $Pb(Mg_{1/3}Nb_{2/3})O_3$ powders, the temperature of the maximum dielectric permittivity and the values of the freezing temperature as determined from Vogel–Fulcher analysis versus particle size were determined. Similar to other ferroelectrics, permittivity values in nanoceramics reduce when diminishing grain size down to 15 nm, while the maximum permittivity and frequency relaxation remains similar as in coarse ceramics. The Vogel–Fulcher law describes the temperature evolution of dynamic properties of the materials (both in ceramic and powder form) related to their polar nanoregions. However, the dielectric properties of the finest powder (particle size of 15 nm) are rather unusual compared to the coarse ones and of ceramics, that is two weak relaxation processes are present, unlike in coarser-grained powders, where only one process was found in the dielectric spectra.

The chapter also describes size effects on the broadband dielectric properties of another classical relaxor, $PbSc_{1/2}Nb_{1/2}O_3$ [12], with various grain sizes down to 20 nm. At such small grain sizes, the maximum permittivity versus temperature is completely suppressed, which was explained as determined by the existence of grain boundaries, which limit the percolation of polar nanoregions. Only a low-frequency process assigned to flipping of polar nanoregions is influenced by the grain size reduction, while high-frequency processes were mostly unaffected. A core–shell structure is suitable to qualitatively explain the diminution of the dielectric anomaly. However, hypotheses concerning the modifications of bulk properties by grain size are needed for quantitative explanations concerning the reduction of the dielectric constant and shifts of the characteristic temperatures; in such mechanisms the polar nanoregions are playing an important role.

Lead-free Aurivillius relaxor ferroelectrics described by the formula $(Bi_2O_2)^{2+}$ $(A_{m-1}B_mO_{3m+1})^{2-}$ in which the relaxor character is attributed to the structural disorder, which is either intrinsic or introduced by doping, are finally addressed. The electrical properties of this type of compound are strongly anisotropic, with the maximum value of conductivity and the major component of spontaneous polarization parallel to the $(Bi_2O_2)^{2+}$ layers [13]. In those compounds the bismuth layer is acting as an insulator against charge transport. There have been limited reports about the grain size effect on dielectric and relaxor properties of the Aurivillius type of ceramics. Unlike in the case of $BaTiO_3$, some non-monotoneous trends of material property versus grain size were reported. The authors discuss the role of grain size on the electrical properties of $BaBi_4Ti_4O_{15}$ ceramics obtained by two different processing methods: the conventional solid-state method and the mechanochemically supported solid-state method, for which an increase of permittivity and of polarization was observed for a larger average grain size. The role of various dopant additions on the dielectric relaxation properties and conductivity of $BaBi_4Ti_4O_{15}$ ceramics is also discussed.

Chapter 18, *Local Field Engineering for Tuning Dielectric and Ferroelectric Properties in Nanostructured Ferroelectrics and Composites*, presents a numerical modeling approach based on finite element modeling for the tailoring of the electrical properties in composites via local field engineering controlled by microstructure. The main idea of this approach is based on the fact that in a real ceramic material the field acting locally may be very different to that in pure homogeneous systems [14]. Due to the presence of grain boundaries with different properties as compared with the ceramic bulk, due to the porosity, and interfaces between dissimilar phases in composites or interfaces between ferroelectric and electrodes, the field line suffers from fringes as described by the electrical boundary conditions and can be diluted or concentrated in some areas. This may help in reducing or enhancing some properties for specific microstructures. Based on this idea, the authors proposed the concept of local field engineering, which consists in designing composite materials (e.g. dielectric–ferroelectric, ferroelectric–ferroelectric, dielectric–metallic particles, etc.) with well-controlled microstructures to tailor local field distribution in order to reach desired properties.

The introductory part describes the general properties of ferroelectrics and mostly the non-linear dielectric character (tunability) and P(E) ferroelectric switching, and explains the origin of field inhomogeneity in real ferroelectric ceramics. Then the finite element method is described and its implementation to calculate local fields, permittivity, polarization, and tunability in systems with inhomogeneous structures presented.

The role of local field inhomogeneity on the tunability properties is described for a few main types of composite systems: (i) nanostructured ferroelectric ceramics in which a low-permittivity non-ferroelectric grain boundary and ferroelectric non-linear grain core with high permittivity were considered; in this case, the decreasing permittivity with reducing grain size and linearization of tunability versus field as in experimental reports were tracked down as a result of the simulations; (ii) porous ferroelectrics (composites formed by ferroelectric matrix and air pores), for which it is demonstrated that some configurations are advantageous for reducing permittivity and increasing tunability due to the concentration of field lines in some ferroelectric regions; (iii) composites with non-linear dielectric matrix and conductive inclusions, for which an enhancement of both permittivity and tunability can be reached by local field concentrations.

Next the chapter describes a way to consider the field inhomogeneity in real ferroelectric systems by combining two models: finite element calculations for field distributions and the Preisach model for switching. The classical Preisach model is firstly described and then simulations of P(E) responses for homogeneous systems are presented. Then the field distributions as computed by finite element methods in realistic microstructures were introduced in the Preisach model and the P(E) responses were simulated for nanostructured ferroelectrics (simulating the grain size dependence of the switching characteristics) and porous ferroelectrics (simulating the role of porosity on the P(E) response). The conclusion of this study is that local field inhomogeneity plays a crucial role in the macroscopic properties of ferroelectric composites. If properly used, the inhomogeneity of the local electric field can be used as an important factor to tailor the macroscopic response towards desired properties, which can be done by using modeling tools.

Nanoscale Effects: Thin-Film Properties

The effects of nanostructuring on the properties of thin-film materials are reviewed in a second section that consists of three chapters. Epitaxial ultra-thin films play a major role in the section. These model systems are ideal ones to study a number of distinctive film effects that are uncovered when thickness is decreased down to the nanoscale, not only as a result of size effects but also associated with the specific mechanical and electrical boundary conditions imposed by the substrate on to which films are grown, and by the characteristics of the conducting oxide layers chosen to fabricate a capacitor epitaxial heterostructure and enable electrical addressability.

Indeed, the presence of a substrate imposes a well-defined biaxial strain in the film plane (see Chapter 19 for further explanation), whose tailoring (by substrate choice and deposition control) not only allows properties but also phases to be tuned, which is the basis of strain engineering [15]. Examples are the preparation of fully strained (compressive: –1.7%) 50 nm thick, $BaTiO_3$ films on $SrRuO_3/DyScO_3$ substrates with a Curie temperature of 953 K, and of analogous but partially relaxed (–1.3%) 200 nm films with a remnant polarization of 70 $\mu C\ cm^{-2}$ (to be compared with values of 493 K and 26 $\mu C\ cm^{-2}$ for single crystals) [16]. Epitaxial strain has also been shown to turn incipient ferroelectrics like $SrTiO_3$ into a conventional ferroelectric with the transition temperature above room temperature, whose spontaneous polarization can be placed either in the film plane, for partially relaxed (tensile: 0.8%) 50 nm films on $DyScO_3$ substrates [17], or perpendicular to the film plane, for fully strained (compressive: –1.7%) 2.4 nm thick $SrTiO_3$ films on Si [18]. Additional examples are the strain engineering of a ferroelectric morphotropic phase boundary in otherwise rhombohedral $BiFeO_3$, which results in an enhanced electromechanical response [19], and of coexisting ferroelectricity and ferromagnetism in otherwise incipient ferroelectric antiferromagnetic $EuTiO_3$ [20].

Electrical boundary conditions are determined by the oxide layers selected for electrodes, and specifically by their ability to screen the surface bound charges associated with the spontaneous polarization and thus to compensate the depolarization field with a direct effect on the stability field of the ferroelectric state. First principle calculations for short-circuited $SrRuO_3/BaTiO_3/SrRuO_3/SrTiO_3$ heterostructures have shown the existence of a critical thickness of 2.4 nm (six unit cells), below which ferroelectricity vanishes when the finite electronic screening length of the electrodes is taken into account [21].

Though not actual size effects, both previous boundary condition effects are nanostructuring ones in the sense that they are only significant when thickness is decreased down to the nanoscale. Epitaxial strain relaxes through the formation of misfit dislocations (or of ferroelastic/ferroelectric domains, a mechanism specific to these materials) above a critical thickness that usually is of a few tens of nanometers (see again Chapter 19), and the depolarization field directly scales with the reciprocal thickness. Note that the depolarization field can be alternatively minimized by formation of ferroelectric inversion domains, like those described for $PbTiO_3$ films as thin as 1.2 nm (three unit cells) on $SrTiO_3$ substrates [22]. These domains have to be formed against the flexoelectric bias electric field associated with the strain gradient, which effectively couples both effects [23].

The experimental study of these nanostructuring effects in film form, and specifically of the disappearance or appearance and change of order or shift of a ferroelectric transition, is challenging, for epitaxial strain also causes lattice distortions in the paraelectric phase; for instance, cubic $BaTiO_3$ turns into tetragonal and thus a non-polar tetragonal to polar tetragonal ferroelectric phase transition takes place. This hinders its study by conventional diffraction techniques (though a careful analysis of the temperature dependence of the out-of-plane cell parameter must reveal the development of ferroelectric order). Advanced TEM techniques can resolve the relative ion displacements and thus the actual electric dipoles at the unit cell level (see Chapter 10). However, temperature-dependent studies to characterize phase transitions are complex and time consuming, and are not usually addressed. The best alternative then is to carry out temperature-dependent electric measurements searching the dielectric anomalies associated with the transition. This is the topic of Chapter 19, *Ferroelectric Phase Transitions in Epitaxial Perovskite Films*.

The chapter starts by providing the phenomenological background for the study of ferroelectric phase transitions from the temperature dependence of the dielectric permittivity, differentiating it from that shown by relaxor materials (see Chapters 17 and 23 for in-depth descriptions of this latter phenomenon characterized by short-ranged instead of long-ranged polar order). Following this, the specific issues involved in the dielectric characterization of thin-film heteroepitaxial capacitors, resulting from the decrease of the film ohmic resistence with thickness (and from the non-negligible resistivity of the oxide electrodes), are presented and discussed in detail. The difficulties in obtaining the actual permittivity of the film are highlighted and procedures to estimate its value are critically reviewed.

The concept of a *dead layer* is introduced. Even when a sound permittivity value can be obtained for the thin-film capacitor, this is usually not the film value, but it is underestimated by the presence of an interfacial capacitance in series with the ferroelectric layer. The origin of this capacitance has been highly controversial and is related to the presence of a thin low-permittivity, non-ferroelectric layer located at the film–electrode interface, either extrinsic (associated with the local strain state or defect configuration that are strongly preparation dependent) or intrinsic, and widely known as the dead layer. Indeed, first principle calculations have shown that ferroelectricity is intrinsically modified at the metal–ferroelectric interface linked to the bonding characteristics, and that can be either depleted, like for $SrRuO_3/ATiO_3$ (A = Pb, Ba, Sr) and $Pt/PbTiO_3$, or enhanced, like for $Pt/BaTiO_3$ and $Au/BaTiO_3$ [24], as later confirmed by experiments [25].

The chapter ends by proposing a methodology that involves the combined analysis of the temperature dependences of the derivative of the reciprocal permittivity and of the refraction index for the identification and study of ferroelectric phase transitions and relaxor states in films. This is illustrated with a number of examples that reveal (by the only means of analyzing the electrical and optical properties) different thin-film effects for conventional and incipient ferroelectrics and for relaxor systems: the shift of the ferroelectric transition towards higher temperatures (and its transformation from first to second order) for $Pb_{0.5}Sr_{0.5}TiO_3/La_{0.5}Sr_{0.5}CoO_3/MgO$ and $BaTiO_3/SrRuO_3/SrTiO_3$ epitaxial heterostructures, the generation of a ferroelectric phase and the role of the depolarization field for $KTaO_3/SrTiO_3$:Nb, and the hindrance of the relaxor to ferroelectric transition for $PbSc_{0.5}Nb_{0.5}O_3/La_{0.5}Sr_{0.5}CoO_3/MgO$.

The appearance of an interfacial capacitance is only one among the many effects that the film–electrode interface has on the macroscopic electrical response of thin-film heteroepitaxial capacitors, which can determine not only capacitance but also leakage current, ferroelectric switching, and coupling responses, such as the pyroelectric and photovoltaic ones. This is the main topic of Chapter 20, *Interfaces in Epitaxial Ferroelectric Layers/Multilayers and Their Effect on the Macroscopic Electrical Properties*, which provides a thorough revision of work carried out on this topic, mainly focused on

$Pb(Zr,Ti)O_3/SrRuO_3$- and BaTi $O_3/SrRuO_3$-based capacitors with a range of metallic top electrodes. Discussion is supported with spectroscopic and microscopic studies on the specific nature of the interfaces.

The chapter is not limited to a discussion of the film–electrode interface, but also addresses the role of other interfaces present in highly topical heteroepitaxial systems. This is the case of the ferroelectric–semiconductor interface, exemplified by the $Pb(Zr,Ti)O_3/ZnO$ system, in ferroelectric metal–insulator–semiconductor heterostructures for ferroelectric field effect transistors (FE-FET). This device has the potential to enable non-destructive readings in ferroelectric memories, though poor retention, directly associated with depolarization fields and the interface electronic characteristics, has slowed down progress [26]. Other interface phenomena discussed herein are capacitance enhancement in ferroelectric heterostructures, such as ferroelectric–antiferroelectric $Pb(Zr,Ti)O_3$-based superlattices or $Pb(Zr,Ti)O_3$–$BiFeO_3$ multilayers, which also show ferromagnetism, or magnetocapacitance in $BaTiO_3/(La,Sr)MnO_3$ ones. Interface magnetoelectric effects is a topic that concentrates increasing interest [27, 28].

Although not an interface effect, a significant direct magnetoelectric effect (the development of a linear polarization in response to a magnetic field) has been reported for oxide epitaxial heterostructures consisting of ferroelectric and magnetic layers, as a result of the elastic interaction between the ferroic layers [29]. These thin-film multiferroic nanostructures are epitaxial columnar heterostructures of perovskite and spinel oxides, for which magnetoelectric coupling is obtained as a product property of the piezoelectricity and magnetostriction of the components [30].

Electric-field control of magnetism and thus also the converse magnetoelectric effect (the development of a magnetization in response to an electric field) can also be obtained in multiferroic heterostructures, this time via inverse magnetostriction, by generation of a magnetoelastic anisotropy in a ferromagnetic layer under the piezoelectric strains induced in the underlying ferroelectric substrate. This is a reversible (and thus volatile) but limited effect, yet much higher irreversible (remnant) effects can be obtained if ferroelectric/ferroelastic domain reorientation phenomena, and the associated non-linear strains, are used instead. This is the topic of Chapter 21, *Electric-Field Control of Magnetism Based on Elastically Coupled Ferromagnetic and Ferroelastic Domains*, which closes the section. It shows by means of a number of examples how ferromagnetic and ferroelectric domains in multiferroic heterostructures can couple via elastic interactions, until fully correlated domain configurations (the term domain patter transfer is used) are obtained. Physical origins, domain wall pinning by the magnetoelastic anisotropy gradients induced by the ferroelectric/ferroelastic domains, the phenomenon scaling properties, and the resulting distinctive magnetic dynamics are discussed. Finally, the electric-field control of magnetic domains, which is how they can be electrically written and erased, and the reversible movement of magnetic domain walls under electric fields, are illustrated.

Nanoscale Effects: Novel Phenomena and Applications

Novel phenomena and applications are addressed in the third and final section that closes the book. The topics of discussion are diverse. Chapter 22 presents both theoretical and experimental information on novel dipole ordering, with an emphasis on discussions relating to vortex states in ferroelectrics [31]. In the first half of the chapter, the approaches that have been used to model the evolution of dipole configurations in nanoscale ferroelectrics are presented in some detail, from effective Hamiltonian to shell models. The predicted appearance of vortex dipole patterns is presented and the use of the toroidal moment as a useful order parameter for mapping the development of vortex states is discussed. The hope and expectation that dipole vortices should be discovered in reality is then assessed in the second half of the chapter, where a sanguine review of experimental evidence is given. The key issue of generating a simple but accurate definition of what constitutes a vortex state is discussed at some length and the overall view is that although several aspects of dipole ordering needed in order for vortex states to develop have been seen, such as continuous rotation of dipoles under high-resolution transmission electron microscopy TEM [32] and flux-closure states [33], no true vortices have yet been observed.

In Chapter 23, the phenomenon of reentrant phase transition behavior is discussed and its manifestation in relaxor electroceramic systems critically evaluated. The unusual sequence of phase transitions (which is relatively rare) in which an initially disordered state develops order on cooling, only for order to be lost again at lower temperatures, is considered thermodynamically and examples of where it can be seen in magnetic spin glass systems considered. Some of the current understanding in the physics of relaxor electroceramics is then presented before the discussion goes further to suggest that reentrant phase transition phenomena can be seen in ferroelectric relaxors. Both perovskite and tungsten bronze systems are discussed.

Chapter 24 focuses on the highly topical subject of functionally active domain walls (or twin walls) in ferroics. A number of examples, both in theory and in experiment are discussed in which the properties of the domain walls are completely different from the domains that they encapsulate. Polar ordering and the emergence of ferrielectricity in ferroelastic walls in $CaTiO_3$ are categorically demonstrated [34]. The expectation of similar dipole ordering in $SrTiO_3$ domain walls is also shown, with the added expectation that the orientation of the dipoles in these walls should be switchable. In other words, 2D ferroelectricity should exist. The specific role of twin walls as conductors [35] and superconductors [36], phonon scattering entities, and havens for the emergence of suppressed functionality through “breather” states is then considered. This is surely one of the most intriguing aspects in the modern study of ferroelectrics and multiferroics.

In Chapter 25, a comprehensive overview of the recent claims of single-phase room temperature multiferroics is given. While systems such as $Pb(Zr, Ti, Fe, Ta)O_3$ are discussed [37], the main thrust of the chapter is a consideration of the evidence for room temperature multiferroic behavior and coupling in various Aurivillius phase ceramics [38].

Chapter 26 presents an elegant summary of how photoexcitation in non-centrosymmetric materials can lead to the development of a potential difference and hence, under short-circuit conditions, a photocurrent. The way in which broken symmetry causes unequal probabilities of photoelectron excitation to positive and negative wavevectors is clearly and simply explained. The specific role of ferroelectrics as a subgroup of non-centrosymmetric materials is then discussed, with particular emphasis on $BiFeO_3$ [39]; other important ferroelectric photovoltaic groups, such as the niobates, are also acknowledged and discussed. Finally, the role of electrode–ferroelectric heterointerfaces and domain wall homointerfaces are considered. Given the great potential of ferroelectric photovoltaics in future technology, this chapter is a fitting way to end the book.

References

(1) Setter, N. and Waser, R. (2000) Electroceramic materials. *Acta Materialia* **48**, 151–178.

(2) Ho, J., Jow, T.R., and Boggs, S. (2010) Historical introduction to capacitor technology. *IEEE Electrical Insulation Magazine*, **26**, 20–25.

(3) Gong, H., Wang, X., Zhang, S., et al. (2014) Grain size effect on electrical and reliability characteristics of modified fine-grained $BaTiO_3$ ceramics for MLCCs. *Journal of the European Ceramic Society*, **34**, 1733–1739.

(4) Ragulya, A.V., Skorokhod, V.V., and Polotai, A.V. (2001) Synthesis and sintering of nanocrystalline $BaTiO_3$ powder under non-isothermal conditions. Structure, grain boundaries and dielectric properties obtained by various sintering methods. *Powder Metallurgy and Metal Ceramics*, **40**, 25–33.

(5) Buscaglia, M.T., Viviani, M., Buscaglia, V., et al. (2006) High dielectric constant and frozen macroscopic polarization in dense nanocrystalline $BaTiO_3$ ceramics. *Physical Review B*, **73**, art. no. 064114.

(6) Deng, X., Wang, X., Wen, H., et al. (2006) Phase transitions in nanocrystalline barium titanate ceramics prepared by spark plasma sintering. *Journal of the American Ceramic Society*, **89**, 1059–1064.

(7) Deng, X.Y., Li, D.J., Li, J.B., et al. (2009) Preparation of nanocrystalline $BaTiO_3$ ceramics. *Science China Serie E – Technological Sciences*, **52**, 1730–1734.

(8) Damjanovic, D. (2009) Comments on origins of enhanced piezoelectric properties in ferroelectrics. *IEEE Transactions on Ultrasonics, Ferroelectrics and Frequency Control*, **56** 1574–1585.

(9) Saito, Y., Takao, H., Tani, T., et al. (2004) Lead-free piezoceramics, *Nature*, **432**, 84–87.

(10) Zou, T., Wang, X., Zhao, W., and Liu, L. (2008) Preparation and properties of fine-grain $(1-x)BiScO_3$–$xPbTiO_3$ ceramics by two-step sintering. *Journal of the American Ceramics Society*, **91**, 121–126.

(11) Hungría, T., Amorín, H., Algueró, M., and Castro, A. (2011) Nanostructured ceramics of $BiScO_3$–$PbTiO_3$ with tailored grain size by spark plasma sintering. *Scripta Materialia*, **64**, 97–100.

(12) Ivanov, M., Banys, J., Bogicevic, C., and Kiat, J.M. (2012) Size effects on dielectric properties of nanograin PSN ceramics. *Ferroelectrics*, **429** (1), 43–47.

(13) Kennedy, B.J., Zhou, Q., Ismunandar, et al. (2008) Cation disorder and phase transitions in the four-layer ferroelectric Aurivillius phases $ABi_4Ti_4O_{15}$ (A = Ca, Sr, Ba, Pb). *Journal of Solid State Chemistry*, **181** (6), 1377–1386.

(14) Padurariu, L., Curecheriu, L., Buscaglia, V., and Mitoseriu, L. (2012) Field-dependent permittivity in nanostructured $BaTiO_3$ ceramics: modeling and experimental verification. *Physical Review B*, **85** (22), art. no. 224111.

(15) Schlom, D.G., Chen, L.Q., Eom, C.B., et al. (2007) Strain tuning of ferroelectric thin films. *Annual Review of Materials Research*, **37**, 589–626.

(16) Choi, K.J., Biegalski, M., Li, Y.L., et al. (2004) Enhancement of ferroelectricity in strained $BaTiO_3$ thin films. *Science*, **306**, 1005–1009.

(17) Haeni, J.H., Irvin, P. Chang, W., et al. (2004) Room temperature ferroelectricity in strained $SrTiO_3$. *Nature*, **430**, 758–761.

(18) Warusawithana, M.P., Cen, C., Sleasman, C.R., et al. (2009) A ferroelectric oxide made directly on silicon. *Science*, **324**, 367–370.

(19) Zeches, R.J., Rossell, M.D., Zhang, J.X., et al. (2009) A strain-driven morphotropic phase boundary in $BiFeO_3$. *Science*, **326**, 977–980.

(20) Lee, J.H., Fang, L., Vlahos, E., et al. (2010) A strong ferroelectric ferromagnet created by means of spin-lattice coupling. *Nature*, **466**, 954–959.

(21) Junquera, J. and Ghosez, P. (2003) Critical thickness for ferroelectricity in perovskite ultrathin films. *Nature*, **422**, 506–509.

(22) Fong, D.D., Stephenson, G.B., Streiffer, S.K., et al. (2004) Ferroelectricity in ultrathin perovskite films. *Science*, **304**, 1650–1653.

(23) Zubko, P., Catalan, G. and Tagantsev, A.K. (2013) Flexoelectric effect in solids. *Annual Review of Materials Research*, **43**, 387–421.

(24) Stengel, M., Vanderbilt, D., and Spaldin, N.A. (2009) Enhancement of ferroelectricity at metal-oxide interfaces. *Nature Materials*, **8**, 392–397.

(25) Chang, L.W., Alexe, M., Scott, J.F., and Gregg, J.M. (2009) Settling the "dead layer" debate in nanoscale capacitors. *Advanced Materials*, **21**, 4911–4914.

(26) Baldia, L., Beza, R., and Sandhub, G. (2014) Emerging memories. *Solid-State Electronics*, **102**, 2–11.

(27) Rondinelli, J.M., Stengel, M., and Spaldin, N.A. (2008) Carrier-mediated magnetoelectricity in complex oxide heterostructures. *Nature Nanotechnology*, **3**, 46–50.

(28) Valencia, S., Crassous, A., Bocher, L., et al. (2011) Interface-induced room-temperature multiferroicity in $BaTiO_3$. *Nature Materials*, **10**, 753–758.

(29) Oh, Y.S., Crane, S., Xheng, H., et al. (2010) Quantitative determination of anisotropic magnetoelectric coupling in $BiFeO_3$–$CoFe_2O_4$ nanostructures. *Applied Physics Letters*, **97**, art. no. 052902.

(30) Zheng, H., Wang, J., Lofland, S.E., et al. (2004) Multiferroic $BaTiO_3$–$CoFe_2O_4$ nanostructures. *Science*, **303**, 661–663.

(31) Naumov, I.I., Bellaiche, L., and Fu, H. (2004) Unusual phase transitions in ferroelectric nanodisks and nanorods. *Nature*, **432**, 737–740.

(32) Jia, C.L., Urban, K.W., Alexe, M., et al. (2011) Direct observation of continuous electric dipole rotation in flux-closure domains in ferroelectric $Pb(Zr,Ti)O_3$. *Science*, **331**, 1420–1423.

(33) McQuaid, R.G.P., McGilly, L.J., Sharma, P., et al. (2011) Mesoscale flux-closure domain formation in single-crystal $BaTiO_3$. *Nature Communications*, **2**, art. no· 404.

(34) Van Aert, S., Turner, S., Delville, R., et al. (2012) Direct observation of ferroelectricity at ferroelastic domain boundaries in $CaTiO_3$ by electron microscopy. *Advanced Materials*, **24**, 525–527.

(35) Seidel, J., Martin, L.W., He, Q., et al. (2009) Conduction at domain walls in oxide multiferroics. *Nature Materials*, **8**, 229–234.

(36) Aird, A. and Salje, E.K.H. (1998) Sheet superconductivity in twin walls: experimental evidence of $WO_{3\text{-}x}$. *Journal of Physics: Condensed Matter*, **10**, L377–L380.

(37) Evans, D.M., Schilling, A., Kumar, A., et al. (2013) Magnetic switching of ferroelectric domains at room temperature in multiferroic PZTFT. *Nature Communications*, **4**, art. no. 1534.

(38) Keeney, L., Maity, T., Schmidt, M., et al. (2013) Magnetic field-induced ferroelectric switching in multiferroic Aurivillius phase thin films at room temperature. *Journal of the American Ceramic Society*, **96**, 2339–2357.
(39) Yang, S.Y., Seidel, J., Byrnes, S.J., et al. (2010) Above-bandgap voltages from ferroelectric photovoltaic devices. *Nature Nanotechnology*, **5**, 143–147.

15

Nanostructured Barium Titanate Ceramics: Intrinsic versus Extrinsic Size Effects

Liliana Mitoseriu and Lavinia P. Curecheriu

Faculty of Physics, University “Alexandru Ioan Cuza”, Romania

15.1 Introduction

Among the wide class of smart multifunctional materials, ferroelectric oxides brought an important contribution in various technological applications and, in particular, in microelectronics, during their short history of about 60 years [1–3]. Besides intensive investigation in fundamental and applied solid state chemistry and physics, their successful exploitation became basically possible by outstanding contributions in material (ceramic) science and engineering. As reviewed by Bell [4], the greatest engineering impact of the most important ferroelectric oxides is closely related to the progressive growing knowledge in the synthesis of micro/nanostructured oxide particles to the defect chemistry and to the control of ceramic processing and sintering mechanisms.

First observed in 1921 in hydrogen-bonded Rochelle salt (potassium sodium tartrate, $NaKC_4H_4O_6$) [5], ferroelectricity rapidly began to play an important role in electronics applications starting with the 1950s of the last century, after the discovery of the first ferroelectric oxide: barium titanate ($BaTiO_3$). Barium titanate was independently discovered by US, Japanese, and Russian scientists in the 1940s [1–3], as result of war-driven efforts to substitute mica in capacitors and quartz or Seignette salt as piezoelectric elements in underwater sonar transducers. Since then, it remained one of the most extensively employed

Nanoscale Ferroelectrics and Multiferroics: Key Processing and Characterization Issues, and Nanoscale Effects, First Edition. Edited by Miguel Algueró, J. Marty Gregg, and Liliana Mitoseriu.
© 2016 John Wiley & Sons, Ltd. Published 2016 by John Wiley & Sons, Ltd.

materials in the microelectronics industry, in particular for passive components as multilayer ceramic capacitors (MLCCs) and embedded capacitors in printed circuit boards, as well as for pyroelectric devices, microactuators, non-linear dielectric (tunable) materials for radio and communication filters and wireless applications, medical diagnostic transducers, ultrasonic motors, positive temperature coefficient (PTC) sensors and switches, and ferroelectric memories. $BaTiO_3$ was firstly used as a piezoelectric ceramic transducer until better piezoelectric performances were discovered in $Pb(Zr, Ti)O_3$ solid solutions. In his historical review *Ferroelectric Ceramics: History and Technology*, Haertling [6] considered that the discovery of non-linear dielectric properties (tunability) in $BaTiO_3$, combined with its high values of permittivity and low losses, was crucial for the development of a new generation of materials for microelectronic devices since its discovery until today. Hence, barium titanate, also considered the prototype ferroelectric ceramic oxide, is among the most systematically studied and widely used ferroelectrics.

Ferroelectricity is present in solid crystalline materials with a non-centrosymmetric unit cell and comprises a few typical phenomenological features, such as: (i) the existence of a *spontaneous polarization* and cooperative long-range ferroelectric order, usually produced by off-centre displacement of some active ions among equivalent positions, e.g. Ti in $BaTiO_3$; (ii) the *switching* character, which represents the ability of polarization (order parameter) to be switched between equivalent energy states by an appropriate driving force (electric field), where the switching process is characterized by *hysteresis*, which represents a fingerprint of ferroelectricity; and (iii) the transition from the low-symmetry ferroelectric (polar state) to the paraelectric state with high symmetry (non-polar), which represents a *phase transition* characterized by a specific Curie temperature and is accompanied by thermal anomalies of the physical properties. Ferroelectrics belong to a subclass of piezo- and pyroelectric materials, which are highly multifunctional materials, due to the fact that their electrical, mechanical, optical, and thermal properties are sensitive to multiple external parameters, such as electric field, mechanical forces (stress, pressure), and temperature. From a microscopic point of view, ferroelectric order is assigned to the existence of ferroelectric domains with ordered spontaneous polarization, separated by domain walls [7, 8]. Their configuration and dynamic properties are determined by the crystalline symmetry and external factors. The most typical ferroelectric domain walls separate domains with opposite polarizations (180° walls) or with perpendicular polarizations (90° walls), the last ones being both ferroelectric and ferroelastic because they separate regions with different orientations of polarization and strain. Domain patterns are determined by minimum energy conditions and they assume a complex structure in a real ferroelectric crystal, which is also influenced by defects, electrical and mechanical boundary conditions, driving force history, and temperature.

Ferroelectrics belong to a class of *non-linear dielectrics*, because the $P(E)$ relationship is nonlinear and hysteretic. Low fields can only induce reversible domain oscillations and give rise to a non-switching linear $P(E)$ response, whereas progressively increasing fields also start to produce small irreversible domain wall movements, but still a non-switching $P(E)$ response (Rayleigh [9–11]). If ferroelectrics are subjected to higher fields (overcoming a coercive field), domains are irreversibly switched between bistable states of polarization $\pm P_s$ and the polarization-field $P(E)$ dependence is hysteretic. The polarization-electric field hysteresis loop is often used for the identification of ferroelectric behavior. By comparison with linear dielectrics, which exhibit a field-independent permittivity, a non-linear and hysteretic function of permittivity upon the as-applied field $\varepsilon(E)$ (denoted as tunability) does exist in ferroelectrics. Permittivity of ferroelectrics assumes very large values, with at least one order of magnitude higher than for the best non-ferroelectric dielectric oxides (e.g. $\varepsilon \sim 1000$ in $BaTiO_3$ as compared to $\varepsilon \sim 100$ in TiO_2). In addition to the $P(E)$ hysteretic response, polarization switching by an external field leads to a strain–electric field $S(E)$ hysteresis. From the briefly mentioned phenomenological properties, it clearly outperforms the multifunctional character of ferroelectrics, which in the same structure combine intercorrelated electrical, mechanical, and thermal complex properties, which explains their large-scale usefulness as smart materials in various types of advanced technological applications. The discovery of the $BaTiO_3$ features was also crucial from a fundamental point of view, because it was the first oxide to demonstrate ferroelectric switching, a property that until that moment was assigned to hydrogen-bonded structures only.

From the structural point of view, $BaTiO_3$ is one of the most important members of the perovskites ABO_3 group, the principal class of ferroelectrics with corner-sharing oxygen octahedral structures [12]. In the perovskite structure, the large A cations are surrounded by twelve anions in cubo-octahedral coordination and smaller B cations are surrounded by six anions in octahedral coordination, while oxygen anions are coordinated by two B-site cations and four A-site cations. The perovskite structure has been shown to be the most versatile ceramic host. In fact, with its high structural flexibility it allows various simple or complex ionic combinations in A and/or B sites and this gives rise to vast possibilities for designing new structural and physical properties. From an electrical point of view only, perovskite oxides can have dielectric, ferro/piezoelectric, ionic, or mixed ionic and electronic conductor, semiconductor, or superconductor character, and they can even show giant magnetoresistance properties. $BaTiO_3$ experiences a series of polymorphic phase transitions. At high temperatures it has a cubic symmetry with space group $Pm3m$ and is non-ferroelectric. With decreasing temperature, the perovskite unit cell distorts to tetragonal $P4mm$ at the Curie temperature (120–130 °C), then to orthorhombic $Amm2$ at 0 °C, and rhombohedral $R3m$ at –90 °C (first-order phase transitions). All the distorted polymorphs are ferroelectric due to a spontaneous ionic polarization along the distortion axis and the corresponding spontaneous polarization is oriented along one of the <100>, <110>, or <111> orientations, respectively. The structural transitions are accompanied by anomalies of the unit cell parameters, specific heat, thermal expansion, and of the electrical, mechanical, pyro- and piezoelectric and electro-optic properties [1,2]. Usually, the development of the ferroelectric ordered state on cooling in displacive ferroelectrics can be explained by the existence of a *soft mode* behavior (i.e. the frequency of an optical mode lattice vibration decreases to zero at the Curie temperature), resulting in a sharp dielectric anomaly and in the Curie–Weiss behavior of the static permittivity in the paraelectric state: $\varepsilon = C/(T - T_0)$ [13], where C is the Curie constant and T_0 is the Curie–Weiss temperature (slightly smaller than the Curie temperature). The permittivity of $BaTiO_3$ single crystals is strongly anisotropic: along the a axis, the dielectric constant can be as high as 5000 near room temperature, but only about 250 along the c axis [14].

In spite of the fact that all functional properties are averaged (and often reduced) as a consequence of the random orientations of grains in ceramics by comparison with a single crystal, the main ferroelectric characteristics with interest for applications are retained in ferroelectric ceramics. The ceramic structures have the important advantage of cheap and easy processing and easy integration in multicomponent devices. As pointed out by Jaffe

[7], the discovery of the relationship between high permittivity and ferroelectric character of the new class of ferroelectric perovskites, together with the ability to align polarization by poling, was a critical step in understanding the ferro/piezoelectricity in oxide ceramics and their further large-scale use in microelectronics. It is worth mentioning that extrinsic phenomena such as domain walls motion, space charges, or defects may also influence the macroscopic properties (e.g. permittivity, piezoelectric response, polarization) of polycrystalline ferroelectrics.

15.2 Applications of $BaTiO_3$ Ceramics; Actual Demands for Passive Components

In addition to the switching properties of ferroelectrics whose main applications are related to the production of memory devices, the high nonlinear optical activity, piezo- and pyroelectricity found interesting applications as sensors, transducers, and actuators in various fields, while the non-linear permittivity $\varepsilon(E)$ is exploited in devices required by modern wireless technologies, for example for reconfigurable microwave circuits, varactors, tunable filters, phase shifters, tunable microstrip line strctures, voltage-controlled oscillators, etc. [15]. However, the major application of $BaTiO_3$-based ceramics is still related to its high permittivity. The wide compositional tolerance and the strong composition dependence of ferroelectric phase transitions allowed the exploitation of perovskite ceramics to increase the volume capacitance in multilayer ceramic capacitors (MLCCs), formed by a number of individual capacitors stacked together in parallel and contacted via the terminal surfaces (Figure 15.1(a)). The need for high-volume capacitance was strongly required by the tremendous need for miniaturization imposed by the last decade's progress in microelectronics. An early example of this possibility was the modification of $BaTiO_3$ by

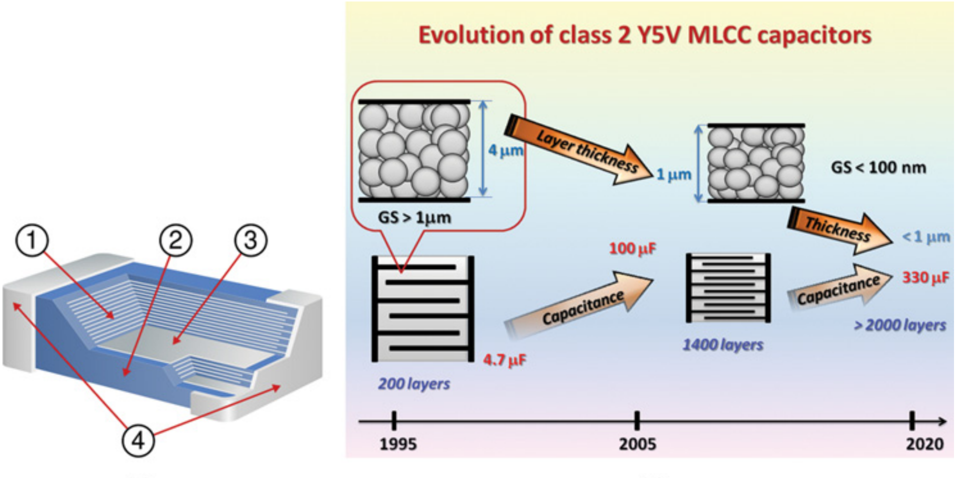

(a) (b)

Figure 15.1 *(a) Detailed construction of a multilayer ceramic chip capacitor: (1) dielectric ceramic, (2) ceramic or lacquered coating, (3) metallized electrodes, (4) connecting terminals. (b) Schematic representation of development of class 2 Y5V MLCCs [20]* isovalent substitutions (e.g. Sr^{2+} on to Ba positions) [16], enabling the shift of permittivity peak at the ferroelectric phase transition towards room temperature and enabling unprecedented high capacitance to be achieved. The growth of the MLCC market is proportional to the growth of the integrate circuit chip production since MLCCs are inseparable components of every integrated circuit [17]. The ceramic chip capacitors were the driving force for the conversion of electronic devices from through-hole mounting to surface-mount on the IC package substrate technology in the 1980s. In 2000, the annual production of MLCCs exceeded 100 billion [18, 19], while in 2012 the year production of devices employing MLCCs was about 10^{12} [20, 21]. Presently, the MLCC high capacitors up to 100 μm can replace tantalum or electrolytic capacitors in most applications and the major challenge is related to their use in high-voltage applications.

$BaTiO_3$ is the main component of Class 2 MLCCs with high permittivity (200 to 14 000) and Class 3 ceramic capacitors (barrier layer or semiconductive ceramic capacitors with giant permittivity up to 50 000). Class 2 MLCCs are characterized by a non-linear change of capacitance versus applied voltage and temperature change. They are suitable for bypass, coupling, and decoupling applications or for frequency discriminating circuits where low losses and high stability of capacitance are less important. Some specifications commonly used for Class 2 ceramic capacitor materials are: *X7R* (capacitance variation of maximum ±15% in the range of −55 to 125 °C), *Y5V* (capacitance variation of +22/−82% in the range of −30 to 85 °C), etc. [20]. Apart from the mentioned microelectronics applications, MLCCs recently became highly required for inverters in hybrid cars, where larger capacitance in the range 100–2000 mF under high superimposed DC and AC fields is needed.

The capacitance per unit volume of an MLCC is determined by the material relative permittivity ε_r, the number of dielectric layers n, and thickness d of one individual layer. In recent decades the progressive miniaturization of digital electronics asked for a higher volume capacitance, which was realized through a gradual reduction in the thickness of the dielectric layer with the simultaneous increase of both the number of layers and the permittivity. Whereas the minimum thickness of the dielectric layers was about 4 μm in 1995, in 2005 some manufacturers produced MLCC chips with a thickness around 1 μm, which was further reduced to 0.5 μm in 2010 (Figure 15.1(b)) [20,21]. To reduce the thickness of an individual layer below 1 μm and to maintain reproducible dielectric properties, a layer should contain at least ~7–9 ceramic grains in thickness, by considering the strong dielectric anisotropy of $BaTiO_3$. Therefore, dense $BaTiO_3$ ceramics with a grain size below 150–200 nm had to be produced and investigated. In order to end up with nanostructured ceramics with such a grain size, ultra-fine primary powders of tenths of nm were necessary, as well as appropriate sintering conditions to avoid grain growth. From a technological point of view, the manufacturing process became more precisely controlled in order to include more stacked layers (increase n and reduce d). From a material science point of view, due to the scalability of the material properties with a reduction size in ferroelectrics, it was a great challenge to determine whether $BaTiO_3$ ceramics with such a small grain size would preserve a high permittivity in the range of ~1000, because otherwise the decrease of the thickness layer d would be compensated in the volume capacitance by the decrease in permittivity when reducing the grain size. This technological-driven interest in investigation of induced size effects in properties when reducing grain sizes in $BaTiO_3$ ceramics has motivated our studies in past decades, firstly for grain sizes below 1 μm [22–25] and, more recently, down to tenths of nanometers [26–33].

15.3 Size-Dependent Phenomena in Ferroelectrics

15.3.1 General Properties

The downscaling of ferroelectrics represents one of the most largely debated subjects, due to its high technological impact [34–38]. With the continued demand for portability in consumer electronics, it is becoming increasingly important to understand the effects of miniaturization on the properties of the active components in microelectronics. From a basic science point of view, to find the ultimate structure still retaining ferroelectricity is a key issue still open in ferroelectricity. Theoretical models predicted progressive reduction both of spontaneous polarization and lattice strain, of the Curie temperature, together with a broadening of the phase transition and reduction of the material constants (dielectric, pyro- and piezoelectric constants, electro-optic, caloric) when reducing the system's size down to nanoscale [39–42]. Properties related to size effects in free-standing ferroelectric nanoparticles [43,44], grain size phenomena in dense nanosized ceramics [27–33, 45–48], thickness-driven properties in ultra-thin films [36, 37, 49–51], or lateral size effects in unsupported nanoislands, nanodots, or 1D structures [52–58] have been largely investigated, mostly in $BaTiO_3$ and in other perovskite ferroelectrics. However, it is worth remembering that the extensive experimental data basis related to size effects in ferroelectrics is difficult to integrate and interpret unambiguously, due to the inability to compare samples produced by various synthetic routes, having different geometrical constraints, electrical and mechanical boundary conditions, surface properties, defects, and internal structures. All of these parameters become essential when the system's size is reduced to the nanoscale. Like other ferroics, ferroelectricity is a cooperative long-range-order phenomenon generated by collective interaction of dipolar units. When the number of dipoles decreases as a result of size reduction, the ferroelectric state becomes unstable and important property changes with respect to the bulk state are expected. Until recently it was generally agreed that the reduction of the physical size of ferroelectrics leads to a progressive decrease of spontaneous polarization up to a critical size (particle, grain size, thickness) corresponding to the transition to the cubic phase and disappearance of ferroelectricity is reached, as an *intrinsic size effect* [35–41].

Due to the influence of several superimposed extrinsic contributions to the properties that also substantially change when reducing the system's size, a scattered range of values for such *critical size*, even for the same system, was experimentally determined or predicted by calculations [35–41, 47–49, 59,60]. Another opinion is that the size effects in ferroelectrics are strictly determined by extrinsic factors related to the processing procedure and should not be found in defect-free high-quality nanosystems [45, 61, 62]. Recent detailed structural analysis based on high-energy XRD and atomic PDF calculations clearly demonstrated the absence of a *critical size* in nanosized $BaTiO_3$ down to 5 nm particle size; instead, the progressive loss of ferroelectricity would have an intrinsic origin connected with the increasing atomic positional disorder in spatially confined physical systems [63]. Therefore, the problem of the existence of a critical size in ferroelectrics is still under discussion and efforts are currently under progress to produce novel downscale ferroelectric nanostructures with specific geometries, to probe their properties as a function of their size and to determine whether intrinsic or extrinsic effects are at the origin of the observed features. The ultimate volume below which the spontaneous ferroelectric polarization vanishes was often referred to as the *superparaelectric limit*. All the primary ferroics (ferromagnetics, ferroelectrics, and ferroelastics [64]) show some common characteristics related to the reduction of their physical size. The superparamagnetic state is typical of ensembles of ferromagnetic non-interacting particles, whereby a lowering of the switching energy barrier down to thermal energy kT values is achieved when reducing the system's size and the spin flipping between the two equilibrium states is thermally activated [65]. As a result, the magnetization field $M(H)$ hysteresis curve changes to a non-linear non-hysteretic (Langevin-type) dependence, accompanied by specific time-dependent phenomena (relaxation) in the superparamagnetic state. Similarly, it was believed that a superparaelectric state might be induced in down-scale non-interacting ferroelectric particles. A rough estimation of the superparaelectric size limit, determined by the size of a ferroelectric structure, for which the energy to coherently flip the polarization vector becomes comparable to the thermal excitation energies [36], gave a critical volume of 2–8 nm for $BaTiO_3$ by considering coercivities in the range of (0.5–1) kV cm^{-1} and remanent polarizations of (5–10) μC cm^{-2}. For the case of $PbTiO_3$, the depth of its energy double well is typically in the range (0.1–0.2 eV) cells $units^{-1}$, about 4 to 8 times the higher thermal energy kT at room temperature, leading one to consider that in principle one unit cell of a ferroelectric material may survive to thermal fluctuations and retain ferroelectricity [37]. In reality this is not true, because ferroelectricity is limited by electrical and mechanical boundary conditions and, most frequently, by practical problems involved in the production of high-quality samples on the extreme nanoscale (i.e. thickness of a few unit cells). Although invoked by some authors and calculated from different approaches, the *superparaelectric state* has never been demonstrated without any doubt. Only a few local switching experiments performed in ferroelectric nanoislands or in supported nanograins [66–68] seem to prove such behavior in some particular small grains, but local parameters (substrate, local defects, local field gradients, thermal fluctuations) may also play a role in the observed local properties. Practically, no macroscopic experiments clearly demonstrated the existence of the superparaelectric limit in well-defined ferroelectric structures. A *superparaelectric* approach is used to describe the dynamics of nanopolar clusters giving rise to frequency-dependent dielectric properties in relaxors [69].

15.3.2 Theoretical Description of Size-Dependent Phenomena in Ferroelectrics

The scaling down of the ferroelectric structures and experimental observations of size-dependent properties stimulated a growing interest in describing theoretically the observed properties. The main theoretical approaches are summarized in Figure 15.2, together with the corresponding time and length scales:

(i) *Ab initio* and atomistic models (not involving empirical inputs), which describe systems at atomic scale taking into account the electronic structure by solving the Schrödinger equation within a certain approximation.

(ii) Mesoscale models, especially the continuum methods, describe phenomena related to the ceramic processing, domain switching, or other macroscopic properties of ferroelectric ceramic structures, usually based on constitutive theory and balance laws of solid-state physics or Ginzburg–Landau thermodynamic equations. Discrete approaches as Monte Carlo or Ising models do not rely on explicit input of thermodynamic and kinetic characteristics and are able to describe either material processing

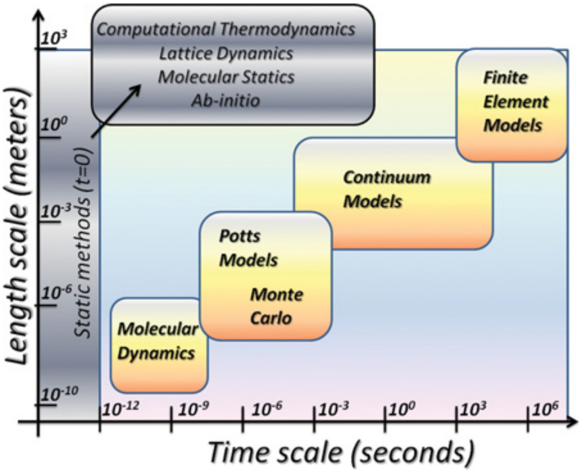
Computational Thermodynamics
Lattice Dynamics
Molecular Statics
Ab-initio
Finite Element Models
Continuum Models
Potts Models
Monte Carlo
Molecular Dynamics
Static methods (t=0)
Length scale (meters)
10^3
10^0
10^{-3}
10^{-6}
10^{-10}
10^{-12}
10^{-9}
10^{-6}
10^{-3}
10^0
10^3
10^6
Time scale (seconds)

Figure 15.2 *Schematic representation of modeling techniques for ferroelectrics, covering different time and length scales*

phenomena (grain growth, sintering) and macroscopic properties (switching, phase transitions).

(iii) Macroscale models are particularly useful for describing the material's behavior and simulate its response in real structures. Macroscopic properties are commonly described by empirical or semi-empirical *physical models*. Among them, finite element methods (FEMs) successfully predicted thermomechanical, electromagnetic, and optical properties in ferroelectrics with realistic microstructures. Additional approaches like computational thermodynamics using the laws of thermodynamics and thermodynamic data for predicting phase diagrams and chemical stability of single, binary, and multiple phase ferroelectric systems at various external parameters are uniquely applicable to all length scales.

The size-dependent properties of ferroelectric systems can be explained by considering the role of a few main factors [35, 40]:

1. Intrinsic size effect, caused by the reduction of long-range ferroelectricity as a result of the progressive decrease in the number of interacting dipolar units and intensity of interaction when reducing grain size. Ferroelectricity is a collective phenomenon resulting from the competition between short-range covalent repulsions and long-range Coulomb interactions [70]. Going down from bulk to nanoscale, the delicate interplay between these factors will be modified in favor of short-range phenomena.
2. The single-domain state, energetically favorable in ferroelectric structures with a small grain size, influences the functional properties (e.g. domain walls contribute to the dielectric and piezoelectric constants, switching characteristics, etc.). This effect does not directly influence the structural stability of the polar phase with grain size reduction and therefore the domain walls contributions to the size-dependent properties are extrinsic.

3. The depolarizing field effect [71] created by uncompensated surface charges (located at boundaries, interfaces with electrodes), which may be partially or completely screened by electrodes or compensated by residual conduction charges existing in non-ideal dielectrics. A destabilization of ferroelectricity and reduction of ferroelectric polarization by the depolarization field is mainly expected in fine powders and unsupported films rather than in bulk ceramics. This effect is strongly influenced by the sample conductivity, nature of electrode, and quality of the ceramic–electrode interface.
4. Surface/interface effects can give both intrinsic and extrinsic contributions to the size-dependent properties of ferroelectrics [35, 40].
   (a) *Intrinsic contributions*. Changes of the local symmetry take place near the surface due to the broken translational invariance, thus changing the local internal field and long-range dipolar interaction and the soft-mode behavior responsible with ferroelectric stability. The total free energy is altered by surface effects by a surface energy term proportional to the total surface area (surface tension). As the physical size of the system decreases, the ratio between interface/volume effects becomes particularly important at meso- and nanoscale.
   (b) *Extrinsic contributions*. This is related to the fact that by reducing the system's size, the fraction of atoms located at the interfaces considerably increases. They are structurally associated with their corresponding surface or interfacial environments. According to the processing, the interfaces in powders, ceramics (grain boundaries), or films (electrode–ceramic interfaces) are regions with unavoidable and uncontrollable defects (e.g. modified chemical bonding, structural inhomogeneity and defects, stoichiometry variations), which modify the macroscopic properties by comparison with those in bulk.

15.3.2.1 Size Effects Described by ab initio Models

The main theoretical approaches used to derive the characteristics of scale-dependent properties of ferroelectric structures will be briefly reviewed. First-principles density-functional (*ab initio*) calculations have been used to study ferroelectricity in perovskites LDA [1, 72]. King-Smith, Vanderbilt and co-workers performed a systematic study of the structural and dynamic properties and energy surfaces for a few common perovskites [72–74]. They showed that ferroelectricity is a result of the delicate balance between long-range electrostatic forces that favour ferroelectricity and short-range repulsion that promote the cubic non-polar phase. These calculations accurately predicted the ground-state structure of the occurrence of ferroelectric phases and some zero-temperature properties for certain perovskites. The method was applied to study structural phase transitions and finite-temperature properties of $BaTiO_3$ and other ferroelectric perovskites [74]. Such calculations allowed determination of the temperature dependence of the order parameter and polarization, the sequence of structural phases, the temperature–pressure phase diagram, the order–disorder or displacive character of the transition, and the role of each energy term in the effective Hamiltonian on the macroscopic properties.

Calculations performed for single crystals showed that ferroelectricity has a collective effect (similar to ferromagnetism and superconductivity), for which a different order degree is expected to occur near surfaces or interfaces, leading to an intrinsic dependence of properties on sample size. However, the size-dependent phenomena in ferroelectrics are even more complicated to describe, because the polarization is also determined by local composition, strain, and charge, and if these variables are uncontrolled, large extrinsic contributions to the properties are generated. In confined structures, both short- and long-range interactions are modified with respect to the bulk situation and it is commonly believed that ferroelectricity is altered and eventually totally suppressed when the system reaches a *critical size*, referred as the *ferroelectric correlation volume* [1]. Due to the very complicated mechanical and electrical boundary conditions, to the characteristic inhomogeneity of polycrystalline ceramics and to the large number of uncontrolled local parameters, first-principle calculations are not the most suitable to describe such systems. However, there are some attempts to describe the succession of structural transformations in $BaTiO_3$ down to 8 nm grain size [75] and a recently proposed core–shell $BaTiO_3$ nanoceramics model consisting of core–shell nanoparticles, nanowires, or nanoplanes was described using *ab initio*-derived effective Hamiltonian calculations [76]. Thus, we will remember the main results on the basis of this approach in describing confinement effects in very simple structures, such as films and nanowires (2D and 1D systems), with the observation that some of the conclusions and possible size-effects-related properties are also valid for ceramic structures.

The effect of the thickness reduction on the thin-film ferroelectricity has been observed for a long time, but has not yet been fully understood. Early experiments and calculations based on the Landau–Ginzburg–Devonshire (LGD) theory have suggested that below a *critical correlation volume* [1] of the electrical dipoles (of around approximately 10–100 nm), ferroelectricity vanishes due to an *intrinsic size effect* [77, 78]. A reduction of the polarization stability when reducing the thickness in films with the polar axis perpendicular to the surface was explained by the formation of a depolarizing field because of incomplete compensation of surface charges due to non-ideal electrodes [71, 79]. However, single-domain ferroelectric phases have been recently observed in ultra-thin films (thickness below 10-unit cells) [80–82]. Furthermore, it was demonstrated that ferroelectric phases can be stable down to ≈ 12 Å (3-unit cells) in $PbTiO_3$ films by forming 180° stripe domains, suggesting that no fundamental limit of thickness is imposed by the intrinsic size effect in thin films [83]. This idea was verified by *ab initio* calculations carried out on perovskite films, which indicate that there is no critical thickness for polarization parallel to the surface [84] and that polarization perpendicular to the surface can exist in films of only 3-unit cells if the depolarization field is artificially removed [85, 86]. Furthermore, recent calculation have revealed that $BaTiO_3$ films with $SrRuO_3$ electrodes lose ferroelectricity below 24 Å (6-unit cells) [87], thus suggesting that a minimum thickness limit still exists for some structures of ferroelectric films. The problems of the depolarizing field in ultra-thin films and of the ferroelectric–electrode interfaces were examined in works devoted to the study of ferroelectricity in ultra-thin films (<10 Å) with realistic electrodes [87–89]. Calculations showed that appropriate electrical and chemical boundary conditions are essential in stabilizing ferroelectricity: single-domain ferroelectricity can persist down to one unit cell in $PbTiO_3$, but not in $BaTiO_3$ films with the same electrodes. The difference has been explained as due to different screening caused by the difference in the work functions at oxide surfaces resulting in different values of ferroelectric polarizations. From these calculations, the important role of parameters such as electrode screening, terminal stoichiometry, electrical and mechanical boundary conditions, in-plane atomic displacement of the ferroelectric (here considered as fixed to the bulk value), in-plane strain caused by the heteroepitaxy, as well as the film thickness in stabilization of the ferroelectic phase was clearly demonstrated.

The finite size effects on the ferroelectric stability in low-dimensional systems such as nanorods, nanodisks, and nanowires [90–95] were also investigated by first principles methods. Individual $BaTiO_3$ clusters assembled in infinite chains combining themselves in wires of increasing diameters and periodic boundary conditions were considered for calculations [93]. A critical diameter was identified below which the ferroelectric distortion along the wire axis is completely suppressed. The ferroelectric instability exhibits a marked "chain-like" character, so that in nanowires it might *a priori* be preserved down to very small dimensions. However, at small radii, low atomic coordinations at the surface produce a contraction of the unit cell responsible for the suppression of the ferroelectric distortion at a critical radius estimated at around 1.2 nm, below which ferroelectricity disappears in the $BaTiO_3$ nanowires. Thus the ferroelectric behavior of nanowires seems to be monitored by the strong sensitivity of ferroelectricity to the unit cell volume, which is affected by low coordination effects at the free surfaces. The ferroelectric distortion parallel to the wire surface is enhanced at the TiO_2 and reduced around the BaO surfaces, which is a similar characteristic found in the case of free-standing slabs [94], which might explain the stoichiometry effects on the tetragonal distortion found in bulk systems.

15.3.2.2 Size Effects Described by Mesoscale Models

Two main approaches (mean-field theories) have commonly been used to describe mesoscale-dependent phenomena: continuum theories based on Landau–Ginzburg–Devonshire (LGD) theory [1, 96–98] and discrete models. The LGD approach was derived from the Landau general theory of phase transitions in which the thermodynamic potential is developed as a power series of the order parameters (components of the ferroelectric distortion or corresponding polarization) [96]. The polarization is a function of time and space coordinates within the sample and the relationships between the conjugated parameters (polarization–field $P(E)$, stress–strain $X(x)$, and entropy–temperature $S(T)$) and the coupling between mechanical, electrical, and thermal parameters result by minimizing the free energy [96–98]. The time-dependent phenomena describing kinetic phenomena during phase transitions, metastable states, ferroelectric switching, and domain wall dynamics are obtained by solving the master (Landau–Khalatnikov) differential equation [99–101] completed with specific boundary conditions [101, 102].

Some size-dependent properties were predicted even within this simple approach, considering renormalized size-dependent Landau coefficients. Their size (g) dependence and the critical sizes for the ferroelectric stability have been determined from dielectric, calorimetry, structural, or spectroscopy data, as in the case of $BaTiO_3$ powders and ceramics with different particle/grain sizes [35, 36, 101], in nanocrystalline $PbTiO_3$ [35, 103], or in ultrathin $PbTiO_3$ films [104]. Another route is to impose empirical grain size dependencies of the Landau parameters, as employed for single-domain unclamped $BaTiO_3$ nanocrystalline ceramics, in order to explain the size-induced changes in tetragonal phase stability and deviations of the dielectric data with respect to the bulk values, to find the existence of a field-induced metastable tetragonal phase in the cubic state [105], or to describe the role of the Curie temperatures distribution on the caloric and dielectric properties of $BaTiO_3$ nanoceramics [105, 106].

Instead of using empirical size-dependent Landau parameters, a more rigorous approach was to include in the free-energy expression [35, 76, 78, 107–114] additional terms due to: (a) shape-dependent depolarization field effects [115]; (b) spatial gradients of polarization components due to various types of local inhomogeneities; (c) surface/interface screening effects due to imperfect charge screening at the electrode-ferroelectric interface (an effect mainly present in thin films) [37, 81] or Laplace surface tension for isolated powder particles [78, 109]; (d) elastic clamping and stress terms describing the effect of the external mechanical loads and residual (internal) stress due to the processing and microstructural particularities and electromechanical coupling terms dependent on the crystalline symmetry [116]. In addition, electrical and mechanical boundary conditions (free surfaces, clamping conditions, constant charge or voltage conditions at the interfaces, and information on the domain structure, like single-domain or 180° domains hypothesis, etc.) are imposed to the system. As a result of these contributions, a renormalization of the Landau coefficients (that become size-dependent) is again obtained. In this way, size-driven ferroelectric–paraelectric phase transitions and the critical size of powders, ceramics, or films with various shapes and geometry have been predicted, as well as size-dependent changes in the nature of the phase transition (from first to second order when reducing the particle size) [78], the spatial dependence of the polarization in films with domain structures, the thickness-dependence of the domain width, free energy, and Curie temperature [109, 110]. More accurate calculations considered the anisotropic correlation length of the electric dipoles in confined systems and demonstrated that the critical thickness is closely associated with the transverse critical size [40]. This conclusion explains to some extent the absence of thickness-dependent Curie temperature and the lack of broadening in the dielectric data for $BaTiO_3$ free-standing nanocapacitors with thickness down to 75 nm, but larger lateral size [53].

Discrete (or dipolar) models used as an alternative in describing confinement effects seem to be more appropriate for discrete ferroelectric systems. Chains (1D) and 2D or 3D networks of interacting polar units (dipole lattice [117–119], Ising, or Preisach systems) were also largely employed: the equilibrium and time-dependent behavior of each dipolar entity was determined at given temperatures and external and local fields (the last of which being either averaged within the effective field approximation, Lorentz, Onsager, etc., or numerically calculated as a vectorial sum of the overall dipolar field contributions). Once the time evolution of each dipole has been determined, the total polarization of the system is calculated, together with other characteristics. Size effects result by imposing geometrical and critical barrier limitations of the polar units to describe margins/confinement effects, nucleation (latent nuclei) and defect sites initiating/inhibiting the polarization reversal and the non-ferroelectric boundaries. It is interesting to note that the average of the total free-energy of such discrete systems with confinement and interaction effects can be described again by a Landau model with renormalized size-dependent coefficients [102].

Ising models described phase transitions in ferroelectric films [120] and characterized size effects in ferroelectric particles [121, 122]. In this approach, interacting dipole ensembles characterized by identical individual "spins" are described by a transverse Hamiltonian containing an interaction term that considers the interaction range (between the nearest-neighbor model and infinite-range interaction). The interaction is a long-range Coulomb one in ferroelectrics. With a decrease of the particle size, the Curie temperature and all the radial components of the polarization together with the average value fall to zero for a critical size, because of a weakening of the long-range interaction among the pseudo-spins below this size. The calculations have shown that the interaction range significantly influences size-dependent effects and for a fixed Curie temperature corresponding to the bulk, a system with long-range interactions needs a larger size to stabilize its ferroelectricity. It is worth noting that the free-energy calculated within Ising models in some structures also lead to a Landau-type dependence of the free energy over the order parameter. The Landau-based models remain a landmark reference in describing the critical phenomena in polar systems, including ferroelectrics. Other discrete models considering collectives of interacting dipoles are derived from the micromagnetic approach, in which individual dipole dynamics and reciprocal interactions are calculated not by effective field approximation but by a numerically estimated sum of the overall contribution of the dipole fields [120]. Even in these systems it is possible to take into account the confinement effects, leading to polarizing/depolarizing or internal field effects on polarization switching [121].

15.3.2.3 Size Effects Described by Macroscale Models

Only a few examples of macroscale models have been reported to describe ferroelectric characteristics, but not finite-size effects. Finite element modeling has been used to describe some electrode–ferroelectric structures in the equilibrium state or under rate-dependent loads, as multilayer ceramic capacitors and ferroelectric and piezoelectric devices, in which the ferroelectric is mostly considered as a continuum [123, 124]. Landau models combined with FEMs have also been used for modeling of the piezoresponse in particular nanostructured ferroelectric films [125] and further steps in employing FEM models combined with empirical permittivity-field dependences [31, 32]. Switching models such as the one using the Preisach approach [126–128] have been recently developed in order to describe dielectric and tunability properties dependent on grain size in nanostructured ferroelectric ceramics. The results of this approach will be described in detail in Chapter 18 of this book. The main difficulty is to have available thermodynamic parameters sufficient to properly describe the boundary conditions and then to numerically solve a large number of coupled differential equations. Physical models combining empirical or semi-empirical approximations with energy relationships (order–disorder models; see Jiles [129, 130]) indirectly take into account scaling effects through phenomenological parameters derived from experiments. They are able to derive some scaling-dependent properties of the ferroelectric responses (such as $P(E)$ loops, switching currents, etc.) in some specific structures, without giving any fundamental insight into the origin of these parameters.

The examples of models deriving confinement-dependent properties have been mainly developed for simple structures (isolated powders, thin films) and only under serious simplifications. Given the high degree of complexity of the problem, no model for grained ceramics is known. In addition, it becomes practically impossible to derive a general behavior of the size-dependent properties and the critical size for a given ferroelectric system (such as nanowire, nanorod, thin or thick film, ceramics) without fully knowing the specific characteristics and the exact boundary conditions and without considering the role of all relevant parameters involved in these phenomena. Almost all the theoretical approaches predicted a family of common scaling effects, as follows:

1. Gradual decrease of tetragonal distortion *c/a* and of the corresponding spontaneous polarization with decreasing size. At a critical size, tetragonality vanishes and

ferroelectricity is no longer sustainable. This can be interpreted as a size-driven ferroelectric-to-paraelectric transition.

2. Reduction of critical temperatures (Curie and Curie–Weiss) when reducing the physical size of the ferroelectric system, with a non-linear variation: a sharp decrease takes place when approaching the critical size whereas almost no variation is observed at large sizes. For each system a critical size determines the ferroelectric stability: a size-driven ferroelectric–paraelectric phase transition takes place at a given temperature.
3. Broadening of the phase transition at smaller sizes was mainly explained as a result of the rapid change in $T_C(g)$ at small sizes. Large fluctuations and large distributions of critical temperatures, characteristic of systems at small dimensions, give rise to a wide temperature range for the ferro–para transition, as demonstrated by the temperature dependence of macroscopic properties (permittivity, polarization, heat capacity, and pyroelectric and piezoelectric constants).
4. Depressed values are typical of the physical constants at small dimensions, by comparison with bulk values. A lower permittivity is expected in some ferroelectrics as a result of changes in the soft-mode dynamics, as an intrinsic effect. More generally, the reduction of long-range order diminishing the dipolar interaction strength while reducing grain size causes the reduction of the mentioned constants. However, important extrinsic contributions to this reduction at small size are commonly accepted.
5. Changes of the domain structure as reducing the system's size. As the physical size becomes small, the minimum free-energy condition is fulfilled for a simpler domain structure. The single domain state is stable at small sizes in all types of fine structures (fine powder grains, ultra-thin films, and fine ceramics). The domain walls provide an important extrinsic contribution to the dielectric and piezoelectric constants. Thus, the reduced values mentioned in item 4 are also due to the lack of domain walls at small size, as an extrinsic effect.
6. Variation of the domain wall dynamics occurs when the moving domains meet grain boundaries or defective structures. Smaller values for the switching polarization and currents and a reduction of coercivity and loop area were derived by several models.

In the following, the role of the mentioned factors on the properties of $BaTiO_3$ nanostructured ceramics, when their grain sizes reduce down to a few tenths of nanometers, will be discussed in detail.

15.4 Size-Dependent Properties in $BaTiO_3$ Ceramics: Intrinsic versus Extrinsic Size Effects

15.4.1 Size-Dependent Properties of $BaTiO_3$ Ceramics with Grain Size in the Range of Micrometers

The first studies concerning grain size (GS)-dependent phenomena in $BaTiO_3$ started with the observation that ferroelectricity in single crystals disappears if crystal thickness is below 1 μm [131]. For ceramics, one of the first observation was related to the enhanced values of permittivity for grain sizes around 1 μm [132], which was explained by Arlt et al. [133] as due to the stress related to the transitions from polydomain (twinned) to single-domain structures that takes place around this size in $BaTiO_3$ ceramics. Kinoshita and

Yamaji [134] reported a reduction of the tetragonal distortion *c*/*a* and of the Curie temperature when reducing GS in $BaTiO_3$ ceramics with sizes in the range of 1.1–53 μm [134]. A small reduction of Curie temperature when reducing GS was reported by Kanata et al. [135] for $BaTiO_3$ ceramics having GS in the range of 0.1–200 μm, while a fast decrease of the ferroelectic–paraelectric transition temperature was reported by Uchino and co-workers [136–138] below 1 μm. They also reported that tetragonal phase changes into cubic in powders with grains of 0.12 μm, which was at that time considered a critical size for the existence of ferroelectricity in $BaTiO_3$ powders. They also noticed that the Curie temperature of $BaTiO_3$ ceramics is always lower than for powders with a similar particle size. These observations allowed the conclusion to be made that the moment where a critical size for the stability of the ferroelectric phase in $BaTiO_3$ ceramics at room temperature may lie between 0.2 and 0.12 μm. Further, ceramics with a smaller grain size should exhibit a pronounced decrease in their Curie temperature below room temperature.

Coarse-grained ceramics of pure $BaTiO_3$ with an average GS between 20 and 50 μm show permittivity of 1500–2000 at room temperature and values in the range of 1000–1500 were reported for GS above 3 μm by the large majority of authors [139]. There are some disagreements concerning the shape of permittivity–temperature dependence and both a sharp maximum at the ferroelectric–paraelectric transition [134, 140] as well as smeared peaks were reported for ceramics with GS in the range from 0.3 to 30 μm [132, 141–143]. The diffuse character of the ferroelectric–paraelectric phase transition was explained as due to a distribution of distributed Curie temperatures as a result of inhomogeneities due to different types of defects existing in the ferroelectric ceramics, to various local densities, and to different types of grain boundaries, resulting in various processing methods and the use of different raw precursors and processing and sintering methods. There is a general agreement concerning the maximum of permittivity (≈4000–6000) around 0.8–1 μm [35, 132, 133, 141], followed by a strong depression in the submicrometer range, in which even larger scattering of the Curie temperature and permittivity data were reported, as will be reviewed in the next section. In conclusion, the large majority of publications showed that variations in the functional properties of $BaTiO_3$ ceramics with reducing GS start when approaching GS to about 1 μm, but major deviations from the bulk properties are expected in the submicrometer range.

15.4.2 Size-Dependent Properties of $BaTiO_3$ Nanoceramics

In spite of the large volume of literature dedicated to the GS effects on the properties of $BaTiO_3$ ceramics, reliable data have been mostly obtained for ceramics with GS $\geq$ 400 nm, due to the difficulty of producing fully dense ceramics below this size by classical sintering methods. Many results reported for samples with smaller grains are likely to be strongly affected by the high degree of porosity [35]. A porosity level above 5% generally leads to a strong depression of the apparent dielectric constant. Moreover, for a correct comparison and conclusions, the role of GS has to be investigated in ceramic systems with similar densities, due to the fact that porous ceramics are in completely different electric and mechanical boundary conditions than the dense ones. This is due to the facts that: (i) grains partially surrounded by pores have increased possibility to accommodate the strain resulting from the paraelectric to ferrolectric transition and (ii) gas–solid interfaces have a different energy in comparison to solid–solid interfaces (grain boundaries GBs). Therefore, for a correct analysis of the role of grain size on the functional properties of $BaTiO_3$ ceramics and to derive some general trends, only dense ceramics with a large range of grain sizes should be compared.

The densification of nanocrystalline oxide powders, including perovskites, to ultra-fine ceramics (grain size below 300 nm) with relative density above 90–95% still represents a challenge. In most cases, the classical sintering procedure is always associated with grain growth, so that the nanostructure of the starting ultra-fine powders is often lost [144, 145]. Recent developments in the densification procedures and the continuing improvements in synthesis techniques of nanopowders made possible the production of ceramic oxides characterized by high density and extremely small grain size down to a few nanometers. This opened the possibility to realize bulk materials whose functional properties are partially or totally defined by their nanostructure. Dense $BaTiO_3$ ceramics with grains below 100 nm have been produced from ultra-fine powders in the last few years, using special densification methods like ultra-high pressure sintering in a multianvil press (GS down to 70 nm, 98% relative density) [45], the combined sintering method (GS down to 90 nm, 99% relative density) [46, 146], or by multistep sintering (down to 30 nm, 98% [147, 148] or even down to 8 nm GS, which represents to date the finest $BaTiO_3$ ceramic with extraordinary high density of 99.6% relative density [47]). Spark plasma sintering was largely employed [144,145 and references therein] for densification of $BaTiO_3$ ceramics with 95–98% relative density. We used the same sintering technique to produce various series of nanostructured $BaTiO_3$ ceramics with the finest grain size down to 30 nm and density of 97%, starting from fine particles of about 5 nm (Figure 15.3) and a comprehensive investigation of the role of the grain size and grain boundaries on the caloric, dielectric, local, and macroscopic ferroelectricity, while tunability and lattice properties have also been reported [27–33].

The general properties obtained in our studies together with ones reported in the literature for such dense ceramics when reducing grain size below 1 μm and proposed interpretations of the observed features are presented in the following.

15.4.2.1 Structural Modifications Induced by the GS Reduction

Ferroelectricity in $BaTiO_3$ originate from the off-centre displacement of the Ti ion, causing a tetragonal distortion of the unit cell, which is stable at heating until the Curie

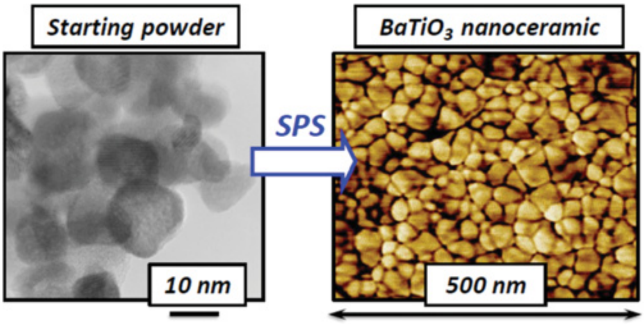

Figure 15.3 *TEM micrograph for the starting $BaTiO_3$ powder [149] and microstructure of a dense ceramic with average GS = 30 nm densified by spark plasma sintering. Reprinted (Figure 1(b)) with permission from [29]. Copyright (2006) by the American Physical Society*

temperature is reached (115–120 °C), when a tetragonal–cubic structural transition takes place. The reduction of ceramic grain size modifies the relative stability between the two polymorphs and promotes a stabilization of the cubic phase at lower temperatures, that is causes a reduction of the Curie temperature. The gradual loss of ferroelectricity when reducing grain size is supported by the long-range order character of ferroelectricity, and resulted from calculations within Landau-type models and Ising and physical models, as largely described in Section 15.3.2.

The structural modifications induced by grain size reduction in $BaTiO_3$ ceramics indicate a gradual diminishing of the tetragonal splitting and shows a transition from tetragonal to a pseudocubic state [45–47]. An example of such dependence is shown, for example, in Figure 15.4 for GS in the range of 20 nm–3 μm [47]. As a consequence, a reduction of tetragonality *c*/*a* when reducing grain size was reported as a general trend in the large majority of studies. However, it is worth mentioning that when diminishing GS below 200 nm, the discrimination of crystalline phases becomes difficult because of the very small structural distortions. With the support of detailed XRD and Raman analyses, authors concluded that even in fine structures with GS of tenths of nm all the polar phases existing in single crystals and coarse ceramics are evidenced, and the nanoceramics undergo the same succession of structural phase transitions. Unlike in coarse ceramics, the structural transitions become less sharp towards very diffuse when reducing GS down to tenths of nm and they take place in large temperature ranges when more structural modifications might coexist [13, 28, 30, 45–47]. The stability temperature range for the tetragonal distortion is reduced in fine-grained ceramics, due to a decrease of tetragonal–cubic and increase of orthorhombic–tetragonal transition temperatures [13, 28, 30, 47, 148]. These features have been explained within Landau-based approaches (see [151] and references therein). At room temperature, nanocrystalline $BaTiO_3$ ceramics is predominantly tetragonal, but orthorhombic–tetragonal or cubic–tetragonal phase coexistence [47, 152] has been also reported in ultra-fine dense ceramics [152, 153]. In any case, the general trend is the reduction of temperature range for the tetragonal phase and an increasing amount of non-tetragonal modification at the expense of the tetragonal one, when reducing GS [153]. Since the polar phases are maintained in very fine structures, a critical temperature for the existence of polar distortion and ferroelectricity was not unambiguously determined by structural investigations.

15.4.2.2 Grain Size Dependence of Permittivity and Curie Temperature: Intrinsic versus Extrinsic Size Effects

Permittivity versus temperature dependence becomes depressed and broadened for small ceramic grain sizes, that is it becomes less temperature-sensitive by comparison with bulk $BaTiO_3$. An example of such dependence, which gives a general trend reported by the large majority of authors, is shown in Figure 15.5 for a series of dense $BaTiO_3$ nanostructured ceramics sintered by SPS, with grain sizes in the range of 50–1500 nm, similar to those reported earlier [27, 28]. One should stress that dielectric properties do not exclusively reflect the intrinsic ceramic properties, but they are also strongly dependent on extrinsic effects, as due to residual uncompensated charges and oxygen vacancies, giving rise to the Maxwell–Wagner phenomena, besides contributions determined by structural defects, porosity, and possible secondary phases. Therefore, it is difficult to compare dielectric data from different studies, since permittivity values are often affected by these phenomena.

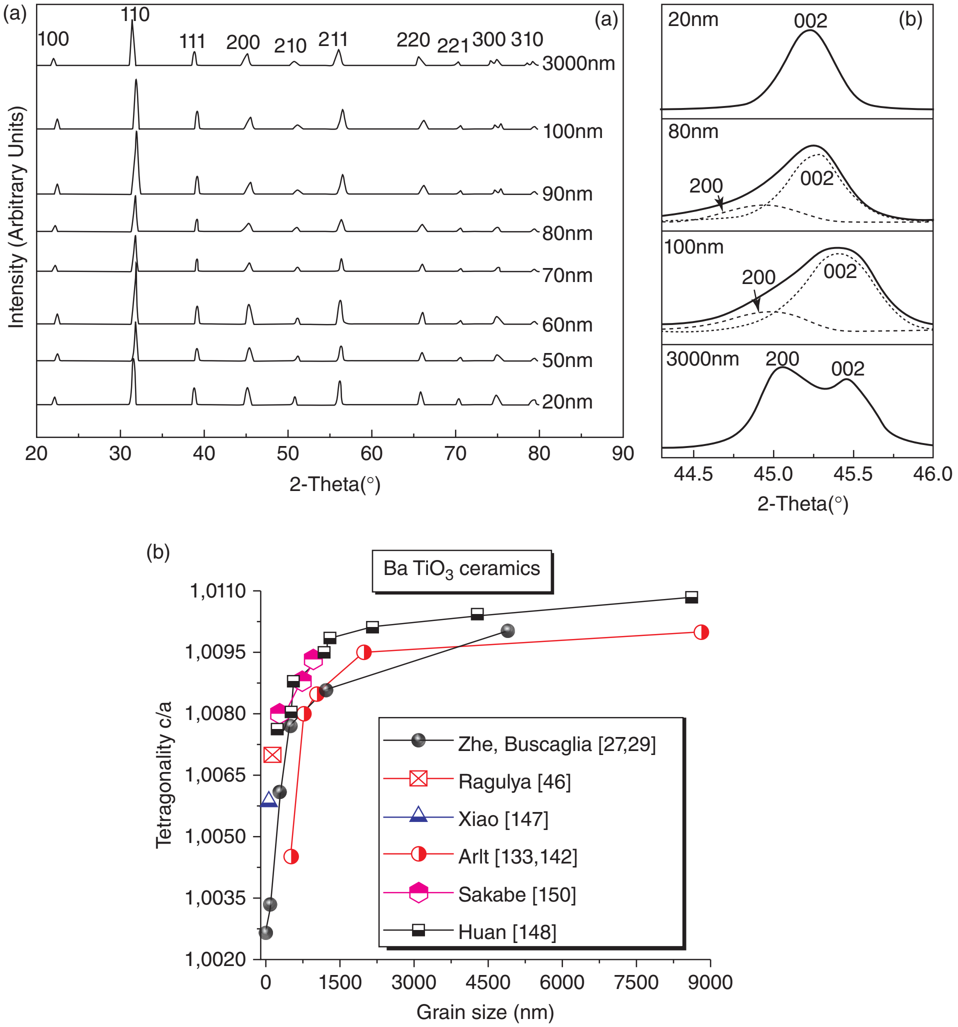

Figure 15.4 *(a) Diffraction profiles around 2θ = 45° (200-002 splitting) for BaTiO$_3$ with various grain sizes (reprinted with permission from [47]. Copyright © [2006] [The American Ceramic Society]). (b) Tetragonal distortion c/a as a function of grain size (data collected from [45] to [47]). For a color version of this figure, see color plate section.*

Usually the ultra-fine ceramics show quite reduced losses and the room temperature permittivity, the key parameter for application of BaTiO$_3$ nanostructured ceramics in MLCCs, shows a strong GS dependence.

Relevant room temperature dielectric data corresponding to dense ceramics with relative density above 95% with variable grain size, down to the smallest value ever reported of GS of 8 nm with ultrahigh density, are summarized in Figure 15.6(a) [27–33, 45, 46, 133, 142, 146, 148, 153–162]. All recent observations confirmed the early results of Arlt [133],

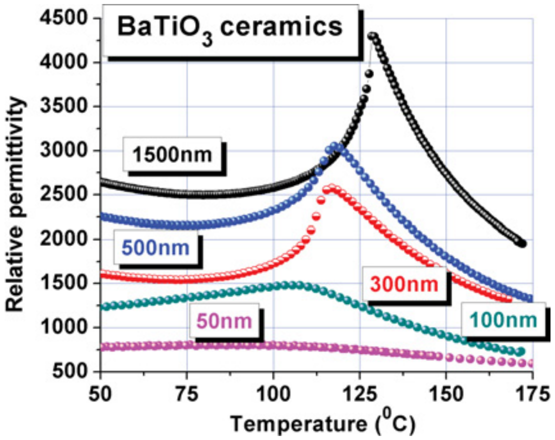

Figure 15.5 *Grain size dependence of permittivity versus temperature curves in dense nanostructured ceramics with GS in the range 50–1500 nm*

described in Section 15.4.1, concerning the enhanced values of room temperature permittivity and of piezoelectric coefficients for GS around ~1.1 μm [148, 160]. This behaviour was explained as due to extrinsic contributions of 90° ferroelectric domain walls [133, 148, 160] to the dynamic dielectric and piezoelectric properties. When reducing GS from coarse ceramics, the 90° domains width decreases and a high domain wall density is formed. The high domain wall density enhances the dipole and ionic polarizabilities and, as a consequence, the permittivity increases and reaches a maximum in the range of 6500–7000 for GS of about ~1.1 μm (Figure 15.6(a)). In contrast, these polarizabilities decrease when GS reduces below 1 μm. This indicates that extrinsic domain wall contributions are progressively weakened and eventually lost when the grain size decreases towards nanoscale, as

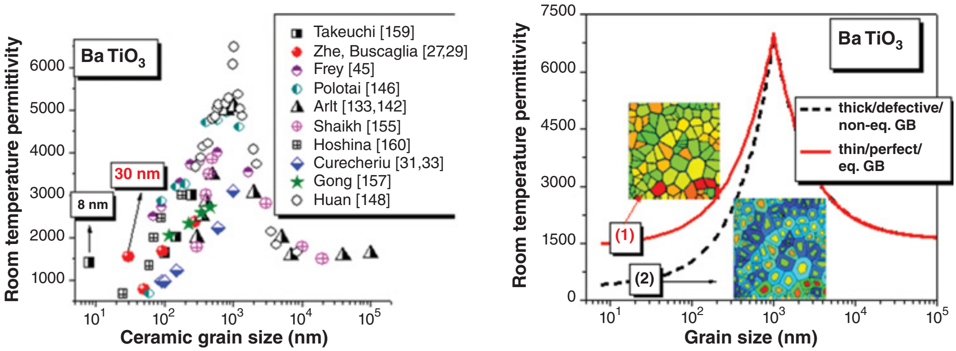

(a) (b)

Figure 15.6 *(a) Grain size dependence of the room temperature permittivity reported to date for dense BaTiO$_3$ ceramics. (b) Schematic representation of permittivity versus grain size in relationship to the ceramic grain boundaries: (1) thin, perfect equilibrium ground boundaries, (2) thick, defective, non-equillibrium grain boundaries. For a color version of this figure, see color plate section.*

the result of a strong enhancement of high compressive stresses associated with an increasing number of grain boundaries. The two competing effects create the general trend of the permittivity versus GS dependence reported in Figure 15.6(a).

If the permittivity data reported by various groups of above 1 μm are quite similar, a very wide spread range of values are noticed at nanoscale, where the micro/nanostructural characteristics like, for example, the nature and properties of grain boundaries (as derived by various synthesis routes and sintering procedures) play a major role. For example, authors reported room temperature permittivities in the range of 1750–4200 for GS = 500 nm, of 975–3000 for GS = 100 nm, of 650–2000 for GS = 50 nm, and of 600–1515 for GS ~ 20–30 nm. Understanding these variations is a key task for the MLCC applications, in which a small GS preserving high permittivity is highly required. There is general agreement concerning the fact that the type and properties of grain boundaries are essential for the properties of nanostructured $BaTiO_3$ ceramics, because their contribution (surface/interface contribution) prevail with respect to the volume contribution (grain bulk contribution) on to the effective functional properties. To explain the permittivity and Curie–Weiss decay at small GS, the widely accepted approach is to consider ceramics as composites, in which ferroelectric grains are surrounded by low permittivity, non-ferroelectric, or "dead-layer" grain boundaries (brick-layer model [45, 46, 27–30, 146]). Within this approach, by using effective field models, a renormalization of the Curie–Weiss law causing the reduction of permittivity and Curie–Weiss temperature takes place. If permittivity of the grain boundary is considered to be about 100–130, as for non-ferroelectric titanates, the thickness of such a grain boundary layer could be estimated to be in the range of 0.4–4 nm [45], of 2–3 nm [27–30], of 1.4 nm [163], and of 1 nm for GS = 30 nm [29] by comparison with 2.5 nm for GS = 50 nm [27]. Therefore, the dielectric size effect can be derived as an extrinsic property due to the "dilution effect" related to increasing weight of grain boundaries when reducing GS at nanoscale, if one admits that grain core intrinsic properties remain the same. Even these calculations provided approximate estimations for the thickness of such a "dead layer", for the idea is generally accepted that the dispersion of permittivity values reported for nanostructured ultra-fine ceramics is related to the different nature and properties of their grain boundaries. High permittivity values of permittivity even above 1500 can be reached in ultra-fine $BaTiO_3$ ceramics with GS down to tenths of nm, if the grain boundaries are clean (free of secondary phases), their thickness is minimized (below 1 nm), and the intergrain contact is perfect. The relationship between the nature of grain boundaries and permittivity values of ultra-fine ceramics is schematically described in Figure 15.6(b). By considering the essential role of grain boundaries, the synthesis and processing methods and parameters should be properly adapted and optimized to meet these desired conditions, in order to have high permittivity at ultra-fine GS. For some reasons not well clarified yet, it seems that in the recently reported almost full-dense ceramics of GS = 8 nm (Figure 15.6 (a)) such conditions related to the grain boundaries have been reached [158].

The reported values for the Curie temperature versus grain size are also quite spread, due to variations of the microstructural characteristics of nanostructured ceramics produced by different groups. Only few relevant data for extremely fine dense ceramics are available in the literature. All of them reported a gradual reduction of the Curie and Curie–Weiss temperatures when reducing GS down to nanoscale, as shown in Figure 15.7. Only Frey and Payne [45] found the same value for the Curie temperature, irrespective of GS, in a large range from 1.7 μm down to 40 nm, but their report lacks explanations for such

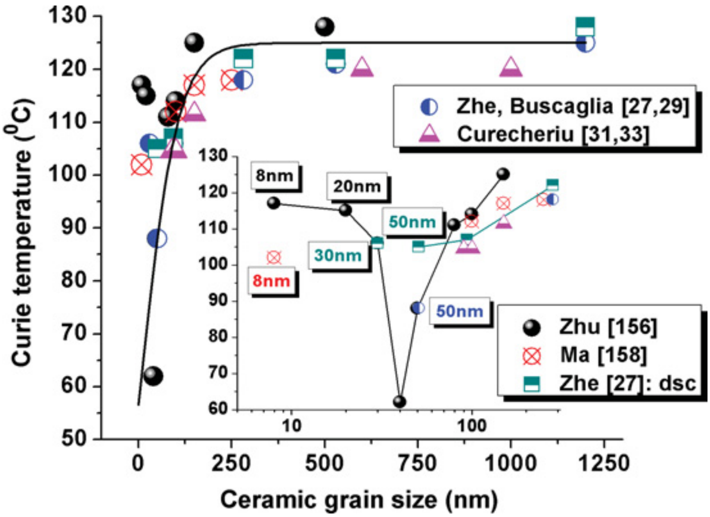

Figure 15.7 Curie temperature reported for dense $BaTiO_3$ ceramics (the line is a guide for the eyes). Inset: Curie temperatures for ceramics with grain sizes below 100 nm. All the represented Curie temperatures were determined by dielectric measurements, with the exception of data from [27], determined from differential scanning calorimetry (DSC). For a color version of this figure, see color plate section.

behavior and no comparison with other literature data for similar GS was provided. All the data in Figure 15.7 were collected only from macroscopic measurements, that is from the permittivity and calorimetry peaks assigned to the Curie temperature. The gradual reduction and broadening of permittivity peaks in ultra-fine ceramics makes it sometimes impossible to detect the ferro–para phase transitions. Vibrational spectroscopy (IR and Raman) analyses provided useful additional information about the room temperature polar states and location of the structural phase transitions, including the Curie (tetragonal–cubic) one [13, 28, 30, 47]. However, large ranges of temperatures with phase superposition or the impossibility to discriminate among the existing polar phases with low distortions (denoted as "pseudo-cubic") make it impossible to make an unambiguous determination of the Curie temperature in very fine ceramics.

The decay of the physical properties (e.g. tetragonality, as shown in Figure 15.4(b)), spontaneous polarization, or Curie temperature, as in Figure 15.7, when reducing GS down to nanoscale is a general trend in ferroics (see [62] and [63] and references therein), which leads to the idea of a critical GS limiting the stability of the polar state (ferroelectricity). Spread values for such critical temperatures, experimental limits to detect it at progressive smaller GS, the lack of samples with a large range of GS produced from the same powders in order to minimize the extrinsic effects related to inherent variations of microstructures, purity, defect levels related to the synthesis of powders, and sintering of ceramics left the existence of such a critical size still under debate [162]. Additionally, recent studies seem to indicate a ferroelectricity re-entrance for ultra-high dense ceramics with an extremely small GS (8 nm) [158, 156], accompanied by an increase in the Curie temperature and in permittivity by comparison with values corresponding to 40 and 50 nm (inset of Figure 15.7).

These ultra-fine dense samples show permittivity values of about 1500 and a Curie temperature in the range of 102–116 °C (Figures 15.6(a) and 15.7), which are extremely high for such a small GS. Even in our studies, we found a higher room temperature permittivity of about 1500 for samples with GS = 30 nm, by comparison with permittivity less than 1000 for GS = 50 nm [27, 29]. However, our mentioned series of nanostructured ceramics have been densified by SPS from different types of powders produced under various conditions and they might show differences not only related to their GS. The increase of Curie temperature for ultra-low GS, as indicated in the inset of Figure 15.7, claimed by the authors as re-entrance of ferroelectricity due to the high internal pressure in ultrafine ceramics [156, 158], contradicts the general trend of property versus GS dependence in ferroics. No other experimental observations confirmed such a trend. In any case, the range of GS below 100 nm is still highly interesting and needs further attention in order to clarify the origin of these contradictions.

15.4.2.3 High-Field Properties: Switching and Tunability

As a consequence of reducing the off-centre tetragonal distortion and the Curie temperature, the switching properties and $P(E)$ loops are affected when reducing GS, as comparatively shown for samples with GS = 90 nm and GS = 1000 nm in Figure 15.8(a). The same trend is noticed even at ultra-high fields in dense $BaTiO_3$ thick films with GS from 170 down to 24 nm produced by aerosol deposition [48, 160] in Figure 15.8(b). A similar trend was reported by many authors and is schematically drawn in Figure 15.8(c). The spontaneous and remanent polarization, rectangularity factor (P_r/P_{sat}), and coercive field tend to reduce with a diminishing GS. Coercive fields of about 2–3 kV cm^{-1} and values of remanent polarization P_r in the range of 8–10 μC cm^{-2} were reported for coarse $BaTiO_3$ ceramics with good saturation of polarization above 10 kV cm^{-1}, while for GS = 70 nm, P_r was only 3 μC cm^{-2} [45]. The reduction of GS down to 30 nm produced a linearization of the $P(E)$ dependence, similar to that shown in Figure 15.8(a) for GS = 90 nm, and practically no switching was observed until very high field values of 80 kV cm^{-1} [29]. Experimental macroscopic $P(E)$ loop evolution with diminishing GS is characterized by a progressive reduction of the remanent polarization and of the hysteresis area and a gradual tilting of the $P(E)$ loops, which remain unsaturated when GS is very fine [45, 159]. We have shown for our finest ceramic sample with GS = 30 nm with no leakage that switching was not produced even under very high fields and the $P(E)$ behavior describes a frozen-like polarization behavior. The tetragonal distortion c/a related to the spontaneous polarization (indeed it was reduced to about 1.0025 compared with c/a = 1.01 in coarse ceramics) indicated, however, a higher theoretical polarization than experimentally observed [29]. Therefore, the intrinsic reduction of tetragonality at small GS cannot alone describe such hysteresis loops for ultra-fine GS. Additional extrinsic factors mostly related to the absence of 90° domains below 1 μm have been proposed. The reduced number of 90° domains can strongly affect the polarization behavior and the piezoelectric properties of ferroelectric ceramics in $BaTiO_3$. According to Damjanovic [164], a strong reduction of the remanent polarization and of the Rayleigh constant in ceramics is expected if 90° domains are absent or pinned by defects. In ultrafine ceramics, the domain walls are clamped to a considerable degree by the large number of grain boundaries and defects.

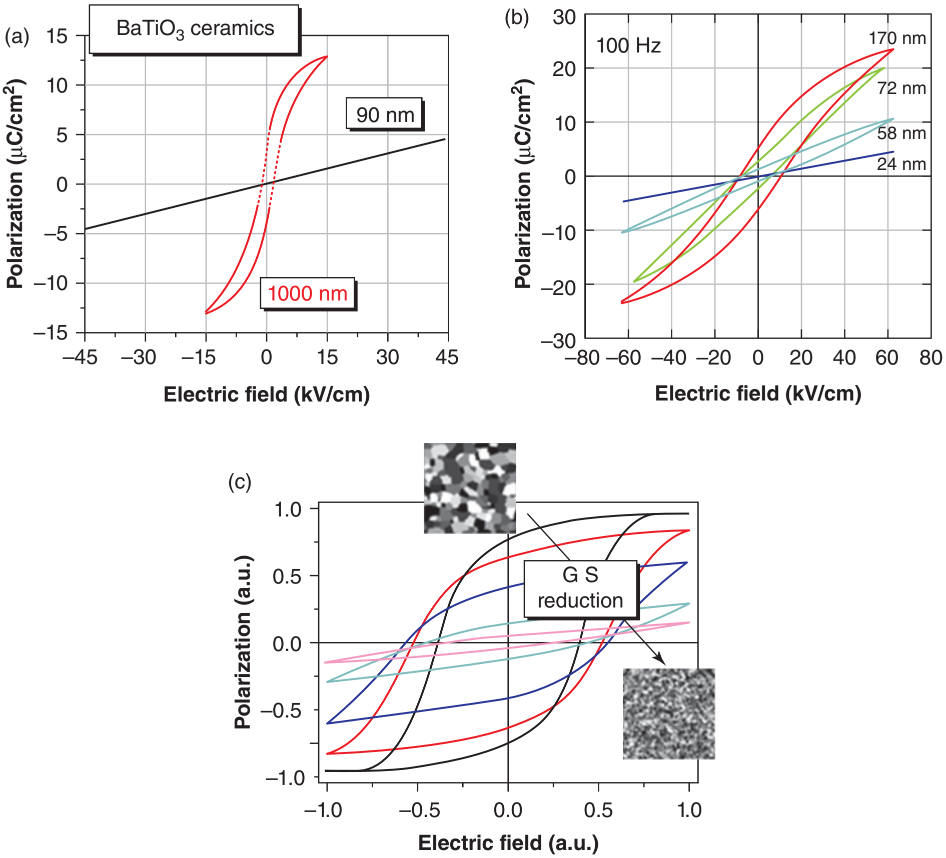

Figure 15.8 *The role of grain size on polarization–field dependence: (a) P(E) hysteresis loops for ceramics with GS = 90 nm and 1000 nm; (b) P(E) loops for ultra-high fields for thick* $BaTiO_3$ *films with GS in the range 24–170 nm (reproduced from [160] with permission. Copyright 2010. The Japan Society of Applied Physics); (c) schematic representation of the grain size dependence of P(E) hysteresis in ferroelectrics*

Based on a Rayleigh analysis, it was concluded that the suppression of ferroelectric hysteresis in nanocrystalline $BaTiO_3$ ceramics results from a frozen domain structure, which is stable under external fields, meaning that domain wall movement and nucleation of new domains becomes difficult when GS reduce down to a few tens of nanometers. The estimated threshold field corresponding to the onset of the irreversible domain wall movement and the Rayleigh constant values were found to be close to ones determined in doped ferroelectric ceramics with strongly pinned domain walls, rather than of pure coarse barium titanate. Grain boundaries and charged defects segregated at grain boundaries were considered to be responsible for the domain wall clamping and the hindrance of polarization reversal. In conclusion, high-field properties are also strongly influenced by extrinsic phenomena via grain boundaries. Even the macroscopic $P(E)$ response indicated almost no switching for such small GSs and the ferroelectric character was locally confirmed at nanoscale by

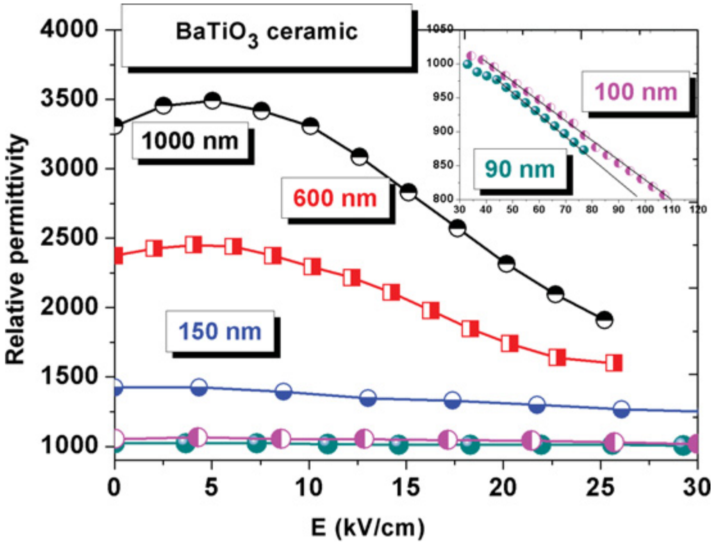

Figure 15.9 Permittivity versus field dependence for BaTiO$_3$ dense ceramics with various grain sizes down to 90 nm. Inset: high-field linear behavior for the finest ceramics

piezoforce microscopy experiments down to 50 nm [27], 30 nm [29], 20 nm [47], and 8 nm [47]. A general trend was observed of lowered local piezoelectric responses, smaller local hysteresis, and coercivity when reducing grain size, in comparison with bulk. In addition, for dense nanoceramics with clean grain boundaries, ferroelectric domains comprising more grains (transgranular ferroelectric domains) have been detected [27, 29].

Tunability properties of nanostructured ceramics were far less investigated than the low-field dielectric properties, with the exception of our series of studies [31–33]. Such a study was limited by the need for very high DC fields to probe the $\varepsilon(E)$ non-linearity and very good quality ceramics (dense and leakage-free) in order to hold high voltages. At low fields, permittivity firstly shows a slight increase, then reaches a maximum corresponding to the static coercive field, and then monotonously decreases up to the saturation for high fields (Figure 15.9). When reducing GS down to tenths of nm, a strong trend towards linearization of the $\varepsilon(E)$ curves was noticed at high fields (inset of Figure 15.9). Since a linear $\varepsilon(E)$ dependence is strongly needed, especially for high-power applications and for spectrally packed communication systems, this linear permittivity-field dependence was until now achieved through circuit design rather than by acting on the material parameters. Therefore, the reduction of ceramic GS at nanoscale seems to be a valid alternative method to induce such a linear permittivity–field $\varepsilon(E)$ variation. The remarkable linear decrease of permittivity with field, combined with the reduced permittivity below 1000 and reduction of domain wall associated losses at microwaves, makes BaTiO$_3$ nanostructured ceramics interesting for tunability applications. However, it is worth mentioning that such a linear feature is typical of very high fields, which can be easily reached in film structures. In conclusion, the grain size reduction in BaTiO$_3$ to nanoscale seems to be an alternative route to the traditional ones to accomplish the requirements of high-tunability, non-hysteretic

$\varepsilon(E)$ dependence, and permittivity in the range of 1000, which are requirements for tunable applications.

The explanation for the permittivity reduction and linearization of the $\varepsilon(E)$ dependence when reducing GS was given by using a model of composite to describe the nanostructured ceramics, in which a ferroelectric core (grain bulk) is surrounded by a non-ferroelectric low-permittivity layer (grain boundary). By comparison with other approaches in which effective field models gave an estimation of the nanoceramic low-field permittivity [45, 163], we proposed a finite element model [31,32], in which the role of local fields determined by specific ceramic nano/microstructures could be considered in calculations. This approach is described in detail in Chapter 18. What is important to notice is the fact that in a real ceramic structure, the local field producing switching or non-linear permittivity behavior is never equal to the applied field, as in homogeneous coarse ceramics or single crystals. As small as the grain size is and as inhomogeneous becomes the local field, the average sample response will be strongly dependent on this field inhomogeneity. An important percentage of the applied field will actually act on the low-permittivity grain boundaries, which are perpendicular on the applied field direction, and the ferroelectric cores are subjected to much smaller fields. Therefore, in nanostructured ceramics, higher fields than for coarse ceramics are necessary for inducing switching (Figure 15.5(b)) and permittivity non-linearity $\varepsilon(E)$. The local field reduction is the main reason for why no $P(E)$ and $\varepsilon(E)$ saturated loops have ever been reported in dense nanostructured ceramics. By considering that ferroelectric cores (grain bulk) behave as a normal ferroelectric and their permittivity non-linearity $\varepsilon(E)$ is similar to that in bulk, the tunability linearization in nanostructured ceramics can be described, as well as grain size dependence of the $P(E)$ loops, which is similar to ones from Figure 15.8 by this approach. In conclusion, by considering that no intrinsic ferroelectric decay is present in $BaTiO_3$ ceramics down to a few nanometers in the ceramic grains, the presence of a low-permittivity dielectric layer can explain the reduction of the low-field permittivity, of $P(E)$ loops and the $\varepsilon(E)$ linearization, as an extrinsic effect determined by the increasing weight of grain boundaries with respect to the grain cores when reducing GS at nanoscale. A high-energy XRD study performed on $BaTiO_3$ ceramics and powders with a grain size ranging from 1200 down to 5 nm demonstrated that the gradual loss of ferroelectricity when reducing grain size has an intrinsic origin related to the increased atomic positional disorder in spatially confined physical systems, without any conclusion being found relating to the nature of grain boundaries [63]. According to this study, even grain sizes of a few unit cells remain tetragonally distorted and ferroelectric, but the coherence length in the nanostructured materials is greatly reduced. If indeed intrinsic ferroelectricity is preserved in $BaTiO_3$ down to a few unit cells and only the structural coherence is lost at very small sizes, it means that the large majority of size-dependent reported properties can be explained as caused by a major contribution of the extrinsic effects and no critical size for the ferroelectric stability seems to exist as a fundamental limit. This means that ferroelectricity does not disappear abruptly at a critical system size [63], but only gradually weakens, below the instrumental limit detection.

15.4.2.4 Grain Boundaries

Together with sophisticated tools for observing the characteristics of grain boundaries in polycrystalline ceramic materials recently developed along with the increased capability for detailed chemical microanalysis and nano/microstructure determination, an understanding of the importance of grain boundaries for the ceramic effective properties has grown. In order to describe the nature and properties of ceramic grain boundaries, one should understand the grain boundary chemistry, which depends on the nature and arrangement of ions in the boundary. By comparison with grain bulk, grain boundary regions are rich in crystalline defects (dislocations and point defects). Usually, segregation of impurities takes place at grain boundaries, as well as at the triple points, due to the fact that solutes that lower the interface energy relative to the bulk phase decrease the free energy of the system by concentrating at the interfaces.

From an electrical point of view, the grain boundary is a space charge region. In pure materials, an intrinsic electric boundary charge arises from localized surface states for charged ions and for electrons and charged vacancies with energies different from the bulk values. The resulting boundary compositions, stoichiometry, and associated electric charges are strongly dependent on the nature of the ceramic material, chemical purity, processing, and sintering procedure. A general random grain boundary contains many steps and kinks that can act as sources and sinks for ion vacancies and the requirement for charge neutrality into the bulk gives rise to a boundary charge and an associated space charge region. Aliovalent ions in solution affect the vacancy concentrations in the bulk and the electric charge on the boundary, while heterovalent substitutions cause the formation of depleted regions at the grain boundaries and Schottky barriers (when a notable difference between the bulk and grain boundary conductivity exists due to the segregation of dopants at grain boundaries). Grain boundary electrical properties are essential in ceramics used for varistor applications such as zinc oxide-based compositions or positive temperature coefficient resistive materials such as n-doped semiconductor $BaTiO_3$ ceramics, for giant permittivity materials such as ceramics with semiconductor grains and high-insulating grain boundary layers, or in ferrite ceramics for which the impedance and magnetic properties are strongly dependent on the nature and properties of grain boundaries.

As already mentioned, a brick-layer model was usually employed for describing polycrystalline ferroelectric ceramics, with a ferroelectric grain bulk and a low-permittivity (linear dielectric) grain boundary. There are some physical reasons to suppose that the grain boundary region is less ferroelectric than bulk (sometimes denoted as the "dead layer"). (i) The presence of grain boundary structural defects (e.g. distortions, loss of long-range order, disordered or amorphous regions) and substitutions with dopants may cause a reduction or even the disappearance of ferroelectric character and transformation of this region into one similar to a linear dielectric. (ii) Polarization in perovskite ferroelectrics is assigned to a structural unit cell distortion and in polycrystalline ceramic the rotation of the polarization vector between adjacent grains would be accompanied by high stresses and deformations, which are usually not allowed due to energy considerations. Therefore, the only possibility for a transition between two different polarization states P_1 and P_2 with different orientations in two adjacent grains, when crossing a grain boundary, is by reducing the module of polarization of P_1 to zero at the boundary and growing from zero to the value of $P_{2,}$ while keeping their constant directions within each grain (i.e. a gradient of polarization module across the grain boundary). This means that the grain boundary region is characterized by a zero spontaneous polarization [108], which again corresponds to a non-ferroelectric material (linear dielectric). The hypothesis of a low-permittivity grain boundary can explain effective permittivity and tunability reduction when reducing grain size at nanoscale, by

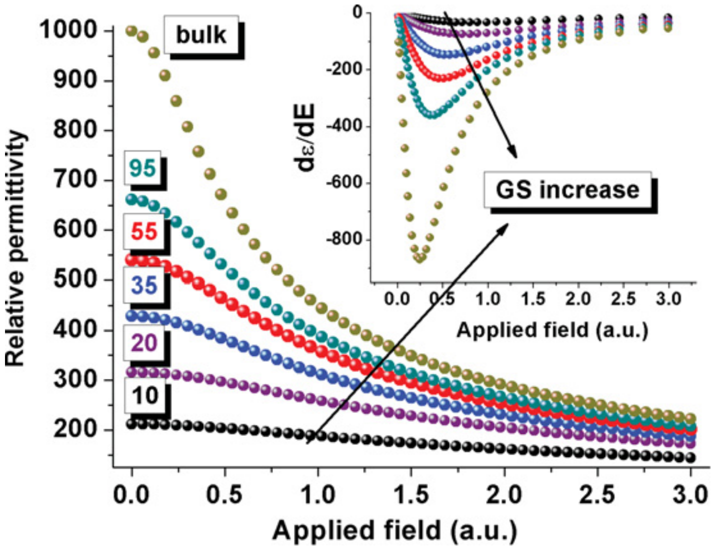

Figure 15.10 *Theoretical permittivity versus field dependence simulating the role of grain size on the tunability properties by considering a non-ferroelectric low-permittivity grain boundary layer and a tunable ferroelectric grain core*

taking into consideration the electric field fringes at the grain boundaries. The presence of a large number of grain boundaries in nanostructured ceramics completely changes the field distribution inside the ceramic volume into a highly inhomogeneous one. Practically, the highest voltage is applied to the low-permittivity grain boundaries, which are placed perpendicular to the field lines [32]. As a result, a much smaller field is actually acting on the ferroelectric part of the material and this explains why nanostructured ferroelectric ceramics show a frozen-like polarization or they need much larger fields for switching in comparison to their coarse counterparts. Due to the local field distribution inside the ceramic, tunability linearization in nanostructured ceramics as observed in Figure 15.9 can be explained by using a proper model for describing the core non-linearity (see Figure 15.10). The experimental observation of high leakage at grain boundaries is also related to the concentration of field lines at low-permittivity grain boundaries.

Literature reports also indicated a collective influence of grain boundaries on the observed domain structure and domain wall mobility in ferroelectrics, with coupling of domain structures across grain boundaries as a result of the long-range electric and elastic fields [165,166]. The role of the domain wall pinning centers located at grain boundaries in reducing the domain wall mobility and irreversible domain wall contributions to the dielectric and piezoelectric responses were also reported [9, 167]. Changes in the domain wall configurations at the grain boundary have been recently observed in PZT bicrystals with a single grain boundary [168]. Large-angle tilt grain boundaries result in a modification of the preferred domain wall orientation near the grain boundary and cause a decreased non-linear response, thus providing an explanation for the properties observed in nanostructured ceramics (reduced polarization switching and linearization of permittivity versus field dependence).

Although some hypothesis concerning the properties and thickness of grain boundaries in nanostructured ceramics have been assumed, only very few studies were aimed at probing and describing nanoceramic grain boundaries themselves. Grain boundary layers of about 1 nm thick were recognized as fine doped $BaTiO_3$ ceramics [150, 169], together with dopants located at the boundary layer and triple points of the grains for doped $BaTiO_3$, but no heterogeneous layer was found in the grain boundary of the pure $BaTiO_3$ nanostructured ceramics. The nature of the grain boundary was found to be strongly dependent on the processing of powders and sintering methods in nanostructured ceramics, which explains the spread of functional property data for ultra-fine nanostructured ceramics. For example, narrow GBs (planes formed throughout the entire extent by one and the same crystallographic planes of the adjoining crystals), atomically smooth and with a low angle, have been determined in controlled-rate sintered $BaTiO_3$ nanoceramics [46]. They were considered equilibrium GBs, are narrow and have a well-distinguished periodic structure, and do not contain any amorphous phase. Such a boundary is not a Schottky barrier and does not create any significant depolarization field into the ferroelectric material. Therefore, permittivity in samples with such types of GB is maintained very high, even for extremely small grain sizes (e.g. case (1) in Figure 15.7). Oppositely, in nanostructured ceramics sintered under high pressure, other two types of grain boundaries were formed: coherent twins and high-angle boundaries, which are usually incoherent because they had atomic structures with low atom densities, varying misorientation angles at a constant angle of misorientation between the grains, and have a low strength [46]. Such characteristics correspond to non-equilibrium grain boundaries, which exhibit variable atomic coordination and, consequently, are highly defective and have a high free volume. Such polycrystalline structures in the ferroelectric ceramic leads to stronger depolarization fields, lower dielectric permittivity, and increased dielectric losses (they correspond to case (2) in Figure 15.7). For comparison, the ultrafine ceramics with GS down to 8 nm [157, 159] with high values of permittivity and Curie temperature most probably contain perfect equilibrium defect-free grain boundaries.

Besides other grain size dependent functional properties in $BaTiO_3$ nanostructured ceramics, we end by mentioning the observation of an enhanced p-type of conductivity of about 1–2 orders in magnitude higher than in microcrystalline counterparts and with a lower activation energy for ceramics with a grain size as small as 35 nm [170] and it was explained as a reduction of oxidation enthalpy of nanocrystalline $BaTiO_3$. The grain size effect on the thermal conductivity in $BaTiO_3$ nanoceramics with GS in the range of 30–100 nm produced by a low-temperature high-pressure technique was also reported [171]. It was found that the thermal conductivity of $BaTiO_3$ nanoceramics systematically decreased when reducing GS and this observation may offer a tool to control thermal conductivity via grain size in nanoceramics. For the finest ceramics the thermal conductivity was similar to that for glasslike materials, whereas for larger grains it behaves as in crystalline dielectrics.

In conclusion, the impact of grain boundaries on the macroscopic functional properties of ferroelectric ceramics is enhanced when reducing their grain size down to tenths of nanometers due to the presence of a large amount of grain boundaries with respect to the bulk ceramic grain cores. Practically, the functional properties of nanostructured ceramics are determined to a large extent by their grain boundaries and the key lies in tailoring them for achieving useful characteristics required in applications is to understand, control, and engineer their grain boundaries.

15.5 Conclusions

Grain size dependent functional properties and mainly ferroelectric and dielectric characteristics of electroceramics remain a hot topic related both to basic science and mainly applicative interests. Since the first observations related to size-driven effects in ferroelectrics, important progress in understanding such phenomena has been achieved, also related to the progressive increase of the capability to produce dense ultra-fine structures with grain sizes down to a few tenths and even units of nanometers and of the instrumental ability to probe nanoscale properties. As grain sizes are so small, the functional properties become defined more by extrinsic phenomena rather than by an intrinsic reduction of ferroelectricity (spontaneous polarization and tetragonal distortion). The large majority of experimental data for nanostructured ceramics can be explained by considering inhomogeneous composite-like structures with grain boundaries and grain bulk regions with different structural, electrical, and mechanical properties. If properly processed, well-controlled ultra-thin, defect-free, and clean grain boundaries may be produced in nanostructured ceramics. For such grain boundaries, high values for the material constants (dielectric, ferroelectric, piezo- and pyroelectric) can be preserved even in ultra-fine $BaTiO_3$ nanostructures and these recent results give optimistic predictions for the possibility of achieving a volume functional efficiency beyond the present state of the art in future miniaturized electronic devices.

Acknowledgments

The authors are grateful to Dr Vincenzo Buscaglia and Dr Maria Teresa Buscaglia (Institute for Energetics and Interphases Genoa, Italy) for the fruitful discussions and long-lasting collaboration in the field of size effects in nanostructured $BaTiO_3$. The financial support from the Romanian Project PN-II-ID-PCE-2011-3-0745 and COST MP0904 Actions are highly acknowledged.

References

(1) Lines, M.E. and Glass, A.M. (1977) *Principles and Applications of Ferroelectrics and Related Materials*, Clarendon Press, Oxford.
(2) Jona, F. and Shirane, G. (1963) *Ferroelectric Crystals*, Elsevier, Amsterdam.
(3) Jaffe, B., Cook, W.R., and Jaffe, H. (1971) *Piezoelectric Ceramics*, Academic Press, London.
(4) Bell, A.J. (2008) Ferroelectrics: the role of ceramic science and engineering. *Journal of the European Ceramic Society*, **28**, 1307–1317.
(5) Valasek, J. (1920) Piezoelectric and allied phenomena in Rochelle salt. *Physical Review*, **15**, 537; and (1921) **17**, 475.
(6) Haertling, G.H. (1999) Ferroelectric ceramics: history and technology. *Journal of the American Ceramic Society*, **82** (4), 797–818.
(7) Jaffe, H. (1958) Piezoelectric ceramics. *Journal of the American Ceramic Society*, **41** (11]), Part II, 494–498.
(8) Xu, Y. (1991) *Ferroelectric Materials and Their Applications*, North-Holland Elsevier Science Publishers, Amsterdam.

(9) Damjanovic, D. and Demartin, M. (1996) The Rayleigh law in piezoelectric ceramics. *Journal of Physics D: Applied Physics*, **29**, 2057; and (1997) *Journal of Physics: Condensed Matter*, **9**, 4943.

(10) Bolten, D., Bottger, U., and Waser, R. (2003) Reversible and irreversible polarization processes in ferroelectric ceramics and thin films. *Journal of Applied Physics*, **93**, 1735–1742.

(11) Bassiri-Gharb, N., Fujii, I., Hong, E., et al. (2007) Domain wall contributions to the properties of piezoelectric thin films. *Journal of Electroceramics*, **19**, 47–65.

(12) Bhalla, A.S., Guo, R., and Roy, R. (2000) The perovskite structure – a review of its role in ceramic science and technology. *Materials Research Innovations*, **4**, 3–26.

(13) Petzelt, J. (2008) Soft mode behavior in cubic and tetragonal $BaTiO_3$ crystals and ceramics: review on the results of dielectric spectroscopy. *Ferroelectrics*, **375**, 156–164.

(14) Merz, W.J. (1949) The electric and optical behavior of $BaTiO_3$ single-domain crystals. *Physical Review*, **76**, 1221–1225.

(15) Tagantsev, A.K., Sherman, V.O., Astafiev, K.F., et al. (2007) Ferroelectric materials for microwave tunable applications. *Journal of Electroceramics*, **19**, 47–65.

(16) Vendik, O.G. and Zubko, S.P. (2000) Ferroelectric phase transition and maximum dielectric permittivity of displacement type ferroelectrics ($Ba_xSr_{1-x}TiO_3$). *Journal of Applied Physics*, **88**, 5343–5350.

(17) Steele, B.C.H., Newnham, R.E., and Evans, A.G. (1997) Ceramics, composites and intergrowths. *Current Opinion in Solid State and Materials Science*, **2**, 563–565.

(18) He, Y. (2004) Heat capacity, thermal conductivity, and thermal expansion of barium titanate-based ceramics. *Thermochimica Acta*, **419**, 135–141.

(19) Setter, N. and Waser, R. (2000) Electroceramic materials. *Acta Materialia*, **48**, 151–178.

(20) http://en.wikipedia.org/wiki/Ceramic_capacitor#Multi-layer_ceramic_capacitors_.28MLCC.29.

(21) Ho, J., Jow, T.R., and Boggs, S. (2010) Historical introduction to capacitor technology. *IEEE Electrical Insulation Magazine*, **26**, 20–25.

(22) Mitoseriu, L., Ricinschi, D., Harnagea, C., et al. (1996) Grain size dependence of switching properties of ferroelectric $BaTiO_3$ ceramics. *Japanese Journal of Applied Physics*, **35** (9B), 5210–5216.

(23) Tura, V., Mitoseriu, L., Papusoi, C., et al. (1998) Investigation of grain size influence on the ferroelectric-to-paraelectric phase transition in $BaTiO_3$ ceramics by means of AC calorimetry. *Japanese Journal of Applied Physics*, **37** (4A), 1950–1954.

(24) Mitoseriu, L., Tura, V., Papusoi, C., et al. (1999) A comparative study of the grain-size effects on ferro–para phase transition in barium titanate ceramics. *Ferroelectrics*, **223**, 99–106.

(25) Mitoseriu, L., Tura, V., Ricinschi, D., and Harnagea, C. (2000) Grain size dependence of the Rayleigh coefficients of BT ceramics. *Ferroelectrics*, **240**, 51–58.

(26) Mitoseriu, L., Harnagea, C., Nanni, P., et al. (2004) Local switching properties of dense nanocrystalline $BaTiO_3$ ceramics. *Applied Physics Letters*, **84**, 2418–2420.

(27) Zhao, Z., Buscaglia, V., Viviani, M., et al. (2004) Size effect on ferroelectric behavior of dense nanocrystalline $BaTiO_3$ ceramics. *Physical Review B*, **70**, 024107.

(28) Buscaglia, M.T., Buscaglia, V., Viviani, M., et al. (2004) Ferroelectric, properties of dense nanocrystalline $BaTiO_3$ ceramics. *Nanotechnology*, **15**, 1113–1117.

(29) Buscaglia, M.T., Viviani, M., Buscaglia, V., et al. (2006) High dielectric constant and frozen macroscopic polarization in dense nanocrystalline $BaTiO_3$ ceramics. *Physical Review B*, **73**, 064114.

(30) Buscaglia, V., Buscaglia, M.T., Viviani, M., et al. (2006) Grain size and grain boundary – related effects on the properties of nanocrystalline barium titanate ceramics. *Journal of the European Ceramic Society*, **26**, 2889–2898.

(31) Curecheriu, L., Buscaglia, M.T., Buscaglia, V., et al. (2010) Grain size effect on the nonlinear dielectric properties of barium titanate ceramics. *Applied Physics Letters*, **97**, 242909.

(32) Padurariu, L., Curecheriu, L., Buscaglia, V., and Mitoseriu, L. (2012) Field-dependent permittivity in nanostructured BaTiO3 ceramics: modeling and experimental verification. *Physical Review B*, **85**, 224111.

(33) Curecheriu, L., Balmus, S.B., Buscaglia, M.T., et al. (2012) Grain size-dependent properties of dense nanocrystalline barium titanate ceramics. *Journal of the American Ceramic Society*, **95**, 3912–3921.

(34) Randall, C.A., Kim, N., Kucera, J.P., et al. (1998) Intrinsic and extrinsic size effects in fine-grained morphotropic-phase-boundary lead zirconate titanate ceramics. *Journal of the American Ceramic Society*, **81**, 677–688.

(35) Akdogan, E.K., Leonard, M.R., and Safari, A. (1999) Size effects in ferroelectric ceramics, in *Handbook of Low and High Dielectric Constant Materials for Applications*, vol. 2, edited by H.S. Nalwa, Academic Press, San Diego, CA.

(36) Shaw, T.M., Trolier-McKinstry, S., and McIntyre, P.C. (2000) The properties of ferroelectric films at small dimensions. *Annual Review of Materials Science*, **30**, 263–298.

(37) Lichtensteiger, C., Dawber, M. and Triscone, J.M. (2007) In *Physics of Ferroelectrics: A Modern Perspective, Topics in Applied Physics*, vol. 105, edited by K. Rabe, K.H. Ahn, and J.M. Triscone), Springer Verlag, Berlin, Heidelberg, pp. 305–338.

(38) Gregg, J.M. (2009) Ferroelectrics at the nanoscale. *Physica Status Solidi* (a), **206**, 577–587.

(39) Zhong, W.L., Wang, Y.G., Zhang, P.L., and Qu, B.D. (1994) Phenomenological study of the size effect on phase transitions in ferroelectric particles. *Physical Review B*, **50**, 698.

(40) Li, S., Eastman, J.A., Li, Z., et al., (1996) Size effects in nanostructured ferroelectrics. *Physics Letters A*, **212**, 341.

(41) Jiang, B. and Bursill, L.A. (1999) Phenomenological theory of size effects in ultrafine ferroelectric particles of lead titanate. *Physical Review B*, **60**, 9978.

(42) Glinchuk, M.D., Eliseev, E.A., and Morozovska, A.N. (2008) Superparaelectric phase in the ensemble of noninteracting ferroelectric nanoparticles. *Physical Review B*, **78**, 134107.

(43) Yashima, M., Hoshina, T., Ishimura, D., et al. (2005) Size effect of crystal structure of barium titanate nano-particles. *Journal of Applied Physics*, **98**, 014313.

(44) Ray, S., Kolenko, Y., Fu, D., et al. (2006) Direct observation of ferroelectricity in quasi-zero-dimensional barium titanate nanoparticles. *Small*, **2**, 1427–1431.

(45) Frey, M.H. and Payne, D.A. (1996) Grain-size effect on structure and phase transformations for barium titanate. *Physical Review B*, **54**, 3158; and Frey, M.H., Xu, Z., Han, P., and Payne, D.A. (1998) The role of interfaces on an apparent grain size effect on the dielectric properties for ferroelectric barium titanate ceramics. *Ferroelectrics*, **206–207**, 337.

(46) Ragulya, A.V., Skorokhod, V.V., and Polotai, A.V., (2001) Synthesis and sintering of nanocrystalline $BaTiO_3$ powder under non-isothermal conditions. Structure, grain boundaries and dielectric properties obtained by various sintering methods. *Powder Metallurgy and Metal Ceramics*, **40**, 25–33.

(47) Deng, X., Wang, X., Wen, H., et al. (2006) Phase transitions in nanocrystalline barium titanate ceramics prepared by spark plasma sintering. *Journal of the American Ceramic Society*, **89**, 1059–1064; Wang, X., Deng, X., and Wen, Li, H. L. (2006) Phase transition and high dielectric constant of bulk dense nanograin barium titanate ceramics. *Applied Physics Letters*, **89**, 162902; and Deng, X.Y., Li, D.J., Li, J.B., et al. (2009) Preparation of nanocrystalline $BaTiO_3$ ceramics. *Science China Serie E – Technological Sciences*, **52**, 1730–1734.

(48) Hoshina, T., Furuta, T., Yamazaki, T., et al. (2012) Grain size effect on dielectric properties of $Ba(Zr, Ti)O_3$ ceramics. *Japanese Journal of Applied Physic*s, **51**, 09LC04-1-5.

(49) Dawber, M., Stucki, N., Lichtensteiger, C., et al. (2007) Tailoring the properties of artificially layered ferroelectric superlattices. *Advanced Materials*, **19**, 4153–4159.

(50) Schilling, A., Bowman, R.M., Catalan, G., et al. (2007) Morphological control of polar orientation in single-crystal ferroelectric nanowires. *Nano Letters*, **7**, 3787.

(51) Vrejoiu, I., Alexe, M., Hesse, D., and Gösele, U. (2009) Ferroelectric nanostructures. *Journal of Vacuum Science and Technology B*, **27**, 498.

(52) Ma, W.H., Harnagea, C., Hesse, D., and Gösele, U. (2003) Well-ordered arrays of pyramid-shaped ferroelectric BaTiO3 nanostructures. *Applied Physics Letters*, **83**, 3770.

(53) Saad, M.M., Baxter, P., Bowman, R.M., et al. (2004) Intrinsic dielectric response in ferroelectric nano-capacitors. *Journal of Physics: Condensed Matter*, **16**, L451–456.

(54) Cojocaru, C.V., Harnagea, C., Rosei, F., et al. (2005), Complex oxide nanostructures by pulsed laser deposition through nanostencils. *Applied Physics Letters*, **86**, 183107.

(55) Buscaglia, M.T., Harnagea, C., Dapiaggi, M., et al. (2009), Ferroelectric $BaTiO_3$ nanowires by a topochemical solid-state reaction. *Chemistry of Materials*, **21**, 5058.

(56) Schilling, A., Byrne, D., Catalan, G., et al. (2009), Domains in ferroelectric nanodots. *Nano Letters*, **9**, 3359.

(57) Roelofs, A., Schneller, T., Szot, K., and Waser, R. (2003) Towards the limit of ferroelectric nanosized grains. *Nanotechnology*, **14**, 250.

(58) Rudiger, A., Schneller, T., Roelofs, A., et al. (2005) Nanosize ferroelectric oxide – tracking down the superparaelectric limit. *Applied Physics A – Materials Science and Processing*, **80**, 1247–1255.

(59) Ahn, C.H., Rabe, K., and Triscone, J.M. (2004) Ferroelectricity at the nanoscale: local polarization in oxide thin films and heterostructures. *Science*, **203**, 488–491.

(60) Dawber, M., Rabe, K.M., and Scott, J.F. (2005) Physics of thin-film ferroelectric oxides. *Reviews of Modern Physics*, **77**, 1083.

(61) Chang, L.W., McMillen, M., Morrison, F.D., et al. (2008) Size effects on thin film ferroelectrics: experiments on isolated single crystal sheets. *Applied Physics Letters*, **93**, 132904.

(62) Chang, L.W., Alexe, M., Scott, J.F., and Gregg, M. (2009) Settling the "dead layer" debate in nanoscale capacitors. *Advanced Materials*, **21**, 4911–4914.

(63) Petkov, V., Buscaglia, V., Buscaglia, M.T., et al. (2008), Structural coherence and ferroelectricity decay in submicron- and nano-sized perovskites. *Physical Review B*, **78**, 054107.

(64) Wadhawan, V.K. (2000) *in Introduction to Ferroic Materials*, Gordon & Breach, New York.

(65) Roduner, E. (2006) In *Nanoscopic Materials: Size-Dependent Phenomena*, RSC, Cambridge, and references Therein.

(66) Rudiger, A., Schneller, T., Roelofs, A., et al. (2005) Nanosize ferroelectric oxides – tracking down the superparaelectric limit. *Applied Physics A – Materials Science and Processing*, **80**, 1247.

(67) Tiruvalam, R., Kundu, A., Soukhojak, A., et al. (2006) Observing the superparaelectric limit of relaxor $(Na_{1/2}Bi_{1/2})_{0.9}Ba_{0.1}TiO_3$ nanocrystals. *Applied Physics Letters*, **89**, 112901.

(68) Polking, M.J., Han, M.G., Yourdkhani, A., et al. (2012) Ferroelectric order in individual nanometre-scale crystals. *Nature Materials*, **11**,700–709.

(69) Ye, Z.G. (1998), Relaxor ferroelectric complex perovskites: structures, crystals, properties and phase transition. *Key Engineering Materials*, **155–156**, 81–122.

(70) Cohen, R.E. (1992) Origin of ferroelectricity in perovskite oxides. *Nature*, **358**, 136–138.

(71) Batra, I.P. and Silverman, B.D. (1972) Thermodynamic stability of thin ferroelectric films. *Solid State Communication*, **11**, 291–294.

(72) King-Smith, R.D. and Vanderbilt, D. (1992) A first-principles pseudopotential investigation of ferroelectricity in barium titanate. *Ferroelectrics*, **136**, 85; and (1994) First-principles investigation of ferroelectricity in perovskite compounds. *Physical Review B*, **49**, 5828.

(73) Zhong, W., King-Smith, R.D., and Vanderbilt, D. (1994) Giant LO-TO splittings in perovskite ferroelectrics. *Physical Review Letters*, **72**, 3618.

(74) Zhong, W., Vanderbilt, D., and Rabe, K.M. (1995) First-principles theory of ferroelectric phase transitions for perovskite compounds: the case of $BaTiO_3$. *Physical Review B*, **52**, 6301.

(75) Deng, X.Y., Zhang, H.T., Li, T., et al. (2010) Ferroelectricity of nanocrystalline $BaTiO_3$ ceramics by first principle calculation. *Chinese Science Bulletin*, **55**, 2182–2185.

(76) Anoufa, M., Kiat, J.M., Kornev, I., and Bogicevic, C. (2013) Vortices of polarization in $BaTiO_3$ core–shell nanoceramics: calculations based on *ab initio* derived Hamiltonian versus Landau theory. *Physical Review B*, **88**, 144106.

(77) Kretschmer, R. and Binder, K. (1979) Surface effects on phase transitions in ferroelectrics and dipolar magnets. *Physical Review B*, **20**, 1065.

(78) Zhong, W.L., Wang, Y.G., Zhang, P.L., and Qu, B.D. (1994) Phenomenological study of the size effect on phase transitions in ferroelectric particles. *Physical Review B*, **50**, 698.

(79) Mehta, R.R., Silverman, B.D., and Jacobs, J.T. (1973) Depolarization fields in thin ferroelectric films. *Journal of Applied Physics*, **44**, 3379.

(80) Tybell, T., Ahn, C.H., and Triscone, J.M. (1999) Ferroelectricity in thin perovskite films. *Applied Physics Letters*, **75**, 856.

(81) Lichtensteiger, C., Triscone, J.M., Junquera, J., and Ghosez, P. (2005) Ferroelectricity and tetragonality in ultrathin $PbTiO_3$. *Physical Review Letters*, **94**, 047603.

(82) Bune, A.V., Fridkin, V.M., Ducharme, S., et al. (1998) Two-dimensional ferroelectric films. *Nature*, **391**, 874–877.

(83) Fong, D.D., Stephenson, G.B., Streiffer, S.K., et al. (2004) Ferroelectricity in ultrathin perovskite films. *Science*, **304**, 1650–1653.

(84) Almahmoud, E., Navtsenya, Y., Kornev, I., et al. (2004) Properties of $Pb(Zr,Ti)O_3$ ultrathin films under stress-free and open-circuit electrical boundary conditions. *Physical Review B*, **70**, 220102.

(85) Ghosez, P. and Rabe, K.M. (2000) Microscopic model of ferroelectricity in stress-free $PbTiO_3$ ultrathin films. *Applied Physics Letters*, **76**, 2767.

(86) Meyer, B. and Vanderbilt, D. (2001) *Ab initio* study of $BaTiO_3$ and $PbTiO_3$ surfaces in external electric fields. *Physical Review B*, **63**, 205426.

(87) Junquera, J. and Ghosez, P. (2003) Critical thickness for ferroelectricity in perovskite ultrathin films. *Nature*, **422**, 506–509.

(88) Dawber, M., Chandra, P., Littlewood, P.B., and Scott, J. F. (2003) Depolarization corrections to the coercive field in thin-film ferroelectrics. *Journal of Physics: Condensed Matter*, **15**, L393.

(89) Sai, N., Kolpak, A.M., and Rappe, A.M. (2005) Ferroelectricity in ultrathin perovskite films. *Physical Review B*, **72**, 020101.

(90) Fu, H. and Bellaiche, L. (2003) Ferroelectricity in barium titanate quantum dots and wires. *Physical Review Letters*, **91**, 257601.

(91) Naumov, I., Fu, H., and Bellaiche, L. (2004) Unusual phase transitions in ferroelectric nanodisks and nanorods. *Nature*, **432**, 737–740.

(92) Staichiotti, M.G. (2004) Ferroelectricity in $BaTiO_3$ nanoscopic structures. *Applied Physics Letters*, **84**, 251.

(93) Geneste, G., Bousquet, E., Junquera, J., and Ghosez, P. (2006) Finite-size effects in $BaTiO_3$ nanowires. *Applied Physics Letters*, **88**, 112906.

(94) Padilla, J. and Vanderbilt, D. (1997) *Ab initio* study of $BaTiO_3$ surfaces. *Physical Review B*, **56**, 1625.

(95) Shimada, T. and Kitamura, T. (2010) Multi-physics properties in ferroelectric nanowires and related structures from first-principles, in *Nanowires*, edited by P. Prete, INTECH, Croatia (ISBN 978-953-7619-79-4), pp. 414.

(96) Landau, L.D. (1965) *Collected Papers of L.D. Landau*, edited by D. TerHaar, Gordon and Breach, New York.

(97) Ginzburg, V.L. and Levanyuk, A.P. (1958) Light scattering near second-order phase-transition and Curie points. *Journal of Physics and Chemistry of Solids*, **6**, 51; and (1974) *Physics Letters A*, **47**, 345.

(98) Devonshire, A.F. (1949) Theory of barium titanate. *Part I. Philosophical Magazine*, **40**, 1040; (1951) Theory of barium titanate. Part II. *Philosophical Magazine*, **42**, 1065 (1951); and (1954) Theory of ferroelectrics. *Advances in Physics*, **3**, 85.

(99) Tilley, D.R. and Zeks, B. (1984) Landau theory of phase transitions in thick films. *Solid State Communications*, **49**, 823.

(100) Ricinschi, D., Harnagea, C., Papusoi, C., et al. (1998) Analysis of ferroelectric switching in finite media as a Landau-type phase transition. *Journal of Physics: Condensed Matter*, **10**, 477.

(101) Tan, E.K., Osman, J., and Tilley, D.R. (2001) Theory of switching in bulk first-order ferroelectric materials. *Physica Status Solidi (b)*, **228**, 765.

(102) Ricinschi, D., Tura, V., Mitoseriu, L., and Okuyama, M. (1999) Landau theory-based analysis of grain-size dependence of ferroelectric-to-paraelectric phase transition and its thermal hysteresis in BT ceramics. *Journal of Physics: Condensed Matter*, **11**, 1601.

(103) Chattopadhyay, S., Ayyub, P., Palkar V.R., and Multani, M. (1995) Size-induced diffuse phase transition in the nanocrystalline ferroelectric $PbTiO_3$. *Physical Review B*, **52**, 13177.

(104) Fong, D.D., Stephenson, G.B., Eastman J.A., et al. (2004) Ferroelectricity in ultrathin perovskite films. *Science*, **304**, 1650.

(105) Akdogan, E.K. and Safari, A. (2002) Phenomenological theory of size effects on the cubic–tetragonal phase transition in $BaTiO_3$ nanocrystals. *Japanese Journal of Applied Physics*, **41**, 7170.

(106) Morozovska, A.N., Glinchuk, M.D., and Eliseev, E.A. (2007) Phase transitions induced by confinement of ferroic nanoparticles. *Physical Review B*, **76**, 014102.

(107) Glinchuk, M.D. and Bykov, P.I. (2004) The peculiarities of the specific heat and dielectric permittivity related to the grain size distribution in ferroelectric nanomaterials. *Journal of Physics: Condensed Matter*, **16**, 6779.

(108) Shih, W.Y., Shih, W.H., and Aksay, I.A. (1994) Size dependence of the ferroelectric transition of small BaTiO3 particles – effect of depolarization. *Physical Review B*, **50**, 15575.

(109) Zhong, W.L. (1998) Particulate ferroelectrics: finite size effects. *Journal of the Korean Physical Society*, **32**, S265–S269.

(110) Liu, G. and Nan, C.W. (2005) Thickness dependence of polarization in ferroelectric perovskite thin films. *Journal of Physics D: Applied Physics*, **38**, 584.

(111) Cao, H.X., Wu, Y.Z., Dong, W., and Li, Z.Y. (2003) Impact of stress and long-range interaction on ultrathin ferroelectric films. *Physica Status Solidi (b)*, **238**, 213.

(112) Zembilgotov, A.G., Pertsev, N.A., and Waser, R. (2005) Phase states of nanocrystalline ferroelectric ceramics and their dielectric properties. *Journal of Applied Physics*, **97**, 114315.

(113) Fang, C., Chen, L.Y., and Zhou, D.X. (2013) Influence of domain on grain size effects of the dielectric properties of $BaTiO_3$ nanoceramics and nanoparticles. *Physica B*, **409**, 83–86.

(114) Hong, J. and Fang, D. (2008) Size-dependent ferroelectric behaviors of $BaTiO_3$ nanowires. *Applied Physics Letters*, **92**, 012906.

(115) Glinchuk, M.D., Eliseev, E.A., Stephanovich, V.A., and Farhi, R. (2003) Ferroelectric thin films properties: depolarization field ferroelectric thin film properties – depolarization field and renormalization of a “bulk” free energy coefficients. *Journal of Applied Physics*, **93**, 1150.

(116) Akcay, G., Alpay, S.P., Rossetti, G.A., and Scott, J.F. (2008) Influence of mechanical boundary conditions on the electrocaloric properties of ferroelectric thin films. *Journal of Applied Physics*, **103**, 024104.

(117) Ishibashi, Y. (1990) Structure and physical properties of domain walls. *Ferroelectrics*, **104**, 299.

(118) Omura, M., Adachi, H., and Ishibashi, Y. (1991) Simulations of ferroelectric characteristics using a one-dimensional lattice model. *Japanese Journal of Applied Physics*, **30**, 2384.

(119) Ricinschi, D. and Okuyama, M. (2002) Relationships between macroscopic polarization hysteresis and local piezoresponse of fatigued Pb(Zr, Ti)O_3 films within a Landau theory-based lattice model. *Applied Physics Letters*, **81**, 4040.

(120) Brown Jr, W.F. (1963) *Micromagnetics*, John Wiley & Sons, Inc., New York; and Wang, Y.G., Zhong, W.L., and Zhang, P.L. (1997) Ferroelectric films described by transverse Ising model with long-range interactions. *Solid State Communications*, **101**, 807.

(121) Williams, W. and Dunlop, D.J. (1989) Three-dimensional micromagnetic modelling of ferromagnetic domain structure. *Nature*, **377**, 634; and Zhong, W.L. (1998) Particulate ferroelectrics: finite size effects. *Journal of the Korean Physical Society*, **32**, S265.

(122) Wang, C.L., Xin, Y., Wang, X.S., and Zhong, W.L. (2000) Size effects of ferroelectric particles described by the transverse Ising mode. *Physical Review B*, **62**, 11423.

(123) Vu-Quoc, L., Srinivas, V., and Zhai, Y. (2003) Finite-element analysis of advanced multilayer capacitors: field computation and post-processing for lumped parameters. *International Journal for Numerical Methods in Engineering*, **58**, 397.

(124) Kim, S.J. and Jiang, Q. (2002) A finite element model for rate-dependent behavior of ferroelectric ceramics. *International Journal of Solids and Structures*, **39**, 1015.

(125) Li, J.H., Chen, L., Nagarajan, V., et al. (2004) Finite element modeling of piezoresponse in nanostructured ferroelectric films. *Applied Physics Letters*, **84**, 2626.

(126) Meyer, V., Sallese, J.M., Fazan, P., et al. (2003) Modeling the polarization in ferroelectric materials: a novel analytical approach. *Solid-State Electronics*, **47**, 1479–1486.

(127) Stancu, A., Ricinschi, D., Mitoseriu, L., et al. (2003) First order reversal curves diagram for the characterization of ferroelectric switching. *Applied Physics Letters*, **83**, 3767–3669.

(128) Stoleriu, L., Stancu, A., Mitoseriu, L., et al. (2006) Analysis of the switching properties of porous ferroelectric ceramics by means of the first-order reversal curves (FORC) diagrams. *Physical Review B*, **74**, 174107.

(129) Jiles, D.C. and Atherton, D.L. (1986) Theory of ferromagnetic hysteresis. *Journal of Magnetism and Magnetic Materials*, **61**, 48.

(130) Smith, R.C. and Hom, C.L. (1999) A domain wall model for ferroelectric hysteresis, in *SPIE, Smart Structures and Materials*, vol. **3667**, Newport Beach, CA, March 1–4, p. 150.

(131) Kniepkamp, H. and Heywang, W.Z. (1954) Depolarization effects in polycrystalline $BaTiO_3$. *Zeitschrift für Angewandte Physik*, **6**, 385.

(132) Jonker, G.H and Noorlander, W. (1962) Grain size of sintered barium titanate, in *Science of Ceramics*, Academic Press, London.

(133) Arlt, G., Hennings, D., and de With, G. (1990) Dielectric properties of fine-grained barium titanate ceramics. *Journal of Applied Physics*, **58**, 1619; and Arlt, G. (1985) Twinning in ferroelectric and ferroelastic ceramics: stress relief. *Journal of Materials Science*, **25**, 2655.

(134) Kinoshita, K. and Yamaji, A. (1976) Grain-size effects on dielectric properties in barium titanate ceramics. *Journal of Applied Physics*, **47**, 371.

(135) Kanata, K., Yoshikawa, T., and Kubota, K. (1987) Grain-size effects on dielectric phase transition of $BaTiO_3$ ceramics. *Solid State Communication*, **62**, 765.

(136) Uchino, K., Sadanaga, E., and Hirose, T. (1989) Dependence of the crystal structure on particle size in barium titanate. *Journal of the American Ceramic Society*, **72**, 1555.

(137) Uchino, K., Sadanaga, E., Oonishi, et al. (1990) *Ceramic Dielectrics – Ceramic Transactions*, American Ceramic Society, Westerville.

(138) Uchino, K. (2000) *Ferroelectric Devices*, Marcel Dekker, Inc.

(139) Hennings, D. Klee, M., and Waser, R. (1991) Advanced dielectrics – bulk ceramics and thin-films. *Advanced Materials*, **3** (7–8), 334–340.

(140) Zhong, W., Zhang, P., Wang, Y., and Ren, T. (1994) Size effect on the dielectric properties of $BaTiO_{3.}$ *Ferroelectrics*, **160**, 55.

(141) Lee, B.W. and Auh, K.H. (1995) Effects of grain size and mechanical processing on the dielectric properties of $BaTiO_{3.}$ *Journal of Materials Research*, **10**, 1418.

(142) Arlt, G. (1990) The influence of microstructure on the properties of ferroelectric ceramics. *Ferroelectrics*, **104**, 217.

(143) Smolenskii, S.A., Bokov, V.A., Isupov, V.A., et al. (1984) *Ferroelectrics and Related Materials*, Gordon and Breach, New York.

(144) Hungria, T., Galy, J., and Castro, A. (2009) Spark plasma sintering as a useful technique to the nanostructuration of piezo-ferroelectric materials. *Advanced Engineering Materials*, **11**, 615–631.

(145) Maglia, F., Tredici, I.G., and Anselmi-Tamburini, U. (2013) Densification and properties of bulk nanocrystalline functional ceramics with grain size below 50 nm. *Journal of the European Ceramic Society*, **33**, 1045–1066.

(146) Polotai, A.V., Ragulya, A.V., and Randall, C.A. (2003) Preparation and size effect in pure nanocrystalline barium titanate ceramics. *Ferroelectrics*, **288**, 93–102.

(147) Xiao, C.J., Zhang, W.W., Chi, Z.H., et al. (2007) Ferroelectric $BaTiO_3$ nanoceramics prepared by a three-step high-pressure sintering method. *Physica Status Solidi (a)*, **204**, 874–880.

(148) Huan, Y., Wang, X., Fang, J., and Li, L. (2013) Grain size effects on piezoelectric properties and domain structure of $BaTiO_3$ ceramics prepared by two-step sintering. *Journal of the American Ceramic Society*, **96** (11), 3369–3371; and (2014) Grain size effect on piezoelectric and ferroelectric properties of $BaTiO_3$ ceramics. *Journal of the European Ceramic Society*, **34**, 1445–1448.

(149) Buscaglia, M.T. and Buscaglia, V., unpublished work.

(150) Sakabe, Y., Wada, N., and Hamaji, Y. (1998) Grain size effects on dielectric properties and crystal structure of fine-grained $BaTiO_3$ ceramics. *Journal of the Korean Physical Society*, **32**, S260–264.

(151) Lin, S., Lu, T., Jin, C., and Wang, X. (2006) Size effect on the dielectric properties of $BaTiO_3$ nanoceramics in a modified Ginsburg–Landau–Devonshire thermodynamic

theory. *Physical Review B*, **74**, 134115; and Fang, C., Zhou, D.X., and Gong, S.P. (2010) Size-induced phase transition in $BaTiO_3$ nanoceramics described by nanodomains and long-range interaction. *Modern Physics Letters B*, **24**, 2161–2170.

(152) Xiao, C.J., Jin, C.Q., and Wang, X.H. (2008) Crystal structure of dense nanocrystalline $BaTiO_3$ ceramics. *Materials Chemistry and Physics*, **111**, 209–212.

(153) Li, B., Wang, X., Li, L., et al. (2004) Dielectric properties of fine-grained $BaTiO_3$ prepared by spark-plasma-sintering. *Materials Chemistry and Physics*, **83**, 23–28.

(154) Zheng, P., Zhang, J.L., Tan, Y.Q., and Wang, C.L. (2012) Grain-size effects on dielectric and piezoelectric properties of poled $BaTiO_3$ ceramics. *Acta Materialia*, **60**, 5022–5030.

(155) Shaikh, A.S., Vest, R.W., and Vest, G. (1989) Dielectric properties of ultrafine grained $BaTiO_3$. *IEEE Ultrasonics, Ferroelectrics and Frequency Control*, **36**, 407–412.

(156) Zhu, J.L., Lin, S., Feng, S.M., et al. (2012) Pressure tuned ferroelectric reentrance in nano-$BaTiO_3$ ceramics. *Journal of Applied Physics*, **112**, 124107.

(157) Gong, H., Wang, X., Zhang, S., et al. (2014) Grain size effect on electrical and reliability characteristics of modified fine-grained $BaTiO_3$ ceramics for MLCCs. *Journal of the European Ceramic Society*, **34**, 1733–1739.

(158) Ma, S., Wang, X., Zhou, J., et al. (2010) Thermal stability of the nanostructured $BaTiO_3$ determined by long and short range interactions: a dual-shell model. *Journal of Applied Physics*, **107**, 064102.

(159) Takeuchi, T., Capiglia, C., Balakrishnan, N., et al. (2002) Preparation of fine-grained $BaTiO_3$ ceramics by spark plasma sintering. *Journal of Materials Research*, **17**, 575–581.

(160) Hoshina, T., Furuta, T., Kigoshi, Y., et al. (2010) Size effect of nanograined $BaTiO_3$ ceramics prepared by aerosol deposition method. *Japanese Journal of Applied Physics*, **49**, 09MC02; and Hoshina, T. (2013) Size effect of barium titanate: fine particles and ceramics. *Journal of the Ceramic Society of Jap*an, **121**, 156–161.

(161) Yang, C.C. and Jiang, Q. (2005) Size and interface effects on critical temperatures of ferromagnetic, ferroelectric and superconductive nanocrystals. *Acta Materialia*, **53**, 3305–3311.

(162) Mitoseriu, L. and Buscaglia, V. (2011) About the superparaelectric state in $BaTiO_3$-based nanocrystals: comment on "high K capacitors and OFET gate dielectrics from self-assembled $BaTiO_3$ and $(Ba,Sr)TiO_3$ nanocrystals in the superparaelectric limit". *Advanced Functional Materials*, **21**, 3210–3211.

(163) Emelyanov, Yu., Pertsev, N.A., Hoffmann-Eifert, S., et al. (2002) Grain-boundary effect on the Curie–Weiss law of ferroelectric ceramics and polycrystalline thin films: calculation by the method of effective medium. *Journal of Electroceramics*, **9**, 5–16.

(164) Damjanovic, D. (1998) Ferroelectric, dielectric and piezoelectric properties of ferroelectric thin films and ceramics. *Reports on Progress in Physics*, **61**, 1267.

(165) Cao, W. and Randall, C.A. (1996) Grain size and domain size relations in bulk ceramic ferroelectric materials. *Journal of Physics and Chemistry of Solids*, **57**, 1499.

(166) Jang, J.W., Youn, H.J., Byun, C., et al. (1999) Ferroelectric domain structures of polycrystalline $PbTiO_3$ thin films prepared by MOCVD. *Ferroelectrics*, **227**, 15.

(167) Griggio, F. and Trolier-McKinstry, S. (2010) Grain size dependence of properties in lead nickel niobate–lead zirconate titanate films. *Journal of Applied Physics*, **107**, 024105.

(168) Marincel, D.M., Zhang, H., Kumar, A., et al. (2014) Influence of a single grain boundary on domain wall motion in ferroelectrics. *Advanced Functional Materials*, **24**, 1409–1417.

(169) Wada, N., Hiramatsu, T., Tamura, T., and Sakabe, Y. (2008) Investigation of grain boundaries influence on dielectric properties in fine-grained $BaTiO_3$ ceramics without the core–shell structure. *Ceramics International*, **34**, 933–937.

(170) Guo, X., Pithan, C., Ohly, C., et al. (2005) Enhancement of p-type conductivity in nanocrystalline $BaTiO_3$ ceramics. *Applied Physics Letters*, **86**, 082110; and Guo, X. (2013) Peculiar size effect in nanocrystalline $BaTiO_{3.}$ *Acta Materialia*, **61**, 1748–1756.

(171) Jezowski, A., Mucha, J., Pazik, R., and Strek, W. (2007) Influence of crystallite size on the thermal conductivity in $BaTiO_3$ nanoceramics. *Applied Physics Letters*, **90**, 114104.

16

The Effects of Ceramic Nanostructuring in High-Sensitivity Piezoelectrics

Harvey Amorín, Ricardo Jiménez, Jesús Ricote, Alicia Castro, and Miguel Algueró

Instituto de Ciencia de Materiales de Madrid (ICMM), Consejo Superior de Investigaciones Científicas (CSIC), Spain

16.1 Technological Drive for Ceramic Nanostructuring of High-Sensitivity Piezoelectrics

Ceramic nanostructuring is a highly topical area of research in ferroelectric materials that is driven by current technological trends in consumer electronics like, for instance, mobile phones; namely, that of enhancing performance while reducing size. The evolution of multilayer ceramic capacitors (MLCCs) is a case study of this trend. This ubiquitous discrete surface-mount electronic component (a mobile phone contains thousands of them) consist of high-permittivity $BaTiO_3$-based ceramic layers with Ni electrodes, and is mass produced to accomplish a range of functions from charge storage and power decoupling to signal filtering and general impedance matching in electronic circuits. MLCCs have undergone a steady improvement in performance over the last decades, from total and specific capacitances of 10^{-2} μF and 10 μF cm^{-3} in 1994, up to figures that approached 100 μF and 10^5 μF cm^{-3} in 2010, at the same time as the device was miniaturized below 1 mm^3. This was only possible by the simultaneous increase in the number of ceramic layers and decrease in their thickness. Current multilayer ceramic capacitors consist of nearly 1000

Nanoscale Ferroelectrics and Multiferroics: Key Processing and Characterization Issues, and Nanoscale Effects, First Edition. Edited by Miguel Algueró, J. Marty Gregg, and Liliana Mitoseriu.
© 2016 John Wiley & Sons, Ltd. Published 2016 by John Wiley & Sons, Ltd.

layers with an individual thickness well in the submicrometer range. This poses stringent requirements to grain size for reliability that must be reduced down to the nanoscale [1,2].

This electronic component has an electromechanical analog: the ceramic multilayer actuator (CMA), with which it not only shares its geometry but also its main development lines. Like that of MLCCs, the performance of CMAs (displacement/force under voltage or what is the same, the effective piezoelectric reponse) increases with the number of layers, and it is not jeopardized by the decrease of individual thickness (as long as dielectric breakdown does not take place at the resulting enhanced electric field). There is thus a technological drive for increasing the number of layers while maintaining, or even better reducing, thickness. Though developments somehow lag behind those of MLCCs, and current devices consist of hundreds of layers with an individual thickness of several tens of micrometers, an analogous evolution can be anticipated that will also ultimately lead to ceramic nanostructuring. CMAs based on ceramic layers of high-sensitivity piezoelectric Pb(Zr, Ti)O_3 with Ag–Pd or Cu electrodes are at the core of a number of technologies like piezoelectric fuel injectors, ink-jet printers, or positioning systems in scanning probe microscopes – to name three in the automotive and manufacturing sectors, and in nanotechnology, respectively [3,4].

Actuators are only one example among the wide range of successful technologies that have been enabled by Pb(Zr, Ti)O_3-based high-sensitivity piezoelectric ceramics, which also covers sensors (like acceleration ones, flowmeters), smart systems (basically combinations of sensors and actuators for applications like active vibration damping or adaptative optics), ultrasound transducers, either for non-destructive testing or for medical imaging, underwater acoustics, and many others [5,6]. Besides, piezoelectric ceramics are also under consideration for novel applications like energy harvesting and magnetoelectric transduction [7,8]. None of these piezoelectric ceramic technologies is oblivious to miniaturization.

A main line within this trend, research and development are intense in the integration of piezoelectric ceramic thick films; these understood as layers prepared by a powder suspension-based processing route, with mechanical elements in microelectromechanical systems (MEMS) for sensing and actuation [9]. Processing compatibility issues with the mechanical components require a significant decrease of the sintering temperatures from 1200–1400 °C down to 750–950 °C, which can have a strong impact on ceramic microstructure, and specifically in grain size that often enters the submicrometer range [10].

A further step forward in miniaturization is the use of thin-film technologies, and the film direct integration into silicon-based MEMS. Much more complex compatibility issues arise in this case, though developments benefit from those made in the frame of ferroelectric memories, and processes compatible with typical deposition temperatures between 600 and 700 °C have been developed [11]. Though textured, columnar films are usually preferred, and epitaxial films have also been successfully grown on Si-based substrates, further reduction of processing temperatures to also enable the integration of piezoelectric MEMS with the CMOS electronics, or even the substitution of Si by flexible organic substrates, naturally leads to extremely fine nanostructures with typical sizes approaching the reported thresholds for ferroelectricity [12,13].

In spite of the large potential impact of these miniaturized piezoelectric technologies, their feasibility, either they are bulk, thick, or thin-film technologies, will depend on how the functional properties of the high-sensitivity piezoelectric ceramic elements scale with the grain size decrease across the submicrometer range and down to the nanoscale. This is the issue this chapter deals with. However, and before describing the nanostructuring effects, the state of the art ferroelectric materials commercially used or under extensive investigation for piezoelectric technologies will be introduced.

16.2 State of the Art Ferroelectric Materials for Piezoelectric Technologies

16.2.1 Commercial, PZT-Based Hard and Soft Piezoceramics

State of the art ferroelectric material for piezoelectric technologies is perovskite ABO_3 $Pb(Zr,Ti)O_3$ (PZT) at the morphotropic phase boundary (MPB) between the rhombohedral $R3m$ and tetragonal $P4mm$ polymorphic phases [14]. The very good functional response of commercial PZT-based high-sensitivity piezoelectric ceramics is the combination of two effects: (1) an enhanced crystal piezoelectric response at the ferroelectric instability and (2) tailored extrinsic contributions associated with the dynamics of ferroelectric/ferroelastic domain walls [15].

Though piezoelectric coefficients across the $PbZrO_3$–$PbTiO_3$ binary system have long been known to show the largest figures at the morphotropic phase boundary [16], the actual mechanism responsible for this enhancement at the ferroelectric instability has not been understood until quite recently. It is currently acknowledged that the large piezoelectric response is a direct consequence of the presence of a monoclinic Cm phase between the rhombohedral and tetragonal polymorphs in the phase diagram, which provides a structural bridge between them [17]. The main features of the phase diagram across the MPB region are presented in Figure 16.1(a). Unlike the rhombohedral and tetragonal phases, whose spontaneous polarizations are fixed by symmetry to lie along the <111> and <001> directions, respectively, electrical polarization in the intermediate monoclinic phase is only constrained to lie within the (110) plane, and can actually rotate between the <111> and <001> directions under the electric field. This effect is especially significant at the monoclinic–tetragonal boundary, at which the crystal lattice shows a maximum in transverse polarizability and thus a very high shear piezoelectric response that is ultimately responsible for the large effective piezoelectric coefficients of ceramics [18, 19]. This mechanism, often referred to as polarization rotation, is also responsible for the ultra-high piezoelectricity of rhombohedral $Pb(Zn_{1/3}Nb_{2/3})O_3$–$PbTiO_3$ and $Pb(Mg_{1/3}Nb_{2/3})O_3$–$PbTiO_3$ single crystals along the <001> direction [20, 21].

This single-crystal piezoelectric contribution only accounts for one-third of the total electromechanical response of MPB $Pb(Zr,Ti)O_3$ ceramics; the d_{33} piezoelectric coefficient of ~245 pC N^{-1} is basically dominated by ferroelectric/ferroelastic (hereinafter referred to as non-180° in order to distinguish them from inversion, i.e. 180° domains) domain wall contributions [22]. Domain configurations at the MPB show a distinctive hierarchical structure that consists of a first level of submicrometer size non-180° lamellar domains (actually superdomains), within which a substructure (or second level) of nanoscale regular twinned domains exist [23]. It is the dynamics of these second-level nanoscale domains that is responsible for the high domain wall contribution to the piezoelectric coefficients [24]. Therefore, not only single-crystal but also domain wall contributions are enhanced at the MPB.

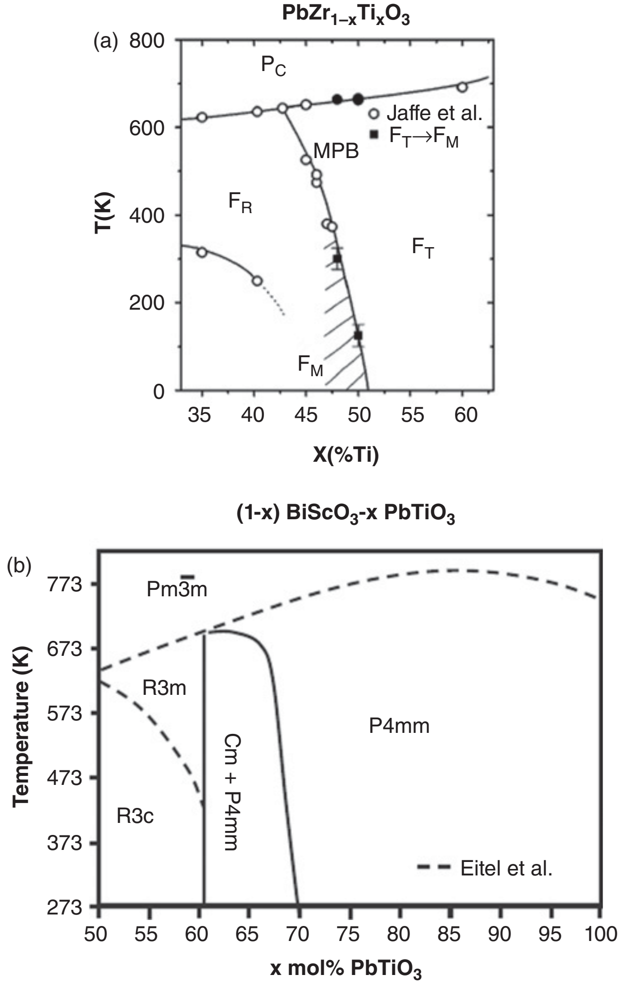

Figure 16.1 *Comparison between the phase diagrams of (a) Pb(Zr; Ti)O_3 (reprinted with permission from [17]. Copyright (2000) by the American Physical Society) and (b) $BiScO_3$–$PbTiO_3$ (reprinted with permission from [32]. Copyright (2007) by The American Physical Society), across their MPB regions*

Indeed, a point defect engineering has been developed for tailoring the dynamics of domains and thus the properties of Pb(Zr,Ti)O_3. Substitutions of trivalent species, such as Fe^{3+} replacing Ti/Zr^{4+} in the B-site causes the formation of acceptor species–oxygen vacancy dipolar defects that can interact with the spontaneous polarization and effectively clamp the domain configuration [25,26]. This is the basis of commercial hard PZTs, which show reduced dielectric and mechanical losses and are used for high-power applications. Substitutions of pentavalent species, such as Nb^{5+} or Sb^{5+} replacing Ti/Zr^{4+} in the B-site, or trivalent ones, like La^{3+} substituting for Pb^2+ in the A-site, introduce cation vacancies and reduce conductivity while enhancing ferroelectric domain mobility [26]. This is the basis of commercial soft PZTs, which can show piezoelectric coefficients as high as 600 pC N^{-1} and are used for high-sensitivity applications. Reaching these very high coefficients also requires introducing an additional isovalent substitution like Sr^{2+} for Pb^{2+}, which reduces the ferroelectric transition temperature and shifts the dielectric anomaly towards room temperature, further increasing the coefficients.

Though PZT piezoceramics are a successful and mature material technology nowadays that has enabled a wide range of piezoelectric devices, research and development of alternative high-sensitivity piezoelectrics that could outperform PZT-based materials in different ways is very active. The main ones are introduced in the next section.

16.2.2 Novel High-Sensitivity Piezoelectrics

16.2.2.1 High-Temperature Materials

A major limitation of PZT-based materials and especially of soft piezoceramics is their temperature operation range, which cannot usually exceed 200 °C. This is caused by the thermal depoling of the materials on approaching the ferroelectric transition and thus high-sensitivity piezoelectrics with higher Curie temperatures than PZT are sought.

A lot of attention is currently focused on $BiScO_3$–$PbTiO_3$ that will also play a main role in this chapter. Therefore, the system is described here in some detail. This is the most promising binary system among $BiMeO_3$–$PbTiO_3$ (where Me is a trivalent cation in octahedral coordination) perovskite solid solutions with ferroelectric morphotropic phase boundaries and high Curie temperatures T_C, which are under extensive research for extending the temperature operation range of high-sensitivity piezoceramics up to 400 °C. These perovskite systems were proposed after an empirical relation was established between the perovskite tolerance factor of an ABO_3 compound with crystal symmetry lower than tetragonal, not necessarily with a polar space group but that did show a ferroelectric MPB across its solid solution with tetragonal $PbTiO_3$, and the Curie temperature of the ferroelectric phases at the MPB, such that the Curie temperature increased as the tolerance factor decreased [27]. Attention was thus directed towards low-tolerance factor perovskites, among which bismuth-based oxides stood out.

Specifically, $BiScO_3$ is a metastable perovskite oxide that has only been obtained at high pressure and crystallizes in the centrosymmetric monoclinic *C2/c* space group [28]. High-pressure synthesis was also necessary for obtaining perovskite phases across the $(1 - x)BiScO_3$–$xPbTiO_3$ system up to $x = 0.55$, range in which ferroelectricity was found from $x = 0.4$ [29]. Apparently, rhombohedral phases only developed above $x = 0.5$, though a later study on samples alternatively obtained by mechanosynthesis reported them already for $x = 0.4$ [30]. Perovskite phases can be prepared by conventional means from $x > 0.5$, and a tetragonal phase has been described for $x > 0.65$ [31]. A morphotropic phase boundary thus existed in the system, which showed coexistence of the rhombohedral $R3m$ and tetragonal $P4mm$ polymorphs for $0.62 < x < 0.65$. A following Rietveld study of high-resolution XRD data indicated the presence of a monoclinic Cm phase between the rhombohedral and tetragonal ones, and coexistence of monoclinic and tetragonal phases for $0.60 < x < 0.70$ [32]. Also, a low-temperature $R3c$ phase has been described by electron diffraction at the rhombohedral side [33]. Main features of the phase diagram across the MPB region are presented in Figure 16.1(b).Therefore, the phase diagram maintains a strong resemblance with that of Pb(Zr,Ti)O_3 and both systems have qualitative analogous MPB regions.

Morphotropic phase boundary $BiScO_3$–$PbTiO_3$ has a Curie temperature of 450 °C, which is 100 °C above that of Pb(Zr, Ti)O_3, and a d_{33} piezoelectric coefficient of 450 pC N^{-1} [31], though coefficients as high as 700 pC N^{-1} have been reported [34]. These figures are comparable to those of soft PZT. Besides, single crystals with a composition at the rhombohedral side of the MPB and <001> orientation have been grown and shown to present ultra-high piezoelectric coefficients [35]. Piezoelectric functionality has been demonstrated far beyond 200 °C and even above 400 °C for doped ceramics, which makes them suitable for operation in harsh environments like diesel fuel injection systems [36, 37]. This requires the processing of multilayer ceramic actuators, which was recently reported [38]. Additionally, sol–gel films on Si-based substrates have also been prepared [39].

Ceramic nanostructuring of $BiScO_3$–$PbTiO_3$ has been studied in depth for the last 5 years, which has not been the case for Pb(Zr,Ti)O_3. This is why this material is chosen here as representative of a first group of systems with PZT-like MPBs, instead of PZT itself. It is expected that material properties show similar down-scaling behavior within this group.

16.2.2.2 High Sensitivity and Power Materials

A main drawback of hard PZTs is their comparatively low piezoelectric coefficients, which limits sensitivity in high-power applications. Alternatively, the main limitation of soft PZTs is their high dielectric and mechanical losses, which cause extensive heating under high driving fields. There is then an interest in developing high-sensitivity materials for power applications that simultaneously provide high piezoelectric coefficients with low losses. A landmark in the field in 1997, ultra-high piezoelectricity with effective d_{33} coefficients exceeding 2500 pC N^{-1} and associated strain levels larger than 0.6% with minimal hysteresis were reported for $Pb(Zn_{1/3}Nb_{2/3})O_3$–$PbTiO_3$ and $Pb(Mg_{1/3}Nb_{2/3})O_3$–$PbTiO_3$ single crystals [40]. These values were recorded for rhombohedral compositions next to the respective MPBs, along the <001> direction. As already anticipated, they are only possible by taking full advantage of the mechanism of polarization rotation, as described for Pb(Zr,Ti)O_3 [20, 21].

Although commercial ultra-high piezoelectricity crystals are already available, and their performance and reliability have steadily improved during the last few years [41], crystal growth is still complex and time consuming (several days) and resulting crystals are fragile. This has fostered a large effort, mostly concentrated in $Pb(Mg_{1/3}Nb_{2/3})O_3$–$PbTiO_3$, to develop textured ceramics with piezoelectric coefficients approaching those of single crystals. Materials with high field effective d_{33} coefficients of 1600 pC N^{-1} and also low field values in resonance of 855 pC N^{-1} have already been obtained [42, 43] and attention is now directed towards the up-scaling issues of the processing [44].

Conventional (non-textured) bulk ceramics are also under consideration, for they can present d_{33} piezoelectric coefficients of 500 pC N^{-1} while showing losses significantly lower than soft PZT [45].

Ceramic nanostructuring of $Pb(Mg_{1/3}Nb_{2/3})O_3$–$PbTiO_3$ and $Pb(Zn_{1/3}Nb_{2/3})O_3$–$PbTiO_3$ have also been recently studied. These materials show very distinctive features that differentiate them from PZT, namely how ferroelectric order develops that involves the appearance of high-temperature relaxor states from the paraelectric phase, and the formation of the ferroelectric phase on cooling in the presence of the evolving polar nanoregions characteristic of relaxors [46]. Not independently, different phases are found in the MPB regions, with two intermediate monoclinic phases with P_m and C_m space groups between the tetragonal and rhombohedral ones in the case of $Pb(Mg_{1/3}Nb_{2/3})O_3$–$PbTiO_3$ [47]. Short-range chemical order is thought to play a major role both in the appearance of the relaxor state [48] and also in the phases present at the MPB [49]. Therefore, these two systems are chosen here as representative of a second group of high-sensitivity piezoelectrics characterized for presenting nanoscale inhomogeneity, for which the ferroelectric phase develops from an intermediate high-temperature relaxor state and whose properties will be shown to have very different down-scaling behavior to that of PZT-like MPB materials.

16.2.2.3 Lead-Free Materials

European Union 2002 directives currently enforced require the restriction of the use of lead, among a list of hazardous substances, in electrical and electronic equipment. Though PZT-based piezoceramics are exempted until a technically viable lead-free alternative is developed, the situation is reviewed every four years, and extensive research is being carried out to find suitable alternatives.

This alternative was thought to have been found in 2004, when piezoelectric coefficients above 300 pC N^{-1} were reported for compositions in the $(K_{0,5}Na_{0.5})NbO_3$–$LiTaO_3$–$LiSbO_3$ ternary system at an apparent orthorhombic tetragonal morphotropic phase boundary, which were further increased above 400 pC N^{-1} by ceramic texturing [50]. However, it is currently acknowledged that an actual MPB does not exist in the system, but that the high coefficients are related to the shift of the orthorhombic to tetragonal polymorphic transition of $(K,Na)NbO_3$ down to room temperature by compositional modification. This is a different mechanism for high sensitivity that entails large temperature dependences, which limit performance [51].

A real rhombohedral–tetragonal morphotropic phase boundary exists in the $(Bi_{1/2}Na_{1/2})TiO_3$–$BaTiO_3$ system, for which high field effective d_{33} coefficients above 500 pC N^{-1} have been reported for textured ceramics [52]. This time, however, the system evolves towards an antiferroelectric phase on heating at a transition temperature that actually shows a minimum value of 150 °C for MPB $(Bi_{1/2}Na_{1/2})TiO_3$–$BaTiO_3$. Piezoelectricity does vanish at this transition, as expected, and the term depolarization temperature has often been used [51]. Indeed, the actual existence of an antiferroelectric phase is under debate, though ferroelectricity undoubtedly disappears [53, 54].

The presence of lone-pair cations at the perovskite A-site has recently been considered essential for piezoelectric high sensitivity [55]. This has concentrated further attention towards $Bi_{1/2}Na_{1/2}TiO_3$ -based materials like $(Bi_{1/2}Na_{1/2})TiO_3$–$BaTiO_3$–$(K,Na)NbO_3$ [56] and $(Bi_{1/2}Na_{1/2})TiO_3$–$(Bi_{1/2}K_{1/2})TiO_3$ [57]. Large electromechanical responses have been described for these systems, though they are related to phase-change phenomena rather than to the piezoelectric effect.

Therefore, a suitable material has not yet been found, which most probably explains why ceramic nanostructuring has hardly been studied for lead-free systems.

16.3 Nanostructuring Effects in Perovskite Systems with PZT-like MPBs

16.3.1 Basic Phenomenology

The most noticeable effect of decreasing the grain size of a high-sensitivity piezoelectric ceramic into the submicrometer range, and further down to the nanoscale on its dielectric properties, is a progressive broadening and depletion of the maximum of permittivity at the temperature of the ferroelectric transition, until its disappearance below a certain threshold size. This evolution is illustrated in Figures 16.2 and 16.3 for $(1-x)\mathrm{BiScO_3}$–$x\mathrm{PbTiO_3}$ with $x = 0.64$, where the temperature dependences of the real and imaginary permittivities of a coarse-grained ceramic are compared with those of a submicrometer grain-sized material at the gate of the nanoscale, and with those of a nanostructured material with a grain size of a few tens of nanometers. This is the lowest size for which dense materials have been processed by spark plasma sintering (SPS) of nanocrystalline powders [58]. Closed porosity, that is a densification of at least 90–92%, is required for carrying out a sound electrical characterization, though results shown here are for materials with values above 95% that approach 99% in the case of those processed by SPS.

The composition $x = 0.64$ was selected, for it is widely reckoned to be the composition at the core of the MPB region that presents the largest piezoelectric coefficients, but the same trend was found for all compositions across the MPB.

Results at five frequencies between 100 Hz and 1 MHz are given. A distinctive feature of this system is the presence of a large frequency dispersion in the dielectric permittivity across the temperature range where the ferroelectric transition takes place: ~450 °C for $x = 0.64$, which overlaps with and partially masks the transition anomaly. This is not an issue in the case of other ferroelectric materials with lower Curie temperature than $\mathrm{BiScO_3}$–$\mathrm{PbTiO_3}$ like $\mathrm{Pb(Zr,Ti)O_3}$ or $\mathrm{BaTiO_3}$ with transitions at 350 and 125 °C, respectively. Back to $\mathrm{BiScO_3}$–$\mathrm{PbTiO_3}$, note that dispersion is maximum at the transition anomaly, such as the maximum permittivity drops from 40 000 at 100 Hz down to 20 000 at 1 MHz for the coarse-grained ceramic shown in Figure 16.2(a). These phenomena have previously been associated with the perovskite defect dynamics that are triggered at high temperature. Oxygen vacancies are usually proposed to play a major role [59], mainly by hopping causing Debye-type relaxations, like the one clearly visible in the real permittivity of the nanostructured ceramic (marked with an arrow in Figure 16.2(c)). Long-range oxygen vacancy displacements also result in high-temperature conductivity (and thus, often in Maxwell–Wagner type relaxations), as indicated by the exponential increase of the imaginary component with temperature and by its characteristic linear dependence with the reciprocal frequency (in addition to dielectric relaxations; see Figure 16.3). It must be noted that the actual defect concentration, and even the defect nature in a material, can be processing dependent and thus differences might exist among the three materials here selected that were processed by conventional sintering, hot pressing, and spark plasma sintering of the same nanocrystalline powders obtained by mechanosynthesis. Differences may also exist with previous reports of materials synthesized by conventional means or by sol–gel by a number of groups [31, 34, 60]. These differences, however, are quantitative rather than qualitative, as indicated by the description of a similar phenomenology for all cases. Indeed, dispersion is maintained down to the nanoscale. This is to say, defects exist in varying concentrations and play a role for all materials. Nonetheless, we will show later that this dispersion is mostly just a consequence of the presence of grain boundaries with differentiated properties.

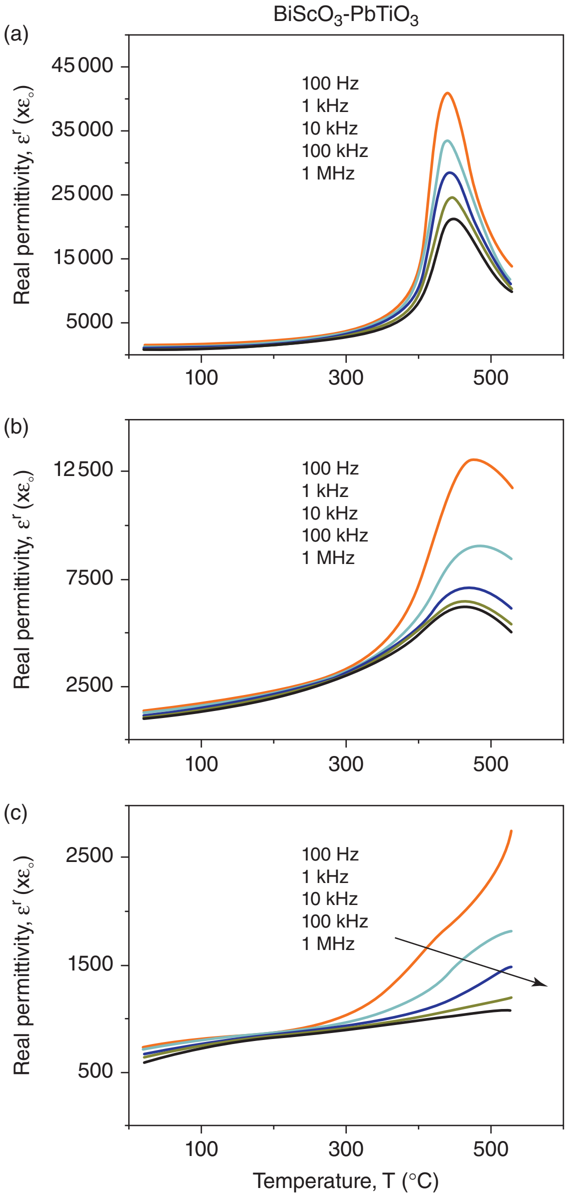

Figure 16.2 *Temperature dependence of the real permittivity for (1 − x)*$BiScO_3$–$xPbTiO_3$ *ceramics with x = 0.64 and an average grain size of (a) 1.3 μm, (b) 0.15 μm, and (c) 25 nm, at several frequencies*

Conductivity contributions are minimized at high frequency and so the temperature dependence of permittivity is shown in Figure 16.4 at 1 MHz for a full series of materials with decreasing grain size down to 25 nm. As already described, the main effect of decreasing size down to the submicrometer range on permittivity was the strong depletion

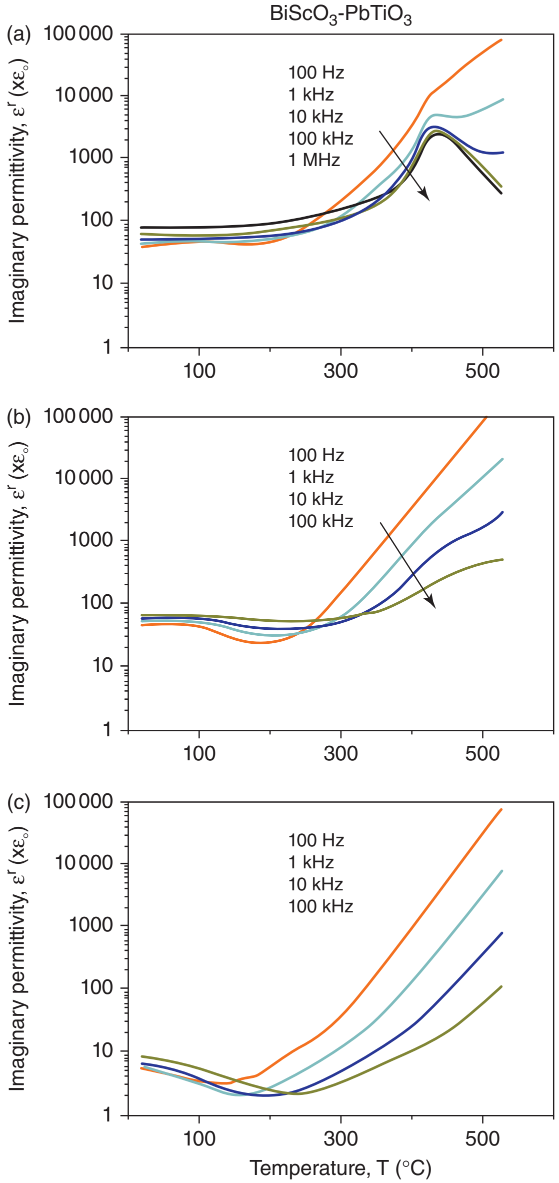

Figure 16.3 Temperature dependence of the imaginary permittivity for the same $(1 - x)BiScO_3–xPbTiO_3$ ceramics with $x = 0.64$ and an average grain size of (a) 1.3 μm, (b) 0.15 μm, and (c) 25 nm, shown in the previous figure

and broadening of the dielectric anomaly associated with the transition, though its position is basically maintained (actually, it seems to fluctuate between 445 and 460 °C with no systematic trend with size, which reflects the overlapping of the dielectric anomaly with a dielectric relaxation, whose position slightly changes among samples).

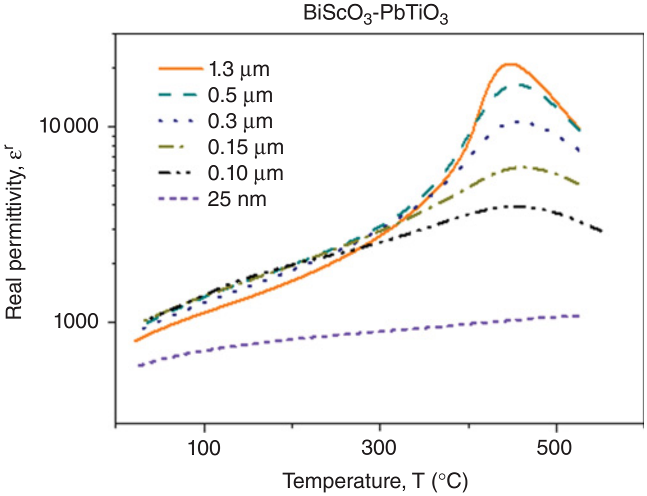

Figure 16.4 *Temperature dependence of the real permittivity for (1 − x)BiScO$_3$–xPbTiO$_3$ ceramics with x = 0.64 and decreasing average grain size at 1 MHz*

The anomaly is further smeared out across the nanoscale, until a threshold size of around 50 nm is reached, below which it disappears. This might be, and actually has often been interpreted as, an indication of the vanishing of ferroelectricity as a size effect, which is apparently supported by the simultaneous disappearance of ferroelectric switching, illustrated in Figure 16.5(a) for the same series of materials. Note the high-field response of the material with an average grain size of 25 nm that is typical of a lossy dielectric. However, the Raman spectra of a nanostructured material with a grain size of 24 nm is analogous to that of a coarse-grained ceramic [61]. Besides, nanocrystals as small as 15 nm maintain the monoclinic *Cm* crystal structure [62]. All these structural investigations indicate the persistence of the polar state. This apparent contradiction has recently been addressed and solved, an issue that we will come back to later.

These results are fully consistent with our previous reports on Fe-doped $(1-x)\text{BiScO}_3$–$x\text{PbTiO}_3$ materials with $x = 0.625$ [58, 61, 63, 64]. Fe^{3+} has been shown to replace Sc^{3+} in the B-site of the perovskite and to cause a shift of the MPB position towards lower x values [37]. Indeed, these materials rather belong to the $(1-x-y)\text{BiScO}_3$–$y\text{BiFeO}_3$–$x\text{PbTiO}_3$ ternary system than to the binary one. A $y \sim 0.06$ has been estimated, for which the MPB is placed at $x = 0.61$. Therefore, $x = 0.625$ locates in the tetragonal field, though close to the boundary with the monoclinic phase. Fe doping also has a hardening effect analogous to that described for PZT materials, which strongly suggests the reduction of a fraction of the dopant to Fe^{2+} and its association with existing oxygen vacancies to form dipolar defects. This is indicated by the changes in the frequency dispersion of the room temperature permittivity, shown in Figure 16.6(a). Note the logarithmic frequency dependence of the permittivity for all cases that has been attributed to a Rayleigh process, the contribution of domain wall movements across a field of randomly distributed pinning centers [65]. The dispersion is significantly reduced for the Fe-doped material as compared with the undoped

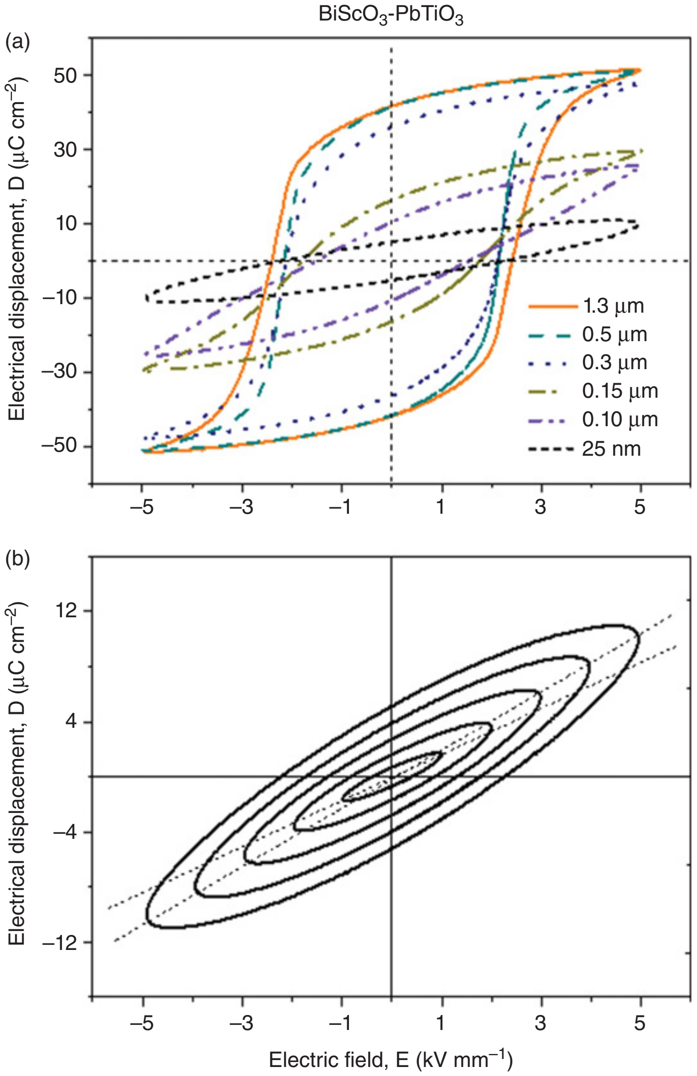

Figure 16.5 *Room-temperature ferroelectric hysteresis loops for* $(1-x)BiScO_3$–$xPbTiO_3$ *ceramics with* $x = 0.64$ *and (a) a decreasing average grain size and (b) a grain size of 25 nm under an increasing driving field, at 0.1 Hz*

one, which indicates a reduction of the domain wall mobility, which is to say the hardening. This mobility is further reduced in the tetragonal phase as expected [66].

The presence of Fe^{2+} in the doped materials is also indicated by the appearance of an additional low-temperature contribution to conductivity with an activation energy of 0.6 eV, a value that agrees with a mechanism of electronic hopping between Fe^{2+} and Fe^{3+} species. High-temperature conductivity with an activation energy of 1 eV is present in all materials; doped or not, and is usually associated with the electromigration of oxygen vacancies.

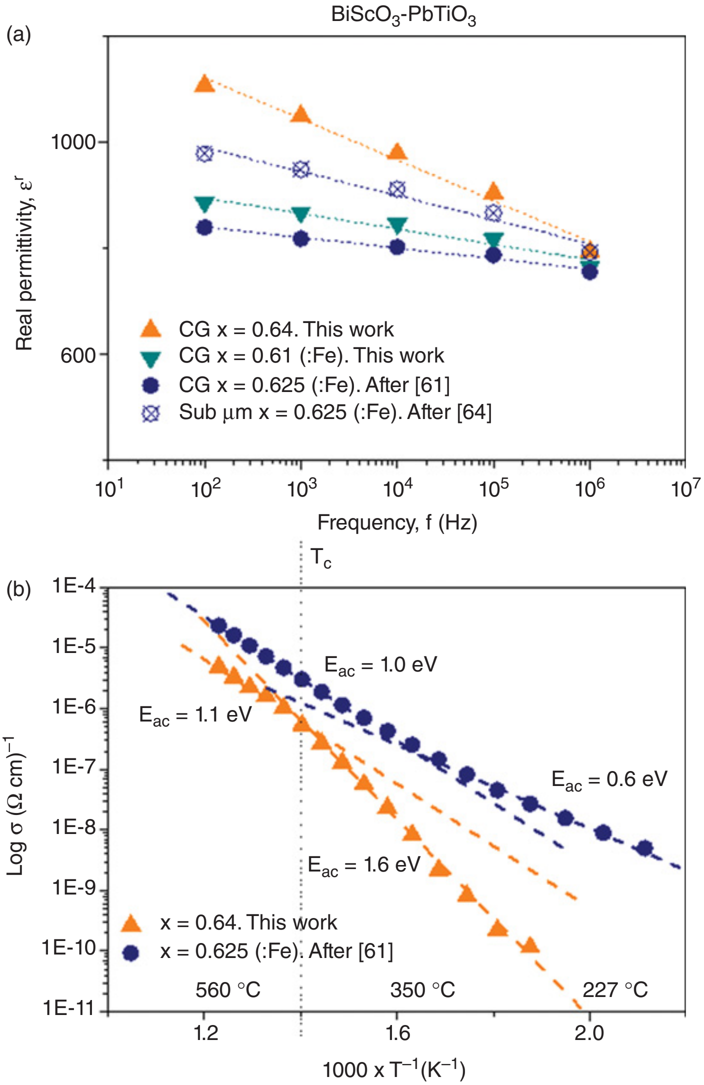

Figure 16.6 *(a) Frequency dispersion of the room temperature permittivity for undoped and Fe-doped (:Fe) (1 – x)BiScO*$_3$*–xPbTiO*$_3$ *ceramics with different x (CG: coarse grained, sub µm: submicrometer grain size). (b) Arrhenius plots for the conductivity of coarse-grained undoped and doped ceramics*

Arrhenius plots for the conductivity of doped and undoped materials are shown in Figure 16.6(b). Note in the case of the undoped ceramic the increase of the activation energy below the ferroelectric transition, which might indicate domain walls to be an obstacle to the movement of the vacancies.

Results are also consistent with those reported for Nb-doped (soft) Pb(Zr,Ti)O$_3$, though the smallest grain size reported was 0.18 µm in that case, for which the anomaly could be clearly observed. No shift of the Curie temperature was found [67]. They are also analogous to those reported for $BaTiO_3$, for which the dielectric anomaly was still observed for materials with a grain size of 50 nm, though its position in this case had shifted from 125 °C for a coarse-grained material with a grain size of 1.2 μm down to 88 °C for 50 nm. This was supported by the DSC results, though a smaller shift was found in this case, from 127 down to 105 °C [68]. Curie temperatures of 106 and 115 °C were later reported for materials with an average grain size of 30 and 20 nm, respectively [69, 70].

16.3.2 Grain Size Dependence of Room Temperature Properties

16.3.2.1 Permittivity

Experimental values for the room temperature dielectric permittivity of 0.36 $BiScO_3$–0.64 $PbTiO_3$ ceramics as a function of grain size are shown in Figure 16.7(a), where the figures for the series of materials processed from nanocrystalline powders obtained by mechanosynthesis, whose properties were presented and preliminarily discussed in the previous section are compared with those of the only independent report on grain size effects in the system [60]. This latter study was carried out on submicrometer-sized $(1-x)BiScO_3$–$xPbTiO_3$ ceramics with $x = 0.64$ that had been processed by two-step sintering of nanoscale powders synthesized by a sol–gel method. Ceramic materials with an average grain size ranging from 0.8 down to 0.2 μm were obtained by tailoring the sintering of the initial powders with a particle size around 10 nm. Permittivity figures between 1173 and 1281 were obtained at 1 kHz.

Error bars represent the dispersion between 100 Hz and 1 MHz when available, which has been associated with the domain wall contribution in the case of coarse-grained materials. Comparable values have been found for materials processed either by two-step sintering, hot pressing, or spark plasma sintering of powders synthesized by sol–gel or mechanosynthesis, and a grain size between 0.8 and 0.15 μm. Values vary between 1100 and 1300 with no clear size dependence, though they are larger than those of ceramics processed by conventional sintering of the mechanosynthesized powders with a grain size above the micrometer, ~950.

The large difference between these values and the permittivity reported for a coarse-grained material in the pioneering work of 2002 is remarkable [31]: 2000 against a value below 1000. However, this former value was for a poled material and a comparably large increase; from 2400 up to 3900 has been reported for similarly coarse-grained (10 μm) soft PZT upon poling [71]. Reasons behind this are not clear, but cannot be associated with an enhancement of the domain wall contribution, for wall density must be strongly reduced upon poling. It might be a consequence of the anisotropy in single-crystal permittivity; this is ε_{33}, being significantly higher than ε_{11}, but experimental permittivity values for poled ceramics do not indicate this to be the case (note also that the transverse polarizability is expected to be very high at the monoclinic to tetragonal boundary) [72]. Changes in the stress state or/and in the percentage of phases in coexistence at the MPB upon poling could be responsible for the permittivity increase.

The main conclusion that can be drawn from Figure 16.7(a) is the absence of a significant maximum in permittivity at any grain size, unlike the case of $BaTiO_3$ [73]. A large maximum has been described for the model ferroelectric around a size of 1 μm, at which permittivity increases from values of 2000 for 2 μm up to 5000, to reach back to 2000 for

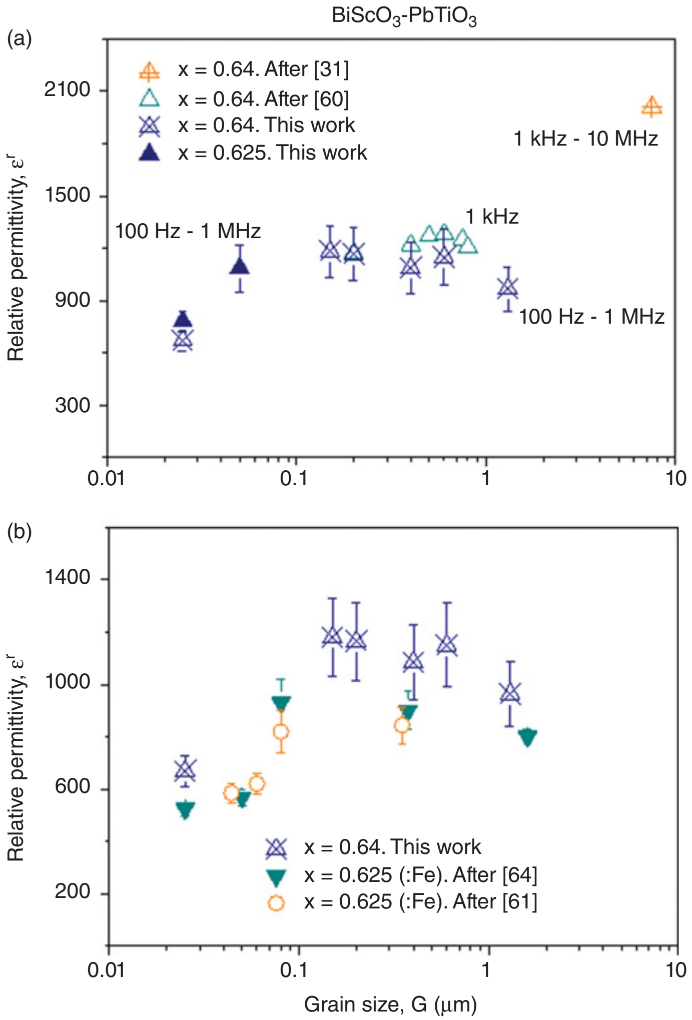

Figure 16.7 *Room temperature permittivity for (1 − x)BiScO$_3$–xPbTiO$_3$ ceramics with decreasing average grain size: (a) undoped with x = 0.64 and x = 0.625 from different sources, (b) undoped with x = 0.64 and Fe doped with x = 0.625 from mechanosynthesized powders*

0.3 μm. This maximum is associated with the dynamics of domain walls and reflects the increase in wall density with the size reduction across the range where lamellar domain configurations exist, and an increasing wall clamping as the evolving configurations stop being able to relax the ceramic stress field. BaTiO$_3$ presents a complex 3D configuration of 90° domains above a grain size of 10 μm that is capable to fully relax ceramic stresses. Domain wall density does not change in this region and thus neither does permittivity, which maintains figures around 2000. Below 10 μm, the former configuration is not energetically favorable and lamellar configurations develop. A distinctive relationship between domain size and grain size holds in this range, such as domain size decreases with the square root of grain size. This involves the increase of the wall density and thus of permittivity with the size reduction. Below 1 μm, lamellar configurations still exist, but a deviation of domain size from the square root law is found (towards smaller values, that is even higher wall densities), down to the disappearance of the 90° walls below a grain size of 0.3 μm. This is the size for which the decrease in elastic energy does not compensate the energy of the wall. However, permittivity decreases for sizes between 1 and 0.3 μm, in spite of the increasing potential wall contribution. Reasons for this are not clear, but it is likely to be related to the clamping of the walls by the ceramic stress field [73–75].

The question is why this mechanism does not hold for high-sensitivity piezoelectrics like $BiScO_3$–$PbTiO_3$ or $Pb(Zr,Ti)O_3$. Permittivity has been reported not to change between 10 and 2 μm for commercial PZT materials [71], but systematic data in the submicrometer range do not exist for them. This observation might reflect differences in the evolution of the domain configurations (note the different phases, where high-sensitivity piezoelectrics are monoclinic close to ferroelectric instabilities while $BaTiO_3$ is tetragonal). Though an evolution of complex 3D configurations towards simpler lamellar structures has also been described for PZT at a similar threshold size of 10 μm, typical domain sizes are an order of magnitude smaller than for $BaTiO_3$ with sizes around 100 nm for a grain size of 10 μm that decrease down to a few tens of nm in the submicrometer range [76]. If this evolution is compared with the hierarchical domain configuration recently described for coarse-grained $Pb(Zr,Ti)O_3$ ceramics, the typical size scales of the two levels can be identified, and one is tempted to suggest the disappearance of the large first level banded structure (superdomains) with the grain size decrease, but the persistence of the fine second level ordered nanotwins. These nanoscale twinned domains are still present in materials with a grain size of 0.18 μm and have been proposed to be responsible of the wall contributions to the linear coefficients. A maximum in permittivity thus would not be expected in high-sensitivity piezoelectrics, as found.

This is further indicated by the frequency dispersion of permittivity for all materials that is given in Figure 16.8(a). Note that a similar slope is maintained all across the submicrometer range, which suggests similar domain wall mobility.

A second conclusion can be drawn from Figure 16.7(a), which is a step-like decrease of permittivity at the nanoscale. This is observed for MPB $x = 0.64$ and also for rhombohedral $x = 0.625$. This decrease is further studied in Figure 16.7(b), where the permittivity of the $x = 0.64$ materials are compared with those reported for the Fe doped $x = 0.625$ ones, all processed from analogous nanocrystalline powders. Data for two sets of doped materials are included: (1) a series of materials processed by SPS under tailored conditions for obtaining decreasing grain sizes [64] and (2) a series of materials with increasing grain size obtained by heating the previous SPS material with the smallest grain size [61]. Note that consistent results were obtained.

A previous aspect worth noting is that lower values are consistently obtained for the doped materials, as expected because they are hard ceramics. Note also the smaller error bars that indicate reduced frequency dispersion. An issue that has not been discussed but that cannot be just taken for granted is dopant incorporation during processing by SPS. Indeed, the submicrometer structured material included in Figure 16.6(a) shows intermediate frequency dispersion between those of the coarse-grained doped and undoped materials. However, nanostructured doped materials do show a reduced dispersion as compared with

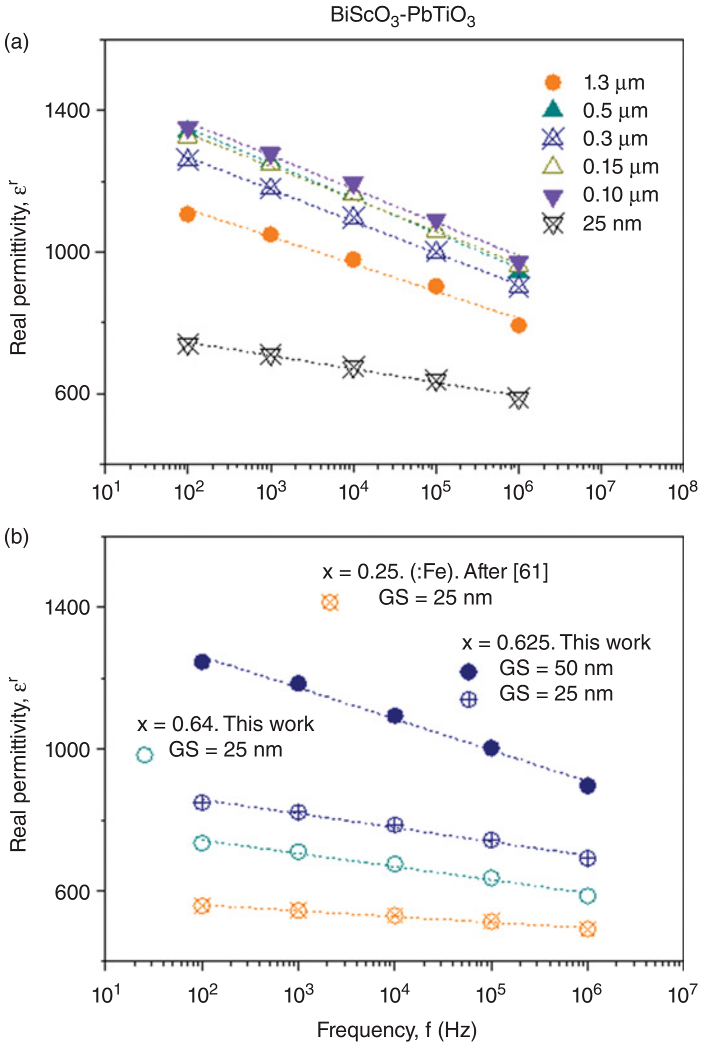

Figure 16.8 *Frequency dispersion of the room temperature permittivity for (a)* $(1-x)BiScO_3-xPbTiO_3$ *ceramics with* $x = 0.64$ *and decreasing grain size and (b) nanostructured undoped and Fe doped materials*

undoped ones, as illustrated in Figure 16.8(b), and thus a partial dopant incorporation seems to have taken place.

The step decrease in permittivity is then found for all materials, undoped or doped, and takes place at a size between 80 and 40 nm, depending on the actual nanostructured ceramics. The pertinent question this time is which one is its origin.

One possible mechanism might be the step being related to the final disappearance of nanotwins within the grains. However, a very recent piezoresponse force microscopy (PFM) study has shown that domains have already disappeared in materials with an average grain

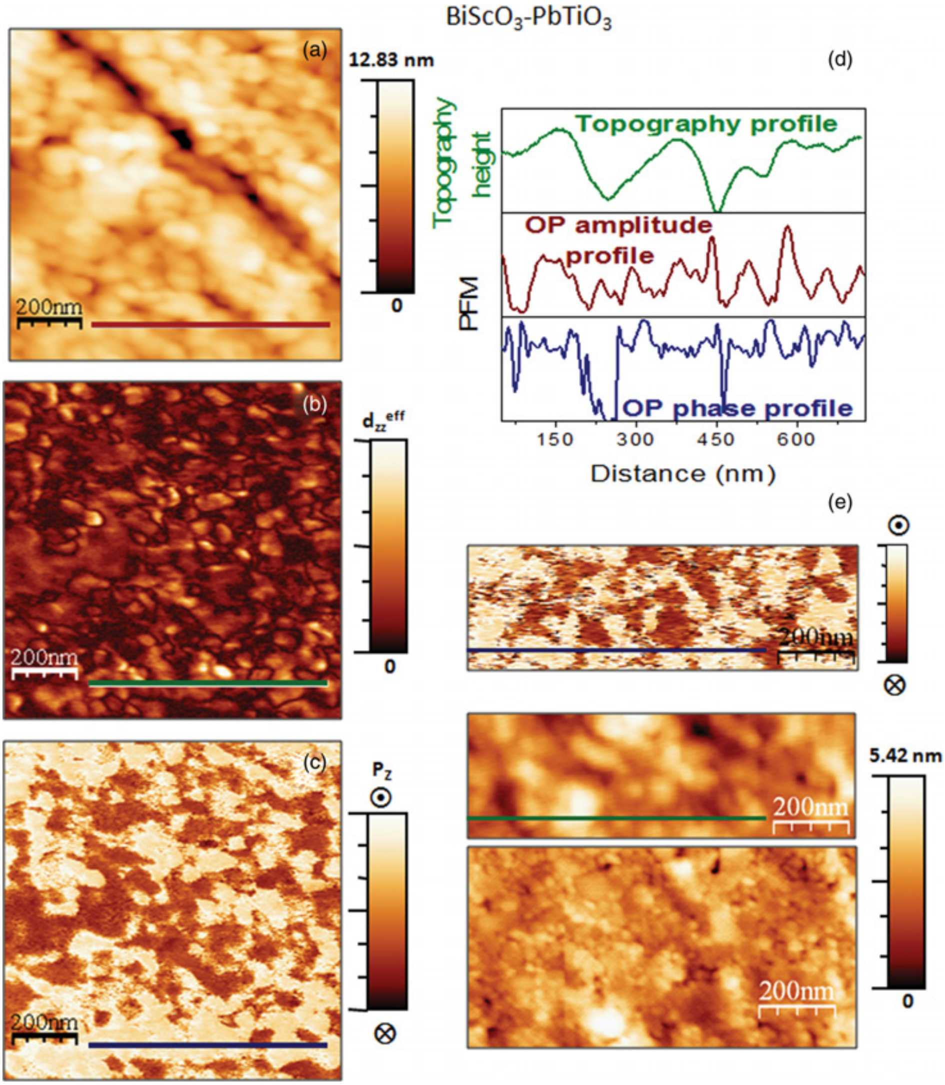

Figure 16.9 PFM results for Fe-doped (1 – x)BiScO$_3$–xPbTiO$_3$ nanostructured ceramics with x = 0.625 and average grain size of 80 (a to d) and 28 nm (e). Reprinted with permission from [77]. Copyright [2014], AIP Publishing LLC

size of 80 nm and that grains are single domain all across the nanoscale, as illustrated in Figure 16.9 [77].

A related issue is the origin of the residual frequency dispersion in the materials with the smallest grain size. We cannot assume it to be associated with ferroelectric domain wall displacements, for they have been shown not to exist. However, the high-field response displayed in Figure 16.5(b) shows a clear increase in the slope, which is of the effective permittivity with the amplitude of the driving electric field. This is a typical Rayleigh-type

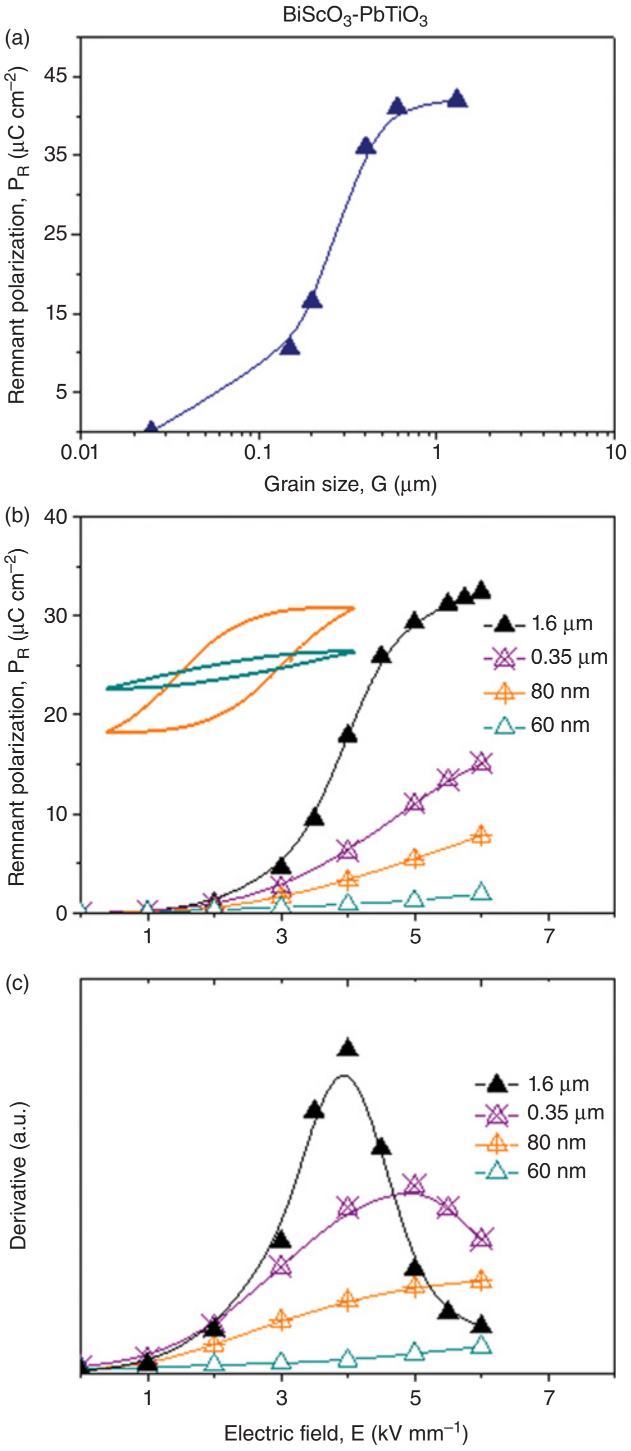
BiScO3-PbTiO3
(a)
Remnant polarization, P_R (μC cm^−2)
45
35
25
15
5
0.01
0.1
1
10
Grain size, G (μm)
(b)
40
30
20
10
0
Remnant polarization, P_R (μC cm^−2)
1.6 μm
0.35 μm
80 nm
60 nm
1
3
5
7
(c)
Derivative (a.u.)
1.6 μm
0.35 μm
80 nm
60 nm
1
3
5
7
Electric field, E (kV mm^−1)

behavior that has the logarithmic frequency dispersion associated with it [65, 78] and is generally caused by the movement of interfaces across a field of defects with which they interact [79]. If this is the case for the nanostructured material, it is necessary to identify both the mobile interfaces and the pinning defects. Indeed, the same PFM study that showed grains to be single domain also revealed the existence of correlations among the polarization of adjacent nanoscale grains, such as regions that spread over several grains and showed an equal sense of out-of-plane components of the electrical polarization vector [77]. These regions have been called inversion superdomains and are thought to appear for minimizing the electrostatic energy, just as inversion domains do in bulk ferroelectric crystals. The inversion superdomain walls might play the role of domain walls in nanostructured materials and their dynamics may be responsible for the Rayleigh behavior of permittivity. Grain boundaries are obvious candidates for the interacting defects.

The alternative mechanism is a grain boundary effect. Grain boundaries have been reported to present differentiated properties, namely a lower dielectric permittivity than grain bulk or even a paraelectric state. They have been reckoned to be responsible for the progressive depletion of the permittivity of nanostructured $BaTiO_3$ ceramics with decreasing grain size [68, 80]. Indeed, the permittivity of materials with a grain size of a few tens of nm can be doubled by the tailoring of grain boundaries [69]. We will address this issue in detail in the next section.

16.3.2.2 Ferroelectric Hysteresis Loops

Ferroelectric hysteresis loops for $(1-x)BiScO_3$–$xPbTiO_3$ ceramics with $x = 0.64$ and decreasing grain size down to the nanoscale have already been shown in Figure 16.5(a), where the gradual disappearance of ferroelectric switching can clearly be seen.

The corresponding values of remnant polarization are given in Figure 16.10(a). Remnant polarization slowly decreases when entering the submicrometer range from 42 down to 36 μC cm^{-2} as the average grain size was reduced from 1.3 down to 0.3 μm. Below this value, polarization suddenly drops down to 16.5 and 10.5 μC cm^{-2} for 0.15 and 0.10 μm, respectively. No ferroelectric switching was observed for the nanostructured material with a grain size of 25 nm.

The remnant polarization versus size curve holds a strong resemblance to a typical remnant polarization against the electric field curve, for which the inflection point defines the coercive field. An example for an Fe-doped coarse-grained ceramic with $x = 0.625$ is given Figure 16.10(b). The curve derivative is shown in Figure 16.10(c). Note the maximum at 4 kV mm^{-1} that corresponds to the coercive field of this tetragonal hard composition. This suggests that the grain size dependence actually reflects an increase of effective E_C or effectively a decrease of the experimental E/E_C ratio as the grain size decreases.

Figure 16.10 *(a) Remnant polarization for $(1-x)BiScO_3$–$xPbTiO_3$ ceramics with $x = 0.64$ as a function of grain size, (b) remnant polarization for Fe-doped $(1-x)BiScO_3$–$xPbTiO_3$ ceramics with $x = 0.625$ and decreasing grain size as a function of the driving field (reprinted with permission from [61]. Copyright © [2014] [The American Ceramic Society]), and (c) derivatives of the previous curves (also reprinted with permission from [61]. Copyright © [2014] [The American Ceramic Society])*

This seems to be confirmed by the previously reported evolution of the remnant polarization versus electric field curves for the series of Fe-doped ceramics with decreasing grain size, also given in the figure [61]. Note the significant increase of the coercive field in the submicrometer range up to a value of 5 kV mm^{-1} for the material with an average grain size of 0.35 μm. Note also the presence of measurable remnant polarization for materials with a grain size of 80 and 60 nm, even though inflection points (maxima in the derivative) in the P_R versus E curves were not reached at electric fields as high as 6 kV mm^{-1}. This indicates the coercive field to be higher than the maximum electric fields attained in the measurements. Infinitely high fields cannot be applied because electrical breakdown takes place.

This increase in the effective coercive field is most probably an effect of the presence of grain boundaries with reduced permittivity. Indeed, a finite element analysis study has shown that actual electric fields across individual grains in $BaTiO_3$ nanostructured ceramics present a broad distribution with an average value well below the external, applied electric field when the differentiated properties of the boundaries are taken into account [81]. Note the broadening of the maximum in Figure 16.10(c) that gives further support to this explanation.

An issue worth discussing is the occurrence of partial (or incipient) ferroelectric switching in nanostructured materials with an average grain size of 80 and 60 nm that present single-domain grains. Ferroelectric loops are given in the inset of Figure 16.10(b). This is most probably enabled by the presence of the inversion superdomains already introduced, and whose dynamics under the electric field has already been hinted at by the Rayleigh-type behavior of permittivity. This provides a mechanism for the reported macroscopic switching in nanostructured materials, though saturation cannot be attained unless electric fields above the effective coercive ones could be applied.

16.3.2.3 Piezoelectric Coefficients

Piezoelectric charge coefficient d_{33} values for $(1 - x)BiScO_3$–$xPbTiO_3$ ceramics with $x = 0.64$ and decreasing grain size down to the nanoscale are given in Figure 16.11. Poling was accomplished under 4 kV mm^{-1} at 100 °C, conditions that were varied to 5 kV mm^{-1} at 150 °C for the nanostructured materials.

The piezoelectric coefficient slowly decreases when entering the submicrometer range from 440 down to 365 pC N^{-1} as the average grain size was reduced from 1.3 down to 0.3 μm. Below this value, the coefficient suddenly drops down to 170 and 55 pC N^{-1} for 0.15 and 0.10 μm, respectively. Residual but measurable piezoelectricity was obtained for the nanostructured material with a grain size of 25 nm. Reported data for the series of Fe-doped materials are also included for comparison [61]. A consistent trend was found.

These curves show a strong resemblance with a typical polarization curve, widely carried out to identify the actual poling electric field required to achieve the saturation of properties. Indeed, that for $(1 - x)BiScO_3$–$xPbTiO_3$ ceramics with $x = 0.64$ has the same shape and shows the inflection point at the same size as the corresponding remnant polarization curve shown in Figure 16.10(a). Therefore, the distinctive decrease of the piezoelectric coefficients most probably reflects how one moves away from the saturation conditions as the effective coercive field increases with decreasing grain size as an effect of the grain boundaries.

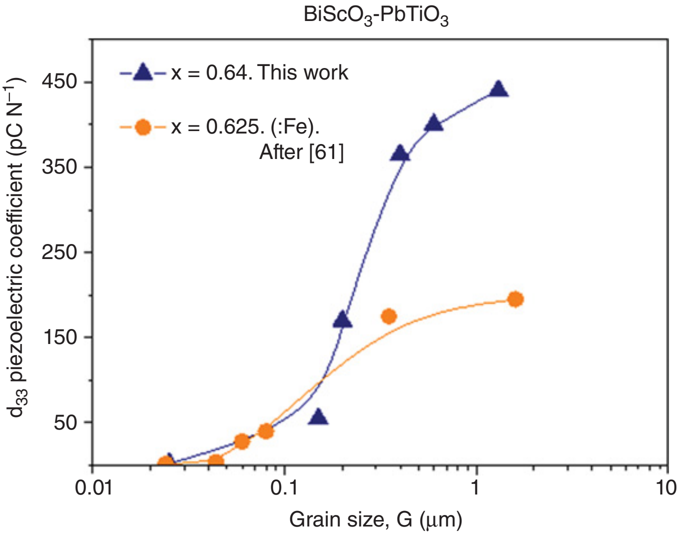

Figure 16.11 Piezoelectric d_{33} coefficient for undoped and Fe-doped $BiScO_3$–$PbTiO_3$ ceramics as a function of grain size after poling with electric fields up to 5 kV mm^{-1} at temperatures between 100 and 150 °C

Results for $BiScO_3$–$PbTiO_3$ can be compared with those reported for soft PZT materials. In the only work that addressed grain size effects in PZT, a continuous decrease of the piezoelectric coefficients, from a d_{33} of ~500 pC N^{-1} for 3.95 µm down to ~340 pC N^{-1} for 0.18 µm, was found, which was associated with the progressive hindrance to domain wall movements as a result of the evolution of the domain configurations and their dynamics with the size reduction [67]. An increase of the coercive field with size reduction was reported, but fields above the coercive ones could be applied in this case for all materials down to a grain size of 0.18 µm. This was helped by the low bulk coercive field of PZT as compared with that of $BiScO_3$–$PbTiO_3$. Therefore, the initial decrease of d_{33} with size for the latter system, from 440 down to 365 pC N^{-1}, is most probably associated with the same effect.

16.3.3 Grain Size Against Boundary Effects

16.3.3.1 Separation of Contributions by Impedance Spectroscopy Analysis

Grain bulk and boundary contributions to the electrical response of an electroceramic can be isolated using impedance spectroscopy analysis. This is a powerful technique for separating the electrical response of a material into their component parts [82]. It rests on the hypothesis, shown valid for a large number of cases, that the (electrically) different regions of the material are characterized by a resistance and a capacitance usually in parallel and that it is possible to identify the different (RC) elements in the impedance spectrum and to assign them to appropriate regions of the electroceramic sample. This is done by studying how the (RC) elements vary with experimental parameters like the processing ones, final microstructure, or temperature; for instance a ferroelectric bulk component is readily

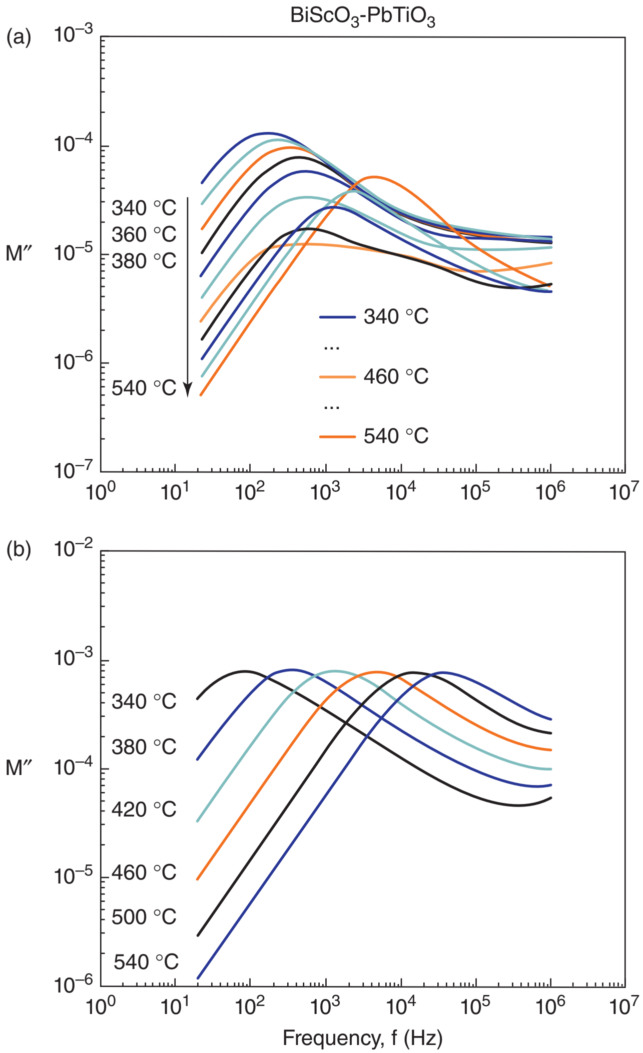

Figure 16.12 *Frequency dependence of the imaginary electrical modulus for Fe-doped (1 – x)BiScO$_3$–xPbTiO$_3$ ceramics with x = 0.625 and grain sizes of (a) 1.6 μm and (b) 24 nm at several temperatures across the ferroelectric transition. Reprinted with permission from [61]. Copyright © [2014] [The American Ceramic Society]*

identified by its distinctive temperature dependence on capacitance, which must reflect the dielectric anomaly at the ferroelectric transition.

This was recently done for two Fe-doped (1 – x)BiScO$_3$–xPbTiO$_3$ materials with x = 0.625 and average grain sizes of 1.6 μm and 24 nm [61]. Impedance data for the coarse-grained ceramic are presented in Figure 16.12(a). The complex modulus formalism was chosen, for it picks out those elements with the smallest capacitance like that corresponding to the bulk of the grain.

Two relaxation peaks can be identified (see the imaginary modulus M'' at 460 °C). Experimental data were then modeled by using two-component equivalent electrical circuits, and a best fit was obtained with a series connection of a first (RQC) element (where Q stands for a constant phase element, which are introduced to take into account the non-Debye behavior exhibited by the polarization characteristics of many materials) and a second (RQ) one that simulated the low- and high-frequency relaxations, respectively. The temperature dependence of the effective capacitance of the first (RQC) element is shown in Figure 16.13(a). Capacitance clearly shows a maximum at ~460 °C that can be readily associated with the dielectric anomaly at the ferroelectric phase transition. This allows the assignment of this first element to the contribution of the bulk of the grain. Capacitance values for the second (RQ) element are also given in the figure. Note that values are consistently higher than those of the grain bulk, as expected for a contribution from the grain boundary, and therefore assigned to it

Capacitance values are given normalized to sample geometry (area and thickness). The actual permittivity for the bulk of the grain can be directly estimated from the capacitance value in this case (coarse-grained material) and a value of ~35 000 is obtained at the transition temperature. An estimation for the grain boundary permittivity requires a hypothesis for the boundary thickness. A value of 650 is obtained at the same temperature under the assumption that the boundary thickness/grain size ratio is 0.01 [61].

Resistance values are also displayed. The Arrhenius plots for the effective conductivity are shown in Figure 16.13(b). Note that conductivity is controlled by the bulk of the grain for this coarse-grained material. An activation energy of 1.1 eV is obtained. This is the same high-temperature mechanism already discussed for the total conductivity in Figure 16.6(b) and that was associated with the electromigration of oxygen vacancies. Note the higher conductivity for grain boundaries with slightly larger activation energy of 1.3 eV. This might indicate a higher concentration of charge carriers at the boundaries, and also of defects.

Electrical modulus data for the nanostructured ceramic are presented in Figure 16.12(b). Unlike the case of the coarse-grained material, only one relaxation peak can be identified. Then experimental data were modeled by using a single (RQC) element. The effective capacitance is shown in the inset of Figure 16.13(a). Note that the temperature dependence is qualitatively analogous to that obtained for the grain boundary contribution of the coarse-grained material. A direct calculation of permittivity provides a value of 500, also in good agreement with the estimated grain boundary permittivity of the former ceramic. Therefore, it can be said that the (RQC) element corresponds to the grain boundary response.

The behavior of the resistance gives further support to this assignment. The Arrhenius plot for the conductivity shows a highly resistive element with an activation energy of 1.3 eV, once again the same value obtained for the conductivity of grain boundaries in the coarse-grained material.

These results clearly demonstrated the electrical response of the nanostructured materials to be fully dominated by grain boundaries. Therefore, a vanishing of ferroelectricity as a size effect cannot be concluded from the disappearance of the dielectric anomaly associated with the transition.

The same methodology was applied to the series of Fe-doped ceramics with increasing grain size, obtained by thermal treatment of the previous nanostructured material [61]. Grain bulk and boundary contributions could be separated from average grain sizes above

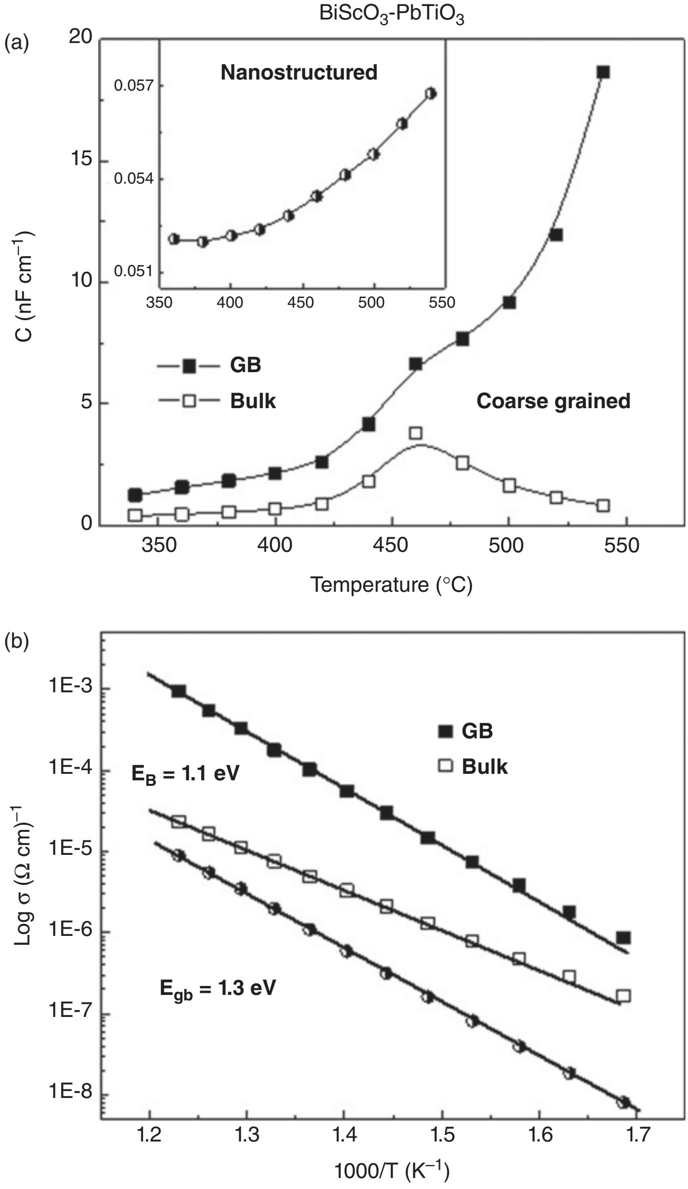

Figure 16.13 *Results of the impedance spectroscopy analysis for the Fe-doped* $(1-x)\mathrm{BiScO_3}$–$x\mathrm{PbTiO_3}$ *ceramics with* $x = 0.625$ *and grain sizes of 1.6 μm and 24 nm. (a) Temperature dependence of the normalized capacitance and (b) Arrhenius plots of conductivity. Bulk and grain boundary (GB) contributions are given. Reprinted with permission from [61]. Copyright © [2014] [The American Ceramic Society]*

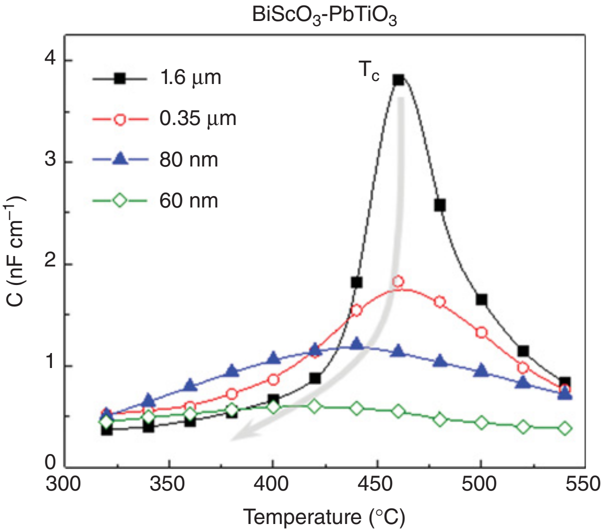

Figure 16.14 *Temperature dependence of the bulk grain normalized capacitance, obtained by impedance spectroscopy analysis for Fe-doped (1 − x)$BiScO_3$–x$PbTiO_3$ ceramics with x = 0.625 and varying grain size. Reprinted with permission from [61]. Copyright © [2014] [The American Ceramic Society]*

60 nm. Results for the capacitance of the grain bulk contribution in ceramics with increasing grain size are shown in Figure 16.14. Note that the dielectric anomaly associated with the transition is observed for all materials. A grain size effect on the transition temperature can be established; T_C did not change when entering the submicrometer range and was still around 460 °C for a material with a grain size of 0.35 μm. A slight decrease, down to 440 and 420 for sizes of 80 and 60 nm, took place at the nanoscale. This is in good agreement with Raman spectroscopy results for the material with a grain size of 24 nm, for which the soft mode was identified and a transition temperature of 405 °C was then defined [61].

Note that a direct comparison among the grain bulk capacitance values for materials with increasing grain size cannot be done, for the evaluation of permittivity would require knowledge of geometrical factors that change with grain size.

16.3.3.2 Simulation of the Electrical Response from the Grain Bulk and Boundary Contributions

The previous analysis provided values for the grain bulk and boundary permittivities, as well as for their conductivity. This enables a simulation to be carried out of the electrical response of ceramic materials with an increasing fraction of grain boundaries; this is to say, decreasing grain size and constant grain bulk properties that should be a great help in differentiating boundary and size effects.

This was done in two steps. Firstly, the effective permittivity of a bulk ceramic with negligible boundaries was obtained starting from the single-crystal values. A dielectric tensor was introduced and the dielectric anomaly associated with the transition was incorporated with two asymmetric Gaussian functions with adjustable height and width. Parameters were

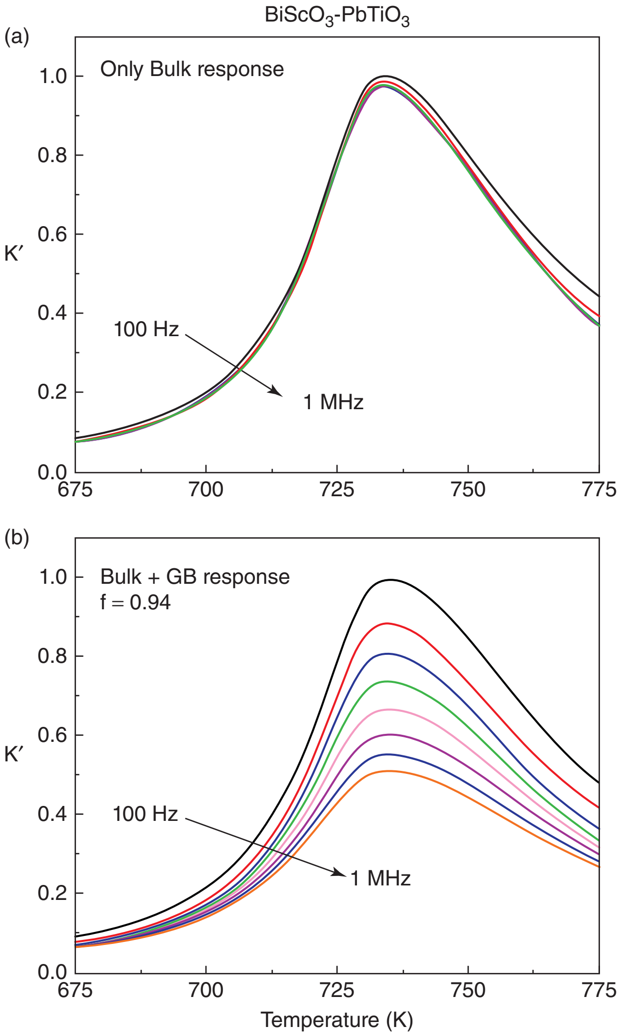

Figure 16.15 *Simulation of the temperature dependence of permittivity for a Fe-doped (1 − x)*$BiScO_3$*–x*$PbTiO_3$ *ceramic with x = 0.625 and a grain size of 1.6 μm (a) without considering grain boundaries and (b) introducing grain boundaries with a volumetric fraction f of 0.94 (10 nm thickness) at several frequencies*

varied to obtain a curve that fitted the value of 35 000 estimated for the permittivity of the grain bulk at T_C and have a width of the dielectric anomaly similar to the one obtained by impedance spectroscopy analysis, as shown in Figure 16.13(a). The effective medium theory with percolation was used [83, 84]. A second phase was used to take into account the actual densification: 95% for coarse-grained materials. Spherical particles and a typical percolation threshold of 0.33 were assumed. Results at several frequencies are presented in Figure 16.15(a). Note the absence of dispersion across the temperature range where the transition takes place.

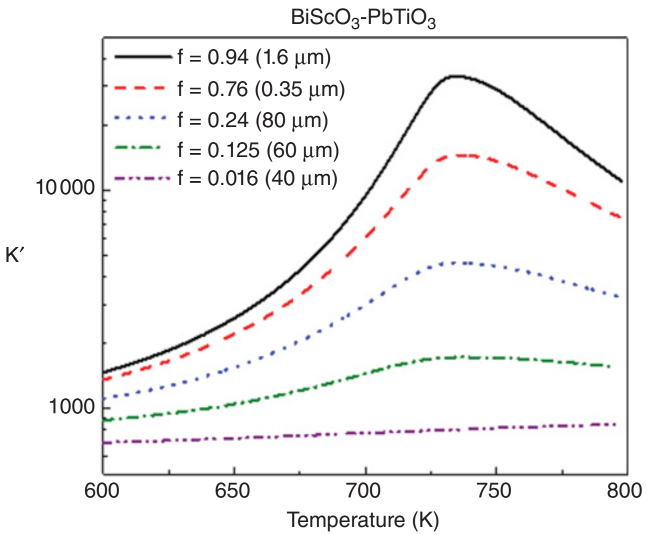

Figure 16.16 *Simulation of the temperature dependence of permittivity for Fe-doped (1 − x)*$BiScO_3$*–x*$PbTiO_3$ *ceramics with x = 0.625 and an increasing volumetric fraction of grain boundaries; that is to say, decreasing grain size*

Grain boundaries were introduced in a second step. A non-ferroelectric character was assumed and thus no temperature dependence of permittivity was introduced. A percolation threshold of 0.99 was considered this time to have non-contacting grain bulk elements for any boundary thickness, which was varied to reproduce the experimental results for the coarse-grained material shown in Figure16.2(a). Best agreement was obtained for a boundary thickness of 10 nm, which corresponds to a volumetric fraction, *f*, of 0.94 in the case of this material with a grain size of 1.6 μm. Results of the simulation are given in Figure 16.15(b). Dispersion across the temperature range where the transition takes place appears now to resemble that of the experimental curves (see Figure 16.2(a)). This clearly demonstrates this dispersion to be a grain boundary effect. Furthermore, it also shows the low-frequency curve to be the closest one to the bulk response.

The results of the simulation for an increasing volumetric fraction of grain boundaries (with 10 nm thickness) are given in Figure 16.16, which should be analogous to a decreasing grain size. Note this time the very good agreement between the simulation and the experimental results shown in Figure 16.4. This corroborates the strong broadening and depletion of the dielectric anomaly, down to its disappearance to be a grain boundary effect. Note also that the temperature position of the dielectric anomaly does not change with the increase in volumetric fraction. Therefore, this confirms the experimental shift in Curie temperature to be an actual size effect.

16.3.3.3 Tailoring of Properties by Modification of the Grain Boundaries

The previous results clearly illustrate how grain boundary effects are as important as grain size effects to understand the properties of nanostructured electroceramics, and specifically of high-sensitivity piezoelectrics. Grain boundaries with differentiated properties have been shown to exist in $BiScO_3$–$PbTiO_3$ ceramic materials and to cause the broadening and depletion of the dielectric anomaly when size decreases, until its disappearance for a grain size of a few tens of nanometers. They also cause a significant increase of the effective coercive field, up to values larger than ceramic electrical breakdown fields, which make impossible ferroelectric switching and thus the poling of the ceramics in the case of materials with the smallest grain size. As a matter of fact, it can be said that the degradation of functionality upon ceramic nanostructuring is basically a grain boundary effect.

This raises the possibility of tailoring ceramic properties and then enhancing functionality by modification of the grain boundaries. This possibility is somehow hinted at when one plots the piezoelectric coefficients for the series of Fe-doped materials with decreasing grain size down to the nanoscale as a function of the material total resistivity. The curve is shown in Figure 16.17(a) and a threshold resistivity is suggested, above which effective poling is not possible. Though resistivity is controlled by the bulk grain for coarse-grained materials, grain boundaries readily take over the process when their density increases as the submicrometer range is entered. Basically, changes in resistivity reflect the progressive disappearance of the contribution of electron hopping between Fe^{2+} and Fe^{3+} species, as illustrated in Figure 16.17(b).

A proof of concept is provided in Figure 16.18, where two Fe-doped materials with an average grain size of 80 nm, but very different conductivities, are compared. Basically, the mechanism of electron hopping between Fe^{2+} and Fe^{3+} species is active in one case, but not in the second one. This has a dramatic effect on ferroelectric switching, which is enhanced in the materials with higher conductivity. Saturation is approached in this case and a remnant polarization of 19 $\mu C\ cm^{-2}$ is achieved as compared with 5 $\mu c\ cm^{-2}$ for the highly resistive material.

This concept opens the door to obtain functional materials with grain sizes of a few tens of nanometers. Indeed, d_{33} piezoelectric coefficients of ~20 $pC\ N^{-1}$ have recently been reported for $BiScO_3$–$PbTiO_3$ ceramics with an average grain size of 23 and 33 nm processed by the combination of SPS and two-step sintering of sol–gel powders [85]. This can be compared with a value of 28 $pC\ N^{-1}$ for a material with a grain size of 60 nm, processed from nanocrystalline powders obtained by mechanosynthesis [61]. The same authors reported in a subsequent study a coefficient of ~20 $pC\ N^{-1}$ for an even smaller size of 11 nm in a material with grain boundaries with negligible thickness as seen by HRTEM [86].

16.4 Nanostructuring Effects in Perovskite Systems with Intrinsic Chemical Inhomogeneity

The first report of grain size effects on the properties of high-sensitivity piezoelectric $(1 - x)Pb(Mg_{1/3}Nb_{2/3})O_3$–$xPbTiO_3$ materials was focused on $x = 0.35$, the composition at the core of the morphotropic phase boundary region that presents the highest piezoelectric coefficients in ceramic form and indicated the destruction of the ferroelectric long-range order below a threshold size of 0.2 μm and the appearance of a relaxor state [87].

However, a later Rietveld study of X-ray diffraction data for a series of $(1 - x)Pb(Mg_{1/3}Nb_{2/3})O_3$–$xPbTiO_3$ ceramics with $x = 0.2$, this time the composition at the $Pb(Mg_{1/3}Nb_{2/3})O_3$ edge of the MPB region, and decreasing grain size down to

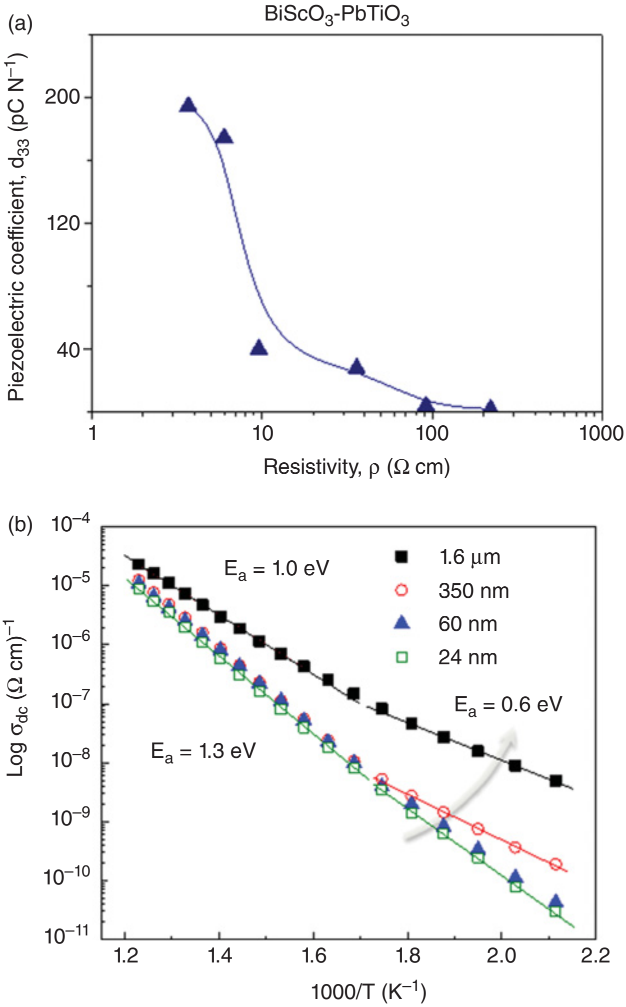

Figure 16.17 *(a) Piezoelectric d_{33} coefficient for Fe-doped $(1 - x)BiScO_3$–$xPbTiO_3$ ceramics with $x = 0.625$ and decreasing grain size as a function of the ceramic resistivity and (b) Arrhenius plots for the conductivity of the previous materials. Reprinted with permission from [61]. Copyright © [2014] [The American Ceramic Society]*

0.1 μm revealed the persistence of the ferroelectric state just next to the nanoscale [88]. The main size effect was an evolution of this phase, from monoclinc *Cm* to rhombohedral *R*3*m* between 0.25 and 0.15 μm, which was accompanied by a continuous rotation of the spontaneous polarization, whose modulus did not significantly change across this size range.

Similar results were subsequently reported for $x = 0.35$, for which the same monoclinic *Pm* phase in coexistence with a minor amount of tetragonal *P*4*mm* was found for materials with an average grain size of 4 and 0.15 μm [89]. The main difference was a slight decrease of the fraction of the later phase, from 11 down to 5% with the size decrease. This was in

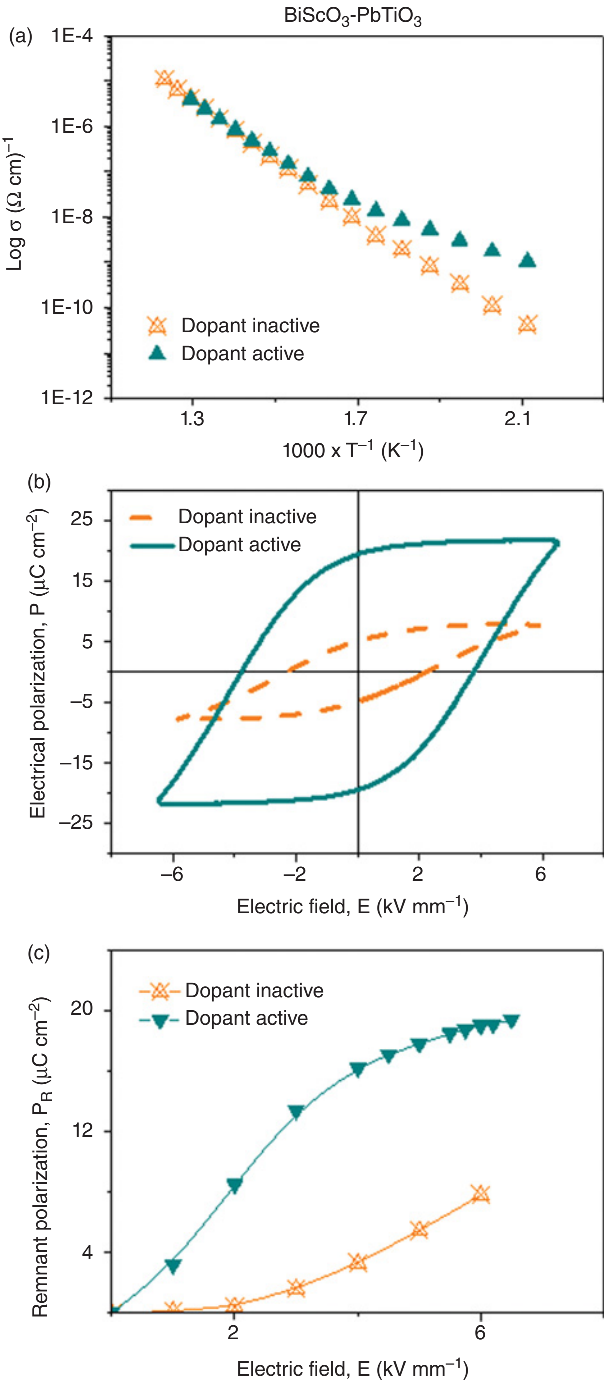

Figure 16.18 *(a) Arrhenius plots for the conductivity of two Fe-doped* $(1-x)BiScO_3$–$xPbTiO_3$ *ceramics with* $x = 0.625$ *and 80 nm grain size that show different levels of dopant activation, (b) ferroelectric hysteresis loops at 0.1 Hz, and (c) remnant polarization as a function of the driving field for the previous materials*

apparent contradiction with the electrical properties that clearly indicated the presence of a relaxor state, in agreement with previous reports [87].

An evolution from micrometer-sized lamellar domains towards submicrometer/nanometer-sized crosshatched domains was also found [89]. These domain configurations had previously been described across the $Pb(Mg_{1/3}Nb_{2/3})O_3–PbTiO_3$ system and were considered to be intermediate states between the relaxor and ferroelectric ones, sometimes written as: “long-time present precursors of the ferroelectric long-range order” [90]. This drove some authors [89] to propose that size effects were the consequence of the slowing down of the ferroelectric transition when size decreases down to the submicrometer range, approaching the nanoscale.

This idea was inspired by the two-stage model for the development of ferroelectric long-range order in relaxor systems [46]. According to this model, and in a first stage at high temperature, polar nanoregions (PNRs) start to nucleate at a given temperature, named the Burns temperature [91]. The presence of nanoscale chemical inhomogeneity, specifically of charge-ordered regions (CORs), is thought to promote their condensation in the highly polarizable medium [48]. The number and size of these PNRs and, thus, their volume fraction, increases as temperature decreases until approaching the temperature of the ferroelectric transition [92]. At this point, ferroelectric fluctuations are triggered and the ferroelectric phase develops. The kinetics of the transition depends on the volume fraction of PNRs at that temperature, and it slows down as this fraction increases. This means that there is a threshold temperature below which the kinetics drastically decreases. This determines the final polar states, as described for the $(1 - x)Pb(Mg_{1/3}Nb_{2/3})O_3–xPbTiO_3$ system. Indeed, the slowing down has been experimentally observed for $x = 0.2$ between 71 and 61 °C [93]. For compositions with a higher transition temperature, such as $x = 0.3$, a long-range monoclinc C_m phase develops, while for $x = 0.2$ intermediate states are arrested [94].

Grain size effects were addressed in depth in a following paper [95], in which the slowing down of the relaxor to a ferroelectric transition was directly described as the grain size was decreased from 0.36 down to 0.21 μm. This kinetic effect was driven by the primary lowering of the transition temperature with the size decrease, from values above the temperature of the slowing down in the system to values below it.

An in-depth comprehensive review of the effects in the submicrometer range can be found elsewhere [96]. Further down at the nanoscale, the disappearance of the relaxor state and the appearance of a paraelectric phase below a grain size of 30 nm was reported for $(1 - x)Pb(Mg_{1/3}Nb_{2/3})O_3–xPbTiO_3$ with $x = 0.35$ [87].

A number of subsequent studies focused on $Pb(Zn_{1/3}Nb_{2/3})O_3–PbTiO_3$-based nanostructured ceramics and, unlike the former work, they reported the presence of relaxor states for grain sizes as small as 15 nm. This is also a perovskite relaxor–ferroelectric solid solution qualitatively analogous to $Pb(Mg_{1/3}Nb_{2/3})O_3–PbTiO_3$; the ferroelectric phase develops from a high-temperature relaxor state and it also has a ferroelectric MPB between the rhombohedral and tetragonal phases [97], of which single crystals show an even higher electromechanical response [40]. It has attracted less attention than its $Pb(Mg_{1/3}Nb_{2/3})O_3$ analog because the perovskite phase is thermodynamically unstable at typical ceramic processing temperatures [98], which makes it extremely difficult to obtain single-phase materials. Indeed, ceramic samples suitable for electrical characterization could only recently be obtained by SPS of nanocrystalline powders obtained by mechanosynthesis, and they unambiguously showed relaxor behavior [99].

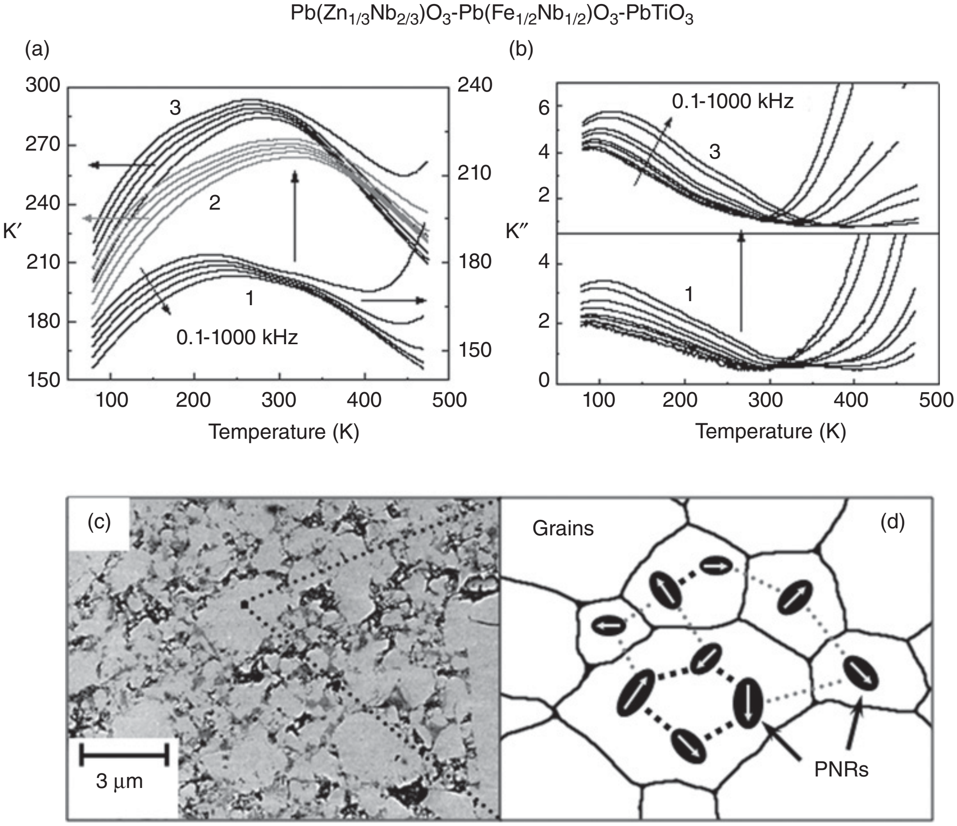

Figure 16.19 Temperature dependence of the (a) real and (b) imaginary permittivity for $(1 - x - y)Pb(Zn_{1/3}Nb_{2/3})O_3–yPb(Fe_{1/2}Nb_{1/2})O_3–xPbTiO_3$ nanostructured ceramics with $x = 0.08$ and $y = 0$ (1), 0.1 (2), and 0.4 (3), at several frequencies. (c) Ceramic microstructure and (d) schematic of proposed correlations among PNRs at the nanoscale. Reprinted with permission from [100]. Copyright [2009], AIP Publishing LLC

This was further investigated in a set of $Pb(Zn_{1/3}Nb_{2/3})O_3–Pb(Fe_{1/2}Nb_{1/2})O_3–PbTiO_3$ nanostructured materials. Two independent Vogel–Fulcher-type relaxations were found, and it was proposed that they were associated with intra- and intergranular correlations among PNRs with freezing temperatures slightly below room temperature and around liquid nitrogen, respectively [100]. Typical sizes of PNRs are around 10 nm [101], and thus considering the average grain size of 20 nm and the finite width of the grain size distribution, grains with a single PNR and grains with a few PNRs must be present. A schematic of this situation, along with the discussed dielectric relaxations are shown in Figure 16.19.

The apparent contradiction between these results and those obtained for $Pb(Mg_{1/3}Nb_{2/3})O_3–PbTiO_3$ might be associated with the different achieved densification levels. Figures of 80% were obtained for the $Pb(Zn_{1/3}Nb_{2/3})O_3–PbTiO_3$-based materials, while the former ones presented densifications of only 60%.

These studies on the $Pb(Mg_{1/3}Nb_{2/3})O_3–PbTiO_3$ and on $Pb(Zn_{1/3}Nb_{2/3})O_3–PbTiO_3$ relaxor–ferroelectric solid solutions have provided a consistent picture of the grain size effects on the properties of relaxor-based materials across the submicrometer and nanoscales, down to a few tens of nanometers. Effects have been shown to originate from the slowing down of the relaxor to ferroelectric transition, up to the final stabilization of the relaxor state at room temperature. This is clearly a distinctive feature of systems with nanoscale intrinsic chemical inhomogeneity, but does not apply to materials with conventional ferroelectric transitions like Pb(Zr,Ti)O_3 and $BiScO_3$–$PbTiO_3$.

Grain size effects in these latter systems have been shown to be mostly associated with the presence of grain boundaries with differentiated properties. This mechanism might also be present in relaxor-based systems. Indeed, grain boundaries with differentiated properties in $(1 - x)Pb(Mg_{1/3}Nb_{2/3})O_3$–$xPbTiO_3$ with $x = 0.2$ have been proposed to be responsible for the modification of the dynamics of the relaxor state at the nanoscale. An increase in the activation energy from 30 to 47 eV and a decrease in the freezing temperature from 77 to 67 °C have been described when the grain size was decreased down to 90 nm. The presence of a fraction of material, most probably the grain boundary that undergoes the ferroelectric transition below room temperature, has also been reported [95].

16.5 Summary and Future Perspectives

The research reviewed here clearly indicates the necessity of differentiating perovskite systems with PZT-like MPBs from those with nanoscale intrinsic chemical inhomogeneity when addressing the effects of ceramic nanostructuring in high-sensitivity piezoelectrics.

The extensive work carried out during recent years on high Curie temperature $BiScO_3$–$PbTiO_3$, a high sensitivity piezoelectric perovskite system with a phase diagram analogous to that of Pb(Zr,Ti)O_3 across the morphotropic phase boundary region, has unambiguously demonstrated that high-resistivity grain boundaries mostly dominate the functional properties of nanostructured ceramics. The main effect is a dramatic increase in the effective coercive field up to values that can exceed the material dielectric strength, which ultimately will prevent poling. Piezoelectric functional nanostructured ceramics thus cannot easily be obtained. Future work must be directed towards the tailoring of grain boundaries, namely of its conductivity, for fully revealing the bulk grain response. Preliminary results involving doping have provided the proof of concept for this approach and Fe-doped $BiScO_3$–$PbTiO_3$ nanostructured ceramics with a d_{33} coefficient of 40 pC N^{-1} have been obtained in this way [63].

A pending issue is the investigation of whether there are actual size effects, besides the described boundary ones, on the properties across the nanoscale. This requires the processing of series of nanostructured materials with decreasing grain size and tailored grain boundaries, which could be poled to saturation (or as close to it as possible). It is worth remarking that ferroelectric domains have been shown not to exist at the nanoscale, neither 180° nor non-180°, and thus domain wall contributions to the linear coefficients, and specifically to the piezoelectric ones, cannot be expected.

Poling of these domain-free materials is only possible thanks to the formation of inversion superdomains across several grains and to the movement of the superdomain walls under the electric field. Strain does not result from this movement, so extrinsic contributions to piezoelectricity are not expected. The single-crystal contribution to the room temperature d_{33} piezoelectric coefficient of PZT ceramics is 80 pC N^{-1} [22] and a similar value, 87 pC N^{-1}, has recently been reported for $BiFeO_3$–$PbTiO_3$ at its multiferroic MPB [102], a system with very high lattice strain and basically clamped non-180° walls. Therefore, the figure of 40 pC N^{-1} reported for a material with a grain size of 80 nm, and for which saturation could not be attained during poling, is not so far from these values. $BiScO_3$–$PbTiO_3$ materials with a grain size as small as 11 nm and 20 pC N^{-1} have also been reported [86]. Differences might indicate a size effect, but this cannot be concluded without knowing the level of poling achieved in the different reports. A decrease of the local out-of-plane effective piezoelectric coefficient (obtained by piezoresponse force microscopy) from 9 to 1.5 pm V^{-1} has been reported for $BiScO_3$–$PbTiO_3$ nanostructured ceramics when the grain size is decreased from 80 down to 24 nm [77], which might also indicate a size effect, for grain boundary contributions can in principle be ruled out in these highly localized measurements.

The scenario is very different for perovskite systems with nanoscale intrinsic inhomogeneity like the relaxor–ferroelectric $Pb(Mg_{1/3}Nb_{2/3})O_3$–$PbTiO_3$ and $Pb(Zn_{1/3}Nb_{2/3})O_3$–$PbTiO_3$ solid solutions. Actual size effects have been described for these systems, associated with the slowing down of the relaxor to ferroelectric transition when the grain size decreases.

Intermediate domain configurations result from this slowing down for submicrometer range structured ceramic materials, which usually have associated a degradation of functionality. However, the kinetics of the transition can be accelerated by the application of a high electric field during the relaxor to ferroelectric transition, which enables full development of the ferroelectric long-range order in materials that otherwise would have been arrested at the intermediate states. Indeed, $Pb(Mg_{1/3}Nb_{2/3})O_3$–$PbTiO_3$ materials with a grain size of 0.15 μm and d_{33} coefficients as high as 300 pC N^{-1} could be obtained by tailored poling [89].

Ferroelectric long-range order can also be partially developed from the intermediate submicrometer/nanometer-scale domain configurations by the application of a high enough electric field at room temperature, a process that involves considerable strain. This is actually a functional response, although non-linear and hysteretic, that has not been properly explored. Indeed, similar effects are currently being investigated in bulk $Bi_{1/2}Na_{1/2}TiO_3$ materials for actuation applications [103].

Further below at the nanoscale, relaxor states are stabilized. Relaxor $(1-x)Pb(Mg_{1/3}Nb_{2/3})O_3$–$xPbTiO_3$ ceramics with $x \sim 0.1$ are used for electrostrictive actuators [104]. The possibility of using the electrostriction of nanostructured ceramics for high positioning accuracy actuators has not yet been investigated.

To close the chapter and as a sort of general conclusion, results here reviewed and updated for a number of systems show that ceramic nanostructuring of high-sensitivity piezoelectrics while maintaining functionality seems feasible. Obviously more research is needed in order to fully investigate their potential. These nanostructured materials might be key enabling technologies for a range of piezoelectric miniaturized and integrated devices.

Acknowledgments

This research has been funded by MINECO (Spain) through the MAT2014-58816-R Project. Technical support by Ms I. Martínez (ICMM) is acknowledged. Work has strongly benefited from synergies established within the ESF COST Action MP0904 SIMUFER.

References

(1) Pithan, C., Hennings, D., and Waser, R. (2005) Progress in the synthesis of nanocrystalline $BaTiO_3$ powders for MLCC. *International Journal of Applied Ceramic Technology*, **2**, 1–14.

(2) Brennecka, G.L., Ihlefeld, J.F., Maria, J.P., et al. (2010) Processing technologies for high permittivity thin films in capacitor applications. *Journal of the American Ceramic Society*, **93**, 3935–3954.

(3) Uchino, K. and Takahashi S. (1996) Multilayer ceramic actuators. *Current Opinion in Solid State and Materials Science*, **1**, 698–705.

(4) Randall, C.A., Kelnberger, A., Yang, G.Y., et al. (2005) High strain piezoelectric multilayer actuators – a material science and engineering challenge. *Journal of Electroceramics*, **14**, 177—191.

(5) Haertling, G.H. (1999) Ferroelectric ceramics: history and technology. *Journal of the American Ceramic Society*, **82**, 797–818.

(6) Setter, N. (ed.) (2002) *Piezoelectric Materials in Devices*, Ceramics Laboratory EPFL, Lausanne.

(7) Anton, S.R. and Sodano, H.A. (2007) A review of power harvesting using piezoelectric materials (2003–2006). *Smart Materials and Structuctures*, **16**, R1–R21.

(8) Nan, C.W., Bichurin, M.I., Dong, S., et al. (2008) Multiferroic magnetoelectric composites: historical perspective, status, and future directions. *Journal of Applied Physics*, **103**, art. no. 31101.

(9) Wilson, S.A., Jourdain, R.P.J., Zhang, Q., et al. (2007) New materials for micro-scale sensors and actuators. An engineering review. *Materials Science and Engineering R – Reports*, **56**, 1–129.

(10) Dorey, R.A., Rocks, S.A., Dauchy, F., et al. (2010) Integrating functional ceramics into microsystems. *Journal of the European Ceramic Society*, **28**, 1397–1403.

(11) Ishiwara, H. (2012) Ferroelectric random access memories. *Journal of Nanoscience and Nanotechnology*, **12**, 7619–7627.

(12) Muralt, P. (2008) Recent progress in materials issues for piezoelectric MEMS. *Journal of the American Ceramic Society*, **91**, 1385–1396.

(13) Eom, C.B. and Trolier-McKinstry, S. (2012) Thin-film piezoelectric MEMS. *MRS Bulletin*, **37**, 1007–1017.

(14) Uchino, K. (1998) Materials issues in design and performance of piezoelectric actuators: an overview. *Acta Materialia*, **46**, 3745–3753.

(15) Damjanovic, D. (1998) Ferroelectric, dielectric and piezoelectric properties of ferroelectric thin films and ceramics. *Reports on Progress in Physics*, **61**, 1267–1324.

(16) Jaffe, B., Roth, R.S., and Marzullo, S. (1954) Piezoelectric properties of lead zirconate–lead titanate solid solution ceramics. *Journal of Applied Physics*, **25**, 809–810.

(17) Noheda, B., Gonzalo, J.A., Cross, L.E., et al. (2000) Tetragonal-to-monoclinic phase transition in a ferroelectric perovskite: the structure of $PbZr_{0.52}Ti_{0.48}O_3$. *Physical Review B*, **61**, 8687–8695.

(18) Guo, R., Cross, L.E., Park, S.E., et al. (2000) Origin of the high piezoelectric response in $PbZr_{1-x}Ti_xO_3$. *Physical Review Letters*, **84**, 5423–5426.

(19) Damjanovic, D. (2009) Comments on origins of enhanced piezoelectric properties in ferroelectrics. *IEEE Transactions on Ultrasonics, Ferroelectrics and Frequency Control*, **56**, 1574–1585.

(20) Fu, H. and Cohen, R.E. (2000) Polarization rotation mechanism for ultrahigh electromechanical response in single crystal piezoelectrics. *Nature*, **403**, 281–283.

(21) Noheda, B., Cox, D.E., Shirane, G., et al. (2001) Polarization rotation via a monoclinic phase in the piezoelectric 92% $PbZn_{1/3}Nb_{2/3}O_3$–8% $PbTiO_3$. *Physical Review Letters*, **86**, 3891–3894.

(22) Zhang, Q.M., Wang, H., Kim, N., and Cross, L.E. (1994) Direct evaluation of domain-wall and intrinsic contributions to the dielectric and piezoelectric response and their temperature dependence on lead zirconate titanate ceramics. *Journal of Applied Physics*, **75**, 454–459.

(23) Schmitt, L.A., Schöau, K., Theismann, R., et al. (2007) Composition dependence of the domain configuration and size in $Pb(Zr_{1-x}Ti_x)O_3$ ceramics. *Journal of Applied Physics*, **101**, art. no. 074107.

(24) Theismann, R., Schmitt, L.A., Kling, J., et al. (2007) Nanodomains in morphotropic lead zirconate titanate ceramics: on the origin of the strong piezoelectric effect. *Journal of Applied Physics*, **102**, art. no. 024111.

(25) Robels, U. and Arlt, G. (1993) Domain wall clamping in ferroelectrics by orientation of defects. *Journal of Applied Physics*, **73**, 3454–3460.

(26) Morozov, M.I. and Damjanovic, D. (2010) Charge migration in $Pb(Zr,Ti)O_3$ ceramics and its relation to ageing, hardening and softening. *Journal of Applied Physics*, **107**, art. no. 034106 (2010).

(27) Eitel, R.E., Randall, C.A., Shrout, T.R., et al. (2001) New high temperature morphotropic phase boundary piezelectrics based on $Bi(Me)O_3$–$PbTiO_3$ ceramics. *Japanese Journal of Applied Physics*, **40**, 5999–6002.

(28) Belik, A.A., Ikubo, S., Kodama, K., et al. (2006) $BiScO_3$: centrosymmetric $BiMnO_3$-type oxide. *Journal of the American Chemical Society*, **128**, 706–707.

(29) Inaguma, Y., Miyaguchi, A., Yoshida, M., et al. (2004) High pressure synthesis and ferroelectric properties in perovskite type $BiScO_3$–$PbTiO_3$ solid solution. *Journal of Applied Physics*, **95**, 231–235 (2004).

(30) Algueró, M., Ricote, J., Hungría, T., and Castro, A. (2007) High sensitivity piezoelectric, low tolerance factor perovskites by mechanosynthesis. *Chemistry of Materials*, **19**, 4982–4990.

(31) Eitel, R.E., Randall, C.A., Shrout, T.R., and Park, S.E. (2002) Preparation and characterization of high temperature perovskite ferroelectrics in the solid solution $(1 - x)BiScO_3$–$xPbTiO_3$. *Japanese Journal of Applied Physics*, **41**, 2099–2104.

(32) Chaigneau, J., Kiat, J.M., Malibert, C., and Bogicevic, C. (2007) Morphotropic phase boundaries in $(BiScO_3)_{1-x}(PbTiO_3)_x$ $(0.60 < c < 0.75)$ and their relation to chemical composition and polar order. *Physical Review B*, **76**, art. no. 094111.

(33) Eitel, R.E., Zhang, S.J., Shrout, T.R., et al. (2004) Phase diagram of the perovskite system $(1–x)BiScO_3$–$xPbTiO_3$. *Journal of Applied Physics*, **96**, 2822–2831.

(34) Zou, T., Wang, X., Wang, H., et al. (2008) Bulk dense fine-grain $(1–x)BiScO_3$–x $PbTiO_3$ ceramics with high piezoelectric coefficient. *Applied Physics Letters*, **93**, art. no. 192913.

(35) Zhang, S., Randall, C.A., and Shrout, T.R. (2003) High Curie temperature piezocrystals in the $BiScO_3$–$PbTiO_3$ perovskite system. *Applied Physics Letters*, **83**, 3150–3152.

(36) Zhang, S., Eitel, R.E., Randall, C.A., and Shrout, T.R. (2005) Manganese modified $BiScO_3$–$PbTiO_3$ piezoelectric ceramic for high temperature shear mode sensor. *Applied Physics Letters*, **86**, art. no. 262904.

(37) Algueró, M., Ramos, P., Jiménez, R., et al. (2012) High temperature piezoelectric $BiScO_3$–$PbTiO_3$ synthesized by mechanochemical methods. *Acta Materialia*, **60**, 1174–1183.

(38) Chen, J., Liu, G., Li, X., et al. (2013) High-temperature actuation performance of $BiScO_3$–$PbTiO_3$ ceramics and their multilayer configuration. *IEEE Transactions on Ultrasonics, Ferroelectrics and Frequency Control*, **60**, 446–450.

(39) Xiao, J., Wu, A., and Vilarinho, P.M. (2008) Sol–gel derived morphotropic phase boundary $0.37BiScO_3$–$0.63PbTiO_3$ perovskite thin films. *Applied Physics Letters*, **92**, art. no. 032902.

(40) Park, S.E. and Shrout, T.R. (1997) Ultrahigh strain and piezoelectric behavior in relaxor based ferroelectric single crystals. *Journal of Applied Physics*, **82**, 1804–1811.

(41) Zhang, S.J. and Li, F. (2012) High performance ferroelectric relaxor–$PbTiO_3$ single crystals: status and perspective. *Journal of Applied Physics*, **111**, art. no. 031301.

(42) Kwon, S., Sabolsky, E.M., Messing, G.L., and Trolier-McKinstry, S. (2005) High strain, $< 001 >$ textured $0.675Pb(Mg_{1/3}Nb_{2/3})O_3$–$0.325PbTiO_3$ ceramics: templated grain growth and piezoelectric properties. *Journal of the American Ceramic Society*, **88**, 312–317.

(43) Poterala, S.F., Trolier-McKinstry, S., Meyer Jr, R.J., and Messing, G.L. (2011) Processing, texture quality, and piezoelectric properties of $< 001 >_C$ textured $(1 - x)Pb(Mg_{1/3}Nb_{2/3})TiO_3$–$xPbTiO_3$ ceramics. *Journal of Applied Physics*, **110**, art. no. 014105.

(44) Amorín, H., Ursic, H., Ramos, P., et al. (2014) $Pb(Mg_{1/3}Nb_{2/3})TiO_3$–$PbTiO_3$ textured ceramics with high piezoelectric response by a novel templated grain growth approach. *Journal of the American Ceramic Society*, **97**, 420–426.

(45) Algueró, M., Alemany, C., Pardo, L., and Pham-Thi, M. (2005) Piezoelectric resonances, linear coefficients and losses of morphotropic phase boundary $Pb(Mg_{1/3}Nb_{2/3})TiO_3$–$PbTiO_3$ ceramics. *Journal of the American Ceramic Society*, **88**, 2780–2787.

(46) Ye, Z.G., Bing, Y., Gao, J., et al. (2003) Development of ferroelectric order in relaxor $(1 - x)Pb(Mg_{1/3}Nb_{2/3})O_3$–$xPbTiO_3$ $(0 <= x <= 0.15)$. *Physical Review B*, **67**, art. no. 104104.

(47) Singh, A.K. and Pandey, D. (2003) Evidence for M_B and M_C phases in the morphotropic phase boundary region of $(1 - x)[Pb(Mg_{1/3}Nb_{2/3})O_3]$–$xPbTiO$): a Rietveld study. *Physical Review B*, **67**, art. no. 064102.

(48) Burton, B.P., Cockayne, E., and Waghmare, U.W. (2005) Correlations between nanoscale chemical and polar order in relaxor ferroelectrics and the lengthscale for polar nanoregions. *Physical Review B*, **72**, art. no. 064113.

(49) Haumont, R., Al-Barakaty, A., Dkhil, B., et al. (2005) Morphotropic phase boundary of heterovalent perovskite solid solutions: experimental and theoretical investigation of $PbSc_{1/2}Nb_{1/2}O_3$–$PbTiO_3$. *Physical Review B*, **71**, art. no. 104106.

(50) Saito, Y., Takao, H., Tani, T., et al. (2004) Lead-free piezoceramics. *Nature*, **432**, 84–87.

(51) Shrout, T.R. and Zhang, S.J. (2007) Lead-free piezoelectric ceramics: alternatives for PZT? *Journal of Electroceramics*, **19**, 111–124.

(52) Yilmaz, H., Trolier-McKinstry, S., and Messing, G.L. (2003) (Reactive) template grain growth of textured sodium bismuth titanate ($Na_{1/2}Bi_{1/2}TiO_3$–$BaTiO_3$) ceramics – II. Dielectric and piezoelectric properties. *Journal of Electroceramics*, **11**, 217–226.

(53) Dittmer, R., Jo, W., Rodel, J., et al. (2012) Nanoscale insight into lead-free BNT–BT–xKNN. *Advanced Functional Materials*, **22**, 4208–4215.

(54) Schutz, D., Deluca, M., Krauss, W., et al. (2012) Lone-pair-induced covalency as the cause of temperature- and field-induced instabilities in bismuth sodium titanate. *Advanced Functional Materials*, **22**, 2285–2294.

(55) Rodel, J., Jo, W., Seifert, K.T.P., et al. (2009) Perspective on the development of lead-free piezoceramics. *Journal of the American Ceramic Society*, **92**, 1153–1177.

(56) Zhang, S.T., Kounga, A.B., Aulbach, E., et al. (2007) Giant strain in lead free piezoceramics of the $Bi_{0.5}Na_{0.5}TiO_3$–$BaTiO_3$–$K_{0.5}Na_{0.5}NbO_3$ system. *Applied Physics Letters*, **91**, art no. 112906.

(57) Moosavi, A., Bahrevar, M.A., Aghaei, A.R., et al. (2014) High field electromechancial response of $(Bi_{1/2}Na_{1/2})TiO_3$–$(Bi_{1/2}K_{1/2})TiO_3$ across its morphotropic phase boundary. *Journal of Physics D: Applied Physics*, **47**, art. no. 055304.

(58) Hungría, T., Amorín, H., Algueró, M., and Castro, A. (2011) Nanostructured ceramics of $BiScO_3$–$PbTiO_3$ with tailored grain size by spark plasma sintering. *Scripta Materialia*, **64**, 97–100.

(59) Elissalde, C. and Ravez, J. (2001) Ferroelectric ceramics: defects and dielectric relaxations. *Journal of Materials Chemistry*, **11**, 1957–1967.

(60) Zou, T., Wang, X., Zhao, W., and Liu, L. (2008) Preparation and properties of fine-grain $(1-x)BiScO_3$–$xPbTiO_3$ ceramics by two-step sintering. *Journal of the American Ceramic Society*, **91**, 121–126.

(61) Amorín, H., Jiménez, R., Deluca, M., et al. (2014) Nanostructuring effects in piezoelectric $BiScO_3$–$PbTiO_3$ ceramics. *Journal of the American Ceramic Society*, **97**, 2802–2809.

(62) Hungría, T., Houdellier, F., Algueró, M., and Castro, A. (2010) Monoclinic symmetry of twin-free nanocrystals in the $BiScO_3$–$PbTiO_3$ solid solution as revealed by aberration-corrected TEM. *Physical Review B*, **81**, art. no. 100102.

(63) Algueró, M., Amorín, H., Hungría, T., et al. (2009) Macroscopic ferroelectricity and piezoelectricity in nanostructured $BiScO_3$–$PbTiO_3$ ceramics. *Applied Physics Letters*, **94**, art. no. 012902.

(64) Amorín, H., Jiménez, R., Ricote, J., et al. (2010) Apparent vanishing of ferroelectricity in nanostructured $BiScO_3$–$PbTiO_3$. *Journal of Physics D: Applied Physics*, **43**, art. no. 285401.

(65) Damjanovic, D. (1997) Logarithmic frequency dependence of the piezoelectric effect due to pinning of ferroelectric–ferroelastic domain walls. *Physical Review B*, **55**, R649–R652.

(66) Eitel, R.E., Shrout, T.R., and Randall, C.A. (2006) Non-linear contributions to the dielectric permittivity and converse piezoelectric coefficient in piezoelectric ceramics. *Journal of Applied Physics*, **99**, art. no. 124110.

(67) Randall, C.A., Kim, N., Kucera, J.P., et al. (1998) Intrinsic and extrinsic size effects in fine-grained morphotropic phase boundary lead zirconate titanate ceramics. *Journal of the American Ceramic Society*, **81**, 677–688.

(68) Zhao, Z., Buscaglia, V., Viviani, M., et al. (2004) Grain size effects on the ferroelectric behavior of dense nanocrystalline $BaTiO_3$ ceramics. *Physical Review B*, **70**, art. no. 024107.

(69) Buscaglia, M.T., Viviani, M., Buscaglia, V., et al. (2006) High dielectric constant and frozen macroscopic polarization in dense nanocrystalline $BaTiO_3$ ceramics. *Physical Review B*, **73**, art. no. 064114.

(70) Deng, X., Wang, X., Wen, H., et al. (2006) Ferroelectric properties of nanocrystalline barium titanate ceramics. *Applied Physics Letters*, **88**, art. no. 252905.

(71) Kamel, T.M. and de With, G. (2008) Grain size effect on the poling of soft $Pb(Zr,Ti)O_3$ ferroelectric ceramics. *Journal of the European Ceramic Society*, **28**, 851–861.

(72) Zhang, S., Alberta, E.F., and Shrout, T.R. (2005) Elastic, piezoelectric and dielectric characterization of modified $BiScO_3$–$PbTiO_3$ ceramics. *IEEE Transactions on Ultrasonics, Ferroelectrics and Frequency Control*, **52**, 2131–2139.

(73) Arlt, G., Hennings, D., and de With, G. (1986) Dielectric properties of fine-grained barium titanate ceramics. *Journal of Applied Physics*, **58**, 1619–1625.

(74) Arlt, G. and Sasko, P. (1980) Domain configuration and equilibrium size of domains in $BaTiO_3$ ceramics. *Journal of Applied Physics*, **51**, 4958–4960.

(75) Arlt, G. (1990) Twinning in ferroelectric and ferroelastic ceramics – stress relief. *Journal of Materials Science*, **25**, 2655–2666.

(76) Cao, W. and Randall, C.A. (1996) Grain size and domain size relations in bulk ceramic ferroelectric materials. *Journal of Physics and Chemistry of Solids*, **57**, 1499–1505.

(77) Salazar, N., Algueró, M., Amorín, H., et al. (2014) Local characterization of nanostructured high sensitivity piezoelectric $BiScO_3$–$PbTiO_3$ ceramics by piezoresponse force microscopy. *Journal of Applied Physics*, **116**, art. no. 124108.

(78) Damjanovic, D. and Demartin, M. (1996) The Rayleigh law in piezoelectric ceramics. *Journal of Physics D: Applied Physics*, **29**, 2057–2060.

(79) Nattermann, T., Shapir, Y., and Vilfan, I. (1990) Interface pinning and dynamics in random systems. *Physical Review B*, **42**, 8577–8586.

(80) Frey, M.H., Xu, X., Han, P., and Payne, D.A. (1998) The role of interfaces on an apparent grain size effect on the dielectric properties for ferroelectric barium titanate ceramics. *Ferroelectrics*, **206–207**, 337–353.

(81) Padurariu, L., Curecheriu, L., Buscaglia, V., and Mitoseriu, L. (2012) Field dependent permittivity in nanostructured $BaTiO_3$ ceramics: modeling and experimental verification. *Physical Review B*, **85**, art. no. 224111.

(82) Irvine, J.T.S., Sinclair, D.C., and West, A.R. (1990) Electroceramics: characterization by impedance spectroscopy. *Advanced Materials*, **2**, 132–138.

(83) Pecharroman, C. and Iglesias, J.E. (1994) Effective dielectric properties of packed mixtures of insulator particles. *Physical Review B*, **49**, 7137–7147.

(84) Jiménez, R. (1996) Application of the percolation effective medium theory (PEMT) to solid electrolyte pressed powder pellets. 2. Electrically anisotropic solid electrolyte particles. *Solid State Ionics*, **92**, 225–241.

(85) Zhang, S., Wang, X., Wang, H., and Li, L. (2014) Grain boundary region and local piezoelectric response of $BiScO_3$–$PbTiO_3$ nanoceramics prepared by combination of SPS and two-step sintering. *Journal of the European Ceramic Society*, **34**, 2317–2323.

(86) Zhang, S., Wang, X., Wang, H., and Li, L. (2014) The microstructure and ferroelectricity of $BiScO_3$–$PbTiO_3$ nanoceramics at morphotropic phase boundaries. *Scripta Materialia*, **82**, 45–48.

(87) Carreaud, J., Gemeiner, P., Kiat, J.M., et al. (2005) Size driven relaxation and polar states in $Pb(Mg_{1/3}Nb_{2/3})O_3$ based systems. *Physical Review B*, **72**, art. no. 174115.

(88) Carreaud, J., Kiat, J.M., Dkhil, B., et al. (2006) Monoclinic morphotropic phase and grain size induced polarization rotation in $Pb(Mg_{1/3}Nb_{2/3})O_3$–$PbTiO_3$. *Applied Physics Letters*, **89**, art. no. 252906.

(89) Algueró, M., Ricote, J., Jiménez, R., et al. (2007) Size effect in morphotropic phase boundary $Pb(Mg_{1/3}Nb_{2/3})O_3$–$PbTiO_3$. *Applied Physics Letters*, **91**, art. no. 112905.

(90) Viehland, D., Kim, M.C., Xu, Z., and Li, J.F. (1995) Long-time present tweedlike precursors and paraelectric clusters in ferroelectrics containing strong quenched randomness. *Applied Physics Letters*, **67**, 2471–2474.

(91) Burns, G. and Dacol, F.H. (1983) Crystalline ferroelectrics with glassy polarization behavior. *Physical Review B*, **28**, 2527–2530.

(92) Dkhil, B., Kiat, J.M., Calvarin, G., et al. (2001) Local and long range polar order in the relaxor–ferroelectric compounds $PbMg_{1/3}Nb_{2/3}O_3$ and $PbMg_{0.3}Nb_{0.6}Ti_{0.1}O_3$. *Physical Review B*, **65**, art. no. 024104.

(93) Jiménez, R., Jiménez, B., Carreaud, J., et al. (2006) Transition between the ferroelectric and relaxor states in $0.8Pb(Mg_{1/3}Nb_{2/3})O_3$–$0.2PbTiO_3$ ceramics. *Physical Review B*, **74**, art. no. 184106.

(94) Algueró, M., Jiménez, B., and Pardo, L. (2005) Transition between the relaxor and ferroelectric states for $(1-x)Pb(Mg_{1/3}Nb_{2/3)}O_3$–$xPbTiO_3$ with $x = 0.2$ and 0.3 polycrystalline aggregates. *Applied Physics Letters*, **87**, art. no. 082910.

(95) Jiménez, R., Amorín, H., Ricote, J., et al. (2008) Effect of grain size on the transition between ferroelectric and relaxor states in $0.8Pb(Mg_{1/3}Nb_{2/3})O_3$–$0.2PbTiO_3$ ceramics. *Physical Review B*, **78**, art. no. 09103.

(96) Algueró, M., Ricote, J., Ramos, P., et al. (2008) Size effects on the macroscopic properties of the relaxor–ferroelectric $Pb(Mg_{1/3}Nb_{2/3})O_3$–$PbTiO_3$ solid solution, in *Handbook of Advanced Dielectric, Piezoelectric and Ferroelectric Materials: Synthesis, Properties and* Applications, edited by Z.G. Ye, Woodhead Publishing Ltd, Cambridge, pp. 447–471.

(97) Xu, G.Y., Gehring, P.M., and Shirane, G. (2006) Coexistence and competition of local- and long-range polar orders in a ferroelectric relaxor. *Physical Review B*, **74**, art. no. 104110.

(98) Algueró, M., Ricote, J., and Castro, A. (2004) Mechanosynthesis and thermal stability of piezoelectric perovskite $0.92Pb(Zn_{1/3}Nb_{2/3})O_3–0.08PbTiO_3$ powders. *Journal of the American Ceramic Society*, **87**, 772–778.

(99) Algueró, M., Hungría, T., Amorín, H., et al. (2007) Relaxor behaviour, polarization buildup, and switching in nanostructured $0.92Pb(Zn_{1/3}Nb_{2/3})O_3–0.08PbTiO_3$ ceramics. *Small*, **3**, 1996–1911.

(100) Amorín, H., Jiménez, R., Hungría, T., et al. (2009) Relaxor behaviour in nanostructured $Pb(Zn_{1/3}Nb_{2/3})O_3–Pb(Fe_{1/2}Nb_{1/2})O_3–PbTiO_3$ ceramics. *Applied Physics Letters*, **94**, art. no. 152902.

(101) La-Orauttapong, D., Toulouse, J., Ye, Z.G., et al. (2003) Neutron scattering study of the relaxor ferroelectric $(1 - x)Pb(Zn_{1/3}Nb_{2/3})O_3–xPbTiO_3$. *Physical Review B*, **67**, art. no. 134110.

(102) Amorín, H., Correas, C., Fernédez-Posada, C.M., et al. (2014) Multiferroism and enhancement of materials properties across the morphotropic phase boundary of $BiFeO_3–PbTiO_3$. *Journal of Applied Physics*, **115**, art. no. 104104.

(103) Sapper, E., Gassmann, A., Gjodvad, L., et al. (2014) Cycling stability of lead-free BNT–8BT and BNT–6BT–3KNN multilayer actuators and bulk ceramics. *Journal of the European Ceramic Society*, **34**, 653–661.

(104) Nomura, S. and Uchino, K. (1982) Electrostrictive effect in $Pb(Mg_{1/3}Nb_{2/3})O_3$ type materials. *Ferroelectrics*, **41**, 117–132.

17

Correlation between Microstructure and Electrical Properties of Ferroelectric Relaxors

Jelena D. Bobic[1], Jan Macutkevic[2], Robertas Grigalaitis[2], Maksim Ivanov[2], Mirjana M. Vijatovic Petrovic[1], Juras Banys[2], and Biljana D. Stojanovic[1]

[1]*Institute for Multidisciplinary Research, University of Belgrade, Serbia*
[2]*Faculty of Physics, Vilnius University, Lithuania*

17.1 Introduction

Relaxor ferroelectrics or relaxors are a class of disordered crystals possessing a peculiar structure and properties. Relaxor ferroelectrics are found in many applications in electronics such as multilayer ceramic capacitors, electro-optical devices, and medical imaging devices [1]. At high temperatures they exist in a non-polar paraelectric phase, which is similar in many respects to the paraelectric phase of normal ferroelectrics. Upon cooling they transform into the ergodic relaxor state in which polar regions of nanometer scale (polar nano regions PNRs) with randomly distributed directions of dipole moments appear. This transformation, which occurs at the so-called Burns temperature (T_B) [2], cannot be considered a structural phase transition because it is not accompanied by any change of the crystal structure on the macroscopic or mesoscopic scale. Nevertheless, the polar nanoregions affect the behavior of the crystal dramatically, giving rise to unique physical properties. For this reason the state of materials at $T < T_B$ is often considered as a new phase different from the paraelectric one. At temperatures close to T_B the polar nanoregions are mobile and

---

Nanoscale Ferroelectrics and Multiferroics: Key Processing and Characterization Issues, and Nanoscale Effects, First Edition. Edited by Miguel Algueró, J. Marty Gregg, and Liliana Mitoseriu.
© 2016 John Wiley & Sons, Ltd. Published 2016 by John Wiley & Sons, Ltd.

their behavior is ergodic. On cooling, their dynamics slows down enormously and at a low enough temperature, T_0 (typically hundreds degrees below T_B), the polar nanoregions in the canonical relaxors become frozen into a non-ergodic state, while the average symmetry of the crystal still remains cubic.

A similar kind of non-ergodicity is characteristic of a dipole glass (or spin glass) phase. The existence in relaxors of an equilibrium phase transition into a low-temperature glassy phase is one of the most interesting hypotheses that have been intensively discussed. The freezing of the dipole dynamics is associated with a large and wide peak in the temperature dependence of the dielectric permittivity with characteristic dispersion observed at all frequencies practically available for the dielectric measurements. Usually, the peak value of dielectric permittivity in relaxors is very high (more than 10 000), similarly as in ferroelectrics. In contrast to ferroelectrics the dielectric anomaly is highly diffused and its temperature shifts with frequency due to the dielectric dispersion. Similarly, as in typical displacive ferroelectrics, the soft phonon modes also exist in ferroelectric relaxors [3]. The critical temperature of the soft phonon modes is close to T_B and the soft mode is ferroelectric soft mode inside polar nanoregions. Moreover, in the strong bias electric field in $Pb(Mg_{1/3}Nb_{2/3})O_3$ (PMN), a typical displacive ferroelectric phase transition was observed by means of Raman, polarization hysteresis, and calorimetric measurements [4, 5]. Nevertheless, the contribution of the soft phonon modes to the static dielectric permittivity for relaxors without a bias electric field is quite low and no dielectric anomaly was observed in the temperature dependence of the static dielectric permittivity of ferroelectric relaxors close to T_B [6]. Moreover, the non-ergodic relaxor state existing below T_0 can be irreversibly transformed into a ferroelectric state by a strong enough external electric field. This is an important characteristic of relaxors, which distinguishes them from typical dipole glasses. Upon heating, the ferroelectric phase transforms to the ergodic relaxor one at the temperature T_C, which is very close to T_0. In some relaxors the spontaneous (i.e. without the application of an electric field) phase transition from the ergodic relaxor into a low-temperature ferroelectric phase still occurs at T_C and thus the non-ergodic relaxor state does not exist.

Compositional disorder, that is the disorder in the arrangement of different ions on the crystallographically equivalent sites, is the common feature of relaxors. The relaxor behavior was first observed in the perovskites with disorder of non-isovalent ions, including the stoichiometric complex perovskite compounds, for example $Pb(Mg_{1/3}Nb_{2/3})O_3$ (PMN) [7] or $Pb(Sc_{1/2}Ta_{1/2})O_3$ (PST) [8] (in which Mg^{2+}, Sc^{3+}, Ta^{5+}, and Nb^{5+} ions are fully or partially disordered in the B-sublattice of the perovskite ABO_3 structure) and non-stoichiometric solid solutions, for example $Pb_{1\text{-}x}La_x(Zr_{1\text{-}y}Ti_y)_{1\text{-}x/4}O_3$ (PLZT) [9, 10], where the substitution of La^{3+} for Pb^{2+} ions necessarily leads to vacancies on the A-sites. Recently, an increasing amount of work on lead-free disordered piezoelectrics has shown that many homovalent solid solutions, for example $Ba(Ti_{1\text{-}x}Zr_x)O_3$ (BTZ) [11, 12], and $Ba(Ti_{1\text{-}x}Sn_x)O_3$ [13], can also exhibit relaxor behaviour.

Bismuth layer-structured ferroelectrics (BLSFs) with Aurivillius structure are revealed as a promising alternative to lead-based relaxor materials for many electronic applications. Many lead-based materials with remarkable electromechanical properties, such as PLZT and PMN, are deemed to be banned due to EU environmental regulations. A lot of literature sources about lead-free ferroelectric ceramics are available nowadays, but the deeper research is needed in order to substitute lead-based materials.

The most important theory on transition in relaxors from the ergodic to the non-ergodic state is the spherical random-bond–random-field (SRBRF) model proposed by Pirc and Blinc [14, 15], in which the Hamiltonian is formally written as:

$$H = H_1 + H_2 \tag{17.1}$$

The first term is written in a standard form:

$$H_1 = -\sum_{ij} J_{ij} \boldsymbol{S}_i \cdot \boldsymbol{S}_j \tag{17.2}$$

where pseudospins $\boldsymbol{S}_i$, proportional to the dipole moments of polar nanoregions, are introduced so that the relation:

$$\sum_i (\boldsymbol{S}_i)^2 = 3N \tag{17.3}$$

is satisfied (N is the number of pseudospins in the crystal). It is assumed that each component of $\boldsymbol{S}_i$ can fluctuate continuously and take any value, that is $-\infty < \boldsymbol{S}_{i\mu} < +\infty$.

J_{ij} (in Equation (17.2)) are the random interactions (bonds) between polar nanoregions, which are assumed to be infinitely ranged. The second term in the Hamiltonian (in Equation (17.1)) describes the interaction of pseudospins with quenched random electric fields $\boldsymbol{f}_i$:

$$H_2 = -\sum_i \boldsymbol{f}_i \cdot \boldsymbol{S}_i \tag{17.4}$$

Both random bonds J_{ij} and random fields $\boldsymbol{f}_i$ obey the (uncorrelated) Gaussian probability distributions with a variance of ΔJ and Δf, respectively. The mean value of the distributions equals J_0 (for random bonds) and zero (for random fields). In the absence of random fields ($\Delta f = 0$), if $J_0 > \Delta J$, the theory predicts the transition from the paraelectric phase (in the model this phase is equivalent to the ergodic relaxor phase) into an inhomogeneous ferroelectric phase with a non-zero spontaneous polarization; if $J_0 < \Delta J$, the system transforms, at a well-defined temperature $T = \Delta J/k_B$, from the paraelectric to a spherical glass phase without long-range order, and the glass order parameter (which is equivalent in this model to the well-known Edwards–Anderson order parameter, q) decreases linearly from 1 at $T = 0$ to zero at $T = \Delta J/k_B$. The presence of random fields ($\Delta f \neq 0$) destroys the phase transition so that q remains non-zero at $T = \Delta J/k_B$, and approaches zero when the temperature further increases [15].

Recently, the SRBRF model has been generalized into a compressible spherical dipolar glass (CSDG) model assuming that for relaxors in the ergodic phase valid Landau model [16]:

$$F = F_0 + {}^1\!/\!_2 aP^2 + {}^1\!/\!_4 bP^4 + {}^1\!/\!_6 cP^6 + \cdots - EP \tag{17.5}$$

where the coefficient a is related to the inverse static dielectric permittivity, namely, $a = 1/\varepsilon_0$, and for temperature dependence of the static dielectric permittivity $\varepsilon(0)$ the valid SRBRF relation is:

$$\varepsilon\,(0) = \frac{1}{\varepsilon_0} \frac{Q\,(1-q)}{T - \left(J_0/k\right)(1-q)} \tag{17.6}$$

Moreover, an electrostrictive coupling between the dielectric polarization and strain or stress tensor fluctuations is taken into account in CSDG theory. CSDG theory describes well the heat capacitance anomaly of relaxors under a bias electric field [16].

The current research activity in relaxor physics is mostly concentrated on differences and similarities between the relaxors, the ferroelectrics and the dipolar glasses. It was demonstrated, for example, that the dipolar glasses can be obtained by doping relaxors [17]. On the other hand, the differences between the relaxors and the displacive ferroelectrics were recently explained by a phonon localization idea [18]. Moreover, the formation of polar nanoregions was attributed to intrinsic local modes in terms of discrete breathers [19, 20]. Thus, the existence of such modes should be the main difference between the relaxors and the displacive ferroelectrics [19]. The differences between various ferroic systems becomes very important in the case of new disordered materials [21].

The Vogel–Fulcher law is a common characteristic of relaxor and dipolar glasses [17]. It can be applied for the relaxation time:

$$\tau = \tau_0 \exp \frac{E_{\mathrm{A}}}{k_{\mathrm{B}}(T - T_0)} \tag{17.7}$$

where τ_0 is the attempt relaxation time, E_A is the activation energy, T_0 is the freezing temperature, and k_{B} is the Boltzmann constant. The Vogel–Fulcher law usually manifests in disordered materials expecting a ”freezing” of its dynamic at some finite temperature above 0 K such as relaxor compounds (see, for example, [6]) or for the position of the maximum of real or imaginary part of the complex dielectric permittivity:

$$\nu = \nu_{\mathrm{o}} \exp \left\{ \frac{-E_{\mathrm{A}}}{k_{\mathrm{B}}\left(T_{\mathrm{m}} - T_{\mathrm{f}}\right)} \right\} \tag{17.8}$$

where ν_0 is the attempt frequency of dipole reorientation, E_{A} is the activation energy (i.e. the energy barrier between two equivalent polarization states), k_{B} is the Boltzmann's constant, and T_{f} is the static freezing temperature of the polarization fluctuations (i.e. the temperature below which the dynamic reorientation of the dipolar cluster polarization can no longer be thermally activated). Note that the parameters obtained by fitting experimental data with Equations (17.7) and (17.8) will always be different, except for the Debye medium case [22].

Another important problem is the structure and the behavior of polar nanoregions. The percolation of polar nanoregions was claimed to exist close to the freezing temperature [23] and in a strong DC electric field close to the transition from the relaxor to the ferroelectric state [24]. However, the nature of such percolations of course should be different. A fractal structure of polar nanoregions was observed in a typical relaxor PMN by means of broadband light scattering spectroscopy [25]. A fractal dimension in PMN at $T < 200$ K was estimated of about 2.61, in good agreement with that theoretically obtained in 3D space [25].

It is well known that the properties of ferroelectric ceramics are very sensitive to their microstructure. There are many factors that could have an influence on final properties of a material such as the powder synthesis method, grain size, and defects (dependent on the processing method type, temperature and time of sintering, additives, etc.). Besides that, the perovskite oxide materials are known to be great hosts for various dopants and the majority of well-studied relaxors are of this structure. However, there are known limitations, for example perovskite multiferroics are scarce [26], and search for materials with alternative structures is of interest [27]. Thus, in this chapter the modifications of electrical properties of relaxor ferroelectrics by grain size reduction and introduction of dopants will be reviewed on the basis of three different families: "classical" relaxor PMN, relaxor ferroelectrics PSN with perovskite structure, and relaxor ferroelectrics $BaBi_4Ti_4O_{15}$ (BBT) with Aurivillius structure.

17.2 Perovskite Relaxors

17.2.1 Nanosized PMN Powders and Nanostructured Ceramics

The influence of the grain size on the dielectric properties of relaxors and mixed ferroelectrics close to the morphotropic phase boundary was studied mainly at low frequencies (i.e. below 1 MHz) [28–31]. It was established that the dielectric permittivity of PMN at low frequencies decreases with reducing grain size and the effect can be explained by a core–shell model [32], which assumes the existence of a dead layer on the surface of the grains and the permittivity of the layer is much lower than of the grain itself. The model predicts a diminution of the overall dielectric permittivity with a decrease of the grain size due to grain boundary "dilution". The dielectric anomaly typical for relaxors completely vanishes in PMN ceramics with 30 nm grain size [32]. The smeared dielectric response of nanograin ceramics was explained in [33] as due to the clamping of PNRs by the grain boundaries. In [31] these observations have been interpreted as the consequence of the continuous disappearance of the correlations between the PNRs that, in turn, gives rise to a transition from a relaxor (interacting PNRs) to a superparaelectric (independent PNRs) state. However, the dielectric investigations of the grain size effect in a wide frequency range could reveal much more interesting features. For example, it was established that in $PbMg_{1/3}Nb_{2/3}O_3$–$PbTiO_3$ (PMN–PT) the ferroelectric phase transition transforms into a relaxor-like anomaly with reduction of the grain size down to 150 nm [33]. The opposite behavior, that is the transition from relaxor to ferroelectric with reducing grain size, could also be possible, if the decrease of the random fields and random bonds would be more rapid than the decrease of the mean interaction energy, according to the spherical bond random (SBRF) model [14]. Moreover, the shift of the dielectric anomaly in PMN with different grain sizes to lower temperatures was observed [34]. Thus, it was necessary to perform broad-band dielectric investigations to estimate the correct behavior of the freezing temperature and other relaxor parameters [6].

Therefore it appears interesting to study the dielectric permittivity in a broader frequency range (20 Hz–1 GHz) and to compare the properties of powders with the properties of ceramics with different grain sizes. Additional comparisons with published data on large grain size ceramics and single-crystal structures have also been performed. In particular, we determined the distribution of the relaxation times from these new measurements.

Powders with various grain sizes in the range of 15 nm to 1000 nm were obtained by annealing a PMN nanopowder (15 nm) prepared by direct mechanical activation of PbO and columbite $MgNb_2O_6$. Nanograin PMN ceramics with 50, 70, and 115 nm grain size and the relative density of 88, 91, and 97%, respectively, were prepared by hot pressing at temperatures of 700, 750, and 800 °C under 90 MPa pressure. The dielectric permittivity of PMN nanoceramics has been measured in a 150–450 K temperature region and 20 Hz–1 GHz frequency range. In the case of PMN powders (15, 30, 40, 65, and 150 nm), it was possible to make measurements in the 20 Hz–1MHz frequency range due to the difficulties to put them into a coaxial line. The frequency range has been covered by two different techniques: by the impedance analyzer HP4284 in a low-frequency range (20 Hz–1 MHz) and by the Agilent 8714 vector network analyzer in the high-frequency range (1 MHz–1 GHz). More detailed experimental procedures are described by in [35].

17.2.1.1 Dielectric Investigations of PMN Nanopowders

The temperature and frequency dependencies of the real part of the dielectric permittivity of PMN powders with a few selected grain sizes (15, 40, and 150 nm [35,36]) are presented in Figure 17.1. The dielectric permittivity values were normalized to maximum permittivity obtained for each specimen due to the impossibility of determining the powder-to-air ratio in the specimen. As seen in Figure 17.1, the dispersion occurs below room temperature; thus, to highlight the dispersion region, we show the temperature dependences only below 300 K. Two main features of the dielectric behavior can be indicated. Firstly, a remarkable shift of the dispersion region to the higher temperatures with the grain size increase (Figure 17.1(a), (b), and (c)) is observed. Secondly, a diminution of the dielectric dispersion on

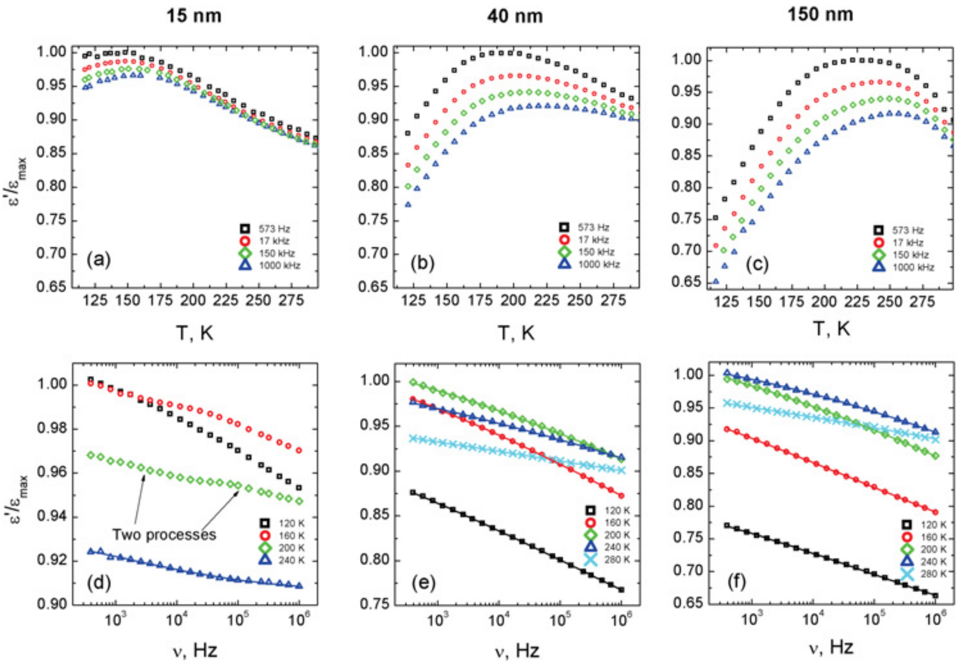

Figure 17.1 *Temperature (a, b, and c) and frequency (d, e, and f) dependences of the real part of normalized dielectric permittivity of PMN nanopowders with different grain sizes. Solid lines in frequency dependences represent Cole–Cole fits. Adapted from [35]. © IOP Publishing. Reproduced by permission of IOP Publishing. All rights reserved*

the decrease of the grain size of powders is also clearly visible, especially if one compares 150 nm [36] and 15 nm [35] curves (Figure 17.1(a) and (c)). To go into a deeper analysis we presented the dielectric data in the frequency domain. The frequency dependencies of the dielectric permittivity (Figure 17.1(d), (e), and (f)) show a substantial dispersion in all investigated frequency ranges.

The experimental data were approximated using the conventional Cole–Cole formula:

$$\varepsilon^* = \varepsilon_\infty + \frac{\Delta\varepsilon}{1 + (i\omega\tau)^{1-\alpha}} \tag{17.9}$$

where $\Delta\varepsilon$ is the relaxator strength, τ is the average Cole–Cole relaxation time, α is the coefficient of the distribution of relaxation times, ε_∞ is the contribution of all higher frequency processes to the dielectric permittivity, and $\omega = 2\pi\nu$ is the measurement angular frequency.

The fit lines are in a good agreement with experimental data (Figure 17.1). The analysis of the data revealed that the dielectric dispersion broadens upon cooling, especially below 200 K, and shifts to lower frequencies. These frequency dependencies are much broader than the usual Debye-type dispersion, except for the smallest (15 nm) grain size powders. Two overlapping relaxation processes were observed in the former case at temperatures below 200 K and therefore a superposition of two Cole–Cole processes has been used in the fitting procedure. The mean relaxation time obtained from the Cole–Cole fits (Figure 17.2) has been analyzed in terms of the Vogel–Fulcher law (Equation (17.7)).

Good approximation of the data (solid lines in Figure 17.2) has been obtained for all grain size powders except for the smallest ones, for which almost no temperature dependence of τ is observed, in agreement with previous observations of the disappearance of relaxor character at the smallest grain sizes [28].

To find out the influence of the mean grain size to the properties of PMN powders the temperature of the maximum dielectric permittivity, $T_{\max}$, and the values of freezing temperature, T_0, versus grain size are presented in Figure 17.3. Here the experimental points for micrometric PMN ceramics, single-crystal and 150 nm powders, taken from our earlier

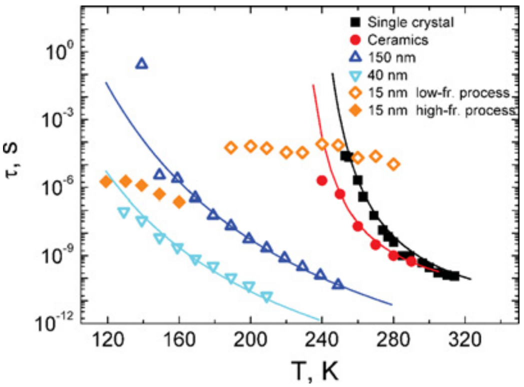

Figure 17.2 *Temperature and grain size dependence of the mean relaxation time obtained from the Cole–Cole formula for PMN powders. Solid lines represent Vogel–Fulcher fits. Adapted from [35]. © IOP Publishing. Reproduced by permission of IOP Publishing. All rights reserved*

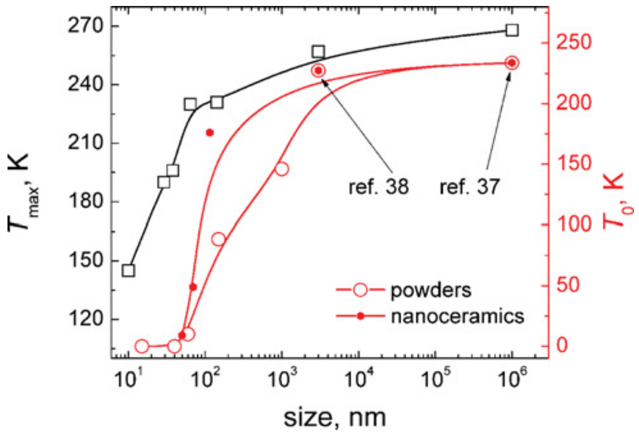

Figure 17.3 *Grain size evolution of T_{max} at 1 kHz frequency (squares) in PMN powder samples and dipole freezing temperatures obtained from Vogel–Fulcher fits for PMN powders (open circles) and nanograin ceramics (filled hexagons). The two rightmost points are taken from Grigalaitis et al. [37,38]. Solid lines are guidelines for eyes. Adapted from [35]. © IOP Publishing. Reproduced by permission of IOP Publishing. All rights reserved*

investigations [35–38] have been added for comparison. All these data behave coherently: from micrometric sizes T_{max} decreases smoothly with reducing grain size, but an abrupt decrease of T_{max} occurs below 60 nm. The evolution is similar to the grain size dependence of the Curie temperature obtained for $BaTiO_3$ [39] or $PbTiO_3$ [40] perovskites, despite the fact that no ferroelectric phase transition takes place in PMN without a bias electric field [41].

Grain size dependence of the freezing temperature is very similar. The T_0 is almost grain size independent if grains are bigger than ~300 nm. However, an abrupt decrease of the freezing temperature occurs with reducing grain size from 300 to 40 nm. Finally, the freezing temperature reaches zero in PMN powders with grain sizes smaller than 40 nm.

17.2.1.2 Dielectric Properties of PMN Nanoceramic

Similarly to the behavior of nanopowders, broad maxima of both real and imaginary parts of the complex dielectric permittivity are observed in nanoceramics with grain sizes of 50, 70, and 115 nm [35] (Figure 17.4). The dielectric anomaly is very similar to the one observed in PMN crystals or coarse-grained ceramics [37,38]. However, the values of dielectric permittivity (at the same temperature) decrease with reducing grain size in all measured frequency ranges from 20 Hz to 1 GHz. At lower frequencies (below 1 MHz), the temperature of the maximum of dielectric permittivity at a selected frequency shifts to the higher temperatures with reducing the grain size, and this decrease is in a good agreement with results presented by Carreaud et al. [32]. On the other hand, at higher frequencies (above 1 MHz) the position of the maximum of the dielectric permittivity shifts to the lower temperatures with reducing the grain size, that is it follows the opposite behavior.

The effect cannot be described by a core–shell model by assuming a frequency independent dielectric permittivity of the shell [32]. This suggests that the grain size influence

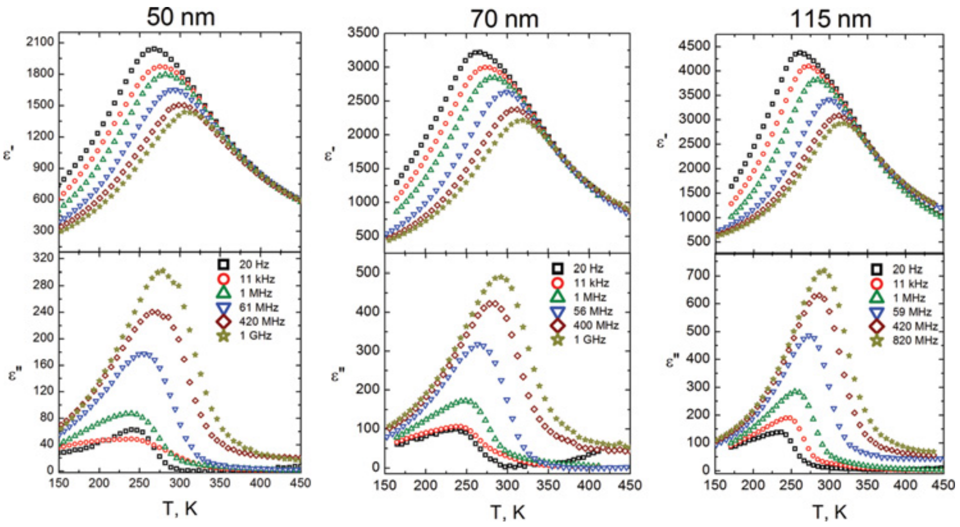

Figure 17.4 Temperature and grain size dependence of dielectric permittivity of PMN nanoceramics. Adapted from [35]. © IOP Publishing. Reproduced by permission of IOP Publishing. All rights reserved

is more pronounced at lower frequencies. This behavior is in a good agreement with the observed weak grain size dependence of the soft mode frequency found in ceramics [33].

The dielectric behavior of PMN nanoceramics, represented in the frequency domain (Figure 17.5), is more complicated than in the case of powders. Here the main dispersion region is located in the GHz range and broadens on cooling, but is nearly frequency-independent. In addition to that, at low frequencies (below 1 MHz), another relaxation process can be distinguished. In the finest nanoceramics (15 nm), it can be well separated from the main dispersion region, but it broadens on the increase of the mean grain size and in the nanoceramics with 115 nm grain size, it substantially overlaps the high-frequency one. Again, this process is not frequency-independent and it moves towards lower frequencies on cooling. This is especially clearly evident when one examines the behavior of the imaginary part of the dielectric permittivity in the 50 nm grain size ceramics, but the same tendencies are also observed in other nanoceramics. It needs to be emphasized that in micrometer-sized PMN ceramics [38] one can see only one broad dispersion extending over all the frequency region where both relaxation processes in nanoceramics are visible.

It is clear that such complicated dispersion cannot be described by the simple Cole–Cole formula (Equation (17.9)). Thus, in order to get a better description of the frequency dependences and to obtain a more detailed information about the relaxation processes in these nanoceramics, the distribution of relaxation times $f(\tau)$ was calculated for each sample, according to the formula:

$$\varepsilon^*(\nu) = \varepsilon_\infty + \Delta\varepsilon \int_{-\infty}^{\infty} \frac{f(\tau) d \lg \tau}{1 + i\omega\tau} \tag{17.10}$$

by using a method described by Banys et al. [42].

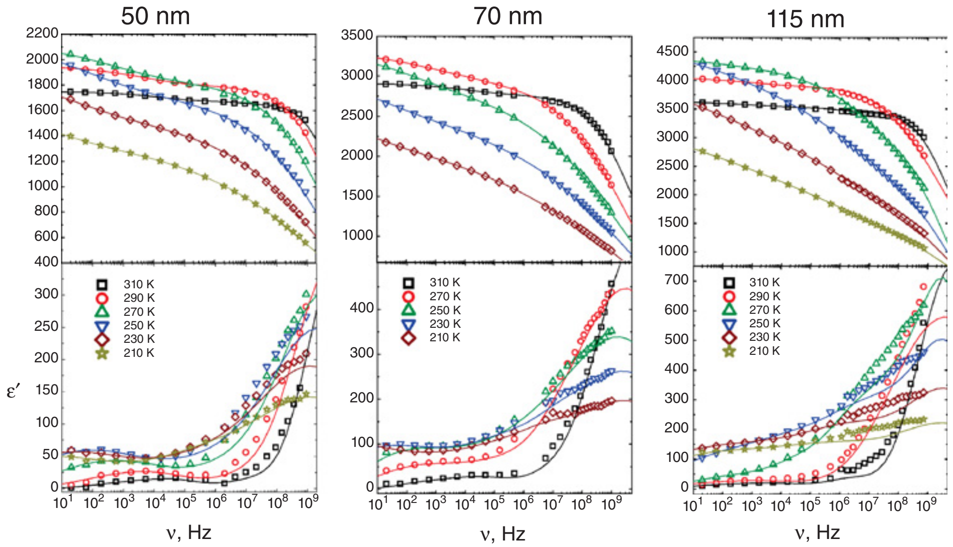

Figure 17.5 *Frequency and grain size dependence of dielectric permittivity of PMN nanoceramics. Solid lines show fits obtained from the distribution of relaxation times. Adapted from [35]. © IOP Publishing. Reproduced by permission of IOP Publishing. All rights reserved*

The distribution of relaxation times, calculated for 50 nm grain size ceramics [35] (Figure 17.6(a)) consists of two components: one contribution, which is nearly stable with the temperature, with a peak at 100–10 ps and another one that strengthens and broadens towards longer relaxation times on cooling. Such distributions of relaxation times are similar to the ones observed in micrometric PMN ceramics [38], single crystals [37], or in mixed $PbMg_{1/3}Nb_{2/3}O_3$–$PbSc_{1/2}Nb_{1/2}O_3$–$PbZn_{1/3}Nb_{2/3}O_3$ compounds [6]. The distributions of relaxation times, for both 70 and 115 nm grain size (Figure 17.6(b) and (c)) ceramics are qualitatively similar. However, the significant differences are observed in the analysis of the behavior of the longest relaxation times edge in the distribution of relaxation times (see inserts in Figure 17.6), which corresponds to the dynamics of the largest PNRs in the sample.

The dependence was fitted with the Vogel–Fulcher law (Equation (17.7)). A strong decrease in the freezing temperatures down to almost 0 K is observed: 176 K for 115 nm ceramics, 49 K for 70 nm ceramics, and 9 K for 50 nm ceramics. The grain size dependence of T_0 is in a good agreement with the freezing temperature dependence on the mean grain size of the PMN nanopowders (Figure 17.3). Moreover, the decrease of the freezing temperature of the longest relaxation times should be related to the narrowing of the distribution of freezing temperatures [33]. The last effect can be caused by narrowing of the volume distribution of PNRs; that is PNRs bigger than the grain size cannot exist. The narrowing the volume distribution of PNRs is also expressed by a suppression of the relaxation at longer relaxation times with reducing the grain size (Figure 17.6).

Several similarities can be noticed between the results. First of all, dielectric investigations of both powders and ceramics show that the Vogel–Fulcher law describes

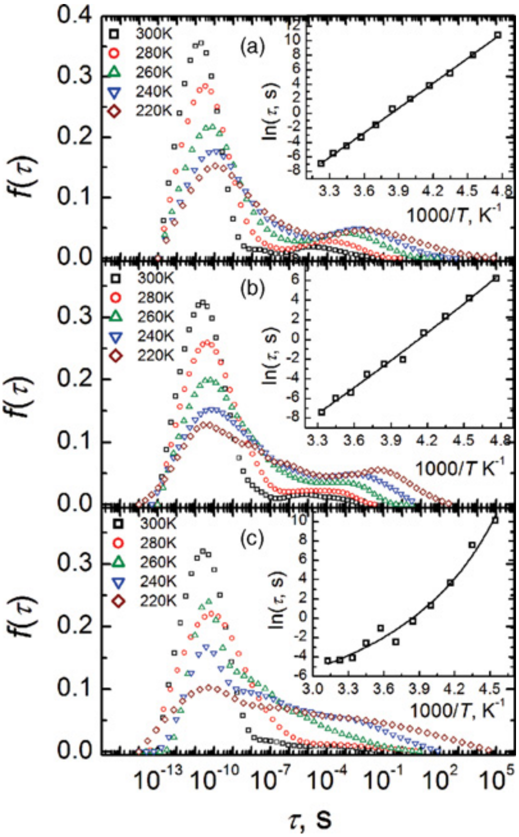

Figure 17.6 Distribution of relaxation times of PMN nanoceramics with various grain sizes: (a) 50 nm, (b) 70 nm, and (c) 115 nm nanoceramics. Inserts show the inverse temperature dependence of the longest relaxation times edge of distributions of relaxation times. Adapted from [35]. © IOP Publishing. Reproduced by permission of IOP Publishing. All rights reserved

temperature evolution of dynamic properties of the material related to the polar nanoregions. In this respect, our data correlates well with results for bulk PMN [37,38].

Secondly, the bigger the grains, the higher the freezing temperature derived from the Vogel–Fulcher law. According to high-resolution X-ray investigations of micrometer PMN, the correlation length associated with the mean size of PNRs is higher than 40 nm below 200 K [43]. In contrast, in nanometric samples it is limited by the grain size [28]. On the other hand, the Vogel–Fulcher law is well known to be a manifestation of cooperative interaction of some types of entities (PNRs in the case of relaxors) [44]. Grain boundaries can be expected to limit the interaction between PNRs in different grains. In that case, the smaller the grain size, the smaller is the interaction and correlation length between the PNRs. This means that the freezing temperature is expected to be lower in the case of smaller grains, and would vanish in the case of very small grains. This is exactly what we observed with a critical grain size of 40 nm. In the case of smaller grains, no freezing (glass behavior) is observed in both dielectric and nuclear magnetic resonance (NMR) measurements [35].

As was already evident from the frequency dependences of the dielectric permittivity (Figure 17.5), there are two overlapping relaxation processes in PMN ceramics. One of them has a quite short relaxation time, around 10^{-11} s, which is nearly temperature independent. Another one has a longer than 10^{-8} s relaxation time. The longest relaxation times of this process follow the Vogel–Fulcher law. The presence of these two processes is quite typical for ferroelectric relaxors [6].

Another important observation is that the temperature corresponding to the maximum of dielectric permittivity T_{max} shifts to the higher values with an increase of grain size in both powders and ceramics. This could be related to the fact that in the case of powders, the relaxation time is proportional to the grain size. It is unknown if the static permittivity of relaxors has a peak, as it is expected to be observable at infinitely low frequencies at low temperatures [45]. The peak observed at a fixed frequency is due to the fact that the static permittivity increases on cooling (Figures 17.1 and 17.4), but the mean and longest relaxation time also increases according to the Vogel–Fulcher law (Figures 17.2 to 17.5) [35]. A selected relaxation time is observed at higher temperatures for powders with bigger grains, and thus T_{max} increases. However, this observation is only weakly valid for higher frequencies in the case of ceramics, and at lower frequencies the trend is opposite – the bigger the grains, the smaller is T_{max}. These effects can be explained by the fact that in the case of ceramics, the distribution of short relaxation times is nearly unaffected by the grain size, while the long relaxation times are suppressed in smaller grains due to the absence of big PNRs. As a result, a more pronounced dispersion of the dielectric permittivity is observed in bigger grains, and T_{max} shifts to higher temperatures. However, it remains unclear why the relaxation time is proportional to the grain size in powders, and why short relaxation times are nearly grain size-independent in ceramics. Probably some kind of interaction between grains exists in ceramics, which is absolutely absent in powders. This interaction could be related to the strain, as dipolar interactions should be of a shorter range and are thus a less likely mechanism. This mechanism could be the subject of a separate investigation. However, a similar effect has been previously observed in barium titanate [46].

Furthermore, it was observed that the bigger the grain size, the bigger the dielectric permittivity of the ceramics is. This fact could be explained by a core–shell structure of the grains [32]. This model assumes that the effective permittivity of the material is determined by two contributions – the grain and the grain surfaces. The former is related to bulk properties of the material, while the latter depends on the contamination of intergrain volume, strain effects, disorder and defects, pinning of dipolar entities, and many more. Usually permittivity of the grain shell is relatively small, but in coarse-grained ceramics it also has a small volume and thus does not give any relevant contribution to effective value. However, it is not the case for nanograined ceramics, for which the properties of the shell also become important. Thus, permittivity is smaller in the case of smaller grains. However, this does not explain shifts of the characteristic temperatures. It is important to note that Curie–Weiss temperature of ferroelectric materials is shifted with grain size, but the transition temperature should remain constant [47]. Modifications of the properties of the grains, primarily interactions of grains and suppression of big PNRs with long relaxation times, must also be taken into account in the present case.

The dielectric properties of smallest (15 nm) grain size PMN powders [35] are rather unusual compared to the other ones. Here we see two weak relaxation processes, unlike in coarser-grained PMN powders where only one process is observed in the dielectric spectra.

To explain this behavior, nuclear magnetic resonance (NMR) measurements of ^{93}Nb were performed [35]. Here it was shown that the behaviour of the spin-lattice relaxation time is a two-component one. The latter fact could mean that one of the NMR-active processes is related to the non-polar mechanism (e.g. grain boundaries). We think that in our case there are three processes involved. It is most likely that in smaller grains a process that determines dielectric properties diminishes. As a result, the NMR-related processes are no longer obscured. They are probably also present in the dielectric properties of coarse-grained ceramics, but are overshadowed by the main relaxational process, which is responsible for relaxor properties of the material.

In summary, very complex size effects on the properties of PMN nanopowders and nanostructured ceramics were observed. The evolution of the dielectric properties at various grain sizes could be approximately explained by a core–shell structure of the grains. However, this model alone is insufficient and modification of bulk properties by grain size must also be taken into account. Grain boundaries limit growth and interactions of PNRs, which is very important for defining the freezing temperature and relaxation times of PNRs. However, interactions between adjacent grains are probably still present in ceramics if they are separated by perfect and thin grain boundaries.

17.2.2 Nanostructured $PbSc_{\frac{1}{2}}Nb_{\frac{1}{2}}O_3$ Ceramics

Relaxor ferroelectric $PbSc_{\frac{1}{2}}Nb_{\frac{1}{2}}O_3$ (PSN) is one of the classic relaxor materials. Its main difference from other classic relaxor materials like PMN is the presence of a spontaneous first-order phase transition from the relaxor to the ferroelectric state at 367 K during a zero-field cooling cycle [48, 49]. The situation is not unique as similar properties are exhibited by other materials, like a very similar $PbSc_{\frac{1}{2}}Ta_{\frac{1}{2}}O_3$ (PST) [8] or much more complicated ternary solid solutions [50]. PSN (as well as PST) has several important properties. B-site ions could be ordered or completely disordered or have any type of ordering in between. A spontaneous ferroelectric phase transition occurs in the case of complete ordering without any relaxor behavior. The latter is exhibited only in the case of a B-site disorder, although the spontaneous phase transition still takes place if the compound is stoichiometric and no lead vacancies are introduced. Thus size effects in stoichiometric disordered PSN ceramics might be different from both classic relaxors and classic ferroelectrics.

The first study of nanostructured disordered PSN was reported by Kiat et al. [51]. It contained investigations with X-ray and dielectric spectroscopy in the 1–1000 kHz range, mainly focused on structural data. It was reported that structure of the samples is actually a mixture of rhombohedral $R3m$ and monoclinic Pm structures at the temperature of 85 K (Figure 17.7). The structure is predominantly (but not pure) rhombohedral at big grain sizes and monoclinic at small ones, with an almost step-like change of structure concentration at around 65 nm, which cannot be explained by a different crystal structure at the surface of the grains. At high temperatures the ceramics are reported to be cubic $Pm\bar{3}m$, independently of grain size. This fact is important for two reasons. Firstly, this implies that variation of grain size modifies the mechanism of phase transition resulting in a discontinuous change in the ground-state symmetry. Furthermore, the presence of a phase transition means that the compound is stoichiometric, as phase transition is expected to be suppressed otherwise [48]. Moreover, it was found that the crystal lattice becomes increasingly strained when

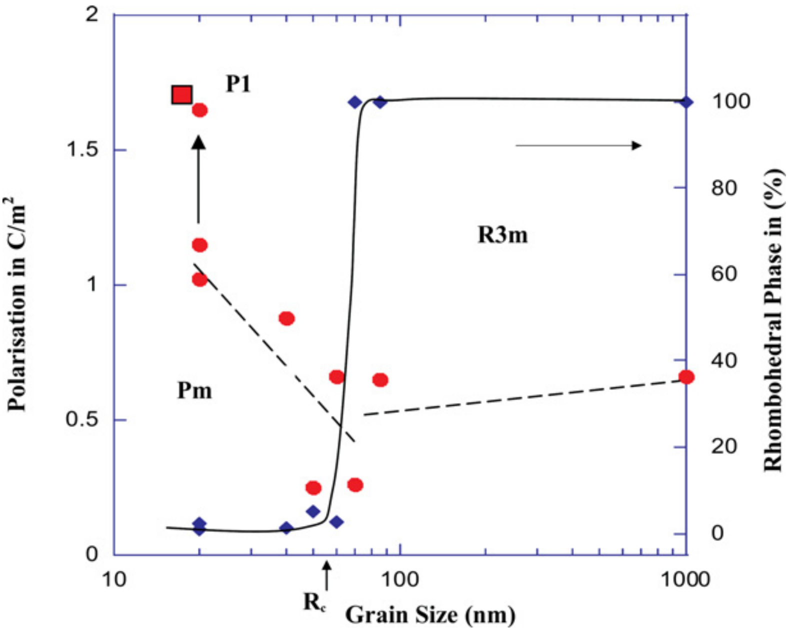

Figure 17.7 *Right: percentage of rhombohedral phase at 85 K (diamond). Left: magnitude of the polarization (dots and square), as calculated from structural refinements and effective charge of ions. All samples are chemically disordered (dots) except one (square) that is chemically ordered with a characteristic grain size of 20 nm (and that adopts the P1 symmetry. Reprinted (Figure 2) with permission from [51]. Copyright (2010) by the American Physical Society*

the grain size is reduced below a critical size, which is accompanied by an increase of polarization, as estimated from the Rietvield refinement (Figure 17.7).

Later, some of the samples studied in Kiat et al. [51] were investigated by means of broadband dielectric spectroscopy in the 100 Hz–55 GHz frequency range [52]. The grain sizes were 20, 40, and 80 nm, which are around the previously reported critical size of 65 nm. The temperature dependencies of dielectric permittivity of 20 and 80 nm ceramics are presented in Figure 17.8. There are several important differences with respect to the bulk ceramics. Firstly, the dielectric anomaly around 400 K is suppressed. This could be qualitatively explained by the coated spheres model [32, 53]. The smaller the grains, the smaller the permittivity. However, a spontaneous phase transition is invisible and the ceramics exhibit purely relaxor-like properties. A similar effect had previously been observed in PMN-35%PT [33]. In the latter case the phase transition was observed in coarse-grained (4 μm) ceramics, which were sintered from the same starting powder as the fine-grained (150 nm) ones. The absence of the transition was explained by the existence of grain boundaries, which would limit the percolation of polar nanoregions (PNRs). Furthermore, only low-frequency process assigned to flipping of the PNRs was influenced by the grain size, while high-frequency processes were mostly unaffected. Only a small broadening and suppression of the dielectric anomaly of PMN–PT was observed at 250 GHz. In PSN both substantial broadening and suppression of the anomaly were observed at 30 GHz (Figure 17.8).

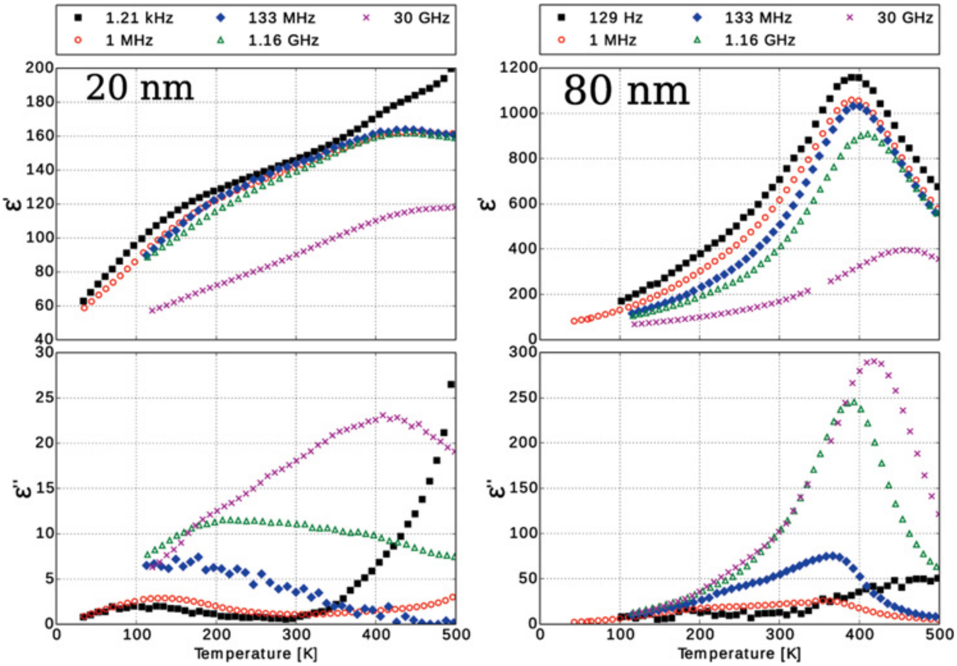

Figure 17.8 *Temperature dependencies of the real (top) and imaginary (bottom) parts of complex dielectric permittivity of 20 nm (left) and 80 nm (right) grain size PSN ceramics. Adapted from [52]*

This could be due to several reasons. Firstly, lower frequencies are compared in PSN. Secondly, grain sizes were much bigger in the case of PMN–PT. Nonetheless, both suppression of percolation and smearing of the anomaly should be taken into account to explain the observed effects in PSN. Moreover, X-ray studies clearly showed the presence of structural phase transition. This means that in reality grain size does not suppress the transition itself, but dielectric anomaly is mostly influenced by other extrinsic processes (like contribution of PNRs or domain walls in the ferroelectric state). The presence of grain boundaries suppresses these contributions, which, in turn, influence the crystal symmetry of the ferroelectric state.

Another important feature of the dielectric spectra of PSN is the low-temperature relaxation. To the best of our knowledge it has been mostly ignored previously, as the process is very faint at low frequencies and is obscured by the main anomaly, but it is very nicely seen in 20 nm ceramics (Figure 17.8). The process takes place at low temperatures (below 200 K even at 1 GHz), making analysis of its dynamics very difficult. The actual mechanism of this process is obscure, as very little data are available. It could be related to some type of disorder in the material, for example second relaxor-like process or coexistence of dipolar glass and ferroelectric states similar to RADA crystals [54]. Another possible mechanism is contribution of ferroelectric domains. In the latter case, relaxation time usually follows Arrhenius law (see, for example, $BaTiO_3$ in [55]) with some exceptions (i.e. Vogel–Fulcher

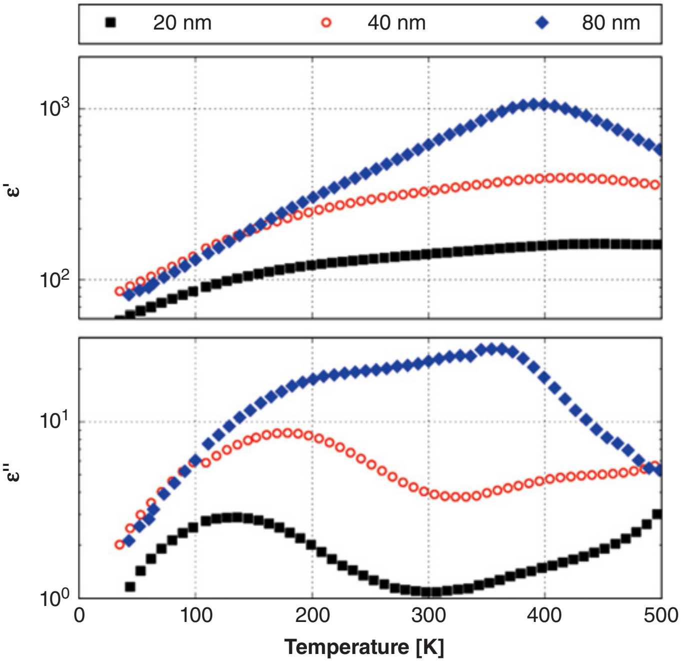

Figure 17.9 Temperature dependencies of the real (top) and imaginary (bottom) parts of complex dielectric permittivity of PSN ceramics with different grain sizes at 1 MHz. Adapted from [52]

behavior in the KDP family) without a proper explanation (see, for example, [56] and [57]). Similar behavior has also been previously observed in other relaxor materials with a spontaneous ferroelectric phase transition [50].

Additional information becomes available when the temperature dependencies of the dielectric permittivity of ceramics with different grain sizes at a selected frequency are compared. In Figure 17.9 we can see that the grain size reduction suppresses the anomaly around 400 K and its temperature is actually shifted to higher temperatures. The shift cannot be explained by the rise of electrical conductivity at smaller grain sizes, as from Figure 17.8 we can see that dispersion at 1 MHz in the finest ceramics is virtually non-existent. Moreover, the values of the dielectric permittivity tend to become very similar at low temperatures, although the finest ceramics exhibit somewhat smaller permittivity. The latter fact could be explained by potentially smaller density of the sample and high strain of the lattice, as reported from X-ray studies [51].

From the evolution of the dielectric losses (Figure 17.9) we can see that the low-temperature process is shifted to lower temperatures when the grain size is reduced, while the dielectric losses become smaller. Another important fact is that dielectric losses related to the anomaly around 400 K are reduced much faster than the dielectric permittivity itself. Moreover, the losses in 80 nm ceramics are bigger at 400 K than at low temperatures, but it is vice versa in 20 nm ceramics.

The interpretation of all these observations is not an easy task. The shift of the low-temperature process to lower temperatures with reduction of grain size could be explained if we assume that this process is related to either PNRs or dipolar glass-like regions in the ferroelectric matrix. In that case the same train of thought as used to explain size effects in PMN can be used. The interactions between the polar entities would be limited at smaller grain sizes. Besides, the average sizes of these regions would be smaller. This means that entities with a much lower volume (and mass) are moved by the electric field in smaller grains, which would make shorter the associated relaxation times. Another possible (and equivalent) interpretation is the suppression of long relaxation times by the grain boundaries. On the other hand, the relaxation times would still increase upon cooling. However, the same relaxation time would be achieved at lower temperatures in ceramics with smaller grains. This would manifest itself as a shift of the anomaly to lower temperatures upon reduction of the grain size. The material itself is a relaxor (albeit with a phase transition) and thus it is most likely that PNRs and not dipolar glass-like regions are present in the material. In that case the shift of this anomaly would have the very same mechanism as in case of a shift of $T_{\max}$ in PMN powders or in case of high frequencies in the ceramics.

It is also possible to assume that the shift of anomaly is related to EMA effects. In a core–shell structure, the smaller the grains, the shorter is the relaxation time in the case of the grain boundary medium having a smaller dielectric constant [53]. However, the effect would be visible only if there is a big difference in grain size, which we do not have in this case. This supports the idea of PNR-related effects. The anomaly around 400 K is also suppressed, but in a slightly different manner. The behavior is very similar to that of the PMN ceramics at low temperature: the smaller the grain, the higher is the $T_{\max}$. It is very likely that the mechanism in this case is also very similar. We can assume that contribution of very small PNRs and polar phonons is unaffected by grain size and their contribution has a maximum at temperatures slightly higher than 400 K. In the case of coarse-grained ceramics, flipping of PNRs would take place with a long relaxation time. It means they would produce an anomaly at a little lower temperature, just above the spontaneous phase transition. However, if the flipping of the big PNRs (or their existence) is suppressed, this would be manifested in an apparent shift of the anomaly. It is probable, however, that the temperature of the phase transition is not shifted in reality.

In summary, the size effects on the dielectric properties of PSN ceramics are very similar to the ones observed in PMN. A core–shell structure is suitable to qualitatively explain the reduction of the dielectric anomaly. However, modifications of bulk properties by grain size are needed to take into account to make quantitative explanations on the reduction of the dielectric permittivity and shifts of the characteristic temperatures. Apparently, PNRs are playing a key role in these mechanisms. On the other hand, the spontaneous phase transition is not driven by PNRs alone, as suppression of the anomaly leads to a modification of the ground state, but the phase transition is not eliminated.

17.3 Aurivillius Lead-Free Ferroelectric Relaxors

Many authors deal with relaxors systems, most of them being the lead-containing perovskites, such as the previously mentioned $PbMg_{1/3}Nb_{2/3}O_3$ and $PbSc_{1/2}Nb_{1/2}O_3$. A considerable number of compositions from the Aurivillius family also exhibit a relaxor ferroelectric behavior. The existing surveys concerning lead-free relaxors with an Aurivillius structure are 15 years old and have received special attention in the last few years because of the observed unusual dielectric properties. A typical representative of lead-free BLSFs with the least complicated chemical composition is $Bi_4Ti_3O_{12}$ with $n = 3$ (BiT). This material is intensively investigated in view of its potential application in electronics (ceramic capacitors, piezoelectric transducers, sensors, high-density random access memories, etc.) [58,59]. In general, BLSFs have a highly anisotropic structure, which is composed of n number of perovskite $(A_{n-1}B_nO_{3n+3})^{2-}$ unit cells sandwiched between $(Bi_2O_2)^{2+}$ slabs along the pseudo-tetragonal c axis (n is an integer between 1 and 5). The 12-coordinate perovskite-like A-site is typically occupied by large cations (from 1.34 to 1.61 Å) such as Na^+, K^+, Ca^{2+}, Sr^{2+}, Ba^{2+}, Pb^{2+}, Bi^{3+}, or Ln^{3+} and the 6-coordinate perovskite-like B-site by smaller cations (from 0.59 to 0.65 Å), such as Fe^{3+}, Cr^{3+}, Ti^{4+}, Nb^{5+}, or W^6.

Among BLSFs, most members have a normal ferroelectric–paraelectric phase transition, while only a few of them (Ba-based ferroelectrics with a Bi-layered structure), such as $BaBi_4Ti_4O_{15}$, $BaBi_2Ta_2O_9$, and $BaBi_2Nb_2O_9$, are interesting from the point of view of the relaxor behavior [60, 61]. As already mentioned, the dielectric properties of a relaxor ferroelectric are explained in the literature in terms of small regions of local polarization (so-called polar regions), which appear at temperatures much higher than T_m (at the Burn's temperature T_B) [62]. Unlike perovskite $A(B_1B_2)O_3$ relaxors whose B-site is occupied by heterogeneous cations (which causes structural disorder responsible for relaxation), Aurivillius compounds with a relaxor character would have no cation disorder at first glance at the formula $(Bi_2O_2)^{2+}(A_{m-1}B_mO_{3m+1})^{2-}$. It seems that each site is occupied by only one kind of cation. Some characteristic parameters for various Ba-based bismuth layered compounds are listed in Table 17.1.

Similar to materials with the perovskite structure, the relaxor behavior in Ba-based Bi-layered compounds is attributed to the structural disorder, which is either inherent or introduced by doping. In the case of $BaBi_4Ti_4O_{15}$, but in contrast to familiar compounds $ABi_4Ti_4O_{15}$(A = Ca, Sr, and Pb), which are not relaxors, relaxation is a consequence of disorder between Bi from $[Bi_2O_2]^{2+}$ layers and the perovskite-like A-type cations [66]. Crystallographic studies of most of the authors [67–69] demonstrated the necessity to partially substituting Bi for Ba in the $[Bi_2O_2]^{2+}$ slabs, but the ratios given for mixed Ba/Bi sites could be different [67]. When a bismuth ion enters an A-site, it can easily go off-center (contrary to Ba^{2+}), leading to local polarization and stimulating the appearance of

Table 17.1 *Dielectric and relaxor characteristics of some Ba-based Bi-layered compounds*

Composition	Phase transition	ε_m (100 kHz)	T_m (K) (100 kHz)	ΔT_{relax} (K) (1 kHz–1 MHz)	Reference
$BaBi_2Nb_2O_9$, $n = 2$	Relaxor	600	~443	100	[63]
$BaBi_2Ta_2O_9$, $n = 2$	Relaxor	525	~353	60	[62]
$BaBi_4Ti_4O_{15}$, $n = 4$	Relaxor	2429	688	16	[64]
$Ba_2Bi_4Ti_5O_{18}$, $n = 5$	Relaxor	2100	625	30–40	[65]
$BaBi_8Ti_7O_{27}$, $n = 8$	Non-relaxor DPT	1200	~ 768	/	[60]

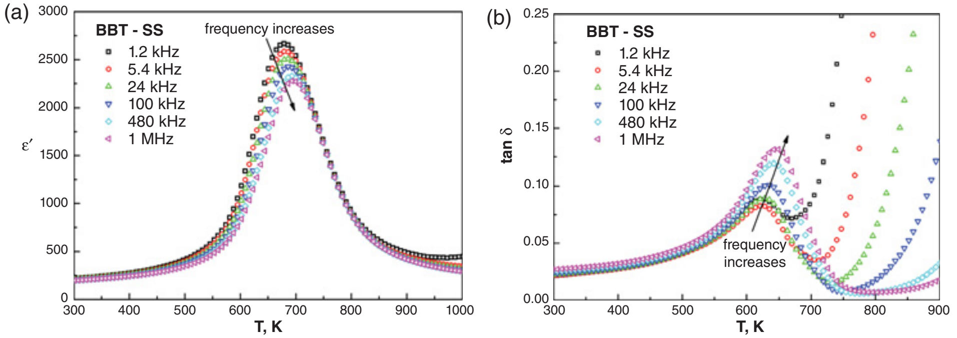

Figure 17.10 *(a) Real part of dielectic permittivity (ε′) and (b) dielectric losses in BBT-SS ceramics as a function of temperature. Reprinted from [64], Copyright (2012), with permission from Elsevier*

PNRs. Concurrently, the cation redistribution leaves positive point charges in perovskite slabs where Bi^{3+} replaces Ba^{2+} and negative point charges in $[Bi_2O_2]^{2+}$ layers where Ba^{2+} replaces Bi^{3+}. These point charges result in an inner electric field along the c axis, which breaks up the long-range polar ordering and prevents macroscopic ferroelectric ordering in $BaBi_4Ti_4O_{15}$ [60]. On the other hand, considering the large difference in the ionic radii of Ba^{2+} and Bi^{3+} cations, locally the tolerance factor would be strongly affected by such local changes in the Ba/Bi ratio. For zones with a high content in Ba, this may lead locally to undistorted structure and eventually non-polar domains [67].

Huang and co-authors [70] have investigated how incorporation of Ba^{2+} in the Sr^{2+} sites of $SrBi_2Nb_2O_9$ ceramics provides a complex dielectric response with a transition from a normal to a relaxor behavior. The Ba^{2+} ions not only substitute the Sr^{2+} ions in the A-site of the perovskite block but enter the $(Bi_2O_2)^{2+}$ layers, leading to an inhomogeneous distribution of barium and local charge imbalance in the layered structure.

17.3.1 Relaxor $BaBi_4Ti_4O_{15}$ Ceramic System

Figure 17.10 shows the temperature dependence of the real parts of the dielectric permittivity (ε′) and dielectric losses (tan δ) at several frequencies (from ~1 kHz to 1 MHz) for the $BaBi_4Ti_4O_{15}$ ferroelectric ceramic system, which was obtained by the solid–state reaction method (abbreviation BBT-SS). Typical characteristics of relaxor ferroelectric behavior are observed. As the frequency increases, the dielectric maximum shifts to a higher temperature (from 679 to 695 K) and the dielectric constant became smaller (from 2668 to 2277) [64].

The degree of relaxation behavior of $BaBi_4Ti_4O_{15}$, obtained by formula $\Delta T_{\text{relax}} = T_{m\,(1\text{ MHz})} - T_{m\,(1\text{ kHz})}$ is found to be 16 K (Table 17.1) [64]. The shift of $T_{\max}$ with frequency is comparable with ΔT_{relax} of perovskite relaxors where the degree of relaxation is ~20 K and ~ 14 K in PMN and PLZT(8/65/35) ceramics [63, 71]. A much more pronounced relaxation is observed in Aurivillius $BaBi_2Nb_2O_9$ compounds ($\Delta T_{\text{relax}} = 110$ K), where 13.4% of barium atoms change their positions with bismuth atoms in the $[Bi_2O_2]^{2+}$. Chen and co-authors [60] consider that the main driving force for this kind of cation redistribution may be the requirement of relieving the size mismatch in the *a*–*b* plane between the perovskite slabs and bismuth oxide slabs. They also consider that similar cation redistribution probably occurs in $BaBi_4Ti_4O_{15}$ and $BaBi_8Ti_7O_{27}$, but the degree of redistribution would not be as big as the lateral sizes of their unit cells are smaller than those of $BaBi_2Nb_2O_9$, which means less size mismatch in the structure and less driving force for cation redistribution. This driving force is so small in $BaBi_8Ti_7O_{27}$ that just diffuse phase transition takes place without relaxation phenomena.

The dielectric constant of relaxor materials follows the Curie–Weiss (CW) law only above the CW temperature (T_{cw}), which is much higher than T_{max} (temperature of dielectric maximum), for $T > T_{max}$. A modified CW law is often used to describe the ε' peak and the diffuseness of the phase transition at the high temperature side [72]:

$$\frac{1}{\varepsilon'} - \frac{1}{\varepsilon'_{max}} = \frac{(T - T_{max})^{\gamma}}{C} \tag{17.11}$$

where ε'_{max} is the maximum value for the real part of the dielectric permittivity and γ and C are constants. For an ideal relaxor ferroelectric $\gamma = 2$, while for a normal ferroelectric $\gamma = 1$ and the system follows the Curie–Weiss law. The value of γ obtained for $BaBi_4Ti_4O_{15}$ ceramics by Khokhar et al. [73] and γ obtained in our investigation are different (1.79 and 1.96, respectively) but still such values of γ imply a relaxor-like behavior of the ceramics. Since ε'_{max} and T_{max} (used to determine the diffuseness parameter γ using Equation (17.11)) are frequency dependent for relaxor materials, γ is not adequate to describe the frequency-independent dielectric behavior at high temperatures ($T > T_{max}$) [74]. According to that, several relations have been used to describe the dielectric permittivity of the relaxor at $T > T_{max}$, one of which is the Lorenz-type empirical relation proposed by Bokov and Ye [75]:

$$\frac{\varepsilon_A}{\varepsilon} = 1 + \frac{(\mathrm{T} - \mathrm{T_A})^2}{2\delta_A^2} \tag{17.12}$$

where the temperature (T_A) and the magnitude (ε_A) of the Lorenz height generally differ from the T_{max} and ε_{max} of the experiments. The parameter δ, which is frequency independent, characterizes the diffuseness of the peak. The results of fitting by the Lorenz equation (δ, ε_A, T_A) at low ($T < T_{max}$) and high ($T > T_{max}$) temperature part of dielectric permittivity for two group of authors are shown in Table 17.2 and Figure 17.11. It is interesting to find that $\varepsilon(T)$, the fitting parameters, are very close in the two temperature ranges, $T < T_{max}$ and

Table 17.2 *The room temperature dielectric constant (ε_{RT}), the peak dielectric constant (ε_{max}), temperature of the dielectric maximum (T_{max}), the degree of diffuseness (γ), the degree of relaxation behavior (ΔT_{relax}), and fitting parameters (δ, ε_A, T_A) of the Lorenz-type formula, which are measured at 1 MHz for different compositions*

					$T < T_{max}$			$T > T_{max}$		
	ε'_{RT}	ε'_m	T_{max} (K)	ΔT_{relax}	δ	ε_A	T_A (K)	δ	ε_A	T_A (K)
Khokhar et al. [73]	204	2113	693	25	41.5	2358	676	77.5	2452	663
Bobic et al. [64]	204	2277	695	16	48.9	2267	691	58.1	2270	697

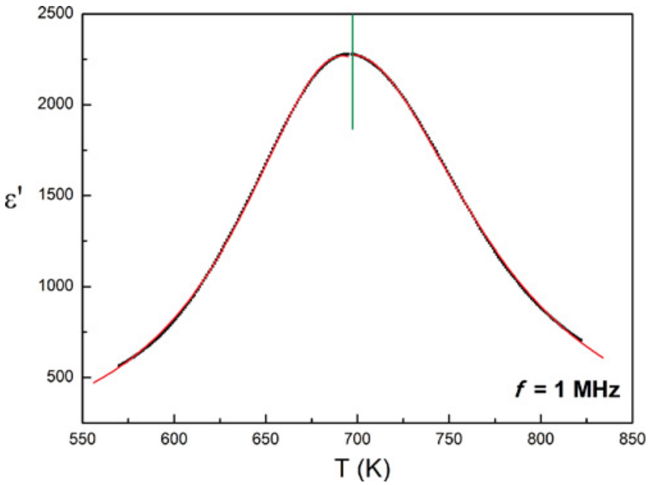

Figure 17.11 *Lorenz fitting of the dielectric constant versus temperature of the BBT-SS ceramics at 1 MHz*

$T > T_{max}$, which indicates that there is one polarization process in the BBT system. Higher values of δ for $T > T_{max}$ in comparison with δ values for $T < T_{max}$ suggest an increase in the diffuseness of the dielectric peak at high temperatures, which might be associated with the thermally activated flips of the PNRs.

The frequency dispersion characterized by the Vogel–Fulcher relation (Equation (17.8)) gave the fitting parameters E_a, T_f, and ν_o of BBT ceramics as being 0.097 eV, 616 K, 10^{12} Hz and 0.034 eV, 654 K, 10^{10} Hz, respectively [73, 64]. The obtained parameters are in agreement with those reported for other relaxors belonging to the Aurivillius family of oxides. The difference between the Vogel–Fulcher parameters obtained by different authors is probably caused by different technological conditions during ceramics preparation. The difference in thermal treatment and sintering conditions (temperature and time) result in the change in the structural disorder [76]. The latter may significantly affect the polar properties and dynamics of dipoles of this material, which are responsible for the relaxor-like properties.

17.3.2 Grain Size-Dependent Electrical Properties of $BaBi_4Ti_4O_{15}$ Ceramics

There have been limited reports about the grain size effect on dielectric and relaxor properties of the Aurivillius type of ceramics. It is well known that plate-like grain formation is a typical characteristic of BLSFs. The layered structure is described by a high value of c-parameter in comparison with parameters a and b of the orthorhombic cell and leads to a high anisotropy of the crystallographic structure, which is directly connected with the high anisotropy of the electric properties.

In order to investigate the influence of grain size on the electrical properties, BBT ceramics were obtained by two different processing methods: the conventional solid-state method and the mechanochemically supported solid-state method [77]. The first one was obtained by homogenization of starting oxides (BaO, Bi_2O_3, and TiO_2) in isopropanol for 24 h and

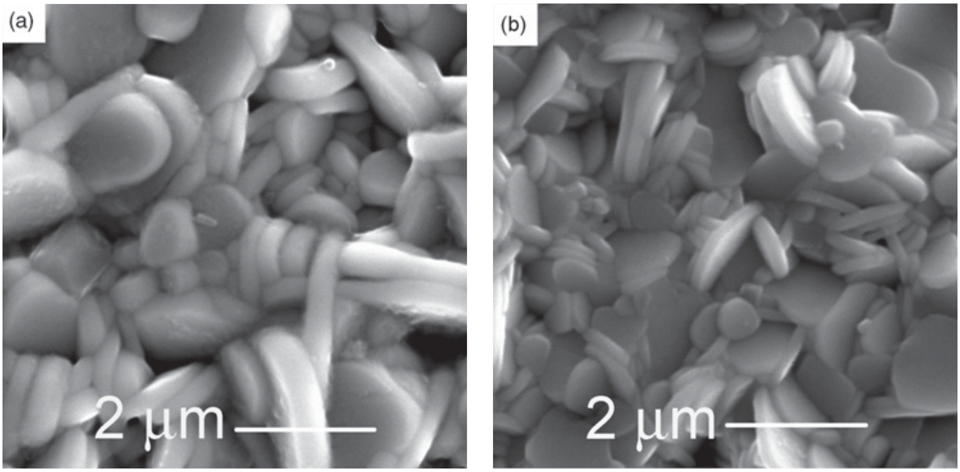

Figure 17.12 BBT ceramics with randomly oriented plate-like grains observed by SEM: (a) obtained by the solid-state method and (b) the mechanochemically supported solid-state method. Reprinted from [77], Copyright (2015), with permission from Elsevier

then calcinated at 950 °C. Another method was to use 6 h milling of the same starting mixture, after which the Aurivillius layered perovskite phase is formed. Milled powder was calcinated at 850 °C for 4 h to obtain a well-crystallized BBT structure (denoted as BBT-MA). The obtained powders were sintered in sealed alumina crucibles to avoid bismuth loss. The microstructures of the sintered samples of BBT-SS (Figure 17.12(a)) show plate-like grains with a random orientation of the plate faces with a size of 2–3 µm and 0.5 µm thick. The grain size of BBT-MA ceramics is smaller in comparison with BBT-SS, around 1.0 µm in length and 0.2 µm in thickness (Figure 17.12(b)). In comparison with the BBT-SS, reduction in the average grain size of BBT-MA ceramic is due to the decrease in the particle size of the milled powders. The relative density of the BBT-SS and BBT-MA pellets were determined to be 89 and 93%, respectively.

Figure 17.13 shows the temperature dependence of the dielectric constant and loss of BBT-SS and BBT-MA ceramics at 100 kHz. According to the large majority of authors [78, 79] the dielectric constant should increase with decreasing grain size in most investigated barium titanate ceramics, and then decrease with a further decrease of grain size. In contrast to that, Ferrer et al. found that Aurivillius $SrBi_4Ti_4O_{15}$ ceramics with the highest platelet size showed the largest dielectric permittivity [80]. Recent investigation of the grain size-dependent electrical properties of $Bi_4Ti_3O_{12}$ ceramics showed that when the grain size is reduced from 4.2 µm to 1.65 µm, a slight decrease of the dielectric permittivity at T_C is observed. However, when the grain size is further reduced to 0.57 µm, an opposite change can be noticed [81]. In our investigation, the higher value of permittivity close to the ferro-paraelectric phase transition of the BBT-SS samples in comparison with BBT-MA can be explained by the brick-wall model, where high permittivity grains are isolated by low permittivity grain boundaries, similarly to the case of PMN and PSN ceramics. The Curie temperature (T_C) was found to slightly decrease in BBT-MA in comparison to BBT-SS.

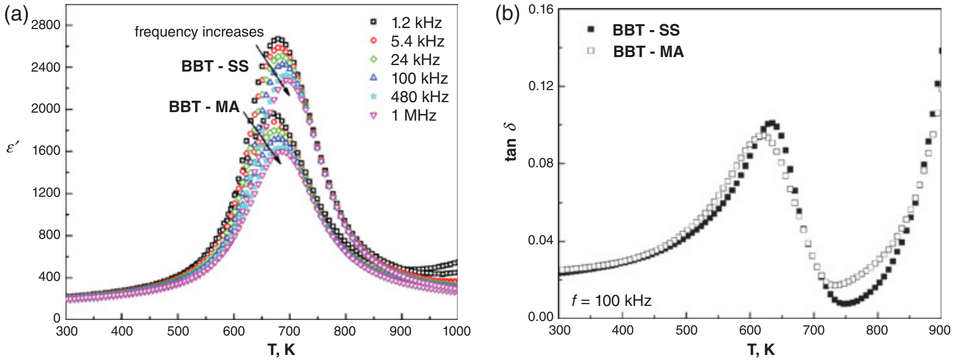

Figure 17.13 *Temperature dependence of (a) the dielectric constant at different frequencies and (b) the dielectric loss at 100 kHz of BBT-SS and BBT-MA ceramics. Reprinted from [77], Copyright (2015), with permission from Elsevier*

This was possibly due to the decrease in crystallite size of the mechanochemically treated sample.

In Table 17.3 are presented some relaxor properties of BBT-SS and BBT-MA ceramics. According to results of $\Delta T_{\mathrm{relax}}$, the synthesis method (in fact, grain size) did not influence the relaxation process, which confirms that the degree of structural distortion is the same in both ceramics. As mentioned above, there is no distinct influence of grain size on relaxation properties and diffuseness of the ε'–T peak in BBT ceramics. It is possible that more expressive relaxation will be manifested in the case of smaller grains. The insignificant differences in relaxation parameters could probably be assigned to the difference in thermal treatment and sintering conditions that results in a change in the structural disorder.

One problem in application of BLSFs for many devices is their high conductivity. There are a huge number of papers that deal with the suppression of conductivity by reduction of grain size or by donor doping. In comparison with the almost isotropic (cubic) structure of BT, PMN, and PZT [82–84], the intrinsic electrical properties of the Aurivillius type of compounds are anisotropic, with the maximum value of conductivity and the major component of spontaneous polarization parallel to the $(Bi_2O_2)^{2+}$ layers [85]. In those compounds the bismuth layer is acting as an insulator against the charge transport. At high temperatures the main conductive species in bismuth-layered compounds are oxygen vacancies, which are assumed to be related to the evaporation of Bi [86].

DC conductivity, which was theoretically predicted from extrapolation of AC conductivity data on the y axis from σ_{AC} versus frequency graph, enable determination of the activation energy for the conduction process (E_{DC}) according to the Arrhenius law:

Table 17.3 *Some relaxor parameters of BBT-SS and BBT-MA ceramics at 100 kHz*

Samples	$\varepsilon'_{\mathrm{RT}}$	$\tan\delta_{\mathrm{RT}}$	$\varepsilon'_{\mathrm{m}}$	T_{m} (K)	$\Delta T_{\mathrm{relax}}$	E_{A} (eV)	ν_{o}(Hz)	T_{f} (K)
BBT-SS	205	0.024	2429	688	16.3	0.034	1.85×10^{10}	654
BBT-MA	200	0.025	1723	677	16.9	0.025	7.08×10^{9}	652

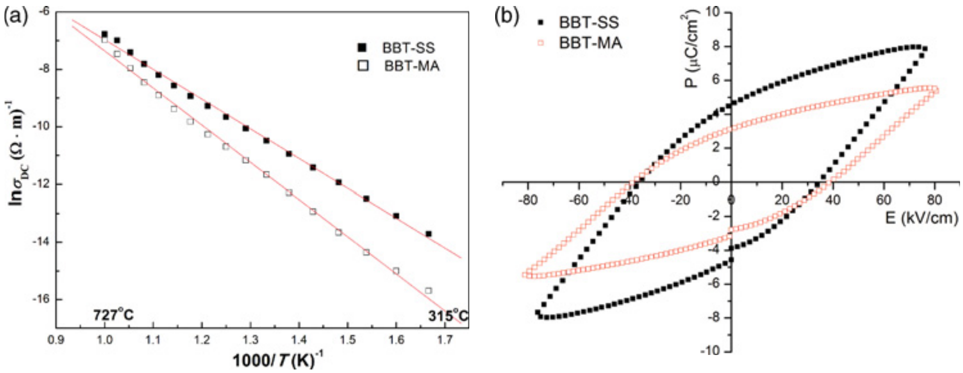

Figure 17.14 *(a) Arrhenius plots of DC conductivity of BBT-SS and BBT-MA ceramics. (b) Ferroelectric hysteresis loop recorded at room temperature for BBT-SS and BBT-MA ceramics. Reprinted from [77], Copyright (2015), with permission from Elsevier*

$\sigma_{DC} = \sigma_0 \exp(-E_{DC}/kT)$. This is graphically presented in Figure 17.14(a) as $\ln(\sigma_{DC})$ versus $1000/T$. The values of activation energies obtained by linear fitting of the experimental data are 0.89 eV and 1.11 eV for BBT-SS and BBT-MA ceramics, respectively. The activation energies of conductivity for both samples are close to 1 eV, which may be attributed to the oxygen vacancies related phenomena. Similarly, as for other Aurivillius compounds, it was confirmed that conductivity decreases with reduction of the grain size, due to the increase in the number of grain boundaries. Differences in grain size could be seen in Figure 17.13.

The P–E hysteresis loops at 100 Hz frequency and maximum electric field of 80 kV/cm were measured at room temperature for the both BBT ceramics and are shown in Figure 17.14(b). The ferroelectric behavior is clearly observable. The remnant polarization (P_r) and coercive field (E_c) were 4.54 μC cm^{-2}, 34.4 kV cm^{-1} and 3.08 μC cm^{-2}, 39.5 kV cm^{-1} for BBT-SS and BBT-MA, respectively. P_r was decreased with decreased grain size because the reduced number of domain variants in smaller grains lowers domain wall mobility. E_C was increased with decreased grain size, which was ascribed to the higher internal stresses in fine-grain ceramics. Lower electric conductivity in BBT-MA samples allows the application of higher poling fields in comparison with the BBT-SS sample.

17.3.3 $BaBi_4Ti_4O_{15}$ Doped Ceramics

A good feature of Aurivillius compounds is their compositional flexibility due to the perovskite block, which allows easy incorporation of various cations on A- and/or B-sites of perovskite-like slabs with ions of the proper ionic radii and valence. The mixing of different elements into these sites determines the structural and dielectric properties for these materials. For the most investigated $Bi_4Ti_3O_{12}$ ceramics, many researchers have used donor dopants such as W^{6+}, Nb^{5+}, and V^{5+} to substitute the Ti^{4+} in order to decrease their conductivity. As already mentioned, low electrical conductivity allows the application of high poling fields, which is beneficial to achieve high polarization and high piezoelectric properties of ceramics [86]. The addition of Nb allowed a decrease in conductivity by three orders of magnitude in the composition $Bi_4Ti_{2.96}Nb_{0.04}O_{12}$, but this composition with the lowest conductivity did not possess the highest piezoelectric response. The highest piezoelectric coefficient $d_{33} = 20$ pC N^{-1} was achieved in the $Bi_4Ti_{2.86}Nb_{0.14}O_{12}$ composition [87]. The conclusion is that decreasing the conductivity in bismuth titanate is a necessary but not sufficient condition for achieving a useful piezoelectric response.

It is believed that the chemical stability of the perovskite layer against oxygen vacancies is drastically improved with isovalent A substitution of Bi^{3+} for La^{3+}. Most of the authors found that the optimal doping content for improvement of ferroelectric properties of bismuth titanate was $La_{0.75}Bi_{3.25}O_{12}$ [88]. Park and Kang [59] reported that rare earth-modified BLSF material, namely $La_{0.75}Bi_{3.25}Ti_3O_{12}$ (BLT) films, possess a fatigue-free behavior up to 3×10^{10} switching cycles and thus they are suitable candidate for FRAM devices.

There are also many investigations about compositional modification of $BaBi_4Ti_4O_{15}$ ceramics by donor, acceptor, and isovalent doping on dielectric and electrical properties (Ti^{4+} substitution with Zr^{4+}, Ce^{4+}, Nb^{5+}, and V^{5+} and Ba^{2+} and Bi^{3+} substitution with La^{3+} and Nd^{3+}).

Chakrabarti and Bera [89] studied isovalent substitution of Ti^{4+} with Zr^{4+} ions in BBT ceramics with the formula $BaBi_4Ti_{4\text{-}x}Zr_xO_{15}$ ($x = 0.1$, 0.2, 0.3, and 0.5). It was shown that relaxor-like properties are suppressed with increasing substitution level and vanish at $x = 0.5$ composition, but the effect of this substitution on the conductivity of the BBT ceramics was not examined. They found that the maximum relative permittivity values remain almost the same as that of BBT but decrease when the level of zirconium addition reaches $x = 0.5$.

The effects of Ce^{4+} as a donor-substituting Bi^{3+} were studied by Diao et al. [90]. The authors noticed that with increasing Ce^{4+} content, the temperature of the dielectric maximum was lowered and the peak of the dielectric constant was significantly suppressed in comparison with pure BBT ceramics. It was found that Ce^{4+} decreases the concentration of oxygen vacancies, but a higher cerium content increases the defect concentration contributing to the increase of dielectric losses.

A similar phenomenon was observed in Nb^{5+}-doped BBT ceramics by Pribošič et al. [91]. In both cases, and generally for donor doping, the conductivity decreases with donor doping to a minimum value where the concentration of electron holes matches the electron concentration. With further increase in the donor concentration the conductivity becomes n-type and starts to increase again. In both cases, SEM images showed that introduction of Nb^{5+} and Ce^{4+} in the BBT structure reduced the grain size of ceramics.

We have also investigated in our previous work the influence of niobium substitution according to formula $BaBi_4Ti_{4\text{-}5/4x}Nb_xO_{15}$ (BBNTx, $x = 0$, 0.05, 0.15, 0.30) prepared by the solid–state reaction method [64]. It was shown that grain size of BBNT specimens becomes more homogeneous with the increase of niobium content. Nb-doped samples exhibit slightly improved density, which is attributed partly to the decreased aspect ratio of the grains. The temperature dependence of the dielectric constant of the BBNT specimens at different frequencies is shown in Figure 17.15(a). The frequency dispersion of the dielectric constant is detected in the BBT and the BBNT5 samples, indicating a relaxor behavior. The degree of relaxation behavior, obtained by $\Delta T_{\text{relaxor}} = T_{\text{m(1 MHz)}} - T_{\text{m (1.21 kHz)}}$ was found to be 16 K for the BBT and 23 K for the BBNT5 sample. For the BBNT15 and the BBNT30, the degree of relaxation is expected to be larger with an increase of niobium concentration. This occurrence is difficult to observe due to the dielectric dispersion that emerges at low frequencies around and above the Curie temperature. This is possibly related

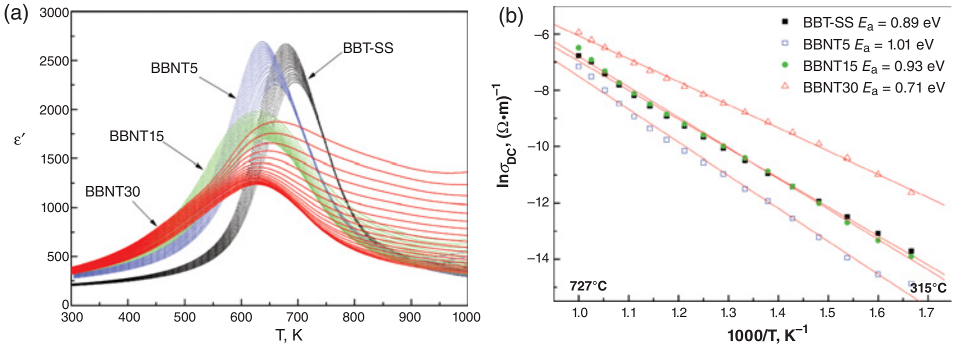

Figure 17.15 *Temperature dependence of the dielectric constant for BBNT ceramics (left) and Arrhenius plots of DC conductivity of BBNT ceramics (right). Reprinted from [64], Copyright (2012), with permission from Elsevier*

to the polarization mechanism associated with the thermally activated conduction of mobile ions and/or other defects [92]. Figure 17.15(b) shows the Arrhenius plot of conductivity of pure and doped samples, which are linear over a temperature range of 315 to 727 °C. In the BBNT5 ceramic an increase in the activation energy as compared with BBT is an indication of the reduction of the amount of oxygen vacancies and, consequently, a reduction of conductivity. With a further increase of the dopant concentration, E_{DC} decreases as a result of the increase of conducting species in the samples.

Just a few reports in regard to isovalent La^{3+} substitution of Bi^{3+} in BBT ceramics are available in the literature. Chakrabarti and Bera [93] reported that La addition results in a significant reduction of the DC conductivity for the $x = 0.3$ composition of $BaBi_{4\text{-}x}La_xTi_4O_{15}$ ceramics prepared through a chemical method, but they did not compare it with the undoped one. A significant frequency dispersion of permittivity is observed with increasing substitution, which indicated enhanced relaxor behavior.

Investigations of Kumar and Varma [94] on partial donor substitution of Ba^{2+} with La^{3+}ions ($Ba_{1\text{-}(3/2)x}La_xBi_4Ti_4O_{15}$) showed that the value of ΔT_{relax} decreases from 10 K for $x = 0$ to 6 K for the composition corresponding to $x = 0.2$, confirming the decrease of the relaxation behavior. For the samples with composition $x = 0.3$ and 0.4, the temperature of the dielectric maximum was found to be frequency independent (non-relaxor diffuse phase transition (DPT)). As has already been mentioned, the Ba-rich zone is potentially non-polar and a possible explanation for the suppression of relaxor behavior with the increase in La should probably be attributed to the increase in the size of the polar regions. Substitution of Ba^{2+} by smaller La^{3+} ions suppressed the formation of non-polar microdomains of Ba-rich zones and resulted in a reduction of frequency dispersion (ΔT_{relax}). The authors found that substitution by La^{3+} resulted in a significant reduction of DC conductivity for all the studied compositions ($x = 0.05$–0.4).

Contrary to the above-mentioned research, we found in our investigation [95] that La^{3+} substitution at the Bi^{3+}site (according to formula $BaBi_{4\text{-}x}La_xTi_4O_{15}$) increases the conductivity in comparison with undoped ceramics. For a small amount of La a certain quantity of oxygen vacancies is formed by La in BBT ceramics, causing an increase of the conductivity by comparison to one of pure BBT. After that, for higher concentrations of La ($x > 0.05$)

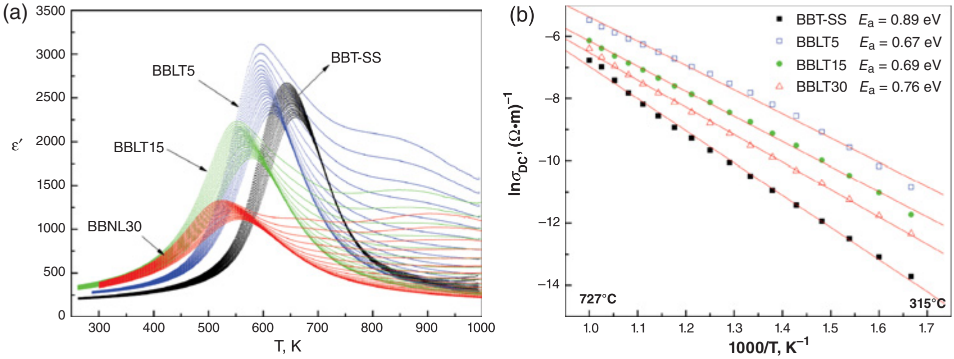

Figure 17.16 Temperature dependence of the dielectric constant for BBLT ceramics (left) and Arrhenius plots of DC conductivity of BBLT ceramics (right). Reprinted from [95], Copyright (2013), with permission from Elsevier

conductivity starts to decrease, but remains still higher than one of undoped ceramics. This observation was confirmed by calculation of activation energy for DC conduction (E_{DC}), shown in Figure 17.16(a). We assumed that further incorporation of La^{3+} ions will reduce conductivity and this should be further investigated.

By examining the effect of La substitutions on the relaxation behavior we observed an increase of relaxation strength with an increase of dopant concentration (Figure 17.16(b)). This is likely to be related to the fact that, in spite of the same charges and very similar ionic radii of Bi^{3+} and La^{3+}, when the off-center bismuth cations with lone pair 6s electrons is substituted with spherical lanthanum ions the chemical and structural inhomogeneity is enhanced and leads to the increase of relaxor character.

From the presented results, it can be concluded that doping of BLSFs is very complex and different types and concentrations of dopants (donor, acceptor, or isovalent dopants) cause different effects on the functional properties in the investigated materials. Oxygen vacancies play an important role in the mechanism of conduction, and their amount can be controlled with dopants. Generally, it can be concluded that the degree of relaxation (ΔT_{relax}) decreases only in the case when the Ba content decreases because the barium leads to a locally undistorted structure and eventually non-polar regions. The observed improvements in basic properties with compositional modification due to substitution at the A- or B-sites have been accompanied in most cases by a decrease in the phase transition temperature and a decrease in the maximum dielectric permittivity.

17.4 Conclusions

Properties of the relaxor materials can be tailored in two most general ways – by physical or by chemical means. Physical modifications include processing conditions, but from the point of view of physics the most interesting is to control the grain size of the ceramics. Two main mechanisms can be highlighted in this case. Firstly, qualitatively the core–shell (and the complementary brick wall) model can explain evolution of the dielectric properties with grain size in cases of both perovskite and Aurivillius structures. Dielectric properties of the shell can be considered to be insulating with a relatively low dielectric constant in comparison with bulk material. Thus, the resulting ceramics generally become less conductive and have a smaller permittivity if the grains are small. Secondly, polar nanoregions are highly important to have a complete understanding of the size effects in ferroelectric relaxors, especially in the reviewed PMN and PSN systems. Grain boundaries limit growth of the PNRs and interactions between the PNRs in different grains. This results in shifts of characteristic temperatures: freezing temperature and temperature of the maximum dielectric permittivity $T_{\max}$. These shifts are related to suppression of the PNRs with long relaxation times (probably PNRs with big volume) and limitation of their interaction by grain boundaries. A spontaneous phase transition is obscured in PSN (similarly to PMN-35%PT), but the phase transition is known to take place from XRD studies. This means that even though the PNRs give a major contribution to the dielectric properties of relaxor ferroelectrics at low frequencies, they are not pivotal for phase transitions.

On the other hand, according to results of ΔT_{relax}, the synthesis method (in fact, the grain size) did not influence the relaxation process in the investigated BBT ceramic. This implies that the PNRs are either less important in relaxors with Aurivillius structure or that they are much smaller than in the case of perovskite relaxors. In contrast, the influence of PNRs is more important when Aurivillius materials are doped. The degree of relaxation decreases in the case when the Ba content decreases because the barium leads locally to undistorted structure and eventually non-polar domains. The increase in relaxation is noticed when the Bi^{3+} and Ti^{4+} are substituted, which causes structural disorder that deteriorates ferroelectric long-range ordering in BLSF compounds.

References

(1) Park, S.E. and Shrout, T.R. (1997) Ultrahigh strain and piezoelectric behavior in relaxor based ferroelectric single crystals. *Journal of Applied Physics*, **82** (4), 1804–1811.

(2) Burns, G. and Dacol, F.H. (1983) Glassy polarization behavior in ferroelectric compounds $Pb(Mg_{1/3}Nb_{2/3})O_3$ and $Pb(Zn_{1/3}Nb_{2/3})O_3$. *Solid State Communications*, **48** (10), 853–856.

(3) Hlinka, J., Petzelt, J., Kamba, S., et al. (2006) Infrared dielectric response of relaxor ferroelectrics. *Phase Transitions*, **79** (1–2), 41–78.

(4) Fu, D., Taniguchi, H., Itoh, M., et al. (2009) Relaxor $Pb(Mg_{1/3}Nb_{2/3})O_3$: a ferroelectric with multiple inhomogeneities. *Physical Review Letters*, **103** (20), art. no. 207601.

(5) Novak, N., Pirc, R., Wencka, M., and Kutnjak, Z. (2012) High-resolution calorimetric study of $Pb(Mg_{1/3}Nb_{2/3})O_3$ single crystal. *Physical Review Letters*, **109** (3), art. no. 037601.

(6) Macutkevic, J., Kamba, S., Banys, J., et al. (2006) Infrared and broadband dielectric spectroscopy of PZN–PMN–PSN relaxor ferroelectrics: origin of two-component relaxation. *Physical Review B*, **74** (10), art. no. 104106.

(7) Viehland, D., Jang, S.J., Cross L.E., and Wuttig, M. (1990) Freezing of the polarization fluctuations in lead magnesium niobate relaxors. *Journal of Applied Physics*, **68** (6), 2916–2921.

(8) Chu, F., Setter, N., and Tagantsev, A.K. (1993) The spontaneous relaxor–ferroelectric transition of $Pb(Sc_{0.5}Ta_{0.5})O_3$. *Journal of Applied Physics*, **74** (8), 5129–5134.

(9) Dai, X., Xu Z., and Viehland, D. (1994) The spontaneous relaxor to normal ferroelectric transformation in La-modified lead zirconate titanate. *Philosophical Magazine B*, **70** (1), 33–48.

(10) Krumins, A., Shiosaki, T., and Koizumi, S. (1994) Spontaneous transition between relaxor and ferroelectric states in lanthanum-modified lead zirconate titanate (6–7)/65/35. *Japanese Journal of Applied Physics*, **33** (1), no. 9A, 4940–4945.

(11) Sciau, P., Calvarin, G., and Ravez, J. (1999) X-ray diffraction study of $BaTi_{0.65}Zr_{0.35}O_3$ and $Ba_{0.92}Ca_{0.08}Ti_{0.75}Zr_{0.25}O_3$ compositions: influence of electric field. *Solid State Commununications*, **113** (2), 77–82.

(12) Simon, A., Ravez, J., and Maglione, M. (2004) The crossover from a ferroelectric to a relaxor state in lead-free solid solutions. *Journal of Physics: Condensed Matter*, **16** (6), 963–970.

(13) Yasuda, N., Ohwa, H., and Asano, S. (1996) Dielectric properties and phase transitions of $Ba(Ti_{1-x}Sn_x)O_3$ Solid Solution. *Japanese Journal of Applied Physics*, **35** (Part 1) no. 9B, 5099–5103.

(14) Pirc, R. and Blinc, R. (1999) Spherical random-bond–random-field model of relaxor ferroelectrics. *Physical Review B*, **60** (19), 13470–13478.

(15) Blinc, R., Dolinšek, J., Gregorovič, A., et al. (1999) Local polarization distribution and Edwards–Anderson order parameter of relaxor ferroelectrics. *Physical Review Letters*, **83** (2), 424–427.

(16) Pirc, R., Kutnjak, Z., and Novak, N. (2012) Compressible spherical dipolar glass model of relaxor ferroelectrics. *Journal of Applied Physics*, **112** (11), art. no. 114122.

(17) Macutkevic, J., Banys, J., Grigalaitis, R., and Vysochanskii, Y. (2008) Asymmetric phase diagram of mixed $CuInP_2(S_xSe_{1-x})_6$ crystals. *Physical Review B*, **78** (6), 1–11.

(18) Manley, M.E., Lynn, J.W., Abernathy, D.L., et al. (2014) Phonon localization drives polar nanoregions in a relaxor ferroelectric. *Nature Communications*, **5**, art. no. 3683.

(19) Bishop, A.R., Bussmann-Holder, A., Kamba, S., and Maglione, M. (2010) Common characteristics of displacive and relaxor ferroelectrics. *Physical Review B*, **81** (6), art. no. 064106.

(20) Macutkevic, J., Banys, J., Bussmann-Holder, A., and Bishop, A.R. (2011) Origin of polar nanoregions in relaxor ferroelectrics: nonlinearity, discrete breather formation, and charge transfer. *Physical Review B*, **83** (18), art. no. 184301.

(21) Patwe, S.J., Achary, S.N., Manjanna, J., et al. (2013) Observation of a new cryogenic temperature dielectric relaxation in multiferroic $Bi_7Fe_3Ti_3O_{21}$. *Applied Physics Letters*, **103** (12), art. no. 122901.

(22) Macutkevic, J., Banys, J., and Grigalaitis, R. (2011) Comment on "Revisit of the Vogel–Fulcher freezing in lead magnesium niobate relaxors". *Applied Physics Letters*, **98** (1), art. no. 016101.

(23) Pirc, R. and Blinc, R. (2007) Vogel–Fulcher freezing in relaxor ferroelectrics. *Physical Review B*, **76** (2), art. no. 020101.

(24) Prosandeev, S., Wang, D., Akbarzadeh, A.R., et al. (2013) Field-induced percolation of polar nanoregions in relaxor ferroelectrics. *Physical Review Letters*, **110** (20), art. no. 207601.

(25) Koreeda, A., Taniguchi, H., Saikan, S., and Itoh, M. (2012) Fractal dynamics in a single crystal of a relaxor ferroelectric. *Physical Review Letters*, **109** (19), art. no. 197601.

(26) Hill, N.A. and Filippetti, A. (2002) Why are there any magnetic ferroelectrics? *Journal of Magnetism and Magnetic Materials*, **242–245** (Part 2), 976–979.

(27) Lee, C.H., Orloff, N.D., Birol, T., et al. (2013) Exploiting dimensionality and defect mitigation to create tunable microwave dielectrics. *Nature*, **502** (7472), 532–536.

(28) Carreaud, J., Gemeiner, P., Kiat, J.M., et al. (2005) Size-driven relaxation and polar states in $PbMg_{1/3}Nb_{2/3}O_3$-based system. *Physical Review B*, **72** (17), art. no. 174115.

(29) Jiménez, R., Amorín, H., Ricote, J., et al. (2008) Effect of grain size on the transition between ferroelectric and relaxor states in $0.8Pb(Mg_{1/3}Nb_{2/3})O_3$–$0.2PbTiO_3$ ceramics. *Physical Review B*, **78** (9), art. no. 094103.

(30) Carreaud, J., Kiat, J.M., Dkhil, B., et al. (2006) Monoclinic morphotropic phase and grain size-induced polarization rotation in $Pb(Mg_{1/3}Nb_{2/3})O_3$–$PbTiO_3$. *Applied Physics Letters*, **89** (25), art. no. 252906.

(31) Algueró, M., Ricote, J., Jiménez, R., et al. (2007) Size effect in morphotropic phase boundary $Pb(Mg_{1/3}Nb_{2/3})O_3$–$PbTiO_3$. *Applied Physics Letters*, **91** (11), art. no. 112905.

(32) Carreaud, J., Bogicevic, C., Dkhil, B., and Kiat, J.M. (2008) Dielectric evidences of core–shell-like effects in nanosized relaxor $PbMg_{1/3}Nb_{2/3}O_3$. *Applied Physics Letters*, **92** (24), art. no. 242902.

(33) Bovtun, V., Kamba, S., Veljko, S., et al. (2009) Broadband dielectric spectroscopy of phonons and polar nanoclusters in $Pb(Mg_{1/3}Nb_{2/3})O_3$–35%$PbTiO_3$ ceramics: grain size effects. *Physical Review B*, **79** (10), art. no. 104111.

(34) Papet, P., Dougherty, J.P., and Shrout, T.R. (1990) Particle and grain size effects on the dielectric behavior of the relaxor ferroelectric $Pb(Mg_{1/3}Nb_{2/3})O_3$. *Journal of Materials Research*, **5** (12), 2902–2909.

(35) Grigalaitis, R., Ivanov, M., Macutkevic, J., et al. (2014) Size effects in a relaxor: further insights into PMN. *Journal of Physics: Condensed Matter*, **26** (27), art. no. 272201.

(36) Banys, J., Grigalaitis, R., Ivanov, M., et al. (2008) Dielectric behaviour of a nanograin PMN powders. *Integrated Ferroelectrics*, **99** (1), 132–139.

(37) Grigalaitis, R., Banys, J., Kania, A., and Slodczyk, A. (2005) Distribution of relaxation times in PMN single crystal. *Journal de Physique IV – Proceedings*, **128**, 127–131.

(38) Grigalaitis, R., Banys, J., Sternberg, A., et al. (2006) Dynamics of polar clusters in PMN ceramics: comparison with PMNs crystal. *Ferroelectrics*, **340** (1), 147–153.

(39) Zhao, Z., Buscaglia, V., Viviani, M., et al. (2004) Grain-size effects on the ferroelectric behavior of dense nanocrystalline $BaTiO_3$ ceramics. *Physical Review B*, **70** (2), art. no. 024107.

(40) Grigalaitis, R., Banys, J., Lapinskas, S., et al. (2006) Dielectric investigations and theoretical calculations of size effect in lead titanate nanocrystals. *Materials Science Forum*, **514–516**, 235–239.

(41) Mathan, N. de, Husson, E., Calvarn, G., et al. (1991) A structural model for the relaxor $Pb(Mg_{1/3}Nb_{2/3})O_3$ at 5 K. *Journal of Physics: Condensed Matter*, **3** (42), 8159–8171.

(42) Banys, J., Lapinskas, S., Kajokas, A., et al. (2002) Dynamic dielectric susceptibility of the betaine phosphate (0.15) betaine phosphite (0.85) dipolar glass. *Physical Review B*, **66** (14), art. no. 144113.

(43) Xu, G., Shirane, G., Copley J.R.D., and Gehring, P.M. (2004) Neutron elastic diffuse scattering study of $Pb(Mg_{1/3}Nb_{2/3})O_3$. *Physical Review B*, **69** (6), art. no. 064112.

(44) Rault, J. (2000) Origin of the Vogel–Fulcher–Tammann law in glass-forming materials: the α–β bifurcation. *Journal of Non-Crystalline Solids*, **271** (3), 177–217.

(45) Colla, E.V., Koroleva, E.Y., Okuneva, N.M., and Vakhrushev, S.B. (1992) Low-frequency dielectric response of $Pb(Mg_{1/3}Nb_{2/3})O_3$. *Journal of Physics: Condensed Matter*, **4** (13), 3671–3677.

(46) Buscaglia, M.T., Viviani, M., Buscaglia, V., et al. (2006) High dielectric constant and frozen macroscopic polarization in dense nanocrystalline $BaTiO_3$ ceramics. *Physical Review B*, **73**(96), art. no. 064114.

(47) Emelyanov, A.Y., Pertsev, N.A., Hoffmann-Eifert, S., et al. (2002) Grain-boundary effect on the Curie–Weiss law of ferroelectric ceramics and polycrystalline thin films: calculation by the method of effective medium. *Journal of Electroceramics*, **9** (1), 5–16.

(48) Chu, F., Reaney, I.M., and Setter, N. (1995) Spontaneous (zero-field) relaxor–to–ferroelectric-phase transition in disordered $Pb(Sc_{1/2}Nb_{1/2})O_3$. *Journal of Applied Physics*, **77**(4), 1671–1676.

(49) Malibert, C., Dkhil, B., Kiat, J.M., et al. (1997) Order and disorder in the relaxor ferroelectric perovskite (PSN): comparison with simple perovskites $BaTiO_3$ and $PbTiO_3$. *Journal of Physics: Condensed Matter*, **9** (35), 7485–7500.

(50) Svirskas, S., Ivanov, M., Bagdzevicius, S., et al. (2014) Dielectric properties of $0.4Na_{0.5}Bi_{0.5}TiO_3$– (0.6-x)$SrTiO_3$–$x$$PbTiO_3$ solid solutions. *Acta Materialia*, **64**, 123–132.

(51) Kiat, J.M., Bogicevic, C., Karolak, F., et al. (2010) Low-symmetry phases and loss of relaxation in nanosized lead scandium niobate. *Physical Review B*, **81** (14), art. no. 144122.

(52) Ivanov, M., Banys, J., Bogicevic C., and Kiat, J.M. (2012) Size effects on dielectric properties of nanograin PSN ceramics. *Ferroelectrics*, **429** (1), 43–47.

(53) Petzelt, J., Rychetsky, I., and Nuzhnyy, D. (2012) Dynamic ferroelectric-like softening due to the conduction in disordered and inhomogeneous systems: giant permittivity phenomena. *Ferroelectrics*, **426** (1), 171–193.

(54) Trybula, Z., Schmidt, V.H., and Drumheller, J.E. (1991) Coexistence of proton-glass and ferroelectric order in $Rb_{1-x}(NH_4)_xH_2AsO_4$. *Physical Review B*, **43** (1), 1287–1289.

(55) Cheng, B.L., Gabbay, M., and Fantozzi, G. (1996) Anelastic relaxation associated with the motion of domain walls in barium titanate ceramics. *Journal of Materials Science*, **31** (15), 4141–4147.

(56) Nakamura, E. (1992) Anomalous dielectric behavior of KH_2PO_4 type crystals in the ferroelectric phase. *Ferroelectrics*, **135** (1), 237–247.

(57) Kubinec, P., Fally, M., Fuith, A., et al. (1995) A dielectric study of the domain freezing in KH_2AsO_4. *Journal of Physics: Condensed Matter*, **7** (10), 2205–2216.

(58) Jovalekić, Č., Zdujić, M., and Atanasoska, L. (2009) Surface analysis of bismuth titanate by Auger and X-ray photoelectron spectroscopy. *Journal of Alloys and Compounds*, **469** (1–2), 441–444.

(59) Park, B.H. and Kang, B.S. (1999) Lanthanum-substituted bismuth titanate for use in non-volatile memories. *Nature*, **401** (6754), 682–684.

(60) Hou, R.Z., Chen, X.M., and Zeng, Y.W. (2006) Diffuse ferroelectric phase transition and relaxor behaviors in Ba-based bismuth layer-structured compounds and La-substituted $SrBi_4Ti_4O_{15}$. *Journal of the American Ceramic Society*, **89** (9), 2839–2844.

(61) Shvartsman, V.V., Costa, M.E.V., Avdeev, M., and Kholkin, A.L. (2003) Relaxor behavior of $BaBi_2Ta_2O_9$ and $BaBi_2Nb_2O_9$ ceramics. *Ferroelectrics*, **296** (1), 187–197.

(62) Shvartsman, V.V. and Lupascu, D.C. (2012) Lead-free relaxor ferroelectrics. *Journal of the American Ceramic Society*, **95** (1), 1–26.

(63) Miranda, C., Costa, M.E.V., Avdeev, M., et al. (2001) Relaxor properties of Ba-based layered perovskites. *Journal of the European Ceramic Society*, **21** (10–11), 1303–1306.

(64) Bobic, J.D., Vijatovic Petrovic, M.M., Banys, J., and Stojanovic, B.D. (2012) Electrical properties of niobium doped barium bismuth–titanate ceramics. *Materials Research Bulletin*, **47** (8), 1874–1880.

(65) Irie, H., Miyayama, M., and Kudo, T. (2000) Electrical properties of a bismuth layer-structured $Ba_2Bi_4Ti_5O_{18}$ single crystal. *Journal of the American Ceramic Society*, **83** (11), 2699–2704.

(66) Rout, S.K., Sinha, E., Hussian, A., et al. (2009) Phase transition in $ABi_4Ti_4O_{15}$ (A = Ca, Sr, Ba) Aurivillius oxides prepared through a soft chemical route. *Journal of Applied Physics*, **105** (2), art. no. 024105.

(67) Tellier, J., Boullay, P., Manier, M., and Mercurio, D. (2004) A comparative study of the Aurivillius phase ferroelectrics $CaBi_4Ti_4O_{15}$ and $BaBi_4Ti_4O_{15}$. *Journal of Solid State Chemistry*, **177** (6), 1829–1837.

(68) Nalini, G. and Row, G.T. (2002) Structure determination at room temperature and phase transition studies above T_c in $ABi_4Ti_4O_{15}$ (A = Ba, Sr or Pb). *Bulletin of Material Science*, **25** (4), 275–281.

(69) Kennedy, B.J., Zhou, Q., Ismunandar, et al. (2008) Cation disorder and phase transitions in the four-layer ferroelectric Aurivillius phases $ABi_4Ti_4O_{15}$ (A = Ca, Sr, Ba, Pb). *Journal of Solid State Chemistry*, **181** (6), 1377–1386.

(70) Huang, S., Feng, C., Chen, L., and Wang, Q. (2006) Relaxor behavior of $Sr_{1-x}Ba_xBi_2Nb_2O_9$ ceramics. *Journal of the American Ceramic Society*, **89** (1), 328–331.

(71) Pérez-Delfin, E., García, J.E., Vega-Garcíaet, A., et al. (2012) Influence of Mn-doping on phase transition characteristics and relaxor behaviour of lead lanthanum zirconate titanate ceramics. *Journal of the European Ceramic Society*, **32** (8), 1659–1665.

(72) Ke, S., Fan, H., Huang, H., et al. (2008) Dielectric dispersion behavior of $Ba(Zr_xTi_{1-x})O_3$ solid solutions with a quasiferroelectric state. *Journal of Applied Physics*, **104** (3), art. no. 034108.

(73) Khokhar, A., Mahesh, M.L.V., James, A.R., et al. (2013) Sintering characteristics and electrical properties of $BaBi_4Ti_4O_{15}$ ferroelectric ceramics. *Journal of Alloys and Compounds*, **581**, 150–159.

(74) Lei, C., Bokov, A.A., and Ye, Z.G. (2006) Relaxor behavior in $Ba(Ti_{0.72}Sn_{0.28})O_3$ solid solution. *Ferroelectrics*, **339** (1), 129–136.

(75) Bokov, A.A. and Ye, Z.G. (2000) Phenomenological description of dielectric permittivity peak in relaxor ferroelectrics. *Solid State Communications*, **116** (2), 105–108.

(76) Adamczyk, M., Ujma, Z., and Pawełczyk, M. (2006) Dielectric properties of $BaBi_2Nb_2O_9$ ceramics. *Journal of Materials Science*, **41** (16), 5317–5322.

(77) Bobic, J.D., Petrovic, V.M.M., Ilic, N.I., et al. (2015) Lead-free $BaBi_4Ti_4O_{15}$ ceramics: effect of synthesis methods on phase formation and electrical properties. *Ceramic International*, **41**, 309–316.

(78) Luan, W., Gao, L., and Guo, J. (1999) Size effect on dielectric properties of fine-grained $BaTiO_3$ ceramics. *Ceramic International*, **25** (8), 727–729.

(79) Wu, L., Chure, M.C., Wu, K.K., et al. (2009) Dielectric properties of barium titanate ceramics with different materials powder size. *Ceramic International*, **35** (3), 957–960.

(80) Ferrer, P., Algueró, M., and Castro, A. (2008) Influence of the mechanochemical conditions on the processing of $Bi_4SrTi_4O_{15}$ ceramics from submicronic powdered precursors. *Journal of Alloys and Compounds*, **464** (1–2), 252–258.

(81) Chen, H., Shen, B., Xu, J., and Zhai, J. (2013) The grain size-dependent electrical properties of $Bi_4Ti_3O_{12}$ piezoelectric ceramics. *Journal of Alloys and Compounds*, **551**, 92–97.

(82) Vijatovic, M.M., Bobic, J.D., and Stojanovic, B.D. (2008) History and challenges of barium titanate: Part I. *Science of Sintering*, **40** (2), 155–165.

(83) Surowiak, Z., Kupriyanov, M.F., and Czekaj, D. (2001) Properties of nanocrystalline ferroelectric PZT ceramics. *Journal of the European Ceramic Society*, **21** (10–11), 1377–1381.

(84) Lee, B.W. and Lee, E.J. (2006) Effects of complex doping on microstructural and electrical properties of PZT ceramics. *Journal of Electroceramics*, **17** (2–4), 597–602.

(85) Jardiel, T., Caballero, A.C., and Villegas, M. (2008) Aurivillius ceramics: $Bi_4Ti_3O_{12}$-based piezoelectrics. *Journal of the Ceramic Society of Japan*, **116** (1352), 511–518.

(86) Kumar, S. and Varma, K.B.R. (2011) Dielectric relaxation in bismuth layer-structured $BaBi_4T_{i4}O_{15}$ ferroelectric ceramics. *Current Applied Physics*, **11** (2), 203–210.

(87) Shulman, H.S., Testorf, M., Damjanovic, D., and Setter, N. (1996) Microstructure, electrical conductivity, and piezoelectric properties of bismuth titanate. *Journal of the American Ceramic Society*, **79** (12), 3124–3128.

(88) Yao, Y.Y., Song, C.H., Bao, P., et al. (2004) Doping effect on the dielectric property in bismuth titanate. *Journal of Applied Physics*, **95** (6), 3126–3130.

(89) Chakrabarti, A. and Bera, J. (2010) Structure and relaxor behavior of $BaBi_4Ti_{4-x}Zr_xO_{15}$ ceramics. *Current Applied Physics*, **10** (2), 574–579.

(90) Diao, C.L., Xu, J.B., Zheng, H.W., et al. (2013) Dielectric and piezoelectric properties of cerium modified $BaBi_4Ti_4O_{15}$ ceramics. *Ceramic International*, **39** (6), 6991–6995.

(91) Pribošič, I., Makovec, D., and Drofenik, M. (2001) Electrical properties of donor- and acceptor-doped $BaBi_4Ti_4O_{15}$. *Journal of the European Ceramic Society*, **21** (10–11), 1327–1331.

(92) Rout, S.K., Hussian, A., Lee, J.S., et al. (2009) Impedance spectroscopy and morphology of $SrBi_4Ti_4O_{15}$ ceramics prepared by soft chemical method. *Journal of Alloys and Compounds*, **477** (1–2), 706–711.

(93) Chakrabarti, A. and Bera, J. (2010) Effect of La-substitution on the structure and dielectric properties of $BaBi_4Ti_4O_{15}$ ceramics. *Journal of Alloys and Compounds*, **505** (2), 668–674.

(94) Kumar, S. and Varma, K.B.R. (2009) Influence of lanthanum doping on the dielectric, ferroelectric and relaxor behaviour of barium bismuth titanate ceramics. *Journal of Physics D: Applied Physics*, **42** (7), art. no. 075405.

(95) Bobic, J.D., Vijatović Petrovic, M.M., Banys, J., and Stojanovic, B.D. (2013) Effect of La substitution on the structural and electrical properties of $BaBi_{4-x}La_xTi_4O_{15}$. *Ceramic International*, **39** (7), 8049–8057.

18

Local Field Engineering Approach for Tuning Dielectric and Ferroelectric Properties in Nanostructured Ferroelectrics and Composites

Leontin Padurariu and Liliana Mitoseriu

University "Alexandru Ioan Cuza", Romania

18.1 Introduction

Ferroelectric materials are characterized by a non-linear and hysteretic dependence of polarization on the applied electric field below a critical temperature (Curie temperature). The spontaneous polarization can be switched between two bistable energy states if a field higher than the coercive one is applied to the system [1]. The switching property of ferroelectrics has extensive applications in data storage, random access memories, ferroelectric tunneling barriers, and ferroelectric gate transistors [2–4]. Together with the non-linear $P(E)$ dependence, the permittivity is also a hysteretic function of field $\varepsilon(E)$, and this dielectric non-linearity is denominated as tunability. This property makes ferroelectrics highly interesting in wireless communications, for voltage tunable microwave devices, such as oscillators, phase shifters, and varactors, especially in their relaxor or paraelectric state, when the hysteretic character is reduced or absent [5, 6]. The most important material requirements for the large majority of tunable applications are: ability to change the permittivity by reasonable fields (high tunability), not every high

---

Nanoscale Ferroelectrics and Multiferroics: Key Processing and Characterization Issues, and Nanoscale Effects, First Edition. Edited by Miguel Algueró, J. Marty Gregg, and Liliana Mitoseriu.
© 2016 John Wiley & Sons, Ltd. Published 2016 by John Wiley & Sons, Ltd.

permittivity, below 1000 down to a few hundreds, low losses, and non-hysteretic character. These requirements are difficult to accomplish in single-phase ferroelectrics, because usually high tunability is typical of the ferroelectric state or close to the ferroelectric-paraelectric transition, where permittivity and losses are high due to the domain wall contributions, and this limitation imposed the necessity of searching for new materials or combinations of ferroelectrics with dielectrics. For other types of non-ferroelectric dielectrics, such as pyroclore oxides [7] or polymers with potential use in flexible electronics like non-ferroelectric polar dielectrics, a certain tunability is acquired, but at very high fields [8]. However, their tunability is too small by comparison with values of ferroelectric-derived oxides and also permittivity is very low (in the range of units). For such systems, the interest is to increase both permittivity and tunability at reasonable values of the applied fields, while preserving low losses. For tailoring both permittivity and tunability to desired values, combinations of materials in composites are a better option than pure phases.

The interfaces between dissimilar phases in composites introduce an electric field inhomogeneity (field lines fringes), due to the different local permittivity and conductivity and, as result, the macroscopic electrical properties are governed by this inhomogeneity. In fact, it was proved that ferroelectric properties are very sensitive to the modifications of microstructure characteristics. For example, in nanostructured $BaTiO_3$ ceramics, which have been intensively studied in the last few years, substantial modifications of both switching and tunability properties were detected when reducing GS at nanoscale [9–16]. The permittivity versus electric field dependence changes from a Johnson-like behavior [17] to a more linearized shape with reducing GS. The hysteresis loops also change as a result of the GS reduction from a rectangular shape, easily saturated, to more tilted loops with reduced hysteresis area, saturation/remanent polarizations, and hardly saturated even at high fields. Another example that proves the strong sensitivity of ferroelectric/dielectric properties on the microstructural parameters is the role of porosity in ferroelectric ceramics. Porosity caused by imperfect sintering is detrimental for electroceramic applications, since it causes important modifications on the effective permittivity and tunability by comparison with values of a dense material. Permittivity reduces when increasing porosity and usually also tunability, although for some specific values of porosity in particular configurations, a higher tunability than for dense materials has been reported [18]. The switching properties are also strongly dependent on porosity: a decrease of saturation/remanent polarization, a decrease of hysteresis area, and an increase of coercive field with an increasing porosity level has usually been reported [19–21]. Any other types of local inhomogeneities present in ceramics, as secondary phases, imperfect crystallization areas, zones with stoichiometry variations or with localized charged defects, interfaces between dissimilar phases, and ceramic–electrodes interfaces may introduce a certain inhomogeneity to the local electric fields as a result of the local permittivity modifications. For these reasons ferroelectric ceramics can be treated as composites.

Observations related to the modification of ferroelectric/dielectric/tunability properties by microstructural factors have often been reported in the literature [9–16, 18–21], but the interpretation of such properties was not clearly related to the local field inhomogeneity. However, there are some simplified models that tried to relate the deviations of such properties from ones typical for the homogeneous material to some microstructural characteristics. For example, Liou and Chou [22] and Zhang et al. [23] modified Johnson's equation $\varepsilon_{\mathrm{r}}(E)$ [17]:

$$\varepsilon_{\mathrm{r}}(E) = \frac{\varepsilon_{\mathrm{r}}(0)}{[1 + 3\beta\varepsilon_{\mathrm{r}}(0)^3\varepsilon_0^3E^2]^{1/3}} \tag{18.1}$$

in order to describe the experimental dependence of the effective permittivity on the applied field in nanostructured ceramics and porous structures. This equation is derived from the Landau–Devonshire–Ginzburg approximation [24], where $\varepsilon_{\mathrm{r}}(0)$ is zero-field permittivity, ε_0 is the vacuum permittivity, E is the applied electric field, and β is a coefficient describing the non-linearity. Liou and Chou [22] and Zhang et al. [23] observed that Johnson's equation was unable to describe their experimental permittivity versus field dependences for such particular microstructures and artificially modified the electric field term in Jonhson's equation by adding a parameter at the field exponent. Sherman et al. [25] tried to compute a more precise value of the field in the ferroelectric region of a dielectric–ferroelectric composite by taking into consideration the electric field boundary conditions at the planar interfaces and then the effective permittivity and tunability was estimated. All these approaches tried somehow to consider the field deviations in inhomogeneous materials. A more rigorous way to take into consideration the role of the microstructures in changing locally the electric field was proposed by Padurariu et al. [26, 27], who explained the need to modify the electric field term in Johnson's equation in order to fit experimental data of inhomogeneous structures by the local field inhomogeneity.

Recently, new contributions in considering the role of the local field inhomogeniety on switching properties were reported. Whyte et al. [28] demonstrated by local piezoresponce force microscopy (PFM) experiments and finite element method (FEM) calculations that ferroelectric domain structures and switching properties are strongly affected by local electric field inhomogeneity. Other descriptions of switching properties of ferroelectrics have been performed using Kolmogorov–Avrami–Ishibashi models [29–31] by introducing the concept of local field distribution [32, 33].

If the microstructural characteristics are so important in changing local fields, one may ask if inhomogeneities can be used to modify the fields in a controlled way in order to enhance electrical properties. Based on this idea, we recently proposed the concept of *local field engineering* [26, 27, 34], which consists in designing composite materials (e.g. dielectric–ferroelectric, ferroelectric–ferroelectric, dielectric–metallic particles, etc.) with well-controlled microstructures to tailor local field distribution in order to reach desired properties. In this work, the role of local field inhomogeneity on the permittivity, tunability, and switching properties will be described in detail, with examples of a few peculiar microstructures. To describe in a rigorous way the field modifications, the finite element method (FEM) was used.

18.2 Finite Element Method

In the last few years, due to the development of computational mathematics, FEM techniques have been distinguished as very powerful methods of calculation of composite materials properties. By comparison with effective medium approximation (EMA)

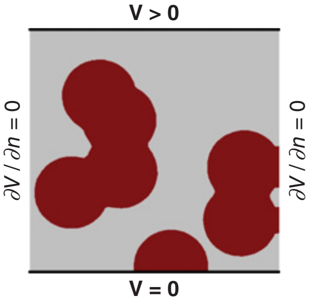

Figure 18.1 *Boundary conditions in FEM for a diphase composite material: light shows a phase with* ε_1 *permittivity; dark shows a phase with* ε_2 *permittivity*

models, traditionally used to estimate effective permittivity in composites [35–39], FEM has the advantage to take into account precisely the microstructural particularities of the composite. In FEM, the macroscopic properties are derived from the local electric field distributions. To compute the local fields in a composite material, Poisson's equation is considered:

$$\nabla \cdot (\varepsilon(\boldsymbol{r})\nabla V(\boldsymbol{r})) = \rho(\boldsymbol{r}) \tag{18.2}$$

where V is the local potential and $\varepsilon(\boldsymbol{r})$ and $\rho(\boldsymbol{r})$represent the local permittivity and charge density in the $\boldsymbol{r}$ position, respectively. This equation together with Dirichlet/Neumann boundary conditions (represented in Figure 18.1) was solved by the FEM procedure. The boundary conditions describe a parallel plate capacitor, which usually represents the commonly used configuration in an experimental dielectric characterization of materials. In the following, we will consider only the case of very good insulator materials and the last term in Equation (18.2) will be considered equal to zero.

The first step in FEM calculations is the meshing of the system in a number of discrete elements. In the case of 2D simulations the most common types of elements are triangular. The local electric calculations are more precise as the number of elements is higher. After meshing, the local electric field is described inside each element as a combination of potentials in the nodes:

$$V(x, y) = p_1V_1 + p_2V_2 + p_3V_3 \tag{18.3}$$

where p_1, p_2, and p_3 are linear interpolation functions. The local potential is approximated better when the elements are very close to an equilateral triangle shape. The advantage of such a meshing procedure is that the elements can describe very well the interfaces between phases in composites materials and numerical errors during the computation procedure are avoided at the interfaces. An example of the mesh for the system represented in Figure 18.1 is represented in Figure 18.2.

The next step in the FEM is the calculation of the local electric potential in each node of the system, based on the Galerkin procedure [40, 41]. The local electric fields are further computed for each eth element as the derivative of the potential:

$$E_x^e = -\left(V_1^e \frac{\partial p_1^e}{\partial x} + V_2^e \frac{\partial p_2^e}{\partial x} + V_3^e \frac{\partial p_3^e}{\partial x}\right) \tag{18.4}$$

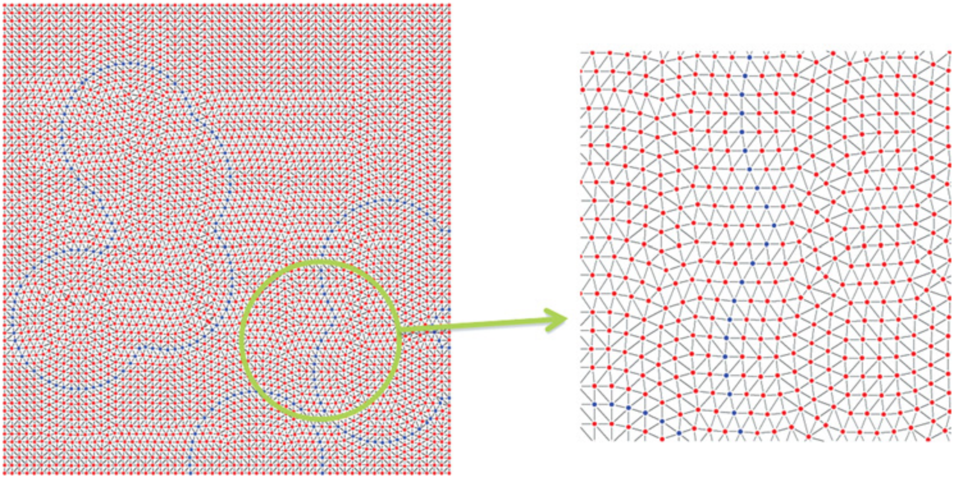

Figure 18.2 *Mesh of the system represented in Figure 18.1 with 50 × 50 nodes (5000 elements)*

$$E_y^e = -\left(V_1^e \frac{\partial p_1^e}{\partial y} + V_2^e \frac{\partial p_2^e}{\partial y} + V_3^e \frac{\partial p_3^e}{\partial y}\right) \tag{18.5}$$

The local electric fields are homogeneous inside an individual element due to the linear interpolation functions (p_1, p_2, and p_3) used in simulations. Then the effective permittivity of the composite material is derived from the total energy of the system computed as the sum of local energies per elements:

$$\frac{\varepsilon_{\text{eff}}}{2}\left(\frac{\Delta V}{d}\right)^2 A_t = \sum_{e=1}^{Ne} \frac{\varepsilon_e E_e^2}{2} A_e \tag{18.6}$$

where ΔV is the voltage applied to the system, d is the distance between electrodes, A_t is the total area of the electrodes, N_e the number of elements, ε_e the local permittivity, E_e the local electric field, and A_e the local area of the eth element.

Together with calculations of the effective permittivity in composites, a very interesting property that can be rigorously estimated by using FEM calculations is the applied field dependence of the effective tunability $\varepsilon_{\text{eff}}(E_{\text{app}})$ of composites containing at least one nonlinear dielectric (or ferroelectric) phase. In this case, the calculations are more complex, since the local permittivity of each element is a function of the local field. As an example, we will show in the following the results of our approach to determine the effective tunability for the case of composites with one tunable phase with field-dependent permittivity described by Johnson's equation $\varepsilon_{\text{r}}(E)$ (Equation (18.1)). As mentioned before, the permittivity versus field dependence of single-phase homogeneous tunable materials is well described by this equation, while for composites it proved to be inappropriate to describe the system of macroscopic tunability. However, Johnson's equation was chosen to describe the $\varepsilon_{\text{r}}(E)$ dependence at the local scale only, for small regions in which the field can be approximated as homogeneous, as in the case of a single-phase tunable material.

In order to describe a composite material, the coupled Laplace and Johnson system of equations should be solved. For a diphase composite with a linear dielectric phase and a non-linear tunable one, the local variation of the potential is described by equation:

$$\nabla(\varepsilon(x, y)\nabla V) = 0, \tag{18.7}$$

where the local permittivity is given by the formula [26,27]:

$$\varepsilon(x, y) = \begin{cases} \varepsilon_{\text{non-lin}}(E_{\text{local}}(x, y)), & \text{for the tunable dielectric regions} \\ \varepsilon_{\text{lin}}, & \text{for the linear dielectric phase} \end{cases} \tag{18.8}$$

The field dependence of the local permittivity of tunable regions is described as:

$$\varepsilon_{\text{non-lin}}(E_{\text{local}}(x, y)) = \frac{\varepsilon_1(0)}{\left[1 + k\varepsilon_1^3(0)E_{\text{local}}^2(x, y)\right]^{1/3}} \tag{18.9}$$

where $\varepsilon_1(0)$ is the zero field permittivity of the non-linear phase and k is a non-linear parameter that includes Johnson's non-linear parameter (1).

In order to compute $\varepsilon_{\text{eff}}(E_{\text{app}})$, the Laplace equation (18.7) is solved in a range of voltages from 0 to $\Delta V_{\max}$ with a small step. For the initial applied voltage (very close to zero) the local permittivities do not depend on the local fields and the calculation is performed as in linear composites. By gradually increasing the applied voltage, the local permittivities are computed as a function of the local field for each element, in accordance with Equations (18.8) and (18.9). As input for these equations, the local electric fields computed at the previous step are considered. Moreover, for each applied voltage step, the partial solution is introduced in Equations (18.7) to (18.9) and a residual is determined. If the residual is higher than an acceptable error, the procedure is repeated until the residual is close to zero and the iteration is stopped. Once the local permittivities are determined, the new local electric fields are again computed and finally the effective permittivity is derived from Equation (18.5). In this way the applied field dependence of the effective tunability in composites is determined: $n(E_{\text{ap}}) = \varepsilon_{\text{eff}}(0)/\varepsilon_{\text{eff}}(E_{\text{app}})$, where $E_{\text{app}} = \Delta V/d$ is the external applied field. On the basis of these calculations, a discussion of the role of local field inhomogeneity was performed and the possibility to optimize tunability by microstructure control was proposed.

18.3 The Role of Local Electric Field Inhomogeneity on Tunability Properties

As discussed in the first part, the main requirements for tunable materials are: moderate dielectric constant (below 1000), high tunability, and low losses (below 3%) [42]. Ferroelectrics are usually characterized by relatively high tunability, but also high permittivity. For these reasons in the last few years material science researchers proposed different methods to reduce permittivity while keeping a high tunability in composites. The simplest solution was to introduce a low-permittivity phase into the ferroelectric matrix. According to this idea, a large number of ferroelectric/dielectric composites have been proposed, using mostly $BaTiO_3$ or its solid solutions, like $Ba(Sr, Ti)O_3$ or $Ba(Zr, Ti)O_3$, as the high-permittivity phase and a linear dielectric low-permittivity phase, like MgO, $MgTiO_3$, or

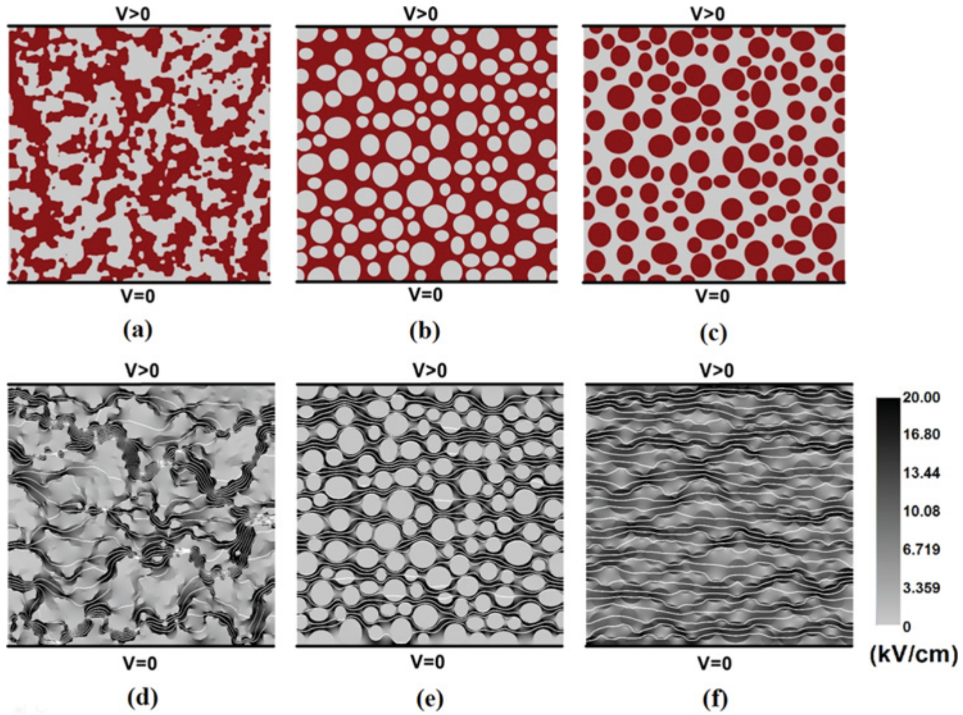

Figure 18.3 *Three composites configurations (a, b, c) and the corresponding local field images (d, e, and f) for the same filling factor: 50% ferroelectric (bright contrast) and 50% linear dielectric (dark contrast) and different distributions of phases: (a) randomly, (b) ferroelectric phase included into a dielectric matrix, and (c) linear dielectric embedded into a ferroelectric matrix. The local electric field intensities are represented in gray scale and the field orientations are perpendicular on the isopotential white lines*

Al_2O_3 [43–47]. Unfortunately, in all these cases in which the microstructure was not controlled and the ferroelectric and dielectric phases were randomly mixed, a reduced tunability together with a smaller permittivity were obtained. In fact, in most cases, the role of starting materials and filling factor on the tunability properties was studied. Accordingly, many new composites have been proposed, but all of them were mainly based on different ferroelectric and linear dielectric choices, but the results were always similar: a reduction of both permittivity and tunability. Although the composite contains a lot of interfaces between dissimilar phases, which introduce a high local field inhomogeneity, this effect was rarely considered.

In order to understand the role of microstructure on the tunability properties, three kind of composites are discussed in the following (Figure 18.3(a) to (c)). All the composites are characterized by the same concentration of phases: 50% ferroelectric (bright contrast) with $\varepsilon_{\mathrm{non-lin}}(0) = 1000$ (zero-field permittivity) and 50% linear dielectric (dark contrast) with $\varepsilon_{\mathrm{lin}} = 10$, but the phases are arranged in totally different ways. The first type of composite (Configuration 1, Figure 18.3(a)) is characterized by a random distribution of the phases, like the real case of the large majority of tunable composites proposed in the literature [43–48]. The second microstructure (Configuration 2, Figure 18.3(b)) is characterized by a ferroelectric phase included in a dielectric matrix, while the third composite (Configuration 3, Figure 18.3(c)) is the reverse of the second one, with the dielectric phase included in the ferroelectric matrix.

The local field images are represented in Figure 18.3(d) to (f). In Configuration 1, it is observed that the local electric field is suppressed on the ferroelectric non-linear component by the low-permittivity phase. In other words, even subjected to a high external field, a large percentage of this field is going to the low-permittivity phase and the ferroelectric phase is subjected to a much reduced field. For this reason, the macroscopic tunable response of such composites is strongly diminished by comparison with a single-phase ferroelectric material, which explains the results of a large number of experimental studies [43–48]. Configuration 2 with the ferroelectric phase included in the dielectric matrix presents an even more unsuitable local field distribution from the point of view of tunability effects: in this case almost all the external field is directed to the linear dielectric phase and the ferroelectric phase is subjected to an almost zero field. Therefore, tunability is expected not to be activated at all. The most promising configuration that concentrates high fields on to the non-linear component is the third configuration, in which the local fields on the ferroelectric component remain high even when the concentration of the dielectric phase is high and, therefore, the tunability in such a configuration is expected to be close to the single–phase values.

The corresponding macroscopic effective responses (permittivity and tunability) of the three configurations are represented in Figure 18.4. All the composites present a reduced permittivity below 300 by comparison with the homogeneous ferroelectric phase (Figure 18.4(a)). The calculations show that only the third configuration, with linear dielectric inclusions into the ferroelectric matrix, can accomplish the requirements of high tunability applications. If in the first two configurations the tunability is smaller than that of the ferroelectric pure phase (and even suppressed to zero for Configuration 2), in the third case the tunability is slightly higher than tunability of the single ferroelectric phase

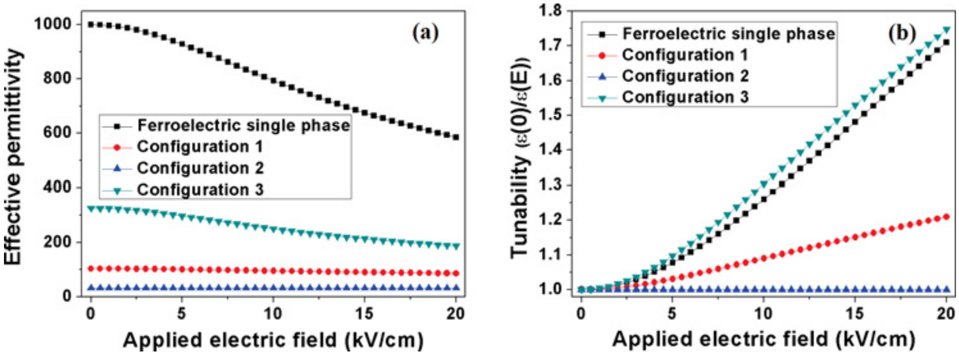

Figure 18.4 *The field dependence of (a) the effective permittivity and (b) tunability for the three configurations: with a randomly distributed phase (Configuration 1), with a ferroelectric phase included in a dielectric matrix (Configuration 2), and with a dielectric phase included in a ferroelectric matrix (Configuration 3)*

(Figure 18.4(b)). This result clearly demonstrates the essential role of intermixing in composites with the same compositions, which is not taken into consideration by effective field model calculations. A major conclusion is the possibility of designing composites to accomplish specific requirements concerning their permittivity and tunability by local field engineering and microstructure control.

The computed results for Configuration 1 are supported by many experimental results for composites with randomly distributed phase microstructures, which represents the most common type of microstructures realized for tunable composites [43–48]. However, our calculations showed that this is not the best configuration from a tunability point of view for a given filling factor.

Derived from these calculations, a few particular systems with microstructures falling in the categories of Configurations 2 and 3 will be further discussed: nanostructured ferroelectric ceramics as a particular case of Configuration 2 and porous ferroelectrics as a particular case of Configuration 3. Additionally, composites with a ferroelectric matrix and conductive inclusions willalso be analyzed.

18.3.1 Nanostructured Ferroelectric Ceramics

A ceramic material can be considered as a composite with grain bulk and grain boundary regions, which usually have different electrical characteristics in terms of permittivity and conductivity [9–12]. The role of grain boundaries in determining the ceramic properties become essential when reducing ceramic grain size down to nanoscale [11, 13, 14]. For explaining dielectric properties of ceramics, the ceramic structure was usually described as a brick-layer model [15, 16, 49] and for the case of ferroelectric nanoceramics, grain boundaries were commonly considered as a non-ferroelectric low-permittivity material [9, 11]. For $BaTiO_3$ and its solid solutions the grain boundary permittivity was considered as being close to one of non-ferroelectric titanates as TiO_2 [9–11, 13, 50], which is a linear dielectric with a permittivity $\varepsilon_{\text{lin}} = 100$, irrespective of the applied field. Since the grain bulk is always surrounded by grain boundaries, a ceramic ferroelectric can be considered as a particular case of Configuration 2.

Ceramics with different grain sizes considered as composites with high-permittivity grains surrounded by low-permittivity grain boundaries have been simulated [26, 51] (Figure 18.5(a) to (c)) and the corresponding local fields have been computed. In Figure 18.5(d) to (f) the local field images for three virtual ceramics with different grain sizes are represented. The grain boundary thickness for all systems was considered the same (~*5* a.u.), irrespective of the grain size (GS). It can be observed that a boundary-free ferroelectric system (e.g. a single crystal) is characterized by a highly homogenous local electric field distribution. The field becomes inhomogeneous in a ceramic composite (Figure 18.5(e) and (f)) and the inhomogeneity degree is higher when increasing the amount of the boundaries in the system. The local electric field in the ceramic with a relatively large GS (Figure 18.5(e)) is still close to the one in the case of a single crystal (Figure 18.5(d)). For this reason the dielectric and tunability properties of a coarse ceramic can be considered similar to ones of the single crystal. A high local field is concentrated on the grain boundaries perpendicular to the field direction, and this is the reason for the field depression on the grain core when GS is strongly reduced. Since the boundary thickness in ferroelectric ceramics is very low, the amount of boundaries in the system becomes significant at nanoscale.

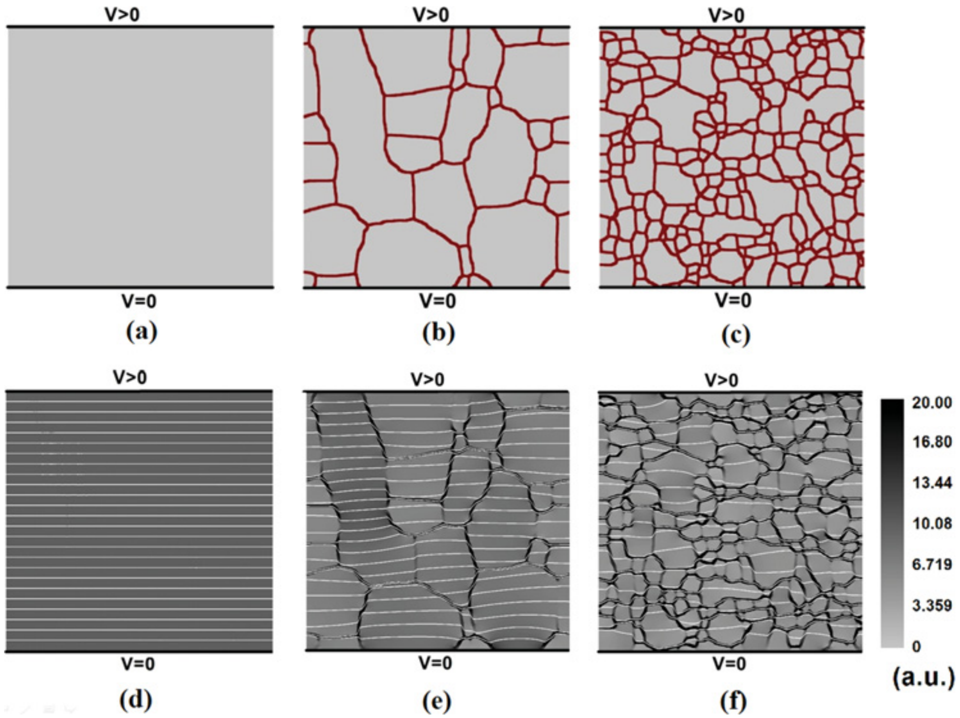

Figure 18.5 *Local field images (d to f) for virtual ceramic microstructures with different grain sizes: (a) single crystal, (b) GS = 100 a.u., and (c) GS = 30 a.u.*

In Figure 18.6 the local electric field distributions $\rho(\alpha)$ as a function of a parameter that represents the ratio between the local field and the external applied field $\alpha = E_{\text{local}}/E_{\text{applied}}$ is shown. The electric field distribution function $\rho(\alpha)$ is defined as the ratio between the area subjected to a local fields with the values between $(\alpha, \alpha + d\alpha)$ and $d\alpha$. If in the case of a single ferroelectric crystal the local electric field distribution is a Dirac function type (Figure 18.6(a)), the distribution becomes broader as the grain size becomes smaller (Figure 18.6(a) and (b)). Another important observation is that the average value of the field acting

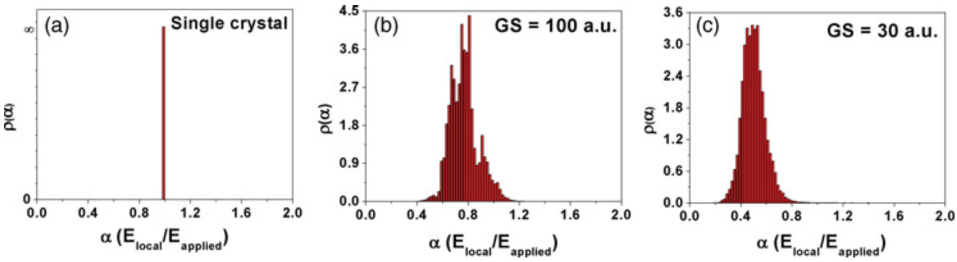

Figure 18.6 *Local electric field distributions at low field on bulk for different GSs: (a) single crystal, (b) GS = 100 a.u., and (c) GS = 30 a.u.*

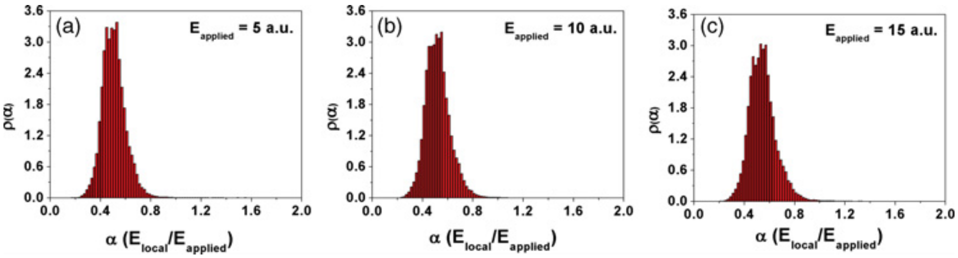

Figure 18.7 *Local electric field distributions computed for the same virtual ceramic (GS = 30 a.u.) for different applied electric field values*

on the grain bulk decreases when reducing GS. This is the reason why a nanostructured ceramic is hardly saturated by comparison with a coarse ceramic, as will be discussed in Section 18.4. It is important to mention that in simulations it is easier to describe a ceramic with a reduced GS with a good statistic of grains (a large number of grains). When a coarse ceramic is considered in simulation, the reduced number of grains in the system makes the local electric field distribution quite noisy.

It is also important to monitor how the local field distribution evolves during applying a high external field, in order to check how the modification of local permittivities under local electric fields affects in turn the local field distribution. Such simulations are shown in Figure 18.7, where the local field distributions for the ceramic with GS = 30 a.u. were computed for different values of applied electric fields (5 a.u., 10 a.u., and 15 a.u.). A slight modification of the local field distribution is observed when the applied electric field increases: the distribution becomes broader and the average α parameter is shifted towards higher values. However, the local field distributions are only slightly affected by the variations of the local permittivities under the local fields and the inhomogenity of the local field is especially related to the microstructure characteristics.

The corresponding computed effective permittivity and tunability versus external field are represented in Figure 18.8. Both permittivity and tunability are smaller when GS is

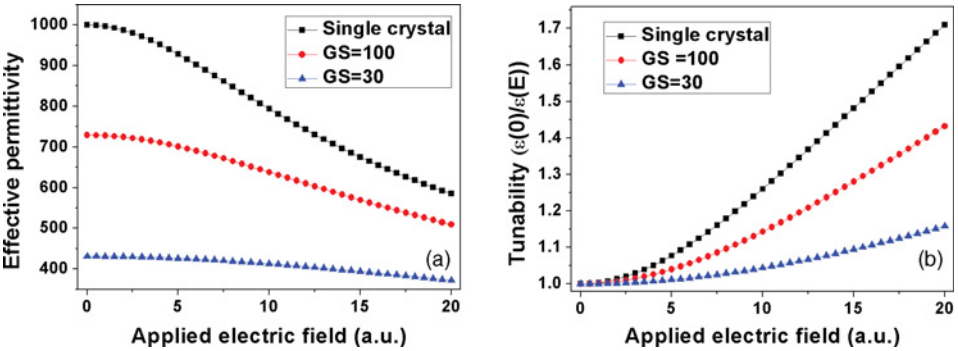

Figure 18.8 *Effective permittivity (a) and tunability (b) responses versus applied electric fields for different GSs: single crystal, GS = 100 a.u., and GS = 30 a.u.*

reduced. In fact, when GS is strongly reduced (which is the case of nanostructured ceramics), an almost constant effective permittivity response under the applied field, as in the extreme case presented in Figure 18.4, is obtained. Therefore, nanostructured ceramics are not promising materials for tunable applications due to a strong reduction of the tunability response, although the reduction of GS is a good way for linearization of the $\varepsilon_{\text{eff}}(E_{\text{app}})$ response in a large field range. A linear $\varepsilon_{\text{eff}}(E_{\text{app}})$ dependence is highly required in tunable applications and this is usually accomplished by circuitry design.

The grain boundary thickness in real nanostructured ceramics like $BaTiO_3$ and its solid solutions is very small (~nm) and important grain size-dependent phenomena appear for ultra-fine dense ceramics (GS ~ 100 nm), where the large amount of grain boundaries give a significant amount of low-permittivity areas in the system. Similar tunability responses like ones simulated within the FEM approach (Figure 18.8) were experimentally determined in nanostructured dense $BaTiO_3$ ceramics with different GSs in the range from 1 μm down to 90 nm [26, 51, 52].

18.3.2 Porous Ferroelectric Ceramics

Among different types of ferroelectric/dielectric combinations, the composites formed by dielectric inclusions embedded into a ferroelectric matrix are of great potential to accomplish the requirements for high tunability. In Figures 18.3 and 18.4 the linear dielectric component was considered to have the permittivity $\varepsilon_{\text{lin}} = 10$. The next step in the investigation of the role of the dielectric inclusions into a ferroelectric matrix was to consider different permittivity values for the dielectric component in order to find the best tunable material. Different simulations have been performed for composites with different low-permittivity phases and the same concentration of the dielectric component (filler factor of 20 %). The results of these calculations for local fields of two such systems (one with $\varepsilon_{\text{lin}} = 50$ and one with $\varepsilon_{\text{lin}} = 1$) are represented in Figure 18.9. The local field images are not very affected by the permittivity of the linear dielectric phase and in both cases the ferroelectric regions are subjected to high local fields.

Although the field distributions look quite similar (Figure 18.9(c) and (d)), the inclusion permittivity affects the dielectric and tunability response, according to Equation (18.5), as presented in Figure 18.10. As expected, a decrease of the composite effective permittivity with a reducing linear dielectric permittivity is observed. More important, this permittivity reduction is accompanied by a non-monotonous variation of tunability with a decrease in ε_{lin}. If for $\varepsilon_{\text{lin}} = 50$ the tunability of the composite is lower than for a dense ceramic, decreasing ε_{lin} results in a larger high-field tunability than for the dense material (Figure 18.10(b)), with the best tunability properties for $\varepsilon_{\text{lin}} = 1$,which corresponds to the case of porous ferroelectric ceramics.

According to the present simulations, porous materials look the most promising candidates for tunable applications. However, from an experimental point of view, it is difficult to produce such porous materials with closed porosity (pores perfectly isolated). Usually in real porous materials, besides this kind of desired closed porosity, additional open porosity may appear as a result of imperfect sintering and their microstructures are closer to Configuration 1 rather than Configuration 3 (Figure18.3 and 18.4). The real challenge for material scientists would be to produce porous materials with perfectly isolated pores (0–3 connectivity) and free of defects in order to hold the application for high fields. From an

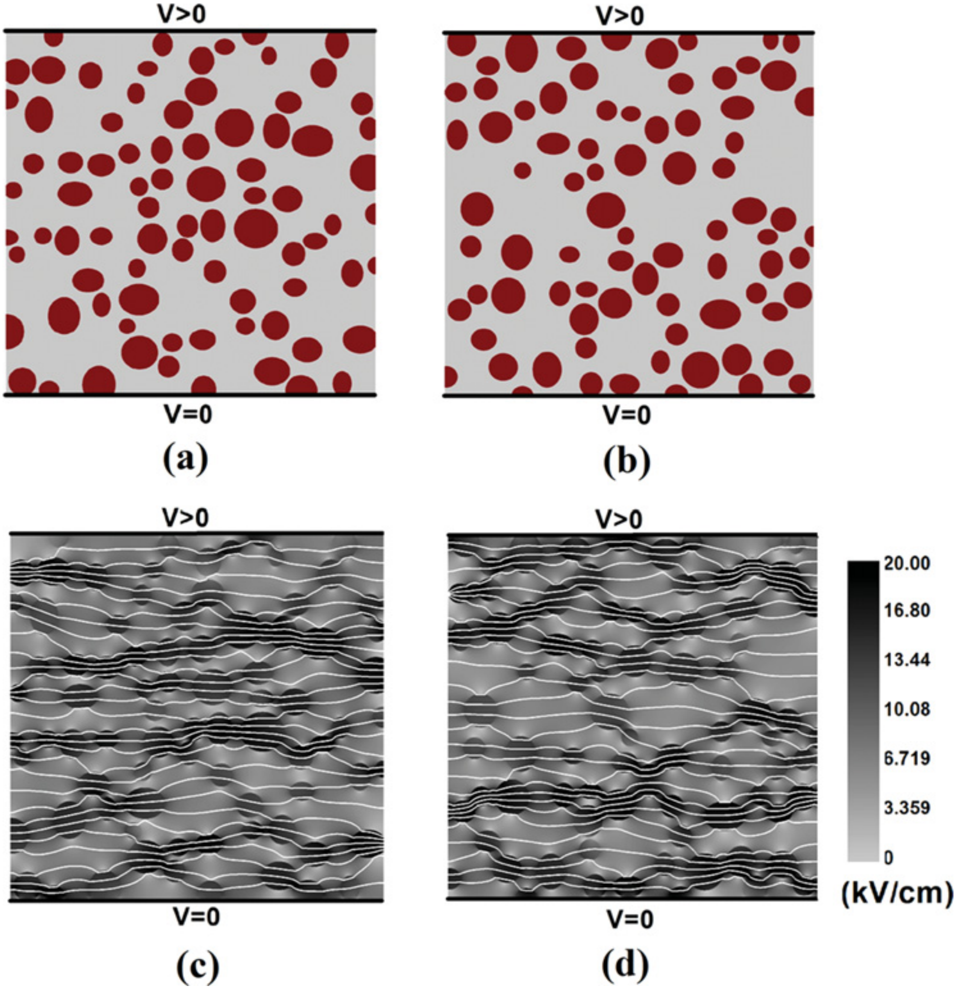

Figure 18.9 *Two ferroelectric/dielectric systems with the same dielectric concentrations (20%) but with different permittivity values of the dielectric component: (a)* $\varepsilon_{lin} = 50$ *and (b)* $\varepsilon_{lin} = 1$ *and the corresponding local field images (c and d)*

experimental point of view, there are some observations related to the beneficial role of porosity in increasing tunability in PZT and $BaTiO_3$ ceramics, which confirm the results of the present calculations [18, 27]. Besides the porosity itself, we recently proposed anisotropy as an additional factor to engineer the local electric fields in order to tailor the tunability properties. The results of the simulations have been experimentally confirmed for porous Nb-doped PZT ceramics with elongated pores [27, 53].

18.3.3 Composites with Non-linear Matrix and Conductive Inclusions

In the previous sections the role of microstructural characteristics of ferroelectric/dielectric composites was investigated in order to find the best configuration that accomplishes the

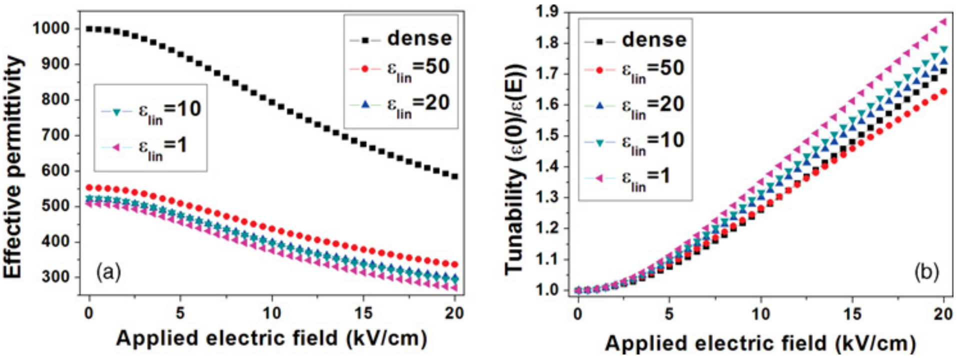

Figure 18.10 *Field-dependence of the (a) effective permittivity and (b) tunability for ferroelectric composites with various low-permittivity inclusions*

requirements of tunable materials in microelectronics: low permittivity and high tunability. Other applications in microelectronics require a very high tunability, irrespective of the permittivity values. In this section, the solution of increasing both tunability and permittivity by introducing conductive fillers in dielectrics will be discussed. This solution is inspired from Configuration 2 presented in Figure18.3 and 18.4. As mentioned before, for composites with ferroelectric inclusions (permittivity of thousands) embedded into a dielectric matrix (permittivity of tens), the ferroelectric component is subjected to an almost zero local field. In this case the field is located predominantly on the low permittivity areas, which are subjected to a much higher field than the average applied electric field. This kind of composite would be a benefit in tunable applications only if the ferroelectric component is of the low permittivity phase. The best solution is to introduce inclusions into a ferroelectric matrix with permittivity much higher than the permittivity of the matrix. However, since the matrix is ferroelectric and its permittivity is already high (thousands), it is difficult to find another material to be used for inclusions with permittivity of a few orders in magnitude higher than the matrix. The solution is to employ conductive inclusions, whose permittivity tends to infinity when they are perfectly isolated. Conductive isolated inclusions can be considered in simulations to have infinite permittivity due to the presence of the free charges. When they are subjected to an external field, their free charges redistribute and polarize the conductor inclusion in such way that a zero field inside the inclusions is realized.

Different composite systems have been generated with different concentrations of the conductive inclusions and the simulated local field images are represented in Figure 18.11. The permittivity values considered in simulations are $\varepsilon_{\text{non-lin}}(0) = 10^3$ and $\varepsilon_{\text{conductive}} = 10^6$.

For all the systems represented in Figure 18.11, an increased local electric field is observed on the matrix, while the local electric field inside the inclusions is zero, as expected inside a conductor. The amount of ferroelectric phase regions subjected to higher fields is higher when the filling factor of the conductive particles increases in the composite system. The applied field dependences of the effective permittivity and tunability represented in Figure 18.12 show a contineous increase of the effective permittivity with increasing concentration of the conductive filler (Figure 18.12(a)). Such an increase was reported both

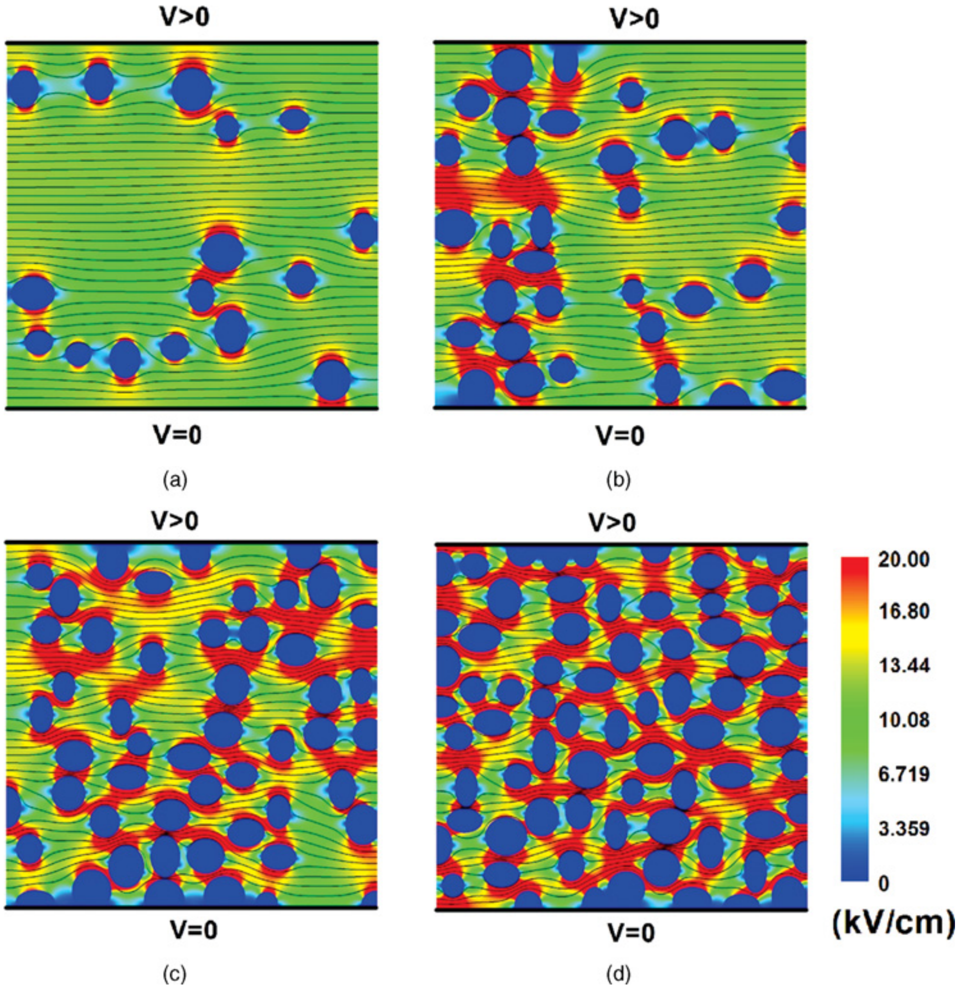

Figure 18.11 *Local field images for four types of composites with conductive inclusions into a ferroelectric matrix, for different concentrations of inclusions: (a) 10%, (b) 20%, (c) 30%, and (d) 40%*

as results of calcualtions based on FEM [54] and also by experimental data for barium titanate-based composites with (Ni, Zn)$Fe_{2+x}O_4$ as conductive inclusions [55]. A spectacular contribution of the conductive inclusions on tunability is observed: an increase from 1.7 in the ferroelectric single phase to 3 for the composite with 40% conductive particles embedded in the ferroelectric. Such trends have been confirmed experimentally in composites formed by silver nanoparticles inclusions into a BST ceramic matrix [56].

New composite materials with tunable properties can be designed following this idea. For example, starting from polar dielectrics with a low permittivity (e.g. polymers) and weak tunability [7], by adding conductive inclusions in the system, the tunability can be

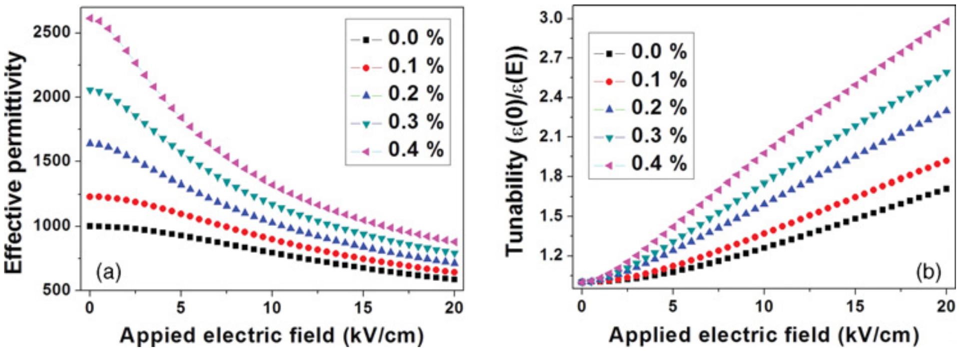

Figure 18.12 *Permittivity (a) and tunability (b) dependencies on the applied electric field for different conductive particle concentrations in a ferroelectric matrix*

increased, together with the permittivity. Recently we proposed such a composite formed by a chitosan matrix filled with gold nanoparticles [34] or with BT nanoparticles [57].

18.4 Switching Properties in Inhomogeneous Ferroelectrics

For describing the P(E) dependence in inhomogeneous ferroelectrics, a combined approach based on a switching model was developed. In this case, the classical Preisach model (CPM) was chosen combined with finite element method (FEM) calculations to exactly determine the local fields as a function of microstructures.

18.4.1 Classical Preisach Model

The Preisach model was originally proposed to describe hysteretic phenomena in magnetic materials [58, 59], and more recently it was used in describing the field dependence of the electric polarization in ferroelectrics [60–70]. The major hypothesis of the Preisach approach is that the system with a switchable behavior is composed of microscopic bistable units called *hysterons*, characterized by elementary rectangular hysteresis loops with constant polarization as an absolute value, but switchable at two electric field values: E_α, from *down* to *up*, and E_β, from *up* to *down* (Figure 18.13 (a)). Unlike in magnetism, for which

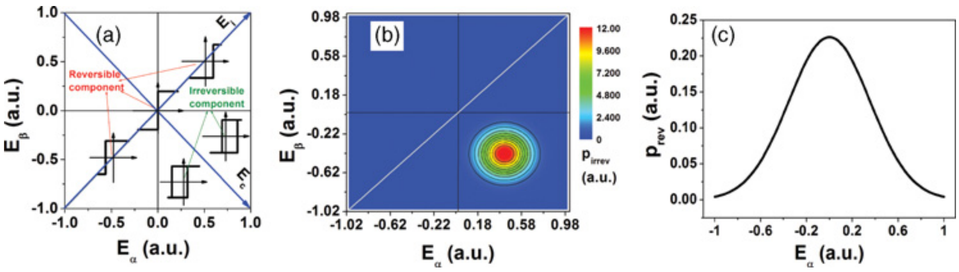

Figure 18.13 *Irreversible and reversible hysterons in the Preisach plane (a) and their corresponding distributions: (b) irreversible component and (c) reversible component*

hysteron is characteristic of a single domain ferromagnetic particle, in ferroelectrics it was impossible to assign it to a physical entitiy or phenomenon (e.g. ferroelectric domain wall, local ferroelectric loop, dipolar unit, etc.). Therefore, CPM was applied for such systems only by postulating the existence of the collection of *hysterons*, without any experimental evidence. Recently, piezoresponce PFM switching experiments proved the local switchable character of ferroelectrics at different electric fields [71, 72] and this was considered by some authors as an experimental support for the existence of hysterons, although the PFM experiment provides an effective response over a larger number of switchable units and, in addition, it takes place under a strong inhomogeneous field created by the tip. Therefore, CPM is applied in ferroelectrics without considering an interpretation for the *hysteron* entity. The different values for the switchable fields of *hysterons* result in a distribution in the Preisach plane, determined by E_α and E_β axes (Figure 18.13(b)), while a system with identical dipolar units (which are switchable all at the same field values) will be characterized by a delta function type of Preisach distribution. In the Preisach plane, the quantity $p_{\text{irrev}}(E_\alpha, E_\beta)\,dE_\alpha\,dE_\beta$ represents the total polarization of the hysterons with *down*-to-*up* switching fields between $(E_\alpha,\ E_\alpha + dE_\alpha)$ and *up*-to-*down* switching fields in the range $(E_\beta,\ E_\beta + dE_\beta)$. Generally, a macroscopic ferroelectric hysteresis is symmetric with respect to the two switching fields, which are equal in absolute value. For this reason, the large majority of *hysterons* are located around the second bisector in the fourth quadrant of the Preisach plane.

The distribution of hysterons in ferroelectrics is composed of two components: an irreversible one, with two distinct switching fields (Figure 18.13(b)), and a reversible one (Figure 18.13(c)). The existence of these two distinct components was put in evidence by the first-order reversal curves (FORCs) analysis [66–69, 73]. The reversible component is formed by hysterons with identical switching fields (or, equivalently, with zero coercivity) and corresponds to the first bisector in the Preisach plane. Practically, the quantity $p_{\text{rev}}(E_\alpha)\,dE_\alpha$ is the total polarization of the reversible hysterons with the switching field between E_α and $E_\alpha + dE_\alpha$.

For computing the system's polarization it is necessary for the Everett integral [74], which is defined as the polarization corresponding to the triangle determined by the first bisector, the horizontal line E_β = constant, and the vertical line E_α = constant, to be:

$$e(E_\alpha, E_\beta) = \int_{E_\beta}^{E_\alpha} \left[\int_{E_\beta}^{a} p_{\text{irrev}}(a, b) db \right] db + \int_{E_\beta}^{E_\alpha} p_{\text{rev}}(a) da \tag{18.10}$$

The maximum polarization of the system is the Everett integral computed under the minimum electric field $E_\beta = -E_{\text{max}}$ and the maximum electric field $E_\alpha = E_{\text{max}}$:

$$P_{\text{max}}(E_{\text{max}}) = e(E_{\text{max}}, -E_{\text{max}}) = \int_{-E_{\text{max}}}^{E_{\text{max}}} \left[\int_{-E_{\text{max}}}^{a} p_{\text{irrev}}(a, b) db \right] db + \int_{-E_{\text{max}}}^{E_{\text{max}}} p_{\text{rev}}(a) da \tag{18.11}$$

This value is considered with the minus sign for *down* configuration (Figure 18.14(a)) and with the plus sign for *up* configuration (Figure 18.14(b)).

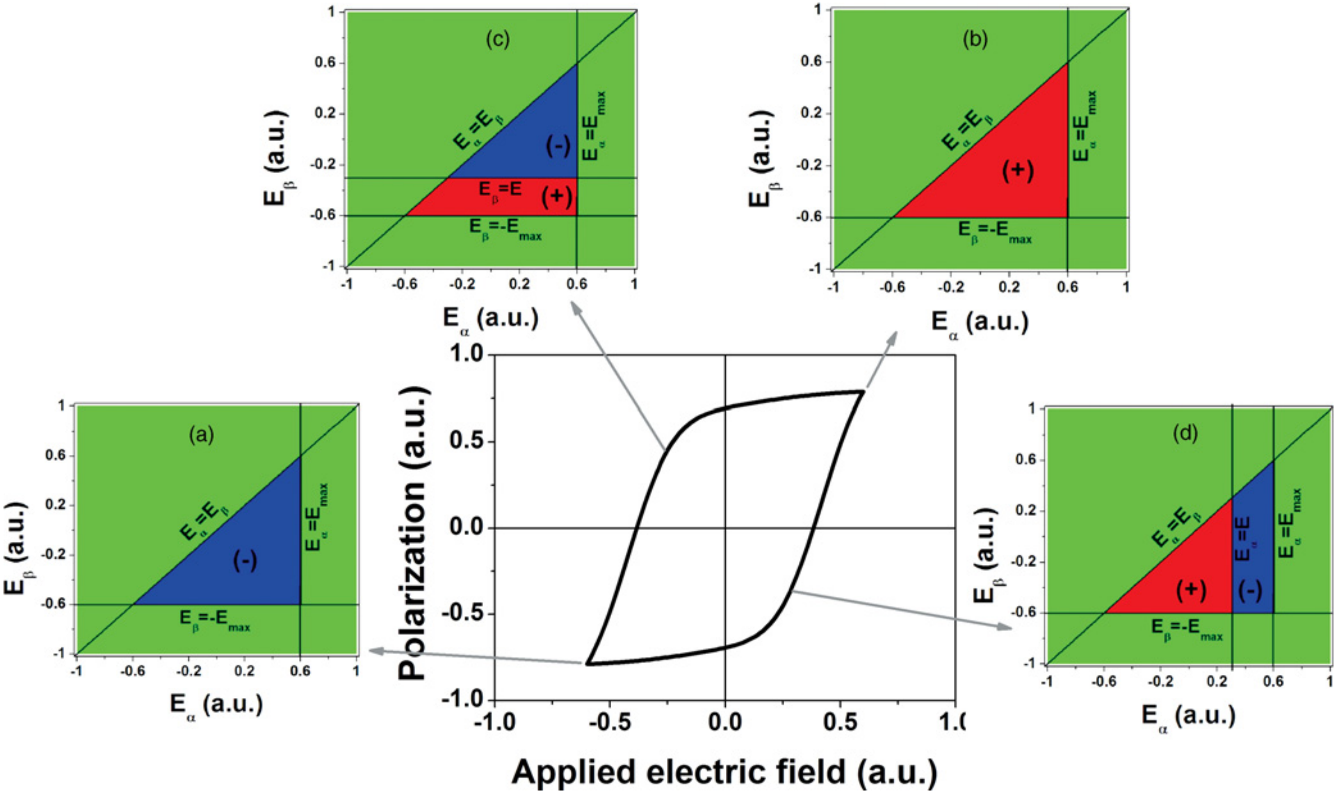

Figure 18.14 *States of hysterons for different values of the applied electric field: (a)*$E=-E_{max}$*, (b)* $E=E_{max}$*, (c)* $-E_{max}<E<E_{max}$ *for the downward curve, (d)* $-E_{max}<E<E_{max}$ *for the upward curve*

In order to compute the system's polarization at a given applied electric field E on the downward curve (from *up* to *down*), the total polarization corresponding to the *down hysterons* (characterized by the switching field $-E_\beta > E$) needs to be calculated. These *down hysterons* are located inside the triangle determined by the edges $E_\alpha = E_\beta$, $E_\alpha = E_{\max}$, and $E_\beta = E$ (Figure 18.14(c)), and therefore their polarization is $e(E_{\max}, E)$. This value, multiplied with 2 is extracted from the maximum polarization (Equation (18.11)) in order to obtain the total polarization of the system:

$$P_{up \to down}(E, E_{\max}) = e(E_{\max}, -E_{\max}) - 2e(E_{\max}, E) \tag{18.12}$$

In a similar way, for computing the polarization at an applied electric field E on the upward curve (from *down* to *up*), the polarization corresponding to the *up hysterons* with $E_\alpha < E$ (Figure 18.14(d)) is $e(E, -E_{\max})$. The system's polarization is determined as the sum of the minimum polarization and $2e(E, -E_{\max})$:

$$P_{down \to up}(E, E_{\max}) = -e(E_{\max}, -E_{\max}) + 2e(E, -E_{\max}) \tag{18.13}$$

If we perform a change of the variables: $E_c = (E_\alpha - E_\beta)/\sqrt{2}$, $E_i = (E_\alpha + E_\beta)/\sqrt{2}$, where E_c has the meaning of the hysteron coercive field and E_i is the interaction (bias) field, then the Preisach distribution will describe the distribution of *hysterons* over their coercive and interaction fields.

As input of the present simulations, a double Gaussian distribution of the irreversible component was considered:

$$p_{\text{irrev}}(E_c, E_i) = \frac{K_{\text{irrev}}}{2\pi\sigma_c\sigma_i} \exp\left(-\frac{(E_c - E_{c0})^2}{2\sigma_c^2}\right) \exp\left(-\frac{E_i^2}{2\sigma_i^2}\right) \tag{18.14}$$

where $\sigma_c = 0.15\,\text{a.u.}$, $\sigma_i = 0.15\,\text{a.u.}$, $E_{c0} = 0.6\,\text{a.u.}$, while the reversible component is characterized by zero coercivity and is a Gaussian function upon the interaction field E_i only:

$$p_{\text{rev}}(E_i) = \frac{K_{\text{rev}}}{\sigma_\gamma(2\pi)^{1/2}} \exp\left(-\frac{E_i^2}{2\sigma_r^2}\right) \tag{18.15}$$

where $\sigma_r = 0.5\,\text{a.u.}$ The σ parameters were chosen in such way that all *hysterons* have switching fields between –1 a.u. and 1 a.u., accordingly to the "3σ" law, and hence the system is saturated at a maximum field: $E_{\max} = 1\,\text{a.u.}$ K_{irrev} and K_{rev} parameters were chosen in such a way that the reversible component represents 10% from the saturation polarization and the saturation polarization is equal to 1 a.u.:

$$s = P_{\text{rev}}/(P_{\text{rev}} + P_{\text{irrev}}) = 0.1 \tag{18.16}$$

$$P_{\text{sat}} = P_{\text{rev}} + P_{\text{irrev}} = 1\,\text{a.u.} \tag{18.17}$$

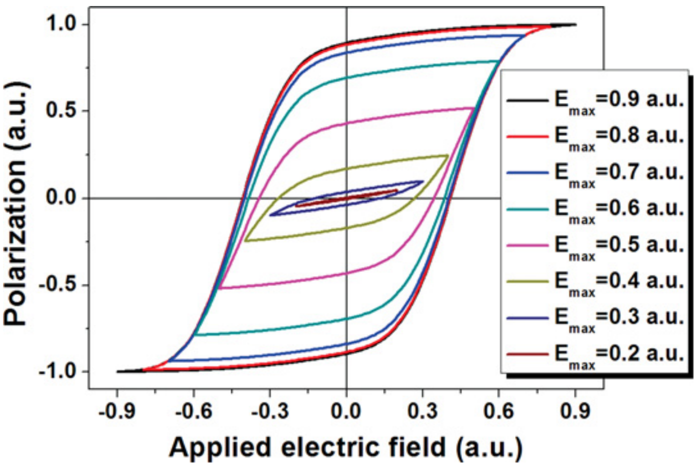

Figure 18.15 *Simulated major/minor P(E) hysteresis loops for different amplitudes of the applied electric field according to Equations (18.12) and (18.13)*

where

$$P_{\text{irrev}} = \int_{-1}^{1} \left[\int_{-1}^{\alpha} p_{\text{irrev}}(a,b) \right] db \tag{18.18}$$

and

$$P_{\text{rev}} = \int_{-1}^{1} p_{\text{rev}}(a) da \tag{18.19}$$

According to Equations (18.12) and (18.13), the Preisach model is able to describe any $P(E)$ hysteresis loops for different maximum applied fields. Such curves were simulated and the results are represented in Figure 18.15. By comparison with other models of hysteresis, CPM is able to describe minor $P(E)$ hysteresis loops, which is one of the most important strengths of this approach. Major/minor $P(E)$ loops in Figure 18.15 were calculated with the assumption that the electric field is homogeneous in the sample and these results describe a fully dense ferroelectric material with no interfaces.

Further, it is important to take into account these minor/major hysteresis loops in developing a more appropriate hysteresis model for composites or porous ferroelectrics, due to the fact that, as we shall see in the following, the hysteresis of the porous system is, in fact, a mixing of such local hysteresis loops, due to the local electric field inhomogeneity. The next step for applying CPM for inhomogeneous ferroelectrics is to introduce the local electric field inhomogeneity.

The total polarization of the system is an average value of the local polarization under local electric fields computed according to Equations (18.12) and (18.13). For example, for an applied field E and a maxim applied field $E_{\max}$on the upward curve the macroscopic polarization is:

$$P_{\text{eff}}(E_{\text{app}}, E_{\max}) = \frac{\iiint\limits_{\Omega} P_{down\to up}(E_{\text{local}}, E_{\text{local max}})dxdydz}{\iiint\limits_{\Omega} dxdydz} = \frac{\iiint\limits_{\Omega} P_{down\to up}(E_{\text{local}}, E_{\text{local max}})dxdydz}{V_t} \tag{18.20}$$

where V_t is total volume of the system. By changing the variables Equation (18.20) becomes:

$$P_{\text{eff}}(E_{\text{app}}, E_{\max}) = \frac{\int\limits_{0}^{\infty} P_{down\to up}\left(\alpha E_{\text{app}}, \alpha E_{\max}\right) \rho(\alpha)d\alpha}{V_t} \tag{18.21}$$

In a similar way, the downward curve is determined with the equation:

$$P_{\text{eff}}(E_{\text{app}}, E_{\max}) = \frac{\int\limits_{0}^{\infty} P_{up\to down}\left(\alpha E_{\text{app}}, \alpha E_{\max}\right) \rho(\alpha)d\alpha}{V_t} \tag{18.22}$$

The $\rho(\alpha)$ distribution is computed by FEM at low field by taking into account the microstructural characteristics of the system. As discussed in Section 18.3.1, the local electric field distribution is also slightly affected by the local modifications of permittivities under the local electric field. In the simulations presented in the following, the local electric field distribution $\rho(\alpha)$ is approximated to be constant at each applied electric field, but one should be aware that in fact it suffers some modifications during switching. The approximation of the constant local field distribution during switching was employed in order to reduce the computation time and resources.

18.4.2 Switching in Nanostructured Ferroelectric Ceramics

In Section 18.3.1 the local electric fields were computed for three virtual ceramic microstructures with different GSs (single crystal, GS = 100 a.u. and GS = 30 a.u.). The corresponding local electric field distributions are represented in Figure 18.6. These distributions were used as input in Equations (18.21) and (18.22) in order to compute the minor/major hysteresis loops. The evolution of the computed $P(E)$ loops when reducing grain sizes are reported in Figure 18.16.

The computed $P(E)$ responses show that the grain size has a major role for the switching properties of ferroelectric nanostructured ceramics. If in a single crystal or coarse ceramics the hysteresis loops are more rectangular, in the fine-grained ceramics the hysteresis loops gradually become narrow, polarization reduces, and apparent coercivity increases and they are hardly saturated (higher fields are necessary for saturation, e.g. a tendency towards *frozen* polarization). The main modifications introduced by the reduction of GS are: a decrease of the saturation/remanent polarization and hysteresis area and a crossover

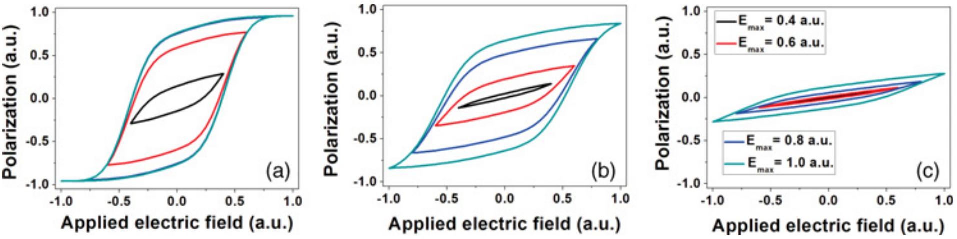

Figure 18.16 Major/minor hysteresis loops computed by the combined CPM/FEM model for virtual ceramics with different GSs: (a) single crystal, (b) GS = 100 a.u., and (c) GS = 30 a.u.

from a rectangular hysteresis loops to a more tilted one. All these modifications were experimentally observed in the case of $BaTiO_3$ nanostructured ceramics [13, 51] and other nanostructured ferroelectrics [75].

18.4.3 Switching in Porous Ferroelectrics

As described in Section 18.3.2, different porous structures with porosity levels in the range from 0 to 40% have been generated and their corresponding local electric field distributions were computed by FEM. As an example, in Figure 18.17, the local electric field distributions are represented for three porosity levels: 0%, 20%, and 40%.

For a dense ferroelectric microstructure (Figure 18.17(a)) the local field is highly homogeneous and has the same value as the applied one. As a consequence, the local and macroscopic hysteretic behaviors are identical. For porous microstructures (Figure18.17(b) and (c)), the local electric field becomes inhomogeneous and the $P(E)$ hysteresis loops will be affected by this inhomogeneity because the local dipolar units (*hysterons*) are evolving under different fields. For this reason, the Preisach model can be applied only locally for porous ferroelectric structures. The local field distributions vary from the Dirac distribution (Figure 18.17(a)), characteristic of the dense ferroelectric structure, to a Gaussian-type of distribution (Figure 18.17(b)) for low levels of porosity and tends towards a lognormal distribution (Figure 18.17(f)) for very high levels of porosity, due to the fact that the maximum shifts towards smaller field values while the distribution is very broad (i.e. it extends asymmetrically towards higher fields).

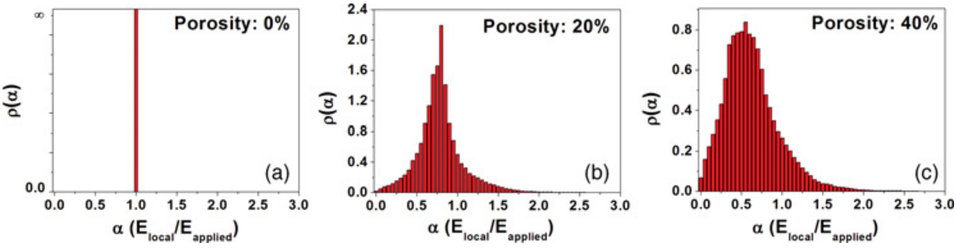

Figure 18.17 Local electric field distributions computed by FEM for different porosity levels: (a) 0%, (b) 20%, and (c) 40%

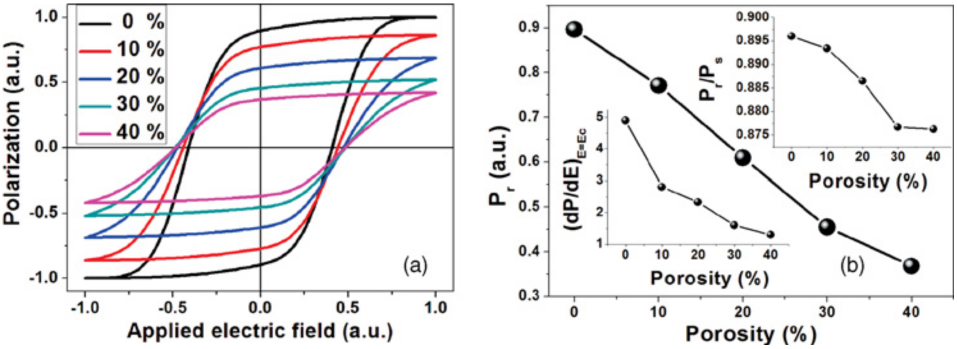

Figure 18.18 *(a) P(E) hysteresis loops simulated for different porosity levels of the ferroelectric ceramics and (b) dependences of remanent polarization on the porosity level. Inset: porosity dependence of the rectangularity factor and susceptibility at the coercive field*

Further, $P(E)$ hysteresis loops have been simulated for different porosity levels, according to Equations (18.21) and (18.22) and the results are represented in Figure 18.18. In all the simulations, the local Preisach distributions were considered the same, irrespective of the degree of porosity. The results show that the $P(E)$ macroscopic hysteresis loops are clearly influenced by the porosity through the local field inhomogeneity. The saturation and remanent polarizations and the area of the hysteresis loop gradually decrease, while the coercive field slightly increases with increasing porosity (Figure 18.18(b)). The shape of the hysteresis loop modifies from an almost rectangular to a tilted one, as shown in the representation of the loop rectangularity factor P_r/P_s in the insets of Figure 18.18(b). Both rectangularity factor and the derivative of the polarization at the coercive field (susceptibility at the coercive field, giving a measure of the loop tilting) decrease with increasing porosity. A dense ferroelectric structure can be more easily saturated than a porous one, a feature that is known in the field of ferroelectric memories, in which very dense structures are required. The saturated state in porous ferroelectrics is not so easy to reach, due to the presence of areas subjected to much lower fields than the applied one (i.e. they need a higher field to switch). The results of these calculations are in a very good agreement with the non-linear dependence of the saturation polarization on porosity experimentally observed in the case of porous PZTN ceramics by FORC measurements [19–21].

18.5 Conclusions

The local field inhomogeneity plays a crucial role in the macroscopic properties of ferroelectric composites. If properly used, the inhomogeneity of the local electric field can be used as an important factor to tailor the macroscopic response towards desired properties. The calculations based on the finite element method offer an excellent approach in designing new composites in which the macroscopic responses are simulated based on realistic microstructures. The effective permittivity and tunability and switching properties of a few examples of composite systems have been reviewed. For example, nanostructured ceramics with GSs around hundreds of nanometers is a good solution for a linear dependence of the effective permittivity on the applied electric field. For other tunable applications that require a reduced permittivity and high tunability, the simulations predicted that composites with dielectric inclusions into a ferroelectric matrix are the most suitable composites. Among them, porous materials present the lowest effective permittivity and highest tunability. Composite materials based on ferroelectrics with conductive inclusions are very attractive for tunability applications because they are characterized by a high tunability and permittivity in comparison with the single ferroelectric phase.

The FEM calculations can complete any switching model in order to describe switching properties and $P(E)$ dependency in composites or inhomogeneous ferroelectric structures. A very good description of switching properties of such ferroelectric systems was realized by using a combined CPM–FEM model. This model explained the transition from rectangular hysteresis loops to a more tilted one, saturation polarization and hysteresis area when reducing GS in nanostructured ferroelectric ceramics. The same approach explained modifications introduced by porosity on the switching properties in ferroelectric materials: decrease of the saturation/remanent polarization, reduction of the hysteresis area, and increase of the tilting degree. Among all the hysteresis models for ferroelectrics existing in literature, the CPM was chosen in this work to describe switching phenomena in ferroelectrics because of its ability to correctly describe minor loops. However, instead of CPM other hysteresis models can be employed, but the local electric field should always be taken into consideration when dealing with inhomogeneous ferroelectrics or ferroelectric-based composites.

Acknowledgments

The financial support of the Romanian CNCS-UEFISCDI Projects No. PN II-ID-PCCE-2011-2-0006 and PN II-RU-TE-2012-3-0150 is greatly acknowledged.

References

(1) Lines, M. and Glass, A. (1979). *Principles and Applications of Ferroelectrics and Related Materials*, Clarendon Press, Oxford.

(2) Scott, J.F. (2000) *Ferroelectric Memories*, Springer, Berlin.

(3) Zhuravlev, M.Y., Sabirianov, R.F., Jaswal, S.S., and Tsymbal, E.Y. (2005) Giant electroresistance in ferroelectric tunneljJunctions. *Physical Review Letters*, **94** (24), art. no. 246802.

(4) Tarui, Y., Hirai, T., Teramoto, K., et al. (1997) Application of the ferroelectric materials to ULSI memories. *Applied Surface Science*, **113**, 656–663.

(5) Im, J., Auciello, O., Baumann, P.K., et al. (2000) Composition-control of magnetron-sputter-deposited $(Ba_xSr_{1-x})Ti_{1+y}O_{3+z}$ thin films for voltage tunable devices. *Applied Physics Letters*, **76** (5), 625–627.

(6) Canedy, C.L., Li, H., Alpay, S.P., et al. (2000) Dielectric properties in heteroepitaxial $Ba_{0.6}Sr_{0.4}TiO_3$ thin films: effect of internal stresses and dislocation-type defects. *Applied Physics Letters*, **77** (11), 1695–1697.

(7) Tagantsev, A.K., Lu, J., and Stemmer S. (2005) Temperature dependence of the dielectric tunability of pyrochlore bismuth zinc niobate thin films. *Applied Physics Letters*, **86** (3), art. no. 032901.

(8) Mikheev, E., Stolichnov, I., Tagantsev, A.K., and Setter, N. (2012) Polarization screening in polymer ferroelectric films: uncommon bulk mechanism. *Applied Physics Letters*, **101** (13), art. no. 132905.

(9) Frey, M.H., Xu, Z., Han, P., and Payne, D.A. (1998) The role of interfaces on an apparent grain size effect on the dielectric properties for ferroelectric barium titanate ceramics. *Ferroelectrics*, **206** (1–4), 337–353.

(10) Emelyanov, A. Yu, Pertsev, N.A., Hoffmann-Eifert, S., et al. (2003) Grain-boundary effect on the Curie–Weiss law of ferroelectric ceramics and polycrystalline thin films: calculation by the method of effective medium. *Journal of Electroceramics*, **9** (1), 5–16.

(11) Zhao, Z., Buscaglia, V., Viviani, M., et al. (2004) Size effect on ferroelectric behavior of dense nanocrystalline $BaTiO_3$ ceramics. *Physical Review B*, **70** (2), art. no. 024107.

(12) Buscaglia, M.T., Buscaglia, V., Viviani, M., et al. (2004) Ferroelectric Properties of dense nanocrystalline $BaTiO_3$ ceramics. *Nanotechnology*, **15** (9), 1113–1117.

(13) Buscaglia, M.T., Viviani, M., Buscaglia, V., et al. (2006) High dielectric constant and frozen macroscopic polarization in dense nanocrystalline $BaTiO_3$ ceramics. *Physical Review B*, **73** (6), art. no. 064114.

(14) Petzelt, J. (2010) Dielectric grain-size effect in high-permittivity ceramics. *Ferroelectrics*, **400**, 117–134.

(15) Verkerk, M.J., Middelhuis, B.J., and Burggraaf, A.J. (1982) Effect of grain-boundaries on the conductivity of high purity ZrO_2–Y_2O_3 ceramics. *Solid State Ionics*, **6** (2), 159–170.

(16) Kidner, N.J., Homrighaus, Z.J., Ingram, B.J., et al. (2005) Impedance/dielectric spectroscopy of electroceramics. *Journal of Electroceramics*, **14** (3), 283–291 and 293–301.

(17) Johnson, K.M. (1962) Variation of dielectric constant with voltage in ferroelectrics and its application to parametric devices. *Journal of Applied Physics*, **33**, 2826–2831.

(18) Zhang, Y., Wang, G., Wang, K., et al. (2008) The model of electric field dependent dielectric properties for porous ceramics. *Journal of Applied Physics*, **103** (11), art. no. 114103.

(19) Stoleriu, L., Stancu, A., Mitoseriu, L., et al. (2006) Analysis of switching properties of porous ferroelectric ceramics by means of first-order reversal curve diagrams. *Physical Review B*, **74** (17), art. no. 174107.

(20) Piazza, D., Stoleriu, L., Mitoseriu, L., et al. (2006) Characterisation of porous PZT ceramics by first-order reversal curves (FORC) diagrams. *Journal of the European Ceramic Society*, **26** (14), 2959–2962.

(21) Mitoseriu, L., Stoleriu, L., Stancu, A., et al. (2009) First order reversal curves diagrams for describing ferroelectric switching characteristics. *Processing and Application of Ceramics*, **3** (1–2), 3–7.

(22) Liou, J.W. and Chiou, B.S. (2000) Analysis of the dielectric characteristics for polycrystalline $Ba_{0.65}Sr_{0.35}TiO_3$ (II) – d.c. field dependence with a modified bias equation. *Journal of Material Science – Materials in Electronics*, **11** (8), 645–651.

(23) Zhang, G., Jiang, S.L., Zeng, Y.K., et al. (2009) The modified model of the dielectric characteristics for porous $Ba_{0.6}Sr_{0.4}TiO_3$ ceramics. *Journal of Applied Physics*, **106** (3), art. no. 034110.

(24) Devonshire, A.F. (1049, 1951) Theory of ferroelectrics. *Philosophical Magazine*, **40**, 1040; **42**, 1065.

(25) Sherman, V.O., Tagantsev, A.K., and Setter, N. (2004) Tunability and loss of the ferroelectric–dielectric composites, in IEEE International Ultrasonics, Ferroelectrics and Frequency Control Joint 50th Anniversary Conference.

(26) Padurariu, L., Curecheriu, L., Buscaglia, V., and Mitoseriu, L. (2012) Field-dependent permittivity in nanostructured $BaTiO_3$ ceramics: modeling and experimental verification. *Physical Review B*, **85** (22), art. no. 224111.

(27) Padurariu, L., Curecheriu, L., Galassi, C., and Mitoseriu, L. (2012) Tailoring non-linear dielectric properties by local field engineering in anisotropic porous ferroelectric structures. *Applied Physics Letters*, **100** (25), art. no. 252905.

(28) Whyte, J.R., McQuaid, R.G.P., Sharma, P., et al. (2014) Ferroelectric domain wall injection. *Advanced Materials*, **26**, 293–298.

(29) Kolmogorov, A.N. (1937) On the statistical theory of the crystallization of metals. *Bull. Acad. Sci. USSR, Math. Ser.*, **1**, 355–359.

(30) Avrami, M. (1939) Kinetics of phase change. I. General theory. *Journal of Chemical Physics*, **7** (12), 1103–1112.

(31) Ishibashi, Y. (1992) Theory of polarization reversals in ferroelectrics based on Landau-type free energy. *Japanese Journal of Applied Physics*, **31**, 2822–2824.

(32) Zhukov, S., Genenko, Y.A., Hirsch, O., et al. (2010) Dynamics of polarization reversal in virgin and fatigued ferroelectric ceramics by inhomogeneous field mechanism. *Physical Review B*, **82** (1), art. no. 014109.

(33) Genenko, Y.A., Zhukov, S., Yampolskii, S.V., et al. (2012) Universal polarization switching behavior of disordered ferroelectrics. *Advanced Functional Materials*, **22** (10), 2058–2066.

(34) Cazacu, A., Curecheriu, L., Neagu, A., et al. (2013) Tunable gold-chitosan nanocomposites by local field engineering. *Applied Physics Letters*, **102** (22), art. no. 222903.

(35) Sareni, B., Krahenbuhl, L., and Brosseau, C. (1996) Effective dielectric constant of periodic composite materials. *Journal of Applied Physics*, **80** (3), 1688–1696.

(36) Jylha, L. and Sihvola, A. (2007) Equation for the effective permittivity of particle-filled composites for material design applications. *Journal of Physics D: Applied Physics*, **40** (16), 4966–4973.

(37) Bottcher, C.J.F. (1952) *Theory of Electric Polarization*, Elsevier, Amsterdam.

(38) Lichtenecker, K. (1926) Die Dielektrizitätskonstante Künstlicher und Natürlicher Mischkörper. *Physikal Z.*, **27**, 115–158.

(39) Lichtenecker, K. and Rother, K. (1931) Die Herleitung des Logarithmischen Mischungsgesetzes als Allegemeinen Prinzipien der Staionaren Stromung. *Physikal Z.*, **32**, 255–260.

(40) Gockenbach, M.S. (2006) *Understanding and Implementing the Finite Element Method*, Society for Industrial and Applied Mathematics, Philadelphia.

(41) Becker, E.B., Carey, G.F., and Oden, J.T. (1981) *Finite Elements: An Introduction*, Prentice-Hall, Englewood Cliffs, NJ.

(42) Tagantsev, A.K., Sherman, V.O., Astafiev, et al. (2003) Ferroelectric materials for microwave tunable applications. *Journal of Electroceramics*, **11**(1—2), 5–66.

(43) Chung, U.C., Elissalde, C., Maglione, M., et al. (2008) Low-losses, highly tunable $Ba_{0.6}Sr_{0.4}TiO_3$/MgO composite. *Applied Physics Letters*, **92** (4), art. no. 042902.

(44) Kozyrev, A.B., Kanareykin, A., Nenasheva, E., et al. (2009) Observation of an anomalous correlation between permittivity and tunability of a doped (Ba, Sr)TiO_3 ferroelectric ceramic developed for microwave applications. *Applied Physics Letters*, **95** (1), art. no. 012908.

(45) Maiti, T., Guo, R., and Bhalla, A.S. (2007) Tailored dielectric properties and tunability of lead free relaxor $Ba(Zr_xTi_{1-x})O$:MgO composites. *Ferroelectrics*, **361**, 84–91.

(46) Chou, X., Zhai, J.W., and Yao, X. (2007) Relaxor behavior and dielectric properties of $MgTiO_3$-doped $BaZr_{0.35}Ti_{0.65}O_3$ composite ceramics for tunable applications. *Journal of the American Ceramic Society*, **90** (9), 2799–2801.

(47) He, Y.Y., Xu, Y.B., Liu, T., et al. (2011) Tunable dielectric properties of $BaZr_{0.2}Ti_{0.8}O_3$–Mg_2SiO_4–MgO composite ceramics. *Journal of Alloys and Compounds*, **509** (3), 904–908.

(48) Liang, X.F., Wu, W.B., and Meng, Z.Y. (2003) Dielectric and tunable characteristics of barium strontium titanate modified with Al_2O_3 addition. *Material Science and Engineering B*, **99** (1–3), 366–369.

(49) Kidner, N.J., Perry, N.H., Mason, T.O., and Garboczi, E.J. (2008) The brick layer model revisited: introducing the nano-grain composite model. *Journal of the American Ceramic Society*, **91** (6), 1733–1746.

(50) Polotai, A.V., Ragulya, A.V., and Randall, C.A. (2003) Preparation and size effect in pure nanocrystalline barium titanate ceramics. *Ferroelectrics*, **288**, 93–102.

(51) Curecheriu, L.P., Buscaglia, M.T., Buscaglia, V., et al. (2010) Grain size effect on the nonlinear dielectric properties of barium titanate ceramics. *Applied Physics Letters*, **97** (24), art. no. 242909.

(52) Curecheriu, L.P., Balmus, S.B., Buscaglia, M.T., et al. (2012) Grain size-dependent properties of dense nanocrystalline barium titanate ceramics. *Journal of the American Ceramic Society*, **95** (12), 3912–3921.

(53) Olariu, C.S., Padurariu, L., Stanculescu, R., et al. (2013) Investigation of low field dielectric properties of anisotropic porous Pb(Zr, Ti)O_3 ceramics: experiment and modeling. *Journal of Applied Physics*, **114** (21), art. no. 214101.

(54) Myroshnychenko, V. and Brosseau, C. (2008) Effective complex permittivity of two-phase random composite media: a test of the two-exponent phenomenological percolation equation. *Journal of Applied Physics*, **103** (8), art. no. 084112.

(55) Huang, J., Du., P., Homg, L., et al. (2007) A percolative ferromagnetic–ferroelectric composite with significant dielectric and magnetic properties. *Advanced Materials*, **19** (3), 437–440.

(56) Wang, Z., Hu, T., Li, X., et al. (2012) Nano conductive particle dispersed percolative thin film ceramics with high permittivity and high tunability. *Applied Physics Letters*, **100** (13), art. no. 132909.

(57) Neagu, A.M., Curecheriu, L.P., Cazacu, A., and Mitoseriu, L. (2014) Impedance analysis and tunability of BaTiO3–chitosan composites: towards active dielectrics for flexible electronics. *Composites Part B*, **71**, 210–217.

(58) Preisach, F. (1935) Über die Magnetische Nachwirkung. *Z. Physik*, **94**, 277–302.

(59) Mayergoyz, I. (1986) *Mathematical Models of Hysteresis*, Springer, New York.

(60) Robert, G., Damjanovic, D., Setter, N. and Turik, A. V. (2001) Preisach modeling of piezoelectric nonlinearity in ferroelectric ceramics. *Journal of Applied Physics*, **89** (9), 5067–5074.

(61) Meyer, V., Sallese, J.M., and Fazan, P. (2002) A novel approach to modeling the polarization in ferroelectric materials. *Ferroelectrics*, **268**, 251–256.

(62) Cima, L. and Labouré, E. (2004) A model of ferroelectric behavior based on a complete switching density. *Journal of Applied Physics*, **95** (5), 2654–2659.

(63) Tsang, C.H. and Shin, F.G. (2003) Simulation of nonlinear dielectric properties of polyvinylidene fluoride based on the Preisach model. *Journal of Applied Physics*, **93** (5), 2861–2865.

(64) Stancu, A., Ricinschi, D., Mitoseriu, L., et al. (2003) First-order reversal curves diagrams for the characterization of ferroelectric switching. *Applied Physics Letters*, **83** (18), 3767–3769.

(65) Wen, X.Y., Yu, J., Ren, T.L., et al. (2008) Studies on the fatigue behavior of ferroelectric film unsing Preisach approach. *Integrated Ferroelectrics*, **99** (1), 3–12.

(66) Mitoseriu, L., Ciomaga, C.E., Buscaglia, V., et al. (2007) Hysteresis and tunability characteristics of Ba(Zr, Ti)O_3 ceramics described by first order reversal curves diagrams. *Journal of the European Ceramic Society*, **27** (13–15), 3723–3726.

(67) Fujii, I., McKinstry, S.T., and Nies, C. (2011) Effect of grain size on dielectric nonlinearity in model $BaTiO_3$-based multilayer ceramic capacitors. *Journal of the American Ceramic Society*, **94** (1), 58–63.

(68) Deluca, M., Stoleriu, L., Curecheriu, L.P., et al. (2012) High-field dielectric properties and Raman spectroscopic investigation of the ferroelectric-to-relaxor crossover in $BaSn_xTi_{1-x}O_3$ ceramics. *Journal of Applied Physics*, **111** (8), art. no. 084102.

(69) Deluca, M., Vasilescu, C.A., Ianculescu, A.C., et al. (2012) Investigation of the composition-dependent properties of $BaTi_{1-x}Zr_xO_3$ ceramics prepared by the modified Pechini method. *Journal of the European Ceramic Society*, **32** (13), 3551–3566.

(70) Guo, S., Ovchinnikov, O.S., Curtis, M.E., et al. (2010) Spatially resolved probing of Preisach density in polycrystalline ferroelectric thin films. *Journal of Applied Physics*, **108** (8), art. no. 084103.

(71) Ovchinnikov, O., Jesse, S., Guo, S., et al. (2010) Local measurements of Preisach density in polycrystalline ferroelectric capacitors using piezoresponse force spectroscopy. *Applied Physics Letters*, **96** (11), art. no. 112906.

(72) Seal, K., Jesse, S., Nikiforov, M.P., et al. (2009) Spatially resolved spectroscopic mapping of polarization reversal in polycrystalline ferroelectric films: crossing the resolution barrier. *Physical Review Letters*, **103** (5), art. no. 057601.

(73) Yoon, S.H., Kim, S.J., Kim, S.H., and Kim, D.Y. (2013) Influence of excess Ba concentration on the dielectric nonlinearity in Mn and V-doped $BaTiO_3$ multi layer ceramic capacitors. *Journal of Applied Physics*, **114** (22), art. no. 224103.

(74) Stancu, A. (2006) *Magnetization Processes in Particulate Ferromagnetic Media*, Cartea Universitara, Iasi.

(75) Amorin, H., Jimenez, R., Ricote, J., et al. (2010) Apparent vanishing of ferroelectricity in nanostructured $BiScO_3$–$PbTiO_3$. *Journal of Physics D – Applied Physics*, **43** (28), art. no. 285401.

19

Ferroelectric Phase Transitions in Epitaxial Perovskite Films

Marina Tyunina

Microelectronics and Materials Physics Laboratories, University of Oulu, Finland

19.1 Introduction

Perovskite-type ferroelectrics (FEs) have been studied for many decades; nevertheless, they continue to be the focus of modern research. The main driving force for this scientific interest in FEs is both the established commercialized applications and the advanced innovations that are enabled by such remarkable properties as a huge piezoelectric coefficient (to several thousands of pm V^{-1}), very large dielectric permittivity (reaching several thousands), a high optical index of refraction with strong linear and non-linear electro-optic effects, and other response functions and effects in FEs [1–11]. In particular, capacitors employing large permittivity of FE ceramics dominate the modern multibillion dollar market of discrete capacitors. Moreover, the markets of electromechanical devices and components using FEs and of the corresponding FE materials are orders of magnitude larger. Also, electro-optic and non-linear optical devices employing FE ceramics or crystals represent a highly competitive field of FE applications. Besides these mainstream applications of FEs, many others have been developed and more are envisaged. The devices using FEs benefit from their strong unique responses. Specifically, the response functions of FEs are known to reach their maxima in the vicinity of phase transitions (PTs). Thus, the ability to control FE PTs is essential for advanced applications.

Nanoscale Ferroelectrics and Multiferroics: Key Processing and Characterization Issues, and Nanoscale Effects, First Edition. Edited by Miguel Algueró, J. Marty Gregg, and Liliana Mitoseriu.
© 2016 John Wiley & Sons, Ltd. Published 2016 by John Wiley & Sons, Ltd.

The global trend to miniature and compact high-performance electronic devices has stimulated the development of technology for FE layers with thicknesses smaller than 1 μm and the components based thereon. A remarkable progress in the fabrication of thin FE layers and films has been achieved in the last few decades [12, 13]. It is worth mentioning that modern FE capacitors and microelectromechanical systems (MEMS) employ ceramic layers with a thickness of only 0.5 μm. Apart from ceramic-type polycrystalline films, single-crystal-type epitaxial films of FEs have also been intensively explored in the last 20 years [14,15]. Because the epitaxy requires expensive single-crystal substrates, epitaxial FE films have long been attracting only fundamental interest. However, the breakthrough development of epitaxial growth of FEs into commercial Si substrates has opened breathtaking opportunities for innovations using epitaxial FE films [16, 17]. Also, owing to the structural and chemical compatibility of the perovskite-type FEs with many other metal oxides, epitaxial FE films have become an important constituent in the rapidly growing field of oxide microelectronics [18]. Correspondingly, the knowledge-based control of response functions in epitaxial FE thin films is of increasing practical importance. Again, since the FE response functions peak near PT, studies of FE PTs in epitaxial thin films have a straightforward practical impact. Simultaneously, better fundamental understanding of the FE PT and of the nature of ferroelectricity may lead to the design of new multiferroic materials and structures with unusual functions.

Here, the phenomenological background and the main experimental methods of dielectric studies of PTs in thin-film FEs are briefly described. The experimental results obtained in epitaxial films of FE $Pb_{0.5}Sr_{0.5}TiO_3$ and $BaTiO_3$, paraelectric $KTaO_3$, and relaxor ferroelectric $PbSc_{0.5}Nb_{0.5}O_3$ are summarized. The films were grown by pulsed laser deposition (PLD) and their crystal structure was systematically characterized using X-ray diffraction (XRD). The details of PLD processes and XRD analysis can be found in the corresponding references and are omitted here for brevity.

19.2 Experimental Study of Phase Transition

19.2.1 Bulk Ferroelectrics and Relaxors

The term “ferroelectrics” is generally applied to materials exhibiting different types of polar ordering. They include normal FEs possessing a long-range ordered spontaneous polarization that can be switched by electric field, antiferroelectrics (AFEs) with antipolar dipole arrangement, and relaxor ferroelectrics (RFEs), which lack a macroscopic polarization but possess local polarization.

For normal FEs, with increasing temperature *T*, the FE polarization decreases and then disappears at a certain temperature θ (Curie point), at which the high-temperature non-polar paraelectric phase (PE) is formed. This FE-to-PE PT (or PE-to-FE PT on cooling), or FE PT, is conventionally described using the macroscopic phenomenological Landau–Ginzburg–Devonshire (LGD) theory [19]. The Gibbs free energy density *G* can be expressed as a polynomial of polarization *P:*

$$G = F - EP = F_0 + \frac{\alpha}{2}P^2 + \frac{\beta}{2}P^4 + \frac{\gamma}{2}P^6 - EP \qquad (19.1)$$

where F_0 is the free energy of the PE phase (at $E = 0$), E is the electric field, and the coefficients α, β, and γ may depend on temperature and pressure. For the second-order FE PT, the coefficients are:

$$\alpha = \frac{1}{c}(T - \theta), \beta > 0, \gamma = 0 \tag{19.2}$$

where $c > 0$ is the Curie–Weiss constant. The temperature of the phase transition is equal to θ, there is no jump in polarization, and no latent heat of transition. The inverse dielectric permittivity can be expressed as:

$$\frac{1}{\varepsilon} = \frac{1}{c}(T - \theta), T > \theta \tag{19.3}$$

$$\frac{1}{\varepsilon} = \frac{2}{c}(\theta - T), T < \theta \tag{19.4}$$

At the first-order FE PT, the polarization experiences a small but finite jump and the coefficients can be written as:

$$\alpha = \frac{1}{c}(T - \theta), \beta < 0, \gamma > 0 \tag{19.5}$$

Correspondingly, when the transition point is approached from below, the inverse permittivity is:

$$\frac{1}{\varepsilon} = \frac{8}{c}(\theta - T) + \frac{3\beta^2}{4\gamma}, T \to \theta^- \tag{19.6}$$

and when approaching it from above it is:

$$\frac{1}{\varepsilon} = \frac{1}{c}(T - \theta) + \frac{3\beta^2}{16\gamma}, T \to \theta^+ \tag{19.7}$$

As seen from Equations (19.6) and (19.7), the high-temperature (low-temperature) phase can persist below (above) θ as a metastable phase, that is manifested in thermal hysteresis: the temperature of the dielectric maximum T_m is higher than θ if reached from below and lower if reached from above.

Using expression (19.1) for equilibrium conditions $(\partial F/\partial P = 0)$ and considering the alternating electric field $E_0 \exp(i\omega t)$, it is possible to write:

$$\mu P'' + \nu P' + \frac{\alpha}{2}P + \beta P^3 = \frac{1}{2}E_0 \exp(i\omega t) \tag{19.8}$$

where μ and ν are the coefficients as defined in [19] and [20]. By presenting the derivatives of polarization in the form $-\omega^2 P$ and $i\omega P$, the dielectric permittivity at $T > \theta$ can be obtained:

$$\varepsilon(\omega) = \varepsilon_\infty + \frac{2\pi/\mu}{\omega_i^2 - \omega^2 + i(\nu/\mu)\omega} \tag{19.9}$$

where ε_∞ is the high-frequency electronic permittivity and $\omega_i{}^2 = \alpha/(2\mu)$. From the dispersion relationship (19.9) one can arrive at the Lyddane–Sachs–Teller equation:

$$\frac{\varepsilon(0)}{\varepsilon_\infty} = \frac{\omega_L^2}{\omega_T^2} \tag{19.10}$$

where ω_L and ω_T are the frequencies of longitudinal and transverse optical phonons. Taking into account expressions for α and ω_i, it is easy to understand that a transverse phonon mode, whose frequency tends to zero on cooling to the temperature θ, should exist in PE. This is the so-called "soft mode", which sometimes is interpreted as causing ferroelectricity, although here it is rather a consequence of the LGD polynomial (19.1). It should be emphasized that the phenomenological LGD theory does not reveal microscopic, atomistic mechanisms of ferroelectricity. Nevertheless, the LGD approach has been and continues to be successfully applied for describing numerous FE phenomena and materials.

As follows from expressions (19.3), (19.4) and (19.6), (19.7), the occurrence and the order of the FE PT can be identified experimentally by inspecting the temperature dependence of the inverse permittivity $1/\varepsilon(T)$. The expressions (19.3), (19.4) can also be applied to studies of AFE PTs [1,2, 19,20]. The experimental studies of FE PTs can also use inspections of the temperature-dependent soft-mode behavior. Importantly, the FE PTs are closely connected with structural phase transitions in perovskite-type FEs. The crystal structure of the high-temperature PE phase is cubic in most FEs and the low-temperature FE phases have a crystal structure of lower symmetry. Correspondingly, experimental investigations of the FE PTs often include studies of crystal structure using X-ray, electron, and/or neutron diffraction or scattering [1, 2].

RFEs outperform normal FEs in many aspects, and numerous applications of RFEs have been developed and envisaged [4, 6, 9]. However, an extensive use of RFEs is hindered by insufficient understanding of physical mechanisms responsible for the remarkable properties of these materials. The problem stands as a challenge since the discovery of RFEs almost 60 years ago [4]. RFEs differ from normal FEs. The PTs from the high-temperature non-polar PE phase possessing cubic crystal symmetry to the low-temperature FE state take place in normal FEs on cooling (Figure 19.1(a)). One of the manifestations of the FE PT is a sharp peak in the temperature dependence of the dielectric permittivity $\varepsilon(T)$, which can be explained in terms of the LGD theory. On the contrary, RFEs exhibit broad dielectric peaks with frequency dispersion in both the permittivity and the temperatures T_m of the peaks (Figures 19.1(b) and 19.1(c)). In contrast to normal FEs, the relaxor (R) state is characterized by the presence of microscopic short-range order of polarization and the absence of long-range ordered spontaneous polarization. The macroscopic electrical response functions of RFEs are often described using a widely accepted model of a glass-like ensemble of randomly interacting dipolar entities with statistical distributions of their size and dipolar

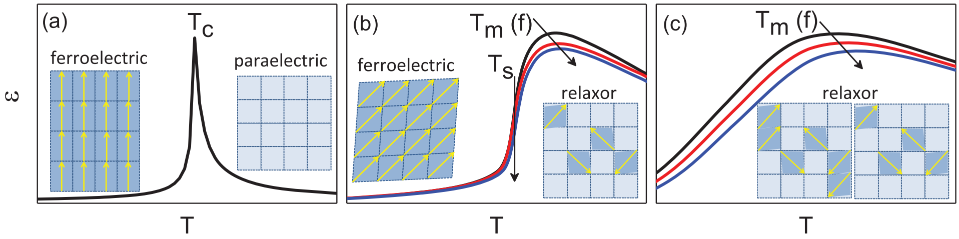

Figure 19.1 *Schematic illustration of the temperature dependence of the real part of the dielectric permittivity, ε(T), at (a) a paraelectric-to-ferroelectric transition, (b) a relaxor-to-ferroelectric transition, and (c) in a relaxor*

strength [4, 5, 9, 21, 22]. The polarization reorientation, or flips, of a dipole are activated thermally and/or by electric field. Although the microscopic nature of the polar entities is under research and debate, the dipolar approach can explain the main features of RFEs such as the broad dielectric peak $\varepsilon(T)$ around temperature T_{m} with a strong frequency dispersion of ε and T_{m}, the Vogel–Fulcher relationship between the temperatures T_{m} and the dipolar relaxation times, the divergence between static and dynamic responses, electric-field-induced transformations, and the effects of high hydrostatic pressure. Notice that the dielectric peak around T_{m} in RFEs is not related to FE PT. A phase transition from the R to FE state can take place spontaneously on cooling to a certain temperature $T_{\mathrm{s}} < T_{\mathrm{m}}$ (see the drop of the permittivity at the temperature T_{s} in Figure 19.1(b)) or it can be induced by applying a large enough electric field. The spontaneous R–FE transition is absent in such RFEs as $PbMg_{1/3}Nb_{2/3}O_3$ (Figure 19.1(c)), where the FE state can be gradually achieved at very low temperatures below T_{m}.

The PE-like state is believed to exist in RFEs at high temperatures above the so-called Burns temperature (T_{B}), although this is still under debate [23]. The deviation from the Curie–Weiss behavior above and around T_{m} has been described using an Edwards–Anderson-type glass order parameter $q(T)$ [21, 24, 25]:

$$\varepsilon = \frac{c\,[1 - q\,(T)]}{T - \theta\,[1 - q\,(T)]} \tag{19.11}$$

The parameter $q(T)$ is a linear function of temperature in many RFE crystals. Although the connection between $q(T)$ and the dipolar relaxation-time spectrum has been analyzed theoretically [26], its microscopic origin remains disputable. Another approach to the analysis of the dielectric peaks in perovskite-structure RFEs has been suggested by Bokov et al. [27]. In a wide range of temperatures above T_{m}, the dielectric permittivity ε can be fitted by an empirical scaling law:

$$\frac{\varepsilon_{\mathrm{ST}}}{\varepsilon} = 1 + \frac{(T - T_{\mathrm{ST}})^2}{2\delta^2} \tag{19.12}$$

where the parameters $\varepsilon_{\mathrm{ST}}$ and T_{ST} have the meaning of the magnitude and temperature of the maximum static permittivity, respectively, and the parameter δ describes the degree of diffuseness of the dielectric peak. Also for the expression (19.12), its atomistic origin is unclear.

As seen from Figure 19.1 and expressions (19.11) and (19.12), the dielectric peaks in RFEs are broader than those in FEs. In general, broad dielectric peaks can be observed also in normal FEs, where the presence of grains with non-FE boundaries and/or other defects can cause peak broadening and frequency dispersion of the dielectric permittivity [28]. The Vogel-Fulcher-type relationship (19.13) between the temperatures T_m and frequency f is considered to be the key peculiarity of the RFE-type broad dielectric peak:

$$f = f_0 \exp\left[-\frac{T_{\mathrm{A}}}{(T_{\mathrm{m}} - T_{\mathrm{f}})}\right] \tag{19.13}$$

Here f_0, T_{A}, and T_{f} are fitting parameters.

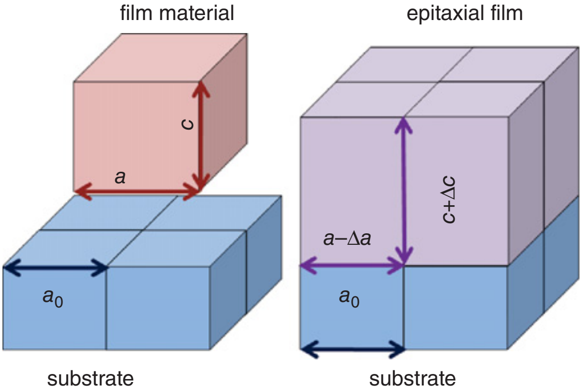

Figure 19.2 Schematics of the cube-on-cube-type epitaxial growth

The expressions (19.3), (19. 4), (19. 6), (19.7), and (19.11) to (13) make it possible to identify FE PTs and RFEs. Hence, the experimental study of the temperature and frequency dependence of the dielectric permittivity $\varepsilon(f, T)$ is a basic tool for analysis of these phenomena.

19.2.2 Epitaxial Thin Films

When a thin film of perovskite FE is grown epitaxially on top of a single-crystal substrate, the crystal structure and the lattice parameters of the FE film are dictated by the substrate and thus can differ significantly from those of the bulk prototype. The simplest case of the cubic substrate and the cube-on-cube-type epitaxial film is illustrated in Figure 19.2.

The epitaxial relationship here is *film*[100](001) ‖ *substrate*[100](001). If the in-plane (parallel to the substrate surface) lattice parameter a of the film material is larger than the lattice parameter a_0 of the substrate surface and the film grows coherently (i.e. the in-plane lattice parameter of the film is equal to that of the substrate), a biaxial in-plane misfit strain s arises in the film. The in-plane strain s is defined as:

$$s = \frac{a_0 - a}{a} \tag{19.14}$$

The sign of s is negative (positive) if the film is compressed (stretched) in the in-plane directions. Correspondingly, compared to the bulk prototype, the out-of-plane lattice parameter of the film can be elongated (for in-plane compressive strain) or become shorter (for in-plane tensile strain). A difference between thermal expansion coefficients of the film and the substrate materials can lead to an additional thermal strain, which depends on temperature.

The perovskite-type epitaxial FE films can grow coherently on the cubic substrates with no or very small misfit. With increasing thickness of the film possessing a misfit strain, the elastic energy of the system increases. The strain should relax in order to minimize the energy. The main mechanism of strain relaxation is through the formation of dislocations. Also specific arrangements of structural and FE domains, formation of three-dimensional defects, and growth of islands or columns are possible [29,30]. There is a critical thickness at which the strain relaxation starts. As shown experimentally, the critical thickness is approximately 100 nm for $|s| = 1\%$ and less than 10 nm for $|s| = 2\%$ [31,32]. For $|s| \geq 3\%$, strain relaxes at the film–substrate interface, but this does not destroy the cube-on-cube epitaxy [33].

A phenomenological theoretical analysis of the effects of strain in epitaxial perovskite FE films has been performed in the seminal work by Pertsev et al. [34], where the strain–temperature (s–T) phase diagrams have been introduced. It has been shown that compared to bulk, the presence of epitaxial strain can lead to new crystal and FE phases, increase of the temperatures of FE PTs, change of the order of FE PTs, and enhancement of polarization in the films. Moreover, the strain can induce the FE state in heteroepitaxial films of non-FE materials [35]. Later, the phenomenological and the first-principles diagrams have been developed for a number of films. Today, the paradigm of the strain-controlled functions is well established and expanded to a very broad range of oxide materials and structures.

In contrast to extensive research of epitaxial films of normal FEs performed in the last 20 years (see [12] to [14] and references therein), epitaxial RFE films have remained practically unexplored. The compositional complexity and insufficient fundamental understanding of RFEs make the theoretical analysis of epitaxial RFE films very difficult. The extrapolation of tendencies found in films of normal FEs to films of RFEs suggests that the epitaxial strain may favor new structural and FE phases with increased temperatures of the FE transitions in RFE films. This, however, has not been confirmed experimentally [36–38].

The theoretical (s–T) phase diagrams [34] have important implications for experimental studies of FE PTs in epitaxial films. Firstly, they show that a metrically tetragonal unit cell (see Figure 19.2) can be centrosymmetric and non-FE. This means that identifying the FE phase and the FE PT in thin and ultra-thin films by conventional X-ray methods may be very difficult if not impossible. Secondly, it is demonstrated that the Curie–Weiss-type dielectric behavior is not changed, and thus it can be used for detecting FE PTs. Finally, the diagrams predict the temperatures, types, and sequences of PTs, different from bulk. Again, similarly to bulk, the temperature dependence of the dielectric permittivity is a basis for experimental studies of PTs in epitaxial films.

19.3 Dielectric Permittivity in Thin Films

19.3.1 Thin-Film Capacitor

The most common way of measuring permittivity of a dielectric is by sandwiching a piece of dielectric between electrodes and measuring impedance of the formed parallel-plate capacitor. A typical arrangement for measuring impedance Z^* at frequencies $f = 10^{-3}$–10^8 Hz ($\omega = 2\pi f$) is sketched in Figure 19.3(a). Let us consider a capacitor built of bulk FE with thickness $d > 100$ μm and metal electrodes. The resistance R_F of FE is determined mainly by dielectric losses (described by R_ε) due to the large ohmic resistance R_Ω of bulk FE. The resistance R_E of electrodes and contacts is negligibly small. The bulk FE capacitor can be treated as an ideal capacitor, whose equivalent circuit is shown in Figure 19.3(b).

The complex impedance of the ideal FE capacitor is:

$$Z^* = R - iX = R_\varepsilon - i\frac{1}{\omega C} \tag{19.15}$$

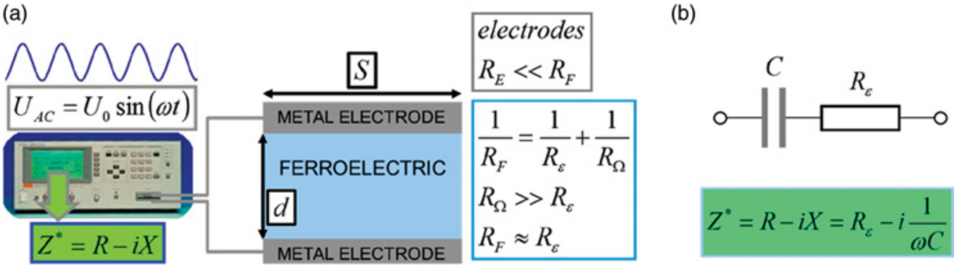
(a)
$U_{AC} = U_0 \sin(\omega t)$
$Z^* = R - iX$
S
METAL ELECTRODE
FERROELECTRIC
d
METAL ELECTRODE
electrodes
$R_E << R_F$
$\frac{1}{R_F} = \frac{1}{R_\varepsilon} + \frac{1}{R_\Omega}$
$R_\Omega >> R_\varepsilon$
$R_F \approx R_\varepsilon$
(b)
C
R_ε
$Z^* = R - iX = R_\varepsilon - i\frac{1}{\omega C}$

Figure 19.3 *(a) Typical setup for measuring impedance and (b) equivalent circuit of the FE capacitor*

The capacitance C and the loss factor $\tan\delta$ are, respectively:

$$C = \frac{1}{\omega X} \equiv C_S \tag{19.16}$$

$$R_\varepsilon = \frac{d}{\omega \varepsilon_0 \varepsilon'' S} \tag{19.17}$$

$$C = \frac{\varepsilon_0 \varepsilon S}{d} \tag{19.18}$$

$$\tan\delta = \frac{\varepsilon''}{\varepsilon} = \frac{X}{R} \tag{19.19}$$

where ε and ε'' are the real and imaginary parts of the dielectric permittivity of FE, S is the area of electrodes, and C_S denotes the capacitance determined for the series connection of C and R_ε (Figure 19.3(b)). The real and imaginary parts of the dielectric permittivity can be easily extracted from the measured C_S and $\tan\delta$.

In contrast to the straightforward connection between the measured impedance and the dielectric permittivity in the bulk FE capacitor (expressons (19.15) to (19.19)), the impedance of a FE thin-film capacitor depends not only on the dielectric properties of the FE film but also on the capacitor design. First of all, with decreasing thickness d of the FE film to hundreds of nanometers, the ohmic resistance R_Ω of the FE film decreases and can become comparable or even larger than R_ε:

$$R_\Omega \approx \rho \frac{d}{S} \tag{19.20}$$

where ρ is the resistivity of the FE film. The thin-film capacitor should thus be treated as a leaky capacitor. Additionally, epitaxial FE thin-film heterostructures often employ thin-film oxide electrodes. The resistance R_E of such electrodes cannot be neglected. Strictly, the inductance of electrodes should also be considered, but is omitted here for simplicity. An equivalent circuit of an FE thin-film capacitor is presented in Figure 19.4. The impedance of such a capacitor is:

$$Z^* = R - iX = R_E + \frac{R_F}{1 + (\omega C R_F)^2} - i\frac{\omega C R_F^2}{1 + (\omega C R_F)^2} \tag{19.21}$$

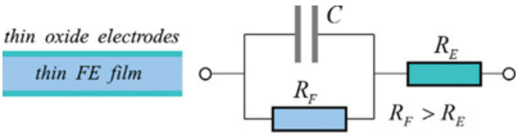

$$Z^* = R - iX = R_E + \frac{R_F}{1+(\omega CR_F)^2} - i\frac{\omega CR_F^2}{1+(\omega CR_F)^2}$$

Figure 19.4 *Equivalent circuit of a thin-film FE capacitor*

As seen from expression (19.21), an accurate retrieval of capacitance from the measured impedance is practically impossible. The capacitance C can be estimated using approximations that depend on the measurement frequencies. For instance, a leaky capacitor approximation C_p can be used for lower frequencies:

$$(\omega CR_\mathrm{F})^2 \ll 1 \tag{19.22}$$

$$R_\mathrm{E} < R_\mathrm{F} \tag{19.23}$$

$$C \approx \frac{X}{\omega(R^2 + X^2)} \equiv C_\mathrm{p} \tag{19.24}$$

$$\tan\delta = \frac{R}{X} \tag{19.25}$$

At higher frequencies, a formal ideal-capacitor approximation C_s may be better suited:

$$(\omega CR_\mathrm{F})^2 > 1 \tag{19.26}$$

$$R \approx R_\mathrm{E} \tag{19.27}$$

$$C \approx \frac{1}{\omega X} \equiv C_\mathrm{s} \tag{19.28}$$

$$\tan\delta = \frac{X}{R} \tag{19.29}$$

It should be emphasized that the expressions (19.24) and (19.28) are approximations only. The estimated capacitance can have significant “extrinsic” frequency dispersion even in the case when the dielectric permittivity of the FE film lacks “intrinsic” frequency dispersion. It is easy to show that the extrinsic dispersion of capacitance at lower frequencies is connected with the relatively small resistance R_F of the FE film, and the relatively large resistance R_E of the electrodes determines the higher-frequency dispersion [39].

An example of the frequency dispersion of the estimated C_s and C_p is shown in Figure 19.5. Here C_med is the capacitance in a medium frequency range, where $C_\mathrm{s} = C_\mathrm{p}$. The capacitor is formed by a 130 nm thick epitaxial film of FE (Pb, Sr)TiO_3 and (La, Sr)CoO_3 bottom electrode on MgO substrate and Pt top electrode. The measurement temperature was 500 K. (More details can be found in [39].)

Most importantly, the expressions (19.21), (19.25), and (19.29) show that the loss factor measured in the FE thin-film capacitor is not directly related to dielectric losses of the FE film, but is determined by the whole capacitor. By varying parameters in expression (19.21),

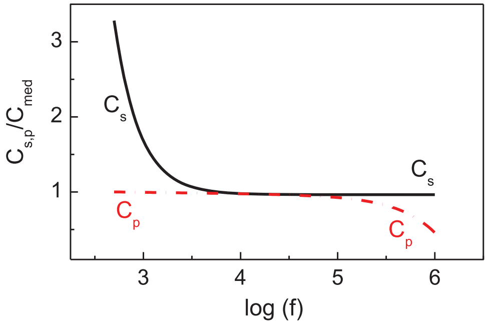

Figure 19.5 The normalized estimated capacitances as a function of logarithm of frequency f (Hz) in an FE thin-film capacitor Pt/$Pb_{0.5}Sr_{0.5}O_3$/$La_{0.5}Sr_{0.5}CoO_3$/MgO

it is possible to calculate tan δ, which fits well to the measured data. An example of such calculation is presented in Figure 19.6. The capacitor is the same as for Figure 19.5. The measurement temperature was 300 K. Thus, in contrast to the analysis of the imaginary part of the dielectric permittivity, which is usually performed in studies of bulk PTs using the measured loss factor, such an analysis is practically impossible in thin films.

Generally, the approximation (19.24) works fairly well for a certain range of frequencies and when the resistance R_F of the FE film is large enough. However, as can be understood from expressons (19.21) to (19.24), the capacitance may be overestimated if the resistance R_F decreases. For instance, the presence of defects and mobile charges may lead to a decrease of R_F on heating and result in an apparent increase of the estimated capacitance. Often such an increase makes it difficult to analyze the high-temperature behavior of thin FE films correctly.

Moreover, with decreasing thickness of the FE film to a few tens of nanometers or smaller, the resistance R_F may become so small that the resistances of the electrodes and of the FE nanofilm appear to be nearly equal (Figure 19.7):

$$R_F \approx R_\Omega \approx R_E \tag{19.30}$$

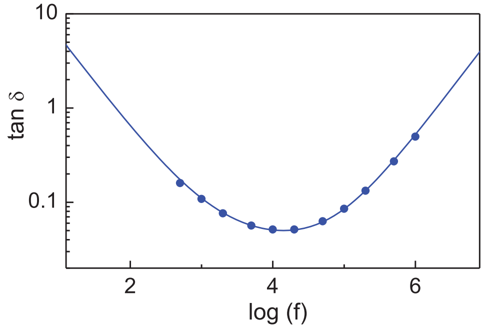

Figure 19.6 The calculated (line) and measured (solid circles) loss factor as a function of the logarithm of frequency f (Hz) in the FE thin-film capacitor Pt/$Pb_{0.5}Sr_{0.5}O_3$/$La_{0.5}Sr_{0.5}CoO_3$/MgO

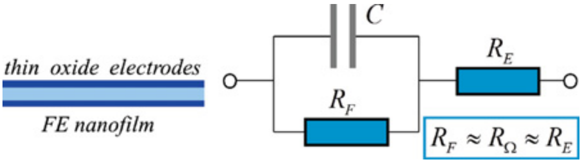

Figure 19.7 *Equivalent circuit of the FE nanofilm capacitor*

Then the approximations (19.24) and (19.28) can no longer be applied. In the case of nanofilms, the imaginary part of the impedance X can be analyzed instead of the complex impedance Z^*, since X does not depend on the resistance R_E of the electrodes:

$$X = \frac{\omega C R_\mathrm{F}^2}{1 + (\omega C R_\mathrm{F})^2} \tag{19.31}$$

The capacitance can be found from the imaginary part X:

$$C \approx \frac{1}{2\omega X}\left(1 + \sqrt{1 - \frac{4X^2}{R_\Omega^2}}\right) \equiv C_X \tag{19.32}$$

This approach in expression (19.32) requires additional measurements or estimations of the ohmic resistance R_Ω of the FE nanofilm. Despite this difficulty and possible related uncertainty, the estimation (19.32) gives realistic values in contrast to completely unrealistic ones obtained using expressions (19.24) or (19.28). This dramatic difference is illustrated in Figure 19.8. The capacitor is formed by a 45 nm thick epitaxial film of RFE $Pb_{1/3}Mg_{2/3}NbO_3$, (La, Sr)CoO_3 bottom electrode on MgO substrate and Pt top electrode. The measurements frequency was 1 MHz. (More details can be found in [36].)

19.3.2 Derivative of Inverse Permittivity

Figures 19.3 to 19.8 and expressions (19.15) to (19.32) explain a basic route for extracting capacitance of an FE thin-film heterostructure (C_H) from the measured impedance.

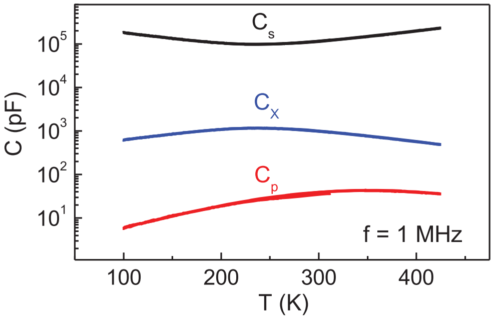

Figure 19.8 *The capacitances of the RFE nanofilm capacitor Pt/$PbMg_{1/3}Nb_{2/3}O_3$/$La_{0.5}Sr_{0.5}CoO_3$/MgO estimated using different approximations as a function of temperature. Notice the logarithmic scale for capacitance*

Unfortunately, the knowledge of C_{H} is insufficient for determining the real part of the dielectric permittivity in FE film. It has been known since the early 1990s [40] that the capacitance C_{H} of the FE thin-film capacitor can be modeled as a series connection of capacitance C_{F} of the FE film and some interfacial capacitance C_{INT}:

$$\frac{1}{C_{\mathrm{H}}} = \frac{1}{C_{\mathrm{F}}} + \frac{1}{C_{\mathrm{INT}}} \tag{19.33}$$

The capacitance C_{INT} can be thought as that of a thin low-permittivity non-FE layer located at the film–electrode interface:

$$C_{\mathrm{INT}} = \frac{\varepsilon_0 \varepsilon_{\mathrm{INT}} S}{d_{\mathrm{INT}}} \tag{19.34}$$

where $\varepsilon_{\mathrm{INT}}$ and d_{INT} are permittivity and thickness of the interfacial layer, respectively. The state-of-the-art first-principles analysis is able to explain the fundamental microscopic origin of the interfacial layer [41,42]. Besides the fundamental reasons for C_{INT}, technological factors such as contamination, intermixing, formation of dislocations, or other defects at the film–electrode interface can also contribute to C_{INT}.

The expression (19.33) can be rewritten in the form:

$$\frac{d_{\mathrm{F}}}{\varepsilon_0 \varepsilon_{\mathrm{H}} S} = \frac{d_{\mathrm{F}} - d_{\mathrm{INT}}}{\varepsilon_0 \varepsilon_{\mathrm{F}} S} + \frac{d_{\mathrm{INT}}}{\varepsilon_0 \varepsilon_{\mathrm{INT}} S} \tag{19.35}$$

If the thickness d_{INT} of the interfacial layer is small compared to the thickness d_{F} of the FE film, the following approximation is valid:

$$d_{\mathrm{INT}} \ll d_{\mathrm{F}} \tag{19.36}$$

$$\frac{1}{\varepsilon_{\mathrm{H}}} \approx \frac{1}{\varepsilon_{\mathrm{F}}} + \frac{d_{\mathrm{INT}}}{\varepsilon_{\mathrm{INT}}} \frac{1}{d_{\mathrm{F}}} \tag{19.37}$$

Thus, by measuring the apparent dielectric permittivity ε_{H} in capacitor heterostructures with different thicknesses d_{F} of similar FE films and by plotting $(1/\varepsilon_{\mathrm{H}})$ as a function of $(1/d_{\mathrm{F}})$, the normalized interfacial permittivity $(\varepsilon_{\mathrm{INT}}/d_{\mathrm{INT}})$ can be extracted from the linear fit of expression (19.37). This approach has been applied to a variety of FE thin-film capacitors and the interfacial parameters $(\varepsilon_{\mathrm{INT}}/d_{\mathrm{INT}})$ have been estimated. Consequently, the intrinsic permittivity ε_{F} of the FE film itself can be found using expression (19.37).

The approach (19.37) has limitations. It cannot be applied to ultra-thin FE films. Its correctness is under question for films with thickness-dependent intrinsic properties, which may exist, for instance, as a result of strain relaxation in epitaxial films. The term $(1/C_{\mathrm{INT}})$ in expression (19.33) may originate not only from the film–electrode interface but also from other boundaries or defects in the FE film. In the case of epitaxial FE films, the major problem is connected with the thickness dependence of intrinsic properties.

An important consequence from expression (19.37) for studies of PTs is that the dielectric permittivity ε_{H} determined in the capacitor heterostructure is smaller than the true intrinsic permittivity ε_{F} of the FE film. Correspondingly, the measured apparent dielectric peak $\varepsilon_{\mathrm{H}}(T)$ is significantly broader than the peak $\varepsilon_{\mathrm{F}}(T)$ in the film. This is schematically illustrated in Figure 19.9.

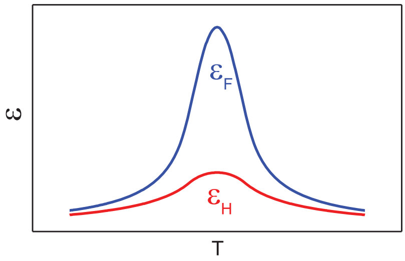

Figure 19.9 Schematic dielectric peaks: the permittivity ε_F of the FE thin film and the permittivity ε_H in the capacitor with this film as a function of temperature

The broadening of the dielectric peak $\varepsilon_{\mathrm{H}}(T)$, which is caused by the presence of interfacial capacitance, can be accompanied by the frequency dispersion of $\varepsilon_{\mathrm{H}}(f)$, which is determined by the capacitor design (as discussed above). The dielectric peak $\varepsilon_{\mathrm{H}}(f, T)$ measured in a thin-film capacitor of normal FE may be "relaxor-looking" (Figure 19.10). It should be emphasized that this "relaxor-look" is of extrinsic nature and does not indicate intrinsic RFE behavior of the film. Additionally, the possible presence of defects in the FE film itself may also lead to frequency dispersion of ε_{F} (for instance, due to Maxwell–Wagner relaxation). A special analysis is required in order to separate intrinsic dispersion of ε_{F} from the capacitor-related extrinsic dispersion of ε_{H}.

In contrast to experimental studies of bulk FE PTs using the straightforward analysis of the measured impedance, such studies are impossible in thin FE films. A solution has been found in the course of discussion [43–45]. It has been suggested that the dielectric peaks in FE thin-film capacitors can be analyzed using derivative ξ of the measured inverse permittivity $(1/\varepsilon_{\mathrm{H}})$:

$$\xi = \frac{\partial}{\partial T}\left(\frac{1}{\varepsilon_{\mathrm{H}}}\right) \tag{19.38}$$

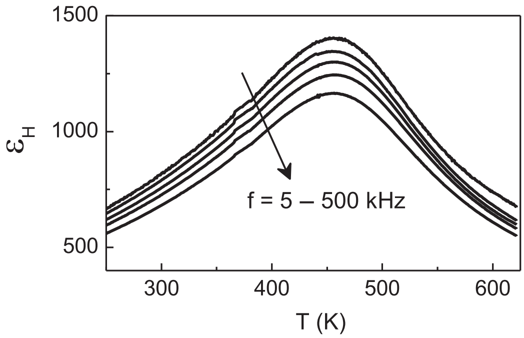

Figure 19.10 The permittivity ε_H as a function of temperature and frequency in the thin-film capacitor Pt(70nm)/$Pb_{0.5}Sr_{0.5}TiO_3$(130 nm)/$La_{0.5}Sr_{0.5}CoO_3$(100nm)/MgO (001). Arrow shows the direction of frequency increase from 5 to 500 kHz

Assuming that the temperature dependences of the extrinsic factors (R_E, R_F, and C_{INT}) are very weak compared to the strong temperature dependence of the intrinsic permittivity ε_F of the FE film (e.g. see expressions (19.2) to (19.7)), it follows from expressions (19.37) and (19.38) that the measured derivative describes the intrinsic behavior of the film:

$$\frac{\partial}{\partial T}\left(\frac{1}{\varepsilon_H}\right) \cong \frac{\partial}{\partial T}\left(\frac{1}{\varepsilon_F}\right) \tag{19.39}$$

The temperature dependences of the permittivity obtained in the LGD theory and those found experimentally in bulk FE and RFE materials can be employed in the analysis of the intrinsic behavior of ξ in thin films. For instance, the modified Curie–Weiss law has been revealed in the PE state of many perovskite-type FEs [46]:

$$\varepsilon = \frac{c}{T-\theta} + \varepsilon_L \tag{19.40}$$

where ε_L is the lattice contribution. Correspondingly, the derivative ξ is equal to:

$$\xi = \frac{c}{(\varepsilon_L(T-\theta)+c)^2} \tag{19.41}$$

It is easy to see from expressions (19.3) and (19.7) that for the second-order FE PT the derivative is:

$$\xi \cong \frac{1}{c}, T > \theta \tag{19.42}$$

$$\xi \cong -\frac{2}{c}, T < \theta \tag{19.43}$$

For the first-order PT, the derivative is:

$$\xi \cong \frac{1}{c}, T \to \theta^+ \tag{19.44}$$

$$\xi = -\frac{8}{c}, T \to \theta^- \tag{19.45}$$

In the case of the empirical scaling law in RFE, the derivative is a linear function of T:

$$\xi = \frac{T - T_{ST}}{\varepsilon_{ST}\delta^2} \tag{19.46}$$

The temperature dependence $\xi\,(T)$ can reveal directly the presence and type of FE PT, and indicate the high-temperature RFE behavior. Unfortunately, no analytical description of the low-temperature RFE behavior of $\xi\,(T)$ in RFEs exists. As a reference for thin-film analysis, experimental proof of expressions (19.41) to (19.46) in bulk FEs and additional inspection of the dielectric peaks in bulk RFE are desirable. Thus prior to investigations of thin films, the derivative $\xi\,(T)$ has been analyzed in bulk samples including crystals of FE $BaTiO_3$ and RFE $PbMg_{1/3}Nb_{2/3}O_3$ and ceramics of FE $Pb_{0.5}Sr_{0.5}TiO_3$ and RFE $PbSc_{0.5}Nb_{0.5}O_3$.

The behavior $\xi\,(T)$ obtained on cooling at $f = 1$ MHz in single-crystal $BaTiO_3$ is shown in Figure 19.11. The temperature T_m of the dielectric maximum is that at which $\xi = 0$. The PE state is evidenced by a positive and practically temperature independent ξ at $T > T_m$. The decrease of ξ at $T > 650$ K is related to the increase in conduction, often observed in perovskite FEs. The jump of ξ at T_m is consistent with the first-order PT. The low-temperature

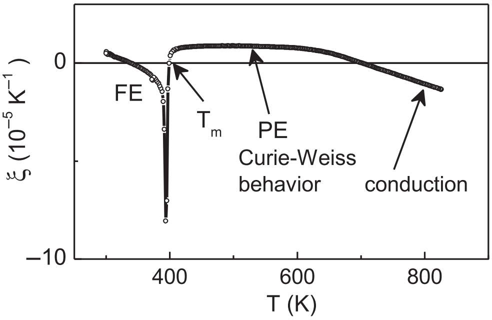

Figure 19.11 *Derivative ξ at f = 1 MHz as a function of temperature in the single-crystal BaTiO$_3$*

Curie–Weiss-type behavior cannot be seen clearly due to the presence of another PT around 270 K.

Both high-temperature and low-temperature Curie–Weiss-type parts of ξ (T) are seen in ceramic $Pb_{0.5}Sr_{0.5}TiO_3$ (Figure 19.12). The PE and the FE states are observed at temperatures that are almost 100 K higher and lower than T_m, correspondingly. The broad PT region can be a consequence of the presence of grains and non-FE grain boundaries in ceramics compared to a single-crystal FE.

The character of ξ (T) in single-crystal RFE $PbMg_{1/3}Nb_{2/3}O_3$ (PMN) is dramatically different from that in normal FE crystals and ceramics (Figure 19.13). The shape of ξ (T) can be approximated by an exponential decay in the whole studied range of temperatures. The derivative ξ (T) tends asymptotically to the high-temperature Curie–Weiss behavior, although this behavior is not reached at temperatures as high as 600–700 K. The linear fit is satisfactory in a narrow range of temperatures between 310 and 390 K. The low-temperature ξ (T) at $T < T_m$ has no signs of FE-type behavior.

The shape of ξ (T) in ceramic RFE $PbSc_{0.5}Nb_{0.5}O_3$ (PSN) has the features of both the high-temperature PMN-like behavior (marked by R in Figure 19.14) and the low-temperature normal FE behavior (marked by FE in the same figure). The high-temperature part of ξ (T) can be approximated by an exponential decay, similarly to PMN. The

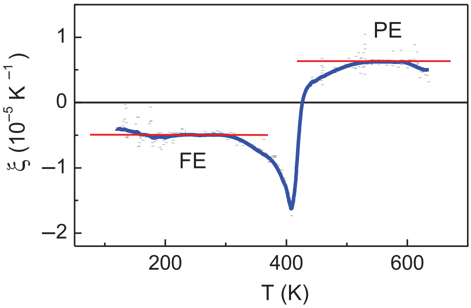

Figure 19.12 *Derivative ξ at f = 1 MHz as a function of temperature in ceramic Pb$_{0.5}$Sr$_{0.5}$TiO$_3$*

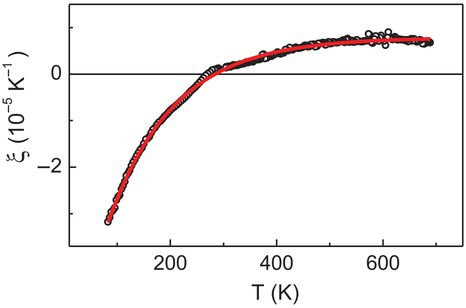

Figure 19.13 *Derivative ξ at f = 76 kHz as a function of temperature in single-crystal* $PbMg_{1/3}Nb_{2/3}O_3$. *Open circles are obtained using experimental data from [47]. Solid line is an exponential fit*

low-temperature $\xi(T)$ at $T < 350$ K evidences the FE state. The observed jump in $\xi(T)$ suggests that the spontaneous R to FE transition is a first-order PT.

As seen from Figures 19.11 to 19.14, the shapes of $\xi(T)$ are clearly different for bulk PE, FE, and R phases. By plotting $\xi(T)$ it is easy to visualize and determine the state of material, temperature, and width of PT, type of PT, and Curie constants. However, precautions should be taken when the measured impedance is influenced by the presence of defects, grains, and grain boundaries.

Compared to bulk samples, plotting $\xi(T)$ for thin-film capacitors has additional advantages. Firstly, it removes extrinsic frequency dispersion of the measured capacitance and permittivity (see Figures 19.5 and 19.10). Indeed, for the measured permittivity $\varepsilon_H(T)$ in Figure 19.10, the derivatives $\xi(T)$ determined at different frequencies merge into one curve (Figure 19.15), confirming the validity of expression (19.39). The data obtained at lower frequencies is scattered due to contact effects, and the higher-frequency $\xi(T)$ is preferable for analysis.

Another advantage of $\xi(T)$ is that it makes it possible to estimate the intrinsic permittivity of the FE film and the interfacial properties ($\varepsilon_{INT}/d_{INT}$) in a definite thin-film capacitor without inspecting a batch of capacitors with different thicknesses of FE films. For

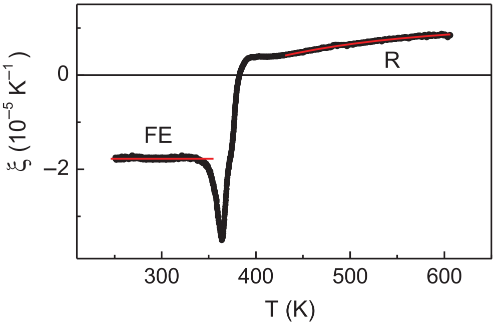

Figure 19.14 *Derivative ξ at f = 1 MHz as a function of temperature in ceramic* $PbSc_{0.5}Nb_{0.5}O_3$. *Solid lines show fits*

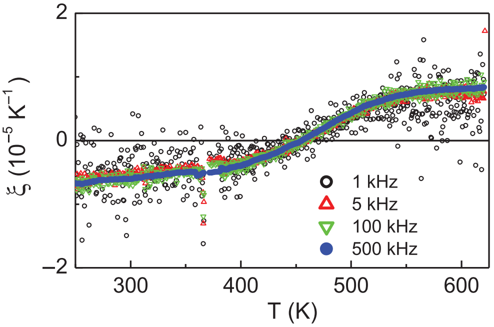

Figure 19.15 *The derivative ξ as a function of temperature and frequency $f = 1$–500 kHz in thin-film capacitor Pt(70nm)/$Pb_{0.5}Sr_{0.5}TiO_3$(130 nm)/$La_{0.5}Sr_{0.5}CoO_3$(100nm)/MgO (001)*

instance, the derivative ξ (T) determined at $f = 200$ kHz in a thin-film capacitor of 400 nm thick $Ba_{0.4}Sr_{0.6}TiO_3$ (BSTO) film is shown in Figure 19.16(a). The high-temperature fit to the modified Curie–Weiss law (19.41) is good for $T > 260$ K and for the following fitting parameters: $c = 0.8 \times 10^5$ K, $\theta = 180$ K, and $\varepsilon_L = 80$. The intrinsic permittivity ε_F of the BSTO film can be found using these parameters and expression (19.40). Then the measured inverse permittivity $1/\varepsilon_H$ can be compared with the intrinsic $1/\varepsilon_F$ (Figure 19.16(b)). The

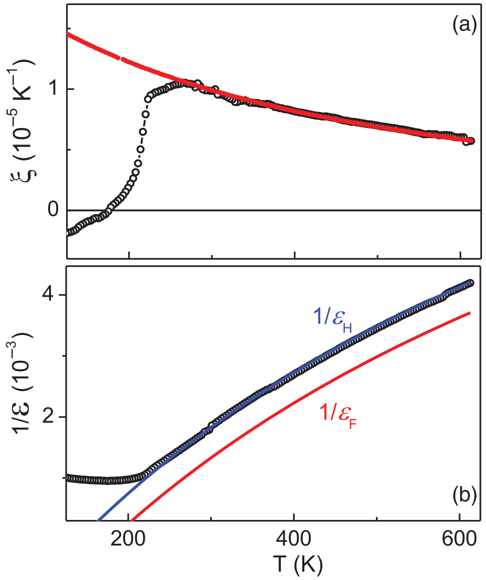

Figure 19.16 *(a) The derivative ξ as a function of temperature at frequency $f = 200$ kHz in thin-film capacitor Pt/$Ba_{0.4}Sr_{0.5}TiO_3$(400 nm)/$La_{0.5}Sr_{0.5}CoO_3$(100nm)/MgO (001). Solid line shows fit to the modified Curie–Weiss behavior. (b) The inverse permittivity as a function of temperature measured in this capacitor ($1/\varepsilon_H$) and calculated ($1/\varepsilon_F$) using the fit in (a)*

difference between them is temperature independent, confirming the validity of expressions (19.39) and (19.37). The difference is equal to:

$$\frac{1}{\varepsilon_H} - \frac{1}{\varepsilon_F} \approx \frac{d_{INT}}{\varepsilon_{INT}} \frac{1}{d_F} \tag{19.47}$$

For the known thickness $d_F = 400$ nm, the normalized interfacial permittivity is found to be approximately 5 nm^{-1}.

Although the suggested analysis of the derivative $\xi\ (T)$ makes it possible to explore intrinsic properties of thin FE films, it still has limitations. In particular, the high-temperature behavior at $T > T_m$ cannot be analyzed accurately for films with high $T_m > 500$–600 K and/or temperature-dependent resistance. The region of intrinsic PT also cannot be found from the low-frequency dielectric data because of inevitable smearing due to extrinsic factors. An additional complementary method of experimental studies of PT is highly desirable.

19.3.3 Thermo-optical Behaviour

The experimental studies of the low-frequency dielectric response in FE thin films are not free from ambiguities due to capacitor design and extrinsic factors, as explained above. The studies of PT using dielectric characterization can be combined with studies of crystal structure. However, because of epitaxial strain, it may be difficult to distinguish between nonpolar centrosymmetric and polar non-centrosymmetric perovskite-type structural phases using conventional thin-film X-ray diffraction techniques. Such methods as Raman scattering and Fourier-transform infrared spectroscopies, employed for experimental studies of bulk FE PTs, are restricted to certain substrate materials, sufficiently thick films, and, unfortunately, may be misleading when applied to thin films [48].

Among other properties, intrinsic optical properties can be unambiguously assessed in thin and ultra-thin films on arbitrary substrates using the state of the art variable angle spectroscopic ellipsometry (VASE) [49–52]. In contrast to the low-frequency dielectric characterization, the optical constants (such as index of refraction n and extinction coefficient k) of thin films can be measured without the need for electrodes. The studies of intrinsic FE PTs in thin films can be carried out by direct inspection of optical properties. Indeed, as follows from a simplified thermodynamic description, a first-order PE–FE PT is accompanied by a jump ΔE_g of bandgap E_g in perovskite-structure FEs [53]. A second-order phase transition is accompanied by a change in the slope of linear temperature dependence of $E_g(T)$ for $\Delta E_g = 0$. Although the simplified model in [53] does not consider exact band structure and its possible changes upon PTs, the experimental observations in single-crystal and some thin-film FEs have really shown the changes in E_g to be consistent with the model [53,54]. For E_g in FEs being typically about 2–4 eV, studies of optical absorption in the visible and ultraviolet spectral ranges may reveal intrinsic PTs in films.

More importantly, the phenomenological description also suggests that the FE PT can be accompanied by changes in the index of refraction n determined in the transparency range [55]. Although the band structure is not taken into account in this modeling either, the experimentally observed deviations of the index $n(T)$ from the linear temperature dependence ($n \propto T$) are widely accepted as indicating the appearance of polarization [56, 57]. Additionally, it is shown experimentally that the PE–FE PTs in single-crystal FEs (such as $BaTiO_3$, $KNbO_3$, and $PbTiO_3$) and the R–FE PTs in RFEs (such as $PbSc_{0.5}Ta_{0.5}O_3$ and

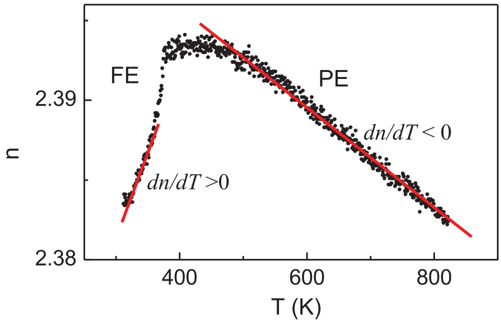

Figure 19.17 *Index of refraction n as a function of temperature in single-crystal $BaTiO_3$*

$PbSc_{0.5}Nb_{0.5}O_3$) are manifested by a jump of *n* [56–64]. Although microscopic mechanisms responsible for optical properties of FEs and RFEs are not fully understood, intrinsic FE PTs can be identified by inspecting the temperature evolution of *n*, or thermo-optical behavior $n(T)$.

As a reference, the thermo-optical behavior in single-crystal $BaTiO_3$ is shown in Figure 19.17. The temperature evolution of index of refraction *n* is measured in the transparency range (photon energy $E_{h\nu} = 2$ eV) [65]. The high-temperature linear increase of *n* on cooling or negative sign of the slope of $n(T)$, $dn/dT < 0$, evidences the PE state and is consistent with the PE state revealed by the high-temperature Curie–Weiss behavior of the derivative ξ in Figure 19.11. The drop of *n* at approximately 400 K observed on cooling indicates the appearance of FE polarization and the FE PT. The sign of dn/dT changes to positive in the FE state. The nature of $n(T)$ is still under investigation [66], but the dependence $n(T)$ can be employed in experimental studies of the PTs in thin films. The combination of ξ (T) and $n(T)$ gives unambiguous knowledge of PTs in thin FE and RFE films, as demonstrated below.

19.4 Phase Transitions in Epitaxial Films

19.4.1 $Pb_{0.5}Sr_{0.5}TiO_3$

The epitaxial heterostructure of a 130 nm thick strain-free film of FE $Pb_{0.5}Sr_{0.5}TiO_3$ (PSTO) and an oxide $La_{0.5}Sr_{0.5}CoO_3$ (LSCO) bottom electrode layer is formed on (001) MgO substrate. The PSTO film is polydomain, containing approximately 75% of *c*-oriented domains (elongated lattice parameter perpendicular to the film plane) and 25% of *a*-oriented domains (elongated lattice parameter in the film plane). For both domain types, the cube-on-cube-type epitaxial relationships are revealed. More details of microstructure can be found elsewhere [33, 39, 67].

The temperature dependence of the derivative ξ (T) and the thermo-optical behavior $n(T)$ in the PSTO film are shown in Figure 19.18. Both the modified high-temperature Curie–Weiss behavior of ξ and the negative high-temperature sign of dn/dT evidence the PE state in the film at temperatures $T > 570$ K. The low-temperature FE state is indicated by both a temperature-independent negative value of ξ and the positive sign of dn/dT. However,

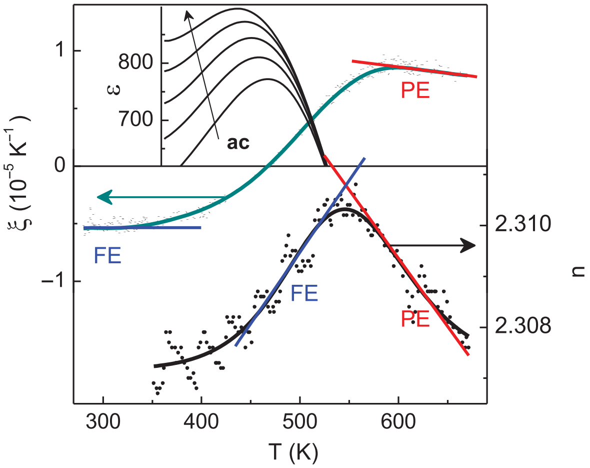

Figure 19.18 *The derivative ξ (left axis), index of refraction n (right axis), and dielectric permittivity ε (inset) as a function of temperature in the PSTO film. The permittivity is measured at different amplitudes of the probing AC voltage. Direction of voltage increase from 5 to 500 mV is shown by the arrow*

the temperature T_m of the dielectric peak is approximately $T_m \approx 465$ K, but the highest temperature T_O, at which the sign of dn/dT is positive, is $T_O \approx 545$ K, significantly higher than T_m. Moreover, the FE state exists at temperatures $T < 350$ K according to the derivative ξ (T), but the index $n(T)$ suggests the existence of the FE state also at higher temperatures $T < 530$ K. Correspondingly, the "dielectric" width of the PT region determined from ξ (T) is over 200 K, whilst the "optical" width according to $n(T)$ is significantly smaller, about 20–40 K only.

The optical observations seem to contradict the dielectric data. However, it is worth emphasizing that the dynamic dielectric response employed for detecting ξ (T) and T_m can be strongly non-linear in the FE state. It is known that the permittivity measured in FE at subswitching levels of AC excitation can increase with increasing amplitude of AC drive in the presence of FE domains [68]. Such an increase is observed also in the studied polydomain epitaxial PSTO film (inset in Figure 19.18): with increasing amplitude of the probing AC field the measured permittivity increases and the apparent position of the dielectric maximum shifts to lower temperatures. Obviously, the minimum available probing AC voltage (typically 5 mV) is large enough to cause a non-linear response in thin FE films. Consequently, the low-temperature permittivity is overestimated and the temperature T_m is underestimated. Here this mechanism is confirmed as due to the combined analysis: the dielectric non-linearity $\varepsilon(V_{ac})$ is detected below 540 K in PSTO, that is at temperatures where the FE state is evidenced optically. The present dielectric and optical observations do not contradict each other; they are self-consistent and confirm that indeed the intrinsic PE–FE transition takes place at a temperature between 530 and 570 K.

Thus, the PE and the FE states, the temperature and width of the intrinsic PE–FE PT, and the broadening of the dielectric peak due to FE dynamic non-linearity are detected thanks to the combination of dielectric and thermo-optical analyses. Compared to the first-order

PT at 400 K in ceramic PSTO, the second-order PT at approximately 550 K is detected in the epitaxial PSTO film. The increase in the temperature and the change in the order of PT in the film are in general agreement with Pertsev's phase diagrams.

19.4.2 $BaTiO_3$

The combined low-frequency dielectric and thermo-optical analysis of FE PT is performed also for epitaxial films of FE $BaTiO_3$ (BTO) grown on (001) $SrTiO_3$ substrate using an $SrRuO_3$ bottom electrode. Because of an approximately 2% misfit between the lattices of BTO and epitaxial $SrRuO_3$ on $SrTiO_3$, the critical thickness for strain relaxation is smaller than 10 nm. The BTO films with thicknesses of 100 nm and larger are practically free of misfit strain. The room-temperature lattice parameters of the *c*-oriented 100–250 nm thick cube-on-cube-type (001) BTO films on $SrTiO_3$ are close to those of bulk BTO.

The temperature dependence of the derivative ξ (T) and the thermo-optical behavior $n(T)$ in the epitaxial BTO films on $SrTiO_3$ are shown in Figure 19.19. The PE state is evidenced at temperatures $T > 500$ K by both the derivative ξ (T) and the index $n(T)$. The FE state is detected at temperatures $T < 180$ K according to the dielectric response ξ (T), and at much higher temperatures $T < 500$ K according to the optical behavior $n(T)$. Similarly to the behavior of the PSTO film, here the temperature T_m of the dielectric peak $T_m \approx 330$ K is also significantly lower than the temperature $T_O \approx 500$ K. The "dielectric" width of the PT region determined from ξ (T) is very large, ~ 320 K, whilst the "optical" width according to $n(T)$ is only about 20–30 K. Similarly to the PSTO film, the dynamic dielectric non-linearity can also explain discrepancies between the "dielectric" and "optical" temperatures and widths of the FE PT in the BTO film (see insert in Figure 19.19). The combined observations show that the intrinsic PE–FE transition takes place at ~ 500 K.

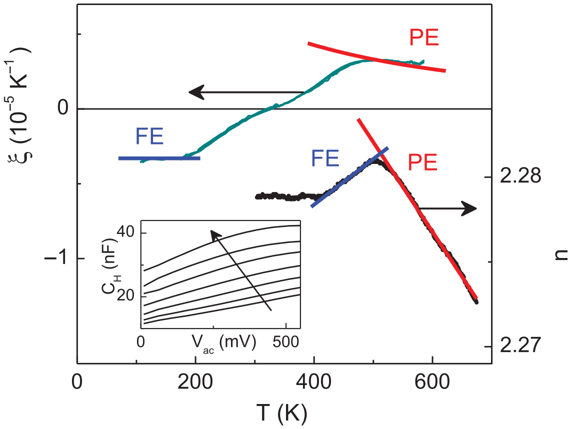

Figure 19.19 *The derivative ξ (left axis) and index of refraction n (right axis) as a function of temperature in the BTO film. Insert shows capacitance C_H as a function of amplitude V_{ac} of the probing AC voltage at different temperatures T = 103–293 K (from the lower curve up, as shown by the arrow)*

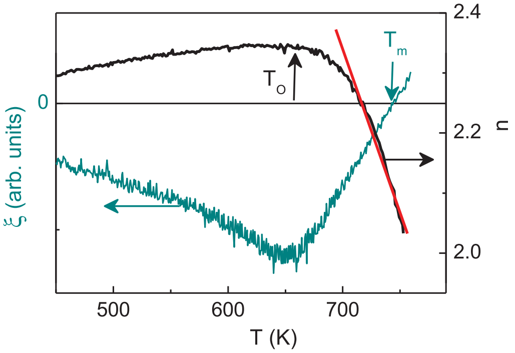

Figure 19.20 The derivative ξ (left axis) and index of refraction n (right axis) as a function of temperature in the $KTaO_3$ film

19.4.3 $KTaO_3$

Potassium tantalate $KTaO_3$ (KTO) in its bulk unstressed form is PE at all temperatures. When epitaxial KTO film is grown coherently on (001) $SrTiO_3$ substrate, the biaxial in-plane compressive strain as large as 2.1% can be achieved at room temperature [36, 69]. The FE PT in KTO films has been predicted theoretically for biaxial compression larger than 1% [70]. The strain-induced FE PT is evidenced by the derivative ξ (T) and the index $n(T)$ in the epitaxial KTO film (thickness ~ 9 nm) grown on conducting Nb-doped $SrTiO_3$ (Figure 19.20). Contrary to the temperature T_m being lower than the temperature T_O in the films of PSTO and BTO (Figures 19.18 and 19.19), the KTO film exhibits an inverse relationship: $T_m > T_O$. Notice that the temperature T_m is determined from the dielectric response which is measured using a Pt top electrode, while the optical properties are inspected using the bare surface of the thin KTO film. The top electrode ensures better screening of polarization charges than the surface of KTO. An incomplete screening suggests the presence of a depolarizing field acting against polarization and leading to lowering of the temperature of the FE PTs with decreasing film thickness [12–15, 71,72]. The observed difference between T_m and T_O is related to different screening conditions on the surface of the KTO nanofilm.

19.4.4 $PbSc_{0.5}Nb_{0.5}O_3$

Perovskite-structure films of RFE $PbSc_{0.5}Nb_{0.5}O_3$ (PSN) grow epitaxially on (001) MgO substrate using an $La_{0.5}Sr_{0.5}CoO_3$ bottom electrode layer despite the large lattice misfits in the heterostructure. A biaxial in-plane compressive strain exists in the cube-on-cube-type PSN film due to a mismatch between the thermal expansion coefficients of PSN and MgO. Here the crystal structure of PSN is metrically tetragonal, that is the out-of-plane lattice parameter c is larger than the two similar in-plane lattice parameters a: $(c/a - 1) \approx$ 0.4% [37].

The spontaneous R–FE PT is known to take place in bulk PSN at $T_s = 350–400$ K [69, 73 –78]. The main peculiarity of the derivative ξ (T) in the PSN film (Figure 19.21) is that indications of the low-temperature FE state are absent. Notice that the low-temperature

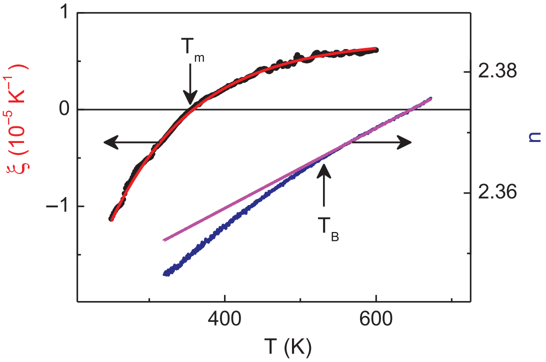

Figure 19.21 The derivative ξ (left axis, $f = 3$ kHz) and index of refraction n (right axis) as a function of temperature in the $PbSc_{0.5}Nb_{0.5}O_3$ film

Curie-type behavior evidencing the FE state is seen clearly in the bulk ceramic PSN sample (Figure 19.14). The derivative ξ (T) in the PSN film resembles the behavior ξ (T) in bulk PMN (Figure 19.13), without a spontaneous R–FE PT.

The index $n(T)$ in the PSN film is free of jumps or inflections, which could be ascribed to R–FE transition (Figure 19.21). The high-temperature part of $n(T)$ can be approximated by a linear dependence, as shown in Figure 19.21. The index $n(T)$ deviates from the linear behavior on cooling below ~ 550 K. The temperature at which the deviation starts is often interpreted as the Burns temperature T_B, which indicates the formation of polar entities in RFEs [56, 57]. The temperature T_B found in the PSN film is consistent with that in bulk PSN [23].

The derivative ξ (T) and the index $n(T)$ show that the spontaneous R–FE transition is frustrated in the PSN film. Additional studies of dynamic polarization and investigations of optical properties in epitaxial PSN films with different lattice strains have confirmed the absence of the FE state [37, 78]. Such a behavior cannot be explained in the frame of existing models. Further studies of possible mechanisms behind it are in progress.

19.5 Concluding Remarks

The measurement of the low-frequency dielectric response is a basic routine in characterization of thin films of the well-known FEs and RFEs, and of the novel materials. However, the intrinsic dielectric properties of the films cannot be extracted from the measured data in a straightforward manner as it can be done for bulk samples. The presence of extrinsic factors is inevitable in a thin-film capacitor, and ignoring this presence can bring misleading interpretations. To a certain extent, ambiguities can be reduced by extending ranges of conditions for dielectric measurements by varying frequency, temperature, and electric field. A careful equivalent circuit modeling and/or derivative analysis can help estimating intrinsic properties. A combination of the low-frequency dielectric characterization with thermo-optical studies can give a better insight into the intrinsic properties of thin films.

As shown here, the combination of methods can be successfully applied for analysis of the FE PTs. One of the intriguing observations enabled by the combined study is the narrow region of the intrinsic PE–FE PTs contrasted with broad dielectric peaks. Moreover, the temperature of the dielectric peak can be 100–150 K lower than that of PT. Another unexpected observation is the frustration of FE PTs in RFE films. A more detailed study is ongoing in order to gain a better insight into the observed behavior.

The combined analysis using optical characterization may reveal new physical phenomena in epitaxial FE films. It is worth mentioning that VASE is a rapidly progressing technique ensuring accurate analysis of optical constants in films of wide bandgap FEs with thicknesses as small as only a few nanometers and in the spectral range from infrared to deep ultraviolet. Theoretical support for studies of optical properties in epitaxial FE films is still missing and is urgently wanted.

Though this chapter has been focused on epitaxial films, the described methodologies may also be useful for studies of polycrystalline films. Moreover, the derivative analysis may be convenient for analysis of FE PTs and RFE behavior, not only in thin films but also in bulk ceramic or single-crystal samples.

Acknowledgments

The author is grateful to J. Levoska for fruitful discussions and valuable comments on the manuscript. She acknowledges her collaborators for their past and ongoing contributions: I. Jaakola, J. Narkilahti, and M. Plekh for sample preparation and dielectric measurements, D. Chvostova, E. Chernova, and A. Dejneka for optical characterization, P.-E. Janolin for encouragement and cooperation in studies of relaxors, and V. Trepakov for stimulating discussions. The author is thankful to I. Pintilie and L. Pintilie for cooperation in electrical characterization of thin films and to COST Action MP0904 for enabling this cooperation.

References

(1) Lines, M.E. and Glass, A.M. (2004) *Principles and Applications of Ferroelectrics and Related Materials*, Clarendon Press, Oxford.
(2) Strukov, B.A. and Levanyuk, A.P. (1998) *Ferroelectric Phenomena in Crystals: Physical Foundations*, Springer-Verlag, Berlin and Heidelberg.
(3) Fridkin, V.M. (1980) *Ferroelectric Semiconductors*, Consultants Bureau, New York.
(4) Smolenskii, G.A., Bokov, V.A., Isupov, V.A., et al. (1984) *Ferroelectrics and Related Materials*, Gordon and Breach, New York.
(5) Blinc, R. (2011) *Advanced Ferroelectricity*, Oxford University Press, Oxford.
(6) Uchino, K. (2000) *Ferroelectric Devices*, Marcel Dekker, New York.
(7) Buchanan, R.E. (ed.) (2004) *Ceramic Materials for Electronics*, Dekker, New York.
(8) Setter, N. (ed.) (2005) *Electroceramic Based MEMS*, Springer, New York.
(9) Ye, Z.G. (ed.) (2008) *Handbook of Advanced Dielectric, Piezoelectric and Ferroelectric Materials – Synthesis, Properties and Applications*, Woodhead Publishing Ltd, Cambridge.

(10) Ferraro, P., Grilli, S. and De Natale, P. (eds) (2009) *Ferroelectric Crystals for Photonic Applications: Including Nanoscale Fabrication and Characterization Techniques*, Springer, Berlin and Heidelberg.

(11) Knopf, G. and Otani, Y. (2013) *Optical Nano and Micro Actuator Technology*, CRC Press, Taylor and Francis Group, Boca Raton.

(12) Paz de Araujo, C., Taylor, G.W., and Scott, J.F. (eds) (1996) *Ferroelectric Thin Films: Synthesis and Basic Properties*, Gordon and Breach, Amsterdam.

(13) Setter, N., Damjanovic, D., Eng, L., et al. (2006) Ferroelectric thin films: review of materials, properties, and applications. *Journal of Applied Physics*, **100**, art. no. 051606.

(14) Schlom, D.G., Chen, L.Q., Eom, C.B., et al. (2007) Strain tuning of ferroelectric thin films. *Annual Review of Materials Research*, **37**, 589–626.

(15) Fridkin, V. and Ducharme, S. (2014) *Ferroelectricity at the Nanoscale: Basics and Applications*, Springer, Berlin and Heidelberg.

(16) McKee, R.A., Walker, F.J., and Chisholm, M.F. (1998) Crystalline oxides on silicon: the first five monolayers. *Physical Review Letters*, **81**, 3014–3017.

(17) McKee, R.A., Walker, F.J., and Chisholm, M.F. (2001) Physical structure and inversion charge at a semiconductor interface with a crystalline oxide, *Science*, **293**, 468–471

(18) Tsymbal, E.Y., Dagotto, E.R.A., Eom, C.B., and Ramesh, R. (eds) (2012) *Multifunctional Oxide Heterostructures*, Oxford University Press, Oxford.

(19) Гинзбург, В. Л. (2001) Фазовые переходы в сегнетоэлектриках. *Успехи Физических Наук*, **171**, 1091–1097, and references therein.

(20) Maksimov, E.G. (2009) Theoretical investigations of the ferroelectric transition. *Uspekhi Fizicheskikh Nauk*, **179**, 639–651.

(21) Blinc, R., Dolinšek, J., Gregorovič, A., et al. (1999) Local polarization distribution and Edwards–Anderson order parameter of relaxor ferroelectrics. *Physical Review Letters*, **83**, 424–427.

(22) Pirc, R. and Blinc, R. (1999) Spherical random-bond–random-field model of relaxor ferroelectrics. *Physical Review B*, **60**, 13470–13478.

(23) Bobnar, V., Filipič, C., Levstik, A., and Kutnjak, Z. (2010) High-temperature dielectric response of $(1 - x)Pb(Mg_{1/3}Nb_{2/3})O_3{-}xPbTiO_3$: Does Burns temperature exist in ferroelectric relaxors? *Journal of Applied Physics*, **107**, art. no. 084104

(24) Viehland, D., Jang, S.J., Cross, L.E., and Wuttig, M. (1992) Deviation from Curie–Weiss behavior in relaxor ferroelectrics. *Physical Review B*, **46**, 8003–8006.

(25) Sherrington, D. and Kirkpatrick, S. (1975) Solvable model of a spin-glass. *Physical Review Letters*, **35**, 1792–1796.

(26) Vugmeister, B.E. and Rabitz, H. (2000) Coexistence of the critical slowing down and glassy freezing in relaxor ferroelectrics. *Physical Review B*, **61**, 14448–14453.

(27) Bokov, A.A., Bing, Y.H., Chen, W., et al. (2003) Empirical scaling of the dielectric permittivity peak in relaxor ferroelectrics. *Physical Review B*, **68**, art. no. 052102.

(28) Zhao, Z., Buscaglia, V., Viviani, M., et al. (2004) Grain-size effects on the ferroelectric behavior of dense nanocrystalline $BaTiO_3$ ceramics. *Physical Revew B*, **70**, art. no. 024107.

(29) Speck, J.S. and Pompe, W. (1994) Domain configurations due to multiple misfit relaxation mechanisms in epitaxial ferroelectric thin films. I. Theory. *Journal of Applied Physics*, **76**, 466–476.

(30) Speck, J.S., Seifert, A., Pompe, W., and Ramesh, R. (1994) Domain configurations due to multiple misfit relaxation mechanisms in epitaxial ferroelectric thin films. II. Experimental verification and implications. *Journal of Applied Physics*, **76**, 477–483.

(31) Tyunina, M., Narkilahti, J., Levoska, J., et al. (2009) Ultrathin $SrTiO_3$ films: epitaxy and optical properties. *Journal of Physics: Condensed Matter*, **21**, art. no. 232203.

(32) Narkilahti, J. and Tyunina, M. (2012) The structure of strained perovskite $KTaO_3$ thin films prepared by pulsed laser deposition. *Journal of Physics: Condensed Matter*, **24**, art. no. 325901.

(33) Tyunina, M., Yao, L., Plekh, M., et al. (2013) Epitaxial ferroelectric heterostructures with nanocolumn-enhanced dynamic properties. *Advanced Functional Materials*, **23**, 467–474.

(34) Pertsev, N.A., Zembilgotov, A.G., and Tagantsev, A.K. (1998) Effect of mechanical boundary conditions on phase diagrams of epitaxial ferroelectric thin films. *Physical Review Letters*, **80**, 1988–1991.

(35) Pertsev, N.A., Tagantsev, A.K., and Setter, N. (2000) Phase transitions and strain-induced ferroelectricity in $SrTiO_3$ epitaxial thin films. *Physical Review B*, **61**, R825–R829.

(36) Tyunina, M., Plekh, M., and Levoska, J. (2009) Intrinsic dipolar glass behavior in epitaxial films of relaxor $PbMg_{1/3}Nb_{2/3}O_3$. *Physical Review B*, **79**, art. no. 054105.

(37) Tyunina, M., Levoska, J., Janolin, P.E., and Dejneka, A. (2013) Low-temperature relaxor state induced by epitaxial compression in $PbSc_{0.5}Nb_{0.5}O_3$ films. *Physical Review B*, **87**, art. no. 224107.

(38) Tyunina, M., Pintilie, I., Iuga, A., and Pintilie, L. (2014) Electric-field-induced transformations in epitaxial relaxor ferroelectric $PbMg_{1/3}Nb_{2/3}O_3$ films. *Physical Review B*, **89**, art. no. 094106.

(39) Tyunina, M., Plekh, M., Antonova, M., and Kalvane, A. (2011) Ferroelectric transitions in epitaxial $Pb_{0.5}Sr_{0.5}TiO_3$ films studied by dielectric analysis. *Physical Review B*, **84**, art. no. 224105.

(40) Miller, S.L., Nasby, R.D., Schwank, J.R., et al. (1990) Device modeling of ferroelectric capacitors. *Journal of Applied Physics*, **68**, 6463–6471.

(41) Junquera, J. and Ghosez, P. (2003) Critical thickness for ferroelectricity in perovskite ultrathin films. *Nature*, **422**, 506–509.

(42) Stengel, M. and Spaldin, N.A. (2006) Origin of the dielectric dead layer in nanoscale capacitors. *Nature*, **443**, 679–682.

(43) Tyunina, M. and Levoska, J. (2006) Application of the interface capacitance model to thin film relaxors and ferroelectrics. *Applied Physics Letters*, **88**, art. no. 262904.

(44) Gregg, J.M. (2006) Comments on "Application of the interface capacitance model to thin film relaxors and ferroelectrics". *Applied Physics Letters*, **89**, art. no. 196101.

(45) Tyunina, M. and Levoska, J. (2006) Response to Comments on "Application of the interface capacitance model to thin film relaxors and ferroelectrics". *Applied Physics Letters*, **89**, art. no. 196102.

(46) Rupprecht, G. and Bell, R.O. (1964) Dielectric constant in paraelectric perovskites. *Physical Review*, **135**, A748–A752.

(47) Bovtun, V., Kamba, S., Pashkin, A., et al. (2004) Central-peak components and polar soft mode in relaxor $PbMg_{1/3}Nb_{2/3}O_3$ crystals. *Ferroelectrics*, **298**, 23–30.

(48) Nuzhnyy, D., Petzelt, J., Kamba, S., et al. (2011) Infrared phonon spectroscopy of a compressively strained (001) $SrTiO_3$ film grown on a (110) $NdGaO_3$ substrate. *Journal of Physics: Condensed Matter*, **23**, art. no. 045901.

(49) Woollam, J.A., Johs, B., Herzinger, C., et al. (1999) Overview of variable angle spectroscopic ellipsometry (VASE), Part I: Basic theory and typical applications. *SPIE Proceedings*, **CR72**, 3–28.

(50) Johs, B., Woollam, J.A., Herzinger, C., et al. (1999) Overview of variable angle spectroscopic ellipsometry (VASE), Part II: Advanced applications. *SPIE Proceedings*, **CR72**, 29–58.

(51) Hilfiker, J., Bungay, C., Synowicki, R., et al. (2003) Progress in spectroscopic ellipsometry: applications from vacuum ultraviolet to infrared. *Journal of Vacuum Science and Technology A*, **21**, 1103–1108.

(52) Hilfiker, J., Singh, N., Tiwald, T., et al. (2008) Survey of methods to characterize thin absorbing films with spectroscopic ellipsometry. *Thin Solid Films*, **516**, 7979–7989.

(53) Fridkin, V.M. (1980) *Ferroelectric Semiconductors*, Consultants Bureau, New York.

(54) Dejneka, A., Aulika, I., Trepakov, V., et al. (2009) Spectroscopic ellipsometry applied to phase transitions in solids: possibilities and limitations. *Optics Express*, **17**, 14323–14338, and references therein.

(55) Fousek, J. and Petzelt, J. (1979) Changes of refractive indices of crystals induced by structural phase transitions. *Physica Status Solidi (A)*, **55**, 11–40.

(56) Burns, G. and Scott, B.A. (1973) Index of refraction in "dirty" displacive ferroelectrics. *Solid State Communications*, **13**, 423–427.

(57) Burns, G. and Dacol, F.H. (1982) Polarization in the cubic phase of $BaTiO_3$. *Solid State Communications*, **42**, 9–12.

(58) Kleemann, W., Schafer, F.J., and Fontana, M.D. (1984) Crystal optical studies of spontaneous and precursor polarization in $KNbO_3$. *Physical Review B*, **30**, 1148–1154.

(59) Bhalla, A.S., Guo, R., Cross, L.E., et al. (1987) Measurements of strain and the optical indices in the ferroelectric $Ba_{0.4}Sr_{0.6}Nb_2O_6$: polarization effects. *Physical Review B*, **36**, 2030–2035.

(60) Korshunov, O.Y., Markovin, P.A., and Pisarev, R.V. (1992) Thermo-optical study of precursor polarization in ferroelectrics with diffuse phase transitions. *Ferroelectrics Letters*, **13**, 137–142.

(61) Markovin, P.A., Kleemann, W., Lindner, R., et al. (1996) A crystal optical study of phase transitions in $Sr_{1-x}Ba_xTiO_3$ single crystals. *Journal of Physics: Condensed Matter*, **8**, 2377–2394.

(62) Merz, W.J. (1949) The electric and optical behavior of $BaTiO_3$ single-domain crystals. *Physical Review*, **76**, 1221–1225.

(63) Kleemann, W., Schafer, F.J., and Rytz, D. (1986) Crystal optical studies of precursor and spontaneous polarization in $PbTiO_3$. *Physical Review B*, **34**, 7873–7879.

(64) Wiesendanger, E. (1973) Dielectric, mechanical and optical properties of orthorhombic $KNbO_3$. *Ferroelectrics*, **6**, 263–281.

(65) Tyunina, M., Dejneka, A., Rytz, D., et al. (2014) Ferroelectricity in antiferroelectric $NaNbO_3$ crystal. *Journal of Physics: Condensed Matter*, **26**, art. no. 125901.

(66) Trepakov, V., Dejneka, A., Markovin, P., et al. (2009) A soft electronic band and the negative thermooptic effect in strontium titanate. *New Journal of Physics*, **11**, art. no. 083024, and references therein.

(67) Tyunina, M., Dejneka, A., Chvostova, D., et al. (2012) Phase transitions in ferroelectric $Pb_{0.5}Sr_{0.5}TiO_3$ films probed by spectroscopic ellipsometry. *Physical Review B*, **86**, art. no. 224105.

(68) Bassiri-Gharb, N., Fujii, I., Hong, E., et al. (2007) Domain wall contributions to the properties of piezoelectric thin films. *Journal of Electroceramics*, **19**, 47–65, and references therein.

(69) Malibert, C., Dkhil, B., Kiat, J.M., et al. (1997) Order and disorder in the relaxor ferroelectric perovskite $PbSc_{1/2}Nb_{1/2}O_3$ (PSN): comparison with simple perovskites $BaTiO_3$ and $PbTiO_3$. *Journal of Physics: Condensed Matter*, **9**, 7485–7500.

(70) Tyunina, M., Narkilahti, J., Plekh, M., et al. (2010) Evidence for strain-induced ferroelectric order in epitaxial thin-film $KTaO_3$. *Physical Review Letters*, **104**, art. no. 227601.

(71) Lai, B.K., Kornev, I.A., and Bellaiche, L. (2005) Phase diagrams of epitaxial $BaTiO_3$ ultrathin films from first principles. *Applied Physics Letters*, **86**, art. no. 132904.

(72) Kouser, S., Nishimatsu, T., and Waghmare, U.V. (2013) Ferroelectric domains and diffuse transitions in ultrathin films of $PbTiO_3$: effects of strain and electrodes. *Physical Review B*, **88**, art. no. 064102.

(73) Chu, F., Reaney, I.M., and Setter, N. (1995) Spontaneous (zero-field) relaxor-to-ferroelectric-phase transition in disordered $Pb(Sc_{1/2}Nb_{1/2})O_3$. *Journal of Applied Physics*, **77**, 1671–1676.

(74) Perrin, C., Menguy, N., Suard, E., et al. (2000) Neutron diffraction study of the relaxor–ferroelectric phase transition in disordered $PbSc_{1/2}Nb_{1/2}O_3$. *Journal of Physics: Condensed Matter*, **12**, 7523–7538.

(75) Abdulvakhidov, K.G., Mardasova, I.V., Myasnikova, T.P., et al. (2001) Phase transitions in lead scandoniobate $PbSc_{0.5}Nb_{0.5}O_3$. *Physics of the Solid State*, **43**, 508–512.

(76) Bidault, O., Perrin, C., Caranoni, C., and Menguy, N. (2001) Chemical order influence on the phase transition in the relaxor $Pb(Sc_{1/2}Nb_{1/2})O_3$. *Journal of Applied Physics*, **90**, 4115–4121.

(77) Raevskii, I.P., Eremkin, V.V., Smotrakov, V.G., et al. (2000) Spontaneous phase transition from relaxor to macrodomain ferroelectric state in single-crystal $PbSc_{0.5}Nb_{0.5}O_3$–$BaSc_{0.5}Nb_{0.5}O_3$ solid solutions. *Physics of the Solid State*, **42**, 161–164.

(78) Lynnyk, A., Chvostova, D., Pacherova, O., et al. (2013) Optical properties of epitaxial relaxor ferroelectric $PbSc_{0.5}Nb_{0.5}O_3$ films. *Applied Physics Letters*, **103**, art. no. 132901.

20

Interfaces in Epitaxial Ferroelectric Layers/Multilayers and Their Effect on the Macroscopic Electrical Properties

Lucian Pintilie, Andra G. Boni, Cristina Chirila, Luminita M. Hrib, Alin Iuga, Lucian Trupina, Ioana Pintilie, Iuliana Pasuk, Raluca Negrea, Corneliu Ghica, Mihaela Botea, Nicoleta Apostol, and Cristian M. Teodorescu

National Institute of Materials Physics, Romania

20.1 Introduction

Ferroelectric materials exhibit a string of non-linear properties, making them very attractive for applications, such as spontaneous polarization that can be reversed by applying an external electric field and that can be modified by applying a mechanical stress (piezoelectric effect) or a temperature variation (pyroelectric effect); a large dielectric constant that can be tuned with the electric field, magnetic field (in the case of multiferroics with a magnetocapacitive effect), and temperature; birefringence; photovoltaic properties; etc [1]. For a long time these materials were used in applications in the bulk form as single crystals or ceramics. Among the most known ferroelectrics are those with a perovskite structure like $BaTiO_3$ (BTO), $Pb(Zr, Ti)O_3$ (PZT), $LiTaO_3$, $LiNbO_3$, etc., but also organic crystals like triglycine sulfate (TGS) or polymers like polyvinylidene fluoride (PVDF) [2–5]. Ferroelectrics were first used mainly for sensing and actuation, as pyroelectric detectors in applications like

---

Nanoscale Ferroelectrics and Multiferroics: Key Processing and Characterization Issues, and Nanoscale Effects, First Edition. Edited by Miguel Algueró, J. Marty Gregg, and Liliana Mitoseriu.
© 2016 John Wiley & Sons, Ltd. Published 2016 by John Wiley & Sons, Ltd.

intruder alarms, motion sensors, thermal imaging, or as ultrasonic transducers for defectoscopy, such as piezoelectric motors, etc. [6]. However, the reversible polarization made the ferroelectrics attractive for applications in non-volatile memories, considering that the two opposite orientations of polarization can be associated to Boolean bits 0 and 1. In this case the ferroelectrics have to be in the form of thin films [7–10]. The most used methods to deposit thin films are chemical (sol–gel, metal–organic decomposition), radio-frequency (RF) magnetron sputtering, and pulsed laser deposition (PLD) [11–13]. Each method has its advantages and drawbacks: chemical methods, especially sol–gel combined with spinning, are of low cost and are suitable for deposition on large areas with uniform thickness and composition, but the films are polycrystalline in the vast majority of cases; RF sputtering is suitable for deposition on large areas with uniform thickness, both polycrystalline and epitaxial films, but has some problem in terms of composition uniformity; PLD can deliver high-quality epitaxial films with uniform thickness and composition, but only on small areas. The continuous improvement of the deposition methods has allowed researchers: to reduce the size of many of the devices based on ferroelectrics and to integrate them with the driving circuits based on semiconductors; to investigate the intrinsic properties of those ferroelectrics that cannot be prepared as bulk crystals (e.g. PZT) by studying epitaxial films in which the extrinsic contributions related to grain boundaries were removed [14–18].

The macroscopic properties of ferroelectrics such as polarization, dielectric response, leakage current, pyroelectricity, and photovoltaic activity are usually studied on samples with capacitor geometry known also as metal–ferroelectric–metal (MFM) structures. In this case the ferroelectric layer is sandwiched between two metal electrodes that can be of the same material or of different materials. Therefore, there will be two interfaces between the ferroelectric and the metal electrodes that can influence the macroscopic electrical properties. The effect of the interfaces at the macroscopic level is dependent on the structural quality of the ferroelectric and on the weight of the interface regions compared to the bulk. It is thus expected that the effect of electrode interfaces is negligible in bulk capacitors, especially in those based on ceramics, or in polycrystalline thin films [19, 20]. In these cases the grain boundaries can dominate the macroscopic electrical properties, hiding the effect of electrode interfaces. The situation may change in the films with columnar texture or in the epitaxial samples. Especially in the last case the effect of the electrode interfaces can dominate the macroscopic electrical properties [21, 22]. The study of the electrode interfaces is thus important in the case of epitaxial films in order to separate their contribution from those coming from the ferroelectric bulk.

The interfaces can also play a major role in the case of multilayers or superlattices, including those of epitaxial quality. An example of a multilayer is the metal–ferroelectric–semiconductor (MFS) structures with potential of application in non-volatile memories [23]. The capacitance–voltage (C–V) characteristic of such a structure is describing a hysteresis associated with polarization reversal, which has to be counterclockwise if the semiconductor is n-type and clockwise in the case of p-type semiconductor [24]. The width of the capacitive hysteresis is called the “memory window”. The larger the window the better is the retention of the written memory in the memory cell. However, if interface states are present these can introduce a parasitic hysteresis that adds destructively to the one associated with ferroelectric polarization, making the retention poorer [25]. MFS structures were deposited on Si, but it was found that the ferroelectric–Si interface is not very clean, especially for PZT [26,27]. This affects the memory window so buffer layers were used to obtain better interfaces. However, an insulating buffer layer such as SiO_2 may be detrimental for the magnitude of the polarization in the ferroelectric layer because it is not able to provide the necessary free carriers for compensating the depolarization fields [28]. Better results are obtained if ferroelectric buffers are used or if the Si is replaced with an oxide semiconductor like ZnO [29].

Another example of multilayer in which the interfaces play a major role is the artificial multiferroics combining layers of ferroelectric and ferromagnetic materials [30–32]. The mechanical coupling between the magnetostriction present in the ferromagnetic layer with the piezoelectricity present in the ferroelectric film can lead to a considerably enhanced magnetoelectric response compared to single-phase multiferroics like $BiFe_3$ (BFO). Electrostatic coupling between the layers can also result in the magnetoelectric effect [33]. In any case, the quality of the interface is important to obtain a good coupling between the two phases that can be used in four-state memory cells with an electric readout of the written information [34].

Generally speaking, interfaces in multilayers and superlattices can lead to many other new interesting effects, such as a considerable increase in the dielectric constant through polarization effects of the Maxwell–Wagner type [35]; the occurrence of polarization in materials that are not ferroelectric at room temperature, as, for example, $SrTiO_3$ (STO) [36]; the occurrence of 2D electron gas at interfaces between perovskite oxides [37, 38]; and thickness-driven phase transitions in ferroelectric–antiferroelectric superlattices [39]. Therefore, theseresults show that the study of the interfaces in relation to macroscopic properties is essential for a better understanding of the ferroelectric-based structures designed for specific applications like memories, sensors, or energy harvesting.

Several examples will now be given based on the study of interfaces in samples, including epitaxial ferroelectric thin films: electrode interface in MFM structures with the same bottom electrode ($SrRuO_3$–SRO) but with different metals as top contacts; PZT–ZnO MFS structures; and ferroelectric–ferromagnetic multilayers as "artificial multiferroics". Most of the results have been published but some new results that have not been published will also be presented.

20.2 Electrode Interfaces in Ferroelectric Capacitors

20.2.1 Interface Effects on the Macroscopic Properties

As mentioned in the introduction, the electrode interfaces are very important in the case of the epitaxial ferroelectric thin films because they seem to dominate the macroscopic electrical properties. This was indicated by recent theoretical and experimental studies suggesting a connection between the polarization and electronic properties of the interface [40–42]. The picture emerging from previous reports is that, at least in the case of epitaxial films, an MFM structure can be assimilated in a back-to-back connection of two Schottky diodes with a ferroelectric volume in between [43]. A model was developed taking into consideration the presence of the interfaces, and the effect of the bound polarization charges on the Schottky contact characteristics such as the built-in potential, the maximum electric field at the interface, the width of the depletion region, and the height of the potential barrier [44, 45]. The model was successfully applied to explain macroscopic electrical properties of epitaxial PZT and BTO thin films with a tetragonal distortion, such as leakage current and thickness dependence of the dielectric constant [18, 46–48]. All these studies have revealed that the polarization charges are in fact determining the interface characteristics and thus also controlling the properties of the MFM structures. This assumption is supported by the fact that the magnitude of the ferroelectric polarization, as well as the orientation of the internal electric field, are not dependent on the metal used as top contact; the height of the potential barriers and the position of the Fermi level are quasi-independent on the work function of the metal used as top electrode; and the dielectric constant is only slightly dependent on the metal used as the top contact.

20.2.1.1 Leakage Currents

As mentioned above, the model has been applied to both PZT and BTO films. It was found that this model works reasonably well only at relatively low voltages. At higher voltages the properties seem to be controlled by the bulk, suggesting that the conduction mechanism changes from interface-controlled Schottky emission (governed by the Simmons equation [49]) to something that may be space-charge limited currents (SCLC, although the thickness dependence is not fulfilled) or thermally activated hopping [50].

This is illustrated in Figure 20.1, where the current –voltage (*I*–*V*) characteristics of epitaxial tetragonal PZT and BTO films are compared. The circles indicate the voltage range where the conduction mechanism changes. One can see that at low voltages the temperature dependence is large, in agreement with Schottky emission over the potential barrier that is present at the electrode interface. At higher voltages the temperature dependence is significantly reduced, suggesting a change in the conduction mechanism.

Current–voltage (*I*–*V*) measurements were performed on epitaxial PZT and BTO films of 300 nm thicknesses, with different metals as top electrodes, and having the same bottom SRO electrode. Some influence on the shape of the *I*–*V* characteristics and on the magnitude

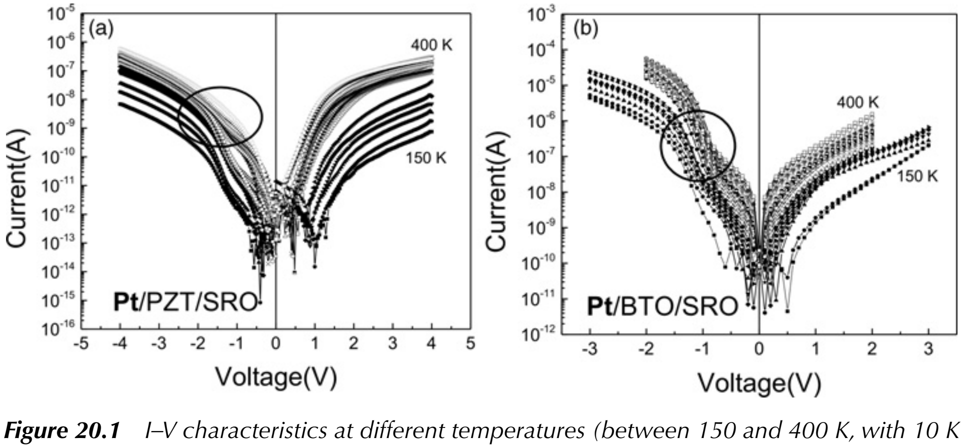

Figure 20.1 *I–V characteristics at different temperatures (between 150 and 400 K, with 10 K steps) for (a) PZT and (b) BTO tetragonal epitaxial films. In both cases the top electrode was Pt. The circles on the negative polarity show the change of the conduction mechanism at voltages of about 1.5 V and temperatures of about 290 K*

of the current was found, but the height of the extracted potential barriers is about the same although the work functions of the used metals are different [48]. Conduction mechanisms were investigated also in PZT compositions close to the morphotropic phase boundary. The experimental results are similar to those reported in the case of the PZT films with a tetragonal structure, suggesting a mixture between interface-limited mechanisms such as Schottky emission and bulk-limited mechanisms such as ohmic, space-charge limited, or thermally activated hopping. Under the action of the applied voltage, carriers are injected from electrodes into the film. At low voltages this process is controlled by the electrode interfaces. The carriers injected at one electrode are drifted by the applied voltage until they leave the film at the opposite electrode. This process is controlled by the bulk through carrier mobility. The height of the potential barrier was estimated using the same procedure as in [46] and [50]. The obtained values are 0.1 eV for top SRO, 0.4 eV for top Pt and Ir, and 0.2 eV for top Ru. It needs to be mentioned that Ir and Ru may oxidize at the interface with the PZT film, forming a very thin layer of metal oxide. RuO_2 is conductive and thus it may appear natural that the barrier height for the top Ru electrode is close to that of SRO. Pt and Ir are in the same period in Mendeleev's table and have similar work functions; thus they may give similar potential barriers. One can mention also that the effect of polarization on the barrier height seems to be less pronounced for PZT close to the morphotropic phase boundary compared to the PZT with a tetragonal structure. This may be due to the fact that the out-of-plane component of polarization is considerably reduced, but more studies are necessary to clarify this aspect.

20.2.1.2 Capacitance/Dielectric Constant

The dielectric constant at low frequencies, known also as the static dielectric constant, is calculated from capacitance. Usually the voltage and the frequency dependencies of capacitance are measured. In the case of ferroelectrics, the capacitance–voltage (*C–V*) characteristic has a butterfly shape, which is a fingerprint for the presence of switchable polarization. The presence of Schottky type contacts is indicated by the *C–V* measurements performed on PZT and BTO of different thicknesses [18]. An example is given in Figure 20.2 for BTO. The capacitance–voltage (*C–V*) characteristics in this case suggest that BTO film may reach a full depletion-like state easier than the PZT-based capacitors (see Figure 20.2(a)). This state is characterized by constant capacitance, which should be equal to the geometrical capacitance of the MFM structure. It can be seen in Figure 20.2 that for BTO films the capacitance reaches nearly constant values for voltages higher than 1 V, especially for negative polarity. In the case of the PZT the capacitance is still voltage-dependent up to the maximum voltage used for measurements. The fact that BTO films behave somehow differently compared to PZT can be related to the finding that the Ba–O bond is ionic in nature while the Pb–O bond has a high degree of covalency [51]. Therefore, on one hand BTO is closer to an insulator ferroelectric but on the other hand PZT is rather similar to a wide-gap semiconductor.

The effect of changing the top electrode has also been investigated. This was carried out on PZT compositions at the morphotropic phase boundary. Films with a Zr/Ti ratio of 52/48 were grown by PLD, both on single-crystal STO substrates with (001) orientation and on Si substrates with an epitaxial buffer layer of STO grown by MBE [52]. The growth of good-quality PZT on STO buffered Si wafers is an important step forward for the integration

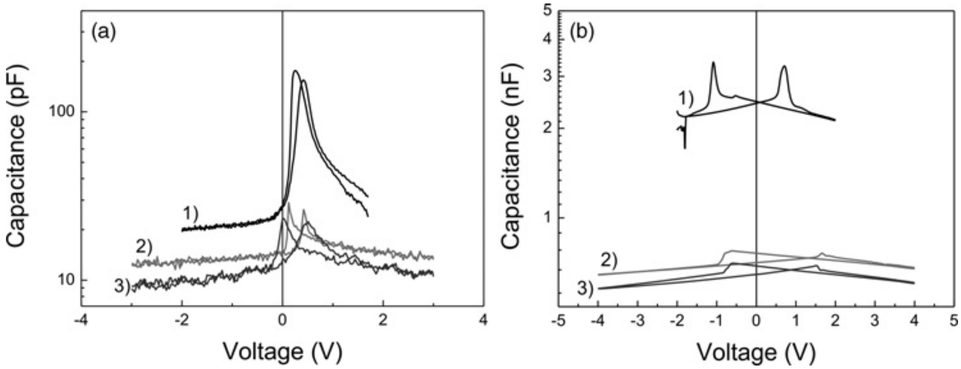

Figure 20.2 *C–V characteristics for (a) BTO layers of thickness of 25 nm (1), 56 nm (2), and 165 nm (3), the area of the top Pt contact is 40 x 40 μm^2, with an SRO bottom contact; and (b) PZT layers of thickness of 24 nm (1), 90 nm (2), and 216 nm (3), the area of the top SRO/Pt contact is 0.1 mm^2, with an SRO bottom contact*

of the PZT-based applications like piezoelectric transducers and actuators, or pyroelectric detectors, with the driving/signal processing circuitry.

Different metals were deposited as top electrodes, using RF sputtering or PLD in conjunction with a shadow mask leaving and an active area of 100 × 100 μm^2. The metals used were Pt, SRO, Ir, and Ru. Figure 20.3 presents the capacitance–voltage characteristics recorded at room temperature. Results are discussed along ferroelectric hysteresis loops presented in the next section.

20.2.1.3 Ferroelectric Hysteresis Loops

Corresponding ferroelectric hysteresis loops are shown in Figure 20.4.

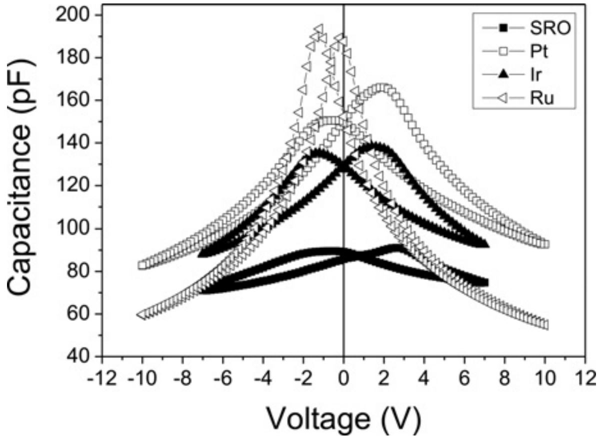

Figure 20.3 *C–V characteristics for a PZT layer (Zr/Ti = 52/48) deposited on an STO buffered Si substrate, with a bottom SRO electrode and different top ones*

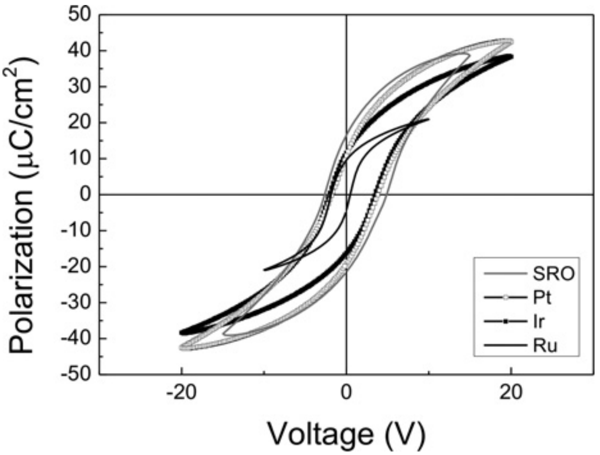

Figure 20.4 *Hysteresis loops for a PZT layer (Zr/Ti = 52/48) deposited on an STO buffered Si substrate, with bottom SRO electrode and different top ones*

It can be seen from Figure 20.3 and 20.4 that the simple change of the metal used for top contact triggers significant changes in the macroscopic properties, as follows:

- The shape of the *C–V* characteristic and hysteresis loop is changing, suggesting that the switching kinetics is dependent on the nature of the top interface. However, although the bottom electrode is always the same (SRO) and the metals used as top contacts are very different (the work functions are: 4.6–4.9 eV for SRO; 4.71 eV for Ru; 5.65 eV for Pt; 5.67–5.72 eV for Ir) [53,54], both the *C–V* characteristic and the hysteresis loop remain fairly symmetric in terms of capacitance and polarization values. This finding is consistent with the fact that the presence of the ferroelectric polarization is a property of the PZT layer. What can change when the top metal is changed is the switching mechanism (e.g. the nucleation of opposite domains at the interface is different for different metals) and the time for compensating the depolarization field.
- The dielectric constant that can be extracted from the *C–V* characteristic is not related only with the PZT layer but with the entire MFM structure. This means that interface-related capacitances are important.
- The shift observed on the voltage axis for some metals suggest the presence of an internal electric field. The shift is small in the case of top Pt and Ir although the work function difference compared to the bottom SRO electrode is significant. On the other hand, the shift is important in the case of the Ru top electrode although the work function difference is negligible. The shift towards negative voltages in this case (hot electrode on top) suggests an electric field oriented towards the bottom SRO contact. These results suggest that the voltage shift (imprint) is not related to the work function difference and should have other origins: non-uniform distribution of charged defects (e.g. oxygen vacancies as it will be illustrated later), different properties of interfaces, etc.

The above results point towards a strong effect of electrode interfaces on the electric properties as well as towards a strong influence of ferroelectric polarization on the characteristics of these electrode interfaces. In a perfect ferroelectric, a monodomain state means that all the elementary dipoles are oriented in one direction. At the end there will be a sheet of positive charges at one electrode and a sheet of negative charges at the other electrode. This situation will generate a depolarization field. In order to preserve the monodomain state, the depolarization field has to be immediately compensated with an electric field of opposite direction so that the total field in the MFM structure is zero. This can be done with free carriers from the ferroelectric film itself or from the electrodes. The compensation charges have to be located in the electrode interface region. Therefore, the picture emerging is that the MFM structure is practically depleted in the volume and that all the charges, either bound polarization charges or free charges for compensation, are located in the interface region. In order to have a stable situation, the free charges for compensation have to be blocked somehow in the interface region. This is possible by having potential barriers blocking the spillover or by trapping. When the polarization is switched, then all the charges for compensation have to move from one interface to the other. If the trapped charge involved in the compensation process of the depolarization field is negligible then the hysteresis loop should be close to rectangular because the free charges can move more easily from one interface to the other, while the trapped charges need some time to be emitted from the trapping center (emission time reversal proportional to the emission rate) into the conduction or valance band [55]. A few other details have to be mentioned and discussed in relation to hysteresis loops of MFM structures:

- Almost perfect rectangular loops can be obtained in the case of epitaxial PZT tetragonal films grown on (001) STO layers [17, 18, 46, 47].
- In the case of epitaxial PZT films for which the polarization direction is not perpendicular to the electrodes, the loop is no longer rectangular. This is because the applied electric field only switches the polarization component perpendicular to the electrodes. This makes the compensation of the depolarization field more complicated, because of the charges involved in compensating the in-plane polarization component. Therefore, the compensation of the total polarization charges responsible for the depolarization field may be only partial. This leads to backswitching effects, reflected in a more elongated shape of the loop, with remnant polarization smaller than the saturated one. This is the case for the films with a Zr/Ti ratio of 52/48, which seems to be a mixture of tetragonal, rhombohedral, and monoclinic phases (see Figure 20.4) [56].
- In polycrystalline films the amount of structural defects is very high, much higher than in epitaxial structures. These mean that the density of the trapping centers affecting the movement of the free carriers involved in compensation of the depolarization field is larger, leading to significant delays in compensation when the polarization is switched. This leads to backswitching phenomena in the hysteresis loops, manifested in elongated loops even for PZT layers with Zr/Ti ratios corresponding to the tetragonal structure (see Figure 20.5, hysteresis for epitaxial and polycrystalline PZT with the same composition).

It is clear that the difference in structural quality has a significant impact on the polarization switching, reflected in the shape of the hysteresis loop and on the magnitude of the current density, which is about two orders of magnitude lower in polycrystalline films. The reasons for this fact can be a lower mobility of the charge carriers and a lower density of free carriers, both results of the high density of structural defects acting as trapping and/or scattering centers.

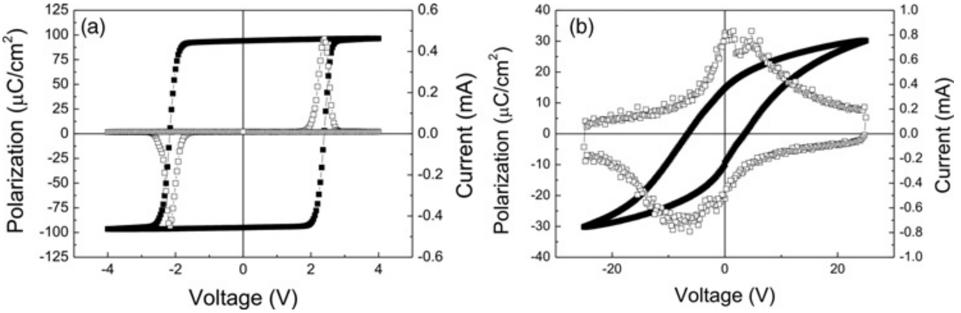

Figure 20.5 *(a) Hysteresis loops for current and polarization in the case of an epitaxial PZT tetragonal film (Zr/Ti ratio of 20/80, thickness about 200 nm) grown on (001) STO, with a bottom SRO contact and top Cu electrodes (0.0057 mm^2). (b) Hysteresis loops for current and polarization in the case of a polycrystalline PZT film (Zr/Ti ratio of 20/80, thickness about 300 nm) grown on Pt/Si substrate and top Pt electrodes (0.275 mm^2)*

20.2.1.4 Photovoltaic Properties

The photovoltaic properties of the ferroelectric also reflect the role of the interfaces. The photovoltaic properties have been investigated by measuring the short-circuit current under illumination with light of appropriate wavelength. It is known that the existence of a bulk photovoltaic effect in ferroelectric ceramics and crystals is able to produce voltages much larger than the band-gap of the material, which was previously reported by Fridkin and Popov [57]. However, it was found that in thin films the magnitude and orientation of the short-circuit current is dependent on the metal used as the top contact, suggesting in this way that, at least in thin films, the origin of the photovoltaic effect may be related to the presence of the Schottky contacts in the same way as in the case of meta–semiconductor contacts [58]. Figure 20.6 present spectral distributions of the short-circuit current recorded for the case of different metals used as top contacts.

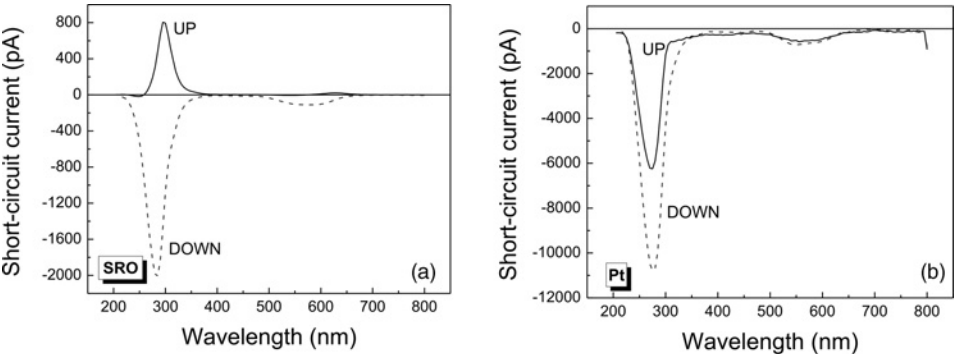

Figure 20.6 *Short-circuit photocurrent recorded in the case of an epitaxial PZT layer after imposing different orientations of polarization (UP: polarization towards the top electrode; DOWN: polarization towards the bottom electrode). The bottom contact was SRO in both cases, while the top electrode was SRO in (a) and Pt in (b)*

Regarding Figure 20.6, it has to be mentioned that the measuring protocol was as follows: in the first stepthe sample was poled UP or DOWN by applying a suitable voltage on the top electrode (negative for UP and positive for DOWN); in the second step the short-circuit current was measured after removal of the poling voltage. It can be seen that:

- The sign of the photocurrent is dependent on the polarization orientation for the top SRO contact. This fact suggests that the imprint (internal electric field) is negligible and the orientation of the polarization set by the poling procedure is not affected. For top Pt the photocurrent has the same sign, although the magnitudes are different. This fact suggests that the imprint is strong enough to impose a certain direction of polarization after removal of the poling voltage. In this case the internal electric field is favoring the DOWN polarization. Therefore, although the sample was poled also as UP, the imprint has switched most of the polarization to the DOWN orientation after removing the external voltage. This is the reason why the short-circuit current has the same sign for the top Pt contact [59].
- The magnitude of the photocurrent is dependent on the metal used as the top contact [60]. This is a result supporting the hypothesis that in ferroelectric epitaxial thin films the origin of the photovoltaic effect is related more to the Schottky contacts present at the electrode interfaces than to the bulk effect found in crystals or ceramics.
- A signal is present at wavelengths well below the absorption threshold (around 600 nm). This is possible if there are defect levels located deep into the gap. The carriers trapped on these levels can be excited with light if the wavelength corresponds to the energy difference between the trapping level and the nearest band (conduction band for electrons or valence band for holes) [18].

Previous studies have shown that the band-gap of the PZT materials can be modified by varying the Zr/Ti ratio [61]. For good-quality epitaxial films the forbidden band can vary between 3.9 eV for Ti-rich compositions up to 4.4 eV for Zr-rich compositions. This fact opens good perspectives in using PZT epitaxial films for UV detection. However, the temperature stability of the detector characteristics is an important issue in this case. Therefore it is important to know if the magnitude of the band-gap is changing with temperature. This will give an indication of whether the spectral domain of sensitivity is changing with the ambient temperature of the detector. To clarify this aspect, spectral distributions at different temperatures were performed on an epitaxial PZT thin film with a Zr/Ti ratio of 20/80. The bottom and top electrodes were SRO. SRO was preferred as the top contact because the signal is higher in this case, as shown in Figure 20.6. The width of the band-gap was estimated from the onset of the spectral distribution at large wavelengths. The results are presented in Figure 20.7.

It can be seen that the band-gap is approximately constant up to about 250 K and then starts to decrease with increasing temperature. The decrease is of about 1 meV K^{-1}. The change in band-gap could be related to the changes in the lattice constant, knowing that the tetragonal distortion and the associated polarization decreases with temperature until they disappear at the structural phase transition taking place at the Curie temperature. This result shows that the spectral response of a UV detector manufactured from a tetragonal, epitaxial PZT film can change at elevated temperatures. Such a finding is important for applications.

As mentioned above, the existence of a short-circuit current at wavelengths corresponding to energies below the width of the band-gap (see Figure 20.6) suggests the presence of

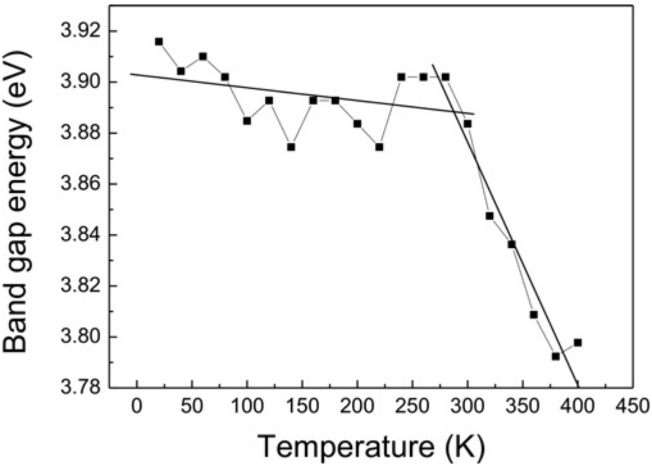

Figure 20.7 *The temperature dependence of the band-gap in epitaxial tetragonal PZT thin films with top and bottom SRO electrodes*

some trapping levels in the gap. This was partly confirmed by performing "optical charging spectroscopy" (OCS) measurements. This is a method used to investigate trapping levels. Basically it consists of the following steps: (1) cooling down the sample in short circuit; (2) charging the traps at low temperature by illumination with light; (3) heating the sample and recording the short-circuit current generated by emptying the trapping levels; (4) cooling down the sample again and recording the "dark" current, the current measured without filling the traps with illumination; and (5) subtraction of the "dark" current from the current measured after filling the traps with light, to obtain the true OCS signal [62]. Figure 20.8 presents an OCS spectra for an epitaxial PZT film with top and bottom SRO contacts.

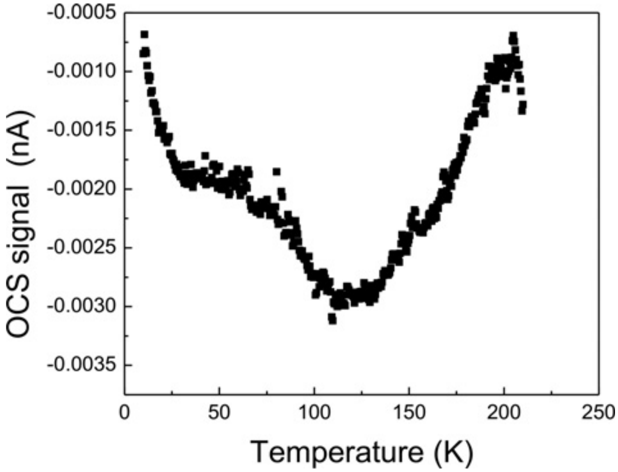

Figure 20.8 *OCS spectra for a PZT capacitor. The filling of the traps was performed with white light*

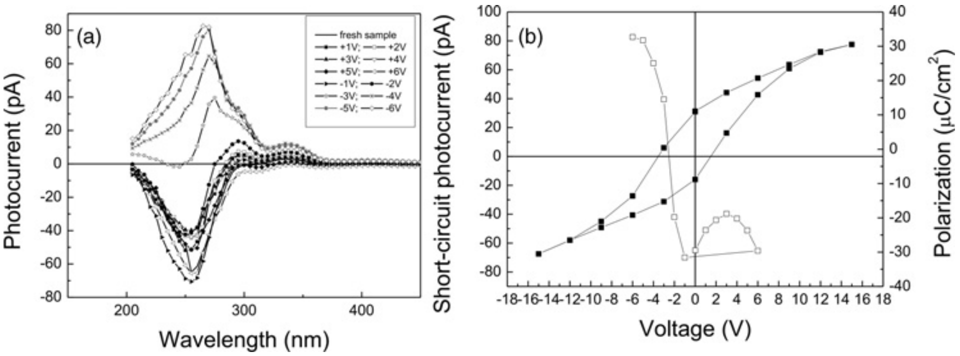

Figure 20.9 *(a) The spectral distributions recorded for a polycrystalline film of PZT, with top and bottom Pt electrodes, after applying different poling voltages, between −6 V and +6 V, step 1 V; (b) the static hysteresis (recorded at 100 Hz with a waiting time of 1 s and an integration time of 1 ms [63]) and the short-circuit photocurrent measured at a wavelength of 280 nm for the different poling voltages used for (a)*

It can be seen that there are traps in the PZT that are releasing free carriers up to about 200 K. The increase of the OCS current at very low temperatures can be an artifact due to the measured values, which were at the measurement limit of the Keithley 6517 electrometer. In any case, it appears that there is a first group of levels discharging around 50 K and then a level discharging near to 200 K. The defects associated with these trapping levels are hard to localize. They can be point defects from the volume or defects located just near the interface, but more probably near the top one because the top contact was usually deposited at room temperature. Therefore it can be assumed that there are more defects at the top interface than at the bottom one.

The short-circuit photocurrent was measured also in polycrystalline PZT thin films deposited by sol–gel on Pt/Si substrate. Results are presented in Figure 20.9.

Looking at Figure 20.9, it can be seen that the shape of the spectral distribution is changing with the poling voltage, suggesting a change in the internal electric field during illumination [59]. The photocurrent does not describe a full hysteresis loop as in the case of epitaxial films [61]. However, the photocurrent has about the same magnitude but with opposite signs for maximum poling voltage. This result is in agreement with previous reports [61]. Another finding is that the photocurrent is with at least one order of magnitude smaller than in the case of epitaxial samples due to the structural defects (mainly grain boundaries) acting as trapping and scattering centers, leading to lower values for the lifetime of the photogenerated carriers.

20.2.1.5 Pyroelectric Properties

Pyroelectric properties in MFM structures in relation to structural quality and type of substrate were also studied. The pyroelectric signal was measured under IR irradiation with the active element mounted to work in the voltage mode [64]. The frequency dependence of the signal was found to have a plateau at low frequencies (constant signal), followed by a linear decrease (in log–log scale) at high frequencies, as shown in Figure 20.10(a) for an epitaxial PZT film deposited on SRO/STO substrate. An interesting result is obtained for

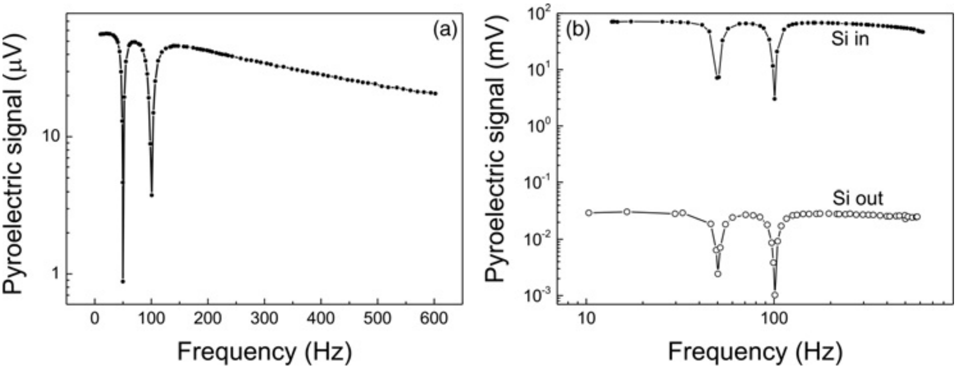

Figure 20.10 *(a) The frequency dependence of the pyroelectric signal of an epitaxial PZT film; (b) the frequency dependence of a polycrystalline ferroelectric film grown on a Pt/Si substrate. Illumination was performed with 800 nm wavelength in both cases. "Si in" and "Si out" means that the Si substrate was included or not in the measuring circuit of the pyroelectric signal. The drops in signal registered at 50 and 100 Hz are due to the notch filters used to suppress the parasitic influence of the power supply network*

polycrystalline layers deposited on Pt/Si substrates (Pt/PZT/Pt/Si structures): at illumination with 800 nm the signal is about three orders of magnitude larger when the Si substrate is included in the circuit of the pyroelectric element compared to the case when it is not included. The Si is not included in the circuit when the external contacts are on the Pt electrodes sandwiching the ferroelectric layer. If the "bottom" contact is made by covering with silver paint the bottom surface of the Si substrate (the surface opposed to the one on which the Pt/PZT/Pt sandwich is deposited) then the Si is included in the circuit. In the latter case the structure is Pt/PZT/Pt/Si/Ag, with one external contact on the top Pt electrode and the other on the bottom Ag electrode. In this case, the Si resistance changes due to the carriers that are photogenerated in the semiconductor by the modulated light falling on the top surface of the structure, whenever the wavelength of the incident light is absorbed in the Si substrate. This change in resistance affects the distribution of the electric fields in the entire structure, influencing the polarization magnitude in the PZT layers via the Pt electrode located between the Si and PZT. Therefore, an extrinsic contribution is brought to the intrinsic pyroelectric signal generated by the standard MFM structure represented by the Pt/PZT/Pt sandwich. The intrinsic pyroelectric signal is the one measured when the Si substrate is not included in the circuit. Further studies are needed in order to clarify this curious phenomenon. Figure 20.10(b) shows a comparison between signals measured with and without the Si substrate included in the measuring circuit. It was also found that the "pyroelectric coefficient" is larger for epitaxial samples compared to polycrystalline ones with up to about one order of magnitude [65]. This may be due to the fact that the polarization value is larger, as well as to the fact that ferroelectric domains can move more easily due to a lower concentration of structural defects.

20.2.1.6 Only-One Schottky Diode Structures

It was found that for some top electrodes single Schottky diodes with ferroelectric behavior can be found, as for the case for top Ta or top Al [66, 67]. The typical *C–V*

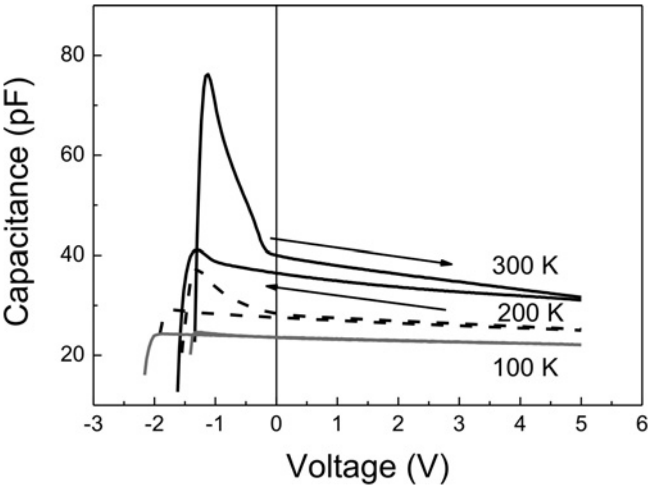

Figure 20.11 *The C–V characteristics for a Schottky-type ferroelectric diode based on an SRO–PZT–Ta structure. The arrows show the direction of the voltage sweep*

characteristics of a Schottky diode are obtained, but these only show hysteresis when the voltage is swept up and down, in agreement with the presence of the spontaneous polarization in the ferroelectric layer (see Figure 20.11, presenting recorded *C–V* characteristics for different temperatures).

It is interesting to observe that the difference in the measured capacitance when the voltage is swept up and down increases with the temperature. This fact can be related with the concentration of free carriers in the PZT film. At low temperatures the concentration is very low, the film is fully depleted, and the difference in the capacitance values when the polarization is oriented UP or DOWN is negligible. Practically the capacitance is voltage independent except in the case when free carriers are injected into the film through the assumed rectifying interface (in the present case the SRO–PZT interface). This corresponds to forward bias, when the capacitance of the space charge region associated to the Schottky contact is, practically, disappearing (manifested as an abrupt drop, going even to negative values [66]). As the temperature increases the concentration of the free carriers increases and the film becomes partly depleted. The contribution of the capacitance related to the space charge region to the measured values is increasing. When the voltage applied on the top Ta contact (assumed to be ohmic) is swept up from negative to positive values the polarization starts with an UP orientation (towards the top contact). This means a negative polarization charge near the bottom SRO–PZT interface. Electrons are repelled and holes are attracted for compensation. On the other hand, the negative applied voltage has an opposite effect, pushing electrons towards the SRO–PZT interface (forward bias). The overall effect is a high capacitance value, corresponding to a significant density of free carriers able to respond to the small-amplitude AC voltage used for capacitance measurements. Polarization switching occurs at some point, increasing the voltage from negative to positive. This means the DOWN polarization and positive bound charges near the SRO–PZT interface. Electrons will be attracted for compensation, but the effect of the applied positive

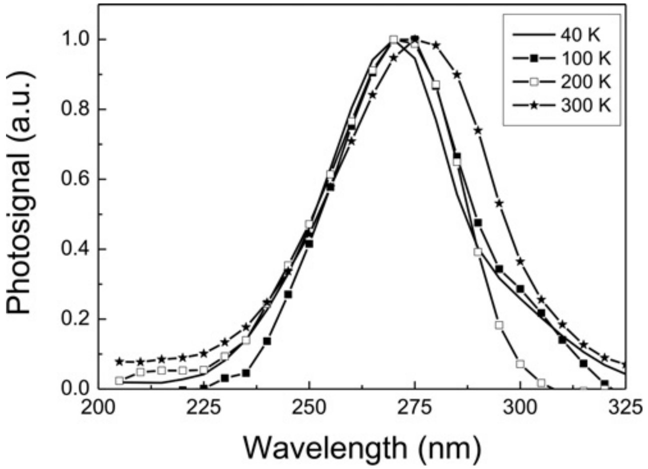

Figure 20.12 *Spectral distributions of the short-circuit photocurrent recorded at different temperatures for a Schottky-type ferroelectric diode based on a Ta–PZT–SRO structure (the signal was normalized to the maximum value)*

voltage is opposite (reverse bias). Both DOWN polarization and applied voltage are blocking free carriers, reflected in the low value of capacity. The change occurs near zero volts at 300 K. When the voltage is swept down from positive to negative the reverse processes take place: polarization starts with the DOWN orientation and ends UP, while the rectifying SRO–PZT contact starts with a reverse bias and ends with a forward one. The capacitance is low at the beginning and starts to increase below –1 V. However, the increase is lower in this case. This is because the UP orientation is less stable than the DOWN one [66]. As can be seen from Figure 20.8(a) the capacitance for DOWN is almost twice the value for UP polarization at a voltage of –1 V and 300 K. This difference could have been speculated in a memory cell, associating high capacitance to bit 1 and low capacitance to bit 0. Unfortunately, the instability of the UP orientation of polarization makes this impossible.

Figure 20.12 shows the spectral distributions of the short-circuit photocurrent for a single ferroelectric Schottky diode at different temperatures. It can be seen that the maximum in the spectral distribution shifts to higher wavelengths as the temperature increases, suggesting a smaller band-gap, in agreement with the results presented in Figure 20.7. The onset of photocurrent is also dependent on temperature. At low temperatures there is a tail at long wavelengths, suggesting the presence of some occupied states just near the bands. It appears that these are emptied at 200 K, when the tail disappears. This result is in agreement with the OSC measurements presented in Figure 20.8 and showing broad OCS peaks up to about 200 K. The peaks correspond to thermal emptying of trapping levels responsible for the tail in the spectral distributions.

Figure 20.13 shows that a ferroelectric Schottky diode can act as a photovoltaic cell. It can be seen that the current under illumination with UV light is significantly larger than the dark current. This result opens the perspective to use ferroelectrics in new generations of solar cells. The problem is that the conversion efficiency is very small, well below 1%. It can be improved by combining ferroelectrics with oxide semiconductors having smaller band-gap (e.g. CuO_x) [68].

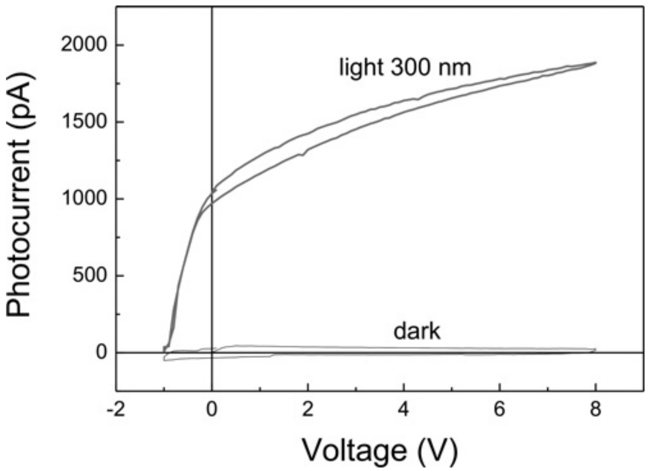

Figure 20.13 *Current–voltage characteristics under illumination with 300 nm wavelength and in dark for an epitaxial Ta–PZT–SRO structure with Schottky-like behavior*

As a conclusion to the present section, one can say that electrode interfaces have a considerable impact on the macroscopic electrical properties and that the interface characteristics are largely controlled by the ferroelectric polarization. The effect of polarization on quantities such as barrier height, built-in potential, and photovoltaic voltage is clearly visible in the case of epitaxial films. The influence starts to diminish in polycrystalline films, where the volume grain boundaries start to have a significant impact on the polarization switching and on the charge transport. Electrode interfaces can also mediate interaction with substrate, as observed for the abnormal pyroelectric effect in ferroelectric films deposited on Pt/Si and illuminated with light absorbed in Si.

20.2.2 Analysis of Free Surfaces and of Electrode Interfaces by AFM/PFM, XPS, and TEM

In order to establish a relation between the macroscopic properties and the microscopic properties (structure, composition, domain structure, etc.) of ferroelectric thin films some studies were performed using techniques such as AFM/PFM (piezo-force microscopy coupled with atomic force microscopy), XPS (X-ray photoelectron spectroscopy), and TEM (transmission electron microscopy). AFM/PFM technique can be used to determine the polarization orientation in the films and the polarization stability on the free surface. Firstly, the amplitude and phase of the out-of-plane PFM signal was recorded on the surface of the film (see Figure 20.14(a) for an epitaxial tetragonal PZT film of about 150 nm). It can be seen that the phase has a nearly homogeneous contrast, suggesting a preferential out-of-plane orientation of polarization. If 180° domains had been present, then areas of different contrast would have been observed in the phase signal, but this is not the case. However, the characteristic grid of 90° domains is visible in the amplitude signal. The presence of these domains is normal in films above 100 nm thickness [69]. Further on, areas of opposite orientation of polarization have been “written” by applying suitable voltages on the AFM

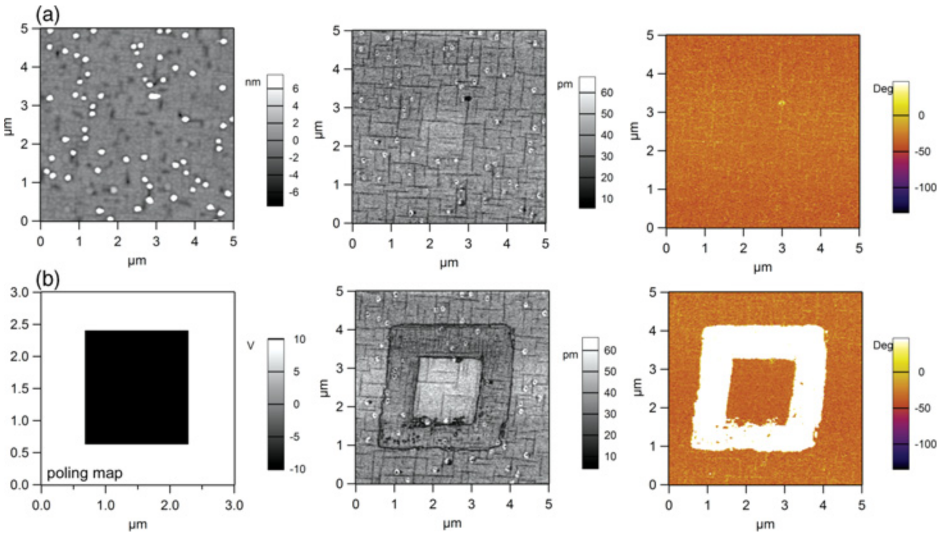

__Figure 20.14__ (a) The topography, the amplitude of the PFM signals, and the phase of the same signal as recorded on the free surface of an unpoled sample; (b) the poling map, the amplitude, and the phase for artificially written domains using the PFM tip

tip (see Figure 20.14(b)). It can be seen that areas with opposite orientations of polarization have a very different contrast in the phase signal. Comparing the contrast of these areas with the initial contrast of the phase signal one can find the dominant orientation of polarization in the unpoled PZT film. In the present case the dominant orientation seems to be UP (towards the surface), but this is dependent on various conditions (substrate, oxygen content) and may change in time due to the ambient atmosphere [70, 71].

The stability of the polarization can also be checked with PFM. For this purpose areas of opposite orientations are "written" with the PFM tip and their phase signal is monitored with time. If one of the orientations is not stable, then the contrast of the respective area changes with time. Examples are presented in Figure 20.15(a) for a PZT layer grown on a single-crystal STO substrate (the same from Figure 20.14), while in Figure 20.15(b) the time evolution for artificially written domains is presented in the case of a BTO film with a thickness of about 100 nm. It can be seen that in the first case both directions of polarization are stable with time (up to one hour) while in the second case one direction of polarization is not stable. In Figure 20.15(b) it can be seen that after 30 minutes changes in the contrast of the phase signal occurs on the area poled with –10 V applied on the tip, suggesting that the UP polarization is not stable in this case. As mentioned above, the stability of polarization direction can be influenced by many factors such as: the imprint (manifested as the shift of the hysteresis loop along the voltage axis due to some internal electrical field); surrounding atmosphere that can change the surface chemistry; structural defects, etc. In the present case it was found that the BTO film is imprinted negatively (hysteresis shifted towards negative voltages), corresponding to an internal electric field oriented from the surface towards the bottom SRO electrode. Such a field will favor the DOWN orientation of

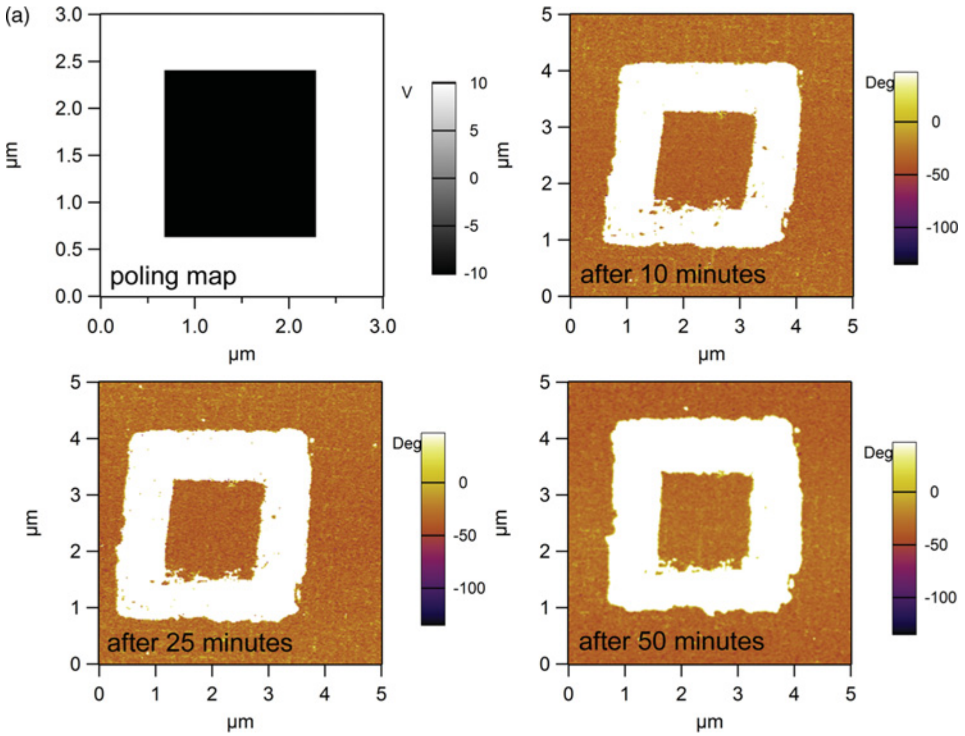

__Figure 20.15__ (a) The polarization stability investigated on the free surface of an epitaxial tetragonal PZT film grown on an STO single crystal with a bottom SRO electrode (thickness about 150 nm); (b) the polarization stability investigated on the free surface of a BTO film grown on an STO single crystal with a bottom SRO electrode (thickness about 100 nm)

polarization, making the UP orientation less stable, in agreement with the results presented in Figure 20.15(b).

Interesting results were obtained also in the case of different top metals. For example, it was found that the polarization stability is different on the free surface and on Ta top contact. Figure 20.16(a) shows the time evolution of the poled areas on the free surface and on the Ta electrode. The poling was done using the same poling map as in Figure 20.15(a) only that the poled areas are located partly on the free surface and partly on the Ta contact (represented by the triangle on the right side of the figures). It was found that on the free surface both UP and DOWN polarizations are relatively stable in time (as in the case of Figure 20.15(a)). This is suggested by the fact that the contrast for the phase signal corresponding to areas of opposite orientations of polarization does not change. For the Ta contact neither polarization orientation seems to be stable, as the contrast evolves to the values found from the beginning on the Ta electrode (see the contrast outside the poled area). This fact suggests that the Ta contact does not form a potential barrier with the PZT layer, able to block the free carriers for compensation. Therefore, it can be assumed that Ta on PZT behaves as an ohmic contact, in agreement with the results of electrical measurements performed on SRO–PZT–Ta structures showing Schottky-like behavior (see Figure 20.11). The same

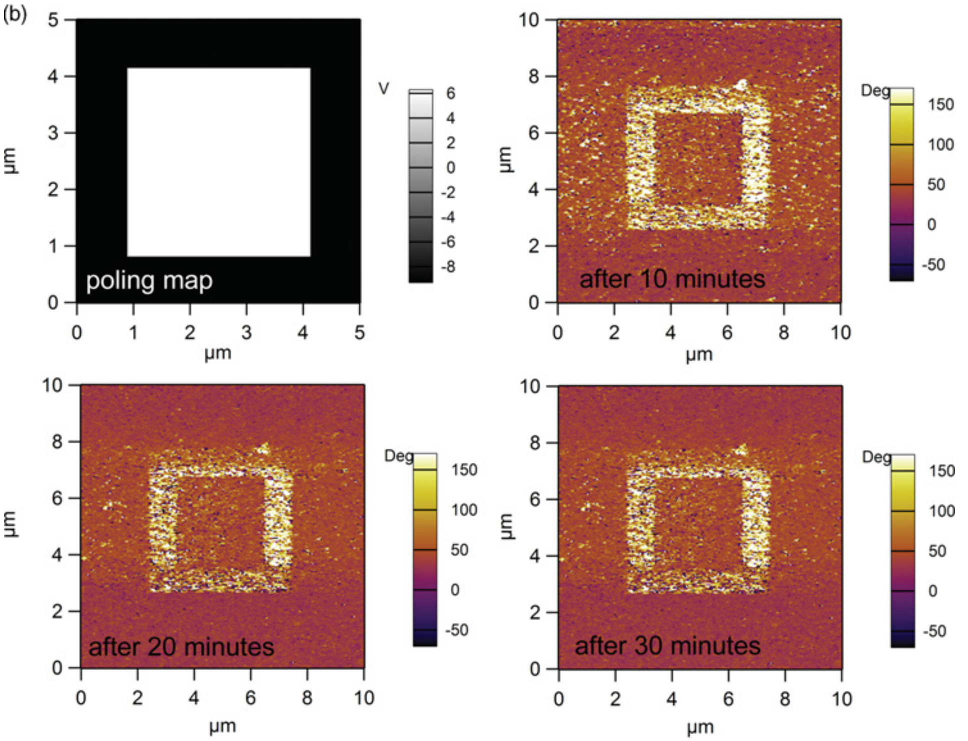

Figure 20.15 (Continued)

experiment performed for top Au suggests that the polarization is stable with time both on the free surface and on the Au electrode (see Figure 20.16(b)). This is in agreement with the results of electrical measurements showing the presence of a potential barrier of about 0.2–0.3 eV at the PZT/Au interface [48].

Further information regarding the properties of surfaces/interfaces in ferroelectric thin films can be obtained from X-ray photoelectron spectroscopy (XPS). This technique can reveal the position of the Fermi level at the surface/interface, the band bending at the surface/interface, possible influence of polarization on the band bending, and the surface/interface composition. Indeed, the XPS studies performed on the free surface have revealed the fact that the values for the binding energies are dependent on the polarization orientations which, in turn, are dependent on the sample history [70, 72]. The binding energies are higher if the polarization is UP or P+ (meaning that the polarization charge at the surface is positive) and are lower if the polarization is DOWN or P– (meaning that the polarization charge is negative). For in-plane polarization or P0 the binding energies are in between the values for P+ and P–. The as-deposited samples seem to be mostly P+ (UP polarization) as an effect of the strain imposed by the substrate. However, with time the surface is contaminated and the polarization switches to P0 (large percent) and P– (small percent). Therefore, a moderate thermal annealing is necessary to remove the contaminants and to restore as much as possible the initial conditions, respectively the P+ orientation

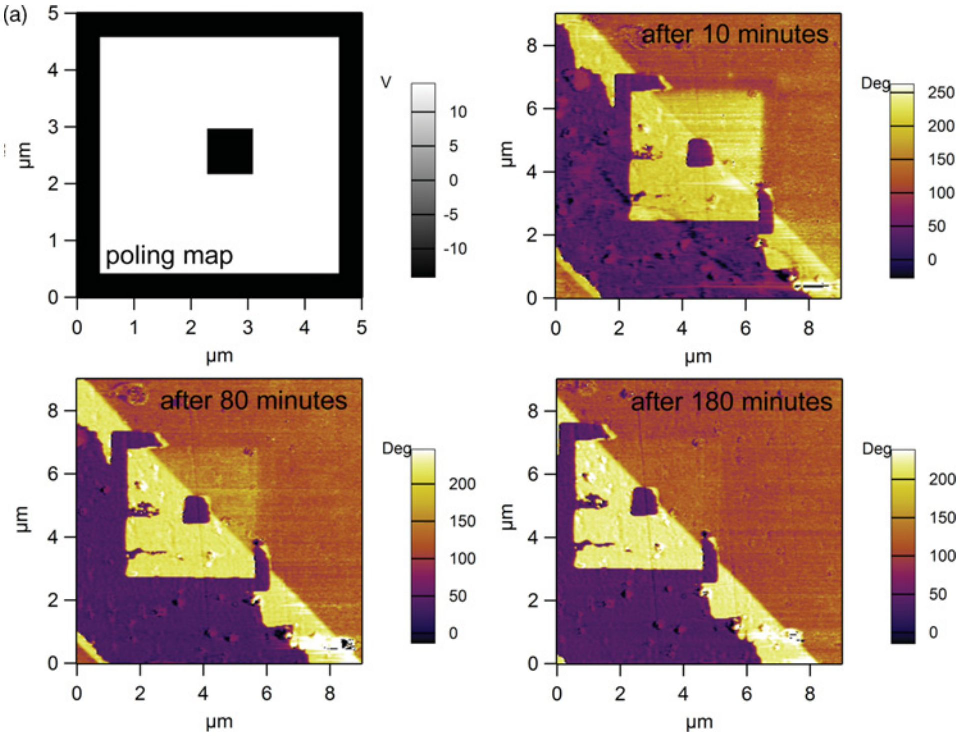

Figure 20.16 (a) The time stability of polarization on the free surface and top Ta electrode; (b) the time stability of polarization on the free surface and top Au electrode. The poling areas were located partly on the bare surface and partly on the metal electrodes, which are located on the surface of the same epitaxial tetragonal PZT film of thickness comparable with that of the film presented in Figure 20.14 (this explains the presence of the 90° domain grid)

[70]. This result demonstrates once more how sensitive the polarization orientation is to different factors, including the environment conditions (e.g. contaminants from the atmosphere), and why the stable orientation of polarization may change with time from UP in as grown (possible deficit of oxygen at the surface) films to DOWN in films stored for some time in air (partial compensation of oxygen vacancies in the surface layer).

The formation of the electrode–ferroelectric interface was also studied by XPS. Au, Cu, and Pt were deposited by MBE on the surface of epitaxial layers of PZT and BTO. The metal layers were deposited in steps starting with 0.2 nm and ending with 10 nm. After each deposition step the XPS spectrum was recorded. It was found that the binding energies corresponding to the core levels of the component elements of the ferroelectric film are slightly moving as the metal thickness increases. This fact suggests a band-bending at the metal electrode interface [48, 73, 74] that can be associated with the formation of a potential barrier, as suggested by macroscopic I–V measurements. Also, it was found that the position of the Fermi level is close to the middle of the band-gap [48]. These results suggest that the ferroelectric films act as almost intrinsic semiconductors and that potential barriers develop at electrode interfaces. Depending on sample history the ferroelectric films can be slightly

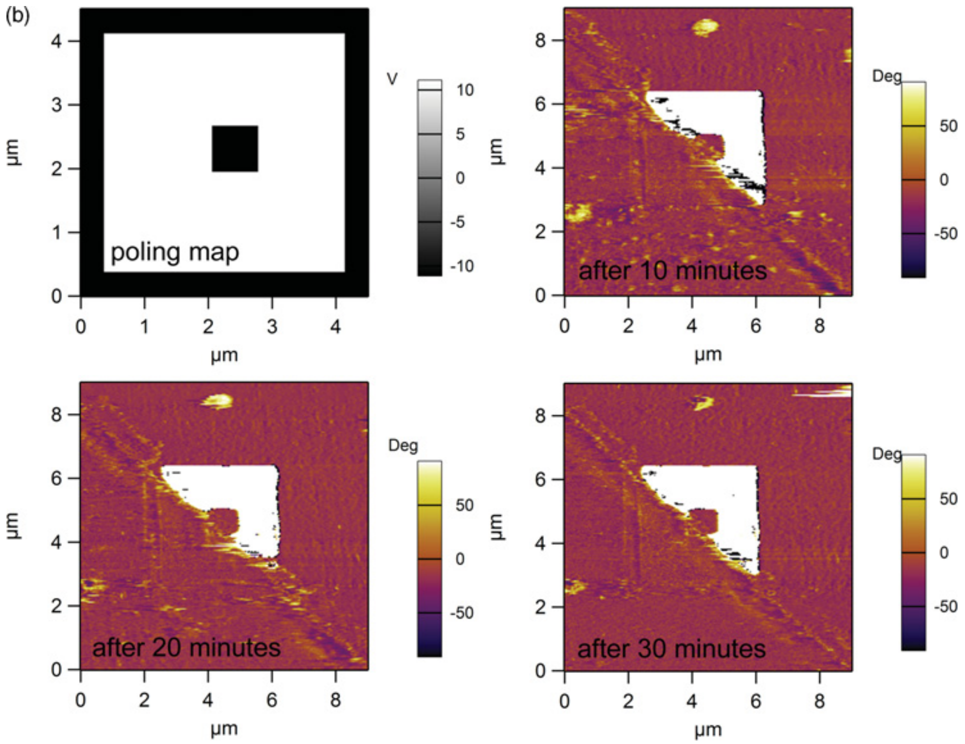

Figure 20.16 (*Continued*)

n-type or p-type, but the free carriers are blocked at the interfaces in order to compensate for the bound polarization charges. The emerging picture is that the bulk of a ferroelectric film is depleted of free carriers and that the band-bending at the interface is controlled by the polarization [48].

The TEM investigations have revealed that metals deposited by MBE on the surface of epitaxial ferroelectric layers are not very adherent and do not form a continuous layer all the time. For example, Au is not continuous and forms nanocrystals on the surface of PZT as well as on the surface of BTO [48, 73]. Cu forms a continuous layer but it seems to oxidize at the interface with the PZT layer [48, 74]. Interesting findings were observed also at the SRO–PZT interface. An apparent "mixed" layer was observed by EELS analysis, suggesting interdiffusion of SRO and PZT. However, the atoms are not randomly distributed and the epitaxial quality is preserved at the interface. Most probably this is an effect of the fact that the PZT film is grown on a terraced substrate.

TEM studies have also revealed that the oxygen content is not uniform throughout the film thickness, as presented in Figure 20.17. The Ti/O ratio has been measured across the BTO layer in order to evidence a possible gradient of oxygen composition. For this purpose, a spectrum image has been acquired across the BTO layer (Figure 20.17(a)). The ADF STEM image in Figure 20.17(b) presents the location from where the spectrum image has been acquired. The area marked "Spatial Drift" has been used to monitor and correct for specimen drift during the spectrum image acquisition. For the spectrum image acquisition

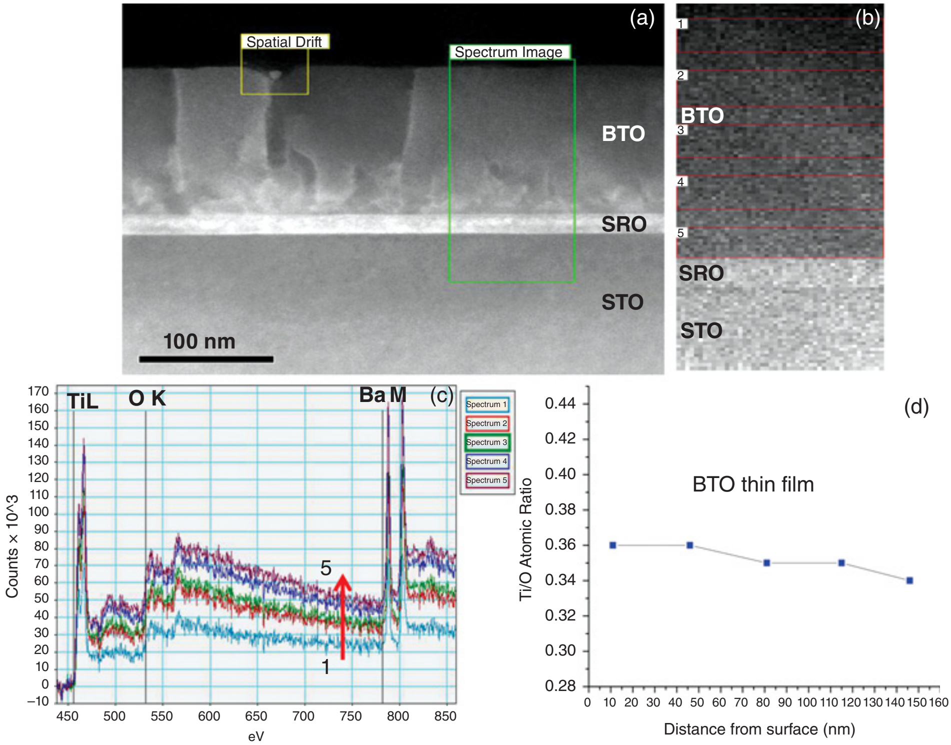

Figure 20.17 *(a) Low magnification HAADF STEM image of the BTO/SRO/STO sample indicating the areas for spectrum image acquisition and spatial drift correction; (b) spectrum image; (c) EELS spectra extracted from the 5 areas indicated in (b) (the arrow indicated the direction from area 1 to 5); and (d) variation of the Ti/O atomic ratio across the BTO layer*

we used a beam convergence semiangle of 32 mrad, a collection semiangle of 36 mrad, and a pixel time of 0.05 s. Five EEL spectra (Figure 20.17(c)) have been extracted from the spectrum image afterwards in five different areas across the BTO layer, numbered with 1 to 5 from surface to bottom (Figure 20.17(a)). In order to compensate for possible sample thickness variations between the five analyzed areas, the Ti/O atomic ratio has been calculated instead of the absolute values in atoms/nm^2 for Ti and O. The quantitative results regarding the Ti/O ratio indicate, on the one hand, a slightly substoichiometric value for the oxygen content and, on the other hand, a slow decrease of the Ti/O ratio from top to bottom (Figure 20.17(d)). This fact points to a slightly poorer oxygen content towards the layer surface and, therefore, a larger concentration of oxygen vacancies in the top part of the BTO layer. The gradient in oxygen vacancies can explain the imprint manifested as a shift of the hysteresis loop or of the *C–V* characteristic along the voltage axis.

All the microscopic investigations show that the formation of the electrode–ferroelectric interface is a complex phenomenon involving subtle changes in surface/interface composition and in band alignment. The fact that the work function of the metal used for electrodes does not play an important role in setting the position of the Fermi level, the height of the potential barriers, and the band-bending at the interface suggests that the interface properties are controlled by the ferroelectric polarization.

20.3 Interfaces in Complex Structures

20.3.1 PZT/ZnO

The metal–ferroelectric–semiconductor (MFS) structures were investigated as alternative for non-volatile memories [10, 75, 76]. The *C–V* characteristic of a MFS structure presents a hysteresis associated with the ferroelectric polarization. The hysteresis is counterclockwise if the semiconductor is n-type and clockwise if the semiconductor is p-type. A "memory window" is defined as the difference between coercive voltages. However, the development of real devices based on MFS structures was hindered by the fact that the ferroelectric–Si interface is not always clean [27]. The introduction of a buffer layer (metal–ferroelectric–insulator–semiconductor MFIS structures) may give a cleaner interface with Si but generates problems with the magnitude and stability of the ferroelectric polarization because of the lack of compensation charges for the depolarization field [77]. Therefore the replacement of Si with an oxide semiconductor such as ZnO is considered a solution for further developments. Recently ZnO-based MFS structures were fabricated and characterized, with ferroelectric either $BaTiO_3$ or $Pb(Zr,Ti)O_3$ (PZT) [78, 79]. A strong temperature–induced change in the hysteretic behavior of the *C–V* characteristic was recently reported in the last case [80]. Later on it was shown that this temperature change is dependent on the PZT/ZnO interface quality [81]. For the epitaxial structures the hysteresis is counterclockwise at any temperature between 100 and 400 K, as should be on an n-type semiconductor like ZnO. For polycrystalline structures the hysteresis is counterclockwise only at elevated temperatures, over 300 to350 K. This behavior was discussed in terms of defect states located at the PZT/ZnO interface.

Conventional polarization hysteresis measurements (HM) have been performed over a large temperature scale, starting from 150 K, up to 450 K, where the response of the sample became unstable. The following measurements have been performed: (a) direct HM – starting with positive voltage on ZnO (ZnO in depletion); (b) inverse HM – starting with negative voltage on ZnO (ZnO in accumulation); and (c) remnant hysteresis test (RHT). The RHT consists of a sequence of four HM. The first is a direct HM and is preceded by a negative pulse. The second is an inverse HM preceded by a positive pulse. The third is a direct HM preceded by a positive pulse and the fourth is an inverse HM preceded by a negative pulse. Thus, the first two HM show both the switching and no switching dipoles while the last two HM show only the non-switching dipoles. An RHT consists of an assembling of two parts. The positive voltage part is obtained by subtracting the third HM from the first HM on the positive voltage side. The negative voltage part is obtained by subtracting the fourth HM from the second HM on the negative voltage side. The results of the HM for 200 and 450 K are shown in Figure 20.18. It can be observed that the behavior of the sample is highly asymmetric and is strongly dependent on both the temperature and the applied voltage sequence on the MFS structure. A notable difference is that the gaps in polarization occur in the direct HM at low temperature and in the inverse HM at high temperature (see Figure 20.18(a) and (b)). The shape of the hysteresis is in all cases subject to distortions due

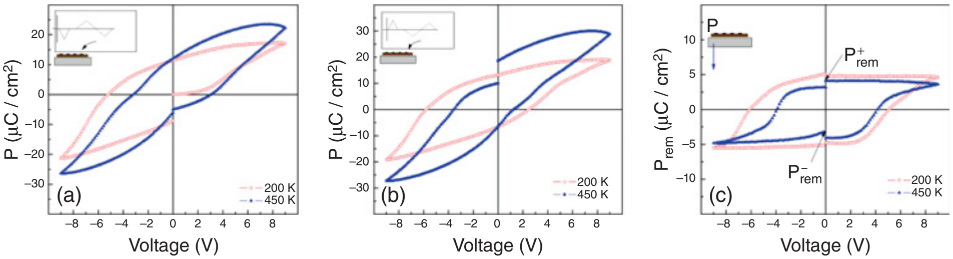

Figure 20.18 *Hysteresis loops at 200 and 450 K: (a) direct hysteresis; (b) inverse hysteresis; (c) direct remnant hysteresis*

to leakage and backswitching effects. RHT eliminates all the distortions connected with the non-switching processes. The results are shown in Figure 20.18(c). The remnant polarization is only around 5 μC cm^{-2} compared with 35 μC cm^{-2} on a single PZT layer. This is the effect of the lower polarization in ZnO. One can observe some discontinuities at 0 V, which are negligible at 200 K and of a significant magnitude at 450 K. This fact suggests the presence of an important imprint at 450 K, caused by an internal electric field with the orientation shown by the arrow of the inset of Figure 20.18(c)).

Figure 20.19(a) summarizes the results of the RHT showing the temperature dependence of the difference between the remnant polarizations ($\Delta P_{\mathrm{rem}} = P^+_{\mathrm{rem}} - |P^-_{\mathrm{rem}}|$). Unexpected is the increase in the values of the ΔP_{rem} above 250 K. This can be explained if one considers the presence of some temperature-dependent internal electric fields in the heterostructure. These fields can affect the shape of the RHT loop both in the lower and the upper saturation segments by creating steps in the remnant polarization values at 0 V. This situation occurs for the RHT at 450 K but not at 200 K (see Figure 20.18(c)), indicating that an internal electric field is building up with increasing temperature. The positive values of ΔP_{rem}

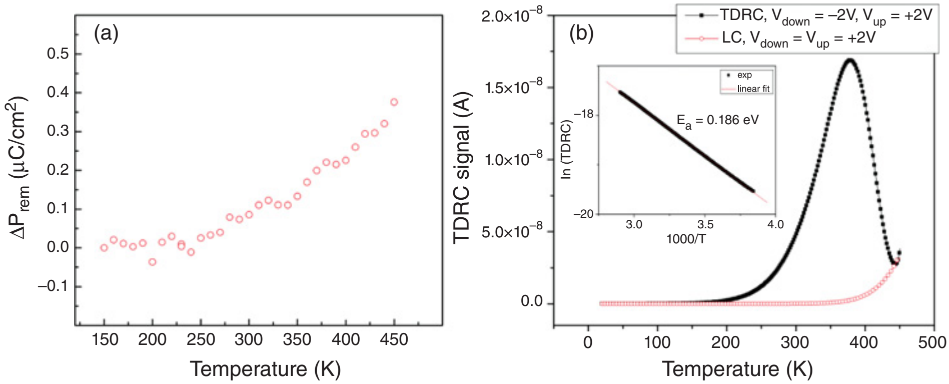

Figure 20.19 *(a) ΔP_{rem} versus temperature; (b) TDRC spectrum and the leakage current (LC) with the inset representing the Arrhenius plot used for evaluation of the interface state activation energy. The TDRC spectra were obtained after cooling the sample in accumulation (V_{down} = –2V) and heated under a positive bias (V_{up} = +2V). For the leakage current (LC) measurement the bias applied was V = +2 V during both the cooling and the heating*

above 250 K prove that the built-up internal electric field is favoring the positive remnant polarization and is opposing the negative one. All these changes observed in the hysteretic behavior of the PZT layer take place in the same temperature range where changes in the hysteresis orientation and shape of the *C*–*V* characteristics occurs [80]. One can assume that these temperature-dependent changes are all related to the presence of defect states at the PZT/ZnO interface.

The thermally dielectric relaxation current (TDRC) technique was used to investigate the presence of trapping interface states in the PZT/ZnO structure. The sample was cooled down to 50 K with a negative bias on ZnO (–2 V, accumulation) in order to charge the interface states with electrons. Then a reverse bias was applied and the sample was heated to 450 K with a constant rate, $\beta = 11$ K min^{-1}, while recording the current due to the carriers released from the traps. The results of TDRC measurements are shown in Figure 20.19(b) (the bias applied on depleted ZnO during heating is +2 V). The measurements reveal the existence of a large amount of defect states giving rise to a peak in the TDRC spectra at ~370 K that grows in magnitude when repeating the TDRC measurements. The possibility to relate the peak to the pyroelectric effect was disregarded because no peak was obtained without bringing the MFS structure in accumulation during cooling – compare the TDRC curve with the one labeled LC (leakage current) in Figure 20.19(b). The increasing part of the TDRC peak can be used to evaluate their activation energy and the apparent carriers capture cross-section. From the corresponding Arrhenius plot activation energy of ~0.19 eV was determined. The resulting apparent capture cross-section for electrons is anomalously small (10^{-26} cm^2), suggesting a supplementary large energy barrier for the capture and emission process. In our opinion this could be caused by the ferroelectric polarization in the PZT film. Through integrating the TDRC peak the density of interface states was evaluated to be about 1×10^{14} cm^{-2} in the first TDRC spectrum and about 2.5×10^{15} cm^{-2} after the sixth consecutive TDRC measurement. If the first value is comparable with the ferroelectric polarization in PZT film (see Figure 20.18) the latter one is one order of magnitude higher. Our explanation for this behavior is that the long time exposure of the samples to a DC voltage (one TDRC measurement takes about 4 h) degrades the interface generating more defects acting as traps, possibly extending from the interface into the bulk of PZT and ZnO films. It is worth noting that precisely in the temperature range where the interface defect states start to release the trapped negative charge in the TDRC spectrum, the $\Delta P_{\mathrm{rem}} = P^{+}_{\mathrm{rem}} - |P^{-}_{\mathrm{rem}}|$ starts to increase (see Figure 20.19(a)). The occurrence of an internal electric field favoring the P^{+}_{rem} direction of the PZT ferroelectric polarization in this temperature range can be explained by the charge stored at the PZT/ZnO interface only if the interface states are donor-like and therefore positively charged when empty. The presence of some interface states at the PZT/ZnO interface was also considered to explain the clockwise hysteresis at ambient temperatures and below [80, 81].

20.3.2 Ferroelectric/Multiferroic Multilayers

Interfaces were found to play an important role in the case of ferroelectric/multiferroic multilayers. For example, it was found that a "phase transition", driven by thickness, occurs in epitaxial superlattices composed of ferroelectric and antiferroelectric PZT layers [39]. If the thickness of the component layers is over a certain critical value (in the present case about 10 nm) the structure presents a mixture of ferroelectric and antiferroelectric behavior reflected in a sort of triple hysteresis loop. When the thickness of the component layers drops below 10 nm then the entire structure behaves as ferroelectric. Structural analysis has revealed that this “phase transition” takes place because the antiferroelectric component assumes the structure of the ferroelectric phase. Further on, it was found that the capacitance of such a multilayer can be increased by increasing the number of pairs and thus the number of interfaces [82]. This was explained by the presence of an interfacial polarization or by the presence of trapped interface charges giving rise to an interfacial capacitance that appears in parallel with the normal capacitance of the multilayer.

A rather similar behavior was observed in the case of the sol–gel deposited Pb(Zr, Ti)O_3–BiFeO_3 (PZTBFO) multilayers. Although both materials are ferroelectric it was found that for symmetric structure, involving only three layers (PZT–BFO–PZT), the hysteresis loop is similar to the one obtained for an antiferroelectric material [83]. When the number of layers increases then the hysteresis loop looks like that for a ferroelectric. It was found again that the capacitance increases with the number of interfaces, a fact that suggests that the “dielectric constant” of a multilayer can be tuned from the number of component films [84]. Moreover, magnetic hysteresis was recorded in the case of BFO–PZT multilayers. This fact was explained by the disorder present at interfaces may induce some ferromagnetic order in an antiferromagnetic material.

“Artificial multiferroic” structures were also tested by combining ferroelectric and ferrimagnetic layers such as PZT (or BTO) and $CoFe_2O_4$ (CFO). Both asymmetric (one ferroelectric layer and one CFO layer, deposited in this order by PLD on single-crystal STO substrates with a bottom SRO electrode) and symmetric (ferroelectric–CFO–ferroelectric) structures were investigated. All show ferroelectric and magnetic hysteresis, acting thus as multiferroics [85]. Other “artificial multiferroics” were obtained by combining (La, Sr)MnO_3 (LSMO) layers with ferroelectric films, with LSMO as the bottom and top electrodes. Capacitance–voltage measurements were performed at low temperatures under an external magnetic field applied perpendicular to the LSMO electrodes. The results are presented in Figure 20.20. It can be seen that there is a variation of the capacitance when the magnetic field is applied simultaneously with the electric field. The magnitude of the capacitance variation depends on the polarity of the applied fields, being larger for positive voltages. Also, it can be seen that the capacitance variation with the magnetic field is decreasing with increasing temperature. These results suggest the presence of a magnetocapacitive effect, which may be mediated by the LSMO–ferroelectric interfaces. The effect

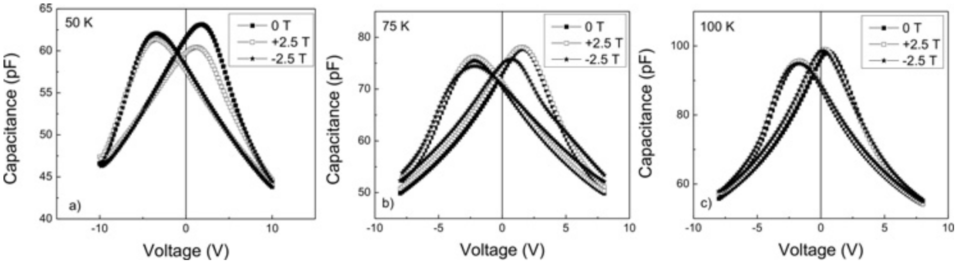

Figure 20.20 *C–V characteristics at different temperatures and for different magnitudes/orientations of the applied magnetic field: (a) 50 K; (b) 75 K; (c) 100 K. The structure was LSMO–BTO–LSMO*

seems to be significant, considering the fact that the applied magnetic field is perpendicular on the in-plane magnetization of LSMO. It can be assumed that the changes induced in the LSMO electrodes by the applied magnetic field are affecting the polarization charges located near the interface, leading to changes in capacitance values [86].

20.4 Conclusions

The results presented in the summary above show that the interfaces in ferroelectric-based structures can have an important impact on the macroscopic electrical properties. The effect can become dominant in the case of epitaxial layers or structures. Referring to the electrode interfaces, the recent studies, combining macroscopic electrical measurements with microscopic investigations performed by XPS and HR-TEM, point towards the fact that the ferroelectric polarization is actually controlling the interface properties. The work function of metals used as electrodes seems to have no role in defining the potential barrier. Very thin layers of metal oxide may develop at the electrode interfaces if needed to enhance a potential barrier able to preserve the compensation charges, allowing at the same time their rapid movement from one electrode to the other when the polarization switching take place. This may explain why the potential barriers estimated from macroscopic *I–V* measurements are of the order of 01–0.3 eV.

The interfaces in multilayers combining materials with ferroelectric, semiconductor, and magnetic properties can induce phenomena that are representative for the multilayer and not for the component phases, such as: thickness-driven phase transitions; changes in the orientation of the capacitive hysteresis in MFS structures; magnetocapacitive effects in “artificial multiferroic” structures, etc.

One can conclude that the study of interfaces in ferroelectric-based structures is very important. Understanding the phenomena taking place at the interfaces will allow the design of new functionalities and optimization of macroscopic electrical/magnetic properties by controlling the structure and chemistry at the microscopic level.

Acknowledgments

The collaboration within the COST MP0904-SIMUFER action is recognized. The authors acknowledge the financial support of the Romanian Ministry of Education – Executive Unit for Funding High Education, Research, Development and Innovation (MEN-UEFISCDI) through the Idea – Complex Research Grant PN-II-ID-PCCE-2011-2-0006 (Contract no. 3/2012). Mihaela Botea and Andra G. Boni wish to thank also the Strategic Grant POSDRU/159/1.5/S/137750, in the Project “Project Doctoral and Postdoctoral Programs Support for Increased Competitiveness in Exact Sciences Research” cofinanced by the European Social Fund within the Sectorial Operational Program Human Resources Development 2007–2013.

References

(1) Lines, M.E. and Glass, A.M. (1977) *Principles and Applications of Ferroelectrics and Related Materials*, Clarendon Press, Oxford.

(2) Jona, F. and Shirane, G. (1962) *Ferroelectric Crystals*, Pergamon Press, Oxford.

(3) Nalwa, H.S. (ed.) (1995) *Ferroelectric Polymers: Chemistry, Physics, and Applications*, CRC Press, New York.

(4) Volk, T. and Wöhlecke, M. (2009) *Lithium Niobate: Defects, Photorefraction and Ferroelectric Switching* Springer Series in Materials Science, Springer, Berlin.

(5) Mitoseriu, L. (ed.) (2007) *New Developments in Advanced Functional Ceramics*, Transworld Research Network, Kerala.

(6) Uchino, K. (2000) *Ferroelectric Devices*, Marcel Dekker, New York.

(7) Scott, J.F. (2000) *Ferroelectric Memories*, in Advanced Microelectronics Series, edited by K. Itoh and T. Sakurai, Springer-Verlag, Berlin, Heidelberg, Germany.

(8) Scott, J.F. (1998) High-dielectric constant thin films for dynamic random access memories (DRAM). *Annual Review of Materials Science*, **28**, 79–100.

(9) Waser, R. (2009) Resistive non-volatile memory devices. *Microelectronic Engineering*, **86**, 1925–1928.

(10) Miller, S.L. and McWhorter, P.J. (1992) Physics of the ferroelectric nonvolatile memory field effect transistor. *Journal of Applied Physics*, **72**, 5999–6010.

(11) Malic, B., Arkon, I., Kodre, A., and Kosec, M. (2006) Homogeneity of Pb(Zr, Ti)O_3 thin films by chemical solution deposition: extended X-ray absorption fine structure spectroscopy study of zirconium local environment. *Journal of Applied Physics*, **100**, art. no. 051612.

(12) Chilibon, I. and Marat-Mendes, J.N. (2012) Ferroelectric ceramics by sol–gel methods and applications: a review. *Journal of Sol–Gel Science and Technology*, **64**, 571–611.

(13) Martin, L.W., Chu, Y.H., and Ramesh, R. (2010) Advances in the growth and characterization of magnetic, ferroelectric, and multiferroic oxide thin films. *Materials Science and Engineering R*, **68**, 89–133.

(14) Scott, J.F. (2007) Applications of modern ferroelectrics. *Science*, **315**, 954–959.

(15) Gruverman, A. and Kholkin, A. (2006) Nanoscale ferroelectrics: processing, characterization and future trends. *Report on Progress in Physics*, **69**, 2443–2474.

(16) Catalan, G., Seidel, J., Ramesh, R., and Scott, J.F. (2012) Domain wall nanoelectronics. *Review of Modern Physics*, **84**, 119–156.

(17) Vrejoiu, I., Le Rhun, G., Pintilie, L., et al. (2006) Intrinsic ferroelectric properties of strained tetragonal $PbZr_{0.2}Ti_{0.8}O_3$ obtained on layer-by-layer grown, defect-free single-crystalline films. *Advanced Materials*, **18**, 1657–1661.

(18) Pintilie, L., Vrejoiu, I., Hesse, D., et al. (2007) Extrinsic contributions to the apparent thickness dependence of the dielectric constant in epitaxial Pb(Zr, Ti)O_3 thin films. *Physical Review B*, **75**, art. no. 224113.

(19) Zhong, C.F., Wang, X.H., Fang, J.A., et al. (2010) Investigation of thickness dependence of structure and electric properties of sol–gel-derived $BiScO_3$–$PbTiO_3$ thin films. *Journal of the American Ceramic Society*, **93**, 3305–3311.

(20) Chen, F., Schafranek, R., Wachau, A., et al. (2010) Barrier heights, polarization switching, and electrical fatigue in Pb(Zr, Ti)O_3 ceramics with different electrodes. *Journal of Applied Physics*, **108**, art. no. 104106.

(21) Nelson, C.T., Gao, P., Jokisaari, J.R., et al. (2011) Domain dynamics during ferroelectric switching. *Science*, **334**, 968–971.

(22) Nagarajan, V., Prasertchoung, S., Zhao, T., et al. (2004) Size effects in ultrathin epitaxial ferroelectric heterostructures. *Applied Physics Letters*, **84**, 5225–5227.

(23) Lee, S.K., Kim, Y.T., Kim, S.I., and Lee, C.E. (2002) Effects of coercive voltage and charge injection on memory windows of metal–ferroelectric–semiconductor and metal–ferroelectric–insulator–semiconductor gate structures. *Journal of Applied Physics*, **91**, 9303–9307.

(24) Ren, T.L., Shao, T.Q., Zhang, W.Q., et al. (2003) Fabrication and properties of silicon-based PZT thin films for MFSFET applications. *Microelelectronic Engineering*, **66**, 554–560.

(25) Nicollian, E.H. and Brews, J.R. (1982) *MOS (Metal Oxide Semiconductor) Physics and Technology*, Wiley-Interscience, New York.

(26) Lin, Y., Zhao, B.R., Peng, H.B., et al. (1999) Asymmetry in the hysteresis loop of $Pb(Zr_{0.53}Ti_{0.47})O_3/SiO_2/Si$ structures. *Journal of Applied Physics*, **86**, 4467–4472.

(27) Li, W.P., Zhang, R., Shen, J., et al. (2000) Evidence for ferroelectric border traps near the SrBi2Ta2O9/Si interface through capacitance–voltage measurement. *Applied Physics Letters*, **77**, 564–566.

(28) Juan, P., Hu, Y., Chiu, F., and Lee, J.Y. (2005) The charge trapping effect of metal–ferroelectric ($PbZr_{0.53}Ti_{0.47}O_3$)–insulator (HfO_2)–silicon capacitors. *Journal of Applied Physics*, **98**, art. no. 044103.

(29) Yu, S., Chen, R., Zhang, G., et al. (2006) Ferroelectric enhancement in heterostructured $ZnO/BiFeO_3$–$PbTiO_3$ film. *Applied Physics Letters*, **89**, art. no. 212906.

(30) Ma, J., Hu, J., Li, Z., and Nan, C.W. (2011) Recent progress in multiferroic magnetoelectric composites: from bulk to thin films. *Advanced Materials*, **23**, 1062–1087.

(31) Martin, L.W., Crane, S.P., Chu, Y.H., et al. (2008) Multiferroics and magnetoelectrics: thin films and nanostructures. *Journal of Physics: Condensed Matter*, **20**, art. no. 434220.

(32) Nan, C.W., Bichurin, M.I., Dong, S., et al. (2008) Multiferroic magnetoelectric composites: historical perspective, status, and future directions. *Journal of Applied Physics*, **103**, art. no. 031101.

(33) Molegraaf, H.J.A., Hoffman, J., Vaz, C.A., et al. (2009) Magnetoelectric effects in complex oxides with competing ground states. *Advanced Materials*, **21**, 3470–3474.

(34) Scott, J.F. (2007) Multiferroic memories. *Nature Materials*, **6**, 256–257.

(35) Shen, M., Ge, S., and Cao, W. (2001) Dielectric enhancement and Maxwell–Wagner effects in polycrystalline ferroelectric multilayered thin films. *Journal of Physics D: Applied Physics*, **34**, 2935–2938.

(36) Haeni, J.H., Irvin, P., Chang, W., et al. (2004) Room-temperature ferroelectricity in strained $SrTiO_3$. *Nature*, **430**, 758–761.

(37) Thiel, S., Hammerl, G., Schmehl, A., et al. (2006) Tunable quasi-two-dimensional electron gases in oxide heterostructures. *Science*, **313**, 1942–1945.

(38) Brinkman, A., Huijben, M., van Zalk, M., et al. (2007) Magnetic effects at the interface between non-magnetic oxides. *Nature Materials*, **6**, 493–496.

(39) Boldyreva, K., Pintilie, L., Lotnyk, A., et al. (2007) Thickness-driven antiferroelectric-to-ferroelectric phase transition of thin $PbZrO_3$ layers in epitaxial $PbZrO_3/Pb(Zr_{0.8}Ti_{0.2})O_3$ multilayers. *Applied Physics Letters*, **91**, art. no. 122915.

(40) Bloom, P.W.M., Wolf, R.M., Cillessen, J.F.M., and Krjin, M.P.C.M. (1994) Ferroelectric Schottky diode. *Physical Review Letters*, **73**, 2107–2110.

(41) Stengel, M., Vanderbilt, D., and Spaldin, N.A. (2009) First-principles modeling of ferroelectric capacitors via constrained displacement field calculations. *Physical Review B*, **80**, art. no. 224110.

(42) Chen, F., Schafranek, R., Wu, W., and Klein, A. (2011) Reduction-induced Fermi level pinning at the interfaces between Pb(Zr, Ti)O_3 and Pt, Cu and Ag metal electrodes. *Journal of Physics D: Applied Physics*, **44**, art. no. 255301.

(43) Ge, C., Jin, K., Wang, C., et al. (2012) Effect of ferroelectric parameters on ferroelectric diodes. *Journal of Applied Physics*, **111**, art. no. 054104.

(44) Pintilie, L. and Alexe, M. (2005) Metal-ferroelectric-metal heterostructures with Schottky contacts. I. Influence of the ferroelectric properties. *Journal of Applied Physics*, **98**, art. no. 124103.

(45) Pintilie, L., Boerasu, I., Gomes, M.J.M., et al. (2005) Metal–ferroelectric–metal structures with Schottky contacts. II. Analysis of the experimental current–voltage and capacitance–voltage characteristics of Pb(Zr, Ti)O_3 thin films. *Journal of Applied Physics*, **98**, art. no. 124104.

(46) Pintilie, L., Vrejoiu, I., Hesse, D., et al. (2007) Ferroelectric polarization–leakage current relation in high quality epitaxial Pb(Zr, Ti)O_3 films. *Physical Review B*, **75**, art. no. 104103.

(47) Pintilie, L., Vrejoiu, I., Hesse, D., and Alexe, M. (2008) The influence of the top-contact metal on the ferroelectric properties of epitaxial ferroelectric $Pb(Zr_{0.2}Ti_{0.8})O_3$ thin films. *Journal of Applied Physics*, **104**, art. no. 114101.

(48) Pintilie, I., Teodorescu, C.M., Ghica, C., et al. (2014) Polarization-control of the potential barrier at the electrode interfaces in epitaxial ferroelectric thin films. *ACS Applied Materials and Interfaces*, **6**, 2929–2939.

(49) Simmons, J.G. (1965) Richardson–Schottky effect in solids. *Physical Review Letters*, **15**, 967–968.

(50) Boni, A.G., Pintilie, I., Pintilie, L., et al. (2013) Electronic transport in (La, Sr)MnO_3-ferroelectric-(La, Sr)MnO_3 epitaxial structures. *Journal of Applied Physics*, **113**, art. no. 224103.

(51) Cohen, R.E. (1992) Origin of ferroelectricity in perovskite oxides. *Nature*, **358**, 136–138.

(52) Niu, G., Saint-Girons, G., Vilquin, B., et al. (2009) Molecular beam epitaxy of $SrTiO_3$ on Si (001): early stages of the growth and strain relaxation. *Applied Physics Letters*, **95**, art. no. 062902.

(53) Lide, D.R. (1995) *C.R.C. Handbook of Chemistry and Physics*, 76th edition, CRC Press Inc., Boca Raton, New York, London, Tokyo.

(54) Hartmann, A.J., Neilson, M., Lamb, R.N., et al. (2000) Ruthenium oxide and strontium ruthenate electrodes for ferroelectric thin-films capacitors. *Applied Physics A: Materials Science and Processing*, **70**, 239–242.

(55) Schroder, D.K. (1998) *Semiconductor Material and Device Characterization*, Wiley-Interscience, New York.

(56) Bell, A.J. (2006) Factors influencing the piezoelectric behavior of PZT and other "morphotropic phase boundary" *ferroelectrics. Journal of Materials Science*, **41**, 13–25.

(57) Fridkin, V.M. and Popov, B.N. (1978) Anomalous photovoltaic effect in ferroelectrics. *Soviet Physics Uspekhi*, **21**, 981–991.

(58) Sze, S.M. (1981) *Physics of Semiconductor Devices*, 2nd edition, John Wiley & Sons, Inc., New York.

(59) Pintilie, L., Stancu, V., Vasile, E., and Pintilie, I. (2010) About the complex relation between short-circuit photocurrent, imprint and polarization in ferroelectric thin films. *Journal of Applied Physics*, **107**, art. no. 114111.

(60) Pintilie, L., Dragoi, C., and Pintilie, I. (2011) Interface controlled photovoltaic effect in epitaxial Pb(Zr, Ti)O_3 films with tetragonal structure. *Journal of Applied Physics*, **110**, art. no. 044105.

(61) Pintilie, L., Vrejoiu, I., Le Rhun, G., and Alexe, M. (2007) Short-circuit photocurrent in epitaxial lead zirconate–titanate thin films. *Journal of Applied Physics*, **101**, art. no. 064109.

(62) Pintilie, I., Pintilie, L., Petre, D., et al. (1998) Theoretical background of the optical charging spectroscopy method used for investigation of trapping levels. *Applied Physics Letters*, **73**, 1685–1687.

(63) Pintilie, L., Pasuk, I., Negrea, R., et al. (2012) The effect of the top electrode interface on the hysteretic behavior of epitaxial ferroelectric Pb(Zr, Ti)O_3 thin films with bottom $SrRuO_3$ electrode. *Journal of Applied Physics*, **112**, art. no. 064116.

(64) Whatmore, R.W. (2004) Pyroelectric arrays: ceramics and thin films. *Journal of Electroceramics*, **13**, 139–147.

(65) Botea, M., Iuga, A., and Pintilie, L. (2013) Giant pyroelectric coefficient determined from the frequency dependence of the pyroelectric signal generated by epitaxial $Pb(Zr_{0.2}Ti_{0.8})O_3$ layers grown on single crystal $SrTiO_3$ substrates. *Applied Physics Letters*, **103**, art. no. 232902.

(66) Pintilie, L., Stancu, V., Trupina, L., and Pintilie, I. (2010) Ferroelectric Schottky diode behavior from a $SrRuO_3$–$Pb(Zr_{0.2}Ti_{0.8})O_3$–Ta structure. *Physical Review B*, **82**, art. no. 085319.

(67) Pintilie, L. (2011) Charge transport in ferroelectric thin films, in *Ferroelectrics: Physical Effects*, edited by Mickael Lallart, INTECH.

(68) Cao, D., Wang, C., Zheng, F., et al. (2012) High-efficiency ferroelectric-film solar cells with an n-type Cu_2O cathode buffer layer. *Nano Letters*, **12**, 2803–2809.

(69) Le Rhun, G., Vrejoiu, I., Pintilie, L., et al. (2006) Increased ferroelastic domain mobility in ferroelectric thin films and its use in nano-patterned capacitors. *Nanotechnology*, **17**, 3154–3159.

(70) Apostol, N.G., Stoflea, L.E., Lungu, G.A., et al. (2013) Band bending at free Pb(Zr,Ti)O_3 surfaces analyzed by X-ray photoelectronspectroscopy. *Materials Science and Engineering B*, **178**, 1317–1322.

(71) Apostol, N.G., Stoflea, L.E., Lungu, G.A., et al. (2013) Band bending in Au/Pb(Zr, Ti)O_3 investigated by X-ray photoelectron spectroscopy: dependence on the initial state of the film. *Thin Solid Films*, **545**, 13–21.

(72) Chen, F. and Klein, A. (2012) Polarization dependence of Schottky barrier heights at interfaces of ferroelectrics determined by photoelectron spectroscopy. *Physical Review B*, **86**, art. no. 094105.

(73) Apostol, N.G., Stoflea, L E., Lungu, G.A., et al. (2013) Charge transfer and band bending at Au/$Pb(Zr_{0.2}Ti_{0.8})O_3$ interfaces investigated by photoelectron spectroscopy. *Applied Surface Science*, **273**, 415– 425.

(74) Apostol, N.G., Stoflea, L.E., Chirila, C., et al. (2014) Schottky barrier versus surface ferroelectric depolarization at Cu/Pb(Zr,Ti)O_3 interfaces. *Journal of Materials Science*, **49**, 3337–3351.

(75) Ishiwara, H. (1997) Current status and prospects MFSFETs and related devices. *Integrated Ferroelectrics*, **17**, 11–20.

(76) Lee, H.N., Kim, Y.T., and Park, Y.K. (1999) Memory window of highly *c*-axis oriented ferroelectric $YMnO_3$ thin films. *Applied Physics Letters*, **74**, 3887–3889.

(77) Yoshimura, T., Fujimura, N., Ito, D., and Ito, T. (2000) Characterization of ferroelectricity in metal–ferroelectric–insulator–semiconductor structure by pulsed C–V measurement; ferroelectricity in $YMnO_3$–Y_2O_3–Si structure. *Journal of Applied Physics*, **87**, 3444–3449.

(78) Voora, V.M., Hofmann, T., Brandt, M., et al. (2008) Interface-charge-coupled polarization response of Pt–$BaTiO_3$–ZnO–Pt heterojunctions: a physical model approach. *Journal of Electronic Materials*, **37**, 1029–1034.

(79) Cagin, E., Chen, D.Y., Siddiqui, J.J., and Phillips, J.D. (2007) Hysteretic metal–ferroelectric–semiconductor capacitors based on PZT/ZnO heterostructures. *Journal of Physics D: Applied Physics*, **40**, 2430–2434.

(80) Pintilie, L., Dragoi, C., Radu, R., et al. (2010) Temperature induced change in the hysteretic behavior of the capacitance–voltage characteristics of Pt–ZnO–Pb($Zr_{0.2}Ti_{0.8}$)O_3–Pt heterostructures. *Applied Physics Letters*, **96**, art. no. 012903.

(81) Pintilie, I., Pasuk, I., Ibanescu, G.A., et al. (2012) The impact of the Pb(Zr,Ti)O_3–ZnO interface quality on the hysteretic properties of a metal–ferroelectric–semiconductor structure. *Journal of Applied Physics*, **112**, art. no. 104103.

(82) Pintilie, L., Boldyreva, K., Alexe, M., and Hesse, D. (2008) Capacitance tuning in antiferroelectric–ferroelectric $PbZrO_3-Pb(Zr_{0.8}Ti_{0.2})O_3$ epitaxial multilayers. *New Journal of Physics*, **10**, art. no. 013003.

(83) Pintilie, L., Stancu, V., Dragoi, C., and Vlaicu, M. (2008) Antiferroelectric-like behavior in polycrystalline Pb($Zr_{0.2}Ti_{0.8}$)O_3–$BiFeO_3$ multilayers prepared by sol–gel method. *Journal of Optoelelectronics and Advanced Materials*, **10**, 3144–3149.

(84) Stancu, V., Dragoi, C., Kuncser, V., et al. (2011) The study of the electric and magnetic properties of $PbZr_{0.2}Ti_{0.8}O_3$–$BiFeO_3$ multilayers. *Thin Solid Films*, **519**, 6269–6277.

(85) Chirila, C., Ibanescu, G., Hrib, L., et al. (2013) Structural, electric and magnetic properties of Pb($Zr_{0.2}Ti_{0.8}$)O_3–$CoFe_2O_4$ heterostructures. *Thin Solid Films*, **545**, 2–7.

(86) Singh, M.P. and Prellier, W. (2007) Oxide superlattices for multiferroics: opportunities, issues, and challenges. *Philosophical Magazine Letters*, **87**, 211–222.

21

Electric Field Control of Magnetism Based on Elastically Coupled Ferromagnetic and Ferroelectric Domains

Kévin J.A. Franke, Tuomas H.E. Lahtinen, Arianna Casiraghi, Diego López González, Sampo J. Hämäläinen, and Sebastiaan van Dijken

NanoSpin, Department of Applied Physics, Aalto University School of Science, Finland

21.1 Introduction

While ferromagnetism and ferroelectricity have long been a centerpiece of solid-state and materials research due to their relevance for memory devices, sensors, and microwave components, studies on multiple ferroic order coexistence has been limited for a long time. The reasons for this are related to the mutual exclusivity of the conventional mechanisms that drive ferromagnetism and ferroelectricity [1] and to the inability of early studies to establish strong coupling effects [2]. Stimulated by advances in thin-film growth techniques and improved computational capabilities, studies on multiferroics have greatly intensified in the last decade. This has led to the identification of new single-phase materials with different mechanisms for the coexistence of multiple ferroic order (for reviews see [3] to [9]). Another rapid development in this field is based on composite material systems [10–12], in which ferromagnetic and ferroelectric compounds are artificially assembled in thin-film heterostructures. One particularly promising prospect of efficiently coupled multiphase systems is the ability to tailor magnetic properties with an electric field at temperatures

---

Nanoscale Ferroelectrics and Multiferroics: Key Processing and Characterization Issues, and Nanoscale Effects, First Edition. Edited by Miguel Algueró, J. Marty Gregg, and Liliana Mitoseriu.
© 2016 John Wiley & Sons, Ltd. Published 2016 by John Wiley & Sons, Ltd.

that are compatible with device applications in technology fields such as spintronics and magnonics.

Spintronics relies on the spin of electrons rather than their charge to store information, sense magnetic fields, or perform logic operations [13–15]. With the commercialization of several devices such as the read head of computer hard-disk drives and magnetic random access memory (MRAM), spintronics has become a successful field of nanotechnology. Major advantages of magnetism-based technologies over conventional semiconductor-based electronics include a high switching speed, a high storage density, and non-volatility. Most spintronic devices under investigation utilize the spin-transfer torque (STT) effect to switch the magnetization of small magnetic elements or move magnetic domain walls along narrow wires [16–19]. Promising examples include STT-MRAM and racetrack memory [20]. STT is obtained when a spin-polarized electric current is passed through a narrow magnetic entity. The critical current density for magnetic switching or domain wall motion by STT is high, of the order of $J \approx 10^{12}$ A m^{-2}, which causes undesirable heat dissipation and considerable power losses. Electric field control of magnetism in composite multiferroic structures is under investigation as a low-power alternative. A promising approach to attain this goal is offered by heterostructures in which ferroelastic domains of a ferroelectric material strain a ferromagnetic film, inducing magnetoelastic anisotropy via inverse magnetostriction. Full correlations between ferromagnetic and ferroelectric domains can be obtained in such hybrid structures, and switching of the ferroelectric polarization via an electric field enables electric field control of magnetism. Effects that have been demonstrated include electric field induced local magnetic switching, writing and erasure of regular ferromagnetic domain patterns, and electric field driven magnetic domain wall motion. In this chapter, we present a summary of our recent findings on elastically coupled domains in multiferroic heterostructures that consist of a ferromagnetic film and a ferroelectric $BaTiO_3$ substrate.

21.2 Domain Pattern Transfer

Magnetostriction is a property of ferromagnetic materials that causes them to change their shape during magnetization reversal. The inverse effect produces a magnetoelastic anisotropy (K_{me}) in response to an external mechanical stress. In ferromagnetic films, the strength and orientation of the magnetoelastic anisotropy depend on the film stress (σ) and the magnetostriction constant (λ). For isotropic materials, such as amorphous systems, it is given by $K_{me} = -3\sigma\lambda/2$, whereas proper tensor formalism is required to describe inverse magnetostriction in epitaxial systems [21, 22].

One popular approach to achieve electric field control of magnetism via inverse magnetostriction involves the growth of ferromagnetic films on to piezoelectric substrates (see, for example, [10] to [12]). In such systems, the magnetoelastic anisotropy does not vary with sample location and the magnetic response of the ferromagnetic film mimics the butterfly-shaped piezostrain curve of the substrate [23]. Consequently, the change of magnetic anisotropy is approximately linear and mostly reversible (volatile) in an electric field if other symmetry-breaking anisotropies are absent. Typical lattice strains that can be induced in a ferromagnetic film on top of a strong piezoelectric crystal are of the order of 0.1%.

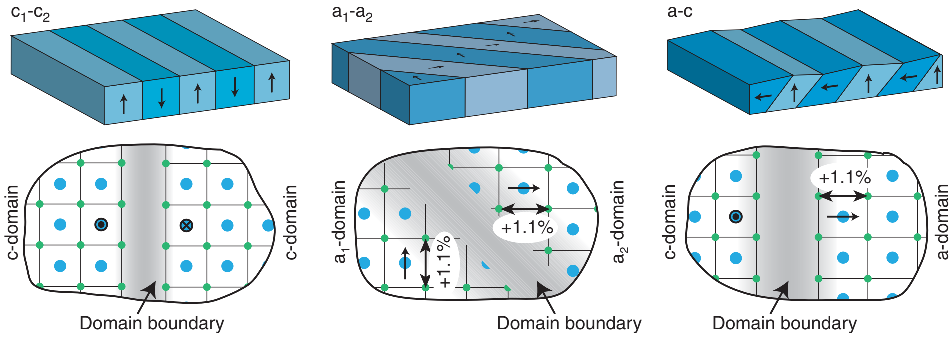

Figure 21.1 *Schematic illustration of three possible domain patterns in tetragonal* $BaTiO_3$ *crystals with a (001)-oriented surface. Ferroelastic* a_1–a_2 *and a–c domain structures can be used to obtain domain correlations between ferroelectric* $BaTiO_3$ *and a ferromagnetic film*

The characteristics of strain transfer from a ferroelectric material with ferroelastic domains are different. If the polarization reversal process involves the nucleation and/or growth of ferroelastic domains, that is ferroelectric domains that are separated by non-180° domain walls, the in-plane lattice parameter changes during ferroelectric switching. This hysteretic response can be used to alter the magnetic properties of an adjacent ferromagnetic film in a non-volatile way. The magnitude of transferrable strain depends on the ferroelectric material, its crystal orientation, and the type of ferroelectric domain pattern. In our experiments, ferroelectric $BaTiO_3$ substrates are used. At room temperature, $BaTiO_3$ exhibits a tetragonal crystal structure with a tetragonality of 1.1% and the ferroelectric polarization aligns with the axis of the largest lattice parameter. Three different domain patterns can form in tetragonal $BaTiO_3$ with a (001)-oriented surface, as illustrated in Figure 21.1. The in-plane lattice structure of stripe domains with alternating up and down polarization (c_1–c_2 domain pattern) is cubic and does not change from one domain to the other. The other two domain patterns are characterized by 90° rotations of the ferroelectric polarization and corresponding changes of the in-plane lattice structure. These configurations therefore exhibit both ferroelectric and ferroelastic properties. For the a_1–a_2 pattern, the unit cell in the (001)-oriented surface is rectangular in both domains, but the axis of unit cell elongation rotates by 90° at domain boundaries. In the case of *a*–*c* stripe domains, the symmetry of the crystal lattice in the (001) plane alternates between cubic (*c* domains) and rectangular (*a* domains).

If a ferromagnetic film is deposited on a $BaTiO_3$ substrate with a_1–a_2 or *a*–*c* domains, pattern transfer from the ferroelectric material to the ferromagnet can be obtained. Full domain correlations in elastically coupled multiferroic heterostructures were first demonstrated for CoFe films on top of $BaTiO_3$ substrates with an a_1–a_2 domain pattern [24, 25], as shown in Figure 21.2(a). In this system, strain-induced magnetoelastic anisotropy dominates over magnetocrystalline anisotropy, which is small because of the atomic composition ($Co_{60}Fe_{40}$ [26]) and polycrystalline structure of the CoFe film. Because of the positive magnetostriction constant of CoFe, the easy magnetoelastic anisotropy axis and ferroelectric polarization are collinear and, as a result, the remanent magnetization of the ferromagnetic

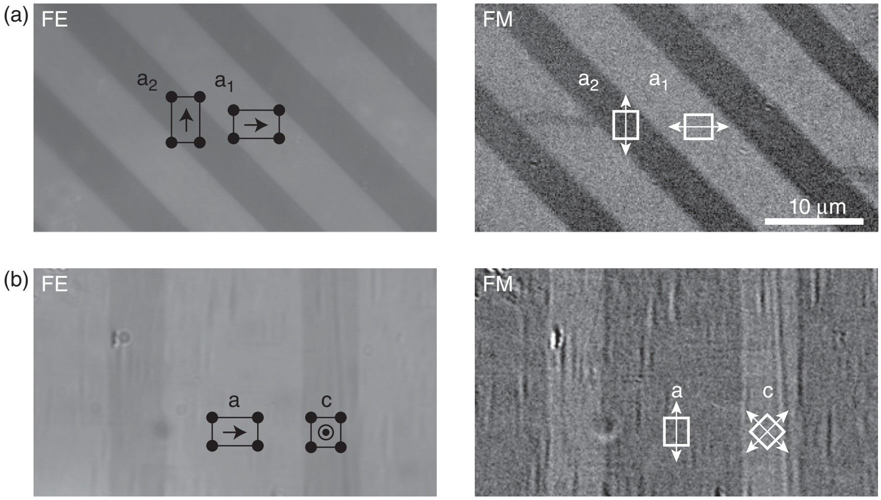

Figure 21.2 *Full pattern transfer (a) from BaTiO$_3$ a_1–a_2 domains to a 15 nm polycrystalline CoFe film and (b) from BaTiO$_3$ a–c domains to a 20 nm epitaxial Fe film. The ferroelectric domain images (FE) were obtained using birefringent contrast in an optical polarization microscope while the ferromagnetic domains (FM) were imaged using the magneto-optical Kerr effect in the same microscope. The single-headed and double-headed arrows indicate the direction of ferroelectric polarization and easy magnetoelastic anisotropy axes, respectively*

film follows the 90° polarization rotations at the a_1–a_2 boundaries. Pattern transfer from BaTiO$_3$ *a*–*c* domains to thin ferromagnetic films has also been realized [27]. An example is shown in Fig. 21.2(b) for epitaxial Fe. Again, the magnetoelastic anisotropy is determined by the structural symmetry of the ferroelectric crystal in the substrate plane. Due to negative magnetostriction of Fe, the magnetic easy axis on top of ferroelectric *a* domains is oriented perpendicular to the ferroelectric polarization, while the two easy axes on top of the *c* domains are aligned at 45°. Besides CoFe and Fe, domain pattern transfer from ferroelectric BaTiO$_3$ crystals has also been obtained for CoFeB [28], CoFe$_2$O$_4$ [29], (La, Sr)MnO$_3$ [30], Ni [31], and NiFe [32], indicating effective strain coupling for a variety of ferromagnetic materials.

The realization of domain pattern transfer in elastically coupled multiferroic heterostructures depends on two main factors:

1. *Competition between magnetoelastic anisotropy and other magnetic anisotropies in the ferromagnetic film.* For large ferroelectric domains, this is the defining criteria. The ferroelectric domain pattern is transferred to the ferromagnetic film if the strain-induced magnetoelastic anisotropy is large compared to other magnetic anisotropies in the system. The figure of merit, $K_{\mathrm{me}}/K_{\mathrm{other}}$, is enhanced by efficient strain transfer (e.g. by epitaxial film growth) and the use of ferromagnetic materials with large magnetostriction and negligible magnetocrystalline anisotropy. In patterned films, the competition between magnetic shape anisotropy and magnetoelastic anisotropy can drastically affect the magnetic microstructure.

2. *Exchange and magnetostatic interactions between neighboring ferromagnetic domains*. If the size of ferroelectric domains becomes comparable to the width of magnetic domain walls, breakdown of domain pattern transfer commences. In this case, the strength of exchange or magnetostatic interactions between neighboring domains starts to overcome the strain-induced magnetoelastic anisotropy, promoting more uniform magnetization. Domain size scaling of pattern transfer is discussed in Section 21.4 of this chapter.

One key characteristic of domain pattern transfer is strong elastic pinning of magnetic domain walls on to ferroelectric domain walls. This effect, which is caused by an abrupt change of magnetic anisotropy on top of ferroelastic domain boundaries, enables full control over the formation of different types of magnetic domain walls in a magnetic field [33] and provides the basis for electric field driven magnetic domain wall motion [34–36]. Magnetic domain wall pinning and related magnetic field effects are described in the next section. Driving of magnetic domain walls with an electric field is discussed in Section 21.6.

Correlations between ferromagnetic and ferroelectric domains have also been obtained in exchange-coupled multiferroic heterostructures, most notably ferromagnetic films on $BiFeO_3$ [37–39]. For a recent review on $BiFeO_3$-based systems we refer to Heron et al. [40]. Although the physics of exchange coupling is different from strain coupling, both produce lateral modulations of magnetic anisotropy. Effects such as magnetic domain wall pinning and finite size scaling of domain pattern transfer do therefore also occur in exchange-coupled multiferroic heterostructures.

21.3 Elastic Coupling Between Magnetic and Ferroelectric Domain Walls

The modification of structural symmetry at ferroelastic domain walls of a ferroelectric material creates magnetoelastic anisotropy boundaries in an adjacent ferromagnetic film via inverse magnetostriction. Magnetic domain walls are strongly pinned by these sudden anisotropy changes and, consequently, strong elastic coupling between magnetic and ferroelectric domain walls is obtained. Experimental results and theoretical calculations indicate that ferroelastic domain boundaries in $BaTiO_3$ are only 2–5 nm wide [41–43], which is considerably smaller than the width of magnetic domain walls in films with in-plane magnetization. The induced anisotropy boundary on top of ferroelectric domain walls can therefore be considered as abrupt. The magnetic pinning potential that is created by an abrupt anisotropy boundary depends on the strength and symmetry of the magnetoelastic anisotropy. The potential profile can be calculated by assuming a lateral displacement of the magnetic domain wall away from the ferroelectric boundary [36]. Such a movement would cause a misalignment between the local magnetization direction and the easy anisotropy axes, thereby enhancing the total anisotropy energy of the system. An example of a pinning potential for an a_1–a_2 domain wall is shown in Figure 21.3. The steep potential well couples the magnetic and ferroelectric domain walls and provides a means to achieve magnetic field tuning of magnetic domain wall profiles and electric field driven magnetic domain wall motion, as will be illustrated below and in Section 21.6.

Magnetization reversal in elastically coupled multiferroic heterostructures exhibiting full domain pattern transfer is characterized by independent magnetization reversal within the

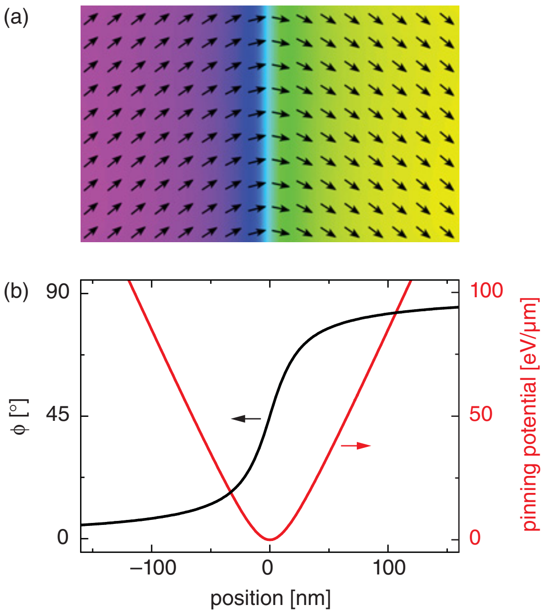

Figure 21.3 *(a) Micromagnetic simulation of the magnetic microstructure in a coupled* a_1*–*a_2 *system and (b) the extracted magnetization angle and calculated pinning potential. The data in (a) and (b) are plotted on the same scale.* $K_{me} = 1.7 \times 10^4\ \mathrm{J\,m^{-3}}$ *was used in the simulations, which corresponds to the experimentally determined anisotropy value for 15 nm CoFe films on* $BaTiO_3$ *[24]*

stripe domains and complete immobilization of magnetic domain walls on top of ferroelectric boundaries. An example for a CoFe film on top of an a_1–a_2 domain pattern is shown in Figure 21.4. Starting from saturation, the magnetization of neighboring stripe domains rotate in opposite directions towards their respective easy anisotropy axes when the magnetic field is reduced. As a result, the spin rotation within the pinned magnetic domain walls varies continuously from zero in saturation, to 90° in remanence, and finally to nearly 180° just before abrupt magnetic switching. Another intriguing consequence of domain wall pinning is the ability to form different types of walls by rotation of the magnetic field in the film plane. Head-to-tail domain walls are stabilized when a non-saturating magnetic field is applied perpendicular to the stripe domains (Figure 21.5(a) and (c) show the remanent configuration). The width of such magnetic domain walls (δ) is determined mostly by the competition between the exchange energy given by the exchange constant (A) and the magnetic anisotropy strength. A good approximation for zero magnetic field is given by $\delta_{uc} \approx \pi(A/2K_{me})^{1/2}$, which is the width of 90° Néel walls in the limiting case of zero magnetostatic energy [21]. Since magnetostatic charges on either side of a head-to-tail domain wall cancel each other, this wall is labeled as magnetically uncharged. If a non-saturating magnetic field is instead applied parallel to the stripe domains, the magnetization aligns in alternating head-to-head and tail-to-tail configurations, which produce equal magnetostatic charges on both sides of the domain wall (Figure 21.5(b) and (d)).

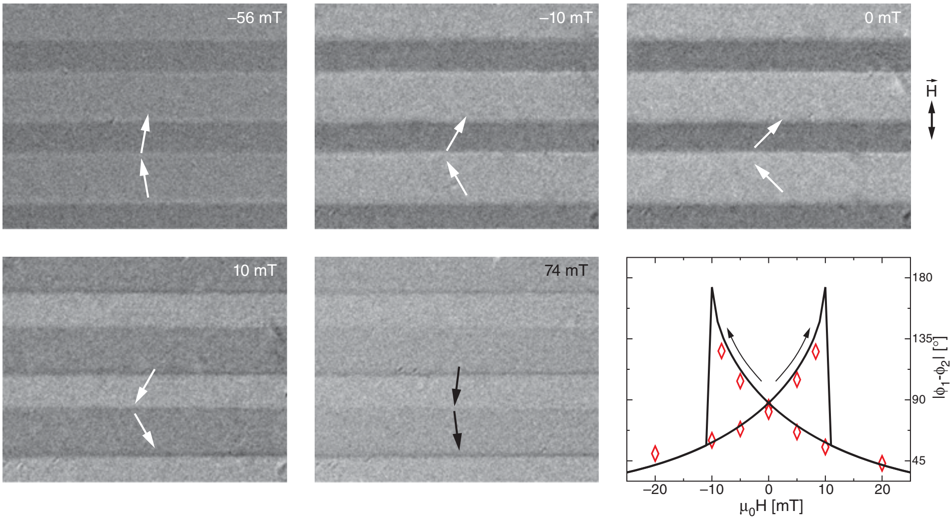

Figure 21.4 Magnetization reversal in a 15 nm CoFe film on top of a $BaTiO_3$ substrate with a_1–a_2 domains. The graph shows the spin rotation between neighboring domains ($|\phi_1 - \phi_2|$) as determined from Kerr microscopy images (symbols) and micromagnetic simulations (line). Data adapted from [33]

The width of these charged walls depends mostly on the magnetostatic energy and magnetic anisotropy. Although an analytical expression is not available, the width of 90° charged walls is approximated by $\delta_c \approx \pi\mu_0 M_s^2 t/8K_{me}$, which is half the width of 180° charged domain walls [44]. Here, M_s is the saturation magnetization and t is the ferromagnetic film thickness. The difference in domain wall width between the uncharged and charged configurations is one to two orders of magnitude for typical ferromagnetic films

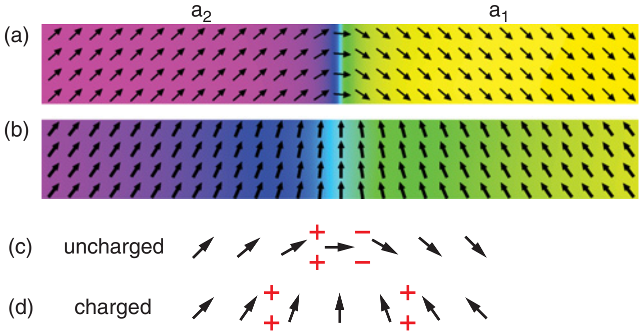

Figure 21.5 Remanent micromagnetic structure on top of an a_1–a_2 ferroelectric domain pattern after the application of a magnetic field (a) perpendicular and (b) parallel to the stripe domains. Schematic illustrations of a narrow uncharged and a broad charged magnetic domain wall are shown in (c) and (d). Data adapted from [33]

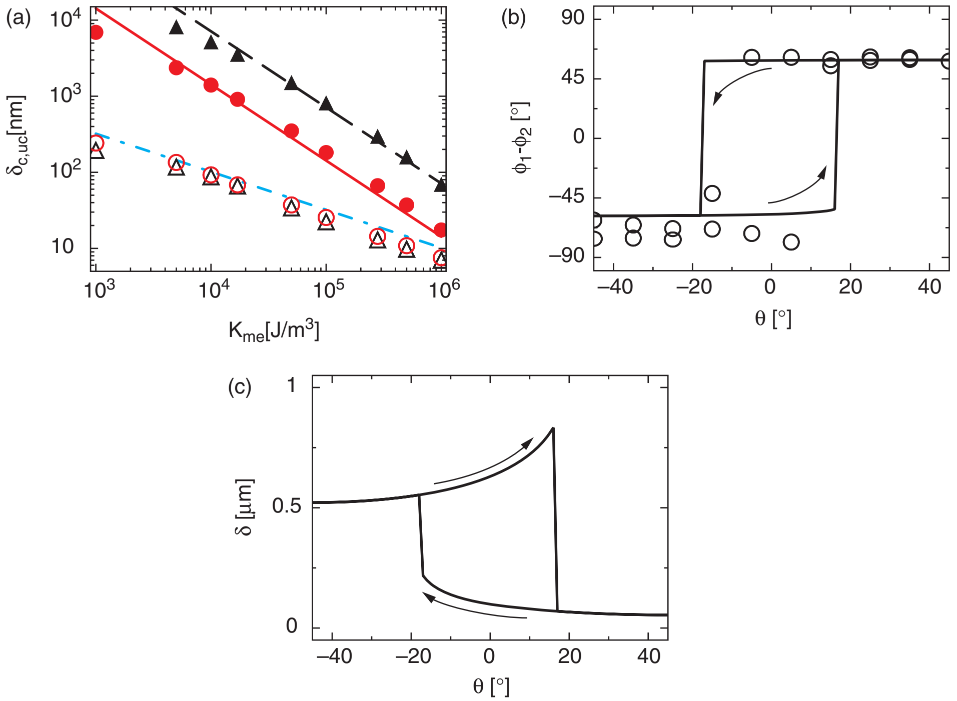

Figure 21.6 *(a) Simulated uncharged (open symbols) and charged (filled symbols) magnetic domain wall width as a function of uniaxial magnetoelastic anisotropy. The circles and triangles indicate data for a ferromagnetic film thickness of 10 and 50 nm, respectively. The lines are calculated using* $\delta_{uc} \approx \pi(A/2K_{me})^{1/2}$ *and* $\delta_c \approx \pi\mu_o M_s^2 t/8K_{me}$. *(b) Dependence of spin rotation* ($\phi_1 - \phi_2$) *and (c) magnetic domain wall width (δ) on the in-plane magnetic field angle. The magnetic anisotropy is* $K_{me} = 1.7 \times 10^4$ J m^{-3} *for both the experimental data (symbols) and the micromagnetic simulations (lines) and the magnitude of the applied magnetic field is 10 mT. Data adapted from [33] and [45]*

and values of K_{me} (Figure 21.6(a)). Consequently, hysteretic switching between broad and narrow magnetic domain walls occurs when a sufficiently large magnetic field is rotated in the film plane (Figure 21.6(b)). The ability to tune the spin rotation, the width, and the type (charged/uncharged) of pinned magnetic domain walls by varying the strength (Figure 21.4) and/or direction (Figures 21.5 and 21.6) of the magnetic field might be useful for magnetic devices wherein domain walls act as functional and controllable elements.

The formation of different types of magnetic domain walls can affect the magnetization reversal process in multiferroic heterostructures, in particular when the energy difference between charged and uncharged walls becomes large in thick ferromagnetic films. An example is given for a 100 nm $Co_{40}Fe_{40}B_{20}$ (hereafter CoFeB) film on $BaTiO_3$ with a_1–a_2 domains. If a magnetic field is applied parallel to the stripe domains (Figure 21.7(a)), charged magnetic domain walls form when the field is reduced from saturation. The magnetostatic energy and width of these walls are initially small, but both increase rapidly when the total spin rotation of the walls grows with decreasing field strength. At some point, the

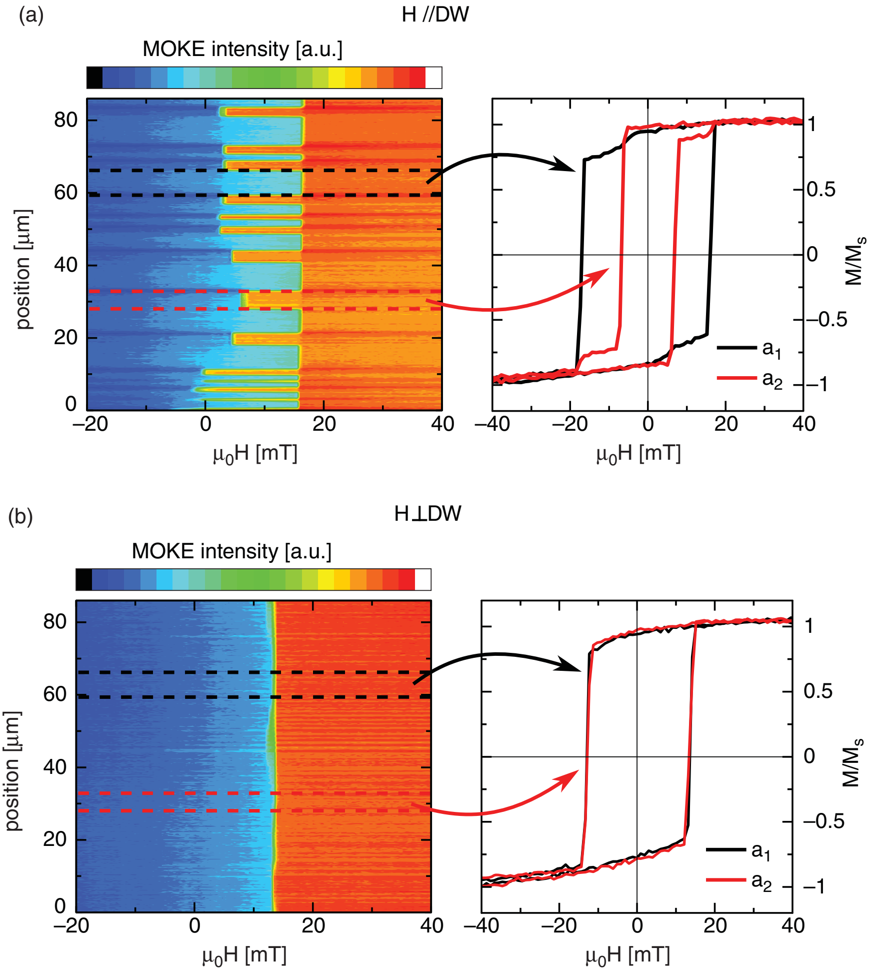

Figure 21.7 *Kerr microscopy data illustrating different magnetic switching behavior for an in-plane magnetic field parallel and perpendicular to the magnetic stripe domains of a 100 nm CoFeB film on top of BaTiO*$_3$. *The images illustrate switching in an area with about 25 stripe domains and the graphs show the corresponding hysteresis curves of an* a_1 *and* a_2 *domain. For a color version of this figure, see color plate section*

large energy difference between charged and uncharged domain walls triggers an abrupt magnetic switching event in every second stripe domain. During this reversal process, all charged domain walls transform into narrow uncharged walls, providing a net energy gain. Magnetic switching in the remaining domains only occurs when a large magnetic field forces the magnetization of neighboring domains to align closely; that is the switch transforms high-angle uncharged domain walls into small-angle charged walls. The reversal process differs when the magnetic field is applied perpendicular to the stripe domains, as shown in Figure 21.7(b). In this case, lower-energy uncharged domain walls form when the field is reduced from saturation and the energy of the ferromagnetic system cannot be lowered by domain wall transformations. In fact, magnetic switching in the domains is now completely synchronized to prevent the formation of higher-energy charged domain walls.

21.4 Domain Size Scaling of Pattern Transfer

Exchange coupling and magnetostatic interactions between neighboring magnetic stripe domains affect the magnetization direction within the domains when the stripes become narrow. Because of this scaling effect, domain pattern transfer can break down. An example is shown in Figure 21.8. For a ferroelectric domain width of $\Delta = 5$ µm, the domains are fully imprinted into the ferromagnetic film. With reducing domain width, however, the magnetization of neighboring domains start to align with each other and the magnetic domains vanish completely when nearly uniform ferromagnetic alignment is obtained for small Δ. The critical length scale for imprinting of ferroelectric domains into a ferromagnetic film depends on the dominant interaction mechanism between neighboring ferromagnetic domains. For uncharged domain walls, the magnetic domains couple via direct exchange. The domain-size dependence of this configuration is therefore characterized by

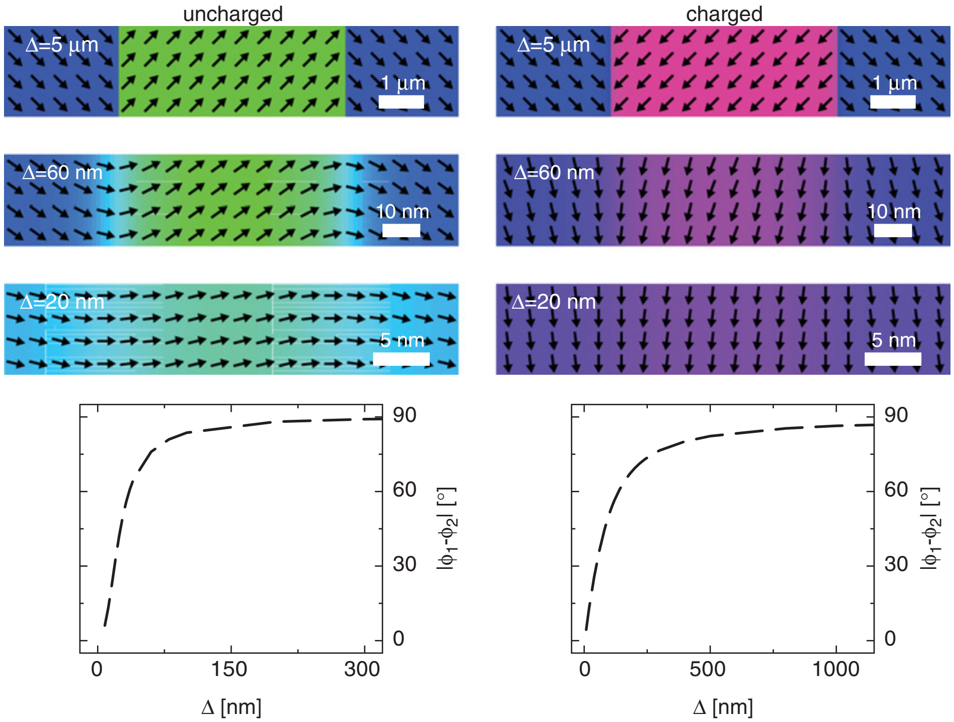

Figure 21.8 *Remanent magnetization state as a function of ferroelectric domain width for uncharged (left) and charged (right) magnetic domain walls and corresponding scaling of spin rotation between domains in a zero applied magnetic field (both for* $K_{me} = 2.8 \times 10^5$ *J m*$^{-3}$*)*

the exchange length, which roughly equals the width of uncharged domain walls. Consequently, the magnetization aligns with the easy anisotropy axes of the individual stripe domains if $\Delta \gg \delta_{\mathrm{uc}}$ (full pattern transfer) while ferromagnetic exchange interactions force the magnetization of neighboring domains to align parallel when $\Delta \ll \delta_{\mathrm{uc}}$ (uniform magnetization). In between these two limiting cases, the spin rotation between domains decreases with reducing ferroelectric domain width (Figure 21.8). For charged domain walls, a similar picture emerges with the distinction that magnetic domains couple via longer-range magnetostatic interactions. In this case, domain coupling is effective over a distance that is comparable to the width of charged magnetic domain walls (δ_{c}). Since δ_{uc} and δ_{c} are good indicators for pattern transfer breakdown, the graph of Figure 21.6(a) can be considered as a phase diagram. In this representation, areas above the curves indicate parameters (ferroelectric domain width and magnetic anisotropy strength) for which ferroelectric domains are imprinted into the ferromagnetic film and areas below the curves represent conditions for which the film magnetization is mostly uniform. Because of the two scaling regimes, it is possible to select a ferroelectric domain width between the widths of uncharged and charged magnetic domain walls. Under this condition, rotation of an in-plane magnetic field would result in the successive writing and erasure of magnetic domain patterns. The experimental data of Figure 21.9 confirm this effect for a 150 nm CoFeB film. Clear magnetic contrast is obtained when the magnetic field is oriented perpendicular to the underlying

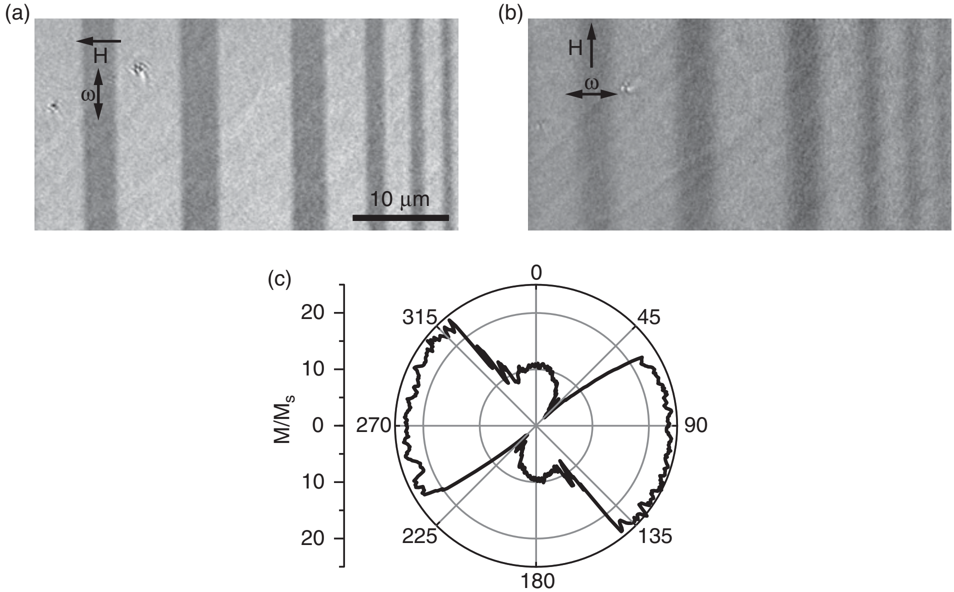

Figure 21.9 *Kerr microscopy images of an a_1–a_2 domain pattern in a 150 nm CoFeB film recorded with an in-plane magnetic field of 40 mT (a) perpendicular and (b) parallel to the stripe domains. The magneto-optical sensitive axis (ω) is perpendicular to the magnetic field in both measurements. The polar plot in (c) shows the spin rotation between domains as a function of the in-plane magnetic field angle. Abrupt switches in this plot are due to domain wall transformations from charged to uncharged and vice versa*

ferroelectric domains ($\Delta > \delta_{uc}$), but the contrast nearly vanishes when the field is rotated by 90° ($\Delta < \delta_c$). Evidence of domain size scaling of pattern transfer has also been obtained for exchange-coupled multiferroic heterostructures. Experiments on CoFe/$BiFeO_3$ indicate a decrease of spin rotation from 90 to 60° for 310 nm wide stripe domains [46], which is in good agreement with a 1D scaling model for uncharged magnetic domain walls [45].

21.5 Electric Field Control of Ferromagnetic Domains

The application of an electric field to multiferroic heterostructures changes the direction of polarization and thereby the in-plane lattice structure of the ferroelectric layer. Via inverse magnetostriction, this alters the magnetoelastic anisotropy of the adjacent ferromagnetic film. The electric field induced modulation of magnetic anisotropy can be significant, particularly if strain transfer is efficient and domain structures are correlated. Many macroscopic measurements of electric field controlled effects in ferromagnetic films on top of $BaTiO_3$ substrates have been conducted using SQUID, vibrating-sample, or magneto-optical Kerr effect magnetometry [47–54] and local switching experiments have been performed using scanning probe microscopy [55]. Ferromagnetic materials that have been used include (La, Sr)MnO_3 [47], Fe [48–51, 54], Ni [52], Fe_3O_4 [53], and $Fe_{81}Ga_{19}$ [54]. In most experiments, the electric field is applied perpendicular to the $BaTiO_3$ substrate plane and changes of the coercive magnetic field or magnetic moment in constant magnetic field are reported. Both effects are explained by electric field induced variations of magnetoelastic anisotropy. Coupling between a ferromagnetic and ferroelectric material driven by an in-plane electric field has also been studied using suspended $BaTiO_3$/FeGa thin-film bilayer structures [56].

The details of electric field controlled magnetic effects depend on the initial ferroelectric domain structure and the efficiency of strain transfer from the ferroelectric layer to the ferromagnetic film. As mentioned above, two types of fully correlated domain patterns can be obtained in systems with a (001)-oriented tetragonal $BaTiO_3$ crystal, as illustrated in Figures 21.1 and 21.2. The application of an out-of-plane electric field to these structures can result in (1) the writing and erasure of regular ferromagnetic stripe patterns via local magnetic switching and (2) reversible motion of magnetic domain walls. In this section, electric field control of ferromagnetic domains is reviewed for a_1–a_2 stripe patterns. Electric field driven magnetic domain wall motion in heterostructures with a–c domains is discussed in Section 21.6.

The application of an out-of-plane electric field to a ferroelectric material with a_1–a_2 stripe domains produces a single c domain in saturation. The micromagnetic response to this polarization switching event in an elastically coupled ferromagnetic film is illustrated in Figure 21.10. In the experiment, regular a_1–a_2 domains of a $BaTiO_3$ substrate are first imprinted into a 50 nm thick CoFeB film during the deposition process. The rectangular in-plane lattice of $BaTiO_3$ induces alternating uniaxial stresses in the ferromagnetic film leading to full domain pattern transfer in the as-grown state. The easy anisotropy axes of the two domains are perpendicular and the magnetization aligns with those axes in zero magnetic field. Out-of-plane switching of the ferroelectric polarization in an electric field of 6 kV cm^{-1} changes the in-plane structure of the $BaTiO_3$ substrate from rectangular to cubic. Abrupt removal of the lattice elongation at the $BaTiO_3$ interface compresses the CoFeB film. The direction of this lattice compression opposes the growth-induced tensile

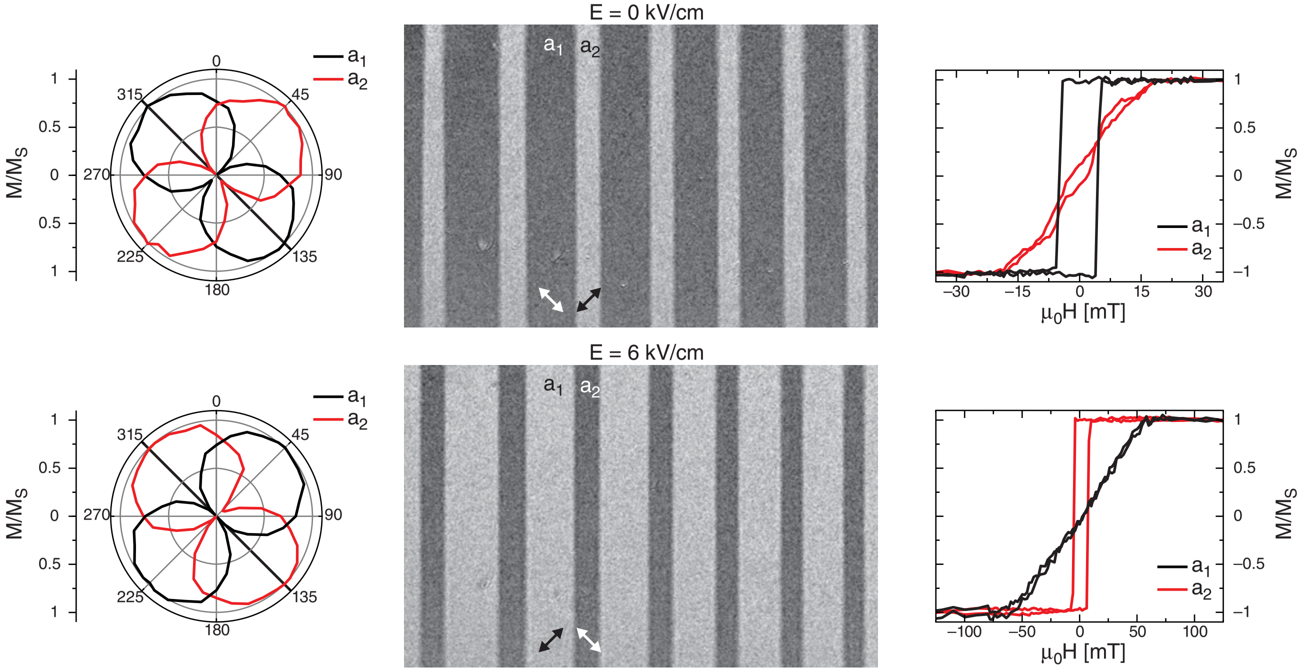

Figure 21.10 Kerr microscopy image, normalized remanent magnetization (polar plot), and hysteresis curves on single a_1 and a_2 domains for a 50 nm CoFeB film on $BaTiO_3$ after growth on a_1–a_2 domains (top row) and after out-of-plane switching of the ferroelectric polarization in an electric field of 6 kV cm^{-1} (bottom row). Switching to a single c domain state in the $BaTiO_3$ substrate induces 90° rotations of the magnetoelastic anisotropy axes in the plane of the CoFeB film, as illustrated by the arrows in the images, rotation of the polar plots, and change from easy- to hard-axis hysteresis behavior on the original a_1 stripe domain (and vice versa for the a_2 domain). Because of symmetry, the overall magnetic stripe pattern is conserved. For a color version of this figure, see color plate section

stress in CoFeB. As a consequence, rotation of the anisotropy axes by 90° and a change of anisotropy strength occur when strain transfer from the $BaTiO_3$ substrate to the CoFeB film is more efficient in an electric field than during film growth. Rotation of the anisotropy axes is clearly illustrated by contrast reversal in the Kerr microscopy images of Figure 21.10. The electric field effect can be described by considering the stress state of the ferromagnetic film (1) after growth on ferroelectric a domains ($\sigma_{\mathrm{growth},a}$) and (2) after electric field induced polarization switching to a single c domain ($\sigma_{\mathrm{electric},c}$). If $\sigma_{\mathrm{electric},c} = -\sigma_{\mathrm{growth},a}$, the magnetoelastic anisotropy is reduced to zero and the growth-induced magnetic stripe pattern is erased in large electric fields. In many experimental systems, however, lattice relaxation during film growth impedes full strain transfer while almost complete strain transfer is obtained during polarization switching because of film–substrate clamping. Therefore, usually, $|\sigma_{\mathrm{electric},c}| > |\sigma_{\mathrm{growth},a}|$ and the magnetoelastic anisotropy axes realign with the new stress state of the ferromagnetic film (90° rotation in the film plane). The magnitude of K_{me} in an isotropic ferromagnetic film after polarization switching can be written as:

$$K_{\mathrm{me},c} = \left| \frac{\sigma_{\mathrm{electric},c} - \sigma_{\mathrm{growth},a}}{\sigma_{\mathrm{growth},a}} \right| K_{\mathrm{me},a} = -\frac{3}{2}\lambda \left| \sigma_{\mathrm{electric},c} - \sigma_{\mathrm{growth},a} \right| . \qquad (21.1)$$

Based on this, an enhancement of magnetoelastic anisotropy is anticipated if less than half of the lattice strain is transferred from the ferroelectric crystal to the ferromagnetic film during the deposition process. In the experiments of Figure 21.10, this is indeed the case. From a fit to the hard-axis hysteresis curves, $K_{\mathrm{me},a} = 1 \times 10^4$ J m^{-3} and $K_{\mathrm{me},c} = 3 \times 10^4$ J m^{-3} are obtained, from which a strain transfer efficiency of 25% during growth is estimated. Due to partial strain transfer during film growth, the magnetic anisotropy remains laterally modulated when the $BaTiO_3$ substrate is switched to a single c domain. The overall magnetic stripe pattern is conserved and, because of 90° rotations of the magnetoelastic anisotropy axes, the magnetic a_1 domains behave as a_2 domains and vice versa in a saturating electric field.

Intermediate states with an alternating ferroelectric a–c domain pattern can also be stabilized by perpendicular electric fields. The transformation from a_1–a_2 to a–c stripe domains in a $BaTiO_3$ crystal alters the magnetic microstructure of the ferromagnetic film in a more complex way [24, 25, 34]. On the new c domains, conservation of the original magnetic stripe pattern with a rotation of the magnetoelastic anisotropy axes by 90° coincide with a change of anisotropy strength, as discussed previously. On the new a domains, the magnetoelastic anisotropy axes of the original a_1 and a_2 domains align in parallel, which erases the growth-induced magnetic stripe pattern in zero magnetic field. An example is shown in Figure 21.11. The growth of ferroelectric c domains in an increasing out-of-plane electric field reestablishes the ferromagnetic a_1–a_2 domain pattern, whereas the magnetic stripes are erased when the polarization of the underlying ferroelectric domain relaxes back into the substrate plane. Back and forth switching between the two magnetic structures is fully reversible.

21.6 Electric Field Driven Magnetic Domain Wall Motion

Domain walls in ferromagnetic thin films or nanowires are conventionally driven by magnetic fields or spin-polarized electric currents utilizing the STT effect. The velocity of

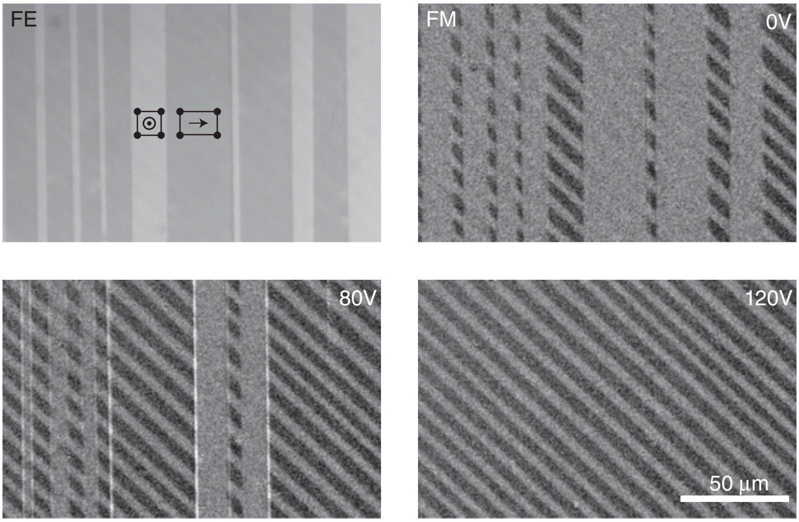

Figure 21.11 *Evolution of the ferroelectric (FE) and ferromagnetic (FM) domain pattern in a CoFe/BaTiO$_3$ heterostructure after switching from an a_1–a_2 domain pattern (growth-induced state similar to Figure 21.2(a), not shown here) to an a–c domain pattern in out-of-plane electric field (top row) and during growth of c domains by lateral domain wall motion under an increasing bias voltage (bottom row). Data adapted from [34]*

magnetic domain walls depends on the driving force and various material properties (magnetic anisotropy, damping constant, saturation magnetization, etc.), which give rise to several dynamic regimes (see, for example, Kleemann [57] and references therein). In the thermally activated creep regime, domain wall motion depends sensitively on the disorder-induced pinning energy barrier and the depinning field. This notion has led to various demonstrations of electric field control over the pinning strength and velocity of magnetic domain walls via voltage-induced changes of magnetic anisotropy. Examples include the use of dielectric gates to manipulate the magnetic anisotropy via charge modulation or band shifting in ultra-thin films [58–63] or coupling to piezoelectric materials [64, 65]. Another promising method utilizes the manipulation of magnetic anisotropy via electric field induced ionic diffusion [66,67]. In all cases, the magnetic domain walls are driven by a magnetic field or spin-polarized electric current and the velocity of the walls is altered by an electric field effect on the magnetic anisotropy.

In elastically coupled multiferroic heterostructures, magnetic domain walls can be driven by an electric field only. This alternative driving mechanism is based on the pinning of magnetic domain walls on top of ferroelectric domain boundaries, as discussed in Section 21.3. Strong elastic coupling between the two ferroic walls forces the magnetic domain wall to follow its ferroelectric counterpart in an electric field. The direction of motion and the domain wall velocity are fully determined by the physics of the ferroelectric subsystem. Reversible motion of magnetic domain walls can be obtained when an out-of-plane electric field is applied to an *a*–*c* domain pattern. An example for an epitaxial Fe film on BaTiO$_3$ is shown in Figure 21.12. If the electric field is aligned along the direction of ferroelectric polarization in the *c* domain of the BaTiO$_3$ substrate (negative bias voltage), the *c* domain

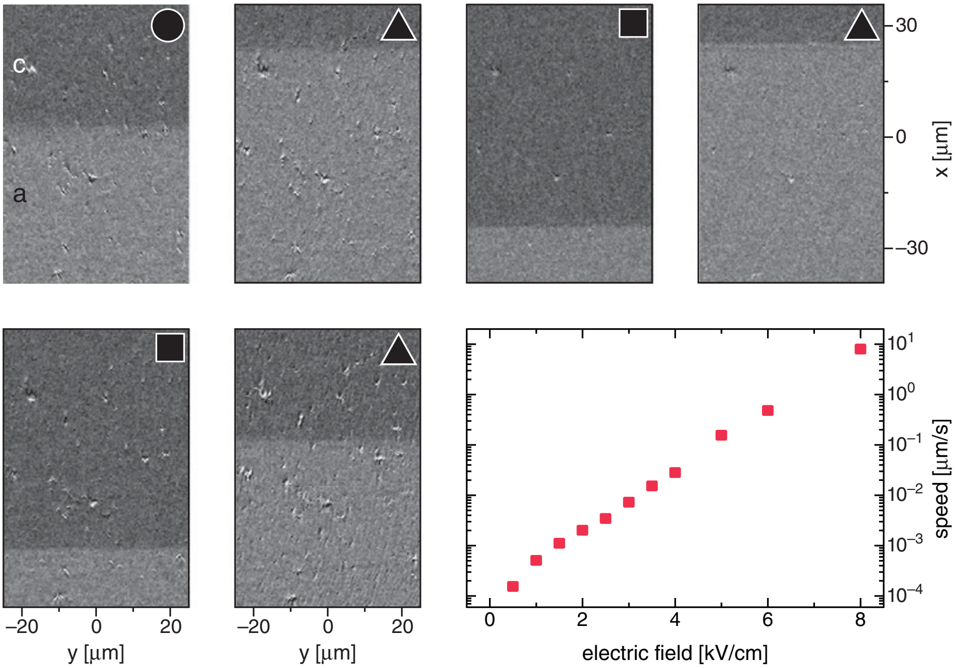

Figure 21.12 *(a) Kerr microscopy images illustrating the motion of a pinned magnetic domain wall in a 20 nm Fe film after the application of positive (triangles) and negative (squares) voltage pulses across the BaTiO$_3$ substrate. (b) Average magnetic domain wall velocity as a function of the applied electric field. All data were obtained in zero magnetic field. Data adapted from [36]*

grows at the expense of the neighboring a domain by lateral wall motion downwards. A positive bias voltage, on the other hand, shrinks the c domain by moving the ferroelectric boundary up. Strong elastic pinning necessitates that the magnetic domain wall in the Fe film strictly follows the displacement of the ferroelectric domain boundary. Other configurations, such as the motion of a_1–a_2 magnetic domain walls driven by in-plane electric fields can also be considered, but this requires a network of planar electrodes and has not yet been explored.

The velocity of elastically coupled magnetic and ferroelectric domain walls depends exponentially on the strength of the electric field pulse, which is characteristic of thermally assisted depinning of ferroelectric domain walls in the strong pinning regime [68]. In the proof-of-principle experiments of Figure 21.12, the domain wall velocity extends over five orders of magnitude. Although unprecedented, the wall velocities are small compared to the maximum reported speed of ferroelectric domain walls in BaTiO$_3$ crystals at room temperature [69]. The main reason is the thickness of the BaTiO$_3$ substrate (0.5 mm), which requires the use of large bias voltages. Considerably faster electric field driven magnetic domain wall motion could likely be attained on top of thinner BaTiO$_3$ crystals.

Another important step towards practical applications involves the patterning of multiferroic heterostructures into nanowire geometries. Interestingly, this offers additional degrees of freedom for the engineering of robust and strongly pinned magnetic domain walls. For example, despite the 45° angle between the magnetoelastic anisotropy axes on top of ferroelectric *a* and *c* domains, near-180° transverse domain walls can be stabilized in magnetic nanowires because of competing shape anisotropy. Fast motion of such walls does not lead to depinning from the ferroelectric boundary up to high driving velocities [36]. In this dynamic regime, deformations of the internal wall structure are small compared to the instabilities that take place during magnetic field or current-driven magnetic domain wall motion. In the latter cases, the spin structure of the magnetic domain wall starts to oscillate above a critical driving force (a phenomenon known as Walker breakdown), leading to a reduction of the domain wall velocity [18]. Micromagnetic simulations predict a very different dynamic behavior for electric field driven magnetic domain walls depending on wall type (uncharged/charged) and other magnetic parameters [35]. For charged magnetic domain walls on top of ferroelectric a_1–a_2 boundaries, simulations indicate the emission of monochromatic spin waves above a critical velocity. The phase velocity of the spin waves matches the speed of the electrically driven ferroelectric domain wall, but their wave number and frequency are different in front and behind the domain walls. More complex dynamic effects, including domain wall depinning and oscillatory domain wall motion are predicted for electrically driven uncharged magnetic walls at high velocities.

Electric field driven magnetic domain wall motion provides a low-power alternative for spintronic devices because of negligible current flow through the ferroelectric layer. The energy advantage over current-driven domain wall motion in magnetic nanowires can be estimated by comparing relevant material parameters and device geometries. In multiferroic heterostructures, the power consumption is determined by the ferroelectric switching process (Joule heating is small and can be neglected). For lateral ferroelectric domain wall motion, it is estimated by $P_{\mathrm{E}} = P_{\mathrm{FE}} E A_{\mathrm{FE}} v_{\mathrm{FE}}$, where P_{FE} and A_{FE} are the polarization and cross-section of the ferroelectric material, E is the applied electric field, and v_{FE} is the wall velocity. For a $BaTiO_3$ nanowire, the power dissipation would be of the order of µW. In current-driven magnetic systems, a large current density (J) is required to move a magnetic domain wall via the STT effect. Normally, the current density is about 10^{12} A m^{-2}. In this case, resistive Joule heating is the main source of power losses and is estimated by $P_{\mathrm{SST}} = \rho_{\mathrm{FM}} V_{\mathrm{FM}} J^2$. Here, ρ_{FM} is the electrical resistivity of the ferromagnetic material (typically permalloy with $\rho_{\mathrm{FM}} \approx 1 \times 10^{-7}$ Ωm) and V_{FM} is the volume of the magnetic nanowire. Thus, a 200 nm wide nanowire with a thickness of 5 nm and a length of 10 µm requires $P_{\mathrm{SST}} \approx 10$ mW. Large figure-of-merit gains in terms of energy efficiency could therefore be obtained if the physics of electric field controlled multiferroic heterostructures can be preserved on the nanoscale.

21.7 Summary and Outlook

Electric field control of elastically coupled multiferroic heterostructures enables the writing and erasure of ferromagnetic domains and the motion of magnetic domain walls. Both effects are based on the manipulation of magnetoelastic anisotropy. Thus far, most experiments have been conducted on ferromagnetic films with in-plane magnetization. In this configuration, the anisotropy axes realign in an electric field because of a variation of the ferroelectric lattice structure in the surface plane. Strain transfer from ferroelastic domains can also be used to modify the properties of ferromagnetic films with perpendicular anisotropy. Reversible switching between in-plane and out-of-plane magnetization requires a relatively small anisotropy (to position the ferromagnetic system close to the spin-reorientation transition) and a large susceptibility to film strain. Possible candidates include Ni and $CoFe_2O_4$ films [70].

Domain pattern transfer from a ferroelectric material to a ferromagnetic film offers attractive means to tune magnetic properties by the application of magnetic or electric fields. The replication of regular stripe patterns and strong pinning of magnetic domain walls on top of ferroelectric domain boundaries could, for example, find uses in new spin-wave-based technologies. Spin waves are normally manipulated in magnonic crystals consisting of periodic antidot or bicomponent lattices (see, for example, [71] and [72]). The reciprocal lattice constant of such crystals enhances the magnonic excitation wave vector. We have recently realized similar effects in CoFeB/$BaTiO_3$ with regular a_1–a_2 domains [28]. Multiferroic heterostructures can thus operate as a magnonic crystal without the creation of geometrical constraints via patterning. Electric field control over ferromagnetic domains is another intriguing feature. Rotations of the magnetic anisotropy axis and variations of its strength in an electric field would modify the spin-wave dispersion relations of a ferromagnetic film. Such effects could be used to realize electric-field controlled spin-wave switches, (de)multiplexers, phase shifters, and interferometers. As the utilization of electric-field effects in magnonics is only emerging, more concepts and ideas are bound to emerge in the coming years.

Besides anisotropy control, electric field induced shifts of magnetic phase transitions can also be realized by strain transfer. Reversible switching between antiferromagnetic and ferromagnetic order has been demonstrated for FeRh films on $BaTiO_3$ substrates near a transition temperature of 350 K [73]. In these experiments, tweaking of the magnetic phase is ascribed to the growth of ferroelectric c domains at the expense of a domains in an out-of-plane electric field. The ferromagnetic Curie temperature can also vary as a function of lattice strain. This phenomenon has been studied extensively for perovskite manganite films on piezoelectric substrates [23, 74–77]. Stronger responses are anticipated when such films are grown on to the ferroelastic domains of a $BaTiO_3$ crystal because of the transfer of larger strains.

Several non-trivial nanoscale effects need to be addressed in future investigations before the fascinating physics of elastically coupled ferroic domains can be utilized in spintronic and magnonic devices. Until now, most studies on domain pattern transfer and electric field control have been conducted on thick $BaTiO_3$ substrates, requiring large bias voltages to switch the polarization. The demonstration of similar effects using thinner crystals or epitaxial ferroelectric films is essential for future device integration and requires a detailed assessment of dynamic switching processes and issues related to domain wall clamping. Ferroelastic domain patterns can be generated in thin films by strain engineering during film growth [78] and polarization switching can be induced by the application of local bias voltages using patterned electrodes [79, 80] or the tip of a scanning probe microscope [81, 82]. While such techniques have been used for the investigation of ferroelectric materials, their utilization in elastically coupled ferromagnetic–ferroelectric heterostructures is only just emerging. Once polarization switching in a ferroelectric layer or nanostructure by short and small voltage pulses is successfully implemented, the dynamic response of a ferromagnetic film can be studied. Micromagnetic and phase-field simulations predict a variety of intriguing dynamic phenomena and the ability to electrically switch the magnetization on nanosecond time scales [35, 83, 84]. The practical realization of electric field induced dynamic switching in elastically coupled ferromagnetic films can be regarded as the next important breakthrough in the field.

Acknowledgments

The authors gratefully acknowledge financial support from the European Research Council and the Academy of Finland.

References

(1) Hill, N.A. (2000) Why are there so few magnetic ferroelectrics? *Journal of Physical Chemistry B*, **104** (29), 6694–6709.
(2) Fiebig, M. (2005) Revival of the magnetoelectric effect. *Journal of Physics D: Applied Physics*, **38** (8), R123–R152.
(3) Prellier, W., Singh, M.P., and Murugavel, P. (2005) The single-phase multiferroic oxides: from bulk to thin film. *Journal of Physics: Condensed Matter*, **17** (30), R803–R832.
(4) Eerenstein, W., Mathur, N.D., and Scott, J.F. (2006) Multiferroic and magnetoelectric materials. *Nature*, **442** (7104), 759–765.
(5) Ramesh, R. and Spaldin, N.A. (2007) Multiferroics: progress and prospects in thin films. *Nature Materials*, **6** (1), 21–29.
(6) Kimura, T. (2007) Spiral magnets as magnetoelectrics. *Annual Review of Materials Research*, **37**, 387–413.
(7) Catalan, G. and Scott, J.F. (2009) Physics and applications of bismuth ferrite. *Advanced Materials*, **21** (24), 2463–2485.
(8) Wang, K.F., Liu, J.-M., and Ren, Z.F. (2009) Multiferroicity: the coupling between magnetic and polarization orders. *Advances in Physics*, **58** (4), 321–448.
(9) Khomskii, D. (2009) Classifying multiferroics: mechanisms and effects. *Physics*, **2**, 20.
(10) Vaz, C.A.F., Hoffman, J., Ahn, C.H., and Ramesh, R. (2010) Magnetoelectric coupling effects in multiferroic complex oxide composite structures. *Advanced Materials*, **22** (26–27), 2900–2918.
(11) Ma, J., Hu, J., Li, Z., and Nan, C.-W. (2011) Recent progress in multiferroic magnetoelectric composites: from bulk to thin films. *Advanced Materials*, **23** (9), 1062–1087.
(12) Vaz, C.A.F. (2012) Electric field control of magnetism in multiferroic heterostructures. *Journal of Physics: Condensed Matter*, **24** (33), art. no. 333201.
(13) Wolf, S.A., Awschalom, D.D., Buhrman, R.A., et al. (2001) Spintronics: a spin-based electronics vision for the future. *Science*, **294** (5546), 1488–1495.
(14) Zutic, I., Fabian, J., and Das Sarma, S. (2004) Spintronics: fundamentals and applications. *Review of Modern Physics*, **76** (2), 323–410.
(15) Chappert, C., Fert, A., and Nguyen van Dau, F. (2007) The emergence of spin electronics in data storage. *Nature Materials*, **6** (11), 813–823.

(16) Berger, L. (1984) Exchange interaction between ferromagnetic domain wall and electric current in very thin metallic films. *Journal of Applied Physics*, **55** (6), 1954–1956.

(17) Slonczewski, J.C. (1996) Current-driven excitation of magnetic multilayers. *Journal of Magnetism and Magnetic Materials*, **159** (1–2), L1–L7.

(18) Thiaville, A., Nakatani, Y., Miltat, J., and Suzuki, Y. (2005) Micromagnetic understanding of current-driven domain wall motion in patterned nanowires. *Europhysics Letters*, **69** (6), 990–996.

(19) Ralph, D.C. and Stiles, M.D. (2008) Spin transfer torques. *Journal of Magnetism and Magnetic Materials*, **320** (7), 1190–1216.

(20) Parkin, S.S.P., Hayashi, M., and Thomas, L. (2008) Magnetic domain-wall racetrack memory. *Science*, **320** (5873), 190–194.

(21) O'Handley, R.C. (2000) *Modern Magnetic Materials: Principles and Applications*, John Wiley & Sons.

(22) Sander, D. (1999) The correlation between mechanical stress and magnetic anisotropy in ultrathin films. *Reports on Progress in Physics*, **62** (5), 809–858.

(23) Thiele, C., Dörr, K., Bilani, O., et al. (2007) Influence of strain on the magnetization and magnetoelectric effect in $La_{0.7}A_{0.3}MnO_3$/PMN-PT(001) (A = Sr,Ca). *Physical Review B*, **75** (5), art. no. 054408.

(24) Lahtinen, T.H.E., Tuomi, J.O., and van Dijken, S. (2011) Pattern transfer and electric-field induced magnetic domain formation in multiferroic heterostructures. *Advanced Materials*, **23** (28), 3187–3191.

(25) Lahtinen, T.H.E., Tuomi, J.O., and van Dijken, S. (2011) Electrical writing of magnetic domain patterns in ferromagnetic/ferroelectric heterostructures. *IEEE Transactions on Magnetics*, **47** (10), 3768–3771.

(26) Hall, R.C. (1960) Magnetic anisotropy and magnetostriction of ordered and disordered cobalt-iron alloys. *Journal of Applied Physics*, **31** (5), 157S–158S.

(27) Lahtinen, T.H.E., Shirahata, Y., Yao, L., et al. (2012) Alternating domains with uniaxial and biaxial magnetic anisotropy in epitaxial Fe films on $BaTiO_3$. *Applied Physics Letters*, **101** (26), art. no. 262405.

(28) Brandl, F., Franke, K.J.A., Lahtinen, T.H.E., et al. (2014) Spin waves in CoFeB on ferroelectric domains combining spin mechanics and magnonics. *Solid State Communications*, **198**, 13–17.

(29) Chopdekar, R.V., Malik, V.K., Fraile Rodríguez, A., et al. (2012) Spatially resolved strain-imprinted magnetic states in an artificial multiferroic. *Physical Review B*, **86** (1), art. no. 014408.

(30) Chopdekar, R.V., Heidler, J., Piamonteze, C., et al. (2013) Strain-dependent magnetic configuration in manganite–titanate heterostructures probed with soft X-ray techniques. *European Physical Journal B*, **86** (6), art. no. 241.

(31) Streubel, R., Köhler, D., Schäfer, R., and Eng, L.M. (2013) Strain-mediated elastic coupling in magnetoelectric nickel/barium-titanate heterostructures. *Physical Review B*, **87** (5), art. no. 054410.

(32) Fackler, S.W., Donahue, M.J., Gao, T., et al. (2014) Local control of magnetic anisotropy in transcritical permalloy thin films using ferroelectric $BaTiO_3$ domains. *Applied Physics Letters*, **105** (21), art. no. 212905.

(33) Franke, K.J.A., Lahtinen, T.H.E., and van Dijken, S. (2012) Field tuning of ferromagnetic domain walls on elastically coupled ferroelectric domain boundaries. *Physical Review B*, **85** (9), art. no. 094423.

(34) Lahtinen, T.H.E., Franke, K.J.A., and van Dijken, S. (2012) Electric-field control of magnetic domain wall motion and local magnetization reversal. *Scientific Reports*, **2**, art. no. 258.

(35) Van de Wiele, B., Laurson, L., Franke, K.J.A., and van Dijken, S. (2014) Electric field driven magnetic domain wall motion in ferromagnetic–ferroelectric heterostructures. *Applied Physics Letters*, **104** (1), art. no. 012401.

(36) Franke, K.J.A., Van de Wiele, B., Shirahata, Y., et al. (2015) Reversible electric-field-driven magnetic domain-wall motion. *Physical Review X*, **5**, art. no. 011010.

(37) Chu, Y.-H., Martin, L.W., Holcomb, M.B., et al. (2008) Electric-field control of local ferromagnetism using a magnetoelectric multiferroic. *Nature Materials*, **7** (6), 478–482.

(38) Lebeugle, D., Mougin, A., Viret, M., et al. (2009) Electric field switching of the magnetic anisotropy of a ferromagnetic layer exchange coupled to the multiferroic compound $BiFeO_3$. *Physical Review Letters*, **103** (25), art. no. 257601.

(39) Heron, J.T., Trassin, M., Ashraf, K., et al. (2011) Electric-field-induced magnetization reversal in a ferromagnet-multiferroic heterostructure. *Physical Review Letters*, **107** (21), art. no. 217202.

(40) Heron, J.T., Schlom, D.G., and Ramesh, R. (2014) Electric field control of magnetism using $BiFeO_3$-based heterostructures. *Applied Physics Reviews*, **1** (2), art. no. 021303.

(41) Zhang, X., Hashimoto, T., and Joy, D.C. (1992) Electron holographic study of ferroelectric domain walls. *Applied Physics Letters*, **60** (6), 784–786.

(42) Hlinka, J. and Márton, P. (2006) Phenomenological model of a 90 degrees domain wall in $BaTiO_3$-type ferroelectrics. *Physical Review B*, **74** (10), art. no. 104104.

(43) Zhang, Q. and Goddard III, W.A. (2006) Charge and polarization distributions at the 90 degrees domain wall in barium titanate ferroelectric. *Applied Physics Letters*, **89** (18), art. no. 182903.

(44) Hubert, A. (1979) Charged walls in thin magnetic films. *IEEE Transactions on Magnetics*, **15** (5), 1251–1260.

(45) Franke, K.J.A., López González, D., Hämäläinen, S.J., and van Dijken, S. (2014) Size dependence of domain pattern transfer in multiferroic heterostructures. *Physical Review Letters*, **112** (1), art. no. 017201.

(46) Trassin, M., Clarkson, J.D., Bowden, S.R., et al. (2013) Interfacial coupling in multiferroic/ferromagnet heterostructures. *Physical Review B*, **87** (13), art. no. 134426.

(47) Eerenstein, W., Wiora, M., Prieto, J.L., et al. (2007) Giant sharp and persistent converse magnetoelectric effects in multiferroic epitaxial heterostructures. *Nature Materials*, **6** (5), 348–351.

(48) Sahoo, S., Polisetty, S., Duan, C.-G., et al. (2007) Ferroelectric control of magnetism in $BaTiO_3$/Fe heterostructures via interface strain coupling. *Physical Review B*, **76** (9), art. no. 092108.

(49) Brivio, S., Petti, D., Bertacco, R., and Cezar, J.C. (2011) Electric field control of magnetic anisotropies and magnetic coercivity in Fe/$BaTiO_3$(001) heterostructures. *Applied Physics Letters*, **98** (9), art. no. 092505.

(50) Venkataiah, G., Shirahata, Y., Itoh, M., and Taniyama, T. (2011) Manipulation of magnetic coercivity of Fe film in Fe/$BaTiO_3$ heterostructure by electric field. *Applied Physics Letters*, **99** (10), art. no. 102506.

(51) Venkataiah, G., Wada, E., Taniguchi, H., et al. (2013) Electric-voltage control of magnetism in Fe/$BaTiO_3$ heterostructured multiferroics. *Journal of Applied Physics*, **113** (17), art. no. 17C701.

(52) Geprägs, S., Brandlmaier, A., Opel, M., et al. (2010) Electric field controlled manipulation of the magnetization in Ni/$BaTiO_3$ hybrid structures. *Applied Physics Letters*, **96** (14), art. no. 142509.

(53) Geprägs, S., Mannix, D., Opel, M., et al. (2013) Converse magnetoelectric effects in Fe_3O_4/$BaTiO_3$ multiferroic hybrids. *Physical Review B*, **88** (5), art. no. 054412.

(54) Xie, Y., Zhan, Q., Liu, Y., et al. (2014) Electric-field control of magnetic anisotropy in $Fe_{81}Ga_{19}$/$BaTiO_3$ heterostructure films. *AIP Advances*, **4** (11), art. no. 117113.

(55) Taniyama, T., Akasaka, K., Fu, D., et al. (2007) Electrical voltage manipulation of ferromagnetic microdomain structures in a ferromagnetic/ferroelectric hybrid structure. *Journal of Applied Physics*, **101** (9), art. no. 09F512.

(56) Brintlinger, T., Lim, S.-H., Baloch, K.H., et al. (2010) In situ observation of reversible nanomagnetic switching induced by electric fields. *Nano Letters*, **10** (4), 1219–1223.

(57) Kleemann, W. (2007) Universal domain wall dynamics in disordered ferroic materials. *Annual Review of Materials Research*, **37**, 415–448.

(58) Bauer, U., Emori, S., and Beach, G.S.D. (2012) Electric field control of domain wall propagation in Pt/Co/GdO_x films. *Applied Physics Letters*, **100** (19), art. no. 192408.

(59) Schellekens, A.J., van den Brink, A., Franken, J.H., et al. (2012) Electric-field control of domain wall motion in perpendicularly magnetized materials. *Nature Communications*, **3**, art. no. 847.

(60) Chiba, D., Kawaguchi, M., Fukami, S., et al. (2012) Electric-field control of magnetic domain wall velocity in ultrathin cobalt with perpendicular magnetization. *Nature Communications*, **3**, art. no. 888.

(61) Bauer, U., Emori, S., and Beach, G.S.D. (2012) Voltage-gated modulation of domain wall creep dynamics in an ultrathin thin metallic ferromagnet. *Applied Physics Letters*, **101** (17), art. no. 172403.

(62) Bernand-Mantel, A., Herrera-Diez, L., Ranno, L., et al. (2013) Electric-field control of domain wall nucleation and pinning in a metallic ferromagnet. *Applied Physics Letters*, **102** (12), art. no. 122406.

(63) Franken, J.H., Yin, Y., Schellekens, A.J., et al. (2013) Voltage-gated pinning in a magnetic domain-wall conduit. *Applied Physics Letters*, **103** (10), art. no. 102411.

(64) Lei, N., Devolder, T., Agnus, G., et al. (2013) Strain-controlled magnetic domain wall propagation in hybrid piezoelectric/ferromagnetic structures, *Nature Communications*, **4**, art. no. 1378.

(65) De Ranieri, E., Roy, P.E., Fang, D., et al. (2013) Piezoelectric control of the mobility of a domain wall driven by adiabatic and non-adiabatic torques. *Nature Materials*, **12** (9), 808–814.

(66) Bauer, U., Emori, S., and Beach, G.S.D. (2013) Voltage-controlled domain wall traps in ferromagnetic nanowires. *Nature Nanotechnology*, **8** (6), 411–416.

(67) Bauer, U, Yao, L., Tan, A.J., et al. (2015) Magneto-ionic control of interface magnetism. *Nature Materials*, **14** (2), 174–181.

(68) Tagantsev, A.K., Cross, L.E., and Fousek, J. (2010) *Domains in Ferroic Crystals and Thin Films*, Springer, New York.

(69) Stadler, H.L. and Zachmanidis, P.J. (1963) Nucleation and growth of ferroelectric domains in $BaTiO_3$ at fields from 2 to 450 kV/cm. *Journal of Applied Physics*, **34** (11), 3255–3260.

(70) Pertsev, N.A. (2008) Giant magnetoelectric effect via strain-induced spin reorientation transitions in ferromagnetic films. *Physical Review B*, **78** (21), art. no. 212102.

(71) Neusser, S., Duerr, G., Bauer, H.G., et al. (2010) Anisotropic propagation and damping of spin waves in a nanopatterned antidot lattice. *Physical Review Letters*, **105** (6), art. no. 067208.

(72) Yu, H., Duerr, G., Huber, R., et al. (2013) Omnidirectional spin-wave nanograting coupler. *Nature Communications*, **4**, art. no. 2702.

(73) Cherifi, R.O., Ivanovskaya, V., Phillips, L.C., et al. (2014) Electric-field control of magnetic order above room temperature. *Nature Materials*, **13** (4), 345–351.

(74) Thiele C., Dörr, K., Fähler, S., et al. (2005) Voltage-controlled epitaxial strain in $La_{0.7}Sr_{0.3}MnO_3/Pb(Mg_{1/3}Nb_{2/3})O_3–PtTiO_3(001)$. *Applied Physics Letters*, **87** (26), art. no. 262502.

(75) Zheng, R.K., Jiang, Y., Wang, Y., et al. (2009) Ferroelectric poling and converse-piezoelectric-effect-induced strain effects in $La_{0.7}Ba_{0.3}MnO_3$ thin films grown on ferroelectric single-crystal substrates. *Physical Review B*, **79** (17), art. no. 174420.

(76) Wang, J., Hu, F.X., Li, R.W. et al. (2010) Strong tensile strain induced charge/orbital ordering in (001)-$La_{7/8}Sr_{1/8}MnO_3$ thin film on $0.7Pb(Mg_{1/3}Nb_{2/3})O_3$-$0.3PbTiO_3$. *Applied Physics Letters*, **96** (5), art. no. 052501.

(77) Kim, J.-Y., Yao, L., and van Dijken, S. (2013) Coherent piezoelectric strain transfer to thick epitaxial ferromagnetic films with large lattice mismatch. *Journal of Physics: Condensed Matter*, **25** (8), art. no. 082205.

(78) Schlom, D.G., Chen, L.-Q., Eom, C.-B., et al. (2007) Strain tuning of ferroelectric thin films. *Annual Review of Materials Research*, **37**, 589–626.

(79) Balke, N., Gajek, M., Tagantsev, A.K., et al. (2010) Direct observation of capacitor switching using planar electrodes. *Advanced Functional Materials*, **20** (20), 3466–3475.

(80) You, L., Liang, E., Guo, R., et al. (2010) Polarization switching in quasiplanar $BiFeO_3$ capacitors. *Applied Physics Letters*, **97** (6), art. no. 062910.

(81) Balke, N., Choudhury, S., Jesse, S., et al. (2009) Deterministic control of ferroelastic switching in multiferroic materials. *Nature Nanotechnology*, **4** (12), 868–875.

(82) Matzen, S., Nesterov, O., Rispens, G., et al. (2014) Super switching and control of in-plane ferroelectric nanodomains in strained thin films. *Nature Communications*, **5**, art. no. 4415.

(83) Hu, J.-M., Yang, T.N., Chen, L.Q., and Nan, C.W. (2013) Voltage-driven perpendicular magnetic domain switching in multiferroic nanoislands. *Journal of Applied Physics*, **113** (19), art. no. 194301.

(84) Yang, T.N., Hu, J.-M., Nan, C.W., and Chen, L.Q. (2014) On the elastically coupled magnetic and ferroelectric domains: a phase-field model. *Applied Physics Letters*, **104** (20), art. no. 202402.

22

Ferroelectric Vortices and Related Configurations

Sergei Prosandeev[1,2], Ivan I. Naumov[3], Huaxiang Fu[1], Laurent Bellaiche[1], Michael P.D. Campbell[4], Raymond G.P. McQuaid[4], Li-Wu Chang[4], Alina Schilling[4], Leo J. McGilly[5], Amit Kumar[4], and J. Marty Gregg[4]

[1]*Physics Department, University of Arkansas, USA*
[2]*Physics Department and Research Institute of Physics, Southern Federal University, Russia*
[3]*Carnegie Institution of Washington, USA*
[4]*School of Maths and Physics, Queen's University Belfast, Northern Ireland, United Kingdom*
[5]*Ceramics Laboratory, École Polytechnique Fédérale de Lausanne (EPFL), Switzerland*

22.1 Insights from Simulations and Theory

22.1.1 Introduction

Phase transition in systems of reduced dimension has been a subject of long-standing interest both fundamentally and technologically [1–4]. Fundamentally, interactions in low-dimensional systems are truncated along certain directions or are screened differently than in bulk, which will significantly alter collective behaviors and relative stabilities of different structural phases. Meanwhile, the thermal fluctuations in low-dimensional systems are more destructive to the formation of ordered phases than in bulks [3]. As a result, phase transformations in reduced dimensions can be profoundly different from what they are in bulk counterparts.

Moreover, when systems are near the critical points of phase transitions, their properties are often very sensitive to small modifications of temperature, pressure, composition, or

---

Nanoscale Ferroelectrics and Multiferroics: Key Processing and Characterization Issues, and Nanoscale Effects, First Edition. Edited by Miguel Algueró, J. Marty Gregg, and Liliana Mitoseriu.
© 2016 John Wiley & Sons, Ltd. Published 2016 by John Wiley & Sons, Ltd.

external strain, which usually leads to exceptionally large responses that have technological applications. This is particularly true in ferroelectric (FE) systems. For instance, when undergoing ferroelectric transitions, these FEs give rise to large piezoelectric, dielectric, or electromechanical responses [5]. The increasing demands of smaller but efficient nanoscale devices require that these large responses continue to remain as devices are miniaturized.

Furthermore, bulk ferroelectrics, which develop non-zero polarization after undergoing the paraelectric-to-ferroelectric phase transformation at the Curie temperature, give rise to bistable or multistable degenerate states. These multistable states can be utilized for storing data in non-volatile ferroelectric random access memories (NFERAMs) [6].

Compared to bulk ferroelectrics, zero-dimensional FE dots promise to increase the storage density of NFERAMs thousandsfold. Obviously, this anticipated benefit would depend on whether phase transitions and multistable states continue to exist in zero-dimensional FE structures. This further explains why phase transitions in ferroelectrics of reduced dimension are technologically relevant, in addition to the fundamental interest described above. Interestingly, the recent intense investigation of FE nanostructures have resulted in the surprising and exciting discoveries of dipolar patterns that do *not* exist in the bulk counterpart, because of electrical and mechanical boundary conditions as well as size effects that are inherent to low-dimensional objects. Examples of such patterns are electric vortices or related flux-closure configurations, which were first predicted by simulations [7–9] and then experimentally confirmed (see [10] to [20]).

The aims of this article are fourfold: (1) to first briefly describe numerical approaches that have been used to discover and further simulate FE vortices and related configurations; (2) to report and discuss findings about such patterns and their original order parameters in FE nanostructures; (3) to emphasize novel possibilities of switching due to these patterns; and (4) to provide examples of other unusual phenomena and effects that originate from FE vortices and other complex dipolar organizations.

22.1.2 Methods

Let us first (briefly) review several different computational and theoretical schemes that have been employed to mimic and study properties of ferroelectric vortices.

22.1.2.1 Effective Hamiltonian Approach

One common scheme is the so-called effective Hamiltonian approach, for which the total energy of ferroelectric nanostructures is generally written as:

$$\varepsilon_{\text{tot}}(\mathbf{u_i}, \mathbf{v}_i, \eta_H) = \varepsilon_{\text{Heff}}(\mathbf{u_i}, \mathbf{v}_i, \eta_H) + \frac{1}{2}\beta \sum_{i} \left\langle \mathbf{E}_{\text{dep}} \right\rangle \cdot Z^* \mathbf{u_i} - \sum_{i} \mathbf{E} \cdot Z^* \mathbf{u_i} - a^3 \sum_{j} \sigma_j \eta_{H,j} \tag{22.1}$$

where the degrees of freedom are: (1) the local soft mode in the unit cell i, $\mathbf{u_i}$, whose product with the effective charge Z^* yields the local electrical dipole, $\{\mathbf{p}_i\}$, in this cell; (2) the homogeneous strain tensor, η_H; and (3) inhomogeneous strain-related (acoustic-type) displacements in unit cell i, $\mathbf{v}_i$ [21]. Note that there are effective Hamiltonians that also include oxygen octahedral tiltings and magnetic dipoles as other degrees of freedom (see, for example, [22] and [23]).

In Equation (22.1) $\varepsilon_{\text{Heff}}$ represents the intrinsic (effective Hamiltonian) energy of the studied ferroelectrics, with its parameters having been generally extracted by performing first-principles calculations on small cells. Analytical expressions of $\varepsilon_{\text{Heff}}$ are typically those of *bulk* systems (see, for example, [21], [24], and [25]), except for two main modifications. The first change consists of adding energetic terms that are associated with the direct interaction between the vacuum surrounding the nanoferroelectric and both the dipoles and inhomogeneous strain near the surface [7, 26]. The second modification consists in replacing the (reciprocal-space-based) matrix associated with long-range dipole–dipole interactions in the bulk [21] by the corresponding matrices characterizing dipole–dipole interactions in the zero-dimensional, one-dimensional, or two-dimensional ferroelectric – implying that no supercell periodic boundary conditions are used to simulate ferroelectric nanostructures. Such matrices are given by Naumov and co-workers [27,28] and correspond to ideal open-circuit (OC) conditions, for which no possible screening of the polarization-induced surface charges can exist. These electrical boundary conditions naturally lead to the existence of a maximum depolarizing field (denoted by $<\mathbf{E}_{\text{dep}}>$ and determined from the atomistic approach of [28]) inside the nanoferroelectric for a non-vanishing polarization.

The second term of Equation (22.1) mimics a screening of $<\mathbf{E}_{\text{dep}}>$ via the β parameter. More precisely, the residual depolarizing field resulting from the combination of the first and second term of Equation (22.1) has a magnitude equal to $(1 - b)|<\mathbf{E}_{\text{dep}}>|$. Therefore $\beta = 0$ corresponds to ideal OC conditions, while an increase in β lowers the magnitude of the resulting depolarizing field; $\beta = 1$ corresponds to ideal short-circuit (SC) conditions for which the depolarizing field has vanished (i.e. for which *all* polarization-induced surface charges are screened).

The third and fourth terms of Equation (22.1) represent the effect of an electric field, $\mathbf{E}$, and applied stress, σ, on properties of the investigated system, respectively [29], with a being the five-atom lattice constant at 0 K and the sum over j in the fourth term running from 1 to 6 for the components of the strain tensor (as consistent with Voigt notations).

Effective Hamiltonians can be implemented within both Monte Carlo (MC) and molecular dynamics (MD) simulations. In the MC scheme, a large number of MC sweeps (typically of the order of 40 000) is used to first equilibrate the system and then compute statistical averages – at each temperature, electric field, and/or stress values. In order to find the ground state, the temperature is usually decreased in small steps, starting from high temperatures (for which any long-range dipolar order is absent). Within the MD technique, statistical quantities can be computed as a function of time and an alternating AC electric field can also be applied.

22.1.2.2 Phase Field Method

In contrast to the effective Hamiltonian method, which is atomistic in nature, the phase field method employs a continuum approach, in which the polarization field, $\mathbf{P}(\mathbf{r})$, is the order parameter. A variation functional $F(\mathbf{P}(\mathbf{r}))$ is developed, which consists of three main energies:

$$F = F_{\text{GL}} + F_{\text{electrost}} + F_{\text{elastic}} \tag{22.2}$$

where F_{GL} is the Ginzburg–Landau contribution:

$$F_{\mathrm{GL}} = \int \left[f_0\left(\mathbf{P}(\mathbf{r})\right) + \frac{1}{2}\beta_{ijkl}\frac{\partial P_i}{\partial x_j}\frac{\partial P_k}{\partial x_l} \right] d^3r \tag{22.3}$$

with

$$\begin{aligned} f_0(\mathbf{P}(\mathbf{r})) = {} & \alpha_1\left(P_1^2+P_2^2+P_3^2\right) + \alpha_{11}\left(P_1^4+P_2^4+P_3^4\right) + \alpha_{12}\left(P_1^2P_2^2+P_1^2P_3^2+P_2^2P_3^2\right) \\ & + \alpha_{111}\left(P_1^6+P_2^6+P_3^6\right) + \alpha_{112}\left(P_1^2\left(P_2^4+P_3^4\right)+P_2^2\left(P_1^4+P_3^4\right)+P_3^2\left(P_1^4+P_2^4\right)\right) \\ & + \alpha_{123}P_1^2P_2^2P_3^2 \end{aligned} \tag{22.4}$$

Here the subscripts 1, 2, and 3 correspond to the x, y, and z Cartesian components, respectively.

The coefficients in this expansion can be found from first-principles calculations or from fitting experimental data. The homogeneous contribution to the free energy expanded into Taylor series with respect to the polarization is $f_0(\mathbf{P}(\mathbf{r}))$, up to the 6th order. The second term in Equation (22.3) gathers the gradient corrections of this expansion.

Moreover, the electrostatic interaction energy, $F_{\mathrm{electrost}}$, appearing in Equation (22.2) is calculated as [30]:

$$F_{\mathrm{electrost}} = \frac{1}{2\varepsilon_0\varepsilon_\infty}\sum_{i=1}^{3}\sum_{j=1}^{3}\int \frac{k_ik_j}{k^2}P_{i\mathbf{k}}P_{j\mathbf{k}}\frac{d^3k}{(2\pi)^3} - \mathbf{E}\cdot\mathbf{P}_0 \tag{22.5}$$

where $P_{i\mathbf{k}}$ is the ith component of the Fourier transform of the polarization field $\mathbf{P}(\mathbf{r})$, and $\mathbf{k}$ is the corresponding wave vector. $\mathbf{P}_0$ is the homogeneous part of the polarization, associated with the zero wave vector. Note that the zero wave vector contribution is excluded from the summation associated with the first term and ε_0 is the dielectric constant of vacuum and ε_∞ is the high-frequency dielectric permittivity.

In Equation (22.2), F_{elastic} is an elastic energy, which is computed as:

$$F_{\mathrm{elastic}} = \frac{1}{2}\sum_{i=1}^{3}\sum_{j=1}^{3}\sum_{k=1}^{3}\sum_{l=1}^{3}C_{ijkl}\int\left[\eta_{ij}(\mathbf{r})\eta_{kl}(\mathbf{r})\right]d^3r - \sum_{i=1}^{3}\sum_{j=1}^{3}\sigma_{ij}\int\left[\eta_{ij}(\mathbf{r})\right]d^3r \tag{22.6}$$

where C_{ijkl} are elastic coefficients, η is the strain, and σ is the external stress. Practically [30], the strain is related to the polarization field, via the electrostriction coefficients Q_{ijkl}:

$$\eta_{ij}(\mathbf{r}) = \sum_{k=1}^{3}\sum_{l=1}^{3}Q_{ijkl}P_kP_l \tag{22.7}$$

A variation method is used to find the polarization field numerically [30], based on the Ginzburg–Landau kinetic equation:

$$\frac{\partial P_i}{\partial t} = -L\frac{\partial F}{\partial P_i} + \xi_i \tag{22.8}$$

where ξ_i is the Cartesian components of the Langevin noise [31].

22.1.2.3 *Shell Model Calculations*

The shell model is an atomistic approach, like the effective Hamiltonian method. However, unlike this latter scheme, the shell model incorporates all structural degrees of freedom but also relies on rather simple analytical forms of interatomic potentials (which we will discuss below). In the shell model, each ion is described as a massive core that is connected to the outer shell by a spring. Notice that, in ferroelectrics, the core–shell interaction is required to be anisotropic, and this anisotropy is crucial for the description of phases having different symmetry (see, for example, [32] and references therein). These shells are also connected to each other by additional springs. Among these springs, some are mimicking long-range electrostatic interactions while others simulate short-range interactions. Two different types of short-range interatomic potentials are usually employed. Firstly, a Rydberg potential, $V(r) = (a + br)\exp(r/p)$, is used, for example for the Pb–Ti, Pb–O, and Ti–O pairs in $PbTiO_3$ systems. Secondly, the Buckingham potential $V(r) = c\exp(r/\zeta) + fr^6$ is often used for O–O interactions, in, for example, $PbTiO_3$ systems. The a, b, ρ, c, ζ, and f coefficients in these potentials are usually found from least-square fitting of first principles calculations or experimental phonon spectra. Then molecular dynamics calculations are typically performed in order to find various properties, including the dipolar pattern.

22.1.2.4 *First-Principles Approach*

First-principles calculations are also atomistic in nature. They do not require any input from experiments and are based on the density functional theory [33]. This theory demonstrates that the many-electron system ground-state properties can be uniquely determined from the electron charge density, once knowing the energy functional (such determination is typically done in a self-consistent way using Kohn–Sham equations). Unfortunately, there is an analytically unknown part of this functional, that is the so-called exchange and correlation term. Various solutions have been proposed and tested for that latter term, and their accuracies were basically found to depend on the type of systems to be investigated [34].

22.1.3 Discovery of Unusual Patterns in Ferroelectric Nanostructures and Their Associated Order Parameters

Properties of FE nanostructures are largely governed by the existence of a depolarization field, which is much stronger than the demagnetization field in magnetic nanosystems. Consequently, polarization and monodomain may vanish in low-dimensional FEs in order to avoid the drastic increase in energy caused by the depolarization field. Even in systems with incomplete screening such as in $SrRuO_3/BaTiO_3/SrRuO_3$ [35], where the depolarization field is significantly weakened as compared to systems under open-circuit electrical boundary condition [36, 37], there is still a critical thickness below which an FE monodomain could disappear.

Ferroelectricity in zero-dimensional dots is even more interesting. A pioneer study revealed that there are large atomic off-center displacements in barium titanate nanodots having less than 5 nm for their lateral size, despite the fact that these dots are under open-circuit electrical boundary condition [7]. These displacements were shown to be robust as different short-range interactions were used to mimic different capping matrix materials. Although the net total polarization vanishes, the existence of large off-center displacements is nevertheless important for the following reason. If we assume that atomic off-center displacements do not exist in dots, very large electric fields will then be required to generate individual dipoles (much like in, for example, semiconductors), which will be detrimental for technological applications. In contrast, with large off-center displacements in FE dots, one may only need a small electric field to generate ferroelectric polarization by aligning the already-existing dipoles, a conclusion which was indeed borne out by theoretical simulations when the electric field was applied in $BaTiO_3$ dots [7].

The vanishing net polarization at all temperatures and the lack of a ferroelectric phase in dots being under open-circuit electrical boundary conditions reveal that there are no polarization-induced multistable states in these dots. One therefore cannot use the polarization itself for the purpose of making non-volatile ferroelectric memories. This initially appeared to be a drawback at the early stage of the FE dot study.

However, the situation quickly changed, mostly because a new type of phase transition was discovered in $Pb(Zr,Ti)O_3$ (PZT) nanosystems [8]. Instead of looking at the net polarization $\mathbf{P} = \sum_i \mathbf{p}_i$, Naumov, Bellaiche, and Fu found and examined a new order parameter, namely the toroidal moment $\mathbf{G} = \sum_i \mathbf{r}_i \times \mathbf{p}_i$, where $\mathbf{p}_i$ is the local dipole moment of site i that is located at $\mathbf{r}_i$. By performing finite-temperature simulations using a first-principles-derived effective Hamiltonian for $Pb(ZrTi)O_3$ nanodisks and nanorods, they showed that this new order parameter vanishes at high temperature due to the fact that dipoles become randomly oriented. However, this order parameter is very large when the temperature is well below a certain critical value, demonstrating clearly the existence of a phase transition [8]. This phase transition originates from the spontaneous formation of the toroidal moment.

The finding of a toroidal phase transition is of fundamental significance since, prior to this, scientists widely believed that there may not be any phase transition in zero-dimensional ferroelectric nanoparticles. The toroidal phase transition thus offers a new and different thinking. Meanwhile, it is useful to point out that the toroidal phase transition found in a single dot does not contradict Landau's phase transition theory. The latter is formulated for the thermodynamic limit, which applies to an array of dots with weak interactions between dots. In [8], an ordered vortex phase occurs in a single dot. When dots form an array as in the thermodynamic limit, the vortices in different dots may become random when the coupling between dots is weak and when thermal fluctuation is sufficiently strong.

The existence of a toroidal phase transition is also technologically important. The toroidal moment **G** may point up or down, therefore representing two degenerate states. These bistable states of the toroidal moment phase can thus be utilized to make ferroelectric memory devices. More specifically, scientists can use one dot to store one data bit. The minimum diameter of the disks that display low-temperature structural bistability was determined to be 3.2 nm [8], enabling an ultimate NFERAM density of $60 \text{ x } 10^{12}$ bits per square inch. Furthermore, since the interaction between toroid moments in different dots is generally weak, the problem of cross-talking between different memory units can thus be largely avoided, which is another advantage.

After the discovery of the toroidal phase transition in PZT nanodisks, ferroelectric vortex structures were subsequently confirmed by other studies using various different methods, such as phase field models, Ginzburg–Landau theory, atomistic simulations, and first-principles density functional calculations. The details of these important studies are described in the following.

Using phase field simulations, Slutsker, Artemev, and Roytburd investigated domain structures in confined nanoferroelectrics of different shapes and sizes [30]. They found an electrostatically compatible circuit of 180 and 90° domains at equilibrium. The formation of 90° domains is very similar to the FE vortex, and the trend to minimize the residual stress and the stray field was found to be responsible for the crater-shaped sets of closed circuits of 90° domains.

Munch and Huber examined the FE closure structures in tetragonal ferroelectric crystals employing a phase-field model, and their study shows a stable polarization vortex of six domains over a narrow range of aspect ratios in freestanding cuboidal nanodots [38]. For other aspect ratios, the authors found that square polarization vortices of four domains are stable. In both cases, the stable FE vortex domains were shown to exist.

By self-consistently solving the Ginzburg–Landau equations and electrostatic equations, Lahoche, Lukyanchuk, and Pascoli found the multivortex toroidal states appearing in nanometric ferroelectric cylinders [39]. The geometrical textures, critical temperatures, and stability regions for these states were calculated, which supports the finding that depolarization energy is the driving force for vortex formation.

Stachiotti and Sepliarsky reported toroidal ferroelectricity in $PbTiO_3$ nanoparticles [40] by using atomistic simulations based on first-principles-derived interatomic potentials. Their simulations revealed the existence of a ferroelectric bubble by the alignment of vortex cores along a closed path. The aspect ratio of the nanostructure was found to play an important role in affecting the topology of the dipole configurations. For certain flat nanostructures, a multibubble state was shown to act as a bridge between the dipole patterns in 0D nanodots and in 2D ultra-thin films.

Other convincing studies that support the existence of a ferroelectric vortex come from direct first-principles calculations. Using density functional calculations, Durgun et al. predicted that polarization vortices appear in germanium telluride crystalline nanoplatelets and nanoparticles when the size is above a diameter of 2.7 nm [41]. The ferrotoroidic ordering is spontaneous and reversible, with the toroidal moment being the order parameter. The authors further emphasized the important role of inhomogeneous strain in stabilizing ferroelectric vortices.

Pilania and Ramprasad reported complex curling vortex configurations of electric dipoles in $PbTiO_3$ nanowires [42] by density functional theory calculations. The critical size for the vortex polarization instability was found to be 16 Å. The authors also showed that strain and surface terminations may cause phase transitions between the curled vortex phase and the conventional rectilinear axial polarization phase.

Furthermore, Shimada et al. demonstrated, also using direct first-principles calculations, a possible coexistence of linear polarization and vortex polarization at twist boundaries in $PbTiO_3$ [43]. Near the twist boundary, in addition to the linear spontaneous polarization along the normal direction, the authors also found a coexisting curled (or toroidal) polarization. The linear polarization is caused by the locally strengthened covalent Pb–O bond, while the curled polarization is caused by rotational in-plane displacements at the twist boundary. It was also revealed that these two types of polarization can be considerably influenced by applying tensile strains. A tensile strain was found to enhance the linear polarization, while it suppresses the vortex polarization.

The ferroelectric vortex also exists in thin films, in addition to FE dots and wires. For instance, first-principles-based calculations conducted on $BiFeO_3$ thin films [44] revealed an array of FE vortices, each having a core located close to the film surface and interface. Interestingly, such a peculiar closed-flux structure was then experimentally confirmed [16]. Similarly, using a first-principles-based effective Hamiltonian approach, Wu et al. determined the ferroelectric pattern in $PbZr_{0.5}Ti_{0.5}O_3$ ultra-thin film [45]. Vortex stripes were reported to form in the FE thin films, with some relation to the 180° domains. The authors also studied how this structure responds to external electric fields. They found that when a local external field is applied, the vortex stripe transforms into the vortex loop structure [45]. In another study, Roy, Sarkar, and Dattagupta investigated the evolution of 180°, 90°, and vortex domains in ferroelectric films, using a Landau-like theory and its time-dependent generalization [46]. It was shown that the formation of the above domains (including FE vortex domains) in thin films depends largely on the choice of electrical boundary conditions and does not require strain fields, which is consistent with the result that FE vortex exists in free-standing FE dots under zero external strain [7].

For the purpose of technological applications, it is always desirable to be able to tune or modify the system properties according to what is needed. This is also true for the ferroelectric vortex structure phase, and scientists have explored different approaches to modify the FE vortex structure. Here we list two interesting possibilities. One was reported by Prosandeev and Bellaiche who investigated properties of ferroelectric nanodots that are embedded in a polarizable medium [47]. The ferroelectric strength of the medium material was found to be important in determining the structural phase of the whole system. Some novel states, such as a state that exhibits a coexistence of two kinds of order parameters, or a state possessing a peculiar order between dipole vortices of adjacent dots, were predicted. Another interesting possibility is by lattice misfit strain, as reported by Naumov and Bratkovsky [48]. Using the first-principles-derived effective Hamiltonian, these authors investigated the effects of external strains on the dipole structures in flat nanoparticles of $BaTiO_3$ and PZT. These authors revealed that strain strongly affects the structural phase by controlling the competition between the depolarizing field and the polarization anisotropy. Compressive strain was shown to favor the formation of 180° stripe or tweed domains, and tensile strain favors the formation of an in-plane vortex. An unusual intermediate phase with the coexistence of both stripe domain and FE vortex was also predicted to be possible. Note that the effect of strain (as well as electrical boundary conditions) on properties of FE nanostructures was also revealed in computational work of [49].

Dipole structures that are more complex than the FE vortex can also occur in ferroelectric systems. In such cases, one needs to define other order parameters. For instance, Prosandeev and Bellaiche introduced another interesting order parameter that involves a double cross product of the local dipoles with their positions [50, 51]. The authors have used this order parameter to describe the helicity of the two domains in the onion states, the curvature of the dipole configuration in flower states, and the simultaneous existence of vortices of opposite chirality. Another example is the formation of the quadrant domain pattern that has been observed and simulated in free-standing single-crystal platelets of $BaTiO_3$ [52]. These quadrant domains self-organize themselves into an antivortex-like configuration, with the relative position of the quadrant core (with respect to the center of the platelet) being adjustable by varying the length-to-width ratio of the platelet sidewalls. These intriguing features were explained by developing a Landau-type phenomenology in which the order parameter is the amount of off-centering of the quadrant core and the thermodynamic driver is the shape anisotropy of the platelet [52]. First-principles calculations conducted in $BaTiO_3$ nanowires [53, 54] also revealed other complex chiral patterns of the electric dipoles and topological defects that can be associated with a large winding number.

Interestingly, electric dipoles can also locally couple with other degrees of freedom, which can result in original phenomena when these electric dipoles organize themselves into vortices. For instance, the coupling between tiltings of oxygen octahedral (also termed antiferrodistortive motions) and ferroelectric vortices was recently predicted to give rise to novel exotic chiral patterns *for the tilting of oxygen octahedra* in zero-dimensional ferroelectric and multiferroic dots [55]. Describing such chiral patterns requires the introduction and use of a novel order parameter, which can be thought of as an extension of the toroidal moment through (i) the replacement of electric dipoles by vectors quantifying antiferrodistortive (AFD) motions and (ii) the introduction of negatives signs for some AFD domains existing inside these chiral patterns [55].

22.1.4 Controlling and Switching of Single, Double, and Multiple Vortex States

The possibility of controlling and, especially, switching ferroelectric vortex or vortices opens exciting opportunities for nanomemory devices, nanomotors, nanotransducers, nanoswitchers, nanosensors, etc. For example, switching between opposite chiralities of (bistable) vortices promises to increase the density of FE non-volatile random access memories by five orders of magnitude [8]. As a new kind of dipolar ordering, vortex FE states exhibit novel coupling with external fields. In fact, the curling dipolar pattern in ferroelectric nanostructures can be affected by homogeneous [56–58], inhomogeneous [59], curled [60–62], or combined (homogeneous plus curled) [60] electric fields. Even a mechanical load can be used as an effective tool to control the vortex structures [63].

Though the homogeneous electric field does not directly interact with the toroidal moment $\mathbf{G}$, it interacts with the local dipoles $\mathbf{p}_i$ at cell i via $-\sum_i \mathbf{E} \cdot \mathbf{p}_i$, and, therefore, can change the initial dipolar pattern. Naumov and Fu [56] studied vortex-to-polarization transformation in $Pb(Zr_{0.5}Ti_{0.5})O_3$ disk-shaped nanoparticles, caused by a homogeneous electric field normal to the vortex plane and parallel to the initial $\mathbf{G}$. By performing first-principles effective Hamiltonian simulations, they found that such a transformation follows an unusual path via a bridging phase, with the toroidal moment rotating by 90° with respect to the initial G_z (Figure 22.1). Later such a path was presumably observed by Gruverman et al. [19] in their experimental study of switching of vertical polarization in small circular PZT capacitors. They discovered that a small domain remains unswitched in the center of the capacitors after switching; this effect was attributed to the formation of a vortex state and to the transformation mechanism predicted by Naumov and Fu [56].

Surprisingly, the homogeneous electric field not only can unwind the curling dipolar pattern but can also switch the toroidal moment in ferroelectric disks or rings if the latter are *asymmetric* in shape; such an asymmetry can be induced, for example, by a cylindrical hole shifted from the central axis. This interesting possibility was demonstrated by Prosandeev et al. [57] in their effective Hamiltonian study of both ferromagnetic ($Ni_{80}Fe_{20}$) and ferroelectric (PZT) asymmetrical nanorings. They found that the homogeneous electric field switches the chirality of the ferroelectric vortices via the formation of antiferrotoroidic pair states where two, large and small, vortices coexist but do not compensate each other, as shown in Figure 22.2. This intermediate phase differs from that in magnetic nanoparticles, where switching of the magnetic toroidal moment $\mathbf{T}$ (by a homogeneous magnetic

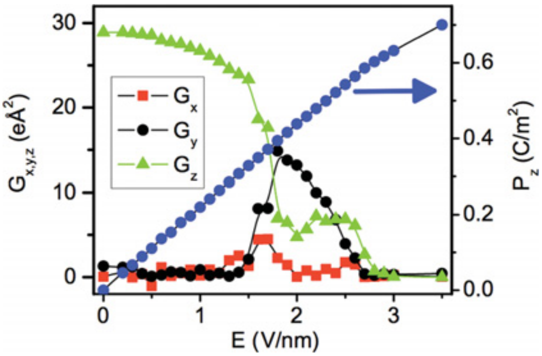

Figure 22.1 *Toroidal moment* **G** *(using the left vertical axis) and net polarization* P_z *(using the right vertical axis) versus the magnitude of the electric field,* **E**, *in a nanodisk with a diameter of 19a, where a is the lattice parameter. As the electric field exceeds ~1.5 V nm*$^{-1}$*, an intermediate phase with non-zero* G_y *occurs. This phase disappears as the field is further increased. Adapted from [56]*

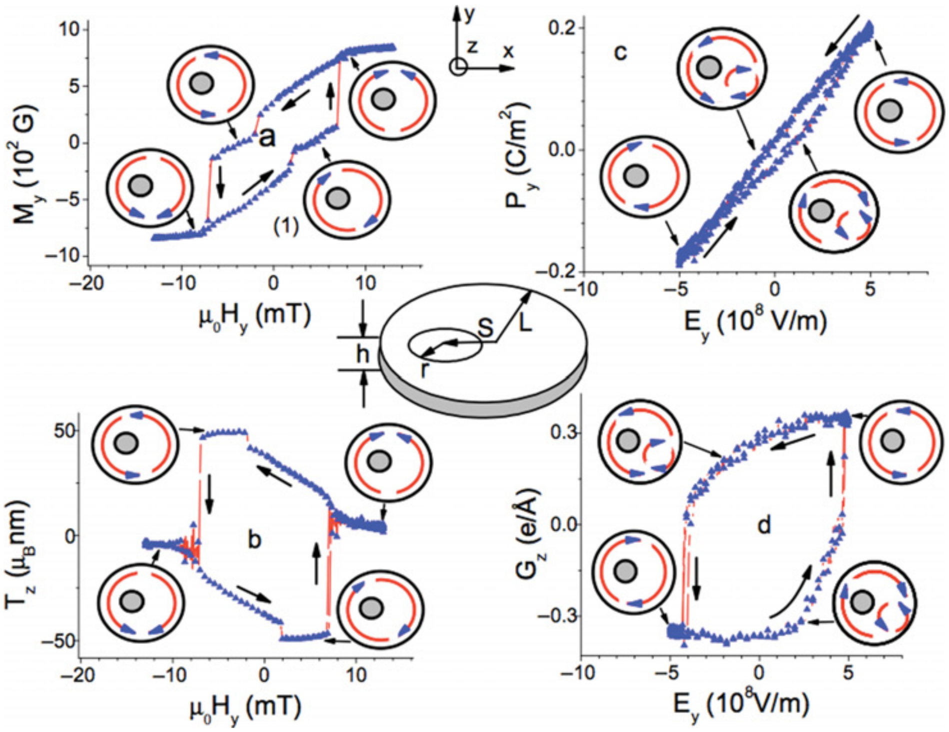

Figure 22.2 *Calculated hysteresis loops in asymmetric ferromagnetic rings (panels (a) and (b)) and in asymmetric ferroelectric rings (panels (c) and (d)). Panels (a) and (b) display the behavior of the magnetization and magnetic toroidal moment, respectively, as a function of the applied homogeneous AC magnetic field. Panels (c) and (d) show the evolution of the polarization and electric toroidal moment, respectively, versus the applied homogeneous AC electric field. Insets schematize the rings' geometry and the dipole arrangement in the (x, y) plane for different states around the hysteresis loops. Reprinted from [57]*

field) involves onion states rather than antiferrotoroidic configurations (cf. Figure 22.2). It is worth noticing that in the context of magnetic nanoparticles, the results of [57] are fully consistent with previous experimental studies (see, for example, [64]).

Some ferroelectric nanoparticles, especially flat ones shaped like the number 8, can posses a double vortex state for which the coexisting two vortices have opposite chiralities. Though the total toroidal moment vanishes here, it is possible to introduce a new order parameter, the hypertoroidal moment **h**, that adequately describes such a peculiar state [50, 51]. Since the moment **h** is different in symmetry from the toroidal moment, the double vortex state responses to the static homogeneous electric field are different than those to a single vortex state. Using an approach similar to that of [57], Prosandeev and Bellaiche [58] showed for their model systems of two ferroelectric disks "welded" together that the moment **h** can be reversed by static electric fields. Such a reversal can be viewed as a *simultaneous* switch of the sense of dipolar rotation (local **G**) in each of two vortices.

As mentioned above, *homogeneous* electric fields can control and even switch the direction of the toroidal moment in *asymmetrical* nanoparticles. Analogously, *inhomogeneous* electric fields are able to interact with the toroidal moment in *symmetrical* nanoparticles. Such an interaction was studied [59] for a 12 × 12 × 12 PZT nanodot with the help of a first-principles-based Monte Carlo scheme. The inhomogeneous field was mimicked by placing several point charges around the nanoparticle whose net charge is zero. Figure 22.3 displays the temperature dependency of **G** in the absence and presence of the external field generated by two, + and −, point charges in the (x, y) plane. Though the field is rather weak, it nevertheless fixes the direction of the forming toroidal moment along the z axis; in the isolated dot this direction could be along any of the six <100> directions.

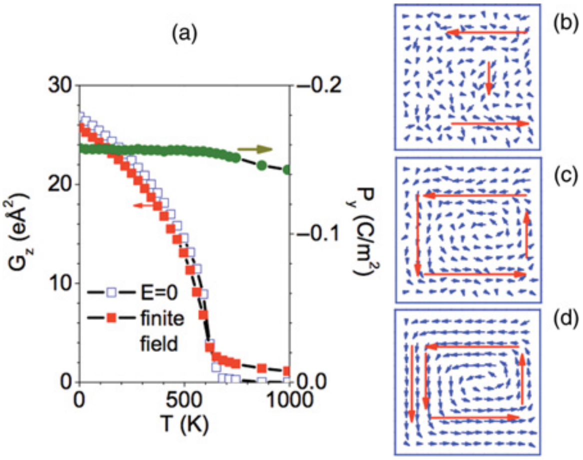

Figure 22.3 *(a) Temperature dependency of the toroidal moment (squares) and polarization (dots) in a 12 x 12 x 12 PZT nanodot, and (b to d) resulting dipole pattern at 625, 300, and 1 K, respectively. The filled symbols of panel (a) correspond to simulations in which the inhomogeneous field is turned on while open symbols show results for an isolated dot. The long and thick arrows of panels (b- to d) are guides for the eyes to show the tendency of some dipoles to align along some specific directions. Reprinted from [59]*

Perhaps the most straightforward way to influence toroidal moment is to use a curled electric field, $\nabla \times \mathbf{E}$, which directly interacts with $\mathbf{G}$; since $\mathbf{G}$ and $\nabla \times \mathbf{E}$ are thermodynamically conjugated parameters, the corresponding term in the thermodynamical potential is simply $(\nabla \times \mathbf{E}) \cdot \mathbf{G}$. It should be stressed that the curled field cannot be generated by static charges, but only by the time-dependent magnetic field via $\nabla \times \mathbf{E} = -\partial \mathbf{B}/\partial t$, as in a focused laser beam with a varying $\mathbf{B}$-field component. In the simulations, it is convenient to present the curled fields in the form $\mathbf{E} = \frac{1}{2}\, \mathbf{S} \times \mathbf{r}$, where $\mathbf{S}$ characterizes the strength and direction of the vorticity. Using first-principles-based Monte Carlo simulations, Naumov and Fu [60] investigated the response of an FE vortex to $\mathbf{S}$ in PZT nanoparticles. They found that the domain coexistence mechanism, when the $-\mathbf{G}$ domain grows while the original $\mathbf{G}$ domain shrinks under external fields, is not valid for the switching of $\mathbf{G}$. Instead dipoles display unusual collective behavior by forming a new intermediate vortex phase with a perpendicular (not opposite) toroid moment, as displayed in Figure 22.4(a), where this phase is denoted as phase II and characterized by a finite G_y moment. The reversal of the vortex

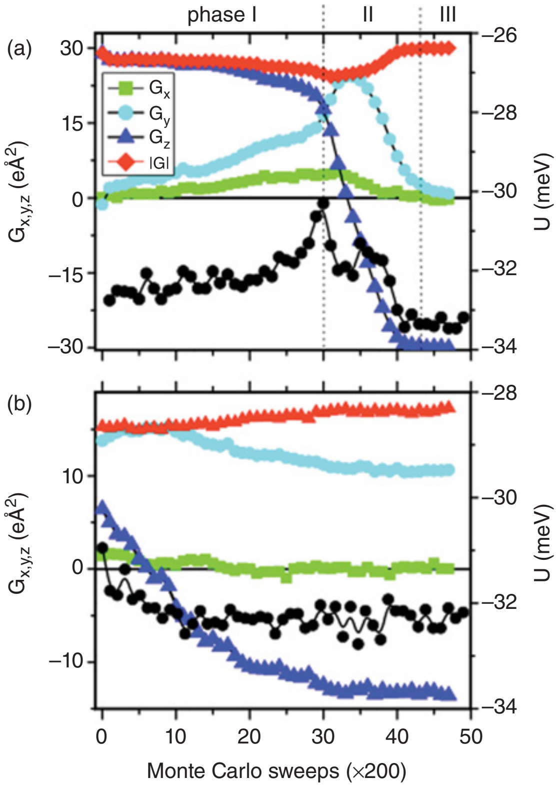

Figure 22.4 *Evolution of the toroidal moment* $\mathbf{G}$ *and its magnitude* $|\mathbf{G}|$ *(using the left vertical axis) and internal U energy per five-atom cell (solid black dots, using the right vertical axis) in a* $d = 19a$ *nanodisk: (a) under an* $S = 0.25$ *mV Å*$^{-2}$ *curled electric field; (b) under the combined action of an* $E = 1.9$ *V nm*$^{-1}$ *homogeneous field and an* $S = 0.04$ *mVÅ*$^{-2}$ *curled field. For clarity of display,* G_z *is plotted after multiplying it by −1. Adapted from [60]*

occurs by undergoing an evolution sequence of $G_z \rightarrow G_y \rightarrow (-G_z)$. Along this path, the amplitude of the moment $|\mathbf{G}|$ (shown in red) changes only slightly, suggesting that the collective hydrodynamical mode for the vortex reversal is simply the rotation of **G**. Among the interesting findings of Naumov and Fu [60] is also the fact that the combined action of homogeneous and curled electric fields can *significantly reduce* the switching energy barrier and drastically (by 600%) decrease the magnitude of the switching curled field (see Figure 22.4(b)). This is due to the fact that both fields can give rise to a lateral vortex, which serves as a bridging phase between the two end states corresponding to $-\mathbf{G}$ and **G**, respectively.

Using phase field simulations, Wang [61] also studied the switching behavior of an FE vortex subjected to a curled electric field in a single-crystal ferroelectric tetragonal nanodot, in contrast to the nanodisks considered by Naumov and Fu [60]. These simulations revealed that the vortex switching in such dots does not begin from the vortex core, as reported [60] but rather from the dot corners (which have the lowest elastic energy density). This discrepancy can be due to a geometry effect or attributed the fact that the direction of polarization in [61] was restricted to the (x, y) plane. Within the same approach, Wang and Kamlah [62] investigated the intrinsic switching of a defect-free vortex in ferroelectric $PbTiO_3$ nanotubes under a curled electric field. It was found that the vortex switching goes through the nucleation of local vortices, which grow at the expense of the original one. In contrast to the results obtained for nanodisks [60], they also found that during the switching a new vortex $-\mathbf{G}$ can coexist with the initial vortex **G**. The difference was attributed to the absence of topological defects in nanotubes.

Furthermore, and as demonstrated recently by using phase field simulations, the vortex domain structure in ferroelectric nanoplatelets can be controlled by a simple mechanical load [63]. Vortex states with more/fewer vortices can be obtained by application of compressive/tensile strains to the nanoplatelet. Such transformations between different vortex states allow one to effectively control the size and the number of vortices; they also lead to a variety of different temperature–stress phase diagrams.

22.1.5 Other Phenomena Related to Vortices and Complex Dipolar Patterns

FE vortices also exhibit several other distinct features. For instance, a nanosystem exhibiting an electric vortex in the (x, y) plane, and thus possessing an electrical toroidal moment along the z axis, is more elongated along the x or y direction than along the z direction. In other words, and as shown by Prosandeev and Bellaiche [65], the η_H *homogeneous* strain has Voigt components for which $\eta_{H,3}$ is smaller than $\eta_{H,2} = \eta_{H,1}$. The axial ratio *c/a* is therefore smaller than 1 for electric vortices, which contrasts with the cases of systems exhibiting a spontaneous polarization [66] or antiferrodistortive motions [67] along the z axis. It was demonstrated [65] that the *inhomogeneous* strain, η_I, is also quite peculiar when an FE vortex state forms. In particular, the $\eta_{I,1}$ and $\eta_{I,2}$ (Voigt) components of the inhomogeneous strain have significant magnitude near the center of the FE vortex. This is because of the elastic elongation (that is induced by the coupling between the strain and electric dipoles) of all the domains forming the vortex. Other unusual signatures of FE vortices are the type of strongly inhomogeneous electric field produced by these vortices outside the nanostructure and the very *weak* interaction between symmetric vortices located at two different dots [65]. This latter interaction varies as $1/R^9$, with R being the distance between the centers of the two dots [65].

Moreover, the facts that the electric toroidal moment (1) is an order parameter and (2) involves the electric dipoles in its definition automatically imply that novel physical responses and tensors can be defined. As an example and as shown in [68], the magnitude, and sometimes even the direction, of the electric toroidal moment can be altered by applying a strain or its conjugate field (i.e. a curled electric field). These effects can be termed as piezotoroidicity and electric toroidal susceptibility, respectively, in analogy with piezoelectricity and electric susceptibility (that relate the change of the electrical polarization with strain and homogeneous electric fields, respectively) in "normal" ferroelectrics.

Several other novel and promising phenomena can also emerge from the existence of ferroelectric vortices. For instance, the combined experimental and theoretical works of [17] reported an enhanced electric conductivity at the FE vortex cores in multiferroic $BiFeO_3$ (BFO). More precisely, the formation of one-dimensional conductive channels that are activated at voltages as low as 1 V (rather than at ~ 3 V, as in the bulk counterpart or in domain walls) was evidenced. Another example of original phenomena was also discovered in BFO: using a first-principles-derived effective Hamiltonian, Ren and Bellaiche [69] demonstrated that the direction and magnitude of the magnetization can be controlled by curled electric fields, because of the inherent interactions between ferroelectric vortices, oxygen octahedral tilts, and magnetic dipoles. This novel magnetoelectric coupling was termed the magnetotoroidic effect and was also found to involve complex intermediate microscopic states, such as electric vortices coexisting with antivortices.

This latter coexistence was also predicted to occur in the ground state of the nanocomposite made of periodic arrays of $BaTiO_3$ nanowires that are embedded in a matrix formed by another FE material [70]. In this ground state, the nanowires all possess FE vortices having the same, clockwise or counterclockwise, rotation while antivortices (and also vortices with identical rotation than in the nanowires) can be found in the matrix. This state is thus analogous to the so-called "phase-locked" phase that has been recently observed in magnetic systems [71]. Interestingly, a spontaneous polarization further exists along the nanowire direction, in addition to the toroidal moment that is associated with the FE vortices. Such a combination was shown to result in natural optical activity and its control by electric fields [72]. In other words, the plane of polarization of linearly polarized light should rotate when passing through the nanocomposite, with the sense of this rotation being switchable by an electric field. Reasons behind this natural optical activity and its control by electric field control are the linear response of the toroidal moment to a homogeneous electric field (thanks to the coupling between electrical polarization and electric vortices) and the field-induced transition between the dextrorotatory and laevororotatory forms of the ground state [72].

Another computational study predicted that gyrotropy can also exist, but in a specific crystallographic state of BFO films that are under compressive strain and that are grown along the (unusual) [–110] direction [73]. This phase has the $P2_12_12_1$ space group and possesses interpenetrated arrays of FE vortices (having the same sense of rotation) and FE antivortices. Such arrays were found to originate from the simultaneous existence of two unstable off-center phonon modes, one at the M-point of the cubic first Brillouin zone and the other one at the X-point of this Brillouin zone.

The nanocomposite studied by Louis et al. [70] was further predicted to exhibit another unusual phenomena, that is a temperature-driven vortex core transition (VCT) for which the vortex cores transforms from being axisymmetric to possessing a "broken symmetry" (that was further found to be correlated to inhomogeneous in-plane polar displacements)

[70]. VCT transitions have been previously known to exist in some complex systems, such as superfluids [74], but never in ferroelectrics before the study of Louis et al. [70].

Furthermore, Prosandeer et al. [75] used an effective Hamiltonian approach within molecular dynamics to study *electrocaloric* effects in PZT nanodots exhibiting an FE vortex. It was found that the changes in temperature, $\Delta T(t)$, induced by a time-dependent change in an AC electric field, $\Delta E(t)$, are related to each other via $\Delta T(t) = \alpha \Delta E(t) + \gamma t$, where α and γ are time-independent positive coefficients. In other words, a variation linear with time, γt, is superimposed on to the usual electrocaloric effect given by $\alpha \Delta E(t)$. Such linear addition originates from the expansion/compression of the vortex pattern (via flipping of dipoles) under the AC field and characterizes a constant heating of the nanodot.

Another original prediction was offered by Prosandeer et al. [76]: simulations using a first-principles-based effective Hamiltonian (within the path-integral quantum Monte Carlo method (PI-QMC) [24, 77, 78]) indicated that quantum, zero-point phonon vibrations lead to the suppression of the ferroelectric vortex, and thus to the annihilation of the electric toroidal moment, in stress-free nanodots made of $KTaO_3$ (KTO) and being under electrical boundary conditions. This suppression was found to be accompanied by the formation of a peculiar local structure that possesses short-range, needle-like correlations of the individual toroidal moments. The annihilation of the global electric toroidal moment in KTO dots is reminiscent of the known fact that quantum vibrations also result in the disappearance of the spontaneous polarization in the so-called incipient ferroelectrics bulks (such as the KTO bulk) [79, 80]. This analogy is at the origin of the term “incipient ferrotoroidics” given by Prosandeer et al. [76] for systems such as KTO dots.

22.1.6 Summary from the Simulations and Theory Perspective

In summary, we have tried to provide a comprehensive review about theoretical and computational studies on FE vortices and related complex patterns of electric dipoles. We hope that this review will be of benefits to expert of this fascinating field of research, but also to “newcomers” interested in learning more about this exciting topic. We also hope that numerous predictions resulting from simulations performed in the last nine years will be experimentally confirmed soon. Finally, we apologize in advance for (involuntary) omissions of works in this rapidly developing and active research direction.

22.2 Insights from Experiments

22.2.1 Introduction

It should be evident from the preceding section of this chapter that theoretical studies, using both atomistic and phenomenological approaches, have made clear predictions about the existence and behaviour of ferroelectric vortices [7, 8, 36, 59, 81]. Spurred on by these predictions, experimentalists have made significant efforts to try to find them in real materials. The fact that magnetic vortex states had already been directly imaged in ferromagnets (whose dipole characteristics are often analogous to ferroelectrics) [82–84] gave genuine confidence of success.

However, after a decade or more of searching, categorical and conclusive observations of genuine ferroelectric vortices have not yet been made. That is not to say that there has been no relevant research progress; on the contrary, a great deal has been learned from the search so far: flux-closure structures, often seen as the precursors for vortex formation, have been discovered to occur in response to depolarizing fields [10–13, 85, 86] or as a result of specific switching experiments [14, 17, 18], and continuous rotations in dipole orientations in ferroelectrics have been directly imaged for the first time [15, 16]. Such observations point strongly to the possibility of vortex formation and perhaps it is only a matter of time before suitable experimental conditions are found in which vortices could be stabilized. For the moment, however, they remain elusive.

It may therefore come as a surprise to find that experimental literature is commonly populated with matter-of-fact statements describing a specific dipole or domain arrangement as a ferroelectric vortex. To critically evaluate the validity, or otherwise, of such statements, let us first examine a number of the defining characteristics of a vortex configuration that, although perhaps not sufficient, are certainly necessary for its existence to be claimed:

(i) The topological winding number of a vortex is $+1$.
(ii) The rotation of local dipoles in the vortex structure should be such that each is oriented perpendicular to the radial vector from the vortex core to that dipole.
(iii) The dipole pattern should only contain a single topological singularity, not a compound set of singularities with a net winding number of $+1$.

22.2.2 Vortices and Topological Winding Numbers

The first characteristic listed above is that the winding number of a dipole pattern needs to be $+1$ for it to even be considered as a possible vortex state [87]. The winding number classification allows different topological patterns to be meaningfully grouped together. To determine the winding number associated with a region of dipoles, a closed path loop in the ferroelectric needs to be considered (Figure 22.5(a)). One should imagine traversing this loop in an anticlockwise sense and then, on a separate diagram, sequentially plotting the orientation of each dipole encountered. In this separate diagram, each dipole considered should be imagined to sit at the centre of a circle, and the point at which the vector direction of the dipole intersects the circle circumference should then be plotted as a pole (Figure 22.5(b)). The number of times that the plotted poles undergo a full rotation, in an anticlockwise sense, is the winding number associated with the dipoles in the region of the ferroelectric enclosed by the initially considered loop. Rotations of dipoles in a clockwise sense are designated as negative winding numbers. Interestingly, a vortex possesses a winding number of $+1$ irrespective of the sense in which it acts (clockwise or anticlockwise; see Figure 22.5(c)). Dipole patterns with winding numbers of -1 are distinctly non-vortex in nature, illustrated by the quadrupole (or perhaps “antivortex”) pattern example given in Figure 22.6(a).

In literature, the topological patterns seen in rare earth manganites are often referred to as vortices [88–90] and yet this claim never seems to be explicitly justified. Without doubt, very interesting domain patterns are present in these improper ferroelectrics; the points at which sets of domain walls intersect are particularly noteworthy as they clearly create some form of line defect around which the sense of the ferroelastic distortion and ferroelectric dipole vector vary. However, the winding number associated with the dipole arrangement around this line defect is rarely discussed. In Figure 22.7, piezoresponse force microscopy (PFM) images from a single crystal of $YbMnO_3$ are shown. As the plane of

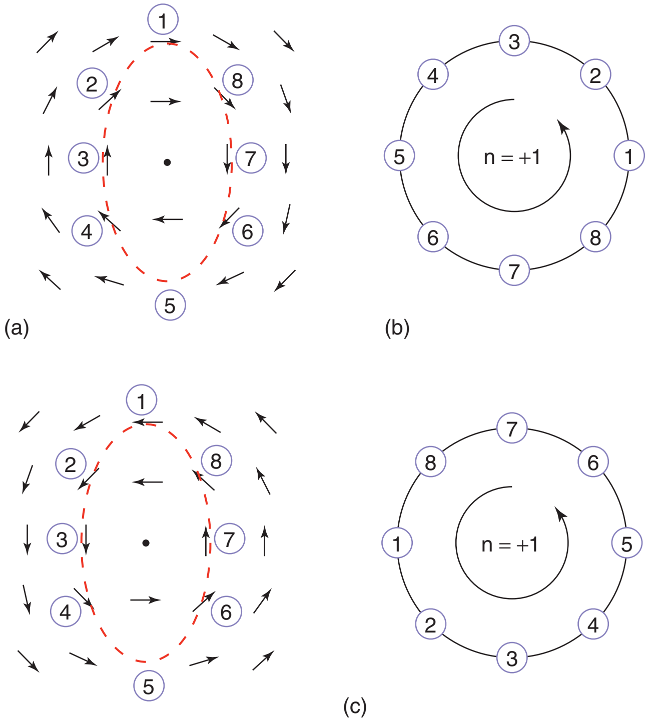

Figure 22.5 The winding number can be determined by considering the way in which dipole orientation varies while traversing around a closed loop (dashed ellipse) in an anticlockwise sense (a). At each point on the journey, encountered dipoles are considered as vectors originating at the centre of a circle; these vectors are then represented, on a second diagram, by the poles at which they intersect the circle circumference (b). The winding number is the number of times sequentially encountered poles describe complete anticlockwise rotations on this second diagram. As can be seen, both clockwise and anticlockwise vortices generate winding numbers of +1 (c)

the section imaged contains the polar axis and this axis is approximately perpendicular to the PFM cantilever, the lateral PFM images completely capture the polar orientations in the various domains (sketched schematically in the same figure). Considering a loop pathway that encapsulates the point at which the domain walls intersect, we can readily generate an associated representation of the topology (Figure 22.7(b)). Each dipole vector is only associated with one of two diametrically opposite poles. While it might be tempting to assign a winding number, it is, in fact, impossible: the sense of rotation, required to move between oppositely oriented domains, is undefined. The vortex terminology, widely used in manganite literature, is therefore baffling and seems unjustified on the basis of the dipole configurations at least.

A very important aspect of this winding number discussion is that, although a value of +1 is necessary for a topological pattern to be described as a vortex, it is not sufficient. Many dipole patterns that are clearly not vortices may also have +1 winding numbers: the radial pattern of dipoles in Figure 22.6(b) is a good example.

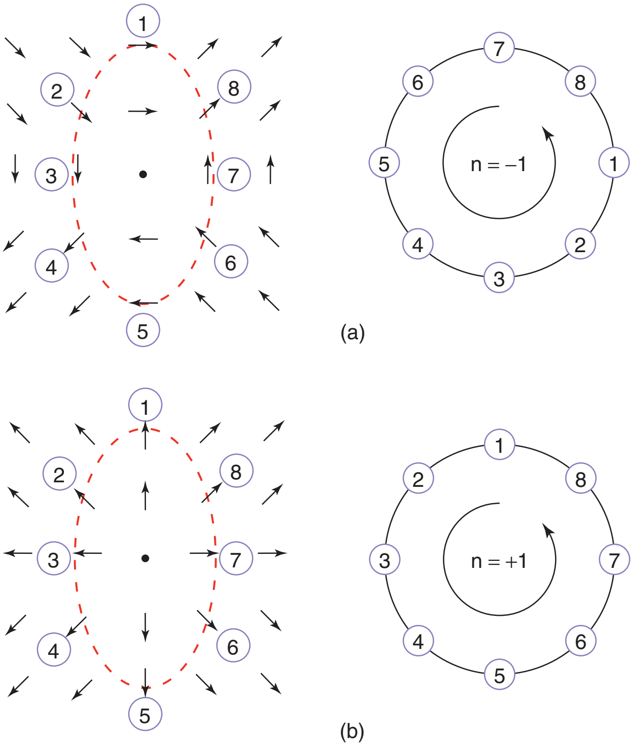

Figure 22.6 A quadrupole, or antivortex, dipole arrangement is an example of a pattern that generates a winding number of −1 (a). A winding number of +1 is a necessary condition for a vortex, but it is not a sufficient one, as can be seen by the radial dipole pattern in (b)

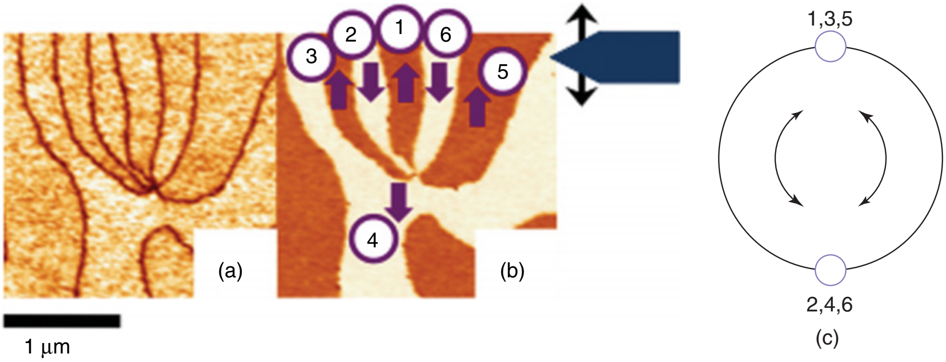

Figure 22.7 Piezoresponse force microscopy (PFM) images (amplitude (a) and phase (b)) of an interesting region of a $YbMnO_3$ single crystal; in this region, domain walls intersect to form a line defect, manifest in the 2D planar section imaged as a point defect. Traversing in a loop around this defect, in an anticlockwise sense, allows for an attempted analysis of winding number (c), as was previously illustrated in Figures 22.5 and 22.6. Here, however, the number of times that the dipole vector rotates in traversing the loop is undefined; even the sense of the rotation across successive 180° domain walls is unclear. A definitive winding number cannot therefore be assigned

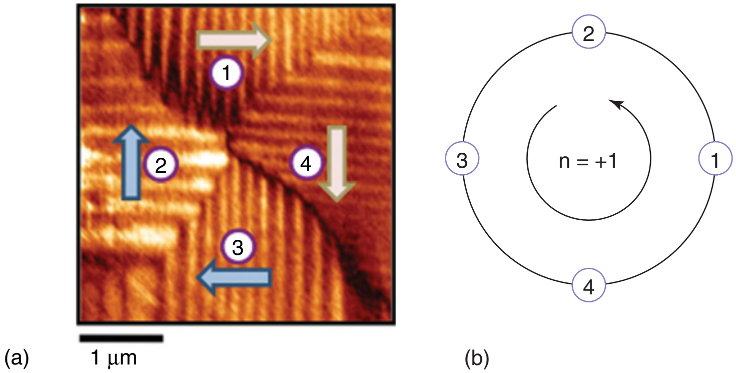

Figure 22.8 *(a) Flux-closure patterns generated by the net polarization in each of four packets of ferroelastic domains (or superdomains). (b) A winding number of +1 can be associated with these kinds of flux-closure arrangements, but the dipole orientation does not vary continuously around the core; rather it changes direction in discrete jumps such that, despite the winding number value, quadrant flux closure cannot be considered as a vortex*

22.2.3 Continuous versus Sudden Dipole rotation

By inspection, the form of a vortex structure (Figure 22.5) is such that there is a continuous rotation in the orientation of dipole vectors around the singularity at the centre of the vortex (the vortex core). Formally, this property might be described by a necessity for dipoles to be oriented perpendicular to the radial vector from the vortex core to the dipole ($\mathbf{r}_i$). In addition, the sense of all dipole vectors (clockwise or anticlockwise) around the core should be the same. Another way to express this might be that, for a given magnitude of local dipole vector ($\mathbf{p}_i$), the magnitude of the ferrotoroidal moment, $\mathbf{G} = \sum_i \mathbf{r}_i \times \mathbf{p}_i$ (discussed extensively in the first half of this chapter), should be at a maximum for the vortex state to be claimed.

Flux-closure structures (Figure 22.8), such as those mapped by McQuaid et al. [12], McGilly and Gregg [11], Ivry et al. [13], Chang et al. [86], and Balke et al. [14, 17], have winding numbers of +1 and could therefore be considered as vortex contenders on the basis of winding number alone. However, it is clear that the rotation of dipole vectors around the core is not continuous; rather its orientation changes abruptly, usually achieved through four distinct 90° rotations in the dipole, or net dipole, orientation. Arguments have been made that, as one moves closer to the centre of a flux closure pattern, there may be a transition from discrete polar rotation to continuous rotation and that, therefore, the existence of flux closure could be sufficient to claim the presence of a localized central vortex that extends over a limited region of space, even if this is not directly observed. This is an interesting point of view. It is certainly topologically allowable for dipole patterns with the same winding numbers to transform from one pattern to another with distance from the topological defect core (see Figure 22.9 for an example of this) [87].

Direct high-resolution mapping of dipoles, using aberration-corrected transmission electron microscopy [15, 16], has definitively shown that continuous rotations of dipoles in a ferroelectric can occur. However, it is telling that, even in the landmark study by Jia and co-workers [15], full 360° polar rotation does not occur around a single core point (only

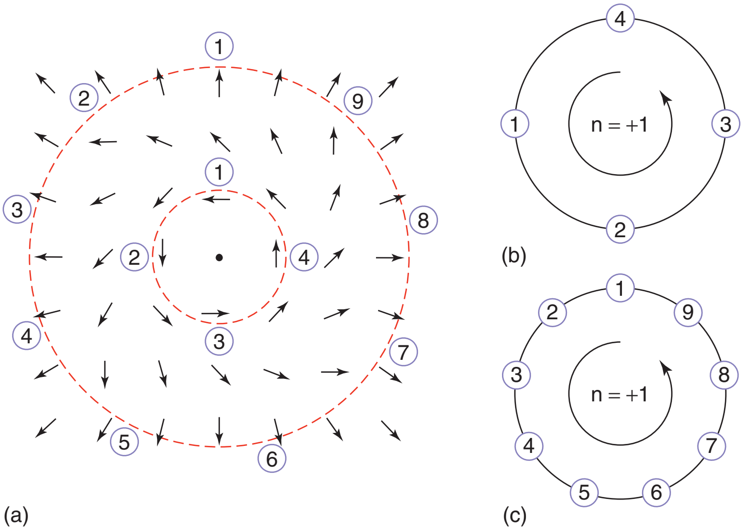

Figure 22.9 *Dipole patterns with the same winding number can transform continuously from one to another as the distance from the topological defect at the center increases. In this example the interior of the pattern in (a) is a vortex, which transforms continuously into a radial pattern. As can be seen, successive dipoles encountered in the loop pathways marked by the dashed lines in (a) both indicate winding numbers of +1 (b and c)*

180° rotation is observed) and thus the dipolar pattern is not associated with a true vortex core singularity. This leads us to the third key feature of a true ferroelectric vortex discussed in detail below.

22.2.4 Unique Core Singularity

When ferromagnetic vortices are imaged, in permalloy disks for example [83, 84], a single vortex core is observed, at which the local magnetic dipole is forced to orient perpendicular to the plane of the vortex structure and around which continuous dipole rotation in the vortex plane is found. In ferroelectrics, the structure of the vortex core may differ. Indeed, local polarization may disappear, rather than reorient, since, in ferroelectrics (unlike ferromagnetics), the magnitude as well as the orientation of local dipoles can vary. Nevertheless, the existence of a single topological defect at the core is still expected, as a signature of the true vortex state.

Despite being necessary for ferroelectric vortices, winding numbers of +1 and continuous uniform dipole rotation do not guarantee the existence of a singular defect core. As pointed out by Mermin [87], an aggregation of topological defects can act in concert to generate apparent winding numbers, at a distance, that are given by the sum of their individual winding numbers, but are not necessarily representative of any one of the individual topological defects within the aggregate. Figure 22.10 illustrates this point: two defects, each with a winding number of $+{}^{1}\!/_{2}$, are in close proximity. While pathway loops enclosing the defects separately clearly demonstrate that neither one has a winding number of +1,

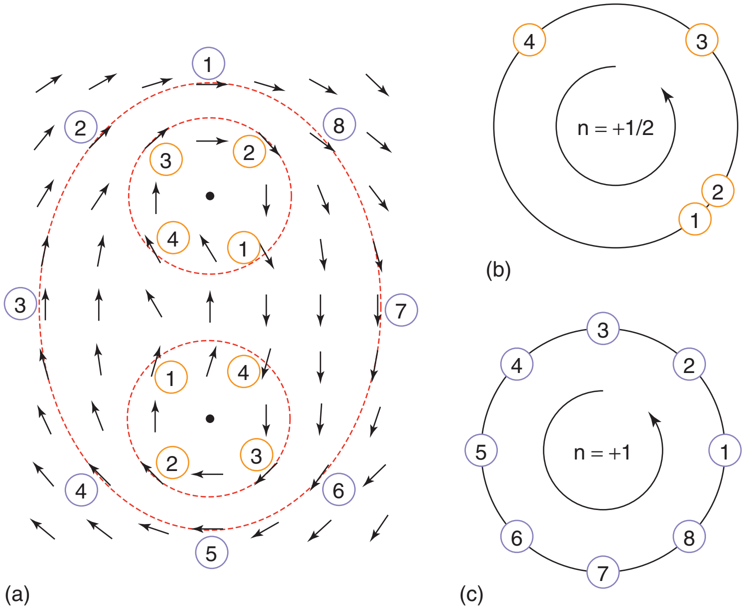

Figure 22.10 *The dipole pattern illustrated in (a) has two topological singularities, each with a winding number of* $+{}^{1}/_{2}$ *(b). If a loop pathway is chosen that encompasses both of these singularities, then the winding number observed will be the sum of their individual winding numbers (c). Thus, something that might appear to have the properties of a vortex on a large scale could be composed of several topological defects, none of which is a true vortex state*

loops that enclose both defects together do indeed generate +1 as the net winding number. One might suggest that the difference between a single vortex core and a compound one, made from potentially many non +1 topological defects, is immaterial. Yet, if a region of dielectric contained an array of equal numbers of both vortex (+1) and antivortex (–1) structures, we would not equate this to a perfectly undisturbed and uniform ferroelectric domain, despite the fact that, for large enough pathway loops, these two dipole patterns would possess the same net zero winding number. Thus, in the limit, a compound set of topological defects, which together generate a +1 winding number, should not be considered to be a true vortex core. Several experimental observations on ferroelectric dipole configurations with winding numbers of +1 (flux-closure states) illustrate a tendency for compound, rather than single, topological core defects. These studies may suggest that a vortex core singularity is energetically unfavorable in ferroelectrics.

McGilly et al. [10] examined the patterns formed at the boundaries between bundles of 90° stripe domains (superdomains) in BaTiO$_3$ single-crystal lamellae and nanostructures. While many of these boundaries were composed of conventional 180° domain walls, they found that some were more complex in form. By considering all possible self-consistent sets of dipole orientations in these more complex junctions (illustrated in Figure 22.11), McGilly et al. concluded, from symmetry arguments, that they had to be comprised of chains of flux-closure and quadrupole pairs. The resolution of STEM allowed for

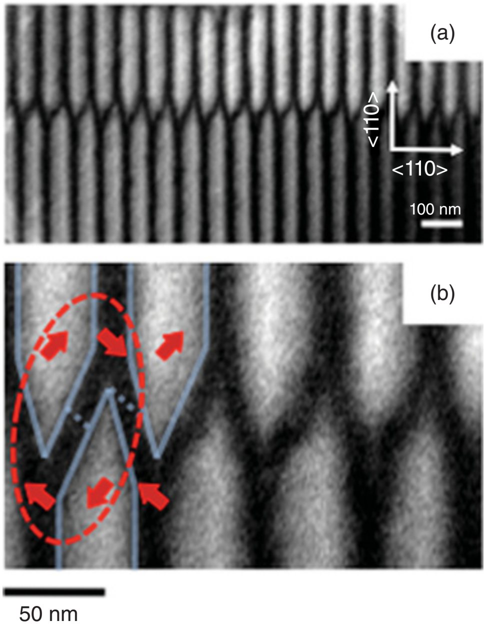

Figure 22.11 *(a) Scanning transmission electron microscopy (STEM) images of a junction between bundles of 90° ferroelastic domains (superdomain bundles), where the existence of flux-closure dipole structures is inferred. (b) Part of the boundary has been magnified and the dipole orientations thought to be present plotted, along with an inferred 180° domain wall not imaged in STEM (interpretation after McGilly et al. [10])*

information to be obtained on the nature of the core structure in these flux-closure objects: in Figure 22.11(b), it is clear that the domains indicated by the light and dark STEM contrast do not converge to a single point. Rather, the light contrast domains show needle-point morphology and stop short of the junction itself. The core region of the flux-closure structure is entirely dark contrast. The implication is that, rather than form a single core at which all four domains converge (a fourfold vertex), a distributed compound core forms, consisting of two threefold vertices, spatially separated by a short 180° domain wall, with little if any contrast on STEM. The two topological defects then form a pair, with a total winding number of +1, but composed of two $+\frac{1}{2}$ objects, conceptually in direct analogy with the schematic given in Figure 22.10.

While the dipole orientations in McGilly et al.'s study were inferred, Chang et al. [86] were able to obtain more direct information, using piezoresponse force microscopy (PFM) on similar flux-closure objects, along the edges of single-crystal lamellae of Pb(Zn, Nb)O_3–PbTiO_3 (PZN–PT). Here superdomain bundles of 90° stripe domains were found to form into flux-closure quadrants on a mesoscale (1–10 μm). Again the form of the flux-closure structure was such that a single fourfold core was avoided and instead two threefold junction structures with $+\frac{1}{2}$ winding number formed (see Figure 22.12(a) to (c)). This PZN–PT study was particularly interesting, as detailed mapping of the boundary between superdomains in the centre of the mesoscale flux-closure structure (Figure 22.12(d) and (e))

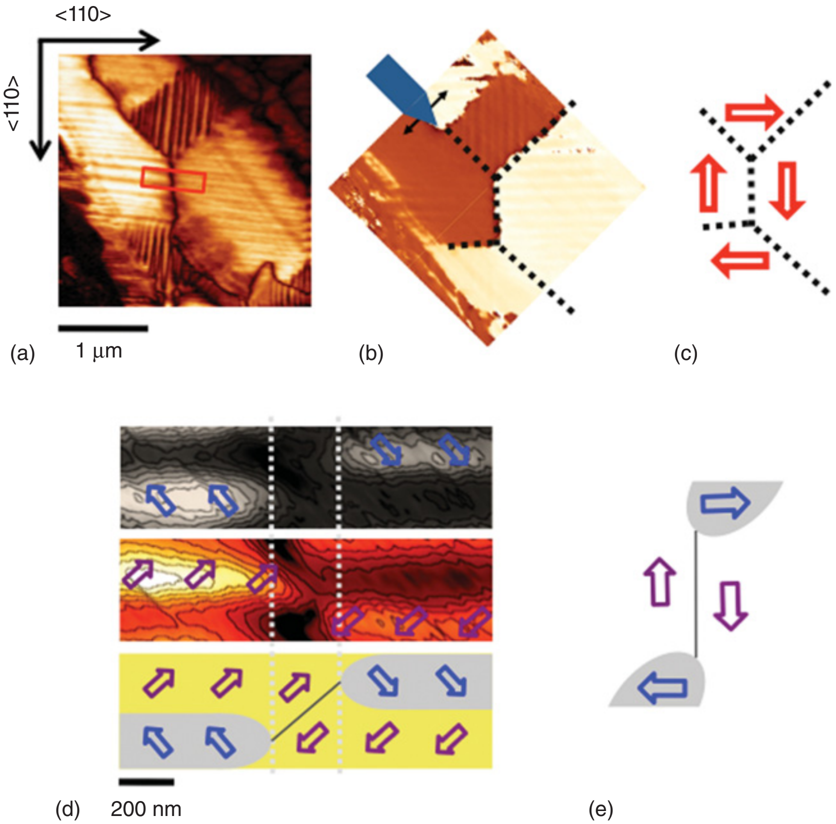

Figure 22.12 *Piezoresponse force microscopy (PFM) imaging of the edge of a thin single-crystal lamella of $Pb(Zn,Nb)O_3$–$PbTiO_3$ (PZN–PT). Piezoresponse amplitude (a) and phase maps (b) revealed the existence of flux-closure structures on length scales between 1 and 10 μm, comprised of four superdomains (distinct bundles of stripe domains) arranged into quadrants (c). Higher resolution mapping of the region enclosed by the rectangular box in (a) showed that, at the junction between bundles of 90° ferroelastic domains, flux closure was again present, but in this case on a length-scale of hundreds of nanometers (d). The two upper panels in (d) show that one set of domains terminates somewhat short of the actual boundary, whereas the other set looks to meet and abut at the boundary. The detailed dipole structure at the junction is hence given by the schematic in the lower panel in (d), a region that has been blown up and rotated in (e). Comparison of the schematics in (c) and (e) clearly suggests that the nested flux-closure structures are self-similar, despite the quite different lengths of scales at which they exist (interpretation after Chang et al. [14])*

revealed another set of flux-closure states in the nanoscale size regime (length scales of order 100 nm). Detailed interpretation of vector PFM information led to a reconstruction of the small-scale flux-closure structures, illustrated schematically in Figure 22.12(e), which were remarkably similar to the mesoscale flux-closure structure in which they were embedded. Such nested self-similar morphology, generating flux closure with a compound rather than a single core, across rather different length scales, strongly suggests that true vortex singularities in ferroelectrics may be too energetically unstable to be generally observed. This may be one of the most serious barriers to ferroelectric vortex formation.

22.2.5 Summary and Conclusions from an Experimental Perspective

There is no doubt that predictions of ferroelectric vortices, resulting from computational simulations, prompted a great deal of excitement in the experimental ferroelectric community. Many researchers sought to be the first to discover ferroelectric vortex states in real materials. This resulted in either speculative interpretations of data in terms of the existence of vortices [19, 20, 91, 92], when other interpretations were equally valid, or in the widespread inappropriate use of the term “vortex” to describe dipole patterns that had either no, or only limited, similarities to genuine vortex patterns in terms of dipole distributions at least [16, 17, 88–90]. After around a decade of searching, we can now afford a frank evaluation of the observations made so far: no true ferroelectric vortices have been unequivocally seen.

However, several phenomena consistent with the possibility of vortex existence have been established: ferroelectric flux-closure states (often seen as a precursor to the formation of vortices) have been found and studied [10–14, 17, 18, 85, 86] and gradual and continuous rotations of electrical dipoles, previously a point of contentious debate, have been directly imaged [15, 16].

Acknowledgments

Work reviewed in Section 22.1 has been financially supported by ONR Grants N00014-11-1-0384 and N00014-12-1-1034. The authors also acknowledge discussion with scientists sponsored by NSF Grant DMR-1066158, ARO Grant W911NF-12-1-0085, and the Department of Energy, Office of Basic Energy Sciences, under Contract ER-46612. Work reviewed and discussed in Section 22.2 has been financially supported by the Engineering and Physical Sciences Research Council (EPSRC) under grant awards: EP/F004869/1, EP/H047093/1, and EP/H04339X/1, by The Leverhulme Trust, under the International Network scheme (F/00 203/V), and by the Department of Employment and Learning (DEL) in Northern Ireland.

References

(1) Landau, L.D. and Lifshitz, E.M. (1980) *Statistical Physics*, Pergamon, New York, Part 1.

(2) Mermin, N.D. and Wagner, H. (1966) Absence of ferromagnetism or antiferromagnetism in one- or two-dimensional isotropic Heisenberg models. *Physical Review Letters*, **17**, 1133–1136.

(3) Bruno, P. (2001) Absence of spontaneous magnetic order at nonzero temperature in one- and two-dimensional Heisenberg and XY systems with long-range interactions. *Physical Review Letters*, **87**, art. no. 137203.

(4) Kittel, C. (1946) Theory of the structure of ferromagnetic domains in films and small particles. *Physical Review*, **70**, 965–971.

(5) Lines, M.E. and Glass, A.M. (1979) *Principles and Application of Ferroelectrics and Related Materials*, Clarendon, Oxford.

(6) Scott, J.F. (2000) *Ferroelectric Memories*, Springer, Berlin.

(7) Fu, H. and Bellaiche, L. (2003) Ferroelectricity in barium titanate quantum dots and wires. *Physical Review Letters*, **91**, art. no. 257601.

(8) Naumov, I.I., Bellaiche, L., and Fu, H. (2004) Unusual phase transitions in ferroelectric nanodisks and nanorods. *Nature*, **432**, 737–740.

(9) Prosandeev, S. Ponomareva, I., Naumov, I., Kornev, I., and Bellaiche, L. (2008) Original properties of dipole vortices in zero-dimensional ferroelectrics. *Journal of Physics: Condensed Matter*, **20**, art. no. 193201.

(10) McGilly, L.J., Schilling, A., and Gregg, J.M. (2010) Domain bundle boundaries in single crystal $BaTiO_3$ lamellae: searching for naturally forming dipole flux-closure/quadrupole chains. *Nano Letters*, **10**, 4200–4205.

(11) McGilly, L.J. and Gregg, J.M. (2011) Polarization closure in nanodots of $PbZr_{(1\text{-}x)}Ti_xO_3$. *Nano Letters*, **11**, 4490–4495 (2011).

(12) McQuaid, R.G.P., McGilly, L.J., Sharma, P., et al. (2011) Mesoscale flux-closure domain formation in single-crystal $BaTiO_3$. *Nature Communications*, **2**, art. no. 404.

(13) Ivry, Y., Chu, D.P., Scott, J.F., and Durkan, C. (2010) Flux-closure vortex-like domain structures in a ferroelectric thin film. *Physical Review Letters*, **104**, art. no. 207602.

(14) Balke, N., Choudhury, S., Jesse, S., et al. (2009) Deterministic control of ferroelastic switching in multiferroic materials. *Nature Nanotechnology*, **4**, 868–875.

(15) Jia, C.L., Urban, K.W., Alexe, M., et al. (2011) Direct observation of continuous electric dipole rotation in flux-closure domains in ferroelectric $Pb(Zr, Ti)O_3$. *Science*, **331**, 1420–1423.

(16) Nelson, C.T., Winchester, B., Zhang, Y., et al. (2011) Spontaneous vortex nanodomain arrays at ferroelectric heterointerfaces. *Nano Letters*, **11**, 828–834.

(17) Balke, N., Winchester, B., Ren, W., et al. (2012) Enhanced electric conductivity at ferroelectric vortex cores in $BiFeO_3$. *Nature Physics*, **8**, 81–88.

(18) Vasudevan, R.K., Chen, Y.C., Tai, H.H., et al. (2011) Exploring topological defects in epitaxial $BiFeO_3$ thin films. *ACS Nano*, **5**, 879–887.

(19) Gruverman, A., Wu, D., Fan, H.J., et al. (2008) Vortex ferroelectric domains. *Journal of Physics: Condensed Matter*, **20**, art. no. 342201.

(20) Rodriguez, B.J., Gao, X.S., Liu, L.F., et al. (2009) Vortex polarization states in nanoscale ferroelectric arrays. *Nano Letters*, **9**, 1127–1131.

(21) Zhong, W., Vanderbilt, D., and Rabe, K.M. (1994) Phase transitions in $BaTiO_3$ from first principles. *Physical Review Letters*, **73**, 1861–1864; (1995) First-principles theory of ferroelectric phase transitions for perovskite compounds: The case of $BaTiO_3$. *Physical Review B*, **52**, 6301–6312.

(22) Kornev, I.A., Lisenkov, S., Haumont, R., et al. (2007) Finite-temperature properties of multiferroic $BiFeO_3$. *Physical Review Letters*, **99**, art. no. 227602.

(23) Kornev, I.A., Bellaiche, L., Janolin, P.E., et al. (2006) Phase diagram of $Pb(Zr, Ti)O_3$ solid solutions from first principles. *Physical Review Letters*, **97**, art. no. 157601.

(24) Iniguez, J. and Vanderbilt, D. (2002) First-principles study of the temperature–pressure phase diagram of $BaTiO_3$. *Physical Review Letters*, **89**, art. no. 115503.

(25) Bellaiche, L., Garcia, A., and Vanderbilt, D. (2000) Finite-temperature properties of Pb(Zr$_{\{1-x\}}$Ti$_x$)O$_3$ alloys from first principles. *Physical Review Letters*, **84**, 5427–5430; (2002) Low-temperature properties of Pb(Zr$_{\{1-x\}}$Ti$_x$)O$_3$ solid solutions. *Ferroelectrics*, **266**, 41–56.

(26) Almahmoud, E., Navtsenya, Y., Kornev, I., et al. (2004) Properties of Pb(Zr, Ti)O$_3$ ultrathin films under stress-free and open-circuit electrical boundary conditions. *Physical Review B*, **70**, art. no. 220102(R).

(27) Naumov, I.I. and Fu, H. (2005) A new method for determining dipole–dipole energy in 1D and 2D systems. ArXiv:cond-mat/0505497 [cond-mat.soft].

(28) Ponomareva, I., Naumov, I.I., Kornev, I., et al. (2005) Atomistic treatment of depolarizing energy and field in ferroelectric nanostructures. *Physical Review B*, **72**, art. no. 140102(R).

(29) Garcia, A. and Vanderbilt, D. (1998) In *First-Principles Calculations for Ferroelectrics: Fifth Williamsburg Workshop*, edited by R.E. Cohen, AIP, Woodbury, New York, p. 54.

(30) Slutsker, J., Artemev, A., and Roytburd, A. (2008) Phase-field modeling of domain structure of confined nanoferroelectrics. *Physical Review Letters*, **100**, art. no. 087602.

(31) Langevin, P. (1908) Sur la theorie du mouvement brownien. *Comptes Rendus de l'Académie des Sciences*, **146**, 530–533.

(32) Sepliarsky, M., Asthagiri, A., Phillpot, S.R., et al. (2005) Atomic level simulation of ferroelectricity in oxide materials. *Current Opinion in Solid State and Materials Science*, **9**, 107–113.

(33) Kohn, W. and Sham, L.J. (1965) Self-consistent equations including exchange and correlation effects. *Physical Review*, **140**, A1133–A1138; Hohenberg, P. and Kohn, W. (1964) Inhomogeneous electron gas. *Physical Review*, **136**, B864–B871.

(34) Kotliar, G., Savrasov, S.Y., Haule, K., et al. (2006) Electronic structure calculations with dynamical mean-field theory. *Reviews of Modern Physics*, **78**, 865–951; Eschrig, H. (1996) *The Fundamentals of Density Functional Theory* (revised and extended version), Edition am Gutenbergplatz, 2003, Cuvillier, Gottingen.

(35) Junquera, J. and Ghosez, Ph. (2003) Critical thickness for ferroelectricity in perovskite ultrathin films. *Nature*, **422**, 506–509.

(36) Kornev, I., Fu, H., and Bellaiche, L. (2004) Ultrathin films of ferroelectric solid solutions under a residual depolarizing field. *Physical Review Letters*, **93**, art. no. 196104.

(37) Stachiotti, M.G. (2004) Ferroelectricity in BaTiO$_3$ nanoscopic structures. *Applied Physics Letters*, **84**, 251–253.

(38) Munch, I. and Huber, J.E. (2009) A hexadomain vortex in tetragonal ferroelectrics. *Applied Physics Letters*, **95**, art. no. 022913.

(39) Lahoche, L., Lukyanchuk, I., and Pascoli, G. (2008) Stability of vortex phases in ferroelectric easy-plane nano-cylinders. *Integrated Ferroelectrics*, **99**, 60–66.

(40) Stachiotti, M.G. and Sepliarsky, M. (2011) Toroidal ferroelectricity in PbTiO$_3$ nanoparticles. *Physical Review Letters*, **106**, art. no. 137601.

(41) Durgun, E., Ghosez, Ph., Shaltaf, R., et al. (2009) Polarization vortices in germanium telluride nanoplatelets: a theoretical study. *Physical Review Letters*, **103**, art. no. 247601.

(42) Pilania, G. and Ramprasad, R. (2010) Complex polarization ordering in PbTiO$_3$ nanowires: a first-principles computational study. *Physical Review B*, **82**, art. no. 155442.

(43) Shimada, T., Wang, X., Tomoda, S., et al. (2011) Coexistence of rectilinear and vortex polarizations at twist boundaries in ferroelectric $PbTiO_3$ from first principles. *Physical Review B*, **83**, art. no. 094121.

(44) Prosandeev, S., Lisenkov, S., and Bellaiche, L. (2010) Kittel law in $BiFeO_3$ ultrathin films: a first-principles-based study. *Physical Review Letters*, **105**, art. no. 147603.

(45) Wu, Z., Huang, N., Liu, Z., Wu, J., Duan, W., and Gu, B.-L. (2007) Unusual vortex structure in ultrathin $PbZr_{0.5}Ti_{0.5}O_3$ films. *Journal of Applied Physics*, **101**, 014112.

(46) Roy, M.K., Sarkar, S., and Dattagupta, S. (2009) Evolution of 180°, 90°, and vortex domains in ferroelectric films. *Applied Physics Letters*, **95**, art. no. 192905.

(47) Prosandeev, S. and Bellaiche, L. (2006) Properties of ferroelectric nanodots embedded in a polarizable medium: atomistic simulations. *Physical Review Letters*, **97**, art. no. 167601.

(48) Naumov, I. and Bratkovsky, A.M. (2008) Unusual polarization patterns in flat epitaxial ferroelectric nanoparticles. *Physical Review Letters*, **101**, art. no. 107601.

(49) Ponomareva, I., Naumov, I.I., and Bellaiche, L. (2005) Low-dimensional ferroelectrics under different electrical and mechanical boundary conditions: atomistic simulations. *Physical Review B*, **72**, art. no. 214118.

(50) Prosandeev, S. and Bellaiche, L. (2008) Order parameter in complex dipolar structures: microscopic modeling. *Physical Review B*, **77**, art. no. 060101.

(51) Prosandeev, S. and Bellaiche, L. (2009) Hypertoroidal moment in complex dipolar structures. *Journal of Materials Science*, **44**, 5235–5248.

(52) Schilling, A., Prosandeev, S., McQuaid, R.G.P., et al. (2011) Shape-induced phase transition of domain patterns in ferroelectric platelets. *Physical Review B*, **84**, art. no. 064110.

(53) Pilania, G., Alpay, S.P., and Ramprasad, R. (2009) *Ab initio* study of ferroelectricity in $BaTiO_3$ nanowires. *Physical Review B*, **80**, art. no. 014113.

(54) Hong, J., Catalan, G., Fang, D.N., et al. (2010) Topology of the polarization field in ferroelectric nanowires from first principles. *Physical Review B*, **81**, art. no. 172101.

(55) Sichuga, D., Ren, W., Prosandeev, S., and Bellaiche, L. (2010) Chiral patterns of tilting of oxygen octahedra in zero-dimensional ferroelectrics and multiferroics: a first principle-based study. *Physical Review Letters*, **104**, art. no. 207603.

(56) Naumov, I. and Fu, H. (2007) Vortex-to-polarization phase transformation path in ferroelectric $Pb(ZrTi)O_3$ nanoparticles. *Physical Review Letters*, **98**, art. no. 077603.

(57) Prosandeev, S., Ponomareva, I., Kornev, I., and Bellaiche, L. (2008) Control of vortices by homogeneous fields in asymmetric ferroelectric and ferromagnetic rings. *Physical Review Letters*, **100**, art. no. 047201.

(58) Prosandeev, S. and Bellaiche, L. (2008) Controlling double vortex states in low-dimensional dipolar systems. *Physical Review Letters*, **101**, art. no. 097203.

(59) Prosandeev, S., Ponomareva, I., Kornev, I., et al. (2006) Controlling toroidal moment by means of an inhomogeneous static field: an *ab initio* study. *Physical Review Letters*, **96**, art. no. 237601.

(60) Naumov, I. and Fu, H. (2008) Cooperative response of $Pb(ZrTi)O_3$ nanoparticles to curled electric fields. *Physical Review Letters*, **101**, art. no. 197601.

(61) Wang, J. (2010) Switching mechanism of polarization vortex in single-crystal ferroelectric nanodots. *Applied Physics Letters*, **97**, art. no. 192901.

(62) Wang, J. and Kamlah, M. (2009) Intrinsic switching of polarization vortex in ferroelectric nanotubes. *Physical Review B*, **80**, art. no. 012101.

(63) Chen, W.J., Zheng, Y., and Wang, B. (2013) Vortex domain structures of an epitaxial ferroelectric nanodot and its temperature-misfit strain phase diagram. *Scientific Reports*, **2**, art. no. 796.

(64) Chien, C.L., Zhu, F.Q., and Zhu, J.G. (2007) Patterned nanomagnets. *Physics Today*, **80** (6), 40–45.

(65) Prosandeev, S. and Bellaiche, L. (2007) Characteristics and signatures of dipole vortices in ferroelectric nanodots: first-principles-based simulations and analytical expressions. *Physical Review B*, **75**, art. no. 094102.

(66) Jaffe, B., Cook, W.R., and Jaffe, H. (1971) *Piezoelectric Ceramics*, Academic Press, London, p. 136.

(67) Kahn, A.H. and Layendeccker, J. (1964) Electronic energy bands in strontium titanate. *Physical Review*, **135**, A1321–A1325.

(68) Prosandeev, S., Kornev, I., and Bellaiche, L. (2007) Tensors in ferroelectric nanoparticles: first-principles-based simulations. *Physical Review B*, **76**, art. no. 012101.

(69) Ren, W. and Bellaiche, L. (2011) Prediction of the magnetotoroidic effect from atomistic simulations. *Physical Review Letters*, **107**, art. no. 127202.

(70) Louis, L., Kornev, I., Geneste, G., et al. (2012) Novel complex phenomena in ferroelectric nanocomposites. *Journal of Physics: Condensed Matter*, **24**, art. no. 402201.

(71) Ruotolo, A., Cros, V., Georges, B., et al. (2009) Phase-locking of magnetic vortices mediated by antivortices. *Nature Nanotechnology*, **4**, 528–532.

(72) Prosandeev, S., Malashevich, A., Gui, Z., et al. (2013) Natural optical activity and its control by electric field in electrotoroidic systems. *Physical Review B*, **87**, art. no. 195111.

(73) Prosandeev, S., Kornev, I.A., and Bellaiche, L. (2011) Phase transitions in epitaxial (–110) $BiFeO_3$ films from first principles. *Physical Review Letters*, **107**, art. no. 117602.

(74) Eltsov, V.B., de Graaf, R., Krusius, M., and Zmeev, D.E. (2011) Vortex core contribution to textural energy in 3He–B below 0.4 T_c. *Journal of Low Temperature Physics*, **162**, 212–225.

(75) Prosandeev, S., Ponomareva, I., and Bellaiche, L. (2008) Electrocaloric effect in bulk and low-dimensional ferroelectrics from first principles. *Physical Review B*, **78**, art. no. 052103.

(76) Prosandeev, S., Akbarzadeh, A.R., and Bellaiche, L. (2009) Discovery of incipient ferrotoroidics from atomistic simulations. *Physical Review Letters*, **102**, art. no. 257601.

(77) Zhong, W. and Vanderbilt, D. (1996) Effect of quantum fluctuations on structural phase transitions in $SrTiO_3$ and $BaTiO_3$. *Physical Review B*, **53**, 5047–5050.

(78) Ceperley, D.M. (1995) Path integrals in the theory of condensed helium. *Reviews of Modern Physics*, **67**, 279–355.

(79) Muller, K.A. and Burkard, H. (1979) $SrTiO_3$: an intrinsic quantum paraelectric below 4 K. *Physical Review B*, **19**, 3593–3602.

(80) Akbarzadeh, A.R., Bellaiche, L., Leung, K., et al. (2004) Atomistic simulations of the incipient ferroelectric $KTaO_3$. *Physical Review B*, **70**, art. no. 054103.

(81) Xue, F., Gao, X.S., and Liu, J.M. (2009) Monte Carlo simulation on the size effect in ferroelectric nanostructures. *Journal of Applied Physics*, **106**, art. no. 114103.

(82) Gomez, R.D., Luu, T.V., Pak, A.O., et al. (1999) Domain configurations of nanostructured permalloy elements. *Journal of Applied Physics*, **85**, 6163–6165.

(83) Shinjo, T., Okuno, T., Hassdorf, R., et al. (2000) Magnetic vortex core observation in circular dots of permalloy. *Science*, **289**, 930–932.

(84) Wachowiak, A., Wiebe, J., Bode, M., et al. (2002) Direct observation of internal spin structure of magnetic vortex cores. *Science*, **298**, 577–580.

(85) Ahluwalia, R., Ng, N., Schilling, A., et al. (2013) Manipulating ferroelectric domains in nanostructures under electron beams. *Physical Review Letters*, **111**, art. no. 165702.

(86) Chang, L.W., Nagarajan, V., Scott, J.F., and Gregg, J.M. (2013) Self-similar nested flux closure structures in a tetragonal ferroelectric. *Nano Letters*, **13**, 2553–2557.

(87) Mermin, N.D. (1979) The topological theory of defects in ordered media. *Reviews of Modern Physics*, **51**, 591–648.

(88) Lilienblum, M., Soergel, E., and Fiebig, M. (2011) Manipulation of ferroelectric vortex domains in hexagonal manganites. *Journal of Applied Physics*, **110**, art. no. 052007.

(89) Zhang, Q.H., Tan, G.T., Gu, L., et al. (2013) Direct observation of multiferroic vortex domains in $YMnO_{3.}$ Scientific Reports, **3**, art. no. 2741.

(90) Geng, Y.N., Choi, Y.J., Cheong, S.W., et al. (2012) Collective magnetism at multiferroic vortex domain walls. *Nano Letters*, **12**, 6055–6059.

(91) Baudry, L., Sene, A., Luk'yanchuk, I.A., and Lahoche, L. (2011) Vortex state in thin films of multicomponent ferroelectrics. *Thin Solid Films*, **519**, 5808–5810.

(92) Sené, A. (2010) *Theory of Domains and Non-Uniform Texture in Ferroelectrics*, PhD Thesis, University of Picardie Jules Verne.

23

Reentrant Phenomena in Relaxors

Alexei A. Bokov and Zuo-Guang Ye

Department of Chemistry and 4D LABS, Simon Fraser University, Canada

23.1 Introduction

The sequence of phases observed in a material in the course of decreasing temperature typically obeys the general rule: a disordered (high-symmetry) phase is followed by a more ordered one. Normally the transition between phases is sharp, i.e. the order parameter, which is zero in the disordered phase, emerges at the transition temperature, T_C, when entering the ordered phase. While the regions of order parameter (fluctuations) may be observed locally at $T > T_C$, they are not stable and, therefore, short-lived. The classical examples of such a kind of behavior are ferromagnetic (FM) and ferroelectric (FE) phase transitions, where the order parameter is magnetization and electric polarization, respectively. However, in some instances this simple picture does not hold. The first example is relaxor ferroelectrics (or relaxors in short) where, between a high-temperature paraelectric (disordered) phase and a low-temperature ferroelectric (ordered) phase, one can observe a so-called ergodic relaxor (ER) phase in a rather wide temperature interval (dozens or even hundreds of degrees). Macroscopically the ER state possesses the same (high) symmetry as the paraelectric phase, but on the nanometer scale it contains areas of randomly oriented local polarization usually called polar nanoregions (PNRs). In contrast to FE fluctuations, PNRs are permanent, but the direction and magnitude of their dipole moments may fluctuate in time, giving rise to the extraordinary properties of relaxors, such as a giant dielectric constant, high electrostriction, characteristic dielectric dispersion, etc.

In a number of relaxor ferroelectrics (sometimes called "canonical" relaxors) the ER phase does not undergo the transition to the FE phase in a zero-field cooling regime and

---

Nanoscale Ferroelectrics and Multiferroics: Key Processing and Characterization Issues, and Nanoscale Effects, First Edition. Edited by Miguel Algueró, J. Marty Gregg, and Liliana Mitoseriu.
© 2016 John Wiley & Sons, Ltd. Published 2016 by John Wiley & Sons, Ltd.

the macroscopic symmetry of the paraelectric phase remains unchanged down to near-zero K. In this case a thermodynamic transition from the ER state to a non-ergodic relaxor (NR) phase can be observed around the freezing temperature, below which the temporal fluctuations of PNRs vanish and their local polarization becomes static. The main microscopic reason for the freezing in canonical ferroelectric relaxors is believed to be the frustrated electric (and probably elastic) interactions among the dipoles of PNRs, which is similar to the one for the freezing in magnetic spin glasses, where the interactions occur among the diluted magnetic spins. Accordingly, many features of relaxor ferroelectrics and spin glasses are similar.

Another kind of unusual phase sequence is also known in which, after having gone through the disordered and the ordered phases, the material reenters a disordered phase upon further cooling. The low-temperature phase is called a reentrant or reappearing phase. It is not exactly the same as the high-temperature parent phase, but it loses the order parameter inherent in the intermediate (ordered) phase. This can happen if the entropy of the reentrant disordered phase is smaller than that of the ordered phase, and it implies that the considered order parameter does not reflect fully the order–disorder processes in the system. Besides the true reentrant behavior, situations are also possible where the order parameter of the intermediate phase is conserved in the low-temperature phase, but the macroscopic properties of the latter resemble the properties of a disordered phase. This can happen if some additional degrees of freedom not influencing the primary order parameter are involved in the reentrant transition. For example, in some magnets undergoing a paramagnetic–ferromagnetic–spin-glass sequence of phases, the primary order parameter (magnetization) increases monotonically from the Curie temperature down to near-zero K, but the spin-glass order appears at the reentrant transition in the direction perpendicular to the magnetization, leading to the coexistence of ferromagnetic and spin-glass orders. Such a kind of quasi-reentrant phase and true reentrant phase are often hardly distinguishable in experiments. Therefore, they are all commonly called reentrant phases.

The present chapter provides a comprehensive review on the reentrant relaxors, that is the materials in which both types of above-mentioned peculiarities (reentrant and relaxor behaviors) are observed.

23.2 Reentrant Phases in Condensed Matter

The first example of a reentrant phase transition was predicted theoretically more than a century ago by G. Tamman (1903) [1]. He considered a pressure–temperature phase diagram containing closed loops with a crystalline phase surrounded by liquid or glass regions, which implied reversible transition from the crystalline to an amorphous phase on cooling. This transition was termed inverse melting. It was initially believed that inverse melting could be seen only under extreme conditions inaccessible in a laboratory, but this phenomenon has since been observed at moderate temperatures and pressures in some polymers [2, 3].

Experimentally the reentrance was first discovered in binary liquid mixtures [4, 5]. It was found that certain homogeneous liquids transform into two separated, coexisting liquid phases at lower temperatures and become homogeneous again when the temperature is further lowered. The reentrant phenomena were studied elaborately in dilute magnets, where the sequence of phases from paramagnetic to ferro- (or antiferro-)magnetic and further to reentrant spin glass (SG) was observed within a particular (usually narrow) concentration range of magnetic atoms. Other examples are superconductors with normal-superconducting-normal phase sequence [6–8] and liquid crystals in which multiple reentrance can be observed when nematic (less ordered) and smectic (more ordered) phases alternate several times as the temperature decreases [9, 10]. Recently a new astrophysical phenomenon of reentrant phase transition has been reported in which a monotonic variation of the temperature yields two phase transitions from large to small, and back to large, black holes [11]. Among ferroelectric crystals reentrant phases are comparatively seldom. Interestingly, however, the reentrant behavior was observed in the first known ferroelectric, Rochelle salt, which exhibits an FE phase between two Curie points (at 24 and –18 °C), that is between two paraelectric phases. KNO_3 and some complex organic compounds also exhibit similar behavior with two Curie points [12].

The equilibrium sequence of phases is determined by thermodynamics, which requires that the stable state of a matter should have a minimal free energy $F = U - ST$. At low temperatures the minimum of F corresponds to the minimum of internal energy, U. The internal energy is determined by the configuration of chemical bonds which are more or less symmetric. At high temperatures the second (negative) term in the free energy expression can prevail, giving rise to a state with large entropy (S), that is a disordered state. The change from the disordered to the ordered state is observed at the phase transition temperature, where the increase of $-TS$ due to ordering is compensated by the decrease of U. However, at lower temperatures where the reentrant transition occurs, the decrease of $-TS$ related to the vanishing of the order parameter leads to a much smaller change of F than the corresponding increase of U. Therefore, some hidden mechanism should exist that keeps the energy low. For example, in binary fluid mixtures, due to the interplay between the van der Waals and hydrogen bonds, a small increase of compositional (related to the order parameter) entropy upon transition to the reentrant phase is accompanied by a more significant decrease of orientational entropy and, as a result, the total entropy actually decreases [13].

To discuss the reentrant behavior in detail we will use as an example the magnetic reentrant spin glasses that are apparently the closest well-studied analogue to the poorly understood reentrant relaxors. Among the magnetic materials the reentrant behavior is typically observed in solid solutions where a "normal" spin-glass phase also exists, but in a different concentration range. Spin-glass phases appear when an FM or AFM system is diluted with magnetic or non-magnetic atoms and the interactions among spins become frustrated, that is a competition between the FM and AFM exchanges develops. A typical phase diagram of such a system is shown in Figure 23.1. As long as the dopant concentration (x) remains small, the original (FM or AFM) exchange dominates and the long-range ordered phase survives, though the transition temperature decreases with increasing x. The degree of frustration increases as well, and above the critical concentration, x_c, the competing FM and AFM interactions become balanced to destroy completely the long-range collinearity among the spins. As a result, the system transforms from the paramagnetic to the spin-glass (SG) phase as the temperature is decreased. However, in a comparatively narrow concentration interval below x_c, where the exchange interactions are frustrated only partially, two phase transitions can be observed. The first one is the Curie (or Néel) point and the second one is a transition to the phase with the properties characteristic of the SG phase, which is usually referred to as reentrant spin glass (RSG). This behavior has been found in

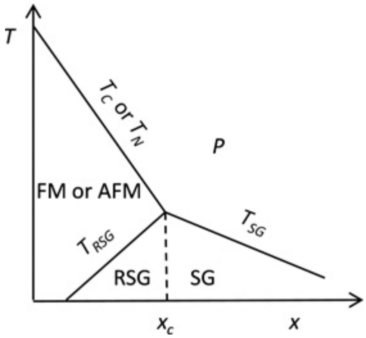

Figure 23.1 *Typical phase diagram of a reentrant spin-glass magnetic system showing paramagnetic (P), ferromagnetic (FM), or antiferromagnetic (AFM), spin-glass (SG) and reentrant spin-glass (RSG) phases; x is the concentration of non-magnetic atoms*

many materials, including polycrystalline metals Au_xFe_{1-x} [14] and $Ni_{1-x}Mn_x$ [15], dilute magnetic semiconductors $Eu_xSr_{1-x}S$ [16], amorphous metals $(Fe_{1-x}Mn_x)_{75}P_{16}B_6Al_3$ [17], etc. Figure 23.2 shows an example of RSG behavior in antiferromagnetic $Fe_{0.55}Mg_{0.45}Cl_2$. The maximum at 8 K in the temperature dependence of the real part of AC susceptibility is associated with the transition from the high-temperature paramagnetic phase to the AFM phase, while the anomaly with a significant dispersion in the frequency range of ~10 Hz–3 kHz observed at ~3 K indicates the transformation to the RSG phase. Magnetic relaxation at such low frequencies is typically absent in FM or AFM phases, but is characteristic of spin glasses.

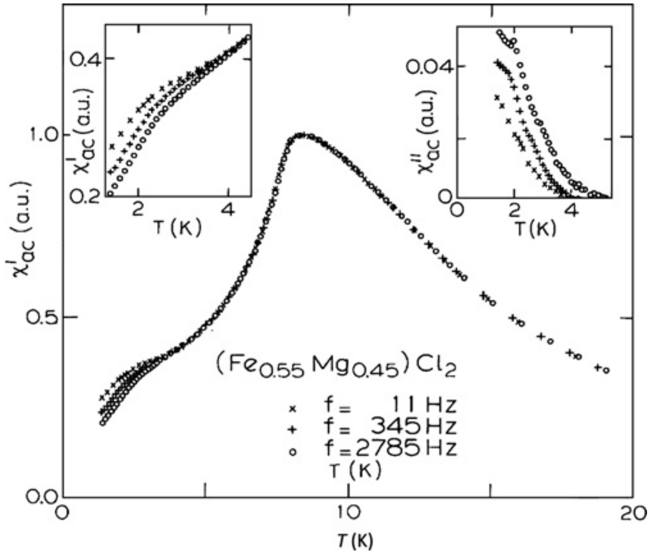

Figure 23.2 *Temperature dependence of the complex ac magnetic susceptibility ($\chi'_{ac} - i\chi''_{ac}$) of the dilute Ising antiferromagnet $Fe_{0.55}Mg_{0.45}Cl_2$ measured parallel to the easy axis at three different frequencies. Reprinted (Figure 2) from [18] with permission from Wong et al. Copyright (1985), American Physical Society*

While numerous experiments demonstrate that the macroscopic properties of RSG and usual SG phases are basically similar, the relations between their magnetic structures and microscopic mechanisms have been topics of intensive debates [19,20]. The phase diagram as depicted in Figure 23.1 was first derived theoretically in the classical work of Sherrington and Kirkpatrick [21], where a mean-field theory of the Ising spin glass with infinite range interactions was developed before experimental discovery of reentrant transitions. They found, in particular, that in a partially frustrated system where the FM interactions prevail over the AFM ones, both FM and SG orders can be observed in different temperature intervals. In this case the FM order parameter gradually grows as the temperature is lowered starting from T_C, then passes through the maximum, and eventually vanishes at T_{RSG}. Therefore, a true RSG phase was predicted to form. The magnetic structure of this phase was found to be similar to that existing in fully frustrated SG systems at $x > x_c$. However, subsequent more realistic theories, computer simulations, and structural investigations have shown that the structural arrangement of the RSG state is typically more complex than in the ordinary spin glass with balanced FM and AFM bonds, and the spin glass and the FM (or AFM) orders may coexist at $T < T_{RSG}$.

Figure 23.3 presents schematically some microscopic models that have been considered in the literature to describe the evolution of the structure of RSG system with temperature. Snapshots of spin configurations are shown in the paramagnetic phase at temperatures well above T_C (upper part of the figure), in the FM phase well below T_C (middle part), and in the RSG phase well below the glassy freezing temperature (bottom part). Red and black arrows represent the dynamic spins whose directions vary with time and the static spins whose motion is frozen due to partially frustrated interspin interactions, respectively. The first of these models (which is referred to as the transverse or xy freezing model) suggests that below T_C the motion of spins becomes partially correlated, that is all of them undergo precession around a single z direction. In other words, the spin possesses a static component along the z axis and a rotating component in the perpendicular xy plane. This magnetic structure has a macroscopic magnetic moment, but the spontaneous magnetization is smaller than that which would exist in the same material in the case of collinear ordering characteristic of the "normal" FM phase. In this picture the subsystem of dynamic spin components fluctuating in the xy plane can be considered as a two-dimensional spin glass, which freezes at the transition temperature T_{RSG} (for this reason the temperature T_{RSG} is often designated in the literature as T_{xy}). Below T_{RSG}, that is in the RSG phase, the spins are completely frozen, but the ideal FM collinearity is still absent: the macroscopic spontaneous magnetization in the RSG phase remains the same as in the high-temperature FM phase (more precisely, the magnetization slowly increases upon cooling through T_{RSG} without any anomalies). This behavior has been confirmed by Monte Carlo simulations performed on a three-dimensional Heisenberg model with moderately frustrated nearest-neighbor interactions [22]. It can be seen from the above consideration that the reentrant phase in the xy model is not truly reentrant, as the degree of disorder does not increase when the system enters this phase. The FM order parameter is preserved and, furthermore, the transverse glassy order parameter appears; thus the resulting state can be characterized by a mixed (ferro-glass) phase where FM and SG orders coexist.

An alternative model has been proposed to explain neutron scattering experiments [17, 23]. It is sketched in the right-hand part of Figure 23.3. The model is based on the fact that in many materials the critical concentration x_c is close to the percolation threshold

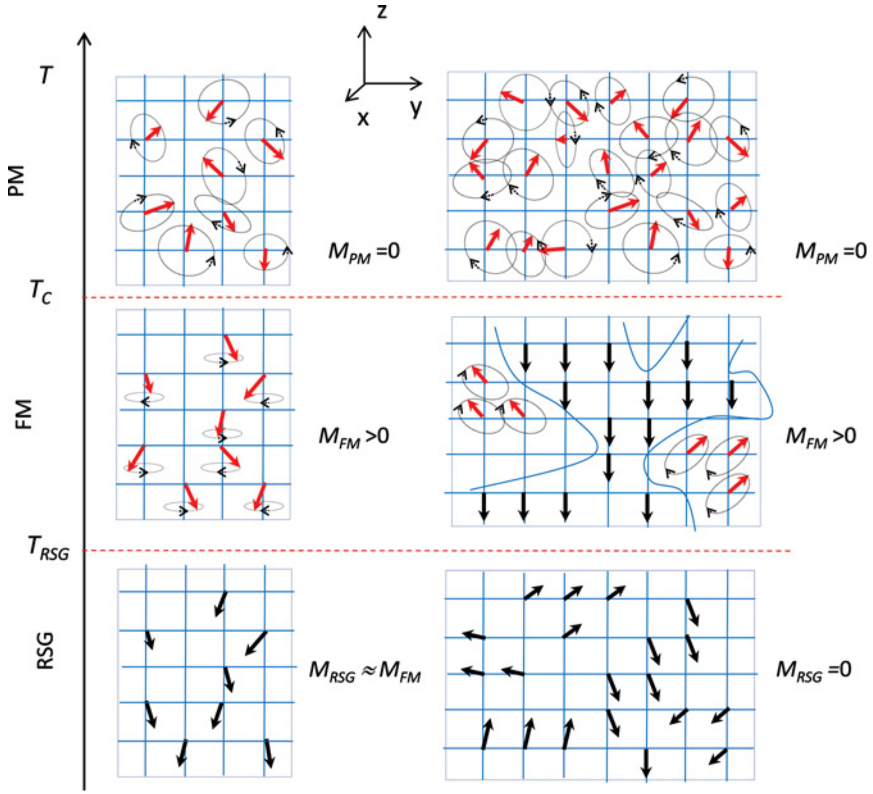

Figure 23.3 *Schematic diagram of the models explaining the RSG behavior: transverse (xy) freezing model (left-hand column) and random-field model (right-hand column). The dynamic and frozen spins are shown by red and black thick arrows, respectively. Infinite FM cluster in the FM phase of the random-field model is outlined. For a color version of this figure, see color plate section*

below which an infinite network of magnetic atoms coupled by the FM interactions cannot be obtained. The spin concentration in an RSG material is believed to be near, but above the percolation threshold. As the temperature decreases through T_C the system becomes decomposed into two intertwined networks: the first one is the static infinite FM cluster and the second one is a set of dynamic finite FM clusters and isolated spins. In entirely ferromagnetic dilute systems without frustrated interactions, the FM phase survives down to near-zero temperature (e.g. in $Mn_xZn_{1-x}F_2$; see Cowley et al. [24]). In the systems with a frustration resulting from, for example, competing FM/AFM first and second neighbor exchanges or the long-range Ruderman–Kittel–Kasuya–Yosida (RKKY) interactions, the spins outside the infinite FM cluster form a spin cluster glass environment. Further evolution of the system is determined by the interaction between these two networks and generally does not imply a true spin-glass transition at T_{RSG} in the sense of the Edwards–Anderson notation. The spins belonging to the SG network can interact with each other and with the infinite FM cluster via different types of interactions including the long-range (dipole and RKKY) and the short-range ones, and the interactions are supposed to be frustrated [17]. This implies a glassy slowing down of spin dynamics in the SG network when approaching T_{RSG} from above. When the relaxation time becomes large and spins are effectively frozen, the fields of long-range interactions act as static random fields on the infinite FM cluster. The static random fields conjugate to the order parameter, even if they are arbitrarily weak, are able to destroy the long-range order in the Heisenberg-type system [25]. According to the "random field" model for reentrant spin glasses [17, 23], this happens at T_{RSG}, and, as a result, the macroscopic FM moment of the infinite FM cluster vanishes. This behavior has been reproduced, in particular, in the Monte Carlo simulation of a dilute classical Heisenberg model with FM nearest neighbor and AFM next-nearest neighbor interactions [26]. It was found that in the RSG phase the infinite FM cluster is broken into FM clusters [26,27], which is an expected result of random local fields. Therefore, in contrast to the transverse freezing model, where the FE order does not change at T_{RSG} but coexists with the glassy order in the RSG phase, in the random field model the FE long-range order is absent at low temperatures; that is the RSG phase is a truly reentrant one.

The random field model has been ruled out in many materials based mainly on investigations combining Mössbauer spectroscopy and spontaneous magnetization measurements (see Ryan [19] for a review). It was argued [19] that as the magnetic properties of all FM-RSG systems are essentially identical, in all cases just the transverse degrees of freedom become frozen at T_{RSG}. However, the random field model is still in use and has found experimental support in a number of materials [27–29].

The *xy* model is not compatible with the Ising magnets as the transverse spin components are impossible there and only longitudinal ordering can be observed. Nevertheless, the coexistence of longitudinal spin-glass and long-range AFM orders has been found in the RSG phase of a dilute Ising antiferromagnet, $\text{Fe}_{0.55}\text{Mg}_{0.45}\text{Cl}_2$ (the susceptibility of this material is shown in Figure 23.2). It was suggested [18] that some spins are ordered within an infinite AFM cluster and some spins are isolated or assembled into isolated finite clusters. The spins not belonging to the infinite cluster become frozen like a spin glass at low temperature. Therefore, in contrast to the *xy* model where the coexisting FE and glassy subsystems are associated with the same atoms (they are just different components of the spins), the spin system in this model is decomposed in space into two phases: a long-range ordered AFM phase and a spin-glass phase.

A similar two-phase percolation model was recently applied to antiferromagnetic complex perovskite $\text{PbFe}_{0.5}\text{Nb}_{0.5}\text{O}_3$ [30] in spite of the fact that this is the Heisenberg-type material and the transverse spin ordering is allowed here. This material is especially interesting in the context of the present review, as it is a multiferroic showing an FE phase transition concomitant with a weak relaxor ferroelectric behavior at ~380 K, a transition from a paramagnetic to an AFM phase at $T_{\text{N}} \approx 150$ K and the RSG behavior below ~12 K. However, a subsequent investigation combining Mössbauer spectroscopy and neutron diffraction experiments [31] ruled out the magnetic phase separation but rather revealed a freezing of a transverse spin component similar to that considered in the *xy* model. An additional feature of this system, besides the AFM order in the intermediate magnetic phase instead of FM order, is that the magnetization of the AFM sublattice slightly decreases upon cooling through T_{RSG}, i.e. the spins experience an additional canting.

23.3 Relaxor Ferroelectrics

Relaxor ferroelectrics are often considered as an electric analog of magnetic spin glasses because they exhibit similar features, such as a quenched disorder in the structure, frustrated interactions, ultra-slow relaxation dynamics, phase transition to a glassy phase under conditions far from equilibrium, aging, rejuvenation and memory effects, etc. However, a striking contrast is that, while spin glasses are basically useless as materials for practical applications, a wide range of applications has been found for relaxors due to their peculiar physical properties (giant piezoelectric effect in the FE phase, large electrostriction and high electric permittivity in the ER phase, etc.). On the other hand, while the theoretical spin-glass models are rather well developed and the behavior is generally understood, comprehensive understanding of the relaxor behavior is still the subject of intensive ongoing investigations and seems to require conceptually more complex models.

The properties of relaxors, the peculiarities of their structure, and the theoretical approaches proposed to explain their behavior have been discussed in a number of recent reviews [32–38]. Therefore, in this section we will present only briefly some basic information that is helpful in understanding the core of this chapter. Emphasis will be placed on the dielectric properties, in particular the dielectric dispersion, which conveniently provides the basic criteria to qualify a material under investigation as a relaxor.

The necessary structural condition for the appearance of relaxor behavior is the quenched (i.e. static at all relevant temperatures) compositional disorder. For example, in the prototypical relaxor $Pb(Mg_{1/3}Nb_{2/3})O_3$ (PMN), the cations Mg^{2+} and Nb^{5+} are partially disordered in the B-sublattice of the perovskite ABO_3 structure. Relaxors belong to the family of ferroelectric materials as their behavior originates from the cooperative FE-type interactions that lead to the development of (local) spontaneous polarization in the ER and NR phases. However, due to the presence of quenched compositional disorder a homogeneous polarization cannot be developed. Instead, the structure comprises nanosize clusters of unit cells with collinear (or nearly collinear) dipole moments, which form the "islands" of spontaneous polarization (i.e. PNRs). The PNRs are surrounded by a non-polar medium where the dipole moment directions of unit cells remain random. Structural data suggest that in PMN the volume fraction of the PNRs steadily increases from 0% in the PE phase to ~30% in the NR phase [39], while their size grows from ~1.5 nm (i.e. about four unit cells) in the ER phase to ~6 nm in the NR phase [40]. The structural difference between relaxors and simple dipole glasses (such as doped alkali halide crystals KCl:OH or KCl:Li) is that in the latter no dipolar clusters are formed and all unit cell dipole moments are randomly directed.

To account for the dielectric properties of relaxors, the PNRs are usually considered as large "molecules". Their thermally activated reorientations provide the main contribution to the dielectric permittivity ($\varepsilon = \varepsilon' - i\varepsilon''$) in the temperature range of the characteristic relaxor $\varepsilon(T)$ peak. The examples of this peak are presented in Figure 23.4, which shows the behavior in PMN and in the PMN–PT solid solution (PT stands for ferroelectric $PbTiO_3$). In both crystals the transition from the paraelectric to the ER state is observed at practically the same temperature $T_B \approx 630$ K, but the low-temperature behaviors are different. In PMN–PT the transition to an FE phase can be clearly seen due to the sharp drop in the $\varepsilon(T)$ curve at the Curie point $T_C = 410$ K. In some other materials the drop can be not so sharp, signifying that the ER–FE transition is

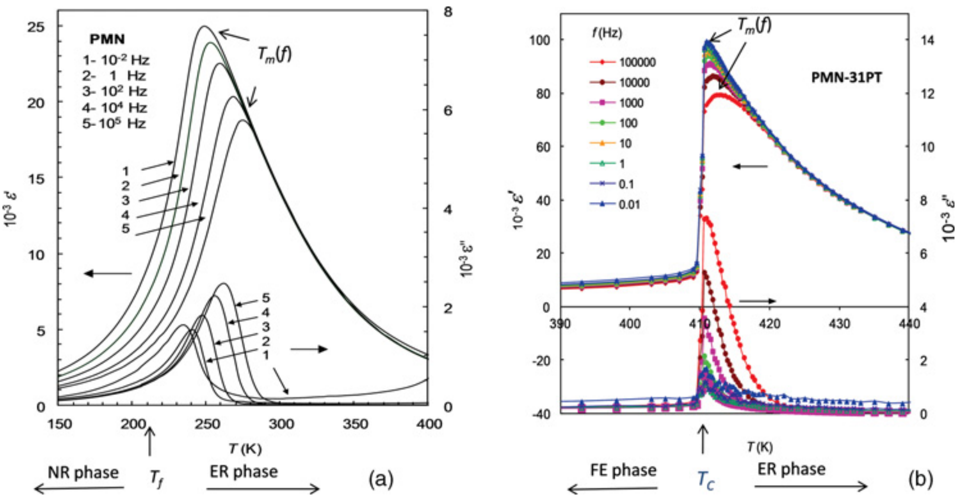

Figure 23.4 *Temperature dependences of the dielectric permittivity (a) in a canonical relaxor* $Pb(Mg_{1/3}Nb_{2/3})O_3$ *crystal and (b) in a crystal with relaxor-to-ferroelectric phase transition,* $0.69Pb(Mg_{1/3}Nb_{2/3})O_3$*–*$0.31PbTiO_3$*, measured at various frequencies. Reproduced from [34] with kind permission from Springer Science and Business Media*

diffuse [41]. In PMN no FE phase is developed. Instead, the phase transition to the glassy NR phase occurs at $T_f \approx 210$ K, which is not accompanied by any noticeable $\varepsilon(T)$ anomaly. In both cases, however, the temperature dependence of permittivity peaks at a frequency-dependent temperature T_m in the ER phase and a pronounced dielectric dispersion is observed around T_m. The dispersion range starts from the phonon frequencies and can spread (in canonical relaxors) down to the lowest measurement frequency available in a laboratory. This behavior contrasts with the behavior in normal ferroelectrics, where the intrinsic relaxation is observed at very high frequencies and disappears when the frequency decreases down to the MHz range.

Similar to a normal FE phase the low-temperature phase of relaxors is nonergodic, that is different configurations of elementary dipoles in the structure can have the same free energy. However, in the FE phase the non-ergodicity is much simpler. In an ideal FE crystal every elementary dipole (the dipole associated with a unit cell) can be in one of a few degenerate states prescribed by the crystal symmetry. For example, in the rhombohedral FE phase (the ground state of classical ferroelectric $BaTiO_3$) there are eight dipole configurations with the same free energy: in each configuration all the elementary dipoles are oriented along the same <111> crystallographic direction of the paraelectric cubic structure. This behavior is the consequence of FE-type interactions between elementary dipoles. In relaxors the FE interactions are local and promote correlations within PNRs only. In the temperature range of the ER–NR transition the PNRs themselves play the role of elementary dipoles. The interactions between them are believed to be frustrated (i.e. both the FE- and AFE-type couplings are present) and lead to the phase transition (cooperative freezing of thermally activated reorientations of PNR dipole moments and appearance of the Edwards–Anderson-type order parameter) at T_f.

While the concept of PNRs is consistent with many experimental results and theoretical considerations, some researchers have questioned about their existence in lead-containing perovskite relaxors [42–44]. Their arguments are based, in particular, on the results of synchrotron diffuse scattering and molecular dynamic simulations. On the other hand, first-principle-based Monte Carlo simulations in lead-free perovskite relaxors clearly point to the presence of PNRs [45]. Recent X-ray fluorescence holography experiments performed in the ER phase of PMN [46] reveal that PNRs indeed exist in lead-containing relaxors, but the traditional picture of the dipole arrangement was oversimplified. In fact, not all elementary dipoles inside PNR appear to be correlated.

Like in normal ferro- and antiferroelectrics, the static dielectric permittivity, $\varepsilon_s \equiv \varepsilon(f = 0)$ in the paraelectric phase of relaxors (i.e. at $T > T_B$) follows the Curie–Weiss law:

$$\varepsilon_s(T) = \frac{C}{T - T_{CW}} + \varepsilon_0 \tag{23.1}$$

where C and ε_0 are constants having the same meaning and the same order of magnitude as in normal ferroelectrics, while T_{CW} is significantly larger than T_m and coincides (at least approximately) with another characteristic temperature T^* (see Dkhil et al. [47] for a discussion concerning this recently discovered characteristic temperature). In the ER phase the temperature dependence of static permittivity typically has the shape of the Lorentz function [48]:

$$\frac{1}{\varepsilon_s(T)} = \frac{1}{\varepsilon_A} + \frac{(T - T_A)^2}{2\varepsilon_A \delta^2}$$

where ε_A is the value of ε_s at the maximum temperature $T_A \leq T_m(f)$ and δ (called sometimes the diffuseness parameter) is the half-width of the Lorentz ε_s (T) peak at two-thirds of the maximum. For a particular material this equation can be verified directly by fitting the data at $T > T_m$, where the dispersion is negligible and, therefore, the static permittivity is measured. Around T_A the dispersion is typically observed down to the lowest measurement frequencies and ε_s cannot be measured directly. It can, however, be derived by appropriate extrapolation of the isothermal relaxation spectra (see, for example, Bokov and Ye [49]).

The relaxation spectrum of relaxors typically comprises several contributions related to different microscopic mechanisms. In canonical relaxors the main dielectric contribution (appearing in the ER phase and dominating in the temperature range around T_m) is typically characterized by the broadening of the relaxation spectrum on cooling and the characteristic relaxation time (τ), which increases faster than the classical Arrhenius law prescribes. In the whole temperature interval where τ can be measured, it follows the Vogel–Fulcher (VF) law, which is well known in the physics of glassy systems:

$$f_r(T) = f_0 \exp\left(-\frac{E_a}{T - T_f}\right) \tag{23.2}$$

where $f_r = 1/(2\pi\tau)$ is the characteristic relaxation frequency, f_0 and E_a are the attempt frequency and activation energy of the relaxation process, respectively, and T_f is the freezing temperature at which τ tends to be infinite. Below this temperature the corresponding relaxation dynamics is supposed to be essentially frozen, which means that at $T < T_f$ the system is non-ergodic, that is T_f delimits the NR and ER phases. Similar to the orientational polarization in ordinary dielectrics the attempt frequency in relaxors typically corresponds to the frequency of optic phonons ($\sim 10^{12} - 10^{13}$ Hz). However, in many relaxors the VF relation (23.2) does not hold and in some others a freezing temperature $T_f = 0$ K is found, which suggests that the canonical NR phase is not achieved.

A different relation has been found virtually in all relaxors within a particular frequency interval. It looks very similar to Equation (23.2) and is also referred to in the literature as the VF law:

$$f = f_m \exp\left(-\frac{E_m}{T_m(f) - T_{VF}}\right) \tag{23.3}$$

where f is the measurement frequency, T_m is the (frequency-dependent) temperature of the $\varepsilon'(T)$ or $\varepsilon''(T)$ maximum, while f_m, E_m, and T_{VF} are the empirical parameters that generally have no physical meaning. In the literature they are often erroneously associated with the attempt frequency, activation energy, and freezing temperature, respectively. Such a misunderstanding arises from the assumption that the positions of the permittivity maxima correspond to the condition $2\pi f\tau(T = T_m) = 1$ and, therefore, the $\tau(T)$ behavior and the relaxation parameters can be derived from the $T_m(f)$ curves. It is, however, known that this condition is often not satisfied in real materials (see p. 103 in Jonscher [50]). In relaxors it can be violated for two reasons. Firstly, several relaxation mechanisms with different parameters often contribute to the $\varepsilon(T)$ maximum and influence T_m. Secondly, the value of T_m at a particular f is determined not only by the relaxation time but also by the behavior of static permittivity, which is strongly temperature dependent in relaxors: it typically has the diffuse Lorentz-shaped maximum at $T_A < T_m$ (see above). As shown theoretically by Tagantsev [51], due to the maximum, Equation (23.3) can be satisfied in some frequency range even when Equation (23.2) does not hold. This can happen under the condition that the relaxation spectrum broadens gradually upon cooling (as often happens in relaxors). Recent numerical simulations showed [49] that the latter condition is not necessary and the relation (23.3) with $T_{VF} > 0$ can be observed even when the relaxation time follows the Arrhenius law and the shape of the spectrum does not change with temperature.

The values of f_m reported for different relaxor materials fall into a wide frequency range of $10^6 - 10^{16}$ Hz or so, and can be very different for the same material when derived from the $\varepsilon'(T)$ and $\varepsilon''(T)$ curves or at different frequency intervals. In canonical relaxors where the freezing of the dielectric spectrum does occur and the relaxation frequency follows the VF law (23.2), the relations $f_{mRe} \approx f_{mIm} \approx f_0$, $E_{mRe} \approx E_{mIm} \approx E_a$, and $T_{VFRe} \approx T_{VFIm} \approx T_f$ are usually satisfied (the subscripts Re and Im denote the parameters derived from the $\varepsilon'(T)$ and $\varepsilon''(T)$ dependences, respectively).

Equation (23.3) can be easily verified in experiment as the temperatures $T_m(f)$ are clearly seen in the $\varepsilon(T)$ curves. On the contrary, verification of Equation (23.2) is often a complicated task. In particular, it requires the analysis of the dielectric spectra (isothermal frequency dependences of permittivity) typically consisting of several overlapping contributions, which should be properly separated.

A large enough external electric field applied to a canonical relaxor at $T < T_f$ can induce irreversibly the FE phase with $T_C = T_f$. The question whether this phase is stable or metastable is under discussion in the current literature, but it can only be destroyed by heating the sample to $T > T_C$. This feature distinguishes relaxors from dipolar glass or spin glass where the field-induced collinear order is unstable. The macroscopic properties of the FE phase in relaxors (canonical and non-canonical) are quite similar to the properties

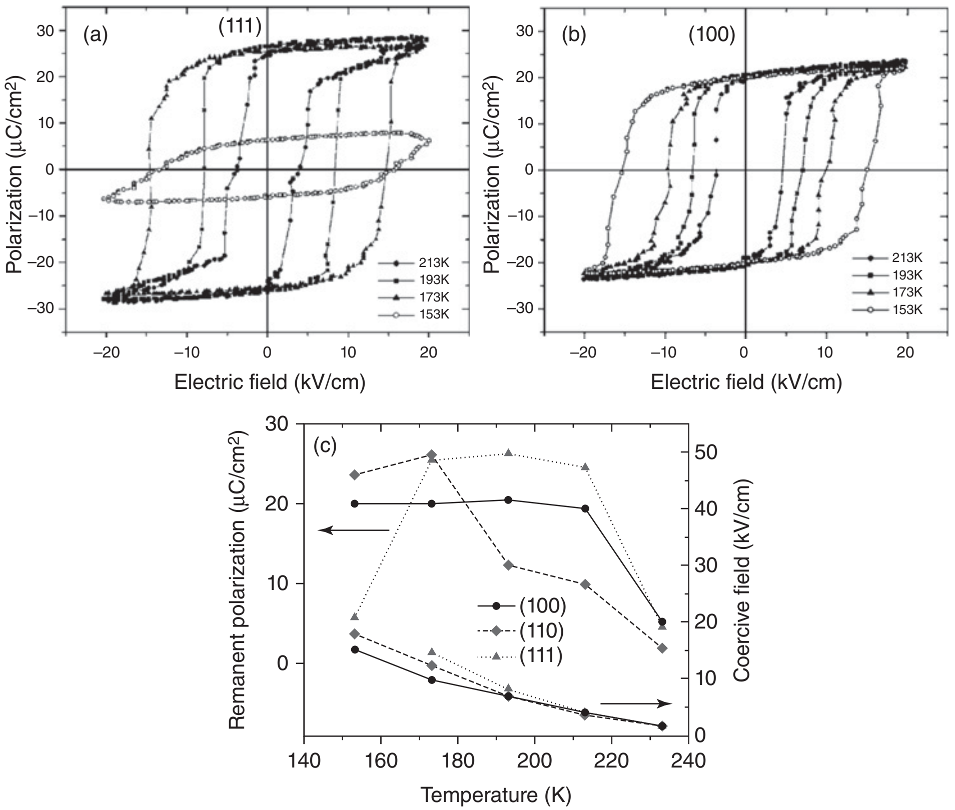

Figure 23.5 *Ferroelectric hysteresis loops displayed in the NR phase of Pb(Mg*$_{1/3}$*Nb*$_{2/3}$*)O*$_3$ *crystal in different crystallographic directions: (a) along [111] and (b) along [100], and (c) the temperature dependences of the remanent polarization and coercive field obtained from these loops. Reprinted (Figures 5(a) and (c) and 6) from [52] with permission from Zhao et al. Copyright (2007) by the American Physical Society*

of the FE phase in normal ferroelectrics. In particular, piezo- and pyroelectric effects are observed. Due to the possibility to induce the FE phase, typical rectangular-shaped ferroelectric $P(E)$ hysteresis loops are observed in the NR phase (in contrast to the opinion expressed in some papers that the hysteresis loops in relaxors are slim). The examples are presented in Figure 23.5 showing the loops in the NR phase of the PMN crystal. Note that in Figure 23.5(c) the temperature dependence of the *measured* remanent polarization (P_r) in the [111] direction reveals a maximum and P_r almost disappears at low temperatures. This looks like a reentrant behavior, but it is not the case. In fact, the low-temperature drop of P_r is a result of the increase in the coercive field to the level above the measurement field rather than a real anomaly in the T dependence of the spontaneous polarization. This is clear, in particular, from the $P_r(T)$ dependence measured in the [100] direction in which the coercive field is smaller, the loops are saturated, and the measured P_r (T) reflects the true behavior of the spontaneous polarization. The latter is practically temperature-independent at low temperatures. Note that the similar problem was discussed (see Section 2.2 in Ryan [19]) in the field of magnetic materials where the maximum in the temperature dependence of zero-field-cooled magnetization was erroneously interpreted by some researchers as the sign of a reentrant transition; it is in fact the result of anisotropy, which exceeds the measuring field.

When discussing the reentrant behavior in relaxors, a number of essentially different situations need to be considered. The first one is the paraelectric–ferroelectric–relaxor sequence of phases upon cooling. In this case the characteristic relaxor-type dielectric dispersion appears at temperatures below a rather sharp dielectric peak associated with the FE Curie point. Alternatively, the notion of reentrant glass (not reentrant relaxor) behavior is applied to describe a more subtle situation where some properties of relaxors (in particular, aging and Barkhausen noise) are apparently similar to the properties of reentrant *xy* spin glasses. This type of behavior can be found even in canonical relaxors, such as PMN, that is in materials where the FE phase is not observed at all under zero-field cooling conditions. Finally, a transformation to the reentrant dipolar glass state has been reported in doped quantum paraelectrics in which relaxor and/or FE transformations have also been observed at higher temperatures. All these scenarios are reviewed separately in the following sections.

23.4 Reentrant Relaxor Behavior in Ferroelectrics

As discussed in the previous section, the typical sequences of phases in relaxor materials are PE–ER–NR or PE–ER–FE. In the former case, a smooth and dispersive diffuse maximum is observed in the temperature dependence of dielectric permittivity at $T_m(f)$. In the latter case a more or less distinct anomaly appears additionally below T_m. The temperature of this anomaly is practically independent of frequency and corresponds to a sharp or diffuse transition to an FE phase. However, some exceptions are known when the temperature $T_m(f)$ of the relaxor-like $\varepsilon(T)$ anomaly is lower than T_C. Recently, this kind of behavior has attracted a great deal of attention. Questions have been raised and discussed as to whether the state below T_m can be considered as a distinct reentrant relaxor phase and what the possible microscopic mechanisms of the phenomenon are.

When considering the origin of reentrant-type relaxor dispersion, the first point to check is the macroscopic homogeneity of the sample. FE crystals and ceramics are often complex compounds or solid solutions, in which inhomogeneities related to composition segregation or regions of different compositional disorder can be expected. In these cases the anomalies of properties at T_m and T_C might be associated with the chemically different mesoscopic or macroscopic regions of the material.

Another possibility is that some extrinsic dielectric contributions can be responsible for relaxor-like dielectric anomalies in the FE phase. Inhomogeneities due to ceramic grain boundaries or material/electrode interfaces often lead to the Maxwell–Wagner-type dielectric response with a very large (up to $\sim 10^5$) dielectric susceptibility and with dielectric dispersion in the frequency range routinely used for dielectric measurements. Significant extrinsic dielectric response may also come from the relaxation of FE domain walls. A noticeable example is given in Figure 23.6, which shows the temperature dependence of the dielectric permittivity in the low-temperature phases of a crystal of the classical ferroelectric $BaTiO_3$. The sharp maxima observed at 180 K and 270 K are caused by rhombohedral–orthorhombic and orthorhombic–tetragonal phase transitions, respectively (the Curie point is located at 440 K outside the range shown in the figure). There are no phase transitions

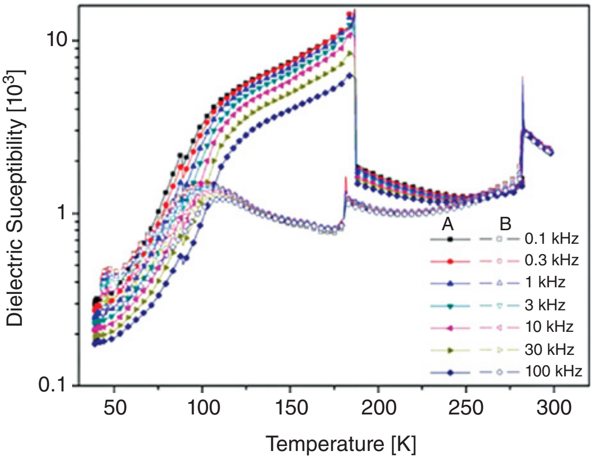

Figure 23.6 *Temperature dependence of small-signal dielectric permittivity of two <111>$_{cub}$ oriented BaTiO$_3$ single crystals. Before measurements sample A was electrically depoled at room temperature with a fast-decayed (from 1 kV/cm to zero within five periods) low-frequency AC field and sample B was annealed at 450 °C for 10 h. Reprinted from [53] with permission from Wang et al. Copyright [2011], AIP Publishing LLC*

below 180 K in this crystal, but a pronounced dielectric anomaly is observed at around 100 K, whose shape and magnitude resemble the behavior of relaxors. In particular, in the crystal annealed at $T > T_C$ (open symbols in Figure 23.6) one can see the diffuse $\varepsilon(T)$ peak with dispersion on the low-temperature slope and the frequency-dependent T_m, similar to the peak typically observed at temperatures above the ER–NR transformation. However, one can hardly expect a relaxor phase in BaTiO$_3$ because the compositional disorder that is a necessary condition for relaxor behavior to occur is absent. Accordingly, the structure of the low-temperature state and the mechanism of the dispersion are completely different from those observed in canonical relaxors. It was shown [53] that the relaxation in the rhombohedral phase of BaTiO$_3$ is related to the motion of the walls of macroscopic FE domains rather than to the dynamics of PNRs. The intrinsic (single-domain) permittivity is comparatively small (~100) and decreases monotonically on cooling in the rhombohedral phase [54]. Accordingly, the dielectric behavior is highly dependent on the domain structure: samples A and B in Figure 23.6 were shown (by means of transmission electron microscopy) to possess very different domain wall densities and configurations.

Below we will discuss examples of reentrant relaxor behavior in such materials where compositional disorder exists and, therefore, relaxor phases can be expected.

23.4.1 Properties of Materials with Paraelectric–Ferroelectric–Relaxor Sequence of States

23.4.1.1 Ferroelectrics with Perovskite Structure

The term "reentrant relaxor" was first applied to a novel perovskite solid solution $(1-x)$BaTiO$_3$–xAgNbO$_3$ (BT–AN) whose end members are the classical ferroelectric BT and

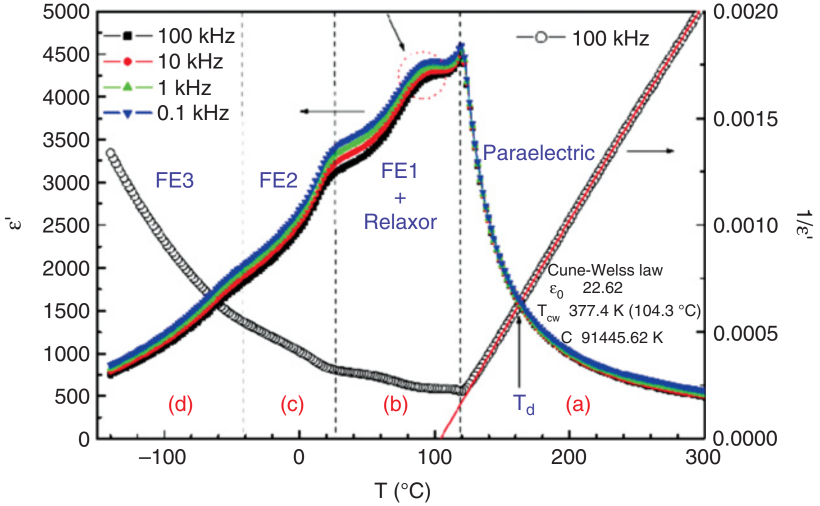

Figure 23.7 Temperature dependences of the dielectric permittivity at different frequencies and the reciprocal of the dielectric permittivity at 100 kHz of the 0.99$BaTiO_3$–0.01$AgNbO_3$ ceramics. Solid line is the fit to the Curie–Weiss law, Equation (23.1). From [55]. © IOP Publishing. Reproduced by permission of IOP Publishing. All rights reserved

the antiferroelectric (at low temperatures) AN [55]. Ceramic samples with $x \leq 0.1$ were prepared and studied [55, 56]. The room-temperature unit cell volume determined using X-ray powder diffraction increased linearly with increasing x while the tetragonality decreased, that confirmed the formation of the solid solution. In all compositions the paraelectric—ferroelectric phase transition was observed almost at the same temperature $T_C \approx 120$ °C as in the pure BT. In Figure 23.7, which shows the temperature dependence of the dielectric permittivity of the 0.99BT–0.01AN ceramics, this transition is clearly seen as a sharp peak. As expected for a normal phase transition, the position of the peak is frequency independent. The anomaly at 25 °C corresponds to the transition from the high-temperature FE phase of tetragonal symmetry (FE1) to the FE orthorhombic (FE2) phase. At –40 °C the FE2 phase transforms into the rhombohedral FE3 phase (the same phase sequence is known to occur in pure BT). However, an additional distinct dielectric anomaly is seen at about 100 °C whose temperature depends on frequency and, therefore, it can hardly be associated with a normal phase transition. With increasing x this anomaly shifts to lower temperatures and becomes much more pronounced, transforming into a diffuse maximum, while the peak at T_C decreases in magnitude, and in the compositions with $x > 0.02$, it is visible only as a comparatively small kink at the high-temperature side of the main diffuse $\varepsilon(T)$ peak [56].

The transition at T_C demonstrates the features characteristic of the normal FE Curie point [55]: in particular, the permittivity at $T > T_C$ follows the CW law with $T_{CW} < T_C$ (see Figure 23.7), the differential scanning calorimetry (DSC) reveals a thermal anomaly at T_C, and the spontaneous polarization (derived from FE hysteresis loops) appears below T_C. On the other hand, in the temperature range of the additional dielectric anomaly at 100 °C no anomalies are observed in the DSC curves or in the temperature dependences of remanent polarization (the behavior characteristic of relaxors). Furthermore, in the frequency range of 400 Hz–1 MHz the temperature of the anomaly follows the VF law for T_m, Equation (23.3), which is a hallmark of relaxor behavior. The best-fit parameters are $f_{mRe} = 9 \times 10^9$ Hz, $E_{mRe}/k = 0.0096$ eV, and $T_{VFRe} = 365$ K. However, it remains unclear whether freezing of the dielectric spectrum actually takes place. The verification of the VF law for the relaxation time, Equation (23.2), appears to be practically impossible due to the complexity of the relaxation spectrum (with the relaxation mechanisms overlapping in frequency). The observed value of f_m is seemingly too low to be considered as the attempt frequency of a relaxor-type dispersion. Besides, in the BT–AN ceramics with $x = 0.1$ [56] the parameters of Equation (23.3) determined from the $\varepsilon'(T)$ and $\varepsilon''(T)$ peaks differ significantly ($f_{mRe} = 9 \times 10^{14}$ Hz, $f_{mIm} = 7 \times 10^{10}$ Hz, $E_{mRe}/k = 0.084$ eV, $E_{mIm}/k = 0.064$ eV, $T_{VFRe} = 154$ K, and $T_{VFIm} \approx 98$ K), which is not typical of canonical relaxors.

The reentrant-like behavior of BT–AN was attributed [56] to the compositional segregation: mesoscopic regions with $x = 0$ were supposed to be responsible for the sharp maximum at ≈120 °C, while the diffuse anomaly at ≈100 °C was due to Ag-rich regions. This interpretation was supported by X-ray diffraction experiments: a mixture of the tetragonal phase and the cubic phase having smaller unit cell volume was observed between ~100 °C and T_C in 0.99BT–0.01AN, while pure tetragonal and cubic phases were found below and above this temperature interval, respectively. It was further proposed that the inhomogeneity has the form of a core–shell microstructure where the compositions of core and shell regions of a ceramic grain are different. Therefore, the state observed below the relaxor-like dielectric anomaly is an FE rather than a glassy state. This is also confirmed by the observation of macroscopic (~1 μm in size) FE domains imaged with the piezoresponse force microscopy (PFM) at room temperature. The relaxor-like dielectric dispersion has been tentatively attributed to the domain wall relaxation and to the relaxation of the boundaries between mesoscopic paraelectric Ag-free regions and the FE phase, which is developed during the diffuse FE transition at $T < T_C$ in the regions with $x > 0$ [56]. We further suggest that the characteristic of relaxor VF law for T_m, Equation (23.3), is due to the maximum in the temperature dependence of static permittivity, which is expected to be developed at the diffuse FE transition. As discussed in Section 23.3, any dispersion may satisfy Equation (23.3) in a certain frequency interval if this maximum exists.

Another BT-based solid solution that shows a reentrant-type dielectric behavior is the $(1 - x)BaTiO_3–xBiScO_3$ [$(1 - x)$BT–xBS] ceramics. Similar to BT–AN considered above, in $(1 - x)$BT–xBS with a comparatively small x, the first, frequency-independent, anomaly is observed in the $\varepsilon'(T)$ dependences at $T \approx 140$ °C, approximately equal to T_C in pure BT (see Figure 23.8), and the second anomaly, observed at a lower temperature, T_m, is not related to a structural phase transition as confirmed by the DSC data [57,58]. The relaxor-type nature of the second anomaly is suggested by the fact that T_m follows the VF relation, Equation (23.3), which was verified for both the $\varepsilon'(T)$ and $\varepsilon''(T)$ dependences. In the temperature range between T_m and T_C the material shows the typical FE characteristics, including $P(E)$ hysteresis loops, macroscopic FE domains observed with PFM and the tetragonal distortion of the perovskite unit cell (according to the X-ray diffraction data). However, with increasing x the distortion gradually decreases and in the samples with $x = 0.1$ the tetragonality almost vanishes (at room temperature) [58]. Our analysis (the details of which will be published elsewhere) of the dielectric data obtained previously [58] shows

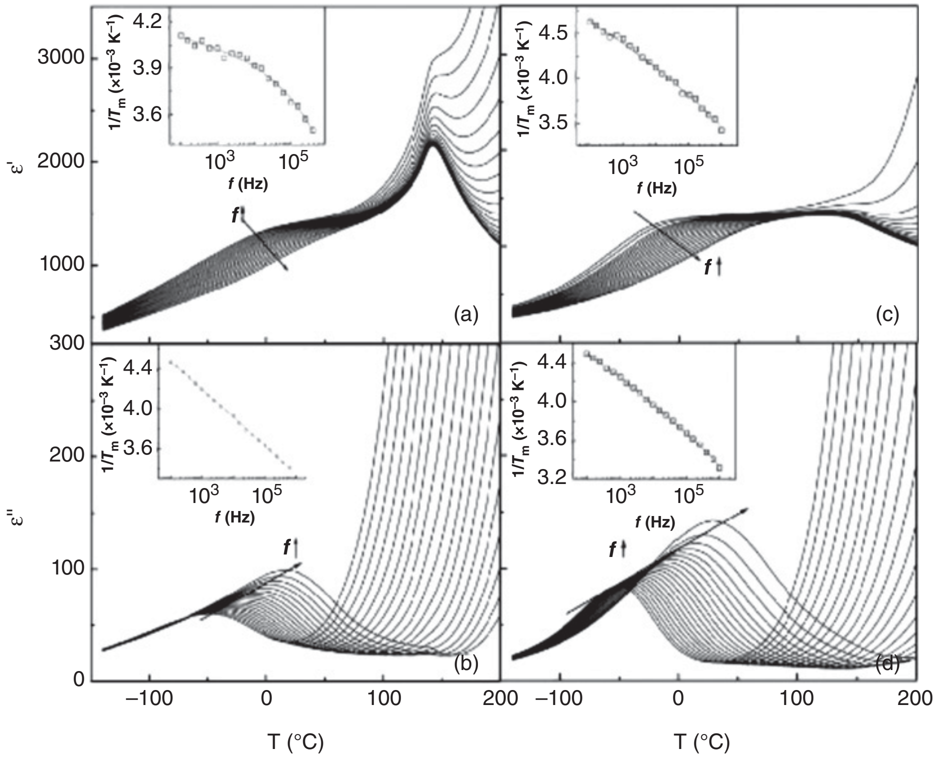

Figure 23.8 *Temperature dependences of the real (a, c) and imaginary (b, d) parts of the dielectric permittivity measured at different frequencies between 10^2 and 10^6 Hz in the (1 – x)$BaTiO_3$–x$BiScO_3$ ceramics with x = 0.05 (a, b) and x = 0.1 (c, d). Arrows indicate the direction of the frequency increase. Insets show the fitting to Equation (23.3). Reprinted from [57] with permission from Guo et al. Copyright [2008], AIP Publishing LLC*

that in the temperature range of the relaxor-type dispersion the $\varepsilon(f)$ dependences obey the Kohlrausch–Williams–Watts relaxation pattern similar to the canonical relaxor PMN. Furthermore, the characteristic relaxation time follows the VF law, Equation (23.2), with the parameters $T_f \approx 110$ K for $x = 0.1$ and $T_f \approx 160$ K for $x = 0.05$. The attempt frequency f_0 is in the phonon frequency range and the activation energy $E_a \sim (1-2) \times 10^3$ K is close to that in PMN. Therefore, these new results suggest the existence of a reentrant relaxor-type non-ergodic state at $T < T_f$. To the best of our knowledge, $(1-x)$BT–xBS is the first and so far the only known material in which the reentrant relaxor dispersion is associated with a true freezing of the relaxation spectrum. However, we do not have enough information to determine what happens with the FE spontaneous polarization and what the microscopic mechanism of the relaxor relaxation is.

In the $(1-x)$BT–xBS solid solutions with comparatively large x, only a single $\varepsilon'(T)$ maximum remains, which looks like those observed in canonical relaxors. Another canonical relaxor feature, that is the cubic macroscopic symmetry, has been revealed there by X-ray and neutron diffraction studies [59]. The glassy aging, rejuvenation, and memory effects similar to those observed in PMN (see Section 23.5) were also found in the ceramics with $x = 0.3$ by Bharadwaja et al. [60]. However, these authors claimed significant differences between some other properties of these ceramics and the properties of canonical relaxors such as PMN. In particular, a considerable drop of remanent polarization determined from the polarization-field hysteresis loops (P_r) was found upon cooling at temperatures significantly lower than T_{VF}, which, as the authors believed, is not characteristic of PMN. Based on this difference a special "reentrant dipole glass" state was suggested to appear in $(1 - x)$BT–xBS at low temperatures. We argue that a similar low-temperature drop of P_r has indeed been observed in PMN (see Figure 23.5(c)) and explained by the increase of the coercive field above the measurement field rather than by the real drop in the spontaneous polarization. Furthermore, we have found (the details will be published elsewhere) that the VF relations (23.2) and (23.3) are fulfilled in $(1 - x)$BT–xBS with $x = 0.3$ with a freezing temperature $T_f = 151$ K and an activation energy $E_a = 0.15$ eV, which is not very different from $E_a = 0.07$ eV observed in PMN. Therefore, it seems that the $(1 - x)$BT–xBS solid solutions with large x are canonical relaxors with the transition from the ergodic to non-ergodic relaxor phase at T_f similar to PMN. Further investigations are needed to examine the low-temperature behavior of remanent polarization, in particular the measurement of a possible pyroelectric current.

The relaxor phase that appears in the temperature range below the FE phase was also reported in $Ba_{0.9}Bi_{0.067}(Ti_{1-x}Zr_x)O_3$ perovskite ceramics with $x < 0.075$ [61]. However, the conclusion about the existence of the transition to the relaxor phase was only supported by the dielectric dispersion observed at $T \ll T_C$ and the FV relation which could confirm the relaxor nature of the dispersion has not been verified.

23.4.1.2 Ferroelectrics with Tungsten Bronze Structure

Besides the perovskite compounds that represent the most widely studied family of ferroelectric materials, ferroelectricity as well as relaxor behavior is also observed in materials with a tungsten bronze structure. However, in contrast to perovskites whose paraelectric phase is cubic, the paraelectric phase of the tungsten bronze compounds generally possesses a centrosymmetric tetragonal *4/mmm* symmetry. They are typically uniaxial ferroelectrics with the tetragonal *4mm* or orthorhombic FE phase. Besides the permittivity maximum observed at the ferroelectric T_C, another $\varepsilon(T)$ peak has been found in many tungsten bronze ferroelectrics at much lower temperatures. This peak was accompanied by the dielectric dispersion which led to the frequency shift of T_m in a similar way as in relaxors. However, for a long time this behavior had not been identified as a reentrant relaxor. Only recently was this identification applied to several tungsten bronze materials including $Ba_2Pr_xNd_{1-x}FeNb_4O_{15}$ [62,63] and $Sr_2NaNb_5O_{15}$ [64].

$Ba_2Pr_xNd_{1-x}FeNb_4O_{15}$ is a solid solution composed of $Ba_2PrFeNb_4O_{15}$, which is a relaxor with $T_m \sim 170$ K (see Figure 23.9), and $Ba_2NdFeNb_4O_{15}$, which is a ferroelectric with $T_C = 323$ K. In the $Ba_2Pr_xNd_{1-x}FeNb_4O_{15}$ ceramics with $0.2 \leq x \leq 0.8$ the reentrant-type coexistence of FE phase transition and relaxor $\varepsilon(T)$ maximum was found [62]. In the T–x phase diagram of the solid solution (Figure 23.10) both T_C and T_m are nearly independent of the composition and the dielectric anomaly related to the FE phase transition and the low-temperature relaxor peak simply disappear at x close to unity and zero, respectively. The X-ray microprobe analysis of the samples showed that uncontrolled phase segregation

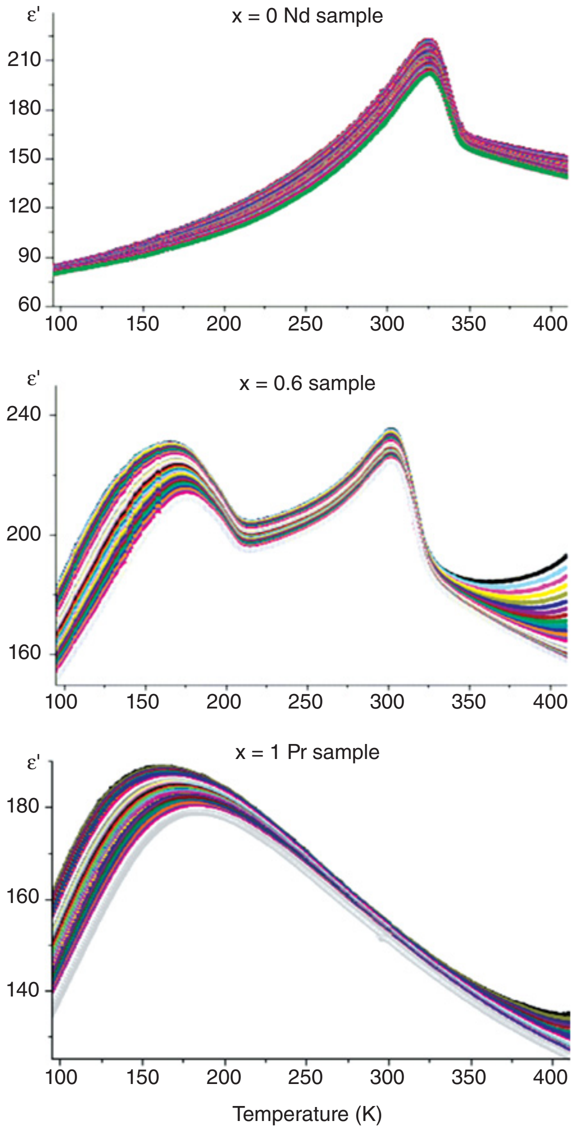

Figure 23.9 *Temperature dependences of the dielectric permittivity of the* $Ba_2Pr_xNd_{1-x}FeNb_4O_{15}$ *ceramics with x = 0, 0.6, and 1, measured on heating at different frequencies from 100 Hz (top curves) to 1 MHz (bottom curves). Reprinted from [62] with permission from Castel et al. © [2009] IOP Publishing. All rights reserved*

that could lead to this behavior is absent. The FE character of the intermediate phase was confirmed by the display of $P(E)$ hysteresis loops and the ultrasonically detected piezoelectric signal, while the observed VF law for T_m, Equation (23.3), confirmed the relaxor character of the low-temperature permittivity maximum [62, 65]. However, the freezing of dielectric spectrum (i.e. the validity of Equation (23.2)) has not been verified.

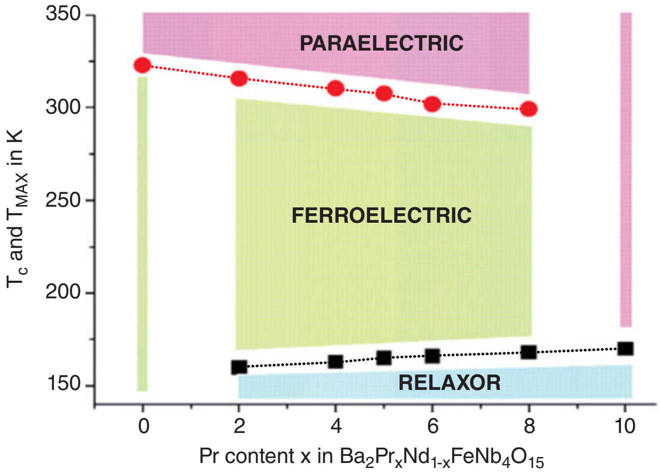

Figure 23.10 *Qualitative phase diagram of* $Ba_2Pr_xNd_{1-x}FeNb_4O_{15}$ *solid solution.* T_C *and* T_m *are shown by circles and squares, respectively. Reproduced from [62] by permission from rom Castel et al. © [2009] IOP Publishing. All rights reserved*

Recent measurements of the $\varepsilon'(T)$ dependences in $Ba_2Pr_xNd_{1-x}FeNb_4O_{15}$ with $0.2 \leq x \leq 0.8$ revealed no reentrant behavior upon cooling from the paraelectric phase: a single diffuse maximum was observed, which is located between the temperatures corresponding to the heating maxima [65]. This was explained by a large temperature hysteresis of T_C on cooling, which resulted in the overlap of the $\varepsilon'(T)$ peak corresponding to T_C with the low-temperature relaxor peak.

Another tungsten bronze compound where the reentrant relaxor behavior was studied in detail is $Sr_2NaNb_5O_{15}$ [64]. The shape of the temperature dependence of permittivity of this ceramic (see Figure 23.11(a)) is very similar to that observed in the above-considered $Ba_2Pr_xNd_{1-x}FeNb_4O_{15}$. The maximum at the frequency-independent temperature of 518 K corresponds to the Curie point. The dielectric permittivity above T_C obeys the CW law with the parameters of $C \sim 1 \times 10^5$ K and $T_{CW} < T_C$, characteristic of a normal PE–FE phase transition [66]. The low-temperature relaxor-like maximum at $T_m \approx 240$ K shifts with frequency according to the VF law, Equation (23.3), typical of relaxor behavior, with the parameters of $T_{VF} = 189$ K, $E_m = 1.9 \times 10^3$ K, and $f_m = 3.7 \times 10^{17}$ Hz. Interestingly, at temperatures close to T_m the anomalies of other properties were observed, suggesting that some structural changes probably occur there. In particular, the remanent and saturation polarizations determined from the well-saturated $P(E)$ hysteresis loops revealed the maximum (Figure 23.11(b)). The anomalies in elastic properties were also found: a minimum of the Young's modulus and a maximum of the mechanical loss tangent. However, the X-ray and neutron diffraction as well as the transmission electron microscopy did not reveal any structural phase transitions: the structure remained orthorhombic (space group *Im2a*) with the fully disordered arrangement of Sr and Na atoms in the whole temperature range between 100 K (the lowest examined temperature) and T_C. At the same time, the Invar effect characteristic of canonical relaxors was observed; that is as the temperature is lowered, the unit cell volume becomes temperature-independent at $T < T_m$. However, in

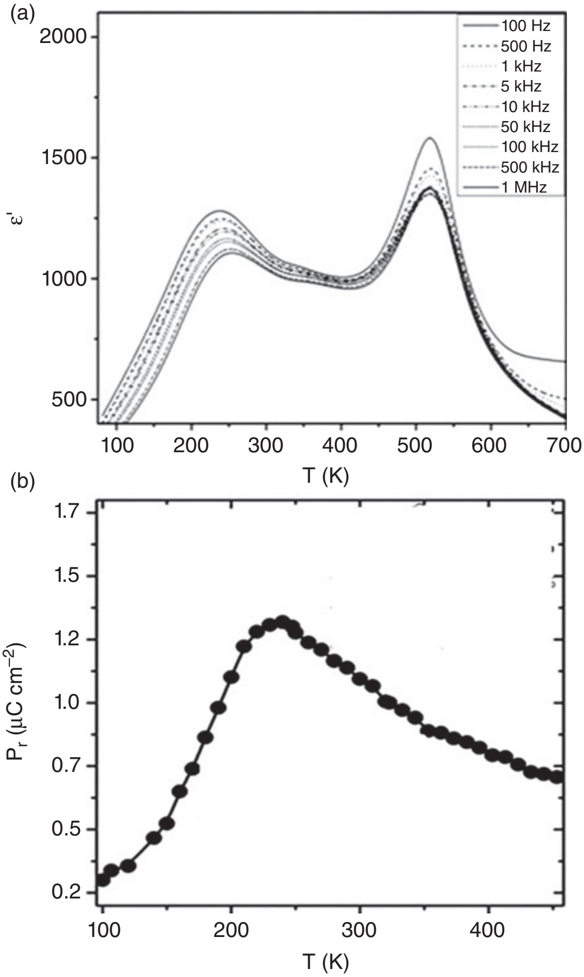

Figure 23.11 *Reentrant relaxor behavior in the $Sr_2NaNb_5O_{15}$ ceramics. Temperature dependences of (a) dielectric permittivity at different frequencies from 100 Hz to 1 MHz and (b) remanent polarization obtained from the P(E) hysteresis loops. Reprinted from [64] with permission from Torres-Pardo et al. Copyright (2011) American Chemical Society*

contrast to canonical perovskite relaxors where the structure is cubic and, therefore, a constant volume is necessarily associated with constant unit cell parameters, in $Sr_2NaNb_5O_{15}$ the orthorhombic lattice parameters a and c increase on cooling below T_m, but the increase is compensated by the decrease of b, giving rise to the Invar effect.

Recently a reentrant relaxor behavior was claimed in the $Ba_5RTi_3Nb_7O_{30}$ (R = La, Nd, Sm) ceramics in spite of the fact that a single $\varepsilon'(T)$ maximum was observed at the frequency-dependent temperature T_m [67]. It was found that the temperature dependence of remanent polarization (P_r) determined from the $P(E)$ hysteresis loops passes through a maximum at $T_r < T_m$, similar to that depicted in Figure 23.11(b). The temperature T_r was defined as a reentrant temperature and it was suggested that below T_r the long-range FE order is broken. We note, however, that the hysteresis loops reported in this paper were very far away from saturation, especially at low temperatures. This suggests that the largest field applied was smaller than the coercive field needed to switch all the FE domains. Therefore, the measured remanent polarization was smaller than the spontaneous FE polarization and the difference between them increased upon cooling (due to an expected increase of the coercive field), giving rise to the $P_r(T)$ maximum. This explanation is supported by the fact that the increase in the maximal measurement field resulted in both a significant increase of P_r and a decrease of T_r. Therefore, similar to the situation in perovskite $(1 - x)$BT–xBS, discussed above, alternative methods for the spontaneous polarization measurement are needed to determine reliably the low-temperature behavior of the long-range FE order. Note that analysis of the pyroelectric effect in a number of different tungsten bronze crystals with the reentrant-type relaxor behavior does not reveal a $P_r(T)$ maximum, as discussed below.

To understand the origin of reentrant relaxor properties in the tungsten bronze compounds, it would be helpful to consider the results obtained on single crystals. Figure 23.12 illustrates a typical situation. In all the tungsten bronze crystals studied that exhibited the reentrant behavior, the low-temperature relaxor-type dielectric peak was found to be absent or significantly suppressed along [001] (i.e. the tetragonal c axis), but was clearly observed at $T_m < T_C$ in the directions orthogonal to [001]. On the contrary, the dielectric peak observed at T_C in the orthogonal directions is very small, or probably completely absent, as it is typically several orders of magnitude

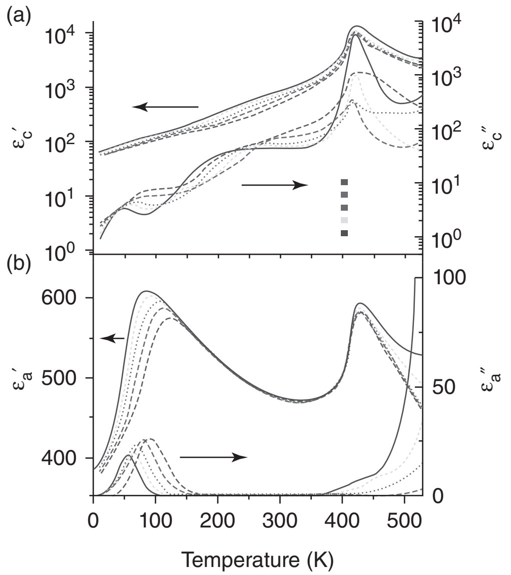

Figure 23.12 Temperature dependences of the real and imaginary parts of dielectric permittivity in the $(K_{0.5}Na_{0.5})_{1.0}(Sr_{0.75}Ba_{0.25})_{4.5}Nb_{10}O_{30}$ crystal doped with 0.04 wt% of CuO, measured along the (a) c axis and (b) a axis of the tetragonal lattice. The probe frequencies are 0.079 (solid), 0.796 (dash), 7.96 (dot), 79.6 (dash–dot), and 796 kHz (dash–dot–dot). Reprinted from [68] with permission from Ko et al. Copyright [2002], AIP Publishing LLC

smaller than along the polar axis, which can be explained [69] by the hardly avoidable small misorientation of the sample studied. This anisotropy was found, in particular, in the $Sr_{0.61}Ba_{0.39}Nb_2O_6$, $(K_{0.5}Na_{0.5})_{1.0}(Sr_{0.75}Ba_{0.25})_{4.5}Nb_{10}O_{30}$, $K_{5.80}Li_{3.82}Nb_{10.88}O_{30}$ [68], $Sr_{0.5}Ba_{0.5}Nb_2O_6$, $Pb_{0.37}Ba_{0.63}Nb_2O_6$, and $(K_xNa_{1-x})_{0.4}(Sr_yBa_{1-y})_{0.8}Nb_2O_6$ [70] crystals. Note that for the last composition the phase transition related to the low-temperature permittivity peak was derived from the X-ray diffraction analysis. The crystal symmetry was reported to change from the tetragonal $4mm$ to the monoclinic m, accompanied by the tilting of polarization away from the c axis of the tetragonal lattice as the temperature decreased. However, for other compositions the phase transition was not confirmed. The specific heat measurements around T_m revealed no latent heat or any significant change in the slope of the Cp versus T curve [70,71]. Analysis of the dielectric response and pyroelectric properties performed by Ko et al. [68] shows that the crystals were isotropic in the plane perpendicular to the c axis. In this plane the characteristic relaxation time, $\tau_r = (2\pi f_r)^{-1}$, determined from the frequency of the $\varepsilon''(f)$ maximum at fixed temperatures around T_m, was found to follow the Arrhenius law (i.e. Equation (23.2) with $T_f = 0$), while the validity of Equation (23.3) was not checked. Upon cooling the relaxation spectrum widened considerably. In $Sr_{0.61}Ba_{0.39}Nb_2O_6$, where the dielectric response was studied by means of IR reflectivity and time domain THz spectroscopy [69], no anomalies in the temperature dependences of the phonon contribution were observed. This suggests the order–disorder mechanism of the FE phase transition. The temperature dependence of the spontaneous polarization was determined in a number of tungsten bronze crystals from the pyroelectric current measurements [68, 70]. A typical result is shown in Figure 23.13, which depicts the behavior of the $(K_{0.5}Na_{0.5})_{0.4}(Sr_{0.60}Ba_{0.40})_{0.8}Nb_2O_6$ crystals. The relaxor-type peak of the dielectric permittivity is observed in the a-plate sample between $T_m = 58$ K (at 1 kHz) and

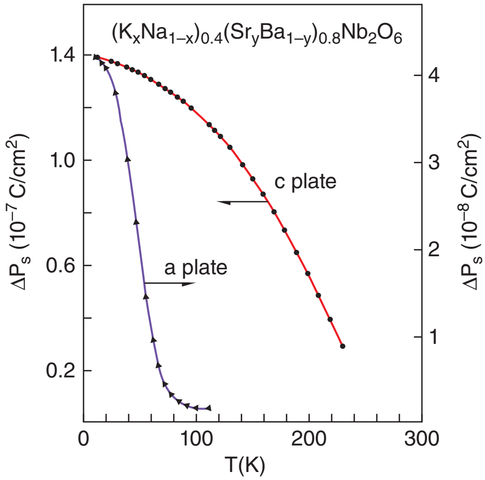

Figure 23.13 *Temperature dependences of the remanent polarization variation obtained by the measurements of the pyroelectric current in the $(K_{0.5}Na_{0.5})_{0.4}(Sr_{0.60}Ba_{0.40})_{0.8}Nb_2O_6$ crystals along the [001] (c-plate) and [100] (a-plate) directions of the tetragonal structure. Reprinted (Figure 9) from [70] with permission from Xu et al. Copyright (1989), American Physical Society*

$T_m = 76$ K (at 100 kHz). In the *c*-plate the dielectric permittivity increases smoothly with increasing temperature, as expected for a ferroelectric with $T_C > 300$ K. It can be seen in the figure that in the [001] direction the polarization gradually decreases with increasing temperature, as expected in an FE phase. In the perpendicular direction the spontaneous polarization is not expected as the symmetry is tetragonal, but the remanent polarization along <100> and <110> was found to exist at $T < T_m$ and vanished only at higher temperatures. It was shown to be practically proportional to the poling field [68], in contrast to highly non-linear behavior characteristic of ferroelectrics. Note that similar proportionality was observed in dipole glasses that show no long-range polar order at any temperature.

23.4.2 Models and Theories

Several models have been proposed to explain the reentrant relaxor behavior in macroscopically homogeneous samples. Kleemann [63] suggested that two peaks in the temperature dependence of the permittivity in $Ba_2Pr_xNd_{1-x}FeNb_4O_{15}$ (and other reentrant relaxors including perovskites) are caused by the coexistence of two phases, which is probable in the framework of percolation theory. In particular, in a solid solution with an *fcc* structure two mutually penetrating infinite percolation clusters can be formed in the composition range of $0.13 < x < 0.87$, which is consistent with the phase diagram in Figure 23.10. In one of these clusters the ferroelectric phase is developed, while the other one seems to include PNRs responsible for the relaxor behavior.

An alternative explanation was suggested in the theoretical work by Stephanovich [72], who applied a replica-symmetric solution of the disordered Ising model to describe the T–x phase diagram and FE hysteresis loops in $Ba_2Pr_xNd_{1-x}FeNb_4O_{15}$. It was believed that the low-temperature phase in the compositions with $x \geq 0.2$ is a dipole glass rather than a relaxor. This conclusion was supported mainly by the opinion that classical relaxors like PMN "never have ferroelectric hysteresis". We argue, however, that well-saturated FE hysteresis loops can in fact be displayed in PMN and other relaxors (see Section 23.3), arising from the induced ferroelectricity [32, 34]. Other proofs are required to discard the relaxor nature of the dielectric relaxation in $Ba_2Pr_xNd_{1-x}FeNb_4O_{15}$.

Schefer et al. [71] contended that high-resolution neutron powder diffraction on $Sr_{0.61}Ba_{0.39}Nb_2O_6$ reveals small changes in the incommensurate modulation of the NbO_6 octahedra with temperature and attributed the low-temperature dielectric peak to this effect. Later, Torres-Pardo et al. [64] questioned this relation as the structural characterization by Schefer et al. was not performed in the range of dispersive dielectric maximum, but at higher temperatures. From the structural study of $Sr_2NaNb_5O_{15}$ by transmission electron microscopy, Torres-Pardo et al. [64] showed that the incommensurate phases are neither present nor stabilized with decreasing temperature and the origin of the reentrant relaxor behavior is different. Based on the analysis of the temperature evolution of the lattice strain, they suggested that a subtle rotation of spontaneous polarization towards the *a* axis occurs upon cooling below T_m, which could be associated with "a smeared-out phase transition into a frustrated ferroelectric/ferroelastic low temperature state". The observed relaxor-type dispersion was attributed to the relaxation of PNRs, which coexist with the FE percolation cluster. The decrease in the measured spontaneous polarization on cooling was explained by the increase in the concentration of PNRs, which reduces the volume of the parent FE phase. However, structural evidence for the existence of PNRs was not obtained.

We point out that the above-described anisotropy of tungsten bronze ferroelectric crystals is compatible with the model of transverse freezing known in the physics of magnetic reentrant spin glasses (Figure 23.3). In this model the spontaneous polarization of the FE phase corresponds to the *z*-component of the order parameter, while the transverse local polarization, which remains dynamic at $T_\mathrm{m} < T < T_\mathrm{C}$ and freezes at lower temperatures, is considered to be responsible for the permittivity peak at T_m (Figure 23.12(b)) and the remanent polarization observed in the (001) plane below T_m (Figure 23.13). The transverse dipole moment can appear due to the shifts of cations away from the symmetry axis of the tetragonal unit cell. The symmetry prescribes the existence of at least four equivalent positions for the shifted cations, and the thermally activated hopping of the cations among these positions can be responsible for the transverse polarization fluctuations. However, the observed Arrhenius behavior of the characteristic relaxation time suggests that a thermodynamic phase transition to the dipolar glass (or non-ergodic relaxor) phase is absent, and the freezing around T_m is purely kinetic (like in many "normal" dipolar glasses and relaxors). Therefore, the transverse remanent polarization observed at $T < T_\mathrm{m}$ is a non-equilibrium quantity. It can be measured by experiment due to a very long relaxation time. Structural verification of this model is yet to be provided.

23.5 Transverse Glassy Freezing and Canonical Relaxors

In the previous section we have considered the examples of materials where the FE phase with the macroscopic polar symmetry exists at temperatures below T_C (as confirmed, for example, by standard X-ray diffraction experiments), and the relaxor behavior appears at lower temperatures. It was noticed [73], however, that even in canonical relaxors where the FE phase is not observed without an external field, some features in the behavior resemble the reentrant rather than "normal" magnetic spin glasses. In particular, the study of the X-ray diffuse scattering in the vicinity of the Bragg peaks in the PMN crystal revealed an unusual behavior of the scattering intensity related to ferroelectric-type fluctuations, which follows a power law $q^{-\alpha}$ at large q with $2 < \alpha < 3$, where q is the deviation of the scattering vector from the reciprocal lattice point. A similar power law dependence was observed in the RSG materials in contrast to the Lorentzian form of scattering found in the materials where the paramagnetic phase transforms directly to the SG phase [17, 23].

The analogy between the reentrant spin glasses and relaxor ferroelectrics is not very surprising, as both are characterized by partially frustrated interactions and both exhibit a mesoscopic or even macroscopic collinear order that exists alongside a glassy order. Subsequent studies based mainly on the analysis of aging phenomena [74–78] provided support to that analogy and suggested that to describe the phase transitions in relaxor ferroelectrics completely, two coexisting order parameters may be needed. In the present section we discuss the results of these investigations.

Aging is a characteristic phenomenon of many disordered materials. The term applies to situations where the properties depend on the time spent by the studied sample under particular conditions. In the context of the present paper we will consider the aging of small-signal AC susceptibility, $\chi = \chi' - i\chi''$ (the dielectric susceptibility and permittivity are related by $\chi = \varepsilon - 1$). One experiment that can conveniently reveal the features of the phenomenon consists in continuous measurements of χ in the course of fast cooling

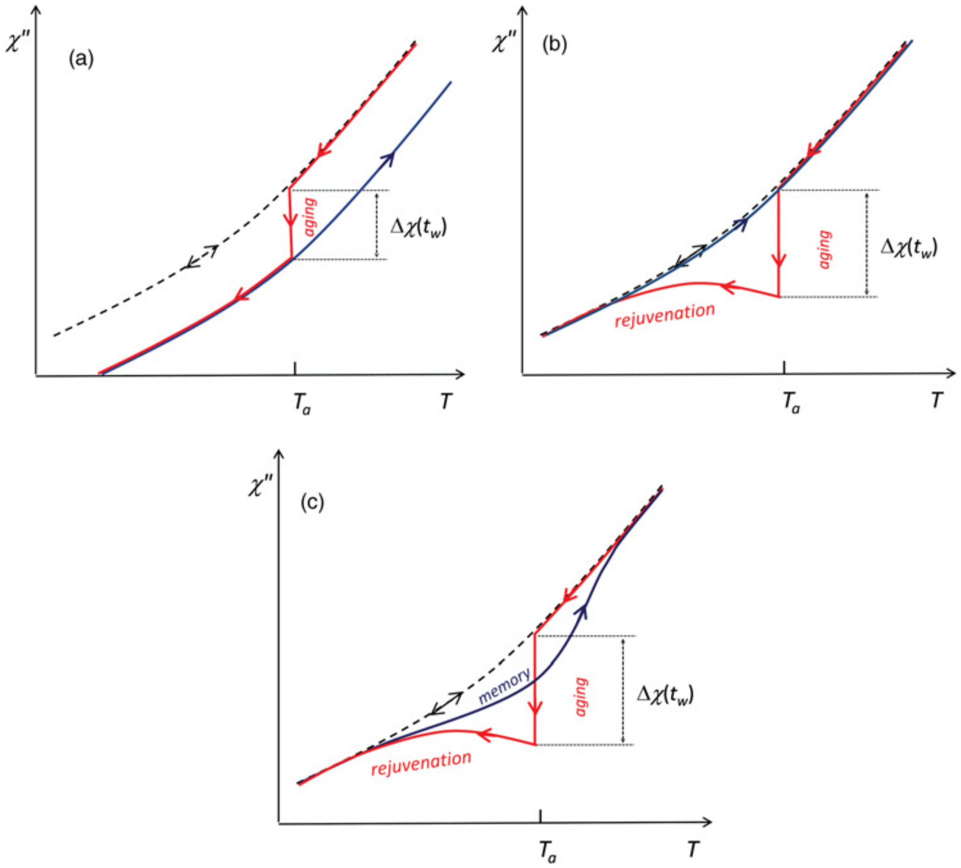

Figure 23.14 *Possible scenarios of aging behavior in ferroic systems: (a) cumulative aging, which can be observed in the FE phase of normal ferroelectrics; (b) aging with rejuvenation, which can be observed in the FM phase of disordered magnets and reentrant spin glasses, and in the FE phase of relaxor ferroelectrics; (c) aging with rejuvenation and memory, which can be observed in the SG phase, RSG phase, and NR phase. In the experiment, the susceptibility is continuously measured while the temperature first decreases, then stabilizes at the aging temperature,* T_a*, for a waiting time,* t_w*, then decreases again (red lines), and finally increases (blue line). The dashed line represents the behavior of the same sample if the temperature varies continuously (without aging). For a color version of this figure, see color plate section*

(quenching) of the sample through the phase transition down to a temperature T_a, stabilizing the temperature during some waiting time t_w, further fast cooling down to $T \ll T_\mathrm{a}$, and then fast heating up through T_a. The possible variants of the behavior are presented schematically in Figure 23.14 for the most typical case where the susceptibility decreases on cooling and with time. The imaginary part of susceptibility is shown, as it usually reveals more pronounced aging effects than the real part. The drop of χ at T_a (aging) can be quite significant (dozens percent). Qualitative differences can occur in the behavior after aging. The cumulative aging (Figure 23.14(a)) is non-reversible, and the initial (non-aged) value of χ can be restored only after heating the sample to the high-temperature phase. In other scenarios (Figure 23.14(b) and (c)), cooling after aging results in a comparatively slow variation of χ within a certain temperature interval below T_a, and at low temperatures the value of χ is the same as it would be without aging. This effect of susceptibility restoration is called rejuvenation. However, in some cases the rejuvenated sample still “remembers” that it was previously aged at T_a and upon subsequent warming a significant dip (or “hole”) is observed in the $\chi(T)$ dependence around T_a (Figure 23.14(c)). A more detailed description of the aging phenomena in magnetic materials can be found in the review by Vincent [79].

Aging indicates that the system is not in equilibrium and moves slowly to a configuration with lower free energy. In normal ferroelectrics the process is generally related to the peculiarities of the domain structure, which influences the susceptibility significantly. Internal stresses and electric fields can appear in the polydomain sample immediately after the phase transition. Their minimization may occur via rearrangement of domain walls and diffusion of lattice defects [80] and, when an optimal configuration is reached, it is no longer influenced significantly by the temperature variation. As a result, aging appears to be cumulative.

The rejuvenation and memory effects stem from hierarchical organization of the metastable states, which is typical of spin glasses and FM phase in disordered magnets [79, 81]. The characteristic memory holes (Figure 23.14(c)) were observed in the “normal” SG phase or in the RSG phase, and the crossover into the rejuvenation (without memory) regime (Figure 23.14(b)) was found after transformation into the FM phase, which can be obtained by heating from the RSG phase or by increasing the concentration of magnetic atoms in an alloy [81]. An analogous crossover between regimes upon variation of composition or temperature was discovered in relaxor ferroelectrics [82]. In particular, the NR phase of the classical relaxor PMN showed the aging behavior to be very similar to the behavior of the SG or RSG phase, including rejuvenation and memory holes as depicted in Figure 23.14(c) and also the scaling effect, which consists of a special relation between the $\chi''(t_w)$ dependences measured at different frequencies during an isothermal aging. All these dependences can be placed onto a single curve, being plotted as χ'' versus the product $t_w f$. In the $(1-x)$PMN–xPT solid solutions with a large enough x the glassy phase is absent and the phase with a collinear long-range (FE) order was observed. Accordingly, the memory was absent and only rejuvenation was found in the FE phase of the 0.72PMN–0.28PT crystal [75]. In the crystal of 0.9PMN–0.1PT with a lower PT concentration the crossover between the regimes was observed upon temperature variation in the same sample [83], similar to the reentrant spin glasses. Note, however, that the behavior of the relaxors is even more complex, and additional cumulative aging was seen in some temperature intervals. This aging seems to be related to additional microscopic mechanisms not existing in magnetic analogs.

The above-described striking parallels allowed Weissman and co-workers [78] to conclude that not only the relaxation properties, but also the microscopic arrangements of the relaxing entities in relaxor ferroelectrics and in reentrant spin glasses are probably similar in some aspects. They agreed with the common belief that in canonical relaxors like PMN the main contribution to the susceptibly in the vicinity of T_m comes from the thermally activated reorientations of the dipole moments of PNRs. However, in the low-temperature phase where these reorientations are effectively frozen, a different relaxation process becomes important. It was proposed that it is the reorientations of the polarization components orthogonal to the spontaneous polarization of PNRs that contribute to the dielectric response and glassy aging phenomena observed at $T < T_f$, similar to the transverse (i.e. *xy*) components of magnetization in the RSG phase. According to this picture, the PNRs in relaxors play the role of FM domains in reentrant spin glasses. The difference lies in the fact that in reentrant magnets the longitudinal and transverse components are subject to FM and glassy ordering, respectively, while the behavior of canonical relaxors is more complex: the FE (longitudinal) ordering that occurs inside PNRs is local. The longitudinal polarization component (the polarization of the particular PNR) remains dynamic in a wide temperature range at $T > T_f$ and freezes at T_f alongside the relatively independent transverse component. Therefore, two distinct glassy order parameters exist in parallel.

A number of experimental data support this model, some of which are summarized as follows:

(i) The results of X-ray diffraction [83] and neutron pair distribution function analysis [39] of PMN and 0.9PMN–0.1PT are consistent with the picture in which the symmetry of every perovskite unit cell inside a PNR is monoclinic with the dipole moment directed between <111> and <100>; thus it can be decomposed into the <111> component and the component orthogonal to <111>. All the <111> components inside a particular PNR are ordered along the same <111> direction (which corresponds to the z axis in the model shown in Figure 23.3), while the directions of the orthogonal components remain disordered and may be frozen upon cooling into a transverse spin-glass-like state (like the xy glass in the RSG phase; see Figure 23.3).

(ii) The glassy aging (the magnitude and form of the memory holes) in the 0.92PMN–0.08PT relaxor is practically unaffected by the (field-induced) remanent polarization of the whole sample [76]. This suggests that the reorientations of the longitudinal dipole moments of PNRs, which determine both the remanent polarization of a poled sample and the main part of the small-signal dielectric response, are not related to the observed aging. The glassy aging and the major dialectic response come from the different degrees of freedom.

(iii) The temperature dependence of Barkhausen noise in PMN suggests that the dipoles participating in the glassy freezing possess moments much smaller than the moments of PNRs. These dipoles could be associated with the transverse components of the unit cell moments [78].

(iv) In the uniaxial relaxor $Sr_xBa_{1-x}Nb_2O_6$ where the dipole moments of all PNRs are collinear and no orthogonal component is expected, a spin-glass-like memory is not observed at low temperatures [74].

(v) The isothermal transformation of the NR phase to the FE phase under an external DC field and the transformation of the field-induced FE phase to the ER phase upon heating were found to occur in two steps, separated in time, corresponding to the development of two distinct order parameters related to the longitudinal and transverse polarization components, respectively [77].

Note that the glassy aging, rejuvenation, and memory effects, qualitatively the same as in PMN, were also found in the $(1 - x)$BT–xBS ceramics with $x = 0.3$ [60]. However, the question whether other relaxors follow a similar behavior is still open.

23.6 Reentrant Dipolar Glass State in Quantum Paraelectrics Doped with Dipolar Impurities

Quantum paraelectrics are the incipient ferroelectrics whose FE phonon soft mode tends to condense at a temperature close to 0 K, but quantum fluctuations prevent the condensation and the material remains paraelectric at all temperatures. Dipolar impurities, that is the impurity (doping) ions shifted from the centrosymmetric sites of the paraelectric unit cell, can stabilize the FE phase when their concentration is larger than a critical value, while a lower concentration results in the formation of a dipolar glass state [33, 85]. Some authors qualify these materials as relaxors. From the structural point of view, moderately doped quantum paraelectrics occupy an intermediate position between the dipolar glasses and the canonical relaxor ferroelectrics. The elementary dipole moments associated with the off-center ionic displacements in distinct unit cells are separated by comparatively large distances (like in simple dipolar glasses); however, due to the high (FE soft mode related) polarizability of the lattice a permanently poled dipole is formed around every off-center ion that resembles a PNR [33, 86]. In contrast to the classical relaxors, the formation of polar nanoregions in this case is not a cooperative effect. The observed broad frequency-dependent peak in the temperature dependence of dielectric permittivity is seemingly identical to that detected in canonical relaxors. An example is shown in Figure 23.15, where the relaxor-like permittivity peak is observed at T_m between 45 and 75 K in the perovskite quantum paraelectric $KTaO_3$ doped with Li and Nb. This peak was related to the glassy freezing of the dipole dynamics of the off-centered Li^+ ions that substitute the K^+ ions in their centrosymmetric positions. However, in contrast to canonical relaxors, T_m follows the Arrhenius law (i.e. Equation (23.3) with $T_{VF} = 0$) and the static permittivity follows the Curie–Weiss law in the temperature range, where the frequency-dependent maximum is

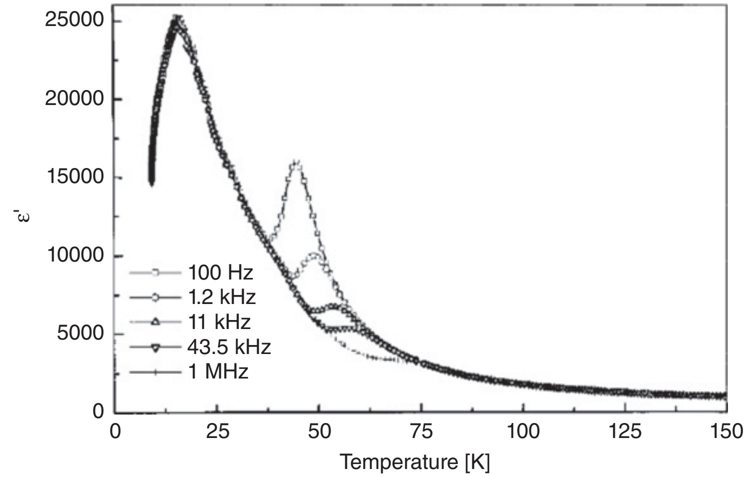

Figure 23.15 *Temperature dependences of the dielectric permittivity in the* $K_{0.9986}Li_{0.0014}Ta_{0.976}Nb_{0.024}O_3$ *crystal measured at different frequencies. Reprinted (Figure 1) from [87] with permission from Trepakov et al. Copyright (2001), American Physical Society*

observed [87,88]. In the $K_{0.9986}Li_{0.0014}Ta_{0.976}Nb_{0.024}O_3$ crystal presented in Figure 23.15, the dopant concentration is close to the critical value. Thus, besides the formation of the dipolar glass in the Li^+ subsystem, the phonon soft mode-driven FE transition was found at $T_C = 39$ K from Raman scattering and dielectric spectroscopy experiments [87,88]. An additional dielectric peak was observed at 15 K. However, it disappeared in a field-cooled crystal. In contrast to the high-temperature dispersive peak, the low-temperature peak was practically frequency-independent. It was supposed to be associated with the transition into a new glass-like phase. As this phase occurred on cooling from the FE phase, it was qualified as a reentrant dipolar glass-like state. However, later neutron diffraction investigation [89] did not confirm the existence of a normal FE phase. While the lattice parameter passed through a minimum at T_C, no splitting or broadening of the (h00) or (hhh) reflections was found, suggesting that the crystal retained the cubic structure at low temperatures. Nevertheless, the sample was found to be most likely heterogeneous, as comparatively small satellites were observed in the vicinity of the (hhh) reflections below $\sim T_C$, which were related to the clusters of the rhombohedral phase embedded into the cubic matrix.

23.7 Summary and Concluding Remarks

Investigation of the reentrant phases and related phenomena in relaxor ferroelectrics is currently just beginning. It appears to be challenging due to the complexity of the objects to be studied. The results published so far have shown a considerable diversity in the reentrant phenomena in relaxors. An unusual dielectric anomaly, that is a diffuse and dispersive $\varepsilon(T)$ peak located within the temperature range of the FE phase, has been reported in a number of perovskite and tungsten bronze materials. However, in most cases the data are not complete enough to distinguish whether this peak signifies a true thermodynamic phase transition into a glassy phase or results from kinetic Arrhenius-type slowing down of an intrinsic or extrinsic relaxation process. The only reentrant relaxor where the non-Arrhenius relaxation has been verified is the $(1-x)BaTiO_3$–$xBiScO_3$ solid solution system, where the Vogel–Fulcher divergence of the relaxation time has been found, suggesting a "true" glassy freezing of the relaxation dynamics at $0 < T_f < T_C$ (see Section 23.4.1.1). On the contrary, the Arrhenius temperature dependence of the relaxation time has been found for the "transverse" reentrant relaxor-like relaxation in a number of tungsten bronze crystals (see Section 23.4.1.2).

In most of the reported reentrant relaxor cases, the experimental data and suggested models indicate a conservation of the high-temperature FE order at temperatures below the relaxor-type permittivity maximum, that is within the reentrant state. The only result that points to the existence of a "true" reentrant phase, that is a phase less ordered than the high-temperature FE phase, is the decreasing remanent polarization below T_m derived from the FE hysteresis loops in $Sr_2NaNb_5O_{15}$ (Figure 23.11) and some other ceramics. However, in view of the difficulties in the interpretation of the low-temperature FE hysteresis loops, as discussed throughout this review, further investigations of the temperature dependence of spontaneous polarization need to be performed.

The models proposed for the reentrant phenomena in relaxors consider two types of coexistence of the FE order and the glassy subsystem of local dipoles in the reentrant state. The first type implies the presence of the spatial macro- or microscopic heterogeneity where the material consists of the FE regions and the regions of the less ordered glassy phase. Alternatively, two orthogonal components of the local dipole moment are supposed to exist. One of the components contributes to the collinear order of the FE domains or PNRs. The other component forms a two-dimensional dipole glass in the plane perpendicular to the direction of the collinear order. Further research is needed to clarify the underlying microscopic mechanisms. A great deal of information concerning the reentrant states in relaxors is expected to be generated in the near future, which will be helpful in understanding the relaxor behavior in general.

Acknowledgments

This work was supported by the United States Office of Naval Research (ONR, Grant No. N00014-12-1-1045) and the Natural Science and Engineering Research Council of Canada (NSERC).

References

(1) Tamman, G. (1903) *Kristallisieren und Schmelzen*, Johann Ambrosius Barth, Leipzig.

(2) Rastogi, S., Newman, M., and Keller, A. (1991) Pressure-induced amorphization and disordering on cooling in a crystalline polymer. *Nature*, **353**, 55–57.

(3) Greer, A.L. (2000) Too hot to melt. *Nature*, **404**, 124–135.

(4) Hudson, C.S. (1904) The reciprocative solubility of nicotine in water. *Zeitschrift für Physikalische Chemie*, **47** (1), 113–115.

(5) Narayanan, T. and Kumar, A. (1994) Reentrant phase transitions in multicomponent liquid mixtures. *Physics Reports*, **239**, 135–128.

(6) Lin, T.H., Shao, X.Y., Wu, M.K., et al. (1984) Observation of a reentrant superconducting resistive transition in granular $BaPb_{0.75}Bi_{0.25}O_3$ superconductor. *Physical Review B*, **29** (3), 1493–1496.

(7) Kim, D.C., Kim, J.S., Kang, H.R., et al. (2001) Observation of anomalous reentrant superconductivity in $Sr_{1-x}K_x\ BiO_3$. *Physical Review B*, **64**, art. no. 064502.

(8) Heera, V., Fiedler, J., Hubner, R., et al. (2013) Silicon films with gallium-rich nanoinclusions: from superconductor to insulator. *New Journal of Physics*, **15**, art. no. 083022.

(9) Indekeu, J.O. and Berker, A.N. (1988) Molecular structure and reentrant phases in polar liquid crystals. *Journal de Physique France*, **49** (2), 353–362.

(10) Mazza, M.G. and Schoen, M. (2011) Structure and dynamics of reentrant nematics: Any open questions after almost 40 years? *International Journal of Molecular Sciences*, **12** (8), 5352–5372.

(11) Altamirano, N., Kubiznak, D., and Mann, R.B. (2013) Reentrant phase transitions in rotating anti-de Sitter black holes. *Physical Review D*, **88** (10), art. no. 101502(R).

(12) Lines, M.E. and Glass, A.M. (1977) *Principles and Applications of Ferroelectrics and Related Materials*, Clarendon Press, Oxford.

(13) Walker, J.S. and Vause, C.A. (1983) Lattice theory of binary fluid mixtures: phase diagrams with upper and lower critical solution points from a renormalization group calculation. *The Journal of Chemical Physics*, **79** (6), 2661–2676.

(14) Coles, B.R., Sarkissian, B.V.B., and Taylor, R.H. (1978) The role of finite magnetic clusters in Au–Fe alloys near the percolation concentration. *Philosophical Magazine B*, **37** (4), 489–498.

(15) Abdul-Razzaq, W. and Kouvel, J.S. (1984) Spin glassiness and ferromagnetism in disordered Ni–Mn. *Journal of Applied Physics*, **55** (6), 1623–1627.

(16) Maletta, H. (1982) Magnetic ordering in $Eu_xSr_{1-x}S$, a diluted Heisenberg system with competing interactions. *Journal of Applied Physics*, **53** (3), 2185–2190.

(17) Aeppli, G., Shapiro, S.M., Birgeneau, R.J., and Chen, H.S. (1983) Spin correlations and reentrant spin-glass behavior in amorphous Fe–Mn alloys: statics. *Physical Review B*, **28** (9), 5160–5172.

(18) Wong, P.Z., von Molnar, S., Palstra, T.T.M., et al. (1985) Coexistence of spin-glass and antiferromagnetic orders in the Ising system $Fe_{0.55}Mg_{0.45}Cl_2$. *Physical Review Letters*, **55** (19), 2043–2046.

(19) Ryan, D.H. (1992) Exchange frustration and transverse spin freezing, in *Recent Progress in Random Magnets*, edited by R.H. Ryan, World Scientific, Singapore, New Jersey, London, Hong Kong, pp. 1–40.

(20) Mirebeau, I., Hennion, M., Mitsuda, S., and Endoh, Y. (1992) Investigation of the reentrant spin glass phase by neutron scattering, in *Recent Progress in Random Magnets*, edited by R.H. Ryan, World Scientific, Singapore, New Jersey, London, Hong Kong, pp. 41–69.

(21) Sherrington, D. and Kirkpatrick, S. (1975) Solvable models of a spin-glass. *Physical Review Letters*, **35** (26), 1792–1796.

(22) Thomson, J.R., Guo, H., Ryan, D.H., et al. (1992) Magnetic ordering in the three-dimensional frustrated Heisenberg model. *Physical Review B*, **45** (6), 3129–3132.

(23) Aeppli, G., Shapiro, S.M., Maletta, H., et al. (1984) Spin correlations near the ferromagnetic-to-spin-glass crossover. *Journal of Applied Physics*, **55** (6), 1628–1633.

(24) Cowley, R.A., Shirane, G., Birgeneau, R.J., and Svensson, E.C. (1977) Critical scattering near the percolation threshold in $Mn_cZn_{1-c}F_2$. *Physical Review Letters*, **29** (14), 894–897.

(25) Imry, Y. and Ma, S.K. (1975) Random-field instability of the ordered state of continuous symmetry. *Physical Review Letters*, **35** (21), 1399–1401.

(26) Abiko, S., Niidera, S., and Matsubara, F. (2005) Reentrant spin-glass transition in a dilute magnet. *Physical Review Letters*, **94**, art. no. 227202.

(27) Niidera, S. and Matsubara, F. (2007) Fluctuating clusters in a reentrant spin-glass system. *Physical Review B*, **75**, art. no. 144413.

(28) Jonason, K., Mattsson, J., and Nordblad, P. (1996) Dynamic susceptibility of a reentrant ferromagnet. *Physical Review B*, **53** (10), 6507–6513.

(29) Dho, J., Kim, W.S., and Hur, N.H. (2002) Reentrant spin glass behavior in Cr-doped perovskite manganite. *Physical Review Letters*, **89** (2), art. no. 027202.

(30) Kleemann, W., Shvartsman, V.V., Borisov, P., and Kania, A. (2010) Coexistence of antiferromagnetic and spin cluster glass order in the magnetoelectric relaxor multiferroic $PbFe_{0.5}Nb_{0.5}O_{3.}$ *Physical Review Letters*, **105**, art. no. 257202.

(31) Chillal, S., Thede, M., Litterst, F.J., et al. (2013) Microscopic coexistence of antiferromagnetic and spin-glass states. *Physical Review B*, **87**, art. no. 220403.

(32) Ye, Z.G. (1998) Relaxor ferroelectric complex perovskites: structure, properties and phase transitions. *Key Engineering Materials*, 155–156, 81–122.

(33) Samara, G.A. (2003) The relaxational properties of compositionally disordered ABO_3 perovskites. *Journal of Physics: Condensed Matter*, **15** (9), R367–R411.

(34) Bokov, A.A. and Ye, Z.G. (2006) Recent progress in relaxor ferroelectrics with perovskite structure. *Journal of Materials Science*, **41** (1), 31–52.

(35) Burton, B.P., Cockayne, E., Tinte, S., and Waghmare, U.V. (2006) First-principles-based simulations of relaxor ferroelectrics. *Phase Transitions*, **79** (1–2), 91–121.

(36) Cowley, R.A., Gvasaliya, S.N., Lushnikov, S.G., et al. (2011) Relaxing with relaxors: a review of relaxor ferroelectrics. *Advances in Physics*, **60** (2), 229–327.

(37) Shvartsman, V.V. and Lupascu, D.C. (2012) Lead-free relaxor ferroelectrics. *Journal of the American Ceramic Society*, **95** (1), 1–26.

(38) Gehring, P.M. (2012). Neutron diffuse scattering in lead-based relaxor ferroelectrics and its relationship to the ultra-high piezoelectricity. *Journal of Advanced Dielectrics*, **2** (2), art. no. 1241005.

(39) Jeong, I.K., Darling, T.W., Lee, J.K., et al. (2005) Direct observation of the formation of polar nanoregions in $PbMg_{1/3}Nb_{2/3}O_3$ using neutron pair distribution function analysis. *Physical Review Letters*, **94**, art. no. 147602.

(40) Xu, G., Shirane, G., Copley, J.R.D., and Gehring, P.M. (2004) Neutron elastic diffuse scattering study of $Pb(Mg_{1/3}Nb_{2/3})O3$. *Physical Review B*, **69**, art. no. 064112.

(41) Bing, Y.H., Bokov, A.A., and Ye, Z.G. (2011). Diffuse and sharp ferroelectric phase transitions in relaxors. *Current Applied Physics*, **11**, S14–S21.

(42) Hlinka, J. (2012) Do we need the ether of polar nanoregions. *Journal of Advanced Dielectrics*, **2** (2), art. no. 1241006.

(43) Bosak, A., Chernyshov, D., Vakhrushev, S., and Krisch, M. (2012) Diffuse scattering in relaxor ferroelectrics: true three-dimensional mapping, experimental artefacts and modeling. *Acta Crystallographica A*, **68**, 117–123.

(44) Takenaka, H., Grinberg, I., and Rappe, A.M. (2013) Anisotropic local correlations and dynamics in a relaxor ferroelectric. *Physical Review Letters*, **110**, art. no. 147602.

(45) Akbarzadeh, A., Prosandeev, S., Walter, E., et al. (2012) Finite-temperature properties of $Ba(Zr,Ti)O_3$ relaxors from first principles. *Physical Review Letters*, **108**, art. no. 257601.

(46) Hu, W., Hayashi, K., Ohwada, K., et al. (2014) Acute and obtuse rhombohedrons in the local structures of relaxor ferroelectric $Pb(Mg_{1/3}Nb_{2/3})O_3$. *Physical Review B*, **89**, art. no. 140103(R).

(47) Dkhil, B., Gemeiner, P., Al-Barakaty, A., et al. (2009) Intermediate temperature scale T^* in lead-based relaxor systems. *Physical Review B*, **80**, art. no. 064103.

(48) Bokov, A.A., Bing, Y.H., Chen, W., et al. (2003) Empirical scaling of the dielectric permittivity peak in relaxor ferroelectrics. *Physical Review B*, **68**, art. no. 052102.

(49) Bokov, A.A. and Ye, Z.G. (2012) Dielectric relaxation in relaxor ferroelectrics. *Journal of Advanced Dielectrics*, **2** (2), art. no. 1241010.

(50) Jonscher, A.K. (1983) *Dielectric Relaxation in Solids*, Chelsea Dielectrics Press, London.

(51) Tagantsev, A.K. (1994) Vogel–Fulcher relationship for the dielectric permittivity in relaxor ferroelectrics. *Physical Review Letters*, **72** (7), 1100–1103.

(52) Zhao, X., Qu, W., Tan, X., et al. (2007) Electric field-induced phase transitions in (111)-, (110)-, and (100)-oriented $Pb(Mg_{1/3}Nb_{2/3}O_3$ single crystals. *Physical Review B*, **75**, art. no. 104106.

(53) Wang, Y.L., He, Z.B., Damjanovic, D., et al. (2011) Unusual dielectric behavior and domain structure in rhombohedral phase of $BaTiO_3$ single crystals. *Journal of Applied Physics*, **110**, art. no. 014101.

(54) Wang, Y.L., Tagantsev, A.K., Damjanovic, D., and Setter, N. (2007) Giant domain wall contribution to the dielectric susceptibility in $BaTiO_3$ single crystals. *Applied Physics Letters*, **91**, art. no. 062905.

(55) Lei, C. and Ye, Z.G. (2008) Re-entrant-like relaxor behaviour in the new $0.99BaTiO_3$–$0.01AgNbO_3$ solid solution. *Journal of Physics: Condensed Matter*, **20** (23), art. no. 232201.

(56) Lei, C. (2008) *Studies of Novel Lead-Free Piezoelectric and Relaxor Ferroelectric Materials*, PhD Dissertation, Simon Fraser University, Burnaby, BC.

(57) Guo, H.Y., Lei, C., and Ye, Z.G. (2008) Re-entrant type relaxor behavior in $(1-x)BaTiO_3$–$xBiScO_3$ solid solution. *Applied Physics Letters*, **92**, art. no. 172901.

(58) Guo, H.Y., Lei, C., and Ye, Z.G. (2009) Dielectric and ferroelectric properties of $(1-x)BaTiO_3-xBiScO_3$ solid solution. *Ferroelectrics*, **380**, 63–68.

(59) Datta, K. and Thomas, P.A. (2010) Structural investigation of a novel perovskite-based lead-free ceramics: $xBiScO_3$–$(1-x)BaTiO_3$. *Journal of Applied Physics*, **107**, art. no. 043516.

(60) Bharadwaja, S.S.N., Kim, J.R., Ogihara, H., et al. (2011) Critical slowing down mechanism and reentrant dipole glass phenomena in $(1-x)BaTiO_3$–$xBiScO_3$ ($0.1 \leq x \leq 0.4$): the high energy density dielectrics. *Physical Review B,* **83**, art. no. 024106.

(61) Simon, A., Ravez, J., and Maglione, M. (2005) Relaxor properties of $Ba_{0.9}Bi_{0.067}(Ti_{1-x}Zr_x)O_3$ ceramics. *Solid State Sciences*, **7** (8), 925–930.

(62) Castel, E., Josse, M., Michau, D., and Maglione, M. (2009) Flexible relaxor materials: $Ba_2Pr_xNd_{1-x}FeNb_4O_{15}$ tetragonal tungsten bronze solid solution. *Journal of Physics: Condensed Matter*, **21**, art. no. 452201.

(63) Kleemann, W. (2012) Random fields in relaxor ferroelectrics – a jubilee review. *Journal of Advanced Dielectrics*, **2** (2), art. no. 1241001.

(64) Torres-Pardo, A., Jimenez, R., Gonzalez-Calbet, J.M., and Garcıa-Gonzalez, E. (2011). Structural effects behind the low temperature nonconventional relaxor behavior of the $Sr_2NaNb_5O_{15}$ bronze. *Inorganic Chemistry*, **50** (23), 12091–12098.

(65) Kinka, M., Josse, M., Castel, E., et al. (2012) Coexistence of ferroelectric and relaxor states in $Ba_2Pr_xNd_{1-x}FeNb_4O_{15}$ ceramics. *IEEE Transactions on Ultrasonics*, *Ferroelectrics, and Frequency Control*, **59** (9), 1879–1882.

(66) Garcıa-Gonzalez, E., Torres-Pardo, A., Jimenez, R., and Gonzalez-Calbet, J.M. (2007) Structural singularities in ferroelectric $Sr_2NaNb_5O_{15}$. *Chemistry of Materials*, **19** (14), 3575–3580.

(67) Li, K., Zhu, X.L., Liu, X.Q., and Chen, X.M. (2013) Re-entrant relaxor behavior of $Ba_5RTi_3Nb_7O_{30}$ (R = La, Nd, Sm) tungsten bronze ceramics. *Applied Physics Letters*, **102**, art. no. 112912.

(68) Ko, J.H., Kojima, S., Lushnikov, S.G., et al. (2002) Low-temperature transverse dielectric and pyroelectric anomalies of uniaxial tungsten bronze crystals. *Journal of Applied Physics*, **92** (3), 1536–1543.

(69) Buixaderas, E., Savinov, M., Kempa, M., et al. (2005) Infrared and dielectric spectroscopy of the relaxor ferroelectric $Sr_{0.61}Ba_{0.39}Nb_2O_6$. *Journal of Physics: Condensed Matter*, **17** (4), 653–666.

(70) Xu, Y., Li, Z., Li, W., and Wang, H. (1989) Phase transition of some ferroelectric niobate crystals with tungsten-bronze structure at low temperatures. *Physical Review B*, **40** (17), 11902–11908.

(71) Schefer, J., Schaniel, D., Pomjakushin, V., et al. (2006) Structural properties of $Sr_{0.61}Ba_{0.39}Nb_2O_6$ in the temperature range 10–500 K investigated by high-resolution neutron powder diffraction and specific heat measurements. *Physical Review B*, **74** (13), art. no. 134103.

(72) Stephanovich, V.A. (2010) Tetragonal tungsten bronze compounds: relaxor versus mixed ferroelectric–dipole glass behavior. *Journal of Physics: Condensed Matter*, **22** (23), art. no. 235902.

(73) Vakhrushev, S., Nabereznov, A., Sinha, S.K., et al. (1996) Synchrotron X-ray scattering study of lead magnoniobate relaxor ferroelectric crystals. *Journal of Physics and Chemistry of Solids*, **57** (10), 1517–1523.

(74) Chao, L.K., Colla, E.V., Weissman, M.B., and Viehland, D.D. (2005) Aging and slow dynamics in $Sr_xBa_{1-x}Nb_2O_6$. *Physical Review B*, **72**, art. no. 134105.

(75) Colla, E.V., Chao, L.K., and Weissman, M.B. (2001) Multiple aging mechanisms in relaxor ferroelectrics. *Physical Review B*, **63**, art. no. 134107.

(76) Colla, E.V., Griffin, P., Delgado, M., and Weissman, M.B. (2008) Polarization-independent aging in the relaxor $0.92PbMg_{1/3}Nb_{2/3}O_3$–$0.08PbTiO_3$. *Physical Review B*, **78**, art. no. 064103.

(77) Colla, E.V. and Weissman, M.B. (2005) Two-step phase changes in cubic relaxor ferroelectrics. *Physical Review B*, **72**, art. no. 104106.

(78) Weissman, M.B., Colla, E.V., and Chao, L.K. (2003) Noise and aging of relaxor ferroelectrics. In *Fundamental Physics of Ferroelectrics 2003 – AIP Conference Proceedings No. 677*, edited by R. Davies and D.J. Singh, AIP, Williamsburg, pp. 33–40.

(79) Vincent, E. (2007) Ageing, rejuvenation and memory: the example of spin-glasses. In *Ageing and the Glass Transition, Lecture Notes Physics 716*, edited by M. Henkel, M. Pleimling, and R. Sanctuary, Springer, Berlin Heidelberg, pp. 7–60.

(80) Damjanovic, D. (1998) Ferroelectric, dielectric and piezoelectric properties of ferroelectric thin films and ceramics. *Reports on Progress in Physics*, **61**, 1267–1324.

(81) Vincent, E., Dupuis, V., Alba, M., et al. (2000) Aging phenomena in spin-glass and ferromagnetic phases: domain growth and wall dynamics. *Europhysics Letters*, **50** (i), 674–680.

(82) Colla, E.V., Chao, L.K., Weissman, M.B., and Viehland, D.D. (2000) Aging in a relaxor ferroelectric: scaling and memory effects. *Physical Review Letters*, **85**, 3033–3036.

(83) Dkhil, B., Kiat, J.M., Calvarin, G., et al. (2001) Local and long range polar order in the relaxor–ferroelectric compounds $PbMg_{1/3}Nb_{2/3}O_3$ and $PbMg_{0.3}Nb_{0.6}Ti_{0.1}O_3$. *Physical Review B*, **65**, art. no. 024104.

(84) Chao, L.K., Colla, E.V., and Weissman, M.B. (2006). Aging in the relaxor ferroelectric $(PbMn_{1/3}Nb_{2/3}O_3)_{0.90}$ $(PbTiO_3)_{0.10.}$ *Physical Review B*, **74**, art. no. 014105.

(85) Hochli, U.T., Knoor, K., and Loidl, A. (1990) Orientational glasses. *Advances in Physics*, **39** (5), 405–615.

(86) Toulouse, J. and Pattnaik, R.K. (1996) Pretransitional condensation in mixed ferroelectrics. *Journal of Physics and Chemistry of Solids*, **57**, 1473–1477.

(87) Trepakov, V.A., Savinov, M.E., Giulotto, E., et al. (2001) Dipole ordering effects and reentrant dipolar glass state in $KTaO_3$:Li,Nb. *Physical Review B*, **63**, art. no. 172203.

(88) Trepakov, V., Galinetto, P., Giulotto, E., et al. (2002) Recent developments in $K_{1-x}Li_xTa_{1-y}Nb_yO_3$ investigations. *Ferroelectrics*, **267**, 221–228.

(89) Borisov, S.A., Vakhrushev, S.B., Koroleva, E.Y.U., et al. (2007) Investigation into the evolution of the structure of $K_{1-x}Li_xTa_{1-y}Nb_yO_3$ single crystals under variations in temperature. *Crystallography Reports*, **52** (3), 440–446.

24

Functional Twin Boundaries: Multiferroicity in Confined Spaces

Ekhard. K.H. Salje[1] **and Xiangdong Ding**[2]

[1]*Department of Earth Sciences, University of Cambridge, United Kingdom*
[2]*State Key Laboratory for Mechanical Behavior of Materials, Xi'an Jiaotong University, China*

24.1 Introduction

Twinning was seen as a bane for experimentalists before the beginning of the twenty-first century, but now much research is focused on how to increase twinning rather than reducing it. The reason for this complete reversal of perspectives is that we understand now that twins are not necessarily a simple structural juxtaposition of adjacent bulk materials, but contain novel structural elements that do not exist in the bulk [1, 2]. As twin boundaries have potentially great applications as functional elements, the chase for "exotic" interfaces has begun. Typical examples are superconducting domain boundaries in insulating materials [3, 4], twin boundaries with high defect mobilities [5–8] two-dimensional electron gas at interfaces [9–12], unusual vortices near twin boundaries [13], or multiferroicity and chirality at domain boundaries [14–16]. A typical example where moving domain boundaries have been shown to serve in magnetic memory devices is the IBM racetrack memory based on the controlled movement of magnetic domain walls. Their movement is registered electromagnetically and their position is used as memory information. The wider industrial consequence of such local structures as memory devices, conductors, holographic templates, or as membranes for batteries have motivated significant research efforts during recent years.

Nanoscale Ferroelectrics and Multiferroics: Key Processing and Characterization Issues, and Nanoscale Effects, First Edition. Edited by Miguel Algueró, J. Marty Gregg, and Liliana Mitoseriu.
© 2016 John Wiley & Sons, Ltd. Published 2016 by John Wiley & Sons, Ltd.

Device materials where the functionality is based on the internal twin structures may need high twin boundary densities. High boundary densities are also needed to detect the functional properties of twin walls in the laboratory environment. The density of atoms inside twin walls is commonly rather low and may be in most thermally quenched materials only one wall atom in 10^6 bulk atoms (1 ppm = one part per million). This ratio can be improved under different experimental conditions and can reach 50 ppm. Ways to generate high domain boundary densities in ferroic nanomaterials were explored in computer simulation studies using two protocols: firstly, the fast quench from a paraelastic into a ferroelastic phase and, secondly, by shear of small samples at low temperatures inside the stability field of the ferroelastic phase. Quenched samples evolve from tweed to junction patterns to stripe patterns. In driven systems, no tweed exists in the plastic regime and the mesoscopic structure "nucleates" rapidly when a yield stress is surpassed. The nucleated domain patterns are long-lived and change towards the single domain state only when the external strain is further increased. The second procedure of "cold shearing" generates higher twin boundary densities and appears to develop into the method of choice for the generation of high boundary densities in domain boundary engineering [17, 18]. It has been argued that materials with high twin boundary densities often have features similar to glass states [19].

Microstructural patterns of twin boundaries and tweed in ferroelastic materials display typical aspects of glasses such as weak ergodicity breaking. The patterns are complex, their dynamics follows Vogel–Fulcher statistics, and their field cooling–non-field cooling hysteresis is similar to certain aspects of spin glasses [20, 21]. Domain glasses do not need extrinsic defects to form although defects may enhance the effect. In the paraelastic phase, which does not contain twin boundaries for symmetry reasons, an intrinsic tweed pattern may dominate a high-temperature precursor regime. Experimentally, massive elastic precursor softening is related to polar standing waves, which are attributed to the glassy relaxation of the tweed pattern. In the ferroelastic phase a complex twin pattern is formed when the sample is strained with a constant strain rate. The dynamics of the pattern formation is athermal at low temperatures and follows Vogel–Fulcher statistics at moderately high temperatures [22, 23]. It is argued that domain boundary patterns can hence evolve glass-like states while the underlying matrix remains fully crystalline without any defect-induced disorder [24].

24.2 Ferroelectric Twin Boundaries

Domain boundaries have never quite the same atomic structure as the surrounding crystal matrix and this is why their physical and chemical properties will often be different from that of the bulk material. Sometimes these differences are small and simply relate to geometrical features as shown in Figure 24.1. An antiferroelectric array of dipoles will usually contain antiphase boundaries (APBs) that change the phase of the up–down pattern of the bulk. In Figure 24.1 the region of an APB is shown in red and it is geometrically obvious that this APB is polar with a dipole moment in the down direction. We expect then that antiferroelectric materials will contain polar domain boundaries. Another typical example is that twinning of the bulk is related to shear strain generated by a structural phase transition that is non-polar. Take the rotation of an oxygen octahedra around a crystallographic *c* axis in a perovskite structure. When the rotation axis is exchanged with the crystallographic *a* axis

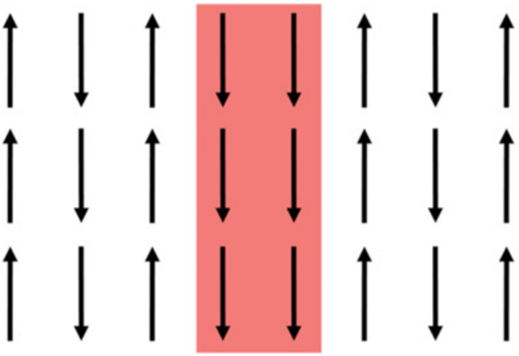

Figure 24.1 Antiphase boundary in an antiferroelectrically ordered array. The antiphase boundary is polar

we observe twinning because the c axis is slightly longer than the equivalent a axis. This is shown in a simple model in Figure 24.2 where the shaded areas represent the region of structural distortions inside the twin boundary. Note that all interatomic distances between nearest neighbors are exactly the same in the wall and the bulk. They are different only for the next nearest neighbor distances and higher distances spanning the twin boundary so that one can expect for most cases only very small structural changes as a weak perturbation of the strain profile of the two ferroelastic domains with the spontaneous strain $+e$ and $-e$. In the case of a second-order phase transition the trajectory is $e(x) \sim \tanh(x/w)$ where the locus of the twin boundary is at $x = 0$ and the thickness of the twin boundary is w.

This scenario can change dramatically if the material is thermodynamically close to structural phase transitions and can flip easily from one structural configuration to another. In particular when one of the incipient phases is itself polar, we may expect that walls and

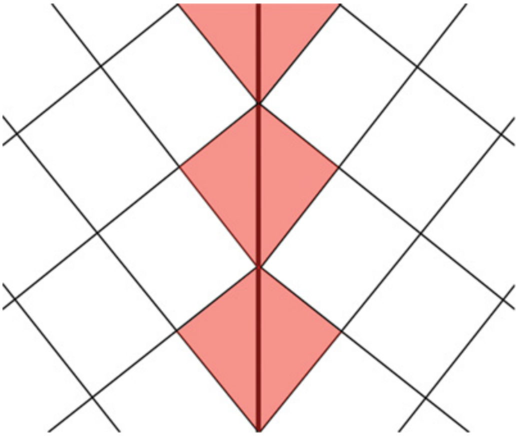

Figure 24.2 A simple model of a twin boundary where the exchange between short and long repetition lengths leads to a lattice distortion inside the shaded area

interfaces have a propensity to be polar, just as in the case of Figure 24.1. The following physical effects typically generate polarity:

1. Polarity and the octahedral rotation repel each other in most perovskite structures. The octahedral rotations often vanish inside twin walls, which allows polarity to emerge in the wall while it remains suppressed in the bulk.
2. The distances between lattice planes across the twin boundary is usually larger by some 1% compared with the lattice repetition unit in the bulk. This makes the formation of new structural elements, such as polarity, easier in the wall simply because there is more space in this part of the material compared with the bulk. It also makes the wall generally elastically softer so that lattice relaxations are easier to achieve.
3. Ionic conductivity is much enhanced in twin boundaries. It is possible, therefore, to inject defects and dopants into the twin boundaries while the bulk remains un-doped. This effect generates novel chemical compounds inside the twin boundaries, which can then be polar. Such local chemical doping is well known for oxygen vacancies and ions such as Ca, Li, and Na and can also be expected for transition metals. Often such chemical enrichments of twin walls occur unwillingly and are unavoidable in complex oxide materials.
4. Twin walls can also be charged as in case of $BaTiO_3$. If the polar vectors in ferroelastic twin boundaries are arranged in head-to-head or tail-to-tail configurations rather than by head-to-tail, as would correspond to a lower energy state, they will locate charges inside the twin walls. This leads to high conductivity and charged twin boundaries need to be characterized by its charge (+ or –) so that geometrically (almost) identical walls are separated by their charges and, thus, interact strongly.

24.2.1 Polar Twin Walls in $CaTiO_3$

Detailed investigations were performed in $CaTiO_3$ and we will use this example to illustrate the relevant mechanisms. The discovery of ferroic properties of twin walls is often related to computer simulations for materials design and the theoretical exploration of extreme physical properties in solids. One of the first examples in solid-state physics, where a spontaneous polarization of the twin boundary was predicted, is the $\{100\}$ twin walls of $CaTiO_3$ (Figure 24.3), a definitely non-polar material [25]. Theoretical simulations [25,26] of these walls show an extremely rich texture of the local polarization at and close to the walls. Local distortions include a strong antiferroelectric component and local non-zero contributions perpendicular to the wall plane, which do not contribute to the macroscopic net dipole moment. Similar studies were performed subsequently by Morozovska et al. [27] and Gu et al. [28].

The great challenge for domain boundary studies is to observe the described singularities experimentally. Van Aert et al. [29] have demonstrated that sufficient advances have been made using aberration-corrected TEM imaging in combination with statistical parameter estimation theory to not only visualize atomic displacements directly inside domain boundaries but also to measure their displacements, atomic layer by atomic layer, with picometer precision. This opens the door for massive advances in the investigation, design, and production of active domain boundaries and local structures that are based on small, local atomic displacements inside extended crystal lattices. They have shown that the predicted structural singularities in $CaTiO_3$ exist and that these features are confined to the

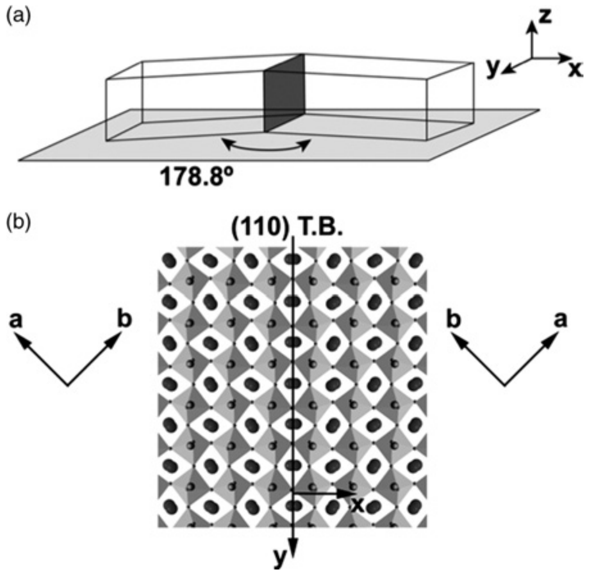

Figure 24.3 *(a) Single twin wall, indicated as a standing dark gray plane, with the chosen (x, y, z) reference system for the definitions of the measured displacements. The angle of 178.8° is the result of the twinning operation from the high-temperature cubic to the low-temperature orthorhombic phase. (b) Atomic configuration on both sides of the (110) twin plane as seen by the electron beam (Ca atoms are marked by large filled circles, Ti atoms by medium-sized shaded circles, and O atoms by small circles). Reprinted with kind permission from [29], Copyright © 2012 Wiley-VCH Verlag GmbH & Co. KGaA, Weinheim*

domain boundaries. The dominant off-centering of Ti was observed while all other structural deformations, such as shifts of the Ca atomic positions, remained too small to be seen (Figure 24.4).

While indirect evidence for the polar behavior in antiphase boundaries, APBs [30], and grain boundaries [31] have been reported before, the results in $CaTiO_3$ is very instructive as it was the first clear indication of twin wall polarity and the underlying structural mechanism for the coupling between strain and dipole moments. $CaTiO_3$ is orthorhombic in its low-temperature form (space group *Pnma*) and is purely ferroelastic. No ferroelectric features of the bulk material have ever been recorded. The TiO_6 octahedron, on the other hand, is well known for its tendency to form polar groups where the Ti position is off-centered with respect to the geometrical center of the surrounding oxygen atoms. Such polar structures exist in compounds such as $BaTiO_3$, $PbTiO_3$, and others. The known competition with octahedral rotation [14, 27, 32] in the tetragonal and orthorhombic phases of $CaTiO_3$ suppresses the off-centering. It is, however, restored when the rotation angle vanishes or when the density of the material decreases. Both conditions are met inside the twin wall and it is thus not entirely unexpected that twin walls should contain dipolar moments. To investigate polar ordering in the ferroelastic walls of $CaTiO_3$, numerical simulations were performed based on an atomic-scale description of the walls in which atoms interact via empirically defined forces [8]. This technique was chosen because a sufficiently large simulation box

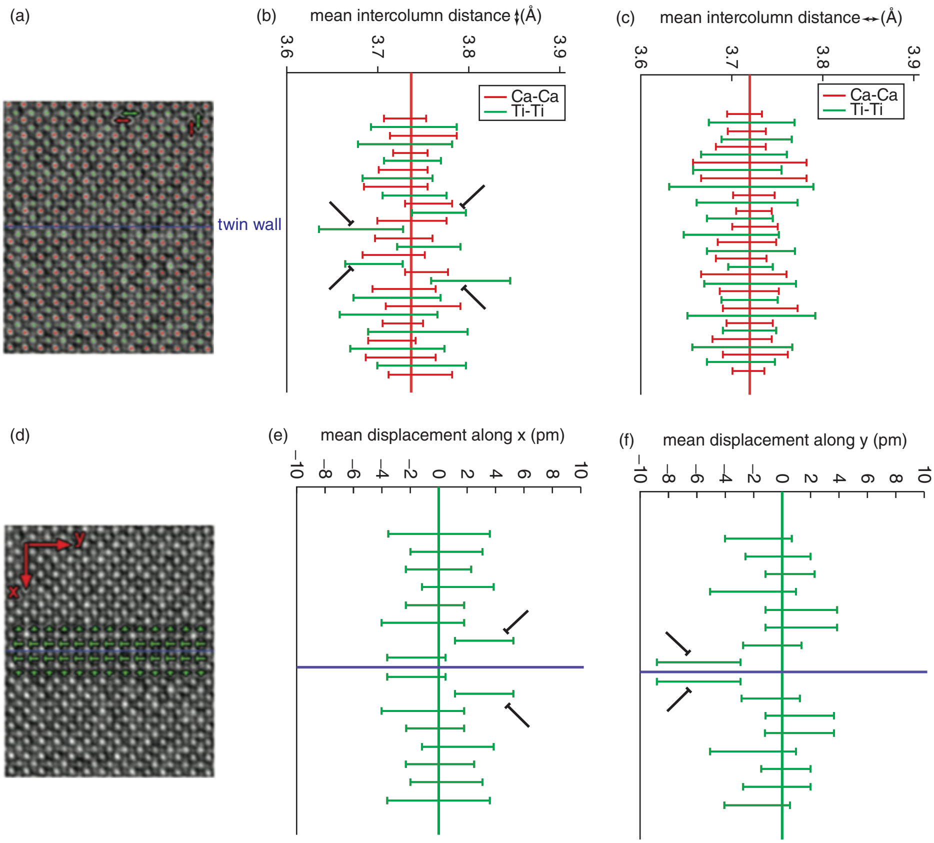

Figure 24.4 *(a) Estimated Ca and Ti atomic column positions shown in red and green, respectively. The horizontal line shows the position of the twin wall. (b) Mean interatomic Ca–Ca and Ti–Ti column distances perpendicular to the twin wall, averaged in the direction parallel with the twin wall, together with their 90% confidence intervals. The vertical line corresponds to the overall mean Ca–Ca interatomic distance. Note the deviations from this line for particular Ti–Ti atomic column distances close to the twin wall (arrows). (c) Mean interatomic Ca–Ca and Ti–Ti column distances parallel with the twin wall, averaged in the direction parallel with the twin wall, together with their 90% confidence intervals. The vertical line corresponds to the overall mean Ca–Ca interatomic distance. No deviations from this line are observed for the Ca–Ca or the Ti–Ti atomic column distances. (d) Mean displacements of the Ti atomic columns from the center of the four neighboring Ca atomic columns and indicated by green arrows. (e and f) Displacements of Ti atomic columns in the x and y directions averaged along and in mirror operation with respect to the twin wall together with their 90% confidence intervals. Reprinted with kind permission from [29], Copyright © 2012 Wiley-VCH Verlag GmbH & Co. KGaA, Weinheim. For a color version of this figure, see color plate section*

was needed, which would not be possible for *ab initio* DFT simulations. Periodic boundary conditions were used in three dimensions. Open boundary conditions in the direction perpendicular to the walls would imply surfaces, which would add unwanted complexity to the problem. Two twin walls are needed to conform to periodic boundary conditions. A

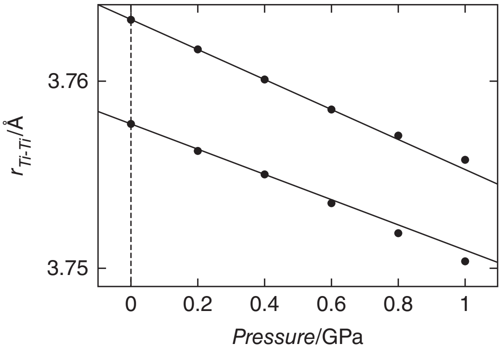

Figure 24.5 *Increased compressibility of the twin wall in CaTiO$_3$. The upper curve (larger Ti–Ti distances) refers to the twin boundaries and shows a shallower slope with increasing uniaxial pressure perpendicular to the twin boundary. This corresponds to a softer elastic response than the bulk (lower curve). Reprinted with permission from [34]. Copyright [2009], AIP Publishing LLC*

supercell was built of 26 unit cells in the direction x perpendicular to the walls, six unit cells in the direction perpendicular to the plane of the twin angle z, and ten unit cells in the bisector of the twin angle y (using the unit cell of the prototypic cubic structure). This gives a total of 7800 atoms. The order parameter Q is a measure of the rotation around the y axis of the oxygen octahedra around each titanium atom, appropriately sign-corrected. The twin wall follows the common $Q \sim \tanh(x/w)$ functional form, which is expected from Landau theory [8]. The wall width lies well within the experimental values as determined previously. In addition to the appearance of polar properties of the walls, an increase in oxygen vacancies was also predicted. The effective self-energy for oxygen vacancies shows that an oxygen vacancy gains ca. 1.1 eV when shifted from the bulk of the material into the twin wall [33]. While this effect is expected from the fact that twin walls in the geological context are known to be decorated by defects, we understand from these calculations that the geometrical requirement for the accommodation of defects may appear negligible, namely ca.1% increase of a lattice spacing in CaTiO$_3$. Such small changes are typical for twin boundaries and other interfaces so that dopants are expected to concentrated in twin boundaries. These localized dopants, on the other hand, can then be used systematically to modify the properties of the walls, for example their conductivity or polarity. Doping with magnetic ions may then lead to magnetic properties of the walls while the same dopants would not necessarily enter the bulk (see Figure 24.5).

24.2.2 Polar Twin Walls in SrTiO$_3$

The polarity of twin boundaries in SrTiO$_3$ provides an additional singularity. The core of the twin walls shows dipolar off-centering of Ti just as in the case of CaTiO$_3$, together with weak off-centering of Sr. The difference stems from the fact that these off-centerings and the position of the twin boundaries are highly frozen in CaTiO$_3$ but highly mobile in SrTiO$_3$ [35–38]. Zykova-Timan and Salje [39] reported that dipole moments in SrTiO$_3$ are thermally activated and commonly switch their orientation (Figure 24.6). The overall

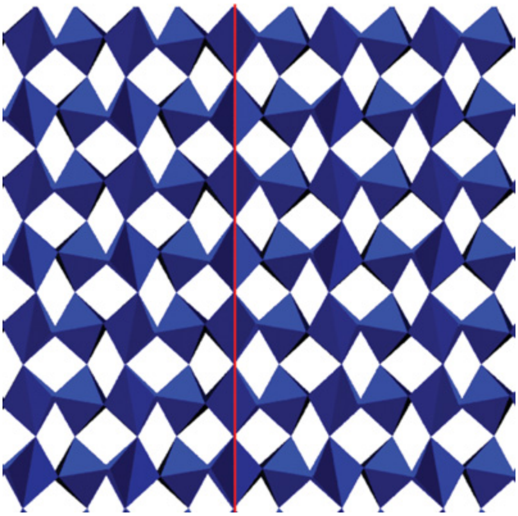

Figure 24.6 Snapshot of the TiO_6 octahedral tilts in the vicinity of the twin wall (vertical red line). Notice the change of the tilting angles across the boundary. Reprinted with permission from [39]. Copyright [2014], AIP Publishing LLC

direction is towards the apex of the twin boundary while the opposite direction also occurs. This reversal is shown in Figure 24.7. Each switch generates a vortex structure between the two opposite dipole directions. These vortexes are hence twin walls inside twin walls and generate a further symmetry breaking so that three processes are involved: the ferroelastic, the ferroelectric, and the vortex symmetry reduction. The symmetry of the system is hence reduced to *P1* rather than the ferroelastic tetragonal symmetry *I4/mcm*.

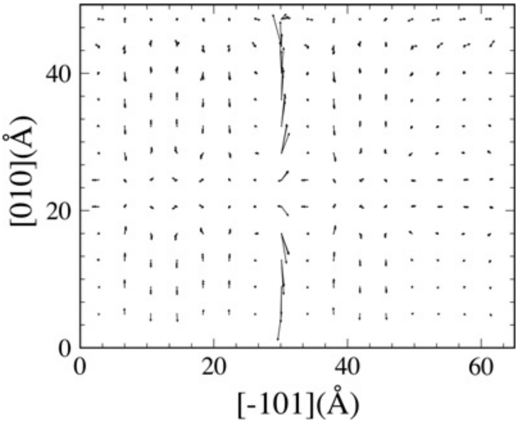

Figure 24.7 In-plane displacements of Ti atoms with respect to the centre of oxygen octahedra. The twin boundary is characterized by the appearance of a vortex. All arrows are amplified by a factor of 20. Reprinted with permission from [39]. Copyright [2014], AIP Publishing LLC

These previously unknown polarization singularities (vortexes) were found very often inside polar $SrTiO_3$ twin boundaries, with pronounced elastic relaxations near the vortex. Usually polarity in twin walls is ferrielectric, whereas vortex excitations lead to true ferroelectricity on a very local scale [39]. As a result, in-plane electric fields can selectively stabilize one of the vortex polarization states and enhance the ability of the walls to move. This behavior can explain the well-known and uniquely high mobility of twin boundaries in $SrTiO_3$. Keeping in mind that nanoscale ferroelectric components are an essential part of possible future memory devices, we envisage a precisely controllable device, where a desired domain wall pattern is manipulated by shifting the vortex position electrically.

The strontium titanate interatomic interactions were modeled by the Buckingham potential, previously parametrized by Akhtar et al. [40]. The corresponding lattice constant was estimated to be within 0.5% of experimentally obtained 3.905 Å at room temperature [39]. By fixing the lattice parameter at the experimental values, we estimated the elastic constants in good correspondence with previous experiments. A twin boundary was created by merging two supercells along the diagonal $[\bar{1}01]$, one with conventional tetragonal a along x and c along z and the other one with short a along z and long c along x. The two structures were rotated by a small angle around the y axis to match the lattice periodicity of the two pieces. The resulting structure was relaxed using steepest descent and further equilibrated in NVT runs for 2 ns at 20 K. The final twin was described in terms of the same tilt order parameter Q and an off-centering distance δ across the twin boundary.

The new phenomenon of switchable polarity in $SrTiO_3$ is not simply due to the appearance of polar displacements in twin boundaries, but the fact that opposing polarities are connected by highly mobile vortexes. Vortexes are totally unrelated to the functional polarity of the walls, which is ferrielectricity, but lead to true ferroelectricity on a very local scale. They should be highly mobile inside each wall and should be easily controlled by an external electric field. In turn, the twin walls are highly mobile under external strain and electric fields [38], causing a rapid change of the dipole moment. An upcoming objective of our research is to model an electric field in simulations to emulate these conditions. A possible application could be in controlled nanoscale memory devices (e.g. non-volatile [41] or reversible electronic switches used in resistive RAM [42]), where a desired domain wall pattern is traced by the vortex position between the electrodes. These new vortex structures have many similarities to the magnetic racetrack arrangement, where magnetic boundaries are shifted inside a magnetic nanowire [43]. The shift of the vortex line can then be monitored electrically (an electric dipole perpendicular to the twin boundary) or magnetically if the velocity of the vortex allows electromagnetic coupling.

24.3 Conducting Twin Boundaries

Hwang and collaborators [9, 44] have systematically investigated interfaces between different perovskite structures where the interfacial carrier concentration relates to the difference in formal chemical charges between the octahedrally coordinated cations, such as Ti^{4+} and Al^{3+} in $LaAlO_3$ and $SrTiO_3$, respectively. While this effect has stimulated a large research effort, high conductivity can also be generated by a much more subtle effect of structural deformation. Typical examples are superconductivity in twin boundaries of WO_3 and high

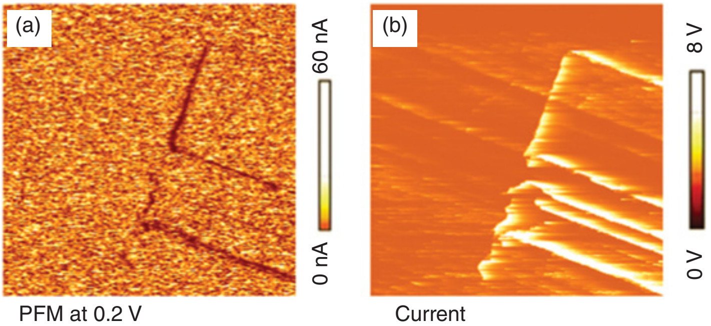

Figure 24.8 *The thickness of the twin boundaries in WO_3 is less than 10 nm with a collapse of the piezoelectric signal in the wall (PFM image) and an increase in conductivity (current image) (after Kim et al., 2010). Reprinted with permission from [4]. Copyright [2010], AIP Publishing LLC*

classic conductivity in multiferroic $BiFeO_3$ [6, 45]. Superconductivity in WO_3 was discovered in 1998 [3, 46] with the introduction of Na and oxygen vacancies in twin walls [5]. The chemical composition of the walls was very slightly modified (e.g. from WO_3 to $WO_{2.95}$), which induced a metal–insulator transition and, at low temperature, led to the appearance of superconductivity in twin walls (Figure 24.8). The highly mobile carriers short-cut the piezoelectric polarization and appear, thus, to destroy the polarity of the twin wall. WO_3 hence inverts the paradigm discussed so far: the high wall conductivity generates non-polar twin walls in a polar matrix while $CaTiO_3$ and $SrTiO_3$ show polar twin walls in non-polar matrices.

A careful analysis of the images in Figure 24.8 also shows that the thickness of the twin boundaries (i.e. the highly conducting sheets) is less than 10 nm [4]. It is unclear whether the role of defects is to introduce the necessary carriers or whether they stabilize the superconducting tetragonal $P\text{-}42_1m$ phase inside the matrix of the low-temperature ferroelectric Pc phase. No systematic studies in most materials have been undertaken to identify the level of defects in twin walls so that we simply do not know whether defects are really required to stabilize the high conductivity in WO_3 or $BiFeO_3$. The crystal structures of the two phases Pc (bulk) and $P\text{-}42_1m$ (twin wall) were reported by Aird et al. [46] and Salje et al. [47]. The superconducting phase has an inherently sheet character: the WO_3 layers are very flat and two-dimensional while the distance between the oxygen is very small. In contrast to the superconducting phase we find the ferroelectric Pc phase to show buckling of the WO_3 layers and highly asymmetric W–O distances along the ferroelectric c-direction. We can now construct a hypothetical twin boundary of the monoclinic Pc phase where the core of the twin boundary has the structure of the superconducting tetragonal $P\text{-}42_1m$ phase. The fit between the interatomic distances in both phases is excellent, which indicates that the tetragonal core of the monoclinic twin is a reasonable proposition. This would link superconductivity to the structural configuration of WO_3 rather than (or in addition to) any chemical modifications. In either case the twin configuration determines the positions of the superconducting layers, which means that nanopatterning of the superconducting structure is possible via the patterning of the twin boundaries (and subsequent doping if needed).

Tungsten oxide, WO_3, and its substoichiometric derivatives are particularly well suited for this research because they display metal–insulator transitions while they remain thermodynamically stable compounds. They display a multitude of structural phase transitions [48] mainly related to shape changes of the WO_6 octahedra and their rotations within an octahedral network. Several of these phases are polar and ferroelectric while the majority of the phase contains inversion centres and are hence non-polar. WO_3 easily releases oxygen and incorporates alkali ions and hydrogen. The facility with which oxygen is released under reducing conditions is less related to the chemical bonding of oxygen but rather to the low energy required to transfer the valence state of localized surplus electrons on the W^{6+} sites to W^{5+}. This tendency to form W^{5+} states near surfaces was directly confirmed by XPS/UPS experiments [49] and indirectly by STM imaging [4]. These W^{5+} states are not localized, however, and form bipolarons in the low-temperature phase [50]. Similarly, conducting twin walls were observed in $BiFeO_3$ [45], where the origin of the conductivity and the structural properties are less established. Other materials equally show enhanced or reduced conductivity in twin boundaries, antiphase boundaries, interfaces, and grain boundaries so that the possibility to design twin boundaries with specific dielectric properties is probably the most advanced activity in domain boundary engineering.

24.4 Thermal Conductivity

In multiferroic materials a massive new design opportunity exists: external fields can change the number of phonon barriers if these barriers are related to multiferroic twinning. All current designs use topological defects inside the nanomaterials (e.g. grain boundaries, kinks) that cannot be removed or generated while the nanodevice is active. Multiferroic materials, martensite wires, and ferroelastic materials have exactly the required properties because their twin density can be changed by strain, electric, or magnetic fields. Within a multiferroic hysteresis, twinning and de-twinning are completely reversible and the twin density depends in most cases only on the value of the applied field. The key connection with the induced variation of the thermal conductivity is that twin boundaries perpendicular to the heat flux reduce the thermal conductivity and this reduction is proportional to the density of twin boundaries. Switchable domain boundaries can therefore replace the previously used topological defects and lead to new, smart designs of thermal bridges, heat sinks, and energy converters, to name a few.

Li et al. [51] investigated coherent twin boundaries because they are most easily manipulated mechanically or by electric and magnetic fields. Previous work has already shown that the morphologies and properties of twin patterns (TPs) can be changed greatly by mechanical deformation. The thermal conductivity of nanomaterials was found to depend sensitively on the number of twin boundaries with an orientation perpendicular to the heat flow. They represent phonon barriers, which directly reduce the thermal conductivity κ_{TC}. Applied fields (strain, electrical, magnetic) reversibly change the twin density, which, in turn, changes the thermal conductivity. We modeled this phenomenon by non-equilibrium molecular dynamics simulations and showed that tuning $1/\kappa_{TC}$ between 0.008 and 0.024 mK W^{-1} via manipulation of the twin morphology and twin density is within the experimentally achievable range of multiferroic, ferroelastic, and martensitic materials (Figure 24.9).

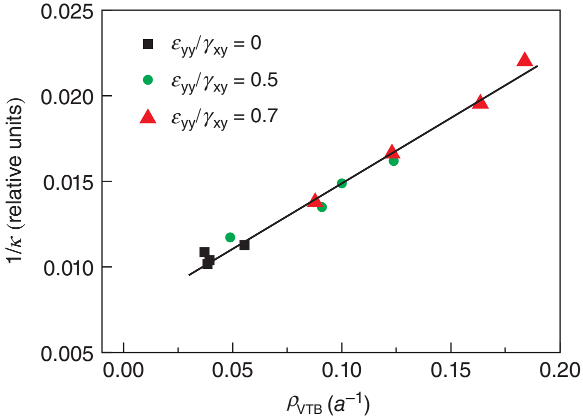

Figure 24.9 *The linear response of the inverse thermal conductivity* $1/\kappa_{TC}$ *with the density* (ρ_{VTB}) *of twin boundaries perpendicular to the heat flux. Reprinted by permission from Macmillan Publishers Ltd: [Scientific Reports] [52]. Copyright © 2014*

24.5 Landau Theory of Coupled Order Parameters in Domain Walls

A good way to capture the structural changes inside domain boundaries is to apply the Landau–Ginzburg theory. A good starting point is the textbook on ferroelastic and co-elastic crystals [53] and a recent didactic summary [54]. The symmetry constraints, which are inherent in Landau theory, allow us to define the structural order parameter that initiates the domain boundary to exist. In the case of transformation twins, the order parameter is the strain and the phase transitions in the case of mobile twin boundaries under external stress are ferroelastic. In case of $CaTiO_3$, an extensive Landau analysis shows the intrinsic instabilities to form polar twin boundaries [27, 28]. More generally, any ferroelastic phase can form twin boundaries where the Landau potential for the strain or strain-related order parameter ($Q \sim u =$ strain) is:

$$G(Q, T, P) = 1/2A\theta_S(\coth\theta_S/T - \coth\theta_S/T_C)Q^2 + 1/4BQ^4 + 1/6CQ^6 + 1/2g\,(\nabla Q)^2 + G(coupling) \qquad (24.1)$$

The first terms lead to the formation of kinks in the order parameter, which for second-order phase transitions ($C = 0$, $B > 0$) has the simple solution with x perpendicular to the twin wall:

$$Q = Q_o \tanh(x/w) \qquad (24.2)$$

where Q_o is the equilibrium value of the order parameter (strain [55]) in the bulk and w is the thickness of the twin wall. This solution is modified when the other terms are considered. The most simple case is a coupling between two second-order transitions in e and P with biquadratic coupling between them:

$$G(coupling) = \lambda Q^2 P^2 \qquad (24.3)$$

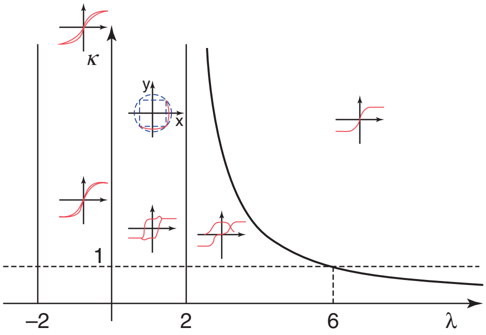

Figure 24.10 Phase diagram of two biquadratically coupled order parameters. The profiles show the parameters Q and P, and the thick lines define the phase boundaries. The parameters λ and κ are the normalized coupling strength and the ratio of the Ginzburg dispersion parameters gQ/gP. A typical situation where coupling originates a second (e.g. functional) property in the domain wall is shown in the figure. From [14]. © IOP Publishing. Reproduced by permission of IOP Publishing. All rights reserved

This coupling is always symmetry allowed while other coupling terms only apply to specific symmetries of the order parameters; for example Salje and Carpenter [56], Salje and Devarajan [57], and Conti et al. [14]) derived the general phase diagram of the wall profiles for a biquadratically coupled order parameter (Figure 24.10).

A simple physical picture for the case in Figure 24.11 emerges when the ferroelastic order parameter $Q = u$ changes sign and becomes zero in the middle of the twin wall. In this case, the coupling energy vanishes and the self-energy of the second-order parameter becomes the solution of the uncoupled Landau potential for P. If this energy is negative (stable) then we will have the generic case where any kink in Q will lead to a breather-like profile in P. The detailed profile is then a solution of the minimization of the Gibbs free energy; the analytical solutions for our case of a biquadratic coupling energy is given

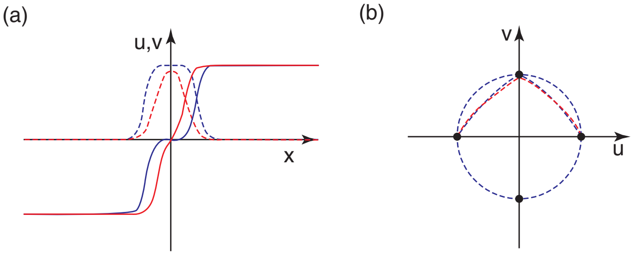

Figure 24.11 Optimal interface for $\lambda = 4$, $\kappa = 1$ (black), and $\kappa = 2$ (gray). The second set of parameters lies on the curve $\lambda = 2 + 4/\kappa$. The optimal paths in the ($Q = u$, $P = v$) plane are not the union of two straight segments. Non-linear trajectories have been called "chiral" because the direction of the renormalized order parameter rotates when it propagates through the interfacial regime. From [14]. © IOP Publishing. Reproduced by permission of IOP Publishing. All rights reserved

by Conti et al. [14]. Similar arguments apply when external forces are applied; the role of stress-induced transitions was discussed by Stepkova et al. [58]. In all these cases new structural features can appear inside the domain wall, which otherwise do not exist in the bulk. These features are related to topological perturbations, the key parameter becomes the "chirality" of the domain wall, a term that was introduced by Houchmanzadeh et al. [32] to describe the rotation of the total order parameter ($= P + Q$) in the order parameter vector space.

24.6 Chiral Twin Walls

It took the genius of Landau to show that hopelessly complicated phase transitions with $3N$ local displacements, spin variables, or other physical parameters can be condensed into a simple pattern function $F(x, y, z)$ multiplied by an amplitude function, which operates in three or less dimensions. Its applications and physical meaning are described in a simple model for ferroelastic materials by Salje et al. [17]. This amplitude is, today, the celebrated "order parameter" of the transition, which is described by the rules of statistical mechanics. The new structural element due to coupling is the chirality of the domain wall in order parameter space. Chirality for twin walls as a generalized concept was first introduced by Houchmanzadeh et al. [32, 59] and evaluated in detail by Conti et al. [14] with concrete examples by Stepkova et al. [58]. The effect of external forces on chiral walls was first described indirectly by Magyari and Thomas [60] in a pioneering paper where they showed that magnetic walls are linearly stable for any strength H of the applied field below a critical value H_o, where it connects to an unstable wall configuration with negative Doering mass. The critical field H_o is lower than the existence limit H_w of the solitary travelling-wave-type domain wall solutions, and represents the threshold of the field region $H_o < H < H_w$ where negative wall mobilities occur. The instability at $H = H_o$ is associated with a non-uniform localized relaxation mode ("corrugating mode") of the plane domain wall. If coupling to the external circuit is taken into account, negative-mobility walls also become unstable against uniform perturbations for sufficiently small circuit resistance. A key finding is that the local state vector space spanned by the coupled-order parameters rotates in the order parameter vector space near the twin wall while the state of the bulk is described by an invariant vector with no spatial dependency. Thomas and his collaborators implicitly used this concept to expand the order parameter vector space of the bulk [53] to domain walls and showed that moving domain walls change their profile in a much more complex way than predicted by simple theories of solitonic waves. The internal structure of the moving wall becomes explicitly field dependent. This effect has never been observed experimentally but it could entail functionalities of moving walls that do not exist in static walls or that moving walls lose their functionality.

In the case of a one-dimensional order parameter (Figure 24.12), the bulk can be described by a scalar quantity (Figure 24.12(c)) while walls need vectors whereby one component remains the bulk-order parameter. The other components relate to the "hidden" degrees of freedom, which become active only in the domain wall. The state vector is then the vector sum of the bulk-order parameter and the hidden-order parameter vectors. This vector is two-dimensional and its progression involves a rotation because the bulk-order parameter and the wall parameters will not have the same change of sign (single chirality)

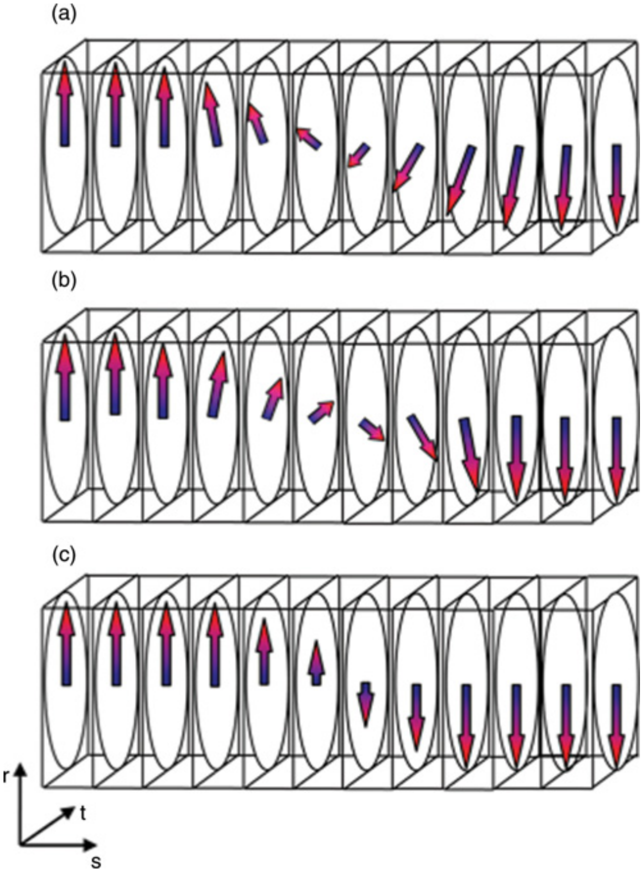

Figure 24.12 *Chirality of two coupled-order one-dimensional parameters. The order parameter vector space is r, t where r is the order parameter of the bulk and t is the order parameter of the wall. The Bloch-type structure (a and b) have positive or negative chirality. In contrast to magnetic Bloch walls, the chiral walls do not necessarily conserve the magnitude of the local vectorial state order parameter. The bulk order parameter transforms like an Ising wall, which is not chiral (c). From [58]. © IOP Publishing. Reproduced by permission of IOP Publishing. All rights reserved*

or not the same space dependence (bichirality) (Figure 24.12(a) and (b) for a single chirality). Stepkova et al. [58] showed that in rhombohedral $BaTiO_3$, both types of 180° domain walls can be stabilized with the bulk order parameter being the ferroelectric polarization. If a twin wall has single chirality but spatially separate with rotations in the clockwise and counterclockwise directions, they will meet in lines where this chirality will be compensated. Houchmazadeh et al. [32] pointed out that these lines (Bloch lines in analogy to magnetic walls) will deform the twin wall locally so that they represent domain boundaries inside a twin wall.

Coupling between chiral magnetic walls and non-chiral twin walls have been reported by Kasama et al. [61]. Their very advanced observation of ferrimagnetic/ferroelastic domain

Figure 24.13 Measured structure factor of a typical tweed structure with high elastic anisotropy (Locherer et al., 1996 [65]). Such structures are precursors of the ferroelastic microstructure in the paraelastic phase. The twin microstructure nucleates under thermal quench from the tweed structure in elastically anisotropic materials. Reproduced with permission from [65], The Royal Society (1996)

interactions in magnetite below the Verwey transition provides a new foundation for the interpretation of the low-temperature magnetic behavior of magnetite, where a strong interaction between twin boundaries and magnetic domain boundaries occurs in this multiferroic material. Twin walls play in this case a specific role in the pinning mechanism of magnetic walls (Figure 24.13). Two types of twin need to be distinguished: twin structures associated with 90° changes in the [001] m easy axis direction play a dominant role in determining low-temperature magnetic properties, while needle twins impede the motion of magnetic domain walls. Twins that produce a 90° rotation of the ferrimagnetic easy axis without significant lattice distortion allow the formation of nanometer-scale magnetic domain structures that are defined strictly by the underlying crystallography. These observations raise the possibility that ultra-fine-scale twin structures may form readily in submicrometer grains and even single-domain grains of magnetite – the dominant carriers of paleomagnetic remanence. Such fine-scale twin domains may be hard to detect microscopically due to the lack of diffraction contrast (in Lorentz microscopy) between them, but their presence may be essential to explain the unusual hysteretic properties of magnetite observed below the transition [62–64]. In such grains, the non-uniform magnetization state above the Verwey transition may provide a template for the formation of such twin boundaries below the transition.

24.7 High Wall Densities

Two alternative routes are usually taken to produce materials with high twin wall densities. Firstly, domain structures nucleate in order–disorder systems when a sample is quenched rapidly from a high-temperature paraelastic phase into a ferroelastic phase. The reason for the formation of microstructures originates from the time evolution of the initial state, which contains thermal fluctuations of the local-order parameter, and the subsequent nucleation of a coarser microstructure. The second approach is to distort a single-domain crystal by shear strain in the low-temperature ferroelastic phase. In this way, a large number of long-lived metastable states are generated kinetically. Experimentally, thin films of one ferroelastic material are deposited on to another ferroelastic material at high temperatures. When the device is cooled to room temperature, the template will shear and impose this shear to the thin film. When this shear strain surpasses the yield strain, the thin film will spontaneously twin with a high twin boundary density. This pattern is then essentially stable under further shear. Driven systems [66] were used experimentally to generate high twin densities [67,68].

When disorder is generated by structural rather than microstructural phenomena, one requires a source of disorder, which is commonly provided by local atomic disorder. In our case, we do not consider random fields, but start from uniform ground states. In this case, quench will freeze in some disorder in the para phase, which represents the initial state in the ferroelastic phase from where the microstructure evolves. Bratkovsky et al. [69] derived the structure factor of the displacement–displacement correlation in the simple case for $T > T_C$ and Ornstein–Zernike fluctuations:

$$S_k \approx \left[1/r_c^2 + a^2 \cos^2\theta + b^2 \sin^4\theta \sin^2 2\phi + gk^2\right]^{-1} \tag{24.4}$$

This function is a four-armed starfish in three dimensions and represents the diffuse diffraction pattern in Figure 24.13 [65, 70–73]. The equivalent microstructure is tweed, which evolves into stripe patterns [1]. The kinetic evolution is then, for the quench experiment, the gradual change from the star to a dog's bone. Simple energy minimization of the relaxation in the stripe pattern for a finite experiment, the gradual change from the star to the dog's bone structure, and the interfacial energy of the twin walls ($\sim g$) lead to the Kittel law:

$$w \approx L^{1/2} \tag{24.5}$$

where w is the distance between the twin walls and L is the sample size.

The alternative way to produce highly twinned materials is by strain-induced microstructures ($\sim$ cold shearing) which differs from the thermally generated twinning by several characterisitc features. The characteristics of the strained twinning were explored in a simple model by Salje et al. [17] and Ding et al. [18]. They simulated the shear instability in a two-dimensional monoatomic lattice. The second nearest neighbor interactions were adjusted to yield a ground state, a sheared lattice with shear angles of 4°. The external driver is a shear strain at the upper and lower edge of the sample, which stabilizes one domain orientation (+4) and destabilizes the other (–4). Increasing strain is initially compensated by an elastic deformation until a threshold is reached where the unstable domain decomposes into a multitude of twinned microdomains (Figure 24.14). The stress–strain curves and the domain patterns depend sensitively on the size of the system and on the elastic moduli of the sample. They tested a hard material (nearest neighbor spring constant $k = 20$) and a soft material ($k = 10$). The hard material displays a small number of vertical domains and few horizontal domain walls (Figure 24.14, right panel). The soft material has a much more complex domain pattern with a large number of vertical walls and some horizontal walls (Figure 24.14, left panel) so that it was concluded that soft materials have a stronger propensity to form complex microstructures than hard materials.

The strain-induced twinning leads to very stable configurations where the domain boundaries inside the unstable (plastic) region hardly change under further strain, and all dynamics

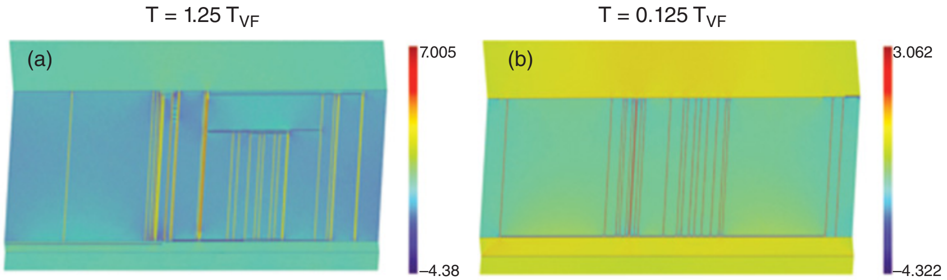

hard material with simple twin configuration

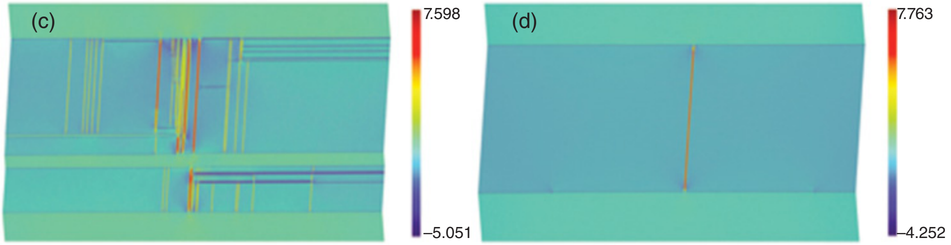

hard material with sandwich twin configuration

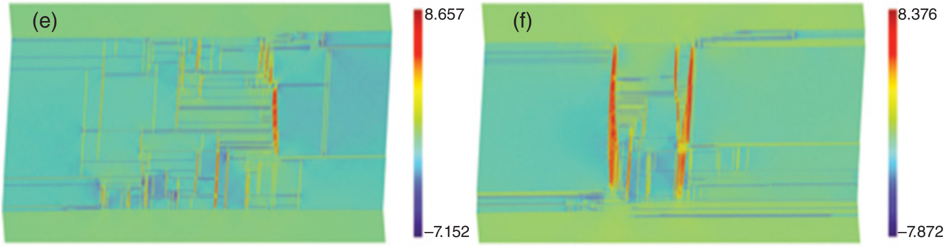

soft material with sandwich twin configuration

Figure 24.14 *Twin patterns at strains larger than the yield strain (in the plastic regime). Shown are domains formed at high temperature (a, c, and e) and low temperature (b, d, and f). Here (a) and (b) show hard materials with simple twin configuration; (c) and (d) show those for a hard material with a sandwich twin configuration, and (e) and (f) are for a soft material. Reprinted with permission from [22]. Copyright (2013) American Physical Society. For a color version of this figure, see color plate section*

are dominated by the progressing front of the large stable domains on the top and the bottom of the sample. A convenient parameter to characterize "complexity" is the number density of intersections between different twin walls. We call these intersections, in accordance with previous experimental observations, "junctions", so that the junction density becomes the key parameter to describe the complexity of our twin patterns. Different tendencies were found for hard and soft materials. The hard materials have fewer junctions and the junction density disappears for small systems when the sample cannot support complex patterns. In contrast to hard materials, we find that soft materials contain generally more complex twin patterns with higher junction densities. The junction density increases with smaller system sizes where the strong relaxation of the systems allows the formation of junctions, even for

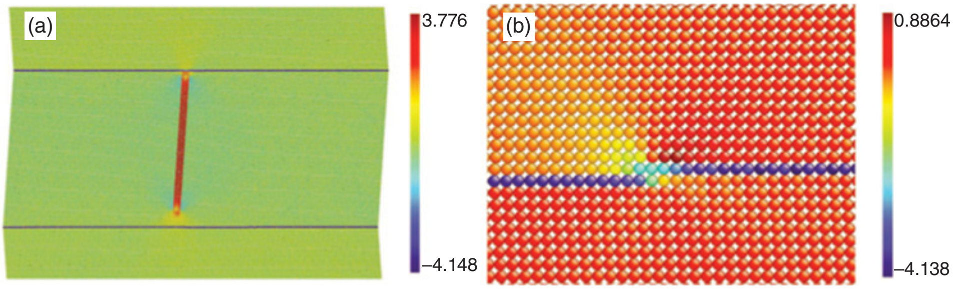

Figure 24.15 Sheared unit cell of a driven system. (a) The single needle domain (red) connects the two horizontal twin boundaries (blue) at the initial stage and then retracts from the lower twin boundary. (b) The kink is seen at the single blue domain wall. It moves to the left under applied external strain. Reprinted with kind permission from [74], Copyright © 2013 Wiley-VCH Verlag GmbH & Co. KGaA, Weinheim. For a color version of this figure, see color plate section

very small samples, before they collapse for systems with fewer than 100 atoms. This shows that the desired materials properties for domain boundary engineering with high boundary and junction densities are best achieved for soft materials. Furthermore, small system sizes do not impede the formation of twin walls but, on the contrary, enable them.

Two elementary dynamic excitations of a domain pattern under weak external strain were found. The first excitation is the progression and retraction of needle domains in Figure 24.15(a) [74]. These needles are attracted to the horizontal twin walls and shrink catastrophically when the needle domain becomes shorter than a critical length. This result mirrors those of earlier theories based on elastic interactions by Novak et al. [75]. Experimental observations of progressing needle domain were reported by Harrison and Salje [67, 76].

The second basic movement is the lateral progression of a twin wall. This mechanism was found to be related to moving kink-excitations in the twin wall (Figure 24.15(b)). Experimentally, such movements were observed by surface techniques (AFM) by Benichou et al. [77] and Faran et al. [78].

24.8 Summary

The functionality of twin boundaries can involve polarity and ferroelectricity or, as in the case of WO_3, the destruction of these properties. A unified description is provided by Landau theory of coupled-order parameters and the emerging property of chiral twin walls. In this paper, only static functional twin boundaries were discussed. Moving twin boundaries are expected to display, under specific boundary conditions and applied fields, another raft of functionalities, which are hitherto unknown. Only a few such functional domain boundaries are known so far but many more may be discovered over the next decade. Future research is needed to explore two sets of open questions: (1) how can functional twin boundaries be electronically addressed in electronic devices and (2) how do dynamical properties modify the static functionalities? We are at the beginning of a major research effort and not much is known about its eventual outcome and the potential industrial products that can be produced using the concept of domain boundary engineering.

Acknowledgment

The work was supported by EPSRC (EP/K009702/1).

References

(1) Salje, E.K.H. (2010) Multiferroic domain boundaries as active memory devices: trajectories towards domain boundary engineering. *Chem. Phys. Chem.*, **11**, 940–950.

(2) Salje, E.K.H. and Zhang, H.L. (2009) Domain boundary engineering. *Phase Transitions*, **82**, 452–469.

(3) Aird, A. and E.K.H. Salje (1998) Sheet superconductivity in twin walls: experimental evidence of WO_{3-x}. *Journal of Physics: Condensed Matter*, **10**, L377–L380.

(4) Kim, Y., Alexe, M., and Salje, E.K.H. (2010) Nanoscale properties of thin twin walls and surface layers in pizeoelectric WO_{3-x}. *Applied Physics Letters*, **96**, art. no. 032904.

(5) Aird, A. and Salje, E.K.H. (2000) Enhanced reactivity of domain walls in WO_3. *European Physical Journal B*, **15**, 205–210.

(6) Seidel, J., Maksymovych, P., Batra, Y., et al. (2010) Domain wall conductivity in La-doped $BiFeO_3$. *Physical Review Letters*, **105**, art. no. 197603.

(7) Calleja, M., Dove, M.T., and Salje, E.K.H. (2001) Anisotropic ionic transport in quartz: the effect of twin boundaries. *Journal of Physics: Condensed Matter*, **13**, 9445–9454.

(8) Calleja, M., Dove, M.T., and Salje, E.K.H. (2003) Trapping of oxygen vacancies on twin walls of $CaTiO_3$: a computer simulation study. *Journal of Physics: Condensed Matter*, **15**, 2301–2307.

(9) Ohtomo, A. and Hwang, H.Y. (2004) A highly-mobile electron gas at the $LaAlO_3/SrTiO_3$ heterointerface. *Nature*, **427**, 423–426.

(10) Pauli, S.A., Leake, S.J., Delley,B., et al. (2011) Evolution of the interfacial structure of $LaAlO_3$ and $SrTiO_3$. *Physical Review Letters*, **106**, art. no. 036101.

(11) Huijben, M., Rijnders, G., Blank, D.H.A., et al. (2006) Electronically coupled complementary interfaces between perovskite band insulators. *Nature Materials*, **5**, 556–560 (2006).

(12) Herranz, G., Basletić, M., Bibes, M., e al. (2006) Co-doped $(La,Sr)TiO_3$: a high Curie temperature diluted magnetic system with large spin polarization. *Physical Review Letters*, **96**, art. no. 027207.

(13) Kalisky, B., Kirtley, J.R., Analytis, J.G., et al. (2011) Behavior of vortices near twin boundaries in underdoped $Ba(Fe_{1-x}Co_x)_2As_{x-2}$. *Physical Review B*, **83**, art. no. 064511.

(14) Conti, S., Muller, S., Poliakovsky, A., and Salje, E.K.H. (2011) Coupling of order parameters, chirality, and interfacial structures in multiferroic materials. *Journal of Physics: Condensed Matter*, **23**, art. no. 142203.

(15) Lubk, A., Gemming, S., and Spaldin, N.A. (2009) First-principles study of ferroelectric domain walls in multiferroic bismuth ferrite. *Physical Review B*, **80**, art. no. 104110).

(16) Lottermoser, T. and Fiebig, M. (2004) Magnetoelectric behavior of domain walls in multiferroic $HoMnO_3$. *Physical Review B*, **70**, art. no. 220407.

(17) Salje, E.K.H., Ding, X.D., Zhao, Z., and Lookman, T. (2012) How to generate high twin densities in nano- ferroics: thermal quench and low temperature shear. *Applied Physics Letters*, **100**, art. no. 222905.

(18) Ding, X., Zhao, Z., Lookman, T., et al. (2012) High junction and twin boundary densities in driven dynamical systems. *Advanced Materials*, **24**, 5385–5389.

(19) Salje, E.K.H., Ding, X.D., and Aktas, O. (2014) Domain glass. *Physica Status Solidi B*, **251**, 2061–2066.

(20) Sillescu, H. (1999) Heterogeneity at the glass transition: a review. *Journal of Non-crystalline Solids*, **243**, 81–108.

(21) Vugmeister, B.E. and Glinchuk, M.D. (1990) Dipole glass and ferroelectricity in random-site electric-dipole systems. *Review of Modern Physics*, **62**, 993–1026.

(22) Ding, X., Lookman, T., Zhao, Z., et al. (2013) Dynamically strained ferroelastics: statistical behavior in elastic and plastic regimes. *Physical Review B*, **87**, art. no. 094109.

(23) Zhao, Z., Ding, X., Sun, J., and Salje, E.K.H. (2014) Thermal and athermal crackling noise in ferroelastic nanostructures. *Journal of Physics: Condensed Matter*, **26**,art. no. 142201.

(24) Guan, P., Chen, M., and Egami, T. (2010) Stress-temperature scaling for steady-state flow in metallic glasses. *Physical Review Letters*, **104**, art. no. 205701.

(25) Goncalves-Ferreira, L., Redfern, S.A.T., Artacho, E., and Salje, E.K.H. (2008) Ferrielectric twin walls in CaTiO$_3$. *Physical Review Letters*, **101**, art. no. 097602.

(26) Lee, W.T., Salje, E.K.H., Goncalves-Ferreira, L., et al. (2006) Intrinsic activation energy for twin-wall motion in the ferroelastic perovskite CaTiO$_{3.}$ *Physical Review B*, **73**, art. n° 214110.

(27) Morozovska, A.N., Eliseev, E.A., Glinchuk, M.D. et al. (2012) Interfacial polarization and pyroelectricity in antiferrodistortive structures induced by a flexoelectric effect and rotostriction. *Physical Review B*, **85**, art. no. 094107.

(28) Gu, Y., Rabe, K., Bousquet, E., et al. (2012) Phenomenological thermodynamic potential for CaTiO$_3$ single crystals. *Physical Review B*, **85**, art. no. 064117.

(29) Van Aert, S., Turner, S., Delville, R., et al. (2012) Direct observation of ferrielectricity at ferroelastic domain boundaries in CaTiO$_3$ by electron microscopy. *Advanced Materials*, **24**, 523–527.

(30) Eitel, R. and Randall, C.A. (2007) Octahedral tilt-suppression of ferroelectric domain wall dynamics and the associated piezoelectric activity in Pb(Zr,Ti)O$_{x\text{-}3}$. *Physical Review B*, **75**, art. no. 094106.

(31) Petzelt, J., Ostapchuk, T., Gregora, I., et al. (2001) Dielectric, infrared, and Raman response of undoped SrTiO$_3$ ceramics: evidence of polar grain boundaries. *Physical Review B*, **64**, art. no. 184111.

(32) Houchmanzadeh, B., Lajzerowicz, J., and Salje, E.K.H. (1991) Order parameter coupling and chirality of domain walls. *Journal of Physics: Condensed Matter*, **3**, 5163–5169.

(33) Goncalves-Ferreira, L., Redfern, S.A.T., Artacho, E., et al. (2010) Trapping of oxygen vacancies in the twin walls of perovskite. *Physical Review B*, **81**,art. no. 024109.

(34) Goncalves-Ferreira, L, Redfern, S.A.T., Artacho, E., and Salje, E.K.H. (2009) The intrinsic elasticity of twin walls: ferrielectric twin walls in ferroelastic CaTiO$_3$. *Applied Physics Letters*, **94**, art. no. 081903.

(35) Salje, E.K.H., Carpenter, M.A., Nataf, G.F., et al. (2013) Elastic excitations in $BaTiO_3$ single crystals and ceramics: mobile domain boundaries and polar nanoregions observed by resonant ultrasonic spectroscopy. *Physical Review B*, **87**, art. no. 014106.

(36) Kityk, A.V., Schranz, W., Sondergeld, P., et al. (2000) Low-frequency superelasticity and nonlinear elastic behavior of $SrTiO_3$ crystals. *Physical Review B*, **61**, 946–956.

(37) Scott, J.F., Salje, E.K.H., and Carpenter, M.A. (2012) Domain wall damping and elastic softening in $SrTiO_3$: evidence for polar twin walls. *Physical Review Letters*, **109**, art. no. 187601.

(38) Salje, E.K.H., Aktas, O., Carpenter, M.A., et al. (2013) Domains within domains and walls within walls: evidence for polar domains in cryogenic $SrTiO_3$. *Physical Review Letters*, **111**, art. no. 247603.

(39) Zykova-Timan, T. and Salje, E.K.H. (2014) Highly mobile vortex structures inside polar twin boundaries in $SrTiO_3$. *Applied Physics Letters*, **104**, art. no. 082907.

(40) Akhtar, M.J., Akhtar, Z., Jackson, R.A., and Catlow, C.R.A. (1995) Computer simulation studies of strontium titanate. *Journal of the American Ceramic Society*, **78**, 421–428.

(41) Zhang, J.X., Xiang, B., He, Q., et al. (2011) Large field-induced strains in a lead-free piezoelectric material. *Nature Nanotechnology*, **6**, 97–101.

(42) Menke, T., Dittmann, R., Meuffels, P., et al. (2009) Impact of the electroforming process on the device stability of epitaxial Fe-doped $SrTiO_3$ resistive switching cells. *Journal of Applied Physics*, **106**, art. no. 114507.

(43) Parkin, S.S.P., Hayashi, M., and Thomas, L. (2008) Magnetic domain-wall racetrack memory. *Science*, **320**, 190–194.

(44) Hwang, H.Y., Iwasa, Y., Kawasaki, M., et al. (2012) Emergent phenomena at oxide interfaces. *Nature Materials*, **11**, 103–113.

(45) Seidel, J., Martin, L., He, Q., et al. (2009) Conduction at domain walls in oxide multiferroics. *Nature Materials*, **8**, 229–234.

(46) Aird, A., Domeneghetti, M.C., Mazzi, F., et al. (1998) Sheet superconductivity in $WO_{3\text{-}x}$: crystal structure of the tetragonal matrix. *Journal of Physics: Condensed Matter*, **10**, L569–L574.

(47) Salje, E.K.H., Rehmann, S., Pobell, F., et al. (1997) Crystal structure and paramagnetic behavior of epsilon-$WO_{3\text{-}x}$. *Journal of Physics: Condensed Matter*, **9**, 6563–6577.

(48) Locherer, K.R., Swainson, I.P., and Salje, E.K.H. (1999) Phase transitions in tungsten trioxide at high temperatures – a new look. *Journal of Physics: Condensed Matter*, **11**, 6737–6756.

(49) Salje, E.K.H., Carley, A.F., and Roberts, M.W. (1979) Effect of reduction and temperature on the electronic core levels of tungsten and molybdenum in WO_3 and $W_xMo_{1\text{-}x}O_3$ – photoelectron spectroscopy study. *Journal of Solid State Chemistry*, **29**, 237–251.

(50) Schirmer, O.F. and Salje, E.K.H., (2001) Conducting bipolarons in low-temperature crystalline $WO_{3\text{-x}}$. *Journal of Physics: Condensed Matter*, **13**, 1067–1072.

(51) Li, S., Ding, X., Ren, J. et al. (arxiv. 1310.2879) Mechanical controlled thermal switch and hysteresis with domain boundary engineered phonon transport.

(52) Li, S., Ding, X., Ren, J. et al. (2014) Strain-controlled thermal conductivity in ferroic twinned films. *Scientific Reports*, **4**, art. n° 6375.

(53) Salje, E.K.H. (1993) *Phase Transitions in Ferroelastic and Co-elastic Crystals*, Cambridge University Press, Cambridge.

(54) Salje, E.K.H. (2012) Ferroelastic materials. *Annual Review of Materials Research*, **42**, 265–283.

(55) Carpenter, M.A., Salje, E.K.H., and Graeme-Barber, A. (1998). *European Journal of Mineralogy*, **10**, 621–691.

(56) Salje, E.K.H. and Carpenter, M.A. (2011) Linear-qudratic order parameter coupling and multiferroic phase transitions. *Journal of Physics: Condensed Matter*, **23**, art. no. 462202.

(57) Salje, E.K.H. and Devarajan, V (1986) Phase transitions in systems with strain-induced coupling between two order parameters. *Phase Transitions*, **6**, 235–247.

(58) Stepkova, V., Marton, P., and Hlinka, J. (2012) Stress-induced phase transition in ferroelectric domain walls of $BaTiO_3$. *Journal of Physics: Condensed Matter*, **24**, art. no. 212201.

(59) Houchmandzadeh, B., Lajzerowicz, J., and Salje, E.K.H. (1992) Interfaces and ripple states in ferroelastic crystals – a simple-model. *Phase Transitions*, **38**, 77–87.

(60) Magyari, E. and Thomas, H. (1982) Instabilities in the classical Heisenberg chain. *Journal of Physics C: Solid State Physics*, **15**, L333–336.

(61) Kasama, T., Church, N.S., Feinberg, J.M., et al. (2010) Direct observation of ferrimagnetic/ferroelastic domain interactions in magnetite below the Verwey transition. *Earth and Planetary Science Letters*, **297**, 10–17.

(62) Smirnov, A.V. (2006) Low-temperature magnetic properties of magnetite using first-order reversal curve analysis: Implications for the pseudo-single-domain state. *Geochemistry Geophysics Geosystems*, **7**, art. no. Q11011.

(63) Smirnov, A.V. (2007) Effect of the magnetic field applied during cooling on magnetic hysteresis in the low-temperature phase of magnetite: first-order reversal curve (FORC) analysis. *Geochemistry Geophysics Geosystems*, **8**, art. no. Q08005.

(64) Kosterov, A. and Fabian, K. (2008) Twinning control of magnetic properties of multidomain magnetite below the Verwey transition revealed by measurements on individual particles. *Geophysical Journal International*, **174**, 93–106.

(65) Locherer, K.R., Hayward, S.A., Hirst, P.J., et al. (1996) X-ray analysis of mesoscopic twin structures. *Philosophical Transactions of the Royal Society A – Mathematical Physical and Engineering Sciences*, **354**, 2815–2845.

(66) Perez-Reche, F.J., Truskinovsky, L., and Zanzotto, G. (2008) Driving-induced crossover: from classical criticality to self-organized criticality. *Physical Review Letters*, **101**, art. no. 230601.

(67) Harrison, R.J. and Salje, E.K.H. (2010) The noise of the needle: avalanches of a single progressing needle domain in $LaAlO_3$. *Applied Physics Letters*, **97**, art. no. 021907.

(68) Gallardo, M.C., Manchado, J., Romero, F.J., et al. (2010) Avalanche criticality in the martensitic transition of $Cu_{67.64}Zn_{16.71}Al_{15.65}$ shape-memory alloy: a calorimetric and acoustic emission study. *Physical Review B*, **81**, art. no. 174102.

(69) Bratkovsky, A.M., Marais, S.C., Heine, V., and Salje, E.K.H. (1994) The theory of fluctuations and texture embryos in structural phase-transitions mediated by strain. *Journal of Physics: Condensed Matter*, **6**, 3679–3696.

(70) Castán, T., Planes, T., and Saxena, T. (2013) Precursor nanoscale textures in ferroelastics: interplay between anisotropy and disorder. *Materials Science Forum*, **155**, 738–739.

(71) Salje, E.K.H. and Parlinski, K. (1991) Microstructures in high-T_c superconductors. *Superconductor Science and Technology*, **4**, 93–97.

(72) Parlinski, K., Heine, V., and Salje, E.K.H. (1993) Origin of tweed texture in the simulation of a cuprate superconductor. *Journal of Physics: Condensed Matter*, **5**, 497–518.

(73) Chrosch, J. and Salje, E.K.H. (1999) Temperature dependence of the domain wall width in $LaAlO_3$. *Journal of Applied Physics*, **85**, 722–727.

(74) Zhao, Z., Ding, X., Lookman, T., et al. (2013) Mechanical loss in multiferroic materials at high frequencies: friction and the evolution of ferroelastic microstructures. *Advanced Materials*, **25**, 3244–3248.

(75) Novak, J., Bismayer, U., and Salje, E.K.H. (2002) Simulated equilibrium shapes of ferroelastic needle domains. *Journal of Physics: Condensed Matter*, **14**, 657–664.

(76) Harrison, R.J. and Salje, E.K.H. (2011) Ferroic switching, avalanches, and the Larkin length: needle domains in $LaAlO_3$. *Applied Physics Letters*, **99**, art. no. 151915.

(77) Benichou, I., Faran, E., Shilo, D., and Givil, S. (2013) Application of a bi-stable chain model for the analysis of jerky twin boundary motion in NiMnGa. *Applied Physics Letters*, **102**, art. no. 011912.

(78) Faran, E. and Shilo, D. (2011) The kinetic relation for twin wall motion in NiMnGa. *Journal of the Mechanics and Physics of Solids*, **59**, 975–987.

25

Novel Approaches for Genuine Single-Phase Room Temperature Magnetoelectric Multiferroics

Lynette Keeney[1], Michael Schmidt[1], Andreas Amann[1,2], Tuhin Maity[1], Nitin Deepak[1], Ahmad Faraz[1], Nikolay Petkov[1], Saibal Roy[1], Martyn E. Pemble[1,3], and Roger W. Whatmore[1,3,4]

[1]*Tyndall National Institute, University College Cork, Ireland*
[2]*School of Mathematical Sciences, University College Cork, Ireland*
[3]*Department of Chemistry, University College Cork, Ireland*
[4]*Department of Materials, Royal School of Mines, Imperial College London, United Kingdom*

25.1 Introduction to Single-Phase Multiferroic Materials

With the seemingly inexorable increase in the use of devices designed to access the Internet for an ever increasing series of applications, there is a constant need for data storage technologies with higher densities, non-volatility, and lower power consumption [1]. Single-phase, room temperature magnetoelectric multiferroic materials are of considerable interest for such applications [2]. The unique advantage of these advanced materials is that not only could they find application in high storage density, low-power memory devices that can be electrically written and magnetically read, but also by constructing devices that exploit the presence of both ferroelectric and ferromagnetic states, memory technologies with four-state logic could be achieved [3] – representing a clear improvement over current two-state logic memory. However, materials that are both multiferroic and magnetoelectric at room temperature are very unusual [4]. In this chapter, we review approaches currently under

---

Nanoscale Ferroelectrics and Multiferroics: Key Processing and Characterization Issues, and Nanoscale Effects, First Edition. Edited by Miguel Algueró, J. Marty Gregg, and Liliana Mitoseriu.
© 2016 John Wiley & Sons, Ltd. Published 2016 by John Wiley & Sons, Ltd.

investigation for the fabrication of single-phase magnetoelectric multiferroics, from bulk ceramics to those in thin-film form. We present an approach of inserting magnetic ions into the Aurivillius phase, layer-structured ferroelectric materials, whereby thin films of average composition $Bi_6Ti_{2.8}Fe_{1.52}Mn_{0.68}O_{18}$ demonstrate room temperature ferroelectricity, ferromagnetism, and magnetoelectric coupling [5]. We discuss the importance of careful microstructural analysis of the materials and the application of a statistical model to determine a confidence level that the observed effects are from genuine single-phase magnetoelectric multiferroics and do not originate from unobserved second-phase ferromagnetic inclusions [6].

To illustrate the unique potential of single-phase multiferroic materials, it is important to clarify the distinction between magnetoelectric materials and multiferroic materials. Electrically polarizable materials possess an electrical dipole moment that can be affected by an external electric field and magnetically polarizable materials possess magnetic dipole moments that are affected by an external magnetic field. As illustrated in the Venn diagram in Figure 25.1, magnetoelectric materials are those where there is coupling between electric and magnetic order parameters such that magnetization can be induced by an electric field and vice versa. This may arise through direct coupling between magnetic and electric polarizations in a single material (e.g. Cr_2O_3, magnetoelectric below 260 K) [8], or indirectly via strain-mediated coupling in a multiphase material (e.g. CoFe-$BaTiO_3$ heterostructures) [9]. Examples of single-phase magnetoelectrics include: Cr_2O_3 (<260 K) [8], CuO (<230 K) [10], $TbMnO_3$ (<27 K) [11], $Ni_3B_7O_{13}I$ (<64 K) [12], and $DyMn_2O_5$ (<43 K) [13]. Strain-mediated indirect magnetoelectric coupling in composite materials can occur, for example, through a magnetostrictive strain (induced in one phase by a change in the applied magnetic field) coupling to a piezoelectrically-induced polarization change in a second phase mechanically coupled to the first. The SI unit of the magnetoelectric coupling coefficient (α) is s m^{-1}, which can be converted to the technical unit V cm^{-1} Oe^{-1} if the permittivity (ε) of the given material is known: s $m^{-1} = 1.1 \times 10^{-11}\ \varepsilon$ V cm^{-1} Oe^{-1}. A magnetoelectric coupling coefficient of 5.90 V cm^{-1} Oe^{-1} has been reported for laminate complexes of lead zirconate titanate (PZT) and Terfenol-D ($TbDyFe_2$) by straining the magnetostrictive phase under a DC magnetic bias of 4.2 T [14], which induces stress on the piezoelectric phase, generating an electric polarization in the piezoelectric phase. Magnetic

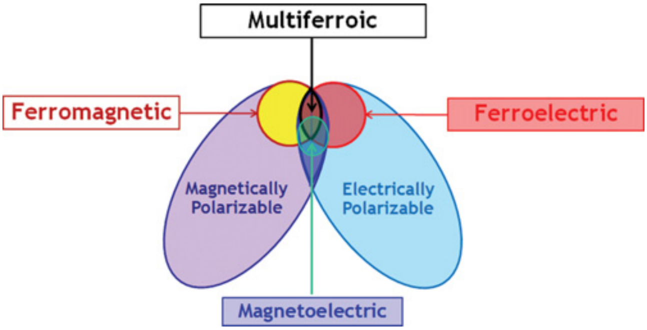

Figure 25.1 *The relationship between multiferroic and magnetoelectric materials. Redrawn from [5] and [7]*

force microscopy imaging of $(BiFeO_3)_{0.65}$–$(CoFe_2O_4)_{0.35}$ nanostructured composite heterostructures [15] demonstrated two electrically switchable perpendicular magnetic states at ambient conditions for ferromagnetic $CoFe_2O_4$ nanopillars embedded in $BiFeO_3$. Additionally, the magnetoelectric coupling effect becomes controllable in a weak perpendicular magnetic field. Thin-film heterostructures [9] of CoFe–$BaTiO_3$ grown by electron-beam evaporation exhibit giant magnetoelectric coupling coefficients (3×10^{-6} s m^{-1}) at room temperature. Lahtinen et al. [9] demonstrated that it is possible to precisely write and erase regular ferromagnetic domain patterns and to control the motion of magnetic domain walls in small electric fields over large areas in these composites by strain-mediated correlations between ferromagnetic domain walls and ferroelastic domain boundaries (see also Chapter 22).

An important subset of the electrically polarizable materials is the ferroelectrics, whose dipole moments can not only be switched by an applied electric field but also their polarization states remain even when the electric field is removed. This is the basis for nonvolatile ferroelectric random access memory, where polarization states are encoded into computer bits at fast writing performances that retain their memory states when the computer is powered-off. Similarly, the ferromagnets are a subset of magnetically polarizable materials such that their magnetic dipole moments align in a magnetic field to give a resultant magnetic moment that is retained when the magnetic field is removed. Ferromagnetic materials are used as recording media in hard disk drives and have increased storage capacity over ferroelectric materials. Spin transfer torque magnetic random access emory (STT-MRAM) has been road-mapped as an emerging memory technology [16]. However, a current drawback of ferromagnetic memory is the considerable power that is usually required for magnetic writing.

As Figure 25.1 illustrates, materials that demonstrate both ferroelectric and ferromagnetic properties within the same phase are known as multiferroic materials. The term “multiferroic” refers to any material in which more than one ferroic effect (ferroelectricity, ferromagnetism, ferroelasticity) exists in the same phase. Magnetoelectricity, on the other hand, is an independent phenomenon that can arise in any material whatever the nature of the magnetic and electrical order parameters, regardless of whether it is multiferroic or not [7]. For example, the first magnetoelectric discovered, Cr_2O_3, is neither ferroelectric nor ferromagnetic [17]. Since the switched states in this material are transient and do not persist, magnetoelectric materials of this type are inadequate for memory storage applications.

In this regard the synthesis of novel room temperature single-phase magnetoelectric multiferroic materials is particularly appealing, because the magnetoelectric and multiferroic coupling interactions could create a range of potential applications. These materials could potentially lead to a new generation of rapid, energy-efficient memory devices with increased data storage densities based on the combined advantages of ferroelectric and ferromagnetic memory. The fabrication of magnetoelectric memory devices that can be electrically written and magnetically read as well as magnetic field sensors where the ferromagnetic resonance could be tuned electrically instead of magnetically are promising avenues for exploitation in technologies requiring reduced energy consumption applications [18,19]. The unique commercial potential of the B6TFMO thin films lies in the opportunity for the creation of a four-state memory technology using the combination of simultaneous ferroelectric and ferromagnetic polarization states (positive and negative in both electrical and magnetic polarizations). The fabrication of memory devices with storage of multiple bits per memory element would significantly advance data storage capabilities to meet consumer demand for increasingly higher data density. Therefore, the design and identification of new mechanisms that can lead to multiferroic–magnetoelectric coupling behavior is in demand.

However, until very recently there were no single-phase ferroelectric/ferromagnetic multiferroics at room temperature. One reason for the scarcity of single-phase multiferroics is the competing electronic requirements for ferroelectricity and ferromagnetism [4]. Hybridization between the cation and anion within the unit cell is the conventional mechanism for stabilizing non-centrosymmetric ferroelectric distortion; therefore the cation driving ferroelectricity must formally be in the d^0 state. Conversely, d-orbital occupancy is a requirement for the existence of magnetic ordering. Hill [4] has suggested that the conditions for obtaining ferroelectricity and ferromagnetism in a single phase can potentially be met by incorporating d^0 and d^n cations into the same structure or where stereochemical activity of the A-site lone pair gives rise to ferroelectricity and magnetism arises from the B-site cation. Multiferroic materials generated by this type of pathway, where ferroelectricity and ferromagnetism have different sources, are classified as Type I multiferroics. Generally, ferroelectric ordering temperatures tend to be higher than the magnetic ordering temperature and coupling between electric and magnetic order parameters tends to be weak in this class of multiferroics. Note that given that there are so few ferromagnetic ferroelectrics, the current trend is to extend the definition of multiferroic materials to include materials possessing the corresponding antiferroic properties such as antiferroelectricity/antiferromagnetism [20]. Examples of multiferroic materials that arise from lone-pair effects are the extensively studied [7, 20–28] room temperature ferroelectric (T_C 110 K)/antiferromagnetic (T_N 643 K) $BiFeO_3$ (which also displays a weak canted ferromagnetic moment) and $BiMnO_3$ [29–31], which is a ferromagnetic oxide ($T_C = {\sim}105$ K) reported to be ferroelectric ($T_C = {\sim}450$ K). Despite the electronic limitations, several multiferroics have been discovered wherein ferroelectricity is induced by clever routes, including a second group of materials in this class called the geometrically driven multiferroics, where ferroelectricity results from long-range dipole–dipole interactions and oxygen rotations [21]. For example, ferroelectricity (T_C ~914 K) in $YMnO_3$ is driven by polyhedral tilting of the MnO_5 block and is compatible with the coexistence of antiferromagnetism (T_N ~80 K) [32–34]. A third route to multiferroism in this class is provided by non-centrosymmetric charge ordering in magnetic materials [22]. This can be seen in compounds containing transition metals, for example $LuFe_2O_4$ (ferroelectric T_C ~330 K and ferromagnetic T_C ~250 K) [35, 36] with formally different valence or bond lengths where formation of inequivalent sites can lead to ferroelectricity. In Type II multiferroics, ferroelectricity is induced by magnetic ordering and the formation of a symmetry-lowering magnetic ground state that lacks inversion symmetry. Since magnetism causes ferroelectricity, there tends to be a strong coupling between order parameters, but ferroelectric polarization tends to be small [22]. In $TbMnO_3$, frustrated magnetism and spiral magnetic ordering (T_N ~41 K) is accompanied by a magnetoelastically induced lattice distortion, which in turn induces ferroelectricity (T_C ~27 K) [10]. Despite research of other materials in this class, for example $TbMn_2O_4$ (T_N ~43 K and T_C ~38 K) [37] and $DyMnO_3$ (T_N ~38 K and T_C ~18 K) [38], the discovery of a rare earth manganite that demonstrates both room temperature ferroelectricity and ferromagnetism still remains [30].

Advances in thin-film growth techniques have allowed the production of high-quality ultra-thin films where "strain tuning" can induce ferroelectric polarization [39, 40], can lead to a significant increase of the spontaneous polarization [41] and can compensate for the adverse influence of thickness reduction and preserve ferroelectricity in ultra-thin perovskite films [42]. Sando et al. [25] investigated the effect of −2.6% (compressive) to +1.3% (tensile) strain on pulsed laser deposition (PLD) grown thin films of $BiFeO_3$ (50–70 nm) on substrates ranging from $(LaAlO_3)_{0.3}$–$(Sr_2AlTaO_6)_{0.7}$ to $PrScO_3$. It was found that high epitaxial strain destroys the bulk-like cycloidal modulation; however, the antiferromagnetic state is stable at high compressive strain. There is a progressive reorientation of magnetic spins from in-plane to out-of-plane as the strain is changed from compressive to tensile, and the authors demonstrate how epitaxial strain in $BiFeO_3$ can tune the exchange bias and giant magnetoresistive response of CoFeB/Cu/Co spin valves [25].

First principles calculations have predicted that epitaxial strain can provide a route to multiferroicity in epitaxial thin films and may lead to an increase in the ferromagnetic Curie temperature [43–46]. The paraelectric ferromagnet EuO (T_C 69 K) is predicted [44] to become ferroelectric under epitaxial strain. A compressive strain of −5.5% is anticipated to yield a polarization of 60 $\mu C\ cm^{-2}$ in the out-of-plane direction and in-plane polarization is predicted under tensile strain while the ferromagnetic state remains unchanged. If a system has a spin–phonon coupling in which the lowest-frequency polar phonon is softer for ferromagnetic ordering than for antiferromagnetic ordering, then epitaxial strain enhancement of a polar instability is expected to decrease the energy of the ferromagnetic–ferroelectric state relative to that of the antiferromagnetic–paraelectric state [46]. Via this mechanism, density functional theory calculates that both tensile (+4.5 ± 1%) and compressive (−4.9 ± 2%) strain can drive the antiferromagnetic–paraelectric $SrMnO_3$ system through a series of phase transitions to a ferromagnetic ($T_C > 92$ K)–ferroelectric ($P_s > 54\ \mu C\ cm^{-2}$) multiferroic state [46]. Fennie et al. [45] proposed a spin–phonon coupling mechanism for epitaxial strain transformation of $EuTiO_3$, an antiferromagnetic–paraelectric insulator in unstrained form, into a single-phase ferroelectric ($P \sim 10\ \mu C\ cm^{-2}$)–ferromagnet (7 μ_B) in epitaxial thin films compressively strained above −1.25%. Strong coupling between magnetic and ferroelectric ordering is realized with spin–phonon coupling through which ferromagnetic spin-alignment softens a low-frequency polar mode that is strongly coupled to biaxial epitaxial strain [45, 47]. Whereas ferromagnetic–ferroelectric multiferroicity remains to be demonstrated experimentally in EuO and $SrMnO_3$, Lee et al. [48] were successful in verifying that spin–lattice coupling converts $EuTiO_3$ into a ferromagnetic–ferroelectric multiferroic. Due to the lack of a suitable substrate to allow for the appropriate biaxial compressive strain (−1.25 to −2%), they calculated that the critical tensile strain to reach the ferroelectric–ferromagnetic ground state of $EuTiO_3$ is +0.75%. The 22 nm (001)-oriented $EuTiO_3$ films grown by reactive molecular beam epitaxy on (110) $DyScO_3$ substrates (strain = +1.1%) demonstrated ferroelectricity below T_C ~250 K and ferromagnetism below T_C 4.24 ± 0.02 K and capacitance measurements demonstrate that the two order parameters are coupled, but unfortunately this magnetoelectric multiferroic phase is only observed at very low temperatures [48].

Chen et al. [49] have demonstrated that substrate-induced epitaxial strain is a valuable approach to the formation of new structures with additional functionality that cannot be grown as equilibrium single crystals. Under identical pulsed laser deposition conditions, thin films of the conventional pseudo-perovskite Bi_2FeMnO_6 structure were obtained on

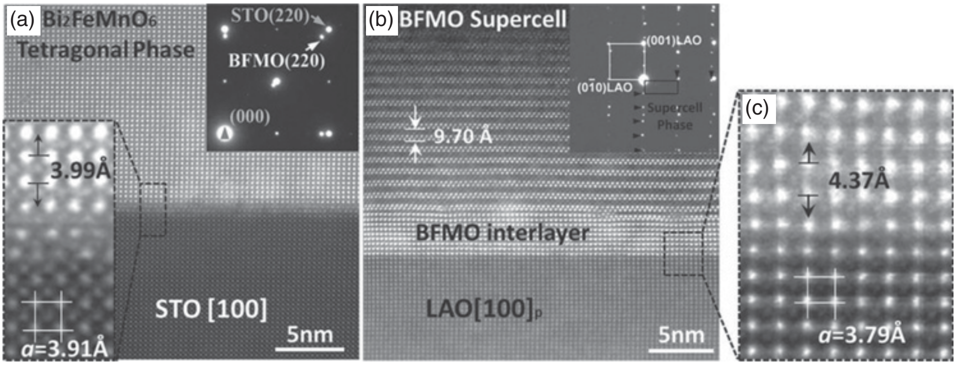

Figure 25.2 *Scanning transmission electron microscopy (STEM) images of (a) the* Bi_2FeMnO_6 *structure obtained on* $SrTiO_3$*(001) and (b) the new* $Bi_3Fe_2Mn_2O_x$ *(BFMO322) supercell structure obtained on* $LaAlO_3$ *substrates. (c) Displays the increased magnification image of the region outlined in (b), demonstrating the coherent interface between the* $LaAlO_3$ *substrate and the BFMO interlayer. Reprinted with kind permission from [49], Copyright © 2013 Wiley-VCH Verlag GmbH & Co. KGaA, Weinheim*

$SrTiO_3$(001) substrates (Figure 25.2(a)), while growth on $LaAlO_3$(001) substrates yielded the new $Bi_3Fe_2Mn_2O_x$ (BFMO322) supercell structure (Figure 25.2(b) and (c)) which demonstrates ferroelectric (P_r (remanent polarization) = 6 μC cm^{-2}, d_{33} (piezoelectric coefficient) ~30 pm V^{-1}) and ferromagnetic (M_s (saturated magnetization) ~ 110 emu cm^{-3}) properties at room temperature. This BFMO322 supercell, with a cation ratio of Bi:Fe:Mn = 3:2:2, is related to the Aurivillius [50] phases and its formation is strongly substrate dependent. A lattice misfit of −2.0% enables growth on $LaAlO_3$ whereas no growth occurs on $SrTiO_3$ (lattice misfit is −0.6%) [49]. Abberation-corrected scanning transmission electron microscopy (Cs-corrected STEM) and optimized geometric phase analysis (GPA) establishes that the formation of biaxial lattice strain distributions and highly strained BFMO transition layers between the $LaAlO_3$ substrate and the BFMO322 supercell are crucial for triggering the growth of the BFMO322 supercell structure [51]. As the thickness of the BFMO interlayers increases, the elastic biaxial strain increases up to thicknesses of ~3–4 nm, whereupon interfacial defects consisting of misfit dislocation partials are generated to relax the mismatch strain. This is followed by the growth of the BFMO322 supercell, which is partially relaxed to ~3.7–4.4% (compared with Bi_2FeMnO_6 on $SrTiO_3$ with a relative strain of −0.33%). The film crystal structure and stoichiometry evolve gradually from the highly distorted pseudo-perovskite structure to the BFMO322 supercell through the interfacial phases, demonstrating that *heteroepitaxial strain* is progressing as a new route for the generation of multiferroic phases [51].

The chemical control of functionality on a site-by-site basis is possible with multicomponent oxide systems. The hexaferrite $Sr_3Co_2Fe_{24}O_{41}$ demonstrates low-field magnetoelectric effects at room temperature, but shows no polarization at zero magnetic field and therefore is not a bilinear magnetoelectric [52]. $SrCo_2Ti_2Fe_8O_{19}$ does exhibit spontaneous polarization at zero magnetic field (~25 μC cm^{-2}) [53] and decreases in magnetization of up to 6.3% on application of a magnetic field of 46 mT and E_{dc} of 22 kV cm^{-1}. Magnetic

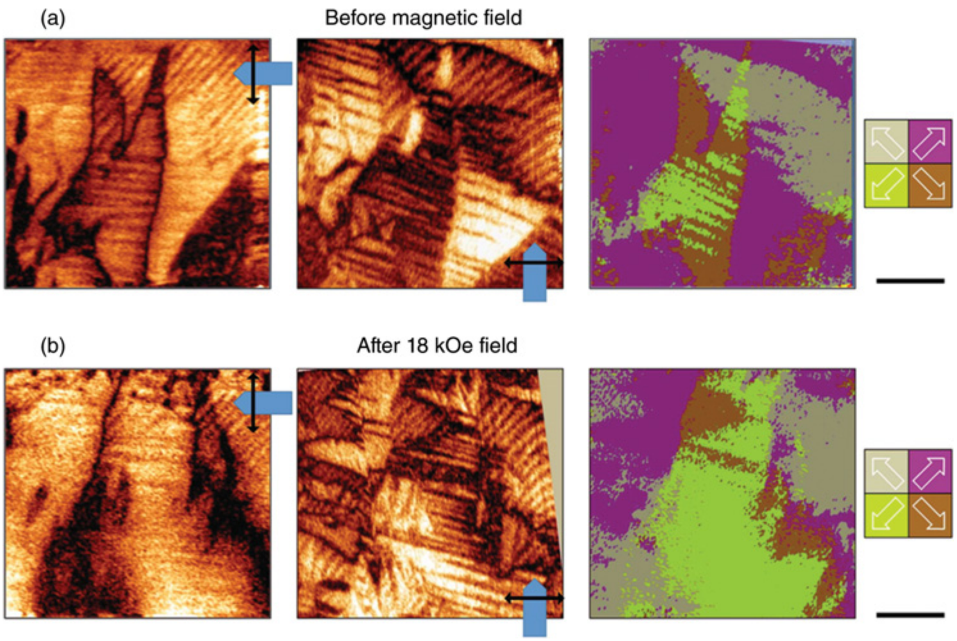

Figure 25.3 Ferroelectric domain configurations of $[Pb(Zr_{0.53}Ti_{0.47})O_3]_{0.6}$–$[Pb(Fe_{0.5}Ta_{0.5})O_3]_{0.4}$ changing dramatically with an applied magnetic field. Lateral piezoresponse force microscopy images (a) before and (b) after the application of 1.8 T magnetic field. Reprinted by permission from Macmillan Publishers Ltd: [Nature Communications] [53], copyright (2013)

force microscopy investigations of this ceramic under various electric fields ($E_{dc} \sim -20$ to $+20$ kV cm^{-1}) demonstrated decreases in magnetic contrast and electric field control of magnetism at room temperature in the absence of a magnetic field bias (converse magnetoelectric effect); however, no change in domain structure could be detected [54].

Recently, a newly discovered single-phase multiferroic, $[Pb(Zr_{0.53}Ti_{0.47})O_3]_{0.6}$–$[Pb(Fe_{0.5}Ta_{0.5})O_3]_{0.4}$, has been shown to exhibit dramatic changes to ferroelectric domain configurations on application of applied magnetic fields (−0.3 to +1.8 T) (Figure 25.3) and significant (∼60% change in polarization) bilinear magnetoelectric coupling in lamellae of the ceramic at room temperature ($\sim 1 \times 10^{-7}$ s m^{-1}) [25, 55, 56]. In addition, magnetic and dielectric anomalies appear at similar temperatures to the elastic data, giving further indications that the multiple ferroic order parameters are strongly coupled [56]. Evans et al. [53] put forward a strain-mediated coupling mechanism for these observations of ferroelectric domain switching in $[Pb(Zr_{0.53}Ti_{0.47})O_3]_{0.6}$–$[Pb(Fe_{0.5}Ta_{0.5})O_3]_{0.4}$ on application of a magnetic field.

For a period in the 2000s, there had been a number of contradictory studies [28, 57, 58] on the multiferroic properties of $BiFeO_3$ thin films. Wang et al. [28] reported an enhancement of room temperature ferromagnetism (∼150 emu cm^{-3} or ∼1 μ_B/Fe) in 70 nm heteroepitaxially strained films compared with the weak ferromagnetism expressed in bulk $BiFeO_3$. However Béa et al. [59] demonstrated that the large ferromagnetic moment was not as a result of epitaxial strain in the films but, rather, virtually all of the ferromagnetic signal observed in $BiFeO_3$ thin films could be attributed to the presence of ferrimagnetic γ-Fe_2O_3 (magnetic moment ~420 emu cm^{-3} or 1.25 μ_B/Fe) precipitates. This parasitic γ-Fe_2O_3 phase was detectable and quantifiable by X-ray absorption spectroscopy (XAS) and X-ray magnetic circular dichroism (XMCD); however, it was not easily detectable by the less-sensitive X-ray diffraction technique. The intrinsic magnetization of $BiFeO_3$, without detectable parasitic phases, is confirmed to be low ($\leq$ 0.02 μ_B/Fe) [59]. This work demonstrates the importance of detailed phase analysis when designating materials as room temperature ferroelectric/ferromagnetic multiferroics.

By inserting magnetic ions into lead-free layered-structured ferroelectric materials in the Aurivillius phase, we outline (Sections 25.3 to 25.6) how Keeney et al. [5] were successful in synthesizing thin films of average composition, $Bi_6Ti_{2.8}Fe_{1.52}Mn_{0.68}O_{18}$ (B6TFMO), which demonstrate ferroelectric and ferromagnetic properties at room temperature. Given that trace levels of magnetic impurity inclusions can significantly affect the observed ferromagnetic response from the main phase [28, 59–61], Section 25.4 reviews how careful phase analysis and statistical treatment of the data confirmed that the B6TFMO phase is a single-phase multiferroic to a confidence level of 99.5%. Section 25.3.4 summarizes how direct evidence of magnetoelectric coupling in the B6TFMO thin films was obtained. This review demonstrates that with materials development and design, the development of room temperature multiferroic materials can be achieved.

25.2 Aurivillius Phase Materials – Candidate Single-Phase Multiferroics?

The layered-structured Aurivillius phase materials (Figure 25.4) [50], described by the general formula $Bi_2O_2(A_{m\text{-}1}B_mO_{3m+1})$, are a particularly attractive class of oxides for the design of prospective new single-phase multiferroic systems as they offer the potential to include substantial amounts of magnetic cations within a strongly ferroelectric system. The materials are members of a homologous family of Bi-layered oxides, where the structure is a naturally layered nanocomposite. The two-dimensional nanostructures have large c axis lattice parameters (the stacking axis), in the nanometer range, and consist of fluorite-structured $(Bi_2O_2)^{2+}$ layers of thickness f (typically ~0.4 nm) lying in the (001) plane. These phases are very flexible, as between the bismuth oxide layers, a wide range of B-site cations can be sandwiched in the form of $mABO_3$ perovskite-type layers. The number of ABO_3 perovskite units (m) per half unit cell can be altered within the range 1 to 9, depending on composition, and a variety of over 50 Aurivillius phase compounds have been reported [62–65]. In Figure 25.4, one unit of $BiFeO_3$ has been inserted into $Bi_4Ti_3O_{12}$ to form the four-layered material, $Bi_5Ti_3FeO_{15}$. The average thickness of the perovskite-type block, h, is influenced by the number of octahedral perovskite units (m) in the block: $h = pm$, where p is the average thickness of the perovskite-like units (also typically ~0.4 nm) [66]. (Note that this is only an approximation, as octahedral tilting, and choice of A and B cations will change the average height of each perovskite unit [67–69].) The value of m can be an integer or fractional [70]. Fractional values of m usually occur with "mixtures" between a pure Aurivillius phase compound and a perovskite end member. These are formed by recurrent intergrowth of the perovskite blocks of two Aurivillius end members; for example $BaBi_8Ti_7O_{27}$ (m = 3.5) is formed from $(Bi_4Ti_3O_{12})_{0.75}$–$(BaTiO_3)_{0.25}$ [71, 72]. The values of f and h

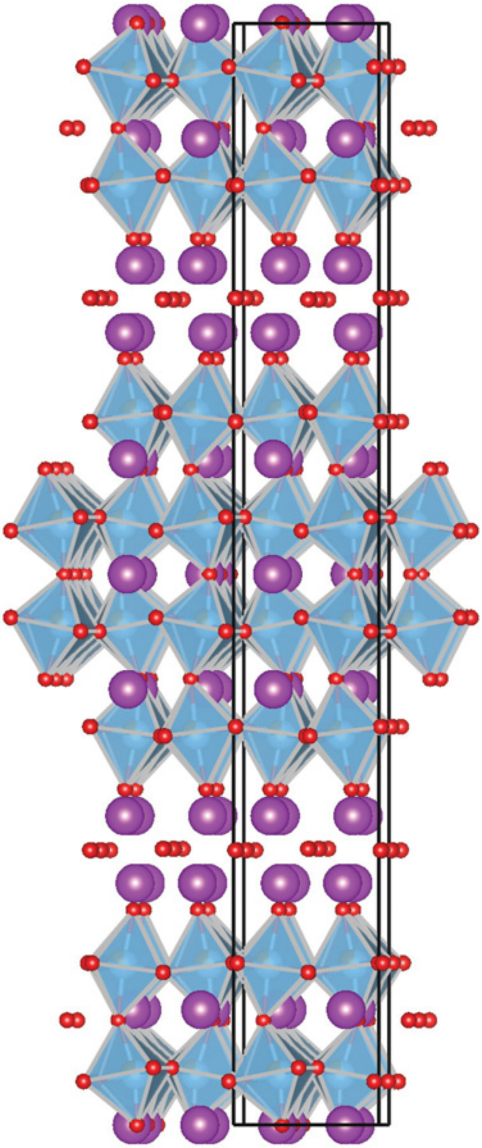

Figure 25.4 *An a axis (plus 4°) projection of the m = 4 Aurivillius phase* $Bi_5Ti_3FeO_{15.}$ *Drawn using structural parameters from Hervoches et al. [76], Crystallographica v1.60d [77], and VESTA 3.0 3D visualization program for crystal structures [78]*

are related to the c cell parameter by $f + h = c/2$. Table 25.1 demonstrates that this formula fits quite well for a variety of Aurivillius phase compositions and it provides a reasonable model from which the values of m can be obtained for any Aurivillius compound.

Table 25.1 *Comparison of c-lattice parameter predicted by f + h = c/2 with that obtained from diffraction data for Aurivillius phase compositions of m = 2–4. Where h = pm and values of 4.11 Å and 4.08 Å for p and f, respectively, were used for the prediction*

Aurivillius phase	*m*	*c* (Å) predicted	*c* (Å) obtained
$SrBi_2Ta_2O_9$	2	24.60	25.02641(50) [73]
$(Bi_3TiNbO_9)_{0.5}$–$(Bi_4Ti_3O_{12})_{0.5}$	2.5	28.71	29.05 [74]
$Bi_4Ti_3O_{12}$	3	32.82	32.8111(4) [75]
$BaBi_8Ti_7O_{27}$	3.5	36.93	37.198 [72]
$Bi_5Ti_3FeO_{15}$	4	41.04	41.197(1) [69]

Lomanova et al. [79] explored a homologous series of ceramics with the general formula $Bi_{m\text{-}1}Fe_{m\text{-}3}Ti_3O_{3m+1}$, and demonstrated the existence of structures with *m* from 4 to 9 using X-ray diffraction and electron probe X-ray microanalysis, including some with fractional *m*. These compounds were achieved by inserting bismuth ferrite units, $BiFeO_3$, into three-layered bismuth titanate, $Bi_4Ti_3O_{12}$. For this particular homologous series, Lomanova et al. [66] have pointed out that, as the number of perovskite-like layers increases, the cell *c* parameter rises almost linearly, implying that the perovskite-like units incorporated into the Aurivillius phase structure experience only slight changes along the *c* axis with increasing *m*. An average thickness of the perovskite layers, $p \cong 4.11$ Å, and the fluorite layers, $f \cong 4.08$ Å, was estimated for this series [66].

Due to the thermodynamic stability curves of the high *m*-number phases being very similar; there is only a small thermodynamic driving force for any individual *m* phase. This leads to a tendency for intergrowths of a mixture of different *m* intergrowths in bulk-processed Aurivillius phase samples, particularly with increasing *m* [80]. Due to the insensitivity of X-ray diffraction to local disorder, this technique is not sufficient to distinguish between large-period superlattices (e.g. $m = 7$) and intergrowths of multiple shorter-period members (e.g. intergrowths of $m = 3$ and $m = 4$) [81, 82]. Therefore, transmission electron microscopy (TEM) is necessary for the confirmation of higher *m*-number Aurivillius phases [81]. Zurbuchen et al. [83] have demonstrated that precise control of temperature and epitaxial growth on to (001) $SrTiO_3$ has enabled the synthesis of an $m = 8$ $Sr_5Bi_4Ti_8O_{27}$ phase by pulsed laser deposition (PLD), which is free from intergrowths of other *m* phases, as confirmed by both X-ray diffraction and TEM.

The Fe distribution over the two non-equivalent octahedral *B* cation sites in the perovskite block (classified as B(1) inside the block and B(2) for the octahedra on the outer sides of the block adjacent to the $Bi_2O_2^{2-}$ layers) has been investigated for the $Bi_{m+1}Fe_{m\text{-}3}Ti_3O_{3m+3}$ series [70]. This report has shown that for $m = 3.5$ to 7, Fe^{3+} ions preferentially occupy the B(1) sites, but the ordered distribution of ions over B(1) and B(2) sites decreases with the increase in the perovskite-like block thickness. At $m \geq 7$, the distribution of Fe^{3+} and Ti^{4+} ions of the perovskite-type block tends to become more random and when the value of *m* increases up to 8–9, concentrations of ions at B(1) and B(2) sites equalize [70].

The Aurivillius phase materials are well-known ferroelectrics, with high Curie temperatures (>500 °C) and large in-plane spontaneous polarizations [60, 84–87]. $SrBi_2Ta_2O_9$ ($m = 2$), $SrBi_2Nb_xTa_{2\text{-}x}O_9$ ($m = 2$) and $Bi_{3.25}La_{0.75}Ti_3O_{12}$ ($m = 3$) Aurivillius phase materials have been developed for commercial use in Fe-RAM (ferroelectric random access memory) devices [88–92]. Interestingly, symmetry differences between structures with even and odd numbers of m means that their ferroelectric properties behave differently, as explained by Newnham et al. [93]. The spontaneous polarization in the Aurivillius phases originates from the rotation and tilt of the BO_6 octahedra in the perovskite block; however, even and odd m-numbered structures rotate differently. At the ferroelectric phase transition, a strong bond is formed between a bismuth ion of the $(Bi_2O_2)^{2+}$ layer and an apex oxygen of the perovskite layer. Therefore the BO_6 octahedra receive strain energy from the bismuth oxide layer. Strain is minimized in even m-numbered structures by retaining mirror symmetry perpendicular to the c axis, but retaining the mirror plane perpendicular to the c axis in the odd m-numbered structures is not energetically favorable as it would result in deformation of the BO_6 octahedral [93]. The presence of a mirror plane results in cancellation of polarizations along that plane. Thus, even m-numbered Aurivillius phase materials exhibit spontaneous polarization along the a axis only because of the glide and mirror planes perpendicular to the b and c axes, respectively, whereas odd m-numbered phases exhibit minor polarization along the c axis and major polarization along the a axis when the glide planes are perpendicular to the b axis [94]. The $(Bi_2O_2)^{2+}$ layer is considered to be paraelectric and it is difficult for the bismuth ions to move in the direction of an applied external field. On increasing the number of m layers, the strain energy that the BO_6 octahedra receive from the bismuth oxide layers decreases and the octahedral cations can move easily towards the direction of the applied electric field. As a result, the saturated coercive field and the minimum electric field for ferroelectric hysteresis loop saturation tends to decrease as m increases [95].

Given that the layered nature of the Aurivillius phase materials also allows for the incorporation of significant amounts of magnetic ions with +3 to +5 oxidation states [96] within the $mABO_3$ perovskite units, the normally conflicting electronic structure requirements for ferroelectricity (unoccupied d orbitals, d^0) and ferromagnetism (partially filled d orbitals, d^n) in a single phase [4] can potentially be circumvented and the fabrication of single-phase magnetoelectric multiferroic materials could conceivably be accommodated.

Weak room temperature ferromagnetism has been reported for $Bi_{m+1}Fe_{m-3}Ti_3O_{3m+3}$ Aurivillius phases with $m = 4$ [97] and antiferromagnetism (80 to 300 K) for $m = 6$ [98] and $m = 7$ [99]. Ferroelectricity was preserved and fine ferroelectric patterns could be written (Figure 25.5) in manganese-substituted $Bi_5Ti_3Fe_{0.7}Mn_{0.3}O_{15}$ ($m = 4$), but the lack of an appreciable room temperature ferromagnetic hysteresis demonstrates

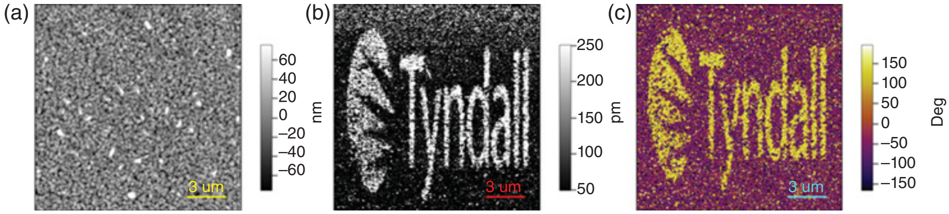

Figure 25.5 *Images of BTF7M3O on SiO_2-Si: (a) topography, (b) out-of-plane PFM (piezoresponse force microscopy) amplitude, and (c) out-of-plane PFM phase after PFM lithography with an applied DC bias of 33.0 V. Reprinted with permission from [100]. Copyright [2012], AIP Publishing LLC*

that it is not a room temperature multiferroic [100]. Zurbuchen et al. [101] revealed that the manganese-substituted $Bi_7Mn_{3.75}Ti_{2.25}O_{21}$ (tetragonal with $m = 6$) was ferromagnetic below 55 K, but not ferroelectric. Ferroelectricity and ferromagnetism above room temperature was reported for cobalt-substituted, four-layered $Bi_5Ti_3Fe_{0.5}Co_{0.5}O_{15}$ ceramic [102], with a small remanent magnetization (7.8 m emu g^{-1}). Subsequent investigations [15, 103–105] of $Bi_5Ti_3Fe_{0.5}Co_{0.5}O_{15}$ ceramics and $Bi_5Ti_3Fe_{0.7}Co_{0.3}O_{15}$ thin films also displayed ferroelectric and ferromagnetic behavior at room temperature. However, extensive microstructural phase analyses detected trace (2 to 3.95 vol%) levels of $CoFe_{2\text{-}x}Ti_xO_4$ second-phase inclusions, not observed by X-ray diffraction but which accounted for the observed magnetization. A remanent magnetization of 7.8 m emu g^{-1}, as observed by Mao et al. [102], would correspond to a trace $CoFe_2O_4$ second (or impurity) -phase level of only 0.03 wt%, which would be very hard to see by any microanalytical method. Additionally, XAS-PEEM (X-ray absorption spectroscopy photoemission electron microscopy) and XMCD-PEEM (X-ray magnetic circular dichroism photoemission electron microscopy) imaging (Figure 25.6) confirmed that the majority of magnetic

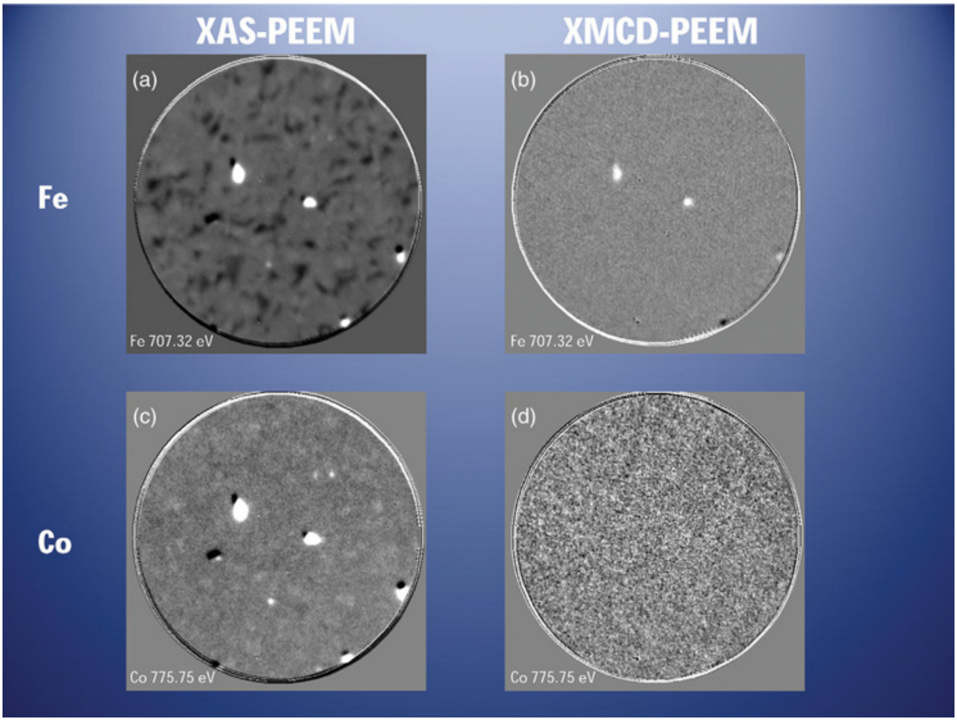

Figure 25.6 *(a) XAS-PEEM image at Fe L-edge resonance (707.32 eV) and (b) XMCD-PEEM image at Fe L-edge resonance (707.32 eV), demonstrating the magnetic signature at the Fe edge for the Fe-rich inclusions. (c) XAS-PEEM image at Co L-edge resonance (775.75 eV) and (d) XMCD-PEEM image at Co L-edge resonance (775.75 eV), demonstrating no magnetic signature at the Co edge for the Co-rich inclusions. Frame of view is 6 μm. Reprinted with permission from [60]. Copyright [2012], AIP Publishing LLC*

responses in the $Bi_5Ti_3Fe_{0.7}Co_{0.3}O_{15}$ thin-film samples arise from the Fe sites of Fe/Co-rich spinel phase inclusions [60]. While the magnetic contribution from the main phase could not be determined by the XMCD–PEEM images, these data, however, imply that it is likely that the $Bi_5Ti_3Fe_{0.7}Co_{0.3}O_{15}$ thin films are not single-phase multiferroics at room temperature. This observation clearly demonstrates the difficulty of explicit assignment of magnetic effects to the parent Aurivillius phase. Other work [106] has reported ferroelectric and ferromagnetic behavior in thin films of $Bi_{4.15}Nd_{0.85}Ti_3Fe_{0.5}Co_{0.5}O_{15}$. Compounds with higher values of m, such as $Bi_6Ti_3Fe_2O_{18}$ (B6TFO, $m = 5$), provide pathways for increasing the proportion of magnetic cations in the Aurivillius phase thin films. For instance, weak ferromagnetic/antiferromagnetic behavior was reported in rare earth and Co-doped B6TFO [107–110] ceramics and thin films, but none of the work presented phase analyses at a level that would exclude the possibility that the ferromagnetic responses were due to trace-level second phases.

In the following sections, we will summarize how at such a higher m an Aurivillius phase material, $Bi_6Ti_{2.8}Fe_{1.52}Mn_{0.68}O_{18}$ ($m = 5$) [5], demonstrates magnetoelectric multiferroicity at room temperature with a confidence level of 99.5% and the effects showing that RE is intrinsic to the Aurivillius phase.

25.3 Magnetoelectric Coupling in Multiferroic $Bi_6Ti_xFe_yMn_zO_{18}$ Systems at Room Temperature

25.3.1 Fabrication and Structural Analysis of $Bi_{m+1}Ti_3(Mn/Fe)_{m\text{-}3}O_{3m+1}$ Thin Films

Liquid injection chemical vapour deposition (LI-CVD), sometimes called atomic vapour deposition since its method of operation lies in between that of atomic layer deposition, is an industrially friendly method for depositing multicomponent oxide thin films [111]. This technique allows high gas-phase saturation of precursors of low volatility and the growth of multicomponent thin films with stoichiometric control at high throughput. Highly oriented and epitaxial thin films of $Bi_4Ti_3O_{12}$ [84] and $Bi_5Ti_3FeO_{15}$ [85] have been successfully grown by LI-CVD. When designing new materials, however, chemical solution deposition methods are often chosen to screen promising compositions since they offer flexibility, control of purity, and homogeneous mixing at molecular level with precursors that are generally significantly cheaper than those used for LI-CVD.

To synthesize thin films of $Bi_7Ti_3Fe_3O_{21}$ ($m = 6$; B7TFO) and $Bi_6Ti_{2.8}Fe_{1.52}Mn_{0.68}O_{18}$ ($m = 5$; B6TFMO) [5], a chemical solution deposition technique was developed by adapting techniques developed for the $m = 4$ materials $Bi_5Ti_3FeO_{15}$ [86], $Bi_5Ti_3Fe_{0.7}Mn_{0.3}O_{15}$ [100], and $Bi_5Ti_3Fe_{0.7}Co_{0.3}O_{15}$ [60]. Metal salts ($Bi(NO_3)_3.5H_2O$, $Fe(NO_3)_3.9H_2O$) and organometallics ($Ti(OCH_2CH_2CH_2CH_3)_4$, $Mn(C_5H_7O_2)_3$) were used as precursors and lactic acid and acetylacetone acted as solvents to prepare 0.03 mol dm^{-3} solutions of B7TFMO/B6TFMO [5]. For all solutions, the reactions were conducted at room temperature and 17.5 mol% excess bismuth [100] was used to compensate for evaporation of bismuth during the annealing process and prevent pyrochlore formation. The films were spin-coated on c-plane sapphire substrates by a commercial spinner operating at 1000 rpm for 30 s. Immediately following this, residual organics were removed from the films by

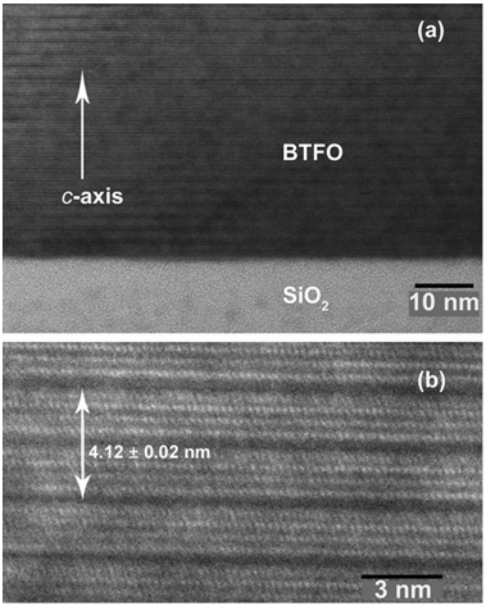

Figure 25.7 *(a) TEM image taken from a cross-section of the annealed* $Bi_5Ti_3FeO_{15}$ *film. (b) HRTEM image of the lattice structure. Reprinted with permission from [87]. Copyright [2012], AIP Publishing LLC*

baking on a calibrated hot plate. The spin-coating/baking steps were repeated to achieve desired thicknesses. Films were annealed in ambient air for 1 hour in a conventional furnace at temperatures of 850 °C. Final thicknesses of ~100 nm and ~200 nm were obtained for B7TFO and B6TFMO, respectively, as observed from cross-section HRSEM (high-resolution scanning electron microscopy) measurements (see Figure 25.7).

In fact, *Keeney* et al. [5] intended to synthesize thin films of $m = 6$ structure only, that is $Bi_7Ti_3Fe_3O_{21}$ ($m = 6$; B7TFO) and $Bi_7T_3Fe_{2.1}Mn_{0.9}O_{21}$ ($m = 6$; B7TFMO). The syntheses were carried out under identical conditions; the only difference for the latter sol was that 30% of Fe was replaced by Mn. However, X-ray diffraction (Figure 25.8) and high-resolution transmission electron microscopy (HRTEM) studies revealed that the intended B7TFMO system fitted with a five-layered B6TFMO system ($a = 5.497$, $b = 5.415$, and $c = 49.280$ Å) with reflections and d-spacings differing from the six-layered B7TFMO system ($a = 5.468$, $b = 5.472$, and $c = 57.554$ Å). Therefore, inclusion of Mn in the B7TFMO sol has driven the film from an $m = 6$ to an $m = 5$ Aurivillius phase. Multiple HRSEM energy dispersive X-ray (EDX) surface scans revealed an average film composition of $Bi_6Ti_{2.8}Fe_{1.52}Mn_{0.68}O_{18}$, which is slightly deficient in Fe and Mn relative to the sol. It was noted that as a considerable excess of Bi is included in the sol, the minor changes in excess given by producing an $m = 5$ rather than an $m = 6$ film is not significant. It was also noted that there were no detectable lines from minor phases visible in the XRD patterns of the films. However, the noise level in any XRD scan places a limit on the detectability on such minor phases and the method is intrinsically unable to detect trace levels (typically

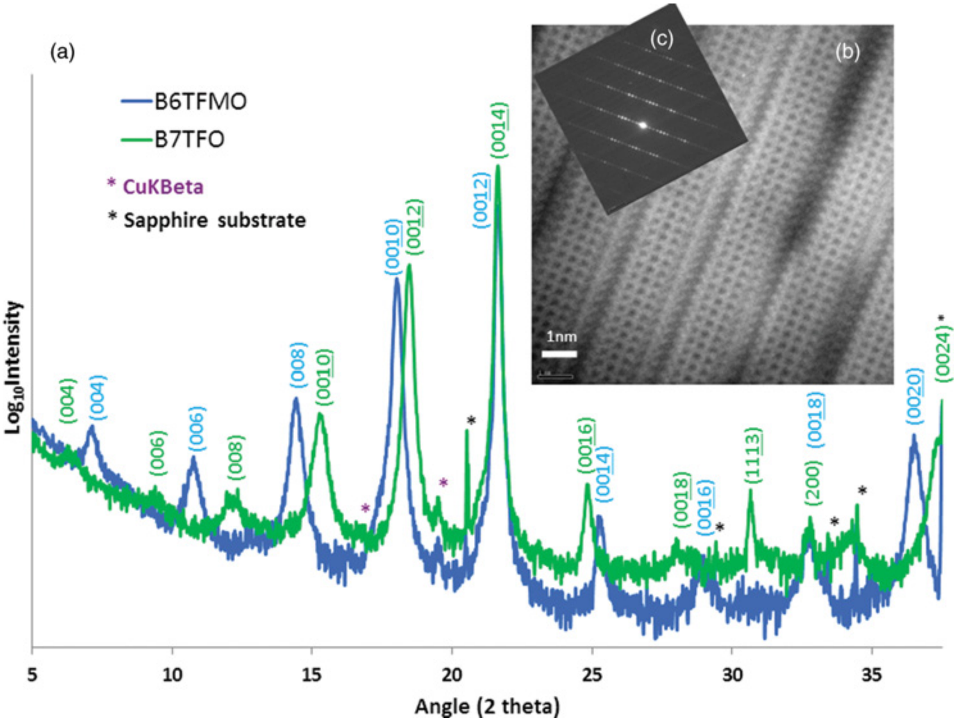

Figure 25.8 (a) XRD patterns from B7TFO and B6TFMO thin films, (b) HR-TEM image, and (c) electron diffraction pattern of B6TFMO. Reprinted from [5], Copyright © 2013 Wiley-VCH Verlag GmbH & Co. KGaA, Weinheim

1–3 vol%) of strongly magnetic secondary phases, which may affect the overall magnetization of the sample [61,62].

AFM (atomic force microscopy) and SEM investigations demonstrated that the B7TFO and the B6TFMO thin films crystallized in the typical Aurivillius phase plate-like morphology. A 72 hour long HRSEM-EDX data collection over a 1600 μm^2 area and signals produced maps that showed areas of excess Fe and Mn for the B7TFO and B6TFMO films. In conjunction with detailed cross-sectional HRTEM/SAED (selected area electron diffraction), these maps showed extremely small amounts (~0.01 vol%) of FeO_x oxide inclusions in B7TFO and slightly larger amounts (~0.1 vol%) of a rock-salt $Mn_{0.53}Fe_{0.47}O$ phase in the B6TFMO. This rock-salt composition is non-ferromagnetic and antiferromagnetic at low temperatures with a Néel point of ∼150 K [112]. Also visible in these surface HRSEM-EDX maps were larger areas (∼1 μm in diameter; ∼1 vol%), similar in shape to the Aurivillius grains, where the Fe content slightly exceeded the surrounding grains. Detailed cross-sectional HRTEM/SAED and HRSTEM-EDX compositional surveys of these grains showed that they were $m = 5$ Aurivillius-structured grains with some $m = 6$ intergrowths possessing a higher Fe content than the average of the film composition determined by surface area HRSEM-EDX. The range of grain compositions spanned both the composition of the sol used in the synthesis ($Bi_6Ti_{2.5}Fe_{1.75}Mn_{0.75}O_{18}$) and the average film composition

$Bi_6Ti_{2.8}Fe_{1.52}Mn_{0.68}O_{18}$ determined by EDX. These microstructural data were important in explaining why a sol which was set up to deliver an $m = 6$ structure could produce an $m = 5$ structure without large amounts of second phase appearing in the film.

Note that in order to make up for the deficiency in Ti^{4+} at the *B*-site of $Bi_6Ti_{2.8}Fe_{1.52}Mn_{0.68}O_{18}$, the charge balance can only be accommodated by a variable valency in Mn: $Bi_6Ti_{2.8}Fe_{1.52}Mn^{III}{}_{0.48}Mn^{IV}{}_{0.2}O_{18}$. It was also noted that the content of Mn^{4+} varied within the ~1 vol% Aurivillius phase structures containing increased Fe content. It is believed that this has important consequences for the magnetic properties of the grains [5], as will be discussed in Sections 25.3.3 and 25.3.4.

25.3.2 Ferroelectric Investigations of $Bi_6Ti_xFe_yMn_zO_{18}$ thin films

The Aurivillius phase materials are well-known ferroelectrics [60, 84–87] where even *m*-numbered Aurivillius phase materials exhibit spontaneous polarization along the *a* axis only, whereas odd *m*-numbered phases exhibit minor polarization along the *c* axis and major polarization along the *a* axis [93, 94]. $Bi_6Ti_3FeO_{18}$ ceramics have ferroelectric Curie temperatures above 1021K [113] and remnant polarization of ~9 μC cm^{-2}, which has been reported [110] to increase to 17.6 μC cm^{-2} on 30% substitution of Fe with Co.

Keeney et al. [5] investigated the local room temperature electromechanical properties of the $Bi_7Ti_3Fe_3O_{21}$ ($m = 6$; B7TFO) and $Bi_6Ti_{2.5}Fe_{1.75}Mn_{0.75}O_{18}$ ($m = 5$; B6TFMO) thin films by using piezoresponse force microscopy (PFM) [114–118]. As these films are preferentially *c*-axis oriented, most of the grains have their crystallographic *a* axis lying in the lateral plane of the film. As a result, the single-frequency lateral PFM images demonstrate greater piezoresponses (25 pm V^{-1} for B7TFO and 19 pm V^{-1} for B6TFMO) than the single-frequency vertical PFM images (3 pm V^{-1} for B7TFO and 8 pm V^{-1} for B6TFMO). Given the minor polarization along the *c* axis for Aurivillius phases with odd numbers of perovskite layers, the difference between lateral and vertical PFM responses for the B6TFMO ($m = 5$) films is less than that of the B7TFO ($m = 6$) films. In order to amplify the weaker vertical piezoresponse and reduce effects of topography cross-talk, the DART-PFM (dual AC resonance tracking piezoresponse force microscopy) mode was employed (Figure 25.9). This method uses the cantilever resonance frequency to boost the piezo signal in the vertical direction, while reducing cross-talk between changes in the sample–tip contact stiffness and the PFM signal by tracking the resonance frequency based on amplitude detection feedback [119]. Investigations of the local room temperature ferroelectric switching behaviour in the films by vertical DART-PFM switching spectroscopy measurements in the absence of an applied DC bias demonstrate clear 180° ferroelectric switching for both types of film (Figure 25.9(a) to (d)). Ferroelectric polarization reversal over areas of the B6TFMO film were achieved by applying an applied field of 525 V μm^{-1} vertically to an area of the thin films via the PFM tip (in a "write" step). The written areas could be detected by a subsequent PFM scan ("read" step) (Figure 25.9(e) and (f)). Tests conducted over an 8 hour period demonstrated that the films retained polarization for this period of time [5].

25.3.3 Assessment of Ferromagnetism in $Bi_6Ti_xFe_yMn_zO_{18}$ Thin Films

Lately the particular class of ferroelectric perovskite compounds $Bi_2O_2(A_{m-1}B_mO_{3m+1})$ containing Fe/Co/Mn ions have been found to exhibit magnetic behavior at room temperature, which have been reported in several papers [98, 99, 120–123]. Ferroelectricity

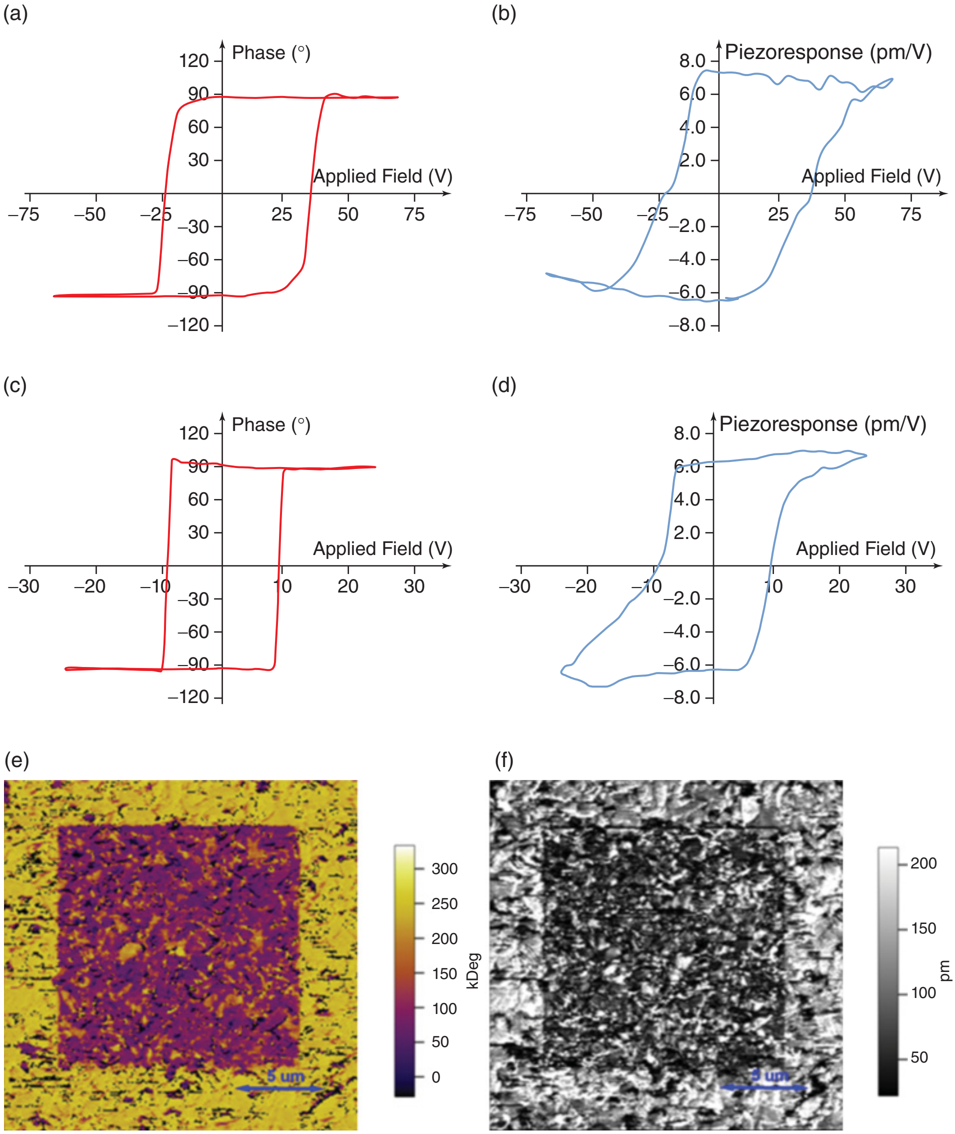

Figure 25.9 *Vertical DART-PFM switching spectroscopy (a) phase and (b) piezoresponse loops of B7TFO and (c) phase and (d) piezoresponse loops of B6TFMO thin films in the absence of an applied DC bias. Images of B6TFMO on c-plane sapphire: (e) out-of-plane PFM phase and (f) out-of-plane PFM amplitude after PFM lithography with an applied electric field of 70 V. Reprinted from [5], Copyright © 2013 Wiley-VCH Verlag GmbH & Co. KGaA, Weinheim*

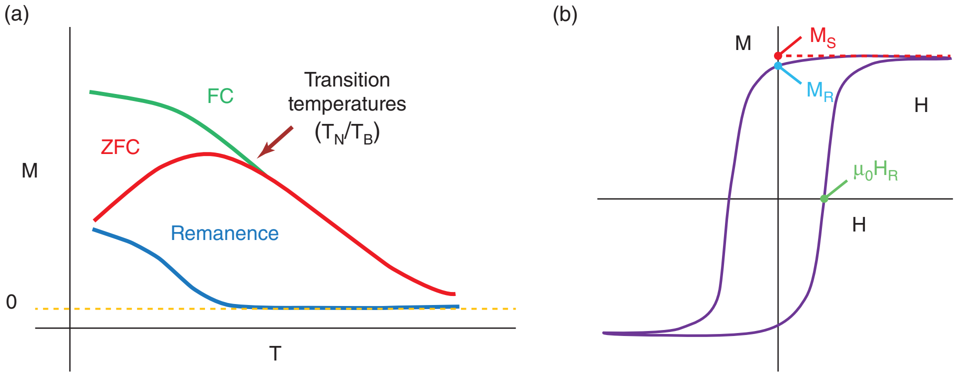

Figure 25.10 *Typical zero field cooled (ZFC)–field cooled (FC)–remanence curve (a) and magnetic hysteresis (M–H) loop (b) measured by a SQUID magnetometer. Reprinted from [5], Copyright © 2013 Wiley-VCH Verlag GmbH & Co. KGaA, Weinheim*

and ferromagnetism above room temperature were reported for the cobalt-substituted, four-layered $Bi_5Ti_3Fe_{0.5}Co_{0.5}O_{15}$ ceramic [102], with a small remanent magnetization. Further investigations [60, 61] of $Bi_5Ti_3Fe_{0.5}Co_{0.5}O_{15}$ ceramics and $Bi_5Ti_3Fe_{0.7}Co_{0.3}O_{15}$ films also demonstrated ferroelectric and ferromagnetic behavior at room temperature. Subsequently, it was observed that the Fe/Co-rich spinel phase, likely to be $CoFe_{2-x}Ti_xO_4$, coexist in the film, which accounts for the observed ferromagnetic moment in the films. In a recent study, room temperature ferromagnetic investigations of thin films of Aurivillius phase $Bi_7Ti_3Fe_3O_{21}$ (B7TFO) and $Bi_6Ti_{2.8}Fe_{1.52}Mn_{0.68}O_{18}$ (B6TFMO) were conducted by an intensive magnetometry examination [5]. The ZFC (zero field cooled)–FC (field cooled) measurement protocol, which has been used in this study, is a widely used protocol to investigate the magnetic properties as a function of temperature and bias field. From the temperature-dependent FC–ZFC magnetization and remanence curves (Figure 25.10(a)), phase transitions are determined. The point at which splitting between ZFC–FC curves occurs denotes the transition temperatures, for example Néel (T_N) or blocking (T_B) temperatures, below which the material is antiferromagnetic or ferromagnetic and result in small or large positive remanences, respectively. Another important measurement is the (*M*–*H*) measurement, where the magnetization (*M*) of the sample is measured as a function of the applied magnetic field (*H*) (Figure 25.10(b)). For paramagnetic and diamagnetic materials, the curves obtained are straight lines through the origin with positive and negative slopes, respectively. For other types of materials (ferromagnetic/ferrimagnetic/antiferromagnetic/superparamagnetic, etc.) the *M*–*H* measurement is nonlinear and takes the form of the schematic hysteresis loop in Figure 25.10(b). Other magnetic parameters such as coercivity, remanence, saturation magnetization, etc., help to determine the type of magnetic materials.

The magnetic behaviour of the B6TFMO and B7TFO thin films (by Keeney et al. [5]) revealed a strong room temperature ferromagnetic signature for the B6TFMO samples, which was evident from SQUID (superconducting quantum interference device) magnetization measurements as a function of magnetic field (Figure 25.11(a) and (b)) and temperature (Figure 25.11(c)), whereas a clear antiferromagnetic behaviour was reported in the

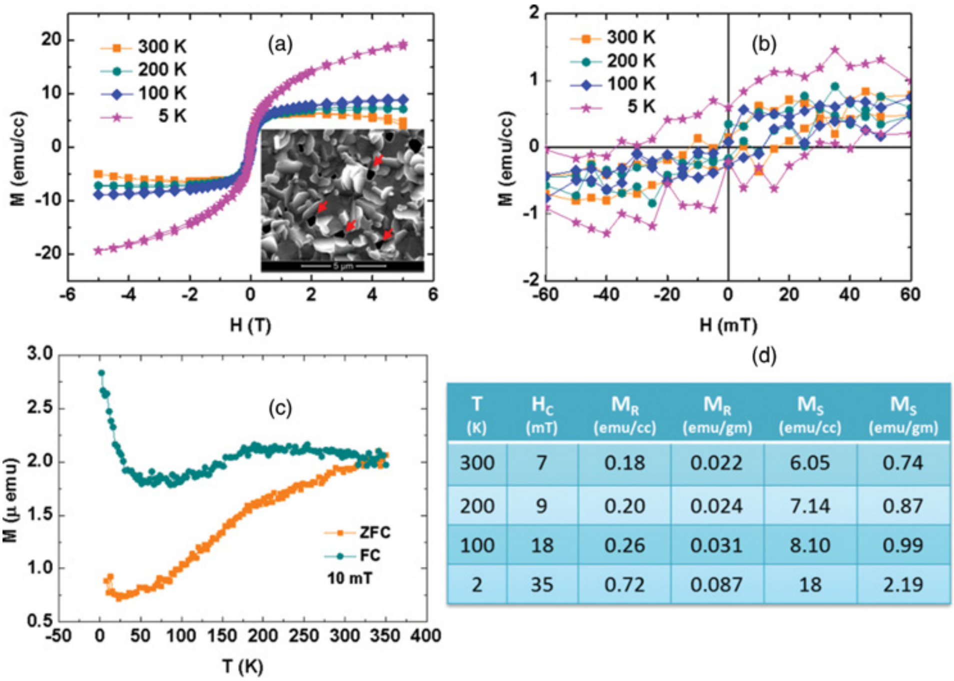

T (K)	H_C (mT)	M_R (emu/cc)	M_R (emu/gm)	M_S (emu/cc)	M_S (emu/gm)
300	7	0.18	0.022	6.05	0.74
200	9	0.20	0.024	7.14	0.87
100	18	0.26	0.031	8.10	0.99
2	35	0.72	0.087	18	2.19

Figure 25.11 *The magnetic properties of the B7TFO phase were investigated. (a) The magnetic hysteresis measured at 2 K. The inset shows hysteresis after direct subtraction of the diamagnetic substrate contribution. (b) The zoomed hysteresis loop of B6TFMO measured at different temperatures. Reprinted from [5], Copyright © 2013 Wiley-VCH Verlag GmbH & Co. KGaA, Weinheim*

case of B7TFO. The geometrical defects of the samples such as roughness and inhomogeneity in sample thickness (including the fact that 2.44% area of the substrate was not covered by the Aurivillius phase thin film due to pore formation; see inset Figure 25.11(a)) were taken into account for a precise calculation of the magnetic properties. The calculated saturation magnetization (M_S) measured for Aurivillius phase B6TFMO is reported as 0.74 emu gm^{-1} with remanent magnetization (M_r) of 0.022 emu g^{-1} (0.18 emu cm^{-3}) and coercivity ($\mu_0 H_c$) of 7 mT at 300 K. The coercivity and remanence increased gradually with a decrease in temperature (Figure 25.11(d)). ZFC–FC measurements (Figure 25.11(b)) with a relatively low field of 10 mT were performed to investigate the magnetization behavior of the B6TFMO sample as a function of temperature. A clear split between the ZFC–FC curves was observed, which demonstrates the ferromagnetic nature of the sample since otherwise the ZFC–FC lines would normally coincide [124] with each other. The compound without Mn substitution, B7TFO ($Bi_7Ti_3Fe_3O_{21}$), demonstrated an antiferromagnetic Néel temperature at 190 K and a magnetic transition to weak ferromagnetism below 35 K (Figure 25.11(c)) as reported previously by Srinivas et al. [98] The antiferromagnetic secondary phase $Mn_{0.53}Fe_{0.47}O$ observed in B6TFMO by HRSEM is reported to have a Néel temperature at ~150 K [112]. However, no magnetic transition at 150 K was detected in the magnetization versus temperature measurement (MT) for B6TFMO by Keeney et al. [5].

Rather, the ZFC–FC curves are well separated below 350 K, which strengthens the evidence for B6TFMO being ferromagnetic, with a T_C greater than 350 K. It was additionally observed that the FC curve of B6TFMO drops down at 190 K and increases again sharply below 35 K, which is similar in nature with the MT behavior of B7TFO (Figure 25.11(c)). A qualitative explanation of the non-monotonic behavior of the FC curve for B6TFMO was described [5]. It is most likely that a significant part of the parent B6TFMO phase was modified to become ferromagnetic at the nanoscale, with the remainder being antiferromagnetic in the same way as in the case of unmodified B6TFO [90, 109, 125, 126]. The variation of magnetization of B6TFMO as a function of temperature (Figure 25.11(c)) was thus non-monotonic in nature due to the influence of a proportion of grains behaving as would be expected from the unmodified parent antiferromagnetic B6TFO phase [125, 126].

In the magnetic hysteresis loop measurement (Figure 25.11(a)), the B6TFMO film shows a saturation magnetization (2.19 emu gm^{-1} at 2 K temperature under 5 T field), which is substantially higher than the unsubstituted B7TFO phase (0.2 emu gm^{-1} at 5 K temperature under a 5 T field). For antiferromagnetic materials the remanent magnetization is understood to be negligibly small (ideally zero) as the opposite spins cancel out each other. The observation of both high remanence and a simultaneous increase of remanence and coercivity of B6TFMO with a decrease in temperature strongly support the existence of ferromagnetism in this material.

A possible mechanism for the observed ferromagnetism in B6TFMO can be explained by assuming that there is Mn^{4+} present in the structure which can couple with Fe^{3+} in a ferromagnetic superexchange interaction via the Goodenough–Kanamori rule. As a result of a transition metal's coordination geometry, the degeneracy of electronic d orbital states is lifted. This occurs because the electrons in the metal d orbitals and the metal ions in the ligands are coordinated to repel each other due to like charge repulsion. In octahedral symmetry, the five d orbitals split into two sets with an energy difference, Δ_{oct}, where one set, the interaxial orbitals (t_{2g} orbitals, comprised of d_{xy}, d_{xz}, and d_{yz}) are lower in energy than the other set, the axial orbitals (e_g orbitals, comprised of $d_z{}^2$ and $d_x{}^2{}_{-y}{}^2$) since these are further from the ligand orbitals and therefore experience less repulsion. The size of the gap, Δ_{oct}, between the sets of orbitals depends on various factors including the ligand type and the geometry of the complex.

According to the Aufbau principle, electrons fill lowest available energy levels first; therefore when Δ_{oct} is large, the t_{2g} orbitals are occupied before the e_g orbitals. As such, coordination environments that generate large splitting energies, Δ_{oct}, lead to "low-spin" complexes. Conversely, "high-spin" complexes are formed when there is a sufficiently small Δ_{oct} to obey Hund's rule, which states that if two or more orbitals of equal energy are available, electrons occupy them singly before filling them in pairs. To obey the Pauli exclusion principle, when two electrons occupy the same energy level they must have opposite spin. The electronic arrangement of the five d electrons of Fe(III) in both its "low-spin" and "high-spin" configurations is displayed in Figure 25.12(a). The use of these splitting diagrams can assist in the prediction of the magnetic properties of transition metal complexes.

If orbital degeneracy is lost in a real environment – by chemical bonding or crystal field effects – the orbital contribution to the total magnetic moment is said to be quenched and the spin-only equation can be used to calculate the effective magnetic moment, μ_{eff} (Bohr magneton): $\mu_{eff} = (n(n + 2))^{1/2}$, where n is the number of unpaired electrons. This relationship holds quite well for first-row transition metal ions at room temperature.

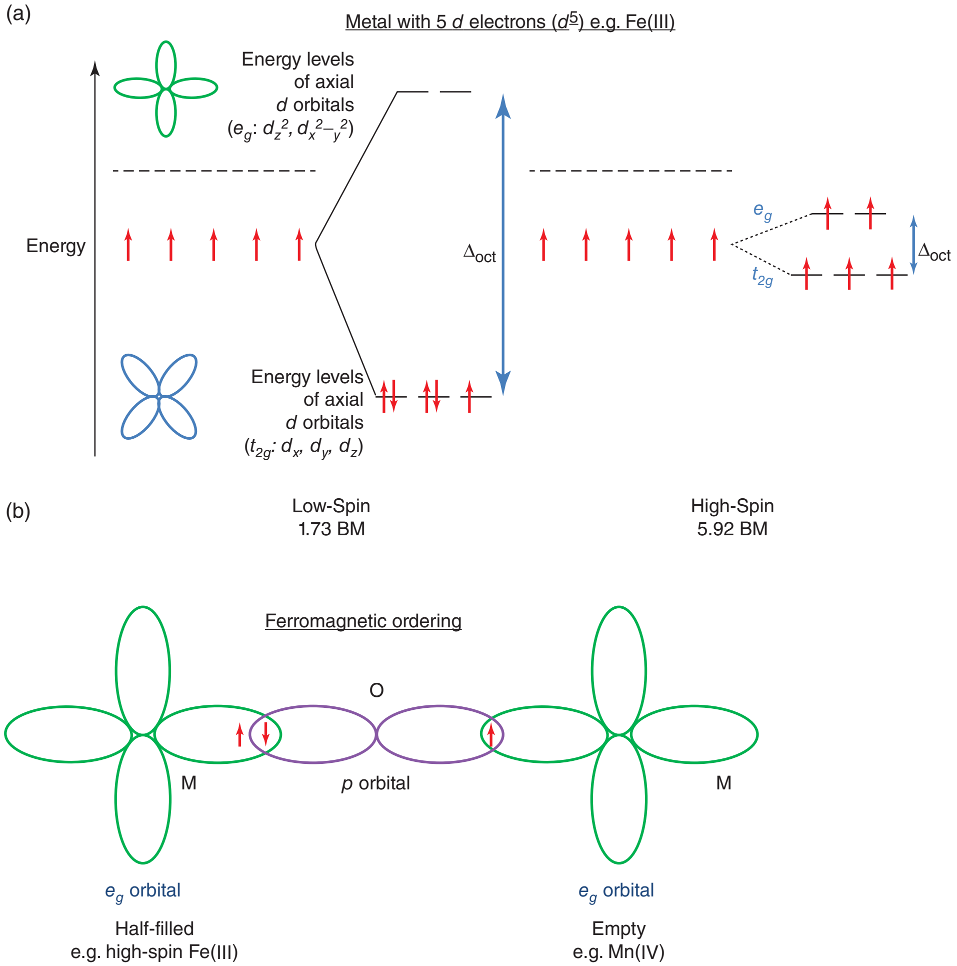
(a)
Metal with 5 d electrons (d5) e.g. Fe(III)
Energy levels of axial d orbitals (e_g: d_{z^2}, $d_{x^2-y^2}$)
Energy
Δ_{oct}
e_g
t_{2g}
Δ_{oct}
Energy levels of axial d orbitals (t_{2g}: d_x, d_y, d_z)
(b)
Low-Spin
1.73 BM
High-Spin
5.92 BM
Ferromagnetic ordering
O
M
p orbital
M
e_g orbital
Half-filled
e.g. high-spin Fe(III)
e_g orbital
Empty
e.g. Mn(IV)

Figure 25.12 *(a) Electronic arrangement of five d electrons in "low-spin" and "high-spin" configurations and (b) mechanism for ferromagnetic ordering*

For transition metals with one to three d electrons only the t_{2g} orbitals will be occupied. Therefore, for Mn(IV) μ_{eff} will be 3.87 BM and the e_g orbitals will be empty in all octahedral coordination environments irrespective of the extent of the octahedral splitting energies Δ_{oct}.

The mechanism involving ligand orbitals to facilitate coupling between metal electrons is referred to as superexchange. According to the Goodenough–Kanamori rule, superexchange interactions are antiferromagnetic where virtual electron transfer is between overlapping orbitals that are each half-filled, for example between the e_g orbitals in high-spin Fe(III). In antiferromagnetic materials, adjacent metal ions couple with their spins antiparallel – there are always equal numbers with the two arrangements so that there is no resultant magnetization in the absence of a magnetic field.

On the other hand, the Goodenough–Kanamori rule predicts that superexchange interactions are strong and ferromagnetic (Figure 25.12(b)) when virtual electron transfer is from a half-filled orbital to an empty orbital, for example between a half-filled e_g orbital in high-spin Fe(III) and an empty e_g orbital in low-spin Mn(III) or in Mn(IV), where the e_g orbitals are always empty regardless of the extent of the octahedral splitting. In *ferromagnetic* materials, the electron spins of each of the atoms couple strongly together to form a resultant unit cell magnetic moment in an applied magnetic field. When the field is then removed, the magnetization does not return to its original value unless heated to the ferromagnetic Curie point temperature.

25.3.4 Room Temperature Magnetoelectric Coupling in $Bi_6Ti_{2.8}Fe_{1.52}Mn_{0.68}O_{18}$ Thin Films

Direct evidence of magnetoelectric coupling in the $Bi_6Ti_{2.8}Fe_{1.52}Mn_{0.68}O_{18}$ (B6TFMO) thin films was demonstrated by Keeney et al. [5] by performing piezoresponse force microscopy under a variable magnetic field to locally image the coupled piezoelectric–magnetic switching. On application of an in-plane magnetic field of +250 mT during single-frequency PFM measurements in the lateral plane (Figure 25.13), two situations were observed: (i) piezoelectric domain formation and (ii) piezoelectric domain switching. Induction of piezoelectric polarization reversal by application of a magnetic field in the positive direction (+250 mT) was also observed by vertical PFM imaging of the out-of-plane piezoresponses (Figure 25.14(e) and (f)). When a magnetic field of 250 mT was applied in the opposite (negative) direction, additional areas exhibiting polarization inversion were obtained (Figure 25.14(h) and (i)). The switching regions were approximately 250 nm in size, clearly related to the Aurivillius grains, of which they were a small fraction of the total number (the average change in polarization was 4% for Figure 25.13 and 7% for Figure 25.14) and widely dispersed throughout the film. The fundamental mechanism mediating the magnetoelectric coupling is not obvious from these experiments, but this direct observation of the switching and formation of a ferroelectric polarization induced by a change in magnetic field within a single phase is significant as it provides strong evidence for the multiferroic character of the B6TFMO thin films. It was proposed that the Aurivillius phase grains that demonstrate magnetoelectric coupling may be those containing the highest levels of Fe/Mn, for which the majority of the Mn will be present as Mn^{4+} [5].

25.4 Confidence Level Assessment of Genuine Single-Phase Multiferroicity

Per definition, the magnetic properties of a single-phase multiferroic material are due to only one phase. It is therefore necessary to exclude the possibility that magnetic effects, for example the remanence magnetization, are caused by the presence of a secondary phase of inclusions. In general, it is not practical to scan the whole sample for inclusions; therefore Keeney et al. [5] needed to resort to statistical methods. A statistical approach was developed that only requires a set of measurements at various resolutions to establish an upper limit for the contribution to the remanence magnetization due to the presence of second-phase magnetic inclusions.

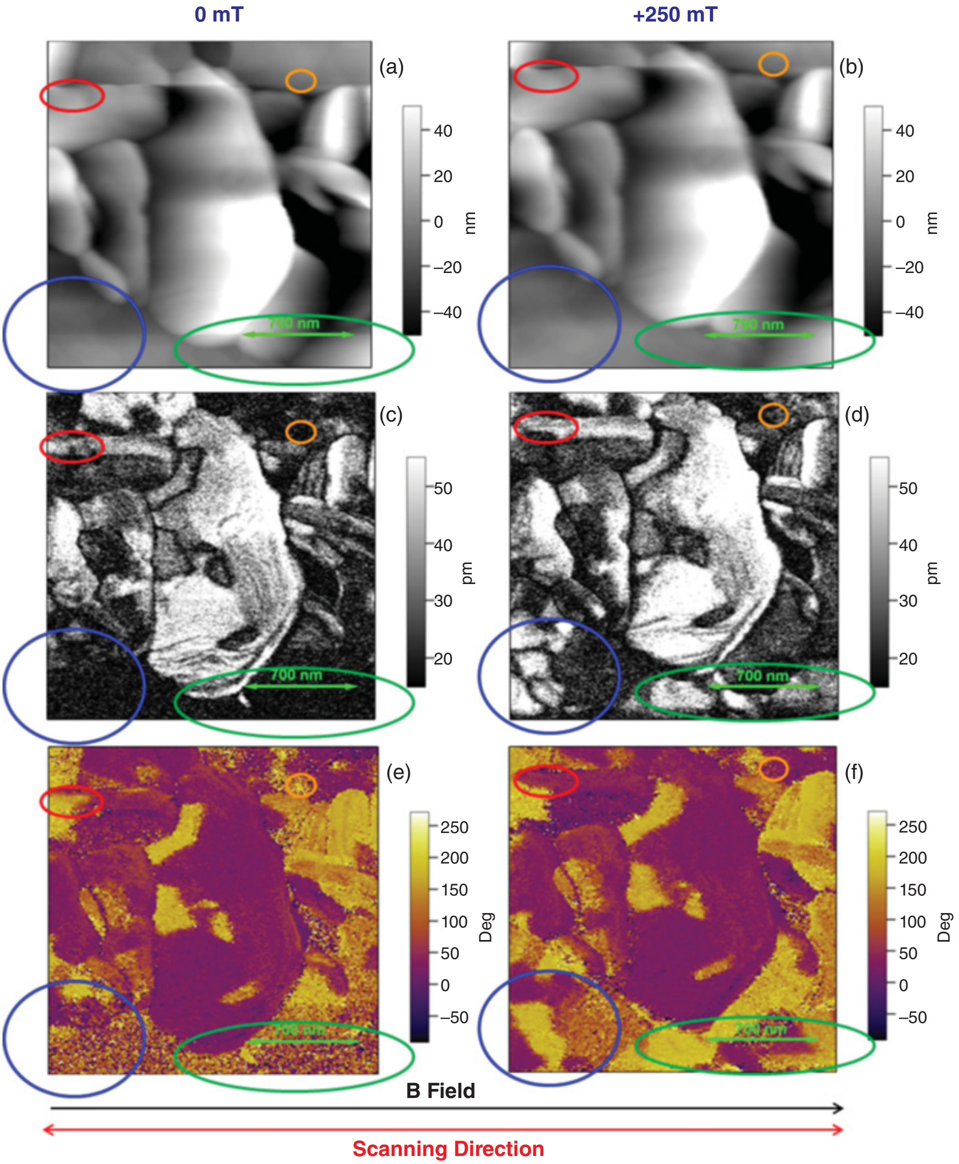
0 mT
+250 mT
(a)
(b)
40
20
0
−20
−40
nm
700 nm
(c)
(d)
50
40
30
20
pm
(e)
(f)
250
200
150
100
50
0
−50
Deg
B Field
Scanning Direction

Figure 25.13 Representative images of B6TFMO thin films: (a) topography, (c) lateral PFM amplitude, and (e) lateral PFM phase under a 0 mT H field and (b) topography, (d) lateral PFM, and (f) lateral PFM phase under a +250 mT H field. Reprinted from [5], Copyright © 2013 Wiley-VCH Verlag GmbH & Co. KGaA, Weinheim

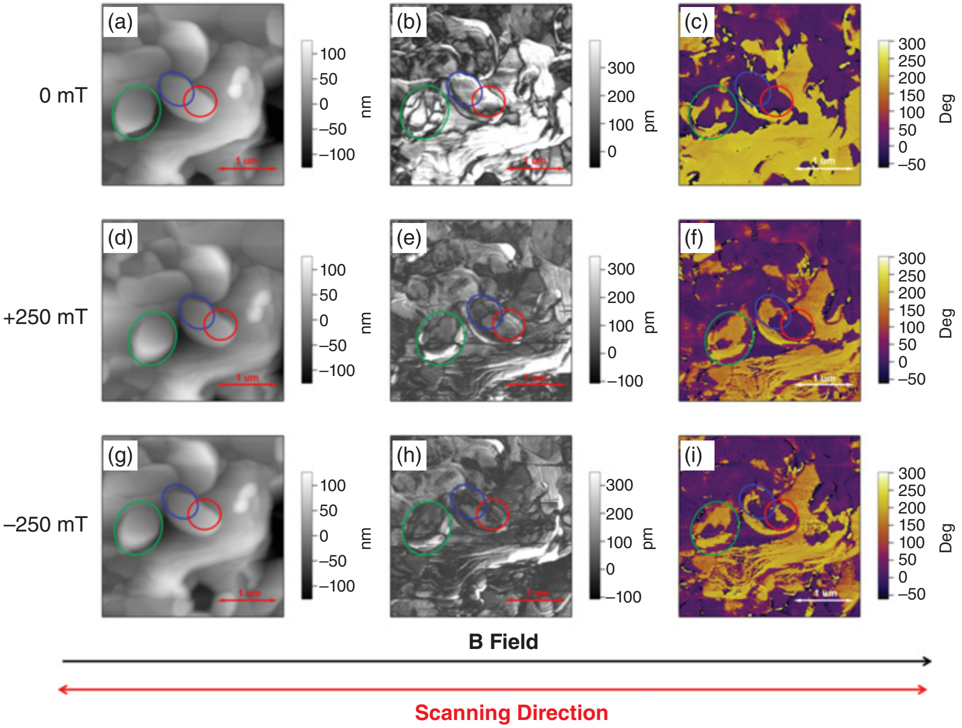

Figure 25.14 Representative images of B6TFMO thin films: (a) topography, (b) vertical PFM amplitude, and (c) vertical PFM phase under a 0 mT H field; (d) topography, (e) vertical PFM amplitude, and (f) vertical PFM phase under a +250 mT H field; and (g) topography, (h) vertical PFM amplitude, and (i) vertical PFM phase under a −250 mT H field. Reprinted from [5], Copyright © 2013 Wiley-VCH Verlag GmbH & Co. KGaA, Weinheim

In the following we will first review the statistics of a single measurement and, following the introduction of the inclusion size distribution function, a set of measurements is generalized at various resolutions. This then allows the provision of an upper limit for the grain size distribution function and the contribution to the remanence magnetization at a given confidence level.

25.4.1 Statistics of a Single Measurement

In a single measurement, a volume of size V is scanned and the number of inclusions in this volume is detected. In general, this volume will be small compared to the sample size. If, in the whole sample, inclusions are present at a volume density ρ and the inclusions are randomly distributed independently of each other, then the probability $P(N)$ of finding precisely N inclusions is given by the Poisson distribution:

$$P(N) = \frac{(\rho V)^N}{N!}\, e^{-\rho V} \tag{25.1}$$

This formula also predicts the probability of finding no inclusions:

$$P(0) = \exp(-\rho V) \tag{25.2}$$

This probability decreases exponentially with the scan volume V.

A slightly different situation is now assumed, where rho (ρ) is not known and in a given scan of a volume V no inclusions are found. Then formula (25.2) can be used to provide an upper bound for the inclusion density ρ. For this it is assumed that the event of not finding any inclusions happened with a probability of more than 0.5%, i.e. P(0) > 0.5%. Solving formula (25.2) for the inclusion density and introducing the symbol $\gamma = 1 - 0.5\% = 99.5\%$ for the confidence level, an estimation for the upper bound of rho (ρ) is obtained:

$$\rho < \rho_{\mathrm{u}} = \frac{-\ln(1-\gamma)}{V} \approx \frac{5.3}{V} \tag{25.3}$$

Subject to this confidence level, the ρ_{u} defined in Equation (25.3) establishes an upper bound for the unknown inclusion density ρ.

25.4.2 The Inclusion Size Distribution Function

For a realistic sample, inclusions can be present at various sizes and the volume density might vary with the inclusion size. Therefore an inclusion size distribution function, $p_{\mathrm{G}}(d)$, can be defined such that for small Δd the quantity, $p_{\mathrm{G}}(d)\Delta d$ is the density of inclusions with diameters in the interval $[d, d + \Delta d]$ u. The approach is now generalized from the previous section to the case of a size-dependent distribution function. If in a scan of a certain volume V no inclusions are present that are larger than a given minimal detectable size d_{m}, then the upper bound from Equation (25.3) becomes a constraint on the size distribution function given by:

$$\int_{\mathrm{d_m}}^{\infty} dq p_{\mathrm{G}}(q) < \rho_{\mathrm{u}} \tag{25.4}$$

25.4.3 Series of Measurements at Varying Resolutions

In practice, the minimal detectable inclusion size decreases with the scan volume. It is therefore often necessary to scan a sample at a number of different resolutions to detect for the presence of inclusions. It is therefore assumed that a number of K scans at different volume sizes V_k and different minimal detectable grain sizes d_k were performed. Here the index k runs from 1 to K, starting at large d_k (i.e. $d_k > d_{k+1}$). It is also assumed that there is a physical upper bound $d_{\mathrm{o}} > d_1$ on the grain size. The probability that no inclusion was detected in measurement number k is given by P_k (0). If the grain distribution function $p_{\mathrm{G}}(d)$ is known, P_k (0) is given by:

$$P_k(0) = \exp\left(-V_k \int_{d_k}^{d_{\mathrm{o}}} dq p_{\mathrm{G}}(q)\right) \tag{25.5}$$

It is again assumed that in each individual scan no inclusion larger than the minimal inclusion size, d_k, was found. The probability for this zero outcome is given by the product of the probability for not detecting inclusions over all scans, that is $P(0) = P_1(0)P_2(0) \ldots P_{Nm}(0)$.

Using Equation (25.5), it then follows that the condition:

$$V_{Nm} \int_{d_K}^{d_{K-1}} dq p_G(q) + \left(V_K + V_{K-1}\right) \int_{d_{K-1}}^{d_{K-2}} dq p_\mathrm{G}(q) + \\ \dots \quad + \left(\sum_{k=1}^{K} V_k\right) \int_{d_1}^{d_o} dq p_\mathrm{G}(q) < -\ln(1-\gamma) \approx 5.3 \tag{25.6}$$

holds with a confidence level of $\gamma = 99.5\%$. Equation (25.6) gives us an estimate of the upper limit of the grain size distribution function $p_\mathrm{G}(d)$ integrated over grain size intervals from d_k to d_{k-1}. In practice, observable quantities (for example the remanence) are more naturally connected to the volume fractions of the inclusions at certain grain sizes. This motivates the rewriting of Equation (25.6) using volume fractions.

If it is assumed for simplicity that the inclusions are spherical, then the volume fraction φ_k of inclusions between sizes d_k and d_{k-1} can be calculated from the grain size distribution $p_\mathrm{G}(d)$ via:

$$\phi_k = \int_{d_k}^{d_{k-1}} dq p_\mathrm{G}(q) \, \frac{4}{3}\pi \left(\frac{q}{2}\right)^3 \le \left[\int_{d_k}^{d_{k-1}} dq p_\mathrm{G}(q)\right] \frac{\pi}{6} d_{k-1}^3 \tag{25.7}$$

In the last step the worst-case scenario is employed in that the weight of the grain distribution function is located at the large inclusion sizes. Using this inequality in Equation (25.6) yields a convenient upper limit for the allowed volume fractions:

$$V_K \frac{\phi_K}{d_{K-1}^3} + \left(\sum_{k=K}^{K-1} V_k\right) \frac{\phi_{K-1}}{d_{K-2}^3} + \quad \cdots \quad + \left(\sum_{k=K}^{1} V_k\right) \frac{\phi_1}{d_\mathrm{o}^3} \\ < -\frac{\pi}{6} \ln(1-\gamma) \quad \approx \quad 2.8 \tag{25.8}$$

which again holds with a confidence level of γ. It therefore follows that there is an upper limit on the volume fraction φ_k of inclusions with a diameter in the interval $[d_k, d_{k-1}]$ given by

$$\phi_k < \frac{-d_{k-1}^3}{\sum_{j=K}^{k} V_j} \frac{\pi}{6} \ln(1-\gamma) \approx 2.8 \frac{d_{k-1}^3}{\sum_{j=K}^{k} V_j} \tag{25.9}$$

25.4.4 Upper Limit on the Contribution to Remanent Magnetization

So far it has been discussed how the absence of inclusions in a number of volume scans at various resolutions limits the possible inclusion size distribution function $p_\mathrm{G}(d)$. In many applications, however, this quantity is not in itself of primary interest, but a possible physical effect caused by the inclusions. In Keeney et al.'s case the physical quantity of interest is the magnetic remanence and the aim was to find an upper bound for the contribution of

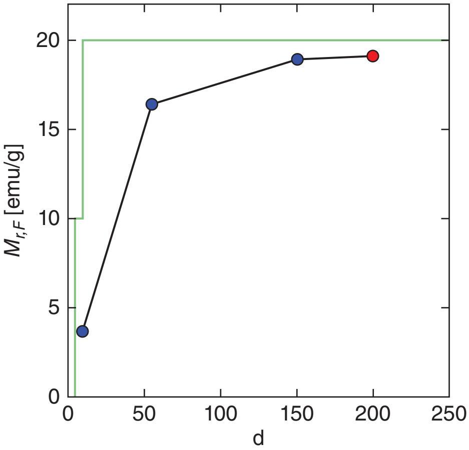

Figure 25.15 *Remanent magnetization $M_{r,F}$ of Fe_3O_4 as function of grain size. The solid lines connecting the dots shows literature data from [127] (first three dots) and [128] (last dot). Because there are only a few literature values, a conveniently chosen (piecewise constant) line is chosen (shown to the left and above the literature values plot), which is assumed to conservatively overestimate (up to the chosen confidence level) the true remanent magnetization for all grain sizes d*

undetected inclusions to this quantity [5]. Using the upper bound estimates for the volume fractions φ_k given in Equation (25.9), the maximal contribution to the remanence from inclusions with diameters in the interval $[d_k, d_{k-1}]$ is given by:

$$M_{r,k} = \frac{-d_{k-1}^3}{\sum_{j=N_m}^{k} V_j} \frac{\pi}{6} \ln\ (1-\gamma)\ M_{r,F}(d_{k-1}) \tag{25.10}$$

Here $M_{r,F}(d)$ is the remanence magnetization of pure Fe_3O_4 grains of diameter d. The literature [127, 128] values for this function are plotted in Figure 25.15. For simplicity it is assumed that $M_{r,F}(d)$vanishes for <5 nm. Furthermore $M_{r,F}(d) = 10$ emu g^{-1} is set for 5 nm $< d <$ 10 nm and $M_{r,F}(d) = 20$ emu g^{-1} for $d >$ 20 nm, which are conservative estimates as shown in Figure 25.15.

The total contribution from inclusions to the remanent magnetization is then simply given as a sum over the contributions from the individual size intervals:

$$M_r = \sum_{k=1}^{K} W_k M_{r,k} \tag{25.11}$$

Because of Equations (25.8) and (25.10) the parameters $W_1, \ldots, W_K, \ldots, W_K$ fulfill the constraint:

$$\sum_{k=1}^{K} W_k = 1 \tag{25.12}$$

with a confidence level γ. Therefore it can be concluded that the contribution to the magnetization remanence from inclusions M_r has an upper bound:

$$M_\mathrm{r} \leq \max_{k=1,\ldots,K} \left\{ M_{\mathrm{r},k} \right\} \tag{25.13}$$

with confidence $\gamma = 99.5\%$. From the analysis by Keeney et al. [5], it was concluded that the contribution to the remanence in the B6TFMO ($Bi_6Ti_{2.8}Fe_{1.52}Mn_{0.68}O_{18}$) thin films from unobserved magnetic inclusions is less than 2.8 m emu g^{-1} with a confidence level better than 99.5%.

25.5 Potential Devices/Applications Based on Single-Phase Magnetoelectric Multiferroics

The semiconductor technology industry has provided remarkable developments in computer processing speeds and miniaturization since Moore's prediction in 1965 [129] and has had a dramatic impact on our lives. However, for future advances in miniaturization, the memory capacity of digital devices will also need to improve at exponential rates. The development of an ideal energy-efficient non-volatile memory having the potential to retain high densities of data in the absence of power or an external stimulus [130] is still an elusive goal. The most common primary memory used in computers and electronic devices today is dynamic random access memory (DRAM), which is a volatile memory allowing each bit of data to be stored in a separate capacitor and accessed at clock cycle times in the order of nanoseconds. However, the data are lost quickly when the power is removed; therefore information must be transferred to a secondary memory, such as a non-volatile magnetic hard drive. Examples of other non-volatile memory devices include EEPROM (electrically erasable programmable read-only memory) and flash type memory. However, both of these memories suffer from limited lifespans, increased write times, and production costs [131].

In the 1970s, Esaki [132] proposed that ferroelectric materials could be ideal candidates for use in non-volatile data storage devices (ferroelectric random access memory (FeRAM)) by taking advantage of their two spontaneously switchable polarization states [133]. Among the known ferroelectric materials, the solid solution $PbZrO_3$–$PbTiO_3$ (PZT) and Aurivillius phase $SrBi_2Ta_2O_9$ (SBT) have been developed for FeRAM applications. Both these materials demonstrate some drawbacks that restrict their applications, such as PZT, which exhibits polarization fatigue, while in the case of $SrBi_2Ta_2O_9$ (SBT), the high processing temperatures required makes them difficult to process in conjunction with functional silicon technologies [134]. In addition, FeRAM has a number of technical drawbacks that restricts their fully fledged production in the memory technology industry. Firstly, the data readout is performed by measuring the net flow of transient current during charge polarization reversal across the circuit. This implies that the readout step is destructive in FeRAM [135]. Secondly, FeRAM-based devices function by charge sensing and when the lateral size of the ferroelectric capacitor is reduced to the submicrometer scale, the stored charges tend to be very small and beyond detectability limits [130].

An alternative to a non-volatile memory with the destructive data readout of FeRAM is magnetic random access memory (MRAM). MRAMs equal or surpass alternative non-volatile memory technologies in terms of access time and endurance [1, 2]. However, a

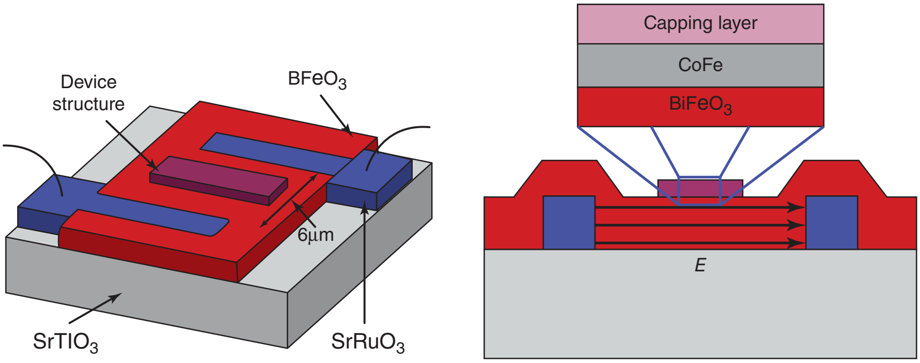

(a) (b)

Figure 25.16 *Dynamic switching device structure. Three-dimensional (a) and cross-sectional (b) schematic diagram of the co-planar epitaxial electrode device showing a structure that could enable controlled ferroelectric switching and electrical control of ferromagnetism. Reprinted by permission from Macmillan Publishers Ltd: [Nature Materials] [136], copyright (2008)*

current drawback of these devices in obtaining a competitive cost/bit is the considerable power that is usually required for magnetic writing. Energy-efficient approaches to reduce the write energy have received much focus recently. One way is to reverse the stored magnetization by spin transfer, employing spin polarization current rather than an external magnetic field. Another way that write-energy could be significantly decreased is by using a write-scheme, which relies on applied voltage rather than current. The ability to control the direction of magnetization in a ferromagnetic layer by purely electrical means would overcome the current requirement of high current densities in spin-transfer torque MRAM and offer *low-power approaches* for spin-based information control. A relatively simple device to demonstrate electric field control of ferromagnetism was shown by Chu et al. [136]. The device (Figure 25.16) consists of in-plane electrodes that enable the application of in-plane electric fields to the $BiFeO_3$ layer, which in turn changes the magnetic state of the CoFe ferromagnetic top layer.

Hence, miniaturization and feature scaling, increased density and processing speeds, non-volatility and decreased power dissipation are major challenges to overcome in the creation of a universal memory that can scale beyond the current state of the art. These physical requirements are potentially achievable by incorporating multistate logic in a memory cell that can be electrically written and magnetically read (or vice versa) in the form of multiferroic magnetoelectric (ME) logic memory. With strong magnetoelectric coupling between the ferroelectric and ferromagnetic states however, the four available switching states ($+P$, $+M$), ($+P$, $-M$), ($-P$, $+M$), and ($-P$, $-M$), where P represents the polarization state and M represents the magnetization state, are not absolutely independent of each other [137] and the only combinations that are independently achievable are either ($+P$, $+M$) and ($-P$, $-M$) or ($+P$, $-M$) and ($-P$, $+M$), which of course is not a four-state memory. This problem can be circumvented by forming a ferromagnetic–magnetoelectric tunnel Néel junction, where combination of electroresistance and magnetoresistance can result in a four-state

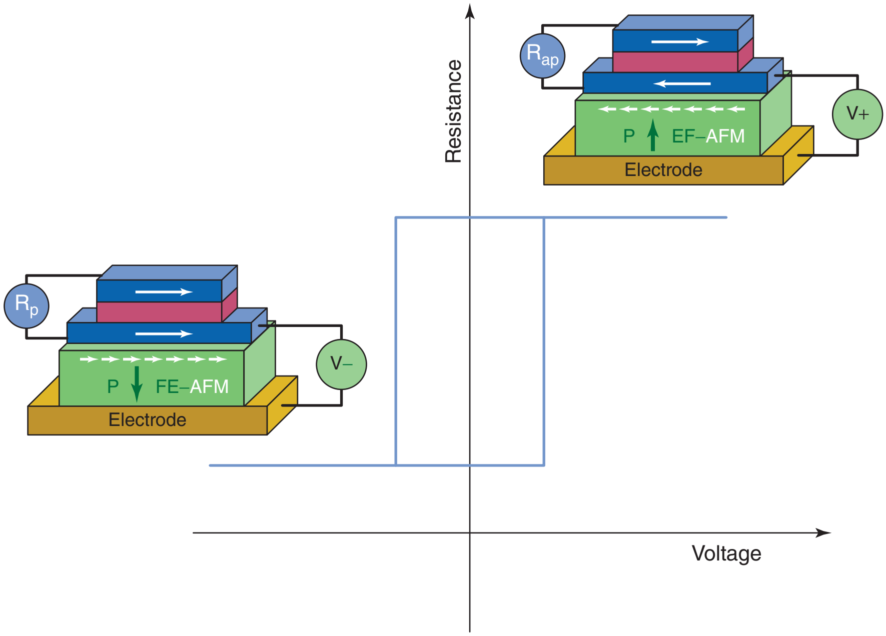

Figure 25.17 *The binary information is stored by the magnetization direction of the ferromagnetic layer, read by the resistance of the magnetic trilayer (R_p when the magnetizations of the two ferromagnetic layers are parallel) and written by applying a voltage across the multiferroic ferroelectric antiferromagnetic layer (FE-AFM). If the magnetization of the lower ferromagnetic layer is coupled to the spins in the multiferroic (small arrows) and if the magnetoelectric coupling is strong enough, reversing the ferroelectric polarization P in the multiferroic changes the magnetic configuration in the trilayer from parallel to antiparallel, and the resistance from R_p to antiparallel (R_{ap}). A hysteretic dependence of the device resistance with voltage is achieved (centre curve). Reprinted by permission from Macmillan Publishers Ltd: [Nature Materials] [135], copyright (2008)*

memory effect [3]. Multiferroic tunnel junctions (MFTJs) (Figure 25.17) consist of two asymmetric oxide and/or metal electrodes separated by an ultra-thin multiferroic barrier layer. The approach exploits the tunneling of electrons through an ultra-thin (<10 nm) multiferroic thin film, providing giant electroresistance/magnetoresistance effects and a means for a non-destructive readout of non-volatile memory states with increased storage densities and data rates with a low-power electrical write operation [3, 138]. Recent investigations of ferroelectric oxide thin films have demonstrated that ferroelectricity can persist down to the nanometre scale [139] and therefore can function as ultra-thin barriers for tunnel junctions. Depending on the direction of the remanent polarization in the ferroelectric, charges are accumulated or depleted in the barrier layer, which influences its electroresistance (ER). Resistive memories can be read more simply than ferroelectric capacitors (where the polarization is read by an applied voltage) by monitoring the source-drain current in a field-effect transistor. If the barrier layer can also act as a ferromagnet, as in the case of single-phase multiferroic materials, the ferromagnetic barrier layer can yield different tunnel barrier heights for spin-up and spin-down electrons. Magnetization may be easily read out from resistance measurements, as is done for magnetic tunnel junctions. Non-polarized electrons from a non-magnetic metal crossing a ferromagnetic–multiferroic barrier will be transmitted differently depending on their spin, thereby acquiring a finite spin polarization, which is referred to as spin-filtering. If a half-metallic ferromagnetic counter electrode is added, aligning its magnetization parallel or antiparallel to that of the barrier yields different resistance levels, where the magnitude of the tunnel magnetoresistance (TMR) is larger for antiparallel arrangements [140].

Ferroelectricity and ferromagnetism have been shown to persist down to a thickness on 2 nm in the single-phase multferroic $La_{0.1}Bi_{0.9}MnO_3$ [3]. A large TMR (90%) and an ER of 22% has been obtained in a 2 V bias operation in a four-resistance-state MTFJ system using this material as a barrier separating $La_{0.66}Sr_{0.33}MnO_3$ and $SrTiO_3$ electrodes; however, these results were obtained at a very low temperature (4 K), requiring liquid helium cooling. The search for an ultra-thin room-temperature multiferroic remains before a four-state logic device based on MTFJs is found to be practically useful [141]. The B6TFMO Aurivillius phase is therefore an ideal candidate for testing the feasibility of an MFTJ function at room temperature based on a single-phase multiferroic barrier layer.

Another application of multiferroic materials is in the fabrication of magnetic field sensors. Magnetic sensors have been used in analysing and controlling various functions for many decades. The high storage capacity of computers is due to the use of magnetic sensors in magnetic storage disks and tape drives. Aeroplanes fly with improved safety standards due to the increased reliability of non-contact switching with magnetic sensors [142]. Magnetic field sensors have other numerous applications, which include automotive sensors, navigation systems, non-destructive material testing, security systems, structural stability, medical sensors, and military instruments. These numerous applications have led to great deal of research in improving upon the current magnetic sensors. There are various ways of preparing magnetic sensors, including fabrication by exploiting various effects such as Faraday's induction law, the Hall effect, the magnetoresistive effect, and using magnetic tunnel junctions. A comprehensive review is provided by James Lenz and Alan S. Edelstein [143] for further reading.

In most of the magnetic field sensors, the basic principle of change in the electrical properties of a material on application of a magnetic field can be exploited [143]. The magnetoelectric multiferroic coupling between two materials can also be used to fabricate magnetic field sensors. This multiferroic coupling can be exploited in two different ways. The first method uses composites made from piezoelectric and magnetostrictive materials. Two different layers of magnetostrictive and piezoelectric materials are glued together with a binder. A magnetostrictive material such as $NiFe_2O_4$ [144], or alloys, e.g. $TbDyFe_2$ (Terfenol-D) [145, 146] is glued with a binder to a piezoelectric material with a high piezoelectric coefficient such as $Pb(Zr,Ti)O_3$ (PZT) [142]. The application of a magnetic field will create a strain in the magnetostrictive layer, which in turn will be transferred to the piezoelectric material. The binder plays an important role as it helps in transferring the strain from one material to another.

The second method is by using single-phase multiferroics showing magnetoelectric switching. These kinds of sensors work on the principle of linear coupling between magnetic and electrical orders. Figure 25.18 shows the structure of a possible magnetic field sensor.

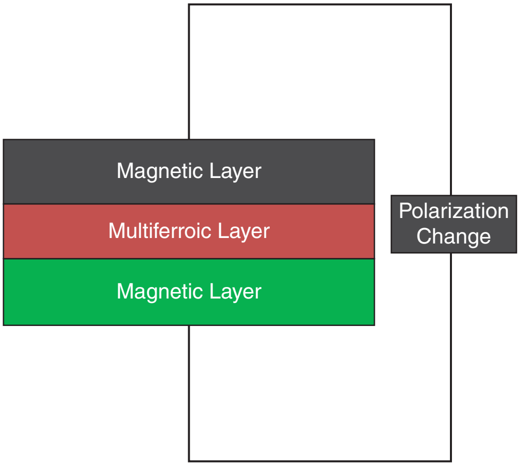

Figure 25.18 *Image of a possible single-phase multiferroic magnetic field sensor where the multiferroic material is sandwiched in between two magnetic electrode layers*

This magnetic field sensor consists of a trilayer structure where the multiferroic material is sandwiched between two magnetic electrodes (Figure 25.18). Any change near the vicinity of the magnetic layer will change the magnetization in the multiferroic layer. Since there is a coupling between magnetic and electric orders, this change in magnetization will change the polarization values in the multiferroic layer with standard circuitry. The only requirement for this kind of device is strong magnetoelectric coupling in a single-phase multiferroic material, which is usually hard to achieve at room temperature. However, recent work on $Bi_6Ti_{2.8}Fe_{1.52}Mn_{0.68}O_{18}$ (B6TFMO) demonstrated multiferroic magnetoelectric coupling, which in principle could be used to prepare future magnetic field sensors. The use of a single-phase multiferroic material has an added advantage of faster response times due to the direct coupling between the ferroic-order parameters. Fabrication of single-phase sensors is a less complex process without the need for a binder layer to couple piezoelectric and magnetostrictive materials. The need for lead-based materials with a high piezoelectric coefficient, such as PZT, for composite sensors should be replaced with less toxic and more environmentally friendly substitutes. Single-phase materials such as B6TFMO, based on bismuth-based systems, are good candidates for fabrication of future magnetic field sensors and can provide a less toxic way of preparing magnetic-based sensing devices.

25.6 Summary and Conclusions

By inserting magnetic ions into layered–structured ferroelectric materials in the Aurivillius phase, Keeney et al. [5] were successful in synthesizing thin films of average composition, $Bi_6Ti_{2.8}Fe_{1.52}Mn_{0.68}O_{18}$ (B6TFMO), which demonstrate ferroelectric and ferromagnetic properties at room temperature. Direct evidence of magnetoelectric coupling was demonstrated by performing piezoresponse force microscopy (PFM) under a variable magnetic field, whereupon magnetic-field-induced ferroelectric domain switching and formation was demonstrated under application of modest (±250 mT) magnetic fields. Although no spinel impurity phases were visible in the XRD patterns, a thorough microstructural phase analysis was performed on the films to investigate whether trace levels of ferromagnetic spinel inclusions could be responsible for the observed ferromagnetism in B6TFMO. This detailed analysis demonstrated no evidence for ferromagnetic impurity inclusions above the detection level of the experiments (0.01 vol%). Statistical analysis based on the volumes inspected placed a confidence of 99.5% that the observed ferromagnetism was not coming from unobserved/undetected ferromagnetic spinel grains. This analysis, coupled with the direct observation of the switching and formation of a ferroelectric polarization induced by a change in the magnetic field within a single phase, is significant as it provides strong evidence that that B6TFMO thin films are single-phase ferroelectric–ferromagnetic–magnetoelectric–multiferroics at room temperature. The body of evidence reported indicates that the origin for the ferromagnetism/magnetoelectric coupling arises from Aurivillius phase grains containing a higher Fe^{3+}/Mn^{4+} content; however, this remains to be verified. The fundamental mechanism for how the ferroelectric- and magnetic-order parameters are coupled also remains to be understood. The study by Keeney et al. [5] demonstrates that with materials development and design, the development of room temperature multiferroic materials can be achieved and that the B6TFMO thin films are exciting candidates for potential use in multiferroic, magnetoelectric logic devices that could potentially meet future industry requirements in energy-efficient, high-density memory applications.

References

(1) *Assessment of the Potential and Maturity of Selected Emerging Research Memory Technologies Workshop and ERD* (Emerging Research Devices)/ERM Working Group Meeting, April 6–7, 2010).

(2) Emerging Research Materials (2009) In *International Technology Roadmap for Semiconductors (ITRS)*, Semiconductor Industry Association, http://www.itrs.net/links/2009ITRS/Home2009.htm.

(3) Gajek, M., Bibes, M., Fusil, S., et al. (2007) Tunnel junctions with multiferroic barriers. *Nature Materials*, **6**, 296–302.

(4) Hill, N.A. (2000) Why are there so few magnetic ferroelectrics? *Journal of Physical Chemistry B*, **104**, 6694–6709.

(5) Keeney, L., Maity, T., Schmidt, M., et al. (2013) Magnetic-field-induced ferroelectric switching in multiferroic Aurivillius phase thin films at room temperature. *Journal of the American Ceramic Society*, **96**, 2339–2357.

(6) Schmidt, M., Amann, A., Keeney, L., et al. (2014) Absence of evidence ≠ evidence of absence: statistical analysis of inclusions in multiferroic thin films. *Scientific Reports*, **4**, art. no. 5712.

(7) Martin, L.W., Crane, S.P., Chu, Y.H., et al. (2008) Multiferroics and magnetoelectrics: thin films and nanostructures. *Journal of Physics – Condensed Matter*, **20**, art. no. 434220.

(8) Folen, V.J., Rado, G.T., and Stalder, E.W. (1961) Anisotropy of the magnetoelectric effect in Cr_2O_3. *Physical Review Letters*, **6**, 607–608.

(9) Lahtinen, T.H.E., Franke, K.J.A., and van Dijken, S. (2012) Electric-field control of magnetic domain wall motion and local magnetization reversal. *Scientific Reports*, **2**, art. no. 258.

(10) Kimura, T., Sekio, Y., Nakamura, H., et al. (2008) Cupric oxide as an induced-multiferroic with high-T_C. *Nature Materials*, **7**, 291–294.

(11) Kimura, T., Goto, T., Shintani, H., et al. (2003) Magnetic control of ferroelectric polarization. *Nature*, **426**, 55–58.

(12) Ascher, E., Rieder, H., Schmid, H., and Stossel, H. (1966) Some properties of ferromagnetoelectric nickel–iodine boracite, $Ni_3B_7O_{13}I$. *Journal of Applied Physics*, **37**, 1404–1405.

(13) Higashiyama, D., Miyasaka, S., Kida, N., et al. (2004) Control of the ferroelectric properties of $DyMn_2O_5$ by magnetic fields. *Physical Review B*, **70**, art. no. 174405.

(14) Ryu, J., Priya, S., Carazo, A.V., et al. (2001) Effect of the magnetostrictive layer on magnetoelectric properties in lead zirconate titanate/terfenol-D laminate composites. *Journal of the American Ceramic Society*, **84**, 2905–2908.

(15) Zavaliche, F., Zhao, T., Zheng, H., et al. (2007) Electrically assisted magnetic recording in multiferroic nanostructures. *Nano Letters*, **7**, 1586–1590.

(16) Hutchby, J. and Garner, M. (2010) *Assessment of the Potential and Maturity of Selected Emerging Research Memory Technologies Workshop and ERD/ERM Working Group Meeting*, April 6–7, 2010.

(17) Borisov, P. and Kleemann, W. (2011) Exchange bias and ferromagnetic coercivity in heterostructures with antiferromagnetic Cr_2O_3. *Journal of Applied Physics*, **110**, art. no. 033917.

(18) Li, J.B., Huang, Y.P., Rao, G.H., et al. (2010) Ferroelectric transition of Aurivillius compounds $Bi_5Ti_3FeO_{15}$ and $Bi_6Ti_3Fe_2O_{18}$. *Applied Physics Letters*, **96**, art. no. 222903.

(19) Christian, G.D. (1994) *Analytical Chemistry*, 5th edition, John Wiley & Sons, Inc.

(20) Martin, L.W. and Schlom, D.G. (2012) Advanced synthesis techniques and routes to new single-phase multiferroics. *Current Opinion in Solid State and Materials Science*, **16**, 199–215.

(21) Ramesh, R. (2009) Materials science: emerging routes to multiferroics. *Nature*, **461**,1218–1219.

(22) Ramesh, R. and Spaldin, N.A. (2007) Multiferroics: progress and prospects in thin films. *Nature Materials*, **6**, 21–29.

(23) Martin, L.W., Chu, Y.H., and Ramesh, R. (2010) Advances in the growth and characterization of magnetic, ferroelectric, and multiferroic oxide thin films. *Materials Science and Engineering R: Reports*, **68**, 89–133.

(24) Chu, Y.H., Cruz, M.P., Yang, C.H., et al. (2007) Domain control in multiferroic $BiFeO_3$ through substrate vicinality. *Advanced Materials*, **19**, 2662–2666.

(25) Sando, D., Agbelele, A., Rahmedov, D., et al. (2013) Crafting the magnonic and spintronic response of $BiFeO_3$ films by epitaxial strain. *Nature Materials*, **12**, 641–646.

(26) Infante, I.C., Lisenkov, S., Dupé, B., et al. (2010) Bridging multiferroic phase transitions by epitaxial strain in $BiFeO_3$. *Physical Review Letters*, **105**, art. no. 057601.

(27) Fischer, P., Polomska, M., Sosnowska, I., and Szymanski, M. (1980) Temperature dependence of the crystal and magnetic structures of $BiFeO_3$. *Journal of Physics C: Solid State Physics*, **13**, 1931–1940.

(28) Wang, J., Neaton, J.B., Zheng, H., et al. (2003) Epitaxial $BiFeO_3$ multiferroic thin film heterostructures. *Science*, **299**, 1719–1722.

(29) Moreira dos Santos, A., Parasharb, S., Rajub, A.R., et al. (2002) Evidence for the likely occurrence of magnetoferroelectricity in the simple perovskite, $BiMnO_3$. *Solid State Communications*, **122**, 49–52.

(30) Rao, C.N.R., Sundaresan, A., and Saha, R. (2012) Multiferroic and magnetoelectric oxides: the emerging scenario. *Journal of Physical Chemistry Letters*, **3**, 2237–2246.

(31) Sharan, A., Lettieri, J., Jia, Y., et al. (2004) Bismuth manganite: a multiferroic with a large nonlinear optical response. *Physical Review B*, **69**, art. no. 214109.

(32) Van Aken, B.B., Palstra, T.T.M., Filippetti, A., and Spaldin, N.A. (2004) The origin of ferroelectricity in magnetoelectric $YMnO_3$. *Nature Materials*, **3**, 164–170.

(33) Smolenskii, G.A. and Bokov, V.A. (1964) Coexistence of magnetic and electric ordering in crystals. *Journal of Applied Physics*, **35**, 915–918.

(34) Huang, Z.J., Cao, Y., Sun, Y.Y., et al. (1997) Coupling between the ferroelectric and antiferromagnetic orders in $YMnO_3$. *Physical Review B*, **56**, 2623–2626.

(35) Ikeda, N., Ohsumi, H., Ohwada, K., et al. (2005) Ferroelectricity from iron valence ordering in the charge-frustrated system $LuFe_2O_4$. *Nature*, **436**,1136–1138.

(36) Serrao, C.R., Sahu, J.R., Ramesha, K., and Rao, C.N.R. (2008) Magnetoelectric effect in rare earth ferrites, $LnFe_2O_4$. *Journal of Applied Physics*, **104**, art no. 016102.

(37) Hur, N., Park, S., Sharma, P.A., et al. (2004) Electric polarization reversal and memory in a multiferroic material induced by magnetic fields. *Nature*, **429**, 392–395.

(38) Goto, T., Kimura, T., Lawes, G., et al. (2004) Ferroelectricity and giant magnetocapacitance in perovskite rare-earth manganites. *Physical Review Letters*, **92**, art. no. 257201.

(39) Haeni, J.H., Irvin, P., Chang, W., et al. (2004) Room-temperature ferroelectricity in strained $SrTiO_3$. *Nature*, **430**, 758–761.

(40) Deepak, N., Caro, M.A., Keeney, L., et al. (2014) Interesting evidence for template-induced ferroelectric behavior in ultra-thin titanium dioxide films grown on (110) neodymium gallium oxide substrates. *Advanced Functional Materials*, **24**, 2844–2851.

(41) Choi, K.J., Biegalski, M., Li, Y.L., et al. (2004) Enhancement of ferroelectricity in strained $BaTiO_3$ thin films. *Science*, **306**, 1005–1009.

(42) Garcia, V., Bibes, M., Bocher, L., et al. (2010) Ferroelectric control of spin polarization. *Science*, **327**, 1106–1110.

(43) Ingle, N.J.C. and Elfimov, I.S. (2008) Influence of epitaxial strain on the ferromagnetic semiconductor EuO: first-principles calculations. *Physical Review B*, **77**, art. no. 121202.

(44) Bousquet, E., Spaldin, N.A., and Ghosez, P. (2010) Strain-induced ferroelectricity in simple rocksalt binary oxides. *Physical Review Letters*, **104**, art. no. 037601.

(45) Fennie, C.J. and Rabe, K.M. (2006) Magnetic and electric phase control in epitaxial $EuTiO_3$ from first principles. *Physical Review Letters*, **97**, art. no. 267602.

(46) Lee, J.H. and Rabe, K.M. (2010) Epitaxial-strain-induced multiferroelectricity in $SrMnO_3$ from first principles. *Physical Review Letters*, **104**, art. no. 207204.

(47) Shvartsman, V.V., Borisov, P., Kleeman, W., Kamba, S., and Katsufuji, T. (2010) Large off-diagonal magnetoelectric coupling in the quantum paraelectric antiferromagnet $EuTiO_3$. *Physical Review B*, **81**, art. no. 064426.

(48) Lee, J.H., Fang, L., Vlahos, E., et al. (2010) A strong ferroelectric ferromagnet created by means of spin-lattice coupling. *Nature*, **466**, 954–958.

(49) Chen, A., Zhou, H., Bi, Z., et al. (2013) A new class of room-temperature multiferroic thin films with bismuth-based supercell structure. *Advanced Materials*, **25**, 1028–1032.

(50) Aurivillius, B. (1949) Mixed bismuth oxides with layer lattice. II. Structure of $Bi_4Ti_3O_{12.}$ Ark. *Kemi.*, **1**, 499–512.

(51) Zhu, Y., Chen, A., Zhou, H., et al. (2013) Research updates: epitaxial strain relaxation and associated interfacial reconstructions: the driving force for creating new structures with integrated functionality. *APL Materials*, **1**, art. no. 050702.

(52) Kitagawa, Y., Hiraoka, Y., Honda, T., et al. (2010) Low-field magnetoelectric effect at room temperature. *Nature Materials*, **9**, 797–802.

(53) Evans, D.M., Schilling, A., Kumar, A., et al. (2013) Magnetic switching of ferroelectric domains at room temperature in multiferroic PZTFT. *Nature Communications*, **4**, art. no. 1534.

(54) Wang, L., Wang, D., Cao, Q., et al. (2012) Electric control of magnetism at room temperature. *Scientific Reports*, **2**, art. no. 223.

(55) Sanchez, D.A., Ortega, N., Kumar, A., et al. (2013) Room-temperature single phase multiferroic magnetoelectrics: $Pb(Fe, M)_x(Zr,Ti)_{(1-x)}O_3$ [M = Ta, Nb]. *Journal of Applied Physics*, **113**, art. no. 074105.

(56) Schiemer, J., Carpenter, M.A., Evans, D.M., et al. (2014) Studies of the room-temperature multiferroic $Pb(Fe_{0.5}Ta_{0.5})_{0.4}(Zr_{0.53}Ti_{0.47})_{0.6}O_3$: resonant ultrasound spectroscopy, dielectric, and magnetic phenomena. *Advanced Functional Materials*, **24**, 2993–3002.

(57) Wang, J., Scholl, A., Zheng, H., et al. (2005) Response to comment on “Epitaxial $BiFeO_3$ multiferroic thin film heterostructures”. *Science*, **307**, 1203.

(58) Eerenstein, W., Morrison, F.D., Dho, J., et al. (2005) Comment on "Epitaxial $BiFeO_3$ multiferroic thin film heterostructures”. *Science*, **307**, 1203.

(59) Béa, H., Bibes, M., Fusil, S., et al. (2006) Investigation on the origin of the magnetic moment of $BiFeO_3$ thin films by advanced X-ray characterisations. *Physical Review B*, **74** art. no. 020101.

(60) Keeney, L., Kulkarni, S., Deepak, N., et al. (2012) Room temperature ferroelectric and magnetic investigations and detailed phase analysis of Aurivillius phase $Bi_5Ti_3Fe_{0.7}Co_{0.3}O_{15}$ thin films. *Journal of Applied Physics*, **112**, art. no. 052010.

(61) Palizdar, M., Comyn, T.P., Ward, M.B., et al. (2012) Cystallographic and magnetic identification of secondary phase in oriented $Bi_5Fe_{0.5}Co_{0.5}Ti_3O_{15}$ ceramics. *Journal of Applied Physics*, **112**, art. no. 073919.

(62) Patri, S., Choudhary, R., and Samantaray, B. (2008) Studies of structural, dielectric and impedance properties of $Bi_9Fe_5Ti_3O_{27}$ ceramics. *Journal of Electroceramics*, **20**, 119–126.

(63) Zhang, P.F., Deepak, N., Keeney, L., et al. (2012) The structural and piezoresponse properties of *c*-axis-oriented Aurivillius phase $Bi_5Ti_3FeO_{15}$ thin films deposited by atomic vapor deposition. *Applied Physics Letters*, **101**, art. no. 112903.

(64) Ahn, S.I., Noguchi, Y., Miyayama, M., and Kudo, T. (2000) Structural and electrical characterization of $Bi_5Ti_3Fe_{1-x}Mn_xO_{15}$ system. *Materials Research Bulletin*, **35**, 825–834.

(65) Keeney, L., Groh, C., Kulkarni, S., et al. (2012) Room temperature electromechanical and magnetic investigations of ferroelectric Aurivillius phase $Bi_5Ti_3(Fe_xMn_{1-x})O_{15}$ ($x = 1$ and 0.7) chemical solution deposited thin films. *Journal of Applied Physics*, **112**, art. no. 024101.

(66) Lomanova, N.A., Morozov, M.I., Ugolkov, V.L., and Gusarov, V.V. (2006) Properties of aurivillius phases in the $Bi_4Ti_3O_{12}$–$BiFeO_3$ system. *Inorganic Materials*, **42**,189–195.

(67) Suarez, D.Y., Reaney, I.M., and Lee, W.E. (2001) Relation between tolerance factor and T_c in Aurivillius compunds. *Journal of Materials Research*, **16**, 3139–3149.

(68) Glazer, A.M. (1972) The classification of titled octahedra in perovskites. *Acta Crystallographica Section B – Structural Science*, **B 28**, 3384–3392.

(69) Hervoches, C.H., Snedden, A., Riggs, R., et al. (2002) Structural behavior of the four-layered Aurivillius-phase ferroelectrics $SrBi_4Ti_4O_{14}$ and $Bi_5Ti_3FeO_{15}$. *Journal of Solid State Chemistry*, **164**, 280–291.

(70) Lomanova, N.A., Semenov, V.G., Panchuk, V.V., and Gusarov, V.V. (2012) Structural changes in the homologous series of the Aurivillius phases $Bi_{n+1}Fe_{n-3}Ti_3O_{3n+3}$. *Journal of Alloys and Compounds*, **528**, 103–108.

(71) Sanson, A. and Whatmore, R.W. (2002) Properties of $Bi_4Ti_3O_{12}$–$(Na_{1/2}Bi_{1/2})TiO_3$ piezoelectric ceramics. *Japanese Journal of Applied Physics*, **41**, 7127–7130.

(72) Sanson, A. and Whatmore, R.W (2005) Phase diagram of the $Bi_4Ti_3O_{12}$–$BaTiO_3$–$(Na_{1/2}Bi_{1/2})TiO_3$ system. *Journal of the American Ceramic Society*, **88**, 3147–3153.

(73) Shimakawa, Y., Kubo, Y., Nakagawa, Y., et al. (1999) Crystal structures and ferroelectric properties of $SrBi_2Ta_2O_9$ and $Sr_{0.8}Bi_{2.2}Ta_2O_9$. *Applied Physics Letters*, **74**, 1904–1906.

(74) Shibuya, A., Noda, M., and Okuyama, M. (2004) Preparation and basic properties of ferroelectric Bi_3TiNbO_9–$Bi_4Ti_3O_{12}$ thin films with different superlattice structures. *Ferroelectrics*, **303**, 83–88.

(75) Kim, Y.I. and Jeon, M.K. (2004) Combined structural refinement of $Bi_4Ti_3O_{12}$ using X-ray and neutron powder diffraction data. *Materials Letters*, **58**, 1889–1893.

(76) Hervoches, H.C., Snedden, A., Riggs, R., et al. (2002) Structural behavior of the four-layer Aurivillius-phase ferroelectrics $SrBi_4Ti_4O_{15}$ and $Bi_5Ti_3FeO_{15}$. *Journal of Solid State Chemistry*, **164**, 280–291.

(77) "Crystallographica, v1.60d, (c) Oxford Cryosystems Ltd," v1.60d (1995–2007).

(78) Momma, K. and Izumi, F. (2011) VESTA 3 for three-dimensional visualization of crystal, volumetric and morphology data. *Journal of Applied Crystallography*, **44**, 1272–1276.

(79) Lomanova, N.A., Morozov, M.I., Ugolkov, V.L., and Gusarov, V.V. (2006) Properties of aurivillius phases in the $Bi_4Ti_3O_{12}$–$BiFeO_3$ system. *Inorganic Materials*, **42**, 189–195.

(80) Anderson, J.S. (1969) Non-stoichiometric and ordered phases:thermodynamic considerations, in *The Chemistry of Extended Defects in Non-metallic Solids: Proceedings of the Institute for Advanced Study on the Chemistry of Extended Defects in Non-Metallic Solids*, edited by L. Eyring and M. O'Keefe, North-Holland Publishing Company, Amsterdam, London, pp. 1–20.

(81) Zurbuchen, M.A., Tian, W., Pan, X.Q., et al. (2007) Morphology, structure, and nucleation of out-of-phase boundaries (OPBs) in epitaxial films of layered oxides. *Journal of Materials Research*, **22**, 1439–1471.

(82) Kobayashi, T., Noguchi, Y., and Miyayama, M. (2005) Enhanced spontaneous polarization in superlattice-structured $Bi_4Ti_3O_{12}$–$BaBi_4Ti_4O_{15}$ single crystals. *Applied Physics Letters*, **86**, art. no. 012907.

(83) Zurbuchen, M.A., Podraza, N.J., Schubert, J., et al. (2012) Synthesis of the superlattice complex oxide $Sr_5Bi_4Ti_8O_{27}$ and its band gap behavior. *Applied Physics Letters*, **100**, art. no. 223109.

(84) Deepak, N., Zhang, P.F., Keeney, L., et al. (2013) Atomic vapor deposition of bismuth titanate thin films. *Journal of Applied Physics*, **113**, art. no. 187207.

(85) Keeney, L., Groh, C., Kulkarni, S., et al. (2012) Room temperature electromechanical and magnetic investigations of ferroelectric Aurivillius phase $Bi_5Ti_3(Fe_xMn_{1-x})O_{15}$ ($x = 1$ and 0.7) chemical solution deposited thin films. *Journal of Applied Physics*, **112**, art. no. 024101.

(86) Keeney, L., Zhang, P.F., Groh, C., et al. (2010) Piezoresponse force microscopy investigations of Aurivillius phase thin films. *Journal of Applied Physics*, **108**, art. n. 042004.

(87) Zhang, P.F., Deepak, N., Keeney, L., et al. (2012) The structural and piezoresponse properties of *c*-axis-oriented Aurivillius phase $Bi_5Ti_3FeO_{15}$ thin films deposited by atomic vapor deposition. *Applied Physics Letters*, **101**, art. no. 112903.

(88) Wouters, D.J., Maes, D., Goux, L., et al. (2006) Integration of $SrBi_2Ta_2O_9$ thin films for high density ferroelectric random access memory. *Journal of Applied Physics*, **100**, art. no. 051603.

(89) Park, B.H., Kang, B.S., Bu, S.D., et al. (1999) Lanthanum-substituted bismuth titanate for use in non-volatile memories. *Nature*, **401**, 682–684.

(90) Yang, J., Tong, W., Liu, Z., et al. (2012) Structural, magnetic, and EPR studies of the Aurivillius phase $Bi_6Fe_2Ti_3O_{18}$ and $Bi_6FeCrTi_3O_{18}$. *Physical Review B*, **86**, art. no. 104410.

(91) Fujii, E. and Uchiyama, K. (2003) First 0.18 μm SBT-based embedded FeRAM technology with hydrogen damage free stacked cell structure. *Integrated Ferroelectrics*, **53**, 317–323.

(92) de Araujo, C.A.P., Cuchiaro, J.D., McMillan, L.D., et al. (1995) Fatigue-free ferroelectric capacitors with platinum electrodes. *Nature*, **374**, 627–629.

(93) Newnham, R.E., Wolfe, R.W., and Dorrian, J.F. (1971) Structural basis of ferroelectricity in the bismuth titanate family. *Materials Research Bulletin*, **6**, 1029–1040.

(94) Watanabe, T. and Funakubo, H. (2006) Controlled crystal growth of layered-perovskite thin films as an approach to study their basic properties. *Journal of Applied Physics*, **100**, art. no. 051602.

(95) Irie, H., Miyayama, M., and Kudo, T. (2001) Structure dependence of ferroelectric properties of bismuth layer-structured ferroelectric single crystals. *Journal of Applied Physics*, **90**, 4089–4094.

(96) Boullay, P., Trolliard, G., Mercurio, D., et al. (2002) Toward a unified approach to the crystal chemistry of Aurivillius-type compounds: I. The structural model. *Journal of Solid State Chemistry*, **164**, 252–260.

(97) Mao, X.Y., Wang, W., and Chen, X.B. (2008) Electrical and magnetic properties of $Bi_5FeTi_3O_{15}$ compound prepared by inserting $BiFeO_3$ into $Bi_4Ti_3O_{12}$. *Solid State Commununications*, **147**, 186–189.

(98) Srinivas, A., Kumar, M.M., Suryanarayana, S.V., and Bhimasankaram, T. (1999) Investigation of dielectric and magnetic nature of $Bi_7Fe_3Ti_3O_{21}$. *Materials Research Bulletin*, **34**, 989–996.

(99) Srinivas, A., Kim, D.W., Hong, K.S., and Suryanarayana, S.V. (2004) Study of magnetic and magnetoelectric measurements in bismuth iron titanate ceramic – $Bi_8Fe_4Ti_3O_{24}$. *Materials Research Bulletin*, **39**, 55–61.

(100) Keeney, L., Groh, C., Kulkarni, S., et al. (2012) Room temperature electromechanical and magnetic investigations of ferroelectric Aurivillius phase $Bi_5Ti_3(Fe_xMn_{1\text{-}x})O_{15}$ ($x = 1$ and 0.7) chemical solution deposited thin films. *Journal of Applied Physics*, **112**, art. no. 024101.

(101) Zurbuchen, M.A., Freitas, R.S., Wilson, M.J., et al. (2007) Synthesis and characterization of an $n = 6$ Aurivillius phase incorporating magnetically active manganese, $Bi_7(Mn,Ti)_6O_{21}$. *Applied Physics Letters*, **91**, art. no. 033113.

(102) Mao, X., Wang, W., Chen, X., and Lu, Y. (2009) Multiferroic properties of layer-structured $Bi_5Fe_{0.5}Co_{0.5}Ti_3O_{15}$ ceramics. *Applied Physics Letters*, **95**, art. no. 082901.

(103) Keeney, L., Kulkarni, S., Deepak, N., et al. (2012) Room temperature ferroelectric and magnetic investigations and detailed phase analysis of Aurivillius phase $Bi_5Ti_3Fe_{0.7}Co_{0.3}O_{15}$ thin films. *Journal of Applied Physics*, **112**, art. no. 052010.

(104) Palizdar, M., Comyn, T.P., Ward, M.B., et al. (2012) Cystallographic and magnetic identification of secondary phase in oriented $Bi_5Fe_{0.5}Co_{0.5}Ti_3O_{15}$ ceramics. *Journal of Applied Physics*, **112**, art. no. 073919.

(105) Nan, C.W., Bichurin, M.I., Dong, S., et al. (2008) Multiferroic magnetoelectric composites: historical perspective, status, and future directions. *Journal of Applied Physics*, **103**, art. no. 031101.

(106) Huang, F.Z., Lu, X.M., Xu, T.T., et al. (2012) Multiferroic properties of Co and Nd co-substituted $Bi_5Ti_3FeO_{15}$ thin films. *Thin Solid Films*, **520**, 6489–6492.

(107) Yang, J., Tong, W., Liu, Z., et al. (2012) Structural, magnetic, and EPR studies of the Aurivillius phase $Bi_6Fe_2Ti_3O_{18}$ and $Bi_6FeCrTi_3O_{18}$. *Physical Review B*, **86**, art. no. 104410.

(108) Yang, J., Yin, L.H., Liu, Z., et al. (2012) Magnetic and dielectric properties of Aurivillius phase $Bi_6Fe_2Ti_3O_{18}$ and the doped compounds. *Applied Physics Letters*, **101**, art. no. 012402.

(109) Prasad, N.V. and Kumar, G.S. (2000) Magnetic and magnetoelectric measurements on rare-earth-substituted five-layered $Bi_6Fe_2Ti_3O_{12}$ compound. *Journal of Magnetism and Magnetic Materials*, **213**, 349–356.

(110) Liu, Z., Yang, J., Tang, X.W., et al. (2012) Multiferroic properties of Aurivillius phase $Bi_6Fe_{2\text{-}x}Co_xTi_3O_{18}$ thin films prepared by a chemical solution deposition route. *Applied Physics Letters*, **101**, art. no. 122402.

(111) Schumacher, M., Baumann, P.K., and Seidel, T. (2006) AVD and ALD as two complementary technology solutions for next generation dielectric and conductive thin-film processing. *Chemical Vapor Deposition*, **12**, 99–108.

(112) Hope, D.A., Cheetham, A.K., and Long, G.J. (1982) A neutron diffraction, magnetic susceptibility, and Mossbauer-effect study of the (Mn,Fel-$)_y$O solid solutions. *Inorganic Chemistry*, **21**, 2804–2809.

(113) Li, J.B., Huang, Y.P., Rao, G.H., Liu, G.Y., et al. (2010) Ferroelectric transition of Aurivillius compounds $Bi_5Ti_3FeO_{15}$ and $Bi_6Ti_3Fe_2O_{18}$. *Applied Physics Letters*, **96**, art. no. 222903.

(114) Kalinin, S.V., Gruverman, A., and Bonnell, D.A. (2004) Quantitative analysis of nanoscale switching in $SrBi_2Ta_2O_9$ thin films by piezoresponse force microscopy. *Applied Physics Letters*, **85**, 795–797.

(115) Kalinin, S.V., Rodriguez, B.J., Jesse, S., et al. (2007) Nanoscale electromechanics of ferroelectric and biological systems: a new dimension in scanning probe microscopy. *Annual Review of Materials Research*, **37**, 189–238.

(116) Varghese, J., Barth, S., Keeney, L., et al. (2012) Nanoscale ferroelectric and piezoelectric properties of Sb_2S_3 nanowire arrays. *Nano Letters*, **12**, 868–872.

(117) Kalinin, S.V., Ye, Z.G., and Kholkin, A.L. (2012) Preface to special topic: piezoresponse force microscopy and nanoscale phenomena in polar materials. *Journal of Applied Physics*, **112**, art. no. 051901.

(118) Kalinin, S.V., Setter, N., and Kholkin, A.L. (2009) Electromechanics on the nanometer scale: emerging phenomena, devices, and applications. *MRS Bulletin*, **34**, 634–642.

(119) Rodriguez, B.J., Callahan, C., Kalinin, S.V., and Proksch, R. (2007) Dual-frequency resonance-tracking atomic force microscopy. *Nanotechnology*, **18**, art. no. 475504.

(120) Mao, X.Y., Wang, W., and Chen, X.B. (2008) Electrical and magnetic properties of $Bi_5FeTi_3O_{15}$ compound prepared by inserting $BiFeO_3$ into $Bi_4Ti_3O_{12}$. *Solid State Communications*, **147**, 186–189.

(121) Srinivas, A., Kim, D.W., Hong, K.S., and Suryanarayana, S.V. (2003) Observation of ferroelectromagnetic nature in rare-earth-substituted bismuth iron titanate. *Applied Physics Letters*, **83**, 2217–2219.

(122) Zhu, J., Mao, X.Y., and Chen, X.B. (2004) Properties of vanadium-doped $SrBi_4Ti_4O_{15}$ ferroelectric ceramics. *Solid State Communications*, **129**, 707–710.

(123) Zurbuchen, M.A., Freitas, R.S., Wilson, M.J., et al. (2007) Synthesis and characterization of an $n = 6$ Aurivillius phase incorporating magnetically active manganese, $Bi_7(Mn,Ti)_6O_{21}$. *Applied Physics Letters*, **91**, art. no. 033113.

(124) Yang, J., Yin, L.H., Liu, Z., et al. (2012) Magnetic and dielectric properties of Aurivillius phase $Bi_6Fe_2Ti_3O_{18}$ and the doped compounds. *Applied Physics Letters*, **101**, art. no. 012402.

(125) Lu, J., Qiao, L.J., Ma, X.Q., and Chu, W.Y. (2006) Magnetodielectric effect of $Bi_6Fe_2Ti_3O_{18}$ film under an ultra-low magnetic field. *Journal of Physics: Condensed Matter*, **18**, 4801–4807.

(126) Srinivas, A., Suryanarayana, S.V., Kumar, G.S., and Kumar, M.M. (1999) Magnetoelectric measurements on $Bi_5FeTi_3O_{15}$ and $Bi_6Fe_2Ti_3O_{18}$. *Journal of Physics: Condensed Matter*, **11**, 3335–3340.

(127) Guan, N., Wang, Y., Sun, D., and Xu, J. (2009) A simple one-pot synthesis of single-crystalline magnetite hollow spheres from a single iron precursor. *Nanotechnology*, **20**, art. no. 105603.

(128) Goya, G., Berquo, T., Fonseca, F., and Morales, M. (2003) Static and dynamic magnetic properties of spherical magnetite nanoparticles. *Journal of Applied Physics*, **94**, 3520–3528.

(129) Moore, G.E. (1965) Cramming more components onto integrated circuits. *Electronics*, **38**, 114–117.

(130) Tsymbal, E.Y. and Gruverman, A. (2013) Ferroelectric tunnel junctions: beyond the barrier. *Nature Materials*, **12**, 602–604.

(131) Garcia, V. and Bibes, M. (2012) Electronics: inside story of ferroelectric memories. *Nature*, **483**, 279–281.

(132) Esaki, L. (1974) Long journey into tunneling. *Science*, **183**,1149–1155.

(133) Scott, J.F. (2012) Applications of magnetoelectrics. *Journal of Materials Chemistry*, **22**, 4567–4574.

(134) Roy, A., Gupta, R., and Garg, A. (2012) Multiferroic memories. Advances in Condensed Matter Physics, art. no. 926290.

(135) Bibes, M. and Barthelemy, A. (2008) Multiferroics: towards a magnetoelectric memory. *Nature Materials*, **7**, 425–426.

(136) Chu, Y.H., Martin, L.W., Holcomb, M.B., et al. (2008) Electric-field control of local ferromagnetism using a magnetoelectric multiferroic. *Nature Materials*, **7**, 478–482.

(137) Fiebig, M., Lottermoser, T., Kneip, M.K., and Bayer, M. (2006) Correlations between magnetic and electrical orderings in multiferroic manganites. *Journal of Applied Physics*, **99**, art. no. 08E302.

(138) Scott, J.F. (2007) Data storage: multiferroic memories. *Nature Materials*, **6**, 256–257.

(139) Fong, D.D., Stephenson, G.B., Streiffer, S.K., et al. (2004) Ferroelectricity in ultrathin perovskite films. *Science*, **304**,1650–1653.

(140) Bibes, M. (2012) Nanoferronics is a winning combination. *Nature Materials*, **11**, 354–357.

(141) Bibes, M., Villegas, J.E., and Barthélémy, A. (2011) Ultrathin oxide films and interfaces for electronics and spintronics. *Advances in Physics*, **60**, 5–84.

(142) Chen, Y., Gillette, S.M., Fitchorov, T., et al. (2011) Quasi-one-dimensional miniature multiferroic magnetic field sensor with high sensitivity at zero bias field. *Applied Physics Letters*, **99** (4), art. no. 042505.

(143) Lenz, J. and Edelstein, A.S. (2006) Magnetic sensors and their applications. *IEEE Sensors Journal*, **6** (3), 631–649.

(144) Srinivasan, G., Rasmussen, E.T., Levin, B.J., and Hayes, R. (2002) Magnetoelectric effects in bilayers and multilayers of magnetostrictive and piezoelectric perovskite oxides. *Physical Review B*, **65** (13), art. no. 134402.

(145) Ryu, J., Carazo, A.V., Uchino, K., and Kim, H.E. (2001) Magnetoelectric properties in piezoelectric and magnetostrictive laminate composites. Japanese Journal of Applied Physics. *Part 1 – Regular Papers Short Notes and Review Papers*, **40** (8), 4948–4951.

(146) Zhai, J., Xing, Z., Dong, S., et al. (2006) Detection of pico-Tesla magnetic fields using magneto-electric sensors at room temperature. *Applied Physics Letters*, **88** (6), art. no. 062510.

26

Semiconducting and Photovoltaic Ferroelectrics

Andrew R. Akbashev[1], Vladimir M. Fridkin[1,2], and Jonathan E. Spanier[1]

[1] *Drexel University, USA*
[2] *Russian Academy of Sciences, Moscow, Russian Federation*

26.1 Introduction

Light–matter interactions in ferroelectric polar materials have attracted attention for decades, driven largely by interest in electronic carrier separation via ferroelectric polarization, observation of anomalously large photovoltages in bulk ferroelectrics, and large optical non-linear susceptibilities. Coupling of light with thin-film electronic materials possessing switchable ferroelectric order is enabling for application of new functionalities, including strain-engineered design of nanoscale ferroelectric domain structure and domain wall variant-dependent electronic and optical properties for manipulating carrier separation resulting in above band-gap voltage output and non-volatile memory based on the ferroelectric photovoltaic effect. Advances, for example, in fundamental understanding of the bulk ferroelectric photovoltaic effect and in optical manipulation of ferroelectric polarization suggest new paradigms for encoding, manipulating, and storing information, optical detection, and sensing that extend well beyond photovoltaic power conversion alone.

In this chapter we review the background and significant advances in the science based on exploiting known and novel light–matter interactions in semiconductor ferroelectrics possessing atomic and mesoscopic-scale degrees of freedom. Novel chemical design strategies for attaining, tuning, and understanding FE and electronic properties through, for example, cation arrangement and cation and O stoichiometry, will be discussed in conjunction with

Nanoscale Ferroelectrics and Multiferroics: Key Processing and Characterization Issues, and Nanoscale Effects, First Edition. Edited by Miguel Algueró, J. Marty Gregg, and Liliana Mitoseriu.
© 2016 John Wiley & Sons, Ltd. Published 2016 by John Wiley & Sons, Ltd.

property characterizations that reveal how new materials have desired polar, light-absorbing and other property combinations. Strategies for synthesizing new complex oxides in both bulk and thin-film form, permitting precise control of stoichiometry and oxidation states and using new methods that are manufacturing-scalable, also will be discussed briefly. Recent advances in understanding coupling of light with switchable polar and orbital degrees of freedom with high spatial, spectral, and/or temporal resolution, and with control of surface environment advance the practical possibilities for using ferroelectrics for applications utilizing light. The promising outlook for materials discovery and innovation in, and applications of, semiconducting ferrroelectrics and multiferroics may be further enhanced through materials genomic approaches.

Ferroelectrics, having intrinsically uncompensated dipolar ordering within the crystal structure, have long been known to exhibit various light-mediated effects that appear in polar and non-polar materials, such as the Dember effect and photorefraction. The intriguing interaction of light with ferroelectrics remains an important frontier area, particularly the photovoltaic effect, understanding of which holds promise for gaining additional insight into the behavior of photoexcited carriers and the development of future photovoltaic materials, devices, and their application. The discussion will cover the key aspects of photovoltaics in ferroelectrics and different mechanisms for the photovoltaic effect taking most known or novel and promising ferroelectric materials as examples. First, we survey the historical and fundamental aspects of photovoltaic effects in various ferroelectrics, providing a comparison with well-known semiconductor materials. Next we highlight various chemical approaches to and design aspects of ferroelectric materials, providing a perspective of the existing or expected photovoltaic properties of such ferroelectrics. In the end, we remark on the outlook for this emerging and captivating field of photovoltaic ferroelectrics. This is a rapidly changing and expanding field; the reader is also referred to the definitive monograph on the subject [1] and other reviews on the subject that have been published recently [2].

26.2 Basic Principles of Photovoltaic Effect in Ferroelectrics

In the 1931 Harry Dember described a photoeffect [3], in which a voltage developed between dark and illuminated sides of a crystal. The so-called Dember effect arises from a difference in electron and hole mobilities produced on the illuminated side of a crystal. In contrast, when a crystal is evenly illuminated, the photovoltage can appear as a result of band bending. It has long been known that for a photovoltaic device based on carrier separation due to band bending at an interface or across a crystal between contacts, the maximum photovoltage developed is ultimately limited by its band-gap value. As early as 1946 anomalously large photovoltages (more than five times the band gap) were reported in films of ThS and PbS [4]. Later, Pensak and Goldstein reported very large temperature- and incident optical intensity-dependent photovoltages in CdTe, exceeding 200V [5,6]. Experiments involving illumination of ferroelectric piezoelectric crystals also revealed photovoltages much larger than the band-gap, first reported by Fridkin and co-workers in SbSI [7] and later in $LiNbO_3$ by Glass et al. [8]. The observation of such anomalous behavior in ferroelectrics opened a new venue in the physics of ferroelectric and light–matter interactions, and the phenomenon was named the "bulk photovoltaic effect" (BPVE). In addition

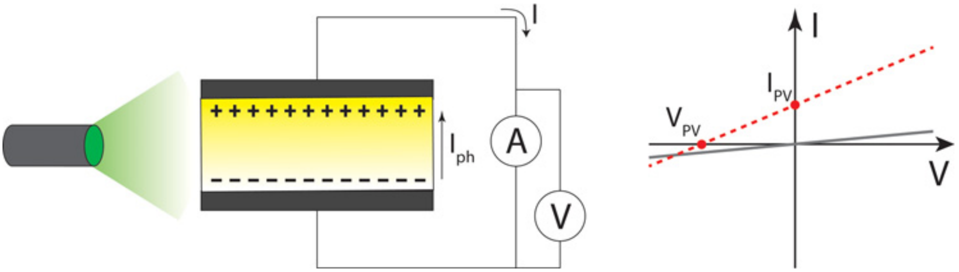

Figure 26.1 Schematic illustration of a photoexcitation of a ferroelectric by a visible light, which results in the development of an open-circuit photovoltage and a short-circuit photocurrent

to a large photovoltage that was observed to be invariant with illumination intensity, short-circuited ferroelectric crystals were shown to enter a steady-state photocurrent regime when exposed to homogeneous light, demonstrating a linear dependency on the light intensity [9, 10]. Illustrated in Figure 26.1(a) is the scheme of current–voltage $I(V)$ measurements in a ferroelectric crystal, poled beforehand along the measured current direction. A typical BPVE response in a ferroelectric crystal is illustrated in Figure 26.1(b). Both the dark current and the photocurrent $I_{\mathrm{ph}}(V)$ are shown. The intersections of the photocurrent curve with the ordinate is I_{PV}, termed as a photovoltaic current, and with the abscissa is V_{PV}, defined as a photovoltage. Notable is the linear photocurrent-voltage response, markedly different from the rectifying character of diode-based photovoltaics that appears under both dark and light conditions.

BPVE can be observed in crystals which belong to 20 point groups lacking a centre of inversion symmetry (including ferroelectrics and piezoelectrics). For a macroscopic, phemonenological description of the phenomenon, let us consider a ferroelectric crystal in a monodomain state, homogenously illuminated (Figure 26.1). For an open-circuit case, the total current density J_{total} emerging in the crystal is a sum of a photovoltaic current density J_{PV} and the current associated with an induced electric field E_{PV} inside the crystal [1, 9, 11]:

$$I_{\mathrm{total}} = I_{\mathrm{PV}} + (\sigma_{\mathrm{dark}} + \sigma_{\mathrm{ph}})\, E_{\mathrm{PV}} \tag{26.1}$$

where σ_{dark} and σ_{ph} are dark conductivity and photoconductivity, respectively. The illumination generates electron-hole pairs and, as a result, charges the ferroelectric capacitor, producing an internal electric field E_{PV}. This electric field, in turn, drives the dark current and photocurrent and is responsible for the appearance of the photovoltage V_{PV}:

$$V_{\mathrm{PV}} = J_{\mathrm{PV}} d/(\sigma_{\mathrm{dark}} + \sigma_{\mathrm{ph}}) \tag{26.2}$$

where d is the distance between the two oppositely charged surfaces of the ferroelectric crystal. From this expression it is immediately seen that the suppression of both σ_{dark} and σ_{ph} conductivities increases the value of the photovoltage V_{PV}. Thus, one can conclude that for a high photovoltage a ferroelectric should not exhibit high conductivity, while a high photovoltaic current in a ferroelectric, on the contrary, does require good conduction properties. In other words, the photovoltaic efficiency of typical ferroelectrics is mediocre due to small currents on the order of 1 nA cm^{-2}.

Several microscopic mechanisms have been proposed for the BPVE. Glass proposed an asymmetric potential well [12]. Belincher and Sturman proposed asymmetric carrier scattering centers producing net current from randomly drifting carriers [13]. Fridkin has proposed the ballistic mechanism, photoexcitation of non-thermalized carriers with asymmetric momenta and also due to relativistic splitting of the conduction band minimum under polarized light (so-called Dresselhaus or Rashba effect [14]). The hot carriers travel ballistically and descend to the conduction band over a thermalization length. In each of these mechanisms the BPVE can be viewed as a result of different direct and reverse probabilities of electron transitions in k-space due to the non-centrosymmetry of the structure. In a centrosymmetric crystal electron photoexcitations from the valence band or impurity level to the state with the momentum $\boldsymbol{k}$ and $-\boldsymbol{k}$ have equal probabilities. When a crystal lacks inversion symmetry, such probabilities become different, resulting in an asymmetric distribution of electron momenta of photoexcited charge carriers. An alternate model involves the so-called shift mechanism of the BPVE; it is quantum-mechanical in nature, obtained by taking into account the non-diagonal elements of the density matrix. The BPVE in this case is caused not by the carrier movement in the band, but by the shift R in real space following the carrier band-band transition. In these models a key length scales in this process are thermalization length (free path) and the magnitude of the so-called shift vector, corresponding to the length over which entangled carrier-photon non-equilibrium. One of the main drawbacks of using the bulk photovoltaic effect in practical solar energy conversion are impractically small power conversion efficiencies apparently due to the rather weak conducting properties of ferroelectrics and the nature of the bulk photovoltaic effect. Thus, the prevailing view has been the following:

(a) Giant photovoltages are caused by photoexcited charge carriers “separated” by ferroelectric polarization.
(b) The current generated by a giant photovoltage remains very small since the ferroelectric naturally cannot exhibit strong conductivity (as a dielectric).
(c) If the ferroelectric exhibits a high leakage current (better conductivity), its polarization may deteriorate.

In 1981 von Baltz and Kraut proposed a theory for calculating short-circuit photovoltaic current in a pure crystal in terms of its Bloch states and energy bands [15]. Neglecting the effect of photon drag, the short-circuit photovoltaic current can be expressed as:

$$j_{\mathrm{PV}} = G_{ijk} I_0 e_j e_k \tag{26.3}$$

where G_{ijk} is the third-rank photovoltaic tensor (the subscripts ijk refer to the Cartesian coordinate system), I_0 is the illumination intensity, and e_j and e_k are unit vectors describing the electric field components [15]. As can be seen from this expression, the shift current originates from a second-order interaction with light (quadratic with electric field), for which the only requirement is the broken inversion symmetry (ferroelectric polarization may be absent). The shift current tensor couples one or two incident EM fields (each having photon energies larger than the band-gap) of a given linear optical polarization state and incident angle with respect to the ferroelectric polarization, crystallographic plane and collected current directions. Perturbative analysis of the electromagnetic field classically yields the following expression for the shift current [15–17]:

$$J_q = \sigma_{rsq} E_r E_S \tag{26.4}$$

Here σ_{rsq} links the current density J_q with the electromagnetic field components E_r and E_s and can be expressed as follows:

$$\begin{aligned}\sigma_{rsq}(\omega) = \pi\, e \left(\frac{e}{m\hbar\omega}\right)^2 \sum_{n',n''} \int d\boldsymbol{k}(f[n''\boldsymbol{k}] - f[n'\boldsymbol{k}])\; x\; \langle n'\boldsymbol{k}\;|\hat{P}_S|\;n''\boldsymbol{k}\rangle \\ \times x\; R_q\; x\; \delta(\omega_{n''}(\boldsymbol{k}) - \omega_{n'}(\boldsymbol{k}) \pm \omega)\end{aligned} \tag{26.5}$$

where n' and n'' are indexes for the bands, $\boldsymbol{k}$ is the wave vector, and $\omega_n(\boldsymbol{k})$ is the energy of the nth band.

The shift vector R_q is

$$R_q(n', n'', \boldsymbol{k}) = -\frac{\partial \phi_{n'n''}(\boldsymbol{k}, \boldsymbol{k})}{\partial \boldsymbol{k}_q} - [\chi_{n''q}(\boldsymbol{k}) - \chi_{n'q}(\boldsymbol{k})] \tag{26.6}$$

where χ_n are the Berry connections for the band n and ϕ_{nn} is the phase of the momentum matrix element between bands n' and n''. The shift current can be understood as the product of terms depending on (1) the transition intensity, which is proportional to the imaginary part of the dielectric function, and (2) the shift vector, which represents the mean distance traveled by coherent carriers during their lifetimes. Using quantum-mechanical calculations within the density functional theory (DFT) framework, Rappe and Young developed a first-principle approach to the calculation of shift current in ferroelectrics [16, 18]. A striking and consistent agreement between the results of such calculations and the experimental values for $BaTiO_3$ is reproduced, including the difference in sign between the majority of the transverse (*xxZ*) and longitudinal (*zzZ*) responses. The calculations reveal a remarkably non-trivial, complex relationship between the shift current and ferroelectric polarization, not evident from Equation (26.5), and this methodology has been applied to the calculation of the shift current in other ferroelectric oxides by these authors, including $BiFeO_3$ [18]. The availability of a DFT approach has opened the possibility of design and simulation of new BPVE materials possessing larger shift current responses and energy conversion efficiencies.

While the shift current is a bulk tensor property that requires non-centrosymmetric (and not necessarily FE) materials, the effect can be more pronounced and it can be manipulated actively through polarization direction, strain, and through materials design in FE materials. For example, the sign of the shift current varies with incident photon energy, incident EM field vector with respect to FE polarization and to collected current directions, and with cation chemistry – even within a group of isostructural FE perovskite oxides of identical symmetry. This enables a new, larger multidimensional parameter space for light-matter coupling with an extraordinary potential for signal encoding and decoding, routing, and manipulation.

26.3 Experimental Evidence of the Bulk Photovoltaic Effect in Ferroelectrics

We next review some of the exemplifying observations of the bulk photovoltaic effect and photocurrent in ferroelectrics. Photovoltaic current in a ferroelectric was first observed in 1955 by A.G. Chynoweth and was proposed to be a consequence of space charge layers at the surface [19]. A single crystal of $BaTiO_3$, *without* an applied electric field, was seen to exhibit pronounced jumps of the electrical current along the polarization direction during illumination, followed by a steady photocurrent state (under no illumination) that was clearly distinct from the pyrocurrent. Afterwards, the photogenerated current was observed in other ferroelectrics, such as $LiNbO_3$ ($LiNbO_3$:Fe) and $KNbO_3$ [8,20], $LiTaO_3$ [21,22], SbSI [23], $SbNbO_4$ [24], $Pb(Ti,Zr)O_3$ [25,26], $BaTiO_3$ [22, 27], $Bi_4Ti_3O_{12}$ [28], $Sn_2P_2O_6$ [29], $KBiFe_2O_5$ [30], as well as various chemical solutions and heterostructures [31,32].

26.3.1 $BiFeO_3$

Bismuth ferrite has recently become one of the most notable multiferroics known today [33]. Having a perovskite crystal structure, $BiFeO_3$ has a record-breaking combination of high-temperature ferroelectric ($T_C = 1103$ K) and antiferromagnetic ($T_N = 643$ K) ordering temperatures, and its renaissance began in 2003, after the discovery of a very high ferroelectric polarization (up to 60 μC cm^{-2}, almost ten times higher than for bulk $BiFeO_3$ at that time) at room temperature found in $BiFeO_3$ thin films [34], initially presumed to be the result of an epitaxial strain. Stimulated by the finding, further research confirmed large values of polarization also in single crystals, indicating that proper crystal growth conditions and approaches are required to reduce charge leakage in $BiFeO_3$ and achieve sufficiently robust ferroelectric properties [35].

As a consequence, the first observation of the photovoltaic current in $BiFeO_3$ under visible light illumination was made only in 2009 by Choi et al. [36]. Thin plates of $BiFeO_3$ single crystals, polished down to ~80–90 μm in thickness, were placed between symmetric Au electrodes and current–voltage ($I(V)$) curves were measured along the polarization with the applied field V being lower than the coercive field of the samples. The experiments demonstrated an intrinsic diode behavior with rather large rectification ratios (159 at 300 K, 488 at 350 K). The diode forward direction appeared to always lie along the FE polarization and could be reproducibly reversed by an application of a polarization-switching electric pulse. In additional to numerous unusual properties, $BiFeO_3$ has one of the narrowest band-gaps of ~2.7 eV among known undoped oxide ferroelectrics, making it an interesting candidate for investigating the PV effect in ferroelectrics. Illuminated through the semitransparent Au electrodes, $BiFeO_3$ exhibited a steady negative photocurrent without any bias applied. The authors present time dependences of the photocurrents for different light wavelengths at room temperature. The steady-state current under 532 nm excitation reaches ~7 μA cm^{-2}, while under 630 nm the current has a thousand times smaller value. Such a significant difference in the steady-state current perfectly matches the expectation that the wavelength of 630 nm lies within the sub-band-gap energy region and cannot excite electrons from the valence to the conduction band. The rotation of the polarization plane of the incident light (or the rotation of the $BiFeO_3$ single crystal after fixing the polarization plane of the beam)

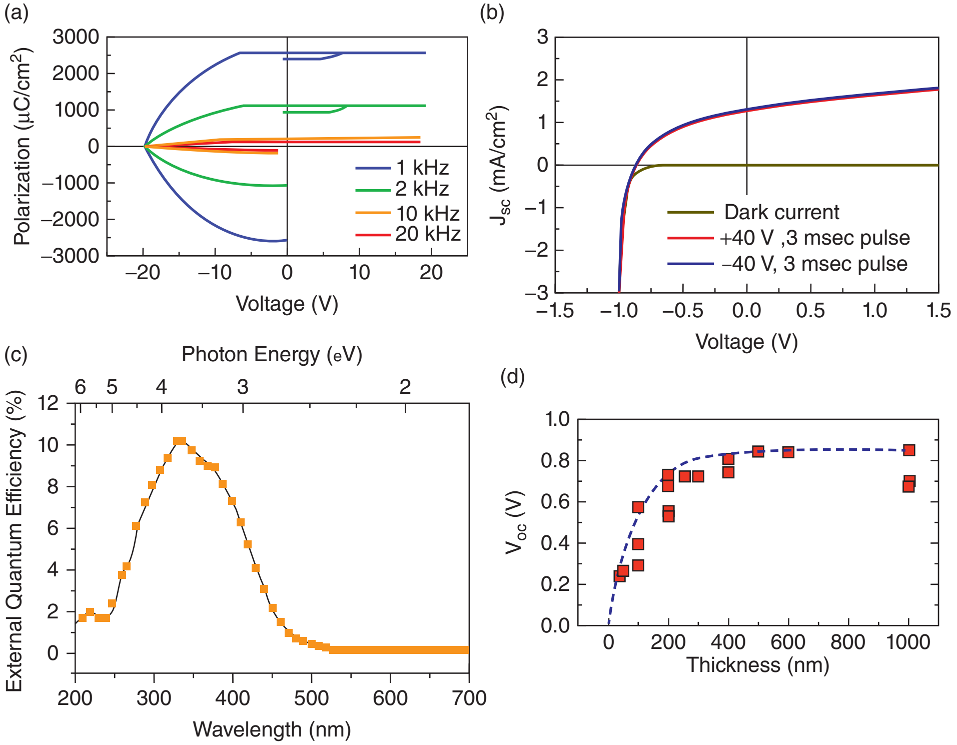

Figure 26.2 *(a) P-E hysteresis loops of the (001)BiFeO$_3$ thin film at different frequencies, (b) I(V) curves in dark and under illumination (2.85 suns) show a photovoltaic effect, and (c) EQE reaches ~10% for the wavelengths close to the corresponding energy of a bandgap. (d) Open-circuit voltage-versus-thickness measurements reveal an interface depletion of 300 nm. Reprinted with permission from [37]. Copyright [2009], AIP Publishing LLC*

caused the photovoltaic current to oscillate concurrently with its maximum corresponding to the light polarization being parallel to the ferroelectric polarization. This sinusoidal behavior was proposed to be the result of a second-order optical response that induces an asymmetric polarization, which in turn is responsible for this optical rectification effect. Further studies of epitaxial BiFeO$_3$ thin films showed that the open-circuit voltages can reach ~16–18 kV cm^{-1} for films thicker than 200 nm with short-circuit current densities of ~1.5 mA cm^{-2} [37]. Figure 26.2(a) and (b) show the corresponding diode-like behavior and photovoltaic effect for BiFeO$_3$ thin films, respectively.

Another important quantity is the *external quantum efficiency* (EQE), which quantifies the photovoltaic current as a function of the incident light wavelength. Such dependence for BiFeO$_3$ is shown in Figure 26.2(c). When the photon energy is larger than the band-gap, the conversion efficiency reaches its maximum of ~10% (the drop in EQE at $\lambda < 325$ nm is due to the light attenuation in the top ITO contact). The authors showed that the diode-like behavior is most likely to be driven by the formation of a Schottky barrier at the BiFeO$_3$–ITO interface, which creates a depletion layer in BiFeO$_3$ with an ionizable impurity density of ~10^{17} cm^{-3} (p-type) and a 1.25 eV offset potential. From Figure 26.2(d) it can be see

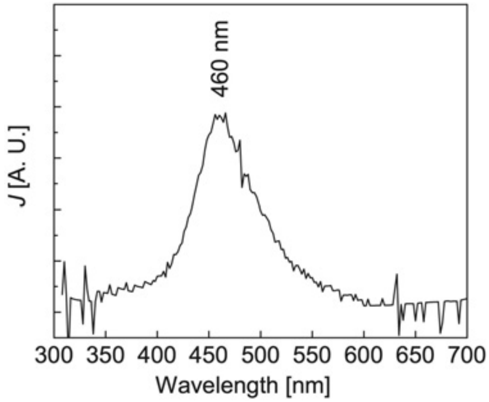

Figure 26.3 *Spectral response for the ITO/BiFeO$_3$(170 nm)/SrRuO$_3$/SrTiO$_3$(001) heterostructure. Reprinted with permission from [38]. Copyright © 2010 Wiley-VCH Verlag GmbH & Co. KGaA, Weinheim*

that the photovoltage saturates to the value of ~0.8 V when the thickness of the BiFeO$_3$ film is 200 nm and above, providing a further, more rigorous, proof that the depletion layer formation plays a major role in the observed phenomena. In order to clarify whether ferroelectric polarization contributes to the photovoltaic, (111)-oriented BiFeO$_3$ thin films with a strong out-of-plane polarization being in a single-domain state were examined. The photocurrent appeared to be a hundred times smaller than in the case of (001)-oriented films and exhibited a reversible one-order-of-magnitude change upon polarization switching by an applied electric field. The change of photovoltage upon polarization switching, on the other hand, was negligible. In another study of BiFeO$_3$ epitaxial films (170 nm thick) the spectral dependence of photocurrent revealed a peak with a different position as well as a smaller value of photovoltage [38] (see Figure 26.3). In contrast to the previous study where the films were grown by metal–organic chemical vapor deposition (MOCVD), in this case BiFeO$_3$ was deposited by radio-frequency (RF) magnetron sputtering. It is also possible that the difference in preparation methods resulted also in a substantial difference in conductivity: RF-sputtered films demonstrated six orders of magnitude lower conductivity (up to 10^{-12} Ω^{-1} cm^{-1} at 300 K) when compared to the MOCVD-grown ones, with a dominant conduction mechanism being Schottky emission (the Schottky barrier height is estimated to be ~0.85 eV). Unexpectedly, such a large difference in conductivity did not lead to a noticeable change in measured photovoltages. It is important to mention, however, that in both works the photocurrent was antiparallel to the FE polarization direction. An interesting point to highlight is that the as-deposited films were a single-domain state and achieved 18 kV·cm^{-1}. We note here that the development of new, cheaper deposition routes for the growth of BiFeO$_3$ may enable the industrial-scale production of photovoltaic devices utilizing BiFeO$_3$ or other oxide perovskites as an active ferroelectric material. Recently, a manufacturing-scalable technique, atomic layer deposition followed by epitaxial stabilization [39], has been used for the growth of phase-pure BiFeO$_3$ epitaxial thin films with crystalline quality equally high when compared to the BiFeO$_3$ films grown by high-temperature techniques (PLD, MBE, MOCVD), which are often viewed as being process incompatible with some materials and device technologies.

Further experiments performed on $BiFeO_3$ single crystals at different temperatures added some new insight into the nature of the photovoltaic effect in bismuth ferrite [40]. The samples exhibited much higher conductivity ($\sim 10^{-8}\ \Omega^{-1}\ cm^{-1}$ at 300 K) and the EQE maximum slightly shifted to smaller wavelengths than in the case of the RF-sputtered thin films, which can be attributed to oxygen vacancies. The results suggested that the electrochemical migration of defects such as oxygen vacancies under a large applied electric field as well as switching of ferroelectric polarization are both essential for the switching of the photovoltaic current and the diode rectification direction. In contrast, a different conclusion was drawn from impedance spectroscopic studies of 350-nm-thick $BiFeO_3$ films sandwiched between ZnO:Al and $La_{0.67}Sr_{0.33}FeO_3$ electrodes fabricated by pulsed-laser deposition [41]. The heterostructure showed an increase of the conductivity by at least three orders of magnitude under weak illumination, with the conductivity remaining almost frequency-independent below 1 kHz. In the high-frequency range (above 10 kHz) the conductivity has an insignificant change under light, leading to the conclusion that the photocurrent is electrode–hole assisted (electrode–FE junction, grain-boundary conduction) without previously proposed participation of heavy ions or oxygen vacancies in the conduction.

26.3.2 Niobates

In 1969 F.S. Chen observed the change of refractive indices under light exposure in poled single crystals of ferroelectric $LiNbO_3$ and $LiTaO_3$. The observed photorefraction effect was proposed to be the result of the drifting of photoexcited electrons out from the illuminated area to the dark one, where they were "retrapped"; the electric field developed between the illuminated and dark sides of the crystal caused the observed effect [21]. Apart from spectacular photorefraction change observations, the photocurrent along the *c* crystallographic axis of $LiNbO_3$ was collected under UV illumination (which was perpendicular to the current) under zero applied bias, the resulting time dependence of which is reproduced in Figure 26.4. The detected current was flowing in the direction opposite to the ferroelectric polarization. The transient current was observed to reach a steady state in about

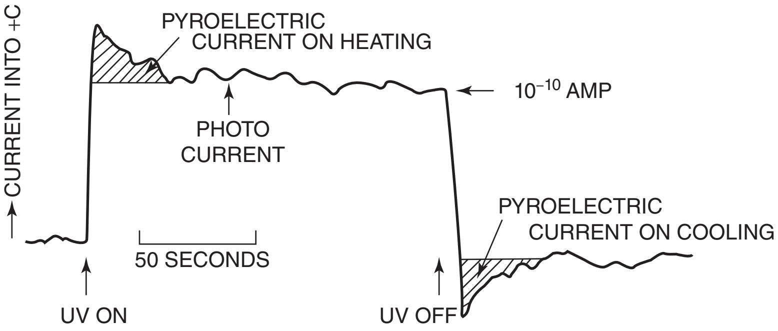

Figure 26.4 *Current-versus-time along the c crystallographic direction of the $LiNbO_3$ crystal when the a face of the crystal was illuminated with a UV light from the mercury discharge lamp. Reprinted with permission from [21]. Copyright [1969], AIP Publishing LLC*

20 s. Later, much effort was devoted to the study of photovoltaic properties of $LiNbO_3$:Fe and $KNbO_3$:Fe crystals, where Fe^{2+} cations are located at the Li^+ and K^+ sites, respectively. From various experiments it became clear that the photocurrent could be observed only along the polar axis of the ferroelectric and is not related to the spontaneous polarization relaxation or pyroelectric effects [8]. When compared to $LiNbO_3$:Fe and $K(Ta,Nb)O_3$, $KNbO_3$:Fe showed a larger photovoltaic effect and photoconductivity, also exhibiting a longer drift length. Spectroscopic studies of absorption constants and photocurrent density of normal (unreduced) and reduced $KNbO_3$:Fe crystals in a short-circuit regime show that the photocurrent is increased for the reduced crystal (Figure 26.5(a)). The absorption peak

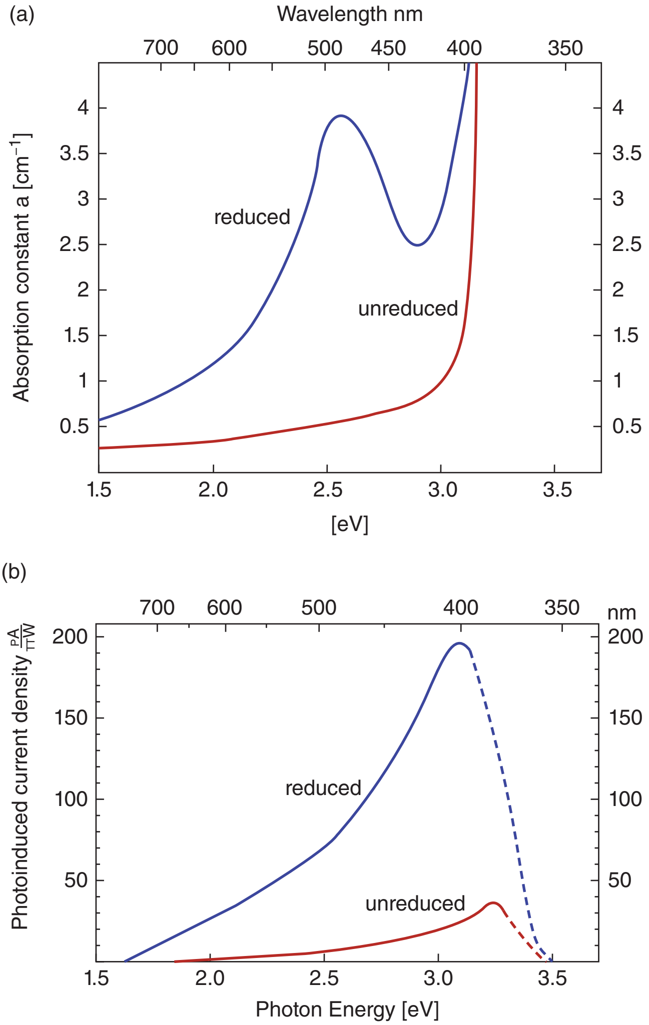

Figure 26.5 Spectral dependences of the absorption coefficient and photoinduced current density of reduced and unreduced $KNbO_3$:Fe. Reprinted from [20] by permission of the publisher (Taylor & Francis Ltd, http://www.tandf.co.uk/journals)

at 2.55 eV does not produce a similar increase in the photocurrent, suggesting an inefficient transition of the photorefractive centers of the $KNbO_3$:Fe crystal, similarly to $LiNbO_3$:Fe.

26.4 The Role of the Schottky Barrier and Depletion Layer

The electrodes on both sides of an active ferroelectric layer are typically either metals (Au, Pt, Cu, etc.) or transparent conducting oxides (doped ZnO, ITO, etc.). The photoresponse of the device in this case can be affected by or arise from (a) the formation of a depletion layer (*p–n* junction), (b) electrochemical migration of defects (mainly oxygen vacancies) and the associated change in electronic structure, (c) Schottky emission from metal contacts, and, finally, (d) the bulk photovoltaic effect itself. Therefore, for the correct design and operation of a ferroelectric photovoltaic device it is crucial to understand the physics behind the observed phenomenon, especially in the light of ongoing debate of the mechanisms and their various contributions. Focusing on the study of the FE layer itself, we should keep in mind the fact that an equally careful study of the effect of the electrodes could provide a significant insight into the origin of the photovoltaic effect in many experiments. One of such studies performed by Zhang et al. showed very different photovoltaic responses when different metals were used as electrode materials [42]. The metal/[300 μm (Pb, La)ZrO_3]/ITO heterostructure (both electrodes were 100 nm thick) illuminated by AM1.5 (air mass coefficient) in the experiments exhibited a hundred times higher short-circuit photocurrent J_{sc} and twice as much of an open-circuit photovoltage V_{oc} when the metal electrode was changed from platinum to silver and then to magnesium (Figure 26.6). A significant change of the response with time is of no clear origin, but the authors presume it may be caused by the pyroelectric effect or a slow transport of electrons from the top to the bottom electrode, which seems unlikely. The difference between the work function of a metal contact ($\varphi_{Pt} = 5.5$ eV, $\varphi_{Ag} = 4.26$ eV, $\varphi_{Mg} = 3.66$ eV) and ferroelectric (Pb, La)ZrO_3 ($\varphi_{PLZO} \approx 3.5$ eV), $\Delta\varphi = \varphi_{PLZO} - \varphi_M$, defines the barrier height at the respective interface. As can be seen, the closer φ_M is to φ_{PLZO}, the lower the energy barrier becomes, resulting in a stronger electron emission from the metal contact directly into the FE layer. This is shown in Figure 26.6, which illustrates the energy band diagram of the photovoltaic cell with and without poling: E_{pi} is the polarization-induced internal electric field in an FE layer and E_{bi} is the field coming from the two Schottky barriers close to the top and bottom electrodes, which can deplete the FE layer.

26.5 Photovoltaic Effect Mediated by Ferroelectric Domain Walls

In 1962 Neumark proposed how greater-than-bandgap photovoltages can occur in non-centrosymmetric materials containing stratifications in the form of crystals containing cubic- and hexagonal-segmented polytypes, producing an additive photovoltage and with reversal of sign with wavelength [43]. This photovoltaic mechanism of charge separation realized in ferroelectrics, fundamentally different from the BPVE, was first proposed and demonstrated by Yang et al. in 2010 [44]. In contrast to the BPVE, the new mechanism relies on the FE domain walls situated periodically perpendicular to the current direction. Such a domain wall array can separate charge carriers in a manner not unlike that in multi-polytype crystals as noted above and in classic *p–n* junctions. In the experiment,

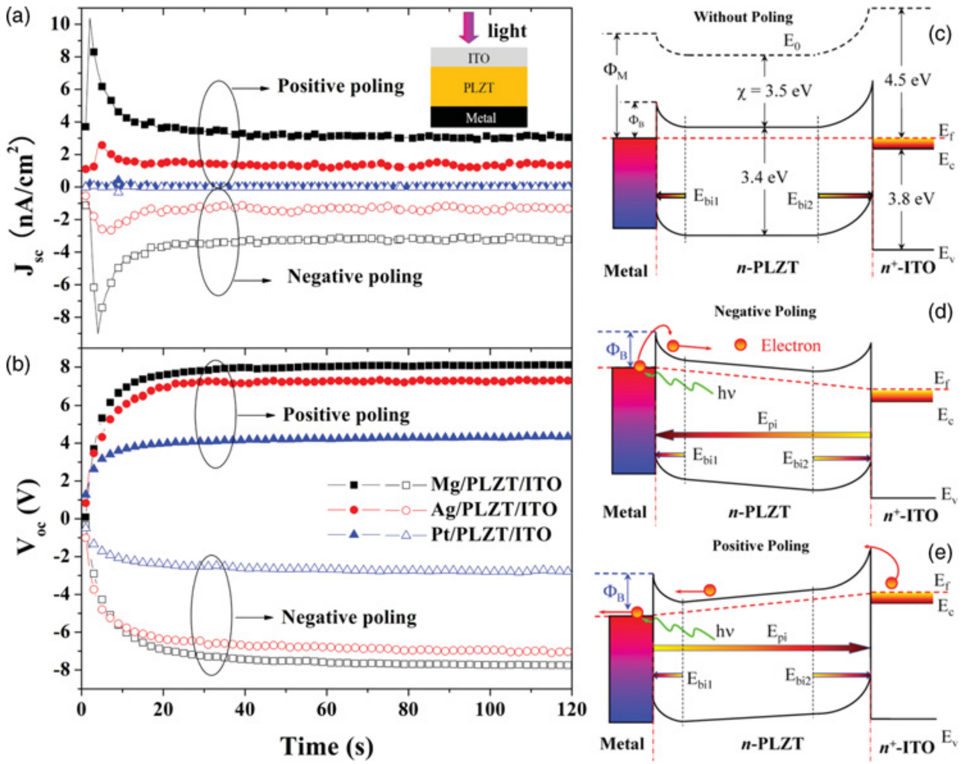

Figure 26.6 (left) Time dependence of a short-circuit photocurrent density and open-circuit photovoltage of the metal/(Pb,La)ZrO_3/ITO photovoltaic cell. (right) Energy band diagrams corresponding to the unpoled, negatively and positively poled ferroelectric layer in the cell. Reprinted by permission from Macmillan Publishers Ltd: [Scientific Reports] [42], copyright (2013)

$BiFeO_3$ thin films were deposited on (110) $DyScO_3$ substrates by MOCVD: 71° domain walls appeared in $BiFeO_3$ when it was grown on the substrates annealed in O_2 (1200 °C, 3 h), while 109° domain walls were found in the films on unannealed substrates. The Pt electrodes were deposited on top of the 100-nm-thick $BiFeO_3$ films with an interelectrode distance of 200 μm, with domain walls being either parallel to the measured electrical current or perpendicular to it. The measurements of $I(V)$ characteristics showed an intriguing photovoltaic behavior: a large photovoltage ($V_{PV} = 16$ V) was observed in the direction perpendicular to the domain walls, but not in the parallel geometry, with a linear dependence on the number of domain walls (Figure 26.7). The absence of a photovoltage both in the parallel direction to the domain walls and for the single-domain sample eliminated the bulk photovoltaic effect as a mechanism for the observed phenomenon.

The proposed mechanism seems conceptually simple and elegant: Each ferroelectric domain wall has a built-in potential that depends on the component of the polarization vector normal to the domain wall, the latter giving rise to the electric dipole in each domain wall. When ferroelectric $BiFeO_3$ is exposed to light, the photogenerated tightly bound excitons require a strong electric field in order to get separated. It turns out that the internal domain wall potential can provide sufficient electric fields needed for the electron–hole

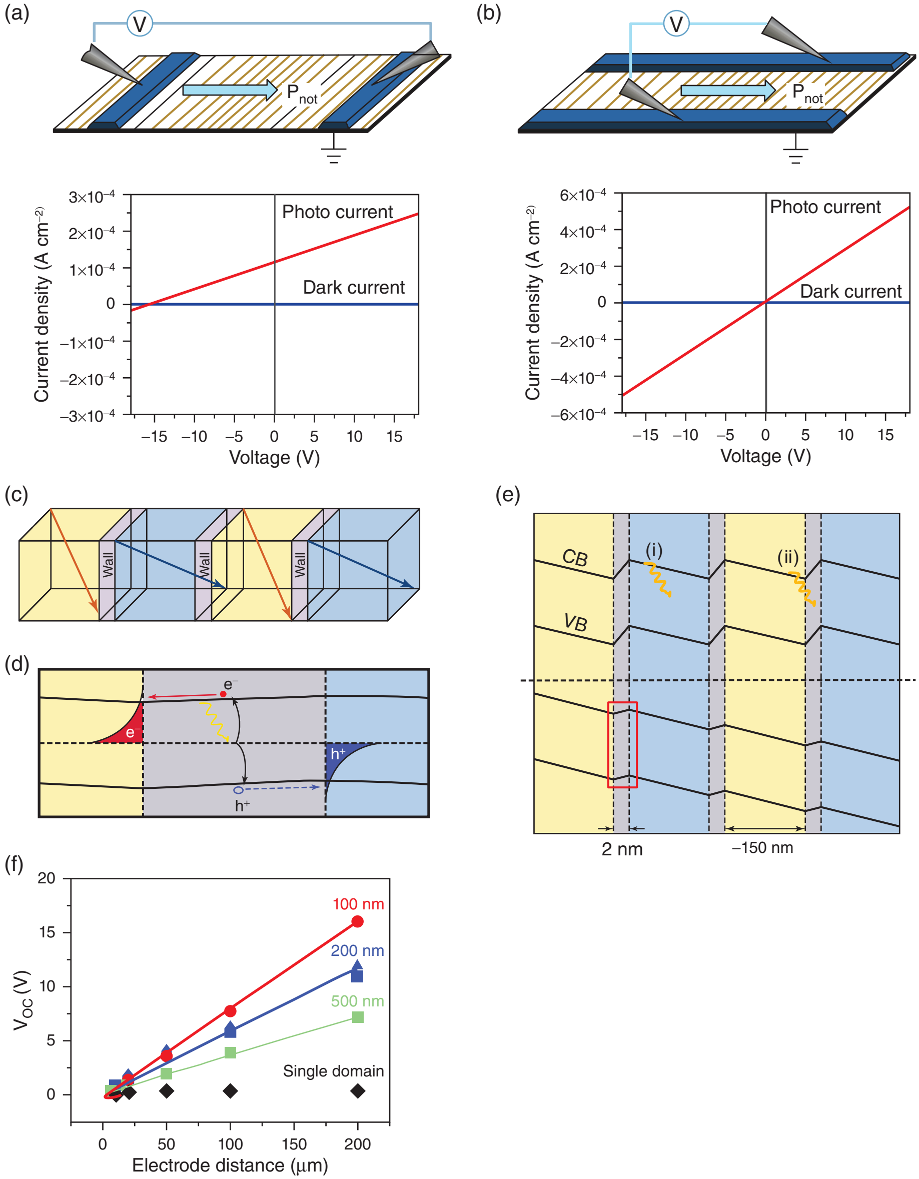

Figure 26.7 *Light and dark I(V) measurements of (a) the perpendicular and (b) the parallel domain wall geometries. (c) Schematic illustration of 71° domains and (d and e) corresponding band diagram across the domain wall (gray). (f) The evolution of open-circuit photovoltage with the distance between the electrodes for the films of different thicknesses (71° domain structure). Reprinted by permission from Macmillan Publishers Ltd: [Nature Nanotechnology] [44], copyright (2010)*

separation. The photoexcited electrons and holes drift to either side of the domain wall (Figure 26.7). This mechanism is in principle similar to the traditional semiconductor *p–n* junction-based solar cell, but with an effective electric field being almost an order of magnitude higher for each domain wall (for the silicon-based junction $V_{PV} = 0.7$ V), greatly overcoming the "band-gap" barrier. The drop of potential at a single domain wall, irrespective of its width, was estimated to be ∼10 mV, being close to the predicted value (20 mV) for 71° domain walls in $BiFeO_3$ [45]. Large photovoltage values could also change sign when the ferroelectric polarization is flipped by the application of an electric field (–200 V, 100 μs). A more rigorous description of the proposed mechanism was published later by Seidel and co-workers [46].

A strikingly different observation was made by Bhatnagar et al. in similar $BiFeO_3$ films grown by PLD on (110) $TbScO_3$ [47]. In contrast to the previously described study, large photovoltages were observed for *both types of geometries*, that is domain walls parallel and perpendicular to the measurement direction, with a stronger effect taking place for the parallel orientation of domain walls. An almost exponential increase of the photovoltage value was measured with decreasing temperature to 17 V for 109° domain and 50 V for 71° domain (both at 80 K). Such an unusual behavior of the photovoltaic effect led the authors to suggest that the previously proposed domain-wall-mediated mechanism is incorrect and does not hold a major contribution to the observed photovoltages. Temperature dependences of dark and photo-conductivities (Figures 26.8 and 26.9), on the contrary, can easily explain the exponential increase of V_{PV} with decreasing temperatures. The resistance is lower in the case of perpendicular domain walls because the equivalent circuit is described by $(\sigma_{total})^{-1} = \sum(\sigma_{bulk})^{-1} + \sum(\sigma_{DW})^{-1}(\sigma_{bulk}$ is the conductivity between the domain walls), while for the parallel domain walls $\sigma_{total} = \sum\sigma_{bulk} + \sum\sigma_{DW}$. It should be remembered that Equation (26.2) shows an inverse proportionality between the conductivity and photovoltage in a material. This simple model also explains why the sample with the 109° domain walls, which are known to be much more conductive than 71° domain walls [48], shows lower photovoltages than the sample with 71° domains. Hence, the authors concluded that for current collected parallel to domain walls, larger-than-bandgap photovoltages can be explained by the BPVE and not the "*p–n* junction"-like accumulation of photovoltage.

26.6 Ferroelectric Solid Solutions: Chemical Tuning of Band-Gap

Because ferroelectrics typically have large band-gaps of more than 3 eV, inefficient absorption of light by such materials leads to their extremely low power conversion efficiency (PCE < 1%) in solar cell applications. Chemical doping of conventional ferroelectric materials has long been a route for introducing higher carrier concentration, spin order, ferroelectric disorder, and better structural stability, and to change various other properties of ferroelectrics. With regard to the field of photovoltaics, chemical substitution enables a tunability of a band-gap of ferroelectrics, especially oxides as most studied ferroelectric materials. In ferroelectric ABO_3 perovskites the electron excitation from the valence band maximum corresponds in a real space to a charge transfer from the oxygen *2p* states to the transition-metal *d* states at the conduction band. Thus, *B*-site partial substitution of typical

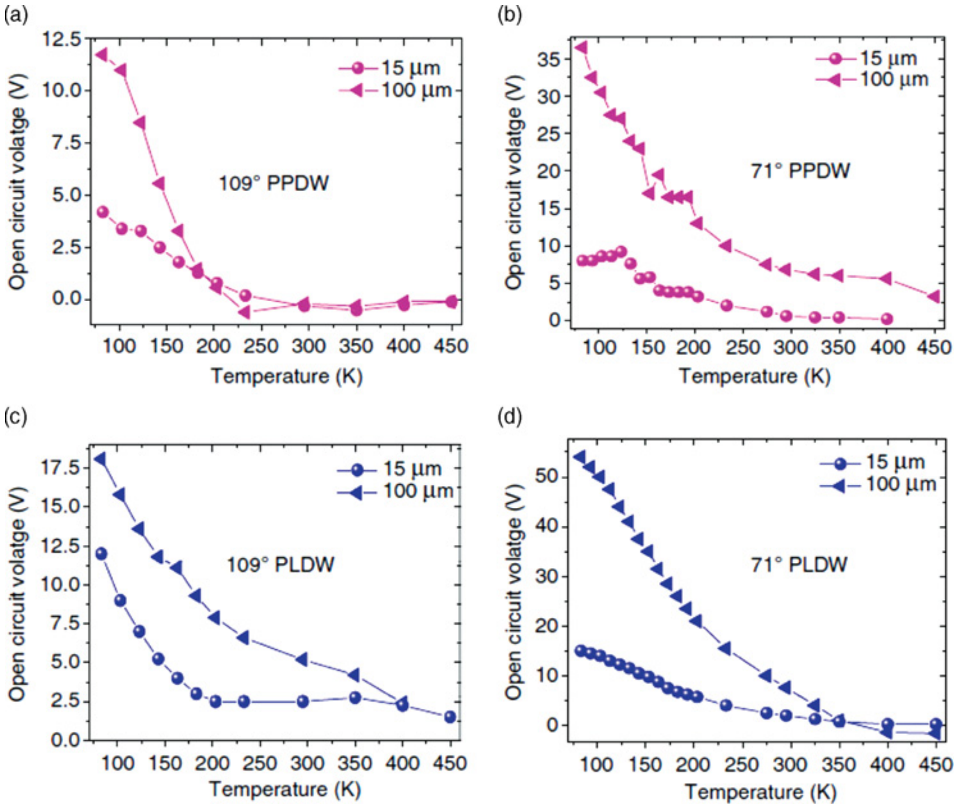

Figure 26.8 *Open-circuit voltage of (100 nm)* $BiFeO_3/TbScO_3(110)$ *in dark and under light for different domain wall types and orientations (PPDW: perpendicular domain wall, PLDW: parallel domain wall). Reprinted by permission from Macmillan Publishers Ltd: [Nature Communications] [47], copyright (2013)*

ferroelectrics such as $BaTiO_3$, $PbTiO_3$, $BiFeO_3$, and $KNbO_3$ by transition metal ions with filled *d* states could be an effective tool for band-gap tuning in ferroelectrics [49, 50].

The double perovskite Bi_2FeCrO_6, the band-gap of which was originally predicted to be less than 2 eV in a ferromagnetic–ferroelectric state, is particularly interesting [51]. Thin films of (001)-oriented Bi_2FeCrO_6 grown by PLD demonstrated a strong photovoltaic effect along the direction perpendicular to the film surface (Figure 26.10) when the sample was illuminated with a red laser (635 nm, 1.5 mW cm^{-2}) [52]. The film with the thickness of 125 nm grown at $T = 660$ °C (Film *A*) exhibited an open-circuit photovoltage of 0.77 V and a photocurrent of 0.99 mA cm^{-2}, both values being higher than in the case of the film grown at $T = 610$ °C (Film *B*, 0.55 V, 0.11 mA cm^{-2}). The single-wavelength PCE was found to be 6.5% at 635 nm for the sample grown at 660 °C, drastically contrasting with PCE = 0.8% obtained for the film deposited 610 °C. Recently, a PCE of 8.1% was achieved by Nechache et al. in a three-layer FE absorber based on atomic ordering of B-site cations in this same BFCO compound, the largest reported to date for an ferroelectric oxide perovskite. Given the shape of the photocurrent-voltage response, smaller-than-bandgap

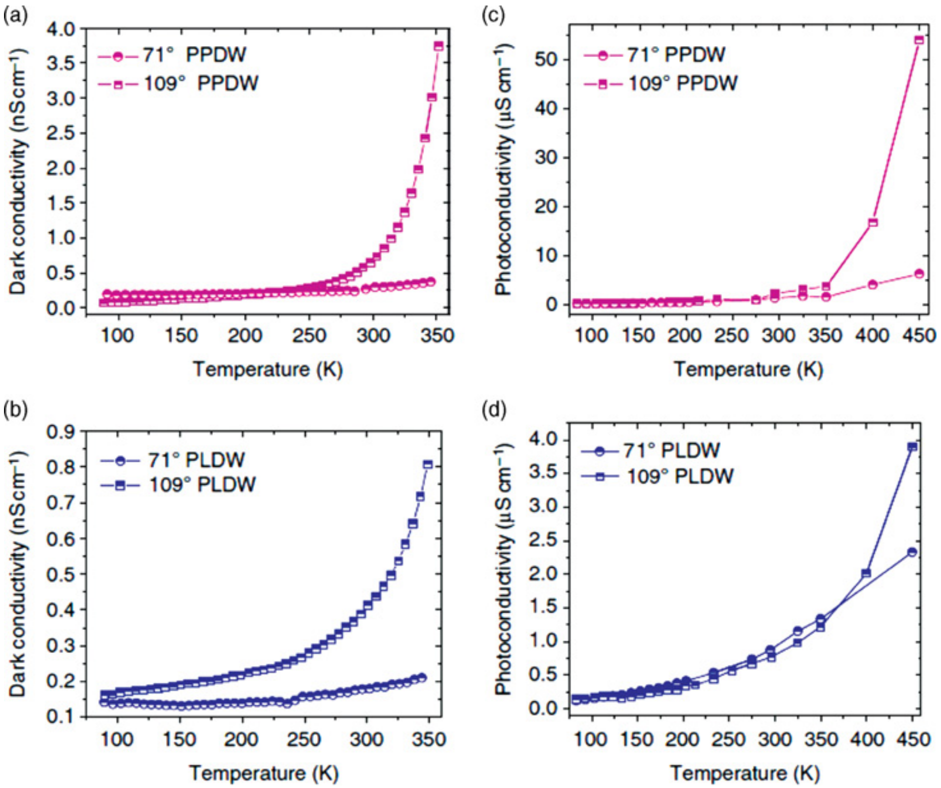

Figure 26.9 *Conductivity measurements of (100 nm) $BiFeO_3/TbScO_3(110)$ in dark and under light for different domain wall types and orientations (PPDW: perpendicular domain wall, PLDW: parallel domain wall). Reprinted by permission from Macmillan Publishers Ltd: [Nature Communications] [47], copyright (2013)*

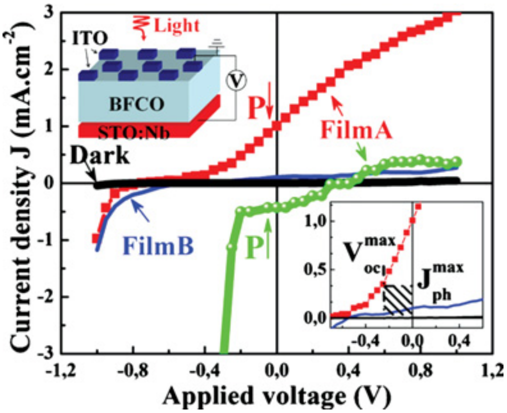

Figure 26.10 *I(V) measurements of (001) Bi_2FeCrO_6 thin films in dark and under light ($\lambda = 635$ nm, 1.5 mW cm^{-2}) for different polarization directions. Film A was grown at 660 °C and film B at 610 °C. Reprinted with permission from [52]. Copyright [2011], AIP Publishing LLC. For a color version of this figure, see color plate section*

photovoltage, and dependence of response on ferroelectric-metal band offsets, the dominant mechanism for carrier separation is not likely due to the BPVE, but rather to band bending [53].

Elemental alloying of binary compound semiconductors permits tuning of optical dielectric function and band-gap, band offsets to drive carrier recombination or separation, optical emission characteristics, all with well-developed dopant technology. A significant obstacle to realizing the potential benefits of ferroelectric semiconductors, however, is that ferroelectric oxide perovskites typically possess an inherently large band-gap E_g, typically >3 eV owing to large electronegativity difference between oxygen and transition metal atoms. Ferroelectric stability is driven by selection of *B*-site transition metal cations, representing a significant materials design and synthesis challenge to propose and realize new materials that are robust, and simultaneously narrower-gap, ferroelectric, and have significant compositional tunability.

Despite intense interest in semiconducting ferroelectrics for photovoltaic applications, until recently there were no ferroelectric oxides having a solar-relevant band-gap. The large energy scale of the direct transition of O 2*p* to transition metal *d* has been understood to be a fundamental aspect of perovskite oxides possessing off-center displacements. Recognizing that *B*-site cations drive ferroelectric distortions, introduction of a substitutional *B*-site cation promoting gap narrowing with a classic FE *B*-site cation such as Nb enabled what had been elusive. The solid solution based on ferroelectric $KNbO_3$ was proposed as a small band-gap end member material with a substantial ferroelectric polarization [54]. The introduction of A and B site cation dopants and O vacancies into $KNbO_3$ reduces the experimental band-gap of the parent phase by more than 2 via the formation of Ni^{2+} and oxygen vacancy $V_O^{\bullet\bullet}$, giving rise to the electronic states in the original band-gap of $KNbO_3$, the largest variation in a band-gap for a single family of polar oxides. According to DFT calculations, such $[KNbO_3]_{1-x}[BaNi_{1/2}Nb_{1/2}O_{3-\delta}]_x$ solid solution (KBNNO) should exhibit ~20 μC cm^{-2} at 0 K, which is only twice as small as the polarization of pure $KNbO_3$ at 0 K. Analysis of spectroscopic ellipsometry studies of ceramic bulk KBNNO indicated that the band-gaps of less than 2 eV for $x < 0.5$ and synchrotron X-ray diffraction experiments along with Raman spectroscopy showed that the solid solution with $x < 0.3$ has a tetragonal crystal structure. Photoresponse of the material with $x = 0.1$ peaked at ~700 nm and had a photoresponse "tail" zeroed at 850 nm, enabling an efficient usage of the visible solar spectrum. Ferroelectric switching measurements of the 20-μm-thick pellets confirmed a ferroelectric order with a polarization value of ~15–20 μC cm^{-2} at 77–170 K. Under broad-spectrum lamp illumination the ceramic samples exhibited a photovoltage and a short-circuit photocurrent of 0.7 mV and 0.1 μA cm^{-2}, respectively, with a reversal of the photocurrent direction on change in the sign of the poling voltage. The room-temperature photocurrent in KBNNO was higher than the photocurrent measured for ferroelectrics such as WO_3-doped (Pb, La)(Zr, Ti)O_3 (9 nA cm^{-2} for a 50-μm sample [55]) or (Na, K)(Mg, Nb)O_3 (25 nA cm^{-2} for a 0.84-μm sample [56]) at 300 K. $BiFeO_3$ ceramic pellets (70 μm thick) discussed in the beginning of this chapter exhibited a comparable light response (4 μA cm^{-2} and 30 mV for 10 mW cm^{-2} green-light illumination) [36]. While these results for KBNNO represent a remarkable achievement in their own right, they suggest that strong integration of materials design with solid-state synthesis and thin-film growth, physical, electronic and functional property characterizations and analyses holds great promise for future progress in this area.

26.7 Conclusions

Ferroelectric photovoltaics have long remained a purely academic curiosity. However, in the last decade this area has flourished, attracting an increasing number of materials scientists and engineers. Because FE photovoltaics are currently under intense investigation, within years we anticipate marked improvements in power conversion efficiency of photovoltaic cells based on ferroelectrics, understanding better the origins of high photovoltages observed and new strategies for maximizing photovoltaic current [57–59] and thus bringing further clarification to and impact on this exciting field. In order to create practical FE photovoltaic devices, considerable efforts must be devoted to harnessing the interesting scientific and technological opportunities that can arise through novel theoretical and chemical approaches to photovoltaic ferroelectrics, including understanding the light–matter interaction, new materials design and property simulations, and experimental methods and analyses. Despite great progress, it can be argued that we are entering a new renaissance for ferroelectrics with potential for application in photovoltaic energy conversion and novel optoelectronics.

Acknowledgment

The authors gratefully acknowledge the Materials Science Division of the US Army Research Office under award no. W911NF-14-1-0500 for support.

References

(1) Sturman, B.I. and Fridkin, V.M. (1992) *The photovoltaic and photorefractive effects in non-centrosymmetric materials*, *Vol. 8* in the series Ferroelectricity and related phenomena, Editor: George W. Taylor, Gordon and Breach Science Publishers.
(2) Butler, K.T., Frost, J.M., and Walsh A. (2015) Ferroelectric materials for solar energy conversion: photoferrics revisited. *Energy Environ Sci*, **8**, 838.
(3) Dember, H. (1931) Über eine photoelektronische Kraft in Kupferoxydul-Kristallen (Photoelectric E.M.F. in Cuprous-Oxide Crystals). *Phys. Zeits.*, **32**, 554.
(4) Starkiewicz, J., Sosnowski, L., and Simpson, O. (1946) Photovoltaic effects exhibited in high-resistance semiconducting films. *Nature*, **158**, 28.
(5) Pensak, L. (1958) High-voltage photovoltaic effect. *Phys. Rev.*, **109**, 601.
(6) Goldstein, B. (1958) Properties of Photovoltaic Films. *Phys. Rev.*, **109**, 601–603.
(7) Fridkin, V., Grekov, A., and Malitskaya, M. (1970) Photovoltages in ferroelectric crystal of SbSI type. *Sov. Crystallographic Reports*, **14**, 500.
(8) Glass, A.M., von der Linde, D., and Negran, T.J. (1974) High-voltage bulk photovoltaic effect and the photorefractive process in $LiNbO_3$. *Applied Physics Letters*, **25** (4), 233–235.
(9) Fridkin, V.M. and Popov, B.N. (1978) Anomalous photovoltaic effect in ferroelectrics. *Soviet Physics Uspekhi*, **21** (12), 981–991.
(10) Fridkin, V.M. (1984) Review of recent work on the bulk photovoltaic effect in ferro and piezoelectrics. *Ferroelectrics*, **53** (1), 69–187.

(11) Fridkin, V.M. (2013) Parity nonconservation and bulk photovoltaic effect in a crystal without symmetry center. *IEEE Transactions on Ultrasonics, Ferroelectrics and Frequency Control*, **60** (8), 1551–1555.

(12) Lines, M.E. and Glass, A.M. (1977) Principles and Applications of Ferroelectrics and Related Materials, Clarendon Press, Oxford.

(13) Belincher, V.I. and Sturman, B.I. (1980) The photogalvanic effect in media lacking a center of symmetry. *Sov. Phys. Usp.*, **23**, 199.

(14) Dresselhaus, G. (1955) Spin-orbit coupling effects in zinc blende strcutures. *Phys. Rev.*, **100** (2), 580–586.

(15) von Baltz, R. and Kraut, W. (1981) Theory of the bulk photovoltaic effect in pure crystals. *Physical Review B*, **23** (10), 5590–5596.

(16) Young, S.M. and Rappe, A.M. (2012) First principles calculation of the shift current photovoltaic effect in ferroelectrics. *Physical Review Letters*, **109** (11), art. no. 116601.

(17) Sipe, J.E. and Shkrebtii, A.I. (2000) Second-order optical response in semiconductors. *Physical Review B*, **61** (8), 5337–5352.

(18) Young, S.M., Zheng, F., and Rappe, A.M. (2012) First-principles calculation of the bulk photovoltaic effect in bismuth ferrite. *Physical Review Letters*, **109** (23), art, no. 236601.

(19) Chynoweth, A.G. (1956) Surface space-charge layers in barium titanate. *Physical Review*, **102** (3), 705–714.

(20) Gunter, P. and Micheron, F. (1978) Photorefractive effects and photocurrents in $KNbO_3$: Fe. *Ferroelectrics*, **18** (1), 27–38.

(21) Chen, F.S. (1969) Optically induced change of refractive indices in $LiNbO_3$ and $LiTaO_3$. *Journal of Applied Physics*, **40** (8), 3389–3396.

(22) Brody, P.S. (1981) Photovoltaic and other outputs from pulsed laser illuminated ferroelectrics. *Ferroelectrics*, **38** (1), 939–942.

(23) Fridkin, V.M., Grekov, A.A., Ionov, P.V., et al. (1974) Photoconductivity in certain ferroelectrics. *Ferroelectrics*, 8 (1), 433–435.

(24) Verkhovskaya K.A, Lobachev A.N., Popov, B.N., et al. (1976) The anomalously large photovoltage effect in antimony orthoniobate. *JETP Letters*, **23**, 476–478.

(25) Land, C.E. and Peercy, P.S. (1978) Photoferroelectric effects in PLZT ceramics. *Ferroelectrics*, **22** (1), 677–679.

(26) Lee, J., Esayan, S., Prohaska, J., and Safari, A. (1944) Reversible pyroelectric and photogalvanic current in epitaxial $Pb(Zr_{0.52}Ti_{0.48})O_3$ thin films. *Applied Physics Letters*, **64** (3), 294–296.

(27) Koch, W.T.H., Munser, R., Ruppel, W., and Würfel, P. (1975) Bulk photovoltaic effect in $BaTiO_3$. *Solid State Communications*, **17** (7), 847–850.

(28) Pintilie, L., Alexe, M., Pignolet, A., and Hesse, D. (1998) $Bi_4Ti_3O_{12}$ ferroelectric thin film ultraviolet detectors. *Applied Physics Letters*, **73** (3), 342–344.

(29) Cho, Y.W., Choi, S.K., and Vysochanskii, Y.M. (2001) Photovoltaic effect of $Sn_2P_2S_6$ ferroelectric crystal and ceramics. *Journal of Materials Research*, **16** (11), 3317–3322.

(30) Zhang, G., Wu, H., Li, G.B., et al. (2013) New high T_c multiferroics $KBiFe_2O_5$ with narrow band gap and promising photovoltaic effect. *Scientific Reports*, **3**, art. no. 1265.

(31) Miyazawa, Y., Uchino, K., and Nomura, S. (1982) Bulk photovoltaic effect in the $PbTiO_3$–$La(Zn_{2/3}Nb_{1/3})O_3$ solid solution ceramics. *Ferroelectrics*, **44** (1), 341–347.

(32) Chakrabartty, J., Nechache, R., Li, S., et al. (2014) Photovoltaic properties of multiferroic $BiFeO_3$/$BiCrO_3$ heterostructures. *Journal of the American Ceramic Society*, **97**, 1837–1840.

(33) Catalan, G. and Scott, J.F. (2009) Physics and applications of bismuth ferrite. *Advanced Materials*, **21** (24), 2463–2485.

(34) Wang, J., Neaton, J.B., Zheng, H., et al. (2003) Epitaxial $BiFeO_3$ multiferroic thin film heterostructures. *Science*, **299** (5613), 1719–1722.

(35) Lebeugle, D., Colson, D., Forget, A., and Viret, M. (2007) Very large spontaneous electric polarization in $BiFeO_3$ single crystals at room temperature and its evolution under cycling fields. *Applied Physics Letters*, **91** (2), art. no. 022907.

(36) Choi, T., Lee, S., Choi, Y.J., et al. (2009) Switchable ferroelectric diode and photovoltaic effect in $BiFeO_3$. *Science*, **324** (5923), 63–66.

(37) Yang, S.Y., Martin, L.W., Byrnes, S.J., et al. (2009) Photovoltaic effects in $BiFeO_3$. *Applied Physics Letters*, **95** (6), art. no. 062909.

(38) Ji, W., Yao, K., and Liang, Y.C. (2010) Bulk photovoltaic effect at visible wavelength in epitaxial ferroelectric $BiFeO_3$ thin films. *Advanced Materials*, **22** (15), 1763–1766.

(39) Akbashev, A.R., Chen, G., and Spanier, J.E. (2013) A facile route for producing single-crystalline epitaxial perovskite oxide thinf. *Nano Letters*, **14** (1), 44–49.

(40) Yi, H.T., Choi, T., Choi, S.G., et al. (2011) Mechanism of the switchable photovoltaic effect in ferroelectric $BiFeO_3$. *Advanced Materials*, **23** (30), 3403–3407.

(41) Katiyar, R.K., Kumar, A., Morelet, G., et al. (2011) Photovoltaic effect in a wide-area semiconductor–ferroelectric device. *Applied Physics Letters*, **99** (9), art. no. 092906.

(42) Zhang, J., Su, X., Shen, M., et al. (2013) Enlarging photovoltaic effect: combination of classic photoelectric and ferroelectric photovoltaic effects. *Scientific Reports*, **3**, art. no. 2109.

(43) Neumark, G.F. (1962) Theory of the Anomalous Photovoltaic Effect of ZnS. *Phys. Rev.*, **125** (3), 828.

(44) Yang, S.Y., Seidel, J., Byrnes, S.J., et al. (2010) Above-bandgap voltages from ferroelectric photovoltaic devices. *Nature Nanotechnology*, **5** (2), 143–147.

(45) Seidel, J., Martin L.W., He, Q., et al. (2009) Conduction at domain walls in oxide multiferroics. *Nature Materials*, **8** (3), 229–234.

(46) Seidel, J., Fu, D., Yang, S.Y., et al. (2011) Efficient photovoltaic current generation at ferroelectric domain walls. *Physical Review Letters*, **107** (12), art. no. 126805.

(47) Bhatnagar, A., Chaudhuri, A.R., Kim, Y.H., et al. (2013) Role of domain walls in the abnormal photovoltaic effect in $BiFeO_3$. *Nature Communications*, **4**, art. no. 2835.

(48) Chiu, Y.P., Chen, Y.T., Huang, B.C., et al. (2011) Atomic-scale evolution of local structure across multiferroic domain walls. *Advanced Materials*, **23** (13), 1530–1534.

(49) Qi, T., Grinberg, I., and Rappe, A.M. (2011) Band-gap engineering via local environment in complex oxides. *Physical Review B*, **83** (22), art. no. 224108.

(50) Bennett, J.W., Grinberg, I., and Rappe, A.M. (2008) New highly polar semiconductor ferroelectrics through d^8 cation-O vacancy substitution into $PbTiO_3$: a theoretical study. *Journal of the American Chemical Society*, **130** (51), 17409–17412.

(51) Baettig, P. and Spaldin, N.A. (2005) Ab initio prediction of a multiferroic with large polarization and magnetization. *Appl. Phys. Lett.*, **86**, 012505.

(52) Nechache, R., Harnagea, C., Licoccia, S., et al. (2011) Photovoltaic properties of Bi_2FeCrO_6 epitaxial thin films. *Applied Physics Letters*, **98** (20), art. no. 202902.

(53) Nechache, R., Harnagea, C. Li, S., et al. (2015) Bandgap tuning of multiferroic oxide solar cells. *Nature Photonics*, **9** (1), 61–67.

(54) Grinberg, I., West, D.V., Torres, M., et al. (2013) Perovskite oxides for visible-light-absorbing ferroelectric and photovoltaic materials. *Nature*, **503** (7477), 509–512.

(55) Poosanaas, P., Dogan, A., Thakoor, S., and Uchino K. (1998) Influence of sample thickness on the performance of photostrictive ceramics. *Journal of Applied Physics*, **84** (3), 1508–1512.

(56) Park, J., Won, S.S., Ahn, C.W., and Kim, I.W. (2013) Ferroelectric photocurrent effect in polycrystalline lead-free $(K_{0.5}Na_{0.5})(Mn_{0.005}Nb_{0.995})O_3$ thin film. *Journal of the American Ceramic Society*, **96** (1), 146–150.

(57) Alexe, M. and Hesse, D. (2011) Tip-enhanced photovoltaic effects in bismuth ferrite. *Nature Communications* **2**, 256.

(58) Zenkevich, A., Matveyev, Yu., Maksimova, K., et al. (2014) Giant bulk photovoltaic effect in $BaTiO_3$. *Phys Rev. B* **90**, 161409.

(59) Wang, F., Young, S.M., Zheng, F., et al. (2016) Substantial bulk photovoltaic enhancement by nanolayering. *Nature Communications* **7**, 10419.

Index

NOTE: Page numbers suffixed with f and t indicate figures and tables, respectively.

Al_2O_3 as low-permittivity linear dielectric, 593
anodic aluminum oxide membranes, 89, 124
antiferroelectrics, 618
antiferromagnetic order, 44
antiferromagnetic spiral structure, 46
antiferromagnetism, 149
applications, *see* devices
aqueous solution–gel route, 166
  chelating agents, 169
  condensation reactions, 167
    initiation, 168
    olation, 168
    oxolation, 168
    propagation, 168
    termination, 169
  electron-donating ligands, 169
  α-hidroxy-carboxylates, 170–171
  metal solvation and hydrolysis in water, 167
  precipitate formation, 170
  solvent evaporation, 169
  water-based precursor solution, 169
  water-soluble metal-ion complexes, 169
aqueous suspensions, *see* colloidal suspensions
artificially engineered multiferroics, 412. *See also* multiferroic composites
atomic force microscopy (AFM), *see* SFM
Aurivillius ferroelectrics, 798. *See also* $Bi_4Ti_3O_{12}$; $SrBi_2Ta_2O_9$
  ferroelectric hysteresis loops, 798, 804
  spontaneous polarization, 799
Aurivillius multiferroics, 799. *See also* $Bi_6Ti_{2.8}Fe_{1.52}Mn_{0.68}O_{18}$
  antiferromagnetism, 799
  $Bi_5Ti_3Fe_{0.7}Co_{0.3}O_{15}$, 800
    magnetic second phase inclusions, 800
  weak ferromagnetism, 799, 806
Aurivillius relaxors, 570
  Ba-based Bi-layered compounds, 571. *See also* $BaBi_4Ti_4O_{15}$
    polar nanoregions (PNRs), 571
    structural disorder, 571
      Ba^{2+}/Bi^{3+} redistribution, 572
Aurivillius structure, 555, 571, 796
  compositional flexibility, 577, 796
    magnetic ions, 796
  crystal properties, 574
    highly anisotropic electrical properties, 574
      conductivity, 576
    plate-like morphology, 574
  highly anisotropic crystallographic structure, 574, 796
  intergrowth patterns, 798
  as naturally layered nanocomposite, 796

Nanoscale Ferroelectrics and Multiferroics: Key Processing and Characterization Issues, and Nanoscale Effects, First Edition. Edited by Miguel Algueró, J. Marty Gregg, and Liliana Mitoseriu.
© 2016 John Wiley & Sons, Ltd. Published 2016 by John Wiley & Sons, Ltd.

$BaBi_{4-x}La_xTi_4O_{15}$, 579
  conductivity, 579
  relaxor characteristics, 580
$BaBi_2Nb_2O_9$ as Aurivillius relaxor, 572
$BaBi_4Ti_{4-5/4\,x}Nb_5O_{15}$, 578
  ceramic microstructure, 578
  conductivity, 579
  relaxor characteristics, 578
$BaBi_4Ti_4O_{15}$, 571
  as Aurivillius relaxor, 572
  cation redistribution mechanism, 572
  compositional modifications, 578
    $BaBi_4Ti_{4-x}Zr_xO_{15}$, 578
    Ce^{4+} substituting for Bi^{3+}, 578
    La^{3+} substituting for Ba^{2+}, 579
    La^{3+} substituting for Bi^{3+}, *see* $BaBi_{4-x}La_xTi_4O_{15}$
    Nb^{5+} substituting for Ti^{4+}, *see* $BaBi_4Ti_{4-5/4\,x}Nb_5O_{15}$
  Vogel–Fulcher law, 574
    freezing temperature, 574
$BaBi_4Ti_4O_{15}$ ceramics, 572
  dielectric properties, 572
    modified Curie–Weiss law, 573
  grain size effects, 574
    conductivity, 576
      Arrhenius plots, 577
    hysteresis loops, 577
    permittivity, 575
    relaxor characteristics, 576
  microstructure, 575
    plate-like grain morphology, 575
  powder synthesis, 574
$BaO–TiO_2–CeO_2$ system, 14
$(Ba,Sr)TiO_3$, 593
  as ferroelectric high-permittivity phase in composites, 593
$BaTiO_3$
  as ferroelectric high-permittivity phase in composites, 593
  A-site substituted, 340
    twofold heterovalent substitution (Na^+, Bi^{3+}), 342
  A/B-site simultaneous substitutions (Bi^{3+}/Yb^{3+}, Fe^{3+}), 342
  B-site substituted, 340
    homovalent substitution (Zr^{4+}), 342
    homovalent substitutione (Sn^{4+}), 342
  Ce-doped
    built-in Ti vacancies, 15–16, 24, 29
    ceramic processing, 22
    ceramic microstructure, 27
      average grain size, 27
      grain size distribution, 30
      porosity, 29
      quantitative EDX analysis, 29
      relative density, 27
    charge compensation mechanism, 14–16, 29
    defect chemistry, 16
    defect model, 16
    dielectric properties, 30
      Curie temperature, 17, 24, 31, 34
      Curie–Weiss law, 36
      frequency dispersion, 30
      temperature dependence of permittivity, 31
    diffuse phase transition, 17, 32, 39
    ferroelectric–paraelectric phase transition, 25, 30, 32
    mixed compensation mechanism, 35
    nanopowders
      morphology, 20
      perovskite phase, 19
      synthesis by modified Pechini method, 18
    orthorrombic–tetragonal phase transition, 33–35
    perovskite structure, 22
      cubic phase, 24
      lattice parameters, 25, 36
      orthorrombic modification, 33, 39
      rhombohedral modification, 37, 39
      tetragonal modification, 24–25
    phase purity, 22
      CeO_2 precipitation, 23, 25, 33
      polytitanate secondary phases, 24, 27, 30, 34
      TiO_2 rich secondary phases, 23, 34

    Raman spectroscopy, 37
    rhombohedral–orthorrombic phase transition, 33–35
    solubility limit, 16–17, 23, 32
  cubic phase, 340, 392, 475
    short-ranged disorder, 342
  critical crystallite size for ferroelectricity, 352
  Curie temperature, 201, 475
  discovery, 473
  discovery of its ferroelectricity, 201
  donor doped, 13–14
  off-centre displacement of Ti, 201
  orthorrombic phase, 341, 393, 475
  rhombohedral phase, 341, 393, 475
  sequence of structural phase transitions, 392, 475
  spontaneous polarization, 201
  spontaneous strain, 201
  substitution-induced structural changes, 342
    chemical clusters, 345
    chemically ordered regions, 342
    disorder, 342
    interatomic spring constants, 343
    loss of ferroelectricity, 342
    relaxor behaviour, 345
  tetragonal phase, 340, 392, 475
  use in the microelectronics industry, 474. *See also* multilayer capacitors
$BaTiO_3$-based nanocomposites, 393
$BaTiO_3$ ceramics, 486
  grain boundaries, 500
  grain size effects, 486, 526
    ceramic stress field, 492, 527
    conductivity, 500
    Curie temperature, 487
    domain configurations, 491, 526–527
    domain dynamics, 526
    ferroelectric phase transition, 487
    permittivity, 487, 491, 525
    tetragonal distortion, 487
$BaTiO_3$ nanoparticles, 128, 393
  critical size for ferroelectricity, 393
  lattice distortions, 393
  structural coherence, 393
$BaTiO_3$ nanorods, 128
$BaTiO_3$ nanostructured ceramics, 353, 487
  composite model, 497
    brick layer model, 498
  critical grain size for ferroelectricity, 353, 493
  domain wall clamping, 495
    frozen domain structure, 495
  ferroelectricity loss, 489, 497
  grain size effects, 353, 487
    Curie temperature, 492–493
    Curie–Weiss law, 492
    extrinsic effects, 354, 493
      defects, 493, 495
      grain boundaries, 354, 495
    intrinsic effects, 354
    permittivity, 489
      dilution effect, 492
      domain wall contributions, 491
      field dependence, 496
      grain boundary contribution, 492. *See also* extrinsic effects
        dead layer, 492
        low-permittivity dielectric layer, 497
      grain bulk contribution, 492
      Rayleigh regime, 494–495
      tunability, 496, 589
    perovskite structure, 353, 489
      coherence length, 497
      spontaneous polarization, 493
      tetragonal distortion, 489
    phase transitions, 353, 489
      vibrational spectroscopy, 493
    switching properties
      ferroelectric hysteresis loops, 494–495, 497
        unsaturated, 589
      piezoresponse microscopy, 496
  processing
    spark plasma sintering, 353, 487
    ultrafine powders, 487
$BaTiO_3$ nanotubes, 128

$BaTiO_3$ nanowires, 215
  critical diameter, 215
$BaTiO_3$ patterned arrays of islands, 124
$BaTiO_3$ porous films, 152
$BaTiO_3$ single crystals
  domain patterns, 679
    a_1–a_2 configuration, 679
    a–c configuration, 679
    c_1–c_2 configuration, 679
    ferroelastic domain wall width, 681
  phase transition, 630
    derivative of the inverse permittivity, 630
    thermo-optical behavior, 635
$Ba(Ti,Sn)O_3$, 345
  dielectric properties, 345
  as relaxor ferroelectric, 555
  sequence of phase transitions, 345, 348
$Ba(Ti,Zr)O_3$, 346
  chemically ordered regions, 347
  dielectric properties, 347
  as ferroelectric high-permittivity phase in composites, 593
  relaxor behaviour, 347
  as relaxor ferroelectric, 555
  sequence of phase transitions, 347–348
$BiCoO_3$, 47
$BiCrO_3$, 47
$BiFeO_3$
  antiferromagnetic ordering, 298, 835
    Neel temperature, 45, 156
  band gap, 835
  canting of the magnetic sublattice, 156
  coupled magnetic and ferroelectric activities, 150
  Curie temperature, 45, 835
  domain wall configurations, 301
  Dzyaloshinskii–Moriya interaction, 156
  ferroelectric polarization, 298
  lattice parameters, 45, 50
  magnetization, 796
    γ-Fe_2O_3 parasitic phase, 796
  oxygen vacancies, 47
  photovoltaic effect, *see* photovoltaic ferroelectrics
  rhombohedral structure, 45, 156, 301
    space group $R3c$, 301
  rotation of the oxygen octahedra, 156, 301
  secondary phases, 47, 50, 156
  spontaneous polarization, 835
  synthesis, 47
    $Bi_{36}Fe_2O_{57}$ intermediate phase, 50
  as type I multiferroic, 792
$BiFeO_3$ epitaxial films
  strain effects, 793
$BiFeO_3$ nanoporous films, 156
  piezoelectric coefficients, 158
  remnant magnetization, 158
$BiFeO_3$ thin films
  low-T processed by aqueous PCSD, 190
$BiFeO_3$-$BiMnO_3$ binary, 48
$BiFeO_3$-$PbTiO_3$ binary, 46–47
  MPB region, 51
  rhombohedral–tetragonal MPB, 53
$Bi_{m-1}Fe_{m-3}Ti_3O_{3m+1}$, as Aurivillus family including magnetic ions, 798
  Fe $^{3+}$ location, 798
$(Bi,La)_4Ti_3O_{12}$
  $Bi_{3.25}La_{0.75}Ti_3O_{12}$ as Aurivillius ferroelectric for memories, 798
  patterned arrays of islands, 124
$BiMnO_3$, 45, 47
  oxygen content, 46
  as type I multiferroic, 792
$BiMnO_{3+\delta}$
  monoclinic P-type structure, 50
  orthorrombic structure, 50
  perovskite decomposition, 50
$BiMnO_3$-$PbTiO_3$ binary, 46–47
  MPB region, 51
  tetragonal–orthorrombic MPB, 53
$BiMO_3$-based solid solutions, 46
$BiMO_3$ perovskites, 45
$(Bi_{1/2}Na_{1/2})TiO_3$-based materials, 348, 518
  depolarization temperature, 350
  dielectric properties, 348
  electromechanical properties, 348
    phase change responses, 518
  high-temperature polymorphic phase transition, 348

- rhombohedral *R*3*c* phase, 348
- short range disorder, 350
- tetragonal *P*4*bm* phase, 348

$(Bi_{1/2}Na_{1/2})TiO_3$-$BaTiO_3$, 518
- ceramic texturing, 518
- high-temperature antiferroelectric phase, 518
  - depolarization temperature, 518
- piezoelectric coefficients, 518

$(Bi_{1/2}Na_{1/2})TiO_3$-$(Bi_{1/2}K_{1/2})TiO_3$, 518

$BiScO_3$, 516
- centrosymmetric monoclinic *C*2/*c* space group, 516
- high-pressure synthesis, 516
- metastable nature, 516

$BiScO_3$–$PbTiO_3$ (BS–PT), 354, 516
- conventional synthesis, 516
- Curie temperature, 516–517
- Fe doping, 522
  - hardening effect, 522
  - low-temperature conductivity, 523
    - electronic hopping, 523
- high-pressure synthesis, 516
- as high-temperature, high-sensitivity piezoelectric, 354, 516
- mechanosynthesis, 516
- monoclinic *Cm* phase, 355, 516
- morphotropic phase boundary, 354, 516
- oxygen vacancies, 519
  - electromigration, 523, 535
- phase diagram, 515f
- rhombohedral *R*3*c* phase, 516
- rhombohedral *R*3*m* phase, 516
- single crystal permittivity anisotropy, 525
- sol–gel synthesis, 519
- tetragonal *P*4*mm* phase, 354, 516

$BiScO_3$-$PbTiO_3$ ceramics, 516
- impedance spectroscopy analysis, 533
  - grain boundary permittivity, 535
  - grain bulk and boundary contributions, 535
  - grain bulk controlled conductivity, 535
- properties, 517
  - high-temperature conductivity, 519
    - Arrhenius plots, 524
    - Maxwell–Wagner type dielectric relaxations, 519
  - permittivity, 522
    - domain wall contribution, 525
    - logatithmic frequency dependence, 519
    - poled state, 525
    - Rayleigh regime, 522
  - permittivity maximum, 519
    - frequency dispersion, 519
  - piezoelectric coefficients, 517
- submicron grain sized, 525

$BiScO_3$-$PbTiO_3$ nanostructured ceramics, 354, 519
- apparent vanishing of ferroelectricity, 522
- basic phenomenology, 519
  - dielectric anomaly, 519
  - ferroelectric switching, 522, 531
- Fe doping, 527
  - dopant incorporation, 527
- grain boundary tailoring for functionality, 540
- grain size effects, 525
  - domain configurations, 527
  - effective coercive field, 531, 532
  - grain boundary effects, 531, 540
  - modelling, 539
  - permittivity, 525
    - mechanisms, 528
    - residual frequency dispersion, 529
      - logarithmic, 531
      - Rayleigh behavior, 531
    - step-like decrease, 527
  - piezoelectric coefficient, 532
  - remnant polarization, 531
  - transition temperature, 537
- impedance spectroscopy analysis, 533
  - grain boundary controlled electrical response, 535
- incipient switching, 532
- inversion superdomains, 531
- monoclinic *Cm* nanocrystals, 522
- piezoresponse force microscopy, 528

$BiScO_3$-$PbTiO_3$ nanostructured ceramics (*Continued*)
  processing
    nanocrystalline powders, 519
    spark plasma sintering, 519
    two-step sintering, 525
  Raman spectra, 519, 537. *See also* Raman spectroscopy
$BiScO_3$-$PbTiO_3$ single crystals, 517
  ultrahigh piezoelectric coefficients, 517
bismuth containing perovskites, 45, 516
bismuth layer-structured ferroelectrics, 555
$Bi_4Ti_3O_{12}$ as a layered perovskite, 202, 571
  applications, 571
  donor doping, 577
  lanthanum doping, 578
$Bi_4Ti_3O_{12}$ thin films, 135
$Bi_{3.25}La_{0.75}Ti_3O_{12}$ thin films, 578
$Bi_6Ti_{2.8}Fe_{1.52}Mn_{0.68}O_{18}$
  as Aurivillius multiferroic with coupled ferroic orders, 790
  ferromagnetic thin films, 807
    remnant and saturation magnetizations, 807
  ferromagnetism, 808
    mechanism, 808
  magnetoelectric coupling, 810
    PFM studies under magnetic fields, 810
  secondary magnetic phases, 810
    statistical analysis, 812
      inclusion size distribution function, 813
      one-image based, 812
      several image based, 813
      upper limit within a confidence level, 814
        contribution to magnetization, 814
$Bi_{m+1}Ti_3(Mn/Fe)_{m-3}O_{3m+1}$ thin films, *see also* $Bi_6Ti_{2.8}Fe_{1.52}Mn_{0.68}O_{18}$
  c-plane sapphire substrates, 801
  fabrication, 801
    chemical solution deposition, 801
      Mn effects, 802
    liquid injection chemical vapour deposition, 801
  high-resolution SEM and TEM studies, 803
    intergrowths, 803
    second phases, 803
  magnetometry studies, 807
  PFM studies, 804
born effective charge tensor, 295. *See also* ferroelectricity, modern theory of polarization
bottom-up methods, 119
  amphilic block copolymer, 153
    self-assembled porous films, 153
  block copolymer approach, 120
  copolymer micelle lithography, 133
  dip-pen nanolithography, 121, 123
  electron-beam direct writing, 119, 121
  electron-beam litography mediated patterning, 121
  gold-nanotube-membrane lithography, 124
  lyotropic liquid–crystal templates, 151
  mesoporous materials, 151
    aluminosilicate, 151
    silica, 151
    TiO_2, 151
  mesoporous non-silica oxide thin films, 151
  micellar templates, 151
  microemulsion (or micelle) mediated, 128
  nanoimprint lithography, 124
  nano shadow mask techniques, 124
  nanosphere lithography, 124
  non-invasive, 119
  parallel generation of nanopatterns, 133
  reactive ion beam etching, 134
  reactive ion etching, 134
  self-assembly, 126
    assisted approaches, 121
    block copolymers
      as templates, 151
    diol-based, 128
    evaporation induced, 151
      nanostructured oxide porous films, 151, 153
    free, 119

- hydrothermal methods, 127
- litographic nanomasks, 133
- microstructural instability, 126
- molecular/atomic, 121
- nanotubes, *see* nanotube synthesis
- nanowires, *see* nanowire synthesis
- site-induced, 119
- template controlled growth, 121
- true, 121
- self-patterning, 121, 126
- sequential patterning techniques, 124
- serial working principle, 133
- serial writing techniques, 123
- thermochemical nanolithography, 138
- TiO_2 patterned seed layers, 132
  - registration, 132
  - focused ion beam technique, 138

- capacitors, 617. *See also* MLCCs
  - embedded, 474
  - polymer composite, 221
  - mica, 473
- $CaTiO_3$, 768. *See also* twin boundaries
  - ferroelasticity, 769
  - orthorhombic *Pnma* symmetry, 769
  - TiO_6 octahedron
    - rotation against off-centering, 769
- ceramic fibers, 213
- ceramic grain boundaries
  - coupled domains across grain boundaries, 499
  - crystalline defects
    - dislocations, 498
    - point defects, 498
  - domain wall pinning, 499
  - giant permittivity materials, 498
  - grain boundary chemistry, 498
  - impurity segregation, 498
  - low permittivity, 498
    - dead layer, 498
  - Schottky barriers, 498
  - semiconducting n-doped $BaTiO_3$ for PTC thermistors, 498
  - space charge region, 498
  - zero spontaneous polarization, 498
  - zinc oxide based ceramics for varistors, 498
- ceramic microstructure
  - grain size histrogram, *see* EBSD data
  - porosity, 487
- ceramic multilayer actuators, *see* multilayer actuators
- ceramic nanostructuring, 62, 512
  - combined sintering method, 488
  - grain size effects, 477
  - local field distribution, 499
  - multistep sintering, 488
  - spark plasma sintering, 488. *See also* ceramic processing
  - as technology-driven, 477, 512. *See also* MLCCs
  - ultra-fine powders, 487
  - ultra-high pressure sintering, 488
- ceramic processing
  - composition control, 57
  - conventional sintering, 55
  - dual-stage sintering, 57
  - electric current sintering, 59
  - electric pulse assisted consolidation, 59
  - ferroelectric oxides, 473
  - field-assisted sintering, 73
  - fine-grained microstructures, 55
  - grain growth, 57
  - hot isostatic pressing, 57
  - hot pressing, 57
  - low-temperature processing, 59–60
  - low-tolerance factor perovskites, 63
    - $Pb(Zn_{1/3}Nb_{2/3})O_3$-$PbTiO_3$, 63
    - $Pb(Zn_{1/3}Nb_{2/3})O_3$-$Pb(Fe_{1/2}Nb_{1/2})O_3$-$PbTiO_3$, 63
    - $ReMnO_3$, 63
  - microstructure control, 47
  - microwave sintering, 57
  - plasma assisted sintering, 59
  - sintering aids, 57
  - spark plasma sintering, 57
    - alkaline niobate materials, 61
    - $BaTiO_3$-based materials, 60–61, 353
      - metastable cubic phase, 61
      - submicron grain size, 60
    - composite materials, 61, 73
      - $BaTiO_3/Al_2O_3$, 61
      - MWCNT–$BaTiO_3$, 61
    - densification, 62

ceramic processing (*Continued*)
        mechanisms, 59–60
            nanostructuring, 353
        $PbTiO_3$-related materials, 61
        tailored stoichiometries, 47
$CoFe_2O_4$
    /$BaTiO_3$ multilayer composites, 150
    mesoporous, 152
    vertical epitaxially-embedded in $BaTiO_3$, 150
colloidal suspensions
    aggregate formation, 101
    aggregation behaviour, 104
    colloidal probe technique, 104
    electrical double layer, 103, 105
    particle–particle interactions, 101, 103
    reagent particles, 101
    surface charge, 106
    Z-potential, 106, 110
composite materials, 589
    adaptative, *see* smart
    dielectric polymer-type, 78, 90
        containing ferroelectric nanowires, 221
    ferroelectric/dielectric, 593
        ferroelectric high-permittivity phase, 593
        linear dielectric low-permittivity phase, 593
        modeled local field distribution, 595
        modeled macroscopic effective responses, 595
            permittivity and tunability, 595
        properties
            breakdown field, 91
            Curie temperature, 80
            dielectric constant, 78, 91
            loss tangent, 78, 81
            permittivity peak, 82
        0–3, 3–0 and 3–3 connectivities, 594–595
    ferroelectric/conductive inclusion, 601
        experimental permittivity and tunability data, 602
        modeled local field distribution, 601
        modeled macroscopic effective responses, 601–602
            permittivity and tunability, 601–602
    local field inhomogeneity, 590
    multiferroic, *see* multiferroic composites
    1–3 connectivity, 233, 236, 252
    organic–inorganic, 163
    processing
        composition gradient, 82
        interface phenomena, 73
            interdiffusion, 73, 82
            intermediate phases, 73
                $Ba_2TiSi_2O_8$ fresnoite, 81–82
                $BaFe_{12}O_{19}$, 90
                $Ba_{12}Fe_{28}Ti_{15}O_{84}$, 90
        polymer-based, 78
        spark plasma sintering, 73
    smart ceramic-polymer, 232
        design flexibility, 232
        incorporating ferroelectric fibers, 232
        with integrated fibers for sensing and actuation, 232
    0–3 connectivity, 78, 84, 91, 252
core-shell particles, *see* core-shell structures
core-shell structures, 72
    as building blocks, 73, 90
        multifunctional composites with 0–3 connectivity, 73
    $Au@SiO_2$, 74
    $BaTiO_3@Al_2O_3$, 83
    $BaTiO_3@BaZrO_3$, 77, 82
    $BaTiO_3@CoFe_2O_4$, 90
    $BaTiO_3@MgO$, 82
    $BaTiO_3@NiFe_2O_4$, 88
    $BaTiO_3@$ polymer particles, 78
    $BaTiO_3@SiO_2$, 80–81, 88, 393
        $Ba_2TiSi_2O_8$ fresnoite, 393
    $BaTiO_3@SrTiO_3$, 82
    $BaTiO_3@TiO_2$, 83
    bimagnetic core-shell particles, 73
        exchange interaction, 73
    $CoFe_2O_4@Pb(Zr,Ti)O_3$, 89

  consolidation, 74
    microstructure-properties relationships, 90
  Fe_2O_3@SiO_2, 74, 88
  Fe_3O_4@SiO_2, 73
  catalytic applications, 73
  multiferroic, 84–85
  $NiFe_2O_4$@$BaTiO_3$, 86–87
  $NiFe_2O_4$@$Pb(Zr,Ti)O_3$, 89
  $Pb(Zr,Ti)O_3$@ $NiFe_2O_4$, 89–90
  silica coatings, 72, 80
  silica-coated nanoparticles, 72
  synthesis
    chemical assembly methods, 74
    electrospinning, 88–89
    heterocoagulation, 75–76
    heteroepitaxial growth, 76, 84
    hydrothermal, 85
    in-situ polymerization, 77, 83
    liquid-phase, 74
    ordered assembly of shell nanoparticles, 74
    precipitation method, 75
    self-assembly of colloids, 74, 88
    shell formation mechanism, 74
    sonochemical, 85
    Stöber process, 75, 80
    surface nucleation and growth, 75
  SiO_2@Au, 73
    optical resonances, 73
Cr_2O_3 as non-multiferroic magnetoelectric material, 790–791
Curie temperature, 201, 474
Curie–Weiss law, 36, 294, 475, 738
  Curie–Weiss temperature, 36, 475
  Curie–Weiss constant, 36, 475

depolarization field, 215
  surface charge screening, 215
devices
  electrical power generation, *see* harvesting devices
  energy harvesters, *see* harvesting devices
  flexible, 164
  functional diversification, 148
  information storage, *see* memories
  integration level, 147
  integration of multiple technologies, 148
  microwave, 153
    reconfigurable circuits, 476
  miniaturization, 118, 476, 618
  multiferroic, *see also* memories
    magnetic field sensors, 791, 819
    tunnel junctions, 818–819
  multifunctional, 148
  optical devices
    electro-optical, 517
    non-linear, 517
  photovoltaic cells, 164
  piezoelectric
    actuators, 149, 153, 201, 258, 513. *See also* multilayer actuators
      microactuators, 474
    microelectromechanical systems, 513, 618
    nanoelectromechical systems, 219, 256
    sensors, 513
    smart systems, 513
    structural health monitoring, 233, 258
    transducers, 149, 201
    ultrasonic motors, 474
    ultrasound transducers, 258, 513
      medical imaging, 474, 513
      non-destructive testing, 513
    underwater acoustics, 513
      sonar transducers, 473
  pyroelectric, 153, 474
    infrared radiation detectors, 201
  radio frequency, 153
    phase shifters, 476
    tunable filters, 474, 476
  sensors, 149, 153, 255
    positive temperature coefficient sensors, 474
  size scaling, 148
  thermistors, 201
  three-dimensional approach, 148

diffraction methods, 391. *See also* neutron scattering techniques, and synchrotron scattering techniques
dipolar glass, 555, 557
  dipole dynamics, 555
    freezing, 555
  Vogel–Fulcher law, 557
domain configurations
  BaTiO$_3$ nanorods
    a–*c* domains by TERS, 361
  BaTiO$_3$ single crystals
    (001) orientation, 679
  flux closure, 276, 715. *See also* ferroelectric vortices
    BaTiO$_3$
      superdomain boundaries, 720
      core structure, 721
    Pb(Zn$_{1/3}$Nb$_{2/3}$)O$_3$-PbTiO$_3$
      mesoscale structures, 721
      embedded nanoscale flux-closure states, 722
    as response to depolarizing fields, 715
    as result of switching, 715
  Pb(Zr,Ti)O$_3$
    nanotwinning, 333
  tetragonal *P*4*mm* ferroelectrics, 280
domain imagining techniques
  conventional transmission electron microscopy, 280
    BaTiO$_3$ as example, 280
    contrast mechanisms, 280–282
  destructive techniques, 435
  domain decoration, 435
  non-destructive techniques, *see* SPM
domain pattern transfer
  CoFe/BaTiO$_3$ with a_1-a_2 domains, 679
  CoFeB/BaTiO$_3$ with a_1-a_2 domains
    electric field writing and erasure of magnetic patterns, 690
    magnetic erasure of transferred patterns, 687
    magnetization reversal, 684–685
  electric field control
    magnetic domain wall reversible motion, 688
    writing and erasure of magnetic patterns, 688
  Fe/BaTiO$_3$ with *a*–*c* domains, 680
    electric field driving of magnetic domain walls, 691
      wall velocity, 692
  magnetic domain wall pinning, 681
    magnetically charged and uncharged walls, 682
      wall width, 683
    magnetization reversal, 682
    pinning potential by an a_1-a_2 wall, 681
  magnetoelastic anisotropy, 680
  nanowire geometry, 692–693
  size scaling effects, 686
    exchange coupling, 686
    imprinting critical length scale, 686
      charged and uncharged walls, 687
    magnetostatic interactions, 686
domain structure
  BiFeO$_3$ epitaxial films, 302, 306
    unit-cell-wise polarization across 109° walls, 306
  PbTiO$_3$ epitaxial films, 299
    unit-cell-wise maps across *a*–*c* twins, 300
domain wall characterization
  high-resolution transmission electron microscopy, 282
domain wall devices
  magnetic, 684
domain wall motion
  magnetic domains, 690
    driving with magnetic field, 690
    driving with spin polarized electric currents, 690
    electric field control, 691
domain walls
  BiFeO$_3$
    DFT calculations, 301
    domain wall engineering, 301
    enhanced conductivity, 301, 425
  BiFeO$_3$ epitaxial films, 302
    109° walls, *see* domain structure
      frozen-in domain wall motion, 306

  coupling with edge dislocations, 276
  inversion domain walls, *see also* $PbZr_{0.2}Ti_{0.8}O_3$ thin films
    atomic scale structure, 276, 283
  new phases
    structural and chemical, 316
  $PbTiO_3$ epitaxial films
    90° walls, *see* domain structure
      strain fields, 285–286
    sharp domain walls, 301
  $PbZr_{0.2}Ti_{0.8}O_3$ thin films
    180° walls, 282–283
  photovoltaic effect, 841
  $TbMnO_3$
    chemical ordering, 316
$DyMnO_3$ as type II multiferroic, 792
$DyScO_3$ as substrate, 285

electric field microscopy, 401. *See also* EFM
electric ordering, 44
electron backscatter diffraction (EBSD), 401, 412
  $BaTiO_3$ ceramics, 417
  $BaTiO_3$-(Ni,Zn)Fe_2O_4 composites
    misorientation angle histrograms, 423
    phase distributions, 419, 421
    phase crystal orientation distributions, 419, 421
    pole figures, 420, 422
  Hough transform, 415
  Kikuchi patterns
    generation process, 413
    indexing method, 413
    recognition process, 413
  KNL–NTS, 416
  $LuMnO_3$ single crystals, 417
  misorientation angle histograms, 419
  multiphase crystallographic relations, 413
  (Ni,Zn)Fe_2O_4 ceramics, 417
  orientation distribution function, 419
  orientation maps, 419
  phase maps, 419
  pole figures, 419
  sample surface preparation, 415, 425
  spatially resolved crystallographic data, 401
  superconductors
    combined EBSD and MFM measurements, 401
  three dimensional EBSD, 426
    EBSD combined with FIB, 426
  Transmission EBSD, 427
    FIB sample preparation, 427
electron beam direct writing (EBDW), *see* bottom-up methods
electron energy loss spectroscopy (EELS)
  atomic resolution spectrum imaging, 310
  chemical and electronic states at interfaces, 307
  EELS spectrometers, 309
  EELS spectrum, 308
    core-loss region, 308
      core-loss edge fine structure, 308
      core-loss edges, 308
    low-loss region, 308
    zero-loss peak, 308
  EELS spectrum imaging
    $BaTiO_3$/Fe interfaces, 314
      Fe–FeO–TiO_2–$BaTiO_3$ interface structure, 315
    $La_{0.7}Sr_{0.3}MnO_3/BiFeO_3$ interfaces, 313
    $LuFe_2O_4$
      atomic resolution mapping, 311
      chemical bonding map, 311
      ELNES fine structure of the O K edge, 311
    $PbTiO_3$ epitaxial films on $SrTiO_3$
      Ti $L_{2,3}$ fine structure, 313
    $TbMnO_3$ domain walls
      chemical ordering, 316
      local ferromagnetism, 316
  electron loss near edge spectroscopy (ELNES), 309
  extended energy loss fine structure (EXELFS), 309
  local chemical properties, 275
electrospinning
  process description, 235
  ultrathin fibers, 213. *See also* nanofibers

electrospun fibers
  defect-free structure, 235
  high surface to volume ratio, 235
  polycrystalline nature, 213
electrostatic force microscopy (EFM), 408, 436
  dielectric constant measurement, 441
  dynamic contact mode (DC–EFM), 436
    similarities with PFM, 440
  ferroelectric domain imaging, 436
    $Gd_2(MoO_4)_3$, 439
    $LiNbO_3$, 441
    potassium titanyl phosphate, 441
  ferroelectric domain relaxation studies, 436
  ferroelectric domain wall studies, 436
  ferroelectric domain writing, 436
    $BaTiO_3$ nanowires, 441
    PZT thin films, 439
  local surface potential mappings, 408
  operating principle, 438
  screening charge effects, 440
  surface charge measurement, 441
electrostrictive coupling, 297
elemental mapping, 243
energy dispersive X-ray spectroscopy (EDXS), 244
environmental awareness, 165
environmental, health and safety properties, 165
environmental impact of preparation, 165
environmental regulations, 518
  European Union directives, 156, 518
environment-friendly materials, 156
epitaxial $BaTiO_3$ films on $SrRuO_3/SrTiO_3$ substrates, 637
  critical thickness, 637
  C–V characteristics, 649
  leakage currents, 648
  oxygen gradients, 666
  phase transition, 637
    derivative of the inverse permittivity, 637
    temperature shift, 637
    thermo-optical behavior, 637
epitaxial $BaTiO_3$ films on $SrTiO_3$ substrates
  PFM studies, 661
    domain writing and stability, 661
    imprint, 661
epitaxial $BiFeO_3$ films on $DyScO_3$ substrates, 302
epitaxial ferroelectric thin film properties
  dielectric permittivity, 649
    C–V characteristics, 649
  leakage currents
    interface-controlled Schotky emission, 648
    metal-electrode work function, 649
    space charge-limited currents, 648
  polarization switching, 652
epitaxial ferroelectric thin films, 201, 618, 622
  biaxial in-plane misfit strain, 622
  bidimensional strain, 201
  coherent growth, 622
  critical thickness, 622
  cube-on-cube type, 622
  epitaxial relationships, 622
  first-principles strain-temperature diagrams, 623
  growth on Si, 618
  phase transition, 623
  phenomenological theoretical analysis, 623
    strain-temperature phase diagrams, 623
  strain effects, 623
    enhanced polarization, 623, 793
    new phases, 623
  strain relaxation, 622
    defects, 622
      dislocations, 622
    ferroelectric domains, 622
    island growth, 622
  thermal strain, 622
  thickness dependence of intrinsic properties, 628
epitaxial $KTaO_3$ films on Nb-doped $SrTiO_3$ substrates, 638
  depolarization field, 638

    derivative of the inverse permittivity, 638
    strain-induced ferroelectric phase, 638
    thermo-optical behavior, 638
epitaxial $LuFe_2O_4$ films, 311
epitaxial $PbSc_{1/2}Nb_{1/2}O_3$ films on $La_{0.5}Sr_{0.5}CoO_3/MgO$ substrates, 638
  phase transition, 638
    derivative of the inverse permittivity, 638
    strain-induced disappearance, 639
    thermo-optical behavior, 638
  relaxor state, 639
epitaxial $Pb_{0.5}Sr_{0.5}TiO_3$ films on $La_{0.5}Sr_{0.5}CoO_3/MgO$ substrates, 635
  domain configuration, 635
  phase transition, 635
    derivative of the inverse permittivity, 636
    first order – second order change, 637
    temperature shift, 637
    thermo-optical behavior, 636
epitaxial $PbTiO_3$ films on $SrRuO_3/DyScO_3$ substrates, 298
  domain configurations, 298
epitaxial $Pb(Zr,Ti)O_3$ films on $SrRuO_3/SrTiO_3$ substrates
  band gap, 654
  C–V characteristics, 649
  ferroelectric hysteresis loops, 652
    crystal structure effects, 652
  leakage currents, 648
  OCS spectra, 655
    trapping levels, 656
  pyroelectric response, 656
  short-circuit photocurrents, 654
epitaxial $Pb(Zr,Ti)O_3$ films on $SrTiO_3$ substrates
  PFM studies, 660
    domain writing and stability, 661
    electrode effects, 662
    90° domain pattern, 660
    self-polarization, 661
epitaxial $Pb(Zr,Ti)O_3$ films on $SrTiO_3/Si$ substrates
  C–V characteristics, 650
    interface-related capacitances, 652
  ferroelectric hysteresis loops, 651
    switching kinetics, 651
  imprint, 651
epitaxial $TbMnO_3$ films, 316
  weak ferromagnetism, 316
epitaxial thin film heterostructures, *see* multilayer structures
  novel properties at interfaces, *see* interfaces
epitaxial thin films, 5
  growth, *see* thin-film fabrication
  $SrTiO_3$ epitaxial layers on single-crystal silicon wafers, 5
  strain-driven multiferroism, 793
    supercell structures, 794
  ultrathin, 5
EuO as predicted strain-driven multiferroic, 793
$EuTiO_3$ as predicted strain-driven multiferroic, 793
extended X-ray absorption fine structure (EXAFS), 392

ferrimagnetism, 149
ferroelastic order, 44
ferroelasticity, 148
  spontaneous strain, 149
ferroelastics, 148
ferroelectric capacitor, 118, 618
  complex impedance, 623
  equivalent circuit, 623
  as geometry to measure the material permittivity, 623
  as metal–ferroelectric–metal (MFM) structure, 646
ferroelectric ceramics, 475
  as effective composite materials, 589
    local field inhomogeneity, 590
  microelectronics, 476
  poling process, 476
  processing and integration, 475
ferroelectric characterization, 250
ferroelectric domains, 201, 474. *See also* domain configurations; walls
  as mechanism for strain relaxation in epitaxial films, 622
ferroelectric fibers, 232

ferroelectric instability, 215
ferroelectric materials
  applications, 645–646
  birefringence, 645
  dielectric permittivity
    losses, 589
    non-linear and hysteretic, 475, 588
      Johnson equation, 590
    tunability, 475, 588, 645
      related applications, 588
  non-linear properties, 645
  photorefraction effect, 831, 838
  photovoltaic effect, 653, 830. *See also* photovoltaic ferroelectrics
  photovoltaic properties, 645
  polarization switching, 200, 294, 474, 588, 645
    Kolmogorov–Avrami–Ishibashi models, 590
    related applications, 588
  strain-electric field hysteretic response, 475
ferroelectric order, 201. *See also* electric ordering
ferroelectric oxides, 201
  defect chemistry, 473
  engineering impact, 473
  as smart multifunctional materials, 473
ferroelectric phase transition, 201, 294, 474. *See also* LGD theory
  displacive type, 329
  experimental studies, 620
  optical soft mode, 329, 475, 620. *See also* vibrations in solids
  order-disorder type, 330
  thermal anomalies of the physical properties, 474
    dielectric anomaly, 475, 620. *See also* Curie–Weiss law
ferroelectric thin film capacitor, 624
  complex impedance, 624
  electrode resistance, 624
  equivalent circuit, 624
  measurement of material permittivity, 625
  ultrathin films, 626
ferroelectric thin films
  ceramic-type polycrystalline, 618
    grain boundaries, 646
  columnar-type textured, 646
  crystal-type epitaxial, 618
    film/electrode interface, 646
  optical characterization
    variable angle spectroscopic ellipsometry, 634
  permittivity measurement, 627, 633. *See also* ferroelectric thin film capacitor
    interfacial capacitance, 628
      fundamental microscopic origin, 628
      technological factors, 628
  phase transition, 629
    bandgap, 634
    derivative of the inverse permittivity, 629, 632
      LGD theory, 630
    dielectric anomaly, 629
    refraction index, 634
    structural studies, 634
  polarization switching, 652
    charge carriers and depolarization field, 652
  pyroelectric properties, 656
  relaxors, 630
    derivative of the inverse permittivity, 630, 632
      empirical scaling law, 630
ferroelectric transition temperature, 45. *See also* Curie temperature
ferroelectric tunnel junctions, 314
ferroelectric vortices
  $BaTiO_3$ nanodots, 704
  $BiFeO_3$ thin films, 707
    ferroelectric vortex arrays, 707
  chiral vortex patterns, 707
    coupled antiferrodistortive motions, 709
  direct imaging of continuous polarization rotation, 718
  domain closure structures, 706

  - 180° and 90° domain circuits, 706
  - stable polarization vortices, 706
- double vortex states, 710
- effective Hamiltonian approach, 701
  - molecular dynamics simulations, 702
  - Monte Carlo simulations, 702
- first-principles approach, 704
  - density functional theory, 704
  - Kohn–Sham equations, 704
- GeTe nanoplatelets and particles, 706
  - ferrotoroidic ordering, 706
- multivortex toroidal states, 706
- $PbTiO_3$ nanoparticles, 706
  - toroidal ferroelectricity, 706
- $PbTiO_3$ nanotubes, 712
  - ferroelectric vortices under curled electric fields, 712
- $PbTiO_3$ nanowires, 706
  - complex curling vortex configurations, 706
- phase field method, 702
  - Ginzburg–Landau energy, 703
  - Ginzburg–Landau kinetic equation, 703
  - variation functional, 702
- $Pb(Zr,Ti)O_3$ asymmetrical nanorings, 708
  - toroidal moment switching, 708
- $Pb(Zr,Ti)O_3$ nanodisks and nanorods, 705
  - electric field induced vortex to polarization transformation, 708
  - spontaneous toroidal moment, 705
  - toroidal phase transition, 705
- $Pb(Zr,Ti)O_3$ nanoparticles, 711
  - ferroelectric vórtices under curled electric fields, 711
- $Pb(Zr,Ti)O_3$ ultrathin films, 707
  - vortex stripes, 707
- shell-model calculations, 704
  - interatomic potentials, 704
- vortex related phenomena, 708
  - conductivity, 713
  - electric toroidal susceptibility, 713
  - electrocaloric effect, 714
    - electrooptical activity, 713
    - magnetotoroidic effect, 713
    - piezotoroidicity, 713
    - toroidal switching, 710
- ferroelectricity
  - as cooperative phenomenon, 201
    - cooperative structural displacements, 375
  - covalent bonding, 382
  - critical size, 118, 352. *See also* scaling effects
  - critical temperature, 588. *See also* Curie temperature
  - depolarization field, 295
  - discovery, 375
  - hysteresis curve, 376, 474
  - linear susceptibility, 295. *See also* ferroelectric materials
  - microscopic origins, 377
    - relative shifts of cations and anions, 382 474
  - modern theory of polarization, 295–296
  - non-centrosymmetric crystal structure, 163, 474
  - spontaneous polarization, 149, 294, 329, 375, 474, 588
    - optical manipulation, 830
    - unit-cell-wise computation, 296
  - switchable polarization, 232
- ferroics
  - crystal symmetry, 148
  - phase transition, 148
- ferromagnetic order, 44
- ferromagnetic thin films
  - piezoelectric substrates, 678
    - electric field induced magnetoelastic anisotropy, 678
  - ferroelectric/ferrolastic substrates, 679. *See also* domain pattern transfer
- ferromagnetism, 148
  - Curie temperature, 149
  - hysteresis curve, 376
  - microscopic origins, *see* magnetic ordering
  - spontaneous magnetization, 149
  - superparamagnetic state, 479

ferromagnets, 148
ferrotoroidal order, 149. *See also* toroidal order
fiber applications
  energy harvesting, 259
  microfiber composite actuators, 259
  structural health monitoring, 258
    smart ceramic–polymer composites, 258
  ultrasonic transducers, 258
    piezoelectric composites, 258
fiber characterization
  mechanical testing, 248
  micromechanical method, 252
    single-fiber properties, 252
  piezoresponse force microcopy, 255
  single fibers, 254
fiber processing
  ALCERU process, 238
  extrusion process, 239
  melt spinning, 238
  polysulfone process, 240
  Pb(Zr,Ti)O_3 materials, 243
  shaping of macrofibruous structures, 236
  sol–gel derived PZT microfibers, 239
  spinning techniques, 233
  viscous suspension spinning process, 237–238
  wet spinning technology, 237
fiber properties
  failure strain, 248
  PZT fibers, 248
    electromechanical, 254
    ferroelectric domain switching, 255
    hardness, 249
    piezoelectric, 253–254
    Young’s modulus, 249
  tensile strength, 248
  yield strain, 248
  Young’s modulus, 248
fibers
  compositional gradients, 243, 249
  grain oriented, 242
  high purity, 237
  lead vacancies, 249
  microstructural gradient, 243
  microstructure, 242
    PZT fibers, 241
  surface morphology, 236
first-principles derived effective Hamiltonian, 215
first-principles density-functional calculations, 481
  $BaTiO_3$ finite-temperature properties, 481
  $BaTiO_3$ phase transitions, 481
  perovskite epitaxial films, 482
    depolarization field, 482
    ferroelectric–electrode interface, 482
    in-plane strain, 482
  perovskite one-dimensional systems
    nanodiscs, nanorods and nanowires, 483
  perovskite oxide ground-state structures, 481
  size dependent phenomena, 481. *See also* scaling effects
    ferroelectric correlation volume, 482
flexible electronics, 164
flexible polymer substrates, 164
  thermal stability, 164
flexible substrates, 163
  paper, 165
  plastics, 165
flexoelectric coupling, 297
flexoelectric rotation of polarization, 276, 286
focused ion beam (FIB) milling, 119. *See also* top-down methods
  Ga-implantation, 120
  three dimension EBSD, 426
frustrated magnets, 282
  competing exchange interactions, 382

harvesting devices
  active fiber composites, 233, 259
  ferroelectric nanowire based, 219, 233, 255
high-pressure techniques, 45

- high-resolution transmission electron microscopy (HRTEM)
  - aberration correction, 282, 288
  - image formation process, 276–277
  - local crystal structure, 275
  - local strain measurements, 282
    - geometric phase analysis method, 284–288
  - local polarization determination, 282
  - microscope optics, 277
  - optical aberrations, 277
    - spherical aberration, 280
  - phase contrast transfer function, 278
    - spherical aberration coefficient, 279
  - point resolution, 279
  - spatial resolution, 282
  - weak phase object approximation, 278
- hollow fiber hybrids, 233
- hollow nanostructures, 212
- hollow spheres
  - hybrid nanostructured, 73
- hybrid materials, 163
  - smart, 233
- hydrothermal synthesis, *see also* nanowire synthesis
  - as environmentally friendly, 234
  - oxygen semiconductor fibrous materials, 235

- impedance spectroscopy analysis, 533
  - application to electroceramics, 533
  - grain bulk and boundary contributions, 533
- incipient ferroelectrics, *see* quantum paraelectrics
- inelastic scattering of light, *see* Raman effect
- integration
  - active non-semiconductor layers, 164
  - CMOS technology, 164, 180
  - functional oxide films, 179
  - high-performance functional layers, 163
- interface effects
  - ferroelectric/electrode interface effects, 651, 660
    - depolarization field compensation, 652
  - metal–ferroelectric–metal structures, 647
- interfaces
  - $BaTiO_3$/Fe
    - interface multiferroicity, 314
    - interface net magnetic moment, 314
  - ferroelectric/metal-electrode, 646
    - back-to-back connected two-Schottky diode structures, 647
    - only-one Schottky diode structures, 657
      - C–V characteristics, 658
      - as photovoltaic cells, 659
      - short-circuit photocurrents, 659
    - Schottky contact, 647
      - photovoltaic effect, 653
    - TEM studies
      - $Pb(Zr,Ti)O_3/SrRuO_3$ interface, 665
    - XPS studies, 664
  - $LaAlO_3/SrTiO_3$
    - 2D electron gas, 312
  - $La_{0.7}Sr_{0.3}MnO_3/BiFeO_3$
    - atomically engineered terminations, 313
- Ising models, 484
  - size dependent effects, 485. *See also* scaling effects

- Kelvin probe force microscopy (KPFM), 437
  - $BaTiO_3$
    - phase transition studies, 442
    - screening mechanism studies, 442–443
  - charge injection, 446
  - distinguishing features with EFM, 438
  - dual harmonic KPFM, 445
  - domain studies
    - $KTiOPO_4$ crystals, 445
    - $LiNbO_3$ crystals, 445
    - PVDF films, 441
    - PZT films, 441

Kelvin probe force microscopy (KPFM) (*Continued*)
  open-loop KPFM, 445
  operating principle, 438
  Pb$(In_{1/2}Nb_{1/2})O_3$- Pb$(Mg_{1/3}Nb_{1/3})O_3$-$PbTiO_3$, 445
  quantitative electrostatic properties, 441
  surface potentials, 438
    $BiFeO_3$ films, 442, 445
    PVDF films, 442, 445
    PZT films, 442, 444–445
    solid–liquid interfaces, 447
  switching spectroscopy, 447
  time resolved KPFM, 447
  tip-sample system modeling, 442
Kirkedall effect, 211. *See also* hollow nanostructures
(K,Na)NbO_3 (KNN) based materials, 518
  ceramic texturing, 518
  $(K_{0.5}Na_{0.5})NbO_3$-$LiTaO_3$-$LiSbO_3$ ternary, 518
  orthorrombic–tetragonal polymorphic transition, 518
  piezoelectric coefficients, 518
$KTaO_3$ as a quantum paraelectrics, 757. *See also* quantum paraelectrics

Landau–Ginzburg–Devonshire (LGD) theory, 483, 618
  Gibbs free energy, 618
  Landau–Khalatnikov differential equations, 483
  Lyddane–Sachs–Teller equation, 619
  size dependent properties, 483–484. *See also* scaling effects
    size driven phase transition, 484
(La,Sr)CoO_3 electrodes, 120
lead-based relaxor-ferroelectrics, 101
lead-free alternatives, 166
life cycle assessment, 165
$LiNbO_3$ as photorefractive material, 838. *See also* photovoltaic ferroelectrics
$LiTaO_3$ as photorefractive material, 838
litography, *see also* top-down methods; bottom-up methods
  electron beam, 119
local field engineering, 590
  composite design for tailored properties, 590
lone pair, 45
  stereochemically active $6s^2$ electron, 298
Lorentz microscopy, 404
low-dimensional systems, 700
  boundary conditions, 701
  electrical vortices, 701. *See also* ferroelectric vortices
  flux-closure configurations, 701
  nanoscale devices, 701
    non-volatile Fe-RAMs, 701. *See also* memories
  phase transition, 700
  size effects, 701
  zero dimensional ferroelectric structures, 701
low-melting point substrates, 163
low-temperature fabrication, 163
low-temperature processing, *see* ceramic processing; thin-film fabrication
low-temperature solution-based deposition method, *see* thin-film fabrication
low-tolerance factor perovskites, 45, 47, 55
  ceramic processing, 63
  phase decomposition, 57
$LuFe_2O_4$
  as type I multiferroic, 792
  charge ordered transition, 310
    ferroelectricity, 792
  ferromagnetic ordering, 310
  layered hexagonal structure, 311

magnetic analogy, 376
magnetic force microscopy (MFM), 401, 436
  high-frequency MFM, 406
  magnetic domains, 406
  magnetic resonance force microscopy, 406
    three dimensional magnetic imaging, 406
  near-field-MFM, 406
  polycrystalline ferrite films, 406

- magnetic imaging, 403
  - sensitivity and resolution, 404
- magnetic ordering, 44
  - spins of electrons in incomplete *d* or *f* shells, 382
- magnetic recording industry, 406
- magnetic resonance imaging, 406
- magnetic spin glasses, 730
  - freezing, 730
  - frustrated interactions, 731
  - phase diagram, 731
- magnetic vortex state, 714
  - imaging, 719
- magnetically active cation, 45
- magnetically induced ferroelectricity, 382. *See also* multiferroic magnetoelectrics
  - Dzyaloshinskii-Moriya interaction, 382
  - exchange-striction mechanism, 382
- magnetism
  - electric control, 678
  - Goodenough–Kanamori rule, 809
- magnetization, 44
- magnetoelastic anisotropy, 678
  - electric field modulated, 688
  - piezoelectrically induced, 678
- magnetoelectric composites, *see* multiferroic composites
- magnetoelectric coupling, 44, 150, 377
  - as interface effect, 377
  - microscopic mechanisms, 377
  - strain-mediated, 377, 790
- magnetoelectric effect, 376, 790
  - crystallographic symmetry requirements, 376
  - magnetoelectric coefficient, 790
- magnetoelectric multiferroics, *see* multiferroic magnetoelectrics
- magnetometry, 806
  - magnetization hysteresis loops, 806
  - zero-field-cooled field-cooled (ZFC-FC) measurement protocol, 806
    - magnetic phase transitions, 806
- magneto-optic imaging, 403
  - Faraday effect, 403
  - Kerr effect, 403
  - magnetic domains, 403
- magnetostriction, 678. *See also* Terfenol-D
  - $Co_{60}Fe_{40}$, 679
  - Fe, 680
- Maxwell–Wagner relaxation, 78
  - as “false” reentrant ferroelectric behaviour, 741
  - ferroelectric thin films, 629
- mechanoactivation techniques, 48
- mechanochemical activation, 48
- mechanochemical reactions, 48
- mechanosynthesis
  - $BiFeO_3$-$BiMnO_3$-$PbTiO_3$, 51
  - $BiFeO_3$-$PbTiO_3$, 51
  - $BiMnO_3$, 48–49
    - amorphous phases, 50
    - nanocrystalline phases, 49
      - pseudocubic symmetry, 49
  - $BiMnO_3$-$PbTiO_3$, 51
  - nanometric particle size, 52
- memories
  - density, 118
  - dynamic random access (DRAM), 816
  - electrically-erasable programmable read-only (EEPROM), 816
  - ferroelectric random access (FeRAM), 5, 816
  - four-state, 789, 791, 817
    - multiferroic tunnel junctions, 818
    - vertically aligned Mn-doped $BaTiO_3$ nanowire arrays, 220
  - hard disk drive, 149
    - magnetic, 816
  - low-power electric-write, non-destructive magnetic read, 149, 789, 791, 817
  - magnetic random access, 816
  - metal-ferroelectric-semiconductor, *see* multilayer structures
  - non-volatile, 201
  - non-volatile ferroelectric random access, 118, 149, 164, 791
    - nanowire based, 233
  - racetrack, 765. *See also* spintronics

- memories (*Continued*)
  - spin transfer torque magnetic random access, 791, 817. *See also* spintronics
  - three dimensional, 148, 202
- metal complexes
  - intrinsically photosensitive, 175. *See also* thin-film fabrication
- metal oxide precursor solutions, 175. *See also* thin-film fabrication
- metal oxides
  - low-temperature solution processed, 163
- MgO as low-permittivity linear dielectric, 593
- MgTiO$_3$ as low-permittivity linear dielectric, 593
- microelectromechanical systems (MEMS), 5. *See also* devices
- microfiber, *see* fiber
- modeling
  - colloidal suspensions, 101
    - aggregate formation, 105, 107
    - Brownian dynamics methods, 105
    - DLVO theory, 103, 105
    - double-layer force, 106
    - Metropolis algorithm, 105
    - Monte Carlo methods, 105
    - particle interactions, 107
    - radial distribution functions, 107
  - finite element (FEM), 485
    - combined CPM–FEM, *see* polarization switching
    - composite materials, 590
      - effective permittivity, 592
      - local electric field distributions, 591
      - tunability, 592
    - electrode–ferroelectric structures, 485
    - piezoresponse, 485
  - grain size effects in ceramics, 537
    - effective medium theory with percolation, 538
      - application to BiScO$_3$-PbTiO$_3$, 539
  - hydrothermal synthesis, 203
    - reaction yield, 203
  - polarization switching, 485, 603
    - classical Preisach model (CPM), 603–607
      - first order reversal curves (FORCs), 604
      - hysterons, 603
    - inhomogenous ferroelectrics, 607–608, 611
- molecular spectroscopy, *see* Raman spectroscopy
- Moore's law, 118, 147
- more than Moore, 148
- morphotropic phase boundary, *see also* perovskite solid solutions
  - strain-driven, 276
- multiferroic composites, 73, 83, 90, 150, 377, 418
  - 0–3 connectivity, 84–85, 150
    - nanoparticulate, 150
  - 1–3 connectivity, 85, 150
    - epitaxial vertical heterostructures, 150
  - 2–2 connectivity, 85, 150
    - multilayered, 150
  - coaxial nanofibers, 85, 89
  - magnetic alloy – ferroelectric oxide type, 426
  - magnetoelectric voltage coefficient, 83, 85, 90
  - magnetoelectricity as product property, 83
  - nanocomposites, 150
  - strain mediated coupling, 83–84, 377
    - Terfenol-D based, 790
  - vertically-aligned nanowire arrays, 85
- multiferroic heterostructures
  - elastically coupled, 681, 791. *See also* domain transfer
  - exchange coupled, 681
  - thin-film epitaxial structures, 84, 677
- multiferroic magnetoelectrics, 44, 73, 150, 677
  - applications, *see* devices

- hexaferrites
  - $SrCo_2Ti_2Fe_8O_{19}$, 794
  - microscopic origins, 377
  - perovskite solid solutions
    - $Pb(Zr,Ti)O_3$-$Pb(Fe_{1/2}Ta_{1/2})O_3$, 795
  - RMn_2O_5 orthorrombic rare-earth manganites
    - ferroelectricity, 383
    - low-temperature magnetic phase diagram, 382
    - magnetoelectric coupling, 383
    - orthorrombic *Pbam* space group, 382
  - scarcity, 792
  - Type I, 792
  - Type II, 792
    - magnetic ferroelectrics, 792
- multiferroism, 44, 791
  - epitaxial strain driven, 793
    - spin–phonon coupling, 793
    - supercell structures, 794
- multifunctionality, 164
- multilayer actuators
  - market technologies, 513
  - materials, 513
    - electrodes, 513
  - performance, 513
- multilayer ceramic capacitors (MLCCs), 14, 201, 474, 512
  - annual production, 477
  - class 2 XTR andY5V ceramic capacitors, 477
  - class 3 ceramic capacitors, 477
  - geometry, 476
  - materials, 477, 512
    - electrodes, 512
  - market technologies, 477, 512
  - miniaturization, 477, 512
    - ceramic nanostructuring requirement, 477, 513
  - specific capacitance, 476, 512
  - volume capacitance, *see* specific capacitance
- multilayer structures
  - dielectric
    - Maxwell–Wagner polarization effects, 647
  - ferroelectric/dielectric
    - $SrTiO_3$ based, 647
  - ferroic
    - ferroelectric/antiferroelectric, 647
      - $Pb(Zr,Ti)O_3$-based, 669
    - ferroelectric/multiferroic, 670
      - $Pb(Zr,Ti)O_3/BiFeO_3$, 670
  - metal–ferroelectric–semiconductor (MFS)
    - as alternative non-volatile memories, 667
    - capacitance-voltage characteristics, 646, 667
    - MFS structures on Si, 646, 667
    - MFS structures on ZnO, 646, 667
    - $Pb(Zr,Ti)O_3$/ZnO based
      - polarization hysteresis, 667–668
      - thermal dielectric relaxation currents, 669
  - multiferroic
    - $BaTiO_3/CoFe_2O_4$, 670
    - $BaTiO_3/(La,Sr)MnO_3$, 670
      - magnetocapacitive effect, 670
    - magnetoelectric coupling
      - electrostatically coupled layers, 647
      - mechanically coupled layers, 647
    - $Pb(Zr,Ti)O_3/CoFe_2O_4$, 670

- nanocapacitors, 135
  - self-organized nanoelectrodes, 135
- nanocomposite multiferroics, *see* multiferroic composites
- nanoelectromechanical systems, 256
- nanoindentation, 247
  - load-displacement curve, 248
  - residual impression, 247
- nanofiber characterization
  - PFM of $BaTiO_3$ nanofibers, 250
- nanofiber preparation
  - electrospinning, 202, 235
- nanofiber properties, 235
  - $BaTiO_3$ aligned nanofibers, 250
- nanofibers, 202, 213
  - as building blocks in nanogenerators, 234

nanopillars
  array preparation, 121
nanoporosity
  as facilitator of film crystallization, 154
nanorods, *see* nanowires
nanoscale disorder, *see* relaxors
nanoscale material properties, 435
nanoscale structural characterization, 390
nanostructured ferroelectric ceramics, 358, 596
  as ferroelectric/dielectric composites, 596. *See also* $BaTiO_3$ nanostructured ceramics
  grain size effects, 478, 596
    modeling of effective permittivity and tunability, 598
    modeling of local field distributions, 596–597, 608
    modeling of polarization switching, 608
  macroscopic ferroelectric response, 358–359
nanotechnology, 435
nanotube synthesis
  topochemical conversion of precursor templates, 211
  vertically aligned arrays, 211
nanotubes, 201, 233
  array preparation, 121
  domain configuration and dynamics, 202
nanowire applications, 221
  nanoelectromechanical systems, 219, 256
    accelerometer using vertically aligned $BaTiO_3$ nanowires, 219
  nanogenerators, 219, 255. *See also* harvesting
  sensors, 255
nanowire characterization
  conductivity
    powder solution composite method, 251
  electrostatic force microscopy, 214
  high-resolution transmission electron microscopy, 214
  piezoresponse force microscopy, 214
    local polarization distribution, 250
    piezoresponse hysteresis loops, 217
  scanning transmission electron microscopy, 214
nanowire properties
  intrinsic size effect, 483
    critical radius, 483
  distributed kinetic friction
    ZnO nanowires, 247
  non-linear dielectric behaviour, 232
  non-linear optical activity, 232
  polarization switching, 217
nanowire synthesis
  hydrothermal, 202–203
    $BaTiO_3$, 204
      topochemical conversion, 207
    $KNbO_3$, 207
      arrays, 208
    $KTa_{1-x}Nb_xO_3$, 208
    $NaNbO_3$, 208
    $PbTiO_3$, 204
      arrays, 208
    $Pb(Zr,Ti)O_3$, 204
      arrays, 208
    $SrTiO_3$, 204
  molten salt, 202, 203
    $BaTiO_3$, 207
  morphological control, 202
  reactive precursor templates, 202, 208
    alkaline titanate nanowires and nanotubes, 208
    anatase nanowires, 210
    heteroepitaxial growth, 208
    topochemical reaction, 208
    topochemical transformations, 211
  solid state synthesis, 212
  solid-state topochemical reactions, 202
  solvothermal, 202–203
  templates, 202
    electrophoretic deposition, 211
    infiltration of sol–gel precursors, 211
    porous membranes with ordered cylindrical pores, 202, 211
  vertically aligned arrays, 211

nanowires, 201, 233
  Curie temperature, 214
  domain configuration and dynamics, 202, 217
    manipulation of patterns, 217
    single-domain, 214
    stripe domain patterns, 216
  Fe@Pb(Zr,Ti)O_3, 89
  local electrical poling, 217
  phase sequence for $BaTiO_3$ and $KNbO_3$, 216–217
  spontaneous polarization, 214
  spontaneous strain, 214
  surface charge screening, 215
  vertically aligned arrays of nanowires
    as positive templates, 211
$NdMn_2O_5$, 383. *See also* multiferroic magnetoelectrics
  ceramic sintering, 384
  multiferroic behaviour, 389
  powder synthesis, 383–384
  single crystal growth, 384
  selected interatomic distances, 385, 388t
  stoichiometry, 385
  structural parameters, 385–386t
  superexchange interactions, 387–388
neutron elastic scattering, 378
neutron facilities, 377, 378, 381t
neutron scattering techniques
  diffraction techniques, 378
  imaging techniques, 378
  spectroscopy techniques, 378
neutron–synchrotron X-ray complementarity, 378
neutron total scattering, 391. *See also* PDF
  $BaTiO_2$@SiO_2 core-shell nanostructures, 393–395
non-linear dielectrics, 474

one-dimensional ferroelectric nanostructures, *see* nanowires; nanotubes
one-dimensional microstructures, *see* fiber
optical charging spectroscopy (OCS), 655
organic ferroelectrics, 164
orientation distribution function (ODF), *see* EBSD data
Ostwald ripening, 204
oxide layers
  flexible substrates, 163
  semiconductor substrates, 163
oxide microelectronics, 618
oxide semiconductors, 163
oxide thin films
  electronic, 163

pair distribution function (PDF) analysis, 391
  chemically resolved, 391
  whole particle refinement, 392
particles
  colloidal, 72, 104
  high reactivity, 48
  magnetic, 72
  magnetic nanoparticles, 73
  nanosized, 48
    size effects, 478
  surface charge, 106
  surface functionalization, 72
  surface properties, 72
patterning, *see* top-down methods; bottom-up methods
$(Pb_{0.76}Ca_{0.24})TiO_3$ thin films on $Pt/TiO_2/SiO_2/Si$ substrate
  ferroelectric hysteresis loops, 183
  high-T processed by CSD, 182
  low-T processed by PCSD, 182
    nanostructuring effects, 184
  microstructure, 183
  lead gradients, 183
$Pb(Fe_{1/2}Nb_{1/2})O_3$
  as reentrant spin glass, 735
(Pb,La)(Zr,Ti)O_3 (PLZT), 333
  ferroelectric to antiferroelectric crossover, 226
  La-driven A-site disorder, 334
  La-induced relaxor state, 334
  as relaxor ferroelectric, 555
  short-ranged displacement of cations, 334

$Pb(Mg_{1/3}Nb_{2/3})O_3$
  average cubic *Pm*-3*m* symmetry, 338
  broad band dielectric investigation, 557
    nanopowders, 559
      particle size effects, 559–561
  chemically ordered regions, 338
  field induced irreversible phase transition to a ferroelectric state, 338, 555
  nuclear magnetic resonance, 566
  polar nanoregions, 338
    monoclinic symmetry, 756
  powder synthesis, 101, 105–106
    columbite method, 101
    conventional solid-state, 101, 109
    mechanochemical synthesis, 101
    secondary pyrochlore phases, 101, 106
    wet chemistry methods, 101
  as relaxor ferroelectric, 555
  soft mode, 338
$Pb(Mg_{1/3}Nb_{2/3})O_3$ ceramics
  detrimental pyrochlore phases, 110
  dielectric properties, 101, 110, 337
    permittivity peak, 110, 338
  electromechanical response, 110
    electrostrictive properties, 337
  grain size effects, 558
    core-shell model, 558
      dead layer, 558
    grain boundary dilution, 558
    permittivity, 558
      low-permittivity grain boundaries, 558
  hot pressing, 558
$Pb(Mg_{1/3}Nb_{2/3})O_3$ nanostructured ceramics
  broad band dielectric investigation, 561
    glass behavior, 564
    grain size effects, 561–565
    polar nanoregions, 563–564
$Pb(Mg_{1/3}Nb_{2/3})O_3$ single crystals
  permittivity broad dispersive maximum, 631
    derivative of the inverse permittivity, 631
$Pb(Mg_{1/3}Nb_{2/3})O_3$-$PbTiO_3$, 101, 514
  chemically ordered regions, 338, 543
  electrostrictive properties, 337
  ferroelectric order development, 518
    two-stage model, 543
  high-temperature relaxor state, 518
  monoclinic phases, 338
    Cm symmetry, 518
    Pm symmetry, 518
  orthorrombic phase, 338
  piezoelectric response, 101, 337
  polar nanoregions, 338, 543
  rhombohedral phase, 338
  spontaneous relaxor to ferroelectric transition, 555
  synthesis, 110
    detrimental pyrochlore phases, 110
    tetragonal phase, 338
$Pb(Mg_{1/3}Nb_{2/3})O_3$-$PbTiO_3$ ceramics, 517
  dielectric properties, 112
    permittivity peak, 112
  ferroelectric hysteresis loops, 112
  grain size effects, 540
    domain configurations, 543
    ferroelectric long-range order destruction, 540, 558
    phase transition kinetics, 543
    polarization rotation, 541
    room temperature relaxor state, 540, 558
  microstructure, 112
  textured, 517
    piezoelectric coefficients, 517
    processing up-scaling, 517
$Pb(Mg_{1/3}Nb_{2/3})O_3$-$PbTiO_3$ single crystals, 514, 517
  ultrahigh piezoelectricity, 514, 517
$Pb(Sc_{1/2}Nb_{1/2})O_3$, 566
  B-site ordering, 566
    order-induced ferroelectric phase, 566
  derivative of the inverse permittivity, 631
  as relaxor ferroelectric, 566
  spontaneous relaxor to ferroelectric transition on cooling, 566

$Pb(Sc_{1/2}Nb_{1/2})O_3$ nanostructured ceramics, 566
  broad band dielectric spectroscopy, 567
  grain size effects, 566
  polar nanoregions, 570
$Pb(Sc_{1/2}Ta_{1/2})O_3$, 555
  as relaxor ferroelectric, 555
$Pb_{0.5}Sr_{0.5}TiO_3$ ceramics
  phase transition, 631
    derivative of the inverse permittivity, 631
$PbTiO_3$
  as aristotype of $Pb(Zr,Ti)O_3$, 298
  Curie temperature, 46
  domain wall configurations, 298
  embedded nanoislands, 137
  epitaxial films, *see* epitaxial
  ferroelectric polarization, 298
  nanodot arrays, 123
  nanoporous films, 154
  ordered epitaxial nanoislands, 129
  porous films, 152
  registered nanosdot arrays, 135
  registered self-assembled nanoislands, 133
  self-assembled nanoislands, 126, 128
  tetragonal phase, 46, 298
  thin fims on $Pt/IrO_2/Ir/SiO_2/Si$ substrate
    ferroelectric loops, 188
    low-T processed by aqueous PCSD, 185
    microstructure, 186, 188
    surface roughness, 186
  thin fims on $Pt/TiO_2/SiO_2/Si$ substrate
    ferroelectric hysteresis loops, 185
    low-T processed by PCSD, 185
$Pb(Zn_{1/3}Nb_{2/3})O_3$-$Pb(Fe_{1/2}Nb_{1/2})O_3$-$PbTiO_3$ nanostructured ceramics
  room temperature relaxor state, 544
    integranular PNR interactions, 544
$Pb(Zn_{1/3}Nb_{2/3})O_3$-$PbTiO_3$ (PZN-PT), 47, 514
  nanostructured ceramics, 543
    room temperature relaxor state, 543
  single crystals, 514, 517
    ultrahigh piezoelectricity, 514, 517
  as thermodynamically unstable perovskite, 543
$Pb(Zr,Ti)O_3$ (PZT), 47, 201, 333, 474, 514
  antiferrodistortive rotation of oxygen octahedra, 334
  domain configurations
    hierarchical structure, 514, 527
      nanoscale regular twinned domains, 333, 514, 527
  embedded nanoislands, 138–139
  La doping, 334. *See also* PLZT
  monoclinic *Cm* phase, 333, 514
  morphotropic phase boundary, 333, 514
  nanotube arrays, 121
  nanotubes, 128
  patterned arrays of islands, 120–121, 124
  as perovskite ferroelectric for FeRAMs, 816
  phase diagram, 515f
  permittivity, 525
    poled state, 525
  piezoelectric response
    domain wall contribution, 514
    single crystal contribution, 514
      polarization rotation mechanism, 514
  polycrystalline films on Pt/Si substrates
    ferroelectric hysteresis loops, 652
    pyroelectric response, 657
      Si substrate extrinsic contribution, 657
    short-circuit photocurrents, 656
  porous films, 152
  PZT-based commercial piezoceramics, *see* piezoelectric ceramics
  rhombohedral *R*3*m* phase, 333, 514
  self-assembled nanoislands, 126
  self-patterned arrays of nanoislands, 131
  as state of the art material for piezoelectric applications, 514
  submicron grain size ceramics, 524
  tetragonal *P*4*mm* phase, 333, 514

perovskite complex oxides, 331. *See also* relaxors
  lead-based complex oxides, 100
perovskite ferroelectrics
  applications, 617. *See also* devices
  properties, 617
  response functions, 617
perovskite reentrant relaxors, *see* reentrant ferroelectric relaxors
perovskite relaxors, *see* $Pb(Mg_{1/3}Nb_{2/3})O_3$ and $Pb(Sc_{1/2}Nb_{1/2})O_3$
perovskite solid solutions, 47, 100
  band-gap tuning, *see* Photovoltaic ferroelectrics
  morphotropic phase boundary systems, 47
perovskite structure, 201, 475
  structural flexibility, 475
    physical properties design, 475
perovskites, 298
phase transitions
  ferroelectric, 729. *See also* ferroelectric phase transition
  ferromagnetic, 729
  high-temperature disordered phase, 729
  low-temperature ordered phase, 729
  order parameter, 729
    fluctuations, 729
  transition temperature, 729
photochemical solution deposition, *see* thin-film fabrication
photorefraction effect, 838
photovoltaic effect, 831
photovoltaic ferroelectrics
  band gap tuning, 844
    perovskite ferroelectrics, 844
      Bi_2FeCrO_6, 844
    perovskite solid solutions, 846
      $KNbO_3$-$BaNi_{1/2}Nb_{1/2}O_{3-\delta}$, 846
  $BiFeO_3$ epitaxial films, 836
    conductivity, 837
      processing effects, 837
    external quantum efficiency, 836
    film-electrode interface, 836
      Schottky barrier, 836
    open-circuit voltages, 836
    short-circuit photocurrents, 836
  $BiFeO_3$ single crystals, 835
    optical rectification effect, 836
    steady-state photocurrents, 835
  bulk photovoltaic effect, 831
    above band-gap photovoltages, 831
    microscopic mechanism, 833
    theory, 833
      shift current, 833
      third-rank photovoltaic tensor, 833
      transition intensity and shift vector, 834
  Dember effect, 831
  domain wall effects, 840
    domain engineered $BiFeO_3$ epitaxial films, 841
    wall conductivity, 843
    wall internal potential, 841
  $KNbO_3$ single crystals, 839
    Fe doped, 839
  $LiNbO_3$ single crystals, 838
  photoresponse contributions, 840
    electrodes, 840. *See also* $BiFeO_3$ epitaxial films
      Schottky barriers, 840
  photovoltaic efficiency, 832
  short-circuit photovoltaic current, 833
  steady-state photocurrent regime, 832
piezoelectric ceramic thick films, 513
  ceramic MEMS, 513
piezoelectric ceramics, 514
  high sensitivity and power, 517
  high temperature, 516
  lead-free, 518
  PZT based high-sensitivity, 514
    grain size effects, 533
    hard PZTs, 515, 517
    point defect engineering, 515
    soft PZTs, 515, 517
    temperature operation range, 516
piezoelectric coupling, 297
piezoelectric effect, 645
piezoelectric fibers, 233
piezoelectric materials, 474
piezoelectric properties, 201

piezoelectric thin films, 513
  flexible organic substrates, 513
  Si-based MEMS, 513
    CMOS electronics, 513
piezoelectricity, 164, 232
piezoresponse force microscopy (PFM), 250, 401, 408, 436
  $BaTiO_3$ nanostructured ceramics, 353, 496
  $BiScO_3$-$PbTiO_3$ nanostructured ceramics, 529f
  ferroelectric domain patterns, 409
  lateral PFM, 409
  parallel PFM and MFM measurements, 409
  vertical PFM, 409
polar materials, *see* pyroelectric materials
polar ordering, 618
polarization, 444
poling process, 201
polycarbonate membrane, 89, 202, 211
polyvinylidene fluoride (PVDF), 221
porous alumina templates, 128, 202, 211. *See also* anodic aluminum oxide membrane
porous ceramics, 487. *See also* porous ferroelectric ceramics
  effective permittivity, 589
  local field inhomogeneity, 590
  switching properties, 589
porous ferroelectric ceramics, 599
  closed and open porosities, 599
  as ferroelectric/dielectric composites with 3–0 connectivity, 599
  modeling of effective permittivity and tunability, 599
  modeling of local field distributions, 599, 609
  modeling of polarization switching, 610
porous silica templates, 128
porous silicon membrane, 202, 211
potassium dihydrogen phosphate (KDP), 201
powder synthesis
  chemical composition, 48
  nanopowders, 48
  particle size, 48
  Pechini method, 17
  sol–gel method, 17
  solid state reaction method, 17
$PrMn_2O_5$, 383. *See also* multiferroic magnetoelectrics
pyroelectric effect, 645
pyroelectric materials, 200, 474
  electrical dipole moment, 200
  non-centrosymmetric structure, 200. *See also* ferroelectricity
  spontaneous polarization, 200. *See also* ferroelectricity
pyroelectric polar groups, 376
pyroelectric properties, 201
pyroelectricity, 164, 232

quantum paraelectrics
  doping, 757
    dipolar glasses, 757
    ferroelectric states, 757
    relaxor states, 757
  Li/Nb doped $KTaO_3$, 757
    reentrant dipolar glass-like state, 758

Raman effect
  classical theory, 326
  inelastic scattering of light, 326
    scattering spectra, 326
  quantum theory, 326
  Rayleigh scattering, 326
  Stokes and anti-Stokes bands, 326
Raman scattering, 328
  first order, 328
  selection rule breaking, 329
    disordered crystals, 329
  selection rules, 328
Raman spectrometer, 328
Raman spectroscopy
  as laboratory scale method, 325
  as method with no need for sample preparation, 325
  as non-destructive method, 325

Raman spectroscopy (*Continued*)
  $BaTiO_3$
    cubic phase, 340
      disorder related Raman activity, 342
    orthorrombic phase, 342
    rhombohedral phase, 341
    tetragonal phase, 340–341
  $BaTiO_3$ nanofibers, 358
  $BaTiO_3$ nanorods, 357
  $BaTiO_3$ nanostructured ceramics, 354
  $BaTiO_3$ nanotubes, 358
  $BaTiO_3$ nanowires, 358
  $Ba(Ti,Sn)O_3$, 345–346
  $Ba(Ti,Zr)O_3$, 346–348
  $(Bi_{1/2}Na_{1/2})TiO_{3-}$ based materials, 350–351
  $BiScO_3$-$PbTiO_3$ nanostructured ceramics, 354–357
    soft mode, 356–357
  crystal orientation, 325
  $KNbO_3$ nanowires, 358
  $PbTiO_3$ nanotubes, 358
  phase studies, 325, 351
    phase gradients, 245
  phase transition studies, 329, 351–352
  PMN, 337–340
  PMN–PT, 338–340
  PLZT, 334–337
  PZT, 334
  relaxor states, 352
  short-ranged order and disorder, 351
  strain measurement, 325
Raman spectrum
  Bose–Einstein correction, 329
  as a fingerprint of substances, 326
reactive ion etching, 119. *See also* top-down methods
  anisotropic etch profiles, 119
  damage, 120
  dry etching, 119
reentrant ferroelectric relaxors, 741
  $Ba_{0.9}Bi_{0.067}(Ti_{1-x}Zr_x)O_3$ as perovskite reentrant relaxor, 746
  $Ba_2Pr_xNd_{1-x}FeNb_4O_{15}$
    dielectric permittivity, 747
    as tungsten bronze reentrant relaxor, 746
  $Ba_5RTi_3Nb_7O_{30}$ (R=La, Nd, Sm) as tungsten bronze reentrant relaxor, 749
  $BaTiO_3$-$AgNbO_3$
    dielectric permittivity, 743
    mesoscale chemical inhomogeneities, 744
      core-shell microstructures, 744
    as perovskite reentrant relaxor, 742
    phase evolution, 743
    solid solution formation, 743
  $BaTiO_3$-$BiScO_3$
    canonical relaxor phases, 746
    dielectric permittivity, 744
    as perovskite reentrant relaxor, 744
    phase evolution, 744
  models
    dipolar glass, 752
    frustrated ferroelectric/ferroelastic state, 752
    transverse freezing, 753
    two-phase coexistence, 752
  reentrant-like behaviour, 741
    ferroelectric domain wall relaxations, 741
      rhombohedral $BaTiO_3$, 742
    Maxwell–Wagner type relaxations, 741
    mesoscale or macroscale chemical inhomogeneities, 741
  $Sr_2NaNb_5O_{15}$
    dielectric permittivity, 748
    Invar effect, 748
    orthorhombic *Im*2*a* symmetry, 748
    as tungsten bronze reentrant relaxor, 748
  tungsten bronze systems, 750
    reentrant behavior crystal anisotropy, 751
    structural phase transition, 751
reentrant phases, 730
  binary liquid mixtures, 730

  - diluted magnets, 730. *See also* reentrant spin glasses
    - paramagnetic–ferromagetic–spin glass phase sequence, 731
  - inverse melting, 730
  - liquid crystals, 731
    - nematic–smetic–nematic phase sequence, 731
  - quasi-reentrant phases, 703
  - superconductors, 731
    - normal-superconducting-normal phase sequence, 731
  - thermodynamics, 731
- reentrant spin glass, 731
  - antoferromagnetic $Pb(Fe_{1/2}Nb_{1/2})O_3$, 735
  - antiferromagnetic $Fe_{0.55}Mg_{0.45}Cl_2$, 732, 735
    - magnetic relaxation, 732
  - Ising spin glass mean-field theory, 733
    - phase diagram, 733
  - microscopic models, 733
    - spin configurations, 733
    - random field model, 735
      - transverse freezing model, 733
    - transverse glassy order parameter, 733
    - two-phase percolation model, 735
- registration, *see* bottom-up methods
- relaxor ferroelectrics, 331, 554, 618, 729
  - as disordered crystals, 554
    - quenched compositional disorder, 736
  - analogy with reentrant spin glasses
    - ageing phenomena, 753
      - rejuvenation effects, 755
    - memory effects, 755
    - transverse glassy freezing, 753
  - analogy with spin glasses, 736
  - Burns temperature, 333, 554, 621
  - canonical relaxors, 729
    - Invar effect, 748
  - chemically disordered regions, 331
  - chemically ordered regions (CORs), 331
  - compositional disorder, 555
  - differences/similarities with dipolar glasses, 557, 736, 739
  - differences/similarities with ferroelectrics, 557, 620
  - ergodic relaxor state, 333, 554, 729
  - field-induced transition to a ferroelectric state, 621, 739
  - freezing temperature, 333, 730, 738
  - heterovalent substituted complex perovskites, 331
  - homovalent substituted complex oxides, 333
  - non-ergodic relaxor state, 333, 555, 730
    - ferroelectric hysteresis loops, 740
  - $(Pb,La)(Zr,Ti)O_3$, *see* PLZT
  - $Pb(Mg_{1/3}Nb_{2/3})O_3$, *see also* PMN
    - B-site partial disorder, 736
  - polar nanoregions (PNRs), 331, 554, 620, 729, 736
    - dynamics, 555
      - freezing, 737
    - interactions, 333, 737
    - growth, 333, 736
    - percolation, 557
    - X-ray fluorescence holography, 738
  - random electric fields, 331, 556
  - soft phonon modes, 555
  - spherical dipolar glass model, 556
  - spherical random-bond–random-field model, 556
  - spontaneous transition to a ferroelectric state, 621
  - Vogel–Fulcher law, 738
- relaxor properties, 331, 554, 620, 729
  - dielectric permittivity, 331, 555, 736
    - broad dispersive maximum, 620, 737
      - PNR thermally activated reorientations, 736
      - Vogel–Fulcher law, 557, 621, 739
    - empirical scaling law, 621, 738
    - modified Curie–Weiss law, 573, 621
    - relaxation spectrum, 738
- relaxors, *see* relaxor ferroelectrics
- Rietveld method, 384. *See also* Synchrotron X-ray diffraction data analysis

Rietveld refinement
  neutron diffraction data for $BaTiO_3$ nanoparticles, 395
  synchrotron X-ray diffraction data for $BaTiO_3$ nanoparticles, 395
Rochelle salt, 201, 473
  physical properties, 376
  reentrant behaviour, 731

scaling effects, 118
  critical size, 478
    extrinsic size effects, 478
    intrinsic size effect, 478, 480
    superparaelectric limit, 478
  depolarization field, 481
  downscaling of ferroelectricity, 390, 478
    Curie temperature, 478, 485
    domain structure, 486
    lattice strain, 478, 485
    phase transition, 478, 486
    spontaneous polarization, 478, 485
  downscaling of material properties, 477, 486
    dielectric, 478, 486
    domain wall contributions, 480, 486
    piezoelectric, 478
    pyroelectric, 478
  surface/interface effects, 481
  technological impact, 478
    piezoelectric technologies, 513
  theoretical description, 479
    ab initio and atomistic models, 479
    macroscale models, 480
      computational thermodynamics, 480
      finite element methods, 480
    mesoscale models, 479
      continuum methods, 479
        Landau–Ginzburg–Devonshire (LGD) theory, 479
    Ising models, 479
    mean-field theories, 483
    Monte Carlo models, 479
scanning electron microscopy (SEM), 241, 400
  digital image processing techniques, 242
  electron backscattered diffraction, 242. *See also* EBSD
    Kikuchi diffraction technique, 242. *See also* EBSD
  image analysis, 242
  main parts of a microscope, 241
  types of signal, 241
scanning force microcopy (SFM), 401, 436
  conductive AFM (c-AFM), 425
  contact modes, 436
  non-contact modes, 436
  tip-sample interaction, 401
  voltage modulated AFM, 436
scanning Hall probe microscopy, (SHPM), 404
scanning near-field acoustic microscopy, 436
scanning probe methods, 400, *see also* SPM
  physical properties analysis, 400
  topographic analysis, 400
scanning probe microscopy (SPM), 245, 435
  atomic force microscope, 246
  contact mode, 256
  friction force microscopy, *see* lateral force microscopy
  lateral force microcopy, 256
  nanoindentation, 256
  non-contact mode, 256
  piezoresponse force microscopy, 245. *See also* PFM
scanning superconducting quantum interference device (SQUID) microscopy, 404
scanning transmission electron microscopy (STEM)
  aberration corrected STEM, 290
  atomic column parameters from HAADF images, 292
  atomic number contrast, 291
  atomic resolution HAADF contrast, 292
  differences with HRTEM, 291
  displacement fields, 297
  dynamic scattering simulations, 292
  HAADF–STEM quantification

    $BiFeO_3$ thin films, 302–305
    $PbTiO_3$ thin films, 299–300
  high-angle annular dark field (HAADF) detector, 291
  image formation, 289
  local crystal structure, 275
  local strain measurements, *see* HRTEM
  mapping of electric polarization, 296
  model-based image analysis, 292–294
    single atomic column contrast model, 292
  scattering formalisms, 291
  unit-cell-wise maps of polarization, 297
  unit-cell-wise maps of strain, 297
  Z-contrast, *see* atomic number contrast
scanning tunneling microscopy (STM), 401, 409, 436
  local density of states, 401
  scanning tunneling spectroscopy (STS), 410
    melt-textured (Nd,Eu,Gd)$Ba_2Cu_3O_x$, 410
    superconducting $Bi_2Sr_2CaCu_2O_8$, 410
  spin-polarized STM, 411
    $La_{0.7}Sr_{0.3}MnO_3$ epitaxial films, 411
  variable temperature STM, 410
second harmonic generation, 200
  frequency doubling, 200
self-assembly, *see* bottom-up methods
semiconductor ferroelectrics, 831
semiconductor multiferroics, 831
semiconductor oxides, 164
semiconductor technology trends, 147
  international technology road map, 164
simulation, *see* modeling
simulation, atomistic
  Pb(Zr,Ti)O_3 nanowires, 215
simulation, full scale dynamic scattering
  HAADF–STEM contrast, 292. *See also* STEM
single-phase multiferroics, *see* multiferroic magnetoelectrics
sintering process, 54
smart hybrid materials, 233
  fiber based, 236
sodium potassium tartrate tetrahydrate, *see* Rochelle salt
Sol-Gel, *see* thin-film fabrication; fiber processing
Sol–Gel processing, *see* thin-film fabrication
solid-state synthesis, 102, 112
  $BaTiO_3$ nanowires, 212
  $Bi_4Ti_3O_{12}$ nanowires and nanotubes, 212
  mechanism of a binary solid-state reaction, 102
  three component system, 103
solvation, *see* Aqueous-solution gel route
spark plasma sintering (SPS), *see* ceramic processing
spin induced ferroelectricity, *see* magnetically induced
spintronics
  advantages against semiconductor devices, 678
  computer hard-disk read-head, 678
  magnetic random access memory (MRAM), 678
    STT–MRAM, 678
  multiferroic heterostructures as low-power alternative, 678
    nanowire geometry, 693
  racetrack memory, 678
  spin-transfer torque (STT) effect, 678
spin wave based technologies, 694
  magnonic crystals, 694
$SrBi_2Nb_xTa_{2-x}O_9$
  as Aurivillius ferroelectric for memories, 798
$SrBi_2Ta_2O_9$
  as Aurivillius ferroelectric for FeRAMs, 798, 816
  nanotubes, 128
  patterned arrays of islands, 120–121, 124
$SrMnO_3$ as predicted strain-driven multiferroic, 793
$SrRuO_3$ as electrode, 124

$SrTiO_3$
  as ferroelastic, *see also* twin boundaries
    tetragonal *I*4/*mcm* symmetry, 772
  as incipient ferroelectric, 202
  as substrate, 124, 312
    Nb-doped, 124
strain engineering, 793
  multiferroic $BiFeO_3$, 793
structure-property relationships, 376
superconducting high T_C oxides, 401
  industrial fabrication of superconducting tapes, 401
  scanning tunneling microscopy, 410
superparaelectric limit, 118
surface enhanced Raman spectroscopy (SERS), 359
synchroton scattering techniques, 378
  diffraction techniques, 378
  imaging techniques, 378
  spectroscopy techniques, 378
synchrotron X-ray diffraction data analysis, 384–385
synchroton X-ray diffraction study of $NdMn_2O_5$, 384
synchroton X-ray elastic scattering, 378
synchroton X-ray facilities, 377–380t
synchroton X-ray total scattering, 391. *See also* PDF
synchrotron X-ray-neutron complementarity, *see* neutron-synchrotron
synthesis
  ferroelectric oxide nanostructured particles, 473
  low-temperature routes, 163
  nanotubes, *see* nanotube synthesis
  nanowires, *see* nanowire synthesis

$TbMnO_3$, 316, 382
  incommensurate antiferromagnet, 316
  low-temperature commensurate spin spiral antiferromagnet, 316
  magnetocapacitance, 382
  magnetoelectric coupling, 316, 382
  magnetoelectric effect, 382
  orthorrombic distorted perovskite, 316
  as type II multiferroic, 792
    magnetic ferroelectricity, 316
$TbMn_2O_4$ as type II multiferroic, 792
Terfenol-D as magnetostrictive material, 790
thermal budget
  circuitry degradation, 165
  cross contamination, 165
thick films, 513
  powder suspension-based processing, 513
thin-film fabrication
  atomic layer deposition, 837
  chemical methods, 646
  chemical solution deposition, 5, 119, 163
    aqueous precursor solutions, 169. *See also* aqueous solution-gel route
      water-based precursor systems, 166
    crystallization, 179
      amorphous oxide phase, 181
      decomposition pathway, 173
    diol-based route, 166
      1,3-propanodiol solvent, 165
    environmental benign solvents, 166
    ozonolysis process, 181
    solution chemistry, 164
    solution deposition, 179
    UV assisted decomposition of precursors, 179
  chemical vapor deposition, 119
  conformal step coverage, 5, 119
  dip coating, 128
    self-assembled porosity, 153
  evaporation, 119
  integration with semiconductor circuits, 646. *See also* integration
  interdiffusion between film and substrate, 165, 182
  liquid source mist chemical deposition, 128

low-temperature deposition methods, 164
  photoinduced densification, 178
  photochemical solution deposition, 164
    flowchart, 180
    light sensitive solutions, 164
    photoactive organic compounds, 170
    photosensitive metal ion complexes, 180
    photosensitive precursors, 164, 175
      charge transfer complexes, 176–177, 185
    photosensitive sol–gel systems, 172
    UV absorber molecules, 164
    UV irradiation, 164
metallo-organic precursors, 119
  alkoxides, 172, 175
  β-diketonates, 172, 175
  Bi(III)-N-methyldiethanolamine, 176
  carboxylates, 172
  titanium di-isopropoxide bis(acetylacetone), 175, 181
metallo-organic chemical vapor deposition, 5, 126
metallo-organic decomposition, 5, 139
molecular beam epitaxy, 5
nucleation and growth-driven process, 119
pulsed laser deposition, 5, 124
reactive radio frequency magnetron sputtering, 120
sol–gel techniques, 5
sputtering, 5, 119
  RF sputtering, 646
textured Pb(Zr,Ti)O_3 films, 132
  TiO_2 seed layers, 132
volatilization of high vapor pressure elements, 165, 183
wet chemistry-based routes, 172
thin-film multilayered composites, 150
thin-film nanostructures
  characterization
    collective top electrode deposition
      chemical mechanical polishing, 136
      flowable spin-on oxide layers, 136
    direct electrical characterization of nanoislands, 137
    electrostatic force microscopy, 123
    piezoresponse force microscopy, 120, 123, 128
  fabrication, *see* top-down methods; bottom-up methods
  ferroic, 118
  formation mechanism, 127
  porous films, 151
  ultra-small trenched, 119
  vertical epitaxially-embedded magnetic phases in ferroelectric matrices, 150
thin film properties
  built-in electric field, 154, 183
  imprint, 154, 183
  intrinsic size effect, 482
    critical thickness, 482
  non-stoichiometric surface, 165, 183
  self-polarization, 154
  substrate-film interface
    Pt_xPb interlayer, 183
    secondary phases, 165
  thickness driven, 478
tip-enhanced Raman spectroscopy (TERS), 359
  $BaTiO_3$ nanorods
    a–c domains, 361
  field enhancement processes, 359
  nanometer scale spatial resolution, 359
  near field signal, 359
  reflection mode, 360
  scanning resolved measurements, 359
  transmission mode, 360
top-down methods
  invasive, 119
    lift-off process, 120

top-down methods (*Continued*)
  nanocolumns by focused ion beam milling, 202, 213
  reactive ion etching, 119
  thin film nanostructures by focused ion beam milling, 119–120
topological patterns, 515. *See also* vortex configuration
toroidal order, 202
transmission electron microscopy, 242
  reciprocity principle, 289
transmission electron microscopy techniques, 275
  aberration corrected instruments, 275, 280
  convergent beam electron diffraction, 276
  electron energy loss spectroscopy, 275–276. *See also* EELS
  electron holography, 319
  electron tomography, 318
  high-resolution transmission electron microcopy, 243, 275–276. *See also* HRTEM
  highly coherent electron sources, 280
  image formation, *see* HRTEM
  information limit, 280
  in-situ electron microscopy, 318
  scanning transmission electron microscopy, 275–276. *See also* STEM
  solid state properties on the atomic scale, 275
  spatial resolution, 280
  spherical aberration corrected microscopes, 280
triglycine sulfate (TGS), 436
tunable dielectrics, 593. *See also* composite materials
tungsten bronze ferroelectrics, 746
  $Ba_2NdFeNb_4O_{15}$, 746
  $Ba_2PrFeNb_4O_{15}$ as tungsten bronze relaxor ferroelectric, 746
  centrosymmetric tetragonal 4/*mmm* symmetry, 746
  orthorhombic ferroelectric phase, 746
  $Sr_xBa_{1-x}Nb_2O_6$ as uniaxial relaxor, 756
  tetragonal 4*mm* ferroelectric phase, 746
  as uniaxial ferroelectrics, 746
tunnel electromagnetoresistance, 314
tunnel electroresistance, 314
twin boundaries
  conducting $BiFeO_3$ twin boundaries, 775
  field control of patterns, 775
  as functional elements, 765
  high-density patterns, 766
    domain boundary engineering, 766
    thin films, 781
  domain glasses, 766
  nanoscale ferroics, 766
  shearing, 781
    soft and hard materials, 782
    tweed patterns, 766
    quenching, 781
  polar $CaTiO_3$ $\{100\}$ twin walls, 768
    HRTEM imaging, 768
    prediction of spontaneous polarization, 768
    oxygen vacancies, 771
    polar ordering, 769
  polar $SrTiO_3$ twin walls, 771
    polarization singularities, 773
      embedded vortex structures, 772
        mobile within the wall, 773
    switchable dipole moments, 771
    twin high mobility, 773
  superconducting WO_3 twin boundaries, 774
    chemical effect, 774
      oxygen vacancies, 774
    non-polar walls within a polar monoclinic *Pc* phase, 774
    tetragonal $P\text{-}42_1m$ symmetry, 774
twin phenomena
  charged domain boundaries, 768
  chirality, 765, 778
  high defect mobilities, 765
    ionic conductivity, 768
  lattice effects, 768

- magnetite, 780
- oxygen octahedral rotations, 766, 768
- polarity, 766
  - antiphase boundaries in antiferroelectrics, 766
- superconducting domain boundaries in insulators, 765
- multiferroicity, 765
- novel chemical compounds, 768
- thermal conductivity, 775
- unsual vortex configurations, 765

twinning, 765
- Landau–Ginzburg theory, 776–777
- multiferroic, 775

UV absorbing molecules, 172–174. *See also* thin-film fabrication

UV activity, 170. *See also* thin-film fabrication
- decomposition products, 171
- precursors, 170

UV irradiation, 178
- gel patterning, 179

UV lamps, 179

variable angle spectroscopic ellipsometry (VASE), 640

vertically aligned nanotube arrays, 221

vertically aligned nanowire arrays, 219, 220. *See also* nanowires

vibration spectroscopy, *see* Raman spectroscopy

vibrations in crystals
- acoustic phonons, 327
- hard mode phonons, 331
- infrared active modes, 329
- mode softening at the ferroelectric transition, 330
  - Cochran law, 338, 356
- optical phonons, 327
- Raman active modes, 329

vortex configuration
- dipolar vortex structures, *see also* ferroelectric vortices
  - localized central vortices within flux closure structures, 718
  - rotation axis of local dipoles, 715
    - continuos rotation, 718
  - unique core singularity, 719
  - winding number, 715
    - domain wall intersections in $YbMnO_3$, 716
- single topological singularity, 715
- topological winding number, 715
- vortex core, 718, 720

wavelength dispersive X-ray spectroscopy, 244

weakly ferromagnetic state, 46

Weiss theory of magnetism, 376

WO_3, 775. *See also* twin boundaries

X-ray absorption fine structure (XAFS), 392

X-ray absorption near-edge structure (XANES), 392

X-ray diffraction, 243

X-ray photoelectron spectroscopy (XPS), 663

$YMnO_3$
- as type I multiferroic, 792
  - geometrical ferroelectricity, 792

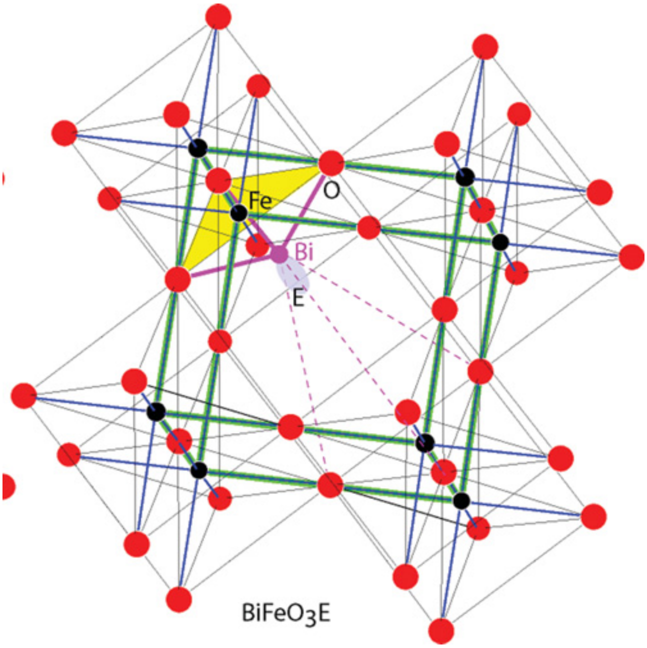
Fe
O
Bi
E
BiFeO3E

Figure 2.1 *Structure of $BiFeO_3$ (E: lone pair of Bi)*

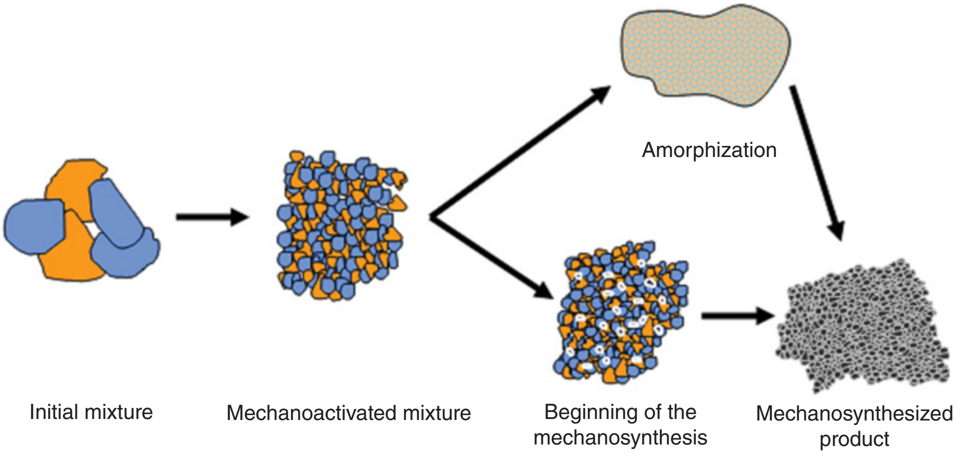
Amorphization
Initial mixture
Mechanoactivated mixture
Beginning of the mechanosynthesis
Mechanosynthesized product

Figure 2.2 *Different possible steps observed during a mechanochemical activation process*

Nanoscale Ferroelectrics and Multiferroics: Key Processing and Characterization Issues, and Nanoscale Effects,
First Edition. Edited by Miguel Algueró, J. Marty Gregg, and Liliana Mitoseriu.
© 2016 John Wiley & Sons, Ltd. Published 2016 by John Wiley & Sons, Ltd.

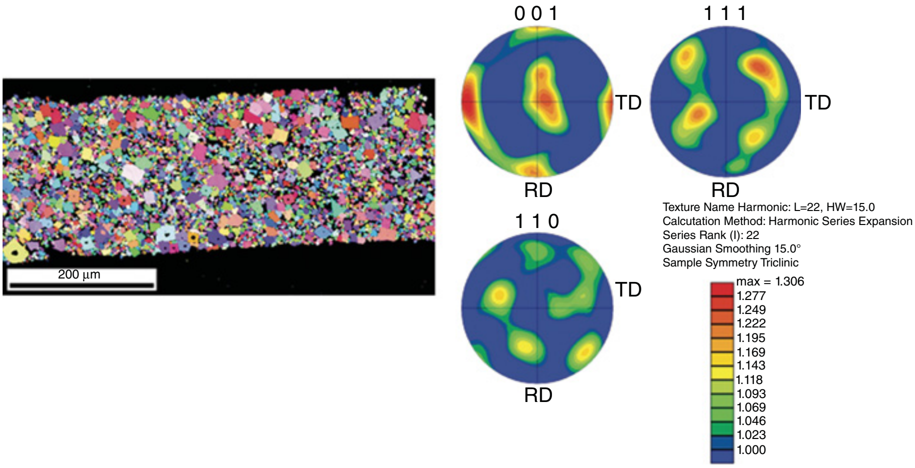

(a) (b)

Figure 9.4 *(a) The crystal orientation of a KNN fibre and (b) the same data plotted as (001), (111), and (110) texture plots of KNN fibre showing limited texturing inside the fibres*

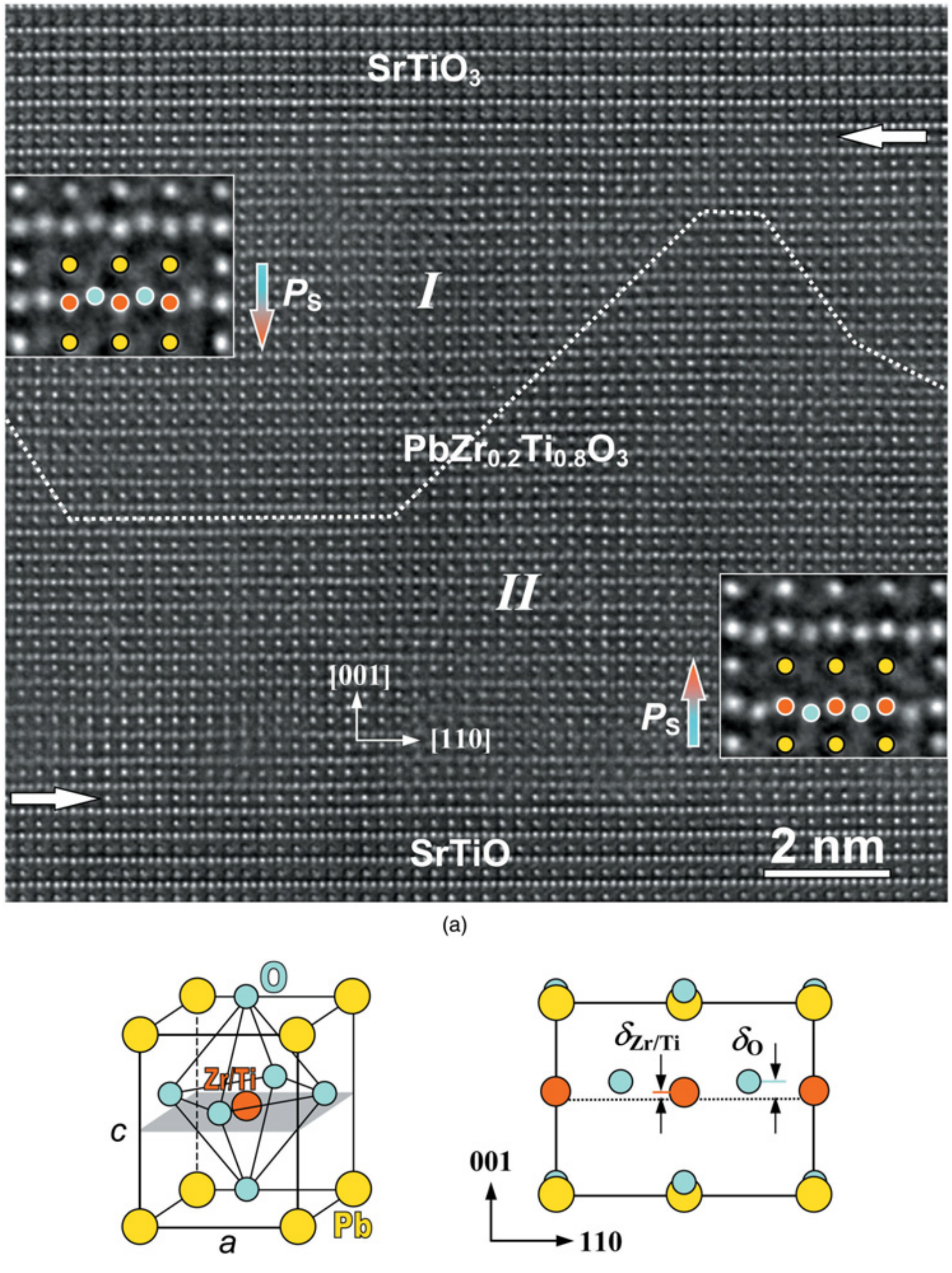
SrTiO$_3$
P_S
I
PbZr$_{0.2}$Ti$_{0.8}$O$_3$
II
[001]
[110]
P_S
SrTiO
2 nm
O
Zr/Ti
c
a
Pb
$\delta_{Zr/Ti}$
δ_O
001
110

(a)

(b)

(c)

Figure 10.5 *Cs-corrected HRTEM image of PZT (a) together with the schematic drawing of the PZT structure (b) projected along [1–10], (c) allowing the polarization change to be studied across a 180° domain wall. Reprinted by permission from Macmillan Publishers Ltd: [Nature Materials] [1]. Copyright © 2008*

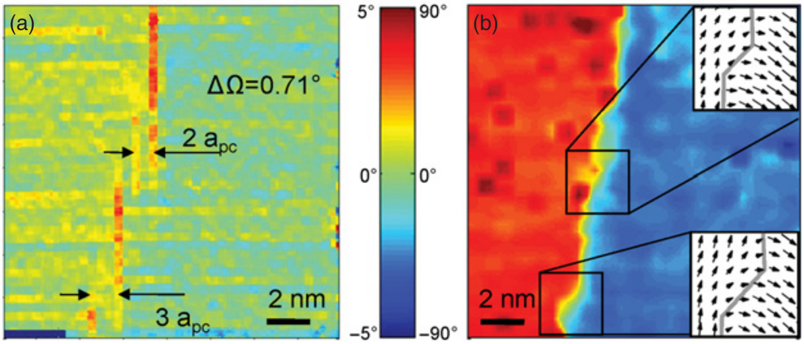

Figure 10.20 *(a) Lattice and (b) polarization rotation field at the BiFeO$_3$ 109° domain wall containing steps. The polarization vector field at the steps (enlarged squares) shows a rotation across a diagonal boundary*

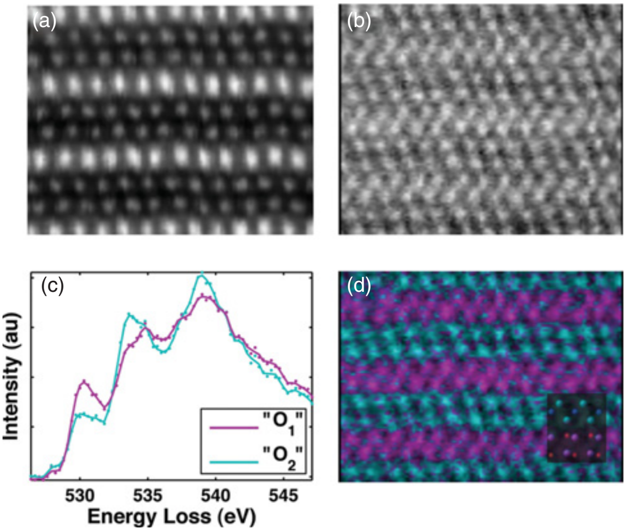

Figure 10.24 *Spectrum imaging of the local oxygen bonding in LuFe$_2$O$_4$ (110). (a) HAADF–STEM collected simultaneously to the EELS spectra. (b) Integrated intensity of the O K edge. (c) EELS fine structure of the two distinct O K edges found in the spectrum imaging, labeled O$_1$ and O$_2$. (d) Spatial distribution of the O$_1$ and O$_2$ chemical environment of oxygen atoms in the structure. Reprinted with permission from [80]. Copyright [2012], AIP Publishing LLC*

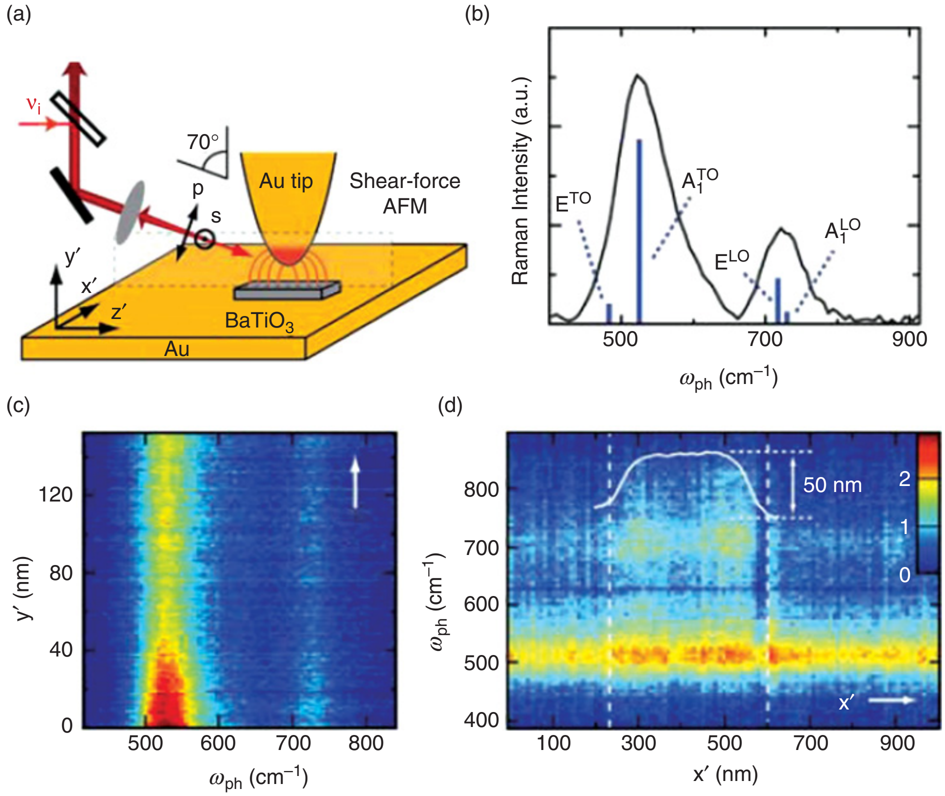

Figure 11.18 *(a) Schematic of the experimental reflection TERS setup for the measurement of BT nanocrystals. (b) TERS spectrum of BT acquired on a nanorod. The fluorescent background has been subtracted and phonon mode assignment is reported on the spectrum. (c) Tip-sample distance dependence and (d) spectrally resolved linescan across a BT nanorod. The abrupt signal change at 580 cm*$^{-1}$ *is due to an acquisition artifact. Reprinted by permission from Macmillan Publishers Ltd: [175], copyright (2009)*

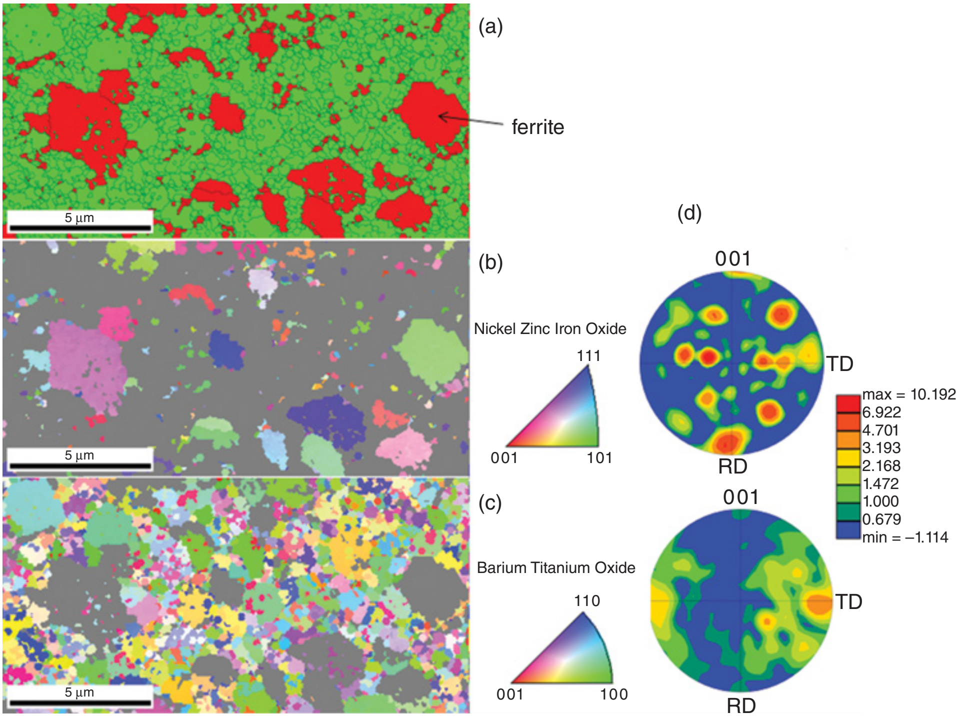

Figure 13.17 *EBSD analysis for sample C, where (a) gives the phase map and (b) gives the inverse pole figure (IPF) map in the (0 0 1) direction for the ferrite only, all other information being plotted in gray. The color code for the orientation is given in the stereographic triangle. (c) The same analysis as for* $BaTiO_3$*. (d) The corresponding pole figures in the (001) direction for the ferrite (left) and* $BaTiO_3$ *(right). Here the intensities are normalized with respect to the NZF data*

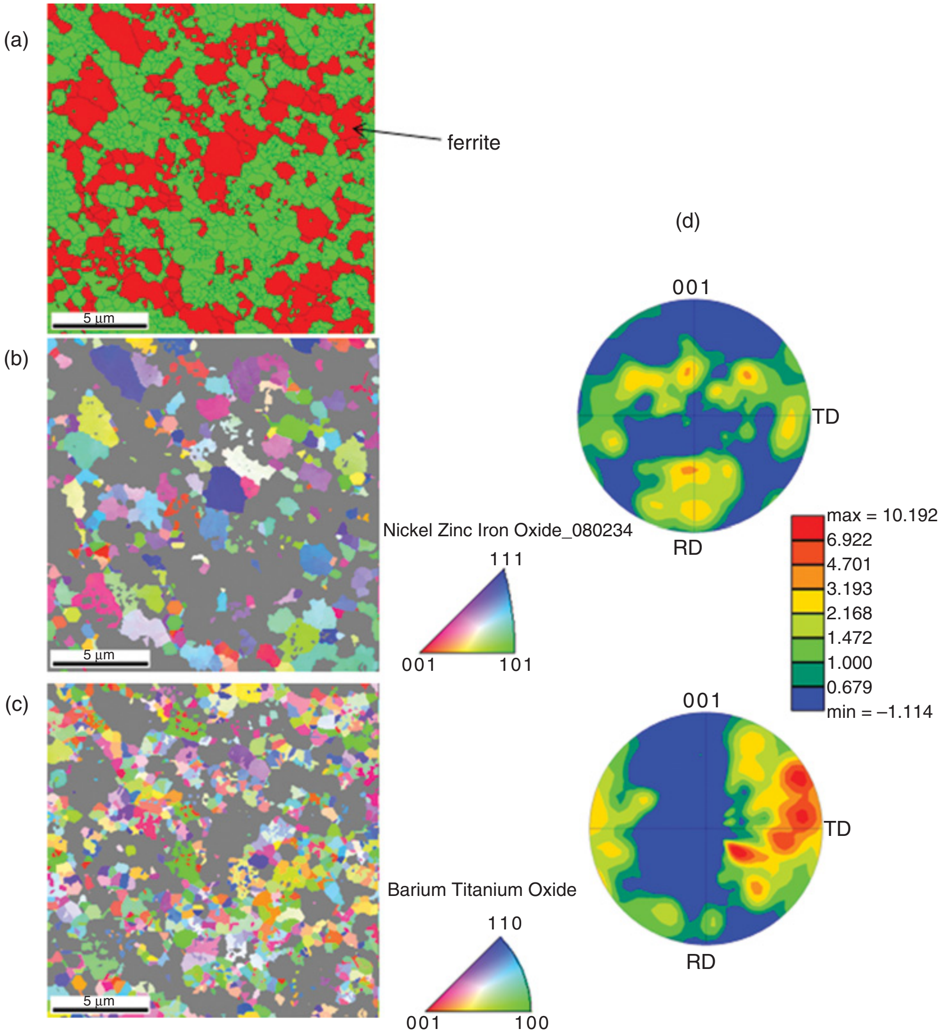

Figure 13.18 *EBSD analysis for sample A: (a) gives the phase map and (b) gives the inverse pole figure (IPF) map in the (0 0 1) direction for the ferrite only; all other information is plotted in gray. The color code for the orientation is given in the stereographic triangle. (c) The same analysis as for* $BaTiO_3$*. (d) The corresponding pole figures for NZF (left) and* $BaTiO_3$ *(right). Here, the recorded intensities are normalized with respect to the NZF data*

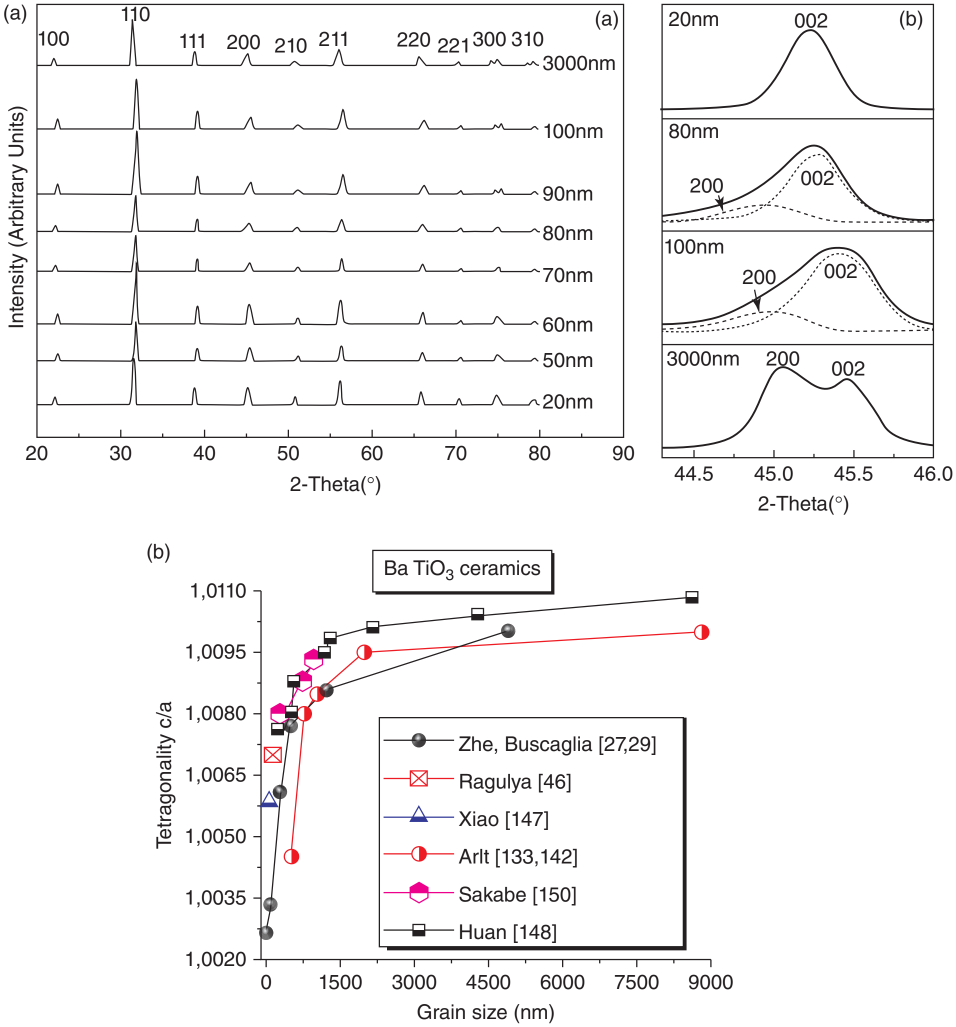

Figure 15.4 *(a) Diffraction profiles around $2\theta = 45°$ (200-002 splitting) for BaTiO$_3$ with various grain sizes (reprinted with permission from [47]. Copyright © [2006] [The American Ceramic Society]). (b) Tetragonal distortion c/a as a function of grain size (data collected from [45] to [47])*

Nanoscale Ferroelectrics and Multiferroics: Key Processing and Characterization Issues, and Nanoscale Effects,
First Edition. Edited by Miguel Algueró, J. Marty Gregg, and Liliana Mitoseriu.
© 2016 John Wiley & Sons, Ltd. Published 2016 by John Wiley & Sons, Ltd.

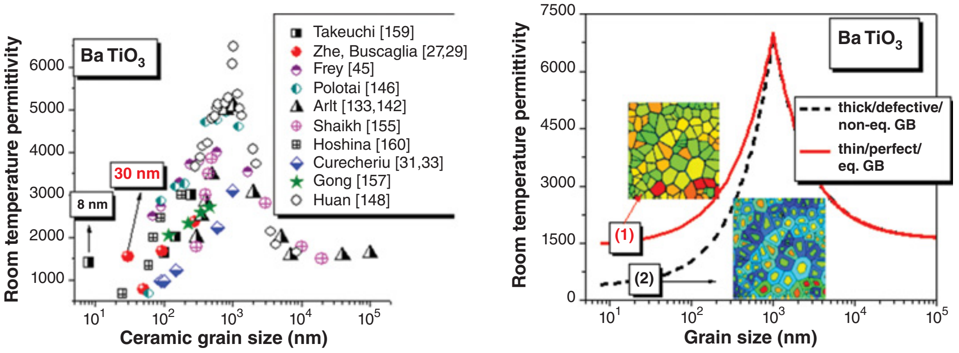

(a) (b)

Figure 15.6 (a) Grain size dependence of the room temperature permittivity reported to date for dense BaTiO$_3$ ceramics. (b) Schematic representation of permittivity versus grain size in relationship to the ceramic grain boundaries: (1) thin, perfect equilibrium ground boundaries, (2) thick, defective, non-equillibrium grain boundaries

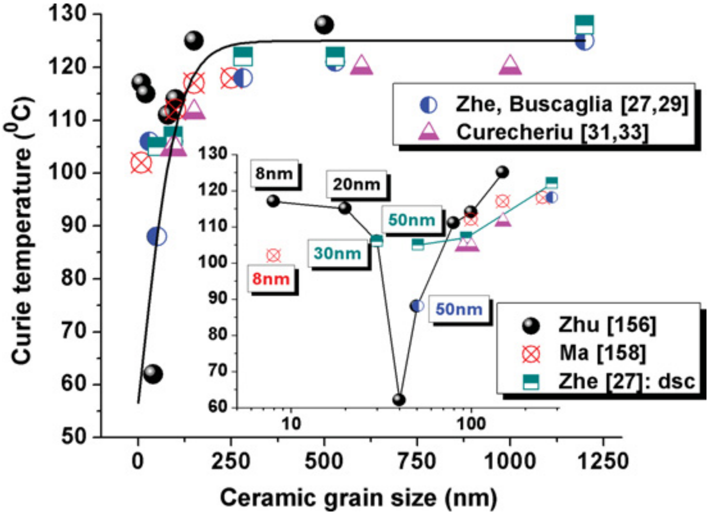

Figure 15.7 Curie temperature reported for dense BaTiO$_3$ ceramics (the line is a guide for the eyes). Inset: Curie temperatures for ceramics with grain sizes below 100 nm. All the represented Curie temperatures were determined by dielectric measurements, with the exception of data from [27], determined from differential scanning calorimetry (DSC)

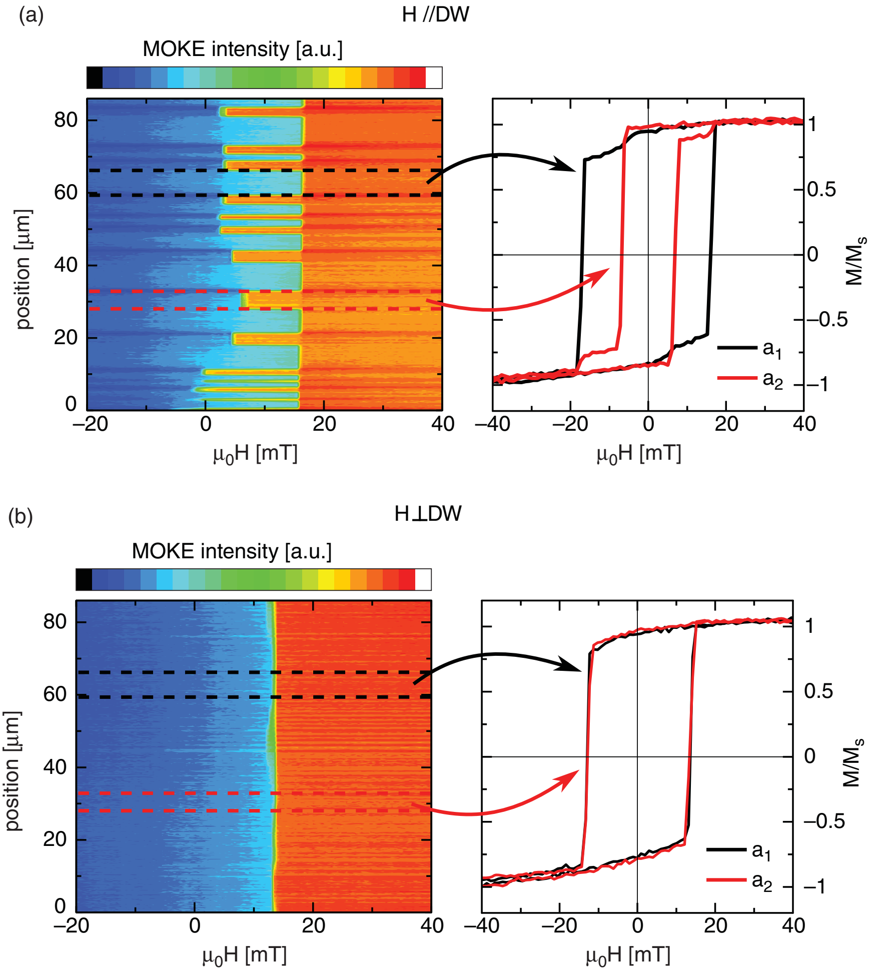

Figure 21.7 *Kerr microscopy data illustrating different magnetic switching behavior for an in-plane magnetic field parallel and perpendicular to the magnetic stripe domains of a 100 nm CoFeB film on top of* $BaTiO_3$*. The images illustrate switching in an area with about 25 stripe domains and the graphs show the corresponding hysteresis curves of an* a_1 *and* a_2 *domain*

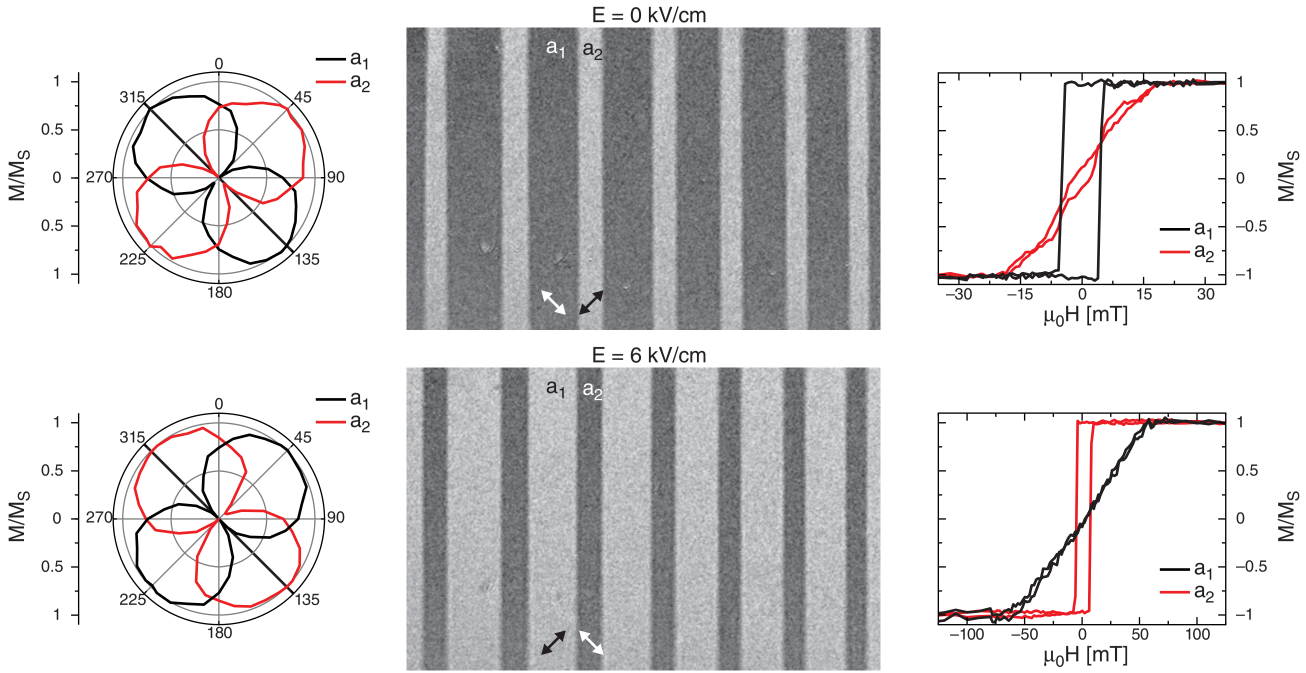

Figure 21.10 *Kerr microscopy image, normalized remanent magnetization (polar plot), and hysteresis curves on single a_1 and a_2 domains for a 50 nm CoFeB film on BaTiO$_3$ after growth on a_1–a_2 domains (top row) and after out-of-plane switching of the ferroelectric polarization in an electric field of 6 kV cm^{-1} (bottom row). Switching to a single c domain state in the BaTiO$_3$ substrate induces 90° rotations of the magnetoelastic anisotropy axes in the plane of the CoFeB film, as illustrated by the arrows in the images, rotation of the polar plots, and change from easy- to hard-axis hysteresis behavior on the original a_1 stripe domain (and vice versa for the a_2 domain). Because of symmetry, the overall magnetic stripe pattern is conserved*

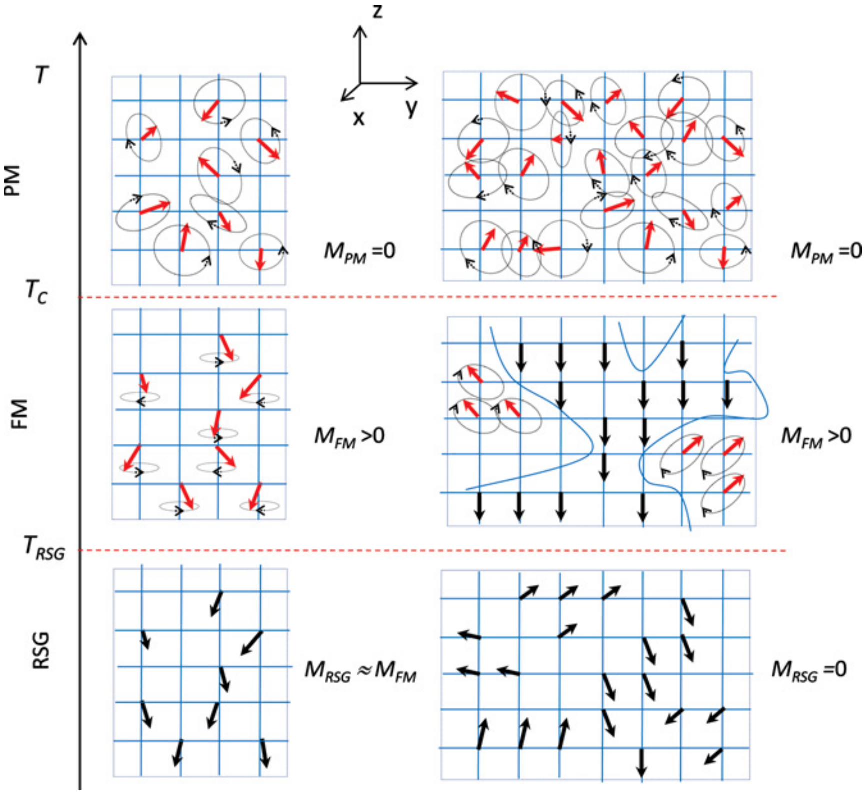
z
x
y
T
PM
M_{PM} =0
M_{PM} =0
T_C
FM
M_{FM} >0
M_{FM} >0
T_{RSG}
RSG
$M_{RSG} \approx M_{FM}$
M_{RSG} =0

Figure 23.3 *Schematic diagram of the models explaining the RSG behavior: transverse (xy) freezing model (left-hand column) and random-field model (right-hand column). The dynamic and frozen spins are shown by red and black thick arrows, respectively. Infinite FM cluster in the FM phase of the random-field model is outlined*

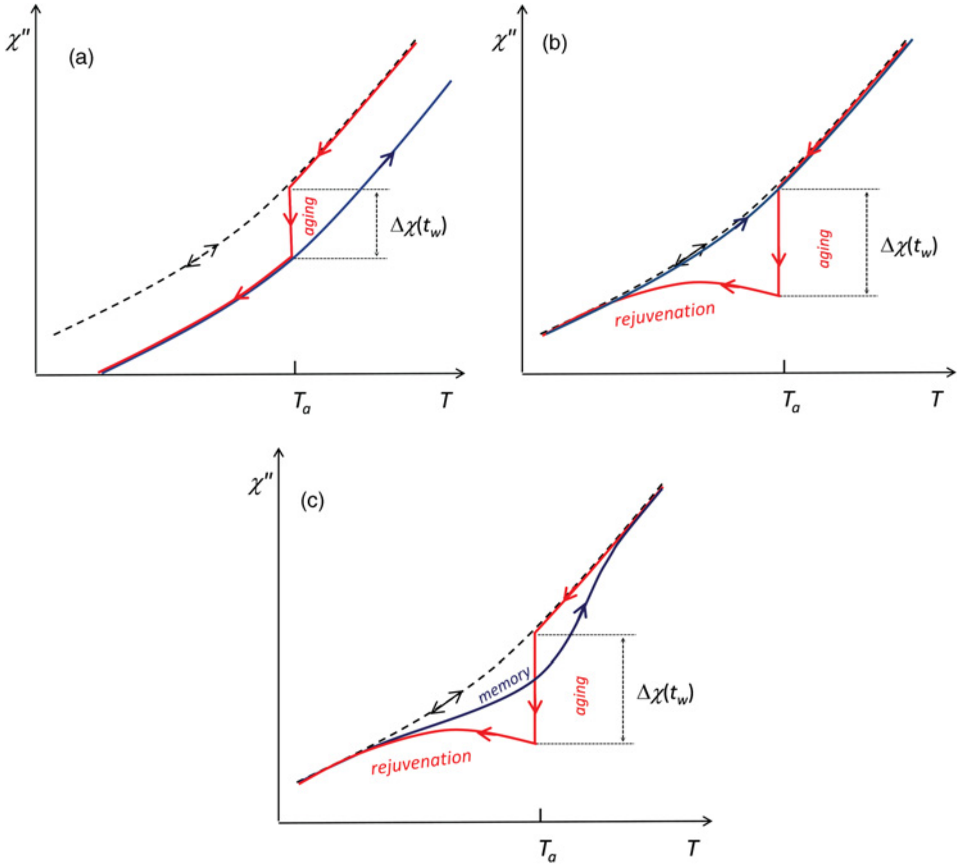

Figure 23.14 *Possible scenarios of aging behavior in ferroic systems: (a) cumulative aging, which can be observed in the FE phase of normal ferroelectrics; (b) aging with rejuvenation, which can be observed in the FM phase of disordered magnets and reentrant spin glasses, and in the FE phase of relaxor ferroelectrics; (c) aging with rejuvenation and memory, which can be observed in the SG phase, RSG phase, and NR phase. In the experiment, the susceptibility is continuously measured while the temperature first decreases, then stabilizes at the aging temperature, T_a, for a waiting time, t_w, then decreases again (red lines), and finally increases (blue line). The dashed line represents the behavior of the same sample if the temperature varies continuously (without aging)*

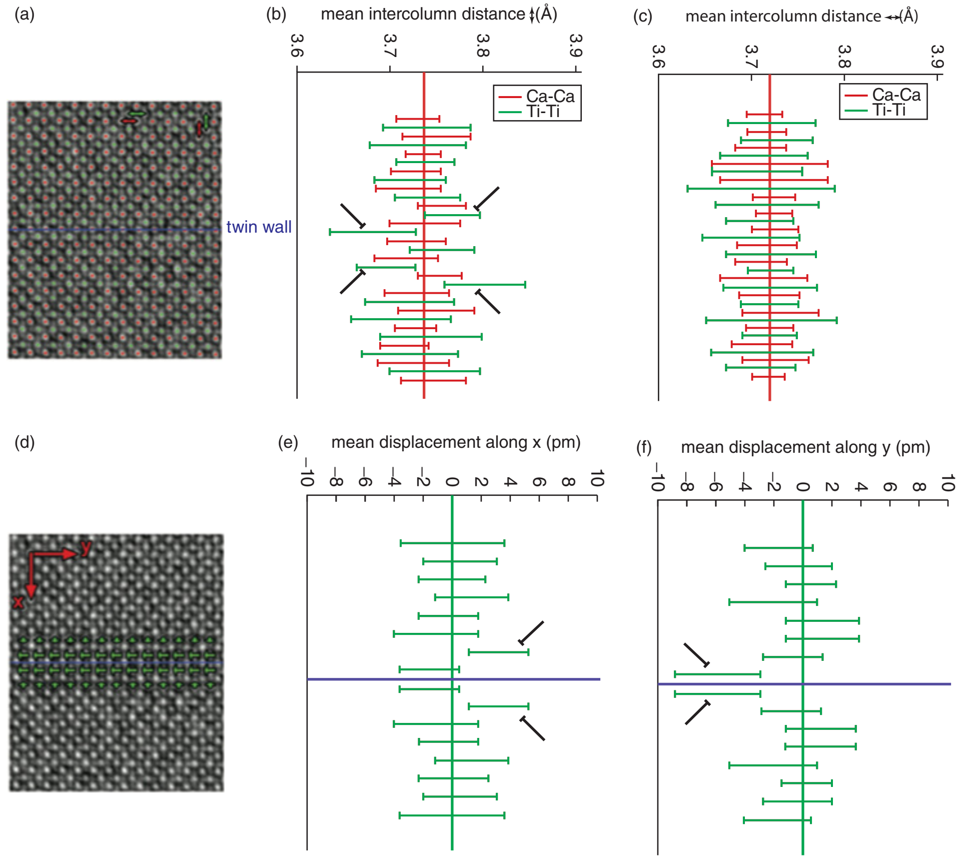

Figure 24.4 *(a) Estimated Ca and Ti atomic column positions shown in red and green, respectively. The horizontal line shows the position of the twin wall. (b) Mean interatomic Ca–Ca and Ti–Ti column distances perpendicular to the twin wall, averaged in the direction parallel with the twin wall, together with their 90% confidence intervals. The vertical line corresponds to the overall mean Ca–Ca interatomic distance. Note the deviations from this line for particular Ti–Ti atomic column distances close to the twin wall (arrows). (c) Mean interatomic Ca–Ca and Ti–Ti column distances parallel with the twin wall, averaged in the direction parallel with the twin wall, together with their 90% confidence intervals. The vertical line corresponds to the overall mean Ca–Ca interatomic distance. No deviations from this line are observed for the Ca–Ca or the Ti–Ti atomic column distances. (d) Mean displacements of the Ti atomic columns from the center of the four neighboring Ca atomic columns and indicated by green arrows. (e and f) Displacements of Ti atomic columns in the x and y directions averaged along and in mirror operation with respect to the twin wall together with their 90% confidence intervals. Reprinted with kind permission from [29], Copyright © 2012 Wiley-VCH Verlag GmbH & Co. KGaA, Weinheim*

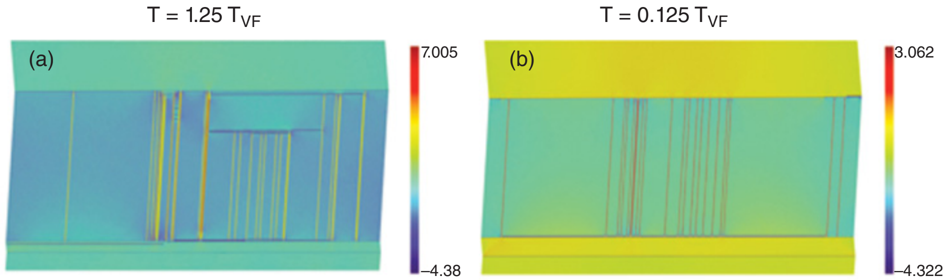

hard material with simple twin configuration

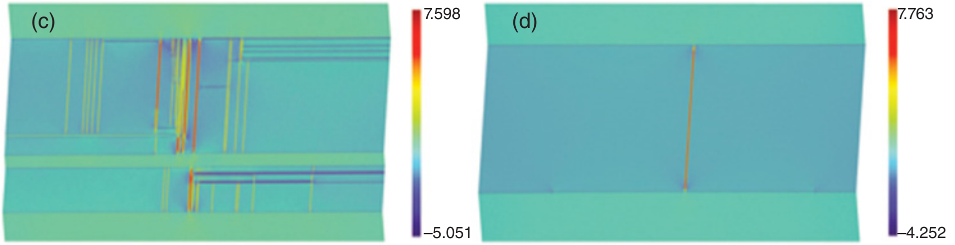

hard material with sandwich twin configuration

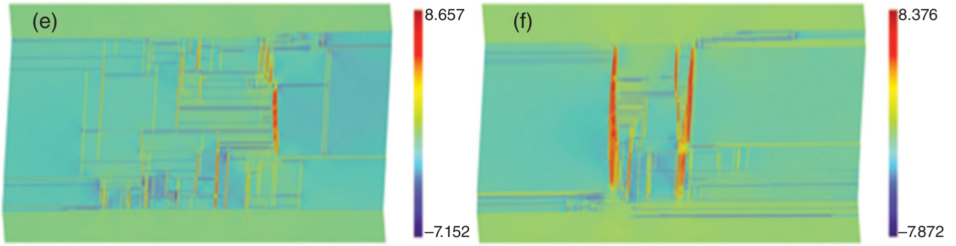

soft material with sandwich twin configuration

Figure 24.14 *Twin patterns at strains larger than the yield strain (in the plastic regime). Shown are domains formed at high temperature (a, c, and e) and low temperature (b, d, and f). Here (a) and (b) show hard materials with simple twin configuration; (c) and (d) show those for a hard material with a sandwich twin configuration, and (e) and (f) are for a soft material. Reprinted with permission from [22]. Copyright (2013) American Physical Society*

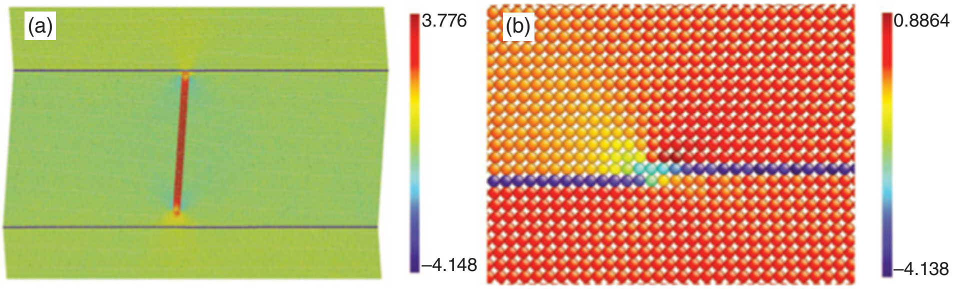

Figure 24.15 Sheared unit cell of a driven system. (a) The single needle domain (red) connects the two horizontal twin boundaries (blue) at the initial stage and then retracts from the lower twin boundary. (b) The kink is seen at the single blue domain wall. It moves to the left under applied external strain. Reprinted with kind permission from [74], Copyright © 2013 Wiley-VCH Verlag GmbH & Co. KGaA, Weinheim

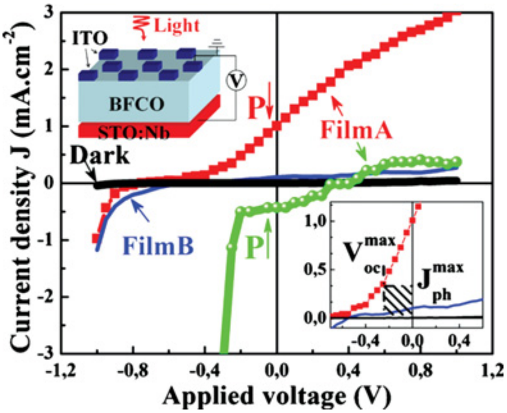

Figure 26.10 I(V) measurements of (001) Bi_2FeCrO_6 thin films in dark and under light (λ = 635 nm, 1.5 mW cm^{-2}) for different polarization directions. Film A was grown at 660 °C and film B at 610 °C. Reprinted with permission from [40]. Copyright [2011], AIP Publishing LLC